

International Conference on Water, Energy and Environment 2011

Promoting a global collaboration among faculty, students, engineers and managers on ecological economics and water, energy and environment resources management.

November 14–17, 2011

Auditorium, Main Building, AUS

Sponsored by:



PROCEEDINGS

The 2011 International Conference
on
Water, Energy and Environment
ICWEE

14-17 November, 2011
Sharjah
United Arab Emirates

Edited by

Nabil Abdel-Jabbar, Raafat Alnaizy and Taleb Ibrahim

College of Engineering
American University of Sharjah
United Arab Emirates

FOREWORD

Under the patronage of his highness Sheikh Dr. Sultan Bin Mohamed Al-Qassimi, Ruler of Sharjah and member of high UAE Rulers council, the American University of Sharjah (AUS), with cooperation of United Arab Emirates University (UAEU) organized “The 2011 International Conference on Water, Energy and Environment (ICWEE)”. The conference is sponsored by the Canadian International Association for Sharing Knowledge and Sustainability (IASKS), Arab Academy of Science (AAS), and Islamic Education, Scientific and Cultural Organization (ISESCO), ADNOC, Bee'ah, Dow Chemical, Huber Technology and Metito. The objective of the ICWEE conference is to promote a global collaboration among faculty, students, engineers, managers on ecological economics, and water, energy, and environment resources management.

The papers appearing in this book contribute significantly to the progress of issues related to water regulation and policies, water resources and sustainable development of the region, water protection and remediation, desalination, wastewater treatment, energy, environmental impact, economic management and development of water resources, environment, and other water related topics.

We thank all the authors and delegates who contributed to the success of ICWEE2011 by sharing their work and knowledge with their colleagues. Our special thanks go to the keynote speakers, session chairpersons, International Advisory Board and all other committee members for their contribution and effort.

Raafat Alnaizy
Taleb Ibrahim
Yousef Alhayek

Sharjah
November 2011

Acknowledgments

The organizing committee acknowledges the support of the Dean of College of Engineering, Dr. Yousef Al Assaf at the American University of Sharjah.

The committee would like to sincerely thank the co-sponsor companies: ADNOC, Bee'ah, Dow Chemical, Metito and Huber.

The committee expresses our sincere thanks to the following AUS offices for their various support activities including, Office of Development & Alumni Affairs, Office of Strategic Communication and Media, and the Office of Public Affairs.

The committee would like to thank our students who assisted in the preparation, especially Yousef Chehade and Saeed Nusri.



METITO



HUBER
TECHNOLOGY
WASTE WATER Solutions

Conference Chairs

Raafat Alnaizy
Taleb Ibrahim
Yousef Haik

Steering Committee

Raafat Alnaizy
Taleb Ibrahim
Yousef Haik
Hans G. Huber
Ibrahim Abu-Reesh
Antonio Baptista
Yung-Tse Hung

Organizing Committee

Yousef Al Assaf
Nabil Abdel-Jabbar
Ahmed Aidan
Mohamed Gadalla
Maruf Mortula
Sofian Kanan
Adnan Badran
Bilal Akash
Elias Baydoun
Fariq Billa
Darwish Gobaisi
John Hillman
Mousa Mohsen
Reyad Sawafta
Ibrahim Kocabas
Mohamed Abouleish
Serter Atabay
Kazi Parvez Fattah
Salwa Mohamed

Web & IT

Khalil Darwish

International Advisory

Board

Mark Holtzapple, USA
Mahmoud El-Halwagi, USA
Ibrahim Dincer, Canada
Clayton Maugans, USA
Karl Rudolph, Germany
Stefania Paris, Germany
Nidal Hilal, UK
L. Rizutti, Italy
V. Nenov, Bulgaria
Tim fuhrmann, Germany
Hisham Ettouney, Kuwait
I. Al-Mutaz, Saudi Arabia
Nabil Fayad, Saudi Arabia
Rodger Macfarlane, UAE
Tamer Gadallah, UAE
Youssef Mouneimne,
Lebanon
Ramdhane Dhib, Canada
Mehrvar Mehrvar, Canada
Fawzi Banat, Jordan
Mousa Abu Orabi, Jordan
S. Al-Sulaiman, Oman
K. Bourouni, Tunisia
Maazuza Othman, Australia
Joonkyu Kim, Korea
Sergio Mussati, Argentina
Tamer Shahin, UAE
Basem Yousef, UAE

Symposium Secretariat

Aileen Yulay

Technical Committee

Nabil Abdel-Jabbar (Co-Chair)
Mohamed Gadalla (Co-Chair)
Serter Atabay (Co-Chair)
Ahmed Aidan
(Tutorial, Exhibition Chair)
Kazi Parvez Fattah
(Poster Session Chair)
Maruf Mortula
Abdallah Shanableh
Naif Darwish
Dana Abouelnasr
Mohamed Ibn Kahla
Zarook Shareefdeen
Sameer Al-Asheh
Hasan A. Hasan
Hassan Arafat
Farouq Mjalli
Jamil Nasser
Bassam Tawabini
Khawla Al-Shayji
Kevin Loughlin
Ibrahim Kocabas
Isaac Wait
Basel Alsayed
Salah Al-Omari
Ali Al Naqbi
Emad Elnajjar
Samir Emam
Mohammad Hamdan
Saud Khashan
Mohamed Younes Selim
Tamer Shahin
Basem Yousef

Table of Contents

Paper #	Page #
1. Stressed Marine Environment - Physico-chemical Evidences from Sulaibikhat Bay, Kuwait	10
2. Impact of Barrages on Water Quality of Rivers Upstream and on Air Entrained in the Hydraulic Jump Downstream	17
3. The Use of GIS and Remote Sensing for Quantitative Evaluation of Water Soil Erosion, Case Study in the West of Algeria	23
4. Optimum Operation of Canal Barrages	27
5. Development of Biochemical Acidogenic Potential Test for Evaluating WAS Digestibility	32
6. Effect of Simplifying the Water Supply Pipe Networks on Water Quality Simulation.....	41
7. Vanadium Recovery from Synthetic Wastewater by Adsorption onto Chitosan.....	47
8. Fabrication of Polymeric Hollow Fiber Membrane for the Production of Safe Drinking Water	51
9. The Effect of Chemical Application and Excessive Extraction of Water Resources on Groundwater Quality and Environment in Saudi Arabia	57
10. Model-Free Control of pH in the Neutralization of Alkaline Waste Water using CO ₂ Gas	64
11. Long Term Water Demand Forecast for the City of Riyadh, Saudi Arabia	68
12. Changing Produced Water from Waste Stream to a Useful Asset in Sudan Oil Fields	73
13. Enzymatic Production of Biodiesel from Waste Cooking Oil	79
14. Prototype Decontamination of Water by Ozone	85
15. Bioelectrochemical Single Chamber Reactor: Enrichment of Autotrophic Perchlorate Reduction for Water Treatment.....	90
16. Removal of Heavy Metals from Aqueous Solution by Poly (Acrylamide-co-Acrylic acid) /Porous Materials .	95
17. Air Pollution by Fine Particles (PM-10, PM-2.5 and PM-1) Size Distribution and Associated Trace Metals Evaluation in the Great Area of Algiers	101
18. Study of Moisture and Leachate Solute Movement during Infiltration Tests.....	106
19. Influence of Hydraulic Gradient and Confining Stress on the Hydraulic Conductivity of Sealing Barriers Materials.....	112
20. Water Resources for Sustainable Development in the Developing Countries.....	117
21. Kinetic, Equilibrium and Thermodynamic Studies for Adsorption of Cadmium (II) Using Modified Agricultural Wastes	123
22. Investigation of Water Quality in Kocasu Creek, Turkey	130
23. Rheological Behavior of RBC Sludge at Different Steps of Treatment	137
24. A Wireless Sensor Network for Water Pipeline Leak Detection.....	143
25. Corrosion and Scale Formation Problems in Water Systems	148
26. Analytical and Numerical Modeling of 2-D Solute Transport in a Fracture/Matrix Aquifer System	154
27. Modeling Sensible Energy Storage in Aquifers	160
28. A Novel Analytical Model of Heat Extraction from Geothermal Reservoirs.....	165

29. A Novel Two Dimensional Analytical Model of Contaminant Transport in Groundwater Aquifers.....	171
30. Integration of Wastewater in the Water Resources of Egypt:.....	179
31. Removal of Phosphorus and BOD from Secondary Effluent using Coagulation	185
32. Copper Removal via Adsorption	188
33. Simplification of a Nonlinear Fuel Cell Model and its System Analysis and Control	195
34. Study on Heavy Metal Resistant Bacteria Isolated From Wastewater	200
35. Adsorption of Two Dyes Water Textiles by Two Biosorbents	207
36. Modification of Magadiite by Organofunctionalization for Use in Removing Pb(II) From Aqueous Media...	211
37. Modelling Groundwater Flow in the Agricultural Area of Ghriiss Plain	217
38. Investigating Geotourism Capabilities of the Gavkhoni Wetland According to the FAS model	221
39. Optimization of Influential Parameter to Biodegrade the Phenol in Batch by Microbial Consortium	228
40. The Impact of Wind Farms on the Stability of Electric Networks	233
41. New Public Management Reforms and Efficiency in Urban Water Service Delivery in Emerging Economies: Blessing or Curse?	237
42. Effects of Skewed Bridge Crossing on Afflux	243
43. Assessment of Runoff Potential for Water Harvesting in Central Butana Rangeland, Sudan.....	249
44. Effect of Alum Addition on the Treatment Efficiency of Cloth-Media Membrane Bioreactor.....	256
45. The Use of Water Treatment Residuals in the Treatment of Textile Industry Wastewater	259
46. Nanofiltration Pretreatment of Desalination Seawater Feed for CO ₂ Release Reduction in MSF Distillers....	263
47. Design Flow Factors for Sewerage Systems in Small Arid Communities	266
48. Hydro-meteorological Impacts of Climate Change in the Middle East: A Review.....	273
49. Decentralized Sewage Reuse for Irrigation Purposes.....	279
50. UV Disinfection of Only Partially Pre-clarified Wastewater for Irrigation Purposes.....	286
51. Copper Cementation on Iron Using Copper Sulphate Solution with Different Organic Solvents	291
52. Conversion and Liquification of Petrochemical Sludge (Biological and Chemical) using Subcritical Water Technology.....	296
53. Plasma Assisted Decomposition of Gaseous Hydrocarbons to Produce CO _x Free Hydrogen.....	301
54. Colloid Particles Deposition in Porous Media: Role of Hydrodynamic and Electrolyte Concentration	307
55. A comparative Life Cycle Assessment (LCA) of Using Virgin Crushed Aggregate (VCA) and Recycled Waste Concrete Aggregate (RCA) in Road Construction	312
56. Enhancing the Remediation Efficiency of Photo-Fenton Reaction by Oxygen and Humic Substances.....	317
57. The Role of the Dynamic Process of Aeration on the Evolution of Dissolved Oxygen and Phosphorus in Water Supplies	323
58. Field Experiment and Numerical Simulation of Point Source Irrigation in Sandy Soil with Multiple Tracers	327
59. Threats to Groundwater Resources due to Uncontrolled Land filling in Jordan: A Review with Some Remedial Measures Recommendations	335

60. Water Scarcity and Solar Desalination Systems in the Eastern Mediterranean Region: A Case of Northern Cyprus	341
61. Study on Amorphous Ag-Doped Manganese Dioxide Electrodes for Electrochemical Supercapacitors Applications	350
62. Effect of Deposition Current on the Capacitive Behavior of Manganese Dioxide/Stainless Steel electrodes..	356
63. Synthesis of Polymethylmethacrylate	361
64. Induced Transboundary Waterborne Emission Savings as Result of National Environmental Policies: the Case of the Danish Packaging Taxation Policy.....	365
65. The Impact of Wind Farms on the Stability of Electric Networks	369
66. A Comparative Study of Vapour Compression Refrigeration Systems under Air to Air and Air to Water Mode	373
67. Energetic and Exergetic Comparison of Water-Water and Water-Air Heat Pumps	379
68. A Simulation Study on Determining the Position and Orientation of a Classic Rectangle-Lengthwise Type Greenhouse System to Have More Benefit from Solar Radiation	386
69. Evaluation of Different Substrate Material of Constructed Wetlands for Bioremediation of Household Sewage	392
70. Mitigating the Impacts of Animal Production on Surface Water Quality in Grassland Ecosystem: Techniques and Measures.....	401
71. Energy Efficiency in Spanish Wastewater Treatment Plants: The Role of the Internal and External Factors ..	406
72. Vortex Ring Buoyant Plume on Porous Body in Thermal Non-Equilibrium	412
73. Study on Amorphous Ag-Doped Manganese Dioxide Electrodes for Electrochemical Supercapacitors Applications	418
74. Adsorption of Dye Pollutants on Hydrothermally Synthesized Mesoporous Copper Phosphate Materials	424
75. Nonlinear Modeling of River Flow	428
76. The Impacts of Wastewaters Discharges on the Quality of Littoral Case of the Coastal Region <i>Ain Temouchent</i> (West Algeria).....	434
77. Treatment of Oilfield Produced Water through NF/RO Membranes: Generating a Sustainable Drinking Water Resource by Reusing a Pollution Source.....	442
78. An Integrated Neural Network-Fuzzy Mathematical Programming for Optimum Long-Term Electricity Price Forecasting in Noisy and Complex Environments	447
79. An Intelligent Approach for Improvement of Short Term Water Consumption Forecasting in a Large and Complex Metropolitan City.....	454
80. A Greedy Randomized Adaptive Search Procedure-Genetic Algorithm for Electricity Consumption Estimation and Optimization in Agriculture Sector.....	460
81. Application of Principal Component Analysis to the Study of Trace Metals in Sediment from Sulaibikhat Bay, Kuwait	466
82. Concentrations of natural and manmade radioactive nuclides for Wadi Al-Numan area in Makkah Al-Mukarramah Province	472

83. Effect of the Type of Water on Leaching of Aluminum Utensils During Food Preparation	482
84. Steady State System Analysis of a Bilinear Fuel Cell Model for Electricity, Heat, and Water Production	488
85. Reduced-Order Observer and Optimal Controller Designs for the Air Flow of a Linearized Model of a 75kW PEM Fuel Cell for Electric Cars.....	492
86. The Effects of Climate Change: How Can Algeria Deal With It	496
87. Simulation of Blue Nile River Using a Distributed Hydrological Model and Global Data Set	500
88. Experimental Testing of the Water Saving Potential of Different Faucet Aerators and their Performance over Time	508
89. The First Water Quality Model From the Arabian Gulf and a New Endogenous Development Capacity in the Region	515
90. Anoxic Water Simulations and Vertical Sub-Meshing to Depict Strong Gradients	529
91. Steady-State Quartz Formation in terms of Water Migration through Nanopores	541
92. On the Control Requirements of Heaving Wave Energy Converters	546
93. Adsorption of Cobalt Ions Onto Immobilized and Non-Immobilized Jordanian Low Grade Phosphate	552
94. Sorption Capacity of Poly-tetra-fluoro-ethylene Sorbent for the Remediation of Oil Polluted Water	559
95. Paper or Plastic? Clearing Misconceptions on Environmental Impacts of Coffee Cups Using Life Cycle Assessment (LCA)	563
96. Modeling Thermal Degradation in Geothermal Reservoirs Due to Reinjection.....	570
97. Africa Energization: Alternative Energy Capacity Building Strategies and Policies	579
98. Concentrations of Natural and Man-Made Radioactivity Soil and Ground Water in Al-Madinah Al-Monawarah	588
99. Analysis of the Water Evaporation and Drift Losses during Irrigation in Semiarid Areas	595

Stressed Marine Environment - Physico-chemical Evidences from Sulaibikhat Bay, Kuwait

Hassan. Alshemmari^{1,2}, Alkhabbaz. Ahmad¹, Saif Uddin¹

¹ Environmental Science Department, Kuwait Institute for Scientific Research, P.O. Box 24885, Kuwait Safat 13109. Email: alkhabbaz@safat.kisr.edu.kw, sdin@kisr.edu.kw

² School of Civil Engineering and Geosciences, Drummond Building, The University of Newcastle upon Tyne, Newcastle upon Tyne, NE1 7RU. Email: hshamari@safat.kisr.edu.kw

ABSTRACT

The Northern Arabian Gulf shows signs of physico-chemical stresses in form of changing water, sediment and biological characteristics. The region in general and Kuwait in particular is affected by these changes, an example is presented from Sulaibikhat Bay. This study investigated the parameters including water depth, temperature, dissolved oxygen content, pH, oxidation–reduction potential (ORP), specific conductivity, salinity and turbidity in the study area. The area is impacted by thermal stress due to presence of desalination plant outfall. Local differences of temperature and salinity (1.2°C and 5.92 mg l⁻¹) were observed within the area. This study recorded the lowest level of DO (5.92 mg l⁻¹) during December, in the southeast of the study area, adjacent to the Ghazali sewage outfall, low ORP values (48.0–188 mV) were also recorded in the southeast of Sulaibikhat Bay, that might be associated with the presence of hydrogen sulphide and pyrite in the bottom sediments, suggesting reducing conditions because of sulphate reduction associated with the decomposition of organic matter. It is observed from this study that tidal flats play a very critical role in maintaining the water quality, acting as filter for effluents. The sediments in the area act as repository of pollutants. There are apparent temporal changes in the biological activity, with absence of fishes, bivalves, crabs in from the area. A low density mud skipper population is only surviving in the area.

Keywords: Sulaibikhat Bay, Kuwait, sewage, desalination plant, salinity

1. INTRODUCTION

The shoreline of Kuwait is having a characteristic embayment 'Kuwait Bay'. The southern shoreline of Kuwait Bay is heavily inhabited, mainly constituting the urban center. The Kuwait bay is characterized by shallow depths, soft sediments, slow tidal currents, and high turbidity (Dames & Moore 1983; Khalaf *et al.* 1981). The deeper portion in Kuwait bay is the trough, which characterizes the navigational channel leading to the Shuwaikh port. The average depth of Kuwait bay water is about 10 m (Dames & Moore 1983; Khalaf *et al.* 1981; Khalaf *et al.* 1982). There are various inlets of stormwater drains, emergency sewage outfalls and other discharges that open into Kuwait Bay, stressing the environmental.

The current study is carried out in southern portion of Kuwait Bay termed as Sulibikhat bay. This is the shallowest water body within the Kuwait Bay system, occupying vast tidal flats upto 4 km wide. The area is having several outfalls; power and desalination plant, hospital and waste water discharge point. Samples were collected from the area to identify changes in ambient concentration of key physico-chemical parameters, that can identify if the environmental stress.

2. STUDY AREA

Sulaibikhat Bay is a small and secured embayment located to the southern part of Kuwait Bay. It is situated between latitude 29° 19.115 and 29 23.198 and longitude 47° 49.023 and 47 55.015 respectively,

covering an area of 45 km². Sulaibikhat Bay, (Figure 1) has undergone considerable development over the years. There is a main cargo port to the east of Sulaibikhat Bay. There are five major recreational and other developments along Sulaibikhat Bay coastline: Entertainment City, Sulaibikhat Sport Club, the Hospital Complex, Kuwait University (KU) and Kuwait Institute for Scientific Research (KISR).

The major environments in Sulaibikhat Bay are tidal channels, rocky flats, mud flats and the shoreline and back-shore area (Khalaf *et al.* 1981; Dames & Moore 1983). The shoreline of Sulaibikhat Bay is generally flat beach formed by the action of back eddies entering the bay from the north (Dames & Moore 1983; Khalaf *et al.* 1981). Landward of the shoreline and towards the west (around Entertainment City) and southwest (near the Sulaibikhat Sports Club), the area is coastal *sabkha* which exists as a continuous inland extension of the intertidal zone. The *sabkha* deposits are generally composed of sand and mud sediments (Khalaf *et al.* 1981).

3. MATERIAL AND METHODS

Temperature, pH, salinity, turbidity, dissolved oxygen, and conductivity were measured in the water column (measurements taken at 0.5 m depth below the surface or just below the surface for shallow depth less than 0.5 m) at each sediment sampling location using a Hydrolab Quanta Water Quality Monitoring System (www.hydrolab.com). This was calibrated, prior to use, using procedures described in the operation manual.

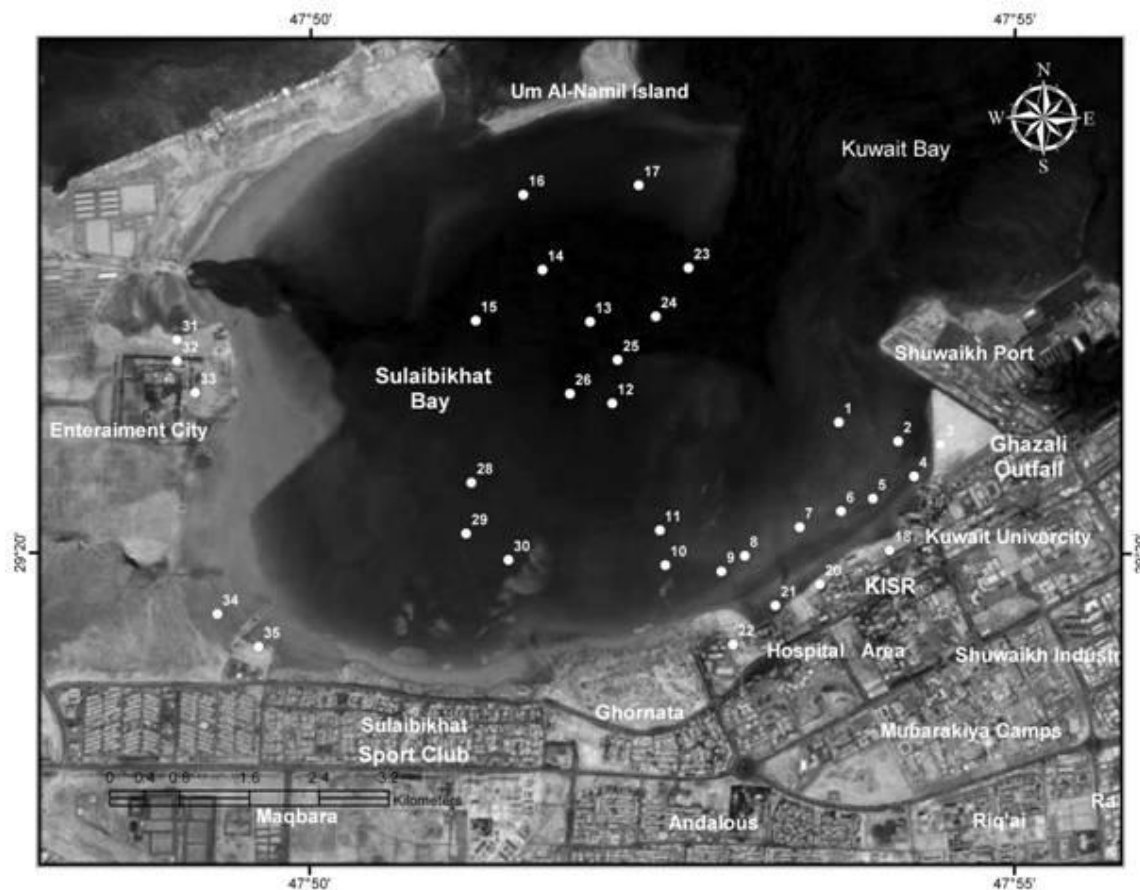


Figure 1: Location of sampling site in the Sulaibikhat Bay.

4. RESULTS

The storm water outfalls are known to add significant quantities of sewage derived from discharges into the storm water network from light industries, or domestic and emergency discharges into the network from overloaded or faulty sewage pumping stations serving the wastewater network in the country (Al-Ghadban *et al.* 2002). The area in front of the Ghazali outfall to the southwest of Shuwaikh Port is occupied by anoxic soft sediments, with anoxic conditions also frequently observed in the shallow overlying water column (Al-Sarawi *et al.* 2002b; KISR 2003). The intertidal environment could have also received significant trace element pollution resulting from abandoned ships and sunken boats in the Shuwaikh Port area.

There are many obvious sources of pollution in the study area (Figure 1), including the Doha West's power and desalination plant, storm water outfalls and the Ghazali sewage discharge. Each of these sources is known to contribute pollutants to the surrounding marine environment (KISR 1999). Petrochemical industries in the Shuwaikh industrial area are also a source of pollution (KISR 1984). These sources are heavily loaded with nutrients and sanitary wastes (Figure 1) (KISR 1999). The power and desalination plants at Doha West discharge large quantities of seawater which is warmer than the sea water. This can

be toxic to marine species. The power plants generate a water discharge 5°C above the ambient water temperature (Al-Ghadban *et al.* 2002; Saeed *et al.* 1999). In summer, when the ambient seawater temperature is 30° to 35°C, the temperature of the seawater discharged by the power and desalination plants at Doha exceeds 40°C, which is stressful to most marine species and has resulted in the loss of temperature-sensitive species (Dames and Moore, 1983).

Water Depth: The deepest water is 5.5 m in the centre of the Bay (Table 1). Previous studies suggest that Sulaibikhat Bay has a central channel, which is ~3 km long, 0.5 km wide and 10.5 m deep (Khalaf *et al.*, 1988, KISR, 2003).

Water Temperature: Figure 2, illustrates measured water temperatures. The temperature in Sulibikhat bay is affected by effluent discharge. The highest temperature (17.7°C) was observed near an effluent discharge from the Doha power plants at the northwest of the Bay, and temperatures gradually decrease towards the southeast coast. The temperature gradient observed reflects the thermal discharge from power plants in the northwest. Seawater used for cooling the power plants is discharged to the sea in the northwest of Sulaibikhat Bay and this is the likely cause of the increase in temperature of the coastal water in this area (Al-Bakri and Kittaneh, 1998).

Table 1: Water column characteristics of Sulaibikhat Bay

Station	Sampling Date	Water Depth (m)	Water Temp (°C)	DO (mg l ⁻¹)	pH	ORP (mV)	Specific Conductivity (mS cm ⁻¹)	Salinity (PSS)	Turbidity (NTU)
SS01	04/12/03	1.22	16.8	5.90	8.57	184	65.6	43.8	16.9
SS02	04/12/03	0.61	16.8	4.01	8.51	160	63.5	42.2	20.1
SS03	04/12/03	0.30	16.9	4.00	8.42	78	62.8	41.6	40.0
SS04	04/12/03	0.30	17.2	5.50	8.55	48	59.3	39.9	14.9
SS05	04/12/03	0.61	17.2	5.83	8.55	82	58.8	38.8	20.1
SS06	04/12/03	0.61	17.2	4.50	8.51	91	45.1	38.6	30.1
SS07	04/12/03	0.61	17.4	4.14	8.25	101	50.4	32.6	35.5
SS08	04/12/03	0.61	16.9	5.51	8.34	109	48.8	31.6	31.8
SS09	04/12/03	0.61	16.8	5.80	8.47	115	50.0	33.0	65.2
SS10	04/12/03	0.61	16.5	6.13	8.66	118	53.2	34.7	45.8
SS11	04/12/03	1.22	17.0	9.34	8.67	127	59.4	39.2	37.2
SS12	04/12/03	1.83	17.2	6.61	8.54	126	64.7	42.8	30.7
SS13	04/12/03	5.49	17.0	6.81	8.42	120	64.8	44.1	9.80
SS14	04/12/03	4.57	17.2	7.76	8.40	124	65.8	43.7	9.20
SS15	04/12/03	2.74	17.7	9.10	8.50	134	66.5	44.5	22.4
SS16	04/12/03	2.26	17.5	7.92	8.48	129	66.5	44.4	42.5
SS17	04/12/03	2.44	17.5	9.14	8.47	135	66.5	44.6	32.5
SS23	11/12/03	0.37	17.1	8.36	8.79	188	64.1	41.2	34.8
SS24	11/12/03	0.37	17.3	8.31	8.79	175	63.3	43.5	40.4
SS25	11/12/03	0.27	17.4	8.77	8.73	170	65.1	44.3	44.2
SS26	11/12/03	0.21	17.7	8.47	8.72	171	65.7	45.3	42.5
SS27	11/12/03	0.12	17.5	9.53	8.80	175	67.2	45.1	75.3
SS28	11/12/03	0.09	17.4	9.90	8.75	165	67.0	44.9	68.1
SS29	11/12/03	0.24	17.2	9.92	8.72	161	65.6	43.6	73.5
SS30	11/12/03	0.12	17.3	9.82	8.72	166	65.8	44.0	67.2
Average		1.14	17.2	7.24	8.57	134	61.4	41.3	38.0
STDEV		1.40	0.30	2.00	0.15	36.9	6.60	4.21	19.4
Max		5.49	17.7	9.92	8.80	188	67.2	45.3	75.3
Min		0.09	16.5	4.00	8.25	48.0	45.1	31.6	9.20

SS01: Surface Sediment and sample number. There are no data for SS18–SS22 from the upper tidal flat.

Dissolved oxygen: (DO) concentrations, Figure 2, show some similarity to temperature variations. The lowest concentrations (4.0 mg l⁻¹) are found in the southeast adjacent to the sewage discharge from the Ghazali outfall (Table 1). Reduced dissolved oxygen concentrations in the southeast likely reflect the high oxygen demand of effluents discharged at the Ghazali outfall. Waste water discharges can have high contents of organic matter, which can lead to shortages of dissolved oxygen (DO) as a result of its consumption by the microorganisms decomposing organic matter (Burdige, 1993). In the case of reduced oxygen concentrations, anaerobic conditions can occur, particularly close to the sediment–water interface. If this happens, a series of secondary oxidants are utilized by microorganisms to degrade organic matter (Calvert and Pedersen, 1993; Alagarsamy, 1997). If sulphate reduction is established, then sulphides will be produced as organic matter is mineralised. The distinctive smell of hydrogen sulphide was noted during sample collection close to the Ghazali outfall; this supports an inter-

pretation of probable reducing conditions in the southeast of the Bay.

Hydrogen Ion Concentration (pH): is the most commonly measured chemical parameter in seawater because it influences many biological and chemical processes. It is necessary to have pH data to understand the speciation of trace elements in seawater (Covington and Whitfield, 1988). The pH of the Sulaibikhat Bay seawater ranged between 8.3 and 8.8 with a mean of 8.6. Values of pH appeared to be more alkaline in the centre of the Bay, with lower values measured in the northwest and southeast.

Oxidation–reduction potential (ORP): is known as redox potential, is measured in millivolts (mV). It is an indication of the equilibrium status of pairs of oxidized and reduced species. Oxygen, iron and sulphur are the most influential substances in determining ORP in many natural environments (UNESCO/WHO/UNEP, 1996). As seen in Figure 2, ORP is highest in the northeast of the Bay and lowest in the southeast, and nearest to the

Ghazali outfall where untreated sewage is discharged. ORP values decrease when dissolved oxygen concentration decrease. Lower ORP values in the southeast are further evidence of reducing conditions in this area.

Specific conductivity: is a measure of the ability of water to conduct electricity. The conductivity of water is highly dependent on its concentration of dissolved salts (i.e. the total dissolved solids or salinity). The conductivity data illustrated in Figure 2 show that the highest concentrations are observed in the west, near the discharge of effluent from the Doha power plant, and in the northwest. The high salt contents in the northwest bear witness to the discharges from the Doha power

plant, which contain concentrated brine. The lowest concentrations are in the southeast and in front of Kuwait University, where storm water and sewage are discharged.

Salinity: is the dissolved salt content of a body of water (UNESCO, 1981). The stations with the highest and lowest recorded salinities (Figure 2) correspond approximately to those showing highest and lowest specific conductivities (Figure 2). The highest salinities observed are in the west and northwest, adjacent to the effluent discharge from the Doha power plant. Salinity then decreases to the southeast towards the storm water and sewage outfalls.

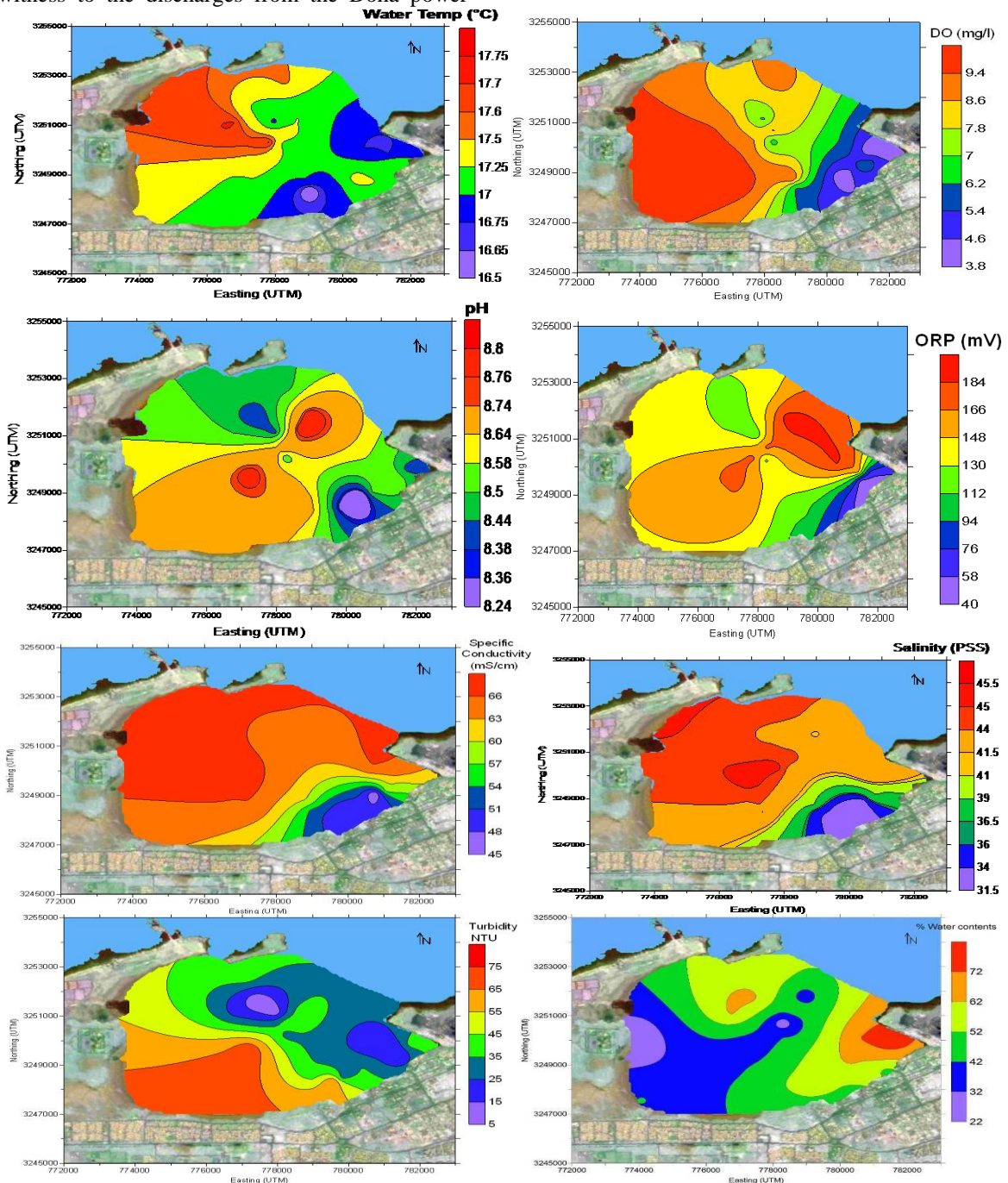


Figure 2: Map distribution of water column characteristics of the study area

Turbidity: reflects the amount of particulate matter that is suspended in seawater. As seen in Figure 2, turbidity is highest in the southwest of the Bay between Entertainment City and the Sulaibikhat Sports Club. Turbidity decreases gradually towards Kuwait Bay, with the lowest turbidities recorded in the deepest parts of Sulaibikhat Bay. Al-Ghadban (2004) observed highly turbid water in the far western part of the Kuwait Bay, and clear water within the eastern part and at the entrance of Kuwait Bay (Al-Ghadban, 2004; Al-Ghadban and El-Sammak, 2005).

Water content: water content of sediments depends on factors such as particle size and packing, pore space, capillary action, time of sampling, and tidal level (flood or ebb) (Al-Bakri and Kittaneh, 1998). The measured water contents are highest in the eastern part of Sulaibikhat Bay near the Shuwaikh Port area, and lowest close to the Entertainment City area in the west. This can be explained by variations in sediment type. Adjacent to Shuwaikh Port, sediments are mainly silty, whereas in the upper tidal flats close to the Entertainment City area, silty sand dominates (as seen in Table 1).

5. DISCUSSION

This study investigated the physiochemical characteristics of Sulaibikhat Bay. The main finding is that local differences in the characteristics of the water column in Sulaibikhat Bay are caused by thermal discharge from power plants and sewage outfall at Ghazali. Local differences of temperature, salinity and DO (1.2°C, 13.7 PSS and 5.92 mg l⁻¹, respectively) were observed in these areas. Changes in water column characteristics because of effluent discharge can have numerous impacts on habitat. Del Pilar Ruso et al. (2008) observed salinity differences of 3.56 PSS in summer and 3.16 PSS in winter in waters adjacent to the Alicante desalination plant in southeastern Spain. They also found that this discharge caused a decrease in the abundance, richness and diversity of a polychaete assemblage along the Alicante coast. At the site of their study, water depth ranged from 4 to 15 m, and the discharged brine accumulated on the seafloor because of its high density. The higher differences of salinity recorded in Sulaibikhat Bay (13.7 PSS) were in water depths between 0.09 and 5.49 m and might be related to the shallower water depth. This study also recorded the lowest level of DO in the southeast of the Bay, adjacent to the Ghazali sewage outfall. The low level of DO is a result of consumption of oxygen by microorganisms decomposing organic matter (Calvert and Pedersen, 1993; Alagarsamy, 1997; Scholz and Neumann, 2007). Bejda et al. (1992) found that, under controlled laboratory conditions, the growth of juvenile fish was significantly reduced at low DO levels, which were varied diurnally between 2.5 and 6.4 mg l⁻¹ over a period of 11 weeks. These findings support the view that the high salinity and low DO found in Sulaibikhat

Bay close to points of effluent discharge might have numerous impacts on local habitats and may not support productive marine communities in the Bay. This suggests that more research and further impact assessment studies are warranted.

In this study, low ORP values (48.0–188 mV) were recorded in the southeast of Sulaibikhat Bay. These may be associated with the presence of hydrogen sulphide and pyrite in the sediments and suggest the possibility that reducing conditions prevail because of sulphate reduction associated with the decomposition of organic matter. The high correlation of pyrite with TOC supports the view that the presence of pyrite is an indicator of the presence of sewage waste under anaerobic conditions (UNESCO/WHO/UNEP, 1996). Scholz and Neumann (2007) found that TOC contents decreased with depth in pyrite-rich sediments, indicating that organic matter had been progressively metabolized by microorganisms. In addition, they found that the release of CO₂ into pore water during metabolism was accompanied by a pH decrease from 7.7 to 6.8. Their findings are consistent with those of this study of Sulaibikhat Bay where, in the core closest to the Ghazali sewage discharge, decreases of TOC with depth from 8.80% to 4.20% were accompanied by the lowest pH recorded in the Bay. This suggests that low pH might be useful as an indicator of active decomposition of organic matter.

6. CONCLUSION

The discharges from the Doha power and desalination plants and the Ghazali sewage outfall all affect the water column within Sulaibikhat Bay. The highest temperature and salinity readings obtained in this study (17.7°C and 45.3 PSS, respectively) were recorded close to effluent discharge points from power and desalination plants. In contrast, there were local reductions in temperature and salinity (16.5°C and 31.6 PSS, respectively) close to the Ghazali outfall. Reduced oxygen concentrations were recorded in the southeast near the Ghazali outfall as a result of the discharge of waste matter with high organic content. This discharge also caused lowering of ORP, so that reducing conditions prevail in this particular area. An abundance of pyrite close to the Ghazali outfall reflects the presence of sewage waste under anaerobic conditions.

ACKNOWLEDGEMENTS

The Authors would like to thank Dr. A. N. Al-Ghadban, Head of the Environmental Science Department at Kuwait Institute for Scientific Research, KISR, for his encouragement and support. The Kuwait Institute for Scientific Research (KISR) is greatly appreciated for its financial support.

REFERENCES

- [1] Alagarsamy, R. (1997) Trace Metals and Organic Matter Diagenesis at the Oman Margin. PhD Thesis. University of Liverpool. 248pp.
- [2] Al-Bakri, D. & Kittaneh, W. (1998) Physicochemical characteristics and pollution indicators in the intertidal zone of Kuwait: implications for benthic ecology. *Environmental Management* 22, 415–424.
- [3] Al-Ghadban, A. N. & El-Sammak, A. (2005) Sources, distribution and composition of the suspended sediments, Kuwait Bay, Northern Arabian Gulf. *Journal of Arid Environments* 60, 647-661.
- [4] Al-Ghadban, A. N. (2004) Assessment of suspended sediment in Kuwait Bay using Landsat and SPOT images. *Kuwait Journal of Science and Engineering* 32, 155-172.
- [5] Al-Ghadban, A., Al-Majed, N. & Al-Muzaini, S. (2002) The state of marine pollution in Kuwait: Northern Arabian Gulf. *Technology* 8, 7-26.
- [6] Al-Sarawi, M. A., Massoud, M. S., Khader, S. R. & Bou-Olyan, A. H. (2002b) Recent trace metal levels in coastal water of Sulaibikhat Bay, Kuwait. *Technology* 8, 27-38.
- [7] Bejda, A. J., Phelan, B. A. & Studholme, A. L. (1992) The effect of dissolved oxygen on the growth of young-of-the-year winter flounder, *Pseudopleuronectes americanus*. *Environmental biology of fishes* 34, 321-327.
- [8] Burdige, J. (1993) The biogeochemistry of manganese and iron reduction in marine sediments. *Earth Science Reviews* 35(3), 249-284.
- [9] Calvert, S. E. & Pedersen, T. F. (1993) Geochemistry of recent oxic and anoxic marine sediments: Implications for the geological record. *Marine Geology* 113, 67-88.
- [10] Covington, A. K. & Whitfield, M. (1988) Recommendations for the determination of pH in sea water and estuarine waters. *Pure & Applied Chemistry* 60, 865-870.
- [11] Dames & Moore (1983) Studies for Sabiya area, Kuwait Bay and development of electrical networks. *Aquatic Biology Investigations*. Ministry of Electricity and Water, Government of Kuwait.
- [12] Del Pilar Ruso, Y., De la Ossa Carretero, J. A., Gimenez Casalduero, F., Sanchez Lizaso, J. L. (2008) Effects of a brine discharge over soft bottom Polychaeta assemblage. *Environmental Pollution* 156, (2) 240-250.
- [13] Khalaf, F. I., Al-Ghadban, A., Al-Saleh, S. & Al-Omran, L. (1982) Sedimentology and mineralogy of Kuwait Bay bottom sediments, Kuwait – Arabian Gulf. *Marine Geology* 46(1-2), 71-99.
- [14] Khalaf, F. I., Al-Ghadban, A., Al-Saleh, S., and Al-Omran, L. (1981) Sedimentology of Kuwait Bay bottom sediments, . KISR, EES-11E, Final report. Kuwait.
- [15] Khalaf, F., Abou-Seida, M., Lo, J. M., Shublaq, W. & Khuraibet. A. (1988) Environmental impact assessment of Al-Akaz Development. KISR-2596, Kuwait Institute for Scientific Research.
- [16] KISR (Kuwait Institute for Scientific Research) (1984) Assessment of trace metal and biological pollution in the marine environment of Kuwait. *EES-31A*, Environmental and Earth Sciences Division; *KISR-605*, Kuwait Institute for Scientific Research.
- [17] KISR (Kuwait Institute for Scientific Research) (1999) Assessment of sediment quality in Kuwait Territorial Waters, Phase 1: Kuwait Bay. *VS006C*, Environmental and Earth Sciences Division, *KISR-565I*, Kuwait Institute for Scientific Research.
- [18] KISR (Kuwait Institute for Scientific Research) (2003) Tidal flow and sediment conditions at the southwest corner of the Shuwaikh Port. *KISR-6659*, Environment and Urban Development Division, Kuwait Institute for Scientific Research.
- [19] Saeed, T., Khordagui, H. & Al-Hashash, H. (1999) Contribution of power and desalination plants to the levels of volatile liquid hydrocarbons in the nearby coastal areas of Kuwait. *Environment International* 25, 553-562.
- [20] Samhan, O., Zarba, M. & Anderlini, V. (1986) Aeolian contributions of trace metals to marine sediments of Kuwait. *Environment International* 12, 001-007.
- [21] Scholz, F. & Neumann, T. (2007) Trace element diagenesis in pyrite-rich sediments of the Achterwasser lagoon, SW Baltic Sea. *Marine Chemistry* 107, (4) 516-532.
- [22] UNESCO (1981) Introduction of the Practical Salinity Scale 1978 and the new International Equation of State of Seawater 1980 January 1982. Deep Sea Research Part A. Oceanographic Research Papers 28(12), 1621.
- [23] UNESCO/WHO/UNEP (1996) Selection of Water Quality Variables. In: Chapman, D. (Ed.). *Water Quality Assessments – A Guide to Use of Biota* (2nd Edition); Chapter 3, Sediments and Water in Environmental Monitoring. ISBN 0 419 21590 5.

APPENDIX

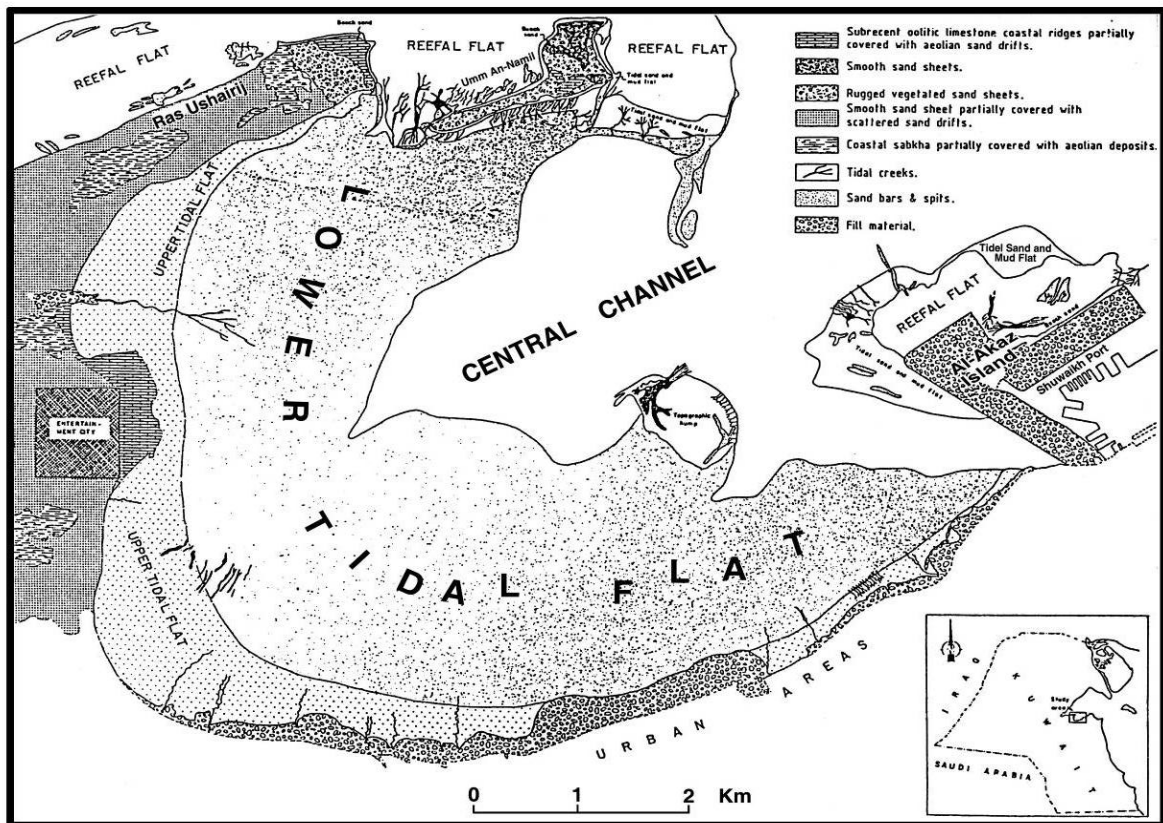


Figure 3: Physiographic map of Sulaibikhat Bay (source; modified after KISR 1986)

Impact of Barrages on Water Quality of Rivers Upstream and on Air Entrained in the Hydraulic Jump Downstream

Emad Hamdy Emam¹, Sherine Ahmed El Baradei²

¹ Professor and Head at the Department of Construction Engineering,
The American University in Cairo, Egypt
(eimam@aucegypt.edu)

² Assistant Professor at the Department of Construction Engineering,
The American University in Cairo, Egypt.
(sbaradei@aucegypt.edu)

ABSTRACT

This research studies the impact of barrages on water quality and self-assimilative capacity of rivers and on their temperature. Constructing barrages in river reaches will alter its hydraulics and thus its water quality and thermal regime. A mathematical model is developed to simulate river hydraulics, water quality and temperature. Diurnal dissolved oxygen concentrations are also investigated. A case of a Nile River reach was studied, to investigate the impact of the existence of the Esna barrage on the water quality and temperature in its upstream reach. The barrage has negative impacts on the upstream self-assimilative capacity of the rivers. The waste load that the river could take was only 54 % (at low flow) and 78% (at high flow) from that load when there was no barrage. When simulating the effects of photosynthesis and respiration the above mentioned percentage was raised to 54% and 91% respectively. Although barrages have negative impacts on the upstream self-assimilative capacity of the rivers, they have positive effect on DO concentrations (increase of 6%) in the downstream. The barrage causes a slight decrease in water temperature of 0.13 degree in the month of June. Any barrage will cause at its downstream formulation of hydraulic jumps under its gates when they are opened. The effect of hydraulic jump on air entrained in water was investigated and it was found that the quantity of air entrained was a function in the numbers of opened gates of the barrage and also a function of the depth of opening of those gates.

Keywords: self-assimilative capacity, water quality, hydraulic structure, barrages, mathematical modeling, dissolved oxygen concentrations, photosynthesis and respiration, thermal regime and water temperature

1. INTRODUCTION

Barrages constructed on a river will change the hydraulic regime of that river by increasing water depths and reducing velocities in the zones of developed backwater curves. This modified hydraulic regime impacts water quality due to changes in the transport and decay processes of pollutants along the rivers. The modified hydraulic regime also impacts the thermal regime the river.

Numerous researchers investigated the effects of hydraulic structures, which create impoundments behind them like dams, on the water quality. Hildyard [9] as an example studied the environmental effects of large dams. There were rare studies investigating the effect of the water level control structures; such as, barrages and weirs on the water quality and its ecosystem. [5] is among the rare researchers who investigated the impact of barrages on water quality in rivers. However Eid used a simplified prismatic river section and considered only atmospheric reaeration and ignored photosynthesis. Many studies such as by Song [11] and Candara [2] were done to simulate water temperatures from air temperatures, but they didn't imply the effect of hydraulic structures on the water thermal regime. Eid

studied this impact, but the simulated water temperature was assumed to obey a linear relation and the lag time between water and air temperature wasn't considered.

This paper studies the impact of barrages on self-assimilative capacity of rivers. In order to do so, water quality indicators were developed aiming to express the impact in a quantifiable manner.

2. RIVER SIMULATION MODEL

The impact of constructing a barrage across a river is numerically modeled. The model consists of two main sub-models; a hydraulic and a water quality sub-models. The water quality sub-model consists of a dissolved oxygen simulator along with its components such as biological oxygen demand, reaeration, photosynthesis, and respiration. An additional sub-model was developed; namely the temperature sub-model.

2.1. Hydraulic Sub-Model

The hydraulic sub-model simulates backwater curves, velocities and areas for a controlled river reach of any geometrical shape using the standard-step method.

2.2. Dissolved Oxygen (DO) Sub-Model

Using the hydraulic parameters calculated via the hydraulic sub-model, the DO sub-model simulates all available sources and sinks (except NBOD and SOD). A mass-balance equation is solved and yielded the following:

$$C_{i+1} = C_i + \frac{\bar{A}\Delta x \{ \bar{P}_a + \bar{K}_a(C_s - C) - \bar{K}_d L - \bar{R} \}_{average}}{Q_i} \quad (1)$$

Where; C_{i+1} = DO concentration at section $i + 1$ in mg/L; C_i = DO concentration at section i in mg/L; \bar{A} = average area of sections i and $i + 1$ in m^2 ; Δx = length of the control volume in m ; Q_i = discharge over the control volume in m^3/day .

The sources and sinks of eqn (1) are explained in the following paragraphs.

In eqn (1), all sources and sinks are taken to be the average of their concentrations between sections (i) and (i+1).

$$L_{i+1} = L_i e^{-K_r \left(\frac{\bar{A}\Delta x}{Q_i} \right)} \quad (2)$$

Where; L_{i+1} = CBOD concentration at section $i + 1$ in mg/L; L_i = CBOD concentration at section i in mg/L; \bar{A} = average area of sections i and $i + 1$ in m^2 ; Δx = length of the control volume in m ; Q_i = discharge over the control volume in m^3/day ; K_r = average decay or loss rate of CBOD in between sections i and $i+1$ day^{-1} ;

$$K_r = K_d + K_s \quad (3)$$

Where; K_d = decomposition rate of CBOD in the stream in day^{-1} ;

K_s = settling rate of CBOD in day^{-1}

$$K_d = 0.3 \left(\frac{h}{8} \right)^{-0.434} \quad [12]; \quad K_s = \frac{v_s}{y} \quad [4] \quad (4\&5)$$

Where; y = average water depth in m ; v_s = settling velocity in m/day.

The exchange of air at the surface of the water makes use of the "two film theory [10]:

$$Reaeration = K_a (C_s - C) \quad (6)$$

where; K_a = volumetric reaeration coefficient in day^{-1}

$$K_a = 3.93 \frac{V^{0.5}}{Y^{1.5}} \quad (7)$$

Where; V = average velocity; Y = average depth in m ;

C_s = saturation concentration of DO at certain section in mg/L; C = DO concentration at certain section in mg/L. The average of the reaeration equation is taken between two successive sections of the control volume.

The essence of photosynthetic process centers about chlorophyll a containing plants which utilize radiant energy from the sun, convert water and carbon dioxide into glucose, and release oxygen. Thus production of oxygen happens only during daylight hours. The variation of light and hence photosynthesis can be idealized by a half sinusoid function, from day to day. Thus swings in oxygen can be induced by diurnal light variations.

A method called "Estimation from observed chlorophyll levels" is used to estimate the value of the photosynthesis over the control volume. This method assumes that the phytoplankton is the principal source of oxygen. This method requires a direct measurement of the concentration of phytoplankton as represented by chlorophyll a in the water. Since photosynthesis is light dependent, the relationship between phytoplankton chlorophyll and photosynthetic production depends on solar radiation, depth, and the extinction coefficient. This is described through the following equations [12].

$$P_a = [a_{op} G_{max} (1.066)^{T-20} P] G(I_a) \quad (8)$$

Where; P_a = average daily growth production (photosynthesis) in mgDO/L.day; a_{op} = mg of DO per

μg of chl_a means chlorophyll a ;

P = phytoplankton chlorophyll in $\mu g/L$; G_{max} =

maximum growth rate of the phytoplankton at $20^\circ C$ in day^{-1} ; T = temperature in $^\circ C$; $G(I_a)$ = light attenuation factor over depth and one day (Unitless)

Respiration is the process by which organisms take up oxygen and discharge carbon dioxide in order to satisfy their energy requirements.

$$R = a_{op} (0.1)(1.08)^{T-20} P \quad (9)$$

Where; R = phytoplankton respiration in mgDO/L.day.

In addition to the atmospheric reaeration that happens to the river, there is another reaeration process that takes place across control structures. This process has a positive effect on the DO concentration at the downstream side of the structure. DO is calculated by Gameson's equation [1]:

$$r = 1 + 0.11(a)(b)(1 + 0.046(T))h \quad (10)$$

Where; r = ratio of upstream DO deficit to downstream deficit; a = water quality factor; b = structure aeration coefficient; T = water temperature, degree C; h = water level difference across the barrage, ft

2.3. Temperature Sub-Model

Water temperature is vital for fauna and flora of water; and for chemical and biological reactions in rivers. Water temperature depends on air temperature and on hydraulic parameters of rivers; such as, depth of water, and geometry of river sections. Constructing a barrage alters the hydraulic regime of water and thus may alter its thermal regime. Heat transferred at the air-water interface is the major factor that induces variation in water temperature. Many researches were done that proved that air and water temperatures are correlated. [11]. The U.S Geological Survey department studied some rivers in Texas and concluded that large streams have a small diurnal temperature change [2]. Heinz [8] revealed that the time lag which exists between the air and water temperatures varies linearly with the depth of the river [8]. From his study it was concluded that, the measured water temperatures follow the air temperatures closely with some time lag.

Diurnal simulation of water temperature using air temperature was done by expanding the equation of Heinz to accommodate the diurnal water temperature changes. This is described via eqns (11) to (13).

$$T_w(t) = A + \frac{\Delta T_w}{\Delta T_a} * T_a(t - \delta) \quad (11)$$

Where; the time t and the time lag δ are in units of days and temperatures are in °C. This equation shows that the water temperature calculated at time t is a function in the air temperature at the time t less the lag time.

To calculate the lag time δ the following equation is used:

$$\delta = \frac{\tau}{2\pi} * \tan^{-1} \left(\frac{2\pi * depth}{\tau * \alpha} \right) \quad (12)$$

Where; τ = cyclic period over which the study is done (here 24 hours); α = thermal diffusivity coefficient:

$$\alpha = \frac{K}{C_p * \rho} ; K = \text{Surface heat exchange conduction}$$

coefficient between the air and the water in $W / m^2 \cdot ^\circ C$;
 C_p = the specific heat of water in $W.S/Kg \cdot C$; ρ =
 density of water in Kg / m^3 ;

$$\frac{\Delta T_{water}}{\Delta T_{air}} = \frac{1}{\sqrt{1 + \left(\frac{2 * \pi * depth}{\tau * \alpha} \right)^2}} \quad (13)$$

3. ASSESSMENT OF THE SELF-PURIFICATION CAPACITY AND ECOSYSTEM

The self-purification capacity of a river is the capacity of its water to accept different waste load concentrations without changing its original quality. To assess the impact of barrages on the self-assimilative capacity of rivers in a quantifiable manner, many indicators were developed. For example introducing waste loads from point sources at different sections along that river be able to compare between the loading capacity of the

river at different hydraulic cases. The DO concentration in the river is kept at a constant level of 5mg/L.

The effects of temperature and photosynthesis on the diurnal DO variation were also tested, because as mentioned earlier the barrage existence has an impact on water temperature. To study this effect, the diurnal change in water temperature is simulated for the four main hydraulic cases.

4. CASE STUDY NILE RIVER (ASWAN-ESNA REACH)

The case study investigates the effect of Esna barrage on the water hydraulic regime; as well as, on water quality upstream the barrage from Esna to Aswan and on downstream air entrained and DO in the river.

4.1. Hydraulic Simulation of Aswan-Esna Reach (Upstream the Barrage)

The Esna Barrage is located downstream the Esna-Aswan reach which is 157.9 Km long. The barrage has 11 gates each of which is 12m in width. In most of the cases the lock is the main structure discharging the river water but at some incidences one or two of the barrage gates are opened to allow relief of excess water. The peak discharge of the High dam is about 2500 m³/s and it occurs in July, whereas, the minimum discharge is about 1000 m³/s and occurs in January. Available river sections are every 5 Km and interpolation was used to generate sections every 100 m in order to do hydraulic calculations via the standard step method in an accurate way. Manning coefficient is assumed to be constant ($n=0.0287$) throughout the simulated reach. The studied reach was simulated under four main hydraulic cases: Cases 1 & 2 study the existence and the non-existence of Esna barrage respectively at low flow conditions; Cases 3 & 4 study the existence and non-existence of barrage respectively at high flow conditions. The results of the calculations and the water level profiles are summarized in the following table:

Table 1: Hydraulic Data of Cases 1 – 4. Station 0 is at Esna . Station 157909 is at Aswan

Station (m)	WL (m)	Max Depth (m)	Energy Head (m)	Area (m ²)	Perimeter (m)
					Velocity (m/s)
Case1 0.0	77.4	6.92	77.41	3707	550 0.270
Case1 157909	82.2	4.39	82.26	2271	526 0.440
Case2 0.0	72.5	4.20	72.51	2250	544 0.444
Case2 157909	83.2	2.87	83.30	1487	523 0.673
Case3 0.0	78.0	7.53	78.04	4034	551 0.620
Case3 157909	84.8	7.00	84.89	3624	532 0.690
Case4 0.0	74.6	6.32	74.65	3386	548 0.738
Case4 157909	85.5	5.18	85.63	2681	528 0.932

4.2. Self-Purification Capacity and Waste Load at Aswan-Esna Reach

Two scenarios were simulated to compare between different cases of waste loadings (W.L). Scenario 1 uses the DO as a function of only CBOD and reaeration. Scenario 2 adds photosynthesis and respiration to the DO. Table 2 summarizes all the waste loading cases [10].

Table 2: Simulation of waste loads at different scenarios

	Case 1	Case 2	Case 3	Case 4
W.L (Kg) day	1405	2612	2118	2705
	Scenario 1	Scenario 1	Scenario 1	Scenario 1
W.L (Kg) day	5684	6218	10971	11768
	Scenario 2	Scenario 2	Scenario 2	Scenario 2

4.3. Diurnal Dissolved Oxygen

DO concentration changes during the 24 hours of the day because of change in water temperature and the change in photosynthetic action of plants throughout the day. Minimum DO concentrations usually occur in the early morning, and maximum concentrations occur in the early afternoon. In the simulation a section with average properties (hydraulically and water quality) was taken using simulated diurnal water temperature. The simulation compared the diurnal DO at cases of existence and non-existence of the barrage. To see the effect of the photosynthesis on the diurnal DO, a trial was done using only the CBOD and the reaeration in calculating the DO as opposed to another trial using the photosynthesis.

The curve representing the diurnal DO in case of having the barrage is slightly higher than that curve of the diurnal DO when not having the barrage. This is so because the diurnal water temperatures in case of having the barrage are less than those in case of not having the barrage because in the case of having the barrage the depths are larger so the DO fluctuations are less. So here, the water temperature is the parameter that has the greater effect on the diurnal DO concentrations; and it is known that the temperature is inversely proportionate with the DO concentration.

4.4. Reaeration across the Barrage (Downstream DO Concentrations)

Gameson equation simulated DO concentrations downstream of the barrage. The calculations which are done under low flow conditions revealed an upstream DO concentration of 8.02 mg/L, an upstream DO

deficit/ downstream DO deficit of 3.90, and a downstream DO conc. of 8.49 mg/L.

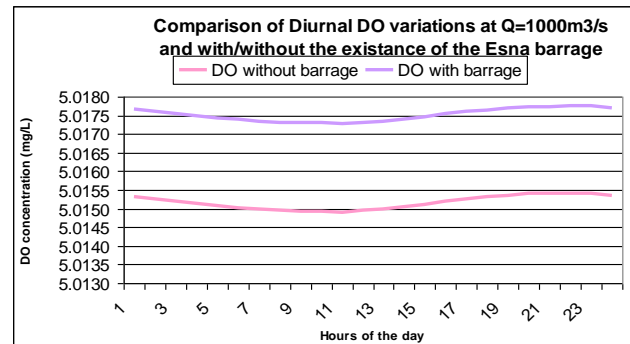


Figure 1: Comparison of diurnal DO variation due to photosynthesis at $Q=1000\text{m}^3/\text{s}$ and with/without the existence of the Esna barrage

4.5. Effect of the Barrage Gates on the Air Entrained in the Hydraulic Jump Formulated Downstream the Barrage

If the gates of the barrages are opened, then hydraulic jumps are generated below those gates. The generated hydraulic jumps are of different kinds [7]. The type of jump is known depending on the calculated Froude number. Depending on the type of the jump, more or less air could be entrained in the water. The ratio between the quantities of air entrained by the hydraulic jump to the water discharge was calculated at different gate openings (namely 0.9 m, 2 m and 3 m) and at low ($1000\text{m}^3/\text{s}$) and high ($2500\text{m}^3/\text{s}$) discharges of the river. Also those conditions were investigated at different numbers of opened gates. The ratio was calculated via the two following equations [3]:

$$Q_{air}^{HJ} / Q_w = 0.014 * (Fr - 1)^{1.4} \quad (14)$$

This equation works for Froude numbers in the following range $5 < Fr < 25$

$$Q_{air}^{HJ} / Q_w = 0.018 * (Fr - 1)^{1.245} \quad (15)$$

This equation works for Froude numbers in the following range $2.4 < Fr < 8.7$

4.7. Simulation of Water Temperature

The effect of Esna barrage on the thermal regime of water was tested. The simulation of the diurnal variations in the water temperatures on a day of the month of June was done for one section that is representative for the whole reach. This section is taken as the section with the average depth throughout the whole reach. The simulation is done for the previously mentioned, four main hydraulic cases. It is observed that the sinusoidal diurnal water temperature curve follows the air temperature curve but with a lag time between water and air temperatures. This lag time increases with increased depth. Figure 2 shows the diurnal air temperature curve along with the diurnal water temperature curves at both cases 1&2. In case 1 the lag time between air and water temperatures is 5.842 hours,

whereas in case 2 it was 5.791 hours. The curves show that in case 2 the diurnal water temperature is higher than in case 1. So in case 2 the maximum water temperature during the whole day is 28.4°C, whereas in case 1 it decreases to reach 27.8°C. This indicates that the existence of the barrage causes a decrease in water temperature. When operating under high flow conditions the diurnal water temperature further decreases. So in case 4 the maximum water temperature during the whole day is 27.5°C, whereas in case 3 it decreases to reach 27.3°C. [6]

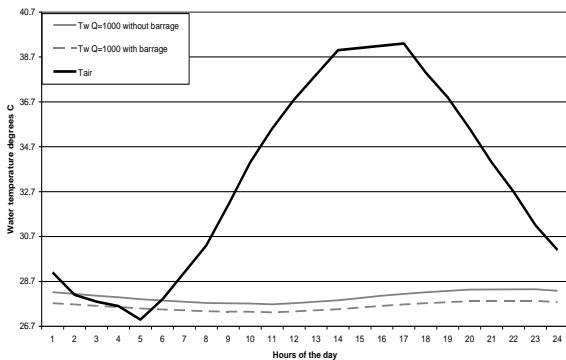


Figure 2: Diurnal air and water temperature at average section and cases of with/without barrage

5. SUMMARY AND CONCLUSIONS

The drawn conclusions are general for any water level control structure, but the calculated percentages are of the Esna barrage case study:

1. The barrage has negative impacts on the upstream self-assimilative capacity of the rivers. At barrage existence the waste load that the river could take (considering CBOD and reaeration only) was only 54 % from that load when there was no barrage and at low

flow conditions. At high flow conditions this load changed to 78%. When adding the effect of the average daily photosynthesis, and respiration the percentages were changed to be 91 % and 93 % respectively. Thus photosynthesis and high flow have positive effect on the self-assimilative capacity of water. As for the diurnal DO variations, it is found to be affected by diurnal water temperatures and photosynthesis values.

2. The barrage has raised the DO concentration downstream by a percentage of 6% from its upstream concentration value.

3. Entrained air in the hydraulic jump downstream the barrage increases with less numbers of gates opened and with decreased depth of gate opening. Also it increases with increased discharge. It is also noted that the entrained air value is calculated to be negative when there is no jump (see tables 4 & 5).

4. The diurnal DO variation is affected by diurnal water temperatures and photosynthesis. The peak DO value that is reached during the 24 hours of the day is increased when photosynthesis component is added to the DO equation.

5. The barrage causes a slight decrease in diurnal water temperature. The average change in diurnal temperature between the cases of with and without barrage is 0.13°C and at high flow and 0.44°C at low flow respectively.

Table 3: Air entrained to discharge ratio at a gate opening of 0.9 m										
Table 4: Air entrained to discharge ratio at a gate opening of 2 m										
# gates opened	Q at 2500m ³ /s per gate	Q at 1000m ³ /s per gate	V in (m/s) at 2500 m ³ /s	V in (m/s) at 1000 m ³ /s	Froude # at 2500m ³ /s	Jump Type	Froude # at 1000m ³ /s	Jump Type	QairHJ/Qw at 2500m ³ /s	QairHJ/Qw at 1000m ³ /s
11	227.3	90.9	9.5	3.8	2.1	Oscillating	0.9	No jump	0.03	-0.003
10	250.0	100.0	10.4	4.2	2.4	Oscillating	0.9	No jump	0.03	-0.001
8	312.5	125.0	13.0	5.2	2.9	Oscillating	1.2	Undular	0.04	0.004
6	416.7	166.7	17.4	6.9	3.9	Oscillating	1.6	Undular	0.07	0.01
4	625.0	250.0	26.0	10.4	5.9	Steady	2.4	Weak	0.11	0.03
2	1250.0	500.0	52.1	20.8	11.8	Strong	4.7	Steady	0.39	0.08
1	2500.0	1000.0	104.2	41.7	23.5	Strong	9.4	Strong	1.10	0.28

Table 5: Air entrained to discharge ratio at a gate opening of 3 m

# gates opened	Q at 2500m ³ /s per gate	Q at 1000m ³ /s per gate	V in (m/s) at 2500 m ³ /s	V in (m/s) at 1000 m ³ /s	Froude # at 2500m ³ /s	Jump Type	Froude # at 1000m ³ /s	Jump Type	Q _{air} HJ/Q _w at 2500m ³ /s	Q _{air} HJ/Q _w at 1000m ³ /s
11.0	227.3	90.9	6.3	2.5	1.2	undular	0.5	No jump	0.004	-0.01
10.0	250.0	100.0	6.9	2.8	1.3	undular	0.5	No jump	0.01	-0.01
8.0	312.5	125.0	8.7	3.5	1.6	undular	0.6	No jump	0.01	-0.01
6.0	416.7	166.7	11.6	4.6	2.1	Weak	0.9	No jump	0.03	-0.003
4.0	625.0	250.0	17.4	6.9	3.2	Oscillating	1.3	Undular	0.05	0.01
2.0	1250.0	500.0	34.7	13.9	6.4	Steady	2.6	Oscillating	0.1	0.03
1.0	2500.0	1000.0	69.4	27.8	12.8	Strong	5.1	Steady	0.4	0.1

REFERENCE

Alabama Department of Environmental Management, Water Division-Water Quality Branch , "The ADEM Spreadsheet Water Quality Mode", Alabama Department of Environmental Management, 2001.

Candara and S.C et al., "Water resources data Texas.,U.S Geological Survey-water data",reportTx-99-4 ,4, 1999.

Chanson, H. " "Air-Water Gas Transfer at Hydraulic Jump with Partially Developed Inflow." *Water Res.*, IAWPRC, Vol. 29, No. 10, pp. 2247-2254, 1995.

Chapra, Steven. "Surface Water Quality Modeling", McGraw-Hill International, 1997

Eid, Dhalia M. "Impact Of Flow Control Structures on Rivers Self Purification Capacity", Dissertation, The American University In Cairo, 1992

El Baradei, Sherine A. "Impact of Control Structure on Ecosystem and Assimilative Capacity of Rivers", Dissertation. Cairo University: faculty of engineering, 2005.

El Baradei. S.A., Emam, E. " Optimum Operating Rules For Barrages", *Icator Journal of Engineering*, Vol. 4, No. 1, pp.17 – 27, 2011.

Heinz, S.G. et al. "Stream Temperature Estimation From Air Temperature", *Water Resources Bulletin* , Vol. 29, No. 1, pp.27-47, 1993.

Hildyard,N..Et al. "The Social and Environmental Effects of Large Dams", San Francisco: Sierra Club Books, 1986

Imam, E, El Baradei, S. "Ecosystem and assimilative capacity of rivers with control structure", 8th Water Pollution Conference. Italy 11-18 September, 2006.

Song, Charles C. S. et al. "Stochastic Properties of Daily Temperature in Rivers", *Journal of The Environmental Engineering Division (ASCE)*, Vol.103, No. 2 , pp. 217-31, 1977.

Thomann, Robert V. "Principles Of Surface Water Quality Modeling and Control", Harper Collins, 1987.

The Use of GIS and Remote Sensing for Quantitative Evaluation of Water Soil Erosion, Case Study in the West of Algeria

Y. Fekir¹, K. Mederbal², B. Belgherbi³, M. A. Hamadouche⁴, D. Anteur⁵

1,2,3,4,5 : Biological System and Geomatics Research Laboratory, Mascara University, Mascara, Algeria

1: youceffekir@yahoo.fr, 2: kmederbal@hotmail.com, 3: belghrebib@yahoo.fr,

4: ham1879@yahoo.fr, 5: anteurdjamel@yahoo.fr

ABSTRACT

This work studies the potential use of remote sensing and the integration of the various factors in a GIS for a quantitative evaluation of the soil losses caused by the water erosion phenomenon.

Using the universal equation of the loss of ground (Universal Soil Loss Equation USLE) revised according to Wischmeier, an estimate of the soil losses enabled us to evaluate then to map the soil erosion risk, after having adapted this model to the local conditions of our study area located at the west of Algeria. The combination of the various factors taken into accounts in USLE model with the geographical information systems (GIS) can inform us about the dominating factor(s) in the phenomenon of erosion, and consequently propose a management plan for the fight against this phenomenon. The validation of the obtained results from the used model requires, in more with the geomatics techniques, the ground studies to be able to provide spatialized results.

Keywords: Water erosion - USLE - Remote sensing – GIS – Mapping

1. INTRODUCTION

Erosion is a very complex phenomenon, linked to natural and anthropogenic factors which are difficult to control, changing both in space and time. This also contributes to the degradation of surface waters by creating problems of turbidity, sedimentation and nutrient and pesticide in excessive amounts for this underworld.

Also, in 1977 Combeau reports that 45% of the area of Algeria is affected by erosion, 100 ha of arable land lost per a day of rain (Rosse 1994). Oppose the magnitude of the situation; a serious problem is placed in terms of land degradation by this phenomena.

This study aims to assess the risk of erosion and quantification of soil loss in a region located in western of Algeria. It consists in using an empirical model USLE (Universal Soil Loss Equation) established by Wischmeier and Smith in 1958 (Wischmeier et al 1985), with which we can estimate the losses caused by water erosion. The idea is to integrate into a geographic information system (GIS), factors contained in the empirical model USLE namely: rainfall erosivity, soil erodibility, the slope factor, land use and conservation practices.

2. PRESENTATION OF THE STUDY AREA

2.1 Geographic Area

The study area, located about 50 kilometers east of Oran, is a depression surrounded by mountains and the sea, separated by a row of dunes. It is bounded on the north by dunes from the Golf and coastal massive of

Arzew, on the east by the fallout south of Mostaganem, on the south by the mountains of Beni Chougrane. The altitude is between 0 and 608.20m. Administratively, the study area spans three wilayas, namely the wilaya of Mascara, Mostaganem and Oran (Figure 1).

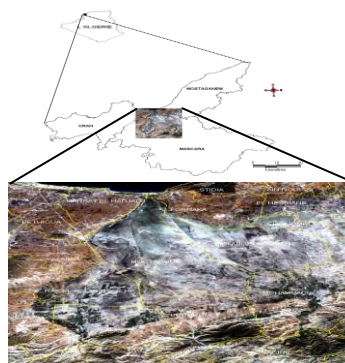


Figure 1: Study area location

This area is one of the major natural regions derived from the geological formation of Tell Atlas Western. It is characterized by altitudes between 0 and 608 m above sea level (Figure 2).

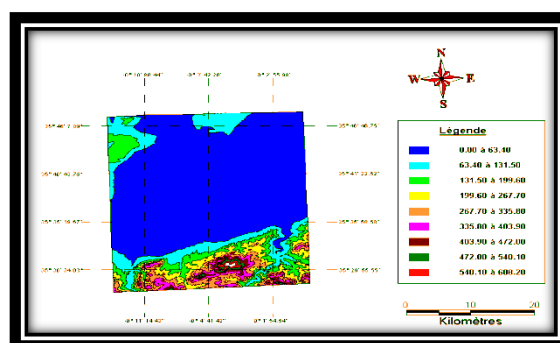


Figure 2: Elevation map of the study area

Pedologic soil properties are determined either by the characteristics of the level of quaternary alluvium which they belong or by the origin and mode of sedimentation of their elements (Gaucher et al 2003). From the soil map (Figure 3), we note the presence of different soil types include:

- Saline soil - Soil shell - encrusted soils - alluvial soils
- LSU (soil Young Mountain) – Dunes

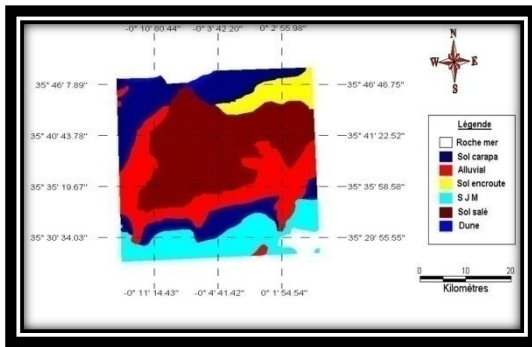


Figure 3: Soil Map of the study area

3. METHODOLOGY

3.1 Model Overview

The universal Soil Loss Equation (USLE), revised according to Wischmeier and Smith (1978), is the most often used model of soil erosion in the world (Lafren et al 2003). It is also very popular in Central Europe, whether in this form or in another adaptation (DIN19708 2005, Mollenhauer et al 2006). This equation is presented as the form:

- The current erosion E_a or "soil loss":
$$E_a = R \cdot K \cdot LS \cdot C \cdot P$$
- The erosion potential E_p or "erosive potential" is the product of physical factors:

$$E_p = R \cdot K \cdot LS$$

Where:

- E = average annual soil loss (t / ha / year)
 - R = rainfall erosivity (climatic factor)
 - K = soil erodibility (lithological factor)
 - LS = topographic factor incorporating the slope and slope length,
 - C = factor for soil protection by vegetation cover. (Cultural factors)
 - P = factor expressing the protection of soil by agricultural practices. (Anthropoic factor).
- Determining the different parameters of the model are detailed in (Wischmeier et al 1985).

3.2 Methodology adopted

Figure 4 summarizes the methodology used to develop maps of soil loss caused by water erosion using the universal equation of soil loss.

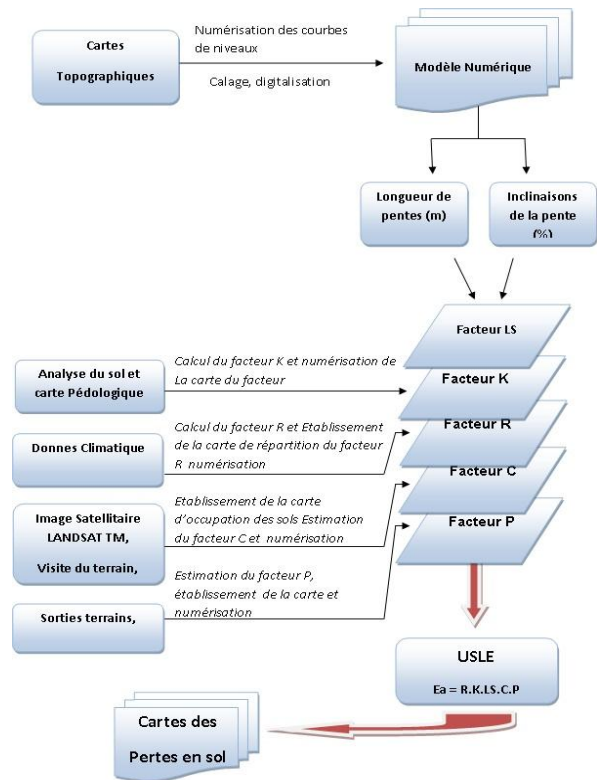


Figure 4: ADOPTED work methodology

4. RESULTS AND DISCUSSIONS

4.1 R Factor

The factor of rainfall erosivity is calculated from rainfall data (intensity of annual and monthly rainfall) recorded at the station of Sidi Abd el MOUMEN in the period of (1983-2000). The obtained R value is in the order of $R = 36.94 \text{ ton / ha / hour}$

4.2 K Factor

To spatialize the K factor, we performed taking samples of each type of soil in the study area (granulometry, organic matter content and permeability). These data are introduced in a GIS to assigning the erodibility K factor for each soil type (Figure 5).

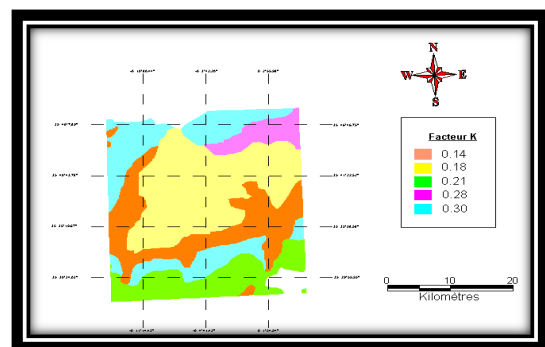


Figure 5: Distribution map of erodibility factor

4.3 Topographic LS Factor

The topographic LS factor is obtained from two parameters (slope, slope length) derived from the DEM. Values of this index varies between 0.82 and 8.28. The distribution map of the LS factor, shows that the highest values are located in the upstream part of the study area (Figure 6).

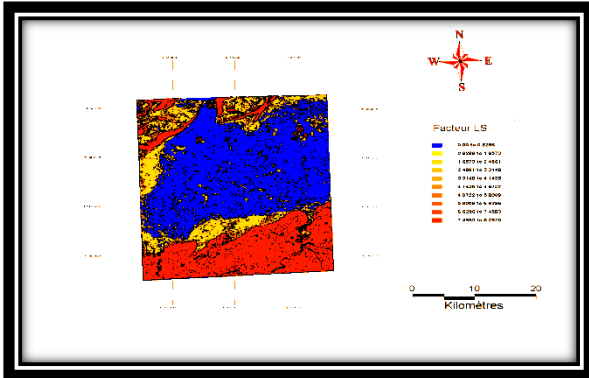


Figure 6: Distribution map of the LS factor

4.4 cultural Factor C

For the determination of C factor, we have used reference tables of Wischmeier and Smith (1978). These tables are described in (Wischmeier et al 1985). This is to express the effect of land use in the study area (Figure 7a).

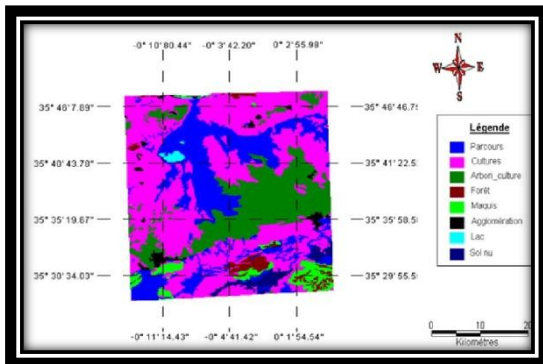


Figure 7.a: Land use map

The value assigned to: Forests: 0.13, range: 0.17, crops: 0.40, arboriculture: bare soil and 0.54: 1. (Figure 7b).

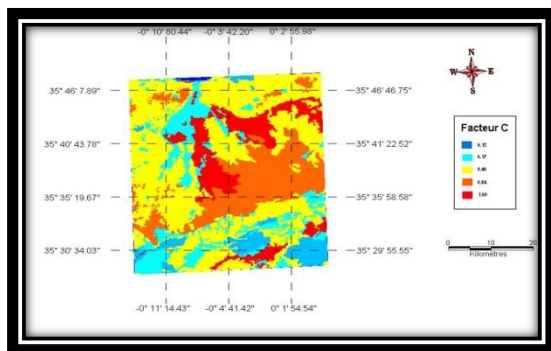


Figure 7b: Distribution map of the C factor

4.5 Factor P

Erosion control practices factor P reflects practices that reduce the amount of runoff and her speed, thus reducing the effects of water erosion.

Throughout the study area, there is no more active facilities against erosion, and farmers do not use conservation tillage. In this context, the value P = 1 was assigned to cover all of the study area.

4.6 Estimated soil loss

Two types of maps have been developed: Map of current losses from water erosion and the map of potential losses.

a. Current loss: The application of the formula of Wischmeier and Smith (1978) taking into account the numerical values of the five factors given the current loss Ea for each point of the study area (Figure 8a):

$$Ea = \text{erosivity} * \text{erodability} * \text{LS factor} * \text{C factor} * \text{P factor}$$

The only parameter which varies from one year to another is the rainfall erosivity R.

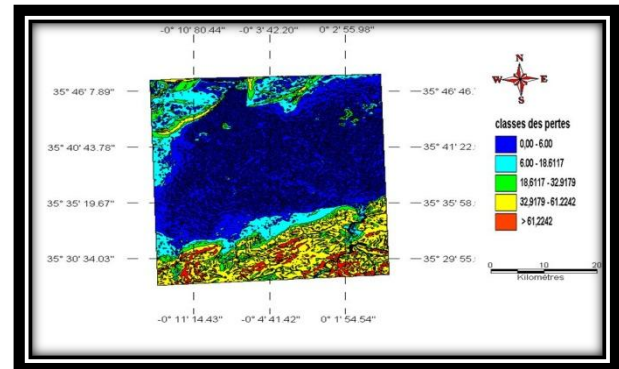


Figure 8.a: Actual Soil Loss map

b. Potential loss: The combination of the following factors: rainfall erosivity R, soil erodibility K, and the LS factor, has produced the map of potential losses from water soil erosion(Figure 8b) :

$$Ep = \text{erosivity} * \text{erodability} * \text{LS}$$

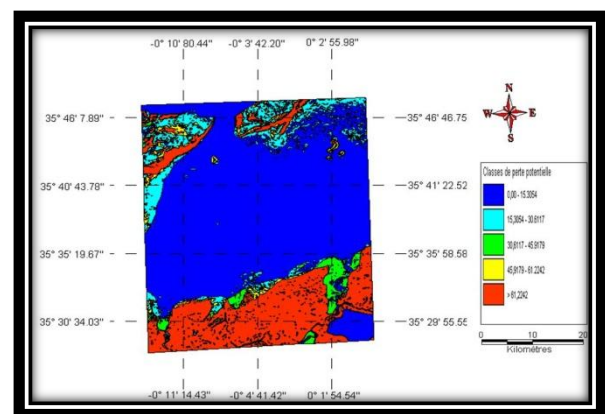


Figure 8.b: Potential Soil Loss map

5. DISCUSSIONS

The average loss by water erosion for all homogeneous units is approximately 45.9184 t / ha / year. The maximum and minimum loss per unit are respectively 91.8361 t/ha/year and 0.08 t/ha/year. The total annual loss in the study area is of 94040.98 tons / year. Erosion rates vary from region to region, depending on the influence of various factors controlling erosion. The distribution of soil loss is not proportional to the surface, in fact, 1.76% of the surface of the study area contribute to loss of 33.33% (Figure 9).

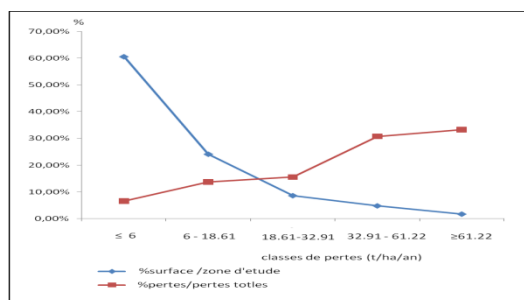


Figure 9: Soil Loss distribution of the study area

The results of calculations of annual net soil loss show:

- Great fragility of the east and south-east of the study area which consists mainly up to 91.8369 tons / ha / year. It Correspond to areas of steep or mountainous terrain.
- The low erosion rate 6.144 t/ha/year mainly dominates the slopes of the central bank of the study area where herbaceous vegetation covers of sandy land.
- The regions of low soil loss or deposition correspond to areas of low slopes or plains that are in the majority at the centre of the study area.

6. CONCLUSION

Maps of potential and current soil loss obtained appeared very useful to identify priority areas on which it is necessary to apply conservation measures to reduce soil erosion and ensure sustainable management of these soils.

Following the mapping of areas susceptible to erosion, field observations were conducted to validate the results. Several signs of water erosion were noticed during the visits to the regions reported as high loss to judge the severity of erosion.

Although the validity of soil loss calculated by the USLE is debatable, the method provides significant help to decision makers and planners to simulate scenarios for the region and plan interventions to fight against

erosion, especially in areas where sheet erosion is predominant on the linear erosion.

REFERENCES

- [1] Arnoldus H., (1981) An approximation of the rainfall factor in the USLE, In: Assessment of Erosion. de Boodt et Gabriels (eds.). John Wiley., 1981, pp 127-132
- [2] Demmak A., (1982) Contribution a l'étude de l'érosion et des transports solide en Algérie septentrionale, Thèse Docteur – Ingénieur, Paris, 1982, p323
- [3] Deumlich D. et al, (2006) Basics of effective erosion control in German agriculture, J. Plant Nutr. Soil Sci., V169, n 3, 2006, pp370-381
- [4] DIN19708, (2005) Bodenbeschaffenheit – Ermittlung der Erosionsgefährdung von Böden durch Wasser mit Hilfe der ABAG, Normenausschuss Wasserwesen im DIN, Beuth Verlag, Berlin, 2005, 25 p.
- [5] Fao, (1996) Mesures de terrain de l'érosion et de l'écoulement des eaux de surface, Bulletin pédologique, vol. 68, 1996, 153p
- [6] Gaucher G. et Simoneau P., (2003) Monographie agricole de la plaine de Saint-de Sig, Terres et Eaux, n°14 et 15, 1952
- [7] Gay M., (1996) Gestion régionale des sols et sensibilité à l'érosion, Laboratoire de Télédétection et de Cartographie Numérique, Ecole Supérieure de Purpan, Toulouse, 1996, pp 1-8.
- [8] Laflen J. M. et Moldenhauer W. C., (2003) Pioneering soil erosion prediction: the USLE story, World Association of Soil and Water Conservation (WASWC), Special Publication, no 1, 2003, 54 p
- [9] Mollenhauer K. et al, (2006) Bodenerosion durch Wasser. Bewertungsmethodik und Instrumente der deutschen Bundesländer, BVB-Materialien 14, Erich Schmidt Verlag, Berlin, 2006, 151 p.
- [10] Riou C. et al, (1997) L'eau dans l'espace rural, production végétale et qualité des eaux, INRA Editions, Universités francophones, 1997, 411 pages
- [11] Rosse E., (1994) Introduction a la gestion conservatoire de l'eau, de la biomasse et de la fertilité des sols (CGES), Bulletin pédologique de la FAO, OROSTOM-Montpellier, France, 1994, P245
- [12] Wischmeier W. H., Smith D. D. et Uhland R. E., (1985) Evaluation of factors in the soil loss equation, Agron. Eng., V39, n 8, 1985, pp 458-462 et 474.

Optimum Operation of Canal Barrages

Emad Hamdy Imam¹, Sherine Ahmed El Brardei²

¹Professor, Department of Construction and Architectural Engineering
The American University in Cairo, Egypt
E-mail: eimam@aucegypt.edu

²Assistant Professor, Department of Construction and Architectural Engineering
The American University in Cairo, Egypt
E-mail: sbaradei@aucegypt.edu

ABSTRACT

Operation of canal barrages used to control their upstream water level at target values requires the identification of feasible operation scenarios for all range of canal flow rates. To investigate the possible operating scenarios and identify the feasible and favorable ones, a hydraulic model is developed to simulate the flow under radial gates of canal barrages with relatively low heads. The hydraulic model is based on the energy-momentum approach to simulate flow under free and submerged jumps conditions. For any discharge, all possible operating scenarios are analyzed and those ones that violate the safe operating criteria (Froude number of jump, location of jump, velocity at exit of stilling basin) are excluded. The hydraulic model was applied to an intermediate barrage across a irrigation canal in Egypt for three typical flowrates (low, medium, and large). In the three cases all operating scenarios were investigated and their relevant hydraulic parameters were characterized. The feasible operating scenarios were identified.

Keywords: radial gates, barrages, irrigation canal, hydraulic jump, submerged and free flow, submergence factor, stilling basins.

1. INTRODUCTION

Barrages and cross regulators use radial or sluice gates to control and raise water levels in their upstream reaches of streams and irrigation canals with mild slopes. These structures are essential for the hydraulic control of these channels to allow the proper feeding of lateral channels or offtakes at all range of flow rates. These water control structures can also measure accurately discharge through them which would reduce the need for the construction of separate dedicated flow measurement structures [1].

The key function of these gated- structures is to maintain the upstream water levels within the desirable range to ensure proper feeding of off takes or to allow navigation when the canal discharges are not large enough to maintain deep normal depths. Barrages are designed as multi vent structures to limit the span of their gates and to provide flexibility in their operation under a variety of operating discharges upto the design maximum discharge. These gated structures usually include stilling basins of various types [6] downstream of the gates to protect the channel bed in the transition between the shooting under-gate flow and the downstream flow. Stilling basins with additional accessories aim to form efficient hydraulic jumps at all operating conditions.

The operating rules for these cross regulators aim to open a selected number of their gates with a certain opening to maintain the target upstream levels while

ensuring the formation of safe hydraulic jumps within the design length of their stilling basin for all combinations of channel discharges and tail water levels.. The number of gates to be opened and the gate opening are the key operating parameters for that purpose. The United States Bureau of Reclamation SBR [6] has proposed modular designs for stilling basins subject to jumps with different Froude's Number. In streams and irrigation canal with mild slopes, prevailing Froude numbers are usually less than 5. Also, tail water depths are usually relatively large which produce hydraulic jumps of the submerged type under most operating conditions.

Radial gates are gaining wider use in comparison to sluice gates especially for medium to large spans. Flows under the gate may be free or submerged depending on the tail water depth. [4]. Computations of flow conditions under radial gates and the formation of hydraulic jumps under free-flow conditions are available in standard references and have reasonable accuracy and ease of use [5], but computations for gates with submerged jumps are often inaccurate. Recent research on radial gates with submerged hydraulic jumps has provided reliable governing equations for computing such cases [2] and [3].

This research develops a hydraulic model to select the feasible operating actions (number of opened gates and gate openings) for control structures with radial gates accounting for all combinations of stream discharges and tail water levels. The key factor is to ensure that the

stilling basin and channel boundary are subject to safe hydraulic conditions.

2. HYDRAULIC MODEL OF FLOW THROUGH THE BARRAGE

2.1. Governing Equations

Figure 1 depicts the flow under a radial gate for both free and submerged flow conditions. Applying the energy equation across the gate, Wahl [1] derived equation 1 to relate the key hydraulic parameters for the case of free flow.

$$Q_g = \delta w b_c \sqrt{\frac{2g(H_1 - \delta w)}{1 + \xi}} \quad (1)$$

Where: Q_g = flow rate through one barrage vent (partially opened gate) (m^3/s); w = vertical gate opening (m); b_c = gate width (m); g = acceleration due to gravity (m/s^2); H_1 = energy head just upstream the gate (m); δ = the contraction coefficient for the flow beneath the gate; and $1 + \xi$ = energy loss and velocity distribution factor.

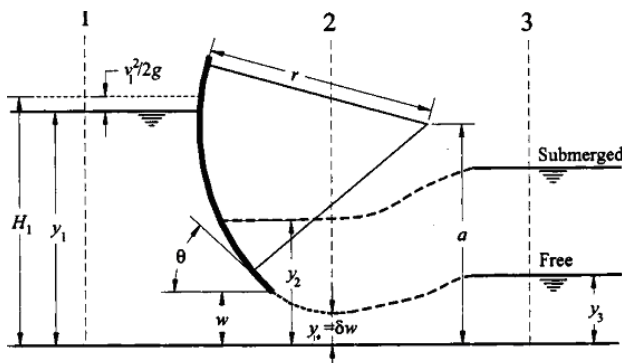


Figure 1: Definition sketch for free and submerged hydraulic jump formed under radial gate

Wahl [1] fitted equation 2 to Buyalski free flow data compute the contraction coefficient δ as a function of the gate leaf angle θ at the edge of the opening in radians for the case of sharp-edged gates.

$$\delta = 1.001 - 0.2349\theta - 0.1843\theta^2 + 0.1133\theta^3 \quad (2)$$

The term $1 + \xi$ can be estimated as a function of Reynolds Number R using equation 3 [3].

$$1 + \xi = 1 + 0.15e^{-5.1 \times 10^{-6} R} \quad (3)$$

where; e = base of natural logarithms; R = Reynolds number = VR_h/ν ; V = characteristic velocity determined at the gate opening and ν is defined as $Q_g / (b_c w)$; and R_h = hydraulic radius just upstream from the gate, between

the gate piers, $R_h = b_1 y_1 / (b + 2y_1)$. The upstream channel width is b_1 , and the upstream flow depth is y_1 .

For the case of submerged flow, Wahl [1] combined both the energy equation across the gate and the momentum equation across the submerged jump to derive equation 4.

$$Q = \delta w b_c \sqrt{\frac{2g(H_1 - y_2 + E_{corr})}{1 + \xi}} \quad (4)$$

Where;

y_2 = flow depth at the now submerged vena contracta location in meters; E_{corr} = energy correction term that accounts for the reduced velocity head of the jet.

Wahl [1] presented equation 5 to refine the energy correction factor based on calibration data for submerged radial gates.

$$E_{corr} = e^{-6.78(Y_2 - Y_j) / H_1} \quad (5)$$

Where y_j = jet thickness at the vena contracta = δW .

Belaud [2] applied the momentum principle between y_2 and y_3 and derived equation 6.

$$S = \sqrt{S'^2 + 4a^2 C_c^2 (1 - S) \left(\frac{1}{S'} - \frac{1}{a C_c} \right)} \quad (6)$$

Where $S' = h_3/H_0$, $S = h_2$ and $a = W/H_0$. At large submergence, h_2 and h_3 are almost equal, and they largely deviate for smaller values of S .

2.2. Identification of Feasible Operating Actions

A barrage should be operated to achieve a target upstream water level which is usually set to facilitate flow diversion to off-takes or to maintain adequate navigation drafts in its upstream reach. Such set target levels are usually constant or they may be reduced at very low flow. To achieve these target levels, the number of partially open gates is selected and the corresponding gate opening should be computed to produce the desired upstream level for the passing channel flow, Q_{CH} . The reach downstream the barrage shall develop a tail water depth corresponding to Q_{CH} that may be either uniform flow depth or a higher depth as a result of control by another downstream structure. For channels with mild slopes, which is usually the case where barrages or regulators are used, the tail water depth, y_3 , existing at the exit to the barrage stilling basin affects the type of the formed hydraulic jump. When y_3 is equal to the downstream conjugate depth (y_{2-conj}) of a jump starting at the vena contracta immediately downstream the gate; then an ideal free

jump is taking place over the stilling basin. If y_3 is smaller than y_{2-conj} , then the jump moves away from the gate and might extend beyond the stilling basin. This “sweep-out” (SO) jump, is not accepted operationally and should be avoided. If y_3 is larger than y_{2-conj} then a submerged hydraulic jump (SJ) will take place. For this case, a different gate-discharge equation shall be used and the tail water affects the upstream water depth. The downstream conjugate depth of a free jump y_{2-conj} is computed from the classical jump equation [5]

$$y_{2-conj} = \frac{y_j}{2} (\sqrt{1 + 8F_1^2} - 1) \quad (4)$$

Where: y_j = upstream conjugate depth of the free jump

at the vena contracta = δW ;

F_1 = Froude number at the upstream end of the jump =

$$\frac{V_j}{\sqrt{gy_j}} ; V_j = \text{velocity at the beginning of the jump} =$$

$$\frac{Q_g}{b_g \delta W} ; Q_g = \text{discharge passing through the gate; and}$$

b_g = gate width.

2.4. Assessment of Feasible Operating Actions

By varying the number of opened gates, and the gate opening, several alternative operating actions are possible and can achieve the set target of the upstream water level for a certain channel discharge. However, these alternative operating actions may not safe for the stilling basin and the downstream channel.

For free hydraulic jumps, the form of the jump and the possible problems it may cause to the channel and the stilling basin is related to the Froude number F_1 [6]. For F_1 between 1.0 and 1.7, there is only a slight difference in the conjugate depths, and a slight ruffle appears on the water surface. Starting with F_1 equal 1.7 small rollers develop on the surface and intensify upto F_1 of 2.5. These “pre-jumps” pose no particular problems to the stilling basin [6] as the water surface is smooth and the velocity distribution is fairly uniform. Research on jumps with Froude number in this range does not detail the effect of tail water submergence on these jumps, but it is anticipated that the behavior will be similar to flow through submerged slots.

For free jumps with F_1 in the range 2.5 to 4.5, the entering jet oscillate from bottom to surface with no regular period which produces large waves of irregular period. Such waves can cause damage to channels side slopes and their protection. Therefore, it is recommended to restrict the potential to form jumps in this range. Again, the effect of submergence on these jumps is not well reported in the literature which makes it safer to retain the previous practical consideration.

Free jumps with F_1 in the range 4.5 to 9.0 are well balanced and their performance is at its best. However, submerged jumps in this range perform less efficiently than their corresponding free ones.

To select the optimum operating actions, several numbers of opened gates are investigated, and the respective gate openings are computed based on the governing equations for free and submerged flow under radial gates. Operating cases with sweep-out jumps are excluded. Free or submerged jumps with F_1 in the range 2.5 to 4.5 are avoided due to the possible generation of damaging waves. For every number of gates investigated, the velocity at the end of the jump is estimated. The velocity at the end of the stilling basin, the first and second zones of the multiple jetissuing from the opened vents is estimated by assuming a 1 to 5 dispersion line. Cases where such exit velocities exceed the scour resistance of the protection zones are also excluded (3 m/s at inlet to the PC protection and 2 m/s at inlet the stone pitching zone).

3. CASE STUDY OF SERIAKOS BARRAGE

3.1. Characteristics of SB and Canal

The Ismailia Canal is a fresh water canal used for irrigation, navigation and domestic use in Egypt. It is supplied with Nile water and runs for a distance of more than one hundred kilometer eastward towards Suez Canal. The canal carries presently a minimum flow of 10 Mm³/day (116 m³/s), and will be enlarged to convey future maximum discharge of 37.7 Mm³/day (436 m³/s). The first reach of the canal is 11 km long and ends at Seriakos barrage (SB). The canal has a trapezoidal cross-section with a future widened bed width of 70 meters, a longitudinal slope of 11 cm/km, and an estimated Manning's coefficient of 0.025. The bed level of the downstream canal reach is (9.00). The tail water level of the SB follows a rating curve closely according the uniform uncontrolled depth in the reach.

The SB has 10 vents each 5 meters clear width, and fitted with radial gates with radii 9.0 meters and pins at heights 6.0 meters. The stilling basin has a bed level of (9.00) and a total length of 50 meters for its RC floor. The piers separating the gates extend for 20 meters. The concrete apron of the basin is followed by 20 meters of perforated PC slab, and another 20 meters of placed pitching stones.

3.3 Feasible Operating Scenarios

Table 1 summarizes the key hydraulic parameters for each operating scenario that can be used to maintain the upstream water level of SB at (15.40) for the case of minimum flow of 10 Mm³/day. For a number of opened gates of 9 or less with gate openings of 0.32 to 1.05 m, all hydraulic jumps are sweep-out unacceptable ones.

The tail water depth for the wide canal is relatively shallow at such a low flow to form the jump just downstream the gates. Therefore all barrage 10 gates should be opened at 0.29 meters to form a submerged jump with a Froude number of 7.62. The velocity at the exit of the stilling basin is 1.02 m/s which is very safe.

Table 2 presents the results for the case of medium flow of 20 Mm³/day. Six or less gates form sweep-out unacceptable jumps. Seven gates produce a free jump just at the gate but within the undesirable range of F_1 . Eight gates with an opening of 0.82 meters produce a submerged jump with $F_1=4.19$ which can be marginally tolerated. The velocity at the exit of the stilling basin is 1.68 m/s which is acceptable. Ten gates can also be used with an opening of 0.7 meters. F_1 equals 4.21 at the vena contracta of the submerged jump, and the velocity at the exit to the basin is 1.34 m/s which is fairly safe.

Table 3 shows the operating scenarios for the case of maximum barrage flow of 37.7 Mm³/day. The acceptable range of opened gates is from 7 to 10 gates with corresponding openings of 2.44 to 1.83 respectively. F_1 of submerged jumps formed for these operating cases is nearly 2, which corresponds to "pre-jump" pose no particular problems to the stilling basin [6] as the water surface is smooth and the velocity distribution is fairly uniform. The velocity at the exit from the stilling basin ranges from 2.49 to 1.74 m/s which is safe the PC protection zone.

4. CONCLUSION

The hydraulic model suggested can simulate the flow under radial gates of canal barrages with relatively low heads. The hydraulic model is based on the energy-momentum approach to simulate flow under free and submerged jumps conditions. For any discharge, all possible operating scenarios are analyzed and those ones

that violate the safe operating criteria (Froude number of jump, location of jump, velocity at exit of stilling basin) are excluded. The hydraulic model was applied to an intermediate barrage across an irrigation canal for three typical flow rates (low, medium, and large). In the three cases all operating scenarios were investigated and their relevant hydraulic parameters were characterized. The feasible operating scenarios were identified.

REFERENCES

- [1] Whal, Tony L. "Refined Energy Correction for Calibration of Submerged Radial Gates", ASCE, Journal of Hydraulic Engineering, Vol.131, No. 6, pp. 457-466, June 2005.
- [2] Belaud, G., Cassan L., and Baume, J. "Calculation of Contraction Coefficient under Sluice Gates and Application to Discharge Measurement", ASCE, Journal of Hydraulic Engineering, Vol. 135, pp. 1086-1091, December 2009.
- [3] Clemmens, A.J., and Strelkoff, T.S., and Replogle, J.A. "Calibration of Submerged Radial Gates", ASCE, Journal of Hydraulic Engineering, Vol. 129, No. 9, pp.680-687, September 2003.
- [4] Lin, C.H, and Yen, J.F., and Tsai, C.T. " Influence of Sluice Gate Contraction Coefficient on Distinguishing Condition", ASCE, Journal of Irrigation and Drainage Engineering, Vol. 128, No. 4, pp. 249-252, July/August 2002.
- [5] Chow, VenTe, "Open Channel Hydraulics", McGraw Hill, 1959.
- [6] Peterka, A. "Hydraulic Design of Stilling Basins and Energy Dissipators", Engineering Monograph No. 25, United States Bureau of Reclamation, Denver, 1984.

APPENDIX

Table 1: Number of opened gates, gate opening, and jump characteristics (Case of $Q=10 \text{ Mm}^3/\text{day}$; $TWL=(11.27)$)

No. of Opened Gates	Gate Opening W	Froude Number of Free Jump, F_1	Conjugate Depth of Free Jump, Y_{2-conj}	Jump Condition	Jet Velocity of free jump, V_1	Contraction Coefficient ?	Submergence Ratio at vena contracta, S	Submergence Ratio of Tail Water, S'	Gate Lip Submergence	Velocity at Exit of stilling basin,
3	1.05	3.92	3.72	SO	10.53	0.70	--	--	--	3.40
4	0.75	4.76	3.33	SO	10.82	0.71	--	--	--	2.55
5	0.60	5.26	2.98	SO	10.79	0.72	--	--	--	2.04
6	0.50	5.71	2.73	SO	10.73	0.72	--	--	--	1.70
7	0.43	6.10	2.53	SO	10.65	0.72	--	--	--	1.46
8	0.36	6.93	2.43	SO	11.09	0.72	--	--	--	1.27
9	0.32	7.33	2.30	SO	11.06	0.72	--	--	--	1.13
10	0.29	7.62	2.17	SJ	10.27	0.73	0.17	0.35	3.67	1.02

• *SO=Sweep-out jump **SJ=Submerged jump

Table 1: Number of opened gates, gate opening, and jump characteristics (Case of $Q=20 \text{ Mm}^3/\text{day}$; $TWL=(12.45)$)

No. of Opened Gates	Gate Opening W	Froude Number of Free Jump, F_1	Conjugate Depth of Free Jump, Y_{2-conj}	Jump Condition	Jet Velocity of free jump, V_1	Contraction Coefficient ?	Submergence Ratio at vena contracta, S	Submergence Ratio of Tail Water, S'	Gate Lip Submergence	Velocity at Exit of stilling basin,
5	1.3	3.48	3.99	SO	10.33	0.69	--	--	--	2.68
6	1.05	3.92	3.72	SO	10.53	0.70	--	--	--	2.23
7	0.89	4.26	3.47	Free Jump	10.56	0.70	--	--	--	1.92
8	0.82	4.19	3.16	SJ	9.99	0.71	0.26	0.54	2.03	1.68
9	0.76	4.15	2.91	SJ	9.55	0.71	0.31	0.54	2.60	1.49
10	0.70	4.21	2.72	SJ	9.30	0.71	0.34	0.54	3.13	1.34

Table 1: Number of opened gates, gate opening, and jump characteristics (Case of $Q=37.7 \text{ Mm}^3/\text{day}$; $TWL=(14.00)$)

No. of Opened Gates	Gate Opening W	Froude Number of Free Jump, F_1	Conjugate Depth of Free Jump, Y_{2-conj}	Jump Condition	Jet Velocity of free jump, V_1	Contraction Coefficient ?	Submergence Ratio at vena contracta, S	Submergence Ratio of Tail Water, S'	Gate Lip Submergence	Velocity at Exit of stilling basin,
7	2.44	1.96	3.72	SJ	7.78	0.66	0.56	0.78	1.43	2.49
8	2.2	1.98	3.42	SJ	7.48	0.66	0.59	0.78	1.73	2.18
9	2.0	2.0	3.18	SJ	7.26	0.67	0.60	0.78	1.99	1.94
10	1.83	2.04	2.99	SJ	7.09	0.67	0.62	0.78	2.18	1.74

Development of Biochemical Acidogenic Potential Test for Evaluating WAS Digestibility

Peiman Kianmehr^{1*}, Wayne Parker², Peter Seto³

¹Department of Civil Engineering, American University in Dubai, UAE

²Department of Civil and Environmental Engineering, University of Waterloo, Canada

³Wastewater Technology Centre, Environment Canada, Burlington, Ontario, Canada

* Department of Civil Eng., American University in Dubai, Dubai, UAE, PO Box 28282 (Email: pkianmehr@aud.edu, Tel: 97143999000 Ext:449)

ABSTRACT

The potential to use the results of biochemical acid potential (BAP) tests to predict the ultimate digestibility of raw and pretreated waste activated sludge (WAS) was investigated. The ultimate methane production from biochemical methane potential (BMP) tests that were conducted on raw and pretreated samples which spanned a range of biodegradability was found to be linearly related to the both volatile fatty acid (VFA) and soluble COD production in corresponding BAP tests. In addition, a linear relationship between NH₄-N production in the BMP and BAP tests was also observed. Despite the linear nature of the relationships, the production of methane in the BMP tests was not equal to the production of VFAs in the BAP tests. WAS samples with low digestibility had ultimate CH₄ yields that were greater than the VFA yields in BAP tests while sludges with high digestibility had lower CH₄ yields than the corresponding VFA yields. This trend contrasted with the NH₄ results where the yields in the BAP tests were consistently less than those observed in the BMP tests. It was hypothesized that the varying relationship between CH₄ and VFA yields was due to the inhibition of anaerobic oxidation of long chain fatty acids (LCFAs) in the BAP tests. LCFAs would be converted to CH₄ in BMP tests but produced as digestion intermediates in the BAP tests and not measured as part of the VFA yield. Hydrogen and acetate were identified as the two most likely intermediates that would accumulate in the BAP tests which would cause inhibition. A stoichiometric model was assembled to facilitate an improved understanding of the biodegradation processes in the BAP and BMP tests. When the model was applied to the BAP tests the anaerobic oxidation of LCFAs and propionate and methanogenesis were excluded from the model. The model was employed to estimate the extent of degradation of lipids, carbohydrates and proteins in the batch tests as a function of the ultimate biodegradability of the sludges. The degradation of lipids was found to decrease while the degradation of carbohydrates and proteins was found to increase as the digestibility of the sludges increased. The varying ratio of lipid to protein and carbohydrate degradability with increasing digestibility of the sludges was found to describe the relationship between VFA production and CH₄ production in the BAP and BMP tests respectively.

Keywords: Anaerobic digestion, waste activated sludge pretreatment, characterization tests, model

1. INTRODUCTION

There is an increasing interest in sludge pretreatment processes that are employed to enhance the digestibility of waste activated sludges (Liu et al., 2009 and Braguglia et al., 2008). However, the ability of a given pretreatment to enhance digestibility has been found to be site-specific and will likely vary with the operating conditions of the activated sludge process from which the sludges are generated (Khanal et al., 2007). There are currently no established methods for predicting the impact that a pretreatment process will have on the digestibility of sludges. Hence, it is common to conduct pilot tests to establish the extent to which sludge digestion will be enhanced. Full scale pilot testing is expensive as compared to batch testing and, with the inherent variability in these systems, it is often difficult to accurately estimate the extent of enhancement that a pre-treatment process is capable of providing.

Biochemical methane potential (BMP) tests are small scale batch tests that can be employed to estimate the

ultimate digestibility of sludges (Shelton and Tiedje, 1984 and Jeong et al., 2005). In this regard, these tests can be conducted under relatively controlled conditions and parameters such as pre-treatment intensity can be evaluated in parallel. However, BMP tests require long term operation (50-70 days) to estimate ultimate digestibility. Gas phase measurements are required and this adds to the complexity and lab equipment that is required to conduct the tests. In addition, successful operation of BMP tests requires that a balance be maintained between the rate of acidification and methanogenesis processes. An imbalance can result in the accumulation of intermediates such as volatile fatty acids (VFAs) that can inhibit the methanogenesis process (Kianmehr et. al., 2008; Kianmehr et. al., 2009).

The biochemical acid potential (BAP) test is an alternative batch digestion test where methanogenesis is inhibited (Martin Ruel et al., 2002). In the BAP test the production of VFAs is monitored as an indicator of the extent to which the anaerobic digestion process will proceed with a given sludge type. A significant benefit

of the BAP test is that it can be conducted in a relatively short period of time (6-10 days) and that only liquid phase measurements are required. In addition, the BAP test is not dependent upon the activity of methanogens and hence the accumulation of inhibitors is not considered to be as challenging for these tests as they are for BMP tests. As the VFAs that are produced in BAP tests would be converted to CH₄ in BAP tests it would be expected that there would be a strong relationship between these responses. However this relationship has not been explored for waste activated sludges.

2. APPROACH

Three sequencing batch reactors (SBRs), each with a volume of 175 L, were operated on screened municipal wastewater at an hydraulic residence time (HRT) of 9.3 hours and SRTs of 1.95, 7 and 15 days respectively. The SBRs were employed as a source of WAS for all of the testing conducted in this study. WAS samples that were generated with different SRTs were used to examine the validity of the BAP test for a range of sludge properties. The pretreatment of WAS samples can provide sludges with different fractions of readily and slowly biodegradable material. Sonication and ozonation were applied as models of physical and chemical pretreatment to examine the validity of the BAP test to characterize pretreated sludges with different rates of biodegradation.

WAS samples from the SBRs were treated by sonication at 45°C in a bench scale apparatus with an operational frequency of 20 kHz and a maximum amplitude of 250 µm. For the unit employed in this study sonication times of 5, 10, 25 and 45 minutes corresponded to ultrasound intensities of 1111, 2222, 5555 and 9999 kJ/L respectively. Ozonation was achieved by diffusing ozone into a sealed glass reactor containing 1100 ml of sludge. Both of the units were operated in a batch mode and for each pre-treatment process a range of treatment intensities were evaluated by collecting samples at different times as the treatment progressed. Additional information about changes in the levels of readily biodegradable material and rate of biodegradation with these pretreatment technologies are discussed in Kianmehr et al. (2008) and Kianmehr et al. (2009).

BAP and BMP tests were conducted in serum bottles with a volume of 500 ml containing 250 ml of sludge sample and 50 ml of anaerobically digested sludge and incubated at 35 °C. BAP and BMP tests containing 300 ml of anaerobically digested sludge were also conducted as controls. Duplicate bottles were employed for each BMP or BAP test. The duplicate serum bottles were employed for liquid sampling and gas measurements separately and sacrificed at the end of test for analysis of digested samples and investigation of the reproducibility of experiments.

Liquid samples were regularly taken by a syringe with a large needle (diameter > 1mm) for measurement of pH, TCOD, filtered COD, TKN and NH₄-N (APHA, 1995). The concentration of acetate, propionate, butyrate, iso butyrate, valerate and iso valerate in liquid samples taken from BAP tests were measured by ion chromatography (Dionex IonPac AS15) with conductivity detection and the total concentrations were converted from VFA mass to COD mass. The generated gas was regularly discharged from bottles for measurement of gas volume with a manometric device. The CH₄ content of the gas was measured by gas chromatography and expressed as COD mass for comparison with TCOD values. Gas volume was measured every day due to considerable accumulation of biogas in bottles in the early days of digestion. Liquid sampling and all gas and liquid analysis were conducted every two days for the first 10 days of digestion. After 10 days of digestion, the measurement and analysis were conducted less frequently depending on the rate of the digestion process.

The profile of ammonia generation in BAP tests was compared to that in BMP tests for most samples. The responses were quite similar (± 4% difference). Hence the ammonia results from both the BAP and BMP tests were employed when investigating the relationship between ammonia and other responses.

3. RESULTS AND DISCUSSION

In this part of study, the VFA and ammonia responses from the BAP tests were compared with the ultimate biodegradability of sludge as measured by the BMP tests. A range of raw and pretreated WAS samples with different SRTs were employed to investigate relationships for sludges with different rates of biodegradation and ultimate biodegradability. The relationship between the VFA and ammonia responses in the early period of the BAP tests and the ultimate ammonia and methane yields in the BMP tests was investigated. A consistent relationship between these responses for the BAP and BMP tests would suggest that the BAP test could be employed as a short term test for estimating the ultimate biodegradability of WAS.

The concentrations of accumulated VFAs after 6 and 10 days in the BAP tests were compared to the ultimate generation of methane in BMP tests (Figure 1). Both responses are presented as fractions of the total COD of the sludge. From Figure 1, it can be seen that for both data sets there was a linear relationship between the concentrations of accumulated VFAs and ultimate methane generation. The best fit linear models can be described by Equations 1 and 2.

$$U_{BMP}^{Methane} = 0.52 \times U_{BAP,6}^{VFA} + 0.23 \quad (1)$$

$$U_{BMP}^{Methane} = 0.50 \times U_{BAP,10}^{VFA} + 0.22 \quad (2)$$

Where:

$U_{BAP,6}^{VFA}$ = VFA fraction in 6 day BAP test (mg COD/mg COD)

$U_{BAP,10}^{VA}$ = VFA fraction in 10 day BAP test (mg COD/mg COD)

$U_{BMP}^{Methane}$ = Methane yield in a BMP test (mgCOD/mgCOD).

Statistical investigations revealed that, the model based on the 10 day BAP test that is described by Equation 2 was deemed to be a better fit of the model to the data as compared to the model described by Equation 1.

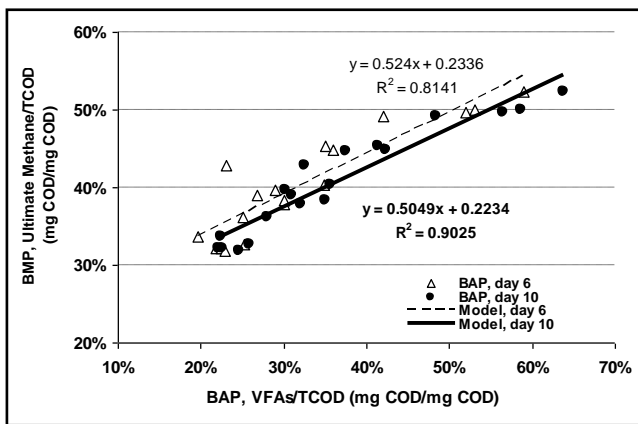


Figure 1: Relationship between methane in BMP tests and VFA responses in 6 day and 10 day BAP test

The adequacy of the linear models for predicting $U_{BMP}^{Methane}$ by the concentration of accumulated VFAs ($U_{BAP,6}^{VA}$) in day 6 and day 10 of the BAP tests was investigated by statistical tests (Montgomery, 2001). The model based on the 10 day BAP test was deemed to be acceptable and was preferable to the model based on the shorter BAP test.

Figure 1 and equation 2 reveal that $U_{BAP,10}^{VFA}$ values were significantly less than $U_{BMP}^{Methane}$ values for all samples with $U_{BMP}^{Methane}$ values smaller than 50%. The difference in responses could be due to the presence of slowly biodegradable material that took longer than 10 days to biodegrade. It also could have been due to inhibition that resulted in the production of non-measured intermediates or the lack of measurement of responses such as hydrogen in the BAP tests. However, the values of $U_{BAP,10}^{VFA}$ were greater than $U_{BMP}^{Methane}$ for sludges with $U_{BMP}^{Methane}$ values greater than 50%. If the VFAs generated in the BAP test were converted to CH_4

in the BMP tests, it would be expected that the values would be similar. The differences between the VFA and CH_4 values could be partly due to uptake of VFAs and conversion of them to non-biodegradable decay products in BMP tests. The underlying reasons for the differences between $U_{BAP,10}^{VFA}$ values and $U_{BMP}^{Methane}$ values are investigated subsequently.

The measurement of COD is much simpler than measurement of VFAs and hence the prediction of ultimate methane generation on the basis of soluble COD in day 10 of the BAP tests was investigated. Figure 2 shows the relationship between accumulated VFA and SCOD in day 10 of the BAP tests. The results reveal that there was a linear relationship between VFA and SCOD in day 10 (Figure 2) and the best fit linear model is shown in Equation 3.

$$C_{BAP,10}^{VA} = 0.61 \times C_{BAP,10}^{SCOD} + 359.5 \quad (3)$$

Where:

$C_{BAP,10}^{VFA}$ = VFA concentration based on COD (mg COD/L) in a 10 day BAP test

$C_{BAP,10}^{SCOD}$ = Soluble COD (mg COD/L) in a 10 day BAP test

Figure 2 and Equation 3 reveal that the $C_{BAP,10}^{SCOD}$ values were consistently greater than $C_{BAP,10}^{VFA}$ values for all sludges. The difference between the responses could have been partially due to the presence of soluble material that required more than 10 days to biodegrade. It also could have been due to inhibition of metabolic pathways that caused accumulation of intermediate products such as LCFAs that were not measured in this study. Since inhibition of the hydrogenotrophic methanogenesis process and accumulation of hydrogen is likely in BAP tests, lack of measurement of generated hydrogen in BAP tests is likely another cause of the differences. An investigation was conducted to explore the underlying reasons of the differences between the $C_{BAP,10}^{SCOD}$ and $C_{BAP,10}^{VFA}$ values and the results of investigation are subsequently presented.

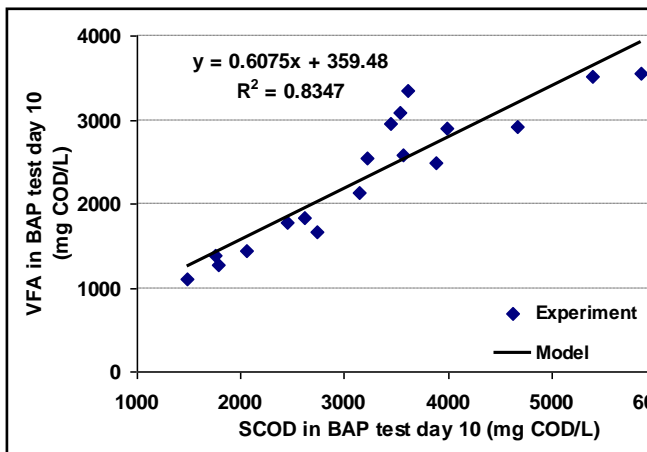


Figure 2: Relationship between soluble COD and VFA responses in BAP test

Figure 3 shows the relationship between accumulated SCOD in day 10 of the BAP tests and ultimate methane yield in the BMP tests and the best fit linear model is shown in Equation 4.

$$U_{BMP}^{Methane} = 0.51 \times U_{BAP,10}^{SCOD} + 0.15$$

(4)

Where:

$U_{BAP,10}^{SCOD}$ = SCOD fraction of TCOD in a 10 day BAP test (mg COD/mg COD).

$U_{BMP}^{Methane}$ = Methane yield in a BMP test (mgCOD/mgCOD).

These results indicate a reasonable fit of the model to the data. The adequacy of the linear models for predicting $U_{BMP}^{Methane}$ by $U_{BAP,10}^{SCOD}$ was investigated with the statistical tests and procedures that were previously employed for the models described in Equation 1 and 2. The statistical investigation revealed that the model was acceptable and could adequately describe the relationship between $U_{BMP}^{Methane}$ and $U_{BAP,10}^{SCOD}$ values.

Figure 3 and Equation 4 reveal that the $U_{BMP}^{Methane}$ values were 1.4% to 17.3% smaller than $U_{BAP,10}^{SCOD}$ values for raw and pretreated sludges. Pretreatment may solubilize particulate inert COD and hence impact on the value of $U_{BAP,10}^{SCOD}$ without increasing the ultimate methane production (Kianmehr et. al., 2008 and Kianmehr et. al., 2009). This may have contributed to the scatter of data when plotting $U_{BMP}^{Methane}$ versus $U_{BAP,10}^{SCOD}$ in Figure 3.

Figure 3 also shows the relationship between $U_{BMP}^{Methane}$ and $U_{BAP,10}^{SCOD}$ for the raw sludges. As can be seen in Figure 3, the $U_{BMP}^{Methane}$ values of this subset of the data

were 1.4% to 12.3% smaller than $U_{BAP,10}^{SCOD}$ values for raw sludges and the r^2 value (0.937) for the linear model for raw sludges in Figure 3 was not much better than r^2 value (0.9) for the model described in Equation 4. These results suggest that solubilization of inert material by pretreatment was likely partially responsible for the difference in responses and the scatter of the data. The results of an investigation that was conducted to explore the underlying reasons of the differences between $U_{BMP}^{Methane}$ and $U_{BAP,10}^{SCOD}$ values are presented subsequently.

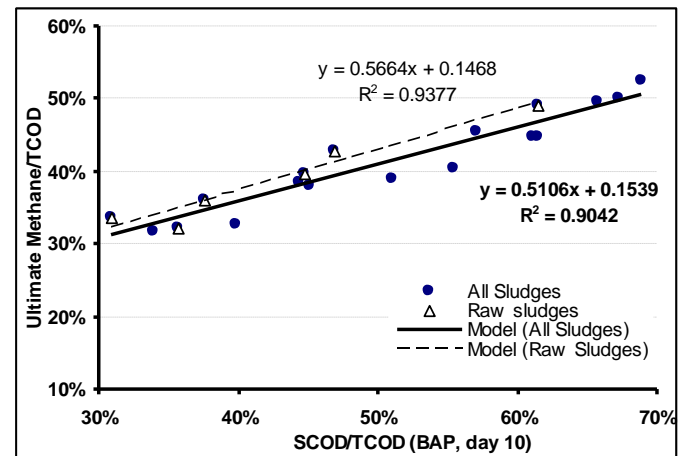


Figure 3: Relationship between soluble COD and methane responses in BAP and BMP tests for all sludges and raw sludges

A comparison of the r^2 values, and the standard errors attributed to estimated slopes and intercepts in the models described in Equations 2 and 4 revealed that there was no clear evidence to suggest that VFA responses were better than SCOD data for predicting ultimate methane generation. Therefore, measurement of SCOD in the BAP tests and employing the linear model described in Equation 4 is a short, simple and widely applicable test to predict the anaerobic biodegradability of sludges as compared to using methane and VFA responses in BMP and BAP tests.

A substantial portion of the organic material that is biodegradable in WAS is proteinaceous. Hence the ammonia and TKN data from the BAP tests were employed to assess the use of BAP tests to predict the ultimate biodegradability of proteinaceous material. Figure 4 shows the ammonia concentrations in day 10 of the BAP tests versus the ultimate ammonia concentrations in the BMP tests. Both responses were normalized with respect to the TKN in the samples. The results indicate that there was a linear relationship between the responses and the best fit linear model was described by Equation 5.

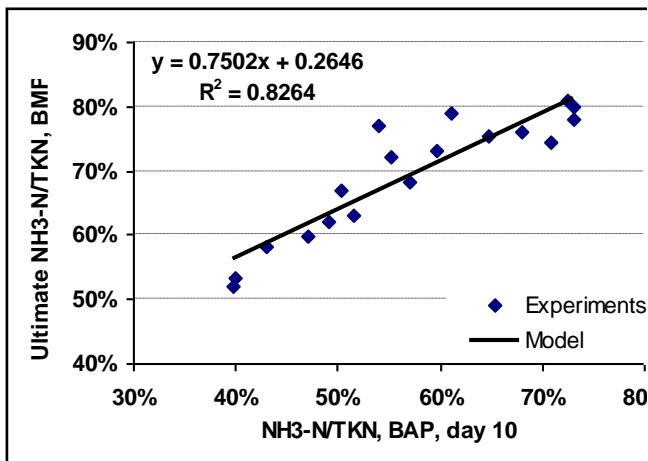


Figure 4: $\text{NH}_3\text{-N}$ fractions of TKN in BMP tests versus 10 day BAP tests

$$U_{BMP}^{Ammon} = 0.75 \times U_{BAP,10}^{Ammon} + 0.26$$

(5)

Where:

$U_{BAP,10}^{Ammon}$ = $\text{NH}_3\text{-N}$ fraction of TKN in 10 day BAP test

U_{BMP}^{Ammon} = Ultimate $\text{NH}_3\text{-N}$ fraction of TKN in BMP test

A linear relationship between the ammonia concentrations in day 10 of the BAP tests and the ultimate ammonia concentration in the BMP tests was observed when both responses were normalized with respect to the TCOD of the sludges. These responses may be easier to employ in practice as the additional measurement of TKN is not required. The best fit linear model is presented in Equation 6. Statistical investigation demonstrated the adequacy of both models mentioned in Eq. 5 and Eq. 6.

$$U_{BMP}^{Ammon} = 0.74 \times U_{BAP,10}^{Ammon} + 0.026$$

(6)

Where:

$U_{BAP,10}^{Ammon}$ = $\text{NH}_3\text{-N}$ fraction of TCOD in 10 day BAP test

U_{BMP}^{Ammon} = Ultimate $\text{NH}_3\text{-N}$ fraction of TCOD in BMP test

Figure 4 reveals that all $U_{BAP,10}^{Ammon}$ values were consistently less than the U_{BMP}^{Ammon} values (i.e. 7.8% to 16.5% of the TKN). The differences in values were likely due to the presence of slowly biodegradable proteinaceous material that took longer than 10 days to biodegrade.

The relationships between the BAP test results and the ultimate biodegradability of WAS as indicated by the BMP results could be effectively employed to characterize WAS biodegradability on the basis of the relatively short term BAP tests. However, the BAP responses (i.e. VFA production) did not directly correspond to CH_4 production in the BMP tests. A

review of the relationships reveals that they varied with the biodegradability of the WAS. For instance, the VFA yields in the BAP tests were less than the CH_4 yields in the BMP tests for samples with low biodegradabilities while this relationship reversed for high biodegradabilities. In addition, VFA and sCOD data from the BAP tests suggested the accumulation of intermediates that were not measured by the VFA analyses.

On the basis of these observations, it was hypothesized that inhibition of selected biochemical pathways had occurred in the BAP tests. The inhibition likely resulted in the accumulation of metabolic intermediates that were not measured by the VFA analysis. In addition, it was hypothesized that the composition of the biodegradable COD with respect to carbohydrates, lipids and proteins changed as the biodegradability of the WAS increased. Given the complex nature of the interactions that occur in anaerobic processes, detailed modeling was conducted to further understand the underlying causes of the observed responses.

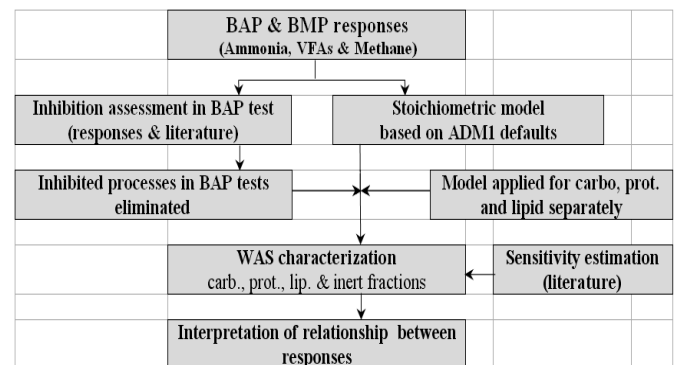


Figure 5: Overview of sludge characterization with BAP and BMP test data.

A simplified stoichiometric model was developed to fractionate the TCOD of the feed sludges based on the flow of COD through the digestion process. The model was built according to the ADM1 model employing default values for parameters and inhibited digestion processes were eliminated from the pathways. An overview of this investigation is shown in Figure 5 and each of these steps is subsequently explained.

In the BAP tests, the presence of inhibitory substances was expected and this inhibition was confirmed through the observed accumulation of VFAs. Figure 6 shows, as an example, the profile of individual VFAs generated in a BAP test (7 day SRT WAS with 5 min. sonication). From Figure 6, it can be observed that the concentrations of acetate, butyrate and propionate increased substantially with time indicating the uptake of these intermediate products was inhibited.

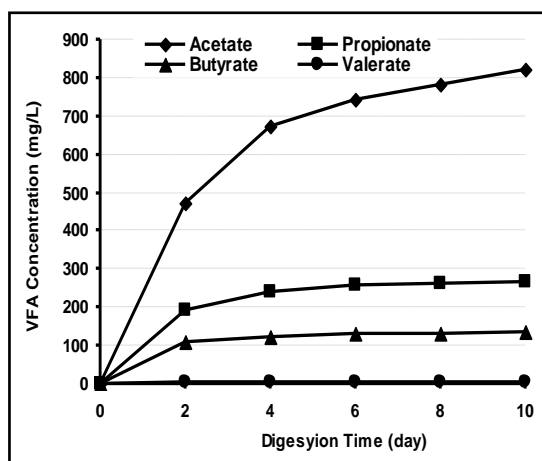


Figure 6: Concentration of Individual VFAs in BAP test

Models of inhibition due to acetate, hydrogen (H_2) and hydrogen ion (pH) were introduced by Siegrist et al. (2002) for the processes in the ADM1 model. Kianmehr (2010) conducted a preliminary estimation of the level of inhibition which may have occurred in the worst possible conditions to understand the importance of inhibition for each anaerobic digestion process and the results are summarized in Table 1. The values of “I” as the inhibition expression are multiplied with the process rates and hence a value of 1 suggests that inhibition was not expected to occur in the tests.

The values of the expression for acetate inhibition (I_{ac}) in the different steps of anaerobic digestion were calculated for the minimum and maximum measured acetate concentrations (700 and 3600 mg COD/L) that were observed in the 10 day BAP tests and are

presented in Table 1. The results indicate that the anaerobic oxidation of LCFAs ($I_{ac,5}$) and also propionate ($I_{pro,6}$) were likely to be partially inhibited by acetate in these tests. Depending on the amount of lipids in the WAS, the inhibition of LCFA oxidation may cause a significant decrease in VFA generation in the BAP test. Since the BAP test is considered as a short test, a significant decrease in the rate of a digestion process would influence the final responses at the end of the test. Hence, the responses in such conditions would not represent the biodegradability of sludge and may result in the underestimation of biodegradability of samples.

The gas analysis results indicated that methane generation was not observed in the BAP tests. Hence, higher hydrogen concentrations were expected in the BAP tests due to the inhibition of hydrogenotrophic methanogenesis. The accumulation of hydrogen gas could have further increased the level of inhibition for anaerobic oxidation of LCFAs and propionate. The stoichiometric model assembled (subsequently presented) for estimation of biodegradability of samples revealed that the accumulated hydrogen in the BAP tests was 2.4% to 9.5% of TCOD of sludge depending on the composition of the biodegradable fraction. The minimum value from this analysis was employed to estimate the levels of inhibition that would result from hydrogen gas accumulation and the results are summarized in Table 1. The results show that such concentrations of hydrogen gas could have substantially inhibited anaerobic oxidation of LCFAs and propionate ($I_{H_2,5} = 0.03$ and $I_{H_2,6} = 0.01$) in the BAP test.

Table 1: Inhibition of Anaerobic Digestion Processes in BAP tests.

rocess	Code	Acetate inhibition $700 \leq S_{ac} \leq 3600$ gCOD/m ³	H ₂ inhibition $H_{2liq} = 94.8$ mgCOD/lit	H ⁺ inhibition pH ≥ 5	NH ₃ inhibition TAN ≤ 702 (g-N m ³) & pH = 7.35
Fermentation of Amino Acids	3	N.I.	N.I.	N.I. ($I_{H,3} = 1$)	N.I.
Fermentation of Sugar	4	N.I.	N.I.	N.I. ($I_{H,4} = 1$)	N.I.
Anaerobic Oxidation of LCFAs	5	Inhibitory ($0.29 \leq I_{ac,5} \leq 0.68$)	Inhibitory ($I_{H_2,5} = 0.031$ at Max. H_{2liq} Conc.)	N.I. ($I_{pH,5} \geq 0.999$)	N.I.
Anaerobic Oxidation of Propionate (& butyrate)	6	Inhibitory ($0.29 \leq I_{ac,6} \leq 0.68$)	Inhibitory ($I_{H_2,6} = 0.015$ at Max H_{2liq} Conc.)	N.I. ($I_{pH,6} \geq 0.999$)	N.I. ($I_{NH_3,6} \geq 0.91$)
Acetotrophic Methanogenesis	7	Already Inhibited in BAP Test by BES Addition			
Hydrogenotrophic Methanogenesis	8	Already Inhibited in BAP Test by BES Addition			

N.I.: Not inhibitor

The values of pH were greater than 6.5 in all BAP tests that were conducted in this study. As indicated in Table 1, pH values of 5 and higher are not significantly inhibitory. This suggests that pH did not cause significant inhibition of any of the digestion processes in the BAP tests in this study. It can be deduced that the control of pH may not be essential in BAP tests.

Free ammonia is inhibitory to the anaerobic oxidation of propionate (Fujishima et al., 2000). Hence, a preliminary estimation of the potential for ammonia inhibition was conducted. Snoeyink and Jenkins (1980) indicated that for pH values lower than 9.3, the dominant part of total ammonia exists in ammonium form which is not inhibitory to the digestion processes. A summary of results for the highest measured pH and TAN values is presented in Table 1. The results show that ammonia may have caused a limited level of inhibition for the anaerobic oxidation processes in the BMP tests.

In summary, theoretical estimation of inhibition showed that the rate of anaerobic oxidation of LCFAs and rate of anaerobic oxidation of propionate and butyrate were likely inhibited in the BAP tests. This issue was considered when building the anaerobic digestion model and interpreting the results of BAP tests.

In addition to inhibition of some of the digestion processes in the BAP tests, a relative change in the composition of the biodegradable COD with respect to lipids, carbohydrates and proteins was likely another reason for the variable relationship between BAP and BMP responses as the digestibility of the sludges increased. For instance, the presence of lipids, whose oxidation was inhibited in the BAP tests would have resulted in higher values of $U_{BMP}^{Methane}$ as compared to $U_{BAP,10}^{VFA}$ (as shown in Figure 1). According to ADM1, a majority of lipids would eventually appear as LCFAs and hence they would not be reflected in $U_{BAP,10}^{VFA}$. The smaller difference between the values of $U_{BMP}^{Methane}$ and $U_{BAP,10}^{VFA}$ for sludges with greater levels of biodegradability could be due to a negligible contribution of lipids to the biodegradable COD of these samples.

The ultimate methane responses in the BMP tests and VFA and ammonia responses in the BAP tests together with a simplified stoichiometric model were employed to evaluate the composition of the feed sludges over a range of biodegradabilities. The characterization of sludge by ADM1 is challenging due to the complexity of the processes and the variety of components that are difficult to measure. Hence, the digestion processes in the model that were believed to be significantly inhibited were eliminated to simplify the model. For ultimate methane generation in BMP tests, it was assumed that all readily and slowly biodegradable COD

would flow through the digestion processes and eventually appear as methane or non-biodegradable decay products regardless of their rate of biodegradation. According to this assumption, the reaction kinetics were eliminated to simplify the model to a stoichiometric model. The default values in ADM1 were employed for stoichiometric and yield parameters.

Figure 7 shows the flow of COD through the digestion process as described by the default ADM1 model with the biodegradable carbohydrates, proteins and lipids each contributing 20% of the TCOD. The solid lines represent the pathways that are common between BMP and BAP tests. The dashed lines represent those reactions that occur in the BMP test which were assumed to be inhibited in the BAP test as already discussed. The accumulated value of each intermediate or final product in the BMP test is described in the related box in Figure 7. In this example 38.8% of the COD was determined to be converted to acetate. As a result of the acetoclastic methanogenesis process, acetate was converted to biomass (1.9%) and methane as byproduct (36.8%). The values for the BAP test (not shown in Figure 7) were calculated by subtracting the values attributed to the inhibited processes.

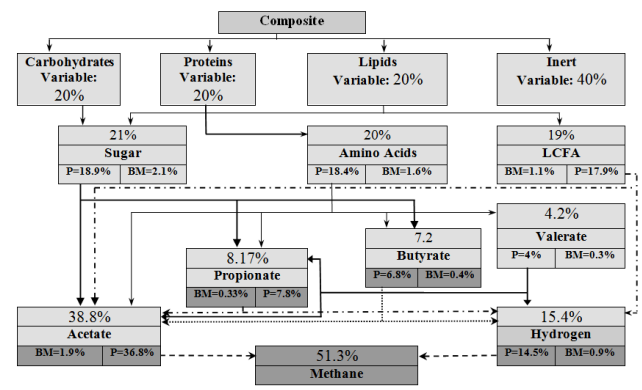


Figure 7: Example of COD distribution in BMP tests (BM – Biomass; P - Product)

VFA and ammonia generation in the BAP tests and methane generation in the BMP tests were considered as experimental responses for model calibration purposes. The VFA, ammonia and methane responses were normalized by dividing by total COD to make the responses from different sludge samples comparable. In all cases, both VFA and ammonia concentrations essentially plateaued by day 10 of the BAP test. An empirical model based on first order reactions in the batch tests was fit to the VFA profiles in the first 10 days to estimate the ultimate ammonia or VFA generation in the BAP tests. The results revealed that the ultimate responses were 0.5 to 3.8 percent greater than the corresponding responses on day 10 of digestion. Further information about this empirical model has been described by Kianmehr (2010). The fractional composition of the feed sludges with respect to non-biodegradable COD, carbohydrates, proteins and

lipids ($f_{li,xc}$, $f_{si,xc}$, $f_{ch,xc}$, $f_{pr,xc}$ and $f_{li,xc}$) were the parameters employed to fit the data in this study. The best fit values for the COD fractions were determined as those that minimized the value of the objective function described by Kianmehr (2010).

In the testing conducted in this study, CH_4 was measured using the offgas while VFAs were measured in the liquid phase. The simplified stoichiometric model was employed to predict the end products that would be expected from the three major carbon sources (carbohydrates, proteins and lipids). The simplified model was then employed to estimate the COD fractions that were present in the feed sludges based upon the results of the BAP and BMP tests.

The best-fit values of carbohydrates ($f_{ch,xc}$), proteins ($f_{pr,xc}$) and lipids ($f_{li,xc}$) and non-biodegradable fractions ($f_{si} + f_{xi}$) versus biodegradable fraction of TCOD are shown in Figure 8. From Figure 8 it can be seen that proteins contributed a substantial fraction of the biodegradable materials in all cases. In addition, the contributions of protein and carbohydrates ($f_{pr,xc}$ and $f_{ch,xc}$) increased as the biodegradability of the sludge increased. The biodegradation of carbohydrates increased from 0% to 28.4% for sludges with biodegradable fraction greater than 40% and the value of $f_{ch,xc}$ was zero for sludges with biodegradable fraction lower than that 40%.

The contribution of lipids ($f_{li,xc}$) was about 7% for low levels of biodegradability and it decreased to zero for sludges with a biodegradability of 50% and higher. The model revealed that 88.7% and 3.6% of COD from lipid substrates would be detected in BMP and BAP tests as CH_4 and VFAs respectively and hence a higher fraction of lipids in the sludge would result in greater differences between BAP and BMP results. As discussed earlier, a lower level of VFA generation was observed in the BAP tests as compared to methane generation in BMP tests when the biodegradability of the samples was smaller than 45% (Figure 1). A significant part of this difference was likely due to the presence of lipids in the sludges with low levels of biodegradability.

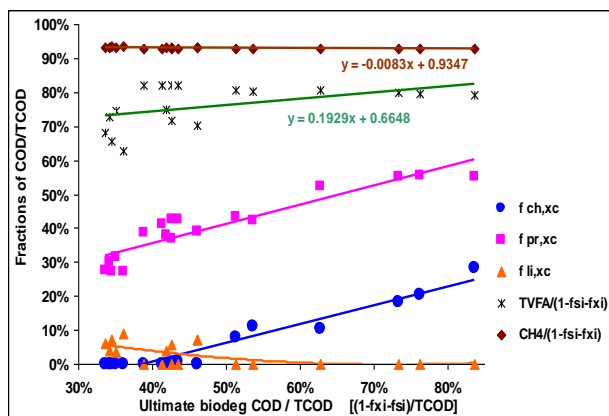


Figure 8: COD fractionation versus biodegradable COD by simplified model

From Figure 8, it can be observed that the ratio of ultimate methane generation to biodegradable fraction of TCOD in the BMP tests (shown in the figure as $CH_4/(1-fsi-fxi)$) was relatively constant for all raw and pretreated sludges regardless of the SRT of the samples or the pretreatment technology (mean and standard error of 0.931 and 0.0004 respectively). According to this result, ultimate methane generation described about 93.1% of the ultimate biodegradability. The difference between ultimate methane generation and ultimate biodegradability was due to the portion of biodegradable material that was converted into cellular mass and eventually resulted in non-biodegradable decay products.

The COD fractionation exercise was repeated using the biodegradable fraction of TKN (as NH_3-N/TKN) as the independent response. Preliminary modeling revealed that the estimated NH_3-N values were highly sensitive to the nitrogen content of the protein (N_{aa}) which had a recommended value is 0.007 in the literature (ADM1). In this part of the investigation, N_{aa} was included as a fitting parameter along with the COD fractions to find its best value.

The COD fractions that were estimated in this exercise (not shown) were similar to the results shown in Figure 8. The slopes of the lines attributed to carbohydrate, protein and lipid fractions (0.87 ± 0.13 , 0.58 ± 0.02 and -0.22 ± 0.07) were similar to the slopes of the lines in Figure 8 (0.57 ± 0.06 , 0.55 ± 0.04 and -0.12 ± 0.04 respectively). Figure 9 presents the estimated values of N_{aa} versus the biodegradable fraction of the COD. From Figure 9 it can be observed that N_{aa} decreased as the biodegradability of the samples increased. This suggests that proteins in sludges with high biodegradability had smaller nitrogen to COD ratio. Such variation of N_{aa} may be due to a change in the population and composition of bacterial from one operational condition to another. For example, the increase of SRT in a reactor causes a reduction of the F/M ratio. The scarcity of substrate in this condition can substantially reduce the population of bacteria present and subsequently change the composition of decay products and byproducts such as EPS.

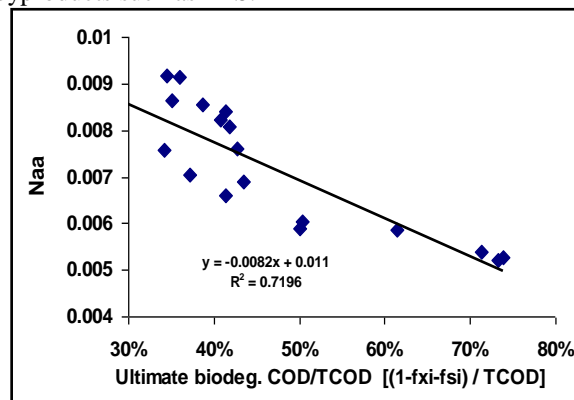


Figure 9: Nitrogen fraction of protein (N_{aa}) vs biodegradable fraction of COD

4. CONCLUSION

Linear equations were developed to describe the relationships that were observed between VFA and $\text{NH}_4\text{-N}$ in short term BAP tests and CH_4 responses in BMP tests. The equations could be employed to predict the ultimate methane and ammonia generation from WAS samples using soluble COD, VFA or ammonia responses in day 10 of BAP test. Hence, the BAP test appears to be a good indicator of WAS digestibility and is much more cost effective than performing long term BMP tests. The experimental results and theoretical estimation of inhibition revealed the anaerobic oxidation of LCFAs (LCFA uptake) is inhibited in BAP tests. This inhibition results in a significant difference between COD attributed to accumulated VFA in BAP test and COD attributed to ultimate methane generation in BMP test.

The biodegradable and non-biodegradable materials in WAS samples were characterized using a simplified anaerobic digestion model. The characterization indicated that the observed differences between VFAs in BAP tests and ultimate methane generation in BMP tests were due to the presence of lipids in the sludges.

REFERENCES

- [1] American Public Health Association, (1995), *Standard Methods for the Examination of Water and Wastewater*, 19th ed; American Public Health Association: Washington D.C.
- [2] Braguglia C. M., Mininni G., Gianico A., (2008), Is Sonication Effective to Improve Biogas Production and Solids Reduction in Excess Sludge Digestion? *Water Science and Technology*, 57(4):479-83.
- [3] Fujishima S., Miyahara T., and Noike T., (2000), Effect of Moisture Content on Anaerobic Digestion of Dewatered Sludge: Ammonia Inhibition to Carbohydrate Removal and Methane Production, *Water Science and Technology*, Vol 41 No 3 pp 119-127.
- [4] Jeong, H-S, Suh, C.-W., Lim, J.-L., Lee, S.-H., Shin, H.-K., (2005), Analysis and Application of ADM1 for Anaerobic Methane, *Bioprocess Biosyst Eng*, V27, 81-89.
- [5] Khanal, S. K., Grewell D, Sung, S. and Van Leeuwen, J. (2007). Ultrasound Applications in Wastewater Sludge Pretreatment: A Review. *Critical Reviews in Environmental Science and Technology*, 37 (4): 277-313.
- [6] Kianmehr P., (2010), Characterization of Pretreatment Impacts on Properties of WAS and Digestibility, *Ph.D. Thesis*, University of Waterloo.
- [7] Kianmehr P., Parker W., and Challen-Urbancic J., (2008), Development of Protocols for Evaluating WAS Pre-treatment Processes, *81st WEFTEC 2008*, Chicago, Illinois, USA.
- [8] Kianmehr P., Parker W., and Seto P., (2009), Characterization of Ozone Impacts on WAS Properties and Digestibility, *82nd Annual Water Environment Federation Technical E*
- [9] *xhibition and Conference*, Orlando, Florida, USA.
- [10] Liu C., Xiao B., Dauta A., Peng G., Liu S. and Hua Z., (2009), Effect of Low Power Ultrasonic Radiation on Anaerobic Biodegradability of Sewage Sludge, *Bioresource Technology*, Vol. 100, 6217-6222.
- [11] Martin Ruel, S.; Comeau, Y.; Heduit, A.; Deronzier, G.; Ginestet, P.; Audic, J. M., (2002), Operating Conditions for the Determination of the Biochemical Acidogenic Potential of Wastewater. *Water Res.*, 36 (9), 2337.
- [12] Montgomery D. C. (2001), Design and Analysis of Experiments, 5th Edition, *John Wiley and sons Inc.*, page 76-86.
- [13] Shelton D. R. and Tiedje J. M., (1984), General Method for Determining Anaerobic Biodegradation Potential. *Applied Environmental Microbiology*, 47(4), 850-7.
- [14] Siegrist, H., Vogt, D., Garsia-Heras, J. L., Gujer, W., (2002), Mathematical Model for Meso- and Thermophilic Anaerobic Sewage Sludge Digestion, *Environ. Sci. Technol.*, Vol. 36, 1113-1123.
- [15] Snoeyink V. L., Jenkins D., (1980), *Water Chemistry*.

Effect of Simplifying the Water Supply Pipe Networks on Water Quality Simulation

Hassan I. Mohamed¹ and Sameh S. Ahmed²

¹Civil Eng. Department, Assiut University, Assiut, Egypt

²Mining Eng. Department, Assiut University, Assiut, Egypt

Both are Currently at: College of Engineering, Majmaah University, Saudi Arabia

e-mail: Hassanmohamed_2000@yahoo.com

ABSTRACT

Domestic water supply distribution systems are important for delivering water to consumers as well as serving as the last process between the treatment plant and the consumer. Hydraulic simplification is an important problem in the design stage of water supply pipe networks. Simplification of pipe networks is recognized by making the original network easier to be understood and analyzed. However, its effect on water quality parameters, including water age, disinfectant residuals and disinfectant by-products is the least understood. In the present article, the effect of using hydraulic equivalent system on water quality estimates is represented by water age and disinfectant residuals, i.e. chlorine decay will be examined. A simple system is used to demonstrate the effect of applying existing series and parallel pipes simplification approaches and effect of demand approximation at pipe ends on water quality estimation. Water quality simulations were performed by using EPANET toolkit for a 24-hours simulation. The results from this study provide invaluable information for understanding current limitations and for improving existing techniques for pipes network simplification. The study showed that while using equivalent pipe equations reveal the same head loss and flow as the full system, it does not ensure that travel times and velocity are equivalent. Since those factors can impact chlorine decay, the equivalent system should be used with care.

Keywords: distribution network, aggregation, residual chlorine, extended period simulation.

1. INTRODUCTION

Aggregation of a water distribution system is not unique. It depends on the aggregation objectives and on the different adopted levels and methods of aggregation. Only few methods have been developed to simplify water distribution systems, focusing only on the system's hydraulic behaviour, Perelman and Ostfeld [1]. Anderson and Al-Jamal [2] introduced a methodology for the simplification of complicated hydraulic networks using a parameter-fitting approach. The layout of the final simplified network is specified a priori; then, pipe conductances and demand distribution are determined by maximizing the fitness between the simplified and the fully system performance. Raczynski et al. [3] developed approach to maintain both hydraulics and water quality for series and parallel pipe systems. The water quality measure that is considered in this study is water age (a zero order reaction). They claimed that since first and second order reactions are a function of water age, using water age as a measure will simplify the calibration method.

Norton and Weber [4] introduced a closed-form mathematical expression for approximation of water age through a distribution network. The model used network storage, number of connections, and flow per connection to develop a relationship between cumulative fraction of population and water age. To improve age representation, Machell et al. [5] introduced an approach which provides information about the component ages contributing to the mean

age. The enhanced model tracks the volumes and ages of different flow contributions, within user defined bands, throughout water distribution systems.

2. THEORETICAL APPROACHES

Hydraulic models are important for the analysis and the design of water pipe networks. They are used for various important tasks by engineers, such as the design of new and analysis of existing distribution networks, long term master and operational planning (Harding and Walski [6]).

2.1 Hydraulic Model

Numerous computer models (computer software) have been developed to solve the network simulation equations. One of the more widely used models is EPANET model which can simulate steady state conditions, extended period simulation, and water quality (Rossman et al.[7], Rossman, [8&9]). EPANET is developed by the U.S. Environmental Protection Agency. This model is an explicit time-driven water-quality modelling algorithm for tracking transient concentrations of substances in pipe networks.

2.2. Water Quality Model

EPANET's water quality simulator uses a Lagrangian time-based approach to track the fate of discrete parcels of water as they move along pipes and mix together at junctions between fixed-length time steps. For each water quality time step, the contents of each segment are subject to reactions, a cumulative

account is kept of the total mass and flow volume entering each node, and the positions of the segments are updated. The chlorine concentration leaving the junction is simply the flow-weighted sum of the concentrations from inflowing pipes and external sources.

3. METHODOLOGY

3.1 Hydraulic Equivalence

Using conservation of energy across a set of pipes in parallel or series, equivalent pipe relationships can be derived. Typically, an equivalent diameter is determined by fixing the equivalent pipe's length and pipe roughness. Jung et al. [10] derived the following equations from the Hazen-Williams head loss equation for calculating the equivalent diameter for series and parallel pipes respectively.

$$\frac{1}{D_e^{4.871}} = \sum_{i=1}^n \frac{1}{D_i^{4.871}} \left(\frac{C_e}{C_i} \right)^{1.852} \frac{L_i}{L_e} \quad (1)$$

and

$$D_e = \left[\sum_{i=1}^n \left(\frac{C_i}{C_e} \right) \left(\frac{L_e}{L_i} \right)^{0.54} D_i^{2.63} \right]^{0.38} \quad (2)$$

Where C_i , D_i , and L_i are the pipe roughness, diameter and length of the pipe in series or parallel and C_e , D_e and L_e are the same parameters for the equivalent system. By fixing two of the three parameters the third can be determined using a form of the above equations. Since these relationships are developed from conservation of energy the equivalent pipes have consistent flow and pressure losses as the original set of pipes.

3.2 Hydraulic and Water Quality Equivalence

Raczynski et al. [3] developed the following equation for computing the water quality equivalent diameter, D_{ew} .

$$D_{ew} = \left[\frac{\sum_{i=1}^n (D_i^2 L_i)}{L_e} \right] \quad (3)$$

D_{ew} ensures that the travel time in the equivalent pipe will equal the series or parallel pipe. However, it does not ensure that the system will be hydraulically equivalent. Since Eq. 3 shows that D_{ew} is independent of C , it is possible to find an equivalent hydraulic system without affecting the travel time equivalence by modifying the pipe roughness. To do so, rather than

solving for D_e for a defined value of C_e in hydraulic equivalence equations (Eq. 1 and 2), D_e is set to D_{ew} , and C_e is solved for as unknown term in Eq. 1 or 2.

4. APPLICATIONS

The network shown in Figure 1 consisting of 9 nodes at the same elevation is representative of a general parallel/series system. Junction 10 has only average demand of 126 L/s and the network is connected to a reservoir of constant head of 59 m. Pipe P1 that feed the system is 300 mm in diameter, 610 m long and have Hazen-Williams coefficient of 100. All other pipes from P2 to P11 are 305 m long. Table 1 shows pipe diameter and Hazen-Williams coefficient for all the pipes in the network.

Table 1: Lengths, diameters and Hazen-Williams coefficient of the different pipes.

Pipe number	Length (m)	Diameter (mm)	Hazen-Williams Coefficient
P1	610	300	100
P2	305	300	130
P3	305	200	150
P4	305	150	160
P5	305	200	150
P6	305	150	160
P7	305	250	140
P8	305	200	150
P9	305	150	160
P10	305	300	130
P11	305	250	140



Figure 1: Simple pipe network (Aggregation level 1).

4.1 Diurnal Curve of Demands

A diurnal curve that makes water demands vary in a periodic way over the course of the day has been used to make the simulation more realistic for analysing an extended period of operation. The diurnal demand curve that was observed by AWWA [11] is used for simulation in this study, as shown in Figure 2.

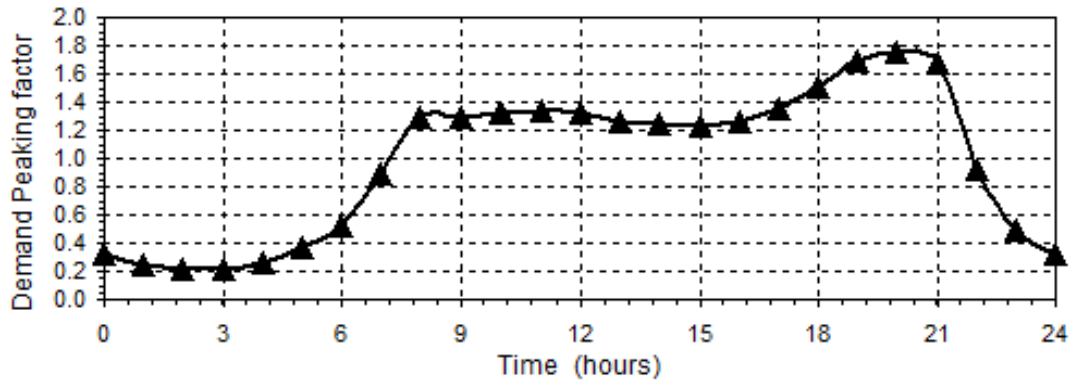


Figure 2: Diurnal demand curve for extended period simulation.

The curve illustrates how the rate of water use varies over a period of 24-hours and provides demand peaking factors as the multipliers that are applied to the average base demand to give the actual demand at a given time.

4.2 Residual Chlorine Reaction Coefficients

Chlorine decay simulation conducted with *EPANET*'s quality model takes into consideration the phenomena of chlorine reaction with chemical species in bulk fluid and pipe walls. Both k_b and k_w can depend on water characteristics, temperature, and moreover, the latter can be correlated to the pipe age and material. A bulk decay coefficient as an average value of the values from literature (Tamminen et al. [12], Mohamed and Abozeid [13]) was used, i.e. -0.36 day^{-1} . Wall decay coefficient obtained by Tamminen et al. [12] was used, i.e. -0.6 m/day^{-1} .

4.3 Simplification Method

The effects of the equivalence methods are evaluated for this system with different levels of skeletonization (aggregation). Skeletonization is loosely defined as the removing of pipes and nodes in a network to make the model simpler. Here, skeletonization or aggregation will simplify the system by replacing a series or parallel set of pipes by a single pipe. Aggregation is applied in a step wise manner. The first level of skeletonization (Level 2) (Figure 3) aggregates the two series pipes between nodes (3,5), (2,10) and (7,9) and removes junctions 4,6 and 8. Since there are no demands at these nodes, no demand reallocation is required. The next level of aggregation (Level 3), shown in Figure 4, aggregates the pipes between nodes (2,10) to one pipe on the upper and lower sides respectively. The final level of aggregation (level 4) (Figure 5) replaces the three pipes with one pipe.

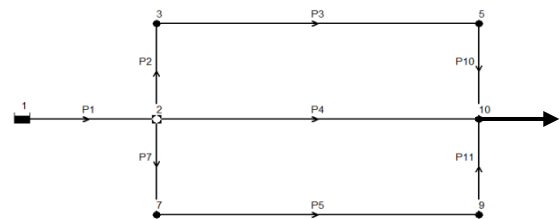


Figure 3: Simple pipe network (Aggregation level 2).

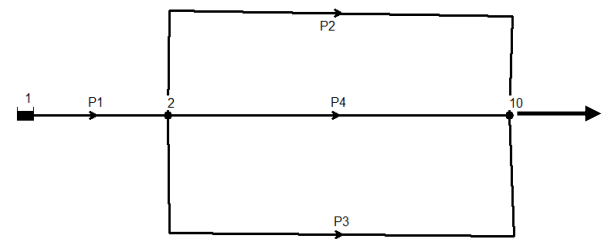


Figure 4: Simple pipe network (Aggregation level 3).



Figure 5: Simple pipe network (Aggregation level 4).

5. RESULTS AND DISCUSSINS

Figure 6 shows the variation of chlorine residual with time at node 10 for aggregation levels 1 and 2. It can be shown the difference in chlorine concentration at the original network (Level 1) and level 2 aggregation for both hydraulic criteria and hydraulic plus water age criteria. Also, it is noticeable that the big difference at the period of high demand (higher than the average). In comparison between hydraulic aggregation and hydraulic plus water age aggregation, we can see that the former slightly better.

Shown in Figure 7 is the variation of chlorine residual with time at node 10 for aggregation levels 1 and 3. It can be shown the difference in chlorine concentration at the original network (Level 1) and level 3

aggregation for both hydraulic criteria and hydraulic plus water age criteria. In comparison between hydraulic aggregation and hydraulic plus water age aggregation, we can see that the former slightly better.

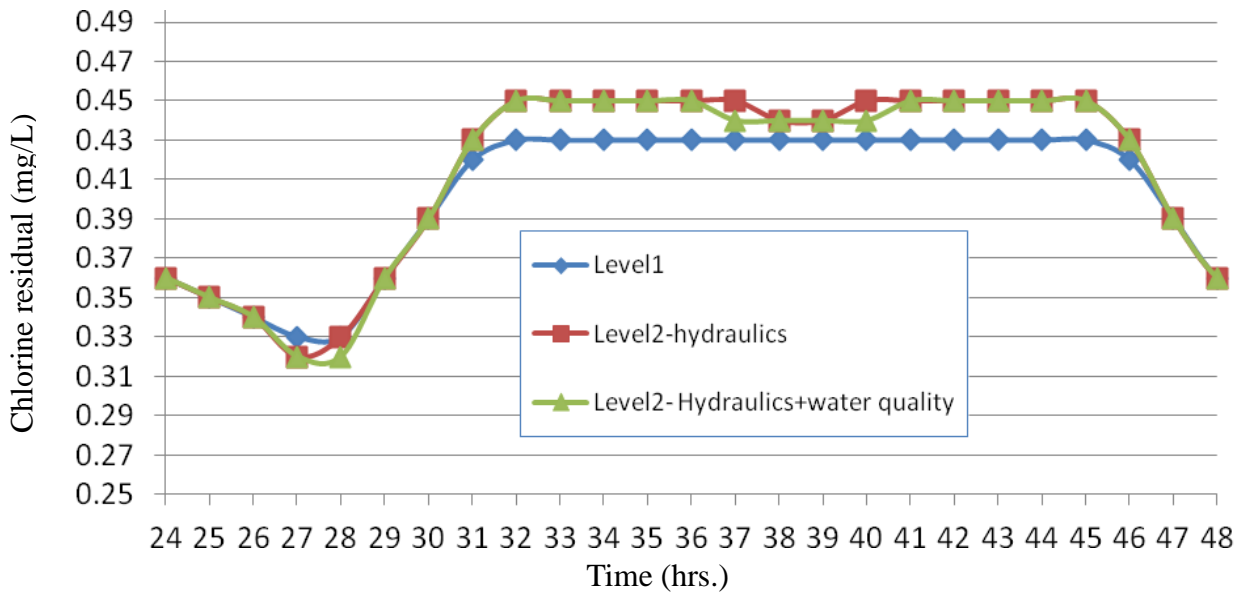


Figure 6: Time series distribution of chlorine concentration at node 10 for aggregation levels 1 and 2.

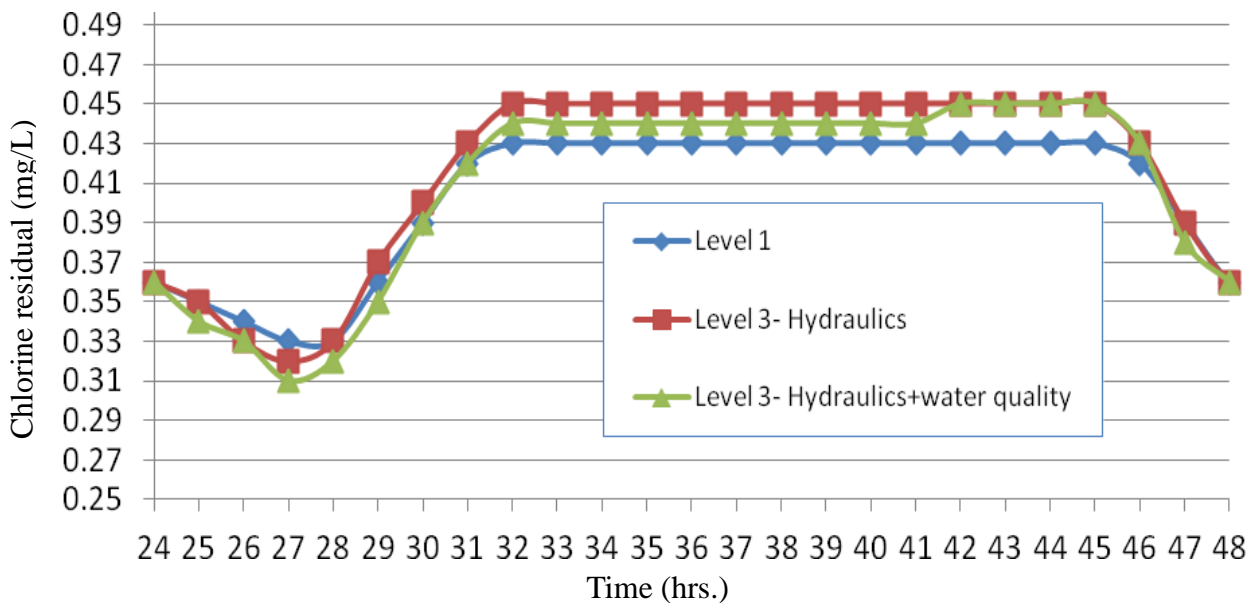


Figure 7: Time series distribution of chlorine concentration at node 10 for aggregation levels 1 and 3.

The variation of chlorine residual with time at node 10 for aggregation levels 1 and 4 is presented in Fig 8. It can be shown the difference in chlorine concentration at the original network (Level 1) and level 4 aggregation for both hydraulic criteria and hydraulic

plus water age criteria. Also, it is noticeable that the large difference at the period of high demand (higher than the average). In comparison between hydraulic aggregation and hydraulic plus water age aggregation, we can see that the former slightly better.

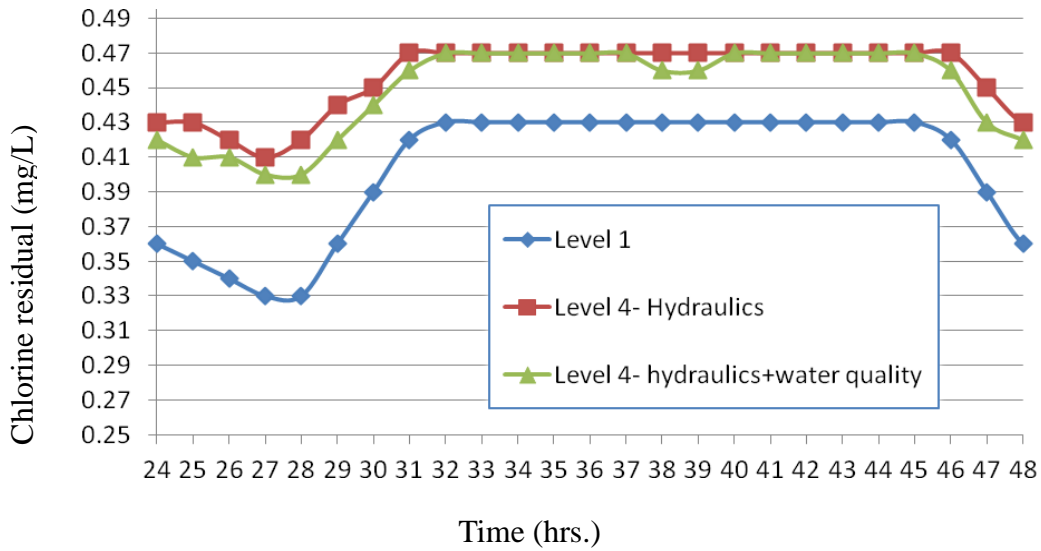


Figure 8: Time series distribution of chlorine concentration at node 10 for aggregation levels 1 and 4.

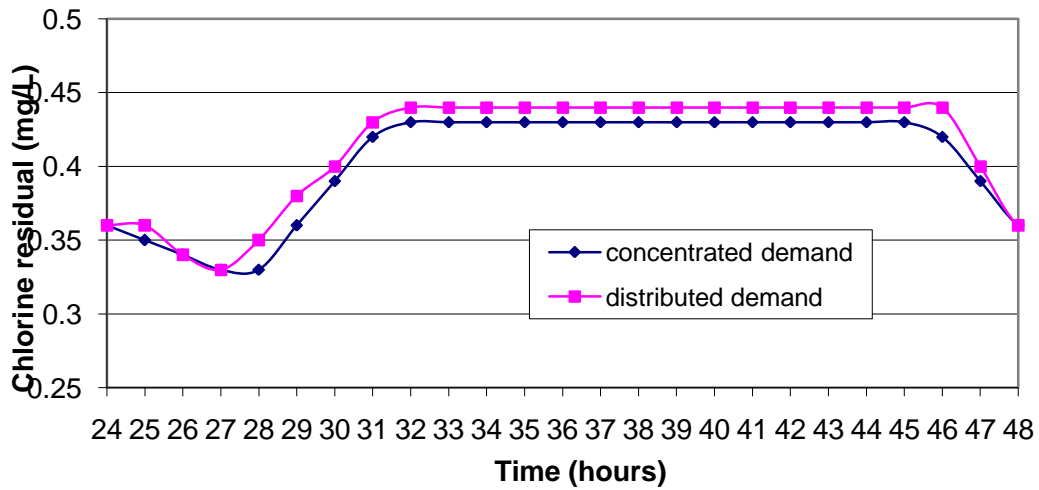


Figure 10: Time series distribution of chlorine concentration at node 10 for concentrated and distributed water demand.

Figure 9 shows the mean relative absolute error for different simplifying levels. It can be shown that the simplification according to hydraulics and water ages gives less error than simplification according to hydraulics only. Also the error due to level 4 simplification is so high compared to level 2 and level 3 and in general the error increase by increasing simplification degree.

To show the effect of water demand distribution on water quality, Figure 10 shows a comparison between time series of chlorine residual when the demand is concentrated at point 10, i.e. level 1, with that when the demand is distributed at the nine nodes. It is clear that demand concentration leads to underestimate of chlorine concentration estimation.

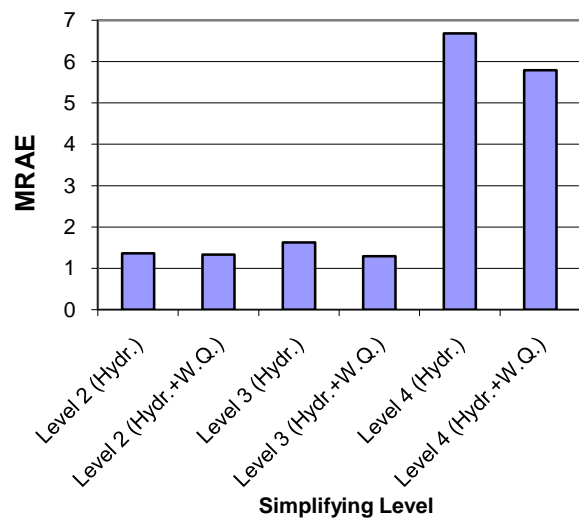


Figure 9: Mean relative absolute error at different simplifying levels.

6. CONCLUSIONS

In this study, effect of water supply pipes network simplification on water quality simulation was explored. Different simplification method which reveal similar hydraulic condition and hydraulic condition plus water age were examined. EPANET model is used for simulation of chlorine decay in a distribution network. It is found that increasing network aggregation can significantly increase the error in water quality simulation.

REFERENCES

- [1] Perelman, L., and Ostfeld, A. "Water distribution system aggregation for water quality analysis", *J. Water Resour. Plann. Manag.*, ASCE, Vol. 134, No. 3, pp. 303-309, 2008.
- [2] Anderson, E. J., and Al-Jamel, K. H. "Hydraulic-Network simplification", *J. Water Resour. Plann. Manag.*, ASCE, Vol. 121, No. 3, pp. 235-240, 1995.
- [3] Raczynski, A., Kirkpatrick, W., Rehnstrom, D., Boulos, P., and Lansey, K. "Developing hydraulic and water quality equivalent systems", Proceed. of the 10th. Annual Water Distr. Systems Conf., WDSA2008, Krugar National Park, South Africa, 2008.
- [4] Norton, J. W., and Weber, W. J. "Closed-Form solution to water age in distribution system", 8th Annual Water Distribution systems Analysis Symposium, Cincinnati, Ohio, USA, 2006.
- [5] Machell, J., Boxell, J. B., and Saul, A. J. "Improving the representation of age of water in drinking water distribution networks to inform water quality", 8th Annual Water Distribution systems Analysis Symposium, Cincinnati, Ohio, USA, 2006.
- [6] Harding, B. L., and Walski, T. M. "long time-series simulation of water quality in distribution system", *J. Water Resour. Plann. Manag.*, ASCE, Vol. 126, No. 4, pp. 199-209, 2000.
- [7] Rossman, L. A., Boulos, P. F., and Altman, T. "Discrete volume element method for network water-quality models", *J. Water Resour. Plann. Manag.*, ASCE, Vol. 119, No. 5, pp. 505-517, 1993.
- [8] Rossman, L. A. "EPANET users manual", Risk reduction engineering lab. US Environmental protection agency, Cincinnati, 1994.
- [9] Rossman, L. A. "Computer models/EPANET", In: Mays, L. A. (ed.) *Water distribution systems handbook*, McGraw Hill, New York, 2000.
- [10] Jung, B., Boulos, P. F., and Wood, D. J. "Impacts of skeletonization on distribution system hydraulic transient models", World Environmental and Water Resources Congress 2007: Restoring our natural habitat, ASCE, 2007.
- [11] AWWA, American Water Works Association, *AWWA Manual M32. "Distribution network analysis for water utilities"*, Denver, Colo.: AWWA, 1989.
- [12] Tamminen, S., Ramos, H., and Covas, D. "Water supply system performance for different pipe materials Part I: water quality analysis", *Water Resour. Manag.*, 22, pp. 1579-1607, 2008.
- [13] Mohamed, H. I., and Abozeid, G. "Dynamic simulation of pressure head and chlorine concentration in the city of Asyut water supply network in abnormal operation conditions", *Arab. J. Science Eng.*, Vol. 36, No. 2, pp. 173-184, 2011.

Vanadium Recovery from Synthetic Wastewater by Adsorption onto Chitosan

Hakimeh Sharififard¹, Mansooreh Soleimani^{2*}, Mahboobeh Nabavi nia¹,
 Mohammad Songolzadeh²

¹Mahshahr branch, AmirKabir University of Technology, Mahshahr, Iran.

²Department of Chemical Engineering, AmirKabir University of Technology, No.424, Hafez Ave., Tehran, Iran, Tel. & Fax: +98(21) 66405847

*E-mail: Soleimanim@aut.ac.ir

ABSTRACT

Vanadium is an important by-product that is used almost exclusively in ferrous and non-ferrous alloys. Due to the limited availability of the primary sources containing this metal, many countries in the world pay considerable attention to the comprehensive utilization of the secondary resources. In this study, the feasibility of vanadium recovery from synthetic wastewater with chitosan, as biosorbent, was investigated. Equilibrium tests were performed for different initial concentrations of vanadium in batch experiments. These equilibrium data were analyzed using equilibrium isotherm correlations, namely, Freundlich and Langmuir models. The adsorption isotherm study exhibited that the maximum adsorption capacity of chitosan was found 90.9 mg/g. The kinetic performance of chitosan has been assessed and the results demonstrate that the adsorption process corresponds to the pseudo- first and second order kinetic models.

Keywords: Vanadium, recovery, chitosan, adsorption

1. INTRODUCTION

Vanadium has strategic and industrial importance due to its applications in many technological fields such as catalysts (in different chemical industries, oil refinery and petrochemical plants) and as an alloying element in steel, iron and titanium alloys. However, primary resources are insufficient to satisfy vanadium demand. Increasing demand and limited resource of vanadium, have encouraged vanadium recovery from secondary metal-containing sources like spent catalysts and dilute industrial wastes [1-3]. Many studies are currently being undertaken to develop new or modified techniques for separation and recovery of metals from dilute solutions.

Adsorption is an effective and versatile method for recovery or removal of heavy metals, particularly in the case of low concentration. In adsorption process, adsorbents should be available at low cost and easy to recycle. Biosorbents are relatively inexpensive and available in large quantities. These adsorbents have high efficiency for metal recovery and potential for easy regeneration. One of the most naturally abundant and cheap biopolymers is chitosan that produced by the alkaline deacetylation of chitin. This adsorbent is characterized by its high percentage of nitrogen, present in the form of amine and amide groups that are responsible for metal ion binding through different mechanisms: chemical interaction, electrostatic interaction. The kind of interaction depends on the metal, its chemistry and the pH of solution [4]. The literature review indicated that chitosan and their derivatives are efficient adsorbents for metal ions separation from dilute solution [4-10].

The objective of this work was to evaluate the potential of chitosan for vanadium recovery from synthetic waste water.

2. MATERIAL AND METHODS

2.1 Material

Chitosan flakes with minimum 80% degree of deacetylation and medium molecular weight (750,000) were purchased from Fluka Co. Stock solutions of the tests were prepared by dissolving vanadium penta oxide (V_2O_5) in sulfuric acid and distilled water. Working solutions were prepared by diluting a different volume of stock solution to achieve the desired concentration. Initial pH of solution was adjusted by H_2SO_4 and NaOH solution with pH meter (Metrohm780). All of the materials have been used in laboratory grade from Merck Company.

2.2 Characterization of chitosan

Characterization of adsorbents is important for their applications in adsorption process. Chitosan was characterized by selected properties.

- To measure bulk density, a 10 ml cylinder was filled to a specified volume with dried adsorbent. The cylinder was weighed. The bulk density was then calculated as [11]:

Bulk density= [weight of dry material (g) / volume of packed dry material (cm^3)]

(1)

- The surface area (S_{BET}) and pore size

distribution of chitosan was determined from adsorption-desorption isotherm of N₂ at 77 K. A Quantachrom NOVA 1000 surface area analyzer was used for determination this parameter by applying the 3-point BET (Brunauer-Emmett-Teller). The pore volumes were calculated by the BJH method.

2.3 Kinetic studies

Kinetic adsorption of vanadium by chitosan was studied by placing 0.3 g adsorbents in flasks containing 50 ml (100 mg/L) metal ion solution at pH 4.0. The contents of the flasks were agitated on an orbital shaker at 250rpm for prescribed periods of time at room temperature. After these periods of time and filtration, the solution concentration was analyzed by inductively coupled plasma (ICP) analyzer (Varian 735ES).

The amount of vanadium recovered by chitosan, q , was determined through following equation:

$$q = \frac{V}{m} (C_0 - C) \quad (2)$$

In this equation C_0 and C are initial and final concentration (mg/L) of vanadium in solution, respectively, V is the solution volume (L) and m is the weight (g) of adsorbent.

2.4 Kinetic models

Different models are applied to evaluate the kinetic mechanism that controls the adsorption process. In this work, pseudo-first-order, pseudo-second-order and intra-particle diffusion. These models are presented in Table 1.

2.5 Equilibrium studies

To evaluate the potential of chitosan for vanadium adsorption, the equilibrium studies of the metal ion adsorption with these adsorbents were carried out by placing 0.3 g of adsorbent in a series of flasks containing 50 mL of metal ions solution at different initial concentrations (50-300 mg/L) and pH 4.0. The flasks were agitated on an orbital shaker at 250 rpm for 24 h at room temperatures. After this period, the metal solution was filtered and the residual concentration of the metal ions was determined by inductively coupled plasma (ICP) analyzer (Varian 735ES). The amount of vanadium adsorbed by chitosan, q , was determined by Eq.(2).

Table 1: Kinetics models

Kinetic model	Equation
Pseudo-first-order ¹	$\log(q_e - q) = \log q_e - \frac{k_1 t}{2.303}$
Pseudo-second-order ²	$\frac{t}{q} = \frac{1}{k_2 q_e^2} + \frac{1}{q_e} t$

Intra-particle diffusion ³	$q_t = k_{id} t^{0.5}$
---------------------------------------	------------------------

¹ $k_1(\text{min}^{-1})$ is pseudo-first-order rate constant, q and q_e are the amounts of solute adsorbed per unit weight of adsorbent (mg/g) at t (min) and equilibrium time, respectively

² k_2 (g/mg.min) is pseudo-second-order rate constant

³ k_{id} (mg/g.min^{1/2})

2.6 Adsorption isotherm

The two most widely used adsorption isotherms are the Langmuir and Freundlich isotherms. In this work, experiments data was analyzed in terms of these two isotherms. The Langmuir adsorption isotherm equation on linear form is:

$$\frac{1}{q_e} = \frac{1}{q_{\max} \cdot K_L} \cdot \frac{1}{C_e} + \frac{1}{q_{\max}} \quad (3)$$

where, q_{\max} is maximum adsorption capacity of adsorbent (mg/g) and K_L is the Langmuir constant related to energy of adsorption (L/mg). K_L and q_{\max} can be calculated from the intercept and slope of the linear plot of $1/q_e$ versus $1/C_e$. Other important parameter, R_L , called the equilibrium parameter was calculated to identify whether an adsorption system is favorable or unfavorable:

$$R_L = \frac{1}{1 + K_L C_0} \quad (4)$$

If the R_L value is between 0 and 1, the adsorption process is favorable.

Linear form of Freundlich model is:

$$\log q_e = \frac{1}{n} \log C_e + \log K_f \quad (5)$$

in this equation, K_f is the Freundlich constant related to adsorption capacity of adsorbent and n is the Freundlich -exponent related to adsorption intensity. These parameters were determined by plotting $\ln q_e$ versus $\ln C_e$.

3. RESULTS AND DISCUSSION

3.1 Characterization of chitosan

The bulk density of chitosan was 0.21 g/cm³. The BET surface area of chitosan was measured and it was found 16.37m²/g. The total pore volume and average pore diameter of chitosan were found as 0.019 cm³/g and 44.9Å.

3.2 Kinetic studies

The experimental data for vanadium recovery by chitosan was analyzed in terms of pseudo-first-order,

pseudo-second-order and intra-particle diffusion models and results illustrated in figures 1-3. The constants and regression coefficient (R^2) of these models were presented in Table 2. The R^2 values for these three models is good ($R^2 > 0.96$), but the plot of q versus $t^{0.5}$, for intra-particle diffusion models, doesn't pass through the origin and has the intercepts (3.148). Therefore, the intra-particle diffusion may not be the rate controlling step. The calculated q_e from pseudo-first and pseudo-second order model are closely similar to experimental q_e for vanadium adsorption by chitosan (11.87 mg/g) and confirm the validity of these models to the adsorption of vanadium. Basis on these result, It could concluded that the overall sorption of this metal by chitosan have been controlled by physico-chemical sorption mechanism.

Table 2: Constants and regression coefficient for kinetic models.

Kinetic models		Chitosan-V
Pseudo-first-order	k_1	0.05
	q_e	10.95
	R^2	0.96
Pseudo-second-order	k_2	0.08
	q_e	12.19
	R^2	0.97
Intra-particle diffusion	k_{fd}	1.27
	intercepts	3.15
	R^2	0.97

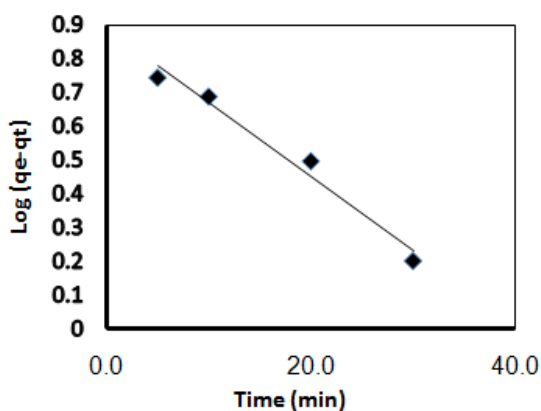


Figure 1: Pseudo-first-order kinetic models for vanadium recovery by chitosan.

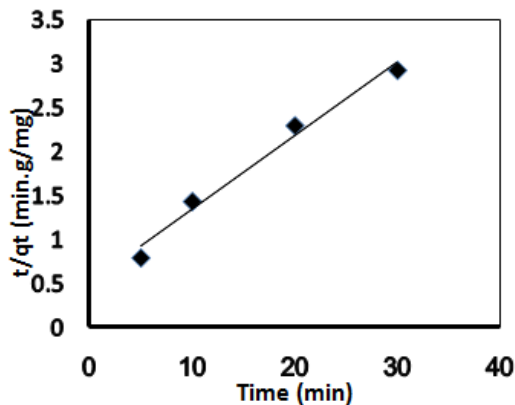


Figure 2: Pseudo- second-order kinetic models for vanadium recovery by chitosan.

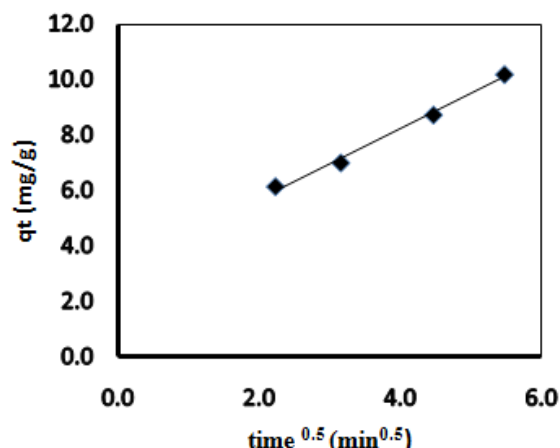


Figure 3: Intra-particle diffusion model for vanadium recovery by chitosan.

3.3 Adsorption Equilibrium

The sorption equilibrium data were fitted for the linear Langmuir and Freundlich isotherms and results illustrated in figures 4 and 5. Constant parameters and regression coefficient (R^2) of these isotherms are presented in Table 3. The R^2 values showed that two models fitted well with the equilibrium data of vanadium adsorption on chitosan.

Maximum capacity of chitosan for vanadium adsorption has been reported in Table 3 by using Eq. (3). The maximum adsorption capacity of this biopolymer is comparable with other adsorbents such as activated carbon [12], Aluminum-Pillared Bentonit [13].

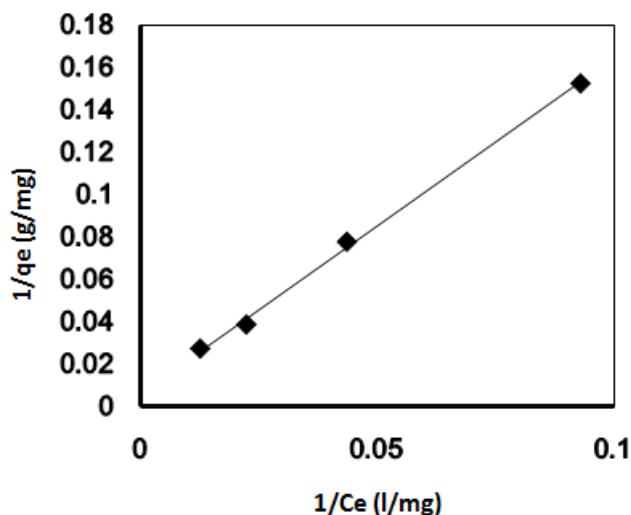


Figure 4: Linear form of Langmuir isotherm for vanadium recovery by chitosan.

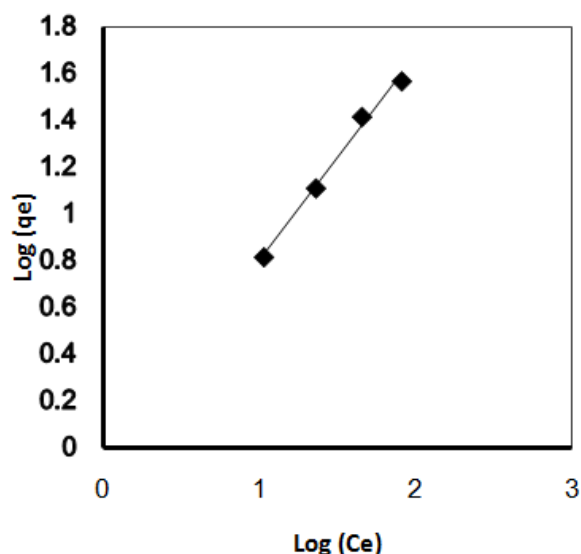


Figure 5: Linear form of Freundlich isotherm for vanadium recovery by chitosan.

Table 3: Constants parameters and regression coefficient for Langmuir and Freundlich isotherms.

Isotherm	Parameters	Chitosan-V
Langmuir	q_{max}	90.900
	L	0.007
	R^2	0.998
Freundlich	K_f	0.832
	n	1.220
	R^2	0.992

4. CONCLUSION

Due to the economical impact of recovery of vanadium metal and their environmental concerns, various techniques employed to recovery these metal ions from aqueous solutions. Results of this work showed that chitosan is suitable adsorbent for vanadium recovery from dilute aqueous solution. Final decisions from this study are as follows:

- From the kinetics studies, it was observed that experimental data were best fitted with Pseudo-first and second order models and this suggests that the overall sorption of this metal by chitosan has been controlled by physico-chemical sorption mechanism.
- Equilibrium results were in good agreement with Langmuir and Freundlich isotherm for vanadium recovery by chitosan.
- Maximum adsorption capacity for vanadium adsorption was 90.9 mg/g, which are comparable with results of other adsorbents.

ACKNOWLEDGEMENT

Sincerely thank Miss Naemeh Zari for analyzing the samples by ICP.

REFERENCES

- [1] Zeng, L., Cheng, C.Y. "A literature review of the recovery of molybdenum and vanadium from spent hydrodesulphurisation catalysts: Part II: Separation and purification", *Hydrometallurgy*, Vol.98, pp.10-20, 2009.
- [2] Moskalyk, R.R., Alfantazi, A.M. "Processing of vanadium: a review", *Mineral Engineering*, Vol.16, pp.793-805, 2003.
- [3] Liu, A., Li, L., Yu, L. "Technology of vanadium extraction from V-bearing solid wastes and its prospect", *Metal Mine*, Vol.328, pp:61-64, 2003.
- [4] Erosa, M.S.D., Medina, T.I. S., Mendoza, R. N., Rodriguez, M. A., Guibal, E. "Cadmium sorption on chitosan sorbents: kinetic and equilibrium studies", *Hydrometallurgy*, Vol. 61, pp. 157-167, 2001.
- [5] Shafaei, A., Zokae, F., Kaghazchi, T. "Equilibrium studies of the sorption of Hg(II) ions onto chitosan", *Chemical Engineering Journal*, Vol. 133, p. 311-316, 2007.
- [6] Zokae, F., Soleimani, M. "Removal of cadmium ions from aqueous solutions by adsorption onto chitosan", *6th ANQUE International Congress of Chemistry*, Pureto de la Cruz, Tenerife, Spain, December 5-7, 2006.
- [7] Guzmán, J., Saucedo, I., Navarro, R., Revilla, J., Guibal, E. "Vanadium Interactions with Chitosan: Influence of Polymer Protonation and Metal Speciation", *Langmuir*, Vol.18, pp. 1567-1573, 2002.
- [8] Sharififard, H., Zokae, F., Soleimani, M. "Comparison of chitosan and activated carbon as adsorbent in palladium separation from dilute acidic solution", *2th International Conference on Chemical Engineering and Advanced Materials (CEAM 2010)*, virtual forum, November, 15-26, 2010.
- [9] Boyac, E., Eroglu, A.E., Shahwan, T. "Sorption of As(V) from waters using chitosan and chitosan immobilized sodium silicate prior to atomic spectrometric determination", *Talanta*, Vol. 80, pp. 1452-1460, 2010.
- [10] Das, N., "Recovery of precious metals through biosorption – A review", *Hydrometallurgy*, pp.1-49, 2010.
- [11] Snell, F.D.; Ettore, L.S. *Encyclopedia of Industrial Chemical Analysis*, vol. 8. 1968.
- [12] Namasivayam, C; Sangeetha, D. "Removal and recovery of vanadium(V) by adsorption onto ZnCl₂ activated carbon: kinetics and isotherms", *adsorption*, Vol.12, pp. 103-117, 2006.
- [13] Manohar, D.M., Noeline, B. F., Anirudhan, T.S. "Removal of Vanadium(IV) from Aqueous Solutions by Adsorption Process with Aluminum-Pillared Bentonite", *Industrial Engineering and Chemical Research*, Vol.144, pp. 6676-6684, 2005

Fabrication of Polymeric Hollow Fiber Membrane for the Production of Safe Drinking Water

Latifa Al-Nuaimi, Nayef Ghasem*, Mohamed Al-Marzouqi

Department of Chemical and Petroleum Engineering,
United Arab Emirates University, Al-Ain city, P.O.Box: 17555

*Corresponding author Email: nayef@uaeu.ac.ae

ABSTRACT

Production of safe drinking water by using micro-filtration and ultra filtration technology become more interesting. Water purification or filtration by using membrane began attracting much attention worldwide, because of its good characteristics such as; high efficiency in removing solid particles, viruses and germs and their low cost. This new technology is useful in industrial waste water treatment. The current study tends to improve the fiber characteristics and make it suitable for the removal of unwanted particles from water. The present work seeks to manufacture cellulose acetate hollow fibers. The fibers were prepared by the nonsolvent induced phase separation (NIPS) method at different spinning conditions. The effect of rheological behavior of the fabricated fibers at different concentrations and temperatures are investigated. The attempt is to clarify the effect of certain parameter on the efficiency of hollow fiber membranes. The work investigated the effect polymer solution flow rate during spinning on the characterizations of hollow fiber membrane. Examine the effect of changing bore fluid flow rate on the properties of hollow fiber; water as inner coagulation at different flow rates; 8, 10, 12, 13, and 16 g/min. Change the distance between the spinneret and external coagulation (water) at different distances (5.5, 7, 9 and 10 cm) in order to study the structure and performance on hollow fiber. Check if the internal coagulation type and composition will be effect on the characterizations of hollow fiber and solids rejection or not. Study the effect of ethanol at different concentration in internal coagulation (Ethanol/Water), while ethanol concentrations in water are 18, 25, 35 and 50%.

Keywords: hollow fibers, cellulose acetate, safe water, ultrafiltration

1. INTRODUCTION

Water filtration is removal of heavy metals and suspended solids from water. It is necessary to keep the water and marine environment clean because the heavy metals and suspended solids accumulate toxic components in the bottom of the sea and lack (2). Membrane filters were ranged from nano-filtration (partial desalination) through ultra-filtration (virus removal) to microfiltration (suspended solids removal).

There are two basic configurations of membrane: flat sheet and hollow fiber (3). In addition, there are many methods and techniques used in the manufacture of the hollow fibers. They are used in various fields. Wet casting, thermally induced phase separation (TIPS) (4) Immersion precipitation method (5), Dry jet wet spinning process (6) and Non solvent induced phase separation (NIPS) (7) are famous examples of making hollow fiber membrane. Membrane separation processes have many advantages in terms of less energy needed, less environmental impacts, capital investments and processes are simple and easy to operate. Membrane separation is given a high quality water, removal or recovery of toxic or valuable components from industries applications and used in food and pharmaceutical industries (8). Cellulose was found in cotton 94% and 50% in wood page. It is obtained by the reacting cellulose with acetic acid or acetic anhydride (9). Cellulose is one of the most ideal membrane materials since it is a kind of most available organic

resource, naturally degradable, biology compatible and hydrophilic. Cellulose and its derivatives are widely used in the manufacture of membranes.

2. EXPERIMENTAL METHODS

2.1 Materials and reagents

Cellulose acetate (CA) was purchased from BASF, Germany. Commercially available *N,N*-dimethylacetamide (DMAc) was used as the solvent of polymer dope solutions. All other chemicals are analytical grade and used without further purification.

2.2 Preparation of hollow fibers

Polymer dope solutions were first prepared by dissolving CA in DMAc as a solvent. The solutions were stirred continuously for 24 hours at room temperature until the solutions were perfectly homogeneous.

In a typical procedure, a homogeneous dope solution was transferred to the dope tank (as shown in Fig. 1) and allowed for two hours without mixing to remove gas bubbles that may exist in the dope solution. The dope solution was then fed into the annulus of the spinneret by a gear pump with a variable speed controller (0.3 cm³/rev). A pulse-free bore fluid was fed into the inner tube of the spinneret through a flow meter using nitrogen as pressurized gas. Once the spinning

dope and the bore fluid met at the tip of the spinneret, coagulation occurs. The hollow fiber membranes were then immersed into the coagulation (water) bath. The ratio of dope flow rate to bore flow rate is maintained almost constant (close to 0.50). All the fibers were produced without any drawing by keeping almost constant ratio of take-up speed to dope extrusion speed (0.94–0.97).

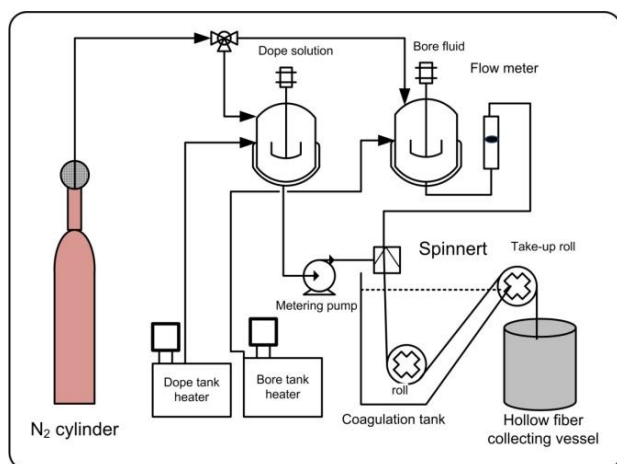


Figure 1: Schematic diagram of the spinning unit for hollow fiber preparation.

2.3 Membrane characterizations

Tensile strengths and elongations of hollow fibers were measured using a tensile apparatus (Shimadzu Autograph AGS-J20N, Japan). For each hollow fiber, four pieces of membrane were continuously measured in a batch of experiment under a 50 mm/min tensile speed. The tensile strengths were calculated on the basis of the cross-sectional areas of hollow fiber membrane. The average of four measurements was taken as the mean tensile strength and elongation.

The contact angles of water drop on membrane surface were measured using sessile drop method (Drop Master DM 300, Kyowa interface science co., Ltd., Japan). A droplet of 0.5 μ l was deposited on the surface then the contact angle was measured.

Water permeability through the membranes was measured by pure water forced to permeate from the inside to the outside of the hollow fibers (Figure 2). The transmembrane pressure was controlled by using an adjusting pressure valve close to the release side, and the average of the readings of the two pressure gauges was taken as the feed pressure. The feed was pumped into the tube side of the hollow fiber membrane and the amount of water permeate through the walls of the hollow fiber membrane was measured. The water permeability was calculated according to the following equation on the basis of the inner surface area of the hollow fiber membrane. The used pressure range is from 0.05 to 0.1 MPa.

$$\text{Water permeability, } P_w = \frac{\text{Volume of water}}{\text{inside wall area of fiber} \times \text{average pressure} \times \text{time}} \quad (1)$$

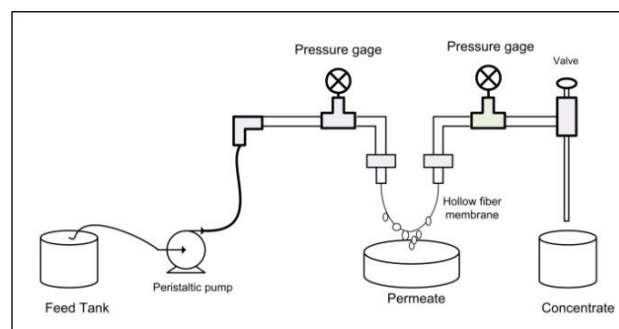


Figure 2: Schematic diagram of ultrafiltration apparatus

2.1 Hollow Fibers Preparation

Hollow fiber membranes were prepared via non-solvent induced phase separation (NIPS) method by a batch extruder. Membranes were prepared from CA/DMAc mixtures of 15%, 18%, 21% and 24% by dissolving a predefined quantity of Cellulose acetate in DMAc for 24 hours until each solution was completely homogeneous. The prepared dope solutions were transferred to the dope mixing tank and remained for 2 hours for degassing so that no bubbles remained in the solution. After 2 hours of degassing the process was started.

Predefined operating conditions were set; such as the dope solution flow rate, pore fluid flow type, pore fluid flow rate, air gap, fibers take up speed and coagulation bath temperature. The experimental setup used in the cellulose acetate hollow fiber fabrication is shown in Figure 3.1. Bore fluid was supplied from a pressurized tank and metered to the spinning process. The pressure was monitored using a pressure gage on a nitrogen (N₂) cylinder. The dope and bore fluids were filtered by a metal filter (25 μ m) and were degassed before spinning to remove the particles and gas bubbles that may exist in the dope. The formed fibers were dropped into a coagulation water bath as a roll of fibers where they were wrapped multiple times around a take up roller with controlled speed. Finally, fibers were collected at the bottom of the hollow fibers collected vessels

3. RESULTS AND DISCUSSIONS

To describe cellulose acetate fibers, the common way is to evaluate its performance in terms of pure water permeability and percent of solid rejection. Five hours is the filtration time of water permeability test. The process of filtration and rejection were investigated. Permeate flux was calculated by using the following equation:

$$\text{Permeate flux} = \frac{\text{Volume of Permeate}}{\text{Time} \times \text{Area of Membrane}} \quad (2)$$

The filtration experiments were done in the first two hours by using distilled water as a feed solution, and BSA solution (1g BSA /1000 ml water) used as feed solution for the next two hours. Finally after that in the last one hour, again distilled water was used as feed solution to clean the inner area of fiber from BSA, because BSA protein molecules could be absorbed on the pore surface and that lead to form BSA layer caused to decrease the flux of water in hollow fiber. The rejection percentage was calculated after two hours of BSA feeding.

3.1 Effect of dope concentration and flow rate

The effect of cellulose acetate concentration in the dope solution on the rejection of BSA is investigated. The rejection ratio for the fibers of 15% CA, 18%CA, 21%CA and 24%CA is presented in the Table1. The percent rejection decreased with increased CA concentration. As the cellulose acetate concentration increased the rejection percentage decreased, because increasing polymer concentration will form denser layers. 15% hollow fiber present a good rejection comparison with other CA concentration.

Table 1: Rejection ratio of BSA at different CA concentrations.

Dope Solution concentration (% CA/DMAc)	Rejection %
15%	16.62
18%	15.42
21%	12.90
24%	9.311

Figure 3 shows that the filtration experiments for 15% CA concentration at variable dope solution flow rate (6 to 10 g/min). The experiments were performed such that, in first two hours deionizer water is used as a feed solution. For a specific fiber, the flux was almost the same at the beginning of filtration. BSA solution of 1mg/ml was used as a feed solution for the next three hours of filtration experiment. Flux of membrane was drastically decreased to the about 50% based on initial flux of in the beginning of filtration for fibers produced at dope solution flow rate of 6 mg/min. The decreasing in the flux at the initial filtration of BSA solution was attributed by absorption or convective deposition of BSA on the membrane surface. Some molecules of BSA adsorbed on the pore surface of membrane and in consequence the formed cake layer caused the decrease in flux. This result matched previous study, cellulose acetate increases membrane hydrophilicity while permeability increases with cellulose acetate concentration because permeability depends on the degree of hydrophilic character of the polymer (10). As

percent CA in the dope solution increased, the decreasing of flux at the initial filtration of BSA solution membrane decreased slightly and gradually mainly at high dope solution mass flow rate, as for 21% CA (Figure 4) because high CA concentration in casting solution suppresses macro-void formation.

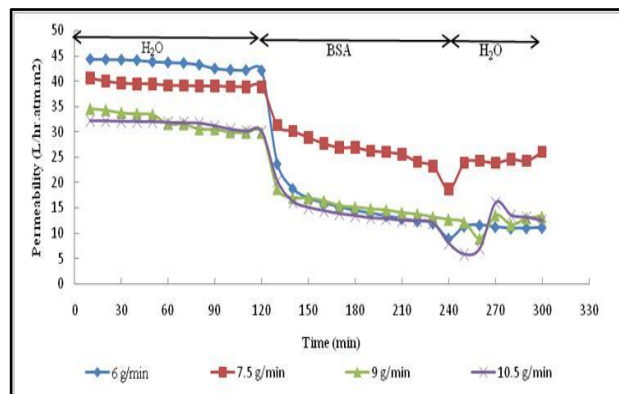


Figure 3: Filtration time of water permeability for 15% CA/DMAc hollow fiber at various dope flow rate.

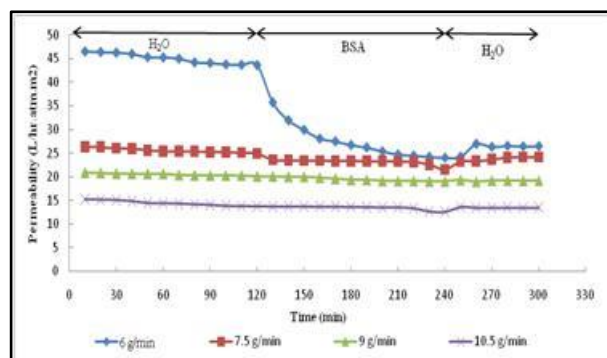


Figure 4: Filtration time of water permeability for 21% CA/DMAc hollow fiber at various dope flow rate

3.2 Effect of bore fluid flow rate

Figure 5 shows the water permeability versus time at various values of bore fluid flow rates (8 to 16 g/min). Results disclosed that, as bore fluid flow rates increased both strength and strain decreased. As the bore fluid flow rate increased the rate of solvent/non-solvent transfer between inner side fiber and bore fluid (non-solvent) increased, consequently, finger like structure at the inner structure increased. The inner side of fiber became more porous and the fiber strength and strain decreased (Figure 6 and Figure 7, respectively). Retention or solute rejection decreased as the bore fluid flow rate increased due to the increase in the macro-voids.

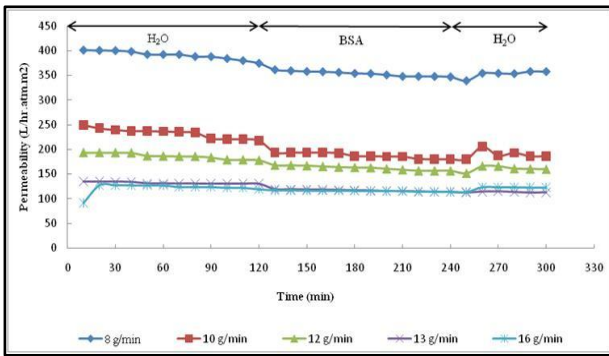


Figure 5: Filtration time of water permeability at different bore flow rate.

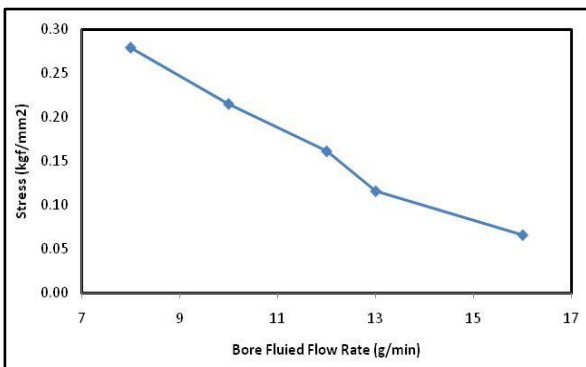


Figure 6: Filtration time of water permeability for variable bore fluid flow rate.

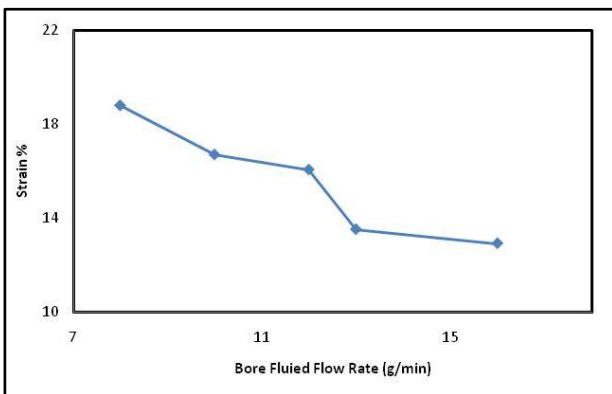


Figure 7: Effect of bore fluid flow rate on the strain of cellulose acetate hollow fibers.

3.3 Effect of bore fluid concentration

Figure 8 shows the water permeability versus time for fibers fabricated at different bore fluid concentration (0 to 50% ethanol). The figure revealed that the water permeability decreased as the ethanol concentration in the bore fluid increased. It was observed that 0% ethanol in bore fluid shows the highest pure water permeation flux and the highest BSA rejection. A summary of the effect of bore fluid concentration (0%, 18%, 25% and 50% ethanol in water) on the hollow fiber membrane BSA rejection is shown in Table 2. As

the percent ethanol increased, percent rejection decreased.

Table 2: Rejection % of BSA at different concentrations of bore fluid.

Ethanol Concentration in Bore Fluid(%Ethanol/H ₂ O)	Rejection %
0%	12.10
18%	10.90
25%	8.31
35%	5.45
50%	4

The morphology of hollow fiber depends on the concentration of bore fluid. The best spinning process was achieved when using pure water as bore fluid. In addition the BSA rejection is 12.10% and that is acceptable. The addition of ethanol (non-solvent) to the bore fluid suppresses formation of macro-voids and leads in low porous membrane.

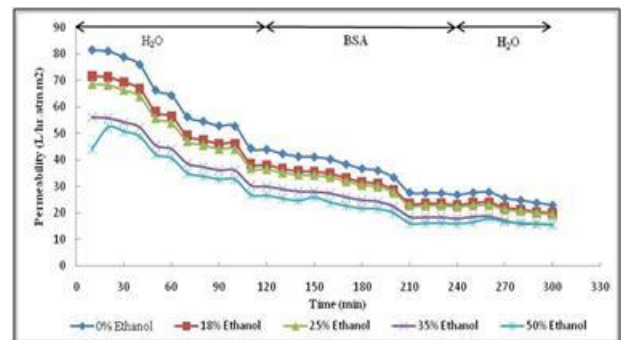


Figure 8: Effect of % ethanol in the bore fluid on the fibers stress.

The effect of ethanol concentration on the membrane tensile stress is shown in Figure 9. Stress decreased as percent ethanol increased. The same trend is observed for the percent strain (Figure 10).

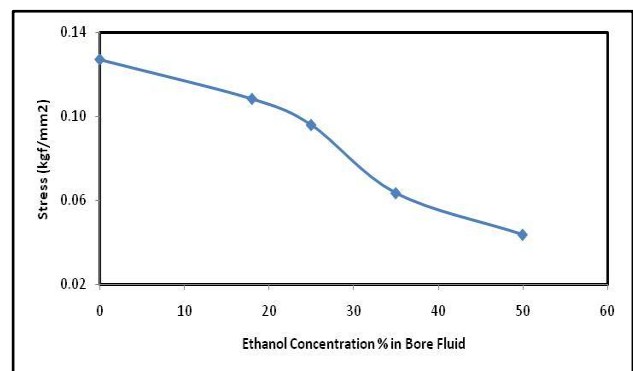


Figure 9: Effect of bore fluid concentration (% ethanol/water) on membrane tensile stress at break.

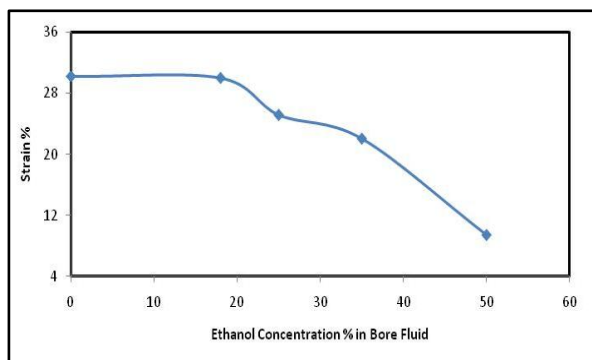


Figure 10: Effect of % ethanol in the bore fluid on the fibers strain.

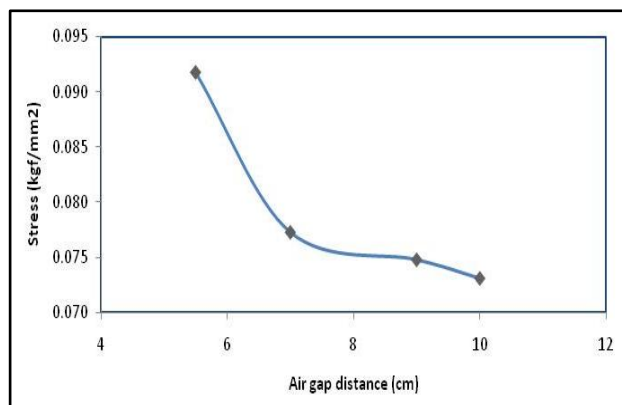


Figure 12: Effect of air gap distance on the stress of fibers fabricated from 21% CA.

3.4 Effect of air gap

The effects of air gap distance on the morphology of the fabricated hollow fiber membranes were studied for air gap distances range 5 to 10 cm and dope solution consisting of 21% CA and 79% DMAc while keeping other operating conditions constant. Figure 11 shows that the water permeability decreased with increased air gap. The longer the nascent hollow fiber membrane is exposed to a humid air gap, the higher the water content in the top layer before de-mixing occurs, resulting in more porous structure and higher permeation rate. Stress and strain were shown to decrease with increased air gap distance (Figure 12 and Figure 13, respectively). This is attributed to the fact that the increased air gap resulted in porous membrane, consequently, weaker structure.

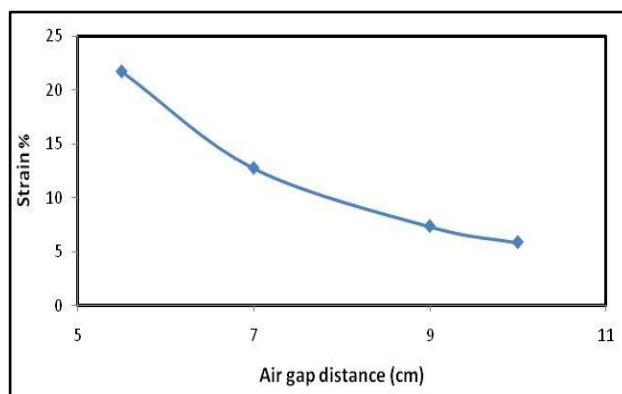


Figure 13: Effect of air gap distance on the strain of cellulose acetate hollow fibers.

5. CONCLUSION

Many preparation factors are known to control the hollow fiber membranes structure and performance. Factors such as dope solution flow rate, air gap distance, the type of bore fluid, bore fluid flow rate and the concentration of polymer in the blending solution had significant effect on membrane morphology and performance. The strength of hollow fiber and hydrophilicity was improved when the cellulose acetate concentration increased in the starting polymer solutions. On the other hand, at a constant cellulose acetate concentration and variable bore flow rate, strength and stain decreased. But when the strength was evaluated, the highest value of strength was achieved at bore flow 8 g/min (air gap of 7cm, 21% CA, the dope solution flow is 6 g/min and using water as bore fluid). The best BSA rejection was obtained at air gap 5.5 cm with 81.49% of BSA rejection. This value of rejection was achieved at bore flow of 15 g/min, dope solution flow rate, 6 g/min dope concentration of 21%CA and using water as bore fluid. The effects of inner coagulation composition on the morphology and performance of cellulose acetate hollow fibers by using different concentrations of ethanol in water indicated that the best results were achieved when using pure water flux as an alternative of using ethanol in water.

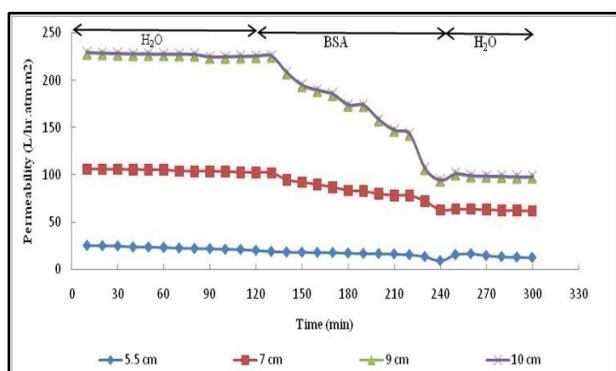


Figure 11: Filtration time of water permeability at different air gap distance.

REFERENCES

- [1] Inzhu Ma, Zhenyn Ding, Guoxiao Wei, Hua Zhao, Tianming Huang. *Sources of Water Pollution and Evolution of Water Quality in the Wuwei Basin of Shiyang River, Northwest China*. 2009, Environmental Management, Vol. 90, pp. 1168-1177.
- [2] Catherine N. Mulligan, Neginmalak Davarpanah, Masaharu Fukue, Tjomohiro Inoue. *Filtration of contaminated suspended solids for the treatment of surface water*. 2009, Chemosphere, Vol. 74, pp. 779-786.
- [3] Shudong Sun, Yilun Yue, Xiaohua Huang, Deying Meng. *Protein adsorption on blood contact membranes*. 2003, Journal of Membrane Science, Vol. 222, pp. 3-18.
- [4] Diana J. Hellman, Alan R. Greenberg, William B. Krantz. *A novel process for membrane fabrication: thermally assisted evaporative phase separation (TAEPS)*. 2004, Journal of Membrane Science, Vol. 230, pp. 99-109.
- [5] Liao-Ping Chenga, Tai-Horng Youngb, Lin Fanga, Jy-Jie Gaa. *Formation of particulate microporous poly(vinylidene fluoride) membranes by isothermal immersion precipitation from the 1-octanol/dimethylformamide/poly(vinylidene fluoride) system*. 1999, Polymer, Vol. 40, pp. 2395-2403.
- [6] Jian-Jun Qin, Juan Gaa, Tai-Shung Chunga. *Effect of wet and dry-jet wet spinning on the shear induced orientation during the formation of ultrafiltration hollow fiber membranes*. 2001, Journal of Membrane Science, Vol. 182, pp. 57-75.
- [7] Sina Bonyadi, Tai Shung Chung, William B. Krantz. *Investigation of corrugation phenomenon in the inner contour of hollow fibers during the non solvent induced phase separation process*. 2007, Journal of Membrane Science, Vol. 299, pp. 200-210.
- [8] Ehsan Saljoughia, Mohtada Sadrzadeha, Toraj Mohammadi. *Effect of preparation variables on morphology and pure water permeation flux through asymmetric cellulose acetate membranes*. 2009, Effect of preparation variables on morphology and pure water permeation flux through asymmetry, Journal of Membrane Science, Vol. 326, pp. 627-634.
- [9] Joel R. Fried, Polymer Science & Technology, 2nd ed. North Bergen, Book Mart and 335-337., 2007. *Polymer Science & Technology*. 2nd Edition. New Jersey: Prentice Hall, 2007. pp. 335-337.
- [10] J. M. Valente, Alexandre Ya. Polishchuk, Victor M. M. Lobo, Hugh D. Burrows. *Transport Properties of Concentrated Aqueous Sodium Dodecyl Sulfate Solutions in Polymer Membranes Derived from Cellulose Esters*. 2000, Langmuir, Vol. 16, pp. 6475-6479.

The Effect of Chemical Application and Excessive Extraction of Water Resources on Groundwater Quality and Environment in Saudi Arabia Najran Region as Study Case

Hussein M. Al-Ghobari

Agric. Eng. Dept., College of food and Agriculture sciences,
King Saud University, Riyadh, Saudi Arabia

ABSTRACT

The main source of water in Najran region is the unconfined shallow aquifer along the Najran Wadi (valley). Ground water quality of Najran region was studied in 43 well water samples collected from different wells in the region. Water samples were chemically analyzed and evaluated using water quality criteria. The investigated water quality parameters revealed the following: Water salinity (EC_w $dS\ m^{-1}$) ranged from 0.35 to 5.99 $dS\ m^{-1}$ (i.e. 227 to 3843 $mg\ L^{-1}$) with an average of 1.95 $dS\ m^{-1}$ (i.e. 1248 $mg\ L^{-1}$), pH value ranged from 7.28 – 7.8 with an average of 7.55. The dominant cation was Ca^{++} followed by Na^+ , Mg^{++} and K^+ while Cl^- was the dominant anion followed by HCO_3^- with an average of 432.4 and 180.2 $mg\ L^{-1}$, respectively. The suitability of this water for irrigation was slight to moderate saline water. Also, about 48.8% of the water had salinity above the recommended level for drinking water. The values of adjusted sodium adsorption ratio (adj. SAR) and residual sodium carbonate (RSC) were in the range of 0.525 to 17.22 and -1.69 to -41.85 with an average of 4.17 and -12.94 $meq\ L^{-1}$ respectively. These results indicated no expected problems with either sodium or permeability from most of the studied wells. Concentration of (NO_3-N) ranged from 0.30 to 33.1 $mg\ L^{-1}$ with an average of 9.48 $mg\ L^{-1}$. All the tested samples have (NO_3-N) concentrations lower than the recommended level for drinking water. Also, it was found that in Najran region a large fraction of farms (more than 35%) which have been equipped with tube wells and irrigation systems have abandoned business and farming as a result of groundwater depletion, this is because the annual groundwater discharge far exceeds the precharge. The excessive extraction of groundwater resources have caused that water for human consumption and agriculture has become an increasingly scarce, which resulted with detrimental effects on the environment by desertification and climate change, especially in Saudi Arabia experiencing drought and hot and dry climate.

Keywords: groundwater; water quality; extraction; environment; Najran

1-INTRODUCTION

The demand for water is not static. It continues to grow as the population increases and living standards improve, and water is becoming scarce not only in arid and drought prone areas but also in regions where rainfall is abundant: water scarcity concerns the quantity of resource available and the quality of the water because degraded water resources become unavailable for more stringent requirements. During the last century, advances in agricultural science and technology have profoundly affected our standard of living and way of life. Agricultural chemicals are an important component of these advances. They contribute substantially to the productivity and efficiency of agriculture and to the well-being of rural and urban communities. Even so, many people are concerned about the possible risks to human health, water quality, and a safe environment resulting from the use of those chemicals. Hence, the quality and quantity of water is a matter of great concern in the world and in particular in arid and semi-arid regions.

There are many parameters to be considered in evaluating quality of irrigation water. The main factors as reported by Ayers (1977) are: salinity, relative amount of sodium, and the other parameters. Many

water quality factors have been considered in order to classify and evaluate the water suitability for irrigation. The influence of The chemical characteristics of water on soil characteristics have been investigated by many researchers including of Richards (1954), Doneen (1958), Rhoades (1972), Oster & Rhoades (1977), Oster & Schroer (1979), Bielorai et al. (1983), Bhivare & Nimbalkar (1984), Moolman (1985), Al Ruwaih et al.(1998) and Al-Kharabshesh (1999).

With growing population, urbanization and irrigated agriculture in arid regions in general and in Saudi Arabia in particular, water shortages are increasing. A major development and progress have been achieved in the agricultural sector in the last 20-30 years in Saudi Arabia because of during the late 1970s and early 1980s, the Saudi government offered free agricultural lands, free-interest loans and farming and investment subsidies for each citizen interested in farming and agriculture. This increased drastically the areas irrigated and hence, the number of wells and the excessive groundwater pumping for irrigation demand. Nowadays agriculture irrigation is the single, largest water demand in the Kingdom of Saudi Arabia accounting for 85-90% of consumptive use (MOP, 2000). This increased drastically the number of wells and the excessive groundwater pumping for irrigation demand. The

excessive extraction of groundwater resources and their resulting problems have influenced the groundwater quality, quantity and the number of wells and farms in each agricultural region in the country, such as, Najran region.

With this fast development of agricultural activities in the country, it has become imperative to study the water quality to assess the chemical characteristics of ground water for the sustainable agriculture management and raising productivity. Several studies were conducted in order to evaluate water quality for irrigation in some areas of the Kingdom of Saudi Arabia, such as, Hamza et al. (1975), Ayed & Mashhady (1982), Mashhady & Yousef (1983), Etewy et al. (1983), Mee (1983), Al-Omran (1987), Bazuhair & alkaff (1989), Hussain & Sadiq (1991), Al-Ghobari (1992), Al-Jaloud & Hussain (1993) and Abdel-Aal et al. (1997). Most of these studies were concentrated in the central and eastern regions of Saudi Arabia. Abdel-Aal et al. (1997) studied the ground water quality for irrigation in two hundred and seventeen well water samples from central Saudi Arabia. They reported that water salinity ranged from 210 to 8200 ppm with an average of 2375 ppm. In general, the information on irrigation water quality classification for agriculture is inadequate as a guideline to optimize the use of groundwater in Saudi Arabia. With the expansion of agriculture lands, the agriculture related pollution sources, such as, pesticides, fertilizers, etc. are gradually contaminating groundwater (El Din et al. 1993). It is, therefore, important to monitor and protect the quality of groundwater from such pollutant. The previous studies concentrated on selected regions and the literature lacks reliable studies on groundwater quality in the southern region of Saudi Arabia, which is considered as one of the major agricultural region of the country. Accordingly, the main objective of this study is to evaluate the ground water quality of Najran region for irrigation on the basis of chemical composition. Also, to show the effect of excessive extraction of groundwater resources on the environment and their resulting problems suffered in the number of wells and farms abandoned after 20-30 years of use in Najran region.

2. MATERIALS AND METHODS

2.1 Description of the studied area

Najran region is semi-mountainous, and located about 980 kilometers from Riyadh region, in the south-western of Saudi Arabia (mean altitude 1250 m above sea level). The region is bordered by the vast Rub Al-Khali desert in the east, the mountainous Assir region in the west and Republic of Yemen in the south. Wadi Najran flows from west to east where the studied wells were located in areas dominated by fertile agriculture lands. Most towns and villages of Najran are located along the banks of the wadi. The groundwater is available in a shallow alluvial aquifer along the Najran

wadi. This aquifer is generally unconfined and the water table fluctuates rapidly in response to the local precipitation and season. Water pumped from wells was generally used for all purposes including domestic, drinking, and cooking, as well as irrigation. The annual average of rainfall is 100- 200 mm.

2.2 Water samples and methods of analysis

Forty three tube well water samples were collected from different locations to represent the agricultural areas located along the banks of Wadi Najran. The water samples were collected for analysis from the delivery pipe of the pumps in clean Agene sample bottles after running for at least five hours and then the bottles were sealed airtight. Water samples were analyzed as follows; electrical conductivity (E_w) and pH of water were determined using standard Electrical Conductivity meter (EC) and pH meter respectively according to Richards, 1954. Soluble calcium (Ca^{++}) and magnesium (Mg^{++}) were determined according to the procedure of Chapman and Pratt, 1961. Carbonate (CO_3^-), bicarbonate (HCO_3^-) and chloride (Cl) were determined as recommended by Chapman and Pratt (1961). Sodium (Na^+) and potassium (K^+) were analyzed using the flame photometer. Nitrate ($NO_3^- - N$) was measured using spectrophotometer according to the method described by Hack, 1998. Also, discharges of the 43 selected tube wells were measured and the daily times of irrigation for each pump were determined.

3. RESULTS AND DISCUSSION

Results of chemical analysis and the calculated water quality parameters are presented in tables 1 and 2. Data indicated that, salinity of the pumped water of the studied wells (EC_w) expressed in dSm^{-1} covers the range of 0.35 to 5.99 dSm^{-1} ; i.e. 227 to 3834 ppm. The average salinity level was 1.95 dSm^{-1} ; i.e. 1248 ppm. These data indicated high variations between the studied wells. Its shows also that application of the relatively high salt content water will add seasonally relatively high quantity of soluble salts to the soil. In that respect Abdel-Aal et al. (1997) reported that using water with 2375 ppm salts in the central region will deposit between 16.6 and 83 $t\ ha^{-1}$ of salt per season for wheat and alfalfa cultivation, respectively. There are several sources, which might have contributed to the high salt concentration values in some of the studied wells. These sources are over-exploitation and excessive pumping, heavy application of inorganic fertilizers, organic amendments and low efficiency irrigation management. The rise in salt contents of well waters by excessive pumping is a phenomenon observed generally in the region. According to the recommendations of the United States Salinity Laboratory (USSL) guideline (Richards 1954) the suitability of the studied well waters is saline to moderate saline water. Previous studies on the quality of irrigation water of the central Saudi Arabia, (Abdel-

Aal et al. 1997) indicated that, water salinity ranged from 210 to 8200 ppm. Application of low quality irrigation water to the soil will increase the concentration of soluble salts in the root zone. It was noticed that with reasonable good irrigation practices the salt content of the saturation extract of soil is 1.5 to 3 times salt content of the irrigation water. Moreover, leaching with ordinary irrigation methods decreases salt accumulation but not eliminate such accumulation. On the other hand, According to the recommended levels in the guideline of the world health organization (WHO 1984) for salinity of drinking water about 48.8% of the wells had salinity values above the WHO standard of 1000 ppm.

Analysis of soluble cations and anions indicated that, the dominant cation was Ca^{++} with an average value of 203.8 ppm for the forty three well water samples followed by Na^+ and Mg^{++} with an average values of 124.33 and 68.43 ppm respectively, (Table 1). The only exception was observed in the highest salt concentration water wells where Na^+ was the dominant cation followed by Ca^{++} and Mg^{++} (well No. 41, 42 and 43). Potassium (K^+) was present in relatively low concentrations, but its concentration was increased with the increase in EC_w values. The dominant anion was Cl^- followed by HCO_3^- while CO_3^- was absent in all the studied samples. The average concentrations were 432.41 and 180.22 ppm for Cl^- and HCO_3^- anions respectively.

It appears that, chloride concentrations increased gradually with the increase in salt contents of the well water. As mentioned by Ayers (1977) water with less than 140 ppm Cl sensitive plants usually show slight to moderate injury. Severe problems are found at Cl

concentrations greater than 350 ppm. Therefore, it should be noticed that the high Cl^- water may cause sever problems for the sensitive and moderately tolerant plants particularly trees and woody ornamentals. The data also indicated that, pH values ranged from 7.88 to 7.80 with an average value of 7.55. It seems that, the obtained pH values did not show significant fluctuations between all the studied wells.

Examining the data for the two sodicity parameters Adj. SAR and RSC as presented in Table (2), it can be observed that the former covers the range of 0.525 to 17.22 with an average of 4.17, whereas the latter ranges between -1.69 to -41.85 with an average of -12.94 meq L^{-1} . It appears that most of the studied water samples have Adj SAR values less 6.0 which indicate no problems with either sodium or soil permeability. As the majority of the soils of Wadi Najran are alluvium soils (i.e. loamy to sandy loam or sandy soils), the sodicity build up is not expected as a result of using these waters to irrigate such soils. This conclusion was also supported by the very low RSC values of all the studied samples. The RSC values (Table 2) are generally low and shows such values are mostly desired.

Concentration of nitrate ($\text{NO}_3 - \text{N}$) ranged from 0.3 to 33.1 ppm with an average value of 9.48 ppm. The levels of ($\text{NO}_3 - \text{N}$) in the studied well waters varied significantly from one well to another. But, in view of the WHO (1984) which put the limit of 45 ppm nitrates as the highest tolerable nitrate content in drinking water, it can be recognized that all the tested wells have a concentrations less than 45 ppm, as shown in table (1). There are several potential sources, which might have contributed to elevated levels of $\text{NO}_3\text{-N}$ in some wells, including human and animal wastes, nitrogenous fertilizers, organic manures and domestic wastes.

Table 1: Chemical composition of irrigation groundwaters for the studied wells from Najran region*

Well No.	EC_w (dSm^{-1})	pH	TDS (ppm)	Ca^{++} (mgL^{-1})	Mg^{++} (mgL^{-1})	Na^+ (mgL^{-1})	K^+ (mgL^{-1})	Cl^- (mgL^{-1})	HCO_3^- (mgL^{-1})	$\text{NO}_3\text{-N}$ (mgL^{-1})
1	0.35	7.26	227	48.4	12.6	11.3	3.1	74.6	108.7	0.3
2	0.53	7.3	339	65.3	18.8	25.5	3.5	74.6	112.2	0.5
3	0.55	7.32	349	69.5	20.2	27.5	3.6	94.7	123.2	0.8
4	0.56	7.35	355	71.6	20.3	27.8	4	106.5	124.4	0.8
5	0.57	7.37	363	73.7	22.9	29.5	4	112.4	125.7	1.1
6	0.57	7.38	365	73.7	24.1	30.3	4.3	142	128.1	1.4
7	0.61	7.44	388	88.4	25.4	31.5	4.4	142	136.6	1.4
8	0.64	7.45	408	88.4	26.6	32.5	4.4	142	142.7	1.5
9	0.72	7.45	463	96.8	28	32.5	4.4	145.69	142.7	1.6
10	0.78	7.46	496	98.9	29.2	32.8	4.5	177.5	150.1	1.7
11	0.82	7.46	522	101.7	30.4	35	4.6	177.5	151.3	2.7
12	0.84	7.48	534	115.8	30.5	36.3	4.6	177.5	153.7	2.7
13	0.85	7.48	543	115.8	30.5	38.3	4.6	195.3	154.9	3
14	0.91	7.48	580	117.9	34.4	42.3	4.7	195.3	156.2	3.7
15	0.95	7.48	609	120	35.5	43.3	4.8	266.3	156.2	3.9
16	0.97	7.51	621	120	35.5	43.5	5.7	266.3	157.4	5.0

17	1.0	7.53	637	122.1	38.1	52	5.7	266.3	158.6	5.1
18	1.19	7.54	759	128.4	38.1	54	6.5	284	162.3	5.2
19	1.33	7.54	848	130.5	40.6	70	6.8	284	163.5	6.4
20	1.38	7.54	884	155.8	49.6	78	7.2	284	167.1	6.5
21	1.47	7.56	940	157.9	56.9	78.8	7.4	301.8	168.4	7.2
22	1.47	7.56	943	166.3	59.6	80.5	7.6	301.8	170.8	7.2
23	1.83	7.57	1170	210.5	59.7	80.5	7.9	355	172	7.6
24	1.96	7.57	1252	218.9	62.1	100.3	7.9	355	173.2	7.9
25	2.07	7.58	1325	225.3	63.4	101.5	8	408.3	175.7	8.6
26	2.1	7.59	1344	237.9	63.6	103.8	8.1	426	176.6	8.6
27	2.13	7.6	1363	240	64.7	104.3	8.2	426	176.9	8.7
28	2.2	7.6	1408	256.8	64.7	105	8.8	426	180.6	9.4
29	2.21	7.61	1414	256.8	67.3	111.3	9.5	426	180.6	9.8
30	2.23	7.62	1427	261.1	73.8	114	9.6	461.5	186.7	9.8
31	2.33	7.64	1491	265.3	76.1	130.3	9.6	514.8	190.3	10.1
32	2.37	7.64	1517	267.4	76.2	131.3	9.6	532.5	191.5	10.7
33	2.38	7.65	1523	269.5	81.3	137.3	10.5	532.5	194	14.6
34	2.53	7.65	1619	271.6	82.5	159.5	10.6	550.3	195.2	15.2
35	2.57	7.66	1645	282.1	95.3	172.8	11.2	603.5	203.7	15.4
36	3.03	7.66	1939	313.7	110.5	173	11.8	642.6	207.4	15.6
37	3.64	7.67	2330	317.9	116.9	175.8	12.1	798.8	214.7	16.0
38	4.07	7.67	2605	334.7	128.2	252.5	12.7	869.8	229.4	20.1
39	4.11	7.68	2630	353.7	130.7	305	13.2	1011.8	230.6	24.4
40	4.14	7.72	2650	406.3	154.9	345	13.3	1047.3	261.1	27.9
41	5.23	7.73	3347	429.6	192.2	462.5	14.1	1171.5	279.4	32.0
42	5.62	7.79	3597	482.1	212.2	567.5	15.1	1278	323.3	32.4
43	5.99	7.8	3834	534.7	258.4	580	26.8	1544.3	391.6	33.1
Average	1.95	7.55	1246.58	203.79	68.43	124.33	8.12	432.41	180.22	9.48

* CO_3 = Not Detected

Table 2: Water quality parameters for the studied well water samples

Well No.	Adj SAR*	RSC**	Well No.	Adj SAR*	RSC**	Well No.	Adj SAR*	RSC**
1	0.525	-1.69	18	2.460	-6.94	35	5.33	-18.71
2	1.104	-2.99	19	2.464	-7.24	36	6.33	-21.77
3	1.302	-3.14	20	2.563	-9.18	37	7.86	-22.12
4	1.344	-3.23	21	2.784	-9.88	38	8.53	-23.58
5	1.344	-3.54	22	3.290	-10.49	39	9.34	-24.80
6	1.351	-3.60	23	3.629	-12.69	40	9.73	-28.94
7	1.40	-4.30	24	3.620	-13.29	41	10.97	-32.92
8	1.40	-4.30	25	3.88	-13.67	42	14.64	-36.39
9	1.470	-4.83	26	3.984	-14.30	43	17.22	-41.85
10	1.704	-4.92	27	3.984	-14.49	Mean	4.17	-12.94
11	1.704	-5.14	28	3.952	-15.27			
12	1.712	-5.81	29	4.430	-15.49			
13	1.720	-5.79	30	4.280	-16.15			
14	1.931	-6.21	31	4.540	-16.49			
15	1.980	-6.40	32	4.540	-16.58			
16	2.42	-6.38	33	4.580	-17.08			
17	2.42	-6.69	34	4.830	-17.26			

*Adjusted Sodium Adsorption Ratio (Adj. SAR) = $SAR [1+(8.4 - pH_C)]$

Where: $pH_c = (pk_2^1 - pk_c^1) + p(Ca^{++} + Mg^{++}) + pAlk$, and $pk_2^1 - pk_c^1$ is obtained from $Ca+Mg+Na$. $p(Ca+Mg)$ is obtained from $Ca+Mg$, and $pAlk$ is obtained from $CO_3^- + HCO_3^-$.

p refers to the negative logarithm, K_2^1 is the second dissociation equilibrium constant of carbonic acid, and K_c^1 is solubility equilibrium constant for calcite.

Concentrations of Ca^{++} , Mg^{++} ,

CO_3^- and HCO_3^- are in $meq L^{-1}$.

** Residual Sodium Carbonate (RSC) = $(CO_3 + HCO_3) - (Ca + Mg)$ $meq L^{-1}$

The discharges for 43 tube wells (Figure 1) and daily irrigation times (Figure 2) varied from one farm to another as shown in the figures. The discharges ranged between 23 to 65 m^3/hr and the times of irrigation ranged between 2 to 20.3 hour/day. It should be mentioned that the groundwater was the only source of irrigation and the surface irrigation was the predominant irrigation method used in the region. Also, it was observed during the visits to the selected farms that most soils were sandy to loamy sands and irrigation channels were not lined and farm lands were not properly leveled. Also, it was noticed that farmers had little knowledge of crop water requirements, and there was excessive water applied during every irrigation. These factors were responsible for heavy water losses during conveyance and field application, and this made the existing annual groundwater discharge exceeded the limited annual recharge. This excessive withdrawal of groundwater lowered the groundwater levels, increased groundwater salinity (Figure 3) and hence affected the discharge of the tube wells in operation, and in fact some of these tube wells dried up and ultimately a number of the farms were abandoned each year in Najran region as shown in the figure (4). The number of tube wells in operation to pump water for irrigation in Najran before 20 years over 4000 and now less than 2000.

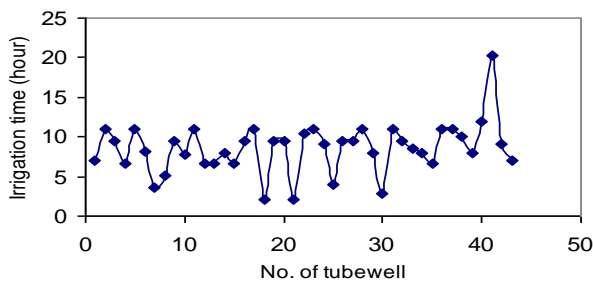


Figure 1: Variation of discharges from 43 tube wells

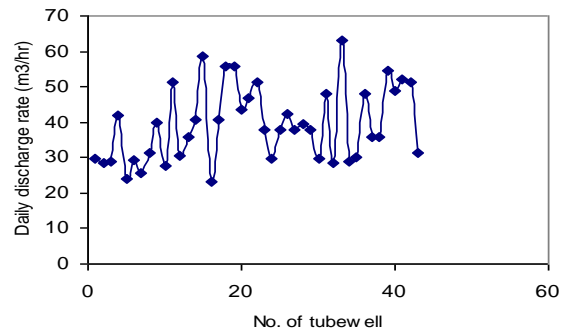


Figure 2: The times of daily irrigation for 43 tube wells

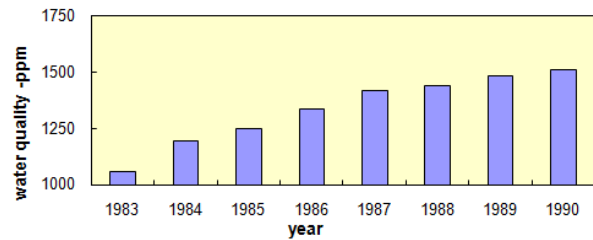


Figure 3: The increase of groundwater salinity caused by excessive pumping of groundwater



Figure 4: Farms of date palm and citrus trees abandoned, as result of groundwater depletion.

4. CONCLUSION

In the light of the preceding results and discussion, the following conclusion can be drawn. The survey of the quality of 43 tube well waters in Najran region has demonstrated high levels of some indicators measured. Elevated concentrations of total dissolved salts were

observed and 48.8% of the wells had salinity levels values above the WHO recommended values. A wide variation of nitrate concentrations was detected, and all the tested wells have lower concentrations lower than 45 ppm.

Also, it was found that in Najran region a large fraction of farms (more than 35%) which have been equipped with wells and irrigation systems have abandoned business and farming as a result of groundwater depletion, because of the increased areas irrigated and hence, the number of tube wells and also, poor irrigation water management. The excessive extraction of groundwater resources have caused that water for human consumption and agriculture has become an increasingly scarce, which resulted with detrimental effects on the environment by desertification (figure 3) and climate change, especially in Saudi Arabia experiencing drought and hot and dry climate.

Therefore, water quality is a major concern in the Region and Groundwater resources can deteriorate as a result of over-exploitation or, when used intensively pesticides, insecticides and without the necessary precautions. In view of the present study, it is suggested that optimizing the application of organic and inorganic fertilizers, and better management of the groundwater, could control the degradation in the quality of some well waters in Najran region. The need for further investigation on more well waters and on a routine bases is imperative to help control sources of water management and accurate evaluation of their magnitude and also, to reduce the number of the abandoned farms each year in Najran region.

5. REFERENCES

- [1] Abdel-Aal, S. I., Sabrah, R. Rabie, R. K. & Abdel Magid, H. M. 1997. Evaluation of ground water quality for irrigation in center Saudi Arabia. Arab Gulf J.Sci. Res., vol.15(2): 361-377.
- [2] Al-Ghobari, H. M. 1992. Influence of Irrigation Water Quality on Soil Infiltration. Irrigation Science 14:15-19.
- [3] Al-Jaloud, A. A. 1999. Use of Saline Water for Irrigation in Saudi Arabia, Journal of Mediterranean Ecology, Vol. 2-106-117.
- [4] Al-Jaloud, A. A. & Hussain, G. 1993. Water quality of different aquifers in Saudi Arabia and its predictive effects on soil properties. Arid soil research and rehabilitation, vol. 7:85-101.
- [5] Al-Kharabshesh, A. 1999. Ground-water quality deterioration in arid areas: a case study of the Zerqa river basin as influenced by Khirbet Es-Samra waste water (Jordan). J. of Arid Environments, vol. 43(3):227-239.
- [6] Al-Omran, A. M. 1987. Evaluation of some irrigation water in central region of Saudi Arabia. J. Coll.Agric. King Saud Univ., vol.9(2):363-369.
- [7] Al Ruwaih, F., Sayed, S. & Al-Rashed, M. 1998. Geological controls on water quality in arid Kuwait. J. of Arid Environments, vol. 38(2):187-204.
- [8] Ayed, I. A. & Mashhady, A. S. 1982. Irrigation water and patterns of soil salinization of Deirab. J. Coll. Agric. King Saud Univ., vol. 4: 139-144.
- [9] Ayers, R. S. 1977. Quality of water for irrigation. J. of irrigation and Drainage Division. ASCE., vol. 103: 135-154.
- [10] Bazuhair, A. S. & Alkaff, A. 1989. Evaluation of ground water quality in wadi Al-Yamaniyah, Saudi Arabia. Arab Gulf Journal of Scientific Research, vol. 7: 21-38.
- [11] Bielorai, H., Shalhevet, J. & Levy, Y. 1983. The effect of high sodium irrigation water on soil salinity and yield mature grapefruit orchard. Irrigation Science, vol. 4:255-266.
- [12] Bhivare, V. N. & Nimbalkar, J. D. 1984. Salt stress effects on growth and mineral nutrition of French beans. Plant and Soil, vol. 80:91-98.
- [13] Chapman, H. D. & Pratt, P. F. 1961 Methods of Analysis for Soils, Plants and water. Univ. California, Berkeley, CA., USA., pp. 1-309.
- [14] Doneen, L. D. 1958. Studies of water quality criteria. Quality of water for irrigation Proc., Water resources center, UC. Davis, Calif., U.S.A.
- [15] El Din, M. N., Madany, I. M. Tayaran, A. Al-Jubair, A. H. & Gomaa, A. 1993. Trends in water Quality of some wells in Saudi Arabia. Sci.Total Environ.,vol.154:110-122.
- [16] Etewy, H., Asseed, M. Al-Barrack, S. & Turjoman, A. M. 1983. Water quality and soil characteristics as related to irrigation and drainage in Al-Hasa area. Saudi Biological Society Proc. 6th Conf. 489-512.
- [17] Hack, D.R. 1998. Analysis of nitrate-nitrogen and Cadmium Reduction Method and Programme No. 2520. pp. 495-502.
- [18] Hamza, A. G., Louty, M. A. Mustafa, A. M. & Hassan, M. M. A. 1975a. Riyadh water and its utilization as mineral water, part II: Anion determination. Bulletin, Faculty of science, Riyadh University, vol. 7: 257-261.

- [19] Hussain, G. & Sadiq, M. 1991. Metal chemistry of irrigation and drainage waters of Al-Hassa Oasis of Saudi Arabia and its effects on soil properties. *Water, Air and Soil Pollution* 57/58: 773-783.
- [20] Mashhady, A. S. & Yousef, A. F. 1983. Evaluation of Al-Qatif irrigation water based on recent concepts of quality appraisal. *J. Coll. Agri. King Saud Univ.*, vol. 5:29-34.
- [21] Mee, J. M. 1983. Saudi ground water chemistry and its significance. *Arab Gulf J. Sci. Res.*, vol. 1: 113-120.
- [22] Moolman, J. H. 1985. The effect of a change in irrigation water quality on the salt load of the deep percolate of a saline sodic soil: a computer simulation study. *Irrigation Science*, vol. 6:19-28.
- [23] National Center for Horticultural Research and Development, Najran, Ministry of Agriculture and Water. Annual technical report (1987-2005) in co-operation with Food and Agriculture Organization of United Nation (FAO), UTFN/006/SAU.
- [24] Oster, J. D. & Rhoades, J. D. 1977. Various indices for evaluating the effective salinity Conference, August 1977, Texas Technical University, Lubbock.
- [25] Oster, J. D. & Schroer, F. W. 1979. Infiltration as influenced by irrigation water quality. *Soil Science Society of America Proceedings*, vol. 43: 44-47.
- [26] Rhoades, J. D. 1972. Quality of water for irrigation. *Soil Science J.*, vol. 113: 277-284.
- [27] Richards, L. A. (ed.). 1954. Diagnosis and Improvement of saline and alkali soils. USDA. Agric. Hand book No. 60. Washington, D. C., pp. 160.
- [28] World Health Organization (WHO). 1984. Guidelines for Drinking Water Quality, Vol. 2. Health criteria and other supporting information, Geneva.

Model-Free Control of pH in the Neutralization of Alkaline Waste Water using CO₂ Gas

E. M. Elkanzi¹, N. Mansoor², M. Bin Daina³

¹Department of Chemical Engineering, University of Bahrain (eme42@hotmail.com)

²Department of Chemical Engineering, University of Bahrain (nmansoor@eng.uob.bh)

³Department of Chemical Engineering, University of Bahrain (mbdaina@uob.edu.bh)

ABSTRACT

Modeling the dynamics of the CO₂ neutralization process involves the coupling of the gas- liquid mass transfer with chemical reactions. Also, due to the nonlinear dependence of the pH value on the amount of titrated reactant, the process will be inherently nonlinear. As a result, it becomes difficult to develop an appropriate mathematical model of the pH process for designing a controller. Control strategies based on experimental titration curve have been proposed to overcome pH control problems of which various variations of model-free control strategies have been implemented. The problem with the experimental titration in gas-liquid systems is its strong dependence on mass transfer. Since the reactions involved are relatively fast, mass transfer resistance would be dominating and dependent on the state of mixing. This paper discusses an alternative approach to solve the experimental titration problem by determining the titration curve at different CO₂ bubbling velocities and choosing the one with the minimum mass transfer resistance. Based on this titration curve a PID control strategy was proposed for which the controller parameters were determined by manual tuning. These parameters were then used for the pH control after disturbance in NaOH flow and the controller successfully returned the process to its set point.

Keywords: CO₂ neutralization, pH, mass transfer, model-free control

1. INTRODUCTION

Most process plants generate a wastewater effluent that must be neutralized prior to discharge or reuse. Industrial, institutional and commercial wastewater management is a process that every business must recognize both as a cost and a potential liability. Wastewater neutralization plays an important role in wastewater treatment processes. It provides the optimum environment for microorganism activity i.e. between pH 6.5 and 7.5, and the right water discharge to the public sewage as mandated by the Department of Environment of between pH 5 and 9 (Environmental Quality Act, 1974). Wastewaters can be classified as: Municipal wastewaters and industrial wastewaters. Municipal wastewaters are produced by domestic activities of the community while industrial wastewaters result from spills, leaks, product washing, etc. The use of CO₂ as a neutralizing agent contributes to the trading of carbon credits, and the likely increasing financial cost of greenhouse gas emissions to individual companies should help promote substantial cuts in incidental carbon dioxide emissions from industry through improved efficiency and greenhouse gas capture. Moreover, strong mineral acids such as sulphuric and hydrochloric acids have traditionally been used to neutralize alkaline waste streams prior to discharge [1]. However, CO₂ is becoming increasingly popular as a replacement for mineral acids for several advantageous reasons. For example, the amount of CO₂ required to neutralize the same amount of alkaline is less than that required by mineral acids [2], as shown in

Fig.1. Adjusting the pH in a waste stream is one of the most difficult processes in wastewater treatment. Good pH neutralization and adjustment includes proper mixing, tank configuration, and instrument control. Consequently, pH control is needed in just about every process plant, and yet a large percentage of pH loops perform poorly. Results are inferior product quality, environmental pollution, and material waste. With ever increasing pressure to improve plant efficiency and tighter regulations in environmental protection, effective and continuous pH control is highly desirable. In CO₂ pH neutralization processes, the control of pH is not only a control problem but also comprises, mass transfer, chemical equilibrium, kinetics, and thermodynamics problems all of which must be considered [3]. The mass transfer problem is the most interesting and challenging one to be solved. Mass transfer varies with the hydrodynamics (mixing and/or gas flow rate) of the process and thus changes the process gain, making it difficult for robust controller design. If the speed of mixing or the inlet gas flow changed, the shape of the titration curve would be altered [4]. As a result, it is difficult to develop a mathematical model of the CO₂ neutralization process and the control may be based on the optimal experimental titration curve, as many previous studies on the control of pH [5,6, and 7] have proposed. Some researchers [8, 9] proposed methods to overcome the nonlinearities and varying titration curve such as online identification using a set point change for PID auto-tuning. Others [10, 11] used strategies based on intelligent control such as fuzzy control, neural net

works or different combinations of intelligent and model-based methods.

This paper discusses an alternative approach to solve the experimental titration problem by determining the titration curve at different CO₂ bubbling velocities and choosing the one with the minimum mass transfer resistance. Based on this titration curve a PID control strategy is to be proposed for which the controller parameters are to be determined by manual tuning. These parameters are then to be used for the pH control after disturbance in NaOH flow.

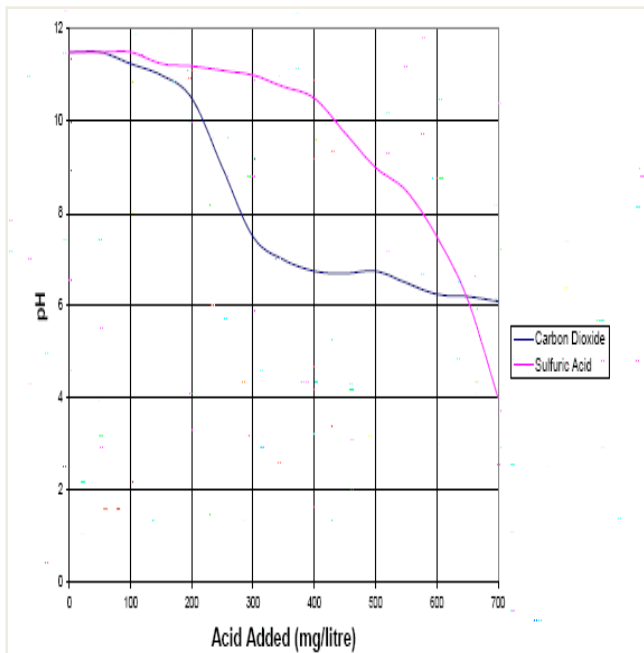


Figure 1: CO₂ H₂SO₄ Comparative Neutralization Curves of an Alkaline Waste Water [2]

2. EXPERIMENTAL WORK

2.1 Experimental Setup

The experimental setup, shown in Figure (2), consists of an adapted Sterifil Aseptic filtration system (Millipore) where the alkaline solution, such as diluted sodium hydroxide solution, is contained in the funnel and the CO₂ gas is bubbled through the spectral/mesh filters (Millipore of sizes 61,51,41,30µm) from the bottom. When operated continuously, the liquid overflows the funnel thus keeping the solution volume constant. The gas and liquid flow rates are measured and controlled by MC series 16 Bit and LC series 16 Bit gas and liquid flow meters (Cole Parmer). The solution pH is measured by a general purpose pH meter (Jenway 3305), operational amplifier (INA114), LabVIEW Card (NISC6-68) and a Dual DC regulated power supply.

2.2 Experimental Procedure

For the dynamic experiments, the setup was operated in a semi-batch manner by bubbling CO₂ through a

constant volume of the sodium hydroxide solution of known pH. The solution pH was measured, online, with time keeping the CO₂ flow rate constant and varying the filter size. The CO₂ flow rate was then varied, from 100 to 500 ml/min STP, using the filter that gave the fastest response in order to determine the best possible flow rate that gives the fastest possible response.

For the control experiments, the setup was operated continuously. The control experiments were run using the fastest possible response curve as the experimental dynamics of the system and constant liquid flow rate of 400 ml/min. In all experiments the temperature was kept constant at 25° C. Closed loop control experiments were run for tuning manually the PID parameters using the Online Method. These parameters are to be used in auto-control of the neutralization process.

3. RESULTS AND DISCUSSION

3.1 Dynamic Experiments Results

The series of semi-batch experiments performed to investigate the mass transfer effect on the dynamic response of the system was to vary the filter size while keeping other variables constant. Figure 3 shows the results for 51, 41 and 30 µm filter sizes. Of the sizes used, the 30 µm filter gave the fastest response. This is due to the fact that the smaller the filter size, the higher is the gas bubbling velocity and consequently the higher is the mass transfer rate. Figure 4 shows the results of the effect of the gas flow rate on the response using the 30 µm filter and gas flow rates of 100 to 500 ml/min STP. Again the higher the gas rate the faster is the response. Therefore the dynamic response using the 30 µm filter and a CO₂ flow rate of 500 ml/min would be the experimental process dynamics to be used in the subsequent continuous control of the neutralization process.

3.2 Continuous Process Control

The controller algorithm used is the PID VI s from labVIEW implemented on a PC with the NISC6-68 I/O device. The PID controller output algorithm is represented by:

$$u(t) = K_c \left(e + \frac{1}{T_i} \int_0^t e dt + T_d \frac{de}{dt} \right) \quad (1)$$

With the following formula representing the current error used in calculating the controller output u(t):

$$eb(k) = (\beta^* SP - PV_f)(L + (1-L)^*) \frac{|\beta SP - PV_f|}{SP_{range}} \quad (2)$$

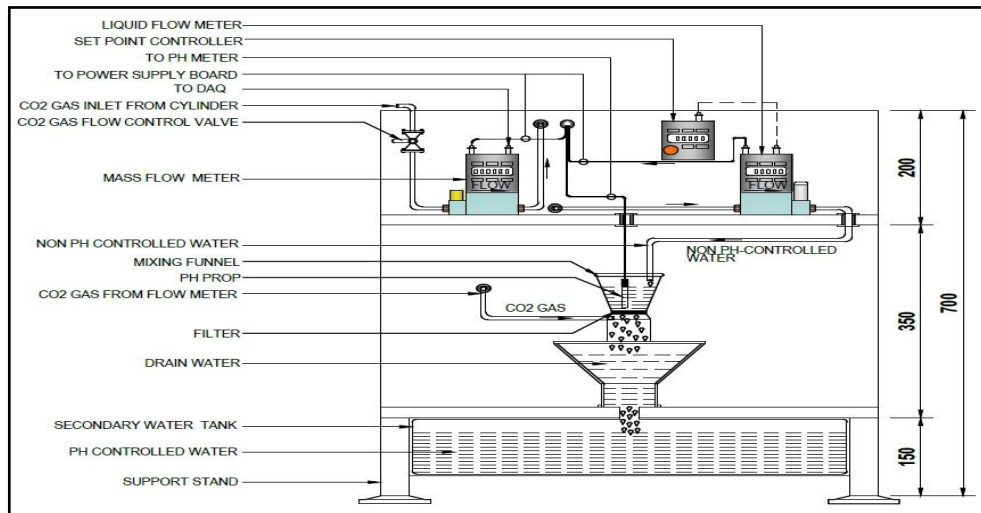


Figure 2: Neutralization process panel front view

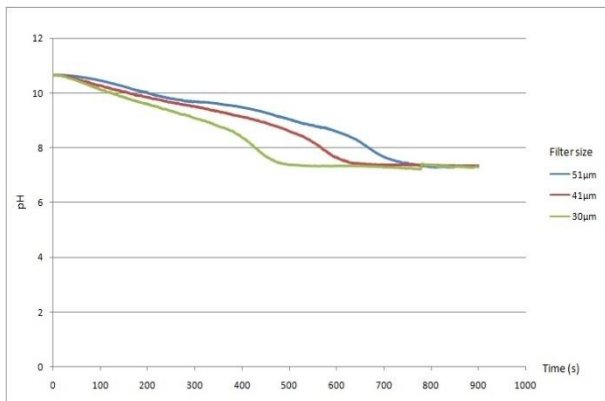


Figure 3: pH change with time for different filter sizes and at constant CO₂ flow rate of 500 ml

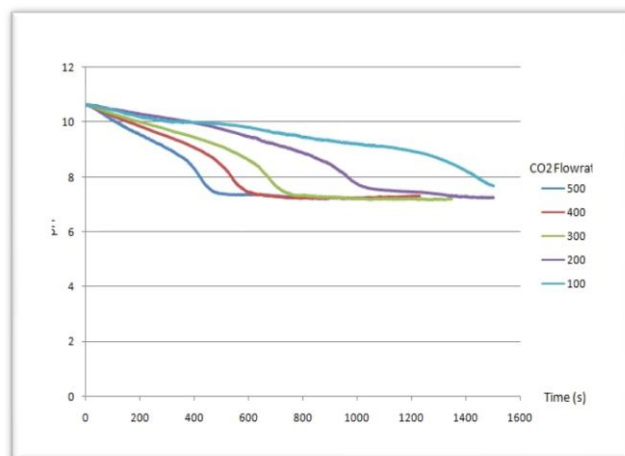


Figure 4: Dynamic responses for filter size 30µm at different CO₂ flow rates

Tuning the PID parameters done by the Manual Tuning (Online method) gave the values of the parameters shown in Table1. These parameters were applied for the continuous neutralization process control using the 30 µm filter, liquid flow rate of 400 ml/min, and set point of 6.5. Figs. 5-7 show the results of the responses.

Table 1: Tuned PID Parameters Values

Parameter	Value
Kc	-8.000
Ti	0.2 (min)
Sampling Time	0.1 (s)
Filter Time Constant	0.3 (s)
β	1.0
Linearity (L)	1.0
Spike limit	0.2

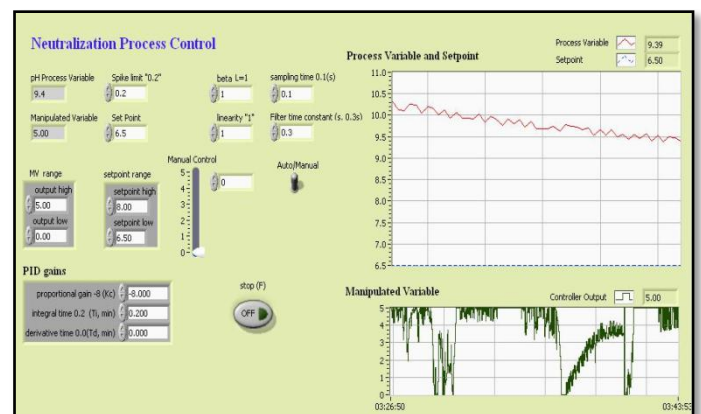


Figure 5: Process variable start decrease under PID controller.

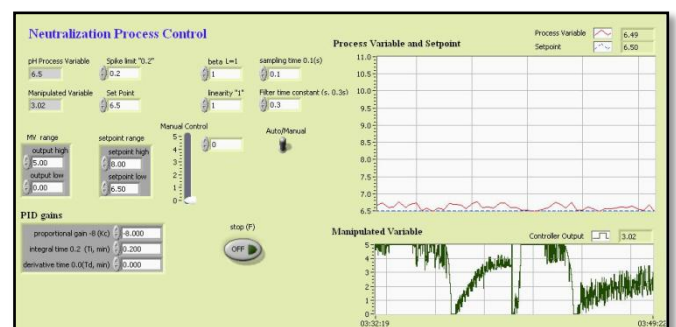


Figure 6: pH regulated at 6.5 under PID controller.

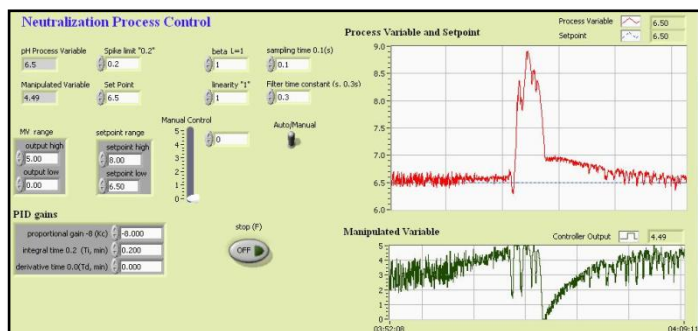


Figure 7: Disturbance rejection under PID controller.

Figure 8 shows the whole auto controlling period with disturbance in the form of Excel data sheet.

The results shown in figures 5-8 show that when using the experimental dynamics of the neutralization process, the pH value successfully reached the desired set point and the controller returns the process value to the desired value even when disturbance is added. No spike and no signal noise occurred during the auto controlling.

4. CONCLUSIONS

The following conclusions may be drawn from this work:

1. Since the model-free control is based on the experimental dynamics, it requires the minimization of mass transfer intrusion in the gas-liquid neutralization process.
2. The auto control results show that the PID controller performed reasonably well using the experimental dynamics of the process.

REFERENCES

- [1] Moore, R.L " Environmental Protection by the Neutralization of Wastewater using pH Control", Instrument Society of America, 2nd ed. (1995).
- [2] Carbon Dioxide Versus Mineral Acids Available: www.astisensor.com/Carbon_Dioxide_Versus_Mineral_acids.pdf.
- [3] Elkanzi, E.M."Using Carbon Dioxide for Alkaline Wastewater Treatment". Available: http://www.co2management.org/proceedings/Elkanzi_ARAMCO_CO2.pdf

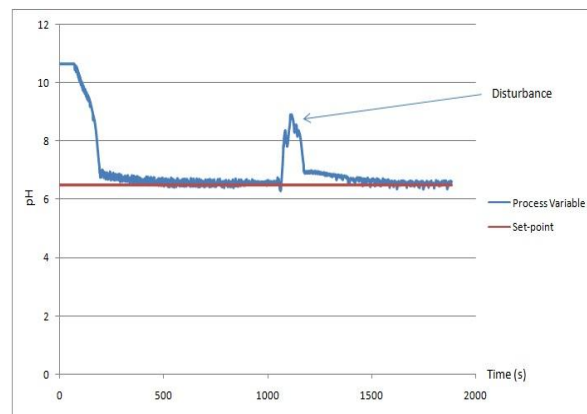


Figure 8 pH regulated at 6.5 under PID controller despite presence of disturbance

- [4] Syafie, S, Tado, F. and Martinez, E. "Model-free learning control of neutralization processes using reinforcement learning" *Engineering Applications of Artificial Intelligence*, Vol.20, pp767-782, 2007.
- [5] Gustafsson, T.K., and Walker, K.V., "Dynamic modeling and reaction invariant control of Ph". *Chemical Engineering Science*, Vol. 38, No.3, pp.389-398, 1983.
- [6] Shinskey, F.G., "pH and plon Control in Process and Waste Streams. Wiley, New York, 1973.
- [7] Wright, R.A. and Karavaris, C."Nonlinear control of pH processes using the strong acid equivalent". *Industrial and Engineering Chemistry Research*, Vol. 30, No.7,pp.1561-1572, 1991.
- [8] Sung, S. and Lee, I., "pH control using a simple set point change". *Industrial and Engineering Chemistry Research*, Vol.34, No. 50, pp. 1730-1734, 1995.
- [9] Kalafatis, A.D., Wang, L. and Cluett, W.R., "Linearizing feed forward-feedback control of pH process based on Weiner model". *Journal of Process Control*, Vol. 15, pp. 103-112, 2005.
- [10] Babuska, R., Oosterhoff, J. and Bruijij, P.M., "Fuzzy self tuning PI control of pH in fermentation". *Journal of Engineering Applications of Artificial Intelligence*. Vol.15, pp. 3-15, 2002.
- [11] Chen, J. and Huang, T.C., "Applying neural networks to on-line updated PID controller for non linear process control". *Journal of Process Control*, Vol. 14, pp. 211-230, 2004.

Long Term Water Demand Forecast for the City of Riyadh, Saudi Arabia

Ibrahim S. Al-Mutaz, Abdel Hamid Ajbar and Emad Ali

Chemical Engineering Dept., King Saud University,

P O Box 800, Riyadh 11421, Saudi Arabia

ABSTRACT

Accurate forecast of residential water demand is critically important for arid and oil rich countries such as Saudi Arabia which depend on costly desalination plants to satisfy the growing demand. Achieving the desired prediction accuracy is a challenging task since the forecast model should take into account a variety of uncertain factors such as economic development, climate conditions and population growth. The task is further complicated given that the water sector in the country is characterized by high levels of unaccounted for water (UFW) and strong government subsidies, which leads to artificially high water demand. This study presents a model for forecasting the long term water demand for Riyadh city, the capital of Saudi Arabia. The proposed model uses historic records of water consumption to calibrate an econometric predictive model for per capita water use. The explanatory variables included household income, persons per household and monthly maximum temperature. Both the effects of unaccounted for water and conservation measures were also included. These results indicate that socio-economic factors and weather temperature are equally dominant for water demand. The results also predict considerable savings in water use if a comprehensive policy for water conservation and UFW management is implemented.

Keywords: Water demand forecast, multiplicative model, water demand management, Riyadh city, long term water demand

1. INTRODUCTION

The forecast of future needs in potable water is important for the planning and management of water resources. The projections of urban water use are required in planning future requirements for water supply, distribution and wastewater systems [1-2]. The forecast of water demand is particularly important in regions of limited natural water resources. The county of Saudi Arabia, for instance, is an arid country characterized by a scarcity of its water resources. The country has no perennial rivers or lakes, and its renewable water resources total 95 cubic meters per capita, well below the 1,000 cubic meters per capita benchmark commonly used to denote water scarcity. In order to satisfy the needs for a growing population, the kingdom is currently relying on desalination plants to satisfy around half of the water demand. Building desalination plants is, however, a costly and time consuming process. It is therefore of importance that policy makers have a reliable estimate of the long term water demand in order to implement the appropriate capital expenditures in the development plans and to avoid any shortage in the domestic water supply.

Water demand forecasting depends on a number of factors (i.e. drivers or explanatory variables) that affect the demand. These include socioeconomic parameters (population, population density, housing density, income, employment, water tariff, etc), weather data (temperature, precipitation, etc), conservation measures as well as cultural factors such as consumer preferences and habits. Various methodologies are available in the literature for water demand forecast. The selection of the forecast methodology is driven in part by the data that can be made available through collection efforts.

The methodologies for the forecast include end-use forecasting, econometric forecasting and time series forecasting [2-3]. End use prediction bases the forecast of water demand on the prediction of uses for water, which requires a considerable amount of data and assumptions. The econometric approach is based on statistically estimating historical relationships between the independent explanatory variables and water consumption, assuming that these relationships will persist into the future. Time series approach, on other hand, forecasts water consumption directly without having to predict other factors on which water consumption depends [3-4].

We propose in this paper to develop an econometric model to predict the long term (20 years) water demand for the city of Riyadh, the capital of Saudi Arabia. The objectives of this study are twofold. The first objective is to develop the mathematical water requirement model for residential water use. The second objective is to analyze the long term water demand (up to year 2030) and to simulate the effects of water conservation strategies and UFW control as well as changes in water price.

2. WATER DEMAND AND SUPPLY

Riyadh city, with a population of around five millions, comprises more than a forth of the total population of Saudi Arabia. Being also the capital and an important administration and industrial centre, it is a focal point for local and international immigration with 30% of the population being non-Saudi. The annual population's growth estimated at 3% puts considerable strains on available water resources. The residential per capita water consumption in the city is estimated in 2010 to be 308 liters per day [5].

On the supply side, the city receives around 48% of its resources from local ground water, after being treated by reverse osmosis plants. The other part of water supply comes from desalination plants located on the sea and transported across 450 km of pipelines. The water supply system in the city is also characterized by large unaccounted for water (UFW), estimated to be 30% of the water supply [5]. This is mainly due to leaks in distribution systems in parts of the old city. As to water pricing, the cost of operating the country's desalination plants and pumping the water to end users is estimated at \$6 per cubic meters and is considered extremely high even with the use of naturally produced oil for energy requirements of thermal desalination plants. The cost of treating local ground water is also high. The government is subsidizing heavily the water consumption making the water virtually free in the country. As result, water is currently largely underpriced which makes demand artificially high and this, itself, leads to its inefficient use.

3. WATER DEMAND MODEL

The following standard functional population model is adopted to estimate the total water use:

$$Q_y = Nq \quad (1)$$

Q is the total annual water use, N the population number and q is the water use per capita. The water use (q) is assumed to depend on a number of explanatory variables (X_i). The projected values for each explanatory variable are required to develop the forecasted per capita use. Projected values for the populations (N) are also required. A variety of econometric models can be used to express the per capita use (q). Overviews on estimations of residential water demand were provided by a number of authors [2,7-9]. The log-log model, where all variables enter the regression equation in a logarithmic form is selected in this work. This model was used extensively in the literature [10-12]. The model relates (q) to the explanatory variables (X_i) using the following equation:

$$\ln q = \alpha + \beta_1 \ln(X_1) + \dots + \beta_n \ln(X_n) \quad (2)$$

Conveniently, the log-log model allows the parameter estimate β_i to be directly interpreted as the elasticity of demand associated with the explanatory variable X_i . One drawback of the model is that it presumes elasticities to be constant over the entire domain of the variables.

The following explanatory variables were selected in this study. These include the household median income (I), the household size (i.e. persons per house) (Hs) and the maximum monthly temperature (T). The selection of the explanatory variables was conditioned by the availability of historical data and also by the anticipated importance of the variable

In order to calibrate the selected model, historical

data for the last seven years were collected from the relevant sources. The water consumption was made available from the ministry of water and electricity while the data pertinent to population number, population growth, median household income and person per house were obtained from the ministry of planning. The maximum temperature was, on the other hand, made available from the local weather authority. It should be noted that the water tariff, being virtually constant over the last years, was not included in the model. Moreover, ample information was obtained concerning the amplitude of unaccounted for water (UFW) and also the conservation plans of the authorities. This information will be used together with the forecast model to predict the effects of conservation and UFW management policies.

4. MODEL CALIBRATION

The proposed log-log model was calibrated using the obtained historical data. The resulting model is:

$$\ln q = 3.11 + 0.25 \log(I) + 0.57 \log(Hs) + 0.24 \log(T) \quad (3)$$

The results of the regression analysis yielded a value of 0.977 for the adjusted R square. The parameter estimates (elasticities) were statistically significant (p-value less than 0.05 and t-stat larger than 2).

For the income, the parameter estimate (0.25) is positive. In general, households with higher incomes are expected to consume more of the complementary commodities associated with water through having dishwashers or even pools. Moreover, our estimates for the income elasticity lie well within the range of the values found in the literature [9, 13].

The parameter estimate (0.57) associated with household size is also positive and is the largest of the three elasticities. As the number of household members increases, per capita water consumption goes up which suggests that several water uses such as washing or even cooking increase more than proportional to the increase in household size. Compared to other countries, it can be noted that in a survey of US and Canadian households, Cavanagh *et al.* [14] found an elasticity of 22%.

Finally, the parameter estimate (0.24) for the monthly maximum temperature is positive and is close to that associated with the income. Higher temperatures are expected to result in higher residential water demand for drinking and taking showers.

5. FORECAST RESULTS

The forecast model, developed in the previous section, is used to predict the long term water demand for the city (i.e. until 2030). Future projections of population as well as these of the explanatory variables were made on the basis of a set of assumptions: The projections for the population growth, for instance, are assumed to

follow the exponential model taking the census data of 1992 and 2004 as reference points. Different annual growth rates (2.95 % and 2.90 %) were assumed for Saudi and non-Saudi populations, respectively. Moreover, because of the uncertainties surrounding the population growth, especially the immigration from outside the country, three scenarios were assumed for the annual growth rate. The most likely growth scenario assumes an annual decrease rate of 0.16 % for Saudi and 0.26 % for non-Saudi. The low growth scenario, on the other hand, assumes a decrease rate of 0.25% and 0.30%, respectively, while the high growth scenario assumes annual decrease rates of 0.1% and 0.2%. These growth rates were provided by the department of statistics (ministry of planning). The projections for the number of houses, on the other hand, follow the arithmetic model taking also the census data for 1992 and 2004 as reference points. The annual growth rate is assumed to be 2.4%, a value also provided by the ministry of planning. The future projections of the median household income are assumed to increase by a constant annual growth rate of 2.2%, a value also provided by the ministry of planning.

The results of the long term water demand are shown in Figs. 1-3. Figure 1 shows the projections for the daily per capita water consumption for the most likely population growth. The per capita consumption is expected to increase from 308 l/day to 341 l/day. The driving force for the increase is the growth in the income and that of the household size, since the projections for the average monthly temperature are assumed to be constant. Figure 2 shows the projected populations for the three scenarios. At the end of the planned period, the city population will reach around 8,100,000 for the fastest growth scenario, 7,000,000 for the lowest growth while the most likely scenario yields a population of 7,600,000. Figure 3 shows the resulting total water demand projections. The most likely scenario would require a demand of 2,600,000 m³/day by the end of the projected period, while the low and high growth scenarios would predict 2,400,000 m³/day and 2,800,000 m³/day, respectively. It can be concluded that for all scenarios and even if we assume that the supply from ground water is maintained at the current level of 48% of the total supply, the projected demand would require investing heavily in new desalination plants, knowing that a medium size desalination plant has a capacity of 30,000 m³/day.

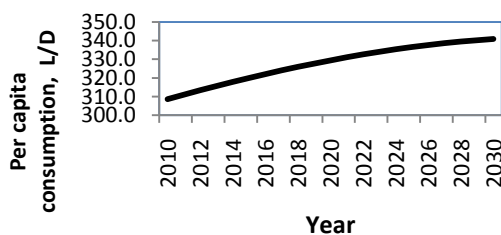


Figure 1: Projected per capita water demand

6. IMPACT OF UFW AND CONSERVATION

In the following section, the forecast model is used to investigate the impact of some management and conservation policies. System losses and conservation measures are not directly accounted for within the predictive model developed in the previous section. However, an unaccounted water use & conservation multiplier will be created to be used in the model. But first, we present the basic assumptions made for the impact of management of UFW and that of conservation

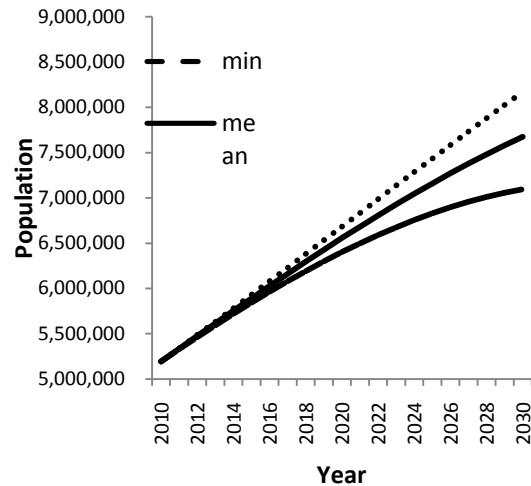


Figure 2: Populations growth scenarios

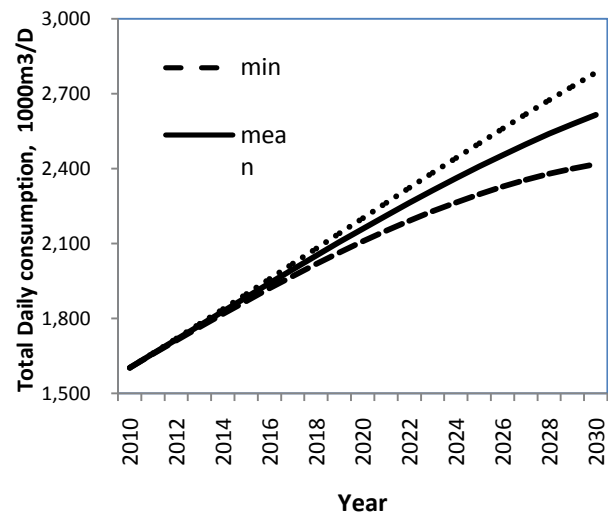


Figure 3: Projected total water demand

6.1 Impact of Management of UFW

The data available from the ministry of water and electricity [5] suggest that UFW in the city is about 30 percent, which means that the per capita water production is even higher than the daily consumption of 308 l/d. The ministry ambitious plan is to reduce the current total UFW down to 15 percent by 2030. Moreover, we assume that only half of UFW is real loss that can be affected by UFW management, with a target of 5 percent real loss by 2030. Therefore the impact on total production is a reduction of 10 percent. Thus, it is reasonable to assume that UFW management could

provide a 10-15 percent reduction in total production by 2030. If 30 percent of total production is UFW in the year 2010, and we have a target of reducing this percentage to 15 percent by the year 2030, then we can interpolate the UFW percent for any year between 2010 and 2030.

6.2 Impact of Water Conservation Measures

Water conservation measures planned by the Ministry of Water include the following:

- Replace toilets using 12 litres per flush with toilets using 6 litres per flush
- Replace showerheads using 22 litres per minute showerheads using 10 litres per minute
- Replace faucets using 15 litres per minute with faucets using 8 litres per minute
- Replace clothes washers using about 50 gallons per load with washers that use about 22 gallons per load

It can be noted that the percent reduction in water use is about 50 percent for toilets, 54 percent for showerheads, 47 percent for faucets, and 56 percent for washers. Overall, we can assume that the replacement program will reduce water use by about 50 percent. We must make a series of assumptions in order to estimate the impact of implementing these conservation measures. The water that is not UFW is used by both the residential customers and the non-residential sector. Based on the data available from the ministry of water, we can make the assumption that the total water production is 30 percent UFW, 50 percent residential and 20 percent non-residential. Next, we make the assumption that 80 percent of residential water use is used in these four types of fixtures compared to only 20 percent of non-residential water use. Finally, we make the assumption that by the year 2030, a total of 90 percent of fixtures will be replaced. If the replacement program starts in 2010 with a target of 90 percent of new fixtures by 2030, then we can interpolate the percent of fixtures replaced each year between 2010 and 2030.

These assumptions can be combined to estimate the impact of conservation measures on total production. A test of these assumptions show that the percent reduction in total production is sensitive to the percent of total production that is residential, and the percent of residential use that is used by these fixtures. A number of alternative assumptions were tested: The most extreme set of assumptions resulted in of 6 and 44 percent reduction in total production. However, the most likely set of assumptions resulted in a range of 20-25 percent reduction.

6.3 Combined Effects of UFW Management and Conservation Measures

The estimated effects of UFW management and conservation measures can be combined to provide an

estimated combined effect on total production. A range of all assumptions were tested resulting in a range extending from 13 to 51 percent reduction in total production by 2030. However, the most likely set of assumptions resulted in a range of about 25–30 percent reduction. Interpolation results of the combined effect between 2010 and 2030 are shown in Table 1.

Table 1: Most probable percent of reduction in water production as result of combined UFW management and conservation measures

Year	Percent Reduction in Total Production
2010	0.0%
2015	6.8%
2020	13.6%
2025	20.4%
2030	27.2%

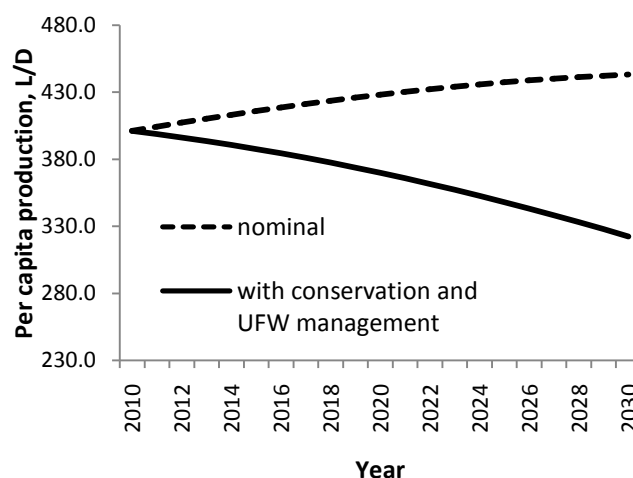


Figure 4: Projected water production per capita with combined UFW management

Figure 4 shows the combined effect of conservation measures and management of UFW. Since the management of UFW affects essentially the water production, it is therefore more convenient to plot the per capita water production rather than consumption. By the end of the projected period, the per capita water production will decrease by 19% from 401 l/day to 322 l/day. The corresponding total water production (Figure 5) would also decrease by about 926,000 m³/day.

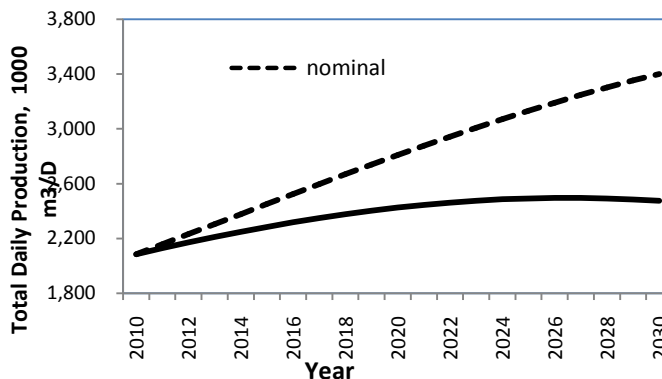


Figure 5: Projected total water production with combined UFW management and conservation measures

8. CONCLUDING REMARKS

This paper attempted to develop a long term water demand forecast model for the city of Riyadh, the capital of Saudi Arabia. The work was also an opportunity to shed some lights on the peculiarities and the challenges for forecasting water demand in an arid and oil rich country. The absence of a rigorous water pricing policy and the high levels of UFW make that the water demand is both artificially high and inefficiently used.

The analysis of historical data showed that a predictive model based on income, temperature and household size could predict well the water consumption trends. The model was used for the forecast of long term water demand for three scenarios of population growth. The predictive model was also used to analyze the combined impact of conservation measures and UFW control. In the absence of policies to reduce the government subsidies of water, it seems that the only realistic option for the reduction of consumption of water is a good policy for control of UFW. Voluntary conservation measures, on the other hand, may not yield consistent and clear impact.

A final note should be made about some aspects of the developed model. It should be noted that the only variable which holds a good deal of certainty is the temperature, barring dramatic future changes in the weather. The other parameters are, on the other hand, characterized by high degree of uncertainties. Both the growths of population and housing units (needed in household size) cannot be predicted with accuracy, given the fluctuations in the immigration from both inside and outside the country. The immigration from outside the country is dependent on the levels of economic activity spurred by oil price, which is another uncertain parameter that introduces a good deal of uncertainty in the income, the third explanatory variable. Therefore, the current deterministic model could be improved significantly by assigning probability density functions to each explanatory variable within the forecasting model and allow the model to become stochastic or probabilistic model.

ACKNOWLEDGEMENT

This work was made possible by a generous grant from the National Plan for Science and Technology (Project # 08-WAT229-02).

REFERENCES

- [1] Bougadis J., Adamowski, K. and Diduch, R. "Short-term municipal water demand forecasting", *Hydrological Process*,
- [2] Davis, W.Y. "Water demand forecast methodology for California water planning areas work plan and model review", Research Report. California Bay-

Delta Authority, CA, USA, 2003.
Vol. 19, pp. 137–148, 2005.

- [3] Khatr, K.B and Vairavamoorthy, K. "Water demand forecasting for the city of the future against the uncertainties and the global change pressures", Case of Birmingham, EWRI/ASCE: 2009, Conference: Kansas, USA May 17-21, 2009.
- [4] Zhou, S.L., McMahon, T.A., Walton, A and Lewis, J. "Forecasting daily urban water demand: A case study of Melbourne", *Journal of Hydrology* Vol. 236, pp. 153–164, 200.
- [5] MOWE, Ministry of Water and Electricity, Riyadh, Saudi Arabia, 2009.
- [6] Arbués F., García-Valiñas, M.A and Martínez-Espiñeira, R "Estimation of residential water demand: a state of the art review", *Journal of Socioeconomics*, Vol. 32, pp. 81–102, 2003.
- [7] Dalhuisen, J.M., Florax, R.J.G.M., de Groot, H. and Nijkamp, P. "Price and income elasticities of residential water demand: a meta analysis", *Land Economics*, Vol. 79, pp. 292–308, 2003.
- [8] Klein, B, Kenney, D, Lowrey, J and Goemans, C. "Factors influencing residential water demand: a review of the literature", University of Colorado Working paper version 1.12.07, 2007.
- [9] Worthington, A. and Hoffman, M. "An empirical survey of residential water demand modelling", *Journal of Economic Surveys*, Vol. 22, pp. 842–871, 2008.
- [10] Mazzanti, M and Montini, A. "The determinants of residential water demand. Empirical evidence for a panel of Italian municipalities", *Applied Economics Letter*, Vol.13, pp. 107–111, 2006.
- [11] Musolesi A and Nosvelli, A. "Dynamics of residential water consumption in a panel of Italian municipalities", *Applied Economics Letters*, Vol. 14:441–444, 2007.
- [12] Nauges, C. and Thomas, A. "Long-run study of residential water consumption", *Environmental and Resource Economics*, Vol. 26, 25–43, 2003.
- [13] Dandy, G., Nguyen, T. and Davies, C. "Estimating residential water demand in the presence of free allowances", *Land Economics*, Vol73, 125–139, 1997.
- [14] Cavanagh, S.M., Hanemann, W.M. and Stavins, R.N. "Muffled price signals: household water demand under increasing-block prices", FEEM Working Paper No. 40, 2002.

Changing Produced Water from Waste Stream to a Useful Asset in Sudan Oil Fields

Suhair A/ Gayoum Mohamed Saad (BSc, MSc. PhD)

College of Water and Environmental Engineering, Sudan University of Science and Technology
(E-mail: suhairag@sustech.edu or suhairag@yahoo.com)

ABSTRACT

Produced water quantities in Sudan oil fields increased largely in recent years as the oil production increased and the old fields matured. Approximately 1.5 million bb/day of water are produced in central region fields. The W/O ratio tends to be 4:1 in most Field **Processing Facilities** (FPFs). Produced water samples were collected from oil fields and analysed for chemical and physical properties (BOD, TDS, pH, COD... etc) and the crude oil content of untreated water was analysed by Gas Chromatograph. Current treatment practices were studied and evaluated carefully. Chemical and physical composition of samples showed normal environmental values of many parameters (BOD, TDS, pH, COD) but the Sodium Content is high. Chromatographic analysis of samples showed that crude oil content is of high value (250-300 mg/l) in untreated produced water. Samples of biologically treated water were also examined for the same parameters and evaluation of the current treatment technology insures the need for improvement of biodegradation rates of hydrocarbons.

Key Words: beneficial uses, biological treatment, W/O ratio.

1. INTRODUCTION

There is tremendous appeal in turning wastewater from oil and gas operations into a useful product [1,]. Developing beneficial uses for produced water could reduce the costs of hydrocarbon development in Sudan; thus increasing the Nation's economically recoverable resources [2]. In addition, the produced water can be used to offset problems created by near-record drought conditions, develop wildlife habitat, and provide water for agriculture, industry, and other uses [3].

Sudan has between 5 billion and 6.7 billion barrels of proven oil reserves, the fifth largest Endowment in Africa [4]. Most of these reserves lie in the Muglad and Melut basins in the south [5], and production hovers around 480,000 barrels per day [6]. Oil is vital to Sudan's economy, to a destabilizing degree. It accounted for 60 percent of government revenues and 95 percent of exports in 2008, and it accounts for 98 percent of southern Sudan's revenues. Unless Sudan begins to diversify its economy, its fortunes will be held hostage to the oil market [7]. This industry has many environmental impacts such as air pollution, soil pollution and hazards associated with waste production [7].

On-shore exploration, like the case in Sudan, carries potential risks for local inhabitants and may cause severe damage to the environment upon which their daily life depends [8]. Also off shore oil production & transportation represent a great risk to the marine environment [9]. The environmental costs of oil development have been extensive. They included destruction of wildlife and biodiversity, loss of fertile soil and degradation of farmland [10].

Oil & gas reservoirs have a natural water layer (formation water) that being denser lies under the hydrocarbons. To achieve maximum oil recovery, in

certain stages of oil field life, additional water is injected in the reservoirs to help force the oil to the surface. Both formation and injected water are eventually produced along with the hydrocarbons. This produced water is the largest volume waste stream in oil production operations. Other wastes that may be generated during this process include the residual wastes that remain after separation of the oil [11].

Almost all oilfields produce large quantities of contaminated water. For every barrel of oil produced around the world approximately 2-10 barrels of water is associated [12]. Water production quantities continue to increase as the oil and gas fields reach maturity [13]. Since great quantities of this water are produced in arid areas, the concept of finding beneficial uses for produced water arises in recent years to convert a high-cost liability into an asset [14].

At the surface, produced water is separated from the oil, treated to remove as much oil as possible, and either discharged or injected back into the wells. The general approach for produced water treatment is de-oiling and de-mineralizing before disposal or utilization [15].

Quality of produced water discharges to surface or re-injected to wells is controlled by rigid environmental regulations in all countries. [16,17] In Sudan the Ministry of Energy and Mining developed national environmental regulations for petroleum industry [18]. Then more detailed regulations had been set in 2005 as a part of the Comprehensive Peace Agreement (CPA) [19].

The composition of produced water is strongly field-dependent and includes a variety of inorganic and organic compounds. Produced water contains small amounts of emulsified oil, organic compounds including

dissolved hydrocarbons, organic acids, phenols and traces of chemicals added during production, inorganic compounds, suspended solids, dissolved solids and natural low-radioactive elements [20].

There are many options for treatment of produced water prior to disposing or re-injecting. [21]. Methods are varying greatly in efficiency and cost. Biological method is one of the cheapest and easiest available options. Both mixed and pure bacterial and fungal cultures have been used successfully in the degradation of hydrocarbons [22]

In this study composition of Heglig Oil fields produced water were analysed. Quantities and treatment practises studied and evaluated carefully. It is expected that the water as waste stream has some significant environmental pollutants and there is a need to upgrade or find new technologies for treatment that the effluent water can be used as useful source for irrigation instead of considered as a waste.

2. MATERIALS & METHODS

This study is carried out in produced water of Heglig oil fields in central Sudan. Heglig fields are lying in Muglad basin which is the largest of the Central African rift basins [5]

2.1 Samples collection

Produced water samples were brought from Heglig oil fields. Samples were taken from different depths of water ponds constructed for bioremediation project [Fig 1], using sterile small bucket, and stored in sterile containers of different sizes.



Figure 1: Produced Water Ponds in Heglig CPF

2.2 Water chemical & physical parameters Identification

To qualify produced water the following chemical & physical parameters were measured using standard methods for the collected samples :color ,odor , pH ,electrical conductivity, TDS, turbidity, BOD , COD ,oil &grease, Nutrients (Nitrate, Ammonia , Phosphorus) and some metals(Cd, Cu, Cr, F, Hg, Mn, Ni, Fe, Zn, Na) . Most of chemical elements identification tests

were made in National Institute of Researches & geology research institute laboratories using flame absorption spectrometer. The standard procedures for these tests were taken from **Atomic Absorption Spectrometry** [23] and **Flame Atomic Absorption Spectrometry** [24]. Other chemical parameters (nitrate, ammonia, COD, BOD) were analysed using titration or other standard methods. Physical tests were carried out in sanitary engineering laboratories in University of Khartoum, following the standard water tests methods [25].

2.3 Oil & grease measurement

Oil is extracted by standard liquid-liquid extraction method .A measured volume of the sample (50 ml=V) was introduced into separating funnel ,20ml of hexane & 10ml of H₂SO₄ were added . The layer of Oil &Hexane was separated in glass tubes and centrifuged at 30,000rpm to remove bacterial cells then transferred into a pre-weighed (W₁(gm))flask and hexane is evaporated in a water bath at 70°C .The flask is reweighed (W₂ (gm)) and the Oil & grease content is Calculated in ppm (mg/l) as :

$$\text{Oil \& grease (mg/l)} = \frac{w_2 - w_1}{V} \times 10^6 \quad (1)$$

2.4 Extraction of oil from produced water for GC tests

Oil is extracted by standard liquid-liquid extraction method. A measured volume of the sample (50 ml=V) was introduced into separating funnel , and 20ml of hexane was added . The layer of Oil &Hexane was separated in glass bottles .Bacterial cells were removed by centrifugation at 30,000 rpm for 15/ min [26].

2.5 Gas chromatography (GC) of Hydrocarbons

Fresh and degraded hydrocarbons were analyzed by gas chromatography using a Varian CP- 3800 series 11 gas chromatograph, equipped with a single flame ionization detector (FID) and fitted with analog digital converter and a Dell computer. A DB-17 silica capillary column of 15 cm length and an internal diameter of 0.32 mm wide bore of 1micron film thickness were used. A temperature program of 35 - 280oC, increasing at 3.0oC per minute for 103.67 min was employed. Hydrogen with a flow rate of 30 ml/min was used as a carrier gas, while the flow rate of air was 300ml/min. The detector temperature was 280oC, while the injection port temperature was 270oC. A sample volume of 0.1 µl was injected and the peaks nC4 – nC34 were recorded.

2.5 Analysis and Evaluation of Produced Water Quantities & Treatment Technologies

Data for water quantities was determined from CPF daily reports. Available treatment technologies was

studied in the field and evaluated according to the analysis of influent and effluent characteristics.

2.6 Current Researches in Sudan Produced Water Treatment.

Data concerning current researches in Sudan produced water treatment was collected from research centres in universities and published scientific papers. And research division in Ministry of Energy.

3. RESULTS

3.1 Composition Of Raw and Treated Produced Water.

Raw & treated produced water in field treatment facility was found to have physical & chemical characteristics as shown in (table1).

Table 1 Composition of Raw & Treated Produced Water in Heglig Oil Fields

Constituent	Heglig Raw produced Water	Heglig Treated Produced water
Color	Brown	colourless
Odour	Mineral oil	odourless
pH-value	8.9 –9.5	8.3-8.6
Total Dissolved Solids mg/l	1000-1210	1000-1100
Oil & Grease mg/l	250-300	30-50
Turbidity (NTU)	100-103	100-103
BOD mg/l	100-130	50
COD mg/l	560-600	20
Cadmium (Cd) mg/l	ND	ND
Chromium mg/l	0.033	0.033
Copper (Cu) mg/l	0.014	0.014
Mercury (Hg) mg/l	ND	ND
Mercury (Hg) mg/l	ND	ND
Sodium (Na) mg/l	90	90
Nickel (Ni) mg/l	0.043	0.043
Ammonia (NH ₃) mg/l	1.12	0.756
Nitrate (NO ₃) mg/l	0.75	<0.001
Phosphorus mg/l	<0.001	ND
Fluoride mg/l	ND	ND
Iron (Fe ₃) mg/l	0.34	0.34
Zinc (Zn) mg/l	0.009	0.006
Manganese (Mn) mg/l	0.064	0.06
Boron (Br) mg/l	0.01	0.01

3.2 Gas Chromatography Results

Gas chromatographs of influent (Fig 2) & Effluent produced water (Fig 3) showed significant values of all peaks (nC₄ - nC₃₄). It is clear that, although treated water showed reduction in peaks, still it has valuable amounts of hydrocarbons.

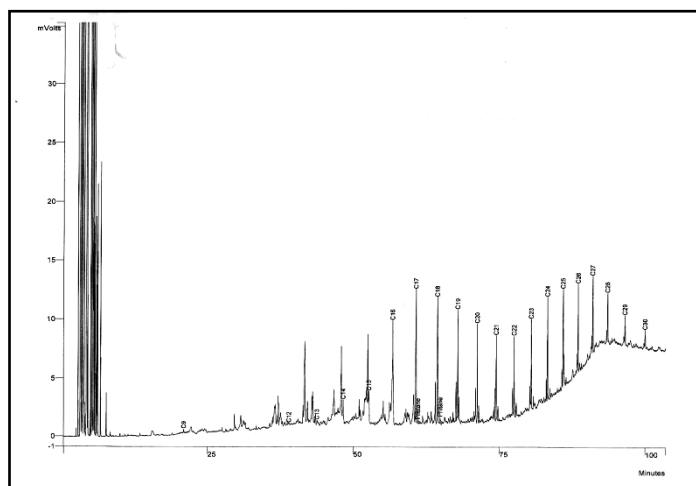


Figure 2: Gas Chromatograph of Raw Produced Water (nC₄- nC₃₄)

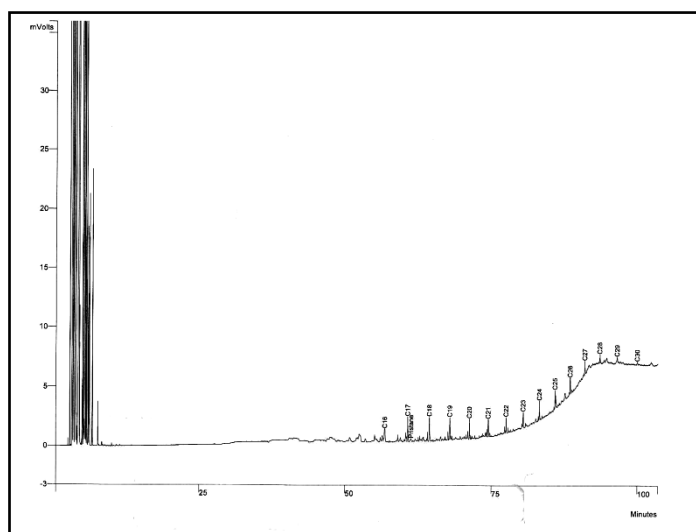


Figure 3: Gas Chromatograph of treated produced water

3.3 Quantities of produced Water

Produced water quantities in Sudan oil fields increased largely in recent years as the oil production increased and the old field matured. IN Sudan Approximately 1.5 million bb/day of water are produced in central Sudan oil fields today. A bioremediation project was constructed in Heglig oil field to treat water coming from central processing facility (CPF) using large beds of reed plants [20,21]. Another small project was constructed in Adar oil fields to treat about 10 thousands bb/d of water by hydro cyclones, but water needs further treatment to meet Sudan environmental regulations. [27]

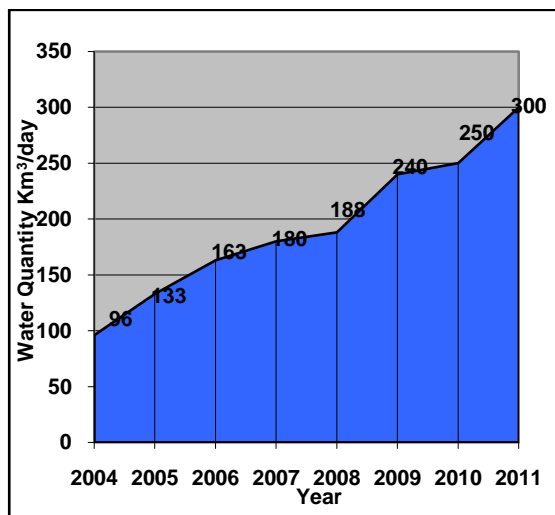


Figure 4: Produced Water Quantities In Central Regions fields (Km³/day)

3.4 Evaluation of Available Treatment Technologies

A bioremediation project was constructed in Heglig oil field to treat water coming from central processing facility (CPF) using large beds of reed plants. It covers a total area of five square kilometres (2.0 km x 2.5 km). The project was commissioned in 2003 as a 2-year Phase I (2003- 2005) experimental pilot project. Owing to the success of Phase I which was approved by the Government of Sudan in 2005, this research programme has been expanded to Phase II (2006 – 2010) for the remaining eight oil fields at Diffra, Bamboo, Neem, Unity, Toma South, El Toor, El Nar, and Munga. Commencing 2006, Phase II project is being planned and implemented in stages, with Diffra, Bamboo and Neem to come on stream in 2006, the remaining fields for the subsequent years. US\$ 15 million has been spent in building the world's largest oilfield waste water treatment system by using living beings and plants. The system can process 250,000 barrels of waste water every day. The oilfield waste water processed by using biological degradation technology, at project initial stages, has all met or exceeded international discharging standards and obtained ISO14001 certification. But as produced water quantities increased and exceeding the design capacity of constructed reed beds, the quality of effluent decreased and the system began to fail [28]. Another small project was constructed in Adar oil fields to treat about 10,000 bb/d of water by hydro cyclones and then reed beds, but water needs further treatment to meet Sudan environmental regulations [29].

Produced water was now being discharged untreated from some fields; volumes were not specified. The reasons given for the lack of treatment were a recent major increase in produced water flow rates and under-sizing of the treatment plants.

3.5 Overview of Current Researches in Developing Produced Water Treatment in Sudan

In Sudan a number of studies were carried to isolate and characterise petroleum degradable microorganisms [30, 31]. However, these studies did not investigate the degradation of produced water hydrocarbons by these isolates until year 2007. An investigation is carried now on the biodegradation of produced water hydrocarbons by a PhD student in the faculty of Science, University of Khartoum, but no results is published so far, only the proposal of work is available[32]. Another Research was carried in Environmental Engineering department – University of Khartoum in which a complete degradation of hydrocarbons in Heglig oil fields produced water was achieved using indigenous bacterial isolates. These isolates were inoculated in a bench scale bioreactor, and able to degrade all hydrocarbons content in a very reasonable retention time (36 hours). A mathematical model for the whole process was developed and the research results were published in year 2009. [33,34] Recently in 2011 Department of researches in Ministry of Energy was funding two Universities (Sudan University of Science & Technology and University of Khartoum) to conduct researches in developing oil industry. Important theme in this research scheme will be the treatment of oily produced water continuing from previous researches results.

4. CONCLUSION

It can be concluded from the aforementioned that:

1. Compared to FAO standards for unrestricted irrigation water [35], central fields produced water can be considered as fresh water and can be used widely to irrigate forests or other crops with ability to resist high values of sodium concentrations after removing hydrocarbons completely from this water.
2. There is a rapid increase in produced water quantities in central Sudan oil fields, and this can harm the environment of those premature regions if not managed carefully.
3. Available technologies of produced water treatment need to be optimized and new methods
4. must be developed to meet the increasing quantities of produced water stream
5. Toxicity of produced water due to high hydrocarbon concentrations, can be reduced using indigenous bacterial species which could result in reducing environmental pollution that affect both land & vegetation .

5. RECOMMENDATIONS

- 1- Further research is essential to study the biodegradability potentials of hydrocarbons using different species of microorganisms.

- 2- Different Bacterial growth methods (suspended, attached or hybrid) must be studied carefully and mathematically modelled to optimize the biological treatment methods.
- 3- Environmental Impact Assessment (EIA) must be carried out in oil fields to evaluate the environmental damages caused by improper disposal of produced water and suggest an action plan for quick remediation.

REFERENCES

- [1] Burnett B. D. (2005) 'Potential for Beneficial Use of Oil and Gas Produced Water' Global Petroleum Institute, Texas Water Resources Institute, Texas A&M University.
- [2] Arnold R ; Burnett B. & et al (2004) "Managing water –From Waste to Resource" Article prepared by number of researchers and oil companies in Oil Review journal.
- [3] UNEP (2007) "Industry and the Environment" Sudan Post-Conflict Environmental Assessment, UNEP Reports.
- [4] Yager TH. R. (2001) 'The mineral industry of Sudan'— U.S. geological survey minerals year book— 2001 page 262- 26.4 .
- [5] Energy Information Administration (2010) "Country Analysis Briefs - Sudan " updated 30 September 2011 available at www.eia.gov/cabs/Sudan/pdf.pdf
- [6] Soliman F.(2007) 'African Focus- Sudan', Petroleum Africa Magazine,pp 187-241
- [7] Derk A. (April 2008) "Sudan Oil Industry Facts and Analysis" A report of project funded by European Union available on line at <http://www.ecosonline.org>.
- [8] International Finance Corporation (IFC)& World Bank Group (WBG) "Environmental, Health, and Safety Guidelines for Onshore Oil and Gas Development" April 30, 2007
- [9] Ekins P.; Vanner R and Firebrace J (2005) 'Management Of Produced Water On Offshore Oil Installations: A Comparative Assessment Using Flow Analysis' Case studies provided by the UK Offshore Operators Association and its member companies , Policy studies Institute , final report .
- [10] Connor J. A.; Newell C. J.'(2006) 'Practical Guidelines for Addressing Impacts of Produced Water Releases to Plants, Soil, and Groundwater' Groundwater API Produced Water Issues Group Publication 4758.
- [11] Veil J .A; Markus G. Puder ,Deborah Elcock ,Robert J. Redweik, Jr.(2004) 'A White Paper Describing Produced Water from Production of Crude Oil' Prepared for : U.S. Department of Energy National Energy Technology Laboratory
- [12] Nature Technology Solution(2006) "Introduction to produced water treatment" Technical paper prepared by Nature Company, USA
- [13] Sumi L. (2005) 'Produced Water from Oil and Gas Production' Paper presented at the 2005 People's oil and gas summit, New Mexico
- [14] William E. Fox & David Burnett (2002) "Produced Water: An Oasis For Arid & Semi-Arid Rangeland Restoration" Technical paper available www.gwpc.org/meetings/special/./Papers/William_Fox_PWC2002.pdf
- [15] Verbeek P., Davies S., (2008) 'Produced water Treatment and Monitoring' paper presented at Tekna Symposium on Produced water Management Stavanger.
- [16] OSPAR Convention (1992) 'Convention For The Protection Of The Marine Environment Of The North-East Atlantic' Text as amended on 24 July 1998, updated 14 November 2000 available at <http://www.mma.es/secciones/biodiversidad/biodiversidad>
- [17] Veil J. A. (2002) 'Regulatory Issues Affecting Management of Produced Water From Coal Bed Methane Wells' Paper prepared for: U.S. department of energy office of fossil energy by Argonne National Laboratory.
- [18] Ministry of Energy & Mining (2002) 'Regulations for Protection of the environmental. Of the petroleum Industry' Khartoum, Sudan
- [19] Ministry of Energy & Mining(2005) 'Advisory Commission for the Environment & Safety' Khartoum, Sudan
- [20] Tibbetts P.J.C ; Buchanan T.I ; Gawel L.J. & Large R. (1992) " A comprehensive determination of produced water composition" Produced Water: Technological/environmental Issues and Solutions , Edited By J. P. Ray, F. Ranier , pp 97-113 .Proceedings of the 1992 International Produced Water Symposium, held February 4-7, 1992, in San Diego, California,
- [21] Veil A. John (2008)"Produced Water Management Options –One Size Does Not Fit All" Society of Petroleum Engineers Distinguished Lecturer Program prepared by Argonne National Laboratory, USA

- [22] Okoh I. A. (2006) "Biodegradation alternative in the cleanup of petroleum hydrocarbon pollutants" *Biotechnology and Molecular Biology Review* Vol. 1 (2), pp. 38-50, June 2006 Available online at <http://www.academicjournals.org/BMBR>
- [23] Welz, B.; Sperling, M.; (1999) "Atomic Absorption Spectrometry," 3rd ed., Wiley-VCH: Weinheim, New York
- [24] Eaton, A.D., Clesceri, L.S. and Greenberg, A.E.,(1995) "Standard Methods for the Examination of Water and Wastewater" 19th Edition, American Public Health Association-American Water Works Association-Water Environment Federation, USA,
- [25] Guihua Ma &Gonzalez G. W (1997) "Flame Atomic Absorption Spectrometry," Daniel Gallagher available at <http://www.cee.vt.edu>
- [26] Dan Caudle (1998) "Measuring Oil And Grease In Produced Water" Sound Environmental Solutions, Inc. , USA.
- [27] GNPOC (2011) "Daily Reports of Higleg oil fields central laboratories" CPF field laboratories reports.
- [28] Gill L. , David T., Khalifa M, Gafar S, Ming L.B; Sabbar A. (Oct. 2006) 'Sudan's more than U.S. \$15 million GNPOC Bioremediation Research Project for Treatment of Produced Water from the Oil Fields in Africa' 20th IPMA World Congress on Project Management Shanghai
- [29] Fayyad S. (2007) 'Produced water treatment project profile, Milut oil Basin Development 'Enviro Arabia presentiaions, Case study, SaudiArabian Environment Water Association.
- [30] Nour M.T,(2004) ' Studies on Aerobic Bacteria Isolated From oil contaminated soil & water in Khartoum state' MSC thesis ,University of Khartoum
- [31] Elkhair M. N. (2006) "Isolation and Characterization of Microorganisms Capable of Degrading Crude Oil Under Aerobic Conditions" PhD Thesis, University of Khartoum.
- [32] Birkeland N.(2006) 'Seed-project in microbiology' Collaboration in mathematics and natural sciences - Sudanese universities and the University of Bergen, Report from visit to Department of Botany, University of Khartoum, 04.12 – 09.12.
- [33] Saad A. S. (2009) 'Biological Treatment of Hydrocarbons in Petroleum Produced Water from Heglig Oil fields- Sudan'' PhD Thesis ,University of Khartoum
- [34] Saad A. S. & etal (2009) "Biological Method for Treatment of Petroleum Produced Water in Sudan" *Sudan Engineering Journal*, Issue No. 51, September 2009.
- [35] D.W. Westcot (1997) " Quality control of wastewater for irrigated crop production. (Water reports - 10)" Food And Agriculture Organization Of The United Nations (FAO) Rome, ISSN 1020-1203

Enzymatic Production of Biodiesel from Waste Cooking Oil

Sulaiman Al-Zuhair¹, Mubarak AlSheraifi¹, Humaid AlShamsi¹, Nayef AlBraik¹, Abdelaziz Suwaidi¹,
Saud AlJahori¹

¹Chemical and Petroleum Engineering Department UAE University, 17555 AlAin, UAE
(s.alzuhair@uaeu.ac.ae)

ABSTRACT

A lab-scale system has been designed and constructed to continuously produce 1 kg/hr relatively pure biodiesel (BD) from waste/used vegetable oil using immobilized lipase (Novozyme 435) in a packed bed bioreactor. The effluent of the reactor is passed through a liquid-liquid extraction and settling units to separate the BD from other components, which is followed by a distillation column for further purification of the product. Complete material and energy balances were carried out using Excel spreadsheets, and detailed equipment sizing were determined. The amount of feed streams of waste oil and makeup methanol and *t*-butanol required were found to be 1.00, 0.11 and 0.14 kg/hr, respectively. The unit resulted in a drop in the kinematic viscosity of waste cooking oil from 30.3 to 6.1 mm²/s.

Keywords: Biodiesel, Immobilized Lipase, Waste oil, Packed bed bioreactor, Continuous Process *keywords*)

1. INTRODUCTION

Biodiesel (BD) is a sustainable biofuel with two favorable properties, which are its availability from renewable resource and its lower negative environmental impact than those of fossil fuels. The high cost of BD, compared to petroleum-based diesel, is a major barrier to its commercialization. It has been reported that 70-80% of the BD cost arises from the cost of the purified feedstock oil [1]. Hence, low cost feedstock, such as waste cooking oil (WCO), should greatly reduce the cost of BD. The transesterification of triglycerides (oil or fat) is conventionally catalyzed chemically by alkaline or acid catalysts. The alkali catalyzed processes are sensitive to free fatty acids (FFA) content in feedstock, which render them not suitable for use with waste cooking oils. Saponification of the FFA consumes the alkali catalyst and at the same time generates soaps that cause the formation of emulsions, which increase the viscosity and create difficulties in downstream recovery and purification of the BD. Therefore, pre-treatment of the oil is required for commercially viable alkali-catalyzed systems [2,3]. On the other hand, the other chemical catalysts, namely acid catalysts, are insensitive towards FFA contents, but they are rarely used because they result in much slower reactions and require careful removal of catalyst, since any catalyst residues can damage the engine parts [4].

A less energy intensive and environmental friendly procedure would be achieved by using enzyme as a biocatalyst. Enzymatic transesterification can overcome the problems facing conventional chemical methods without compromising their advantages [3]. Most importantly, glycerol can be easily recovered without any complex process, FFAs contained in the oils can be completely converted to methyl esters and subsequent wastewater treatment is not required. The reuse of lipase is essential from the economic point of view, which can be achieved by using the lipase in immobilized form. In addition, immobilized enzyme displays improved

stability and activity [5,6]. As continuous processing is favorable economically, the objective of this work was to design and construct a lab-scale system to continuously produce relatively pure BD from waste oil using immobilized lipase in a packed bed reactor (PBR). The system consisted mainly of a PBR (containing the immobilized enzyme), a liquid-liquid extraction (LLE) and settling units and a distillation column (DC).

2. PROCESS DESCRIPTION

As mentioned earlier, WCO was used as a feedstock. The lipase-catalyzed transesterification reaction took place under atmospheric pressure and a temperature of 45°C, which was reported to be the optimum for the (Novozyme 435) [7]. Methanol is the most commonly used alcohol in BD production, mainly because of its high reactivity and relatively low cost. To overcome the methanol inhibition effect and enhance the stability of the enzyme, *t*-butanol was used as an organic solvent [8].

The proposed process flow sheet (PDF) is shown in Fig 1. The WCO initially passed by a filter to remove suspended solids. The FFA and water contents of the filtered WCO (Stream 3) was determined to be 7% FFA 5% water using Acid Value (IP1) [9] and Karl Fisher (737 KF Coulometer, Metrohm) tests, respectively. Stream 3 was mixed with recycled methanol and *t*-butanol (Stream 1), and make up methanol (Stream 2) and *t*-butanol (Stream 3) to sustain their ratios to triglycerides at 6:1 and 8:1 respectively. The ratio of methanol:oil was determined in a preliminary experiment to be the optimum at which the rate of reaction is maximum. Thus result agrees with previous results found in literature [10]. It was found that BD production increases with increasing methanol concentration up to oil to methanol ratio of 6:1 and then decreases when methanol concentration is further increased. In general, it is widely accepted that methanol which is completely dissolved in the substrate

mixture should not inactivate the lipases. However, in contact with insoluble methanol that exists as drops in the oil, water molecules required to activate the lipase will be stripped off, which renders the enzyme inactive. In addition to enhancing the stability of the enzyme, the use of *t*-butanol reduces the viscosity of the mixture and

dissolves the by-product (glycerol), which otherwise would deposit on the immobilized enzyme and block its active sites. It should be noted however, that using *t*-butanol requires the addition of a DC to recover the solvent.

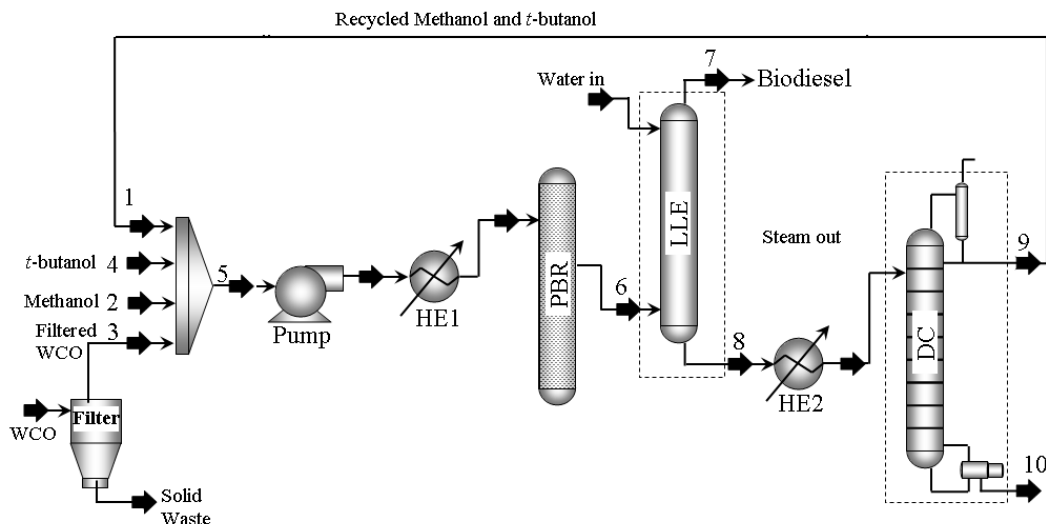


Figure 1. Proposed Process Flow Diagram

For simplicity, the triglyceride in the WCO was assumed to be triolein and the FFA is oleic acid. Although other fatty acids may be present in the triglyceride, it has been proven that non-specific enzymes, like the one selected in this work, do not show different catalytic activities towards different fatty acids [11]. Since the difference in molecular weights of different fatty acids is not significant, this assumption can be justified. The mixture (Stream 5) was brought to the required temperature of 45°C using a shell and tube heat exchanger and then fed to a PBR. The main advantage of PBR in comparison to other conventional Plug Flow Reactor (PFR) or Continuous Stirred Tank Reactor (CSTR) is the higher conversion per weight of catalyst [12]. The main advantages of PBR over Fluidized Bed reactor (FBR) are better ability to provide temperature control, easier to service and clean, lower pumping requirements, and less erosion of internal components. Therefore, PBR has been selected to be used in this work that was packed with desired amount of immobilized lipase and designed to achieve 90% conversion with respect to total triglycerides input. The output of the reactor (Stream 6) consisted of the produced BD and glycerol together with the water, the solvent *t*-butanol, the unreacted WCO and methanol. Distillation was not suitable for separating BD from glycerol, as they both have very high and close boiling points of 320°C and 300°C, respectively [4], which renders distillation unfeasible. Therefore, LLE, which is used to separate compounds based on their relative solubility in two different immiscible liquids, was elected instead. In the LLE tower, water was used as a

solvent to extract glycerol from Stream 6. The organic phase that exited the LLE tower (Stream 7) containing mainly BD, which is considered the main product. The aqueous stream (Stream 8) entered a DC to separate water and glycerol (Stream 10) from methanol and *t*-butanol (Stream 9), which was recycled as Stream 1. Two shell and tubes heat exchangers (HE) were introduced before the PBR and the DC to bring the temperatures of the input streams to the desired values. The separation fractions, extracted from HYSYS and shown in Table 1, are the fractions of the components appearing in the output streams relative to their respective amounts in the input streams. It should be highlighted that the zero values are rounded up as they were too small; however, traces of these components still existed.

Table 1. Molar ratios of components in output relative to input streams

Streams	Molar ratio	
	7 relative to 6	9 relative to 8
Biodiesel	0.99	0
Oil	0.99	0
Methanol	0.05	0.99
<i>t</i> -butanol	0.2	0.95
Glycerol	0.01	0.01
Water	0.01	0.1

Excel spreadsheet was used to carry out the material balance. Since a recycle stream was calculated in the

process, iteration solution was required. Back calculation was also used to determine the amount of inputs required to produce the desired 1 kg/hr of BD. As shown in Table 2, the amount of feed streams of WCO, methanol and *t*-butanol required were found to be 1000, 105 and 142 kg/hr, respectively. Excel spreadsheet was also used to carry out the energy balance, as shown in Table 3.

According to Fig. 1, two shell-and-tubes HEs were used; the first (HE1) was used to raise the temperature of the input stream to the reactor (Stream 5) to the desired 45 °C, and the second (HE2) was used to raise the temperatures of the output streams of the LLE unit (Stream 8) from 44 °C to the desired temperature of 95 °C. The temperature of the output streams of the LLE unit, was found from HYSYS Aspen. The constants of the heat capacity correlations of all the components are presented in Table 4, as extracted from HYSYS Aspen.

Steam at 1.0 bar was used as a heating medium in HE1 and HE2.

3. MAIN EQUIPMENT DESIGN

3.1 Packed Bed Reactor (PBR)

The oil, tert-butanol and methanol mixture enter the reactor which was maintained at a temperature of 45 °C and 1 atm. The reaction was designed to give a conversion of 90% with respect to the input triglyceride. The design equation of the PBR is given by Eq (1)

$$\frac{dX}{dV} = \frac{r_B}{F_{S_o}} \quad (1)$$

Where X is the conversion, V is the volume of the reactor, r_B is reaction rate and F_{S_o} is the molar flow rate of substrate, which was taken to be the ester bond on the triglyceride as defined by [11].

Table 2. Excel spread sheet of the process material balance

Streams	1 (Recycle)		2 (MU Methaol)		3 (WCO)		4 (MU <i>t</i> -butanol)		5 (Reactor Input)	
	(kmol/hr)	(kg/hr)	(kmol/hr)	(kg/hr)	(kmol/hr)	(kg/hr)	(kmol/hr)	(kg/hr)	(kmol/hr)	(kg/hr)
Oil	0.0	0.0	0.0	0.0	1.0	880.0	0.0	0.0	1.0	880.0
Biodiesel	0.0	0.0	0.0	0.0	0.0	0.0	0.0	0.0	0.0	0.0
Glycerol	0.0	0.8	0.0	0.0	0.0	0.0	0.0	0.0	0.0	0.8
Water	0.9	16.5	0.0	5.2	2.8	50.0	0.0	0.0	4.0	71.7
Methanol	2.9	91.4	3.1	99.7	0.0	0.0	0.0	0.0	6.0	191.1
<i>t</i> -butanol	6.0	448.1	0.0	0.0	0.0	0.0	1.9	141.5	8.0	589.6
FFA	0.0	0.0	0.0	0.0	0.2	70.0	0.0	0.0	0.2	70.4
Total	9.8	557	3.1	105	4.0	1000	1.9	142	19.2	1800

Streams	6 (Reactor Output)		7 (Organic Stream)		8 (Aqueous Stream)		9 (Distillate)		10 (Bottom Product)	
	(kmol/hr)	(kg/hr)	(kmol/hr)	(kg/hr)	(kmol/hr)	(kg/hr)	(kmol/hr)	(kg/hr)	(kmol/hr)	(kg/hr)
Oil	0.1	88.0	0.1	87.1	0.0	0.9	0.0	0.0	0.0	0.9
Biodiesel	2.9	826.8	2.8	818.5	0.0	8.3	0.0	0.0	0.0	8.3
Glycerol	0.9	83.2	0.0	0.8	0.9	82.4	0.0	0.8	0.9	81.6
Water	4.2	76.2	0.1	1.7	9.2	164.8	0.9	165	8.2	148.3
Methanol	3.0	97.1	0.2	4.9	2.9	92.3	2.9	91.4	0.0	0.9
<i>t</i> -butanol	8.0	589.6	1.6	117.9	6.4	471.7	6.0	448.1	0.3	23.6
FFA	0.0	0.0	0.0	0.0	0.0	0.0	0.0	0.0	0.0	0.0
Total	19.2	1800	4.7	1031	19.3	820	9.8	557	9.5	264

Table 3. Excel spread sheet of the process energy balance

Streams Temp.	1 77 °C		2 25 °C		3 25 °C		4 25 °C		5 28 °C	
	(kg/hr)	C(kJ/kg.K)	(kg/hr)	C(kJ/kg.K)	(kg/hr)	C(kJ/kg.K)	(kg/hr)	C(kJ/kg.K)	(kg/hr)	C(kJ/kg.K)
Oil	0.0	24.5	0.0	24.4	880.0	24.4	0.0	24.4	880.0	24.4
Biodiesel	0.0	2.1	0.0	1.9	0.0	1.9	0.0	1.9	0.0	1.9
Glycerol	0.8	2.7	0.0	2.6	0.0	2.6	0.0	2.6	0.8	2.6
Water	16.5	4.2	5.2	4.2	50.0	4.2	0.0	4.2	71.7	4.2
Methanol	91.4	1.5	99.7	3.6	0.0	3.6	0.0	3.6	191.1	3.6
<i>t</i> -butanol	448.1	2.8	0.0	2.7	0.0	2.7	141.5	2.7	589.6	2.7
FFA	0.0	2.1	0.0	1.9	70.0	1.9	0.0	1.9	70.4	2.0
Total/Avg	557	2.6	105	3.6	1000	21.8	142	2.7	1800	13.4

Streams	Reactor inlet 45 °C		6 45 °C		Water inlet 25 °C		7 44 °C		8 44 °C	
	(kg/hr)	C(kJ/kg.K)	(kg/hr)	C(kJ/kg.K)	(kg/hr)	C(kJ/kg.K)	(kg/hr)	C(kJ/kg.K)	(kg/hr)	C(kJ/kg.K)
Oil	880.0	24.4	88.0	24.4	0.0	24.4	87.1	24.4	0.9	24.4
Biodiesel	0.0	2.0	826.8	2.0	0.0	1.9	818.5	2.0	8.3	2.0
Glycerol	0.8	2.6	83.2	2.6	0.0	2.6	0.8	2.6	82.4	2.6
Water	71.7	4.2	76.2	4.2	90.2	4.2	1.7	4.2	164.8	4.2
Methanol	191.1	3.7	97.1	3.7	0.0	3.6	4.9	3.7	92.3	3.7
<i>t</i> -butanol	589.6	2.7	589.6	2.7	0.0	2.7	117.9	2.7	471.7	2.7
FFA	70.4	2.0	0.0	2.0	0.0	1.9	0.0	2.0	0.0	2.0
Total/Avg	1800	3.6	1800	3.6	90.2	4.2	1031	4.0	820	3.1

Streams Temp.	Distillation inlet 95 °C		Condenser inlet 90 °C		9 77 °C		Boiler inlet 110 °C		10 110 °C	
	(kg/hr)	C(kJ/kg.K)	(kg/hr)	C(kJ/kg.K)	(kg/hr)	C(kJ/kg.K)	(kg/hr)	C(kJ/kg.K)	(kg/hr)	C(kJ/kg.K)
Oil	0.9	24.5	0.0	24.5	0.0	24.5	2.2	24.5	0.9	24.5
Biodiesel	8.3	2.2	0.0	2.2	0.0	2.1	20.7	2.2	8.3	2.2
Glycerol	82.4	2.7	1.6	2.7	0.8	2.7	203.9	2.7	81.6	2.7
Water	164.8	4.2	33.0	4.2	16.5	4.2	370.7	4.2	148.3	4.2
Methanol	92.3	1.5	182.7	1.5	91.4	1.5	2.3	1.6	0.9	1.6
<i>t</i> -butanol	471.7	1.8	896.2	1.8	448.1	2.8	59.0	1.9	23.6	1.9
FFA	0.0	2.2	0.0	2.2	0.0	2.1	0.0	2.2	0.0	2.2
Total/Avg	820	2.4	1113.5	1.9	557	2.6	658.7	3.5	264	3.5

Table 4. Constants of enthalpy correlation used in HYSYS

	Biodiesel	Oil	FFA	Methanol	Tertbutanol	Glycerol	Water
a	1.093x10 ⁻⁷	-4.953x10 ⁻⁷	3.52x10 ⁻⁷	0	0	0	-5.7296
b	-0.152999	-0.0531265	-0.204165	0.6602	-0.656059	0.0915316	1.9145
c	0.0034338	0.0030014	0.003543	0.0011072	0.0048408	0.0024132	-0.0003957
d	-1.714x10 ⁻⁶	-7.581x10 ⁻⁷	-1.856x10 ⁻⁶	2.693x10 ⁻⁷	-3.188x10 ⁻⁶	-1.144x10 ⁻⁶	8.762x10 ⁻⁷
e	5.228x10 ⁻¹⁰	-1.946x10 ⁻¹⁷	6.04x10 ⁻¹⁰	-2.226x10 ⁻¹⁰	9.855 x10 ⁻¹⁰	2.547x10 ⁻¹⁰	-4.951x10 ⁻¹⁰
f	-7.323x10 ⁻¹⁴	5.915x10 ⁻²¹	-8.948x10 ⁻¹⁴	0	0	0	1.038x10 ⁻¹³

The rate of BD production using immobilized lipase from *Candida antarctica* at interface of the enzyme was described by a Ping-Pong Bi Bi model as presented by Eq.(2) [13],

$$r_B = \frac{0.0098[E]}{\left[\left(1 + \frac{3.8 \times 10^4}{[A]}\right) \left(1 + \frac{[S]}{250}\right) \right] + \left[\frac{2.5 \times 10^4}{[S]} \left(1 + \frac{[A]}{110}\right) \right]} \quad (2)$$

Where, the concentration of the substrate, $[S]$ and methanol $[A]$, are related to the conversion by Eqs (3) and (4), respectively.

$$[S] = (F_{S_0}/v_o)(1 - X) \quad (3)$$

$$[A] = (F_{A_0}/v_o)(1 - X) \quad (4)$$

Where, v_o is the total volumetric flow rate in and F_{Ao} is the input flow rate of alcohol.

The initial activity per gram, E_i , of the *C. antarctica* lipase immobilized on ceramic beads was reported to be 1000 LU/g [13]. Equation (5) was used to relate the activity at any time, E , to the initial activity, E_i . The value of the specific decay constant, α , was determined by assuming the 90% of the activity of the enzyme was lost within three months of operation.

$$E = E_i e^{-\alpha t} \quad (5)$$

The set of equations (Eqs 1-5) were solved simultaneously using POLYMATH and the volume of the reactor required to achieve 90% conversion was determined. As shown in Table 5.

Table 5. Packed-bed Bioreactor specifications

Molar flow rate of Substrate	1.0 mol/hr
Molar flow rate of methanol	6.0 mol/hr
Temperature	45 °C
Catalyst initial activity	1000 LU/g
Volumetric flow rate	$3.8 \times 10^{-5} \text{ m}^3/\text{min}$
Reactor volume	$6 \times 10^{-5} \text{ m}^3$
Weight of catalyst	27 g
Reactor length	0.5 m
Reactor diameter	0.013 m

3.2 Liquid-Liquid Extraction (LLE) Unit

In LLE, a solution to be separated (feed) is made indirect contact with an extracting solvent in order to permit diffusion transfer of the constituents from the feed to the solvent. The equilibrium data of the ternary mixture of water-BD-glycerol was determined using HYSYS Aspen. The ideal number of stages in a counter-current extractor was determined using the modified McCabe-Thiele graphical technique and the mass fraction found from the material balance, which was found to be 2. Using the heuristics tray spacing of 0.376 m and the tower safety addition of 0.3 m [14] the total height and diameter of the LLE unit were determined to be 1.4 and 0.1 m, respectively.

3.3 Distillation column (DC)

McCabe-Thiele graphical method was used to determine the theoretical number of stages for the separation of the solvent *t*-butanol from water. A reflux ratio of 1.5 the minimum reflux ratio, R_{min} and a total condenser were used. The theoretical number of stages was found to be four, and with assuming an efficiency of 70% [15]. From which, the total height of the column was found to be 1.2 m, taking plate spacing to be 0.1 m and clearance of 0.3 m from top and bottom. To determine the diameter of the column, the vapor velocity inside the column was taken to be 0.6 m/s, [15]. The volumetric flow rate of the gas was found from the material balance to be $3.3 \times 10^{-4} \text{ m}^3/\text{s}$. The cross sectional area and the diameter of the column were then determined to be $5.5 \times 10^{-2} \text{ m}^2$ and 0.03 m, respectively.

3.4 Lab-Scale BD Production

Waste cooking oil was collected from a local restaurant and used as substrate after filtration. Lipase from *C. antarctica* immobilized on ceramic particles was obtained from Sigma-Aldrich. All other chemicals were of analytical grade and used as purchased.

The lab-scale production set-up system consists mainly of a PBR (containing the immobilized enzyme), and a LLE and settling units. The DC was not introduced into the system, at this stage. Water from temperature-controlled water bath circulates through the jacket of the PBR to maintain the reaction at 40 °C. A schematic diagram of the BD production system is shown in Fig.2. Waste cooking oil was mixed with methanol and *t*-butanol according to the ratio found in Table 2, namely 6:1 and 8:1 respectively. The mixture was passed through the system using peristaltic pump at two flowrates, namely 0.17 and 0.6 ml/min. The effluent of the bioreactor was mixed with water to extract glycerol. The output of the mixer was fed to a settling unit, where the upper layer was collected as the product, biodiesel.

The kinematic viscosity and density of the produced BD were measured at 40 °C, using Stabinger Viscometer (SVM300, Anton Paar, Austria), and their values were compared to those of the raw material, filtered waste cooking oil. In addition, the kinematic viscosity and density were compared to the standard values of BD and petroleum diesel. The results shown in Table 6 clearly show that.

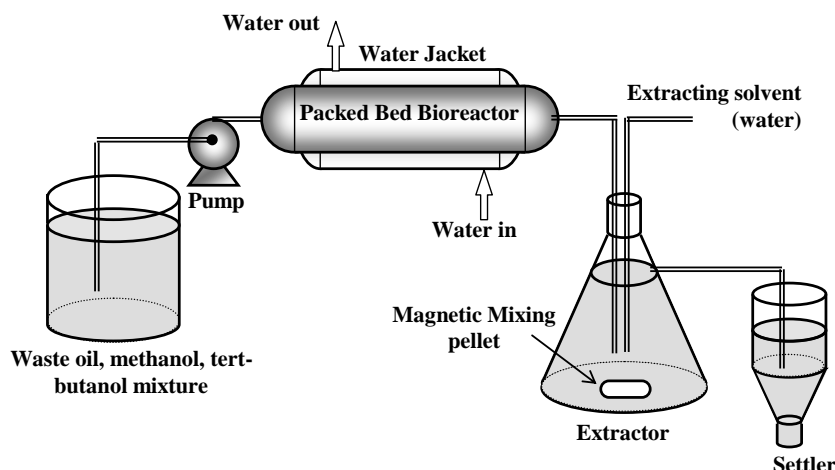


Figure 2. Schematic diagram of the experimental set-up

Table 6. Properties of produced biodiesel compared to raw material, standard biodiesel and petroleum diesel

Property at 40 °C	Waste oil	Produced biodiesel (0.17 ml min ⁻¹)	Produced biodiesel (0.6 ml min ⁻¹)	Standard biodiesel	Petroleum diesel
Kinematic viscosity (mm ² sec ⁻¹)	30.32	6.285	6.684	1.9 – 6.0	1.9 – 4.1
Density (kg m ⁻³)	785.7	864.8	856.5	820 - 950	850

CONCLUSION

A pilot plant has been designed to produce 1 ton/hr BD from waste/used vegetable oil using enzymatic approach. The amount of feed streams of WO, methanol and tert-butanol required were found to be 1138, 130 and 7.6 kg/hr, respectively. The main units in the proposed plant were designed and the economic feasibility of the process was assessed. It was found that the total capital investment required is about US\$ 620,000, which will be paid back within four years of operation.

REFERENCES

- [1] Lai, C.C., Zulaikah, S., Vali, S.R. and Ju, Y. "Lipase-catalyzed production of biodiesel from rice bran oil", *J. Chem. Tech. Biotechnol.* Vol. 80, pp. 331–337, 2005.
- [2] Soumanou, M.M. and Bornscheuer, U.T. "Improvement in lipase-catalysed synthesis of fatty acid methyl esters from sunflower oil", *Enzyme Microbiol. Technol.* Vol. 33, pp. 97-103, 2003.
- [3] Fukuda, H., Kondo, A. and Noda, H. "Biodiesel fuel production by transesterification of Oils", *J. Biosci. Bioeng.* Vol. 92, pp. 405-416, 2001.
- [4] Zhang, Y., Dube, M.A., McLean, D.D. and Kates, M. "Biodiesel production from waste cooking oil: economic assessment and sensitivity analysis", *Bioresour. Technol.* Vol. 90, pp. 229–240, 2003.
- [5] Clark, D.S. "Can immobilization be exploited to modify enzyme activity?", *TIBTECH*, Vol. 12, pp. 439-443, 1994.
- [6] Cowan, D. "Industrial enzyme technology", *TIBTECH*, Vol. 14, pp. 177-178, 1996.
- [7] Harding, K.G., Dennis, J.S., von Blottnitz, H. and Harrison, S.T.L. "A life-cycle comparison between inorganic and biological catalysis for the production of biodiesel", *J. Cleaner Prod.* Vol. 16, pp. 1368-1378, 2007.
- [8] Chen, J.W. and Wu, W.T. "Regeneration of immobilized *Candida antarctica* lipase for transesterification", *J. Biosci. Bioeng.* Vol. 95, pp. 466-469, 2003.
- [9] Institute of Petroleum, *Methods for Analysis and Testing*, Volume 1, Hyden and Son Ltd, London, 1982.
- [10] Royon, D., Daz, M., Ellenrieder, G. and Locatelli, S. "Enzymatic production of biodiesel from cotton seed oil using t-butanol as a solvent", *Bioresour. Technol.* Vol. 98, pp. 648-653, 2006.
- [11] Al-Zuhair, S., Fan, W.L. and Lim, S.J. "Proposed kinetic mechanism of the production of biodiesel from palm oil using lipase", *Proc. Biochem.* Vol. 42, pp. 951-960, 2007.
- [12] Fogler, H.S. *Elements of Chemical Reaction Engineering*, 4th edition, Pearson Education International, USA, 2006
- [13] Al-Zuhair, S., Dowaidar, A. and Kamal, H. "Dynamic modelling of biodiesel production from simulated waste cooking oil using immobilised lipase", *Biochem. Eng. J.* Vol. 44, pp. 256-262, 2008.
- [14] Benitez, W. *Principles and Modern Application of Mass Transfer Operations*, Wiley Interscience, USA, 2002
- [15] Turton, R., Bailie, R.C., Whiting, W.B. and Shaeiwitz, J.A. *Analysis, Synthesis and Design of Chemical Process*, 2nd edition, PH PTR, USA, 1998

Prototype Decontamination of Water by Ozone

Bouregba N¹, Benmimoun Y¹, Tilmatine A²,
Draou A.E.K¹ et Benaoum B¹

¹ University of Mascara, Laboratory of Science and Technology of water (bouregba.n@gmail.com, ybenmimoun2000@yahoo.com, aekdru@hotmail.com, benaoum_benali@yahoo.com)

²University of Sidi Bel Abbes (atilmatine@gmail.com)

ABSTRACT

The decrease of microbiologic contamination and the limitation of the microbiologic degradation of polluted water require the use of chemical disinfectants, like chlorine, which act on the microorganisms themselves, and the use of new technologies, like ozone. In this context, we have initiated research on this technical that uses an effective disinfectant than chlorine and not to act on the bacteria themselves, but also in improving the taste, odor and destruction Color. Following the two prototypes in our laboratory, as well as ozone generators technology for water treatment is established, is disinfection with ozone which is a chemical treatment by oxidation. The advantage of ozone is that it is not persistent in the waters treated. The objective of this study is to produce ozone from an ozone generator to dielectric barrier discharge for two different applications to plates and cylindrical, which is essentially composed of two conducting electrodes held against one of another. The air or oxygen is compressed and then dried, and passes between two electrodes where it is subjected to a corona discharge in a field of high voltage alternating current. Part of the oxygen is transformed into ozone.

Keywords: Decontamination, surface water, ozone generator, ozone, ozonation.

1. INTRODUCTION

Water is omnipresent in daily life and industry. There is no living being that does not drink, or a product that is not at least rinsed with water during its production, and water is an essential component in the production of many food products and chemicals, for instance. A water treatment by ozone is currently considered as one of the best options used for disinfection. Compared to chlorine, ozone has decisive advantages for use in industry for disinfection. It is a natural product, no dangerous derivatives, does not remain water and becomes to oxygen: It is used, for example, for the treatment of ultra pure water, which is not the case of chlorine. It is therefore not storable and is produced locally [07, 14].

This process is used to treat any type of water, from drinking water to wastewater. Our principal working is essentially the completion of laboratory ozone generators to electric discharge and their use in water treatment systems. In this work, we focused our efforts to realize two different experimental designs of water treatment [17].

2. MATERIALS AND METHODS

2.1. Ozonation erection with an ozone generator plate (type 1)

For such a mixture of ozone with water, we use an air blower to pump air into the cell of ozone peaks. The ozone produced in the output is injected into a water reservoir of five liters through small holes. The same

cell was used and placed inside a sealed assembly which consists of a cylinder. We used an HT alternative frequency equal to 50 Hz, delivered by a transformer providing a tension of 14 kV and produce a maximum current of 20 mA (Figure1).

In this work, the main interest is in testing the disinfecting effect of ozone on the treatment of color, using colorful polluted water. We did so in this study in order to allow ourselves a visual analysis of water treatment. The treated water is collected in a tray at the bottom and visually analyzed. We used for these experiments a dielectric barrier of Plexiglas 1 mm thick, the inter-electrode are set at 3mm.

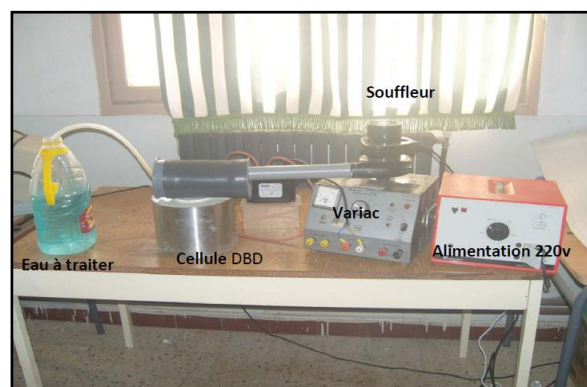


Figure 1: Descriptive representation of the system ozonation type 1.

2.2. Ozonation erection with an ozone generator cylindrical (type 2)

This arrangement is represented by a photograph in front view in figure 2. The processing circuit of the water is closed, polluted water leaves the reservoir and the treated water comes back into the same reservoir. The pump draws the water with a flow rate of about 10 L / min, the Venturi injection system injects the ozone produced by the generator in the water circuit. Indeed an aspiration occurs at the Venturi injector [05].



Figure 2: Descriptive representation of the system ozonation type 2.

3. RESULTS AND DISCUSSION

3.1. Thickness of the dielectric influence

To analyze the influence of the thickness of the dielectric on the DBD, we experimented with three Plexiglas barrier dielectrics of different thicknesses (3mm, 5mm and 8mm). The graph in figure 3, shows the characteristic of current as a function of the tension for each thickness by gradually increasing the tension of 2 kV to 14 kV in 2 kV [01, 03, 06].

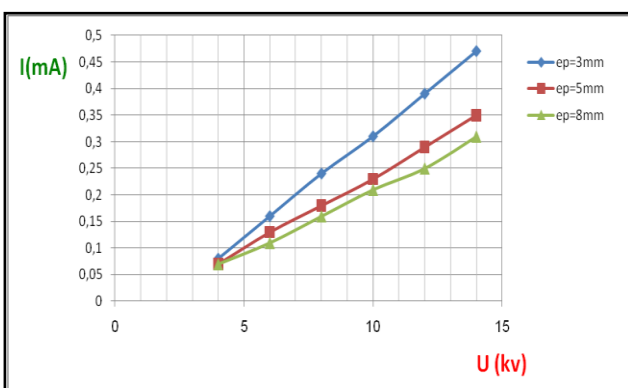


Figure 3: Variation of current as a function of the tension (three values of the thickness of the dielectric).

These results show that the thickness of the dielectric barrier has an important influence on the value of the current product. Indeed, the current decreases with increasing thickness, this is explained by the fact that a greater thickness corresponds to a higher resistance and

therefore the current decreases. Therefore, it recommends the use of dielectric barriers as thin as possible to generate higher powers.

3.2. Interval inter-electrode influence

We repeated the same experiment by increasing the characteristic of current as a function of the tension for several values of the inter-electrode and a thickness of 1 mm (Fig.4). The results show that the interval between the electrodes has an influence on the performance of the cell. Indeed, to produce more ozone, you need more power and higher current values. Therefore, the DBD is less intense for longer distances, and that intervals of one millimeter are recommended [16].

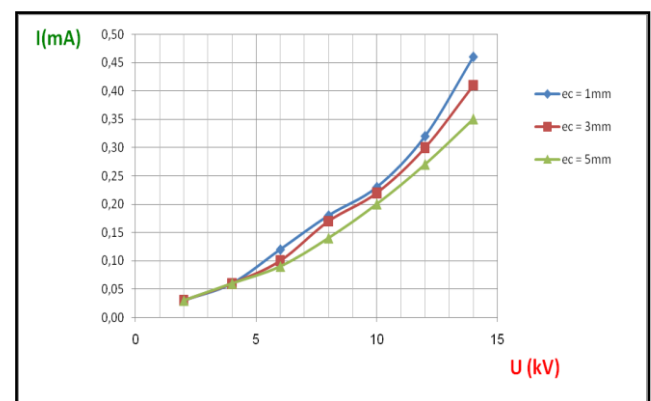


Figure 4 : Variation of current as a function of the tension (three values of the interval inter-electrode).

3.3. Identification and analysis of current oscillograms

The electrical characterization of the DBD is made under the oscillograms of current generated by the used cell. A storage oscilloscope with 250 MHz frequency was used to visualize the electrical current. Figures 5 and 6 give the current oscillograms obtained by the two types of generators respectively [15, 18].

These oscillograms show that the current is composed of very brief pulses produced by the generator plate and pulses of high frequency current produced by the generator cylinder, which are produced mainly in the area where the current at maximum rate. Indeed, each spark is stopped by the barrier dielectric and a new spark occurs. We see that the current pulse can happen up to values of 10 mA in case of a tension of 14 kV and 12 mA at 12 kV respectively.

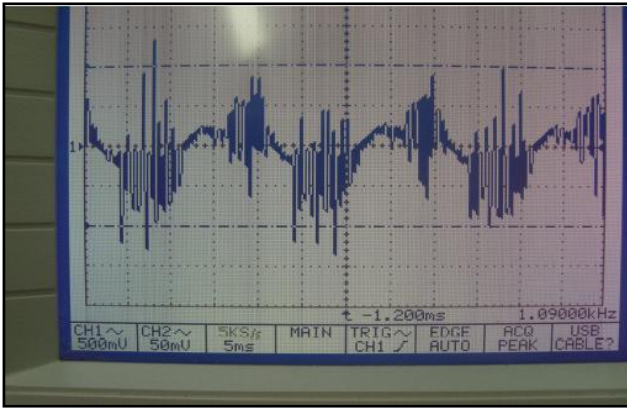


Figure 5 : Oscillograms of the current generated by the plate ozone generator.

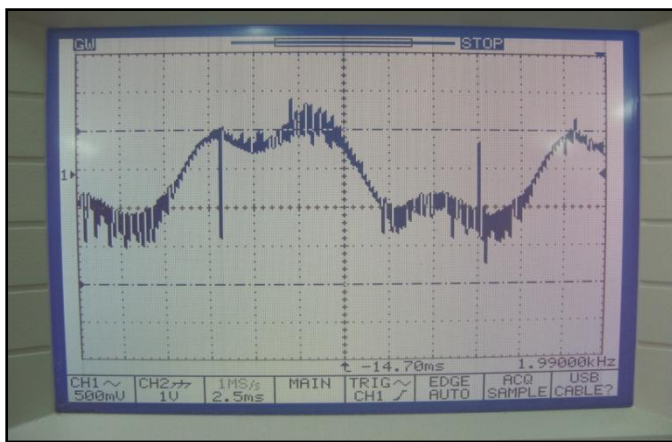


Figure 6 : Oscillograms of the current generated by the cylindrical ozone generator.

3.4. Verification of the efficiency of the process

We have already succeeded in making banks experimental water treatment by ozone, especially two ozone generators that produced results more or less positive. The technological improvements, based on some parameters were targeted.

3.4.1. First device

After a treatment period of 30mn, going over several times the amount of polluted water in the cell of ozonation, we obtained satisfactory results. There was a slight discoloration of water and certainly this is due to the amount of injected ozone. Indeed, the treatment is not completely done, because it acts on the surface and mixing between water with ozone does efficiently not occur (Figure 7).



Figure 7: Utilization of polluted water to visualize the change due to ozone (4 before and 5 after).

3.4.2. Second device

In the first experiment, we used 10 gallons of colored water and we put the process in motion until the discoloration. The effectiveness of this process depends largely on water contact time of with ozone and the amount of injected ozone. Therefore, we collected a sample at of 30 s regular intervals [05].

Water is discolored after 5 min of treatment as shown in figure 8. Water begins to fade from the 2nd min and becomes transparent from the 3rd min. Indeed, ozone attacks the organic matter that gives color to the water. We used a pump giving a maximum throughput of 30 L/min, but as we placed a venturi section of lower water, flow is lower.

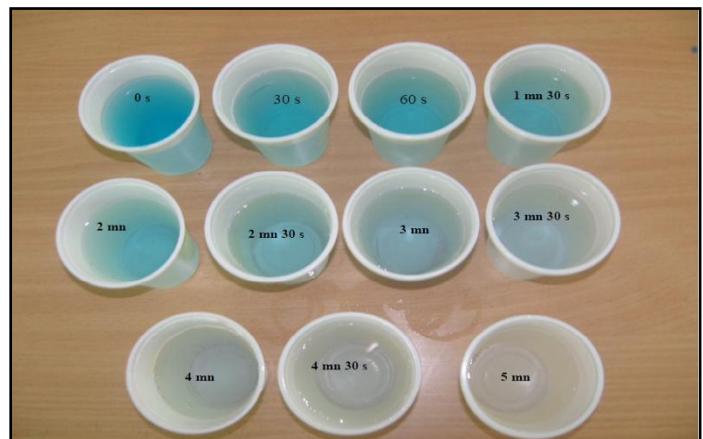


Figure 8 : Progress of the treatment of discoloration in steps of 30 seconds

For the second experiment, the process was applied to a sample taken from the wastewater treatment plant of the region of Mascara. The result shows that the ozone generated by dielectric barrier discharge is very effective for the treatment of wastewater as shown in figure 9.

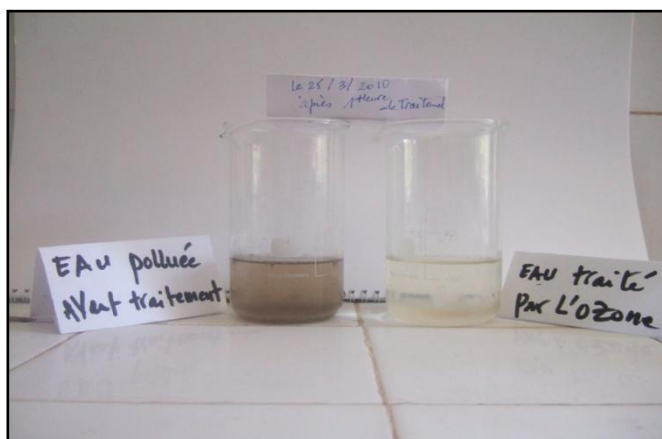


Figure 9 : Result of the process of wastewater

4. CONCLUSION

This work allowed us to master some of the practical water treatment by DBD generated ozone. Indeed, we performed two experimental devices and used for experimental study as electric water treatment as well. It appears from our results, the DBD generates many brief current pulses and high frequency is the cause of generated ozone.

Experiments using polluted and colorful water showed a greater improvement in the visual appearance due to the presence of organic matter, especially for the second device with a cylindrical ozone generator.

Note that this work is the first of its kind carried out jointly at the Universities of Sidi-Bel-Abbes and Mascara, and a lot of work will be done subsequently. We intend in future to design more efficient ozone generators, and use analytical means for more accurate results, and the occurrence of ozone analyzer in air and water to characterize more our experimental cells.

REFERENCES

- [1] Abahazem, A., Merbahi, N., Ducasse, O., Eichwald, O., and Yousfi, M., "Primary and Secondary Streamer Dynamics in Pulsed Positive Corona Discharges", IEEE Transactions on plasma science, vol. 36, No. 4, August, 2008.
- [2] Allen, N.L., and Mikropulos, P.N., "Streamer Propagation aLong Insulating Surfaces in Air", IE EE Trans. Electr. Insul., Vol. 6, No. 3, p. 357-362, 1999.
- [3] Allégraud, K., "Décharge à Barrière Diélectrique de Surface : Physique et Procédé", Thèse de doctorat, Ecole polytechnique, France, 2005.
- [4] Abahazem, A., "Etudes Expérimentales des Décharges Couronne pour la Dépollution des Gaz", Université de Toulouse III, 2009.
- [5] Benaoum, B., " Etude et Réalisation d'un Générateur d'Ozone à Décharge à Barrière Diélectrique", Mémoire de magister, Université de Mascara, 2011.
- [6] Benmimoun, Y., Flazi, S., Tilmatine, A., Rahli, M., "Study and Ralization of an Electric Process to Fight against Harmfull Insects", J. Electrical Systems 3-3, ISSN 11125209, p 144-150, 2007.
- [7] Gottschalk, C., Libra, J.A., Saupe, A., "Ozonation of Water and Waste Water. A Practical Guide to Understanding Ozone and its Applications", Wiley Editions, 2000.
- [8] Jarrige, J., et Vervish, P., "Etude Expérimentale de la Décomposition de COV dans une Décharge Couronne à Pression Atmosphérique", Le Havre, 2004.
- [9] Kip, A.F., "Positive-Point-to-Plane Discharge in Air at Atmospheric Pressure", Physical Review, Vol 54, 1938.
- [10] Lagmich, Y., "Diagnostic et Modélisation d'une Décharge à Barrière Diélectrique pour le Contrôle d'Écoulement", Thèse de doctorat, Université Toulouse III - Paul Sabatier, 2007.
- [11] Larbre, J., "Décontamination de Surface par un Procédé Plasma Froid à Pression Atmosphérique", Thèse de Doctorat, Université Paris Sud XI, 2006.
- [12] Labergue, A., "Etude de Décharges Electriques dans l'Air pour le Développement d'Actionneurs Plasmas - Application au Contrôle de Découlements d'Écoulements", Thèse de doctorat, Université de Poitiers, 2005.
- [13] Ledru, G., " Formation des Excimères et Exciplexes de Garares Corrélés à l'état Métastable Xe (3P2) Peuplé Sélectivement. Application aux Exciplexes KrXe dans une Décharge à Barrières Diélectriques", Thèse de doctorat, Université Paul Sabatier de Toulouse, 2005.
- [14] Martin, L., " Dépollution d'Effluents Chargés en Composés Organiques Volatils Cycliques (Toluène et Bêta-Pinène) par Décharge Couronne à Barrière Diélectrique- Marquage Isotopique et Simulation du Procédé", Thèse de doctorat, Université de Paris VI, 2005.
- [15] Miyoski, Y., Hosokawa, T., and Sakai, O., "Point to plan Discharge Phenomena in Air in Negative Polarity", Nagoya Institute of Technology Bulletin, 1964.
- [16] Naude, N., " Étude Electrique de la Physique d'une Décharge de Townsend à la Pression

Atmosphérique et de son Interaction avec un Générateur : Modèle et Expérience”, Thèse de doctorat, Université de Toulouse III, 2005.

- [17] Ono, R., and Oda, T., “Formation and Structure of Primary and Secondary Streamers in Positive Pulsed Corona Discharge-Effect of Oxygen Concentration and Applied Voltage”, J. Phys. D:

Appl. Phys. 36 1952-1958, 2003.

- [18] Sublet, A., “ Caractérisation de Décharges à Barrières Diélectriques Atmosphériques et Su atmosphériques et Application à la Déposition de Couches d'Oxyde de Silicium”, Thèse de doctorat, Ecole polytechnique fédérale de Lausanne, 2007.

Bioelectrochemical Single Chamber Reactor: Enrichment of Autotrophic Perchlorate Reduction for Water Treatment

Juan-Rodrigo Bastidas-Oyanedel¹, Ali Farhat², Mays N. Atiyeh³, Maren Mieseler⁴, Farrukh Ahmad⁵

BioEnergy and Environmental Laboratory (BEEL), Water and Environmental Engineering Program, Masdar Institute of Science and Technology, PO Box 54224, Abu Dhabi, United Arab Emirates.

¹ jbastidas@masdar.ac.ae, ² afarhat@masdar.ac.ae, ³ matiyeh@masdar.ac.ae, ⁴ mhintz@masdar.ac.ae, ⁵ fahmad@masdar.ac.ae

ABSTRACT

Perchlorate, a toxic compound impeding iodide uptake in humans, is found in industrial waste streams and in many surface and groundwater bodies around the world. Biological treatment of perchlorate contaminated water has been proposed as a cost effective approach; however, this approach often leaves the treated water with poor secondary water quality. To alleviate this problem, a few studies have demonstrated the bioelectrochemical reduction of perchlorate to innocuous chloride ion using an integrated bioanode-biocathode reactor known as microbial fuel cell (MFC), which allows the perchlorate laden water to reside across a membrane from the anodic substrate side of the process. The process relies on biocathodic perchlorate treatment mediated by electroactive perchlorate-reducing microorganisms, which can directly utilize the cathode as an electron donor. However, the enrichment methods for selecting electroactive perchlorate-reducing microorganisms presented in literature need the acclimation of the microorganism with a different electron acceptor other than perchlorate, or require the addition of an electron shuttle compound. In this study, we propose a new enrichment method called bioelectrochemical single chamber (BSC) enrichment for selecting electroactive microorganisms capable of reducing perchlorate. This method uses a simpler apparatus than an integrated MFC, and does not need acclimation nor the use of electron shuttles. The results presented are preliminary.

Keywords: bioelectrochemical system, perchlorate reduction, autotrophic mixed culture, biocathode, microbial fuel cell.

1. INTRODUCTION

Perchlorate (ClO_4^-), a strong oxidant, is commonly found in a variety of products ranging from rocket fuel propellant and fireworks to matches and automobile airbag inflation systems [1]. In the environment, perchlorate exhibits high aqueous solubility and almost no retention in soil, making it a prevalent contaminant [2]. Its toxicity involves impeding iodide uptake by the thyroid gland in humans [3].

The biological transformation of perchlorate to completely innocuous chloride ion (Cl^-) is a cost-effective approach [1,4]. In literature, autotrophic (*i.e.* use of inorganic carbon for growth) reduction of perchlorate have been performed using different electrons donors such as arsenite [5,6], hydrogen [7,8], elemental sulfur [9,10] and zero valent iron [11,12].

A novel approach is the use of a cathode, as an electron donor, in a bioelectrochemical system [4,13]. A biocathode is the result of combining a cathode and electroactive microorganisms growing on its surface. Biocathodes restrain the capacity of specific microorganisms to accept electrons from a solid surface (cathode) [4].

Thrash *et al.* [13] studied the use of an integrated bioanode-biocathode reactor, also known as microbial fuel cell (MFC). In their batch experiments, the anode and cathode chambers were communicated by a cation exchange membrane, and the system imposed a constant

voltage of -0.5 V on the cathode chamber. They observed complete perchlorate reduction ($250 \text{ mg}\cdot\text{L}^{-1}$) only in the presence of the electron shuttle 2,6-anthraquinone disulfonate (AQDS).

Butler *et al.* [4] completely reduced perchlorate, *i.e.* $20 \text{ mg}\cdot\text{L}^{-1}$ influent concentration, using a similar MFC reactor configuration with a constant resistance instead of a constant voltage while operating in a continuous mode. This enrichment experiment lasted for more than 400 days. For the first 84 days the cathode chamber was fed with nitrate (an electron acceptor). Then perchlorate was added to the feeding, gradually increasing the ratio of perchlorate/nitrate until solely perchlorate was fed from day 303.

In this study, we propose a new enrichment method called the bioelectrochemical single chamber (BSC) enrichment for selecting electroactive microorganisms capable of reducing perchlorate. We compare our findings with an MFC-based enrichment procedure commonly reported in literature. The results presented are preliminary.

2. MATERIALS & METHODS

Inoculum. Activated sludge from the Masdar City membrane bioreactor (MBR) was used as inoculum for the electroactive perchlorate-reducing culture enrichment methods.

2.1 Bioelectrochemical single chamber enrichment

A diagram of the bioelectrochemical single chamber (BSC) reactor is shown in Figure 1. BSC Liquid volume was 600 mL and a headspace of 200 mL. The Cathode was made of a treated active-carbon fiber brush. Brush treatment is detailed elsewhere [14]. A Titanium wire acted as an anode. The anode was in contact with the liquid and protected with a plastic cover, in order to avoid any contact with the cathode. Both electrodes were connected to a potentiostat (VMP3, BioLogic Science Instruments, Claix, France).

The reactor was charged with 250 mL of inoculum and 350 mL of perchlorate basal media [10,12,15,16], which consisted on (in $\text{mg}\cdot\text{L}^{-1}$): 620 NaClO_4 , 0.27 $\text{Na}_2\text{MoO}_4\cdot 2\text{H}_2\text{O}$, 0.05 AlCl_3 , 1 $\text{CaCl}_2\cdot 2\text{H}_2\text{O}$, 0.04 $\text{CoCl}_2\cdot 6\text{H}_2\text{O}$, 0.11 $\text{CuCl}_2\cdot 2\text{H}_2\text{O}$, 1 EDTA, 2 $\text{FeCl}_2\cdot 4\text{H}_2\text{O}$, 0.05 H_3BO_3 , 37.5 K_2HPO_4 , 41.25 $\text{MgCl}_2\cdot 6\text{H}_2\text{O}$, 0.49 $\text{MnCl}_2\cdot 4\text{H}_2\text{O}$, 5.1 $\text{Na}_2\text{S}\cdot 9\text{H}_2\text{O}$, 0.07 Na_2SeO_3 , 0.5 $\text{Na}_2\text{WO}_4\cdot 2\text{H}_2\text{O}$, 5.95 NH_4Cl , 0.09 $\text{NiCl}_2\cdot 6\text{H}_2\text{O}$, 0.05 ZnCl_2 , and $3.2\text{ g}\cdot\text{L}^{-1}$ NaHCO_3 . After inoculation the reactor was purge with argon for 30 minutes.

The enrichment was performed at $25\pm 2^\circ\text{C}$, stirring velocity of 100 rpm using a magnetic stirrer, pH 7.5, and a constant potential between the anode and cathode of 1 V, which corresponds to the perchlorate reduction voltage at the experimental conditions.

The culture was operated on a continuous mode at 48 h hydraulic retention time for 2 days in order to wash out any organic carbon present in the inoculum. After that the reactor was operated in a batch mode for 10 days.

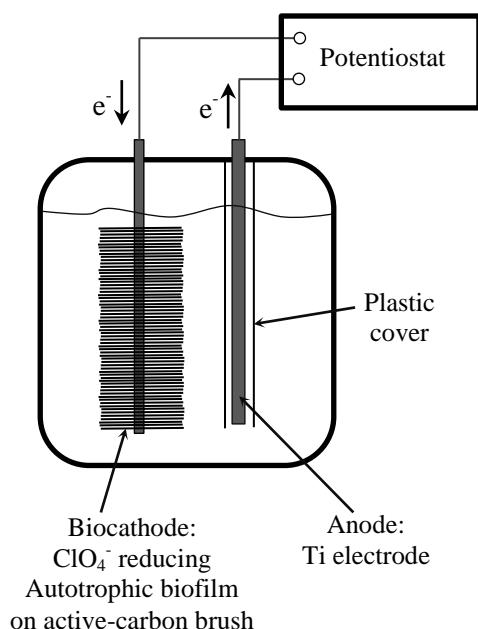


Figure 1: Bioelectrochemical single chamber (BSC) reactor diagram.

2.2 MFC enrichment method

Figure 2 illustrates the MFC enrichment method, which was based on Thrash *et al.* [13] pre-culturing the inoculum on acetate and perchlorate (Figure 2A), and Butler *et al.* [4] using a constant resistance in a batch MFC (Figure 2B).

2.2.1 Inoculum pre-culture

The active sludge inoculum was pre-culture on 60 mL bottles, at $25\pm 2^\circ\text{C}$, stirring velocity of 100 rpm using a magnetic stirrer, and pH 8.5, optimal pH after Butler *et al.* [4]. The basal media [17] contained (in $\text{g}\cdot\text{L}^{-1}$): 4.4 KH_2PO_4 , 3.4 K_2HPO_4 , 2 NaHCO_3 , 0.5 NaCl , 10.2 MgSO_4 , 0.0146 CaCl_2 and 0.4 yeast extract. Before and after inoculation, the media was purge with argon for 30 minutes in order to maintain anaerobic conditions. The inoculum to total culture volume ratio was 1:12 (v/v). The inoculated bottles were fed with 1 mL of $6.8\text{ g}\cdot\text{L}^{-1}$ acetate and $400\text{ mg}\cdot\text{L}^{-1}$ perchlorate solutions.

2.2.2 Constant resistance MFC

The cathode chamber of a MFC reactor was inoculated with 10 mL from the culture grown in section 2.2.1. The MFC was operated in batch mode at $25\pm 2^\circ\text{C}$, with a stirring velocity of 100 rpm and a pH of 8.5. The MFC was operated in open circuit for 1 day before been connected to a 500Ω resistor. This resistance yielded the maximum power density obtained from a polarization curve (data not shown).

The bioanodes of the MFC anodic chamber consisted on an electroactive heterotrophic acetate oxidizing biofilm defined in previous experiments.

Both cathodic and anodic chambers were connected by a CMI-700 cation exchange membrane (Membranes International Inc. Ringwood, NJ, USA). Each chamber had a working volume of 230 mL. Electrodes in both chambers consisted of treated active-carbon fiber brushes [14]. Both electrodes were connected by a resistor and to a data logger (Keithley 2701) to monitor the voltage generated between the two chambers.

The enrichment culture growing in the cathodic chamber was fed with $200\text{ mg}\cdot\text{L}^{-1}$ of NaClO_4 as electron acceptor and basal media (see section 2.2.1). Anodic chamber media contained (in $\text{g}\cdot\text{L}^{-1}$): 2 sodium acetate as electron donor, and 1 NH_4Cl , 0.1 KCl , 5 $\text{NaH}_2\text{PO}_4\cdot \text{H}_2\text{O}$, 9 Na_2HPO_4 , 0.2 yeast extract, 2.5 NaHCO_3 [18]. After inoculation, both chambers were purged with argon for 30 minutes.

2.4 Perchlorate analysis

Perchlorate concentration was analyzed using an ionic chromatograph – tandem mass spectrometer (IC-MS/MS) configuration. This system consisted on a

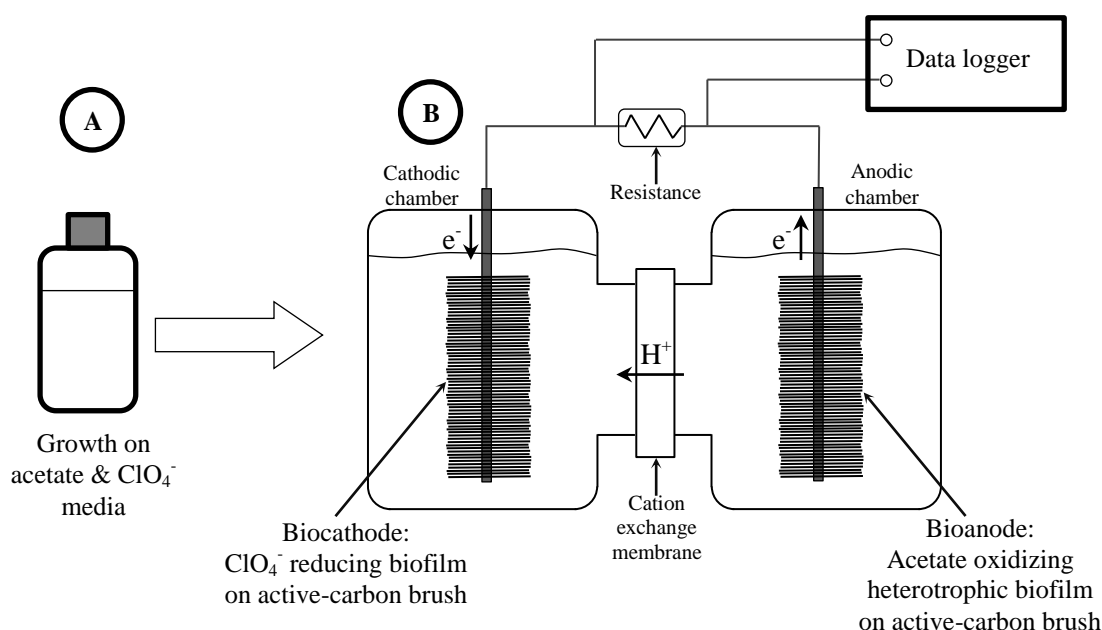


Figure 2: Microbial fuel cell (MFC) enrichment method. A: pre-culture on acetate and perchlorate as electron donor and acceptor, respectively. B: MFC with a constant resistance

Dionex (Sunnyvale, California, USA) ion chromatograph linked to an Applied Biosystems–MDS SCIEX (Foster City, California, USA) API 2000 triple quadrupole mass spectrometer.

Samples from the BSC and MFC reactor were filtered with 0.2 μm syringe filters, and stored at -20°C . Samples were diluted with a factor of 10, and run against a standard calibration curve prepared with an ion chromatography perchlorate analytical standard (IC-ClO₄-10X-1, AccuStandard Europe, Switzerland) using serial dilution for calibration.

3. RESULTS & DISCUSSIONS

3.1 BSC and MFC results

Figure 3 shows the kinetics of perchlorate reduction for both BSC and MFC enrichment methods. The reduction by BSC method (presented in open circles) was followed through 10 days. BSC culture reduced perchlorate at a rate of $24 \text{ mg}\cdot(\text{L}\cdot\text{d})^{-1}$.

MFC culture (black triangles) reduced perchlorate until day 5 at a rate of $15 \text{ mg}\cdot(\text{L}\cdot\text{d})^{-1}$, then no removal was encountered in this system. This stagnation has been observed by Butler *et al.* [4]. One reason for this stagnation phenomenon could be the decay of heterotrophic perchlorate reducing microorganisms (HPRM) in the cathode chamber after the fifth day, due to the fact that no organic carbon source such as acetate was fed to the cathode chamber. HPRM were selected over autotrophic microorganisms in the pre-culturing step (see section 2.2.1 and Figure 2A) since the electron donor consisted of acetate. Another reason could be the depletion of trace nutrients in the catholyte under conditions of electrochemical stress.

3.2 BSC versus MFC enrichment methods

Our preliminary results on BSC reactor proved that this system is an improved tool for the enrichment of electroactive perchlorate-reducing microorganisms over the conventionally reported MFC method. Below, we further compare our BSC method with the conventional MFC method.

BSC method is exempt of a two chamber apparatus, making it simpler than a MFC reactor. Also, the processes conducted on BSC reactor does not depend on cation-exchange membrane related mass transfer limitations or on any anode chamber issues.

Our BSC enrichment did not need an acclimation with other electron acceptors as in the work of Butler *et al.* [4]. Also, the reduction of perchlorate in the BSC reactor was accomplished without any electron shuttle compound - Thrash *et al.* [13] suggested the use of electron shuttles as AQDS for the complete reduction of perchlorate.

3.4 Perspectives

Future work will be focus on two subjects: 1) the characterization of selected electroactive perchlorate-reducing microbial population using the BSC enrichment method; and 2) the optimization of BSC perchlorate reducing microorganism enrichment by

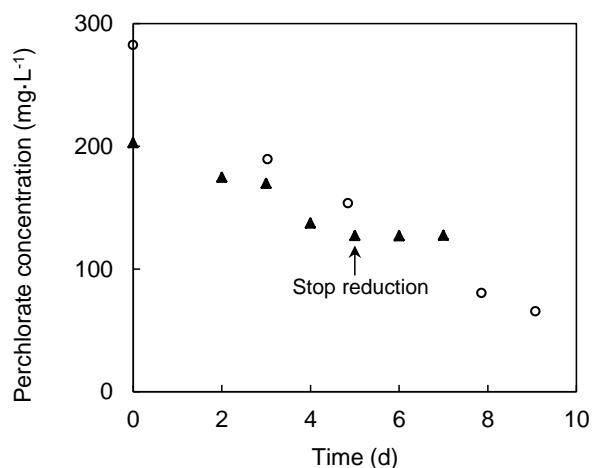


Figure 3: Kinetics of perchlorate reduction by BSC (○) and MFC (▲) electroactive mixed cultures.

studying the influence of environmental parameters such as pH, temperature, and perchlorate concentration.

4. CONCLUSION

Our preliminary results showed that our BSC enrichment method allowed the selection of electroactive perchlorate reducing microbes. Also, BSC method is an excellent tool for selecting other electroactive microbes from environmental samples. Therefore this method can be applied for the enrichment of microorganisms that reduce different contaminants such as nitrate or bromate.

5. ACKNOWLEDGEMENTS

This research was funded and supported by Masdar Institute.

REFERENCES

- [1] Sturchio, N.C., Hatzinger, P.B., Arkins, M.D., Suh, C., and Heraty, L.J. "Chlorine isotope fractionation during microbial reduction of perchlorate", *Environmental Science & Technology*, Vol. 37, No. 17, pp. 3859-3863, 2003.
- [2] Urbansky, E. "Perchlorate as an environmental contaminant", *Environmental Science & Technology*, Vol. 9, No. 3, pp. 187-192, 2002.
- [3] Kucharzyk, K.H., Crawford, R.L., Cosens, B., and Hess, T.F. "Development of drinking water standards for perchlorate in the United States", *Journal of Environmental Management*, Vol. 91, No. 2, pp. 303-310, 2009.
- [4] Butler, C.S., Clauwaert, P., Green, S.J., Verstraete, W., and Nerenberg, R. "Bioelectrochemical perchlorate reduction in a microbial fuel cell", *Environmental Science & Technology*, Vol. 44, No. 12, pp. 4685-4691, 2010.
- [5] Sun, W.J., Sierra-Alvarez, R., and Field, J.A. "Long term performance of an arsenite-oxidizing-chlorate-reducing microbial consortium in an upflow anaerobic sludge bed (USB) bioreactor", *Bioresource Technology*, Vol. 102, No. 8, pp. 5010-51016, 2011.
- [6] Sun, W.J., Sierra-Alvarez, R., Milner, L., and Field, J.A. "Anaerobic oxidation of arsenite linked to chlorate reduction", *Applied and Environmental Microbiology*, Vol. 76, No. 20, pp. 6804-68011, 2010.
- [7] van Ginkel, S.W., Lamendella, R., Kovacik, W.P., Domingo, J.W.S., and Rittmann, B.E. "Microbial community structure during nitrate and perchlorate reduction in ion-exchange brine using the hydrogen-based membrane biofilm reactor (MBfR)", *Bioresource Technology*, Vol. 101, No. 10, pp. 3747-3750, 2010.
- [8] Shrout, J.D., Scheetz, T.E., Casavant, T.L., and Parkin, G.F. "Isolation and characterization of autotrophic, hydrogen-utilizing, perchlorate-reducing bacteria", *Applied Microbiology and Biotechnology*, Vol. 67, No. 2, pp. 261-268, 2005.
- [9] Sahu, A.K., Conneely, T., Nusslein, K.R., and Ergas, S.J. "Biological perchlorate reduction in packed bed reactors using elemental sulfur", *Environmental Science & Technology*, Vol. 43, No. 12, pp. 4466-4471, 2009.
- [10] Ju, X., Field, J.A., Sierra-Alvarez, R., Salazar, M., Bentley, H., and Bentley, R. "Chemolithotrophic perchlorate reduction linked to the oxidation of elemental sulfur", *Biotechnology and Bioengineering*, Vol. 96, No. 6, pp. 1073-1082, 2007.
- [11] Son, A., Schimdt, C.J., Shin, H., and Cha, D.K. "Microbial community analysis of perchlorate-reducing cultures growing on zero-valent iron", *Journal of Hazardous Materials*, Vol. 185, No. 2-3, pp. 669-676, 2011.
- [12] Yu, X., Amrhein, C., Deshusses, M.A., and Matsumoto, M.R. "Perchlorate reduction by autotrophic bacteria in the presence of zero-valent iron", *Environmental Science & Technology*, Vol. 40, No. 4, pp. 1328-1334, 2006.
- [13] Thrash, J.C., Van Trump, J.I., Weber, K.A., Miller, E., Achenbach, L.A., and Coates, J.D. "Electrochemical stimulation of microbial perchlorate reduction", *Environmental Science & Technology*, Vol. 41, No. 5, pp. 1740-1746, 2007.

- [14] Feng, Y., Yang, Q., Wang, X., and Logan, B.E. "Treatment of carbon fiber brush anodes for improving power generation in air-cathode microbial fuel cells", *Journal of Power Sources*, Vol. 195, No. 7, pp. 1841-1844, 2010.
- [15] Zhang, H., Bruns, M.A., and Logan, B.E. "Perchlorate reduction by a novel chemolithoautotrophic, hydrogen-oxidizing bacterium", *Environmental Microbiology*, Vol. 4, No. 10, pp. 570-576, 2002;
- [16] Yu, X., Amrhein, C., Deshusses, M.A., and Matsumoto, M.R. "Perchlorate reduction by autotrophic bacteria attached to zerovalent iron in a flow-through reactor", *Environmental Science & Technology*, Vol. 41, No. 3, pp. 990-997, 2007.
- [17] Clauwaert, P., Rabaey, K., Aelterman, P., De Schamphelaire, L., Pham, T.H., Boeckx, P., Boon, N., and Verstraete, W. "Biological denitrification in microbial fuel cells", *Environmental Science & Technology*, Vol. 41, No. 9, pp. 3354-3360, 2007.
- [18] Nerenberg, R., Rittmann, B.E., and Najm, I. "Perchlorate reduction in a hydrogen-based membrane-biofilm reactor", *Journal American Water Works Association*, Vol. 94, No. 11, pp. 103-114, 2002.

Removal of Heavy Metals from Aqueous Solution by Poly (Acrylamide-co-Acrylic acid) /Porous Materials

¹M. Zendehtdel, ¹H. Alikhani

¹Department of Chemistry, Faculty of Science, Arak University, Arak, Iran
Email: m-zendehtdel@araku.ac.ir/ mojangzendehtdel@yahoo.com

In this study, a series of poly acrylamide-co-acrylic acid/NaY zeolite, poly acrylamide-co-acrylic acid/MCM-41 and poly acrylamide-co-acrylic acid/clinoptilolite nanocomposites synthesized. These materials characterized by using FT-IR spectroscopy, XRD, TGA and SEM. Removal capacity of Pb(II) and Cd(II) ions in aqueous solutions by using these nanocomposites was investigated with controlled time, initial metal ions concentration, pH values, adsorbent content and temperature by using atomic absorption spectrometry. Result show that these nanocomposites have further adsorption related to NaY, MCM-41 and clinoptilolite. Poly (AAM-co-AAc)/NaY, poly (AAM-co-AAc)/MCM-41 and poly (AAM-co-AAc)/Clinoptilolite exhibit superior Pb(II) (about 90-99%) and Cd(II) (about 88-98%) adsorption behavior at room temperature and the poly (AAM-co-AAc)/NaY nanocomposite had the best adsorption behavior. Finally, the equilibrium removal performance of the composites is analyzed according to the langmuir and Freundlich adsorption isotherm model that show result fitted to langmuir model and have monolayer adsorption

Keyword: removal, acrylamide-co-acrylic acid/ zeolite,heavy metals

1. INTRODUCTION

Heavy metals are a class of pollutants that require extensive treatment before discharge in water system. These metals are harmful to human, animals and living creatures. Lead, for example, is the second top priority hazardous substance according to the Agency of Toxic Substances & Disease Registry (ATSDR) in year 2007 [1]. It is a very toxic element, causing brain damage, kidney damage, and gastrointestinal distress to human at short term exposure. Chronic exposure to lead can affect the central nervous center, urinal system, and leads to kidney damage and death. The potential sources of lead come from manufacturing of batteries, metal products, paints, and ceramic glazes.

Cadmium is a natural, usually minor constituent of surface and groundwater too. It may exist in water as a hydrated ion, as inorganic complexes such as carbonates, hydroxides, chlorides or sulfates, or as organic complexes with humic acids [2]. Cadmium may enter aquatic systems through weathering and erosion of soils and bedrock, atmospheric deposition, direct discharge from industrial operations, leakage from landfills and contaminated sites, and the dispersive use of sludge and fertilizers in agriculture. Adverse health effects due to cadmium are well documented and it has been reported to cause renal disturbances, lung problems, bone lesions, cancer and hypertension in humans [3].

In order to reduce heavy metal pollution problem, heavy metals in the environment removed by some processes such oxidation-reduction processes, filtration, electrochemical treatment, evaporation, ion exchange or reverse osmosis and adsorption [4]. Recently, the adsorption process with strong affinity and high loading

capacity for targeted metal ions has developed which much attention has paid to modification of superabsorbent [5-7].

Polymeric nanocomposites consisting of organic polymers and inorganic nanoparticles in a nanoscale regime represent a novel class of materials that have motivated considerable interest in recent years. These composites exhibit new advantageous properties and can be very different from those of their individual counterparts. Although, much preparation have focused on the improvement of the swelling ability, gel strength, mechanical and thermal stability of superabsorbents but adsorption of heavy metals by these composites is very important for selection of suitable adsorbent to metals removal from aqueous solutions [8-10].

In this study, a series of poly (acrylamide-co-acrylic acid), poly (acrylamide-co-acrylic acid)/polyvinyl-alcohol, poly (acrylamide-co-acrylic acid)/NaY zeolite and poly (acrylamide-co-acrylic acid)/clinoptilolite and composites synthesized and characterized. In addition, their removal capacity of Pb (II) and Cd (II) ions investigated in aqueous solutions. Finally, the equilibrium removal performance of the composites is analyzed according to the langmuir and Freundlich adsorption isotherm model.

2. EXPERIMENTAL

2.1 Materials and method

Acryl amide (AM), acrylic acid (AA), potassium hydroxide (KOH), N, N'-methylene bis acryl amide (Bis), N, N, N', N'-tetra methyl ethylene diamine (TMED), ammonium persulfate (APS), aluminum hydroxide, silica gel, sodium hydroxide, methylene blue

dye supplied by Merck and MB was the analytical reagent grade and used as received and polyvinyl alcohol (PVA) purchased from Fluka and Clinoptilolite supplied by the company of pars kansar. We synthesized NaY zeolite with molar ratio: 16 NaOH: 1 Al (OH)₃: 15 SiO₂: 320 H₂O in our laboratory [11]. All of them were used with out further purification. Final product characterized with FT-IR (Galaxy series FT-IR 5000 spectrometer), TGA (Diamond TG/DTA Perkin Elmer) and SEM (Philips, XL30).

2.2 Synthesis of poly (AAm-co-AAc)/NaY and poly (acrylamide-coacrylic acid)/Clinoptilolite composites

The optimum molar ratio of initial materials for preparation of poly (AAm-co-AAc) considered at prior work in our laboratory [12]. Preparation conditions for samples are as follows: At first, Potassium acrylate was prepared by partially neutralizing a diluted acrylic acid solution with a predetermined amount of 50 wt% aqueous potassium hydroxide solution which was added by drop wise in an ice bath. Then, the 0.23g cross-linker (N, N'-methylene bis acryl amide) carefully added to the acryl amide solution (3.19 g). Then, 0.2g of PVA, NaY zeolite or Clinoptilolite that ultrasound for 1h before use for getting nano size was slowly added to stirring monomer mixture. Then the first neutralized solution was added to it. The obtained suspension mixed by a 300-rpm magnetic mixer for 30 minutes. In the next step, TMED and APS (30 wt %) were added to the pore material-polymer mixed solution. After polymerization, the products removed from the beaker, cut to small pieces, and dried 72 to 96 hours in laboratory conditions.

2.3 Adsorption studies

Adsorption experiments were carried out under optimized conditions using the composite as adsorbent in a temperature controlled incubator shaker (IKA-OS₂) set at 300 rpm maintained at 30 °C for 8 h. A known amount of adsorbent was thoroughly mixed with 25 ml of respective Pb(II) and Cd(II) solutions of known concentration and pH. The pH of the solution was measured with a digital pH meter (Metrohm-744). The pH of the reaction mixture was initially adjusted using 0.1 M HNO₃ or NaOH solution. After the flask was shaken for the desired time, the suspension was filtered through Whatman 0.45 mm filter paper and the filtrate after suitable dilution, was analyzed for the Pb(II) and Cd(II) concentrations. Adsorption experiments were evaluated in batch equilibrium mode.

The concentration of Pb(II) and Cd(II) was determined with an atomic adsorption spectrophotometer. The percentage adsorption (%) was calculated by Eq. (1):

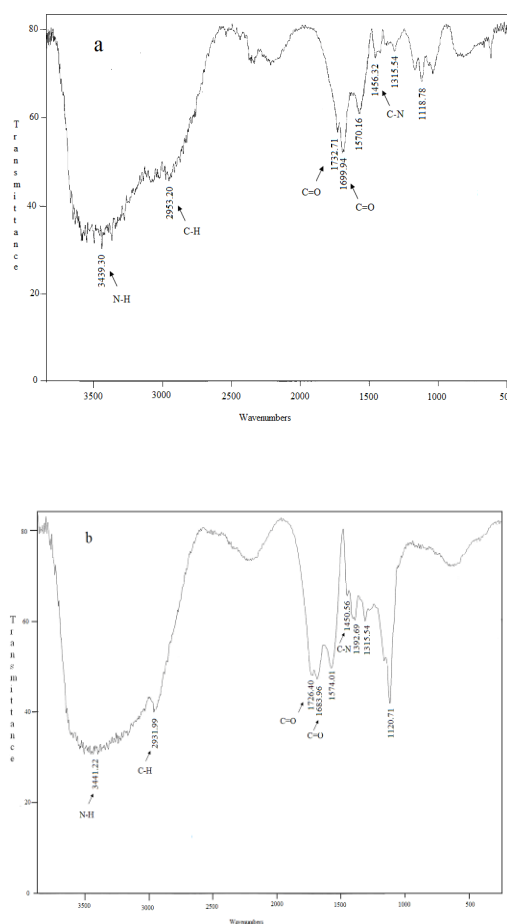
$$\% \text{Adsorption} = (C_i - C_f)100/C_i \quad (1)$$

Where C_i and C_f are the concentration of the metal ions in the initial and final solutions, respectively.

3. RESULTS AND DISCUSSION

3.1 FT-IR analysis

Figure 1 shows FT-IR spectra in the range of 500 to 4000 cm⁻¹ for poly (AAm-co-AAc) and poly (AAm-co-AAc)/PVA respectively. No characteristic stretch vibration peak of C=C is found in them. The broad band in 3439 cm⁻¹ is due to N-H groups of polyacrylamide and the peak at 1700 cm⁻¹ represents the carbonyl group. Also we can see two bonds at 1384 and 1570 cm⁻¹ related to COO⁻ group in polyacrylate and the peaks at 1456, 2953 cm⁻¹ represent the C-N and C-H bonding, respectively [13]. Figure1 shows FT-IR spectra in the range of 500 to 4000 cm⁻¹ for the poly (AAm-co-AAc)/NaY and poly (AAm-co-AAc)/Clinoptilolite, respectively.



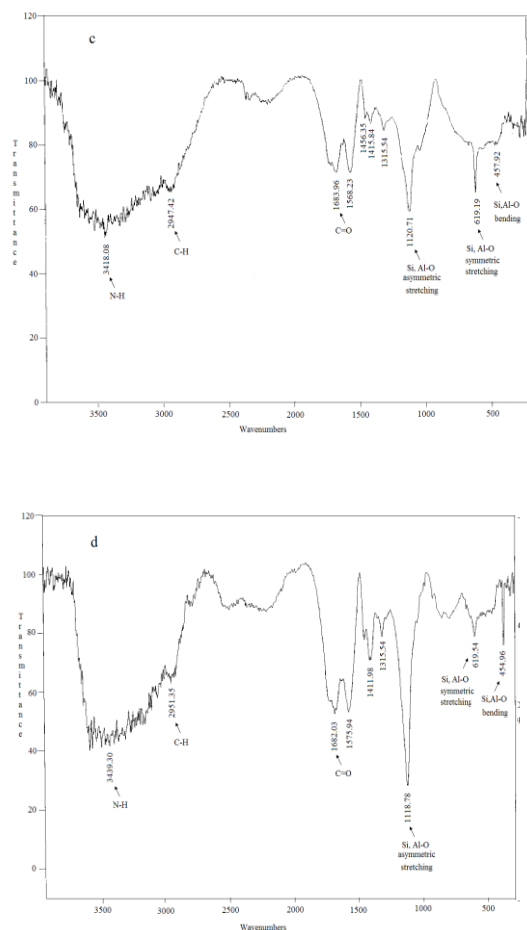


Figure 1: (a) FT-IR spectra of poly (AAm-co-AAc), (b) poly (AAm-co-AAc)/PVA, (c) poly (AAm-co-AAc)/NaY, (d) poly (AAm-co-AAc)/clinoptilolite

3.2 Morphology

SEM images of poly (acrylamide-co-acrylic acid)/PVA, poly (AAm-co-AAc)/NaY zeolite and poly (AAm-co-AAc)/Clinoptilolite are shown in Figure 2a-c, respectively. The micrographs reflected that poly (acrylamide-co-acrylic acid) forms a continuous phase and visibly no phase separation were observed. Uniform pore distribution was observed throughout the matrices. The pores are open ended, well interconnected with well defined boundaries. It means that NaY and Clinoptilolite have good collaborate with poly (AAm-co-AAc) and improves the network of it which may be favorable for Cadmium and Lead adsorption [14]. In (c) and (d) spectrum, the peaks of carbonyl shifted to around 1682 cm^{-1} and the intensity of the peaks at 3400 cm^{-1} correspond to N-H decreased and shifted to lower frequency. It may be because of the formation of hydrogen bonding between COOH, NH_2 of the copolymer and hydroxyl groups of Al-OH and Si-OH in pore materials.

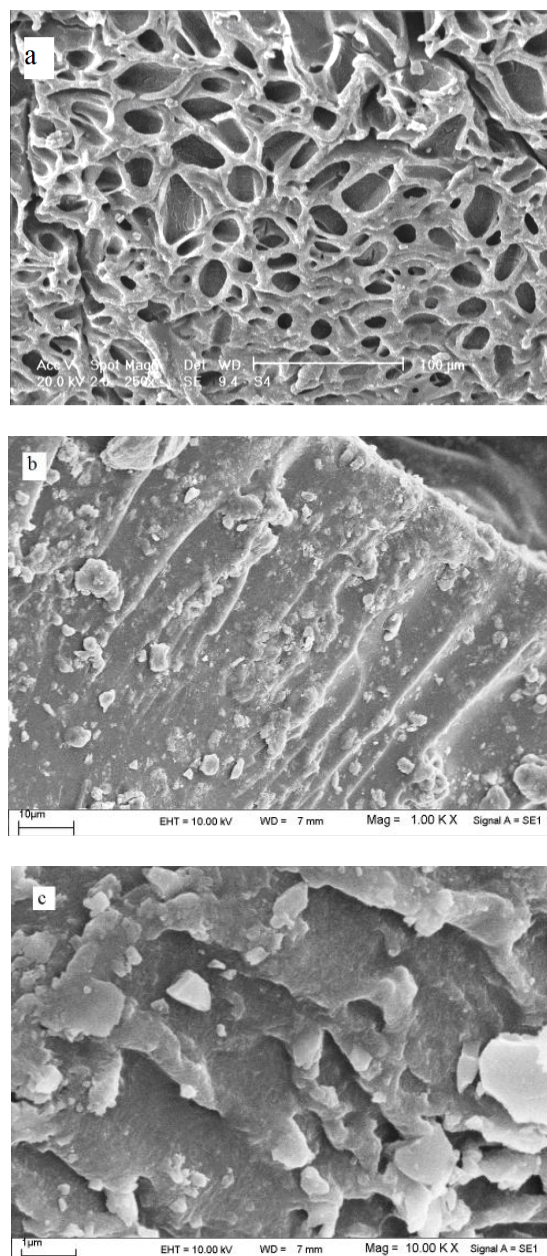


Figure 2: (a) SEM images of poly (acrylamide-co-acrylic acid)/PVA, (b) poly (AAm-co-AAc)/NaY zeolite, (c) poly (AAm-co-AAc)/Clinoptilolite

4. ADSORPTION STUDY OF LEAD AND CADMIUM

4.1 The effect of contact time

Figure 3 shows the adsorption percentage of Lead and Cadmium versus time in the solution of Pb(II) and Cd(II) with 50 mgL^{-1} as initial concentration. The adsorption increase up to 120 min for Pb (II) and 60 min for Cd (II) and then saturated. Thus, it appears that time equilibrium of 120 and 60 min for Pb(II) and Cd(II) ions are required, respectively.

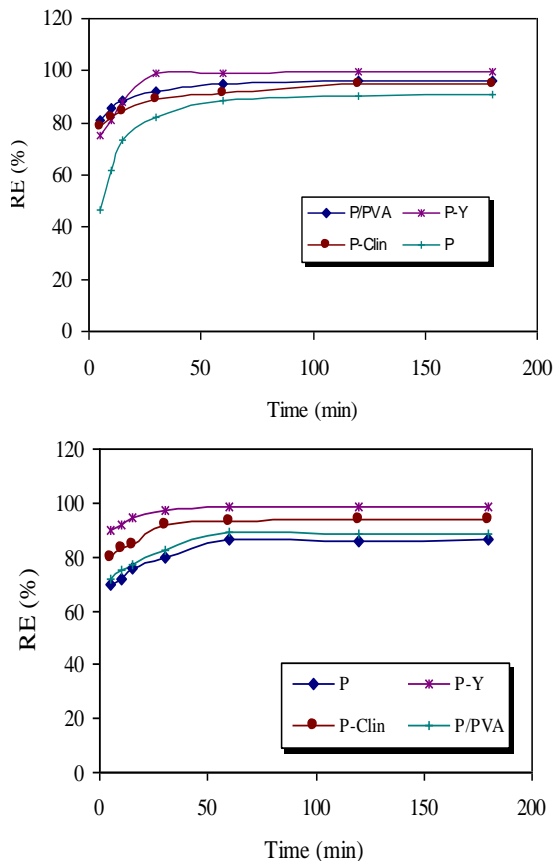


Figure 3: RE of Lead and Cadmium versus time in the solution of Pb (top) and Cd (bottom)

4.2 The effect of initial concentration

Figure 4 shows the effect of initial concentration of heavy metal ions on the percentage adsorption. Results show that the amount of adsorption was significantly increased with initial heavy metal concentration especially in the case of Pb(II) and also for Cd(II) in the studied initial concentration range (50-500 mgL⁻¹). Also, we can see with increasing the initial concentration of Pb(II) and Cd(II) from 500 to 2000 mgL⁻¹ adsorption decreased that due to saturation of the adsorption sites at the adsorbents.

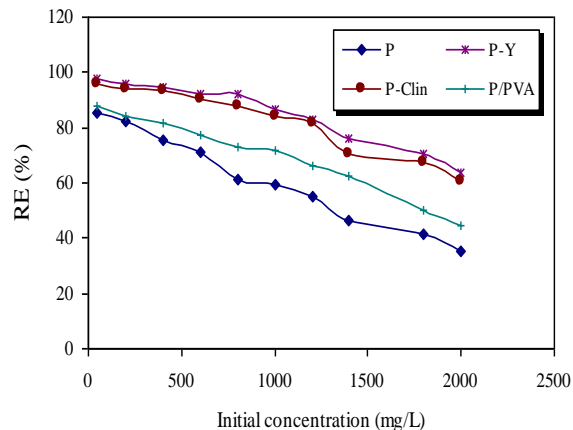
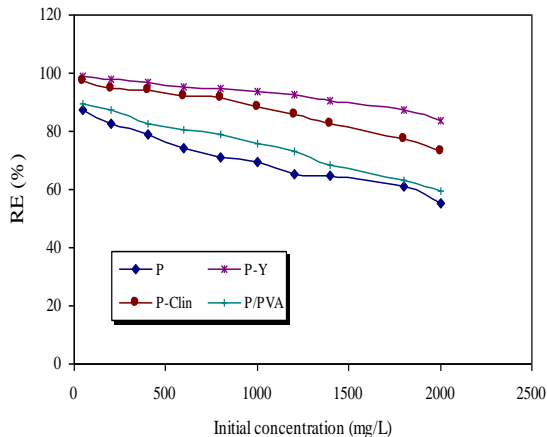


Figure 4: RE of Lead and Cadmium versus initial concentration of Pb (top) and Cd (bottom)

4.3 Effect of pH on Pb (II) and Cd (II) adsorption

Figure 5 shows the effect of equilibrium pH on the amount of Pb(II) and Cd(II) adsorbed on various adsorbents. Results show that the adsorption capacity of heavy metal ions decreased at low pH. Also, the optimum pH for removal of Pb(II) and Cd(II) was determined about 5, 6, respectively. The smaller amount of metals adsorbed at low pH is probably due to competitive adsorption of H⁺ with metal ions. These results confirmed that both metal sites in the NaY zeolite and carboxylate groups in the poly (AAm-co-AAc) play a critical role for absorption metal ions [15-17].

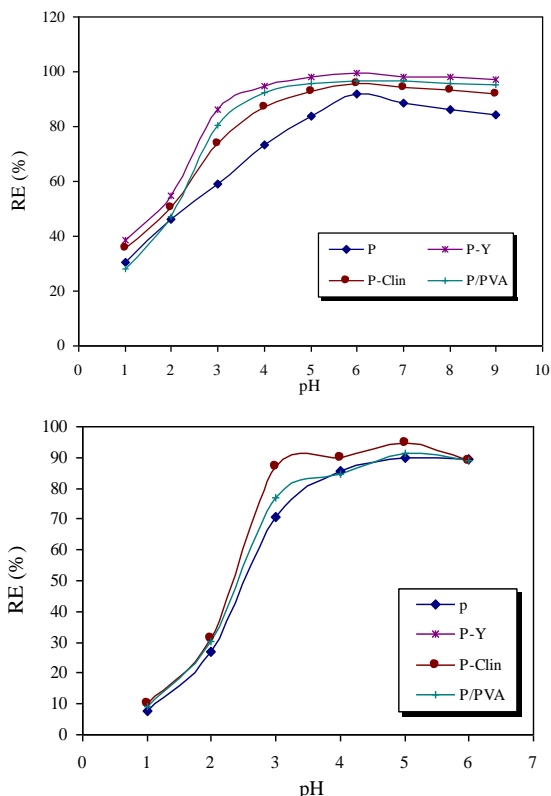


Figure 5: RE of Lead and Cadmium versus pH of Pb (top) and Cd (bottom)

4.4 Effect of adsorbent content

Figure 6 shows the percentage adsorption of Lead and Cadmium at different content of adsorbent. The result show that with increasing of adsorbent content from 5 to 25 mg on 25 ml of 50 mgL^{-1} Cd(II) and Pb(II) solution, the removal of Cd(II) and Pb(II) increased. It seems, further increasing in the adsorbent content had negligible effect on the adsorption.

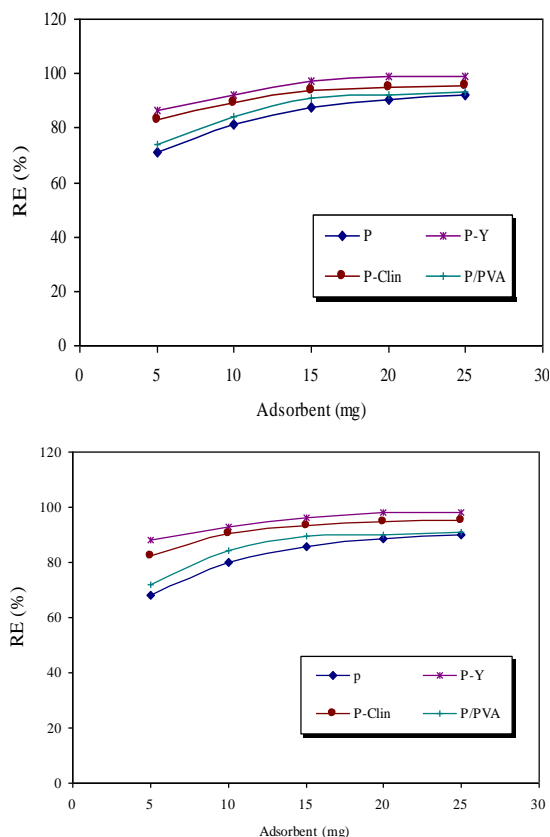


Figure 6: RE of Lead and Cadmium versus different content of adsorbent for Pb (top) and Cd (bottom)

4.5 Effect of temperature

Figure 7 shows the effect of temperature in the range of 283-323 K on the adsorption of heavy metals on the various adsorbent. We can see with increasing of temperature until 303K the adsorption of heavy metals increased. Then, the adsorption process has endothermic nature. In addition, with increasing temperature up to 323K adsorption of heavy metals decreased that may be due to some desorption of heavy metals [18].

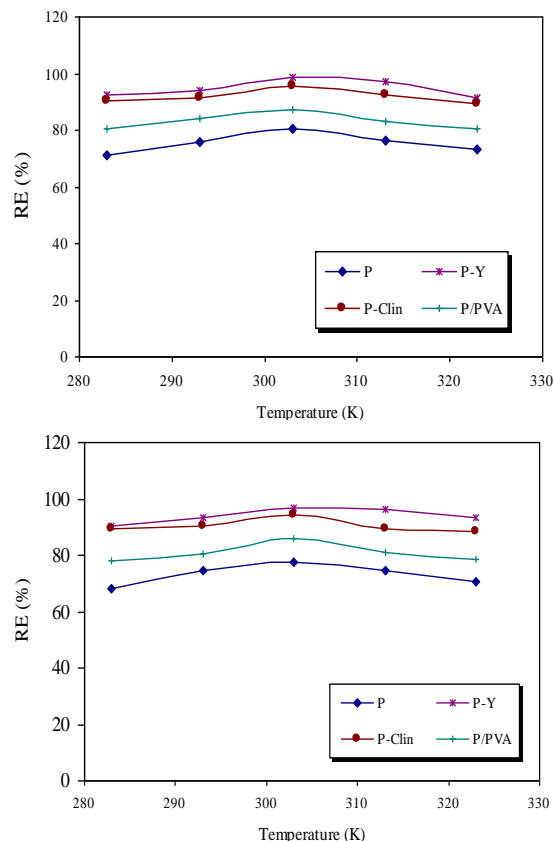


Figure 7: RE of Lead and Cadmium versus temperature of Pb (top) and Cd (bottom)

4.6 Comparison between the poly (AAM-co-AAc)/PVA, poly (AAM-co-AAc)/NaY and poly (AAM-co-AAc)/Clinoptilolite

It seems, NaY zeolite with $\text{Na}_{56} (\text{Al}_{56} \text{Si}_{136} \text{O}_{384})$ formula and by almost spherical cages (12\AA of diameter) tetrahedral interconnected through smaller windows (7.4\AA of diameter) defined by 12 oxygen rings is a good adsorbent for Pb(II) and Cd(II) related to Clinoptilolite with $(\text{Ca}_4 \text{Mg}_{18} \text{Na}_4 \text{K}_{28}) (\text{Al}_{8.16} \text{Si}_{27.84} \text{O}_{72}) (\text{H}_2\text{O})_{25.52}$ formula by smaller channel. These data indicate that the poly (AAM-co-AAc)/NaY and poly (AAM-co-AAc)/Clinoptilolite exhibit more ability in removal of Pb(II) (about 90-99%) and Cd(II) (about 88-98%) than poly (AAM-co-AAc)/PVA. It is Because of there are a lot of charges on the poly (AAM-co-AAc)/NaY and poly (AAM-co-AAc)/Clinoptilolite which adsorbed Pb(II) and Cd(II). Therefore, the composites have good porosity and flexibility for metal ions can be interred into network easily and interact with NaY, clinoptilolite and poly (AAM-co-AAc).

REFERENCES

- [1] ATSDR, CERCLA Priority List of Hazardous Substances, 2007 (cited; available from: <http://www.atsdr.cdc.gov/cercla/07list.html>).
- [2] Organisation for Economic Co-operation and Development (OECD) (1994), Risk Reduction Monograph No. 5: Cadmium OECD Environment Directorate, Paris, France.
- [3] M. P. Waalkes, Cadmium carcinogenesis in review, *J. Inorg. Biochem.* 79 (2000) 241–244
- [4] V. Radhika, S. Subramanian, K. A. Natarajan, Bioremediation of zinc using *Desulfotomaculum nigrificans*: bioprecipitation and characterization studies, *Water Res.* 40 (2006) 3628–3636.
- [5] R. Celis, M. C. Hermosin, J. Cornjo, Heavy metal adsorption by functionalized clays, *Environ. Sci. Technol.* 34 (2000) 4593–4599.
- [6] V. V. Ginzburg, C. Singh, A. C. Balazs, Theoretical phase diagrams of polymer/clay composites: the role of grafted organic modifiers, *Macromolecules*, 33 (2000) 1089–1099.
- [7] I. L. Lagadic, M. K. Mitchell, B. D. Payne, Highly effective adsorption of heavy metal ions by thiol-functionalised magnesium phyllosilicate clay, *Environ. Sci. Technol.* 35 (2001) 984–990.
- [8] M. S. Alhakawati, C. J. Banks, Removal of copper from aqueous solution by *Ascophyllum nodosum* immobilized in hydrophilic polyurethane foam, *J. Environ. Manage.* 72 (2004) 195–204.
- [9] U. Ulusoy, S. Simsek, Lead removal by polyacrylamide-bentonite and zeolite composites: effect of phytic acid immobilization, *J. Hazard. Mater.* 127 (2005) 163–171.
- [10] M. L. Pinto, J. Pires, A. P. Carvalho, M. B. de Carvalho, J. C. Bordado, Synthesis and regeneration of polyurethane/adsorbent composites and their characterization by adsorption methods, *Micropor. Mesopor. Mater.* 89 (2006) 260–269.
- [11] D. W. Breck, N. Y. Tonawanda, Assigned to Union Carbide, pat. no. 3130007, Patented Appr., 21(1964).
- [12] M. Zendejdel, A. Barati, H. Alikhani, A. Hekmat, Removal of methylene blue dye from wastewaters by adsorption on to sIPN hydrogels composed of poly (Acrylamide-co- Acrylic acid) and poly vinyl alcohol, 1st International conference on advances in wastewater treatment and reuse, 10-12 November 2009, Tehran, Iran.
- [13] Y. H. Ni, X. W. Ge, Z. C. Zhang, 2005. Preparation and characterization of ZnS/ poly (AAm-co-AAc) dendritical nanocomposites by γ -irradiation. *Mat.Sci.and eng.* 119: 51-54.
- [14] J. Z. Yi, L. M. Zhang, Removal of methylene blue dye from aqueous solution by adsorption onto sodium humate/polyacrylamide/clay hybrid hydrogels, *Biores. Technol.* 99 (2008) 2182-2186
- [15] C. Quintelas, Z. Rocha, B. Silva, B. Fonseca, H. Figueiredo, T. Tavares, Removal of Cd(II), Cr(VI), Fe(III) and Ni(II) from aqueous solutions by an *E. coli* biofilm supported on kaolin, *Chem. Eng. J.* 149 (2009) 319–324.
- [16] Y. Asc, i, M. Nurbas, Y. Sag Ac, ikel, Sorption of Cd (II) onto kaolin as a soil component and desorption of Cd (II) from kaolin using rhamnolipid biosurfactant, *J. Hazard. Mater. B* 139 (2007) 50–56.
- [17] N. Rangsayatorn, P. Pokethitiyook, E. S. Upatham, G. R. Lanza, Cadmium biosorption by cells of *Spirulina platensis* TISTR 8217 immobilized in alginate and silica gel, *Environ. Int.* 30 (2004) 57–63.
- [18] V. Singh, S. Pandey, S. K. Singh, R. Sanghi, Removal of cadmium from aqueous solutions by adsorption using poly(acrylamide) modified guar gum-silica nanocomposites, *Sep. Purif. Technol.* 67 (2009) 251-261

Air Pollution by Fine Particles (PM-10, PM-2.5 and PM-1) Size Distribution and Associated Trace Metals Evaluation in the Great Area of Algiers

Rabah Kerbachi¹, Ali Bitouche¹, Dalila Belhout¹, Nassima Oucher¹, Ménouer Boughedaoui¹

¹Research Laboratory LSTE, Ecole Nationale Polytechnique, El-Harrach, Alger, Algérie
email: r_kerbachi@yahoo.fr

ABSTRACT

The study presents the levels of air pollution by fine particulates matters PM-10, PM-2.5 and PM-1 at six different sites in the great Algiers. Samples are taken using a high volume sampler HVS-PM-10 equipped with a Sierra-Andersen cascade impactor. Measurements are carried out for a period of one year at each site. The results reveal that pollution by PM-10 and PM-2.5 is very high and exceeds the European and WHO guidelines. At urban site, the average content of PM-10 rises up to 65 $\mu\text{g}/\text{m}^3$ but values higher than 100 $\mu\text{g}/\text{m}^3$ were often reached. The (PM-2.5) average content is 35 $\mu\text{g}/\text{m}^3$ which constitute more than 50 % in mass of the PM-10. The ratio PM-2.5/PM-10 is a characteristic of an urban area influenced by the road traffic. Moreover, it is noted that approximately one third of the PM-10 is composed of very fine fraction of PM-1. It is shown that PM-10 are distributed according to a bimodal distribution with a good correlation between the very fine (PM-1) and the respirable particles (PM-2.5).

The size range analysis of trace metals (Fe, Mn, Pb, Cu, Co and Cd) associated to these particles shows high pollution by lead which is due to the very low use of unleaded fuel in Algeria. It is noticed that major part of toxic metals (Pb and Cd) are distributed on the very fine particles. The heavy metals of soil dust of earth's crust Fe and Mn are enriched in the coarse particles (range 3 - 10 μm). Data of the mass median diameter and the size distribution of trace metals are also discussed.

Keywords: Air pollution, fine particles, PM-i, road traffic, trace metals, size distribution, Algiers

1. INTRODUCTION

Fine particles of different size fractions PM-10, PM-2.5 and PM-1 is an important factor in air pollution, particularly in urban areas where traffic is dense. In terms of health, they represent a major indicator of air quality [1, 2, 3]. Numerous and consistent studies attribute their high responsibility in the occurrence of a wide range of biological and health effects [4, 5]. Because of their physicochemical characteristics, they have on the respiratory and cardiovascular system a high potential for harm. The European Commissioner for the Environment in 2007 estimated that each year 370,000 people in Europe die prematurely from diseases related to air pollution, including 350,000 of them due to respirable particles PM-2.5. Also, after the United States and the WHO, the European Union is considering making more severe standards in effect since 2000.

In Algeria, where urbanization and motorization are developing rapidly, the degradation of air quality and pollution are already collected. Studies have shown that the Greater Algiers (3.5 million people, 1000,000 vehicles) is, like any large urban area, confronted with severe air pollution [6, 7, 8]. The main source of emissions is traffic. Pollution from fine particles has not been the subject of special attention. And also to have accurate data on levels and types of pollution and to arrive at formulating a prevention strategy, we have from 2002 to 2009 conducted a large study on the contamination of the atmosphere by PM10, PM-2.5

PM-1 in different types of sites in the city of Algiers. Heavy metals associated with these particles and their contributions to global pollution were also studied.

2. METHODOLOGY

The study was conducted at six sites: three urban sites U1, U2 and U3 for assessing the exposure rate of urban population to pollution, one site close to road traffic S (site under the direct influence of cars emissions) and two peri-urban sites PU1 and PU2 located at the limit of the urban city (Figure 1).

S: The sampling station is located at the campus of Ecole Nationale Polytechnique (ENP) south-east at about 10 km from central Algiers and directly (8 m) along the main road RN5. This important road is frequented by more than 25,000 vehicles per day with approximately 15% of buses and heavy vehicles diesel. This site is also exposed to natural ventilation.

U1: The station is located at the university campus of Bab-Ezzouar about 15 km southeast of Algiers. It is an urban site with high resident population density (50,000 inhabitants per Km^2).


U2: The sampling site is located within the hospital Mustapha Bacha in central Algiers. This position overlooking the bay of Algiers is to undergo to very good natural ventilation.

U3: This site is like U1, an urban site with high resident population density in the district Badjarah.

PU1: The peri-urban site is located in the district of Dely Brahim (south-Algiers) at the Institute ISMAL.

PU2: This site is located at the end of the district Bouzaréah at the research centre CDER. This well ventilated site, which is the highest point of Algiers, is not under the influence of direct emissions of particles.



Figure 1 : Localisation of measurement sites in Great-Algiers ( sampling site)

In all these sites, sampling is performed at a height of 4 to 12 m from the ground. Samples are taken using a high volume sampler HVS-PM-10 equipped with a Sierra-Andersen cascade impactor with four stage ($< 1\mu\text{m}$, $1-1.5\mu\text{m}$, $1.5 - 3\mu\text{m}$, $3 - 7.2\mu\text{m}$ et $7.2 - 10\mu\text{m}$). The sampling time is 24 hours and the flow $1\text{ m}^3/\text{mn}$. Measurements are carried out for a period of one year at each site (with a sampling average frequency of six daily samples a month). After acid digestion of the collected particulate filters, heavy metals Fe, Pb, Mn, Ni, Cu, Co and Cd, are analyzed by atomic absorption spectrophotometry.

3. RESULTS AND DISCUSSION

3.1 Levels of air pollution by fine particles

The results show that in all sites, concentrations vary daily in a wide range. The diurnal variation is due, firstly, changes in the intensity of emission sources (road traffic), and other meteorological influences (wind, rain). For all sites studied, the mean levels of the three size fractions PM-10 PM-3 and PM-1 are summarized in table 1.

Table 1: Atmospheric mean levels of PM-i in $\mu\text{g}/\text{m}^3$ measured in ambient air in Algiers

Sites	PM-1	PM-3	PM-10	PM-1/PM-10	PM-3/PM-10
S	27.1	43.3	80.4	0.34	0.54
U1	22.2	35.6	69.3	0.32	0.51
U2	18	28.1	48	0.37	0.58
U3	22	38	73	0,30	0,52
PU1	13.1	18.3	27	0.48	0.67
PU2	10.4	20	30	0.35	0.66

It follows that the atmospheric concentrations of PM-i in road traffic site S (site under direct influence of vehicle emissions) are the highest. The lowest levels are measured in peri-urban sites. They are on average two times lower than in urban areas. The ratios PM-1/PM-10 and PM-3/PM-10 giving the mass of fine particles contribute to PM-10 are similar for all sites and show that in the PM-10, the very fine particles are predominant. The very harmful PM-1 are about a third of PM-10 and PM-3 more than half. Figure 2 shows the average mass contributions to PM-10 of different size fractions measured in urban areas.

The respirable fraction PM-2.5 that standards take into consideration is not accessible experimentally by our sampler. It is determined graphically from plotting data for the five size classes on a log-probability diagram the d_i diameter of particles based on the percentage of the cumulative mass of particles with a diameter $\leq d_i$ [9].

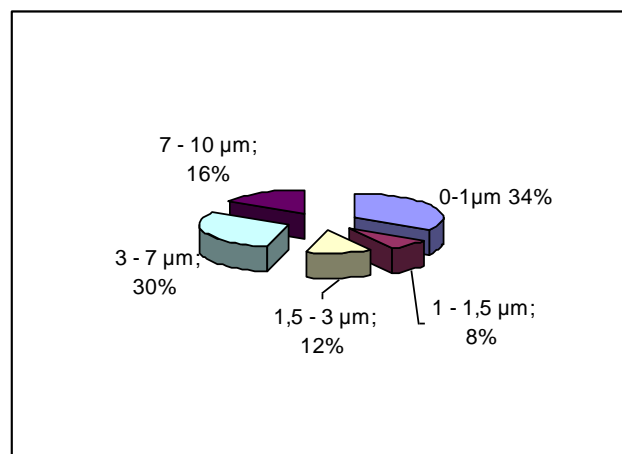


Figure 2: Mass distribution of the PM-10 per size range in urban site

The results obtained show that the PM-2.5 are, according to the type of site, approximately 92 to 94% of PM-3. Thus, by equating the PM-3 to PM-2.5, the error is acceptable.

The comparisons of measured atmospheric concentrations with the PM-10 and PM-2.5 standards of Algeria [10], U.S.A [11], European Union [12 and WHO standards [13] show that compared with the strong guide values of health protecting by of WHO, the

average annual levels of PM-10 and PM-2.5 are substantially exceeded in all types of sites. The European and U.S. standards are met in peri-urban sites. The very little binding Algerian standard (80µg/m³ for PM-10) is respected at all sites. Overall, we find that the fine particle pollution is excessive in both types of site, traffic station as well as urban sites.

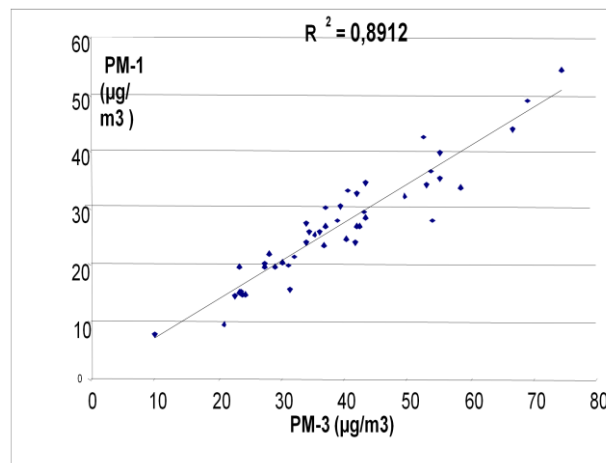
This pollution is alarming in its scale, but also because of the strong presence of very fine particles which increase the potential harm of airborne particles. A comparison with other cities also shows that Algiers accuses a high rate of pollution. The PM-10 levels measured in Algiers are indeed much higher than those observed in European cities like Paris, Lyon and Marseille (22 to 40 ug/m³) [14], but lower than in some cities emerging countries known for their high pollution as Beijing (135.9 g/m³) and Cairo (130 to 250 g/m³) [15].

3.2 Correlations between different size classes

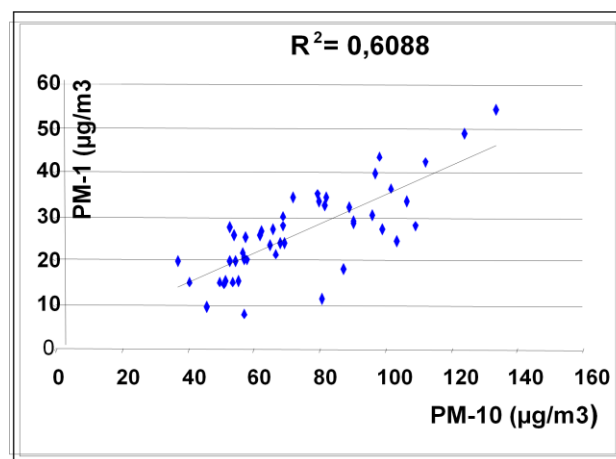
The daily evolution of particulate levels in PM-1, PM-3 and PM-10 shows a similarity in their evolution, particularly between the PM-1 and PM-3. Figure 3 presents some correlations calculate at road traffic site. We notice that for both types of sites, we get very good linear correlations between PM 1 and PM-3 and on other hand between PM-(3-10) and PM-10. The correlation between PM-1 and PM-10 is not satisfactory. This result suggests that very fine particles PM-1 and PM-3 have probably the same origin, road traffic and the secondary particles. The fractions PM-10 and PM-(3-10) which are less fine particles are highly enriched in particles of terrestrial origin and resuspension.

3.3 Particle size distribution

The study of the frequency distribution of levels of different size classes can access the modality of the size distribution of particles measured in Algiers [16]. The statistical analysis of data shows that the particles studied follow a bimodal distribution curve centred on 0.6 and 6µm modes (Figure 4) for urban sites and modes centred on 0.8 and 6 µm on the road traffic site. The literature reports similar bimodal distributions. In some cases, it leads to a trimodal curve when considering also the ultrafine particles.



(a)



(b)

Figure 3: PM-i correlations at traffic station: a) PM-1 / PM-3 b) PM-1 / PM-10

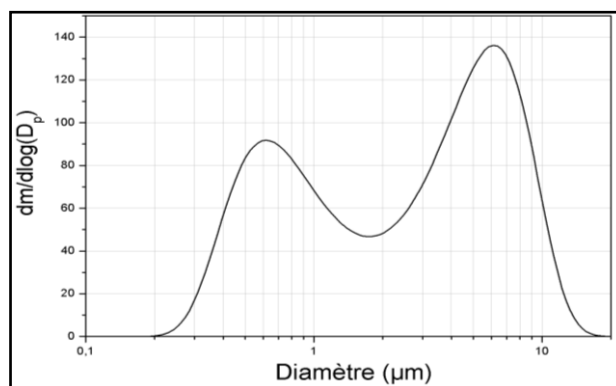


Figure 4: bimodal size distribution of PM-10 in Algiers

3.5 Heavy metals associated with PM-i

The study of heavy metals by particle size (table 2) shows that in almost all fractions and at all sites, the iron is, among the elements studied, the most abundant metal.

In urban areas, with an average content of 470 ng/m³, it is rising 0.64% of PM-10. Lead, in abundance, following the iron. From 300 ng/m³ content at road traffic site, it has now dropped to about 6 ng/m³ in peri-urban site. In urban area, lead levels measured are relatively high and exceed the new European standard of 0.2 µg/m³.

Table 2: Atmospheric levels of heavy metals associated to the PM-i size fractions

PM-i	Sites	Average concentrations (ng/m ³)					
		Fe	Pb	Mn	Cu	Ni	Cd
PM-1	Traffic	148.9	150.8	16.8	32.7	10,1	7.4
	Urban	106.7	117.4	11.3	20.1	8,4	0.6
	Peri-urban	146.6	Nd	15.3	7.9	5,1	nd
PM-3	Traffic	282.9	208.9	31.2	63.2	27.1	12
	Urban	193	147.6	27.3	41.3	19.2	1.1
	Peri-urban	251.4	4.2	28.7	12.8	7.3	nd
PM-10	Traffic	639.8	299.3	57.3	98.9	38,1	21
	Urban	467.1	231.2	41.3	60.8	31.7	1.4
	Peri-urban	440.3	6.1	61.4	22.6	17.2	0.3

Analysis of these data shows that heavy metals are distributed differently on the size classes. So in urban areas, the ratio $Pb_{PM-3}/Pb_{PM-10} = 0.66$ means that 66% of global atmospheric lead has a particle size less than 3µm. In the case of iron, 60% fall on the coarser fraction PM-(3-10). Manganese behaves like iron. This difference in the size of heavy metals is related to their emission source. The metals of the earth's crust (Fe, Mn, Cu) are associated with coarse particles (3-10µm) while lead enriches especially fine particles from road traffic (Figure 5).

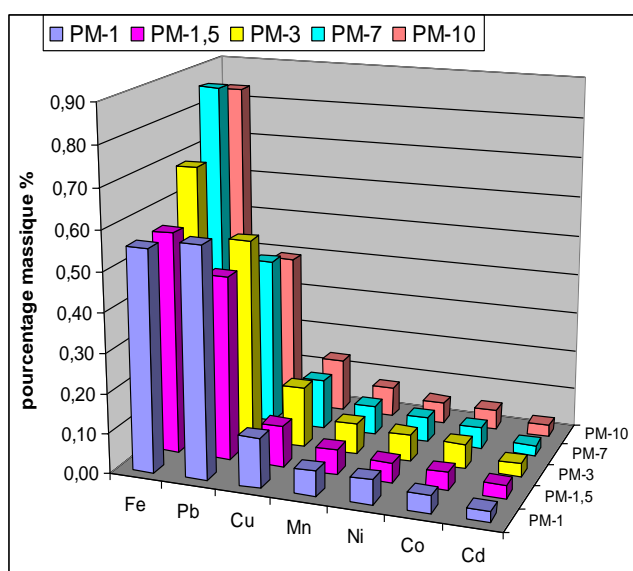


Figure 5: Mass fractions of heavy metals in the PM-i at traffic station

4. CONCLUSION

The study conducted over several years has allowed

access to levels of air pollution by particulate matter (PM-10, PM-2.5 and PM-1) met in Algiers in different types of sites. In urban and at station traffic site, levels of PM-10 and PM-2.5 are excessive and exceed largely international and WHO standards. This pollution is particularly worrying that over 60% of PM-10 particles are respirable. In peri-urban sites, the pollution levels are indeed reduced by half, but reached the levels measured in magnitude in urban sites in major European cities. It also shows that PM-10 following a bimodal distribution centred on 0.6 and 6µm. There are probably three major sources of pollution: road traffic and the secondary particles to PM-3 and terrigenous sources for PM-(3-10). The study of heavy metals showed the presence of high levels of lead associated with very fine particles and Fe-Mn crust in the coarse particles. In Algeria, the vehicle fleet is rather old with a low level of maintenance and the use of leaded fuel are the main reasons of high pollutant emissions of fine particles associated to high levels content of lead particles. In addition, arid climate is a source of a large part of air pollution by coarse particles.

REFERENCES

- [1] Schroeder W.H. "Toxic trace elements associated with airborne particulate matter", A review. *JAPCA*, 37, 11, pp. 1267 – 1285, 1987.
- [2] Janssen N. A. H., D. F.M. Van Mansom, Van Der Jagd K., H. Harsema and Hoek G. " Mass concentration and elemental composition of airborne particulate matter at street and background locations", *Atm. Env.*, vol. 31, N°8, pp. 1185-1193, 1997.
- [3] Chiron M., Quenel P. et Zmirou D. "La pollution atmosphérique d'origine automobile et la santé publique", *Poll. Atm.*, Janvier-mars, pp. 41-52, 1997.
- [4] Dockery D.W., Pope C.A., Xu X., Spengler J.D., M.E. Ware, Fay B.G., Ferris Jr. and Speizer F.E." An association between air pollution and mortality in six US cities" *N. Eng. J. Med.*, 329, pp. 1753 –1759, 1993.
- [5] Pope C.A., Thun M.J., Namboodira M., Dockery D.W., Evans J.S., Speizer F.W. and Heath Jr. C. W." Particulate air pollution as a predictor of mortality in a prospective study of U.S. adults", *Am. J. Respir. Crit. Care Med.*, vol. 151, N°3, pp. 669-674, 1995.
- [6] Boughedaoui M., Kerbachi R. et Joumard R. " Mesure de la pollution plombifère dans l'air ambiant d'Alger", *Poll. Atm.*, N°121, pp. 105-111, 2004.
- [7] Kerbachi R., Boughedaoui M., Bounouna L., keddami M. , "Ambient air pollution by aromatic hydrocarbons in Algiers", *Atm. Env.*, 40, pp. 3995-4003, 2006.
- [8] Kerbachi R., Boughedaoui M., Bitouche A. et Joumard R. " Etude de la pollution de l'air par les particules fines PM-10, PM-2,5 et PM-1 et évaluation des métaux lourds qu'elles véhiculent en milieu urbain", 15^e Colloque international "Transport et pollution de l'air",

proceedings N°107, Vol. 2, Inrets Ed., Arcueil, France, pp. 213-218, 2006. Algiers, 28.9.2011

- [9] Butler J.D. *Air pollution chemistry*, Academic Press , London, pp. 345-352, 1979.
- [10] *Journal officiel de la République algérienne démocratique et populaire* (Décret N° 06-02 du 7 janvier 2006 définissant les valeurs limites, les seuils d'alerte et les objectifs de qualité de l'air en cas de pollution atmosphérique, 2006.
- [11] U.S.- Environmental Protection Agency National ambient air quality standards (NAAQS) for particulate matter, *Federal Register*, vol.62, N° 138, 1997.
- [12] *Journal officiel des Communautés européennes*: L 163/41, directive 1999/30/CE du 27 avril 1999, Bruxelles, 1999.
- [13] WHO, *Air quality guide line, Global update 2005*, particulate matter, ozone, nitrogen dioxide and sulphur dioxide, Genova , 2005.
- [14] Ministère de l'Ecologie, de l'Energie, du Développement durable et de l'Aménagement du territoire, France, Bilan de la qualité de l'air 2006, rapport du 7 mars 2007.
- [15] Gertler A.W., Abu-Allaban M. Lowenthal and D.H. "The mobile source contribution to observed PM-10, PM-2,5 and VOCs in The greater Cairo area", 15^e Colloque international " *Transport et pollution de l'air*", *proceedings N°107*, Vol. 1, Inrets Ed., Arcueil, France, 2006, pp. 263-269, 2006.
- [16] Zhuyun Xu, Gautam M. and Mehta S. "Cumulative frequency fit for particle size distribution", *Appl. Occup. Env. Hyg.* volume 17(8), pp. 538-542, 2002.

Study of Moisture and Leachate Solute Movement during Infiltration Tests

Laouni Gaidi¹, I. Alimi-Ichola², C. Sayad Gaidi¹

¹Lab. W.S.T., Dept. of Civil Eng. & Hydraulic University of Mascara, Algeria, (lgaidi@yahoo.fr)

²LGCIE, INSA of Lyon, France, (ibrahim.alimiichola@insa-lyon.fr)

³Lab. W.S.T., Dept. of Civil Eng. & Hydraulic University of Mascara, Algeria, (sayadchahira@yahoo.fr)

ABSTRACT

The material choice and liner layer thickness depends on soil - pollutant interaction. To carry out the pollutant transfer mode in unsaturated soil and pollutant action onto the soil, infiltration and standard laboratory hydraulic conductivity tests were performed on soil column. During infiltration tests, soil moisture and soil electrical conductivity were measured to observe moisture and leachate solute movement. Infiltration curves were used to describe leachate inflow and the steady infiltration rate. Moisture profiles allowed the observation of the soil saturation process and the determination of the leachate transit time in the soil column. Soil electrical conductivity profiles give the pollutant distribution in the soil column.

Studies have shown that the hydraulic conductivity of compacted soil permeated with leachate can be significantly higher than the hydraulic conductivity of the same soil permeated with water [1-2]. Laboratory permeability tests performed with different water head, carry out the influence of the leachate and the hydraulic gradient on the soil hydraulic conductivity.

Key words: moisture, pollutant, hydraulic conductivity, electrical conductivity profiles, TDR method

1. INTRODUCTION

A laboratory tests are carried out in standard laboratory hydraulic conductivity tests and soil infiltration columns. These columns are equipped with five TDR probes placed at different depths. During infiltration test TDR probes permit to follow the moisture and the impedance (or electric conductivity) profiles evolution i.e. the infiltrated solute movement. The moisture profiles allow also to observe the soil saturation process and to determine the solute transit time through a layer. The soil electric conductivity (or impedance) profiles give the pollutant distribution in the layer.

2. MATERIALS AND METHOD

Pollution tests were performed with leachates produced by leaching waste clinker, lead slag and REFION. The percolation of these leachates through soil layer was compared to water percolation. To achieve test results in a reasonable time, soil used must have a hydraulic conductivity close to 10^{-7} m/s after compaction.

To characterise the tested soil, different geotechnical tests were performed, e.g. particle size distribution, Atterberg limits. Standard permeability tests were performed on compacted soil at different dry unit weight γ_d . These tests results were used to determine the soil unit dry weight to achieve hydraulic conductivity equal 10^{-7} m/s. It is noticed that this hydraulic conductivity value is obtained when the dry unit weight γ_d is equal to 16kN/m^3 . Particle-size distribution and Atterberg Limits tests showed that the used soil is clayey sand (SC). Proctor compaction test gave water

content and dry unit weight at the optimum state. Geotechnical test results are summarised in table 1.

Table 1: Soil Geotechnical Characteristics

w % natural	LL	IP	w _{opt}	(γ_d/γ_w) _{opt}
11	30	19	10	1.9

Soil suction for different volumetric water contents is measured to obtain soil water characteristic curve. Measured data and the Van Genuchten model curve are shown in figure 1. This model proves that the soil suction becomes zero when the volumetric water content reaches 33%.

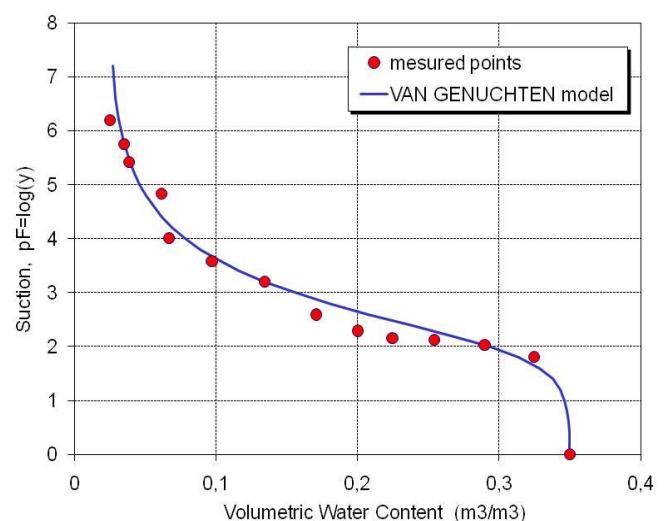


Figure 1: Tested soil water characteristic curve

2.1 Apparatus and Experimental procedure

For different tests, the dry soil was wetted at optimum water content ($w_{opt} = 10\%$) and compacted to achieve a dry unit weight of $16kN/m^3$. During infiltration tests, moisture movement was monitored with TDR probes. Soil water content and electrical conductivity were assessed by TDR pulse analysis.

2.2 TDR Method

Measuring the transit time and the amplitude of an electromagnetic pulse which propagated along a transmission line embedded in soil, soil dielectric constant and voltage reflection coefficient can be calculated. Topp et al. [3] proposed the following relationship to determine the soil volumetric water content when the soil dielectric constant is known:

$$\theta = -0.053 + 0.29K_a - 5.5 \cdot 10^{-4}K_a^2 + 4.3 \cdot 10^{-6}K_a^3 \quad (1)$$

where K_a dielectric constant and θ volumetric water content

To improve volumetric water content determination, TDR probe was calibrated with the different leachates used for infiltration tests. The three used leachates have different pH, different electrical conductivity and different solute concentration. Chemical characteristics of these leachates are shown in table 2.

Table 2: Leachates chemical characteristics

Leachate	pH	Electrical conductivity (mS/cm)	Solute concentration (mg/l)
Waste clinker	7.9	12.63	7996
Lead slag	6.3	53.3	75446
REFIOM	7.6	11.2	6980

Figure 2 shows different devices for calibration tests and for TDR measurement. Dry soil wetted at known water content is compacted in a ring equipped with a three rod TDR probe. Soil dielectric constant versus soil volumetric water content is evaluated with TDR curves. The calibration function of volumetric water content versus dielectric constant for soil used in infiltration tests is computed for the three leachates and water. The following relationships provide volumetric water content assessment during infiltration tests:

water:

$$\theta = 8 \cdot 10^{-5}K_a^3 - 0.0022K_a^2 + 0.0361K_a - 0.043 \quad (2)$$

waste clinker leachate:

$$\theta = -6 \cdot 10^{-7}K_a^3 - 0.0006K_a^2 + 0.0256K_a - 0.0199 \quad (3)$$

lead slag leachate:

$$\theta = 4 \cdot 10^{-5}K_a^3 - 0.0015K_a^2 + 0.0324K_a - 0.043 \quad (4)$$

REFIOM leachate:

$$\theta = 7 \cdot 10^{-5}K_a^3 - 0.0033K_a^2 + 0.0541K_a - 0.0949 \quad (5)$$

In accordance with the studies of Top et al [3], we used the couples (θ , K_a) to establish a new third degree polynomial law. This law represents the four laws mentioned above. The expression of this law is given by equation:

$$\theta = 0.0548 + 0.0153 K_a - 5 \times 10^{-5} K_a^2 + 8 \times 10^{-8} K_a^3 \quad (6)$$

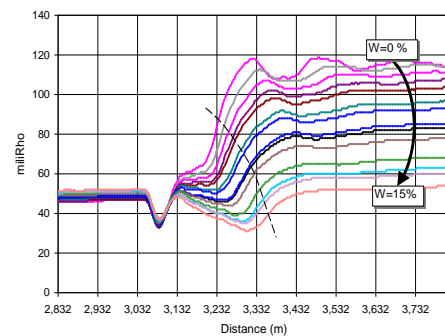
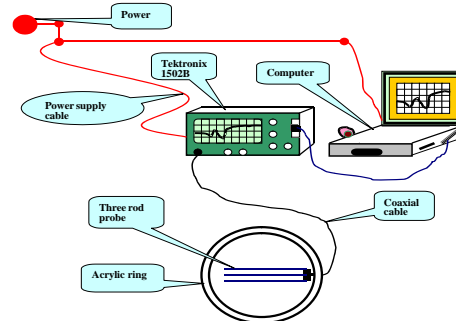


Figure 2: Schematic TDR method devices

Figure 3 gives a representation of this law with experimental points. We will use this relation for the determination of the volumetric water content; K_a is obtained by signal TDR.

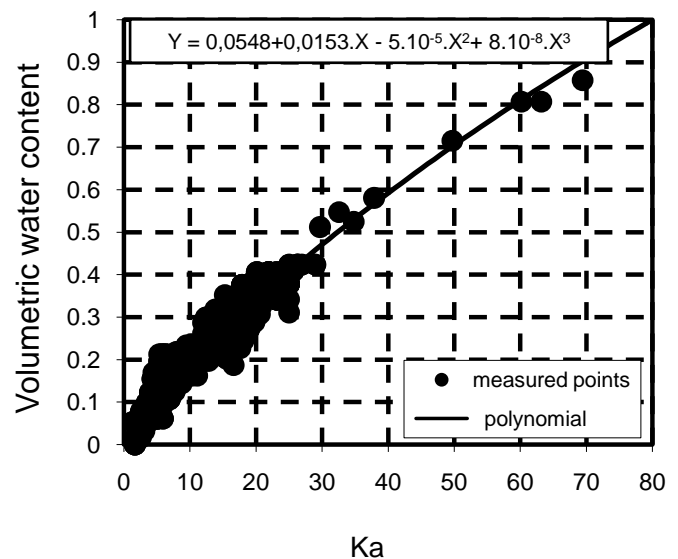


Figure 3: The relation $\theta=f(K_a)$, [4]

2.3 Infiltration Test Device

The infiltration tests are carried out in PEHD column having 550mm in length, composed with rings of 50mm height and 106mm of diameter. The soil was wetted at desired water content and compacted at desired bulk density in each ring. Before soil compaction, five rings were equipped with three rod TDR probe of 80mm length. After the setting of the column, TDR probes are located at 75, 175, 275, 375, 475mm depth. The column is installed as it is shown in figure 4.

The infiltration is performed at constant water head supply h_0 . Table 3 presents the initial conditions for different liquids.

Table 3: Initial water content and unit dry weight during infiltration tests

	Water	Waste clinker leachate	Lead slag leachate	REFIOM leachate
Water content (%)	12.50	11.20	10.98	10.26
Bulk density γ_d/γ_w	1.6	1.6	1.6	1.6
h_0	0	0	0	0

The infiltration is performed at constant water head supply h_0 . Table 3 presents the initial conditions for different liquids. Curves of cumulative infiltration versus time are determined from the variation of water level in Mariotte burette. TDR curves obtained from Tektronix 1502B, are recorded in computer for further analysis. The records are made every 2 hours.

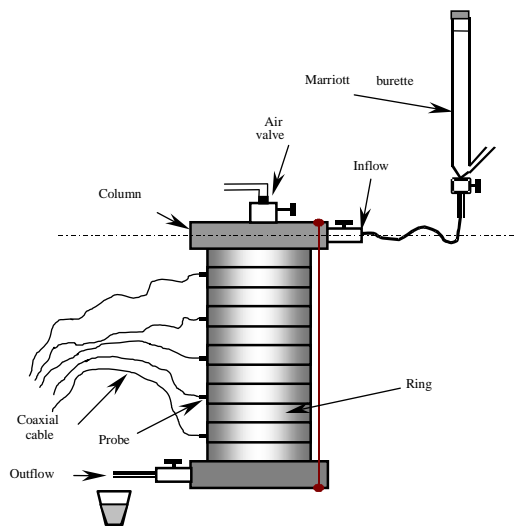


Figure 4: Schematic of soil column used for infiltration tests

3. RESULTS AND DISCUSSION

Experimental results concerned infiltration curves, moisture and bulk electrical conductivity distribution and the trends in the soil permeability coefficient. The

use of different leachates must reveal the leachate action on the soil. Choice of the soil permeability equals to 10^{-7} m/s allows liquid to outflow after one or two days. Moisture profile analysis must show the soil saturation degree when the liquid outflow starts. Soil bulk electrical conductivity profiles associated to water content profiles allow the comparison of moisture and solute migration.

3.1 Infiltration curves analysis

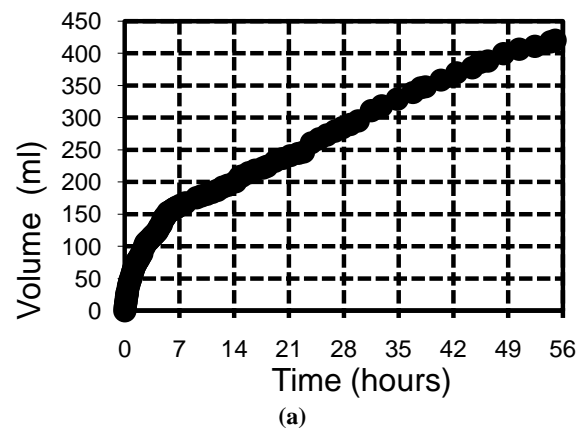
Figures 5 (a) and 6(a) show infiltration curves when water and lead slag leachate inflow the soil column. Water and lead slag leachate infiltration curves are represented in figures 5(b) and 6(b) by the Philip model: $I = S\sqrt{t}$ where I is the cumulative infiltration and S the sorptivity.

It is noticed that the sorptivity is constant during water infiltration but its value changes during the lead slag leachate infiltration. Referring to Philip infiltration theory, the change in the sorptivity value corresponds to the change in the capacity of the soil to absorb or remove water.

Table 4: Soil hydrodynamic parameters

	v_0 , m/s	S , cm/s ^{1/2}	D , m ² /s
Water	$2.01 \cdot 10^{-7}$	$1.148 \cdot 10^{-2}$	$1.60 \cdot 10^{-7}$
Waste clinker leachate	$2.24 \cdot 10^{-7}$	$2.891 \cdot 10^{-2}$	$4.01 \cdot 10^{-6}$
Lead slag leachate	$2.06 \cdot 10^{-7}$	$1.017 \cdot 10^{-2}$	$1.185 \cdot 10^{-7}$
REFIOM leachate	$7.90 \cdot 10^{-7}$	$4.673 \cdot 10^{-2}$	$1.47 \cdot 10^{-5}$

It is shown in table 4 the steady infiltration rate v_0 , the sorptivity and the water diffusivity for water and leachates. These hydrodynamic parameters depend on the liquid infiltrated. The steady infiltration rate and the sorptivity of the REFIOM leachate are four times higher than the water steady infiltration rate. The REFIOM leachate diffusivity is hundred times higher than the water diffusivity. These results prove that the solute contained in leachate change the soil structure. It increases the infiltration rate, the water diffusivity and the sorptivity.



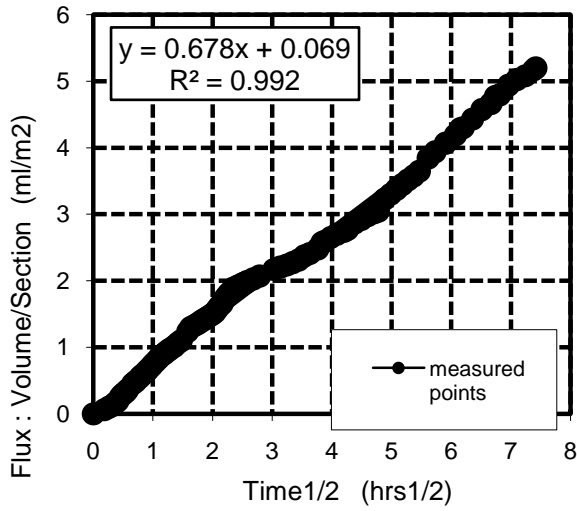


Figure 5: Water infiltration curve

3.2 Soil permeability results

Standard laboratory hydraulic conductivity tests were performed with three water head pressure, 20, 50 and 100cm. Before permeability test, each sample is saturated under water head pressure equals to 50cm. Test results are represented by the average liquid flux q ($m^3/s/m^2$) versus hydraulic gradient $i = dh/dL$. In figure 7, are presented the results of the tests realised with water and REFION leachate. It is noticed that the average water flux is proportional to hydraulic gradient (fig.7 (a)) but REFION leachate flux is not proportional to the hydraulic gradient. Hydraulic conductivity changes when hydraulic gradient applied to move leachate, changes (fig.7 (b)).

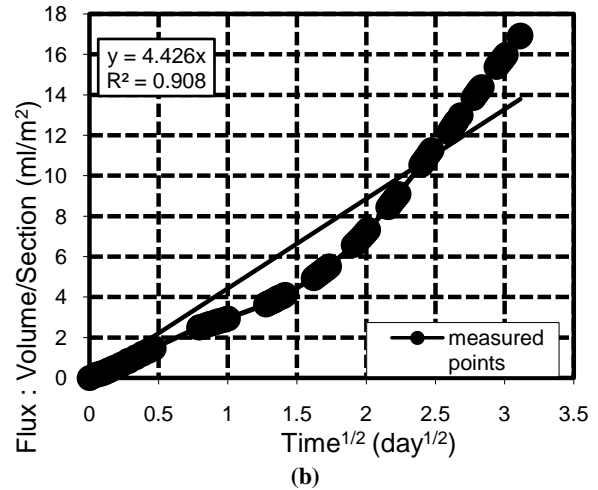
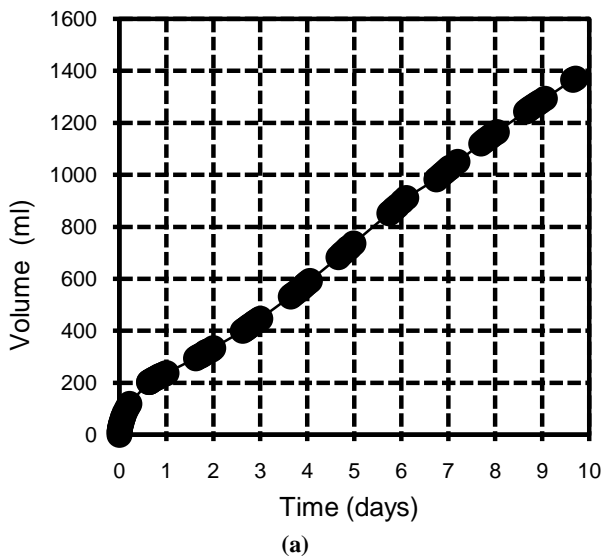


Figure 6: Lead slag leachate infiltration curve

It is shown in table 5 the average value computed with all measured data during the permeability tests, regardless of hydraulic gradient influence. It is noticed that the hydraulic conductivity hardly does not change, when the soil is permeated by water, waste clinker leachate or lead slag leachate. It becomes ten times higher when the soil is permeated by REFION leachate.

Table 5: Average hydraulic conductivity k for water and leachates

	k (m/s)
water	$1.64 \cdot 10^{-7}$
waste clinker leachate	$1.43 \cdot 10^{-7}$
lead slag leachate	$1.46 \cdot 10^{-7}$
REFION leachate	$1.61 \cdot 10^{-6}$

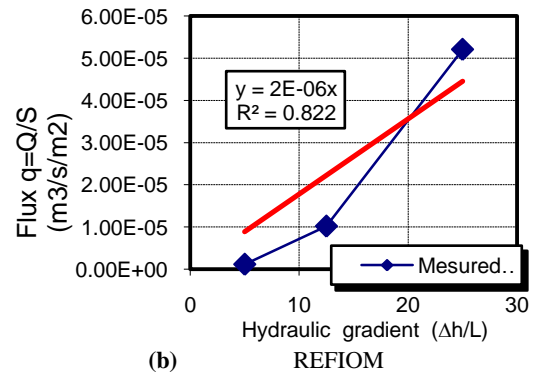
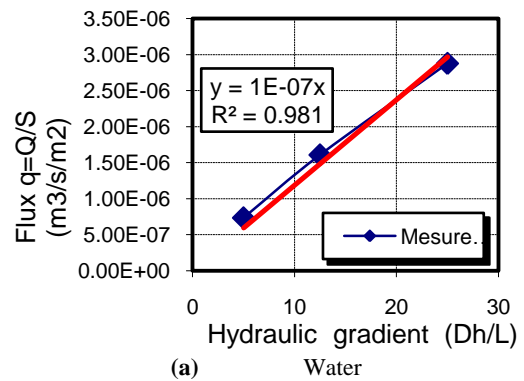


Figure 7: Darcy's law applied to water and REFIOM leachate permeation

3.3 Moisture and Electrical Conductivity Profiles

Figures 8 and 9 present moisture profiles and bulk electrical conductivity profiles in the column during the permeation of waste clinker and lead slag leachates. Soil bulk electrical conductivity is determined with TDR curve, using the method described by Nader et al [5], Rhoades [6] and Alimi [7].

Profiles represented by dash line are the profiles when the leachates outflow the column. Leachate transit times in the soil column are 1.13 and 1.22 days respectively for waste clinker leachate and lead slag leachate. The transit time is not really affected by the leachate quality but it is half time less than water transit time (2 days) in the soil column. At the transit time, moisture is not uniform in the soil column but the reached saturation degree is higher in column infiltrated with waste clinker leachate than in column infiltrated with lead slag leachate. The leachate action on the soil depends on the leachate characteristic. It is noticed also that soil saturation with leachate continues during the outflow. The leachate flows through the soil column before water content becomes uniform in the soil.

The bulk electrical conductivity profiles shown in figures 8 (b) and 9 (b), prove that, the upper layers retain more solute than the lower layer before leachate outflows the soil column. During the waste clinker percolation, pollutant retaining remains more important in upper layer although the water content along the soil column becomes uniform. The soil purifies the percolated leachate.

When the lead slag leachate percolates throughout the soil column, the column upper layer becomes saturated with solute before a uniform water content was obtained along the column. This upper part saturated with solute remains saturated when the uniform water content is reached along the column. The interaction between soil and lead slag leachate is more important than that of waste clinker leachate.

It is shown with these profiles that the soil volumetric water content does not exceed respectively, 26% and 33% when waste clinker and lead slag leachates are percolating. These water content values represent respectively 66% and 85% of the porosity of the soil compacted at the bulk density γ_d/γ_w equal to 1.6. The soil porosity occupied during water percolation reaches 92%. The soil water characteristic curve (Fig.1) shows that soil pF is zero when the volumetric water content is over 33%. So the soil column cannot retain more moisture and the values of the waste clinker leachate sorptivity and diffusivity presented in table 4 explain the reduction of the moisture which is retained.

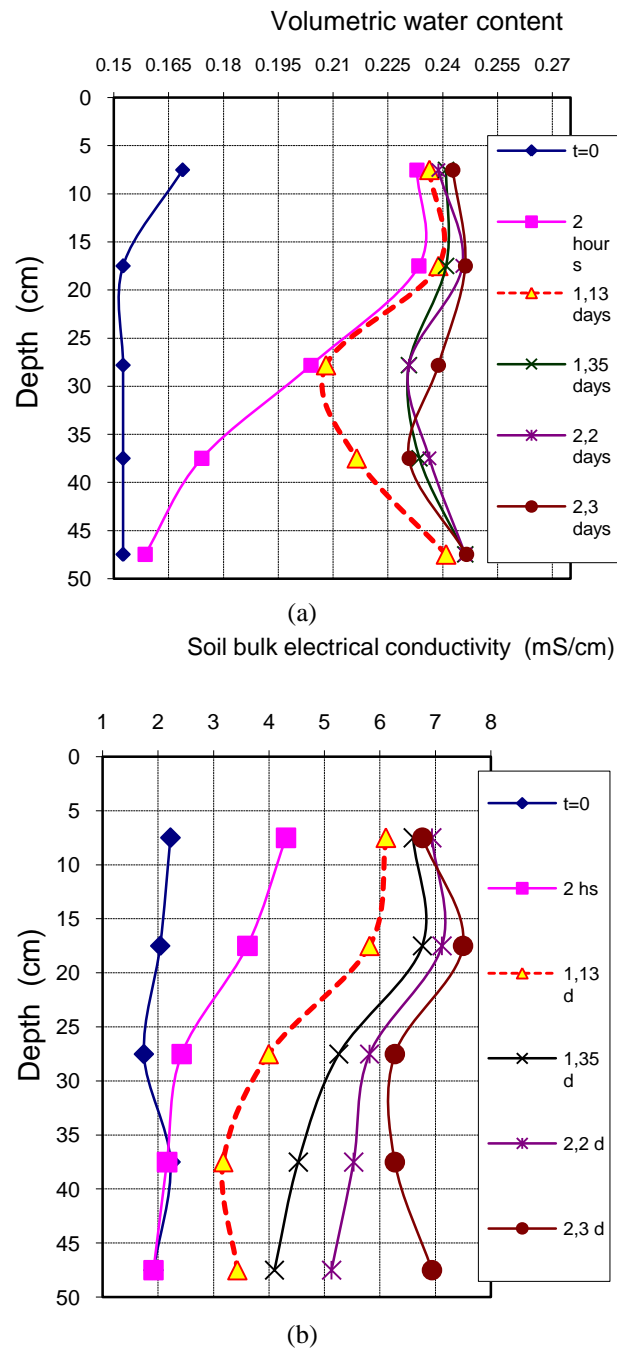


Figure 8: Moisture and bulk electrical conductivity during waste clinker leachate infiltration

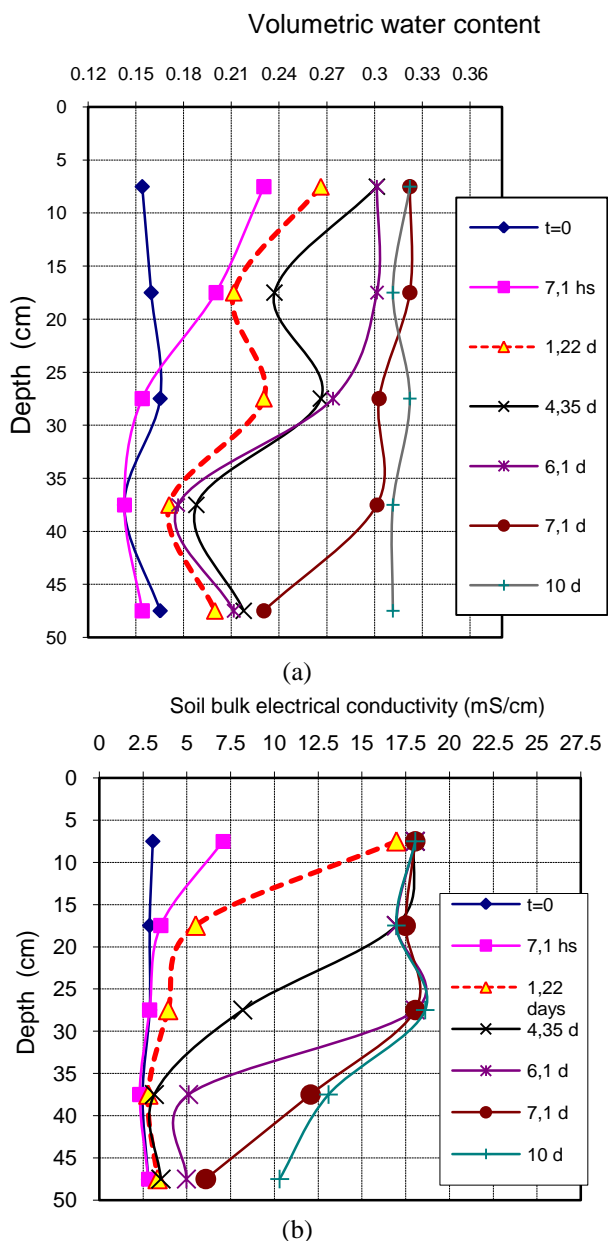


Figure 9: Moisture and bulk electrical conductivity during lead slag leachate infiltration

4. CONCLUSION

This study allows the evaluation of the soil pollution process. It is shown that the solute action on the soil can be described by the transit time, that to say the time for the leachate to percolate unsaturated soil. The reduction of this time for the leachate percolation means that liner layer thickness must be increased to prevent rapid percolation and to secure ground water.

This leachate action is also described by the soil hydraulic conductivity. Standard permeability tests show that the soil permeability coefficient can increase ten times when it is percolated by leachate. This result

proves that the liner must be tested with leachate to determine its permeability and to project its thickness.

The use of TDR probes during infiltration tests allows to observe that the soil is not saturated before water or leachates flows out of the column. When uniform water content is reached in the column, the saturation degree remains less than 95% as it is recommended in hydraulic conductivity test. According to measured data in tables 4 and 5, steady infiltration rate values are close to hydraulic conductivity and are not influenced by this low saturation degree. It seems that the steady infiltration rate estimates the hydraulic conductivity when the infiltration tests are carried out under low water head. This estimation is not influenced by the leachates.

REFERENCES

- [1] A. H. Gipson, (1985) "Permeability Testing on Clayey Soil and Silty Sand Bentonite Mixture Using Acid Liquor", Hydraulic Barriers in Soil and Rock, ASTM STP 874, A. I. Johnson, R. K. Froebel, N. J. Cavalli and C. B. Petterson, Eds., ASTM, West Conshohocken, PA, pp. 140-154
- [2] M. H. Gleason, D. E. Daniel, and G. R. Eykholt, (1997) "Calcium and Sodium Bentonite for Hydraulic Containment Applications", Journal of Geotechnical Environmental Engineering, ASCE, Vol. 123, No 5, pp. 438-445.
- [3] G. C. Topp, J. L. Davis and A. P. Annan, (1980) "Electromagnetic Determination of Soil Water Content: Measurement in Coaxial Transmission Lines", Water Resour. Res. 16: 574-582
- [4] L. Gaidi and I. Alimi, (2000) "Etudes des caractéristiques Hydrodynamique des Sols par la Méthode TDR (Time Domain Reflectometry)", Bulletin of Engineering Geology and the Environment, vol.59 n°3, pp. 247-255.
- [5] A. Nadler, S. Dasberg and I. Lapid, (1991) "Time Domain Reflectometry Measurements of Water and Electrical Conductivity of Layered Soil Columns", Soil Sci. Soc. Am. J. vol. 55: 938-943
- [6] J.D. Rhoades and van Schilfgaard, (1976) "An Electrical Conductivity Probe for Determining Soil Salinity", Soil Sci. Soc. Am. J. vol. 40: 647-651
- [7] I. Alimi-Ichola, (1998) "Use of Time Domain Reflectometry Probes for monitoring unsaturated soil pollution", Proc. of 3rd Int. Cong. On Environmental Geotechnics, Lisboa, Portugal 7-11 Sept. 1998 pp. 107-112

Influence of Hydraulic Gradient and Confining Stress on the Hydraulic Conductivity of Sealing Barriers Materials

C. Sayad Gaidi¹, Laouni Gaidi¹ and S. Taibi²

¹ Lab. W.S.T., Dept. of Civil Eng. & Hydraulic University of Mascara, Algeria
(chahiras@hotmail.com); (lgaidi@yahoo.fr)

² Lab. of Mechanic, Phys. & Geosc., University of Le Havre, France
(taibi.said@univ-lehavre.fr)

ABSTRACT

In the initial phase of design and building of waste disposal sites, the current rules specify permeabilities smaller than 10^{-9} m/s for the natural or compacted fine grained soils. This led to many research works, from the '70, to measure the hydraulic conductivity of fine grained soils with water, natural or laboratory-prepared lixivates as percolating liquids. In this paper, a method for the determination of saturated hydraulic conductivity is proposed. The role of the confining stress (σ_3) and of the hydraulic gradient (i) under constant confinement stress is examined. It is thus possible to validate the expressions of the permeability coefficient versus void ratio and effective confining stress.

Keywords: permeability, clay soils, hydraulic conductivity, system of confining, disposal sites

1. INTRODUCTION

The quantity of waste and pollutants in developed countries continues to grow. One of the major risks associated to domestic and industrial activities is the soil and drinking water resources pollution. It is admitted that the pollution process is the transfer result from source to receptors formed by these resources. Water is the main vehicle for this transfer. Waste stored at the surface or in deep geological formations is subjected to biological, physical and chemical changes in water contact. These phenomena create products that can pollute groundwater and thus be harmful to public health and the environment. In addition, rainwater washes these discharges and releases toxic elements. These toxic elements pollute groundwater.

The objective of this paper is to study the influence of hydraulic gradient and confining stress on the hydraulic conductivity. The flow regime is a steady state. The tests were made on a sandy clay initially compacted to the optimal conditions (OPN) (Taibi and al.2003). we propose an experimental procedure for the determination of saturated hydraulic conductivity. We will study first the role of confining stress (σ_3) on the permeability coefficient (K), and secondly the effect of hydraulic gradient (i) at constant confining stress on the same coefficient (K).

2. MATERIALS

The used material is a mixture composed of 90% kaolinite (P300), 5% Hostun sand (RF) and 5% silica. The principal characteristics are noted in Table 1. Figure 1 contains the particle size distribution curves of the mixture and its constituents. In addition, a compaction test (Figure 2) gives the following optimal

characteristics $w_{OPN} = 18\%$, (γ_d/γ_w) OPN=1.67

Table 1: Geotechnical Material Characteristics

Material	Kaolinite (P300)	Silice (S)	.Hostun sand (RF)	Sandy clay
wL	40			38
IP	20			19
%<80 (μm)	100	97	0	95
%<2 (μm)	59	5	0	53
d10 (μm)	0.15	13	160	
d60 (μm)	2	40	300	3.8
γ_s/γ_w	2.65	2.64	2.65	2.65
w OPN(%)	17			18
γ_d/γ_w OPN	1.73		1.60	1.67

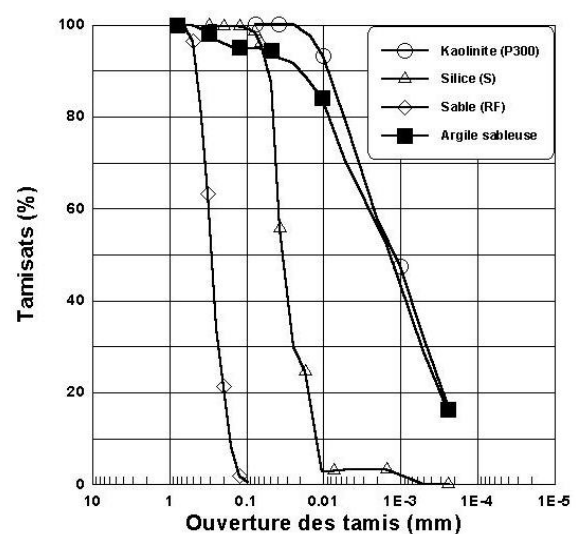


Figure 1: Particle size distribution curves of the mixture and its constituent

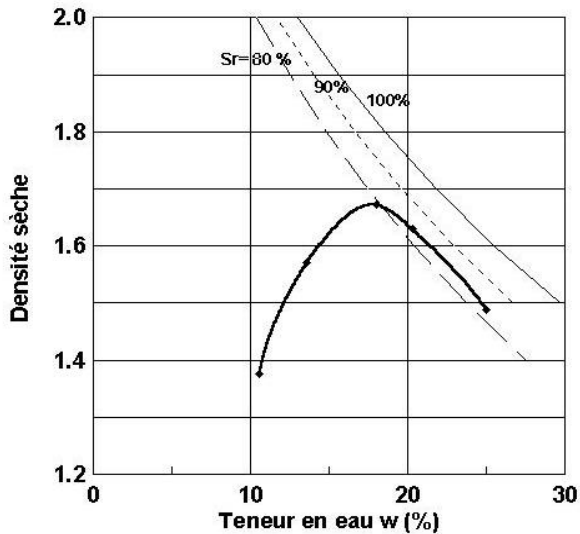


Figure 2: Proctor curve- sandy clay

3. Procedure and permeability measurement method

The experimental device consists of a triaxial cell Bishop-Wesley type, controlled using pressure-volume controllers GDS. This cell is used to test the samples of 35 or 50 mm of diameter and a variable slenderness H/D (Figure 3). Triaxial cell, made of duralumin and reinforced Plexiglas, used to apply an isotropic confining stress (up to 1.7 MPa) and a known deviator stress. The flow is vertical (from bottom to top). Control and / or pressure measurement and / or the volume of water is provided by three controllers:

- Controller 1: Used to apply a confining stress σ_3
- Controller 2: Used to apply interstitial pressure u_e or to inject a known volume of water at the sample base.
- Controller 3: Used to apply interstitial pressure u_s at the head of the sample and measure the volume of water coming out.

The equipment used for the measurement the permeability at high confining pressure contains (Figure 4):

- A high pressure triaxial cell, 200 bars
- Two controllers, pressure / volume (GDS), 30 bars.
- A compressed air cylinder, 240 bars.
- A computer for data acquisition
- A pressure sensor for monitoring the confining stress
- Valves, accumulator, check valve, stainless steel pipes (Φ 6 mm, 200 bars).

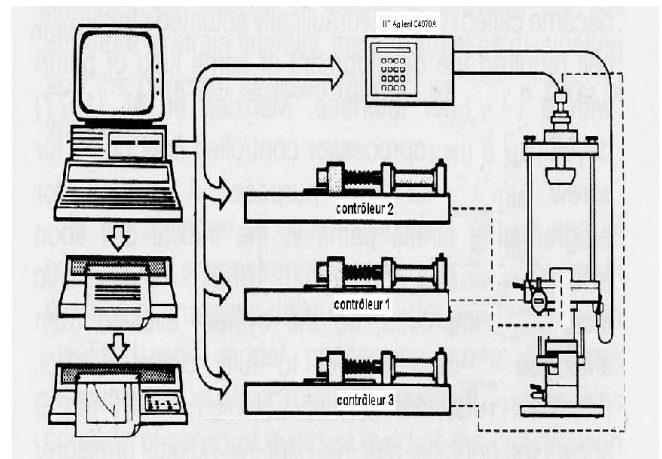


Figure 3: Triaxial permeameter: Wesley Bishop type

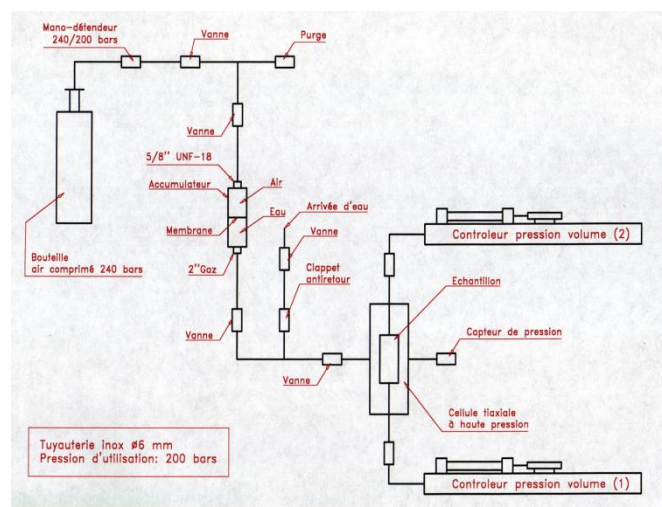


Figure 4: High pressure permeameter

The samples are compacted at optimum conditions ($w = 18\%$ and $\gamma_d = 16.7 \text{ kN/m}^3$) in a cylinder of 35 mm diameter and 50 mm high. Then the sample is placed in the permeameter. All samples are inserted into supple latex membranes for low pressures. For high pressure membranes are made of neoprene. After placing the sample, the saturation starts. In this step, it is based on the measure in undrained conditions of increased pore pressure ΔU under the effect of an increase in the isotropic confining stress $\Delta \sigma_3$. We deduce Skempton coefficient B , with $B = \Delta V / \Delta \sigma_3$. It is estimated that saturation is reached for this material when the value of B is greater than 0.9.

This value is generally reached when the value of pore pressure is 600 kPa. This value is retained for further testing. The sample is then consolidated at levels of isotropic effective stress $\sigma = \sigma_3 - (U_e + U_s) / 2$ from 0.1 MPa to 4.4 MPa and measuring the corresponding flow rate.

Two hydraulic gradients $i = (U_e - U_s) / (\gamma_w h)$ were tested ($i = 30$ and $i = 50$) with U_e : pore pressure at the top, U_s : pore pressure at the bottom, h : height of the sample, and γ_w the water specific weight. Permeability is derived by direct application of Darcy's law, $k [\text{m/s}] = Q / i.S$,

Q is the flow rate [m³ /s], S, section of the sample [m²] and i the hydraulic gradient.

4. RESULTS AND DISCUSSIONS

4.1 Influence of hydraulic gradient

The test was performed in the permeameter of high and low pressure. At each increment of applied stress, two hydraulic gradients were tested (i = 30 and 50). Figure 5 shows some examples of temporal evolution of the water volumes entering and leaving the sample Ve and Vs, for different confining stress ($\sigma_3 = 900$ and 5000 kPa).

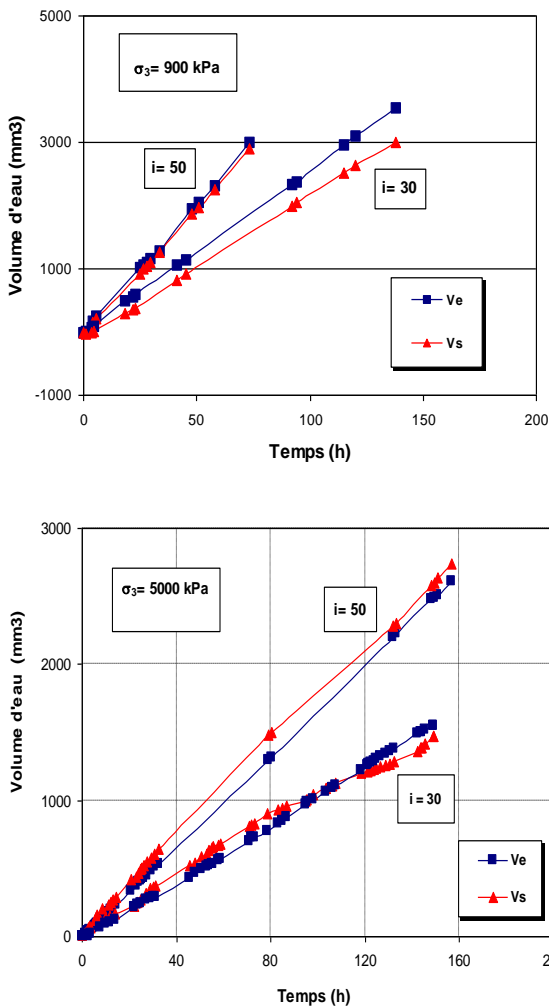


Figure 5: Temporal evolution of the water volumes i = 30 and i = 50

Figure 6 shows the evolution of the flow velocity through the sample versus hydraulic gradient for all the applied confining stress. Linear relationships appear to be a good approximation of experimental points. This linearity indicates the validity of Darcy's law in the range of tested hydraulic gradients. Similar results were obtained by other researchers studying the clays (Macey, 1942 ; Low, 1961 ; Travenas et al., 1983...)

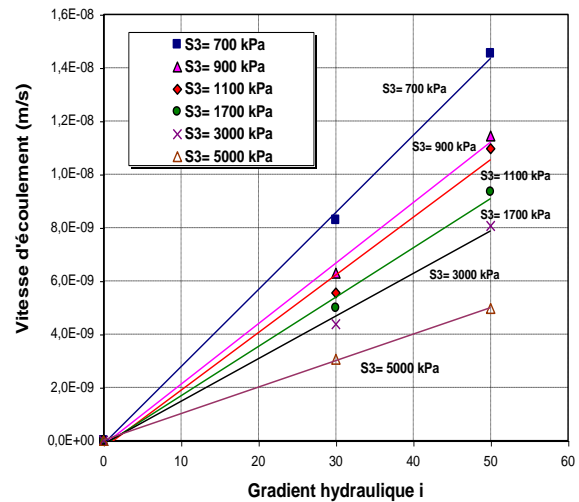


Figure 6: Evolution of the flow velocity through the sample versus hydraulic gradient

Figure 7 presents in the plan [log k, σ_3'] the evolution of the permeability according to the effective confining stress. We note that there is no influence of hydraulic gradient on the coefficient of permeability. These observations support the conclusion that for the range of tested gradients the Darcy's law is valid.

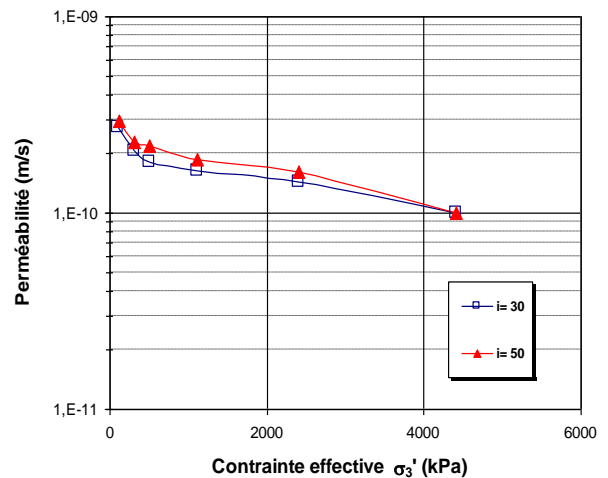


Figure 7: Evolution of the permeability according to the effective confining stress

4.2 Influence of confining stress

Travenas and al., 1983 found a linear relationship between permeability and void ratio. This relation is obtained using a clay samples from Canada, the United States and Sweden. This relationship is given by the equation 1:

$$e = e_0 + C_k \text{Lg} (k/k_0) \tag{1}$$

k_0 is the permeability of the initial void ratio e_0 ,
 k is the permeability,
 e is the void ratio,

C_k variation index of permeability, it is equal the half of the initial soil void ratio (Travenas and al., 1983 ; Leroueil and al., 1990). Mesri et al., 1994 obtained the same relationship by studying the permeability of Boston soft clays.

Figure 8 presents the curves of isotropic compressibility in the plan $[\log \sigma_3', e]$ for all levels of tested stress. We have superposed the compressibility line deduced from correlations with w_L (Biarez and Favre, 1975). We remark the highly over consolidated behavior of the sample, due to initial compaction

In Figure 9, we remark that the permeability decreases when the void ratio decreases. This decrease is due to the closure of the pore space. There is also evidence that this decrease is linear, which is in accordance with the results of the literature presented above.

Figure 10 presents the evolution of permeability versus the effective confining stress. We compared the experimental points to the model of Taylor. We note that this model does not describe the evolution of permeability in this plan. This evolution appears to be well described by a logarithmic law.

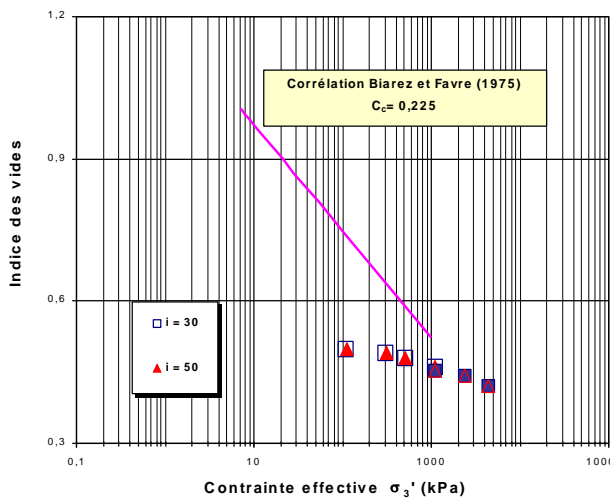


Figure 8: Variation of the void ratio according to the effective confining stress

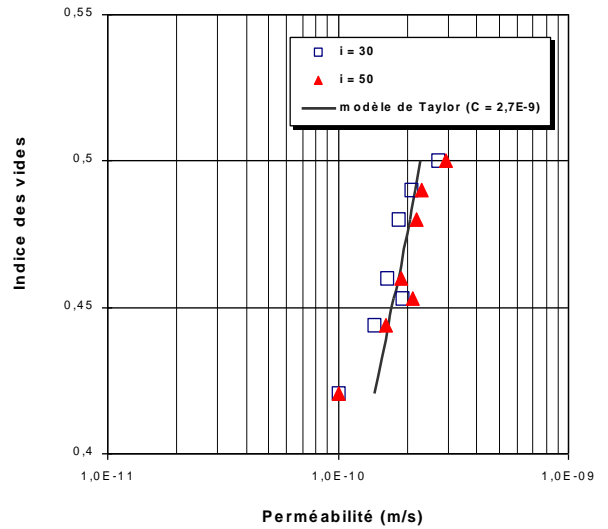


Figure 9: Variation of the void ratio versus the permeability

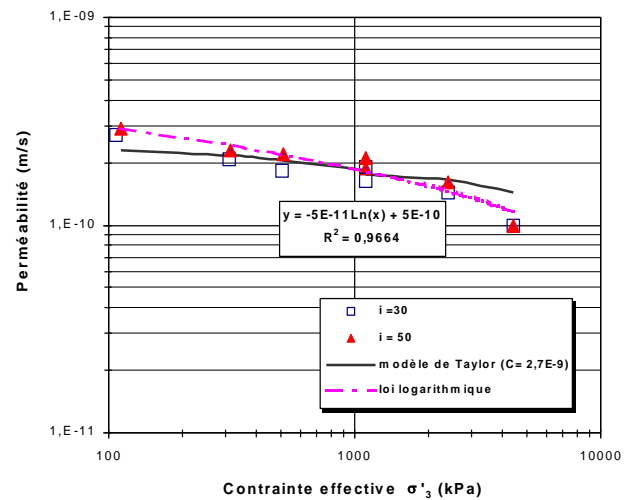


Figure 10: Evolution of the permeability versus the effective confining stress

5. CONCLUSION

The measure of the permeability in steady state has validated the Darcy's law for tested hydraulic gradients ($i=30$ and $i=50$).

Permeability decreases when the effective stress increases: with decreasing the void ratio. This decrease is described by the model of Taylor.

The method of measuring in steady state has the advantage of using a simple formulation and to check the validity of Darcy's law. But the test would take several days or weeks (2 to 4 weeks).

Other techniques for measuring the permeability of the

transitional state, based on the technique of the pulse tests will be used. This method is a recent technique for measuring permeability with variable load. It provides a quick and easy way to estimate the permeability in ranges between 10⁻⁸ and 10⁻¹² m / sec. These results will be subject a next publication.

REFERENCES

- [1] Biarez, J. and Favre, J. L. "Parameters filing and statistical analysis of data in soil mechanics", Proceedings of the 2nd Int. Conf. On Application of Statistics and Probabilities in Soil Mechanics, Vol. 2, Aachen, pp. 249-264, 1975.
- [2] Leroueil, S., Travenas, F., Bouclin, G., and Bergeron, L. "Permeability anisotropy of natural clays as a function of strain", Canadian Geotechnical Journal, No.27, pp. 568- 579, 1990.
- [3] Low P. F., "Physical chemistry of clay- water interaction", Advances in Agronomy, Vol. 13, pp. 269- 327, 1961.
- [4] Macey, H., "Clay- water relationships and the internal mechanism of drying", Transactions of the British Ceramic Society, Vol. 41, N°. 4, pp. 73- 95, 1942.
- [5] Mesri, G., Feng, T. W., Ali, S., and Hayat, T. M. "Permeability characteristics of soft clays", XIII Conférence internationale de mécanique des sols et des travaux de fondation, pp. 452-463, New Delhi-Inde, 1994.
- [6] Taibi, S., Sayad, C., Kheirbek-Saoud, S., and Fleureau, J.M. "Saturated permeability of a barrier made in compacted clay", 13th European Conference on Soil Mechanics & Geotechnical Engineering, Prague, August 2003.
- [7] Tavenas, F., Jean, P., Leblond, P., and Leroueil, S. "The permeability of natural soft clays. Part II: Permeability characteristics", Can. Geotech. J., Vol. 20, pp. 645-660, 1983.

Water Resources for Sustainable Development in the Developing Countries

Ibrahim Yuksel¹, Hasan Arman², Gokmen Ceribasi³ and Mehmet Sandalci⁴

¹Sakarya University, Technology Faculty, Department of Civil Engineering, 54187, Sakarya, Turkey.
(yukse2000@yahoo.com)

²United Arab Emirates University, Faculty of Science, Department of Geology 17551, Al-Ain, UAE.
(harman@uaeu.ac.ae)

³Sakarya University, Technical Education Faculty, Department of Construction, 54187, Sakarya, Turkey.
(gceribasi@sakarya.edu.tr)

⁴Sakarya University, Engineering Faculty, Department of Civil Engineering, 54187, Sakarya, Turkey.
(sandalci@sakarya.edu.tr)

ABSTRACT

The global debate about large dams is at once overwhelmingly complex and fundamentally simple. It is complex because the issues are not confined to the design, construction and operation of dams themselves but embrace the range of social, environmental and political choices on which the human aspiration to development and improved well-being depend. Over the last two decades, global electricity production has more than doubled and electricity demand is rising rapidly around the world as economic development spreads to emerging economies. Not only has electricity demand increased significantly, it is the fastest growing end-use of energy. Therefore, technical, economic and environmental benefits of hydroelectric power make it an important contributor to the future world energy mix, particularly in the developing countries. This paper deals with policies to meet increasing energy production for sustainable development in the developing countries.

Keywords: water resources, energy policy, sustainable development, developing countries

1. INTRODUCTION

With an estimated 95% of population growth in the coming decades likely to be in and around cities, the need for sustainable solutions with compact, interconnected power plants will be ever more pressing. Decentralized schemes, however, will remain important for rural electrification programs. Hydropower can be adaptive and flexible. Depending on the storage capacity involved, a major advantage of hydropower is that generation can be scheduled. Run-of-river schemes can be implemented to provide continuous 'base-load' generation. The operation of a cascade of several run-of-river power plants can be optimized to provide generation when it is needed. This is especially true if there is a reservoir scheme at the head of the cascade. Schemes that include a reservoir are able to store potential energy for production when the demand is highest. When water resources are not available to replenish reservoirs by natural inflow, pumped-storage schemes have been developed to assist in the storage of energy from other generation sources. Therefore, hydropower can substantially improve efficiency in a mixed power system, reducing emissions from fossil-fuel power plants, and backing up intermittent sources such as wind power [1, 2].

Over the past fifteen years, many large hydropower projects in developing countries have been adversely affected by concerns over the environmental and social effects of building large dams. Obtaining loans from international lending institutions and banks to finance

such projects has become more difficult. Consequently, many projects have been delayed or cancelled. Five years ago, hydropower was the world's second-largest source of electricity; now it ranks fourth [3, 4].

The remaining potential in developing countries is still very large. Several developing countries are focusing again on this domestic source of electricity, driven by a rapidly expanding demand for electricity, by the need to reduce poverty and to diversify the electricity mix. Support from international lenders and interest from the private sector is also growing. The majority of reservoirs have been developed for water supply, primarily irrigation. Only about 25% of reservoirs worldwide have any associated hydropower facilities [4].

2. RIVERS AND DAMS

Rivers weave in and out of our lives, providing innumerable benefits to communities across the world. In our planet, the rivers for drinking water, irrigation, aquatic habitat, fisheries, energy, navigation, recreation and simply the natural beauty they bring to our landscapes. Humans have been building dams and other river blockages to harness and control water for centuries, attempting to secure its benefits for human use. On the other hand, by design, dams alter the natural flow regime, and with it virtually every aspect of a river ecosystem, including water quality, sediment transport and deposition, fish migrations and reproduction, and riparian and floodplain habitat and the organisms that

rely on this habitat. Dams also require ongoing maintenance. For example, reservoirs in sediment-laden streams lose storage capacity as silt accumulates in the reservoir. In arid climates reservoirs also experience a high rate of water loss to evaporation [2, 5].

Dams also can have significant economic impacts on dam owners, the surrounding community and society in general. As dams age, maintenance costs and safety hazards often increase, resulting in an increasing financial burden and liability on the dam owner. Depending on the river and the fisheries being impacted by the dam, an owner may also be required to retrofit the structure with fish passage facilities or make other upgrades to comply with water quality standards. When dams diminish fisheries, communities can lose jobs and sustenance, or the source of their cultural or spiritual life. Because of these and other concerns, some dam owners and managers are finding that it makes more sense to remove certain dams, often benefiting the community ecologically and socially, rather than make costly repairs or upgrades. However, when such dams still provide valuable services, alternatives to replace the dams' functions should be considered [2, 5].

3. HYDROPOWER AND SUSTAINABILITY

The hydropower industry is closely linked to both water management and renewable energy production, and so has a unique role to play in contributing to sustainable development in a world where billions of people lack access to safe drinking water and adequate energy supplies. On the other hand, approximately 1.6 billion people have no access to electricity and about 1.1 billion are without adequate water supply. However, resources for hydropower development are widely spread around the world. Potential exists in about 150 countries, and about 70% of the economically feasible potential remains to be developed—mostly in developing countries where the needs are most urgent [2, 6, 7].

Hydropower is available in a broad range of project scales and types. Projects can be designed to suit particular needs and specific site conditions. As hydropower does not consume or pollute the water it uses to generate power, it leaves this vital resource available for other uses. At the same time, the revenues generated through electricity sales can finance other infrastructure essential for human welfare. This can include drinking water supply systems, irrigation schemes for food production, infrastructures enhancing navigation, recreational facilities and ecotourism. Water is a vital resource that supports all forms of life on earth. Unfortunately, it is not evenly distributed by season or geographical region. Some parts of the world are prone to drought, making water a particularly scarce and precious commodity. In other parts of the world, floods that cause loss of life and property are major problems.

Throughout history, dams and reservoirs have been used successfully in collecting, storing and managing water needed to sustain civilization. Hydropower often supports other essential water services such as irrigation, flood control and drinking water supplies. It facilitates the equitable sharing of a common vital resource [1, 2, 8].

Hydropower has very few greenhouse gas emissions compared with other large-scale energy options. In addition, by storing water during rainy seasons and releasing it during dry ones, dams and reservoirs can help control water during floods and droughts. These essential functions protect human lives and other assets. This will be increasingly important in the context of global warming, which implies an expected rising variability in precipitation frequency and intensity. Hydropower projects do not export impacts such as acid rain or atmospheric pollution. Environmental impacts are limited to changes in the watershed for the dam is located. When well managed, these changes can sometimes result in enhancements, and other impacts can be avoided, mitigated. Hydropower can contribute to mitigating the widespread potential human impacts of climate change. Table 1 shows advantages and disadvantages of the hydropower [2].

4. GLOBAL HYDROPOWER PRODUCTION

There is about 700 GW of hydro capacity in operation worldwide, generating 2740 TWh in 2000 (about 19% of the world's electricity production). About half of this capacity and generation is in Europe and North America with Europe the largest at 32% of total hydro use and North America at 23% of the total. However, this proportion is declining as Asia and Latin America commission large amounts of new hydro capacity. On the other hand, small, mini and micro hydro plants also play a key role in many countries for rural electrification. An estimated 300 million people in China, for example, depend on small hydro [4, 9].

As shown in Table 2 the world's gross theoretical hydropower potential is about 40000 TWh/year, of which about 14000 TWh/year is technically feasible for development and about 7000 TWh/year is currently economically feasible. The last figure fluctuates most being influenced not only by hydro technology, but also by the changing competitiveness of other energy/electricity options, the status of various laws, costs of imported energy/electricity, etc. On the other hand, as can be seen in Table 2 the biggest growth in hydro generation is expected in the developing countries where there is still a large potential for hydro development, while relatively little growth is expected in most OECD countries where more than 65% of the economic potential is already in use.

Table 1: Advantages and disadvantages of the hydropower option. Source: [1].

ADVANTAGES	DISADVANTAGES
Economic Aspects	
Provides low operating and maintenance costs	High upfront investment
Provides long life span (50 to 100 years and more)	Precipitation
Provides reliable service	Requires long-term planning
Includes proven technology	Requires long-term agreements
Instigates and fosters regional development	Requires multidisciplinary involvement
Provides highest energy efficiency rate	Often requires foreign contractors and funding
Creates employment opportunities and saves fuel	
Social Aspects	
Leaves water available for other uses	May involve resettlement
Often provides flood protection	May restrict navigation
May enhance navigation conditions	Local land use patterns will be modified
Often enhances recreation	Waterborne disease vectors may need to be checked
Enhances accessibility of the territory and its resources	Requires management of competing water uses
Improves living conditions	
Sustains livelihoods (fresh water, food supply)	
Environmental Aspects	
Produces no pollutants but only very few GHG emiss.	Inundation of terrestrial habitat
Enhances air quality	Modification of hydrological regimes
Produces no waste	Modification of aquatic habitats
Avoids depleting non-renewable fuel resources	Water quality needs to be managed
Often creates new freshwater ecosystems with increased productivity	Temporary introduction of methyl mercury into the food chain needs to be monitored/managed
Enhances knowledge and improves management of valued species due to study results	Species activities and populations need to be monitored
Helps to slow down climate change	Barriers for fish migration, fish entrainment
Neither consumes nor pollutes the water it uses for electricity generation purposes	Sediment composition and transport may need to be monitored/managed

Table 2: Distribution of hydropower plants according to capacity in Brazil (2002). Source: [7]

Capacity Range (MW)	Number of Plants	Installed Capacity (MW)	Percentage of Total
Up to 30	337	1509	2.4
31-100	29	1776	2.7
101-500	36	9219	14.9
501-1000	8	5365	8.7
Over 1000	23	44260	71.4
Total	433	62129	100

Until recent years there has been less than 100 GWh/year of new hydro capacity under construction at any one time, equivalent to less than 15% of the capacity in operation. The figure has now risen, reflecting China's vast construction program, which includes the 18.2 GW Three Gorges Project, now in its second phase of construction. Most new hydro capacity is under construction in Asia and South America. China has by far the most, with about 50 GW under way. Brazil has largest resources in world (800000 GWh/year) of economically exploitable capacity and

Norway depends almost entirely hydro for its electricity needs [4, 7, 9].

5. HYDROPOWER IN DEVELOPING COUNTRIES

All the remaining potential in developing countries is still very large. Several developing countries are focusing again on this domestic source of electricity, driven by a rapidly expanding demand for electricity, by the need to reduce poverty and to diversify the electricity mix. Support from international lenders and

interest from the private sector is also growing. The majority of reservoirs have been developed for water supply, primarily irrigation. Only about 25% of reservoirs worldwide have any associated hydropower facilities [4].

5.1 Brazil

Hydroelectric power is one of Brazil's principal energy assets: the republic has by far the largest hydropower resources on the continent. The Brazilian WEC Member Committee reports that gross theoretical capability exceeds 3000 TWh/yr, with an economically exploitable capability of over 800 TWh/yr, of which nearly 40% has been harnessed so far [3, 4].

Hydroelectricity plants (above 30 MW capacity) represent 78% of the overall Brazilian installed capacity (Table 2). Because of that, electricity generation in Brazil is strongly influenced by the natural flows of rivers and other watercourses [4].

In past decade, hydro generating capacity became more than doubled in Brazil. Brazil shares Itaipu's output with its neighbour Paraguay, which sells back to Brazil the surplus power remaining after its own electricity needs have been satisfied. On the other hand, at the end of 2002, Brazil had over 7 GW of hydro capacity under construction, including a major (4125 MW) extension of capacity at Tucuruí and two additional 700 MW units at Itaipu. Nearly 7 GW of further hydro capacity is planned for future development [3, 4, 10].

Within the overall picture outlined above, small-scale hydro (since 1998, defined in Brazil as plants with a capacity of 1-30 MW) has an economically exploitable capability of about 17 TWh/yr, some 27% of which had been exploited by capacity installed as at end-2002. The 975 MW of small-scale hydro currently in place will be augmented by 2280 MW additional capacity which is under construction or planned. Under current legislation, certain incentives are given to owners/developers of small-scale hydro schemes, in order to improve competition in the electricity market [4].

5.2 China

China's hydroelectric resources are vast, however measured: its gross theoretical potential approaches 6000 TWh/yr, while its economically feasible potential has been assessed as some 290000 MW (1270 TWh/yr)-in both instances, far larger than that of any other country in the world. Current hydro output exceeds 250 TWh/yr, contributing about 17% to the republic's electricity generation. Total amount of hydro capacity under construction is about 35000 MW: as large as the combined current building program of the next four largest hydro developers [4].

More than 50 GW of pure hydroelectric capacity is planned for construction, including five very large schemes: Xiluodu (12800 MW) and Xiangjiaba (6000 MW) in the Yangtze River basin, Nuozhadu (5550 MW) in the Lancang basin, Laxiva (3720 MW) and Jinping I (3300 MW). China has about 5700 MW of pumped-storage capacity, with 6120 MW under construction and about 58 GW planned [3, 4].

5.3 India

India's gross theoretical hydropower potential (2638 TWh/yr) and theoretically feasible potential (660 TWh/yr) are amongst the highest in the world. The public utilities' total installed hydroelectric capacity exceeded 26500 MW at the end of 2002, with a corresponding generation of 68.5 TWh, equivalent to 12.9% of India's public sector electricity generation [3, 4].

There are at least 17 plants of over 300 MW capacity being built, of which the largest are Nathpa Jhakri (1500 MW), Sardar Sarovar (1200 MW), Tehri Stage I (1000 MW) and Narmada Sagar (1000 MW). The Atlas also reports that there are 267 small-scale hydro plants (up to 3 MW) in operation, with an aggregate installed capacity of about 210 MW; a further 140 MW of small-scale capacity is under construction. A total of 3349 schemes, aggregating 2852 MW, have been identified for possible future development [3, 4].

5.4 Turkey

The gross hydroelectric potential and technically utilizable potential of Turkey are estimated as 433 TWh/year and 216 TWh/year respectively. The economically utilizable installed capacity and annual average energy generation have been determined approximately as 35500 MW and 126 TWh/year respectively (Table 3). The gross hydroelectric potential of Turkey is about 1% of the world total and about 14% of the European total. Although Turkey is not affluent in terms of hydroelectric energy potential, it is ranked in the first quartile within European countries. In terms of developing water resources in Turkey, hydraulic energy generation takes a considerable portion [4, 11-17].

It is estimated that there is considerable small hydropower (SHP) potential in Turkey. DSI (State Hydraulic Work) has started a pre-investigation study on "The Place of Small HEPPs (hydroelectric power plants) within Estimated Hydroelectric Potential". These studies conclude that an additional technical hydroelectric energy potential of 57 TWh/year could be utilizable. 38 TWh/year of hydroelectric energy potential, corresponding to two-thirds of this additional potential, has been estimated to be economically utilizable, so the total economically utilizable hydroelectric potential of Turkey will reach 164 TWh/year [4, 13, 14].

Approximately 50% of the additional potential of 38 TWh (that is, 19 TWh) could be realized as small HEPPs, with installed capacities of less than 10 MW. The share of SHP potential in the total, which is 3% at present, would be 14%. In accordance with the results obtained from the pre-evaluation study, about 15 percent increase in 126 TWh/year exploitable energy potential can be achieved by developing additional SHP (Small Hydroelectric Power) potential. However, this study gives only rough results about the additional SHP potential of the country and the potential must be evaluated more precisely, with comprehensive master plan studies for each hydrological basin [4, 14, 15].

So far in Turkey, 566 hydro plants are at various stages of development. As of 2004, 130 plants have been put into operation, 31 are under construction and a further 405 are at various planning stages, see Table 3. The 130 hydropower plants in operation have an installed capacity of 12251 MW and an annual average generation of 44388 GWh. Thus, only 35% of the technically and economically utilizable hydroelectric potential has been developed. On the other hand, 85% of the total hydro capacity in operation has been developed by DSI, corresponding to 9931 MW (49 hydro plants) and 35795 GWh/year respectively. The largest and most comprehensive regional development project ever implemented by DSI in Turkey is "The Southeast Anatolian (GAP) Project", which is located in the region of Southeast Anatolia on the Euphrates and Tigris Rivers and their tributaries, which originate in Turkey [4, 13].

The Ministry of Energy and Natural Resources carries out the general energy planning studies, using an 'MAED' demand model, and TEIAS, (Turkish Electricity Transmission Company) carries out energy generation expansion planning studies, using the DECADES model. The MAED model, which was developed by the International Atomic Energy Agency (IAEA), makes projections of the medium and long-term general electricity demand. It takes into consideration a detailed analysis of social, economic and technical systems. The model is based on low, medium and high case scenarios. It is very important to project the energy demand accurately, because decisions involving huge investments of capital are based on these forecasts [4]. The Ministry of Energy and Natural Resources (MENR) taking into consideration the MAED energy demand model demand outcome. According to the Plan, the installed capacity will increase to 57551 MW in 2010 and to 117240 MW in 2020. The installed hydropower capacity is anticipated to increase to 18943 MW in 2010 and to 34092 MW in 2020. Thus, an additional 1000 MW of hydro capacity should be added to the system annually over the next 20 years. Turkey is thus seeking support for the development of all its economic potential by 2023, which is the 100th anniversary of the foundation of the Turkish Republic [4, 16, 17].

6. CONCLUSION

Hydro-electric power has always been an important part of the world's electricity supply, providing reliable, cost effective electricity, and will continue to do so in the future. Hydro power has environmental impacts which are very different from those of fossil fuel power plants. The actual effects of dams and reservoirs on various ecosystems are only now becoming understood. The future of hydro-electric power will depend upon future demand for electricity, as well as how societies value the environmental impacts of hydro-electric power compared to the impacts of other sources of electricity.

Hydropower currently provides 17% of the world's electricity supply. The contribution of other renewables is currently very small; according to the European Commission's World Energy, Technology and Climate Policy Outlook 2030, in the year 2000 wind and solar power contributed 0.16 and 0.01%, respectively. The report projects these values to have increased by 2010 to 0.6% for wind and 0.12% for solar. It is clear, therefore, that hydropower will remain the major contributor in the renewable power sector for the foreseeable future. The current installed hydropower capacity is some 730 GW and annual generation is around 2700 TWh. In addition, some 100 GW of new capacity is currently under construction.

The hydropower industry is closely linked to both water management and renewable energy production and thus has an important role, in cooperation with the international community, and in striving for sustainable development in a world where billions of people still lack access to safe drinking water and adequate energy supplies. Hydropower emits very few greenhouse gases in comparison with other large-scale energy options and thus helps slowing down global warming. In addition, by storing water in rainy seasons and releasing it in dry ones, dams and reservoirs help control water during floods and droughts. These essential functions, protecting human lives and other assets, will be increasingly important in the context of climate change is expected to give rise to even greater variability in the frequency and intensity of rainfall. Hydropower is a proven, well understood technology based on more than a century of experience. Its schemes have the lowest operating costs and longest plant lives. Hydropower plants also provide the most efficient energy conversion process. Modern plants can convert more than 95% of moving water's energy into electricity, while the best fossil-fuel power plants are only about 60% efficient.

The future of hydro-electric power will depend upon future demand for electricity, as well as how societies value the environmental impacts of hydro-electric power compared to the impacts of other sources of electricity.

Table 3: Distribution of the hydropower potential in Turkey by project implementation status. [13]

	Number of project	Installed capacity MW	Total annual power generation capacity			
			Firm GWh	Mean GWh	Cumulative GWh	Mean %
In operation	130	12251	32 984	44388	44034	35.0
Under construction	31	3338	6 467	10845	55233	9.0
Final design completed	19	3570	7 029	10897	66130	9.0
Under final design operation	21	1333	2 492	4494	70624	4.0
Planned	119	6091	10 861	22324	92948	18.0
Under planning	57	1978	4 214	7602	100550	6.0
Master plan completed	40	2691	5 674	9195	109745	7.0
Reconnaissance completed	107	3920	8 523	15184	124929	12.0
Initial study completed	42	368	526	1180	126109	1.0
Total potential	566	35540	78 770	125129		100.0

REFERENCES

- [1] IHA, International Hydropower Association, “The Role of Hydropower in Sustainable Development”, IHA White Paper, pp. 1-140, 2003.
- [2] Yuksel, I., “Dams and Hydropower for Sustainable Development”, *Journal of Energy Sources, Part B: Economics, Planning, and Policy*, Vol. 4, Number 1, pp. 100-110, 2009.
- [3] WEC, World Energy Council, “Survey of Energy Resources”, www.worldenergy.org, accessed date 05 March 2011.
- [4] Yuksel, I., “Hydroelectric Power in Developing Countries”, *Journal of Energy Sources, Part B: Economics, Planning, and Policy*, Vol. 4, Number 4, pp. 377-386, 2009.
- [5] AR, American Rivers, “Beyond Dams: Options and Alternatives”, A Report by American Rivers and International Rivers Networks, www.americanrivers.org, accessed date 10 March 2011.
- [6] WEC, World Energy Council, “Survey of Energy Resources”, www.worldenergy.org, accessed date 09 April 2011.
- [7] IEA, International Energy Agency, “World Energy Outlook 2005”, OECD/IEA, Paris, 2006.
- [8] WCD, World Commission on Dams, “Dams and Development”, www.wcd.org, accessed date 10 February 2011.
- [9] EIA, Energy Information Administration, “International Energy Outlook 2005”, <http://www.eia-doe.gov>, accessed date 20 April 2011.
- [10] IAEA, International Atomic Energy Agency, “Brazil: a Country Profile on Sustainable Energy Development, Vienna, Austria, 2006.
- [11] Kaygusuz, K., “Sustainable Development of Hydropower”, *Energy Sources*, Vol. 24, pp.803-815, 2002.
- [12] Ozturk, R. and Kincay, O., “Potential of Hydroelectric Energy”, *Energy Sources*, Vol. 26, pp. 1141-1156, 2004.
- [13] DSI, State Hydraulic Works, “Statistics on Hydropower”, Ankara, Turkey, accessed date 10 April 2011.
- [14] MENR, Ministry of Energy and Natural Resources, “Energy Statistics of Turkey in 2005”, available from <http://www.menr.gov.tr>, accessed date 16 March 2011.
- [15] Yuksek, O and Kaygusuz, K., “Small Hydropower Plants As a New and Renewable Energy Source”, *Energy Sources, Part B, Vol. 1*, pp. 279-290, 2006.
- [16] Yuksel, I., “Southeastern Anatolia Project (GAP) for Irrigation and Hydroelectric Power in Turkey”, *Journal of Energy Exploration & Exploitation*, Vol. 24, Number 4-5, pp. 361-370, 2006.
- [17] Yuksel, I., “Development of Hydropower: A Case Study in Developing Countries”, *Journal of Energy Sources, Part B: Economics, Planning, and Policy* Vol.2, Number 2, pp.113-121, 2007.

Kinetic, Equilibrium and Thermodynamic Studies for Adsorption of Cadmium (II) Using Modified Agricultural Wastes

AlOthman, Z. A.^{*1} & Habila, M.A.²

¹ Chemistry Department, College of Science, King Saud University, zaothman@ksu.edu.sa

² Chemistry Department, College of Science, King Saud University, m_a_habeela@yahoo.com
Riyadh 11451, Saudi Arabia

ABSTRACT

Agricultural wastes have a great potential in removal of heavy metal ions from aqueous solution. The contamination of water by toxic heavy metals is a world-wide environmental problem. Unlike organic pollutants, the majority of which are susceptible to biological degradation, heavy metals will not degrade into harmless end products. Discharges containing Cadmium, in particular, are strictly controlled due to the highly toxic nature of this element and its tendency to accumulate in the tissues of living organisms. So this work aims to develop inexpensive, highly available, effective metal ion adsorbents from natural wastes as alternative to existing commercial adsorbents. *Tamrix articulata* wastes were modified chemically by esterification with maleic acid to yield adsorbent which is rich in carboxylic content. The adsorption behavior of treated *Tamrix articulata* wastes for cadmium ions from aqueous solutions has been studied as a function of appropriate equilibrium time, adsorbent dose, temperature and pH in a batch system. Results showed that the maximum adsorption capacity was 195.5mg/g at solution pH 4, temperature 30°C, contact time 120 minute, initial concentration 400 mg/L and adsorbent dose 0.3g/L. The kinetic study was analyzed using the pseudo-first order and pseudo-second order kinetic models. It was shown that the adsorption of cadmium could be described by the pseudosecond order equation. Also the experimental data were analyzed by the Langmuir and Freundlich models of adsorption. Thermodynamic parameters such as ΔG° , ΔH° and ΔS° have also been evaluated and it has been found that the sorption process was spontaneous and exothermic in nature. In conclusion, the treated *Tamrix articulata* wastes investigated in this study showed good potential for the removal of cadmium from aqueous solutions.

Keywords: *Tamrix articulata* wastes, Cadmium removal, Adsorption, Kinetic and Thermodynamic study.

1. INTRODUCTION

Cadmium (Cd) is a toxic heavy metal of significant environmental and occupational concern [1]. It is introduced into water from smelting, metal plating, cadmium nickel batteries, phosphate fertilizers, mining, pigments, stabilizers, alloy industries and sewage sludge [2]. Cadmium has been classified as a human carcinogen and teratogen impacting lungs, kidneys, liver and reproductive organs [1, 3]. The harmful effects of cadmium include a number of acute and chronic disorders, such as renal damage, emphysema, hypertension and testicular atrophy [2] Hence, it is essential to remove Cd(II) from water and wastewater before its transport and cycling into the natural environment. The most important technologies include chemical precipitation, electroflotation, ion exchange, reverse osmosis and adsorption onto activated carbon [4]. Adsorption has been developed as an efficient method for the removal of heavy metals from contaminated water and soil. A variety of adsorbents, including clays, zeolites, dried plant parts, agricultural waste biomass, biopolymers, metal oxides, microorganisms, sewage sludge, ash and activated carbon have been used for cadmium removal [5-16]. Cost is an important parameter for comparing the adsorbent materials [17]. Activated carbon considered as a highly effective adsorbent for heavy metals removal from waste water, but is readily soluble under extreme

pH conditions [18]. Also very high cost [19]. The low cost agricultural waste by-products such as sugarcane bagasse [20], rice husk [21], sawdust [22], coconut husk [23], oil palm shell [24], neem bark [25], etc., for the elimination of heavy metals from wastewater have been investigated. In this study, *Tamrix articulata* wastes were modified chemically by esterification with maleic acid under conditions which yielded adsorbent rich in carboxyl content. The produced adsorbant was used for removal of cadmium (II) ions from water. The sorption process was examined in terms of its equilibria, kinetics and thermodynamics.

2. MATERIALS AND METHODS

2.1 Preparation and characterization of adsorbent

Tamrix articulata wastes were collected from the Saudi Arabian desert, grinded, passed through 200–400 mesh sieves and then washed with hot distilled water until the final effluent was colorless. The resulting material was then dried in an electric oven for 3 h at 60°C. Maleic acid, cadmium acetate and EDTA were all laboratory grade chemicals.

Tamrix articulata wastes were esterified according to the previously described method [26]. For scanning electron microscope (SEM) analysis, samples were mounted on an aluminum stub, coated with a thin layer of gold and

then examined using Jeol (JSM- 6380LA) Japan. Fourier transformation infrared (FTIR) spectra of samples were recorded using a spectrophotometer (Thermo Scientific USA). Elemental analysis of native and maleic acid treated *Tamrix articulata* wastes were performed using a Perkin Elmer Series II CHN analyzer.

2.2 Carboxyl content

The carboxyl contents of the native and modified *Tamrix articulata* wastes were determined according to the method reported in [27]. Previous studies [28, 29] have indicated that carboxylic acids form an anhydride (I) [equation (1)] when subjected to heat treatment. The presence of cellulosic material in the *Tamrix articulata* wastes with maleic acid during the heating process would allow the anhydride (I) to react with the cellulose hydroxyls of the *Tamrix articulata* wastes to form the cellulose maleicate adduct (II) [26].

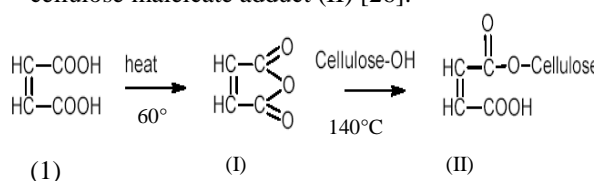


Figure 1 shows the influence of the maleic acid concentration [mmol/(1 g *Tamrix articulata* wastes)] on the extent of esterification as expressed in mequi COOH/100 g sample. The extent of esterification increased significantly as the maleic acid concentration was increased within the range studied. This enhancement in the ester group content could be interpreted in terms of the greater availability of maleic acid molecules to be converted to anhydride (I).

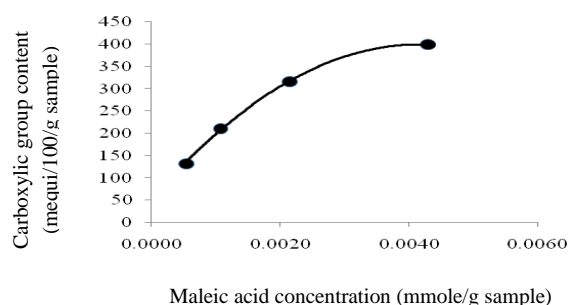


Figure 1: Effect of maleic acid concentration on the carboxyl group content of esterified *Tamrix articulata* wastes.

2.2 Adsorption studies

Known volumes (100 ml) of each prepared Cadmium (II) ion solutions [100–1250 mg/l] were placed in 125 ml Erlenmeyer flasks. Containing 0.03g of adsorbent, and after addition of the corresponding metal ion solution, the contents were shaken at 150 rpm for 2 h in a thermostatted shaking water bath at 30°C. At the end of 2 h, the metal ion solutions were separated by filtration. Blank experiments without added adsorbents

were performed at the same time. Then the metal ion concentrations were determined via direct direction against standard EDTA solutions before and after adsorption.

3. RESULTS AND DISCUSSION

3.1 Properties of native and maleic acid treated *Tamrix articulata* wastes

FTIR data showed bands at 3640–3500 cm^{-1} which are related to the stretching vibrations of the O–H, 3000–2800 cm^{-1} which are related to the stretching vibrations of the C–H, and 1740–1725 cm^{-1} which are related to COO and C–O. Bands at 1130–1000 cm^{-1} are vibration of C–O–C and O–H of polysaccharides. The same peaks are observed for native and maleic acid treated *Tamrix articulata* wastes, the only difference is the increase in peak intensity at 1735 cm^{-1} in case of treated *Tamrix articulata* wastes, which confirms the increase in COO groups due to esterification. The elemental analysis results for native and maleic acid treated *Tamrix articulata* wastes revealed that native wastes are composed of 41.7% carbon, 5.3% hydrogen, and 1.8% nitrogen, while maleic acid treated *Tamrix articulata* wastes are composed of 45.4% carbon, 5.6% hydrogen, and 1.0% nitrogen. The carbon content increase is due to the increase in carboxylic group content. Figure 2 shows the scanning electron microscope (SEM) image, which indicates the rough and microporous structure of the surfaces of native (Figure 2A) and maleic acid treated *Tamrix articulata* wastes (Figure 2B). Esterification did not clearly change the porosity but only introduced carboxylic groups to the surfaces.

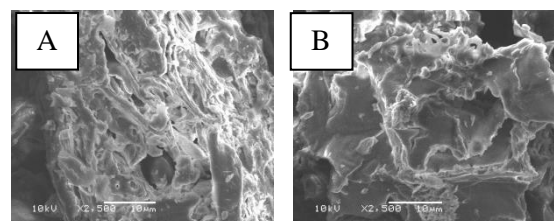


Figure 2: shows the scanning electron microscope (SEM) image of native waste surfaces (A) and maleic acid treated *Tamrix articulata* wastes (B).

3.2 Effect of carboxyl group content of treated *Tamrix articulata* wastes on Cd(II) adsorption

Table 1 shows the effect of the carboxyl group content of the esterified *Tamrix articulata* wastes on their adsorption capacity, q_e (metal uptake per unit weight of adsorbent), toward Cd(II) ions from aqueous solutions. Evidently, increasing the extent of esterification was accompanied by an increase in the adsorption capacity of the treated *Tamrix articulata* wastes. A greater extent of esterification lead to *Tamrix articulata* wastes maleicate with a greater number of carboxyl groups, which would increase the adsorption capacity for Cd(II) ions. Current data show that as the concentration of

maleic acid increased from 0.0005 to 0.0043 mmol/g *Tamrix articulata* wastes, the extent of esterification increased from 131.2 to 399 mg equiv COOH/100 g sample and the adsorption capacity increased from 53.3 to 195.5 mg/g, respectively. These results indicate that the carboxyl groups introduced into the cellulose molecular structure of *Tamrix articulata* wastes via esterification using maleic acid play an effective role in the Cd(II) ion adsorption process.

Table 1: Effect of esterification of *Tamrix articulata* wastes on Cd (II) ion adsorption at 30°C.

Maleic Acid (Mmol/g waste)	Esterification (Mg Equiv - COOH / 100 g Sample)	Adsorption Capacity (qe) (mg/g)
0.0043	399	195.5
0.0022	315	137.70
0.0011	210	88.84
0.0005	131.2	53.3

3.3- Adsorption Studies

3.3.1- Effect of pH

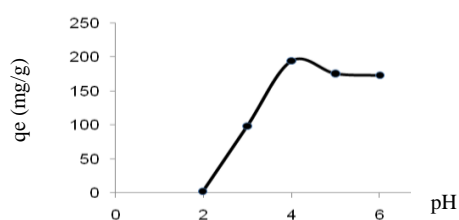


Figure 3: Effect of pH on cadmium biosorption by modified *Tamrix articulata* wastes at 30°C.

As shown in Figure 3, the adsorption capacity, q_e (mg/g), of modified *Tamrix articulata* wastes toward Cd(II) ions increased over the range from 2.6 to 194.5 mg/g at pH values increasing from 2 to 4. Indeed, the maximum adsorption, q_{max} , of Cd (II) ions was attained at a pH value of 4. This could be ascribed to the lower stability of chelates formed in a highly acidic medium. At lower pH values, the H ions present in the system compete with metal cations for the exchange sites on the adsorbent surface and partially release these cations. Heavy metal cations are completely released under extreme acid conditions [30].

3.3.2 Kinetics of adsorption

Information on the kinetics of solute uptake is required to select optimal operating conditions for full-scale batch process. Graph in Figure 4 showed that a contact time of 120 min was sufficient to achieve equilibrium and that the adsorption did not change significantly with further increases in contact time. Therefore, the uptake and un-adsorbed cadmium concentrations at the end of 120 min are given as the equilibrium values.

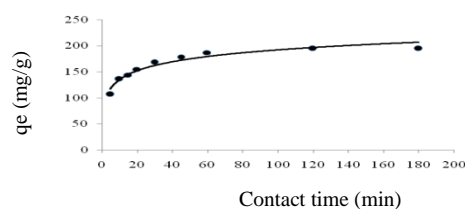


Figure 4: Effect of contact time on cadmium (II) biosorption by modified *Tamrix articulata* wastes at pH 4 and 30°C.

The adsorption kinetic values were analyzed using pseudo-first- and pseudo-second-order kinetic models. These models correlate solute uptake to predict the reactor volume. These models are explained below:

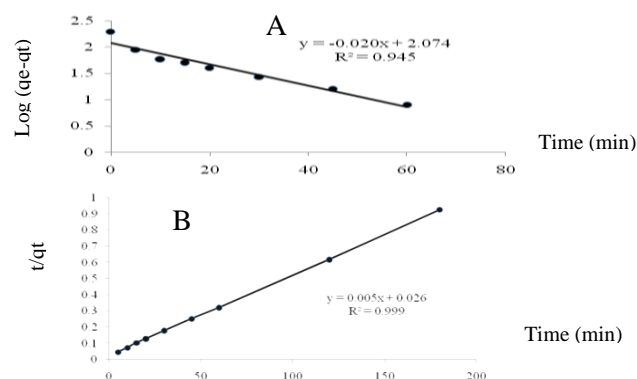


Figure 5: Pseudo-first-order (A) and pseudo-second-order (B) cadmium (II) biosorption by modified *Tamrix articulata* wastes.

The pseudo-first-order equation of Lagergren [31] is generally expressed in equation (2) as follows:

$$dq_t/dt = k_1(q_e - q_t), \quad (2)$$

where q_e and q_t are the sorption capacities at equilibrium and at time t , respectively, and k_1 is the rate constant of pseudo first-order sorption (min^{-1}). After integration and applying boundary conditions, $q_t = 0$ to $q_t = q_t$ at $t = 0$ to $t = t$, the integrated form of Eq. (2) becomes:

$$\log(q_e - q_t) = \log q_e - k_1 t / 2.303. \quad (3)$$

The pseudo-first-order rate constant k_1 can be obtained from the slope of the graph between $\log(q_e - q_t)$ versus time t (Figure 5A). The calculated k_1 values and corresponding linear regression correlation coefficient values are shown in Table 2. The linear regression correlation coefficient value R_1^2 was 0.945, which indicates that this model cannot be applied to predict the adsorption kinetic.

Table 2: Kinetic constants for cadmium (II) adsorption onto maleic acid treated *Tamrix articulata* wastes at an initial concentration of 400 mg/l at 30°C and pH 4.

The pseudo-first-order			The pseudo-second-order		
Rate Constant (K_1)	q_e (mg/g)	(R_1^2)	Rate Constant (K_2)	q_e (mg/g)	(R_2^2)
0.046	118.5	0.945	0.009	200	0.999

The pseudo-second-order chemisorption kinetic rate equation is expressed in eq. (4) [32]:

$$Dq_t/dt = k_2(q_e - q_t)^2, \quad (4)$$

where q_e and q_t are the sorption capacities at equilibrium and at time t , respectively, and k_2 is the rate constant of pseudo-second-order sorption (g/(mg min)). After integration and applying boundary conditions, $q_t = 0$ to $q_t = q_e$ at $t = 0$ to $t = t$, the integrated form of Eq. (4) becomes:

$$t/q_t = 1/Kq_e^2 + t/q_e, \quad (5)$$

where t is the contact time (min) and q_e (mg/g) and q_t^2 (mg/g) are the amount of the solute adsorbed at equilibrium. Figure 5B shows the linear relationship of the graph t/q_t against t , from which q_e and k can be determined from the slope and intercept respectively. The linear regression correlation coefficient R_2^2 value (0.99) was higher than R_1^2 (Table 2). These results confirm that the adsorption data were well represented by the pseudo-second order kinetic model.

3.3.3 Effect of adsorbent dosage

The amount of cadmium (II) adsorbed varied with varying adsorbent dosages. As shown in Figure 6, the adsorption capacity of cadmium decreased from 208.7 to 30.6 mg/g with an increase in adsorbent concentration from 0.3 to 6 g/l for initial cadmium concentration of 400 mg/l. A similar trend was also observed for zinc removal using *Azadirachta indica* as the adsorbent [33].

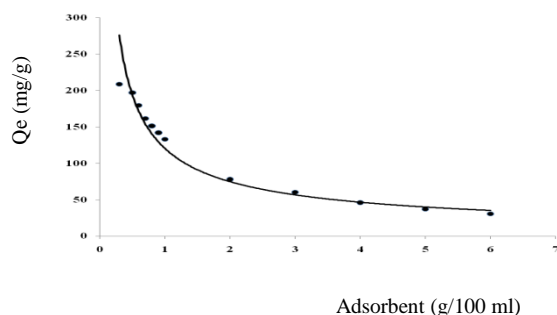


Figure 6: Effect of adsorbent concentration on cadmium (II) biosorption by modified *Tamrix articulata* wastes, 400 mg/L of metal at pH 4 and 30°C.

3.3.4 Adsorption isotherms

Analysis of the isotherm data by fitting different isotherm models is an important step in determining a suitable model for design purposes [34].

Langmuir isotherm

The Langmuir equation (6) [35] was applied to the equilibrium adsorption data for Cd(II) ions onto native and modified *Tamrix articulata* wastes.

$$C_e/q_e = 1/(q_{max} \cdot b) + C_e/q_{max}, \quad (6)$$

where C_e is the equilibrium concentration of the adsorbate (mg/l), q_e is the amount of metal ion adsorbed (mg/g), and q_{max} and b are Langmuir constants related to the maximum adsorption capacity (mg/g) and the adsorption energy, respectively. The Langmuir equilibrium constant, K_L , can be obtained from eq. (7).

$$K_L = q_{max} \cdot b. \quad (7)$$

The linear form of the Langmuir isotherm is shown in Figure 7. The correlation coefficients, R^2 , for the adsorption of Cd(II) ions onto native and maleic acid-treated *Tamrix articulata* wastes are 0.966 and 0.957, respectively, indicating that the adsorption was well fitted by the Langmuir isotherm.

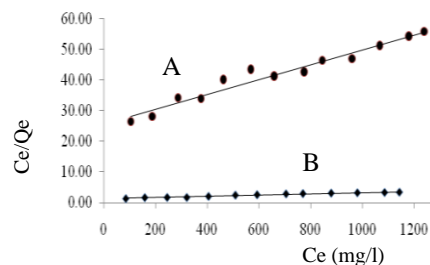


Figure 7: Langmuir biosorption isotherms for cadmium (II) at 0.3 g/l of biosorbent concentration for native (A) and maleic acid-treated *Tamrix articulata* wastes (B).

Freundlich isotherm

As shown in equation 8

$$\text{Log} q_e = \text{log} K + 1/n \text{log} C_e, \quad (8)$$

where C_e is the equilibrium concentration (mg/l) and q_e is the amount of metal adsorbed (mg/g) at equilibrium. The quantities K_F and n are the Freundlich constants, with K_F (mg/g) indicating the adsorbent capacity and n indicating the favorable nature of the process. Plots of $\log q_e$ versus $\log C_e$ should be linear, with the slope and intercept of the line obtained corresponding to $1/n$ and $\log K_F$, respectively (Figure 8).

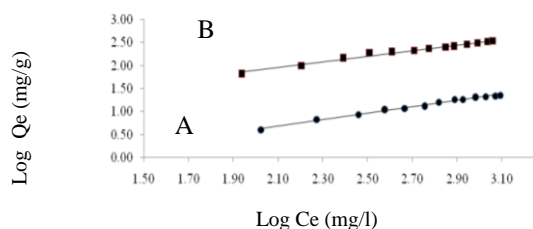


Figure 8: Freundlich biosorption isotherm for cadmium (II) at 0.3 g/l of biosorbent concentration for native (A) and maleic acid-treated *Tamrix articulata* wastes (B).

The calculated results of the Langmuir and Freundlich isotherm constants are given in Table 3. The adsorption of cadmium (II) onto native and maleic acid-treated *Tamrix articulata* wastes was well correlated with the Langmuir equation and Freundlich equation for the concentration range studied.

Table 3: Langmuir and Freundlich constants for the adsorption of Cd(II) Ions onto native and maleic acid-treated plant at pH 4 and 30°C.

	Constant	Native	Maleic acid-
Langmuir constants	K_L	0.024	0.8
	b	0.00057	0.0016
	Q_{max}	41.6	500
	R^2	0.957	0.966
Freundlich constants	K_F	0.168	4.93
	n	1.44	1.66
	R^2	0.991	0.973

3.3.5 Thermodynamic studies

Thermodynamic parameters, such as change in Gibbs free energy (ΔG°), enthalpy (ΔH°) and entropy (ΔS°) were evaluated from eq. (9, 10).

$$\text{Log } K_d = \Delta S^\circ / 2.303R - \Delta H^\circ / 2.303RT \quad (9)$$

$$\Delta G^\circ = -RT \ln K_d \quad (10)$$

where K_d is equilibrium partition constant calculated as the ratio between sorption capacity (q_e) and equilibrium concentration (C_e). R is the gas constant (8.314 J/mol/K). T is the temperature in Kelvin (K). From eq. 9 a plot of $\log K_d$ vs. $1/T$ (Figure 9) would give ΔH° and ΔS° which are given in Table 5.

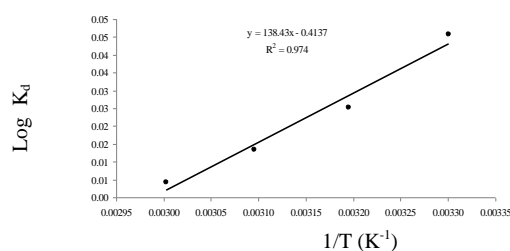


Figure 9: thermodynamic study for adsorption of Cd(II) onto maleic acid-treated *Tamrix articulata* wastes.

Table 5: Thermodynamic parameters for adsorption of Cd(II) onto maleic acid-treated *Tamrix articulata* wastes.

Temperature T(K)	Thermodynamic parameters		
	ΔG° (kJ/mol)	ΔS° (J/mol/K)	ΔH° (kJ/mol)
303	-0.265		
313	-0.151		
323	-0.082	-7.9	-2.6
333	-0.027		

The negative ΔH° value indicates the exothermic nature of the process. Moreover, the negative ΔS° value corresponds to a decrease in the degree of freedom of the adsorbed species. The negative ΔG° value confirmed the reaction feasibility and spontaneous adsorption process. Also the small negative ΔG° values obtained in this study indicate that physical adsorption is the predominant mechanism in the sorption process [36].

4. CONCLUSION

The maleic acid-treated *Tamrix articulata* wastes investigated in this study showed good potential for the removal of cadmium (II) from aqueous solutions. The Maximum adsorption capacity (q_e) occurred at pH 4 with a contact time of 2 hr. The adsorption isotherms were well fitted by the Langmuir equation and Freundlich equation. The biosorption process was best described by the second-order equation. Thermodynamic parameters (ΔG° , ΔH° and ΔS°) showed that the adsorption process is spontaneous and exothermic in nature.

5. ACKNOWLEDGMENTS

This work was supported by NPST program by King Saud University project number 09-ENV656-02.

REFERENCES

- [1] Waalkes, M.P. "Cadmium carcinogenesis in review", *J. Inorganic Biochemistry*, Vol. 79, pp. 241–244, 2000.
- [2] Kadirvelu, K. and Namasivayam, C. "Agricultural by-products as metal adsorbents: sorption of lead (II) from aqueous solutions onto coirpith carbon", *Environmental Technology*, Vol. 21, pp. 1091–1097, 2000.
- [3] Sharma, Y.C. "Thermodynamics of removal of cadmium by adsorption on indigenous clay", *Chemical Engineering Journal*, Vol. 145, pp. 64–68, 2008.
- [4] Poon, C.P.C. "Removal of Cd(II) from wastewaters", In: Mislin, H., Raverva, O. (Eds.), *Cadmium in the Environment. Birkha User Basal, Switzerland*, pp. 6–55, 1986.

- [5] Tan, G.Q. and Xiao, D. "Adsorption of cadmium ion from aqueous solution by ground wheat stems", *Journal of Hazardous Materials*, Vol. 164, pp. 1359–1363, 2009.
- [6] Benguella, B. and Benaissa, H. "Cadmium removal from aqueous solutions by chitin: kinetic and equilibrium studies", *Water Research*, Vol. 36, pp. 2463–2474, 2002.
- [7] Meng, Y.T., Zheng, Y.M., Zhang, L.M. and He, J.Z. "Biogenic Mn oxides for effective adsorption of Cd from aquatic environment", *Environmental Pollution*, Vol. 157, 2577–2583, 2009.
- [8] Soltani, R.D.C., Jafari, A.J. and Khorramabadi, Gh.S. "Investigation of cadmium (II) ions biosorption onto pretreated dried activated sludge", *American Journal of environmental science*, Vol. 5, pp. 41–46, 2009.
- [9] An, H.K., Park, B.Y. and Kim, D.S. "Crab shell for the removal of heavy metals from aqueous solution", *Water Research*, Vol. 35, pp. 3551–3556, 2001.
- [10] Cortes-Martinez, R., Martinez-Miranda, V., Solache-Rios, M. and Garcia-Sosa, I. "Evaluation of natural and surfactant-modified zeolites in the removal of cadmium from aqueous solutions", *Sep. Sci. Technol.*, Vol. 39, pp. 2711–2730, 2004.
- [11] Garg, U., Kaur, M.P., Jawa, G.K., Sud, D. and Garg, V.K. "Removal of cadmium (II) from aqueous solutions by adsorption on agricultural waste biomass", *Journal of Hazardous Materials*, Vol. 154, pp. 1149–1157, 2008.
- [12] Semerjian, L. "Equilibrium and kinetics of cadmium adsorption from aqueous solutions using untreated *Pinus halepensis* sawdust", *Journal of Hazardous Materials*, Vol. 173, pp. 236–242, 2010.
- [13] Li, Z.Z., Katsumi, T., Imaizumi, S., Tang, X.W. and Inui, T. "Cd(II) adsorption on various adsorbents obtained from charred biomaterials", *Journal of Hazardous Materials*, Vol. 183, pp. 410–420, 2010.
- [14] Wang, F.Y., Wang, H. and Ma, J.W. "Adsorption of cadmium (II) ions from aqueous solution by a new low-cost adsorbent-Bamboo charcoal", *Journal of Hazardous Materials*, Vol. 177, pp. 300–306, 2010.
- [15] Tashauoei, H.R., Attar, H.M., Amin, M.M., Kamali, M., Nikaeen, M. and Dastjerdi, M.V. "Removal of cadmium and humic acid from aqueous solutions using surface modified nanozeolite A", *International journal of environmental science and technology*, Vol. 7, pp. 497–508, 2010.
- [16] Visa, M., Bogatu, C. and Duta, A. "Simultaneous adsorption of dyes and heavy metals from multicomponent solutions using fly ash", *Applied surface science*, Vol. 256, pp. 5486–5491, 2010.
- [17] Bailey, S.E., Olin, T.J., Bricka, R.M. and Adrian, D. "A review of potentially low cost sorbents for heavy metal", *Water Research*, Vol. 33, No. 11, pp. 2469–2479, 1999.
- [18] Huang, C.P. and Blankenship, B.W. "The removal of mercury(II) from dilute aqueous Solution by activated carbon", *Water Research*, Vol. 18, pp. 37–46, 1989.
- [19] Ho, Y.S., Chiang, T.H. and Hsueh, Y.M. "Removal of basic dye from aqueous solution using tree fern as a biosorbent", *Process Biochemistry*, Vol. 40, No. 1, pp. 119–124, 2005.
- [20] Chand, S., Aggarwal, V.K. and Kumar, P. "Removal of Hexavalent Chromium from the Wastewater by Adsorption", *Indian Journal of Environmental Health*, Vol. 36, No. 3, pp. 151–158, 1994.
- [21] Srinivasan, K., Balasubramaniam, N. and Ramakrishna, T.V. "Studies on Chromium Removal by Rice Husk Carbon", *Indian Journal of Environmental Health*, Vol. 30, No. 4, pp. 376–387, 1998.
- [22] Ajmal, M., Rao, R.A.K. and Siddiqui, B.A. "Studies on Removal and Recovery of Cr (VI) from Electroplating Wastes", *Water Research*, Vol. 30, No. 6, pp.1478–1482, 1996.
- [23] Tan, W.T., Ooi, S.T. and Lee, C.K. "Removal of Chromium (VI) from Solution by Coconut Husk and palm Pressed Fibre", *Environmental Technology*, Vol. 14, pp. 277–282, 1993.
- [24] Khan, N.A., Shaaban, M.G. and Hassan, M.H.A. "Removal of heavy metal using an inexpensive adsorbent", Proc. UM Research Seminar 2003 organized by Institute of Research Management and Consultancy (IPPP), University of Malaya, Kuala Lumpur, 2003.
- [25] Ayub, S., Ali, S.I. and Khan, N.A. "Efficiency evaluation of neem (*Azadirachta indica*) bark in treatment of industrial wastewater", *Environmental Pollution Control Journal*, Vol. 4, No. 4, pp. 34 – 38, 2001.

- [26] Wing, R.E. and Peoria, I.L. "Corn fiber citrate: preparation and ion-exchange properties", *Industrial Crops and Products*, Vol. 5, No. 4, pp. 301-305, 1996.
- [27] Daul, G.C., Reinhardt, R.M. and Reid, J.D. "The carboxymethylation of cotton", *Textile Research Journal*, Vol. 23, pp. 719-726, 1953.
- [28] Hashem, A., Abdel-Halim, E.S., El-Tahlawy, Kh.F. and Hebeish, A. "Enhancement of the Adsorption of Co(II) and Ni(II) Ions onto Peanut Hulls through Esterification Using Citric Acid", *Adsorption Science & Technology*, Vol. 23, No. 5, pp. 367-380, 2005.
- [29] Andrews, B.A.K., Blanchard, E.J. and Reinhardt, R.M. "Fabric Whiteness Press Finishing with Citric Acid", *Text. Chem. Color*, Vol. 25, No. 3, pp. 52-54, 1993.
- [30] Gong, R., Ding, Y.D., Liu, H., Chen, Q. and Liu, Z. "Lead biosorption by intact and pretreated *Spirulina maxima* biomass", *Chemosphere*, Vol. 58, pp. 125-130, 2005.
- [31] Lagergren, S. and Kungliga S. "Svenska Ventenskapsakademiens", *Handlingar, Band*, Vol. 24, No. 4, pp.1, 1898.
- [32] Ho, Y.S. and McKay, E. "The kinetics of sorption of basic dyes from aqueous solution by Sphagnum moss peat", *Can. J. Chem. Eng.*, Vol. 76, pp. 822-827, 1998.
- [33] Bhattacharyya, K.G. and Sharma, A. "Adsorption of Pb(II) from aqueous solution by *Azadirachta indica* (Neem) leaf powder", *Journal of Hazardous Materials*, Vol. B113, pp. 97-109, 2004.
- [34] El-Geundi, M.S. "Homogeneous surface diffusion model for the adsorption of basic dyestuffs onto natural clay in batch adsorbers", *Adsorption Science & Technology*, Vol. 8, pp. 217-225, 1991.
- [35] Langmuir, I. "The adsorption of gases on plane surfaces of glass, mica and platinum", *Journal of American Chemical Society*, Vol. 40, No. 9, pp. 1361-1403, 1918.
- [36] Horsfall, M., Spiff, A. I. and Abia, A. A. "Studies on the influence of mercaptoacetic acid (MAA) modification of cassava (*Manihot sculenta* cranz) waste Biomass on the adsorption of Cu²⁺ and Cd²⁺ from aqueous solution", *Bulletin of the Korean Chemical Society*, Vol. 25, No. 7, pp. 969-976, 2004.

Investigation of Water Quality in Kocasu Creek, Turkey

Gulgun Yilmaz¹, Recep Bakis²

¹Anadolu University, Porsuk Vocational School, Eskisehir, 26470, Turkey, Eskisehir, Turkey.
guunal@anadolu.edu.tr

²Anadolu University, Department of Civil Engineering, Iki Eylul Campus, 26470, Eskisehir, Turkey.
recepbakis@anadolu.edu.tr

ABSTRACT

The modern agricultural, industrial and chemical revolutions and the explosion of the world's population brought the necessity of investigating the water quality which is used for several purposes within urban areas. The Kocasu Creek is an important tributary of the Kutahya basin, Turkey; is polluted with municipal and industrial waste. All of these released pollutants may have an impact on the water quality of the Kocasu Creek. Kocasu Creek's water is used for irrigation, drinking and as a supply of industrial water in the urban area. The aim of this study is determination of organic pollutants and investigation of its effects. For this purpose, water samples were taken and analyzed using couple plasma – atomic emission spectrophotometry. Concentration of heavy metals (Zn, Fe, Mn, Ni, Cu, Cr, Co and Pb) and major elements (Na, K, Ca, and Mg) were measured in the Kocasu Creek water. The concentrations depended on the sampling season and some metals determined to dominate in Kocasu Creek. This may be explained by geochemical factors and drainage basins of Kocasu Creek.

Keywords: heavy metals, river pollution, water pollution, water quality

1. INTRODUCTION

The need for water quality to be included in international treaties reflects the profound impact of economic, technological and demographic change upon the water environment. Until the modern agricultural, industrial and chemical revolutions, the explosion of the world's population and spread of urbanization, water quality was a non-factor in both domestic and international politics [1]. Kovacs [2] describes river pollution as an integrated, environmental problem resulting, not only from unregulated industrial pollutants and accidental spills, but also from such factors as airborne and other non-point source pollutants, urbanization, erosion and intensified agriculture. In Turkey, environmental pollution is considered an important hindrance to achieve a desired level of sustainable growth and development. In this respect, water contamination is an important issue to be considered accordingly. As in all parts of the world, water is a valuable, economic and strategic natural resource in Turkey as well. In developing and underdeveloped countries, 95 % of domestic wastewaters and 70 % of industrial waste waters are discharged into rivers, seas and creeks without being treated and therefore, clean water resources are also contaminated. Currently, about 1.4 billion people are deprived of clean water and most of the rivers are already contaminated. Finally, 80 % of the diseases in the world are due to contaminated water [3].

Turkey (26-45° E, 36-42° N) is a transcontinental country encompassing an area of 784 000 km². About 97% of the country is in Asia Minor (Anatolia) and 3%

in Europe (Thrace). The population was 68 million in 2000,

corresponding to a density of 87 in /km². The current population growth rate is 1.4% (<http://nkg.die.gov.tr>; Turkey's Statistical year book 2005). Today, about 66% of the Turkish population lives in cities [4].

Turkey is surrounded by the Mediterranean, Aegean, Marmara and Black Seas, with a total coastal length of 10 765 km. The mean altitude of Turkey is 1130. While the European part constitutes a relatively mature low-lying fertile land, Anatolia rises from west to east. Because of its complex geologic, geomorphic and climatic settings, Turkey has many rivers that enter the surrounding seas and neighboring countries of Iraq, Iran and Armenia. Overall, 26 main drainage basins, including 4 basins lacking an outflow to the sea, occur in Turkey. Turkey is drained by major rivers, each with a catchment area > 1500 km² [4].

The water quality of Turkey's rivers shows a wide variability, being influenced by both natural and anthropogenic factors. Natural factors affecting the water quality of these rivers include the precipitation to evapotranspiration ratio, the annual distribution and type of precipitation, topography that determines water residence time and erosion rate, and land use that affects vegetation type and cover. Anthropogenic influences have become more evident since the 1970s, particularly in regions where agricultural and industrial water use had increased [4].

Anthropogenic pollution of Turkey's rivers is caused mainly by domestic (sewage) and industrial waste

waters, and from irrigation return waters. While in large cities administrated by metropolitan municipal authorities domestic waste water is treated before being released into nearby streams, facilities for water treatment do not occur or are out of use in many smaller towns [4].

Starting in the 1970s, systematic water quality measurements have been conducted by associated governmental authorities (i.e. DSI and EIE) [5, 6] in many rivers of Turkey. These systematic measurements include some physical parameters (temperature, conductivity, and pH), major ions (Ca, Mg, Na, K, Cl, SO₄, alkalinity) and other constituents (boron, sodium absorption ratio, residual sodium carbonate, sediment load), but not other environmentally important parameters such as nutrients, agrochemicals and trace elements [4].

In this study, concentration of heavy metals (Zn, Fe, Mn, Ni, Cu, Cr, Cd and Pb) and major elements (Na, K, Ca, and Mg) are determined based on the water samples taken from Kocasu Creek and the degree of contamination is compared with values provided by Water Contamination Control Regulation (WCCR) and other available standards - Mainland Water Resources Classification (MWRC), U.S Environmental Protection Agency (EPA), World Health Organization (WHO) [7], European Union (EU) and Standards of Turkish Drinking Water (TS266) [8].

2. MATERIALS AND METHODS

2.1 Study Area and Sampling

The area of the Kocasu Creek is located within borders of city of Kutahya, Turkey. Exact location (coordinated) is shown on the map given in Figure 1.



Figure 1: Kocasu Creek, Kocasu Basin and the sampling points used for this study. Source: DSI, 5.

The Kocasu Creek has been polluted with municipal and industrial waste. The surface waters flowing into the

creek from basin area have been increased pollution in the Kocasu Creek. This pollution in the creek has been transferred to sediments in the creek and has been diffused by the interaction between surface water, creek water, sediment and the basin ground.

In this study, water samples were collected from 7 points from the Kocasu Creek. In the choice of these points several factors were considered namely Quality Control Stations of State Hydraulic Works, potential pollutant sources (municipal and industrial). The locations of the sampling stations and pollution sources; (1.Çavdarhisar Dam reservoir 2. Downstream of Cavdarhisar Dam (250m) 3. Near the spring of Kocasu Creek 4. Near the bridge of Kocasu Esatlar 5. Upstream of Kayabogazi Dam 6. Downstream of Kayabogazi Dam, near the bridge 7. Treatment plant Purified Water) are given in Figure 1.

Surface water samples were collected from the areas after small streams pour into the creek and where discharged water mix with the creek (30-40 cm below the surface). The samples were collected from the points where contamination is expected to be higher. All the samples had a volume of 2 liters and were kept in sterilized plastic containers. Meanwhile, pH, Electricity conductivity and temperature values of the samples were measured. Later, these plastic containers were labeled and placed in the fridges in the laboratory (4 °C). Sodium, Potassium, Boron and heavy metal analyses were made by using Perkin Elmer Optical Emission Spectrometer Optima 4300 DV (ICP-OES) after water samples were filtrated.

3. WATER POTENTIAL OF KOCASU CREEK

Source of Kocasu Creek is considered to be the spring waters (cells). Bedir Creek is located at the head of Kocasu Creek. Bedir Creek is fed by waters discharged by Cavdarhisar Dam which is a purpose built dam for irrigation and tributaries join from Kizikdere Creek also at the mouth of Cavdarhisar Dam. These waters join with spring waters at the source location and form Kocasu Creek (Figure 1). Kocasu Creek join with other tributaries along the downstream and at the mouth and get the name Orhaneli Creek and then finally spills into Manyas Lake.

Analysis of flow or discharge data was provided by DSI (General Directorate of State Hydraulic Works) 3. Regional Directorate and the data recorded from Flow Gauging Stations (FGS) regarding Cavdarhisar Dam mouth is given with respect to FGS ref: 03-017on Figure2.

Table 1: Average discharge of Kocasu (before the junction with springs sources) in m³/s belong to the upstream of the watershed.

Sources	Month												Total
	October	November	December	January	February	March	April	May	June	July	August	September	
03-017 Bedir Creek, Average q (m ³ /s)	0,162	0,266	1,17	2,239	2,404	2,194	1,46	0,677	0,327	0,188	0,154	0,144	11,385
03-018 Kızık Creek Average q (m ³ /s)	0,047	0,086	0,32	0,591	0,722	0,72	0,609	0,328	0,136	0,049	0,036	0,033	3,677
Monthly average discharge (m ³ /s)	0,209	0,352	1,49	2,83	3,126	2,914	2,069	1,005	0,463	0,237	0,19	0,177	15,062

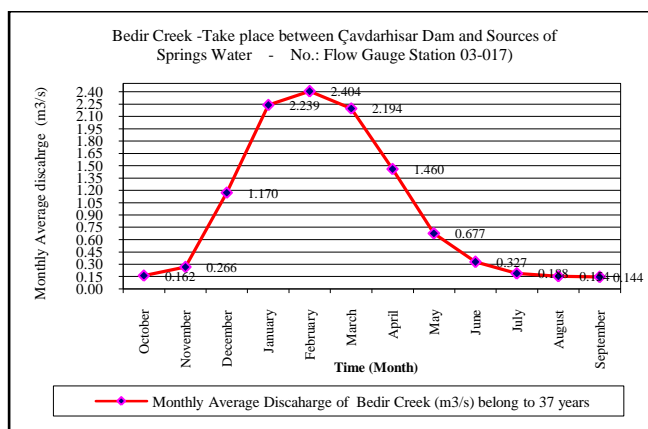


Figure 2: Monthly average discharge of Bedir Creek (m³/sn) belong to 37 years. Source: DSI, 5.

This flow gauge station is located on Bedir Creek. According to record flow measurement carried out by DSI between 1966 and 2005 for a period of 37 years; it is observed that minimum of 0.162 m³/sec (162lt/sec) and maximum of 2.404 m³/sec (2,404 lt/sec) flow rates are recorded related to discharged water from the dam. Although the purpose of Cavdarhisar is an irrigation dam, maximum discharge is set during off season for irrigation. This means, excess water during the months of December to March is discharged at the mouth and consequently leads to the fact that less water is discharged during the irrigation season from Cavdarhisar Dam, which its actual function is to supply water for irrigation. FGS ref: 03-018 is located on Kizikdere Creek (Figure 3).Kizikdere Creek is a left bank tributary to Bedir Creek and its flow is monitored by FGS ref: 03-018 (Figure 3).

According to flow meter measurement between 1967 and 2005 for a period of 36 years; it is observed that minimum of 0.033 m³/sec (33 lt/sec) and maximum of 0.722 m³/sec (722 lt/sec) water flows into Bedir Creek.

Hence the water potential at the location of source head (cells) before joining with spring waters is shown in Table 1.

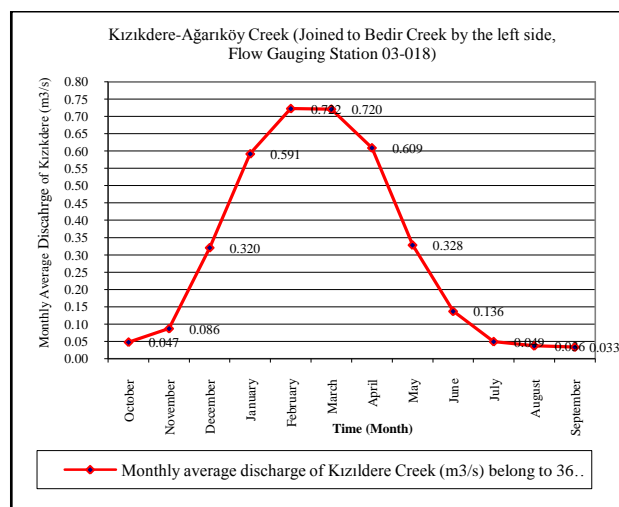


Figure 3: Monthly average discharge of Kızıldere Creek (m³/sn) belong to 36 years. Source: DSI, 5.

This also forms the head waters of Kocasu Creek. The total of flow rates related to Bedir Creek (37 year average) and Kizikdere Creek (36 year average) are plotted on the same graph. Taking into consideration the average monthly flow rates with respect to data obtained in 37 and 36 years, excluding the sources (cells), the minimum and maximum flow rate of Kocasu Creek is determined to be 0.209 m³/sec (209 lt/sec) and 3.126 m³/sec (3126 lt/sec) respectively (Table 1). Flows from main basin are not included in above mentioned figures. Headwaters when joined with these flows will increase the volume of water. Nevertheless it is very difficult to differentiate the amount of head waters and the flow due to absence of a flow gauge station located at end of the source.

Therefore the exact quantity of headwaters cannot be assessed. It is only indicated that the flow rate of a single cell that is located on the left bank of a nearby river is 0.054 m³/sec (54 lt/sec). Considering the formation of a lake at the source region, it has been observed that many small size cells originate underneath the lake waters, creek waters and bottom of rocks. Excess surface waters during rainfall from nearby dried creeks are discharged into Kocasu Creek. Flow gauge station ref: 03-083 is located on Kocasu Creek and monitors

yearlong the amount of water flows coming from Bedir Creek, the sources and river basins. This station is also utilized to measure the flow into Kayabogazi. Monthly average flow rates measured at this station for a period of 7 years is given in Figure 4.

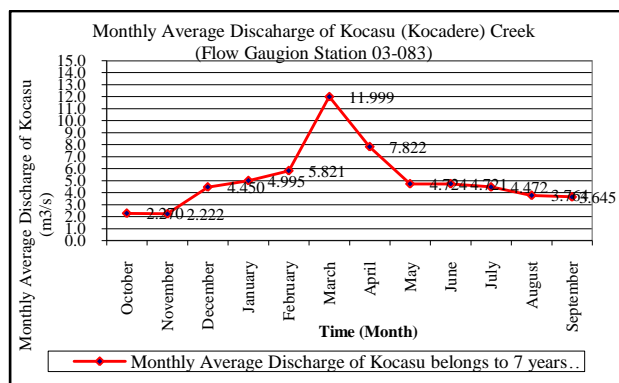


Figure 4: Monthly average discharge of Kocasu Creek (m^3/sn) belong to 7 years. Source: DSI, 5.

The data obtained from this FGS is essential to determine the quantity of water generated by the source locations. It is to be reminded that monitoring carried out during the rainfall seasons will lead to increase in average rates. Source waters are based on the rainfall amount, such that the cells will generate large flows during the rainy periods and small flows during the dry seasons. According to average monthly flow rates over a period of 7 years measured at Kocadere – Esatlar (FGS 03-083) station, minimum flow rate of $2.222 \text{ m}^3/\text{sec}$ ($2222 \text{ lt}/\text{sec}$) is observed during November and maximum flow rate of $11.999 \text{ m}^3/\text{sec}$ ($11999 \text{ lt}/\text{sec}$) is observed during March. S Water source of Kayabogazi Dam is Kocasu Creek and its basin. Purpose of Kayabogazi Dam is to provide irrigation water, flood prevention and supply drinking water (DSI) [5] to the its region. Reservoir water of Kayabogazi is supplied to nearby residential areas as drinking and utility water after process of purification.

As given in Table 2 shows the clean water output of Tavsanlı district water treatment plant (Tavsanlı Municipality). Furthermore, it is observed that Tavsanlı Municipality Water Treatment plant is supplied with average $292.75 \text{ lt. water per second}$ in 2006 was treated as $267.86 \text{ lt. water per second}$ in 2007 by Kayabogazi Dam in order to provide drinking and utility water (Table 2).

Table 2: Produced the amount of clean water in the treatment plant for drinking water of Tavsanlı Municipality (m^3), Turkey.

		Year		
		2006	2007	2008
Months	January	796800	749300	685700
	February	755300	676400	-
	March	823200	683600	-
	April	751000	654300	-
	May	729500	672400	-
	June	747400	661800	-
	July	781600	704700	-
	August	813100	726400	-
	September	772100	727200	-
	October	769800	787000	-
	November	735800	706600	-
	December	756500	697550	-
Total (m^3)		9232100= (292.75 lt/s)	8447250= (267.86 lt/s)	-

Demand for using and drinking (or domestic water) water will increase related to the rate of population increase. Thus, water demand by such residential districts will be supplied by Kocasu Creek tributaries located in upper basin and the cells located at the source of Kocasu Creek. Kocasu creek, being a natural surficial and underground water collection field that serves and will continue to serve as a supply of using and drinking water, shall be preserved in accordance with the “Water Contamination Control Regulation”.

3. CONTAMINATION ANALYSES IN KOCASU CREEK

The results of the analyses were compared with various standards such as Water Contamination Control Regulation (WCCR)[9] - Mainland Water Resources Classification (MWRC)[10], U.S Environmental Protection Agency (EPA)[11], World Health Organization (WHO)[7], European Union (EU)[12] and TS266 [8]. In this study, Mainland Water Resources Classification was chosen as the main standards to compare.

pH Analysis

pH value for Kocasu Creek surface water samples collected in summer from predetermined points were measured by Cole Parmer pH meter. These values are presented in Table 3. The max.and min. pH values for these samples are 8,45 and 7.38 in respectively. The limit values stated in WHO [7] and EU [12] standards are between 6.5 and 8.5.

Table 3: Result values of summer period in surface water samples in Kocasu Creek.

	Sample Station no	Number of samples station and name of the station						
		1	2	3	4	5	6	7
	Location of the samples name	Cavdarhisar Dam reservoir	Downstream of Cavdarhisar dam (250 m)	Near the spring of Kocasu Creek	Near the bridge of Kocasu Esatlar,	Upstream of Kayabogazi Dam	Downstream of Kayabogazi Dam, near the bridge	Treatment plant Purified water
Topographic elevation of the samples location	Elevation from the sea level (m)	1052	1029	957	949	924	896	831
	Feet							
Coordinate of the samples	N (Y)	391029N	391053N	391919N	391939N	392506N	392511N	393218N
	E (X)	0293501E	0293557E	0293801E	0293733E	0293643E	0293712E	0292922E
	Euro user	05974847E 06753070N	05975312E 06755226N	05960749E 06772344N	05959412E 06772144N	05946927E 06779697N	05947455E 06780611N	05921894E 06779631N
	Air temperature during the sampling from the Creek ($^{\circ}\text{C}$)	29	29	32	32	31,5	33	33
	Ph	8,33	7,42	7,38	7,73	8,45	8,12	7,66
	Water temperature of Kocasu Creek, T ($^{\circ}\text{C}$)	25	12	15,5	18	24	21	18
	Electrical Conductivity (mmho/cm, $25^{\circ}\text{C}^{\circ}\text{de}$)	422	490	523	523	398	416	435
	Dissolved Oxygen 8DO)(mg/lt) Above show temperature Down show DO value	<u>at $27,6^{\circ}\text{C}$</u> 7,54	<u>at $13,5^{\circ}\text{C}$</u> 9,36	<u>at 15°C</u> 7,27	<u>at $19,5^{\circ}\text{C}$</u> 8,16	<u>at 23°C</u> 11	<u>at $20,6^{\circ}\text{C}$</u> 8.8	<u>at $21,2^{\circ}\text{C}$</u> 8,23

According to Water Contamination Control Regulation MWCR [10] standards, 6.5-8.5 for Class 1, 6.5-8.5 for class II, 6-9 for class III and $> 6-9$ for class IV. These values show that water quality is determined as “quite contaminated” in terms of pH level; class 3rd and 4th. These values show that surface water quality is determined; class 1rd and 2th.

Electricity Conductivity, EC (μScm^{-1})

As for surface water, EC values were found as max.523 (μScm^{-1}) and min.398. (μScm^{-1}) in (Table 3). According to Mainland Water Resources Classification, no limit values exist regarding Electricity Conductivity for surface water and ground water samples. In TS266 [8], limit values are given as, 650 μScm^{-1} at Class 1-2, Type 1 and 2500 μScm^{-1} at class 2, type 2. In addition, when 2500 μScm^{-1} limits value in WHO [7] and EU [12] standards is considered, no problem is observed in surface water in terms of conductivity.

Temperature (T $^{\circ}\text{C}$)

According to measurements made, the temperature

values for the surface water samples collected from Kocasu Creek are given in Table 3. The average temperature for all points is 19.07°C . The temperature of industrial and drainage waste waters is higher than natural rivers. The increase in the temperature of a river depends on the ratio between total amount of water carried by the river and the amount of waste water that pours into this river as well as the distance flown after this waste water mix with waters of the river. The high temperature caused by industrial and drainage waste water is more obvious during the cold periods of the year, such as late autumn and winter.

Sodium (Na)

According to Water Contamination Control Regulation, total Sodium values are given as 125, 125, 250 ve >250 mgL^{-1} for I., II. III. ve IV class waters respectively. This value is given as 100-200 mgL^{-1} in TS266; and 200 mgL^{-1} in WHO [7] regulations (normal level in natural waters is < 20 mgL^{-1}). Sodium contamination level of Porsuk Creek is displayed in Table 4. The average Sodium values were measured as 6.74 mgL^{-1} .

Potassium (K)

The effects of potassium are very similar to that of Sodium. The factors leading to contamination are generally industrial wastes, agricultural fertilizers and the structure of soil. Water Contamination Control Regulation does not provide a limit value for potassium in its classification. This limit value is given as 12 mgL^{-1} in TS266 [8]. The average potassium (K) values were measured as 2.73 mgL^{-1} .

In order to determine contamination levels of inorganic contamination parameters, the following analyses were made for surface water: Cadmium (Cd), Lead (Pb), Copper (Cu), Chrome (Cr), Nickel (Ni), Zinc (Zn), Manganese (Mn) and Boron (Bo). The limit values of pollutant parameters are taken from WCCR [9] to make a comprehensive comparison of the data obtained from this analysis.

Table 4: Concentration level of heavy metal and other element in surface water samples of Kocasu Creek (mg/L).

Sample no	Ag	Al	As	B	Ba	Ca	Cd	Cr	Ag
1	<0.005	<0.015	<0.005	0,21	0,014	31	<0.0004	<0.0005	<0.005
2	<0.005	<0.015	<0.005	0,155	0,028	46,5	<0.0004	<0.0005	<0.005
3	<0.005	0,172	<0.005	0,125	0,067	39,9	<0.0004	<0.0005	<0.005
4	<0.005	<0.015	<0.005	0,119	0,063	33,5	<0.0004	<0.0005	<0.005
5	<0.005	<0.015	<0.005	<0.007	0,099	49,9	<0.0004	<0.0005	<0.005
6	<0.005	<0.015	<0.005	0,073	0,111	49,5	<0.0004	<0.0005	<0.005
7	<0.005	<0.015	<0.005	0,167	0,056	27	<0.0004	<0.0005	<0.005

Sample no	Cu	Fe	Hg	K	Mg	Mn	Mo	Na	Cu
1	<0.003	0.068	<0.002	3,47	13,4	<0.05	<0.0008	6,61	<0.0013
2	<0.003	0.075	<0.002	3,44	13,8	<0.05	<0.0008	6,50	<0.0013
3	<0.003	0,063	<0.002	2,65	13,8	<0.05	<0.0008	7,44	<0.0013
4	<0.003	0.062	<0.002	2,71	14,2	<0.05	<0.0008	7,07	<0.0013
5	<0.003	0.085	<0.002	1,86	14	<0.05	<0.0008	5,90	<0.0013
6	<0.003	0.083	<0.002	2,47	13,9	<0.05	<0.0008	6,12	<0.0013
7	<0.003	0.088	<0.002	2,57	13	<0.05	<0.0008	7,60	<0.0013

Sample no	P	Pb	Sb	Se	Zn
1	<0.01	<0.003	0,02	0,019	<0.001
2	<0.01	<0.003	<0.0034	<0.005	<0.001
3	<0.01	<0.003	<0.0034	0,01	<0.001
4	0,094	<0.003	0,025	<0.005	<0.001
5	<0.01	<0.003	0,023	<0.005	<0.001
6	0,08	0,109	0,019	<0.005	0,009
7	<0.01	<0.003	<0.0034	0,016	<0.001

Cadmium (Cd)

Along Kocasu Creek, Cadmium level was measured as $\text{Cd} < 3 \mu\text{gL}^{-1}$ in surface water (Table 4). Maximum values were not exceeded in the WCCR [9]. In other words, 1st class quality level was observed in the creek. According to Water Contamination Control Regulation, the limit values are between $3\text{-}5 \mu\text{gL}^{-1}$ for Cd.

Pb (Lead)

Lead contamination level of Kocasu Creek is displayed in Table 4. The average Lead values were measured as $3 \mu\text{g L}^{-1}$. This value decreased $109 \mu\text{g L}^{-1}$ near Downstream of Kayabogazi Dam, near the bridge. In general, Kocasu Creek has the 1st class water quality level in terms of Lead presence WCCR [9], (Table4).

Copper (Cu)

Copper concentration of Kocasu Creek was measured as $0.3 \mu\text{gL}^{-1}$, which is 1st class quality level WCCR [9],

(Table4).

Cr (Chrome)

Chrome concentration of Kocasu Creek was measured as $0.5 \mu\text{gL}^{-1}$, which is 1st quality level WCCR [9], (Table4).

Ni (Nickel)

Nichel concentration of Kocasu Creek was measured as $1.3 \mu\text{gL}^{-1}$, which is 1st quality level WCCR [9], (Table4).

Zn (Zinc)

Zinc concentration of Kocasu Creek was measured as $1.3 \mu\text{gL}^{-1}$. Kocasu Creek had 1st class water quality in terms of Zinc contamination WCCR [9], (Table4).

Mn (Manganese)

Manganese concentration of Kocasu Creek was

measured as $50\mu\text{gL}^{-1}$. The water quality of Kocasu Creek was 1st class in this study WCCR [9], (Table4).

B (Boron)

The highest surface water Boron levels were measured between 210 and $7\mu\text{gL}^{-1}$ in this study. Kocasu Creek had 1st class water quality in terms of Boron WCCR [9], (Table4).

6. CONCLUSION

During the last several decades, accelerating industrial, economic and agricultural development, along with an increasing population and internal migration to cities, has created a tremendous pressure on water resources and associated aquatic ecosystems. These developments not only increased water demands but also caused major water pollution parallel with the amount of use [4].

Recently, it was recognized that there is an urgent need for better coordination among the different governmental organizations that are in charge of the management and conservation of water resources.

The Aegean rivers are not fully regulated yet to meet increasing demands for irrigation, flood control and hydropower generation. However, numerous projects are planned and being implemented to meet these increasing needs[4].

This study deals with surface water contamination in Kocasu Creek. To achieve this purpose, water samples were collected from 7 points. The values in this area were found in the limits stated in Water Contamination Control Regulation (WCCR) for surface water. Surface water was classified as “contaminated” regarding various parameters. Therefore; Surface water resources of Kocasu Creek is “drinkable” and should be used as “drinking water”.

Moreover, the fields irrigated with the water from Kocasu Creek and the plants grown by using surface water. The determination of this contamination level in Kocasu Creek, which is used as the only water resource for domestic, industrial and agricultural uses in the region, and the ground water resources in its basin, is important since they complement the studies done on integrated contamination research at basins level in other regions.

REFERENCES

- [1] Shmueli, D.F., “Water Quality in International River Basin”, *Political Geography*, Vol.18, pp. 437-476, 1999.
- [2] Kovacs, G., Decision Support Systems for Managing Large International Rivers. In: Vlachos,

E., Webb, A., Murphy, I., (Eds.), *The Management of International River Basin Conflicts*, pp.132-133, 1986.

- [3] Gumrukcuoglu, M. and Basturk, O., “Sürdürülebilir Su Yönetiminde Nehir Kirliliği Üzerine Bir Çalışma”, *TMMOB 2. Su Politikaları Kongresi*, pp. 521-529, 2007. (in Turkish)
- [4] Klement, T., Robinson, C.T., and Uehlinger, U., *Rivers of Europe*, Academic Press, Chapter17, pp. 643-673, USA, 2009.
- [5] DSI, State Hydraulic Works, “Statistics on Hydropower”, Ankara, Turkey, www.dsi.gov.tr, accessed date 10 April 2011.
- [6] EIE, General Directorate of Electrical Power Resources Survey and Development Administration, “Water Quality Data for Surface Waters in Turkey”, No: 28, 438 pp., Turkey, 2003. (in Turkish)
- [7] WHO, The World Health Organization, *Drinking Water Standard*, accessed date 25 July 2009.
- [8] TS266, Turkish Drinking Water Standard (p.96), 1997, (in Turkish).
- [9] WCCR, Water Contamination Control Regulation Standard, Ministry of environment and Forestry Turkey, 25687, 31.12.2004.
- [10] MWRC, Mainland Water Resources Classification, 2004.
- [11] EPA 200.7, U.S. Environmental Protection Agency, *Safe Drinking Water is in Our Hands- Existing Standards and Future Priorities*, 1999.
- [12] EU, European Union, Council Directive 98/83/EC of 3 November 1998 on the Quality of Water Intended for Human Consumption, 1998.

RELEVANT WEBSITES

<http://www.dsi.gov.tr>

<http://www.eie.gov.tr/>

<http://nkg.die.gov.tr/>

<http://www.cevreorman.gov.tr/>

http://www.who.int/water_sanitation_health/dwq/guidelines/en/index.html

Rheological Behavior of RBC Sludge at Different Steps of Treatment

Basim Abu-Jdayil¹, Fawzi Banat², Mukheled Al-Sameraiy³

¹ Chemical & Petroleum Engineering Department, U.A.E. University, Al-Ain, UAE

(*Babujdayil@uaeu.ac.ae*)

² Department of Chemical Engineering, Petroleum Institute, Abu-Dhabi, UAE affiliation (*fbanat@pi.ac.ae*)

³ Environmental Research Center, University of Technology, Baghdad, Iraq (*Babujdayil@uaeu.ac.ae*)

ABSTRACT

The rheological characterization of sewage sludge at different steps of wastewater treatment is important since it allows predicting and estimating sludge behavior when submitted to almost all treatment and disposal operations. Rotating biological contactor (RBC) is being widely used for wastewater treatment, which is a biological treatment process following primary treatment. The rheological characterization of RBC sludge at different solid contents was carried out using a rotational viscometer. The effects of mesophilic and thermophilic treatments on the sludge rheological properties were examined. It has been found that the thermophilic treatment of sludge was more efficient than the mesophilic process in modification of the rheological properties of treated sludge.

Keywords: Sludge rheology, activated sludge, RBC sludge, Bingham fluid, thermophilic treatment, mesophilic treatment

1. INTRODUCTION

Wastewater treatment process generates significant quantities of sludge from suspended solid in the feed, biomass generated by biological operations, and precipitates from added chemicals [1]. Raw sludge is an unstable solids suspension that must be subjected to specific and complex treatment before an environmentally acceptable product is obtained for final disposal.

The rheological characterization of sewage sludge at different steps of wastewater treatment is important since it allows predicting and estimating sludge behavior when submitted to almost all treatment and disposal operations.

At the moment, rheological parameters are essentially used in sludges conditioning or for optimizing sludge consistency for the storage, spreading [2-4] and as indicators of sludge quality in aeration tanks [5]. In addition, Hasar et al. [6] have pointed out that the activated sludge viscosity has a major impact on pressure loss in pipes, transport phenomena near the membrane and sludge conditioning in next step. The rheological characteristics of sludge depend on many factors such as source, solid concentration, temperature, and sludge treatment method [6,7] showed that rheological parameters are strongly dependent on the sludge type and total solid content. Battistoni et al. [8] has also observed that sludge rheology is strongly dependent on feed characteristics and conditions applied.

The thermal treatment is integrated in the sludge handling units with the aim to reduce sludge production, enhance biogas production in anaerobic digesters, obtain pathogen inactivation, and/or improve sludge dewaterability.

Rotating biological contactor (RBC) is being widely used for wastewater treatment but there is an apparent lack of knowledge about the rheological properties of the produced sludge. A rotating biological contactor or RBC is a biological treatment process used in the treatment of wastewater following primary treatment, which removes the grit and other solids through a screening process followed by a period of settlement. The RBC process involves allowing the wastewater to come in contact with a biological medium at the rotating biological cofactors in order to remove pollutants from the wastewater. The basis of the practical use of the RBC is that the dissolved oxygen in the reactor did not have significance on treatment efficiency because sufficient amount of oxygen could be supplied during the air exposure cycle [9].

The objective of this work was to study the rheological characteristics of sewage sludge generated from Rotating Biological Contactors (RBC) technology at different steps of treatment. The effects of the solid content on the rheological parameters of RBC sludge were investigated. In addition, the effect of the thermophilic and mesophilic treatment of the rheological properties of RBC sludge was studied. Since the sludge samples were collected from the sludge tank that comes after the RBC unit, the rheological characterization presented here can be used to improve the storage and transportation system of the RBC sludge and the conditioning process.

2. MATERIALS AND METHODS

2.1 Sludge Sample and Treatment Plant

Sludge samples were collected from a wastewater treatment plant located in the campus of Jordan University of Science and Technology (JUST) and

thereafter were stored in a refrigerator at a temperature of 8 °C before being used in the tests. The sludge samples were collected from the sludge tank that comes after the RBC unit. The average biological oxygen demand (BOD) of wastewater is about 400 mg/L. The BOD of the treated wastewater is no more than 10 mg/L. Wastewater passed through several steps of treatment, including physical as well as biological steps. Six rotating biological contactors (RBC) are used in the biotreatment step. The RBC contactors are made from plastic discs supported on a shaft passing perpendicularly through the center of each disc. The discs are slowly rotated at 1.25 rpm in a contour-bottomed tank containing the wastewater. As the surfaces of the discs are alternately exposed to the wastewater and air, biological growth forms on these surfaces. The biological growth will adsorb and assimilate the organic materials in solution. Air is also supplied to the wastewater in the tank to further increase the growth of bacteria. Excess biomass is sloughed off by shearing as the growth passes through the liquid and is kept in suspension by the mixing of the discs. The treated wastewater flows out of the tank into a clarifier to remove the suspended solids. The clarified wastewater was chlorinated before being pumped to the university lake to be used for irrigation purposes. The remaining solids and water in the clarifier, i.e. sludge, is pumped to the sludge tank as shown in Figure 1. Sludge samples tested in this work were collected from the bottom of the sludge tank.

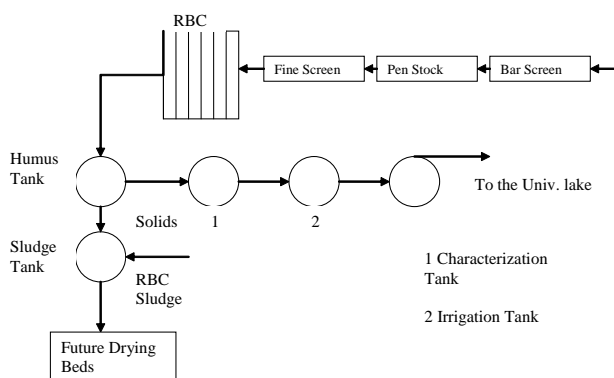


Figure 1: Block diagram for JUST wastewater treatment plant.

2.2 Mesophilic Treatment

The samples of RBC sludge with total solid content of 31.4 g/L were loaded in an open vessel and heated to 37 °C in a jacketed vessel using a circulating water bath. These samples were kept at 37 °C for different periods of time (0.25 to 4 hrs) and then allowed to cool at room temperature before measuring the rheological properties.

2.3 Thermophilic Treatment

Sludge samples with total solid content of 31.4 g/L were inserted in a vessel, which is covered with Para film. A

small hole was made on the surface of the Para film. The vessel was transferred into a water bath maintained at 40, 45, 50, 55 and 60 °C. The treatment time was varied between 1 to 72 hrs. After treatment, the samples were stored for one day at room temperature before conducting the rheological tests.

2.4 Rheological Measurements

The steady rheological properties of RBC sludge were measured using a concentric cylinder viscometer (Haake VT 500, MV1-system), which composed of an inner cylinder rotating in a stationary outer cylinder. The radius of the rotating cylinder is 20.04 mm, the length of the cylinder is 60 mm, and the gap width is 0.96 mm. For every point on the flow curves a constant shear rate was used. After attaining a constant the shear–stress signal, which required about 30 seconds, the values of shear stress and viscosity were recorded. The viscometer was thermostatically controlled with a water circulator (Haake D8) at the desired temperature.

3. RESULTS AND DISCUSSION

3.1 Rheological Properties of Fresh sludge

The rheological properties of sludge material can be significantly affected by variables such as shear rate, temperature and total solids [10]. In many cases, solid concentration was the most important parameter affecting the sludge rheology [6,10-12]. Sewage contains solid materials like bones, stones, wood, rages, etc, which make pumping of sewage difficult. The percentage of solids in sewage gives an indication of the concentration and physical state of its principal constituents. The combination of inorganic and organic solids is called “total suspended solids” [13]. In this work, the effects of total suspended solids (TSS = 32.2 g/L – 50.2 g/L) on the rheological behavior of RBC sludge were investigated.

Figure 2 illustrates the flow curves of RBC sludge at different TSS values. For all investigated TSS, the sludge samples showed shear-thinning behavior with a yield stress. Bingham model (equation 1) has been used to describe the non-Newtonian behavior of sludge suspensions [11,12]:

$$\tau = \tau_o + \eta_B \dot{\gamma} \quad (2)$$

where τ is the shear stress, τ_o is the yield stress; η_B is the Bingham viscosity and $\dot{\gamma}$ is the shear rate. In the sludge samples the yield stress must be reached before flow starts. Its presence is due to the resistance of solid particles opposed to deformation, until the applied stress exceed the yield strength of the solid phase and that the sludge show flow. It is commonly admitted that the yield stress of suspensions is linked to the existence of an interconnected three dimensional network of flocs. The value of the yield stress corresponds to the stress

needed to be applied to overcome the cohesion Van der-Waals forces and induce the flow of the suspension [14].

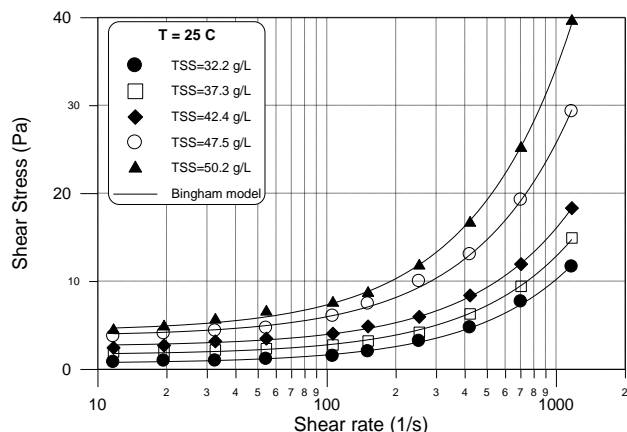


Figure 2: Flow curves of RBC sludge at different solid contents.

Figure 2 also shows the flow curves of RBC sludge for different values of TSS, fitted to the Bingham model, while the model parameters obtained by non-linear regression for different TSS are reported in Table 1. The high regressions coefficients (around 0.99) indicated that the Bingham model describe adequately the rheological behavior of RBC sludges under different TSS. As shown in Table 1, both the yield stress and Bingham viscosity increased as the solid content was increased. The obtained yield stress increased significantly from 697 *mPa* at TSS = 32.2 *g/L* and T = 25 °C to 4354 *mPa* at TSS=50.2 *g/L* and T = 25 °C. On the other hand, the Bingham viscosity exhibited less pronounced evolution, where it increased from 9.6 *mPa · s* at TSS = 32.2 *g/L* to 30.0 *mPa · s* at TSS = 50.2 *g/L*. It is clear that the yield stress is more sensitive than the Bingham viscosity for the variation in solid content.

3.2 Thermal Treatment

The mesophilic treatment process is the anaerobic digestion by biological oxidation by anaerobic action at or below 40 °C while the thermophilic process is the anaerobic digestion at a temperature within the thermophilic range, which is usually considered to be between 40 and 60 °C. Anaerobic reactors are normally operated at mesophilic temperature or at moderate thermophilic temperature. Thermal processes are used to either dry the sludge or to oxidize its organic content. A thermal drying serves as an important preliminary stage for further thermal treatment (incineration and pyrolysis) that minimizes the amount of remaining sludge, improves its hygienic quality and provides the opportunity for an economical resources recovery [15]. During the heat treatment, a very significant change in the apparent viscosity of sludge was observed [16]. This generates significant change in velocity profiles, considerably modify temperature profiles and pressure drops inside the process equipment.

Table 1: Regressed parameter values of Bingham model used to describe the rheological data for different total solid content.

TSS (g/L)	τ_o (mPa)	η_B (mPa · s)
32.2	697	9.6
37.3	1674	11.2
42.3	2630	13.5
47.5	3794	22.0
50.5	4354	30.0

The effect of mesophilic treatment time on the flow curves of RBC sludge measured at room temperature is shown in Figure 3. The shear stress of the untreated samples is less than that of the anaerobically treated samples. Most likely, the sludge structure was changed since the apparent viscosity of the treated sludge increased with the treatment time (Figure 3).

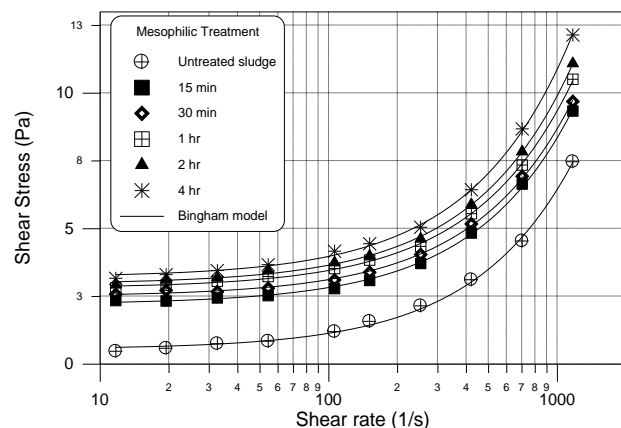


Figure 3: Flow curves of mesophilic treated sludge for different times.

The Bingham model was used to fit the experimental data. The Bingham model constants τ_o and η_B (Table 2) revealed that the mesophilic treatment changes the rheological behavior of the RBC sludge. When the time of treatment was increased to 4 hr, the value of yield stress, τ_o , was 5.85 times that of the untreated sample, while Bingham viscosity, η_B , was 31% higher than that of the untreated sample.

Table 2: Parameter values of Bingham model used to describe the rheological data for mesophilic treated sludge

Treatment	τ_o (mPa)		η_B (mPa · s)	
	Measured directly	Stored	Measured directly	Stored
Untreated sludge	549		5.90	
15 min	2213	2355	6.15	6.20

30 min	2504	2576	6.20	6.56
1 hr	2804	2718	6.56	7.32
2hr	2958	2885	6.96	7.52
4 hr	3210	3254	7.69	7.93

It can be seen from Table 2 that storing the treated sludge for 24 hrs before conducting the rheological tests, led to some increase in the values of rheological parameters (yield stress and Bingham viscosity), which means that some aggregations have been formed during the storage period.

The effects of thermophilic conditions (i.e. the thermal treatment at 40-60 °C) on the rheological properties of RBC sludge were also investigated. The time of thermal treatment was varied between 1 and 72 hrs. The apparent viscosity of the treated samples was measured after one day of storage at 25 °C.

As can be seen in Figure 4, increasing the treatment temperature resulted in a clear increase in the viscosity of the sludge. However, above 55 °C the increase in the sludge viscosity was insignificant. On the other hand, increasing the treatment time led to an increase in the apparent viscosity of sludge, see for example Figure 5. Again, increasing the treatment time above 48 hrs did not result in remarkable increase in sludge viscosity. This clear difference between the treated and untreated sludge can be attributed to the effect of thermophilic treatment, which altered the sludge structure. Cecchi et al. [17] attributed such behavior to the lysis of mesophilic organisms as well as to the increased rate of biodegradation of sludge organic compounds.

The rheological properties of treated sludge were well fitted by the Bingham model, see Figures 4 and 5.

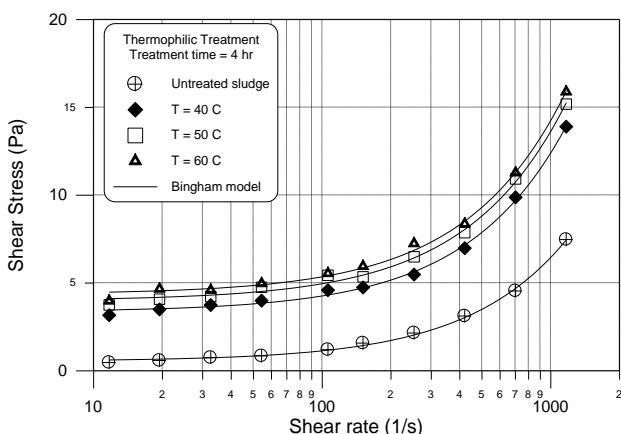


Figure 4: Effect of thermophilic temperature on the flow curves of RBC sludge.

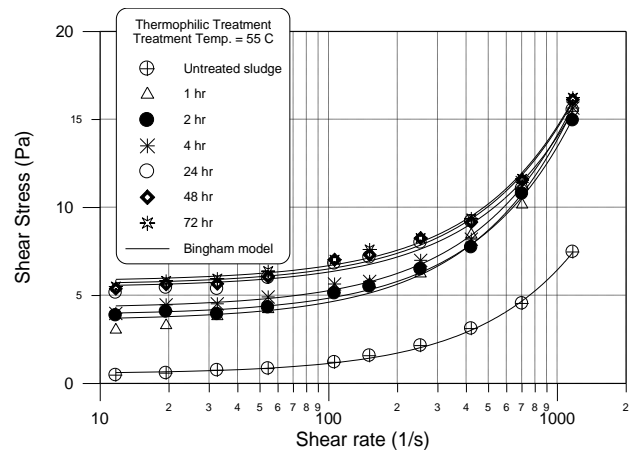


Figure 5: Effect of thermophilic treatment time of the flow curves of sludge.

As is evident from Figure 6, increasing the treatment temperature has increased the yield stress of sludge which reached an equilibrium state at 55 °C. Further increase in the treatment temperature to 60 C did not lead to significant development in the sludge yield stress. On the other hand, Figure 6 shows that increasing the treatment time from 1 to 48 hrs has resulted in noteworthy increase in the yield stress of the sludge; further increase in the treatment time to 72 hrs has no significant effect on the yield stress. The exposure of sludge samples to thermal treatment for different times is believed to cause some dramatic changes in the structure of sludge which in turn change the sludge specific properties.

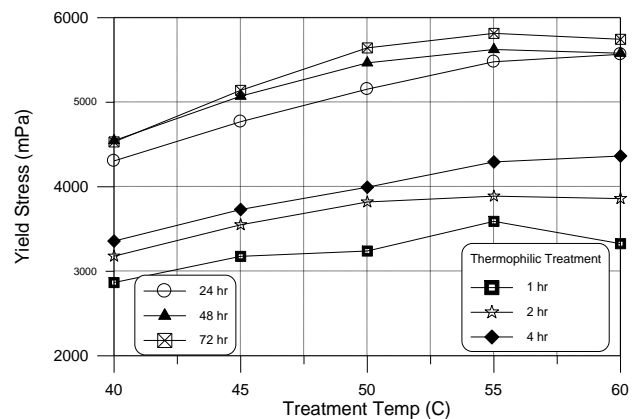


Figure 6: Dependence of the yield stress on thermophilic treatment temperature and time.

The Bingham viscosity has been widely used as a parameter for characterizing sludge rheology. Figure 7 shows the effect of treatment temperature and time on the Bingham viscosity. It is clear that increasing the treatment temperature increased the Bingham viscosity of sludge. At the same time, the treatment time has no clear effect on the Bingham viscosity of sludge.

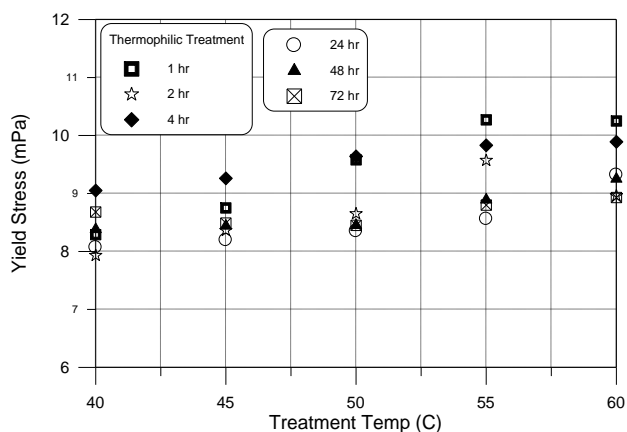


Figure 7: Dependence of the Bingham viscosity on thermophilic treatment temperature and time.

Obviously, the values of the Bingham parameters τ_0 and η_B calculated after mesophilic or thermophilic treatment increased compared to those of untreated samples. For example, at constant treatment time of 4hr, the value of yield stress increased by 6 times after the mesophilic treatment while it increased by more than 6 times after thermophilic treatment at 40 °C and by 10 times after thermophilic treatment at 60 °C. On the other hand, the values of Bingham viscosity increased by 35% after mesophilic treatment while they increased by 53% after thermophilic treatment at 40 °C and by 58% after thermophilic treatment at 60 °C. In conclusion, the thermophilic treatment caused more increase in the apparent viscosity of the RBC sludge than that caused by the mesophilic treatment. This increase in the apparent viscosity was represented by clear increase in the yield stress with small increase in the Bingham viscosity. It seems that the thermal treatment increased the interactions between the sludge particles that led to increase the yield stress, but these interactions were not strong enough to withstand the shearing process where after passing the yield stress most of these interactions were broken that yielded no significant increase in the Bingham viscosity.

4. CONCLUSIONS

In this work, the dependence of rheological properties of RBC sludge on solid content (TSS) has been experimentally investigated. Results revealed that the RBC sludge behaved like a Bingham fluid. When the solid content was increased the Bingham parameters (τ_0, η_B) found to increase accordingly. It was clear that the yield stress was more sensitive than the Bingham viscosity for the variation in solid content. Mesophilic and thermophilic treatments of sludge led to significant increase in the apparent viscosity of sludge. This modification in the rheological behavior of sludge expressed itself mainly by clear increase in the yield stress rather than the Bingham viscosity. On the other hand, the thermophilic treatment of sludge was found to be more efficient than the mesophilic process in

modification of the rheological properties of treated sludge.

REFERENCES

- [1] Sundstorm, D., and Klei, H., *Wastewater Treatment*, Prentice Hall, NJ, 1979.
- [2] Novak, L., Larrea, L., Wanner, J. and Garcia-Herreras, J.L. "Non-filamentous activated sludge bulking in a laboratory scale", *Water Research*, Vol. 27, 1339–1346, 1993.
- [3] Badino Jr, A.C., Facciotti, M.C.R. and Schmidell, W. "Estimation of the rheology of glucoamylase fermentation broth from the biomass concentration and shear conditions," *Biotech Technol*, Vol. 13, pp. 723–6, 1999.
- [4] Trejo-Tapia, G., Jimenez-Aparicio, A. and Villarreal, L. "Rodriguez-Monroy, M. Broth rheology and morphological analysis of *Solanum chrysotrichum* cultivated in a stirred tank," *Biotech Lett*, Vol. 23, pp. 1943–1946, 2001.
- [5] Guibaud, G., Tixier, N. and Baudu, M. "Hysteresis area, a rheological parameter used as a tool to assess the ability of filamentous sludges to settle," *Process Biochemistry*, Vol. 40, pp. 2671–2676, 2005.
- [6] Hasar, H., Kinaci, C., Ünlü, A., Togrul, H. and Ipek, U. "Rheological properties of activated sludge in a SMBR," *Biochemical Engineering Journal*, Vol. 20, pp. 1–6, 2004.
- [7] Pevere, A., Guibaud, G., van Hullebusch, E., Lens, P. and Baudua, M. "Viscosity evolution of anaerobic granular sludge," *Biochemical Engineering Journal*, Vol. 27, pp. 315–322, 2006.
- [8] Battistoni, P., Fava, G., Stanzini, C., Cecchi, F. and Bassetti, A. "Feed characteristics and digester operative conditions as parameters affecting the rheology of digested municipal solid wastes," *Water Science and Technology*, Vol. 27, pp. 37–45, 1993.
- [9] Kubsad, V., Chaudhari, S. and Gupta, S.K. "Model for oxygen transfer in rotating biological contactor," *Water Research*, Vol. 38, pp. 4297–4304, 2004.
- [10] Abu-Jdayil, B., Banat, F. and Al-Samraiy, M. "Steady Rheological Properties of Rotating Biological Contactor (RBC) Sludge," *J. of Water Resource and Protection (JWARP)*, Vo. 2, pp. 1–7, 2010.

- [11] Mu, Y. and Yu, H.Q. "Rheological and fractal characteristics of granular sludge in an upflow anaerobic reactor," *Water Research*, Vol. 40, pp. 3596 – 3602, 2006.
- [12] Mori, M., Seyssiecq, I., and Roche, N. "Rheological measurements of sewage sludge for various solids concentrations and geometry," *Process Biochemistry*, Vol. 41, pp. 1656–1662, 2006.
- [13] Hussain, S.K., *Public Health Engineering*, Tech India Publications, Satya Prakashan, 1990.
- [14] Seyssiecq, I., Ferrasse, J.H. and Roche, N. "State-of-the-art: rheological characterization of wastewater treatment sludge," *Biochemical Engineering Journal*, Vol. 16, pp. 41–56, 2003.
- [15] Hassebrauck, M., and Ermel, G. "Two examples of thermal drying of sewage sludge", *Water Science and Technology*, Vol. 33, pp. 235-242, 1996.
- [16] Russeil, C., and Gordon, C. *Advanced Wastewater Treatment*, 2th edn, New York, 1989.
- [17] Cecchi, F., Pavan, P., Musacco, A., Alvarez, J.M., and Vanllini, G. "Digesting the organic fraction of municipal solid waste: moving from mesophilic (37 °C) to thermophilic (55 °C) conditions", *Waste Management & Research*, Vol. 11, pp. 403-414, 1993.

A Wireless Sensor Network for Water Pipeline Leak Detection

Ahmed Hassanin, Mustahsan Mir, Farooq Mukhtar

amh90@ieee.org, m.mir@ajman.ac.ae, farooqalmukhtar@yahoo.com

Department of Electrical Engineering

Ajman University of Science & Technology, Ajman, UAE

ABSTRACT

This paper details the design, implementation and testing of a wireless sensor network for water pipeline leak detection. The developed prototype system is composed of a number of small wireless nodes distributed along the pipelines in the water supply system. Each node is equipped with a pressure sensor to detect and locate leaks using the pressure point analysis method. If a leak occurs the sudden change in pressure will be sensed by nearby nodes. The nodes will then relay an alarm message to other nearby nodes until this alarm reaches the main control room and the exact location of the leak is identified. The design and simulation of the network protocols run by the nodes as well as the hardware implementation of the nodes are discussed in detail. Furthermore, the power consumption of the nodes was analyzed to determine the power supply specifications and requirements. The paper also compares the developed system to suggested or currently deployed ones. It explains how this system overcomes many of the problems faced by current techniques. The results and analysis show superior performance and huge cost reduction compared to other systems. Further analysis of the leak detection method is needed on larger pipeline models or using accurate simulators.

Keywords: Wireless sensor networks, pipeline leak detection, pressure point analysis, water distribution system.

1. INTRODUCTION

More than 48 billion m³ of water is lost in underground distribution systems worldwide per year. In many regions this water is produced through a long and expensive desalination process. The water leakage can also damage nearby structures causing a huge economical loss. For example, in Croatia more than 41% of the water produced was lost in underground pipelines leaks and periodic scanning of the pipelines reduced the losses by only 4% [1]. However, by continuously monitoring the underground pipelines all the leaks will be detected and located within minutes which will greatly reduce water losses. Furthermore, leak detection can prevent pipeline total failure as reported in [2].

The most commonly used leak detection methods are the acoustic noise correlation and pressure point analysis. In acoustic noise correlation, the noise produced by the escaping fluid can be used to detect and even locate the leak [3]. However many references such as [2] and [4] have indicated that the noise greatly attenuates as the distance from the leak increases, especially in large pipes (pipes larger than 12" in diameter). Furthermore, the noise generated by moving vehicles can interfere with the leak noise causing many false alarms [5].

In pressure point analysis, the fluid pressure is continuously monitored. If a leak occurs the change in pressure will create a wave that will propagate along the pipeline in both directions. If the leak is not big enough to produce a sudden change in pressure then a change in the pressure will develop between points before and after the leak location [4]. This method is widely used in

oil and gas pipeline systems and is not affected by the outside environment. Leaks as small as 0.5% were detected and located by Jun Zhang in [3]. In this paper the pressure point analysis method is utilized for detecting and locating leaks using a wireless sensor network.

The selected leak detection technique needs to be deployed all over the pipeline system for monitoring and detecting leaks in the entire system. Several monitoring systems exist and several others have been suggested by researchers in the past few years. The simplest system consists of a team of trained personnel equipped with geophones; devices that can be used to listen to underground leaks. The team will scan the pipeline system with their equipment looking for leaks as shown in Figure 1. It is obvious that scanning the underground pipeline system of a big city will take months if not years therefore a leak may develop and go unnoticed for a long time.

Recently, fiber optic cables were used to detect and locate leaks in pipeline systems. The cables are normally extended along the pipeline walls and if a leak occurs, the leaked material will change the ambient temperature of the cable. It has been shown that some scattering effects of injected laser light depend on the cable temperature and strain [6]. Therefore the fiber cable can detect and locate the leak up to few meters. However, this approach requires huge installation and maintenance costs since fiber optic cables are expensive and will have to be distributed over tens of kilometers below the surface.

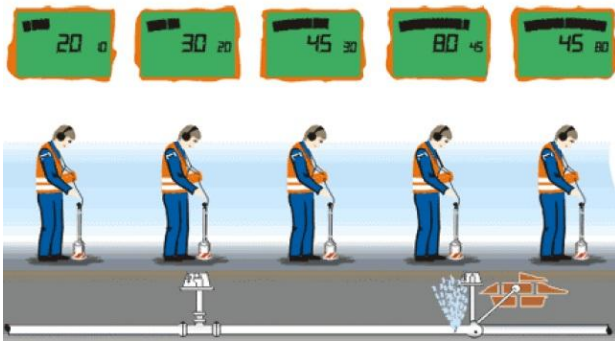


Figure 1: Scanning a pipe using geophones

Recently, the idea of using a wireless sensor network to monitor the underground pipeline system was proposed. Unlike the previous systems, the distributed wireless network can detect and locate leaks in all pipes almost instantly. A wireless sensor network (illustrated in Figure 2) is a group of detection stations or nodes that are spatially distributed over a wide area. Those nodes monitor parameters like temperature, humidity and pressure using specialized sensors. Each node is often equipped with a microcontroller unit that can process and store the sensors output. The nodes utilize wireless transceivers in order to send data to each other. They normally form a wireless ad-hoc network, where nodes function as repeaters, relaying data packets to one or more base stations [7].



Figure 2: Pipeline monitoring using WSN

Researchers in [8] have suggested placing the nodes underground and transmitting their data wirelessly to relay nodes above ground. However, the research indicated that a relatively huge amount of power will be wasted trying to send the data wirelessly in such a hostile channel. In our system, the sensors will be placed underground with wires connecting the sensors to the nodes above ground.

A somewhat different approach is used by Mohammad and Jawhar who have proposed a combined wired and wireless communication network for monitoring pipeline infrastructure [9]. The main problem with this system is that all nodes share a common communication medium. If tens or hundreds of nodes exist, the amount of collisions will hugely degrade the network speed and performance.

Network protocols are typically separated into layers. Layer two is responsible for medium access control and error detection while layer three performs other tasks such as routing data to the destination through the

shortest path. However, research has indicated that a cross-layer architecture can greatly enhance network performance in WSN [7]. In [10] the authors suggested a routing and addressing scheme for a WSN used for monitoring pipelines. The main disadvantage of this scheme (depicted in Figure 3) is that three different node types exist: Basic Sensor Nodes, Data Relay Nodes and Data Discharge Node. Each m number of basic nodes will send their data to one relay node and then every n number of data relay nodes will connect to a data discharge node. Each type is equipped with a different wireless transceiver and is running a different code. This will create huge debugging and installation issues and will create a Tree-like topology. In our system the nodes will gather data and will also relay messages to the next nodes while dedicated nodes will be placed on the edges of the pipeline to collect the data from the sensor nodes. This approach takes advantage of the inherent linearity nature of this application as all nodes are placed in one line.

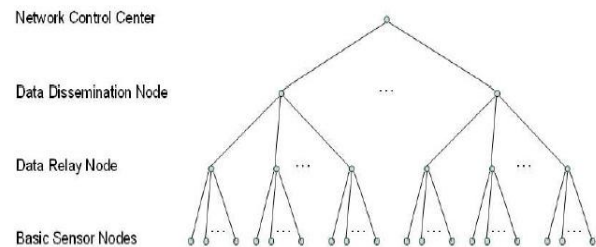


Figure 3: WSN hierarchy suggested in [10]

The design, simulation and implementation of the network protocols run by the nodes are discussed in **Section 2**. Power analysis of the nodes under different operational conditions is detailed in **Section 3**. Finally, **Section 4** briefly describes a prototype pipeline model used to test the proposed leak detection method. Some test results obtained by using this model are also presented in this section.

2. WIRELESS NETWORK PROTOCOL

We decided to design our own network protocol because current wireless protocols do not take into account the unique requirements of wireless sensor networks. For example:

1- Wi-Fi and Bluetooth can extend for 100 meters but will consume 100mW.

2- Zigbee (802.15.4) has a very narrow range (between 10 and 75 meters) which does not suit our application.

Figure 4 shows the wireless transceiver used in implementing a node. It operates at a frequency of 915MHz with a range of 200m LOS. It uses FSK modulation which increases the signal's immunity to noise.



Figure 4: Wireless transceiver from Hope-RF

Figure 5 shows a positioning scheme suggested by [10]. In this scheme, each node should have at least four neighbors so if a node fails on one side, the other nodes can still relay data to that side.

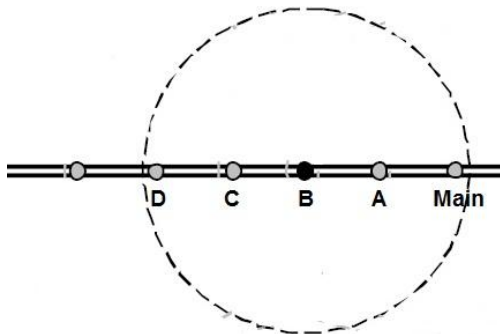


Figure 5: A suggested positioning scheme in [9]

The wireless network protocol works as follows:

- 1- The main node on one end of the pipe will send a broadcast to all nearby nodes containing a reference time to ensure all nodes can be synchronized.
- 2- The main node will ask nearby nodes to send their addresses to confirm their existence. It will then add all received addresses to a list called the children list. All nearby nodes will consider the main node their father node.
- 3- The main node will then ask each node in the children list to synchronize with its own neighbors. In Figure 5, node B will now act as the main node and will synchronize with nodes C and D. It will also add them to its children list.
- 4- The procedure in 1, 2 and 3 will get repeated until all nodes are synchronized and an unbalanced tree topology (similar to the topology in Figure 6) will be created.

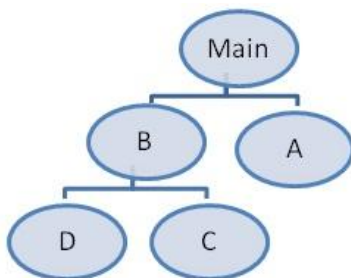


Figure 6: The relation between the nodes after the synchronization stage

5- The main node will issue a get data order to each node separately which will cause the data to recursively flow through the network to the main node.

By ensuring that the network is synchronized, the protocol will allow the whole network to enter the sleep mode and then wake up in almost the same time which will hugely reduce the power consumption as detailed in the next section.

Power consumption will be reduced by yet another feature. Since the protocol eliminates collisions (except possibly in the synchronization stage), the nodes will not need to retransmit data as in CSMA/CA scheme.

The wireless protocol was simulated using a modified setup in ISIS Proteus software, as depicted in Figure 7.

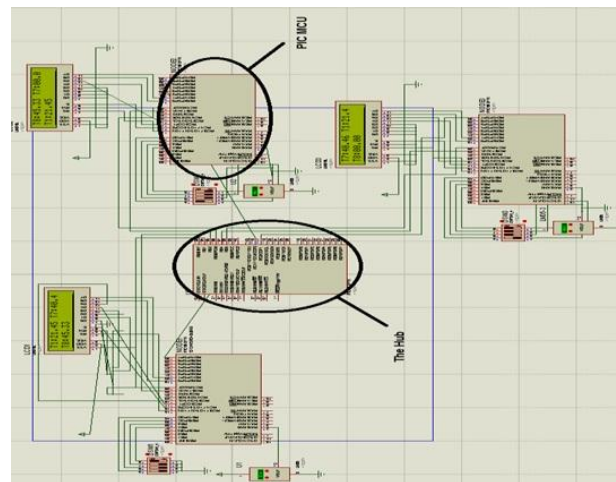


Figure 7: Simulating the protocol on ISIS Proteus

The simulation allowed us to test the protocol operation under different scenarios. Now with the network protocol designed and simulated, the nodes were tested on real hardware. We used a PIC16F877A MCU and LM35 temperature sensor in the first stage. After the wireless protocol was completely tested we replaced the temperature sensor with pressure sensor to monitor pipelines as detailed in the last section. Figures 8 and 9 show the breadboard and PCB implementation of a node.



Figure 8: Testing a node on a project board



Figure 9: PCB Implementation of a node

3. POWER CONSUMPTION ANALYSIS

Since power consumption is the main concern of Wireless Sensor Networks, it is essential to devise a way to continuously measure the power consumed by a node. NI LabVIEW Data Acquisition Card (DAQ) was used for this purpose. We chose LabVIEW because the nodes enter different stages (Transmission, Reception, Processing, etc.) within milliseconds, therefore it is impossible to manually measure the power consumption.

Figure 10 shows the current drawn by the node with the wireless transceiver turned off. The MCU normally draws 1.5mA, but this drops to 1µA in sleep mode. The LCD draws an additional 130mA by itself (as shown in Figure 11). Figure 12 also indicates that when the transceiver is in idle state waiting for data to be sent or received, the node draws an additional 25mA. These facts explain why it is necessary for the nodes to turn off their transceivers and sleep most of the time. The LCD was also removed to reduce the power consumption.

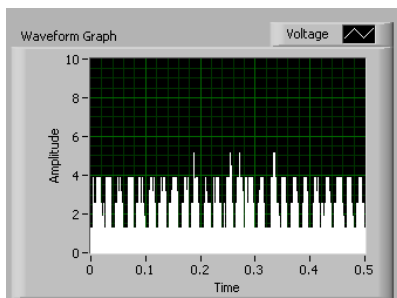


Figure 10: The PIC MCU working only

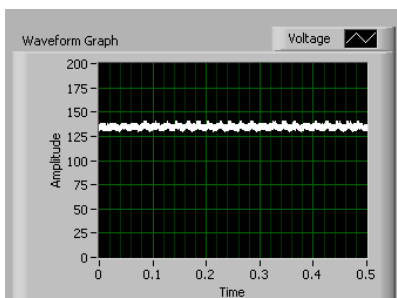


Figure 11: LCD turned on

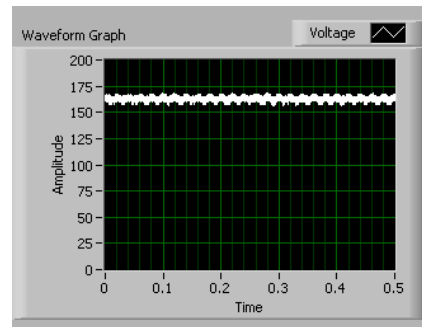


Figure 12: The Transceiver turned on

Finally we observed the power consumed during the transmission stage. Figure 13 shows the large amount of current drawn during transmission. The current jumped more than 30mA. It is therefore essential to reduce the number and duration of transmission. Our protocol accomplishes this task by almost completely eliminating collisions as discussed in the previous section.

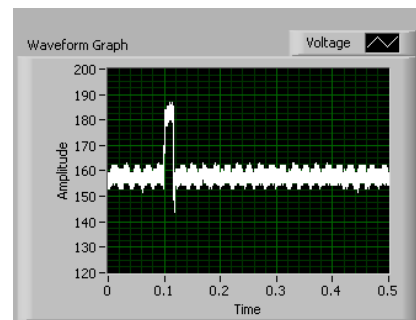


Figure 13: Current drawn during transmission

4. PIPELINE MODEL

A small pipeline model was built to implement and test the pressure point analysis technique in leak detection. The model shown in Figure 14 consists of a pipe carrying water and two small pipes that act as leaks. Three pressure sensors were inserted inside the pipe before and after the leak points. It's worth noting that valves are attached to the leak pipes to control the size of the leak.

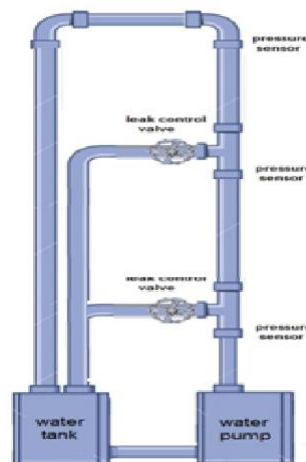


Figure 14: Pipeline model

In this model a pump was used to pump the water from the tank to the pipe. By opening the valves a sudden change in pressure or a pressure difference between the points before and after the leak is reported by the nodes attached to every pressure sensor. Figure 15 shows the built model.



Figure 15: Built pipeline model

The pipeline leak detection system was tested to validate correct and reliable operation. We inserted two pressure sensors; one before and the other after the leak. The sensors' readings showed noticeable difference in pressure for leaks with size of approximately 10%. Compared to existing systems this value is relatively big but this is due to limited accuracy and sensitivity of the available pressure sensor. If more sensitive sensors were used they would have detected much smaller leaks.

A slowly developing leak is not expected to give rise to sudden change in pressure. However, extensive testing using LabVIEW revealed that after some time delay there was significant difference in the pressure values for two sensors; one before and the other after the leak. Thus, it was concluded that even slowly developing leaks can be detected in the built model.

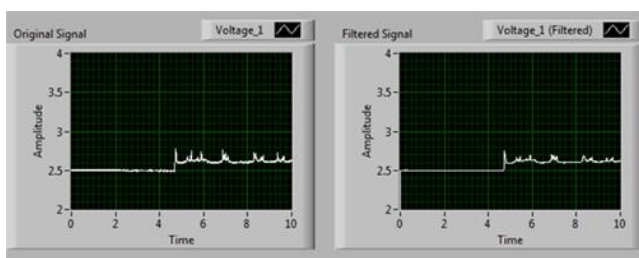


Figure 16: Sudden change in pressure caused by a leak

Although the above tests proved that the system is capable of detecting leaks, it is necessary to perform more tests on real pipelines or using a specialized simulation software to obtain more accurate results.

5. CONCLUSION

The wireless sensor network discussed in this paper can detect leaks and identify their locations by continuously monitoring the entire pipeline system. In our system the nodes are distributed along the pipeline and can detect leaks by monitoring pressure transients inside the pipe.

The nodes periodically report the measured pressure signals to the main node through a wireless sensor network.

After completely simulating, implementing and testing the network protocols run by the nodes, we plan to further test our network on bigger pipeline models or using accurate simulators under different leak conditions and sizes.

REFERENCES

- [1] Blažević, M., Samardžić, I., and Kolumbić, Z. "Leak Detection in Underground Pipelines of Municipal Water Distribution", *Proceedings of the 4th International Conference on Advanced Technologies for Developing Countries*, pp. 481-486, Croatia, 2005.
- [2] Water Utilities Department in the City of Dallas, *Advanced Leak Detection Memorandum*, 2009.
- [3] Zhang, J. "Designing a Cost Effective and Reliable Leak Detection System", *Proceedings of Pipeline Reliability Conference*, pp. 1-11, USA, 1996.
- [4] Stafford, M., and Williams, N., *Pipeline Leak Detection Study*, Health and Safety Executive, London - Great Britain, 1996.
- [5] Tafuri, A.N., Yezzi, J.J., Watts, D.J., and Carlyle, J.M. "Leak Detection and Leak Location in Underground Pipelines", *Proceedings of International Oil Spill Conference*, pp. 379-381, 1997.
- [6] Frings, J., and Walk, T. "Distributed Fibre Optic Sensing Enhances Pipeline Safety and Security", *Oil & Gas European Magazine*, pp. 132-136, 2011.
- [7] Zheng, J. and Jamalipur, A., *Wireless Sensor Networks: A Networking Perspective*, Wiley, Canada, 2009.
- [8] Lin, M., Wu, Y., and Wassell, I. "Wireless Sensor Network: Water Distribution Monitoring System", *Proceedings of Radio and Wireless Symposium IEEE Conference*, pp. 775-778, 2008.
- [9] Mohamed, N., and Jawhar, I. "A Fault Tolerant Wired/Wireless Sensor Network Architecture for Monitoring Pipeline Infrastructures", *Proceedings of International Conference on Sensor Technologies and Applications*, 2008.
- [10] Mohamed, N., Jawhar, I., Mohammad, M., and Aziz, J. "A Routing Protocol and Addressing Scheme for Oil, Gas and Water Pipeline Monitoring Using Wireless Sensor Networks", *Proceedings of the International Conference on Wireless and Optical Communications Networks*, pp. 1-5, 2008.

Corrosion and Scale Formation Problems in Water Systems

Farag Abd El Salam Abd El Aleem¹, Ibrahim S. Al-Mutaz², Ahmed Al-Arifi³ and Farag Abd El Salam Abd El Aleem¹

¹Chemical Engineering Department, College of Engineering
King Saud University, P.O. Box 800, Riyadh 11421, Saudi Arabia

³Saline Water Conversion Corporation (SWCC),
P.O. Box 5988, Riyadh, Saudi Arabia.

ABSTRACT

Corrosion and scale formation are considered among the most important problems affecting the actual performance and economics of industrial water systems especially desalination plants, water treatment processes, energy production units and cooling water equipment.

Each water system has unique combination of metals, water flows, water quality and temperature range that must be considered before selecting the suitable program for corrosion and scale control.

In fact, the presence of water is essential to the low temperature corrosion process, hence metals immersed in water tend to corrode because of their thermodynamic instability. Even pure water "with no dissolved salts" is corrosive due to the presence of oxygen in it.

Concerning scale formation, it directly occurs in water when the thermodynamic solubility of any fouling salt (CaCO₃, CaSO₄, etc.) is exceeded resulting in the precipitation of scale deposit on the surface of the metal in contact with water. The accumulation of this scale layer leads to significant decrease in heat transfer rate of thermal processes in desalination plants and also to a detectable increase in the pressure drop of water pipelines and equipment. In view of the significant practical importance of scale and corrosion problems in water environments, both are investigated, discussed and reviewed in the present work. Moreover, the interaction between scale and corrosion phenomena in water systems are also pronounced and tackled. Various strategies for protection and control of both corrosion and scale formation are finally covered.

1. INTRODUCTION

The presence of water is essential to the low temperature corrosion process. Even pure water "with no dissolved substances" is corrosive to iron; since iron is anodic to hydrogen in the pure water, it will corrode producing hydrogen gas and ferrous hydroxide.

When containing impurities or dissolved substances can be corrosive or non-corrosive depending on the nature of these impurities. Natural waters, e.g. contain dissolved solids, dissolved gases and sometimes colloidal or suspended matter; all these may affect the corrosive properties of water in relation to the metals with which it is in contact. Sea water, on the other hand, is a strong electrolyte containing a relatively high concentration of salts that occurs commonly in nature. These salts are the main reasons for corrosive nature and scaling tendency of water [1-4].

In the present paper, both corrosion and scale formation processes in water systems are discussed and reviewed. The interaction between scale and corrosion is also pronounced and tackled. Various strategies for control of both corrosion and scale are also covered.

2. CONSTITUENTS OR IMPURITIES PRESENT IN WATER

From the practical point of view; we will give examples for natural water composition (including surface water, river water and brackish water). This is given here below in Table (1). Moreover, for seawater, its sample analysis is also given in Table (2). Both tables give the main types of impurities present in each water source. The effect of various water constituents on corrosion will be discussed here below.

Table 1: Gulf seawater composition, pH = 8.2 [6].

Ions	Concentration, mg/L
Calcium Ca ⁺⁺	508
Magnesium Mg ⁺⁺	1,618
Sodium Na ⁺⁺	13,440
Potassium K ⁺	483
Strontium Sr ⁺⁺	17
Bicarbonate HCO ₃ ⁻	176
Chloride Cl ⁻	24,090
Sulphate SO ₄ ⁻	3,384
Bromide Br ⁻	83
Fluoride F ⁻	1
Total dissolved solids	TDS 43,800

Table 2: Typical water analysis (results in mg/liter) [3].

	Very soft lake water	Moderately soft surface water	Slightly hard river water	Moderately hard river water	Hard borehole water (chalk formation)	Slightly hard borehole water containing sodium bicarbonate	Very hard underground water
pH Value	6.3	6.8	7.4	7.5	7.1	8.3	7.1
Alkalinity to methyl orange (CaCO ₃)	2	38	90	180	250	278	470
Total hardness (CaCO ₃)	10	53	120	230	340	70	559
Calcium hardness (CaCO ₃)	5	36	85	210	298	40	451
Sulphate (SO ₄)	6	20	39	50	17	109	463
Chloride (Cl)	5	11	24	21	4	94	149
Silica (SiO ₂)	Trace	0.3	3	4	7	12	6
Dissolved solids	33	88	185	332	400	620	1670

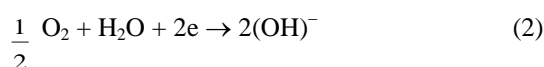
3. EFFECT OF DISSOLVED GASES

Of the dissolved gases present in water, oxygen occupies a special position as it stimulates the corrosion reaction. Carbon dioxide is scarcely less important; but has to be considered in relation to calcium hardness. Other gases, which are occasionally present usually, arise from pollution. Ammonia, which in various forms may be present in wastewater, attacks copper and copper alloys. Hydrogen sulfide and sulfur dioxide are also usually the result of pollution. Both gases may initiate or accelerate corrosion of most metals [3].

Here, we will concentrate only on two gases, i.e. (O₂) and (CO₂).

3.1 Influence of Dissolved Oxygen [5]

Oxygen dissolved in water is probably the most troublesome corrosion producing substance. The product of corrosion of iron by oxygen containing water is a mixture of iron oxides, usually hydrated, and referred to as rust. The following equations illustrate this corrosion process:



The action of oxygen is two fold; it depolarizes the cathode and it oxidizes the ferrous ions to ferric ions, which forms the insoluble ferric hydroxide. In a closed system, this reaction will continue until the dissolved oxygen is used up and the ferrous hydroxide smoothens the reaction. However in a system in contact with air, the oxygen supply is continually replenished. The rate of corrosion in this case, is generally restricted by the transport of oxygen from the air through the water to the metal. Figure 1 shows the effect of dissolved oxygen on the corrosion of iron in water containing sodium chloride.

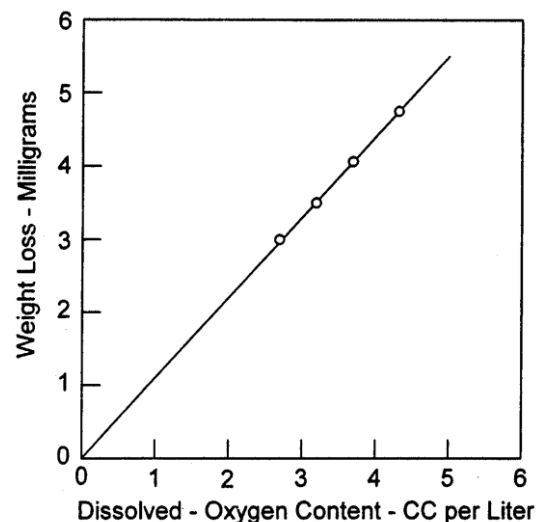
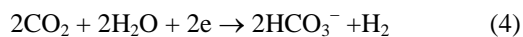


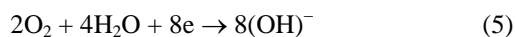
Figure 1: Corrosion in sodium chloride solutions containing dissolved oxygen.

3.2 Influence of Dissolved Carbon Dioxide [5]

Carbon dioxide is present in water as: (1) the carbon dioxide in the, carbonate ions; (2) the carbon dioxide necessary to convert the carbonates to the bicarbonates; (3) the amount of carbon dioxide necessary to keep the bicarbonates in solution; and (4) any excess carbon dioxide. This excess carbon dioxide is referred to as "aggressive" carbon dioxide, and is the most corrosive form. For equal concentrations, carbon dioxide dissolved in water is not as corrosive as oxygen dissolved in water. In corrosion caused by carbon dioxide dissolved in water, the following reaction applies where CO_2 reacts with water to form bicarbonate but not carbonate:



The depolarizing reaction of oxygen at the cathode is:



Comparing of these two reactions indicates that, on the basis of electrons, oxygen dissolved in water should be roughly four times as corrosive as an equal molar amount of carbon dioxide. When dissolved in water, carbon dioxide acts as an acid, so that the acidity of the solution and the corrosion rate are increased by increasing the partial pressure of the carbon dioxide. This is illustrated in Figure 2. It is to be mentioned that; dissolved carbon dioxide influences the solubility of magnesium and calcium carbonates. These salts sometimes precipitate on the surface of metal pipe and form a protective coating.

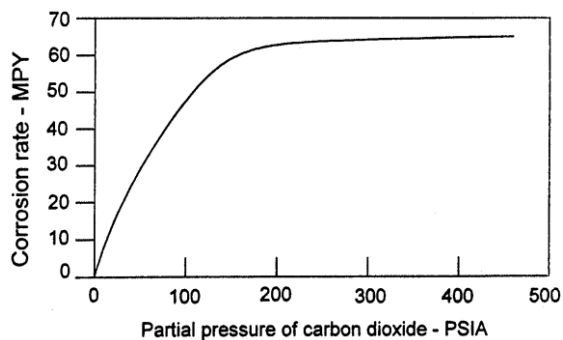


Figure 2: Corrosion of steel in distilled water containing CO_2 at various partial pressure.

3.3 Effect of Hydrogen Ion Concentration "pH" [7]

From the practical point of view, it was found that; at pH values below about 5, both iron and copper corrode rapidly and uniformly, while at values higher than 9, both iron and copper are usually protected. Between pH_5 and 9, pitting is likely to occur if no protective film is present. Figure (3) indicates the effect of pH on the corrosion rate of iron in aerated water. For this

corrosion process, the anodic reaction is as follows for all pH values:



But the corrosion rate varies due to changes in the cathodic reduction reaction. In the acidic solution, below pH_4 , the corrosion rate increases due to the availability of H^+ which will undergo the cathodic reaction "hydrogen evolution" as follows:

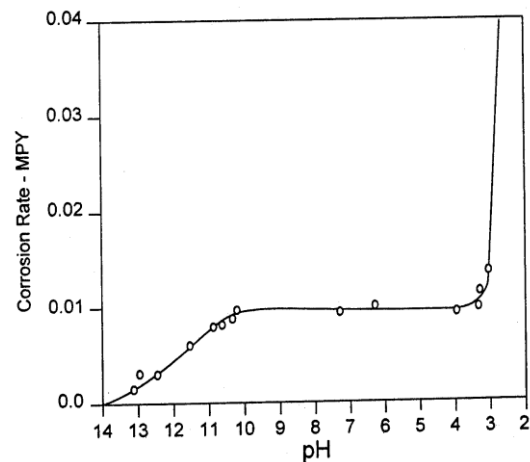
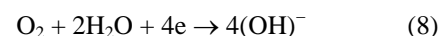


Figure 3: Effect of pH on corrosion of iron using HCl and NaOH to control pH in water containing dissolved oxygen [7].

In the intermediate region, from pH_4 to pH_{10} , the corrosion rate is nearly constant due to the formation of the porous ferrous oxide deposit on the metal surface. The corrosion rate in this case is controlled by the oxygen transfer through this porous deposit layer to the metal surface and the cathodic reaction in this case is:



At higher values of pH "above $\text{pH}= 10$ ", corrosion rate is effectively reduced due to the formation of the passive ferric oxide film which will protect the metal. From the practical point of view; in water systems corrosion problems exist at lower or neutral values of pH, but at higher pH values scale and fouling problems exist [7].

4. INFLUENCE OF DISSOLVED SALTS [5,6,7]

These salts include; sodium chloride "specially in sea water", calcium and magnesium salts " which cause hardness of water" and other salts like sulfates, nitrates, silicates and phosphates. On NaCl will be discussed here below from the corrosion point of view.

4.1 Sodium Chloride and Sea Water [5,7]

It is well known that; sodium chloride is a major constituent of seawater, brackish water and some chemical process water. Hence its effect on the corrosion process of water systems is of special importance. The effect of NaCl concentration on the iron corrosion rate in aerated solutions at room temperature is shown in Figure (4).

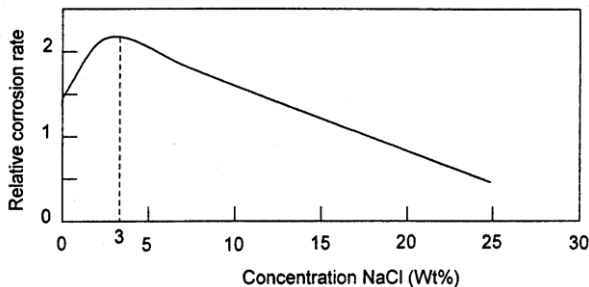


Figure 4: Effect of NaCl concentration on corrosion of iron in aerated solutions.

As shown in this figure, initial increase in the corrosion rate exists for the increase in NaCl solution up to 3%. This is due to the enhancement of the solution conductivity in this concentration range. Higher conductivity permits higher corrosion currents in these systems. However, still higher dissolved salt decreases the solubility of dissolved oxygen and hence, the rate of corrosion will directly decrease beyond the maximum, at about 3% NaCl, as shown in Figure (4).

5. SCALE FORMATION PROBLEMS IN WATER SYSTEMS [9-13]

Scale formation is arising a lot of problems in thermal processes like desalination plants and steam generation power plants. In a typical desalination plant about 20% to 30% of the heat transfer area is provided to allow for scale formation problems. Moreover, high pressures are required to overcome the produced scale resistance by deposits inside pipelines. Uneven scale deposition can also cause pitting corrosion.

The main sources of scale formation in water systems are: fouling salts as CaCO_3 , CaSO_4 , Mg(OH)_2 , Suspended Particles as SiO_2 , Corrosion Products like Iron Oxide and Copper Salts [4].

5.1 Mechanism of Scale Formation [4]

In general scale forming constituents are present in water as ions. Certain combination of these ions form components which have low solubility in water. Once the solubility has been exceeded, the compound precipitate as a solid. Precipitated solids may either remain in suspension in water "sludge formation", or form a coherent scale on the surface "scale formation".

5.2 Main Factors Affecting Scale Formation [4,9,15]

Those factors are as follows:

1. Salt type and concentration.
2. The time period for scale formation.
3. The hydrodynamics and fluid velocity.
4. The operating temperatures.
5. pH of water environments.

Due to size limitations of the papers, only two significant factors, i.e. CaSO_4 concentration and pH will be given here below:

5.2.1 Effect of calcium sulphate concentration [15]

In these experiments, CaSO_4 concentration was changed from 500 ppm to 1500 ppm while the other parameters were kept constant. CaSO_4 deposits for mild steel are plotted in Figure (5).

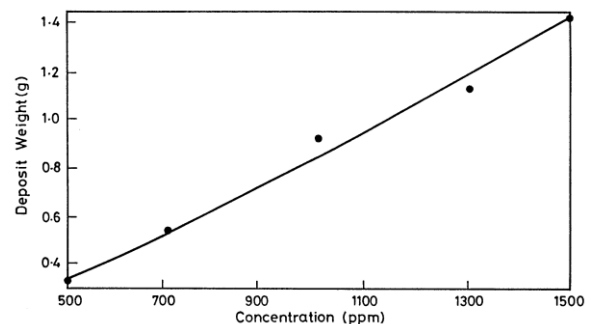


Figure 5: Effect of CaSO_4 concentration on scale deposition (Mild steel tube).

Condition: $U = 0.25$ m/s, $Re = 2000$, $T_i = 40$ °C, $pH = 8$, $q = 31082.03$ W/m², Time = 24 hr.

As shown in Figure (5), the fouling deposit increases directly by increasing the concentration of CaSO_4 in the investigated fluid. This direct effect of salt concentration on fouling is expected as the thermodynamic driving force for scale formation is the super-saturation of the considered salt and hence increasing its concentration in water will increase the super-saturation and produce more scale deposit [4,8,15].

5.2.2 Effect of pH [15]

This parameter has significant importance in scale formation studies. In practice, pH values of the flowing fluids are reduced by acid dosing to minimize scale formation. But on the other hand, this will produce a lot of corrosion problems, hence this parameter (PH) has to be thoroughly investigated to distinguish between its effects on both scale and corrosion problems.

The pH of this solution was varied from 4 to 9 and the total deposit was obtained at the end of each run. These deposits were plotted versus pH of the tested solution in Figure (6). This figure shows the mixed effect of pH on both scale and corrosion as it was noticed also from the quality of the deposit (yellow corrosion products were observed in it). Hence, precise chemical analysis were conducted on the collected samples of the deposit to isolate the corrosion products found CaSO_4 scales and the results were replotted in Figure (7) versus pH of the test solution.

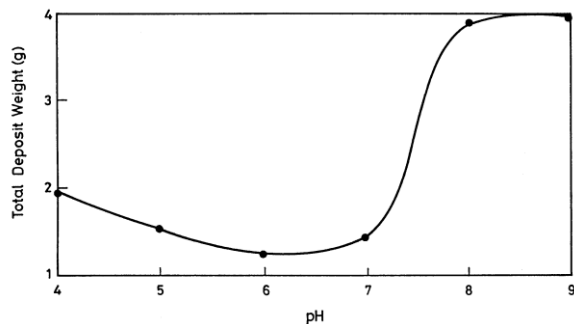


Figure 6: The effect of pH on total deposition of calcium sulfate (Mild steel).

Condition: CaSO_4 conc. 1000 ppm, $u = 0.25$ m/s, $Re = 2000$, $T_i = 40$ °C, Time = 144 hr, $q = 31082.03$ W/m².

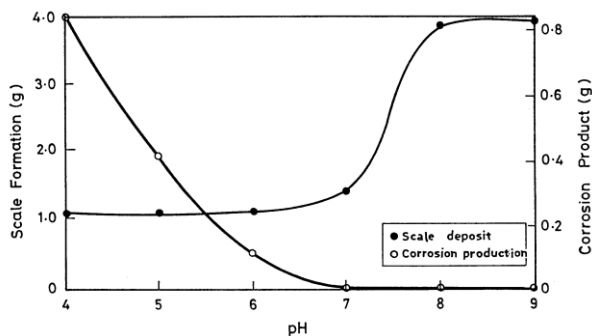


Figure 7: The effect of pH on scale and corrosion (separately) (Mild steel).

Condition: CaSO_4 conc. 1000 ppm, $u = 0.25$ m/s, $Re = 2000$, $T_i = 40$ °C, Time = 144 hr, $q = 31082.03$ W/m².

As shown in this figure scale is always present at higher pH values (>7) where corrosion increases sharply with decrease of pH. These findings are in good agreement with those reported in literature concerning the precise control of pH (at 6-7) to avoid both scale and corrosion problems in water systems [7]. It is worth mentioning that, in practice, acid dosing is applied in desalination plants to reduce scale formation. But this will generate a lot of corrosion problems, hence either corrosion inhibitor is to be added or precise control of pH around (6-7) has to be applied.

6. INTERACTION BETWEEN CORROSION AND SCALE IN WATER SYSTEMS [4,5]

- Utilization of specially formed "thin layer films" scales for corrosion protection.
- More attention has to be given for pitting and crevice corrosion initiated under scale or biofouling layers formed in water systems.
- Corrosion products, in many water systems, accelerates scale formation due to its seeding effects. This type is known as corrosion fouling.
- Water Tendency for both corrosion and scale formation needs better understanding and theoretical modeling of both phenomena.
- Successful treatment strategy of water has to take both corrosion and scale into deep consideration.

7. SCALE CONTROL TECHNOLOGIES [9-14]

- Proper water Treatment strategy.
- Use of suitable antiscalents.
- Acid dosing or PH control.
- Mechanical or chemical cleaning.
- Physical techniques like ultrasonics, magnetic fields or Ion flux.

8. CORROSION PREVENTION AND CONTROL [3-7]

The complete elimination of corrosion is difficult, if not impossible. Several ways exist, however, to reduce or to inhibit corrosion that are within the capability of most of water utilities and plants.

The following principle strategies are usually recommended for corrosion minimization or control in water systems:

- Modify water quality by the suitable water treatment processes.
- Properly select the suitable materials of construction.
- Use of the suitable corrosion inhibitors.
- Apply protective coatings resistant lining or suitable paints.
- Provide cathodic protection.

9. CONCLUSIONS

1. Better understanding of corrosion and scale phenomena in water systems can effectively reduce the tremendous operating and maintenance problems of these systems.
2. The proper treatment strategy of water is a key factor for controlling both corrosion and scale formation in various water systems.
3. Selection of the proper materials of construction at the design stage can minimize the expected future troubles of both corrosion and scale in water environment.
4. Precise monitoring of both corrosion and scale formation in the actual plants is essential for successful control and minimization of any arising problems from scale and corrosion in water systems.

REFERENCES

- [1] Demadis, D.K.; Maverdeki, E.; et al., "Industrial Water Systems: Problems, Challenges and Solutions for Process Industries", *Desalination Journal*, Vol. 213, pp. 38-46, (2007).
- [2] El-Dhshan, M.E., "Corrosion and Scaling Problems Present in Some Desalination Plants in Abu-Dhabi", *Desalination Journal*, Vol. 138, pp. 371-377, (2001).
- [3] Schock, M.R. "Internal Corrosion and Deposition Control", in "Water Quality and Treatment Handbook", edited by Pontius, F. W., 4th ed. 1990, American Water Works Association, Mc-Graw Hill. New York.
- [4] Heitman, H.G. "Saline Water Processing" 1990, Published by VCH, Germany.
- [5] Ostroff, A.G. "Water and Corrosion" in "Introduction to Oil Field Water Technology" Published by NACE" National Association of Water Engineers" 2nd edition 1979.
- [6] Abed El Aleem, Farag, A.; Al- Hazzaa, M.; and El-Dahshan, M.E. "Effect of Hydrodynamic Conditions On The corrosion Of Mild Steel And Stainless Steel Alloys Containing Molybdenum in Seawater Desalination Processes". I.D.A Congress on Desalination and Water Sciences, Abu Dhabi, 1995, Vol. V, pp. 149164.
- [7] Jones, D.A. "Principles and Prevention of Corrosion", Macmillan Publisher, New York, 1992.
- [8] Blochl, R. and Muller, H.S., *Canadian J. of Chem. Eng.*, 1990, v.68, p. 585-591.
- [9] Epstein, N., "Fouling: Technical Aspects" in *Fouling of Heat Transfer Equipment*, Edited by Somerscales, E.F.C. and Knudsen, J.G., Hemisphere, Washington D.C. 1981, p.31.
- [10] Andritsos, N., Kontopoulou, M. and Karabelas, A.J., *Canadian I. of Chem. Eng.* 1996, v. 74, p. 911-919.
- [11] Andritsos, N. and Karabelas, A.J., Presented at "IDA World Congress on Desalination and Water Reuse", Nov. 1995, Abu-Dhabi.
- [12] Knudsen, J.G. "Fouling in Heat Exchangers" in *Hemisphere Handbook of Heat Exchangers Design*", G.F. Hewitt (ed.) 1990 Hemisphere.
- [13] Yiantsios, S.G.; Andritsos, N. and Karabelas, A.J., Presented at "Fouling Mitigation of Industrial Heat Exchangers" Engineering foundation Conference, AIChE and ASME, June 1995, California, U.S.A.
- [14] Kern, D.Q and Seaton, R.E., *British Chem. Eng.* 1959, v. 4, p. 258-262.
- [15] Al-Jalik, S., "Fouling and Scale Formation in Desalination Plants", M.Sc. Thesis, College of Engineering, King Saud University, Saudi Arabia, (1996).

Analytical and Numerical Modeling of 2-D Solute Transport in a Fracture/Matrix Aquifer System

Ismail Kucuk¹, Ibrahim Kocabas²

¹Department of Mathematics, AUS (ikucuk@aus.edu)

²Chemical Engineering Department, AUS, (ikocabas@aus.edu

ABSTRACT

Modeling solute transport in groundwater aquifers serves to explore several environmental problems of great importance. First, it allows assessing the vulnerability of groundwater to contamination due to potential pollutant sources. Second, it allows quantifying the degree of contamination in actual cases of contamination. Finally, it allows estimating the effectiveness of the remediation techniques.

A vast number of analytical and numerical models of solute transport have been presented by earlier researchers. In recent years, however, increasing computing powers have allowed more comprehensive analytical models to be developed, which serves as challenging benchmarks for numerical models as well as more representative interpretation tools of actual data.

In this work, we present a new two dimensional solute transport model which is solved analytically as well as numerically. The solutions are utilized in an integrated manner to validate each other for several scenarios. For instance, the analytical model is used as a benchmark for effectiveness of numerical model in alleviating numerical dispersion and unphysical oscillations and capturing the transport phenomena at and near the fracture/matrix interface. The numerical model, on the other hand, is used as a benchmark for the effectiveness of the analytical model in capturing the 2-D nature of the transport within the system

Thus, we present this new set of analytical/numerical solutions as an integrated and comprehensive modeling tool for studying 2-D solute transport in a fracture/matrix configuration.

Keywords: solute transport, tracer transients, thermal transients, contaminant transport, convection-dispersion equation

1. INTRODUCTION

A high permeability zone located in a low permeability matrix is an important transport system frequently encountered in groundwater aquifers, as well as oil and geothermal reservoirs. For instance a high permeability streak confined by low permeability layers in aquifers and oil reservoirs or a high permeability fracture zone located in a low permeability matrix in geothermal reservoirs are commonly encountered natural subsurface flow systems.

The two and three dimensional solutions have also been developed for uniform homogeneous infinite porous media[1,2,3]. Several notable two-dimensional solutions to the presently discussed system is the steady state solution presented by Costas et al[4], some physically less likely configurations[5,6,7] and an approximate solution developed by Kocabas[8] and an exact but significantly complicated solution for an equal transverse dispersion coefficients in the aquifer and confining layers[9]. Therefore, there remains the need for exact analytical solutions to provide more insight into the transport mechanisms in such systems.

This work presents two dimensional time-variant (transient, unsteady state) analytical solutions for the tracer transport in the high permeability zone. The novel analytical solution is exact and it is expected to serve a stronger benchmark for the numerical simulators.

2. MATHEMATICAL DEVELOPMENTS

Our conceptual model assumes a high permeability zone located in a significantly less permeability matrix of infinite extent. In the high permeability streak the longitudinal convection is much greater than that in the transverse direction, and hence, only longitudinal convection assumed to occur. Even though, the convection in the transverse direction is negligible compared to that in longitudinal direction it can still cause a transverse dispersive transport which is much greater than that of molecular diffusion. Therefore, both longitudinal and transverse dispersions are assumed to take place in the high permeability zone. The matrix receives the tracer at the streak/matrix boundary and only transversal dispersion is assumed to occur in the matrix. This is because the fast fluid travel within the high permeability streak can generate a larger transverse pressure gradient in the matrix than that

exists in the longitudinal direction, and hence give rise to a considerable dispersive transport in that direction. Since longitudinal convection, and dispersion within the matrix are expected to be much smaller than those of the transverse direction they are neglected in the model.

The dispersion of tracer arises due to the microscopic pore fluid velocity variations both in the magnitude and the direction. Such velocity variations are assumed to occur both in the high permeability streak in both directions and in the matrix only in the transverse direction. Thus, in our mathematical model, we have employed not only a longitudinal dispersion but also a transversal dispersion which could be many orders of magnitude greater than pure molecular diffusion

2.1 Governing Equations and Development of the Solution

The two dimensional governing differential equations of the tracer transport in the high permeability streak and the adjacent matrix are:

$$\frac{\partial C}{\partial t} + u \frac{\partial C}{\partial x} - D_L \frac{\partial^2 C}{\partial x^2} - D_t \frac{\partial^2 C}{\partial y^2} = 0 \quad (1)$$

$$\frac{\partial C_m}{\partial t} - D_m \frac{\partial^2 C_m}{\partial z^2} = 0 \quad (2)$$

Note that different independent variables, y and z , are employed for the transport in transverse direction within the high permeability streak and the adjacent matrix. Refer to Fig.1 for the coordinate system employed. Such a formulation does not affect the results but simplifies the algebra greatly. For the continuous injection of a constant concentration fluid into the high permeability streak, the initial and boundary conditions are specified as follows:

$$C = C_m = C_0 \quad \text{at} \quad t = 0 \quad (3)$$

$$C = C_i \quad \text{at} \quad x = 0 \quad (4)$$

Both mediums are assumed to be semi-infinite:

$$C \rightarrow 0 \quad \text{as} \quad x \rightarrow \infty \quad (5)$$

$$C_m \rightarrow 0 \quad \text{as} \quad z \rightarrow \infty \quad (6)$$

The symmetry of the system requires a zero gradient at the centerline of the aquifer.

$$\frac{\partial C}{\partial y} = 0 \quad \text{at} \quad y = 0 \quad (7)$$

Then the two equations are coupled through the equality of concentrations and fluxes at the boundary.

$$C = C_m \quad \text{at} \quad y = b \quad \text{and} \quad z = 0 \quad (8)$$

$$\phi_f D_t \frac{\partial C}{\partial y} = \phi_m D_m \frac{\partial C_m}{\partial z} \quad \text{at} \quad y = b \quad \text{and} \quad z = 0 \quad (9)$$

The mathematical formulation is simplified using following dimensionless variables:

$$C_D = \frac{C - C_0}{C_i - C_0} \quad \text{and} \quad C_{Dm} = \frac{C_m - C_0}{C_i - C_0} \quad (10)$$

$$x_D = \frac{ux}{D_L} \quad \text{and} \quad t_D = \frac{u^2 t}{D_L} \quad (11)$$

$$y_D = \frac{uy}{\sqrt{D_L D_t}} \quad \text{and} \quad z_D = \frac{uz}{\sqrt{D_L D_m}} \quad (12)$$

$$\theta = \frac{\phi_m D_m}{\phi_f D_t} \quad (13)$$

In terms of the dimensionless variables the governing equations and initial and boundary conditions reduce to:

$$\frac{\partial C_D}{\partial t_D} + \frac{\partial C_D}{\partial x_D} - \frac{\partial^2 C_D}{\partial x_D^2} - \frac{\partial^2 C_D}{\partial y_D^2} = 0 \quad (14)$$

$$\frac{\partial C_m}{\partial t_D} - \frac{\partial^2 C_m}{\partial z_D^2} = 0 \quad (15)$$

$$C_D = C_{mD} = 0 \quad \text{at} \quad t_D = 0 \quad (16)$$

$$C_D = 1 \quad \text{at} \quad x_D = 0 \quad (17)$$

$$C_D \rightarrow 0 \quad \text{as} \quad x_D \rightarrow \infty \quad (18)$$

$$C_{mD} \rightarrow 0 \quad \text{as} \quad z_D \rightarrow \infty \quad (19)$$

$$\frac{\partial C_D}{\partial y_D} = 0 \quad \text{at} \quad y_D = 0 \quad (20)$$

$$C_D = C_{mD} \quad \text{at} \quad y_D = y_{Db} \quad \text{and} \quad z_D = 0 \quad (21)$$

$$\frac{\partial C_D}{\partial y_D} = \theta \frac{\partial C_{mD}}{\partial z_D} \quad \text{at} \quad y_D = y_{Db} \quad \text{and} \quad z_D = 0 \quad (22)$$

The solution of the present model based on the inlet boundary condition defined by Eq.4 is called as the constant concentration continuous injection solution. The continuous injection solution is most useful for interpretation of laboratory tracer experiments and the contaminant transport in porous media in case of a persistent source of contamination.

Using the technique of Laplace and Fourier Sine transforms together with the iterated Laplace transform theorem applied to Laplace inversions, we have obtained the exact solution. The complete solution for the continuous injection solution, whose derivation is detailed in Appendix A, may be written as.

$$C_D = \frac{1}{2} \left[\begin{array}{c} \operatorname{erfc}\left(\frac{x_D - t_D}{2\sqrt{t_D}}\right) + \exp(x_D) \\ \operatorname{erfc}\left(\frac{x_D + t_D}{2\sqrt{t_D}}\right) \end{array} \right] - C_{D2} \quad (23)$$

And

$$C_{D2} = \sum_{n=0}^{\infty} \left[\begin{array}{c} \sum_{m=0}^n (-1)^m \binom{n}{m} \int_0^{t_D} \int_0^{\infty} \frac{2^{m+1} \eta^m}{m!} \\ \exp(-\eta^2) H_m(\eta) \frac{x_D}{2\sqrt{\pi}(t_D - \tau)^3} \\ \exp\left(-\frac{(x_D - (t_D - \tau))^2}{4(t_D - \tau)}\right) \\ \left(\operatorname{erfc} \frac{\alpha_1 + 2\sqrt{\tau}\eta / \sqrt{\theta}}{2\sqrt{t_D - \tau}} + \right. \\ \left. \operatorname{erfc} \frac{\alpha_2 + 2\sqrt{\tau}\eta / \sqrt{\theta}}{2\sqrt{t_D - \tau}} \right) du d\tau \end{array} \right] \quad (24)$$

3. CONCLUSIONS

A novel analytical solution has been developed for a two dimensional system which simulates the solute transport in an aquifer. The new two-dimensional model is expected to serve several important purposes. First, the can also be used for interpreting and forecasting more involved two dimensional concentration surfaces of field data. Second, from the two dimensional model we can derive a solution representing the average concentration distribution across the high permeability zone and provide a fast interpretation and forecasting tool as a one dimensional solution. As it will include the influence of additional transverse dispersion process and geometrical effects of the two dimensional transport it will be more accurate than the previously developed one dimensional analytical solutions. Third, the solution can also be used to study the profile obtained/expected at a specific location in the two dimensional domain and the distribution along a streamline. This feature is particularly important because the concentration distribution obtained along a streamline or concentration profiles obtained at a single point in space are single curves and not surfaces. Thus they may be easily adapted for curve fitting process of one dimensional solutions. As a result, we can infer the two dimensional characteristics using only the part of the solution representing distribution along a streamline or profile at a point. The new solutions are able to demonstrate the collective role of the parameters related to processes as well the system geometry.

REFERENCES

- [1] Sauty, J. P., 1980, An analysis of hydrodispersive transfer in aquifers, *Water Resources Research*, 16(1), pp.145-158.
- [2] Leij, F. J., Dane, J. H., 1990, Analytical solutions of the one-dimensional advection equation and two or three dimensional dispersion equation, *Water Resources Research*, 26(7), pp.1475-1482.
- [3] Sim. Y and Chrysikopoulos, C. V. Analytical solutions for solute transport in saturated porous medis with semi-infinite or infinite thickness, *Adv. Water Resources*, Vol. 22. No.5 pp.507-519
- [4] Chrysikopoulos, C. V, Hsuan, P.Y, Fyrrillas, M. M. and Lee, K.Y. Mass transfer coefficients and concentration boundary layer thickness for a dissolving NAPL pool in porous media, *J. Hazardous materials B97* (2003) 245-255.
- [5] Bai, M., Shua, Z., Cao, J., Zaman, M, and Roegiers, J.-C. "A semi-analytical solution for a two-dimensional capacitance model in solute transport," *J. Pet. Sci. and Eng.*, Vol. 22, pp.275-295, (1999)
- [6] West, M. R., Kueper, B. H., and Novakowski, K. S." Semi-analytical solutions for solute transport in fractured porous media using a strip source of finite width," *Advances in water resources*, Vol. 27 No.5, pp. 1045-1057, (2004)
- [7] Zhan,H, Wen,Z., Huang, G. and Sun, D. "Analytical solution of two-dimensional solute transport in an aquifer-aquitard system," *J. Contaminant Hydrology*, Vol. 107, pp. 162-174, (2009)
- [8] Kocabas, I. "Thermal Transients During Nonisothermal Fluid Injection into Oil Reservoirs", *J. Petroleum Science and Engineering*, Vol. 42, pp. 121-133, 2004
- [9] Kocabas, I., "Modeling Tracer Flow in Oil Reservoirs Containing High Permeability Streaks," (SPE Paper 81429, revised version in 2007, Proceedings Of MEOS, June 9-12 2003, Bahrain.)

Appendix A: Derivation of Continuous Injection Solution

The solution to Equations 14 through 21 is developed as follows: Let's define two new dependent variables, χ and χ_m related to the original dependent variables by:

$$C_D = \chi \exp(x_D / 2) \quad (A1)$$

and

$$C_{mD} = \chi_m \exp(x_D / 2) \quad (A2)$$

Then, performing a dependent variable transformation reduces Equations 12 and 13 to:

$$\frac{\partial^2 \chi}{\partial x_D^2} + \frac{\partial^2 \chi}{\partial y_D^2} - \frac{\chi}{4} - \frac{\partial \chi}{\partial t_D} = 0 \quad (A3)$$

$$\frac{\partial^2 \chi_m}{\partial z_D^2} - \frac{\partial \chi_m}{\partial t_D} = 0 \tag{A4}$$

The related initial and boundary condition become:

$$\chi = \chi_m = 0 \quad \text{at} \quad t_D = 0 \tag{A5}$$

$$\chi = 1 \quad \text{at} \quad x_D = 0 \tag{A6}$$

$$\chi \rightarrow 0 \quad \text{as} \quad x_D \rightarrow \infty \tag{A7}$$

$$\chi_m \rightarrow 0 \quad \text{as} \quad z_D \rightarrow \infty \tag{A8}$$

$$\chi = \chi_m \quad \text{at} \quad y_D = y_{Db} \text{ and } z_D = 0 \tag{A9}$$

$$\frac{\partial \chi}{\partial y_D} = \sqrt{\theta} \frac{\partial \chi_m}{\partial z_D} \quad \text{at} \quad y_D = y_{Db} \text{ and } z_D = 0 \tag{A10}$$

Apply the Laplace transformation to (A3) and (A4) with respect to t_D to obtain:

$$\frac{\partial^2 \dot{\chi}}{\partial x_D^2} + \frac{\partial^2 \dot{\chi}}{\partial y_D^2} - (s+a)\dot{\chi} = 0 \tag{A11}$$

where $a=1/4$, and

$$\frac{\partial^2 \dot{\chi}_m}{\partial z_D^2} - s\dot{\chi} = 0 \tag{A12}$$

In this work, the Fourier Sine transform and its inverse transform are defined as follows:

$$\chi(\omega) = \frac{2}{\pi} \int_0^\infty \chi(x_D) \sin(\omega x_D) dx_D$$

$$\chi(x_D) = \int_0^\infty \chi(\omega) \sin(x_D \omega) d\omega$$

Based on the adopted definitions, Fourier sine transform of the second derivative is:

$$\frac{2}{\pi} \int_0^\infty \frac{d^2 \chi}{dx_D^2} \sin(\omega x_D) dx_D = \frac{2}{\pi} \chi(x_D = 0) - \omega^2 \chi(\omega) \tag{A13}$$

Applying Fourier Sine transform to (A11) and (A12) with respect to x_D yields:

$$\frac{\partial^2 \ddot{\chi}}{\partial y_D^2} - (s + \omega^2 + a)\ddot{\chi} = -\frac{2\omega}{\pi} \tag{A14}$$

$$\frac{\partial^2 \ddot{\chi}_m}{\partial z_D^2} - s\ddot{\chi}_m = 0 \tag{A15}$$

The solutions of A14 and A15 are respectively given by:

$$\ddot{\chi} = c_1 \exp(-\sqrt{s+\lambda} y_D) + c_2 \exp(\sqrt{s+\lambda} y_D) + \frac{2\omega}{\pi s(s+\lambda)} \tag{A16}$$

and

$$\ddot{\chi}_m = c_3 \exp(-\sqrt{s} z_D) + c_4 \exp(\sqrt{s} z_D) \tag{A17}$$

where

$$\lambda = \omega^2 + a \tag{A18}$$

Then, first transforming related boundary conditions given by (A5) through (A10) and applying the boundary conditions to determine the solutions constants we obtain the solution in Laplace and Fourier Sine space:

$$\ddot{\chi} = \ddot{\chi}_1 - \ddot{\chi}_2 \tag{A19}$$

Where

$$\ddot{\chi}_1 = \frac{2\omega}{\pi s(s + \omega^2 + a)} \tag{A20}$$

and

$$\ddot{\chi}_2 = \ddot{\chi}_1 \frac{\sqrt{\theta s}}{1 - \frac{(\sqrt{s+\lambda} - \sqrt{\theta s})}{(\sqrt{s+\lambda} + \sqrt{\theta s})} \exp(-2\sqrt{\alpha} y_{Db})} \left[\frac{\exp(-\sqrt{s+\lambda}(y_{Db} + y_D))}{(\sqrt{s+\lambda} + \sqrt{\theta s})} + \frac{\exp(-\sqrt{s+\lambda}(y_{Db} - y_D))}{(\sqrt{s+\lambda} + \sqrt{\theta s})} \right] \tag{A21}$$

Using a binomial expansion for the denominator yields:

$$\ddot{\chi}_2 = \left[\sum_{n=0}^{\infty} \frac{2\omega}{\pi} \frac{\sqrt{\theta s} (\sqrt{s+\lambda} - \sqrt{\theta s})^n}{s(s+\lambda)(\sqrt{s+\lambda} + \sqrt{\theta s})^{n+1}} \left[\frac{\exp(-\sqrt{s+\lambda}((2n+1)y_{Db} - y_D))}{(\sqrt{s+\lambda} + \sqrt{\theta s})} + \frac{\exp(-\sqrt{s+\lambda}((2n+1)y_{Db} + y_D))}{(\sqrt{s+\lambda} + \sqrt{\theta s})} \right] \right] \tag{A22}$$

Using the following relation

$$\left(\frac{(\sqrt{s+\lambda} - \sqrt{\theta s})}{(\sqrt{s+\lambda} + \sqrt{\theta s})} \right)^n = \left(1 - \frac{2\sqrt{\theta s}}{\sqrt{s+\lambda} + \sqrt{\theta s}} \right)^n \tag{A23}$$

$$\sum_m^n (-1)^m \binom{n}{m} \left(\frac{2\sqrt{\theta s}}{\sqrt{s+\lambda} + \sqrt{\theta s}} \right)^m$$

The equation (A22) reduces to:

$$\ddot{\chi}_2 = \left[\sum_{n=0}^{\infty} \left[\frac{\omega}{\pi} \sum_{m=0}^n \binom{n}{m} \frac{(-1)^m 2^{m+1} \theta^{(m+1)/2} s^{(m-1)/2}}{(s + \lambda)(\sqrt{s + \lambda} + \sqrt{\theta s})^{m+1}} \right. \right. \\ \left. \left. \left[\exp(-\sqrt{s + \lambda} ((2n + 1)y_{Db} - y_D)) + \exp(-\sqrt{s + \lambda} ((2n + 1)y_{Db} + y_D)) \right] \right] \right] \quad (A24)$$

Based on A19, the dimensionless concentration solution, C_D may be expressed as:

$$C_D = C_{D1} - C_{D2} \quad (A25)$$

where

$$C_{D1} = \chi_1 \exp\left(\frac{x_D}{2}\right) \text{ and } C_{D2} = \chi_2 \exp\left(\frac{x_D}{2}\right) \quad (A26)$$

The inversion of $\ddot{\chi}_1$ is achieved through the following inverse Fourier Sine and Laplace transform relations respectively

$$\dot{\chi}_1 = F_s^{-1} \frac{2\omega}{\pi s(\omega^2 + s + a)} = \frac{\exp(-\sqrt{s + a} x_D)}{s} \quad (A27)$$

Laplace inverting (A27) and substituting $a = 1/4$ we obtain:

$$C_{D1} = \frac{1}{2} \left[\operatorname{erfc}\left(\frac{x_D - t_D}{2\sqrt{t_D}}\right) + \exp(x_D) \operatorname{erfc}\left(\frac{x_D + t_D}{2\sqrt{t_D}}\right) \right] \quad (A28)$$

The inverse Laplace transform of the first term within summation in A24 is carried out using the following three relations consecutively to obtain (A32):

$$L^{-1}(s^{(m-1)/2} f(\sqrt{s})) = \frac{1}{2^m \sqrt{\pi \tau}^{m+1}} \int_0^{\infty} \exp\left(-\frac{u^2}{4\tau}\right) H_m\left(\frac{u}{2\sqrt{\tau}}\right) f(u) du \quad (A29)$$

$$L^{-1}\left(\frac{1}{(s + a)^{m+1}}\right) = \frac{\tau^m e^{-atD}}{m!} \quad m = 0, 1, 2, 3, \dots \quad (A30)$$

$$L^{-1}\left(\frac{\exp(-\eta\sqrt{s + \lambda})}{(s + \lambda)}\right) = e^{-\lambda} \operatorname{erfc}\left(\frac{\eta}{2\sqrt{x_D}}\right) \quad (A31)$$

$$\dot{\chi}_2 = \sum_{n=0}^{\infty} \left[\sum_{m=0}^n \binom{n}{m} \int_0^{t_D} \frac{(-1)^m}{(\sqrt{\tau})^{m+1}} \int_0^{\infty} \exp\left(-\frac{u^2}{4\tau}\right) H_m\left(\frac{u}{2\sqrt{\tau}}\right) \frac{u^m}{m!} \exp(-\lambda(t_D - \tau)) \frac{2\omega}{\pi} (\) du d\tau \right] \quad (A32)$$

Where

$$F(u) = \operatorname{erfc} \frac{\alpha_1 + u/\sqrt{\theta}}{2\sqrt{t_D - \tau}} + \operatorname{erfc} \frac{\alpha_2 + u/\sqrt{\theta}}{2\sqrt{t_D - \tau}},$$

$$\alpha_1 = (2n + 1)y_{Db} + y_D \text{ and}$$

$$\alpha_2 = (2n + 1)y_{Db} - y_D$$

In order to invert (A32), we need the following relation14:

$$F_s^{-1}\left(\omega \exp(-(\omega^2 + 1/4)(t_D - \tau))\right) = \exp\left(-\frac{t_D - \tau}{4}\right) \frac{\sqrt{\pi} x_D}{4\sqrt{(t_D - \tau)^3}} \exp\left(-\frac{x_D^2}{4(t_D - \tau)}\right) \quad (A33)$$

After the inversion and some additional manipulations we obtain (A34)

$$C_{D2} = \sum_{n=0}^{\infty} \left[\sum_{m=0}^n \binom{n}{m} \int_0^{t_D} \frac{(-1)^m}{(\sqrt{\tau})^{m+1}} \int_0^{\infty} \exp\left(-\frac{u^2}{4\tau}\right) H_m\left(\frac{u}{2\sqrt{\tau}}\right) \frac{u^m}{m!} \frac{x_D}{2\sqrt{\pi}(t_D - \tau)^3} \exp\left(-\frac{(x_D - (t_D - \tau))^2}{4(t_D - \tau)}\right) F(u) du d\tau \right] \quad (A34)$$

Defining $\eta = \frac{u}{2\sqrt{\tau}}$ we obtain:

$$C_{D2} = \left[\sum_{n=0}^{\infty} \sum_{m=0}^n \binom{n}{m} \int_0^{t_D} \int_0^{\infty} \frac{2^{m+1} (-1)^m \eta^m}{m!} \exp(-\eta^2) H_m(\eta) \frac{x_D}{2\sqrt{\pi}(t_D - \tau)^3} \exp\left(-\frac{(x_D - (t_D - \tau))^2}{4(t_D - \tau)}\right) F(\eta) d\eta d\tau \right] \quad (A35)$$

where

$$F(\eta) = \operatorname{erfc} \frac{\alpha_1 + 2\sqrt{\tau}\eta/\sqrt{\theta}}{2\sqrt{t_D - \tau}} + \operatorname{erfc} \frac{\alpha_2 + 2\sqrt{\tau}\eta/\sqrt{\theta}}{2\sqrt{t_D - \tau}}$$

$$\text{and } C_D = C_{D1} - C_{D2}$$

AVERAGE CONCENTRATIONS:

The average concentration across the high permeability streak is defined by Eq.42. Using equations A19 through A26 we can show that:

$$\bar{C}_D = C_{D1} - \bar{C}_{D2}$$

where C_{D1} is given by A29,

$$\bar{C}_{D2} = \frac{\exp(x_D/2)\bar{\chi}_2}{y_{Db}} \quad (\text{A36})$$

and

$$\bar{\chi}_2 = \left[\sum_{n=0}^{\infty} \sum_{m=0}^n \binom{n}{m} \frac{(-1)^m 2^m \theta^{(m+1)/2} s^{(m-1)/2}}{(s+\lambda)^{3/2} (\sqrt{s+\lambda} + \sqrt{\theta s})^{m+1}} \right] \left[\frac{2\omega}{\pi} \left[\exp(-\sqrt{s+\lambda}((2n+1)y_{Db} - y_D)) + \exp(-\sqrt{s+\lambda}((2n+1)y_{Db} + y_D)) \right] \right] \quad (\text{A37})$$

Noticing that only exponent of $(s + \lambda)$ term within the summation differs from that of the continuous injection solution one can develop an expression for average concentrations using the same approach employed above to develop continuous injection solutions.

Modeling Sensible Energy Storage in Aquifers

Ibrahim Kocabas¹, Ismail Kucuk²

¹Chemical Engineering Department, AUS (ikocabas@aus.edu)

²Department of Mathematics, (ikucuk@aus.edu)

ABSTRACT

Sensible energy storage exploits water as the natural substance with the highest specific heat coefficient. It involves heating of water using solar panels during sunshine dominated seasons and injecting this water into a storage aquifer. This sensible energy loaded water is produced back during cold seasons to be utilized as residential or green house heating agent, and so on.

The main design parameters involved in the sensible energy storage operation are those that control various phenomena such as storage capacity of the aquifer, heat losses to the confining layers and heat dispersion within the flow system. The degree of sensible energy loading of water, rate and duration of injection, injection production cycles constitute the main decision variables.

In this work, a thermal injection backflow mathematical model of sensible energy storage is presented. The influence of design parameters and decision variables has been studied via a parametric sensitivity analysis. Then, a nonlinear regression curve fitting technique has been employed to match experimental field values and the model generated curves. The results show that sensible energy storage could be an effective renewable energy source in many parts of the world.

Keywords: sensible energy storage, aquifer thermal energy storage, thermogeology, heat transport through porous media, non-isothermal injection tests

1. INTRODUCTION

Sensible energy storage has been one of the sources of alternative energy[1,2,34]. Recently it has evolved into a full science of thermo-geology[5,6,7] which fundamentally involves storage of heat of summer and cold or “chill” of winter in groundwater aquifers. Depending on the area of interest either heat of summer or cold of winter is first stored in water and the water is injected into an aquifer to be stored until winter or summer during which it is produced back to be used for different purposes such as space heating or cooling. The subsurface storage efficiency is one of the dominating factors controlling the overall efficiency and performance of the system.

Thus designing, monitoring, evaluating and controlling the performance of a sensible energy storage operation requires a fundamental understanding of nonisothermal injection and transport through porous media.

The main design parameters involved in the sensible energy storage operation are those that control various phenomena such as storage capacity of the aquifer, heat losses to the confining layers and heat dispersion within the flow system. The degree of sensible energy loading of water, rate and duration of injection, injection production cycles constitute the main decision variables. In this work, a thermal injection backflow mathematical model of sensible energy storage is presented. The influence of design parameters and decision variables

has been studied via a parametric sensitivity analysis. Then, a nonlinear regression curve fitting technique has been employed to match experimental field values and the model generated curves. The results show that sensible energy storage could be an effective renewable energy source in many parts of the world.

The basic mathematics of sensible energy storage is analogous to mathematics of nonisothermal injection backflow tests in geothermal tests.

Kocabas [2005] has proposed that a joint the interwell tracer test with a thermal injection backflow test for estimating both hydrodynamic and thermal parameters, fast, reliable and in situ. and Kocabas[2010] have also investigated the design of a thermal injection backflow test to estimate the heat transfer parameters with the least uncertainty is an important issue and should be explored in depth.

2. MATHEMATICAL DEVELOPMENTS

This work employs a conceptual model of a constant thickness aquifer of uniform porosity and permeability and a radial flow geometry extending from the wellbore far into the aquifer. The aquifer is confined by two impermeable layers of infinite extend. The temperature across the aquifer thickness is uniform and heat is transferred to/from the confining layers by conduction. The water and rock within the aquifer and the confining layers are in thermal equilibrium. This system

represents a sensible energy storage aquifer (Sauty et. al.1978 and Sauty et. al. 1982). Within that aquifer/aquitarde geological configuration, while heat conduction in the flow direction is neglected, an infinite lateral thermal conductivity in the fracture and a constant thermal conductivity in the matrix are assumed. Thus, the governing equations become:

$$\rho_r c_r \frac{\partial T}{\partial t} + \frac{\rho_w c_w q}{2\pi h} \frac{\partial T}{\partial x} - \frac{2k_m}{h} \frac{\partial T_m}{\partial z} \Bigg]_{z=0} = 0 \quad (1)$$

$$\rho_m c_m \frac{\partial T_m}{\partial t} - k_m \frac{\partial^2 T_m}{\partial z^2} = 0 \quad (2)$$

The initial and boundary conditions are:

$$T = T_m = T_0 \quad \text{at} \quad t = 0 \quad (3)$$

$$T = T_i \quad \text{at} \quad r = 0 \quad (4)$$

$$T_m = T \quad \text{at} \quad z = 0 \quad (5)$$

$$T_m \rightarrow 0 \quad \text{as} \quad z \rightarrow \infty \quad (6)$$

To simplify the mathematical formulation the following dimensionless variables are used.

$$T_D = \frac{T_o - T}{T_o - T_i}, \quad T_{mD} = \frac{T_o - T_m}{T_o - T_i} \quad (7)$$

$$r_D = \frac{4k_m \pi r^2}{\rho_w c_w h q}, \quad t_D = \frac{4k_m t}{\rho_r c_r h^2} \quad (8)$$

$$z_D = \frac{2z}{h}, \quad \text{and} \quad \theta = \frac{\rho_m c_m}{\rho_r c_r} \quad (9)$$

Using the above dimensionless variables yields:

$$\frac{\partial T_D}{\partial t_D} + \frac{\partial T_D}{\partial r_D} - \frac{\partial T_{mD}}{\partial z_D} \Bigg]_{z_D=0} = 0 \quad (11)$$

$$\theta \frac{\partial T_{mD}}{\partial t_D} - \frac{\partial^2 T_{mD}}{\partial z_D^2} = 0 \quad (12)$$

The dimensionless initial and boundary conditions become:

$$T_D = T_{mD} = 0 \quad \text{at} \quad t_D = 0 \quad (13)$$

$$T_D = 1 \quad \text{at} \quad r_D = 0 \quad (14)$$

$$T_{mD} = T_D \quad \text{at} \quad z_D = 0 \quad (15)$$

$$T_{mD} \rightarrow 0 \quad \text{as} \quad z_D \rightarrow \infty \quad (16)$$

Using the Laplace transform, the following Laplace domain solutions of injection period are obtained (Kocabas, 2004):

$$\dot{T}_D = \frac{1}{s} \exp(-sx_D) \exp(-\sqrt{\theta s} x_D) \quad (17)$$

$$\dot{T}_{mD} = \frac{\exp(-sx_D)}{s} \exp(-\sqrt{\theta s} x_D) \exp(-\sqrt{\theta s} z_D) \quad (18)$$

For the backflow period the relevant governing equations must be solved treating the injection period solutions as the initial condition values.

During the backflow period, the governing equations change due to both the reversal in the flow direction and presence of a different backflow rate than that in injection period. Using t_p as the time variable for the backflow period, dimensionless governing equations for the backflow period are:

$$\frac{\partial T_D}{\partial t_{pD}} - \frac{1}{\lambda} \frac{\partial T_D}{\partial r_D} - \frac{\partial T_{mD}}{\partial z_D} \Bigg]_{z_D=0} = 0 \quad (19)$$

$$\theta \frac{\partial T_{mD}}{\partial t_{pD}} - \frac{\partial^2 T_{mD}}{\partial z_D^2} = 0 \quad (20)$$

Where the ratio of the injection rate to backflow rate and dimensionless backflow time are defined respectively as:

$$\lambda = \frac{u}{u_b} \quad (21)$$

and

$$t_{pD} = \frac{k_m t_p}{\rho_r c_r b^2} \quad (22)$$

The other dimensionless variables are defined by Equations 8, 9 and 10. The initial and boundary conditions for the backflow period are specified in Equations 23, 25 and 26:

$$T_D = T_D(t_{Di}, r_D) \quad \text{at} \quad t_{pD} = 0 \quad (23)$$

Where t_i is the total injection time and, hence,

$$t_{Di} = \frac{k_m t_i}{\rho_r c_r b^2} \quad (24)$$

$$T_{mD} = T_{mD}(t_{Di}, x_D) \quad \text{at} \quad t_{pD} = 0 \quad (25)$$

$$T_D = 0 \quad \text{at} \quad r_D = r_{DR} = \frac{k_m q t_i^2}{\rho_w c_w \pi \phi^2 h^3} \quad (26)$$

The boundary conditions for the bounding layer remain unchanged, and hence, Equations 15 and 16 apply.

Using a second Laplace transform with respect to tpD , one may arrive at the solution for the backflow period (Kocabas, 2004,2010) . Since the only point of observation during the backflow period is the injection well, the temperature recovery with time for the feed-zone in the injection well is given by:

$$\ddot{T}_D = \frac{1}{s} \left[1 + \frac{\sqrt{\theta}}{\sqrt{s + \sqrt{p}}} \right] \left[\frac{\lambda}{s + \sqrt{\theta s} + \lambda p + \lambda \sqrt{\theta p}} \right] \quad (27)$$

The real space solution given by Eq. 28, has been obtained by applying the technique of iterated Laplace transform to Eq. 27. The iterated Laplace transform (Sneddon, 1972) is an easy yet highly powerful technique to invert significantly complicated Laplace space equations. The solution obtained using iterated Laplace transform given by Eq. 28 is a different closed form solution than those published earlier(Kocabas, 2004,2010). However, all solutions are mathematically equivalent yielding exactly same numerical results only Eq. 28 takes less computer time during computation of return profiles and it is an apparently simpler expression than its earlier counterparts.

$$T = \lambda \int_0^{\min(1, \frac{t_n}{\lambda})} \operatorname{erfc} \left(\frac{\sqrt{\alpha} \tau}{2\sqrt{(1-\tau)}} \right) G(\tau) d\tau + \lambda \int_0^{\infty} \sqrt{\alpha} \int_0^{\min(1, \frac{t_n}{\lambda})} \operatorname{erfc} \left(\frac{\sqrt{\alpha} \tau + \omega}{2\sqrt{(1-\tau)}} \right) F(\omega) d\tau d\omega \quad (28)$$

where

$$G(\tau) = \frac{\lambda \sqrt{\alpha} \tau}{2\sqrt{\pi}(t_n - \lambda\tau)^3} \exp \left(-\frac{\lambda^2 \alpha \tau^2}{4(t_n - \lambda\tau)} \right) \quad (29)$$

$$F(\omega) = \frac{\lambda \sqrt{\alpha} \tau + \omega}{2\sqrt{\pi}(t_n - \lambda\tau)^3} \exp \left(\frac{-(\lambda\alpha\tau + \omega)^2}{4(t_n - \lambda\tau)} \right) \quad (30)$$

$$\alpha = \theta t_{Di} \quad (31)$$

3. CONCLUSIONS

A novel analytical solution is developed to interpret the non-isothermal injection tests. The model is expected to function as a tool of designing, monitoring, evaluating and controlling the performance of a sensible energy storage in aquifers. It will also serve for a fundamental understanding of nonisothermal injection and transport through porous media.

REFERENCES

[1] Sauty, J. P., Gringarten, A., Landel, P.A., “The effect of thermal dispersion on injection of hot water in aquifers. Proc. The Second Invitational

Well Testing Symposium, Div. Of Geothermal Energy, U.S. Dept. of Energy. Berkeley CA., pp. 122-131, 1978

[2] Sauty, J. P., Gringarten, A., Menjz, A. and Landel, P.A., Sensible energy storage in aquifers: 1. Theoretical study,” Water Resources Research, Vol. 18 No.2, pp.245-252. 1982.

[3] Palmer, C. D., Blowes, D. W., Frind, E. O., and Molson, J. W. “Thermal energy storage in an aquifer 1. Field Injection experiment” Water resources Research, Vol. 28 No.10 pp.2845-2856, 1992.

[4] Rosen, M. A., “Second-law analysis of aquifer thermal energy storage systems” Energy, Vol. 24, pp.167-182, 1999

[5] Banks, D. An introduction to Thermogeology: Ground Source Heating and Cooling, Blackwell Publishing, Oxford, 2008.

[6] Banks, D. “Thermogeological assessment of open-loop well-doublet schemes: a review and synthesis of analytical approaches” J. Hydrogeology, Vol. 17, pp.1149-1155, 2009.

[7] Ditkin, V. A. and Prudnikov, A. P., 1962. Operational Calculus in Two Variables, Int. Series Pure Appl. Math., Pergamon Press, London, pp. 46-47, 1962.

[8] Sneddon, I.A., The use of integral Transforms, MCGraw Hill, NY, 1972

[9] Kocabas, I.. Geothermal reservoir characterization via thermal injection-backflow and interwell tracer testing, Geothermics 34 , pp. 27-46. 2005

[10] Kocabas, I. “Designing Thermal and Tracer Injection backflow Tests,” Proceedings of World geothermal Congress, Bali, Indonesia, April 25-30, 2010.

Appendix A: Derivation of the Real Space Temperature Recovery Profile for a Thermal Injection Backflow Test Applying a double Laplace transform (Ditkin and Prudnikov, 1962) with respect to the dimensionless variables tDi and tpD to the dimensionless backflow equations and their initial and boundary conditions (equations 19 through 26), yields the double Laplace transformed solution of the fracture equation, Eq. 19, given by (B.1):

$$\ddot{T}_D = \ddot{T}_{x_D=0} \left\{ \begin{array}{l} \exp(-sx_D) \exp(-\sqrt{\theta s} x_D) - \\ \exp(-sx_{DL}) \exp(\sqrt{\theta s} x_{DL}) \\ \exp[-\lambda p(x_{DL} - x_D)] \\ \exp[-\lambda \sqrt{\theta p}(x_{DL} - x_D)] \end{array} \right\} \quad (B.1)$$

Where

$$\ddot{T}_{x_D=0} = \left[1 + \frac{\sqrt{\theta}}{\sqrt{s + \sqrt{p}}} \right] \frac{\lambda / s}{s + \sqrt{\theta s} + \lambda p + \lambda \sqrt{\theta p}} \tag{B.2}$$

Since we can only measure the temperatures at the well (i.e. $x_D = 0$), the solution (B.1) at $x_D = 0$ may be expressed as:

$$\ddot{T}_D = \ddot{F}(s, p, \theta) - \ddot{G}(s, p, \theta) \exp(-x_{DL} s) \exp(-\lambda x_{DL} p) \tag{B.3}$$

In real space, (B.3) will have the form:

$$T_D = F(t_{Di}, t_{pD}, \theta) - G(t_{Di} - x_{DL}, t_{pD} - \lambda x_{DL}, \theta) H(t_{Di} - x_{DL}, t_{pD} - \lambda x_{DL}) \tag{B.4}$$

Where H is the Heaviside step function. Since during the injection period the farthest distance

traveled by the injected fluid is equal to ut_i , using Equations 24 and 26, we can show:

$$\frac{t_{Di}}{x_{DL}} = \frac{\phi \rho_w c_w}{\phi \rho_w c_w + (1 - \phi) \rho_s c_s} \leq 1 \tag{B.5}$$

Since, according to Eq. (B.5) $t_{Di} \leq x_{DL}$ the Heaviside step function and as a result the second term of Eq. (B.4) will always be zero. Therefore, the nonzero part of the solution will be the inverse of only (B.2).

To obtain a real space solution, we rewrite (B.2) as: In order to invert (B.5), we employ the method of iterated Laplace transform. In order to proceed let's first divide (B.5) into two parts, namely each part within the left square brackets multiplied by that in the right square brackets and call them TD1, and TD2. Then, iterative Laplace transform inversion is applied to each term separately.

For TD1, the first iteration of Laplace inversion is applied to the s in the denominator of the term in right square brackets to obtain:

$$L_1^{-1} \ddot{T}_{D1} = L_1^{-1} \frac{1}{s} \frac{\lambda}{s + \sqrt{\theta s} + \lambda p + \lambda \sqrt{\theta p}} = \frac{\lambda}{s} \exp(-\sqrt{\theta s} \tau) \exp(-\lambda p \tau) \exp(-\lambda \sqrt{\theta p} \tau) \tag{B.6}$$

The second iteration is applied to the remaining s terms in (B.6) to obtain:

$$L_2^{-1} \frac{\lambda}{s} \exp(-\sqrt{\theta s} \tau) = \lambda \operatorname{erfc} \left(\frac{\sqrt{\theta} \tau}{2\sqrt{t_{Di} - \tau}} \right) \tag{B.7}$$

Since the inversion is applied iteratively, the final result must be convolution of the results of the two steps, yielding:

$$L^{-1} \ddot{T}_{D1} = \dot{T}_{D1} = \int_0^{t_{Di}} \lambda \operatorname{erfc} \left(\frac{\sqrt{\theta} \tau}{2\sqrt{t_{Di} - \tau}} \right) \exp(-\lambda p \tau) \exp(-\lambda \sqrt{\theta p} \tau) d\tau \tag{B.8}$$

Inversion of exponential function in (B.8) with respect to Laplace variable p results in:

$$L^{-1} \left(\frac{\exp(-\lambda p \tau)}{\exp(-\lambda \sqrt{\theta p} \tau)} \right) = H(t_{pD} - \lambda \tau) \frac{\lambda \sqrt{\theta} \tau}{2\sqrt{\pi(t_{pD} - \lambda \tau)^3}} \exp \left(\frac{-\lambda^2 \theta \tau^2}{4(t_{pD} - \lambda \tau)} \right) \tag{B.9}$$

Thus, the double Laplace inversion of TD1 becomes:

$$T_{D1} = \int_0^{\min(t_{Di}, \frac{t_{pD}}{\lambda})} \left\{ \operatorname{erfc} \left(\frac{\sqrt{\theta} \tau}{2\sqrt{t_{Di} - \tau}} \right) \frac{\lambda^2 \sqrt{\theta} \tau}{2\sqrt{\pi(t_{pD} - \lambda \tau)^3}} \exp \left(\frac{-\lambda^2 \theta \tau^2}{4(t_{pD} - \lambda \tau)} \right) \right\} d\tau \tag{B.10}$$

To obtain inversion of TD2, we first the utilize the following operational relation

$$\frac{1}{\sqrt{s + \sqrt{p}}} = \int_0^\infty \exp(-(\sqrt{s + \sqrt{p}})w) dw \tag{B.11}$$

Then, the iterated and double Laplace transform inversions are sequentially applied to obtain:

$$T = \int_0^{\min(t_{Di}, \frac{t_{pD}}{\lambda})} \left(\frac{\lambda^2 \sqrt{\theta} \tau}{2(t_{pD} - \lambda \tau)} \right) G(\tau) d\tau + \lambda \int_0^\infty \sqrt{\theta} dw \int_0^{\min(t_{Di}, \frac{t_{pD}}{\lambda})} \left(\frac{\lambda \sqrt{\theta} \tau + w}{2(t_{pD} - \lambda \tau)} \right) F(w) d\tau \tag{B.13}$$

Where

$$G(\tau) = \left\{ \frac{\exp\left(-\frac{\lambda^2 \theta \tau^2}{4(t_{pD} - \lambda \tau)}\right)}{\sqrt{\pi(t_{pD} - \lambda \tau)}} \operatorname{erfc}\left(\frac{\sqrt{\theta} \tau}{2\sqrt{(t_{Di} - \tau)}}\right) \right\} \quad (\text{B.14})$$

$$F(\omega) = \left\{ \frac{\operatorname{erfc}\left(\frac{\sqrt{\theta} \tau + \omega}{2\sqrt{(t_{Di} - \tau)}}\right) \exp\left(-\frac{(\lambda \sqrt{\theta} \tau + \omega)^2}{4(t_{pD} - \lambda \tau)}\right)}{\sqrt{\pi(t_{pD} - \lambda \tau)}} \right\} \quad (\text{B.15})$$

Normalizing all variables by t_{Di} , and setting the normalized backflow time t_n as:

$$t_n = \frac{t_i}{t_p}, \quad (\text{B.16})$$

we obtain Eq. 28.

A Novel Analytical Model of Heat Extraction from Geothermal Reservoirs

Ibrahim Kocabas

Chemical Engineering Department, AUS (ikocabas@aus.edu)

ABSTRACT

A naturally fractured geothermal reservoir may consist of a network of fractures separated by low permeability matrix blocks. An idealized representation of such systems consists of an infinite number of parallel fractures separated by constant width matrix slabs. A purely convective flow in fractures and a conductive heat flow from the matrix blocks in a geothermal reservoir have been solved analytically in the late seventies. However, the analytical solution for a slightly modified system of a convective dispersive transport along the fractures and conductive transport from matrix block were presented only in Laplace space up to the present and numerical inverters have been employed to compute the solutions.

This work presents real space analytical solutions for the modified heat extraction model described above. The real space solutions have been developed using the powerful tool of iterated Laplace transform. The developed model has been used for 1) assessment of the efficiency of numerical Laplace transform algorithms and 2) investigation of the efficiency of heat extraction from geothermal reservoirs. We have found out that while Fourier series based methods perform better in sharp interface convective-dispersive transport cases. For a given injection rate and a distance between the injector producer pairs, the efficiency of heat extraction is influenced mostly by two important parameters, namely, surface area to volume ratio of fractures and surface area to volume ratio matrix blocks.

Keywords: fractured geothermal reservoirs, geothermal heat extraction, thermal transients, iterated Laplace Transform

1. INTRODUCTION

Reinjection of heat depleted geothermal waters into geothermal reservoirs is widely practiced worldwide as a method of disposal and/or pressure maintenance.

Modeling the thermal transients during reinjection is of great importance for determining the influence of reinjection under present conditions, predicting the future impact for any set of conditions and controlling the propagation of thermal front by engineering the injection conditions.

This work revisits a classical model of heat transport in a fractured geothermal reservoirs for developing a novel closed form analytical solution using the method of iterated Laplace transform.

2. MATHEMATICAL DEVELOPMENTS

A naturally fractured geothermal reservoir may consist of a network of fractures separated by low permeability matrix blocks. An idealized representation of such systems consists of an infinite number of parallel fractures separated by constant width matrix slabs. This is one of the two classical models used in modeling heat and tracer transport in porous media since early seventies.

A purely convective flow in fractures and a conductive heat flow from the matrix blocks in a geothermal reservoir have been solved analytically in the mid seventies [1]. However, the analytical solution for a slightly modified system of a convective dispersive

transport along the fractures and conductive transport from matrix block excluding two cases[2,3] were mostly presented in Laplace space [4,5,6,7] and numerical inverters have been employed to compute the solutions[8,9,10].

2.1 Governing Equations

The mathematical model of heat transport in a boundary conditions dominated system is constructed with the following assumptions: (i) the porous system consists of a single fracture located in low-permeability matrix of infinite extent, horizontal and constant thickness; (ii) a single-phase steady-state incompressible nonisothermal fluid flow takes place in the fracture, and the fluid in the matrix is virtually immobile; (iii) a convective transport and a longitudinal dispersion occurs in the fracture, and only a thermal conduction takes place in the matrix in a perpendicular direction to flow; (iv) the transverse thermal dispersion is of infinite magnitude instantaneously equalizing the temperatures across the fracture and (v) the exchange of heat between the fracture and the matrix occurs at the matrix/fracture interface and is proportional to the transverse temperature gradients in the matrix.

Within that fracture/matrix geological configuration, while heat conduction in the flow direction is neglected, an infinite lateral thermal conductivity in the fracture and a constant thermal conductivity in the matrix are assumed. Thus, the governing equations become:

$$\rho_r c_r \frac{\partial T}{\partial t} + \rho_w c_w \phi u \frac{\partial T}{\partial x} - \left[k_L \frac{\partial^2 T}{\partial x^2} - \frac{k_m}{b} \frac{\partial T_m}{\partial z} \right]_{z=0} = 0 \quad (1)$$

$$\rho_m c_m \frac{\partial T_m}{\partial t} - k_m \frac{\partial^2 T_m}{\partial z^2} = 0 \quad (2)$$

The initial and boundary conditions are specified as follows

$$T = T_m = T_o \quad \text{at} \quad t = 0 \quad (3)$$

$$T = T_i \quad \text{at} \quad x = 0 \quad (4)$$

$$T \rightarrow 0 \quad \text{as} \quad x \rightarrow \infty \quad (5)$$

$$T_m = T \quad \text{at} \quad z = 0 \quad (6)$$

$$\frac{\partial T_m}{\partial z} = 0 \quad \text{at} \quad z = a \quad (7)$$

The mathematical formulation may be simplified using dimensionless variables. Among a large number of alternatives we have selected the following dimensionless as we content that this group of variables allows distinction of the collective roles of individual parameters best in the closed form analytical solutions.

$$T_D = \frac{T_o - T}{T_o - T_i}, \quad T_{mD} = \frac{T_o - T_m}{T_o - T_i} \quad (8)$$

$$x_D = \frac{\rho_r c_r}{\rho_m c_m} \frac{k_m}{\rho_w c_w \phi a^2} \frac{x}{u}, \quad t_D = \frac{k_m t}{\rho_m c_m a^2} \quad (9)$$

$$z_D = \frac{z}{a} \quad \lambda = \frac{\rho_w c_w \phi}{\rho_r c_r} \frac{\rho_w c_w \phi u a}{k} \frac{\rho_m c_m u a}{k_m} \quad (11)$$

Using the above dimensionless variables governing equations become:

$$\frac{\partial T_D}{\partial t_D} + \frac{\partial T_D}{\partial x_D} - \frac{1}{\lambda} \frac{\partial^2 T_D}{\partial x_D^2} - \theta \frac{\partial T_{mD}}{\partial z_D} \Big]_{z_D=0} = 0 \quad (12)$$

$$\frac{\partial T_{mD}}{\partial t_D} - \frac{\partial^2 T_{mD}}{\partial z_D^2} = 0 \quad (13)$$

Similarly the initial and boundary conditions become:

$$T_D = T_{mD} = 0 \quad \text{at} \quad t_D = 0 \quad (14)$$

$$T_D = 1 \quad \text{at} \quad x_D = 0 \quad (15)$$

$$T_D \rightarrow 0 \quad \text{as} \quad x_D \rightarrow \infty \quad (16)$$

$$T_{mD} = T_D \quad \text{at} \quad z_D = 0 \quad (17)$$

$$\frac{\partial T_{mD}}{\partial z_D} = 0 \quad \text{at} \quad z = 1 \quad (18)$$

The dimensionless governing equations, namely Eq. 12 and Eq. 13, are two coupled linear differential equations representing the transport in a representative fracture and matrix element

The Laplace space solutions of Eq. 12 and Eq.13, after applying the relevant boundary conditions are given by Eq. 19 and Eq. 20 respectively [see Appendix B].

$$\bar{T}_D = \frac{1}{s} \exp\left(\frac{\lambda x_D}{2}\right) \exp\left(-\sqrt{\lambda} x_D \sqrt{\frac{\lambda}{4} + s + \theta \sqrt{s} \tanh(\sqrt{s})}\right) \quad (19)$$

$$\bar{T}_{mD} = \bar{T}_D \left[\frac{-\tanh(\sqrt{s}) \sinh(\sqrt{s} z_D) + \cosh(\sqrt{s} z_D)}{\cosh(\sqrt{s} z_D)} \right] \quad (20)$$

One way of deriving a closed form solution to the above equation is to utilize the result of a definite integral relation on semi-infinite domain. This method has been employed by Sudicky and Frind (1982), to develop solutions to the above problem. This solution, although useful, contains a Heaviside step function and this makes it less suitable for regression procedures for parameter estimations. In addition it is not easy to identify the physical components of the modeled processes in the solution. In order to develop a more convenient and physically interpretable solution, we can utilize the concept of iterated Laplace transform[11,12,13] as follows. The first iteration inversion of Eq. 19 is carried out to yield:

$$\dot{T}_D(\tau, s) = \frac{\sqrt{\lambda} x_D}{2\sqrt{\pi \tau^3}} \exp\left(-\frac{\lambda(x_D - \tau)^2}{4\tau}\right) \frac{1}{s} \exp\left(-\theta \tau \sqrt{s} \tanh(\sqrt{s})\right) \quad (21)$$

The second iteration solution can be obtained directly from the solution derived by Skopp and Warrick, (1975).

The Skopp and Warrick,(1982) problem offers a very useful example for deriving the solution and for developing physically meaningful dimensionless variables. For that reason it has been reproduced in Appendix B in terms of most useful dimensionless parameters. Applying the second iteration in accordance with Skopp and Warrick inversion relations (See Appendix B) yields the real space closed form solution as follows:

$$T_D = \int_0^{x_D} \frac{\sqrt{\lambda} x_D}{2\sqrt{\pi\tau^3}} \exp\left(-\frac{\lambda(x_D - \tau)^2}{4\tau}\right) F(t_D - \tau) d\tau \quad (22)$$

Where

$$F = \frac{2}{\pi} \int_0^\infty e^{-\lambda_R} \left[\frac{\sin\left(\frac{\omega^2(t_D - \tau)}{2} - \lambda_I\right)}{+ \sin(\lambda_I)} \right] \frac{d\omega}{\omega} \quad (23)$$

$$\lambda_R = \frac{\theta\tau\omega}{2} \frac{\sinh(\omega) - \sin(\omega)}{\cosh(\omega) + \cos(\omega)} \quad (24)$$

$$\lambda_I = \frac{\theta\tau\omega}{2} \frac{\sinh(\omega) + \sin(\omega)}{\cosh(\omega) + \cos(\omega)} \quad (25)$$

3. SIMULATIONS OF TRANSPORT

For simulating the transport the following definitions can be greatly useful to assume possible ranges of the three parameters of the model. First one may identify a characteristic time for each process, namely convection, thermal dispersion and transverse thermal conduction respectively.

$$t_c = \frac{L}{u}, t_k = \frac{\rho_w c_w \phi L^2}{k}, \text{ and } t_t = \frac{\rho_m c_m a^2}{k_m} \quad (26)$$

and two parameters of heat capacity ratios may be identified:

$$\theta_1 = \frac{\rho_w c_w \phi}{\rho_r c_r}, \text{ and } \theta_2 = \frac{\rho_m c_m}{\rho_r c_r} \quad (27)$$

Finally three normalized variables may be defined as:

$$x_{nD} = \frac{x}{L}, z_{nD} = \frac{z}{a}, \text{ and } t_{pvi} = \frac{ut}{L} \quad (28)$$

Note that while each one of the space variables are normalized by a physical length, the normalized time variable turns out to be equal to number of pore volumes injected.

Using the above variables we can show that some well known dimensionless parameters such as longitudinal and transverse Peclet numbers may be expressed as:

$$Pe = \frac{t_k}{t_c} \quad \text{and} \quad P_t = \frac{t_t}{t_c} \quad (29)$$

It is much easier to guess initial/possible estimates of these numbers for simulation purposes. For instance while a Peclet number of 100 indicates a very small dispersive transport compared to the convective transport. A value of 20 assumes a highly dispersive system. As we expect the magnitude of transverse dispersion is to be small compared to the longitudinal dispersion, the transverse Peclet number is generally assumed to be significantly greater than longitudinal one. Similarly, we can make fairly reliable estimates of the magnitudes of heat capacity ratios and we know the possible ranges of normalized variables in an experiment.

The initial dimensionless numbers of the transport equation then may be written as:

$$x_D = \frac{x_{nD}}{\theta_2 Pe}, \text{ and } t_D = \frac{t_{pvi}}{P_t} \quad (30)$$

$$\theta = \frac{a/b}{\theta_2} \quad \text{and} \quad \lambda = \frac{\theta_1}{Pe P_t} \quad (31)$$

Such arrangements allow much more confident estimates of possible ranges of the dimensionless variables as well as providing insight into the collective role of parameters.

The solutions are computed for a normalized time varying from zero to 2.5 pore volume injection, namely from two possible group of numbers, namely $t_{pvi}=0$ to $t_{pvi}=2.5$. Then the return profiles are computed for Peclet numbers of 100 and 30 and setting each one of the remaining dimensionless and normalized parameters to one.

Eq. 22 distinctly shows that while the transverse diffusion into the adjacent matrix is controlled by two parameters θ and t_D only, the transport within the

fractures is controlled by λ , x_D and t_D . These variables can directly be related to the individual normalized variables of each domain.

The computed values of temperature return profiles are given in Figures 1 through 3. The return profiles can be computed with various methods and among them Fourier transform based numerical Laplace transform techniques is most successful reproducing analytical results. The Stehfest algorithm, although much faster than any other method may sometimes suffers from accuracy as it cannot reproduce profiles containing sharp fronts which is the case for small to medium dispersivity systems. The Fourier series based methods are the most efficient ones, even more efficient than real space analytical solution. The numerical double integration requirement of the analytical solution appears to be hindering a fast computation of the profiles. Therefore, the analytical solution's main function may be sometimes limited to providing an advanced benchmark to compare the accuracy and efficiency of numerical Laplace inversions for such problems.

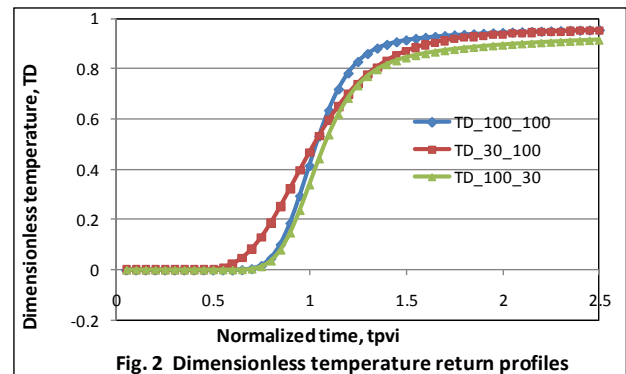
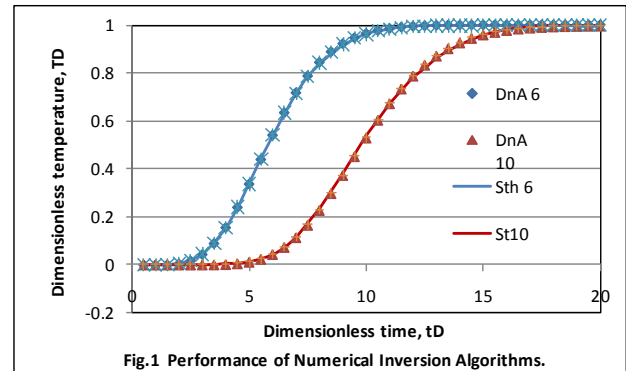
The design of reinjection operations involve obtaining the best estimates of three design variables. The design variables are listed as injection rate, distance between injector producer pairs and expected thermal breakthrough time (i.e. expected life of the project). Fig.2 may be used to compute the dimensionless parameter values for a given T_D value accepted thermal breakthrough. The more the reservoir cools due continued injection of cold water the dimensionless time gets greater increasing to one at complete cooling. A forty percent cooling means a TD of 0.4 which may be considered as the thermal breakthrough time. Fig. shows that while a large longitudinal thermal dispersion adversely influences thermal efficiency, a large transverse thermal conductivity/dispersion delays thermal breakthrough. Once the dimensionless parameters are identified we may solve for the normalized variables after setting critical values of injection rate and the distance between an injection production pair.

4. CONCLUSIONS

A novel analytical model of thermal transients in a parallel fractures geothermal model have been developed. The model is of great importance as it allows to identify the physical components of the modeled processes in the solution. It also provides the collective roles of the individual parameters of the transport. The analytical solutions are used as benchmark to evaluate the efficiency and accuracy of some numerical Laplace transform methods. Fourier transform based methods are found to be extremely accurate and more

importantly more efficient than the analytical model itself.

The developed models have been used to show how to carry out the design of a reinjection operation in a geothermal reservoir as well as computing the efficiency of an ongoing operation.



REFERENCES

- [1] Skopp, J. and Warrick, A.W. "A two phase model for the miscible displacement of reactive solutes in soils", *Soil sci. Soc. Am. Proc.* Vol 38 No. 4, pp. 545-550, 1974
- [2] Tang, D.H, Frind, E. O., and Suducky E. A., Contaminant transport in fractured porous media for a single fracture, *Water Resour. Res.*, Vol.17, No.3, pp. 555-564, June 1981
- [3] Suducky, E. A. and Frind, E. O. "Contaminant transport in fractured porous media: Analytical solutions for a system of parallel fractures", *Water Resour. Res.*, Vol. 18, No. 6, pp. 1634-1642, Dec. 1982.
- [4] Barker, J. A. "Laplace transform solutions for solute transport in fissured aquifers", *Adv. Water resources*, Vol. 5 No.2, pp. 98-104, June 1982
- [5] West, M. R., Kueper, B. H., and Novakowski, K. S. "Semi-analytical solutions for solute transport in fractured porous media using a strip source of finite width", *Adv. WaterResources*, Vol. 27, pp. 1045-1059, 2004

- [6] Chen, S.C., Solutions for Radionuclide Transport From an Injection Well Into a Single Fracture in a Porous Formation., *Water Resour. Res.*, Vol. 22, No. 4, pp. 508-518, April 1986.
- [7] El-Khatib, Noaman A. F. , Transient pressure behavior for a reservoir with continuous permeability distribution in the invaded zone, Proceedings 16th SPE Middle East Oil and Gas Show and Conference, MEOS, V.2, pp. 609-624, 2009.
- [8] Dubner, H., and Abate, J. " Numerical inversion of Laplace transforms by relating them to the Finite Fourier Cosine Transform", *J. ACM*, V Vol.13, No.1, pp.115-123, Jan., 1968.
- [9] Stehfest, H. "Algorithm 368: Numerical inversion of Laplace transform", *D-5 Communication ACM*, Vol. 13, No. 1, pp. 47-4, Jan., 1970.
- [10] DeHoog FR, Knight JH, Stokes AN. An improved method for numerical inversion of Laplace transforms. *SIAM J Scient Statist Comput* Vol. 3, No. 3, pp.357–66, 1982.
- [11] De Smedt, F., and Wierenga, P. J. "A generalized solution for solute flow in soils with mobile and immobile water," *Water Resources. Res.* Vol. 15, No. 5, pp. 1137-1141, 1981.
- [12] De Smedt, F., Brevis, W. and Debels, P. "Analytical solution for solute transport resulting from instantaneous injection in streams with transient storage," *Journal of Hydrology*, Vol. 315, pp. 25-39, 2005.
- [13] Kocabas, I. "Application of iterated Laplace transformation to tracer transients in heterogeneous porous media, *J. Franklin Institute*, Volume 348, Issue 7, Sept. 2011, pp. 1339-1362
- [14] Abramowitz, M. and Stegun I.A., *Handbook of Mathematical Functions*, Dover Publications, NY, 10th Ed. 1972.

APPENDIX A: Skopp and Warrick model.

The earliest analytical model of tracer transients in a similar geometrical configuration is developed by Skopp and Warrick (1982). Adopting Skopp and Warrick model to thermal transients could provide significant intuition to understanding the parallel fractures model.

In the Skopp and Warrick model longitudinal dispersion is neglected, and hence neglecting the longitudinal thermal dispersion reduces the governing equations to A1 and A2

$$\rho_r c_r \frac{\partial T}{\partial t} + \rho_w c_w \phi u \frac{\partial T}{\partial x} - \frac{k_m}{b} \frac{\partial T_m}{\partial z} \Bigg|_{z=0} = 0 \quad (A1)$$

$$\rho_m c_m \frac{\partial T_m}{\partial t} - k_m \frac{\partial^2 T_m}{\partial z^2} = 0 \quad (A2)$$

The initial and boundary conditions are specified the same as those Eq.3 through Eq.7 in the main text except Eq. 5 is not needed for this problem.

The most meaningful and intuitive dimensionless variables suitable for this problem may be the following.

$$t_D = \left(t - \frac{\rho_r c_r x}{\rho_w c_w \phi u} \right) \frac{k_m}{\rho_m c_m a^2} \quad (A3)$$

$$x_D = \frac{k_m x}{\rho_w c_w \phi u a} \quad \text{and} \quad z_D = \frac{z}{a} \quad (A4)$$

Based on A3 and A4 equations A1 and A2 reduces to:

$$\left[\frac{\partial T_D}{\partial x_D} - \frac{\partial T_{mD}}{\partial z_D} \right]_{z_D=0} = 0 \quad (A5)$$

$$\frac{\partial T_{mD}}{\partial t_D} - \frac{\partial^2 T_{mD}}{\partial z_D^2} = 0 \quad (A6)$$

The initial and boundary conditions become the same as Eq.14 through eq.18 in the main text, and again eq.16 is not needed for this problem.

Laplace transforming A6 results in:

$$\frac{\partial^2 \bar{T}_{mD}}{\partial z_D^2} - s \bar{T}_{mD} = 0 \quad (A7)$$

Solving A7 one obtains A8.

$$\bar{T}_{mD} = c_1 \sinh(\sqrt{s} y_D) + c_2 \cosh(\sqrt{s} y_D) \quad (A8)$$

Applying the boundary conditions reduces A8 to A9.

$$\bar{T}_{mD} = \bar{T}_D \left[\frac{-\tanh(\sqrt{s}) \sinh(\sqrt{s} y_D) + \cosh(\sqrt{s} y_D)}{\cosh(\sqrt{s} y_D)} \right] \quad (A9)$$

Using A9 we may derive:

$$\frac{\partial \bar{T}_{mD}}{\partial y_D} \Bigg|_{y_D=0} = -\bar{T}_D \sqrt{s} \tanh(\sqrt{s}) \quad (A10)$$

Substituting A10 into A5 yields:

$$\frac{\partial \bar{T}_D}{\partial x_D} + \sqrt{s} \tanh(\sqrt{s}) \bar{T}_D = 0 \quad (A11)$$

Solving A11 and applying the boundary condition at $x_D = 0$ we obtain:

$$\bar{T}_D = \frac{1}{s} \exp\left(-\sqrt{s} \tanh(\sqrt{s}) x_D\right) \quad (\text{A12})$$

The inversion of A12 is directly obtained from Skopp and Warrick inversion relation given in Appendix C. Substituting x_D in place of A and 1 in place of B in equations C2 through C4 we obtain:

$$F = \frac{2}{\pi} \int_0^\infty \exp(-\lambda_R) \left[\frac{\text{Sin}\left(\frac{\omega^2 t_D}{2} - \lambda_I\right)}{+ \text{Sin}(\lambda_I)} \right] \frac{d\omega}{\omega} \quad (\text{A13})$$

$$\lambda_R = \frac{\omega x_D}{2} \frac{\text{Sinh}(\omega) - \text{Sin}(\omega)}{\text{Cosh}(\omega) + \text{Cos}(\omega)} \quad (\text{A14})$$

$$\lambda_I = \frac{\omega x_D}{2} \frac{\text{Sinh}(\omega) + \text{Sin}(\omega)}{\text{Cosh}(\omega) + \text{Cos}(\omega)} \quad (\text{A15})$$

APPENDIX B: Analytical Solution to Parallel Fractures Model.

The dimensionless governing equation of parallel fractures model are given by Eq. 12 and Eq. 13. Rearranging eq. 12, we obtain B1.

$$\left. \frac{\partial^2 T_D}{\partial x_D^2} - \lambda \frac{\partial T_D}{\partial x_D} - \lambda \frac{\partial T_D}{\partial t_D} + \lambda \theta \frac{\partial T_{mD}}{\partial z_D} \right]_{z_D=0} = 0 \quad (\text{B1})$$

Laplace transforming B1:

$$\left. \frac{\partial^2 \bar{T}_D}{\partial x_D^2} - \lambda \frac{\partial \bar{T}_D}{\partial x_D} - \lambda s + \lambda \theta \frac{\partial \bar{T}_{mD}}{\partial z_D} \right]_{z_D=0} = 0 \quad (\text{B2})$$

The solution of dimensionless matrix diffusion equation, namely Eq. 13 and its derivative at the fracture matrix interface, have already been presented in Appendix A, given by A9 and A10 respectively. Substituting A10 into B2 we obtain:

$$\frac{\partial^2 \bar{T}_D}{\partial x_D^2} - \lambda \frac{\partial \bar{T}_D}{\partial x_D} - \lambda \left(s + \theta \sqrt{s} \tanh(\sqrt{s}) \right) \bar{T}_D = 0 \quad (\text{B3})$$

Solving B3 we obtain:

$$\bar{T}_D = \frac{1}{s} \exp\left(\frac{\lambda x_D}{2}\right) \exp\left(-\sqrt{\lambda^2 + 4\lambda(s + \theta \sqrt{s} \tanh(\sqrt{s}))} \frac{x_D}{2}\right) \quad (\text{B4})$$

Rearranging B4 results in B5 as it lends itself to an easy implementation of iterated Laplace inversion method.

$$\bar{T}_D = \frac{1}{s} \exp\left(\frac{\lambda x_D}{2}\right) \exp\left(-\sqrt{\frac{\lambda}{4} + s + \theta \sqrt{s} \tanh(\sqrt{s})} \frac{\sqrt{\lambda} x_D}{2}\right) \quad (\text{B5})$$

The first step of iterative Laplace inversion [14] result in Eq. 21 and the second iteration would yield Eq. 22 through Eq.25. Note for the second iteration while real space time variables is $(t_D - \tau)$ and A has been replaced with $\theta \tau$ in the Skopp and Warrick inversion relations C2 through C4.

APPENDIX C : Laplace Inversion Relation by Skopp and Warrick

Skopp and Warrick provides the following Laplace transform relation in their notable work in 1976.

$$F(s) = \frac{1}{s} \exp\left(-A \sqrt{s} \tanh(B \sqrt{s})\right) \quad (\text{C1})$$

$$F = \frac{2}{\pi} \int_0^\infty \exp(-\lambda_R) \left[\frac{\text{Sin}\left(\frac{A \omega^2}{2} - \lambda_I\right)}{+ \text{Sin}(\lambda_I)} \right] \frac{d\omega}{\omega} \quad (\text{C2})$$

$$\lambda_R = \frac{A \omega}{2} \frac{\text{Sinh}(B \omega) - \text{Sin}(B \omega)}{\text{Cosh}(B \omega) + \text{Cos}(B \omega)} \quad (\text{C3})$$

$$\lambda_I = \frac{A x_D}{2} \frac{\text{Sinh}(B \omega) + \text{Sin}(B \omega)}{\text{Cosh}(B \omega) + \text{Cos}(B \omega)} \quad (\text{C4})$$

A Novel Two Dimensional Analytical Model of Contaminant Transport in Groundwater Aquifers

Ibrahim Kocabas

Chemical Engineering Department, AUS (ikocabas@aus.edu)

ABSTRACT

Only two percent of waters on earth is freshwater and groundwater plays a central role in freshwater supplies in many parts of the world. In order to assess the degree of contamination or vulnerability to contamination in groundwater aquifers a large number of analytical models have been presented. The models have varied in complexity ranging from a simple one dimensional models to complex two and three dimensional models in infinite as well as bounded aquifers. Among them a fairly comprehensive two dimensional transport model in a homogenous bounded aquifer have been first presented by Batu, 1989. The same system has later been modified by West et al. 2005, to include diffusion into matrix blocks. While the solution by Batu has been presented in real space, West et al. employed a numerical Laplace inversion technique to compute their solution.

In this work, we first demonstrate the inconsistent use of numerical inversion of the Laplace transform technique as the presented solution by West et al must lead to complex concentration function which is physically impossible. Second, we show that consecutive application of Laplace, Fourier Sine and Finite Fourier Cosine transforms does in fact lead to a simpler procedure than that of both Batu and West et al, to develop the solutions to the governing equations. Then we obtained the appropriate real space solutions using Inverse Finite Fourier Cosine, Inverse Fourier Sine and inverse iterated Laplace transform techniques and sequentially. Finally, we employed our real space solution as benchmarks for numerically inverted solutions.

Keywords: Groundwater contamination, convection dispersion, iterated Laplace transform, aquifer remediation

1. INTRODUCTION

Analytical models of solute transport have been only one dimensional for a long period until the development of modern computers as powerful computational tools.

With increasing computational resources a second generation of analytical models have been developed consisting of two coupled one dimensional equations.

In general most of these models have stayed as semi analytical that means the solutions are obtained in Laplace space and they are computed using numerical Laplace inversion algorithms. With the modern computers, the development of two and three dimensional analytical solute transport models have accelerated in order to better represent the actual transport in the field as well as to produce more challenging benchmarks for numerical simulators. Advancement in computational powers have also allowed the use of some powerful but obscure methods to develop closed form analytical solutions in real space and compute them using numerical integration techniques. Thus, this approach allowed comparing the performances of the numerical inversion algorithms as well as providing accurate benchmarks for numerical simulators.

In the following we critically review a number of two dimensional methods of solute transport from the point of physical validity or their accuracy in representing an actual system. Then, we develop real space solutions for one possible system using iterated Laplace transform

technique. Note that the proposed dimensionless parameters and the proposed dependent variable transformation appears to be unique to this work for the two dimensional problems studied.

2. MATHEMATICAL DEVELOPMENTS

The two and three dimensional solutions to convection dispersion equation started with the work of Sauty [1] and later continued with Leij and Dane[2] and Chrysikopoulos, and his co-workers[3,4,5,6], Guyonneta and Neville[7], and Bekhit and Hassan[8] followed. The common feature of these early studies is that they were mostly in infinite medium problems in all directions. then researchers started to develop solutions for bounded media and/or heterogenous coupled media (diffusion into adjacent matrix or pseudo steady state solute exchange between the flowing and stagnant portions) as well. Among them we mention and review the works of Batu[9], Bai et al.[10], West et al [11] and Zhan et al [12]. The work of Batu[9] is based on a conceptual model of a horizontal aquifer of infinite extend in flowing direction and bounded in transverse directions to flow. While both convection and dispersion take place in flowing direction only dispersion occurs in transverse directions. A strip source is assumed to function at the inner boundary and solute decay assumed to occur in the system. Batu[9] has used a Laplace transform technique with subsequent separation of variables to obtain the solutions. The main contribution of Batu[9] was to include a non

symmetrical strip source to the system as the symmetrical source solution has been presented earlier by Bruch and Street (1967) which has been reported by Batu[9]. For this problem obtaining a real space solution was possible. Later West et al [11] have included a matrix diffusion term in the same model. The matrix diffusion was assumed to occur into the confining layers in the third dimension (i.e. space coordinate). The coupling of the equations in main aquifer and confining matrix were achieved using the continuity of concentrations and fluxes at the aquifer matrix interface. The matrix was also assumed to be of finite extent as opposed to many models employing a semi-infinite matrix. The main disadvantage of this model is in this assumption as vertical diffusion is expected to be quite small and an extremely slow process the confining matrix aquitards could have been assumed to be infinite extend which would greatly simplify the solution. The fact that a vertical diffusion into vertically confining layers from a fairly thick aquifer is unlikely to have any significant impact on the transport in the aquifer appears to be a major shortcoming of the model. A second point in this model is that assuming a decay of solute at the inner boundary as formulated in the paper may lead to a nonphysical solution and the reader should have been warned against this possibility. A significant contribution of West et al.[11] is the employment of a Finite Fourier Cosine transform to obtain the solution. Nevertheless, the authors had to resort to numerical Laplace inversion to compute the solutions as they were unable to invert them analytically. A recent study by Zhan et. al [12] considers a similar system in which they assumed convective transport in the semi infinite aquitards in addition to diffusion/dispersion only.

The conceptual model used in their work suffers from the ignoring the convective transport in transverse direction in the aquifer while it has been included in the adjacent aquifers. It is quite unlikely to have two adjacent media while one has a finite fluid velocity the other has zero velocity in the same direction. A second point that needs clarification is that the validity of application of Fourier transform in a composite media as Fourier transform demands a continuous semi-infinite medium. Justification of using such a method has not been elaborated by the authors.

Bai et al [10] developed a different conceptual model of a two dimensional transport in an aquifer than West et al [11] and Zhan et al. [12] They have assumed both convective and dispersive transport in both directions in the aquifer.

The aquifer is assumed to be semi infinite in x direction and bounded in y direction. They have also included a pseudo steady state transfer between the flowing and stagnant portions within the aquifer (a capacitance model). The major drawback of their work is that they have assumed constant concentrations at the aquifer

confining layer interface which is not physically likely to occur in an actual system. Notably the authors used a double Laplace transform technique to develop the two dimensional solutions and a double numerical inversion technique to compute them. The double numerical inversion of Laplace transforms suffer from the same disadvantages of single numerical inversion methods.

In the following sections we will develop real space analytical solutions to a modified West et al . [11] and Bai et al.[10] mathematical models. This modified model uses the concept of two superposed media in a two dimensional flow system. This solution is important since it quite accurately represents two dimensional transport in confined aquifer in y direction with an unsteady state capacitance term included within the aquifer. This is a physically more likely system that may exists in subsurface than those presented by Zhan et al. [12], Bai et al. [10], and West et al. [11].

2.1 Governing Equations

The two dimensional governing differential equations of a chemically conservative tracer transport in a heterogeneous aquifer and the adjacent immobile matrix (aquitard) may be obtained by joining the derivations of Bear [13] and Coats and Smith [14] and Correa et al[15]:

$$f \frac{\partial C}{\partial t} + u \frac{\partial C}{\partial x} - D_L \frac{\partial^2 C}{\partial x^2} - D_t \frac{\partial^2 C}{\partial y^2} + kC + (1-f) \frac{\phi D_m}{b} \frac{\partial C_m}{\partial z} \Big|_{z=0} = 0 \quad (1)$$

$$0 \leq x \leq \infty, 0 \leq y \leq h, 0 \leq z \leq a$$

$$\frac{\partial C_m}{\partial t} - D_m \frac{\partial^2 C_m}{\partial z^2} + kC_m = 0 \quad (2)$$

In Eq.1 and eq. 2 while the tracer is assumed to subject to decay **no tracer adsorption** is assumed in the porous medium, and hence, no retardation term is included. Note the adding retardation would not alter the general form of the above equations.

For an initial concentration of solute, C_i , in the aquifer into which a constant concentration fluid flux continuously enters from a certain section of the boundary along x direction, the initial and boundary conditions are specified as follows:

$$C = C_m = C_i \quad \text{at} \quad t = 0 \quad (3)$$

$$C = C_0 e^{kt} \delta(y - y') \quad \text{at} \quad x = 0 \quad (4)$$

Employing Eq.4 needs attention as it has been prescribed differently by Bear[13], Tang et. al [16,17], Batu [9] and West et al [11]. While Bear [13] and Tang

et al [16] assumed $kt=0$, Batu assumed the same form in Eq.4 and West et. al.[11] assumed $(-kt)$ as the exponent. Mathematically while Batu[9] solution leads to an infinite amount of solute input into the systems as time goes to infinity, West et. al.[11] solution may lead to an unphysical concentration function since it may cause the final solution to be function of a complex variable (See equation A38 in Appendix A). As there were no physical justification in each of the mentioned pieces of work we have employed Batu's specification for mathematical purposes even though we have preferred Bear's and Tang et al's specification.

The aquifer is assumed to be semi-infinite in x direction and confined along y direction.

$$C \rightarrow 0 \quad \text{as} \quad x \rightarrow \infty \quad (5)$$

$$\frac{\partial C}{\partial y} = 0 \quad \text{at} \quad y = 0 \quad (6)$$

$$\frac{\partial C}{\partial y} = 0 \quad \text{at} \quad y = h \quad (7)$$

Then the two equations are coupled through the equality of concentrations and fluxes at the aquifer and matrix boundary.

$$C = C_m \quad \text{and} \quad z = 0 \quad (8)$$

$$\frac{\partial C_m}{\partial z} = 0 \quad \text{at} \quad z = a \quad (9)$$

The mathematical formulation is simplified using following dimensionless variables:

$$C_D = \frac{C - C_i}{C_o - C_i} \quad \text{and} \quad C_{mD} = \frac{C_m - C_i}{C_o - C_i} \quad (10)$$

$$x_D = \frac{ux}{D_L} \quad \text{and} \quad t_D = \frac{u^2 t}{D_L} \quad (11)$$

$$y_D = \frac{uy}{\sqrt{D_L D_t}} \quad \text{and} \quad z_D = \frac{uz}{\sqrt{D_L D_m}} \quad (12)$$

$$\theta = \frac{\phi_m D_m}{\phi_f D_t} \quad (13)$$

In terms of the dimensionless variables the governing equations and initial and boundary conditions reduce to:

$$f \frac{\partial C_D}{\partial t_D} + \frac{\partial C_D}{\partial x_D} - \frac{\partial^2 C_D}{\partial x_D^2} - \frac{\partial^2 C_D}{\partial y_D^2} + \kappa C_D + (1-f) \frac{1}{\lambda} \frac{\partial C_{mD}}{\partial z_D} \Big|_{z_D=0} = 0 \quad (14)$$

$$0 \leq x_D \leq \infty, \quad 0 \leq y_D \leq y_{Dh}, \quad 0 \leq z_D \leq z_{Da} \quad (15)$$

$$\frac{\partial C_m}{\partial t_D} - \frac{\partial^2 C_m}{\partial z_D^2} + \kappa C_{mD} = 0 \quad (15)$$

$$C_D = C_{mD} = 0 \quad \text{at} \quad t_D = 0 \quad (16)$$

$$C_D = C_{mD} = 0 \quad \text{at} \quad t_D = 0 \quad (17)$$

$$C_D = e^{\kappa^* t_D} \delta(y_D - y'_D) \quad \text{at} \quad x_D = 0 \quad (18)$$

The aquifer is assumed to be semi-infinite in x direction and confined along y direction.

$$C_D \rightarrow 0 \quad \text{as} \quad x_D \rightarrow \infty \quad (19)$$

$$\frac{\partial C_D}{\partial y_D} = 0 \quad \text{at} \quad y_D = 0 \quad (20)$$

$$\frac{\partial C_D}{\partial y_D} = 0 \quad \text{at} \quad y_D = y_{Dh} \quad (21)$$

$$C_D = C_{Dm} \quad \text{and} \quad z_D = 0 \quad (22)$$

$$\frac{\partial C_{Dm}}{\partial z_D} = 0 \quad \text{at} \quad z_D = z_{Da} \quad (23)$$

3. Development of Solutions

The solutions of the governing equations are developed through a unique set of steps as follows. first the dependent variables are subject to the following variable transformation. The two new dependent variables, χ and χ_m , related to the original dependent variables by[17]:

$$C_D = \chi \exp(x_D / 2) \quad (24)$$

$$C_{mD} = \chi_m \exp(x_D / 2) \quad (25)$$

After performing a dependent variable transformation of the governing equations and the related initial and boundary condition, we apply a Laplace, a Fourier Sine and a Finite Fourier Cosine transform to the governing equations as well as initial and boundary conditions with respect to the variables $t_D = 0, x_D = 0$ and $y_D = 0$ respectively. The governing equation for the aquifer reduces to an algebraic equation and the solution becomes:

$$\ddot{\chi}_c = \left\{ \frac{2\omega}{\pi(s-\kappa)} \text{Cos}\left(\frac{\pi n y'_D}{y_{Da}}\right) \right. \quad (26)$$

$$\left. \frac{1}{s+a+\omega^2+\kappa+\frac{\pi^2 n^2}{y_{Da}^2}+\beta} \right\}$$

Where

$$\beta = \frac{\sqrt{s+\kappa}}{\lambda} \tanh(\sqrt{s+\kappa} z_{Da}) \quad (27)$$

Note that while the double dots represent the Laplace and Fourier Sine transformation, the subscript c represents the Finite Fourier Cosine transformation of

the variable χ . Also note that Eq. 26 represents the solution for line source located at y'_D . The inversion of this solution and developing strip source solutions are carried out as follows. First the line source solution is inverted back from the Finite Fourier Cosine space resulting in:

$$\ddot{\chi} = \left\{ \frac{\ddot{G}(n=0)}{y_{Da}} + \ddot{G}(n) \sum_{n=1}^{\infty} \left\{ \begin{array}{l} \frac{2}{y_{Da}} \text{Cos}\left(\frac{\pi n y'_D}{y_{Da}}\right) \\ \text{Cos}\left(\frac{\pi n y_D}{y_{Da}}\right) \end{array} \right\} \right\} \quad (28)$$

Where

$$\ddot{G} = \left[\frac{\frac{2\omega}{\pi(s-\kappa)}}{s+a+\omega^2+\kappa+\frac{\pi^2 n^2}{y_{Da}^2}+\beta} \right] \quad (29)$$

To develop the solution for a strip source Eq. 28 is integrated over the strip source to domain to yield:

$$\ddot{\chi} = \frac{\ddot{G}(n=0)2B}{y_{Da}} + \frac{2}{n\pi} \sum_{n=1}^{\infty} \left[\frac{\ddot{G}(n)\text{Cos}\left(\frac{\pi n y_D}{y_{Da}}\right)}{\left[\text{Sin}\left(\frac{\pi n(d+2B)}{y_{Da}}\right) - \text{Sin}\left(\frac{\pi n d}{y_{Da}}\right) \right]} \right] \quad (30)$$

Inverting Eq. 30 with respect to Fourier Sine transform may be best approach for the next step in developing the real space solutions. This involves inverting \ddot{G} with respect to Fourier Sine transform to obtain the Laplace space function.

$$\dot{G} = \frac{1}{(s-\kappa^*)} \exp\left(-\sqrt{fs+a+\kappa+\frac{\pi^2 n^2}{y_D^2}+\beta} x_D\right) \quad (31)$$

The real space solution is obtained by using an iterated Laplace transform method. In this procedure a classical inversion formula [20] is followed by the inversion relation provided by Skopp and Warrick, [18]. The two relations are then joined by a convolution equation to yield:

$$G(t_D) = \frac{2}{\pi} \int_0^{t_D} \exp\left(-\left(a+\kappa+\frac{\pi^2 n^2}{y_D^2}+\beta\right)\frac{\tau}{f}\right) F(t_D-\tau) \frac{\sqrt{f} x_D}{2\sqrt{\pi\tau^3}} \exp\left(-\frac{fx_D^2}{4\tau}\right) d\tau \quad (32)$$

Where

$$F = \frac{1}{\pi} e^{-(\kappa+\kappa^*)(t_D-\tau)} \int_0^{\infty} e^{-\lambda_R} \left\{ \begin{array}{l} \left[\text{Sin}\left(\frac{\omega^2(t_D-\tau)}{2}-\lambda_l\right) + \text{Sin}(\lambda_l) \right] \frac{2}{\omega^2} \\ \left[\text{Cos}\left(\frac{\omega^2(t_D-\tau)}{2}-\lambda_l\right) - \text{Cos}(\lambda_l) \right] \frac{1}{\kappa^*} \end{array} \right\} \frac{d\omega}{\omega} \quad (33)$$

Where λ_R and λ_l are given by equations A43 and A44 in Appendix A. Finally the dimensionless concentrations in the aquifer is obtained from eq. 24 where.

$$\chi = \left\{ \frac{G(n=0)}{y_{Da}} + G(n) \sum_{n=1}^{\infty} \left\{ \begin{array}{l} \frac{2}{y_{Da}} \text{Cos}\left(\frac{\pi n y'_D}{y_{Da}}\right) \\ \text{Cos}\left(\frac{\pi n y_D}{y_{Da}}\right) \end{array} \right\} \right\} \quad (34)$$

This solution is important for several reasons. First, it allows studying the collective role of the parameters representing the controlling processes in model. In fact, it is unique in this aspects as a most systematic approach is used to develop the solutions in dimensionless parameters and variables. Second, the model is fairly comprehensive allowing us to study more practical problems compared to the earlier models. Finally it allows evaluating the efficiency of numerical inversion algorithms and may be used as a benchmark for numerical simulators.

Furthermore the iterative Laplace transform method is quite versatile and may be easily adopted to develop real space solutions to some other problems such as posed by Bai et al and Zhan et al. Those models must however be modified to eliminate those features which are unlikely to exist in actual systems.

Assuming no diffusion into z direction and no decay which means $\beta = 0$, $\kappa = 0$, and $\kappa^* = 0$, will allow us to reproduce the well known solution of Bruch and Street, which is reported by both Batu, (1989) and West et al. (2004).

On non zero decay constant however must be investigated in detail. If a negative κ^* is assumed as in the work of West et.al. (2004) the inversion of Eq. 31 may yield a physically unlikely complex variable solution as demonstrated by inversion relation A38. The reader must be informed against this possibility.

4. CONCLUSIONS

In the present work we have developed novel two dimensional analytical model of contaminant transport in groundwater aquifers. Various forms of the model has been studied by several researchers in the past including some recent ones. The earlier pieces of work suffered several drawbacks which ranged from using inappropriate boundary condition to physically unlikely conditions in actual systems and to having required to use a numerical Laplace inversion technique to compute concentration functions. First we have presented a physically likely system which varied from models of all previous. then we incorporated a mathematically tractable boundary condition. Finally we developed a closed from real space solution as a novel model of the prescribed problem of two dimensional contaminant transport. The new model is expected to function as a fairly comprehensive and quite accurate model of two dimensional transport. It serves as powerful tool of interpreting and evaluating field tracer tests and remediation operations. Finally it allows determining collective role of transport parameters which play dominant role in designing the tests as they allow estimating independence and/correlation of parameters.

REFERENCES

- [8] Sauty, J.P. An analysis of hydro-dispersive transfer in aquifers," *Water Resources Research*, Vol. 16 No. 1 Feb. 1980, pp.145-158
- [9] Leij, F. J. and Dane, J. H. "Analytical solution of one-dimensional advection equation and two and three dimensional dispersion equation," *Water Resources Research*, Vol. 26 No. 7 Jul. 1990, pp.1475-1482.
- [10] Chrysikopoulos, C. V. , Voudrias, E. A. and Fyrrillas, M. M. "Modelling of contaminant transport resulting from dissolution of nonaqueous phase liquid pools in saturated porous media," *Transport in porous Media*, Vol. 16, pp.125-145, (1994)
- [11] Chrysikopoulos, C. V., "Three dimensional analytical models of contamination transport from nonaqueous phase liquid pool dissolution in saturated porous medium," *Water Resources Research* Vol. 31. No. 4, pp. 1137-1145, (April, 1995)
- [12] Sim. Y. and Chrysikopoulos, C. V. "Analytical solutions for solute transport in saturated porous media with semi-infinite or finite thickness," *Advances in water resources*, Vol. 25 No.5, pp. 507-519, (1999)
- [13] Chrysikopoulos, C. V, Hsuan, P.Y, Fyrrillas, M. M. and Lee, K.Y. " Mass transfer coefficients and concentration boundary layer thickness for a dissolving NAPL pool in porous media", *J. Hazardous materials B97* pp. 245-255, 2003.
- [14] Guyonnetta, D. and Neville,C. "Dimensionless analysis of two analytical solutions for 3-D solute transport in groundwater", *J. Contaminant Hydrology*, Vol. 75 , pp.141– 153, 2004
- [15] Bekhit, H. M. and Hassan, A. E. "Two-dimensional modeling of contaminant transport in porous media in the presence of colloids, *Advances in Water Resources*, Vol. 28, No.12, pp.1320-1335, 2005
- [16] Batu, V. " A generalized two-dimensional analytical solution for hydrodynamic dispersion in bounded media with the first-type condition at the source", *Wat. Resour. Res.*, Vol.25 No.6 pp. 1125–1132, 1989.
- [17] Bai, M., Shua, Z., Cao, J., Zaman, M, and Roegiers, J.-C. "A semi-analytical solution for a two-dimensional capacitance model in solute transport," *J. Pet. Sci. and Eng.*, Vol. 22, pp.275-295, (1999)
- [18] West, M. R., Kueper, B. H., and Novakowski, K. S." Semi-analytical solutions for solute transport in fractured porous media using a strip source of finite width," *Advances in water resources*, Vol. 27 No.5, pp. 1045-1057, (2004)
- [19] Zhan,H, Wen,Z., Huang, G. and Sun, D. "Analytical solution of two-dimensional solute transport in an aquifer–aquitard system," *J. Contaminant Hydrology*, Vol. 107, pp. 162-174, (2009)
- [20] Bear, J. *Dynamics of Fluids in Porous Media*, Dover Publications, Inc. 1988
- [21] Coats, K.H., and B.D. Smith.. Dead end pore volume and dispersion in porous media. *SPE J.* Vol. 4 pp73–84, 1964.
- [22] Correa, A. C., Pande, K. K., Ramey, H. J. Jr. and Brigham, W. E.: "Prediction and interpretation of miscible displacement using a transverse matrix dispersion model," *SPE 16704*, (Sep. 1987).
- [23] Tang, D.H, Frind, E. O., and Suducky E. A., Contaminant transport in fractured porous media for a single fracture, *Water Resour. Res.*, Vol.17, No.3, pp. 555-564, June 1981
- [24] Kocabas, I. "Thermal Transients During Nonisothermal Fluid Injection into Oil Reservoirs", *J. Petroleum Science and Engineering*, Vol. 42, pp. 121-133, 2004
- [25] Skopp, J. and Warrick, A.W. " A two phase model for the miscible displacement of reactive solutes in soils", *Soil sci. Soc. Am. Proc.* Vol 38 No. 4, pp. 545-550, 1974
- [26] Haberman, R., *Elementary Applied Partial Differential Equations*, Prentice Hall Inc. 1983, New Jersey. pp. 368.
- [27] Bateman, H and Erdelyi, A., *Tables of Integral Transforms*, Mc Graw Hill 1954, Volume 1.

[28] Suducki, E. A. and Frind, E. O. "Contaminant transport in fractured porous media: Analytical solutions for a system of parallel fractures", *Water Resour. Res.*, Vol. 18, No. 6, pp. 1634-1642, Dec. 1982.

Appendix A:

The solution to Equations 12 through 19 is developed as follows: Let's define two new dependent variables, χ and χ_m , related to the original dependent variables by:

$$C_D = \chi \exp(x_D/2) \quad (A1)$$

And

$$C_{mD} = \chi_m \exp(x_D/2) \quad (A2)$$

Then, performing a dependent variable transformation reduces Equations 12 and 13 to:

$$\frac{\partial^2 \chi}{\partial x_D^2} + \frac{\partial^2 \chi}{\partial y_D^2} - \frac{\chi}{4} - f \frac{\partial \chi}{\partial t_D} - \kappa \chi - (1-f) \frac{1}{\lambda} \frac{\partial \chi_m}{\partial z_D} \Big|_{z_D=0} = 0 \quad (A3)$$

$$\frac{\partial^2 \chi_m}{\partial z_D^2} - \frac{\partial \chi_m}{\partial t_D} - \kappa \chi_m = 0 \quad (A4)$$

The related initial and boundary condition become:

$$\chi = \chi_m = 0 \quad \text{at} \quad t_D = 0 \quad (A5)$$

$$\chi = e^{\kappa^* t_D} \delta(y_D - y_D') \quad \text{at} \quad x_D = 0 \quad (A6)$$

$$\chi \rightarrow 0 \quad \text{as} \quad x_D \rightarrow \infty \quad (A7)$$

$$\frac{\partial \chi}{\partial y_D} = 0 \quad \text{as} \quad y_D = 0 \quad (A8)$$

$$\frac{\partial \chi}{\partial y_D} = 0 \quad \text{at} \quad y_D = y_{Db} \quad (A9)$$

$$\chi = \chi_m \quad \text{and} \quad z_D = 0 \quad (A9)$$

$$\frac{\partial \chi_m}{\partial z_D} = 0 \quad \text{at} \quad z_D = z_{Da} \quad (A10)$$

Apply the Laplace transformation to (A3) and (A4) with respect to t_D to obtain:

$$\frac{\partial^2 \dot{\chi}_c}{\partial x_D^2} - (fs + a + \kappa) \dot{\chi}_c + \frac{1}{\lambda} \frac{\partial \dot{\chi}_m}{\partial z_D} \Big|_{z_D=0} = 0 \quad (A11)$$

where $a=1/4$, and

$$\frac{\partial^2 \dot{\chi}_m}{\partial z_D^2} - (s + \kappa) \dot{\chi}_m = 0 \quad (A12)$$

In this work, the Fourier Sine transform and its inverse transform are defined as follows[19]:

$$\chi(\omega) = \frac{2}{\pi} \int_0^\infty \chi(x_D) \sin(\omega x_D) dx_D \quad (A13)$$

$$\chi(x_D) = \int_0^\infty \chi(\omega) \sin(x_D \omega) d\omega \quad (A14)$$

Hence, Fourier sine transform of the second derivative is:

$$\int_0^\infty \frac{d^2 \chi}{dx_D^2} \sin(\omega x_D) dx_D = \frac{2}{\pi} \chi(x_D=0) - \omega^2 \chi(\omega) \quad (A15)$$

Note that The Laplace transform of inner boundary condition at $x_D = 0$, namely Eq.16, is evaluated as:

$$\chi(0) = e^{\kappa^* t_D} \delta(y_D - y_D') \quad (A16)$$

$$\dot{\chi}(0) = \frac{1}{s - \kappa^*} \delta(y_D - y_D') \quad (A17)$$

Subsequently applying Fourier sine transform to (A11) with respect to x_D yields:

$$\frac{\partial^2 \ddot{\chi}}{\partial y_D^2} - \eta \ddot{\chi} + \frac{1}{\lambda} \frac{\partial \ddot{\chi}_m}{\partial z_D} \Big|_{z_D=0} = \frac{-2\omega \delta(y_D - y_D')}{\pi(s - \kappa^*)} \quad (A18)$$

Where

$$\eta = fs + \omega^2 + a + \kappa \quad (A19)$$

$$\frac{\partial^2 \ddot{\chi}_m}{\partial z_D^2} - (fs + \kappa) \ddot{\chi}_m = 0 \quad (A20)$$

The solution of A20 are in Laplace and Fourier Sine space is given by:

$$\ddot{\chi}_m = c_3 \text{Sinh}\left(-\sqrt{s + \kappa} z_D\right) + c_4 \text{Cosh}\left(\sqrt{s + \kappa} z_D\right) \quad (A21)$$

Transforming A9 and A10 and applying them to determine the constants c_3 and c_4 yields the solution of A18.

$$\ddot{\chi}_m = \ddot{\chi} \text{Cosh}\left(\sqrt{s + \kappa} z_D\right) - \ddot{\chi} \tanh\left(\sqrt{s + \kappa} z_{Da}\right) \text{Sinh}\left(\sqrt{s + \kappa} z_D\right) \quad (A22)$$

Then we will have:

$$\frac{\partial \dot{\chi}_{mc}}{\partial z_D} \Big|_{z_D=0} = -\ddot{\chi} \sqrt{s + \kappa} \tanh\left(\sqrt{s + \kappa} z_{Da}\right) \quad (A23)$$

Then Laplace and Fourier Sine transformed form of Eq.A18 becomes

$$\frac{\partial^2 \ddot{\chi}}{\partial y_D^2} - (\eta + \beta) \ddot{\chi} = \frac{-2\omega}{\pi(s - \kappa)} \delta(y_D - y_D') \quad (\text{A24})$$

where

$$\beta = (1 - f) \frac{\sqrt{s + \kappa}}{\lambda} \tanh(\sqrt{s + \kappa} z_{Da}) \quad (\text{A25})$$

The above equation may best be solved by using a Finite Fourier transform as demonstrated by West et al. In this work, the Finite Fourier Cosine transform and its inverse transform of the Laplace and Fourier sine space variable are defined as follows[19]:

$$\ddot{\chi}_c(n) = \int_0^{z_{Da}} \ddot{\chi}(y_D) \frac{\text{Cos}(\frac{\pi n y_D}{y_{Da}})}{y_{Da}} dy_D \quad (\text{A26})$$

$$\ddot{\chi}(y_D) = \frac{\ddot{\chi}_c(0)}{y_{Da}} + \sum_{n=1}^{\infty} \frac{2\ddot{\chi}_c(n)}{y_{Da}} \frac{\text{Cos}(\frac{\pi n y_D}{y_{Da}})}{y_{Da}} \quad (\text{A27})$$

Finite Fourier cosine transform of the second derivative is:

$$F_c \left\{ \frac{d^2 \ddot{\chi}}{dy_D^2} \right\} = -\frac{\pi^2 n^2}{y_{Da}^2} \ddot{\chi}_c - \left\{ \frac{\partial \ddot{\chi}}{\partial y_D} \Big|_{y_D=0} - \frac{\partial \ddot{\chi}}{\partial y_D} \Big|_{y_D=y_{Da}} \right\} \quad (\text{A28})$$

Finite Fourier Cosine transform of RHS of Eq is evaluated as:

$$\ddot{\chi}_c(x_D = 0) = \frac{2\omega}{\pi(s - \kappa)} \int_0^{y_{Da}} \delta(y_D - y_D') \frac{\text{Cos}(\frac{\pi n y_D}{y_{Da}})}{y_{Da}} dy_D \quad (\text{A29})$$

Carrying out the integration results in:

$$\ddot{\chi}_c(0) = \frac{2\omega}{\pi(s - \kappa)} \frac{\text{Cos}(\frac{\pi n y_D'}{y_{Da}})}{y_{Da}} \quad (\text{A30})$$

Thus Applying Finite Fourier Cosine transform with respect to y_D to A24 results in

$$\left(\eta + \frac{\pi^2 n^2}{y_{Da}^2} + \beta \right) \ddot{\chi}_c = \frac{2\omega}{\pi(s - \kappa)} \frac{\text{Cos}(\frac{\pi n y_D'}{y_{Da}})}{y_{Da}} \quad (\text{A31})$$

Solving for $\ddot{\chi}_c$

$$\ddot{\chi}_c = \left\{ \frac{\frac{2\omega}{\pi(s - \kappa)} \frac{\text{Cos}(\frac{\pi n y_D'}{y_{Da}})}{y_{Da}}}{1} \right\} \left\{ \frac{1}{fs + a + \omega^2 + \kappa + \frac{\pi^2 n^2}{y_{Da}^2} + \beta} \right\} \quad (\text{A32})$$

The following relations are utilized for inversions. The best way may be to invert this solution first with respect to Finite Fourier Cosine transform which yields

$$\ddot{\chi} = \left\{ \frac{\ddot{\chi}_c(n=0)}{y_{Da}} + \sum_{n=1}^{\infty} \frac{2\ddot{\chi}_c(n)}{y_{Da}} \frac{\text{Cos}(\frac{\pi n y_D}{y_{Da}})}{y_{Da}} \right\} \quad (\text{A33})$$

Or

$$\ddot{\chi} = \left\{ \frac{\ddot{G}(n=0)}{y_{Da}} + \ddot{G}(n) \sum_{n=1}^{\infty} \left\{ \frac{2}{y_{Da}} \frac{\text{Cos}(\frac{\pi n y_D'}{y_{Da}})}{y_{Da}} \right\} \right\} \left\{ \frac{\text{Cos}(\frac{\pi n y_D}{y_{Da}})}{y_{Da}} \right\} \quad (\text{A34})$$

This solution, given by A34, is valid for a point source at $x_D = 0$ and $y_D = y_D'$. In order to develop the solution for a strip source at $x_D = 0$ and source length varies from $d1$ to $d1+2B$ where $2B$ dimensionless strip length, A34 is integrated between these limits, resulting in:

$$\ddot{\chi} = \frac{\ddot{G}(n=0)}{y_{Da}} \int_{d1}^{d1+2B} dy_D' + \frac{2}{y_{Da}} \sum_{n=1}^{\infty} \ddot{G}(n) \frac{\text{Cos}(\frac{\pi n y_D'}{y_{Da}})}{y_{Da}} \int_{d1}^{d1+2B} \frac{\text{Cos}(\frac{\pi n y_D}{y_{Da}})}{y_{Da}} dy_D' \quad (\text{A35})$$

Where \ddot{G} is defined by Eq.29 in the main text. Carrying out the integration of A36 we obtain:

$$\ddot{\chi} = \frac{\ddot{G}(n=0)2B}{y_{Da}} + \frac{2}{n\pi} \sum_{n=1}^{\infty} \ddot{G}(n) \frac{\text{Cos}(\frac{\pi n y_D}{y_{Da}})}{y_{Da}} \left[\text{Sin}(\frac{\pi n (d1+2B)}{y_{Da}}) - \text{Sin}(\frac{\pi n d1}{y_{Da}}) \right] \quad (\text{A36})$$

Note for remaining inversions of A36 or Eq.30 in main text, we need to invert only $\ddot{G}(0)$ and $\ddot{G}(n)$. Inverting \ddot{G} with respect to Laplace and Fourier Sine transforms we start with anyone of them and do subsequent inversion of the remaining one. For

instance, first inverting with respect to Fourier Sine transform using

$$F_s^{-1} \left\{ \frac{2\omega}{\pi(s + \varepsilon)} \frac{1}{\omega^2 + \varepsilon} \right\} = \frac{1}{s + \varepsilon} \exp(-\sqrt{\varepsilon} x_D) \quad (\text{A37})$$

Using the relations A37 the inverse of Eq. 29 with respect Fourier sine transform is obtained as Eq. 31 in the main text. With a little digression, the inverse Laplace transform of A37 is given by (A38) [20]

$$L^{-1} \left\{ \frac{\exp(-\sqrt{s} x_D)}{s + \varepsilon} \right\} = \frac{1}{2} \exp(-\varepsilon t) \left[\begin{aligned} &\exp(-i\sqrt{\varepsilon} x_D) \operatorname{erfc} \left(\frac{x_D}{2\sqrt{t_D}} - i\sqrt{\varepsilon t_D} \right) + \\ &\exp(i\sqrt{\varepsilon} x_D) \operatorname{erfc} \left(\frac{x_D}{2\sqrt{t_D}} + i\sqrt{\varepsilon t_D} \right) \end{aligned} \right] \quad (\text{A38})$$

Note that if one were to use the boundary conditions employed by West et al this would have been the result of inverse Laplace operation for the solution which is physically impossible. After we apply an inverse Fourier Sine transform to Eq. 29, Eq. 31 is inverted by using iterated Laplace transformation technique. The first iteration would result in:

$$G(\tau) = \left\{ \begin{aligned} &\exp \left(- \left(a + \kappa + \frac{\pi^2 n^2}{y_D^2} \right) \frac{\tau}{f} \right) \\ &\frac{\sqrt{f} x_D}{2\sqrt{\pi \tau^3}} \exp \left(- \frac{f x_D^2}{4\tau} \right) \frac{1}{(s - \kappa^*)} \\ &\exp \left(- \left(\frac{(1-f)\sqrt{s + \kappa}}{\lambda} \tanh(\sqrt{s + \kappa} z_{Da}) \right) \frac{\tau}{f} \right) \end{aligned} \right\} \quad (\text{A39})$$

The second iteration would and subsequent convolution yields Eq. 31. Eq. 32 is obtained by closely adopting the results of Skopp and Warrick, [18]. Skopp and Warrick[20, 21] provides the Laplace inversion of A40.

$$F = L^{-1} \left\{ \frac{\exp \left(- \left(A\sqrt{s} \tanh(B\sqrt{s}) \right) \right)}{s} \right\} \quad (\text{A40})$$

Then inversion of A41 may be deduced as A42

$$F = L^{-1} \left\{ \frac{\exp \left(- \left(A\sqrt{s + \kappa} \tanh(B\sqrt{s + \kappa}) \right) \right)}{s + \kappa^*} \right\} \quad (\text{A41})$$

$$F = \frac{1}{\pi} e^{-(\kappa + \kappa^*)(t_D - \tau)} \int_0^\infty e^{-\lambda_R} \left\{ \begin{aligned} &\left[\begin{aligned} &\operatorname{Sin}(\omega^2(t_D - \tau)/2 - \lambda_I) \\ &+ \operatorname{Sin}(\lambda_I) \end{aligned} \right] \frac{2}{\omega^2} - \\ &\left[\begin{aligned} &\operatorname{Cos}(\omega^2(t_D - \tau)/2 - \lambda_I) \\ &- \operatorname{Cos}(\lambda_I) \end{aligned} \right] \frac{1}{\kappa^*} \end{aligned} \right\} \frac{d\omega}{\omega} \quad (\text{A42})$$

$$\lambda_R = \frac{A\omega}{2} \frac{\operatorname{Sinh}(B\omega) - \operatorname{Sin}(B\omega)}{\operatorname{Cosh}(B\omega) + \operatorname{Cos}(B\omega)} \quad (\text{A43})$$

$$\lambda_I = \frac{A\omega}{2} \frac{\operatorname{Sinh}(B\omega) + \operatorname{Sin}(B\omega)}{\operatorname{Cosh}(B\omega) + \operatorname{Cos}(B\omega)} \quad (\text{A44})$$

$$A = \frac{(1-f)\tau}{f\sqrt{\lambda}}, \text{ and } B = z_{Da} \quad (\text{A45})$$

Integration of Wastewater in the Water Resources of Egypt: Opportunities and Constrains

Fatma A.El-Gohary

*Water Pollution Research Department, National Research Center
fgohary@hotmail.com*

ABSTRACT

Limited freshwater resources are one of the major obstacles to the economic development of Egypt. The agricultural sector is the highest freshwater consumer. With growing demand on freshwater resources in Egypt, pressure is mounting on the agricultural sector to give up part of its allocation to prime use sectors such as households and industries. This has spurred the search to improve the efficiency of water consumption, and to augment the existing sources of water with more sustainable alternatives. The utilization of treated wastewater saves conventional water resources from pollution and is a viable water demand management strategy that promotes the use of lesser quality water for specific purposes. Despite the perceived potential advantages for a country located in an area with arid and semi-arid climate, the spread of planned water reuse schemes in Egypt is surprisingly slow. The main constraint facing the use of treated wastewater is the low coverage with sanitation systems and/or the implementation of large-scale centralized treatment facilities which produce large amounts of wastewater which in turn cannot be used for irrigation and is often discharged into receiving water bodies. This paper summarizes the existing situation and presents the results of recent research and development efforts to accelerate coverage with sustainable sanitation systems to protect the health of the people, conserve water resources and promote safe use of treated wastewater in Egypt.

Keywords: wastewater treatment, water reuse, opportunities, constraints

1. INTRODUCTION

Egypt is an arid country covering an area of approximately 1 million km². Most of the population is concentrated in only 5.5% of the total area of Egypt, in the Delta & Nile valley. Renewable water resources available to Egypt total approximately 57 billion cubic meters (BCM)/year. Approximately 97 percent comes from the Nile, with the remainder from precipitation, which is mainly confined to the north coast. The quantity of supply is essentially fixed. Water demand, on the other hand, is increasing. Currently, it is estimated at 72 BCM per year, over 80 percent of which is used for agriculture. Projections vary, but all foresee growing requirements, and therefore a growing gap between demand and sustainable supply. Excess demand is accommodated by tapping groundwater (6 BCM) and non-renewable aquifers (1 BCM), plus reuse of agricultural drainage water (about 7.5 BCM) and treated municipal and industrial wastewater (variously estimated at 0.7 to 3 BCM) [1].

The problem of how to accommodate large and growing water requirements is further complicated by pollution from all sources – agricultural, domestic and industrial – which limits how both fresh and wastewater can be used without adverse economic, environmental, and health implications. Renewable water available on a per capita basis is currently under 800 cubic meters /year, a quantity that already places Egypt among water scarce countries. And, with continued rapid growth in population, it is expected that per person availability

will decline to 720 cubic meters by 2017 and 600 cubic meters by 2025 [2]. At the same time, requirements are likely to increase with economic growth, even with improved water efficiency and changes in the composition of economic output in ways that reduce the water intensity of production.

2. USE OF MARGINAL QUALITY WATER

With growing demand on freshwater resources in Egypt, pressure is mounting on the agricultural sector to give up part of its allocation to prime use sectors such as households and industries. Meanwhile, agriculture has to continue producing food and fiber to satisfy current and future demand for food security. Under such circumstances, the use of treated municipal wastewater and agricultural drainage water in irrigation could become important not only to fill a gap in supply, but also to maximize water use efficiency. The utilization of wastewater and drainage water saves conventional water resources and is a viable water demand management (WDM) strategy that promotes the use of lesser quality water for specific purposes. Also, wastewater is available to farmers on demand allowing them to grow crops they would not otherwise be able to grow. It can ensure crops all year round, and is rich with nutrients. Urban wastewater is well suited to agricultural reuse and landscaping because of the reliability of supply, proximity to urban markets, and its nutrient content (depending on the treatment technology). This WDM implies that wastewater be viewed as a resource.

2.1 Municipal Wastewater Use

Water reuse is an old practice in Egypt. Since 1900 settled sewage has been used to cultivate orchards in a sandy soil area at El-Gabal El-Asfar village, near Cairo. The area gradually increased to about 4500 hectares. Egypt is now witnessing a wide range of new projects aiming at expanding the green stretch in the desert by introducing forests plantation (man-made forests), making use of treated sewage water, to produce timber trees of high economic value. The planned horizontal expansion that is based on treated wastewater is some 250,000 feddan. Apart from some 20,000 feddan in Middle Egypt, most of the planned area is located in the Western and Eastern Delta, with Greater Cairo and Alexandria as the main suppliers of treated wastewater. Also, the use of treated wastewater from the New Industrial Cities in the desert, and the Canal Cities will be considered in the future. However, the amount of treated wastewater which is officially used is still very limited.

The main constraint facing the use of treated wastewater in Egypt is the low coverage with sanitation systems and/or the implementation of large-scale centralized treatment facilities which produce large amounts of wastewater which in turn cannot be used for irrigation and is often discharged into receiving water bodies. Consequently, reuse of water is a lost opportunity, as wastewater is either buried away in cesspools or discharged into receiving water bodies. So the amount of wastewater collected and treated makes up a small percentage of the generated quantities, as do the reused amounts. Other constraints are:

- Insufficiency of economic analysis
- Relatively high cost of wastewater treatment and conveyance,
- Technical and social issues affecting the demand for reclaimed water
- Difficulty in creating financial incentives for safe and efficient water reuse.

2.1.1 Trends in the Development of Wastewater Services In Egypt

Several social, cultural, economic and environmental factors have shaped the development of sanitation services in Egypt and will influence the development of wastewater management in the future. Historically, private household sanitation facilities in Egypt were built to satisfy households demand for privacy and convenience.

On-site disposal systems are commonly used in rural areas, un-sewered small communities and un-sewered developments in urban areas. The Sanitary pit privy or earth pit privy is the most commonly used system in rural Egypt. In locations where the soil is heavy and impervious or where there is no room to establish the

sanitary pit privy at a safe distance from drinking water supply wells, the concrete vault privy is used. Where indoor plumbing has been installed, and the house is provided with drinking water supply system, the indoor toilet or privy is connected to an out-door septic tank. As population densities increased, the household water use has increased and on-site systems have begun to threaten the groundwater resources. Efforts financed by National and International Organizations allowed the development of improved on-site sanitation systems which are now under testing [3].

Community wastewater management services in Egypt evolved in three phases. During the first phase, wastewater services were provided to large cities and urban centers. In the second phase, wastewater collection services and some treatment works were provided to secondary towns. Centralized conventional wastewater collection systems were typically provided to large cities and secondary towns. The third phase, currently underway will provide wastewater services to smaller towns and rural areas. Once again the trend is to provide conventional centralized sewerage systems to individual communities and to transport the waste from several individual communities to centralized treatment facilities.

Recently, the acute nature of sanitation problems in rural Egypt has been recognized by the GOE. There have been local government efforts and foreign aid programs that addressed this problem. However the magnitude of the sanitation problems in rural Egypt is much larger than the scope of the projects planned so far. There are about 4,600 villages and 2,000 housing clusters (Nag, Ezba, Kafr), which are expected to accommodate around 40 million people by the year 2017. Consequently, there is an urgent need, in both the short and long term, to address this problem and find appropriate solutions, which are both economically and technically feasible for Egypt. Such solutions must also look at ways to reduce the health hazards and improve the overall environmental conditions of the people of rural Egypt. To do this successfully, requires good planning which in turn should be based on national policy, developed specifically to protect water resources, health of the people and sustain development.

Recently, there is a growing realization between experts and decision makers in Egypt that decentralization of sanitation programs into smaller-scale projects can bring benefits at an affordable cost to those in greatest need. Centralized water based sanitation is in general not economically feasible. Moreover, it produces wastewater which does not always meet the criteria required for sustainability and environmental security. New configurations employing the best practices of sanitation technology and management for rural and urban contexts are needed. The challenge facing decision makers is therefore, to go beyond traditional classification between 'small, appropriate' and

'modern/advanced technologies and to develop rural and peri-urban sanitation with a mix of scales, strategies, technologies, payment systems and decision-making structures, that better fits the physical and human systems for which they are designed. This does not mean that the macro picture should not be considered. On the contrary, the decentralization should take place after an adaptable strategic macro framework has been defined to sketch out the overall direction for sanitation service provision in the project area. Several options have recently been proposed and appear feasible, but necessitate further development.

There is a wide range of innovative sanitation technologies to choose from. In some cases it may be preferable not to install sewers, but to continue to use existing on-site sanitation technologies such as cesspools and septic tanks. In other cases, sewers may be installed only for a block of houses connected to a communal septic tank. Under certain circumstances, however, the high-cost solution of connecting to a citywide sewerage network is the only feasible technical solution.

2.1.2 Technology Options

Intermediate-scale sanitation opens new perspective and may be more cost effective in rural areas. Intermediate does not refer to the technical level or appropriateness of technology, but intermediate in terms of conveyance distance between point of waste generation and the point of treatment. This approach would allow for wastewater management to be broken down to the neighborhood-level. Selection of technology could be made based upon specific site conditions and financial resources of individual communities. Planning decentralized, intermediate distance wastewater treatment and recovery technologies that are linked with agriculture systems appear to be a rational approach to solving the human and environmental health problems that result from discharge of untreated domestic wastewater. These systems could be based on the topography of the local watershed, opposed to sector or citywide collection and treatment schemes, and would result in small-scale facilities equally dispersed through the urban environment. This approach would allow for independent, self-maintained, and self-sustained facilities that are capable of recovering wastewater resources and immediately reusing them in decentralized urban farms. This strategy would reduce the distance that wastewater is conveyed and would eliminate the need to discharge to receiving bodies [3].

If small-scale, easily maintained and operated single or multi-residence treatment systems, providing maximum levels of environmental health and public safety, can be developed and easily replicated, then institutional resources can be directed toward education and supporting their dissemination and incremental upgrading. National policies must be action-oriented

and support institutions that work on the development of innovative technologies.

2.1.2.1 Anaerobic Treatment

Anaerobic treatment technologies, as noted by McCarty [4] were explored as early as 1881. However, low-cost anaerobic treatment technologies such as the mechanized up-flow anaerobic sludge blanket (UASB) have shown considerable promise only recently [5]. Since the early 1980s, considerable research and development has occurred in relation to anaerobic wastewater treatment systems and specifically, UASBs. The UASB technology is characterized by its high organic removal efficiency, low-cost, low capital and maintenance costs and low land requirements [6]. Anaerobic treatment processes are suitable in tropical conditions because anaerobic treatment functions well in temperatures exceeding 20°. They are characterized by low sludge production and low energy needs.

Anaerobic treatment technology offers the opportunity to treat wastewater, convert the organic matter to natural gas and recover the nutrient rich treated effluent for irrigation. Performance data from Egypt showed the effectiveness of UASB reactor removing up to 85% of the COD and about 85% of the incoming suspended solids. Removal of faecal coliforms did not exceed one log. However, the anaerobic sludge bed, apparently is working as an effective sieve for all kinds of helminth ovae. Non of such ovae were detected in the effluent. Examination of the sludge indicated the presence of *Ascaris spp.* in almost all samples examined. As a consequence, excess sludge of the UASB reactor should be handled with care. It is worth mentioning that the two-stage system performed better than the one-stage system when operated at the same HRTs (8 hours) [7]. Anaerobic treatment processes are not considered totally effective in the destruction of pathogens and must be followed by a post-treatment step to meet standards regulating reuse or disposal of treated wastewater into receiving water bodies. Therefore, an adequate polishing step is required.

A systematic assessment of integrated wastewater treatment schemes has been carried out by El-Gohary et al. (1995-2004). The first step in all treatment schemes was a UASB reactor. The use of Algal ponds (AP) [8], Lemna (Duckweed) ponds (LP) and Fishponds [9], a Rotating Biological Contactor [10], wetland (surface & subsurface flow) [11] and a down flow hanging sponge reactor [12], to upgrade the UASB effluent has been investigated. All post-treatment systems were fed continuously with the UASB effluent. The treatment scheme were located out-door, exposed to ambient weather conditions.

The choice of these systems has been based upon initial assessment of cost and technological complexity and feasibility. They are, in general, simpler in design and

operation than most conventional processes and require minimal external energy sources. These characteristics are important when implementing a treatment system in a community where economic resources and technological skills are limited.

The results obtained indicated that all treatment schemes are comparable with regard to the removal of organic pollutants, as reflected by the BOD and COD values and suspended solids. For this reason, the governing design criteria will be the cost, land availability and the intended use.

Recently, a full-scale wastewater treatment plant consisting of an up-flow anaerobic sludge blanket reactor followed by a trickling filter has been constructed in one of the villages of the Delta. The results obtained indicated that the UASB is a promising option as an advanced primary treatment step [13].

2.1.3 Potential Environmental and Health Risks of Water Reuse Schemes

It should however be mentioned that unplanned wastewater use is associated with serious health and environmental risks. The use of raw or partially treated wastewater can cause pollution of soil, surface water and groundwater due to increase in nitrate concentrations. Inappropriate wastewater use poses direct and indirect risks to human health caused by the consumption of polluted crops and fish. Farmers in direct contact with wastewater and contaminated soil are also at risk. Moreover, most of the conventional wastewater treatment plants are not efficient in removing pathogens.

The primary problem associated with using wastewater for agriculture is the inherent health risks from wastewater containing bacteria, viruses, and a wide range of parasitic organisms. Generally, indicator organisms are used to reflect the sanitary quality and its suitability to replace conventional or other non-conventional water sources for irrigation. Typical indicators are fecal coliform content measured as CFU/100mL (colony forming units) and helminth eggs or ova (*Ascaris* and *Trichuris* species and hookworms) present in wastewater.

Waste water can also contain large amounts of suspended solids that have the potential to clog soil pores and irrigation equipment emitters. Clogged soils have a decrease in permeability resulting in poor irrigation efficiencies and water logging due to poor drainage. Irrigation emitters of various types (drip, micro-sprayers, etc) can become clogged by particulate matter and the development of bio-growth or bio-fouling. Wastewater effluent applied through a drip irrigation system typically requires sand filtration as a pretreatment to avoid problems with clogging.

The risks posed vary depending upon the location (for example, relative to houses or watercourses), land capability (such as soil types, slopes, salinity, depth to water table, etc), size of the scheme (volume of wastewater used), application techniques and the end-use (such as irrigation of golf courses or growing food crops). For the use of wastewater, details of risk identification and assessment should be provided in any Environmental Improvement Plan (EIP), thus providing an effective mechanism for third party review.

Risk management provides a series of steps which, when taken in sequence, support better decision-making by allowing greater insight into risks and their impacts. In general, a risk-based approach supports the concept of continuous improvement. The major emphasis for risk management of water reuse schemes is the maximization of water quality whilst at the same time minimizing the risks to the environment, health, and agriculture. Depending on wastewater quality, restrictions on end-uses are needed to control the exposure routes from residual pathogens and chemical contaminants to humans, crops and/or livestock. It is therefore important that suppliers and users of wastewater work together to identify and assess the potential exposure routes associated with their use schemes. Potential exposure routes and/or risks fall into the following categories:

- Environmental;
- Human and stock health;
- Crop (food) safety;
- Legal liability.

Water authorities should develop wastewater use management strategies. The primary objective of which is the production of high quality wastewater with low levels of pathogens and chemical contaminants.

2.2 Agricultural Drainage Water

Agricultural drainage systems collect and dispose of excess surface and subsurface water from cropped fields. Agricultural drainage water has the advantage of coming in large volumes, uncontaminated by pathogens, and is often being located close to or even inside the reuse areas. Reuse of drainage water holds great potential for saving valuable freshwater resources for competing prime uses that require more stringent water quality standards. It can provide a reliable supply of irrigation water and rich nutrients to cropped fields. Furthermore, reuse may alleviate drainage disposal problems in rivers and streams by reducing the volume of drainage water as well as helping in the restoration of natural wetlands. The practice of using drainage water for irrigation reinforces the potential for implementing sustainable integrated water resources management and reducing the number of people deprived of potable water.

In many water-short areas, drainage water turns out to be an important resource with economic value. Policies for integrated water resources management, therefore, give drainage water adequate attention, and many countries now include drainage water management and reuse in their water budget and water national plans.

Farmers in water-scarce countries may use this drainage water for irrigation, if it is of sufficiently good quality, either as a sole source or mixed with fresh canal water. The choice of the use option depends on the volume and quality of drainage water, soil type, crop tolerance to salinity, agro-climatic conditions, and availability of freshwater resources. Reuse of drainage water for irrigation requires a transformation in the drainage system from a disposal-based linear system to recovery-based loop system conserving water and nutrient resources. Drainage water reuse requires low investments, and such investments are add-ons to already existing schemes. Typical add-ons are the construction, operation, and maintenance of pumping facilities to lift water from drains to canals and, in some cases, civil works such as link canals, culverts, and mixing basins. The type and size of the work needed is site specific and depends largely on the volume of drainage water available and the layout of the irrigation and drainage systems.

In Egypt, drainage water reuse is practiced on a very large scale. The official reuse of agricultural drainage water in irrigation amounted to 4.84 BCM/year in 2001. The present aim of the Government of Egypt is to reuse up to 8 km³/year in new reclamation areas in the near future. In addition, there exists significant unofficial wastewater reuse estimated between 2.8 and 4 km³. This unofficial water reuse is not controlled by the government and poses threats to human health and environment. Unless adequate regulations are enforced, the quality of drainage water is threatened.

2.2.1 Potential Environmental and Health Risk

Although reuse of drainage water has met the increased water demand for irrigated agriculture in some countries, but many drainage water reuse plans have been implemented without due regard for likely negative impacts or secondary effects. This has generated new problems as well as tension between water supply agencies and irrigators and between environmentalists and irrigators.

The main quality concern regarding reuse of drainage water for irrigation is its salt content and potential adverse impact on crop productivity. Agricultural chemical residues (nutrients and pesticides) become a concern when drainage water is mixed with canal water that is used for drinking purposes. Moreover, as soon as agricultural water gets into main drainage canals it may mix with wastewater from domestic and industrial sources, which adds another quality concern about

human health. These possible impacts call for careful planning and management. Failure to properly evaluate the risks of reuse and to put tools in place for safe practices may jeopardize crop production, human health, and the environment

Also, drainage water may harm the ecosystem. The most serious threat is the degradation of water quality in downstream water bodies owing to the disposal of saline or polluted drainage water. Where farmers use many agrochemicals, aquatic life may suffer from the disposal of nutrient-rich drainage water in lakes and estuaries that have insufficient assimilation capacity or through-flow. Therefore, environmental impact assessment procedures should be followed during project preparation.

3. CONCLUSIONS

1. Planned reuse is not just about treatment; it requires an integrated approach. Where the planned reuse of effluent should be integrated into the decision to invest in intensive (for example, activated sludge) or extensive (for example, stabilization ponds) technologies, or centralized versus decentralized systems.
2. Because collection and treatment of wastewater are usually under the jurisdiction of a different sector (such as urban water supply and sanitation) from the reuse sectors (such as agriculture and municipalities), inter-sectoral coordination in planning and management is extremely important. The Country Water Assistance Strategies offer an opportunity to ensure such coordination. On the demand side, users should be involved in planning and monitoring the quality of the supplied effluent. Effective advisory/extension services are also extremely important.
3. Key to the success of planned strategic reuse programs are a coherent legal and institutional framework with formal mechanisms to coordinate the actions of multiple government authorities; policies to reduce waste loads through application of the "polluter pays" principle; appropriate practices for wastewater use through crop choice, landscaping, public awareness campaigns to establish social acceptability for reuse; and consistent government commitment over the long term.
4. The private sector can play an important role in promoting treated wastewater reuse. It would be even more attractive for the private sector to invest in wastewater treatment when markets for the treated effluent exist. This arrangement requires policies and regulations that allow the private sector to function and provide reliable services.

REFERENCE

- [1] International Resources Group, Integrated Water Resource Management II, Feasibility of wastewater reuse. Report No.14. June 2010. Contract No. EPP- 00-04-00024-00
- [2] National water resources plan (NWRP). Water for the future 2017, Ministry of water resources and irrigation, Cairo, Egypt, January 2005.
- [3] F.A. El-Gohary (2001). DESAR treatment concepts for comined domestic wastewater” Decentralized Sanitation and Reuse, concepts, systems and implementation. Integrated Environmental Technology Series Edited by piet lens,Grietje Zeeman and Gatzte Lettinga. Puhlised by IWA, pp. 133-163.
- [4] McCarty, P.L. et al., One hundred years of anaerobic treatment, Hughes, E., Stafford, D.A., Wheatley, B.I., Baader, W., Lettinga, G., Nyns, E.J., Verstraete, W., and Wentworth, R.L., Eds), Anaerobic Digestion, Elsevier Biomedical Press BV, Amsterdam, 1981, pp. 3-22.
- [5] Lettinga,G., Van velsen, A.F.M., Hobma, S.W., Zeeuw,W., and Klapwijk,A. Use of the upflow sludge blanket (USB) reactor concept for biological wastewater treatment especially for anaerobic treatment. Biotechnol. Bioeng.,Vol.22 pp.699-734, 1980.
- [6] Lettinga G. and Hulshoff Pol L. W., (UASB process design for various types of wastewater. Wat. Sci. Technol., Vol.24, No. 8, 87-107, 1991.
- [7] El-Gohary, F.A. and Nasr, F.A., Cost effective pre-treatment of wastewater. Wat. Sci. Tech.,Vol.39, No. 5, 97-103, 1999.
- [8] Saber A. El-Shafai, Fayza A. Nasr, F.A. El-Gohary, Huub J. Gijzen. (2007). Nitrogen recovery in an integrated system for wastewater treatment and tilapia aquaculture. The Environmentalist 27, 287–302.
- [9] Saber A. El-Shafai, **F.A. El-Gohary**, Fayza A. Nasr, N. Peter van der Steen and Huub J.Gijzen. (2007). Nutrient recovery from domestic wastewater using a UASB-duckweed ponds system. Bioresource Technology 98, 798-807.
- [10] Tawfik , A. Klapwijk, F.A. El-Gohary, G Lettinga (2005). Potentials of using a rotating biological contactor (RBC) for post-treatment of anaerobically pre-treated domestic wastewater. 25, Issue 1 , 89–98.
- [11] El-Khateeb M. A. and El-Gohary F. A., Combining UASB Technology and Wetland for Domestic Wastewater Reclamation and Reuse. Water Supply, Vol. 3, No. 4, pp. 201-208, (2003).
- [12] Mahmoud, M., Tawfik, A., Samhan, F. El-Gohary, F. Sewage treatment using an integrated system consisting of anaerobic hybrid reactor (AHR) and down-flow hanging sponge (DHS). Desalination and Water Treatment 4, 168–176, 2009
- [13] Nada,T., Moawad,A., El-Gohary,F.A., Farid,M.N. Full-scale municipal wastewater treatment by up-flow anaerobic sludge blanket (UASB) in Egypt. Desalination and Water Treatment. 30,134-145,2011. Cairo, Egypt, October 4, 2011

Removal of Phosphorus and BOD from Secondary Effluent using Coagulation

Maruf Mortula¹, Sina Shabani², Khaled Al Rumaithi³, Waleed Nawaz⁴, Ghanem Kashwani⁵

¹American University of Sharjah (mmortula@aus.edu)

²American University of Sharjah (b00024877@aus.edu)

³American University of Sharjah (b00019661@aus.edu)

⁴American University of Sharjah (b00022655@aus.edu)

⁵American University of Sharjah (b00020099@aus.edu)

ABSTRACT

Coupled removal of phosphorus and BOD is very critical in achieving wastewater treatment objectives. Several experiments were conducted to check the removal of different BOD and phosphorus and their effects on turbidity and PH levels. The Jar test was used to simulate the coagulation and to see the effect of different materials such as alum, lime, dried leaves, and polymer on the removal of BOD and phosphorus and their effect on turbidity and PH levels. The Turbidity changed with the increase in doses of coagulants which can give the optimum coagulant dose as shown later; however, PH levels were not changing significantly. Moreover, the materials showed up to 80-90 % Removal in the levels of phosphorus and BOD.

Keywords: Coagulation, BOD Removal, Phosphorous Removal, Treated wastewater effluent, jar test

1. INTRODUCTION

Phosphorus removal is one of the important objectives of tertiary wastewater treatment. Researchers used many different processes and materials to remove phosphorus, but chemical precipitation has been prominent among these processes [1]. It is used as a tertiary treatment process. Jar test is used as a laboratory representation of chemical precipitation to achieve low level of residual phosphorus, by carrying the test on activated sludge effluent (secondary treatment) [1]. Previous results indicated that iron as coagulant followed by lime precipitation was a feasible solution for removing phosphorus [2]. Since chemical precipitation process generates large amount of waste residuals, it is often avoided as a treatment option. A large number of medium to large sized wastewater treatment plants in the Middle East, do not even treat phosphorus from wastewater, since it is considered expensive for removal as one pollutant. However, there are certain advantages of using chemical precipitation it is capable of removing more than one pollutant from wastewater. Typically secondary effluent can still have some BOD remaining. At times, these BOD levels are higher than many regulatory guidelines. Previous researchers examined the performance of "a new tannin-based coagulant called Tanfloc" and observed 60% BOD removal [3]. Conducting jar tests using aluminum and iron salts resulted in 88% removal of COD [4]. The use of aluminum salts has been studied and a COD removal of up to 96% has been achieved [5].

Even though phosphorus and BOD are removed separately by using coagulation, there have been occurrences of coupled removal and BOD and phosphorus observed in some previous studies. It is observed that riparian reeds can remove phosphorus and BOD in river water [6]. Researchers used alum

coagulation and carbon adsorption and observed both COD and phosphorus removal [7]. Conducting coagulation and carbon adsorption resulted in 57% BOD removal and 87% phosphorus removal [8]. A rapid coagulation process can achieve up to 99% total phosphorus removal and 90% BOD removal [9]. However, these studies were limited within a few known coagulants, and not planned for coupled phosphorus and BOD removal. Therefore, there is a growing necessity to investigate the coupled removal of phosphorus and BOD from treated wastewater.

The objective of this paper was to find the best coagulant materials (such as Alum and leaves) that could reduce BOD and phosphorus from secondary effluent. To assess effectiveness of coagulation process jar tests were used in the laboratory. Wastewaters from two different wastewater treatment plants were used. PH, turbidity and other relevant water quality parameters were monitored.

2. MATERIALS AND METHODS

2.1 Wastewater

The secondary effluents were collected from two wastewater treatment plants in United Arab Emirates. They were collected after biological treatment processes. After being collected, they were stored in a freezer and tests were conducted within a short period of time (<7days).

2.2 Jar test

Coagulation process was simulated in the laboratory by using jar test as shown in figure1 apparatus. In this experiment different types of Coagulants such as lime,

Alum, Polymer, Plant-based material (leaves) were used. One liter of wastewater samples used in each jar for each trial. Doses of the coagulants were added to the jars(5, 10, 15, 20, 25 mg/L or 20, 40, 60, 80 mg/L) and one jar is left for control having zero concentration of the coagulant. Rapid mixing of 300 rpm was used for 2 minutes for coagulation followed by 30 minutes of flocculation with slow mixing of 36 rpm. After all the previous steps the jars were left for one hour for sedimentation. 9 sets of experiments were conducted using different types of coagulants. Each set of experiments were repeated three times to avoid biased results and recording more accurate results by the calculation of the average of three recorded data. Two different samples of wastewater were tested, Tertiary treatment effluent of Sharjah wastewater treatment plant and Secondary treatment effluent of Dubai wastewater treatment plant.

Coagulants: Lime, Alum, Polymer, and Leaves were the coagulants that were used in the experiments. The Coagulants were chosen according to previous studies which showed that these types of materials have caused reduction in BOD and Phosphorous concentration. The Polymer was collected from the Al Aweer wastewater treatment plant, Lime and Alum were purchased from commercial vendors, and Leaves were collected from locally available trees.

2.3 Analytical Methods

The samples collected after the jar tests were analyzed for phosphorus, turbidity, pH and BOD. Hach spectrophotometer (DR 5000- method 8048) was used for testing phosphorus. BOD tests were conducted using Hach BOD Track system. In this test, 420 ml sample of each jar were taken in order to start the experiment. Then the contents of the nutrient buffer pillows were added. Using a funnel the samples were put in the dark bottles. The bottles were closed and the system was run for the specific periods of time. Turbidity was measured in nephelometric turbidity units. The measurement was done using Hach portable turbidity meter (2100P). PH of the samples was also measured using a standard pH meter.

3. RESULTS AND DISCUSSION

Results showed that the coagulation process was effective in removal of the phosphorus and BOD. Table 1 shows the change in pH and Turbidity with the increase in Coagulant dose.

Table 1: Coagulant doses, pH, and turbidity

Lime	Dose (mg/L)	0	5	10	15	20	25
	PH	7.46	7.69	7.8	7.88	7.43	7.8
	Turbidity (NTU)	2.49	3.69	4.03	4.69	5.02	8.1
Lime	Dose (mg/L)	0	20	40	60	80	100

	PH	7.68	7.66	7.69	7.72	7.6	7.7
	Turbidity (NTU)	3.1	2.4	1.9	1.7	1.4	1.9
Alum	Dose (mg/L)	0	5	10	15	20	25
	PH	7.36	7.42	7.35	7.29	7.26	7.1
	Turbidity (NTU)	3.1	3	2.8	3	2.1	2
Alum	Dose (mg/L)	0	10	20	30	50	60
	PH	7.5	7.45	7.48	7.51	7.5	7.4
	Turbidity (NTU)	3.1	3.5	5.1	2.5	2.3	2.1
Alum	Dose (mg/L)	0	20	40	60	80	-
	PH	7.26	7.28	7.33	7.25	7.22	-
	Turbidity (NTU)	2.28	4.28	7.18	1.77	1.3	-
Pol	Dose (mg/L)	0	20	40	60	80	-
	PH	7.68	7.7	7.67	7.63	7.58	-
	Turbidity (NTU)	2.3	1.11	1	1.14	1.88	-
Pol	Dose (mg/L)	0	20	40	60	80	100
	PH	7.64	7.66	7.77	7.6	7.68	7.6
	Turbidity (NTU)	n/a	n/a	n/a	n/a	n/a	n/a
Leaves	Dose (mg/L)	0	20	40	60	80	-
	PH	7.66	7.63	7.57	7.52	7.74	-
	Turbidity (NTU)	2.35	2.29	1.7	2.28	2.7	-
Leaves	Dose (mg/L)	0	20	40	60	80	-
	PH	7.59	7.55	7.53	7.53	7.56	-
	Turbidity (NTU)	2.46	2.4	1.53	1.68	1.9	-

- n/a = Not Available
- Pol= Polymer



Figure 1: Jar test apparatus

Experimental results indicated that the increase in dosage of coagulants were capable of reducing the

phosphorus and BOD concentrations of the wastewater (Figure 1). High percentages of removal are obtained during these experiments. For BOD it was removed 100% in some cases and for phosphorous up to 80 % removal was observed. In Figure 2 the graph is showing the change in phosphorous concentration with the change in Coagulant dosage. Different Doses of Coagulants were used in this experiment which resulted in different levels of removal of phosphorous and BOD. The percentage removals Phosphorous were changing between 30- 80 percent. On the other hand, figure 3 shows the BOD percentage removals were between 71- 100 percent. These values show that coupled removal of BOD and phosphorous can be the target in treatment of wastewater using Coagulation and different types of coagulants can be used.

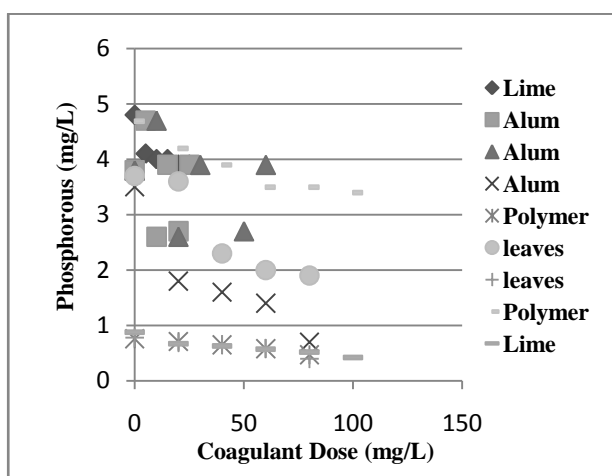


Figure 2: Coagulant dose vs phosphorous concentration

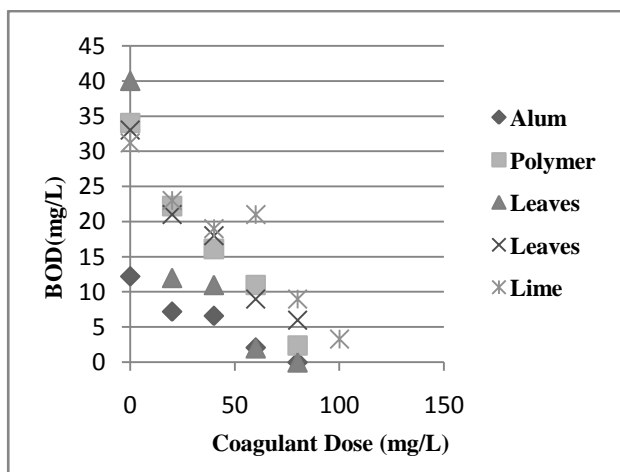


Figure 3: Coagulant dose vs BOD concentration

4. CONCLUSION

The experimental results showed that the materials that are used can significantly reduce the BOD and phosphorus content in the wastewater. In addition, the PH was in most experiments in the normal range which is close to 7 and the turbidity graph also showed the logical pattern of turbidity graphs. Using different and widely available and economical materials such as

alum, lime, dried leaves and polymers is a really great option that can be added to the wastewater treatment process hence we noticed that coagulation with these materials significantly removed the BOD and phosphorus from the secondary wastewater. Future research will be conducted on testing different materials and the efficiency of wastewater treatment at different PH levels and temperatures.

ACKNOWLEDGEMENT

We would like to express our gratitude to graduate student Ahmad Ghadban for helping us getting familiar with the experimental procedures. Moreover, we would like to thank Eng. Aqeel Ahmed for his endless helps in the environmental lab.

REFERENCES

- [1] Schnrid, L. A., and McKinney, R. E., "Phosphate Removal by a Lime-Biological Treatment Scheme", *Water Poll Control Fed*, 41, 1259, 1969.
- [2] O'Tarrell, T. P., and Bishop, D. F., "Lime Precipitation in Raw, Primary, and Secondary Wastewater." *Chemical Engineering Progress Symposium Series*, No. 124, 1971.
- [3] Sanchez-Martin, J., Beltran-Heredia, J., Hernandez, C., "Surface water and wastewater treatment using a new tannin-based coagulant Pilot plant trials", *Journal of Environmental Management*, 91, pp 2051-2058, 2010.
- [4] Kumar, P., Prasad, B., Chand, S., "Treatment of desizing wastewater by catalytic thermal treatment and coagulation", *Journal of Hazardous Materials*, 163, pp. 433-440, 2009.
- [5] Al-Malack, Abuzaid, and Mubarak, "Coagulation of Polymeric Wastewater by Chemical Industry", *Wat. Res.* Vol. 33, No. 2, pp. 521-529, 1999.
- [6] Wang, C., Wang, P., "Retention and Removal of Suspended Solids and Total Phosphorus from Water by Riparian Reeds", *Environmental Engineering ASCE*, pp. 771-777, 2008.
- [7] Paptic, S., Koprivanac, N., Metes, A., "Removal of some reactive dyes from synthetic wastewater by combined Al(III) coagulation/carbon adsorption process", *Dyes and Pigments*, 62, pp. 291-298, 2004.
- [8] Ayoub, G.M., Hamzeh, A., Semerjian, L., "Post treatment of tannery wastewater using lime/bittern coagulation and activated carbon adsorption", *Desalination*, 273, pp. 359-365, 2001.
- [9] Yoon, T.Y., Kim, C.G., "Case studies on rapid coagulation processes to cope with total emission controls", *Desalination*, 231, pp. 290-296, 2008.

Copper Removal via Adsorption

Md. Maruf Mortula¹, Ahmad A. Ghadban², Haider O. Al-Karaghool³, Manal W. Kaakani⁴

¹American University of Sharjah (mmortula@aus.edu)

²American University of Sharjah (b00024256@aus.edu)

³American University of Sharjah (b00022386@aus.edu)

⁴American University of Sharjah (g00039244@aus.edu)

ABSTRACT

Heavy metals are one of the most toxic types of water pollutants and are considered harmful to the environment. One way to remove heavy metals is through adsorption. This paper aims to investigate the efficiency of using adsorption as a treatment method for wastewater in order to get rid of copper. Batch tests were conducted to assess the performance of copper removal via adsorption. A variety of adsorbents were tested and compared with each other in order to determine the most efficient material suitable for the treatment. Water samples were prepared from deionized water via the addition of copper (II) sulfate. Batch tests were conducted using Erlenmeyer flasks. Five flasks were used for each test such that one of them is filled with zero adsorbent concentration (blank) and the other four are filled with different adsorbent concentrations in order to get an idea about the effect of the adsorbent dosages on the adsorption process. All flasks were subjected to a shaking period of 1 hour after which equilibrium is assumed to be reached. Copper concentrations of all water samples were then tested using Hach DR5000 spectrophotometer. Freundlich and Langmuir equations were used to fit the experimental data so that kinetics of the process can be obtained. It was concluded that limestone powder and fly ash are the most suitable adsorbents with about 94% copper removal. Limestone powder was chosen as the superior adsorbent due to the fact that its data were fitted using Freundlich and Langmuir isotherms more robustly than fly ash's data. Additional batch tests were conducted using limestone powder in order to obtain the optimum pH value and study the effect of the adsorbent dosage increments on the removal process.

Keywords: Heavy Metals, Copper, Adsorption, Batch tests

1. INTRODUCTION

Wastewater contains many soluble and suspended solids, that if present in abundance, may result in an adverse effect on the water once it is discharged to the nature. Some of these solids are metals, which when removed from the wastewater, not only reduce risk of contamination in the water bodies, but may also be reused as raw materials in various industries. Heavy metals are one of the most toxic types of water pollutants and are considered harmful to the environment. Wasewar and his colleagues stated that at least 20 metals are considered to be toxic, and approximately half this number is emitted to the environment in quantities that are hazardous to the environment in addition to the human health [1]. One way to remove heavy metals is through adsorption. Adsorption is one of the recovery treatment methods used in low volumes of wastewater to remove heavy metals as they cannot be degraded or destroyed.

In Dubai, many industries are located in the free zone region of Jebel Ali. These industries include metals, textile, paper, dairy processing, pharmaceutical, oilfield and refinery, soft drinks, bakeries, rubber, and power, to name a few. Each of these industries emits different metals, which in aggregate and in combination, will highly pollute and toxify the medium in which the wastewater is being emitted to. The objective of this research is to study the removal of copper from wastewater via adsorption.

Adsorption has been used to remove different types of metals and nutrients in wastewater; however, the process in which it is carried out, along with the mode of adsorption, differs with different metals and nutrients, along with what is available. Activated carbon has been found to be an effective adsorbent for the removal of many types of pollutants in wastewater and other media. Activated carbon has four different forms based on the application and its advantages and disadvantages to the wastewater. These four forms are powder, granular, fibrous, and cloth [2]. However, activated carbon is relatively expensive and hence, the production of a much cheaper low cost activated carbon has yet to be found.

Fruits and vegetations have been successfully used to adsorb metals from wastewater. One of these vegetations is the maize cob [3]. A success rate of removal of 81% for Iron metal was found, and 79% for manganese salt metal from groundwater, after a contact time of 100 minutes. It was stated that the reason for the high percentage of metal adsorption is primarily due to the chemical make-up of the cobs, as they consist of ligno-cellulosic material "with a large number and array of different functional oxygen groups that have a negative charge". Another successful adsorption material is through the use of the waste of the tea factory for the removal of zinc in wastewater [1].

In the Arabian Gulf, dates and palm trees are found in abundance. Dates readily fall off the branches onto the ground once ripened. It is these ripened dates that will

be used in this research. Also, these dates that have fallen to the ground may have decayed slightly. This allows for the production of cyanide on the dates, which has been found to act as a beneficial reagent in adsorption. Date pits are appropriate for activated carbon as it has an excellent natural structure and consists of low ash content [4]. According to research conducted by N.S Awwad, A.A.M Daifuallah, and M.M.S Ali, date pits that had been carbon activated have been successfully used in the uptake of Pb^{2+} , Cd^{2+} , Fe^{3+} , and Sr^{2+} through a one step steam pyrolysis in a batch mode [5]. A summary of experiments and research previously conducted is illustrated in

Table 2.

N.S. Awwad and his colleagues used date pits that were washed, dried in the oven, and crushed to be used as adsorbents in the treatment process. Like other researchers, they also used analytical grade reagents in the chemical analysis, as well as double-distilled water [5]. In previous researches conducted, dried palm seed was added to a solution of H_2SO_4 for 5 hours, and then boiled for 20 hours in a fume hood. They were then placed in an ice bath to cool, then washed over cold water and filtered. The carbon was then placed in the oven to dry, and then immersed in a dilute mixture of $NaHCO_3$ to remove any acid still present in the mixture. The resulting carbon was washed with distilled water until it had a pH of 6. This was then dried in the oven and sieved to a 0.1 mm particle size, then stored in a glass bottle until needed [2].

Different types of carbons have been used [5] which included steam activated carbon, nitrogen activated carbon, steam activated carbon with chemical treatment, and air activated carbon. Steam activated carbon was produced by crushing samples at a gradually increasing temperature at 50°C every 10 minutes. Steam was then introduced through the mixture, and heating continued until the temperature reached 600-800°C. After heating for one hour, the system was shut down, and samples of different temperatures were obtained. For the nitrogen activated carbon, steam and nitrogen were introduced to the hot mass and heating was continued to 700 – 800°C, where they were kept at this temperature for hours of 0.5, 1, and 2, before they were cooled. Their weight was then determined. For the steam activated carbon with chemical treatment, the adsorbent was immersed in a dilute $FeCl_3$ or Calcium acetate solution, and then left in a drying oven overnight. The samples were then placed in a tubular furnace where steam was introduced to the mass, and heat gradually increasing to 700°C, where they remained at this temperature for a duration of 1 hour before they were cooled, and weighed, before being boiled again in a dilute solution of HCl , washed in double-distilled water, then dried. For the air activated carbons, air was passed through the hot water at 350°C, and continued to heat until it reached 700°C, where the temperature remained for 1 hour before the samples were cooled and weighed.

Table 2: Previous studies on heavy metals adsorption

Srl. No.	Heavy Metal	Adsorbent	Test	Studied Variables	Results	Reference
1	Zinc	Tea Factory Waste	Batch test	pH, adsorbent dose, contact time, initial concentration, temperature.	Very good adsorption at pH 4.2 and room temperature. Max adsorption capacity of Zn (II) per gram adsorbent was 8.9 ± 0.08 mg. % removal of Zn increased with dose and decreased with increase in metal conc. % removal decreased with increase in initial conc.	[1]
2	Pb, Cd, Fe, Sr	Date Pits	Batch test	Adsorbent dosage, pH, contact time, temperature.	Carbon type – slight effect on uptake of metals. Carbon dosage – uptake increases with increase in dosage. PH – low uptake at low pH range. Contact time – equilibrium reached after 150 min for Pb, Cd and Fe. 90 min for Sr. Temperature – no effect for Pb, Cd, Fe. Increase in temperature decreased adsorption for Sr.	[5]
3	Fe, Mn	Maize Cobs	Column test	Initial concentration.	Max adsorption capacity at 2.3 mg Mn/g maize cob, and 2.5 Fe. Percent removal – initial concentration 1 to 40 mg/L – 79% to 37% (Mn), 80% to 39% (Fe).	[3]
4	Pb	Natural porous medium (red pozzolan)	Batch and column tests	pH and total lead concentration.	Batch – at 0.1 mol/L NaCl % distribution of Pb was constant (38.8 Pb^{2+} , 55.5 $PbCl$, 5.3 $PbCl_2$) irrespective of pH and total lead conc. Column – lead breakthrough at 0.1 mol/L NaCl solution at pH4, with total concentration of 2.2×10^{-4} mol/L.	[6]

2. MATERIALS AND METHODS

This research aims to investigate the possibility of removing copper from synthetic wastewater via adsorption. Batch tests were conducted to assess the performance of several adsorbents for copper removal. Freundlich and Langmuir equations were used to fit the experimental data obtained from the batch tests so that kinetics of the adsorption process can be obtained.

2.1 Adsorbents

Adsorbents were either collected from nature or purchased from chemical companies in Sharjah, United Arab Emirates (UAE). These materials were subjected to preliminary batch tests for assessment as potential adsorbents for phosphorus. Table 3 describes the various adsorbents that were tested.

2.2 Water Samples

Water samples were artificially made via the addition of copper sulfate (CuSO₄) to deionized water. All water samples were used immediately after preparation. Different copper concentrations ranging from 1 to 15 mg/L were used in the various conducted batch tests.

2.3 Analytical Methods

Water samples were tested for copper concentration using the "Bicinchoninate Method". This method involves the reaction of copper with a salt of bicinchoninic acid to form a purple colored complex in proportion to the copper concentration which is measured at 560 nm. Copper was measured using HACH DR5000 spectrophotometer. All measurements were taken in duplicate. Temperature and pH values of water samples were measured using pH100 probe provided by YSI Environmental.

2.4 Experimental Setup and Approach

A preliminary batch test was conducted on all 8 adsorbents in order to assess their applicability for copper adsorption. This batch test was carried out using 8 Erlenmeyer flasks each filled with the same volume (200 mL) of water samples (1.78 mg/L initial copper concentration (ICC)) and the same amount of adsorbents (10 g/L). The best three adsorbents were further investigated using additional batch tests. Each of these tests was carried out using five Erlenmeyer flasks filled with the same volume (200 mL) of water samples (1.5 mg/L ICC). These flasks were filled with 0, 5, 10, 15, and 20 g/L adsorbent dosages. Additional batch tests were conducted using the best adsorbent in order to obtain the optimum pH value and study the effect of the adsorbent dosage increments on the removal process. These additional batch tests were similar to the previous

ones but with slight differences in ICC and adsorbent dosages in addition to the pH control. In all batch tests, all flasks were subjected to a shaking period of 1 hour after which equilibrium is assumed to be reached. Water samples were then collected from the flasks and tested for copper concentration, pH, and temperature. Graphs of effluent copper concentration (ECC) to influent copper concentration (ICC) ratios vs. adsorbent dosages were then plotted for each batch test.

2.5 Adsorption Isotherm Models

Experimental data obtained from three of the conducted batch tests were all fitted to both Freundlich and Langmuir equations.

2.5.1 Freundlich Isotherm

The equation for Freundlich isotherm is as follows:

$$Q = K_d C_e^{1/n} \quad (1)$$

Where Q is the adsorption density of the adsorbent [= (C_o - C_e) / m], C_e is the adsorbate concentration at equilibrium in the solution, K_d & n are material characteristics, C_o is the initial adsorbate concentration in the solution, and m is the mass of the adsorbent.

2.5.2 Langmuir Isotherm

The equation for Langmuir isotherm is as follows:

$$Q = \frac{abC_e}{1+bC_e} \quad (2)$$

Where a & b are material Characteristics.

These equations can be easily linearized and used to fit the experimental data through a linear regression. There are some other isotherm models but these two are considered to be the most commonly used ones especially for monolayer and noncompetitive adsorption processes which is usually the case for synthetic water with only one metallic ion.

3. RESULTS AND DISCUSSION

The first set of preliminary batch experiments were conducted on synthetic water (deionized water spiked with CuSO₄) with an initial copper concentration of 1.78 mg/L. These experiments were carried out for the purpose of getting an idea about the capability of a wide range of chemical and natural materials to adsorb copper. Figure 5 shows the ECC to ICC ratio for some selected adsorbents at an adsorbent dosage of 10 g/L. By comparing limestone aggregate to limestone powder, one can easily observe that higher surface area results in higher adsorption capacity. Based on Figure 5, only three materials (limestone powder, fly ash, and GAC) stood as possible adsorbents for copper.

Table 3: Adsorbents tested in this research

Srl. No.	Adsorbent	Source and Method
1	Granular Activated Carbon (GAC)	Purchased from Al Rama International Trading L.L.C in Sharjah – UAE.
2	Beach Sand	Collected from Sharjah beaches & then air dried for more than a month.
3	Dune Sand	Obtained from the geotechnical lab at AUS.
4	Limestone Aggregate	Obtained from Sharjah Carbon Factory located in Sharjah – UAE.
5	Limestone Powder	Obtained from the construction lab at AUS.
6	Fly ash	Obtained from the construction lab at AUS.
7	Activated Alumina	Purchased from Oasis Chemical Materials Trading Company L.L.C located in Sharjah – UAE, & sieved to 4 mm particle size.
8	Electric arc furnace (EAF) Slag (Steel Slag)	Obtained from Emirates Steel Industries (ESI) located in Abudhabi – UAE.

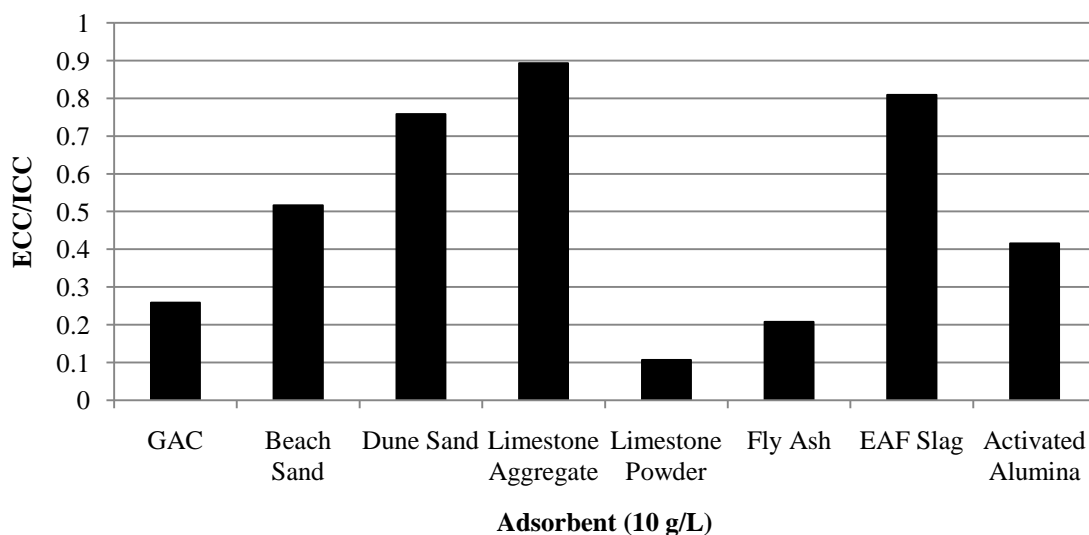


Figure 5: Preliminary batch test's results for 8 different adsorbents

Additional batch tests were conducted using limestone powder, fly ash, and GAC in order to determine the best of them. Synthetic water with an initial copper concentration of 1.5 mg/L was used in these tests. Figure 6 shows ECC/ICC vs. adsorbent dosage for the three adsorbents. It is obvious that GAC is the least efficient among the three; however, it is not clear which one of the other two is better even though limestone powder seems to be more uniform.

Figure 7 shows the fitting of the experimental data obtained from the limestone powder and fly ash batch tests to both Freundlich and Langmuir isotherm equations. It can be observed from the figure that the Freundlich equation was generally more successful in fitting the experimental data for the tests with coefficients of determination equal to 0.9993 and 0.7761 for limestone and fly ash respectively. Also, the data for limestone powder were fitted much nicer than fly ash and with more accuracy, hence, implying the superior suitability of limestone powder for copper adsorption

since an equation can be easily obtained using Freundlich isotherm which can be used to predict the performance of the batch reactor treatment system.

Further batch tests were conducted using limestone powder in order to obtain the optimum pH value and study the effect of the adsorbent dosage increments on the removal process. The batch test conducted at a pH value of 3 and an ICC of 14 mg/L (Figure 8) suggests that acidic conditions are less favored for copper adsorption on limestone powder since 5 g/L of adsorbent was not even enough to remove only 30% of copper concentration. On the other hand, a similar batch test of a pH value of 9 and an ICC of 9.4 mg/L shows that basic conditions are extremely suitable for copper adsorption since, as shown in Figure 8, only 1.25 g/L adsorbent was enough to remove 91% of copper concentration. Additionally, another basic batch test suggests that even after reducing the adsorbent dosage increments from 1.25 to 0.05 g/L limestone powder was still able to adsorb copper very efficiently (Figure 9). It

is also noted that the adsorption density reached a very high value of 55 mg Cu/g at 0.05 g/L adsorbent dosage. The two batch experiments conducted at the neutral condition (pH = 7) with ICCs of 4.4 mg/L and 2.4 mg/L (Figure 8) implies that such conditions are only moderately suitable for copper adsorption with a maximum of 84% copper removal in the later figure.

Furthermore, a third neutral batch test with an ICC of 8.6 mg/L (Figure 10) proved that even increasing the adsorbent dosage increments from 1.25 to 5 g/L was not enough to produce the same performance observed in the basic conditions with only 0.05 g/L adsorbent dosage increments.

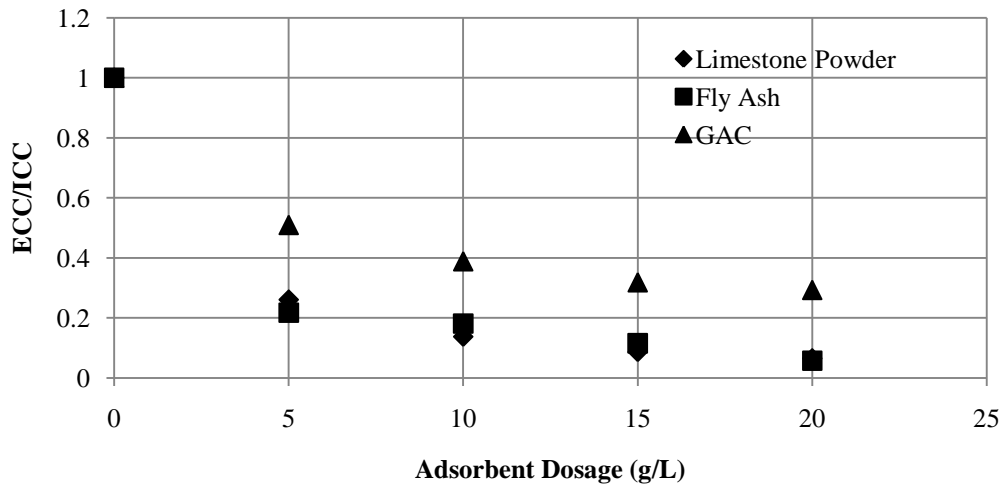


Figure 6: Comparison between three potential adsorbents

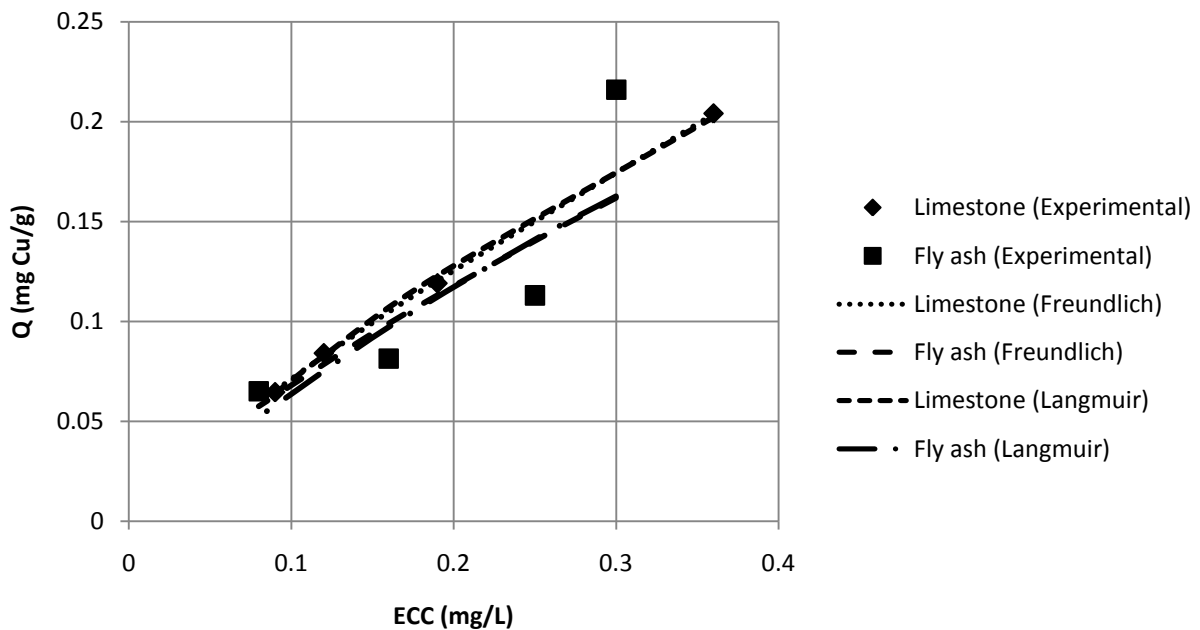


Figure 7: Freundlich and Langmuir isotherms for limestone powder and fly ash

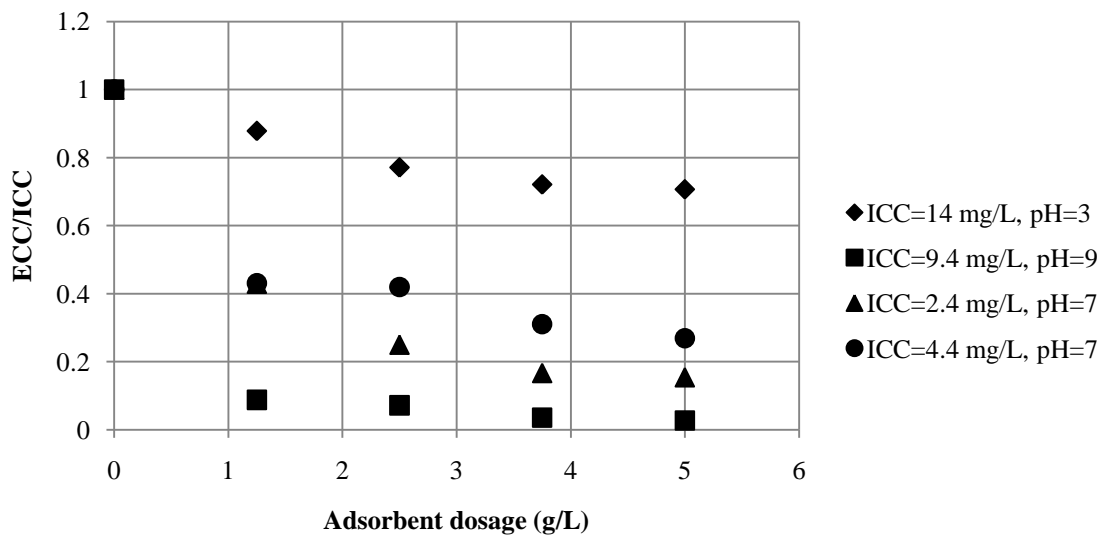


Figure 8: Some batch tests using limestone powder

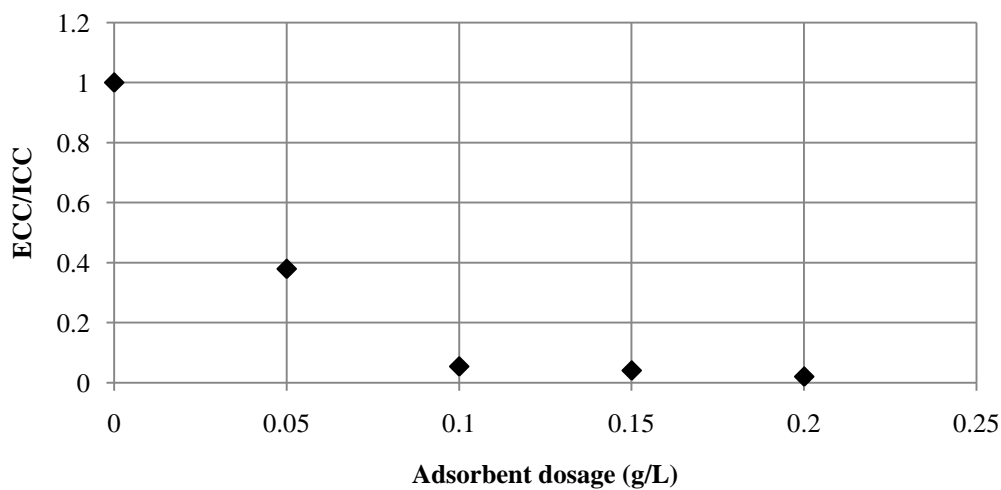


Figure 9: Basic batch test using limestone powder (ICC=4.4 mg/L, pH=9)

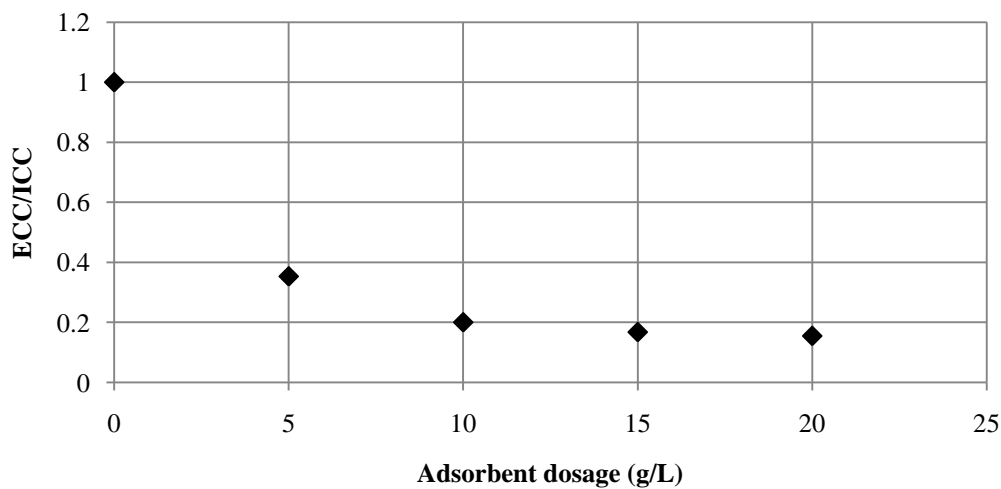


Figure 10: Neutral batch test using limestone powder (ICC=8.6 mg/L, pH=7)

4. CONCLUSIONS

The high heavy metals concentrations in industrial wastewater can result in many problems such as toxicity which is the most severe. Literature review shows the ability of adsorption process as an effective technology to remove heavy metals. In this study, removal of copper via adsorption on various materials was investigated using batch adsorption experiments. It was concluded that limestone powder and fly ash are the most suitable adsorbents for copper. Also, the data for limestone powder were fitted by Freundlich and Langmuir isotherms much nicer than fly ash. Upon further experiments on limestone powder, basic conditions (pH = 9) proved to be the most suitable for copper adsorption even with adsorbent dosage increments of 0.05 g/L. Further investigations can be done in order to study the effects of variations of other parameters such as adsorbent particle size and temperature. Moreover, fixed bed column experiments are highly needed in order to simulate the filtration process which is the most commonly used in treatment plants for adsorption.

REFERENCES

- [1] K. L. Wasewar, M. Atif, B. Prasad, and I. M. Mishra, "Batch adsorption of Zinc on tea factory waste," *Desalination*, vol. 244, pp. 66-71, 2009.
- [2] A. El Nemr, A. Khaled, O. Abdelwahab, and A. El-Sikaily, "Treatment of wastewater containing toxic chromium using new activated carbon developed from date palm seed," *Journal of Hazardous Materials*, vol. 152, pp. 263-275, 2008.
- [3] M. M. Nassar, "Adsorption of Fe³⁺ and Mn²⁺ from ground water onto maize cobs using batch adsorber and fixed bed column," *Separation Science and Technology*, vol. 41, pp. 943-959, 2006.
- [4] M. Belhachemi, R. V. R. A. Rios, F. Addoun, J. Selvestre-Albero, and A. Sepulveda-Escribano, "Preparation of activated carbon from date pits: effect of the activation agent and liquid phase oxidation," *Journal of Analytical and Applied Pyrolysis*, vol. 86, pp. 168-172, 2009.
- [5] N. S. Awwad, A. A. M. Daifuallah, and M. M. S. Ali, "Removal of Pb²⁺, Cd²⁺, Fe³⁺, and Sr²⁺ from aqueous solution by selected activated carbons derived from date pits," *Solvent Extraction and Ion Exchange*, vol. 26, pp. 764-782, 2008.
- [6] M. P. Papini, Y. D. Kahie, B. Troia, and M. Majone, "Adsorption of lead at variable pH onto a natural porous medium: Modelling of batch and column experiments," *Environmental Science Technology*, vol. 33, pp. 4457-4464, 1999.

Simplification of a Nonlinear Fuel Cell Model and its System Analysis and Control

Gun-hyung Park¹, Ameen El-Sinawi², Zoran Gajic¹

¹Rutgers University, Department of Electrical and Computer Engineering
94 Brett Road, Piscataway, New Jersey 08854
(gunhyung@eden.rutgers.edu), (gajic@ece.rutgers.edu)

²American University of Sharjah, Department of Mechanical Engineering,
P.O. Box 26666, Sharjah, United Arab Emirates (aelsinawi@aus.edu)

ABSTRACT

The well-known nonlinear fifth-order model of a proton exchange membrane (PEM, also known as polymer electrolyte membrane) fuel cell appears to be pretty complex. In this paper, we propose a technique to simplify the model while preserving all fundamental model variables and providing the closeness of the trajectories of the simplified and the original model near operating points. We perform linearization of the original model at steady state (around model operating points, equilibrium points) and find the eigenvalues of the obtained linearized model using the MATLAB Symbolic Tool Box. It is important to observe that the obtained equilibrium point is unique. Examining the real parts of the linearized model eigenvalues are able to determine the linearized system stability requirements.

1. INTRODUCTION

In this paper we consider a fifth-order nonlinear model of proton exchange membrane (PEM) fuel cell, developed in [1], see also [2]. The state variables in this model represent respectively the pressures of hydrogen and water at the anode side and the pressures of oxygen, nitrogen, and water at the cathode side, that is

$$x(t) = \begin{bmatrix} p_{H_2}(t) & p_{H_2O_A}(t) & p_{O_2}(t) \\ p_{N_2}(t) & p_{H_2O_C}(t) \end{bmatrix}^T \quad (1)$$

The state space model is given by

$$\dot{x}_1 = \frac{RT\lambda_{H_2}}{V_A} (Y_{H_2} - x_{12}) k_a u_a + \frac{RTC_1}{V_A} (x_{12} - 1) I \quad (1.1)$$

$$\dot{x}_2 = \frac{RT\lambda_{H_2}}{V_A} \left(\frac{\varphi_a P_{vs}}{x_1 + x_2 - \varphi_a P_{vs}} - x_{21} \right) k_a u_a + \frac{RTC_1}{V_A} (x_{21} - 1) I \quad (1.2)$$

$$\dot{x}_3 = \frac{RT\lambda_{air}}{V_C} (Y_{O_2} - x_{345}) k_c u_c + \frac{RTC_1}{2V_C} (x_{345} - 1) I \quad (1.3)$$

$$\dot{x}_4 = \frac{RT\lambda_{air}}{V_C} (Y_{N_2} - x_{435}) k_c u_c \quad (1.4)$$

$$\dot{x}_5 = \frac{RT\lambda_{air}}{V_C} \left(\frac{\varphi_c P_{vs}}{x_3 + x_4 + x_5 - \varphi_c P_{vs}} - x_{534} \right) k_c u_c + \frac{RTC_1}{V_C} \left(\frac{C_2}{C_1} (1 - x_{534}) - 1 - x_{534} \right) I \quad (1.5)$$

$$x_{12} = \frac{x_1}{x_1 + x_2}, x_{21} = \frac{x_2}{x_1 + x_2},$$

$$x_{345} = \frac{x_3}{x_3 + x_4 + x_5}, x_{435} = \frac{x_4}{x_3 + x_4 + x_5}, \text{ and}$$

$$x_{534} = \frac{x_5}{x_3 + x_4 + x_5}$$

where R is the universal gas constant, T is temperature, V_A and V_C are anode and cathode volumes. C_1, C_2 are known constants [1]-[2], φ_a, φ_c are the relative humidity constants, P_{vs} is the saturation pressure, λ_{H_2} and λ_{air} are stoichiometric constants, $Y_{H_2} = 0.99$, $Y_{O_2} = 0.21$, $Y_{N_2} = 0.79$ are reactant fractions. I is the cell current, and it is considered as a disturbance.

The model output variables are defined by

$$y(t) = \begin{bmatrix} p_{H_2}(t) \\ p_{O_2}(t) \end{bmatrix} = \begin{bmatrix} x_1(t) \\ x_3(t) \end{bmatrix} \quad (2)$$

The system control input is given by $u(t) = [u_a(t) \ u_c(t)]^T$ where

$$u_a(t) = \frac{1}{k_a} (H_{2in}(t) + H_2 O_{Ain}(t)) \quad (3)$$

$H_{2in}(t)$ and $H_2 O_{Ain}(t)$ represent inlet flow rates of the anode side hydrogen and water vapor with k_a being known constant, and

$$u_c(t) = \frac{1}{k_c} (O_{2in}(t) + N_{2in}(t) + H_2 O_{Cin}(t)) \quad (4)$$

$O_{2in}(t), N_{2in}(t), H_2 O_{Cin}(t)$ represent respectively inlet flow rates of the cathode oxygen, nitrogen, and water with k_c is known constant.

It is interesting to observe that a similar nonlinear model was considered in [3]. Linear system identification of PEM fuel cells was considered in [4]. A linear PEM fuel cell model with static nonlinearities was obtained in [5].

In this paper, we propose a technique to simplify the model while preserving all fundamental model variables and providing the closeness of the trajectories of the simplified and the original model near the operating points. This has been done using a system linearization technique based around its steady state (operating, equilibrium) points, [6]-[7]. Due to complexity of the obtained steady state system given in terms of five algebraic equations, the solution of these equations has been found using the MATLAB Symbolic Tool Box. An important result obtained is that the equilibrium solution is unique. In addition, using the same tool box we have found the linearized model eigenvalues.

2. MODEL LINEARIZATION

The PEM fuel cell model defined in (1) has the following general nonlinear system form

$$\dot{x}(t) = f(x(t), u(t), I(t)) \quad (5)$$

where f is a function mapping $\mathfrak{R}^n \times \mathfrak{R}^m \rightarrow \mathfrak{R}^n$. An equilibrium point $\bar{x} \in \mathfrak{R}^n$ with a specific input $\bar{u} \in \mathfrak{R}^m$ and disturbance $\bar{I} \in \mathfrak{R}^l$ is satisfying

$$f(\bar{x}(t), \bar{u}(t), \bar{I}(t)) = 0_n \quad (6)$$

Using MATLAB Symbolic Math Toolbox, we obtain a unique equilibrium point for the given system

$$\bar{x}_1 = \frac{\varphi_a P_{vs} \varphi_{11}}{\varphi_{12}} \quad (7)$$

$$\begin{aligned} \varphi_{11} = & C_1^2 I^2 - 2\lambda_{H_2} C_1 I \left(Y_{H_2} - 1 \right) k_a u_a \\ & + \lambda_{H_2}^2 Y_{H_2} \left(Y_{H_2} - 2 \right) k_a^2 u_a^2 \end{aligned} \quad (7.1)$$

$$\begin{aligned} \varphi_{12} = & C_1^2 I^2 - \lambda_{H_2} C_1 I Y_{H_2} k_a u_a \\ & + \lambda_{H_2}^2 \left(Y_{H_2} - 1 \right) k_a^2 u_a^2 \end{aligned} \quad (7.2)$$

$$\bar{x}_2 = \frac{\varphi_a P_{vs} \varphi_{21}}{\varphi_{22}} \quad (8)$$

$$\begin{aligned} \varphi_{21} = & \lambda_{H_2} C_1 I \left(Y_{H_2} - 1 \right) k_a u_a \\ & - \lambda_{H_2}^2 \left(Y_{H_2}^2 - 3Y_{H_2} + 2 \right) k_a^2 u_a^2 \end{aligned} \quad (8.1)$$

$$\begin{aligned} \varphi_{22} = & C_1^2 I^2 - \lambda_{H_2} C_1 I Y_{H_2} k_a u_a \\ & + \lambda_{H_2}^2 \left(Y_{H_2} - 1 \right) k_a^2 u_a^2 \end{aligned} \quad (8.2)$$

$$\bar{x}_3 = \frac{\varphi_c P_{vs} \varphi_{31}}{\varphi_{32}} \quad (9)$$

where

$$\begin{aligned} \varphi_{31} = & I^3 C_1^2 \left(-C_1 + C_2 + (C_1 + C_2) Y_{N_2} \right) \\ & + \lambda_{air} I^2 C_1 \left(3C_1 - (C_1 + 2C_2) Y_{N_2} \right) k_c u_c \\ & + \lambda_{air} I^2 C_1 \left(-4C_2 Y_{O_2} - 2(C_1 + C_2) Y_{N_2} Y_{O_2} \right) k_c u_c \\ & + 2\lambda_{air}^2 I \left(2C_1 - C_1 Y_{N_2} - 4C_1 Y_{O_2} \right) k_c^2 u_c^2 \\ & + 2\lambda_{air}^2 I \left(2(C_1 + C_2) Y_{O_2}^2 \right) k_c^2 u_c^2 \\ & + 2\lambda_{air}^2 I \left((C_1 + 2C_2) Y_{N_2} Y_{O_2} \right) k_c^2 u_c^2 \\ & + 4\lambda_{air}^3 \left(Y_{N_2} + Y_{O_2} - 2 \right) Y_{O_2} k_c^3 u_c^3 \end{aligned} \quad (9.1)$$

and

$$\begin{aligned} \varphi_{32} = & I^3 C_1^2 \left(-C_1 + C_2 + (C_1 + C_2) Y_{N_2} \right) \\ & + \lambda_{air} I^2 C_1 \left(-2(3C_1 - C_2) + (3C_1 + 4C_2) Y_{N_2} \right) k_c u_c \\ & + \lambda_{air} I^2 C_1 \left(2(C_1 + C_2) Y_{O_2} \right) k_c u_c \\ & + 2\lambda_{air}^2 I \left(2C_2 Y_{N_2} + (C_1 + 2C_2) Y_{O_2} - 3C_1 \right) k_c^2 u_c^2 \\ & + 4\lambda_{air}^3 \left(Y_{N_2} + Y_{O_2} - 1 \right) k_c^3 u_c^3 \end{aligned} \quad (9.2)$$

$$\bar{x}_4 = \frac{\varphi_c P_{vs}(\varphi_{41})}{\varphi_{42}} \quad (10)$$

where

$$\begin{aligned} \varphi_{41} = & I^2 C_1 Y_{N_2} ((C_1 - C_2) - (C_1 + C_2) Y_{N_2}) \\ & + \lambda_{air} I Y_{N_2} (-3C_1 + (C_1 + 2C_2) Y_{N_2}) k_c u_c \\ & + \lambda_{air} I Y_{N_2} (2(C_1 + C_2) Y_{O_2}) k_c u_c \\ & + 2\lambda_{air}^2 (-2 + Y_{N_2} + Y_{O_2}) Y_{N_2} k_c^2 u_c^2 \end{aligned} \quad (10.1)$$

and

$$\begin{aligned} \varphi_{42} = & I^2 C_1 ((C_1 - C_2) - (C_1 + C_2) Y_{N_2}) \\ & + \lambda_{air} I (-4C_1 + (C_1 + 2C_2) Y_{N_2}) k_c u_c \\ & + \lambda_{air} I (2(C_1 + C_2) Y_{O_2}) k_c u_c \\ & + 2\lambda_{air}^2 (-1 + Y_{N_2} + Y_{O_2}) k_c^2 u_c^2 \end{aligned} \quad (10.2)$$

$$\bar{x}_5 = \frac{\varphi_c P_{vs} \varphi_{51}}{\varphi_{52}} \quad (11)$$

where

$$\begin{aligned} \varphi_{51} = & I^3 C_1^2 Y_{N_2} (C_1 - C_2 - (C_1 + C_2) Y_{N_2}) \\ & + \lambda_{air} I^2 C_1 (B_1 + B_2 + B_3 + B_4) k_c u_c \\ & - 2\lambda_{air}^2 I (B_5 + B_6 + B_7) k_c^2 u_c^2 \\ & - 4\lambda_{air}^3 (2 + Y_{N_2} + Y_{O_2}) (1 + Y_{N_2} + Y_{O_2}) k_c^3 u_c^3 \end{aligned}$$

$$B_1 = 2(C_1 - C_2) - 7C_1 Y_{N_2}$$

$$B_2 = -2(C_1 - C_2) Y_{O_2}$$

$$B_3 = 4(C_1 + C_2) Y_{N_2} Y_{O_2}$$

$$B_4 = (3C_1 + 4C_2) Y_{N_2}^2$$

$$B_5 = 3C_1 + 2(C_1 - C_2) Y_{N_2}$$

$$B_6 = -(5C_1 + 2C_2) Y_{O_2} + 2C_2 Y_{N_2}^2$$

$$B_7 = 2(C_1 + C_2) Y_{O_2}^2 + 2(C_1 + 2C_2) Y_{N_2} Y_{O_2} \quad (11.1)$$

and

$$\begin{aligned} \varphi_{52} = & I^3 C_1^2 (-C_1 + C_2 + (C_1 + C_2) Y_{N_2}) \\ & + \lambda_{air} I^2 C_1 (-2(3C_1 - C_2) + (3C_1 + 4C_2) Y_{N_2}) k_c u_c \\ & + \lambda_{air} I^2 C_1 (2(C_1 + C_2) Y_{O_2}) k_c u_c \\ & + 2\lambda_{air}^2 I (2C_2 Y_{N_2} + (C_1 + 2C_2) Y_{O_2} - 3C_1) k_c^2 u_c^2 \\ & + 4\lambda_{air}^3 (Y_{N_2} + Y_{O_2} - 1) k_c^3 u_c^3 \end{aligned} \quad (11.2)$$

Using Jacobian linearization around the equilibrium point, the system with input \bar{u} and disturbance \bar{I} can be expressed as

$$\dot{\delta}_x(t) = \left. \frac{\partial f}{\partial x} \right|_{\substack{x=\bar{x} \\ u=\bar{u} \\ I=\bar{I}}} \delta_x(t) + \left. \frac{\partial f}{\partial u} \right|_{\substack{x=\bar{x} \\ u=\bar{u} \\ I=\bar{I}}} \delta_u(t) + \left. \frac{\partial f}{\partial I} \right|_{\substack{x=\bar{x} \\ u=\bar{u} \\ I=\bar{I}}} \delta_I(t) \quad (12)$$

where

$$x(t) = \bar{x} + \delta_x(t)$$

$$u(t) = \bar{u} + \delta_u(t) \quad (13)$$

$$I(t) = \bar{I} + \delta_I(t)$$

with the constant matrices given by

$$\begin{aligned} A = \left. \frac{\partial f}{\partial x} \right|_{\substack{x=\bar{x} \\ u=\bar{u} \\ I=\bar{I}}} \in \mathfrak{R}^{n \times n}, \quad B = \left. \frac{\partial f}{\partial u} \right|_{\substack{x=\bar{x} \\ u=\bar{u} \\ I=\bar{I}}} \in \mathfrak{R}^{n \times m}, \\ G = \left. \frac{\partial f}{\partial I} \right|_{\substack{x=\bar{x} \\ u=\bar{u} \\ I=\bar{I}}} \in \mathfrak{R}^{n \times l} \end{aligned} \quad (14)$$

The linearized system is expressed as

$$\dot{\delta}_x(t) = A \delta_x(t) + B \delta_u(t) + G \delta_I(t) \quad (15)$$

For our model, we have

$$A = \left. \frac{\partial f}{\partial x} \right|_{\substack{x=\bar{x} \\ u=\bar{u} \\ I=\bar{I}}} = \begin{pmatrix} A_1 & 0_{2 \times 3} \\ 0_{3 \times 2} & A_2 \end{pmatrix} \bigg|_{\substack{x=\bar{x} \\ u=\bar{u} \\ I=\bar{I}}} \quad (16)$$

where

$$\begin{aligned} A_1 = & \begin{pmatrix} a_{11} & a_{12} \\ a_{21} & a_{22} \end{pmatrix} \text{ and} \\ A_2 = & \begin{pmatrix} a_{33} & a_{34} & a_{34} \\ a_{43} & a_{44} & a_{43} \\ a_{53} & a_{53} & a_{55} \end{pmatrix} \end{aligned} \quad (16.1)$$

with

$$a_{11} = \frac{RT}{V_A} \left(-\lambda_{H_2} k_a \bar{u}_a + C_1 \bar{I} \right) \frac{\bar{x}_2}{\bar{x}_{12}^2} \quad (16.2)$$

$$\bar{x}_{12} = \bar{x}_1 + \bar{x}_2$$

$$a_{12} = \frac{RT}{V_A} \left(\lambda_{H_2} k_a \bar{u}_a - C_1 \bar{I} \right) \frac{\bar{x}_1}{\bar{x}_{12}^2} \quad (16.3)$$

$$a_{21} = \frac{RT}{V_A} \lambda_{H_2} \left(\frac{-\varphi_a P_{vs}}{(\bar{x}_{12} - \varphi_a P_{vs})^2} + \frac{\bar{x}_2}{\bar{x}_{12}^2} \right) k_a \bar{u}_a$$

$$+ \frac{RT}{V_A} \left(-C_1 \bar{I} \frac{\bar{x}_2}{\bar{x}_{12}^2} \right) \quad (16.4)$$

$$a_{22} = \frac{RT}{V_A} \lambda_{H_2} \left(\frac{-\varphi_a P_{vs}}{(\bar{x}_{12} - \varphi_a P_{vs})^2} - \frac{\bar{x}_1}{(\bar{x}_{12})^2} \right) k_a \bar{u}_a$$

$$+ \frac{RT}{V_A} C_1 \bar{I} \frac{\bar{x}_1}{(\bar{x}_{12})^2} \quad (16.5)$$

$$a_{33} = \frac{RT}{V_C} \left(-\lambda_{air} k_c \bar{u}_c + \frac{C_1}{2} \bar{I} \right) \frac{\bar{x}_4 + \bar{x}_5}{(\bar{x}_{345})^2} \quad (16.6)$$

$$\bar{x}_{345} = \bar{x}_3 + \bar{x}_4 + \bar{x}_5$$

$$a_{34} = \frac{RT}{V_C} \left(\lambda_{air} k_c \bar{u}_c - \frac{C_1}{2} \bar{I} \right) \frac{\bar{x}_3}{(\bar{x}_{345})^2} \quad (16.7)$$

$$a_{43} = \frac{RT}{V_C} \lambda_{air} k_c \bar{u}_c \frac{\bar{x}_4}{(\bar{x}_{345})^2} \quad (16.8)$$

$$a_{44} = -\frac{RT}{V_C} \lambda_{air} k_c \bar{u}_c \frac{\bar{x}_3 + \bar{x}_5}{(\bar{x}_{345})^2} \quad (16.9)$$

$$a_{53} = \frac{RT}{V_C} \lambda_{air} \left(\frac{-\varphi_c P_{vs}}{(\bar{x}_{345} - \varphi_c P_{vs})^2} + \frac{\bar{x}_5}{(\bar{x}_{345})^2} \right) k_c \bar{u}_c$$

$$+ \frac{RT}{V_C} (C_1 + C_2) \bar{I} \frac{\bar{x}_5}{(\bar{x}_{345})^2} \quad (16.10)$$

$$a_{55} = \frac{RT}{V_C} \lambda_{air} \left(\frac{-\varphi_c P_{vs}}{(\bar{x}_{345} - \varphi_c P_{vs})^2} - \frac{\bar{x}_3 + \bar{x}_4}{(\bar{x}_{345})^2} \right) k_c \bar{u}_c$$

$$- \frac{RT}{V_C} (C_1 + C_2) \bar{I} \frac{\bar{x}_3 + \bar{x}_4}{(\bar{x}_{345})^2} \quad (16.11)$$

$$B = \frac{\partial f}{\partial u} \Big|_{\substack{x=\bar{x} \\ u=\bar{u} \\ I=\bar{I}}} = \begin{pmatrix} b_{11} & 0 \\ b_{21} & 0 \\ 0 & b_{32} \\ 0 & b_{42} \\ 0 & b_{52} \end{pmatrix} \quad (17)$$

$$b_{11} = \frac{RT}{V_A} \lambda_{H_2} \left(Y_{H_2} - \frac{\bar{x}_1}{\bar{x}_{12}} \right) k_a \quad (17.1)$$

$$b_{21} = \frac{RT}{V_A} \lambda_{H_2} \left(\frac{\varphi_a P_{vs}}{\bar{x}_{12} - \varphi_a P_{vs}} - \frac{\bar{x}_2}{\bar{x}_{12}} \right) k_a \quad (17.2)$$

$$b_{32} = \frac{RT}{V_C} \lambda_{air} \left(Y_{O_2} - \frac{\bar{x}_3}{\bar{x}_{345}} \right) k_c \quad (17.3)$$

$$b_{42} = \frac{RT}{V_C} \lambda_{air} \left(Y_{N_2} - \frac{\bar{x}_4}{\bar{x}_{345}} \right) k_c \quad (17.4)$$

$$b_{52} = \frac{RT}{V_C} \lambda_{air} \left(\frac{\varphi_c P_{vs}}{\bar{x}_{345} - \varphi_c P_{vs}} - \frac{\bar{x}_5}{\bar{x}_{345}} \right) k_c \quad (17.5)$$

$$G = \frac{\partial f}{\partial I} \Big|_{\substack{x=\bar{x} \\ u=\bar{u} \\ I=\bar{I}}}$$

$$= \begin{pmatrix} \frac{RTC_1}{V_A} \left(\frac{\bar{x}_1}{\bar{x}_{12}} - 1 \right) \\ \frac{RTC_1}{V_A} \left(\frac{\bar{x}_2}{\bar{x}_{12}} - 1 \right) \\ \frac{RTC_1}{2V_C} \left(\frac{\bar{x}_3}{\bar{x}_{345}} - 1 \right) \\ 0 \\ \frac{RTC_1}{V_C} \left(\frac{C_2}{C_1} \left(1 - \frac{\bar{x}_5}{\bar{x}_{345}} \right) - 1 - \frac{\bar{x}_5}{\bar{x}_{345}} \right) \end{pmatrix} \quad (18)$$

2.1 Linearized System Eigen values and System Stability

The matrix A_1 in (16.1) has two eigenvalues

$$\lambda_1, \lambda_2 = \frac{a_{11} + a_{22} \pm \sqrt{(a_{11} + a_{22})^2 + 4(a_{11}a_{22} - a_{12}a_{21})}}{2} \quad (19.1)$$

The matrix A_2 in (16.1) has three eigenvalues. Using the MATLAB Symbolic Tool Box we have found that these eigenvalues are given by

$$\lambda_3 = a + \gamma + \frac{c}{\gamma}$$

$$\lambda_4, \lambda_5 = a - \frac{1}{2} \left(\gamma + \frac{c}{\gamma} \right) \pm i \frac{1}{2} \left(\gamma - \frac{c}{\gamma} \right) \quad (19.2)$$

where

$$a = \frac{a_{33} + a_{44} + a_{55}}{3} \quad (19.3)$$

$$\gamma = \sqrt[3]{-b + \sqrt{b^2 - c^3}} \quad (19.4)$$

$$b = \frac{(a_{33} + a_{44} + a_{55})}{6} \times \alpha - \left(\frac{a_{33} + a_{44} + a_{55}}{3} \right)^3$$

$$+ \frac{a_{33}a_{43}a_{53}}{2} - a_{34}a_{43}a_{53} + \frac{a_{34}a_{44}a_{53}}{2}$$

$$- \frac{a_{33}a_{44}a_{55}}{2} + \frac{a_{34}a_{43}a_{55}}{2}$$

$$\alpha = a_{33}a_{44} - a_{34}a_{43} - a_{34}a_{53} + a_{33}a_{55}$$

$$- a_{43}a_{53} + a_{44}a_{55} \quad (19.5)$$

$$c = \frac{a_{34}a_{43}}{3} - \frac{a_{33}a_{44}}{3} + \frac{a_{34}a_{53}}{3} - \frac{a_{33}a_{55}}{3}$$

$$+ \frac{a_{43}a_{53}}{3} - \frac{a_{44}a_{55}}{3} + \left(\frac{a_{33} + a_{44} + a_{55}}{3} \right)^2 \quad (19.6)$$

The equilibrium point \bar{x} with input \bar{u} and disturbance \bar{I} is stable when real parts of all eigenvalues of equations (19.1) and (19.2) are negative. Using realistic data that stability condition can be easily tested by simply evaluating all parameters defined in (19.1)-(19.5).

3. CONCLUSIONS

We have found the equilibrium (steady state) solution of the well-known nonlinear model of the proton exchange membrane fuel cell using the MATLAB Symbolic Tool Box. It appears that the obtained solution is unique. Even more, we have found the corresponding linearized system around its equilibrium points, and the corresponding linear system eigenvalues.

REFERENCES

- [1] W. K. Na and B. Gou, "Feedback linearization-based nonlinear control for PEM fuel cells, *IEEE Transactions on Energy Conversion*, Vol. 23, 179-190, 2008.
- [2] B. Gou, W. K. Na, and B. Diong, *Fuel Cells: Modeling, Control, and Applications*, CRC Press/Taylor & Francis Group, Boca Raton, Florida, 2010.
- [3] Q. Li, W. Chen, Y. Wang, J. Jia, and M. Han, "Nonlinear robust control of proton exchange membrane fuel cell by state feedback exact linearization," *Journal of Power Sources*, Vol. 194, 338-348, 2009.
- [4] C. Kunusch, A. Husar, P. Puleston, M. Mayosky, and J. More, "Linear identification and model adjustment of a PEM fuel cell stack," *International Journal of Hydrogen Energy*, Vol. 33, 3581-3587, 2008.
- [5] M. Meiler, O. Schid, M. Schudy, and E. Hofer, "Dynamic fuel cell stack model for real-time simulation based on system identification," *Journal of Power Sources*, Vol. 176, 523-528, 2008.
- [6] H. Khalil, *Nonlinear Systems*, Prentice Hall, 3rd edition, 2002.
- [7] Z. Gajic, *Linear Dynamic Systems and Signals*, Prentice Hall, 2003.

Study on Heavy Metal Resistant Bacteria Isolated From Wastewater

Benmalek ¹Y., M.-L. Fardeau²

¹ Université des Sciences et de Technologie Houari Boumediene, Faculté des sciences biologiques, Département de BCM, Laboratoire de Microbiologie, BAB EZZOUAR, Alger, Algérie.

yambenmalek@yahoo.fr

² Université de Provence et de la Méditerranée, Laboratoire de Microbiologie IRD, UMRD180, Microbiologie et Biotechnologie des Environnements Chauds, ESIL, Case 925, 163 Avenue de Luminy, 13288 Marseille Cedex 09, France. marie-laure.fardeau@univmed.fr

ABSTRACT

Removal of metal ions from wastewater using heavy metal-resistant bacteria is the cheaper, economical and efficacious methods. In this study, twenty heavy metal-resistant bacteria were isolated from wastewater of oued El-Harrach in Eastern of Algiers in Algeria. These include zinc, chromium, cadmium and lead-resistant bacteria. Heavy metal bacteria characterized include both Gram negative (75%) and Gram positive (25%). All the isolates showed high resistance to heavy metal ions tested with Minimum Inhibitory Concentration ranging from 100-1400 ug/ml. Seventeen resistant isolates showed co-resistance to other heavy metals used in this study. All the strains also showed antibiotic resistance of which 40% were resistant to two antibiotic and 60% were multi- antibiotic resistant.

Key words: Heavy metal resistance bacteria, antibiotic resistance, bioaccumulation, Wastewater, oued El-Harrach.

1. INTRODUCTION

Heavy metals are one of the major sources of environmental pollution. They are released due to the discharge of effluent into environment by a large number of industrial activities such as metal processing, mining, electroplating, leather tanning and pigments production. The concentration level of these toxic chemical compounds varies widely in the environment. Wastewater contains significant concentration of heavy metals that are not degraded by the conventional process of wastewater treatment. Presence of high concentration of heavy metals in wastewater has a deleterious impact on aquatic life [1]. Mean-while, many heavy metals like zinc, iron and copper are essential trace elements to cell at low levels but they can exert toxic effects at concentration encountered in polluted environments [2]. Usually, chemical agents like mercury, cadmium, lead, chromium and nickel are present in soluble form and are extremely toxic and too dangerous for any biological function and disturbed ecological activity in aquatic environment. Beside that, heavy metals have the ability to form unspecific complex compounds in the cell which lead to toxic effects.

In response to toxic concentrations of metal ions, many micro-organisms including bacteria can develop resistance and become heavy metal-resistant [3, 4]. Among the various mechanisms intra and extra cellular, bioaccumulation [5], bio-sorption [6], bio-mineralization and precipitation [7], enzymatic oxidation or reduction to a less toxic form [8] and efflux heavy metal systems. Stress of heavy metals is well known to shift a native bacterial community to a composition in which resistant and tolerance bacteria become numerously dominant. The heavy metal-

resistant bacteria have an important role in wastewater treatment process and because their detoxifying ability, they can be manipulated for bio-remediation of heavy metals in wastewater.

The present study aimed to isolate, characterized and identified heavy metal-resistant bacteria from wastewater of oued El-Harrach. The co-resistance to other metal-salts used and antibiotics also has been studied extensively.

2. MATERIALS AND METHODS

2.1 Site description

Oued El-Harrach was located in El-Harrach city in East of Algiers/Algeria. It's formed by the confluence of oued Smar, oued Ouchayeh and the Littoral Rive Gauche. Oued El-Harrach receives effluent from many local industries, domestic, agriculture and urban sewage. The wastewater of oued El-Harrach discharge directly in the sea.

2.2 Sampling

Wastewater samples were collected in sterile glass bottles from the surface and transported to the laboratory where they were analyzed within 8h of collection. A total of two samples were taken for the study. The heavy metals concentration was determined according to Dean-Ross and Mills [2]. Samples were acidified with 5ml of concentrated nitric acid per liter. After over night incubation at ambient temperature, the result liquid was diluted and the concentrations of cadmium, lead, zinc and chromium were determined using atomic adsorption spectrophotometer.

2.3 Isolation, characterization and identification of heavy metal-resistant bacteria

Lead, cadmium, zinc and chromium-resistant bacterial strains were isolated from wastewater of oued El-Harrach using nutrient agar (Difco) as basal medium according to Rajbhanshi and Rani et al. [10, 11]. 100 ug/ml of each heavy metal was incorporated separately in the medium. For the isolation, 0.1ml of raw wastewater samples was sown in mass of these media. Then, plates were incubated at 30°C for 24-48h. The isolates and different distinct colonies on the selective media were sub cultured on the same media for purification. After that, the pure culture was characterized and identified on the basis of their morphology, physiology and biochemical characters using standard methods and api 20E system (Bio Merieux).

2.4 Determination of MIC of heavy metals

MIC of the heavy metal ions-resistant bacteria characterized against respective heavy metal was determined by gradually increasing the concentration of the heavy metal 50ug/ml each time on nutrient agar plate. The initial concentration used for this study was 100ug/ml. Each plate was spread with overnight cultures of the bacterial strains. Nutrient agar plates were incubated at 30°C for 24h to 10 days. After incubation, the culture growing on the last concentration was transferred to the higher concentration by streaking on a new plate. MIC was noted when the strains failed to grow on plates even after 10 days [12].

2.5 Study of the co-resistance to other metals

The characterized bacterial strains resistant to their selective heavy metal were tested for their sensitivity or resistance to other metal-salts used in this study. 100ug/ml was used as initial concentration of each heavy metal which was gradually increased 50ug/ml each time until MIC was obtained.

2.6 Study of antibiotic sensitivity of the isolates

As heavy metal-resistance is linked with antibiotic-resistance, the metal-resistance isolates were tested for their sensitivity to 12 antibiotics. The disc diffusion method was used to determine antibiotic resistance and sensitivity of the characterized heavy metal-resistant isolates [13]. Standard antibiotic-impregnated discs were placed on freshly prepared lawns of each isolate on Mueller-Hinton plates. After 24-48h of incubation at 30°C, the diameter of the inhibition zones was measured and the strains were classified as resistant (R), intermediate (I) and susceptible (S) following the standard antibiotic disk chart. Discs containing the following antibiotics were tested: ampicillin (10ug), cefoxitin (30ug), cefalotin (30ug), gentamycin (10ug), kanamycin (30UI), amikacin (30ug), doxycyclin (20ug),

nalidixic acid (30ug), pipemidic acid (20ug), fusidic acid (10ug), nitroxolin (20ug) and lincomycin (15ug).

3 RESULTS AND DISCUSSION

3.1 Heavy metal analysis

Analysis of wastewater samples collected from oued El-Harrach revealed that heavy metal content of the samples from which the bacteria was isolated was estimated as : 0.616 mg/l chromium, 0.846 mg/l lead, 0.548mg/l cadmium and 0.943 mg/l zinc. The results showed that zinc and lead concentration was very important and they were considered as the major pollutants.

3.2 Isolation and characterization of heavy metal-resistant bacteria

A total of twenty heavy metal-resistant bacterial strains were isolated from wastewater of oued El-Harrach and characterized. The heterotrophic metal -resistant isolates identified showed wide varieties of species including Gram-negative and positive. Eight members of these isolates (40%) belong to the family Enterobacteriaceae (Zn^{2+} -resistant *Enterobacter intermedium*, Cd^{2+} -resistant *Salmonella arizonae* and *Enterobacter aerogenes*, Cr^{2+} -resistant *Serratia fonticola* with *Klebsiella oxytoca* and Pb^{2+} -resistant *Enterobacter amnigenus*, *Morganella morganii* and *Klebsiella pneumoniae*) with two species of the genus *Pseudomonas* (Zn^{2+} -resistant *Pseudomonas aeruginosa* and Cr^{2+} -resistant *Pseudomonas pseudomallei*) and the genus *Bacillus* (Zn^{2+} -resistant *Bacillus cereus* and Cd^{2+} -resistant *Bacillus*). Though, *Aeromonas*, *Achromobacter*, *Staphylococcus*, *Micrococcus*, *Alcaligenes*, *Flavobacterium* and *Acinetobacter* species were also characterized and identified by api-20E system and classic tests used. Most of these bacteria like *Pseudomonas*, *Micrococcus*, *Klebsiella*, *Bacillus* and *Flavobacterium* were widely isolated from wastewater by other researchers and well documented for their resistance to chemical antimicrobial agents [14, 6, 10, 11].

3.3 Co-resistance to other heavy metals and antibiotic sensitivity

All the isolates showed high resistance for their relative heavy metals with MIC ranging from 100ug/ml to 1400ug/ml (table.1). Lead and chromium -resistant strains were resistant to higher concentrations than cadmium and zinc-resistant isolates. All the metal -resistant bacteria were tested for their co-resistance to other metal-salts used in this study. It's interesting to note that 17 isolates (85%) were multi -resistant to heavy metals (Table.2). Among the tested microorganisms, Pb^{2+} -resistant *Morganella morganii*, Zn^{2+} -resistant *Enterococcus faecalis* and Cd^{2+} -resistant *Alcaligenes* sp showed co-resistance only to one heavy

Table.1: Heavy metal-resistant bacteria characterized

Bacteria	Resistant to	MIC (ug/ml)
<hr/>		
<i>Micrococcus luteus</i>	Zinc	500
<i>Pseudomonas aeruginosa</i>		300
<i>Enterococcus faecalis</i>		300
<i>Enterobacter intermedium</i>		100
<i>Bacillus cereus</i>		250
<hr/>		
<i>Alcaligenes sp</i>		100
<i>Salmonella arizonae</i>	Cadmium	200
<i>Enterobacter aerogenes</i>		150
<i>Acinetobacter sp</i>		250
<i>Bacillus sp</i>		300
<hr/>		
<i>Serratia fonticola</i>		300
<i>Klebsiella oxytoca</i>		850
<i>Pseudomonas pseudomallei</i>	Chromium	1000
<i>Aeromonas hydrophila</i>		400
<i>Staphylococcus aureus</i>		550
<hr/>		
<i>Enterobacter amnigenus</i>		700
<i>Klebsiella pneumoniae</i>	lead	900
<i>Achromobacter sp</i>		600
<i>Morganella morganii</i>		900
<i>Flavobacterium sp</i>		650

Table 2: Co-resistance of heavy metal-resistance isolates to other heavy metals

Microorganisms	Co-resistance to	MIC (ug/ml)
Zn²⁺- resistant bacteria		
<i>Micrococcus luteus</i>	chromium, lead, cadmium	1000,1400, 350
<i>Pseudomonas aeruginosa</i>	chromium, lead, cadmium	900, 1000, 300
<i>Enterococcus faecalis</i>	lead	800
<i>Enterobacter intermedium</i>	lead, cadmium	550, 250,
<i>Bacillus cereus</i>	chromium, lead, cadmium	450, 450, 350
Cd²⁺- resistant bacteria		
<i>Alcaligenes sp</i>	lead	300
<i>Salmonella arizonae</i>	lead, chromium, zinc	600, 600, 200
<i>Enterobacter aerogenes</i>	lead, chromium, zinc	800, 700, 200
<i>Acinetobacter sp</i>	lead, chromium	700, 400
<i>Bacillus sp</i>	lead, chromium	300, 300
Cr²⁺- resistant bacteria		
<i>Serratia fonticola</i>	lead, zinc, cadmium	600, 200, 200
<i>Klebsiella oxytoca</i>	lead, zinc, cadmium	600, 200, 200
<i>Pseudomonas pseudomallei</i>	lead, zinc, cadmium	600, 700, 300
<i>Aeromonas hydrophila</i>	lead, zinc, cadmium	400, 250, 300
<i>Staphylococcus aureus</i>	lead, zinc	400, 250
Pb²⁺- resistant bacteria		
<i>Enterobacter amnigenus</i>	chromium, zinc, cadmium	550,300, 300
<i>Klebsiella pneumoniae</i>	chromium, zinc, cadmium	600, 200, 200
<i>Achromobacter sp</i>	chromium, zinc, cadmium	600, 200, 200
<i>Morganella morganii</i>	zinc	200
<i>Flavobacterium sp</i>	zinc, cadmium	450, 300

metal, but the strains Pb²⁺- resistant *Flavobacterium* sp, Cr²⁺-resistant *Staphylococcus aureus*, Zn²⁺-resistant *Enterobacter intermedium* and *Bacillus cereus* and Cd²⁺-resistant *Acinetobacter* sp were resistant to two heavy metals. Based on the results of co-resistance study, the strain Zn²⁺-resistant *Micrococcus luteus* was identified as very efficient isolate which was resistant to higher

concentrations than other isolates with 1000 ug/ml (chromium), 1400ug/ml (lead) and 350ug/ml (cadmium) respectively.

In the present study no attempt was made to determine heavy metal-resistance mechanisms in bacteria. However, it has been reported that microbial resistance

to metals include a variety of detoxifying systems and mechanisms developed by resistant-microorganisms such as reduction, precipitation at the cell surface, complexation by exopolysaccharids, blocking cellular uptake by altering the uptake pathway and removal from the cytoplasm by efflux pumps [15, 16, 17].

In antibiotic resistance test, heavy metal resistance capacities of the micro organisms are mainly associated with antibiotic resistance. In this study, all the isolates characterized were resistant to antibiotics of which Zn²⁺-resistant *Micrococcus luteus*, *Enterococcus faecalis* and *Enterobacter intermedium*, Cr²⁺-resistant *Aeromonas hydrophila*, *Staphylococcus aureus* and *Pseudomonas pseudomallei*, Cd²⁺-resistant *Acinetobacter* sp and Pb²⁺ resistant *Enterobacter amnigenus* were found to be bi-antibiotic resistant, while the rest of the isolates were found to be multi-antibiotic resistance (Table.3and Figure.1). The literature reveals that there is an interrelationship between the antibiotic and heavy metal resistance capacities of all the micro organisms [18, 19].

In wastewater, there are some substances that have the potential to select for antibiotic resistance, even though they are not antibiotics themselves. Heavy metals and biocides are two of them. The exposure to heavy metals or biocides results in the selection of bacterial strains also able to resist antibiotics. This happens because genes encoding heavy metals and biocides are located together with antibiotic resistance genes or alternatively because bacteria can have unspecific mechanism of resistance common to different substances including heavy metals, biocides and antibiotics [20]. It is therefore, likely that selective pressure by one such compound indirectly selects for the whole set of resistances. From the above results, the isolate Zn²⁺-resistant *Micrococcus luteus* which was resistant to higher concentration of different heavy metals appeared to be most susceptible to antibiotics. Though, antibiotic-resistance is not correlated with degree of resistance to heavy metals.

4 CONCLUSION

A total of twenty heavy metal-resistance bacteria were isolated and characterized from wastewater of oued El-Harrach, which received industrial, domestic and urban effluents. Among these isolates, 75% were Gram-negative and 25% Gram-positive. Beside resistance to their selective metal, three strains were found to be co-resistant to only one heavy metal. The results of antibiotic study revealed that eight strains were resistant to two antibiotics. However, the heavy metal-resistant bacteria could be a potential agent for bio remediation of heavy metals pollution.

ACKNOWLEDGEMENTS

I would like to acknowledge microbiology laboratory staff of the FSB/USTHB

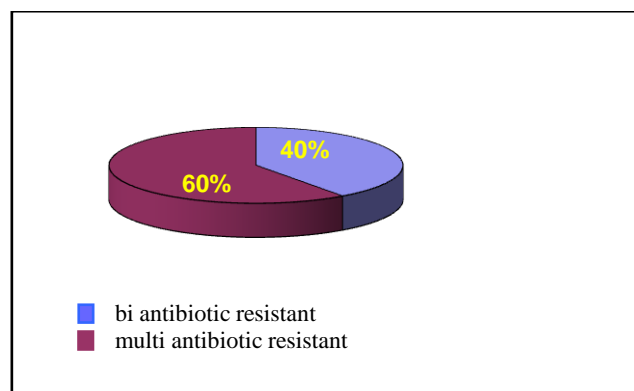


Figure 1: Frequency of bi antibiotic and multi antibiotic resistance among heavy metal-resistant isolates

Table 3: Antibiotic sensitivity of heavy metal- resistant bacteria

Micro organisms	Sensitive to	Resistant to
Zn²⁺- resistant bacteria		
<i>Micrococcus luteus</i>	-AM, FOX, CF, G, K, D, AN, NA,L, FA.	- PI, Ni (I).
<i>Pseudomonas aeruginosa</i>	- G, NA, D, PI, L, AN.	- K, AM, CF, FOX, Ni (I), FA
<i>Enterococcus faecalis</i>	- AM, AN, FOX, CF, G, D, K, Ni, NA, PI.	- L, FA.
<i>Enterobacter intermedium</i>	- AM, CF, FOX, G, K, AN, D, Ni, PI, NA.	- FA, L.
<i>Bacillus cereus</i>	- AN, CF, FOX, AM, D, L, Ni, PI, NA.	- K(I), FA, G (I).
Cd²⁺- resistant bacteria		
<i>Alcaligenes sp</i>	- AN, CF, FOX, G, FA, Ni, L.	- AM, K, D, NA, PI (I).
<i>Salmonella arizonae</i>	- K, AN, NA, Ni, D.	- AM, CF, FOX, G, L, FA, PI (I).
<i>Enterobacter aerogenes</i>	- AN, G, K, D, NA.	- AM, CF, FOX, L, Ni (I), FA, PI.
<i>Acinetobacter sp</i>	-AM, CF, FOX, AN, G, K, Ni, NA, D, PI.	- FA, L.
<i>Bacillus sp</i>	- K, G, AN, AM, CF, FOX, D, L.	- Ni (I), FA, PI, NA.
Cr²⁺- resistant bacteria		
<i>Serratia fonticola</i>	- K, AN, NA, PI, CF.	- AM, CF, G, FA, L, D, Ni (I).
<i>Klebsiella oxytoca</i>	- AN, CF, PI, NA, D.	- K (I), G, CF, AM, Ni (I), FA, L.
<i>Pseudomonas pseudomallei</i>	- K, AN, G, NA, PI, CF, L, FA, D, Ni.	- AM, CF.
<i>Aeromonas hydrophila</i>	- K, G, AN, AM, CF, FOX, D, NA, PI, Ni.	- L, FA.
<i>Staphylococcus aureus</i>	- K, AN, CF, FOX, AM, NA, PI, D, Ni, L.	- G, FA.
Pb²⁺- resistant bacteria		
<i>Enterobacter amnigenus</i>	- NA, FOX, D, PI, AN, CF, AM, L, FA, Ni.	- K (I), G
<i>Klebsiella pneumoniae</i>	- AN, PI, NA, D.	- K (I), G, AM, CF, FOX (I), L, FA, Ni (I).
<i>Achromobacter sp</i>	- AN, FOX, D, NA.	- AM (I), CF, K (I), G, PI, FA, L, Ni.
<i>Morganella morganii</i>	- AN, D, PI, Ni.	- K (I), G, AM, CF, FOX, L, FA, NA.
<i>Flavobacterium sp</i>	- AN, CF, FOX, AM, NA, PI, D.	- K (I), G, L, FA, Ni (I).

AM : ampicillin, CF: cefalotin, FOX : ceftoxitin, G : gentamycin, K : kanamycin, AN : amikacin, D : doxycyclin, Ni : nitroxolin, L : lincomycin, NA : nalidixic acid. PI : pipemidic acid, FA : fusidic acid.

I: intermediate resistance.

REFERENCES

- [1] Moten, A.M & Rehman, A. Study on heavy trace metal ions in industrial waste effluents in Pakistan. Environmental Expert. Com. Article-909, 1998
- [2] Dean-Ross, D., & Mills, A.L. Bacterial community structure and function along a heavy metal gradient. Applied and Environmental Microbiol Vol. 55, N^o.8, pp. 2002-2009, 1989

- [3] Klerks, P.L., & Weiss, J.S. Genetic adaptation to heavy metals in aquatic organisms: a review. *Environ. Microbiol.* Vol. 46, pp. 173-205, 1987
- [4] Kasan, H.C., & Baecker, A.A.W. Activated sludge treatment of coal- gasification effluent in a petro - chemical plant-H. Metal accumulation by heterotrophic bacteria. *Wat. Sci. Tech.* Vol. 21, (4/5), pp. 297-303, 1989
- [5] Blindauer, C.A, Harrison, M.D., Robinson, A.K., Parkinson, J.A., Bowness, P.W., Sadler, P.J., & Robinso, N.J. Multiple bacteria encode metallothioneins and Smt A- like zinc fingers. *Mol Microbiol.* Vol. 45, pp. 1421-1432, 2002
- [6] Leung, W.C, Wong, M.F., Lo, H., Chua, W., Yu, P.H.F., & Leung, C.K. Removal and recovery of heavy metals by bacteria isolated from activated sludge treating industrial effluents and municipal wastewater. *Water Science and Technology.* Vol. 41, n°.12, pp. 233-240, 2000
- [7] Podda, F, P. Zuddas, A. Minacci, Pepi, M., & Baldi, F. Heavy metal co-precipitation with hydro-zincite [Zn (5), (CO) (3) (2), (OH) (6)] from mine waters caused by photosynthetic microorganisms. *Appl Environ Microbiol.* Vol. 66, pp. 5099-5098, 2000
- [8] Silver, S: Bacterial resistance to toxic metal ions. *A Review of Gene.* Vol.179,pp. 9-19, 1996
- [9] Nies, D.H. Efflux mediated heavy metal resistance in prokaryotes. *FEMS Microbiology Reviews.* Vol. 27, pp. 313-339, 2003
- [10] Rajbhanshi, A. Study on heavy metal resistant bacteria in Gushewori Sewage treatment plant. *Our Nature.* Vol. 6,pp. 52-57, 2008
- [11] Rani, J.-M, Hemambika, F B., Hemaprya, J., & Rajeshkannan, V. Comparative assessment of heavy metal removal by immobilized and dead bacterial cells: a biosorption approach. *Global Journal of Environmental Ressearch.* Vol. 4, n° 1, pp. 23-30, 2010
- [12] Shakoori, A.R, Zaidi, K.-S.,& Haq, R. Cadmium resistant *Enterobacter cloacae* and *Klebsiella sp* isolated from industrial effluents and their possible role in cadmium detoxification. *World Journal of Microbiology and Biotechnology.* Vol.15, pp. 249-254 1998
- [13] Baurer, A.W., Kirby, W.M.M., Sherries, J.C., & Twick, M. Antibiotic susceptibility testing by a standardized single disc method. *American Journal of Clinical Pathal.* Vol. 45, pp. 493-496, 199

Adsorption of Two Dyes Water Textiles by Two Biosorbents

A.Ouldoumna^{1,2}, N. Benderdouche², B. Bestani²

¹LRSBG, Faculty of Science and Technology, University of Mascara BP 763, Mamounia, Mascara 29000, Algeria

E-mail: aouldoumna@yahoo.fr

²LSEA2M, Faculty of Science and Technology, University of Mostaganem (UMAB), BP 188, 27000, Algeria
benderdouchen@yahoo.fr

ABSTRACT

The objective of our work under the protection of the environment is to test the power of biosorbents waste of two plants, Eucalyptus and Cinara cardinalcius to remove colored substances from aqueous solutions, especially Methylene blue and red Nylosan; compare the deus biosorbents have been used in its raw state, the elimination capacity of methylene blue by the biosorbent was prepared and studied as a function of pH, dose of biosorbent, and contact time. The iodine and methylene blue index are very important factors in the characterization of the adsorbents studied. The value of iodine was greatest 477.46 mg / g for Cinara-cardinalcius vis-à-vis the biosorbent Eucalyptus 398.2 mg / g indicating an average microporosity for both materials. The Langmuir model applied to the results of experiments in process (batch) yielded a maximum capacity of adsorption by biosorbents very important. The kinetic study of the biosorption of the two dyes by applying the model of Lagergren (pseudo-first order and pseudo-second order) has shown that the attachment is compatible with order kinetics 2. The thermodynamic study showed a process exothermic with methylene blue and another with red Nylosan endothermic. The results found show that the two biosorbents can thus serve as the elimination of organic micropollutants from water.

Key words: sorption, pH of water, methylene blue, red Nylosan, isotherm, biosorbents.

1. INTRODUCTION

Water plays an important role in all areas of life (industry, agriculture, ...) The water becomes increasingly scarce and its quality deteriorates. Water must become everyone's business. The World Health Organization (WHO) considers that 80% of diseases that affect the world's population and are directly transported by water: 400 million people are living permanently gastroenteritis, malaria and 160 million 30 million onchocerciasis [1]. discharges of organic chemicals such as hydrocarbons, aromatics, dyes ... they are considered dangerous micropollutants because they are less remarkable. The health of living is deteriorating slowly, their lives are shortened, their offspring may be suffering from deformities, their likelihood of being affected by cancer increases. The Science and Technology is improving processes of pollution. Many researchers have studied the use of plants to extract heavy metals from water and soil [2-4]. Some plant species have shown a remarkable resistance to certain metals such as copper, zinc and lead [5-9]. Several studies are performed to produce adsorbents from waste plant for the purpose of protecting the environment and presented good results vis-à-vis the fixation of certain pollutants [10-13]. In our study we chose to work with the raw waste from two plants, the card, as the eucalyptus (*Eucalyptus globulus*, *Cinara cadinalcius*) for their availability in our region. Chosen to eliminate the pollutant is the synthetic dye methylene blue as synthetic dyes currently represent a relatively large chemical compounds found in almost all spheres of our

daily lives [10]. Discharges, especially dyes, are toxic to most living organisms. The dyes are characterized by their ability to absorb light radiation in the visible spectrum (380-700 nm). The color results from the transformation of white light into colored light by selective absorption of energy by certain groups of atoms called chromophores. The objective of this work is the use of two waste available to their raw state, to compare the performance of adsorption between the two materials and follow spectrophotometrically the binding of methylene blue and red Nylosan using UV-spectrometry VIS.

2. MATÉRIELS AND MÉTHODES

2.1 Preparation of adsorbents

The biosorbents used are waste of cardoon and eucalyptus, the waste is récolées the region of Mascara western Algeria, were washed with distilled water and dried in an oven at 60 C for 24 hours, they are ground in a mill ball type Croschop Viersen at 90 revolutions per minute and that for a time sufficient to achieve a reduction of grain size, sieved. They are then employed.

2.2. Biosorption of the Methylene Bleu

The study of the adsorption of a compound on an adsorbent allows us to examine the influence of some parameters on retention. It allows us to examine the influence of contact time, dose of adsorbent, pH. We

prepared a solution of concentration 100 mg / L, contact time (180 min), the dose of the adsorbent (2, 4, 8, 12, 16g / l), pH (2, 4, 6, 8, 10, 11) for the two biosorbents studied. An optimal dose for each biosorbent was placed with 25 mL of methylene blue concentration of 30 to 2200 mg / L. after a contact time which was previously determined to reach equilibrium, the solution is filtered and then analyzed by spectrophotometer Jenway UV / Visible Model (6400spectrophotometer). The concentration of methylene blue and red nylosane on the surface of biosorbent, x / m were determined by the following equation (1).

$$q_e = \frac{(C_o - C_e) \cdot V}{M} \quad (1)$$

Where M is the mass of biosorbent used (g) and V the volume of solution (ml).

3. RESULTS AND DISCUSSION

Many studies have shown that pH is an important factor in determining the potential for adsorption of cationic and anionic organic compounds [14-17] The pH of the solution has a very important role in the adsorption . In a series of beakers, were successively introduced a volume of methylene blue solution or red nylosan of known concentration adjusted to a pH of, if necessary with sodium hydroxide or hydrochloric acid concentration (1 N) to which we added a mass of biosorbents (*Eucalyptus globulus*, *Cinara cadinalcius*). The mixture is stirred for a specified time, then filtered and analyzed spectrophotometrically. As part of our work, the study of the biosorption of methylene blue and red Nylosan by biosorbents materials from *Eucalyptus globulus*, *Cinara cadinalcius* is performed for pH values: 2, 4, 8, 10,11 to examine the evolution of the biosorption of the pollutants as a function of pH. Studies conducted by researchers Ray and castrated and all [18] showed that systems based algae with a negative charge or of their affinity for cations. This is consistent with our results found by biosorbents used. The adsorption could be explained by pure electrostatic interaction between the negative charge of biosorbent and the positively charged methylene blue. The results of the biosorption of MB and the RN as a function of pH are shown graphically in Figure 1(a, b).

Figure 1(a) shows the percentage removal of MB depending on the pH of the solution for both biosorbents. One can observe that increasing the pH of the solution results in better elimination of the pollutant. The highest rate of biosorption takes place at an optimal pH of 10 for both biosorbents *Eucalyptus globulus* and *Cinara cadinalcius* A higher pH, the charge on the surface of adsorbent changes and becomes negative, causing a higher electrostatic attraction of cations dye, leading to a higher adsorption for methylene blue [19]. A decrease is observed at pH 2, 4 and 8 can be

explained by the fact that at low pH values, there is an electrostatic repulsion between the ions and the biosorbent surface positively charged. When the pH increases, the ion can replace BM hydrogen ion on the biosorbent surface, leading to an improvement in the adsorption [19].

In Figure 1(b) Can be seen, the best percentages of deletions Red Nylosan are obtained at acidic pH values for all biosorbents.

The increase in adsorption of dye depends on the properties of the adsorbent surface and structure of the dye [20,21]. A decrease in the elimination of the dye is observed beyond a basic pH and may be due to electrostatic repulsion. A similar behavior was reported by researchers [22, 23].

3.1. Adsorption isotherm of two dyes

The adsorption isotherm is the plot of the amount adsorbed per unit mass of biosorbents studied as a function of the concentration of BM and RN in equilibrium at room temperature. There are several equations to describe the adsorption isotherms. The results of these measurements are plotted in Figure 2.

We notice a rapid increase in the amount adsorbed for low concentrations and stabilization at high concentrations. Figure 2 shows clearly that the two materials have different adsorption capacities.

We find that the two biosorbents, *Eucalyptus globulus* and *Cinara-cardinalcius* adsorbs the MB with adsorption capacities of 250 mg / g and 333mg / g respectively. The largest adsorption capacity was obtained for the biosorbent based on the CARD and EUCA with an adsorption capacity of 83.33 mg / g The following table summarizes the results of the biosorption for the Langmuir model study.

The results are very interesting and comparable to those found by some researchers in our laboratory (Benderdouche & all) [10,11,12], as well as other work done by researchers [35].

3. FIGURES AND TABLES

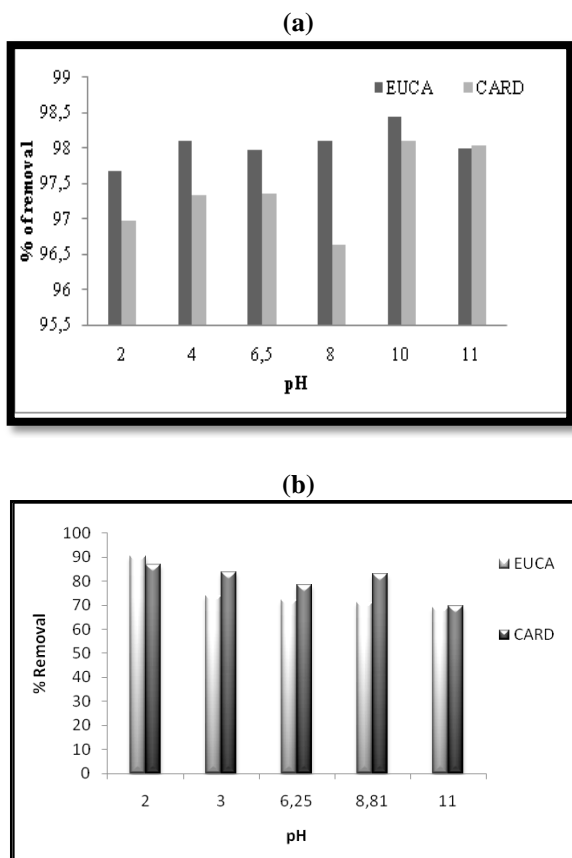


Figure 1: Effect of pH on the biosorption with $C_0 = 100$ mg / L; Methylene blue(a),Red nylosane(b).

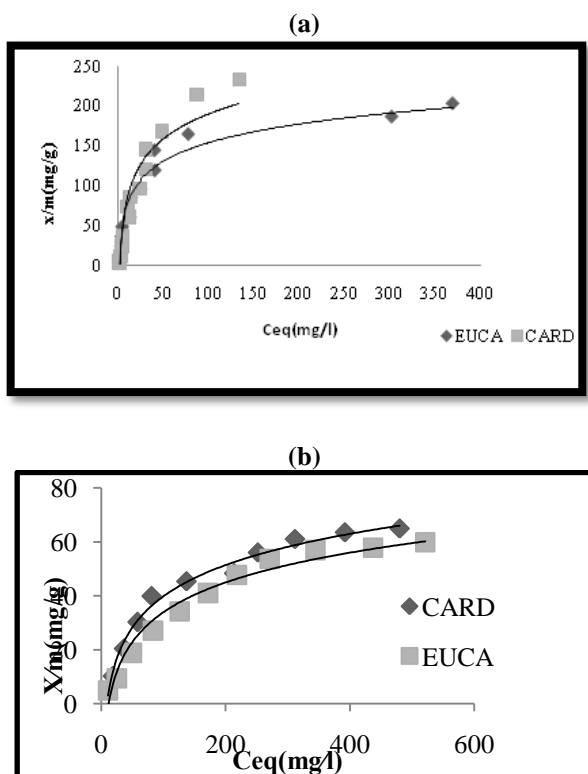


Figure 2: Isotherme of dsorption; ; Methylene blue(a),Red nylosane(b).

Table 1: Results of adsorption isotherms of methylene blue

Component	Biosorbents	Langmuir Constants		
		q_{max} (mg/g)	K_L (L/mg)	R^2
Red Nylosan	CARD	83,33	0,008	0.97
	EUCA	83,33	0,006	0.99
Methylene blue	CARD	333	0.021	0.97
	EUCA	250	0.032	0.99

Figures and tables should be placed as close as possible to where they are cited. Captions should be Times New Roman 10-point. Figures and Tables should be numbered separately and consecutively. Figure’s captions should be flush center below the figures, and Table captions should be in center above the table body. Initially capitalize only the first word of each caption. Table contents should be Times New Roman 9-point. If some figures or tables are so large that they are unreadable presented in left or right column, they should be set across both columns.

5. CONCLUSION

This work has been devoted to the study of the elimination of methylene blue and red Nylosan by natural supports in their states gross waste of Eucalyptus globulus and Cinara-cardinalciu. The results of these tests showed that the studied biosorbents have sorption capacities vis-à-vis the two pollutants.

The following conclusions can be drawn:

- The pH has an important influence on the adsorption process.
- The adsorption isotherms obey the Langmuir model with correlation coefficients of 0.990 for Eucalyptus globulus and 0.97 for Cinara-cardinalcius for both pollutants.
- This study showed that the biosorbents are an excellent example of economic use of waste to protect the environment without any inconvenience.

REFERENCES

- [1] J.W. Moore, Environmental Chemistry, Academic Press, New York, (1979).
- [2] J.G Dean, Basqui, F.L. and Lanouette, K.H Environ. Sci. Technol. 6, 509. (1972).
- [3] Brinckman, F.E. and Olson, G.J. Biotechnol. Bioeng. Symp. 16, 35, (1986).
- [4] C.S. Stefanovic, and Macan, K.M. Int. J. Environ. Anal. Chem. 38, 323, (1990).

- [5] Tiwari, D.P., Romod, K., Mishra, A.K., Singh, R.P. and Srivastov, R.P. *Indian J. Environ. Health* 31,120, (1989).
- [6] N Shukla. and Pandey, G.S. *Biol. Wastes* 32, 145, (1990).
- [7] M.M Nassar, *Adsorp. Sci. Technol.* 15, 609, (1997).
- [8] M.M Nassar. *Water Res.* 32, 3071, (1998).
- [9] M M Nassar, *Water. Sci. Technol.* 7, 133, (1999).
- [10] M. Termoul, B.Bestani, N. Benderdouche, M.Belhakem and E. Naffrechoux. Removal of Phenol and 4-Chlorophenol from Aqueous Solutions by Olive Stone-based Activated Carbon .*ALGERIA Journal of Science And Technolog.* Vol 24, No 5. S, (2006).
- [11] N. Benderdouche & all. Activation d'un précurseur naturel en vue de l'adsorption de Bleu de Methylene (2008).
- [12] N.Benderdouche , B.Bestani ,B.Benstaali , D.Derriche. Enhancement of the adsorptive properties of a desert salsola vermiculata species. *Journal of Adsorption Science & Technology*, vol. 21, No 8, pp. 739–750. (2003).
- [13] M.C. Ncibi, B. Mahjoub, M. Seffen. Kinetic and equilibrium studies of methylene blue biosorption by *Posidonia oceanica* (L.) fibres. *J. Hazard. Mater*, B139, 280–285. (2007).
- [14] Sastri,M.V.C.*India Instt. Science Quart.j.* 1942, 5,162
- [15] Dai,M.J. *Colloid Interface science*,164,223. (1994)
- [16] Gao,S ; Tonada S. ;Abe I. ;Kitagawa,M. ;Martruba, J Tanso ,163,138(1994).
- [17] M.J. Dai, *Colloid interface science*, 164, 223 (1994).
- [18] C. Ray-Castro, P. Lodeiro , Propriétés acide-base de biomasse d'algue .Un modèle reflétant des effets électrostatiques et hétérogénéité chimique. *Entourer Sci Technol* 37 (2003).
- [19] Seco A., Marzal P., and Gabaldon C. Study of the Adsorption of Cd and Zn onto an Activated Carbon: Influence on pH, Cation Concentration, and Adsorbent Concentration. *Separation Science and Technology* 34, 1577.411(1999).
- [20] J.X. Lin, S.L. Zhan, M.H. Fang, X.Q. Qian, H. Yang, Adsorption of basic dye from aqueous solution onto fly ash, *J. Environ. Manage.* 87 193–200, (2008).
- [21] S.D. Khattria, M.K. Singh, Removal of malachite green from dye wastewater using neem sawdust by adsorption, *J. Hazard. Mater.* 167 1089–1094, (2009).
- [22] B.H Hameeda, M.I. El-Khaiary, Equilibrium, kinetics and mechanism of malachite green adsorption on activated carbon prepared from bamboo by K₂CO₃ activation and subsequent gasification with CO₂, *J. Hazard. Mater.* 157 344–351, (2008).
- [23] B.H. Hameed, Spent tea leaves: anewnon-conventional and low-cost adsorbent for removal of basic dye from aqueous solutions, *J. Hazard. Mater.* 161 753–759, (2009).

Modification of Magadiite by Organofunctionalization for Use in Removing Pb(II) From Aqueous Media

Soumia. Benkhatou ¹, Mohamed. Sassi ², Mohamed.Boucekara¹, Abdelkader. Bengueddach²

¹LMEA, University of Mascara, Algeria

² Chemistry Laboratory of Materials, University of Oran Es-Sénia, Algeria

ABSTRACT

In this work, a layered silicate Na-magadiite has been hydrothermally synthesized and then, it has been organically modified by thiourea (MeO/Me) without preintercalation with cationic surfactant. These materials were characterized by X-ray diffraction (XRD), infrared spectroscopy (FT-IR) and scanning electron microscopy (MEB). Comparative batch experiments were performed using Na-magadiite and Na-magadiite/thiourea (MeO/Me) for removing lead from aqueous solutions.

Kinetics study results of lead removal with these materials fit a pseudo-second order model. The adsorption isotherm data follow the Langmuir equation in which parameters were calculated. Na-magadiite/thiourea (MeO/Me) has a better lead removal capacity (19.41mg/g) than Na-magadiite (9.91mg/g) at pH=7.

Keywords: Layered silicate, pollution, adsorption, lead

1. INTRODUCTION

Naturel layered polysilicates form a family which contained six (06) members: magadiite, makatite, kanemite, ilerite and silhydrite. Magadiite was first found in the deposits of lake magadi of kenya and described by Eugster 1967[1]. Magadiite is a layered silicate with the ideal formula $\text{Na}_2\text{Si}_{14}\text{O}_{29}\text{nH}_2\text{O}$ forms a series of sodium polysilicates[2,3].

The layer structure of this mineral is composed of one or multiple negatively charged sheets of SiOH tetrahedra where the negative charge is compensated by interlayer hydrated sodium ions [4]. The surface of magadiite contain silanol group (Si-OH) and siloxide group (Si-O). The interlayer between these layers contain Na⁺ and H₂O. Na-magadiite can be prepared in a laboratory under hydrothermal conditions. It possesses some specific properties: It has a high capacity for ion exchange compared with smectites, interlamellar adsorption of water and polar organic molecules, grafting and transformation into crystalline layered silic acids by proton exchange [5, 6]. These properties could promote its application as cation exchanger or molecular sieves [7], adsorbents for environmental pollutants [8] and supports for catalyst [9].

The most important characteristic of lamellar solids is the possibility to expand their interlayer space which can introduce a large variety of organic molecules to form intercalation host-guest compound, for various applications for example, the intercalation of Na-magadiite with shorter organic cations such as tetrapropylammonium (TPA) is used as intermediate to prepare zeolite materials[10], while, when it is intercalated with longer organic cations such as dodecyltrimethylammonium is used as intermediate to

facilitate the silylation of the interlayer space of magadiite[11], these compounds can be then used as precursors for pillaring reactions[12,13] and formation of polymer-inorganic nanocomposites[14,15].

In this study, Thiourea(MeO/Me) was applied as grafting agent to make organically modified magadiite.

Thiourea modified magadiite was obtained on one step without preintercalated by ion exchanger. It was characterized using X-ray diffraction (XRD), infrared spectroscopy (FT-IR) and scanning microscopy (MEB). These materials are used in liquid-solid extraction of heavy metal like lead. Properties of retention of material with regard to the metal elements in aqueous solution can be appreciated by the layout of different sorption isotherms. Lead removal capacity determined according to the model of Langmuir is higher with exchanged Magadiite thiourea than sodic magadiite.

2. EXPERIMENTAL

Headings are numbered and capitalized. All major headings are centered in bold in 10 fonts. Leave one line above the heading, and one line clear below before the start of the next paragraph or second-level heading.

2.1 Preparation of Na-magadiite

Na-magadiite was hydrothermally synthesized according to the literature [1, 16, 17].

A mixture of colloidal silica, sodium hydroxide, water and ethyl alcohol, with a molar ratio of $\text{SiO}_2/\text{NaOH}/\text{H}_2\text{O}/\text{EthOH} = 1:0.13:14.17:1.78$, was sealed in a teflon-lined autoclave at 150°C for 72h. The product was filtered, washed with distilled water and dried at 80°C for 24h. The resulting white powder was

characterized by X-ray diffraction and infrared spectroscopy. Its cation exchange capacity (CEC), measuring according to Kahr and Madsen [18], was $116.5 \text{ mol kg}^{-1}$.

2.2 Preparation of Thiourea intercalated Na-magadiite

Na-magadiite/thiourea (MeO/Me) was prepared according to the method developed by Cox et al [19, 20], 1mmole of thiourea was added to 20ml of ethyl alcohol and 20ml of distilled water. The mixture was stirred at the temperature of 25°C for 1h. 1g of Na-magadiite was added to the precedent mixture and the mixture obtained was stirred for 1h at the temperature of 25°C . The solid phase (Na-magadiite/thiourea) was separated by centrifugation, then washed with distilled water and dried at 80°C for 24h.

2.3. Kinetic

2.3.1. Models

To identify the correct mechanism, several models must be checked for suitability and consistency over a broad range of system parameters.

Different kinetic models used to fit the experimental data can be summarized as follows:

First-order kinetics model: the First-order kinetics adsorption model was suggested by Lagergren (1898) for the sorption of solid/liquid systems. It has been used by many authors (Namasivayam and Kadirvelu, 1999; Cheung et al, 2000; Chiron et al, 2003) and can be expressed in integrated form:

$$\log(q_e - q_t) = \log(q_e) - \frac{k_1 \cdot t}{2,303} \quad (1)$$

Where k_1 is the rate constant of adsorption (min^{-1}) and q_e and q_t are the adsorption loading of lead (mg/g) at equilibrium and at time t (min) respectively. The equilibrium loading q_e (mg/g) is calculated from the Langmuir adsorption isotherm. By plotting: $\log(q_e - q)$ against t , a straight line is obtained and the value of the rate constant k_1 can be calculated.

Pseudo-second-order kinetics model: Pseudo-second-order kinetics model (Ho and McKay, 1998; Namasivayam and Sumithra, 2004) is expressed as:

$$\frac{t}{q_t} = \frac{1}{k_2 q_e^2} + \frac{1}{q_e} t \quad (2)$$

Where k_2 (g/mg min) is the rate constant of pseudo-second-order adsorption. Plotting t/q_t against t , a line is obtained and the rate constant k_2 as well as q_e can be calculated.

2.3.2. Lead removal kinetic study

The kinetic study was carried out on Na-magadiite (sample A) and Na-magadiite/thiourea (MeO/Me) (sample B) suspensions in 100 mg/l of lead nitrate solution.

Suspensions of 0.05 g sample A and sample B in 50 ml of 100 mg/l lead nitrate solution were stirred at the temperature of 25°C during different time intervals (10 – 180 min). The pH is fixed to 5 and 7 . The obtained phases were separated and centrifuged. The lead concentration in the supernatants was measured by atomic absorption spectrophotometry by measuring the equilibrium pH (pHe).

2.4. Sorption isotherms

For the adsorption of lead, samples of 0.05 g of sodic magadiite, modified magadiite with thiourea were mixed with 100 ml of lead nitrate solution in a range from 2 to 80 mg/l . The suspensions were stirred at the temperature of 25°C for 60 min and the pH was carefully fixed at 5 and 7 . After filtering, the supernatants were analyzed by atomic absorption spectrophotometry.

The data of adsorption are finally treated according to the linearized equations of Freundlich (Eq.3) and Langmuir (Eq.4).

$$\log \frac{x}{m} = \frac{1}{n} \log C_e + \log k \quad (3)$$

$$\frac{1}{x/m} = \frac{1}{Q_0 b C_e} + \frac{1}{Q_0} \quad (4)$$

Where x/m (mg/g): quantity of aqueous solution adsorbed per gram of solid. b , n and k : constants.

C_e (mg/l): equilibrium concentration of solute in solution.

Q_0 (mg/g): maximum quantity of adsorption.

2.5. Techniques of characterization

X-ray diffraction was carried out with $\text{Cu K}\alpha$ monochromatic radiation using a diffractometer Philips PW1830. The infrared spectra of our materials (KBr disc) were recorded on a spectrometer Perkin Elmer FT-IR in the region 500 – 4000 cm^{-1} . The scanning microscopy analyses were performed on a LEO. Sterioscan 440 electron microscope in the backscattered mode. The technique used for the determination of lead is the atomic absorption spectrometer: AA-660, cat No. 206-10000-02, serial No. 28S00354, Shimadzu Corporation.

3. RESULTS AND DISCUSSION

3.1. Characterization of materials

3.1.1. X-ray diffraction

The XRD patterns of Na-mag and Na-mag/thiourea (MeO/Me) are shown in fig 1. The Na-mag showed a basal spacing of 1.54nm, which is very similar to that reported in the literature[21,22 ,23].The reflexions of magadiite after intercalation reactions with thiourea were similar to the (001) reflexions of the original Na-mag, which indicates that the thiourea may be intercalated in the interlayer space of magadiite parallel to silicate layer to form a monolayer lateral arrangement. This results in agreement with the IR spectra, where the characteristic absorption bands of thiourea are exists in the fig 2b.

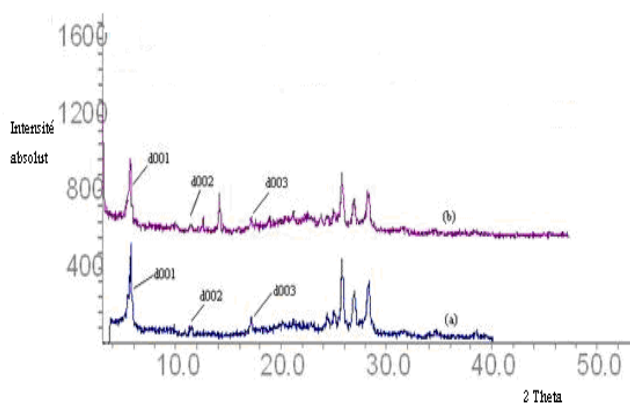


Figure1: X-ray diffractograms of (a) Na-mag and (b) Na-mag/thiourea(MeO/Me).

3.1.2. IR spectroscopy

Infrared spectra of Na-mag, and Na-mag/thiourea (MeO/Me) are shown in fig 2(a) and 2(b) respectively . The IR spectrum exhibits a small sharp band appearing at 3666 cm⁻¹ due to the weakly hydrogen bonded free SiOH stretching of isolated groups on the surface of magadiite. This weakly bonded free SiOH is responsible for silylation reaction. A broad band centered at 3470 cm⁻¹ correspond to the OH stretching vibrations of interlamellar adsorbed water and also the strong hydrogen bonding SiOH stretching. A characteristic band is observed at 1630 cm⁻¹ due to the presence of physisorption water. A band situated at 785 cm⁻¹ due to the symmetric stretching of Si-O.

The IR spectrum of intercalated mag with mixed thiourea fig 2(b) was similar to those of the original magadiite in which the characteristic absorption bands of thiourea appeared completely in fig 2b.

The bands at 3348cm⁻¹ represents N-H stretching vibration, the bands at 3142 cm⁻¹ due to C-H stretching vibration of aromatic group, bands at 2961cm⁻¹ is assigned to C-H stretching vibration of methyl group and C=C stretching vibration at around 1525cm⁻¹. All

of these results confirm the presence of our thiourea in the interlayer space of magadiite.

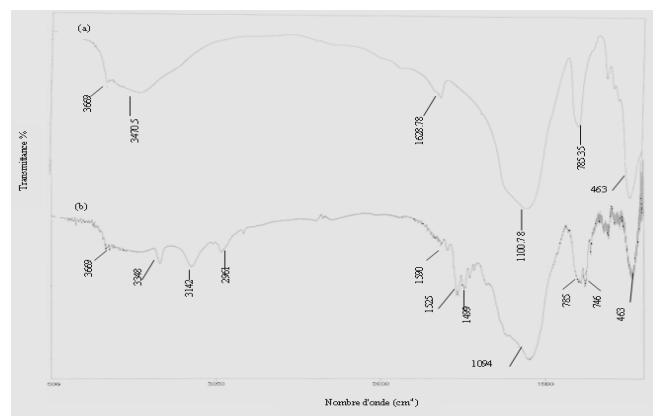


Figure 2: Infrared spectra of (a) Na-mag, and (b) Na-mag/thiourea(MeO/Me).

3.1.3. M.E.B



Figure 3: Electronic scanning microscopy of Na-mag

3.2. Study of lead removal by Na-mag, Na-mag/Thiourea(MeO/Me)

3.2.1. Kinetic Study

Kinetics datta of lead removal with Na-mag, and Na-mag/thiourea (MeO/Me) are shown in fig 4. We have drawn on this figure, the variations of lead concentration versus time.

The curves in figure 4 show two branches: the first from t=0-60min, corresponding to a relatively rapid phase, the second from t > 60min corresponds to the steady state, since the concentration at time t is practically constant (C_e).

The results for the pH 5 and 7 correspond to a removal rate of 40 and 50% for Na-mag, 90 and 95% for Na-mag/thiourea (MeO/Me), respectively. These results show that the adsorption is better at pH7.

Table1: Experimental conditions, kinetic parameters and regression coefficients (R2) for the two kinetic models

	pH	First order			Pseudo-second order		
		1 st order equation	R1 ²	K1(mn ⁻¹)	2 nd order equation	R2 ²	K2 (g.mg ⁻¹ .mn ⁻¹)
Na-mag/ thio mixte	5	Log (q _e -q) = -0,0263 t + 1,5232	0,9975	00,060	t/q _t = 0,0238 t + 0,2769	0,9993	0,0020
	7	log (q _e -q) = -0,0232 t + 1,6444	0,9855	0.053	t/q _t = 0,0171 t + 0,2254	0,9941	0,013
Na-mag	5	Log (q _e -q) = -0.0791t + 1.7696	0.9076	0.0343	t/q _t = 0.01 t + 0,0085	0,9999	0,0117
	7	Log (q _e -q) = -0.0482 t + 1.7423	0.8691	0.0367	t/q _t = 0,0099 t + 0,0164	0,9993	0,006

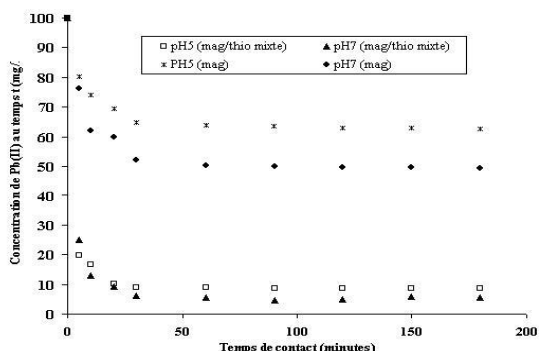


Figure 4: Lead removal kinetic on Na-mag and Na-mag/thio mixed for various pH (5 and 7)

3.2.2. Kinetic models

The plot of log (q_e-q) = f(t), at different pH, we can determine the rate constant for reaction of order 1 (table1).

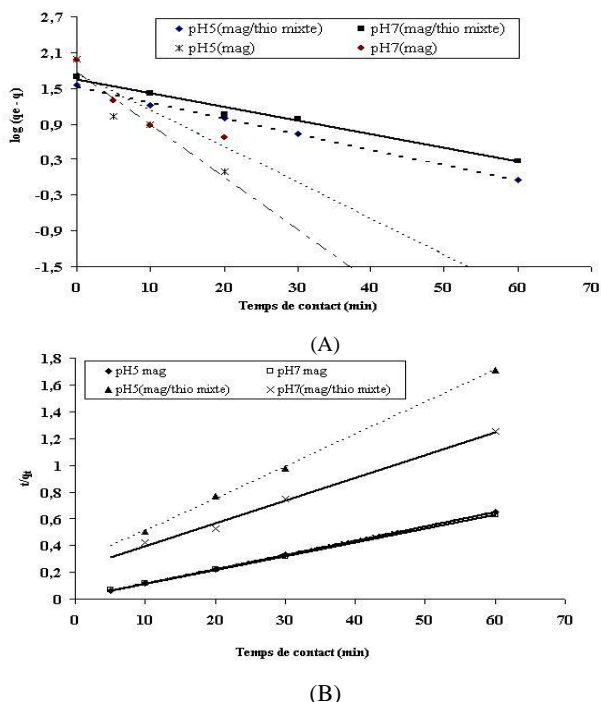


Figure 5: (A) First –order kinetics model, (B) Pseudo-second-order kinetics model for various pH.

The plot of the variation in the ratio t/q_t versus time t (figure 5B) gives a straight 1/q_e slope and intercepts (1/K₂q_e²). The values obtained allow the determination of the rate constant for reaction of order 2 (table1).

Table 1 presents the results of fitting experimental data to first-order and pseudo-second-order models for different value of pH (5 and 7). It can be seen from table1 that the correlation coefficient (R2) varies in the order: pseudo-second-order > first order model under all experimental conditions, which indicates that the pseudo-second order model is the most suitable in describing the adsorption kinetics of thiourea on magadiite. Kinetic data fit this model with a correlation coefficient higher than 0.99.

3.3. Sorption isothermes

3.3.1. Lead sorption isotherms with Na-mag and Na-mag/Thiourea(MeO/Me)

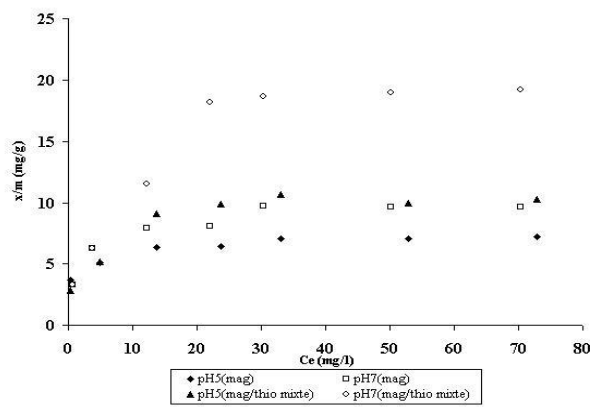


Figure 6. Plots of lead removal isotherms with Na-mag and mag-Na/thio mixed for various pH

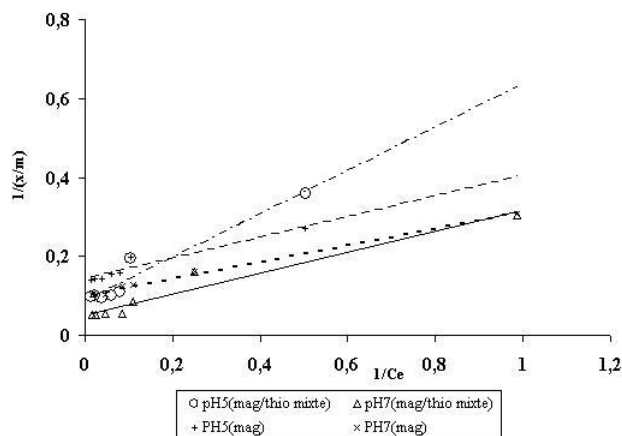


Figure 7: Langmuir Plot for lead removal with Na-mag and mag-Na/thio mixed for various pH (pH5 and 7).

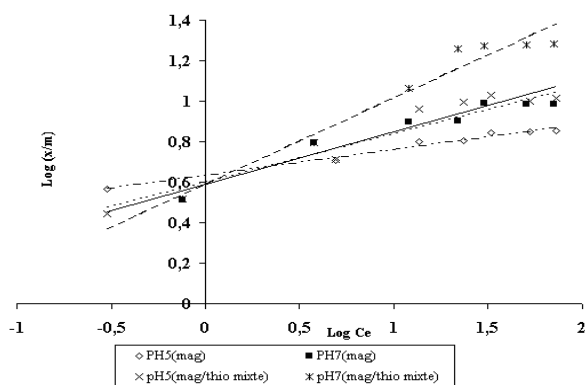


Figure 8: Freundlich Plot for lead removal with Na-mag and mag-Na/thio mixed for various (pH5 and 7).

To assess the effectiveness of each material in the removal of Pb^{2+} , we determined the constants of the two models tracks (Table 2). The findings that we can do from the table 2 on parameters of Freundlich and Langmuir at pH 5 and 7 for the two materials are summarized as follows:

Na-magadiite/thiourea (MeO/Me) has a better lead removal capacity (19.41mg/g) than Na-magadiite (9.91mg/g) at pH=7. Others researchers performed the removal of Lead (II) (16.61 mg/g) by activated carbon [24] and (22 mg/g) by organophilic bentonite [25]. The determination coefficients obtained at pH 5 and 7 by the Langmuir model are superior to those obtained by the Freundlich model with pH 5 and 7, indicating a good fit to the Langmuir model than the Freundlich model (Table 2).

Table 2: Parameters of Langmuir isotherms of Pb^{2+} removal by Na-mag and mag-Na/thio mixed à différents pH (5, 7).

	FREUNDLICH			LANGMUIR		
	K	n	R ²	Q ₀	b	R ²
pH5						
mag-Na	1,43	7,88	0,98	7,358	0,49963	0,9837
mag-Na /Thiourea (MeO/Me)	1,94	3,83	0,9361	13,28	0,13432	0,9735
pH7						
mag-Na	1,77	4,18	0,9251	9,910	0,47616	0,9946
mag-Na /Thiourea (MeO/Me)	1,54	2,34	0,9556	19,417	0,19339	0,9552

4. CONCLUSION

Our work is part of a multidisciplinary field, it falls within the framework of safeguarding the environment while offering a new material "magadiite", a lamellar polysilicate synthesized and used in the treatment of pollutants such as heavy metals.

We have a first approach the method of synthesis of magadiite soda called Mag-Na, and then interpolated with organic molecules complexing "thiourea" for the Mag-Na/Thiourea. The intercalation of thiourea is reached at one stage and the integration is done in layers parallel to the lateral monolayer of siloxane.

The synthesis of our materials Mag-Na and Mag-Na/thiourea mixed allowed the application of the latter in the pollution of heavy metals such as lead.

To assess the effectiveness of each material, we determined the kinetics of elimination of this pollutant by determining the optimum conditions (pH, contact time, kinetic cst). What has drawn the following conclusions:

Applying our results to first-order kinetic model shows that the value of the rate constant increases at pH 7-5 for the three materials. The results of lead mining for the temperature of 25°C for two materials (Na-magadiite, and Magadiite-Na/Thiourea MeO/Me) show their consistency with the pseudo second order kinetic model than the first order kinetic model. The disposal capacity of lead for the temperature of 25°C shows their consistency with the Langmuir model at pH 5 and 7 with good regression coefficients. Na-magadiite/thiourea (MeO/Me) has a better lead removal capacity (19.41mg/g) than Na-magadiite (9.91mg/g) at pH=7

REFERENCES

- [1] H. P. Eugster, *science*, 157, 1177-1180, 1967.
- [2] Okutomo S., Kuroda K., Ogawa M., *App . clay .sci .* 15, 253-264, 1999.
- [3] C.S.Kim, D.M.Yates, P.J.Heanet, *clays clay miner*, 45, 881-885, 1997.
- [4] P.H.Thiesen, K.Beneke, G.Lagaly, *j.mater.chem*, 12, 3010-3015, 2002.
- [5] R.A.Fletcher, D.M.Bibby, *clays clay miner*, 35, 318-320, 1987.
- [6] Lagaly G., beneke K., weiss A, *Am.Miner*, 60, 642-649, 1975.
- [7] Hatsushika.T, Takei.S, Suzuki.T, *muki materiaru*, 3, 319-326, 1996.
- [8] Fujita.L, Kuroda.K, Ogawa. M, *chem.. mater*, 15, 3134-3141, 2003.
- [9] Fudala.A, Konya.Z, Kiyozumi.Y, Niwa.S-L, Toba.M, Mizukami.F, Lenta.P.B, Nagy.J, Kiriesi. L, *microporous mesoporous mater*, 35-36, 631-641, 2000.
- [10] G.Pal-borbely, H.K.Beyer, Y.Kiyozumi, F. Mizukami, , *microporous mater*, 111, 45-51, 1997.
- [11] K.Isoda, K.Kuroda, *chem mater*, 12, 1702-1707, 2000.
- [12] Dailey. J.S, Pinnavaia.T.J, *chem mater*, 4, 855-863, 1992.
- [13] Kwon.O-Y, Shin.H-S, Choi.S-W, *chem mater*, 12, 1273-1278, 2000.
- [14] Wang.Z, Lan.T, Pinnavaia.T-J, *chem mater*, 8, 2200-2204, 1996.
- [15] Wang.Z, pinnavaia.T.J, *chem mater*, 10, 1820-1826, 1998.
- [16] Brindley G.W, *Am. Mineral*, 54, 1583-1591., 1969.
- [17] Graces. J.M., RockE. S. C, Crowder C. E. and Hasha. D. L, *clays clay miner*, 361, 409-418, 1988.
- [18] G.Kahr, F.T.Madsen, *appl clay sci*, 9, 327, 1995.
- [19] Cox.M.,Rus-Romero.J.R.,Sheriff.T.S, *chem.Eng.J*, 84(2), 107-113, 2001.
- [20] Cox M., Rus-Romero.J.R., Sheriff.T.S, *React.Funct.Polym*, 60, 215-222, 2004.
- [21] H. P. Eugster, *science*, 157, 1177-1180, 1967.
- [22] Brindley G.W, *Am. Mineral*, 54, 1583-1591., 1969.
- [23] Graces. J.M., RockE. S. C, Crowder C. E. and Hasha. D. L, *clays clay miner*, 361, 409-418, 1988.
- [24] Shekinoh, P; Kadirvelu, K; Kanmani, P; Senthilkumar, P; Subburam, V. Adsorption of lead(II) from aqueous solution by activated carbon prepared from Eichhornia. *J. Chem. Technol. Biotechnol.* 77, 458-464, 2002.
- [25] S.Andini.S, R.Cioffi, F.Montagnaro, F. Pisciotta, L.Santoro. Simultaneous adsorption of chloro phenol and heavy metal ions on organophilic bentonite. *Applied clay science.* 31, 126-133, 2006.

Modelling Groundwater Flow in the Agricultural Area of Ghriss Plain

Belkacem Bekkoussa¹, Habib Azzaz¹ & Abdelkader Khaldi¹

¹Laboratoire des Sciences et Techniques de l'eau, Université de Mascara, BP 763, Route de Mamounia, Mascara 29000, Algérie (Bekkoub@yahoo.fr)

ABSTRACT

The Ghriss Plain is the most productive agricultural area in the west-northern part of Algeria. Although the aquifer system of the Plain contains an important water resource, excessive pumping in the last three decades, mainly for irrigation, has resulted in a significant depletion of the reservoir. The water table of the Ghriss Plio-Quaternary aquifer decreased drastically in some sectors, by more than 60 meters from 1970 to 2001. The restrictions of groundwater pumping imposed by the authorities since the beginning of 1990 have contributed to a decrease the total withdrawal. The paper reports a groundwater flow model developed to allow the sustainability of the groundwater resource to be estimated such that appropriate environmental policy can be initiated.

Keywords: Groundwater modelling, Ghriss plain, anthropogenic factor, climatic factor.

1. INTRODUCTION

The drought which has been affecting the north western Algeria for the three last decades had important effects on all the water resources and more particularly on groundwater resource [8; 9]. The overexploitation of this resource, in order to supply the various water uses of the local populations and especially the agricultural uses, imperils his perennality. The water-level drawdown of the Ghriss Plio-Quaternary aquifer towards alarming levels causes major apprehension for the population of the area and also for the local and national authorities.

In this article, groundwater flow in the Ghriss plain plio-queternary aquifer was simulated using steady-state numerical model. This unconfined aquifer is located in an agricultural plain in northwest Algeria (**Fig. 1**). The groundwater is the most used resource for the agricultural activities and for the supply water in the study area.

2. STUDY AREA

The Ghriss plain has a semi-arid climate with hot and dry summers, and mild and wet winters. Rainfall measurements are available from 13 pluviometers, taken between 1976 and 2001[9]. The average annual rainfall for this period is about 313 mm. Rainfall mainly occurs in the wet season (October-March) and is generally correlated with altitude. The analysis of the rainfall recharge evolution in the study area showed a clear reduction since 1973 wich is estimated to 25% [3]. The pluviometric deficit was recurrent during several years, which results in the reduction of the flow of the principal river of the Ghriss plain, the Fekan Wadi, before it totally dried this last years. The water table of the Ghriss Plio-Quaternary aquifer decreases drastically up to more than 60 meters between 1970 and 2001 in some sectors. The restrictions of groundwater pumping imposed by the authorities since the beginning of the

1990 have contributed to decrease the withdrawal. The estimated recharge of the Ghriss plain aquifer system is 65,3 million m³/year and the total withdrawn volume is 64,7 million m³/year [4]. A fragile equilibrium is noted since the year 2000, between recharge and withdrawal in the Ghriss plain aquifer system which results in a stabilization of the piezometric heads of the Plio-Quaternary aquifer.

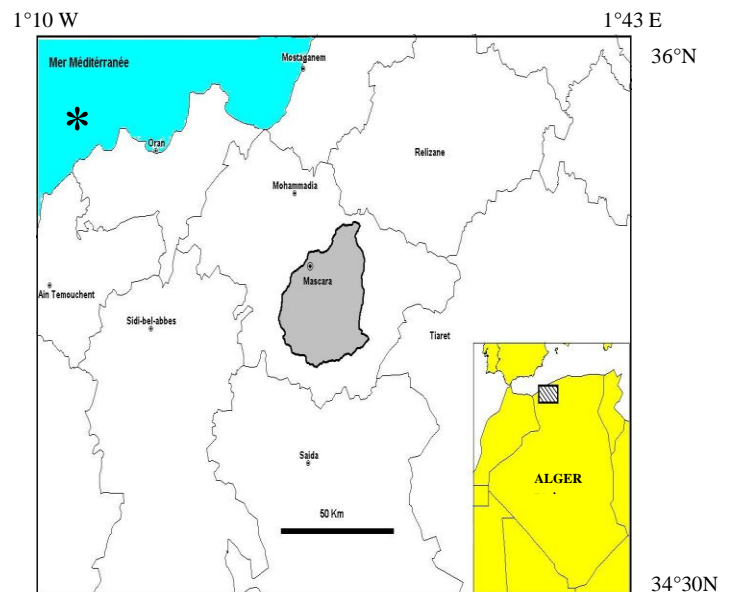


Figure 1: Location of the study area

3. HYDROGEOLOGICAL CONTEXT

The Ghriss plain is composed of three superposed aquifers:

- Plio-queternary aquifer,
- The Pliocene limestone and sandstone aquifer,
- The Jurassic calcareous dolomitic aquifer.

Plio-quaternary aquifer is an unconfined reservoir which extends across the plain with an area of 605 km². It consists of quaternary alluvium, porous white limestone, sand, sandstone and lacustrine limestone. Natural recharge occurs directly as infiltration from precipitation [11]. A significant Lateral flow comes from the Jurassic aquifer in the east southern and the Pliocene aquifer in the north. Other forms of recharge are excess irrigation, which is not evapotranspired. The water table depth ranges from -6 to -80 m. This aquifer is bounded by Miocene marls.

The direction of groundwater flows is from north-east and south to south-west towards a common outlet called Ain Fekan, which is a spring dried in the beginning of 80's. The rainfall infiltration rate is estimated at about 20% (Sourisseau, 1972). Transmissivity values ranges from 5.10^{-5} to 10^{-2} m²/s [2;11].

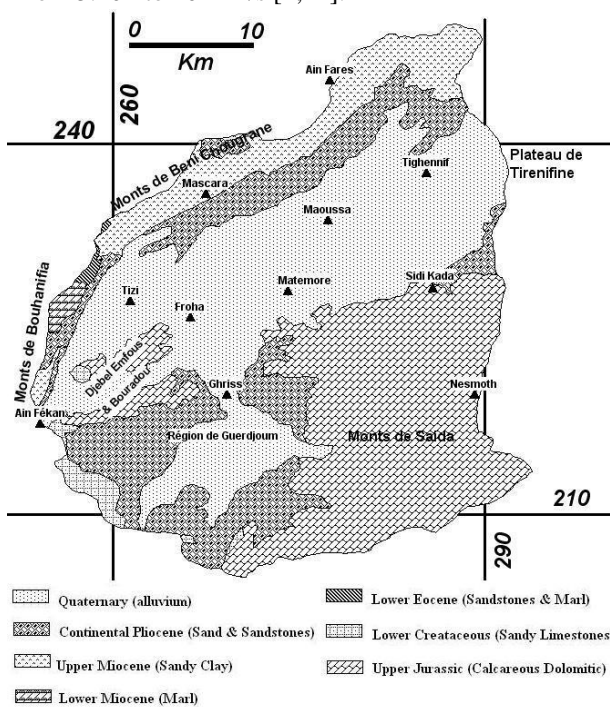


Figure 2: Hydrogeological

4. NUMERICAL MODEL

The code selected to develop the numerical model was MODFLOW; a modular, three-dimensional finite difference groundwater flow model developed by the US Geological Surey [7]. The model grid describes a square mesh of 45 km x 45 km bordering the limits of the Plio-Quaternary aquifer. The grid is formed by 7832 cells. Two types of mesh are used in the model: small mesh (0,202 km²) and large mesh (0.81 km²). The distribution of these cells depends on the density of information available and the desired accuracy. The model was run in steady-state conditions to simulate initial conditions. The boundary of the Ghriss plain was determined by the natural/hydrogeological features (Figure 3).

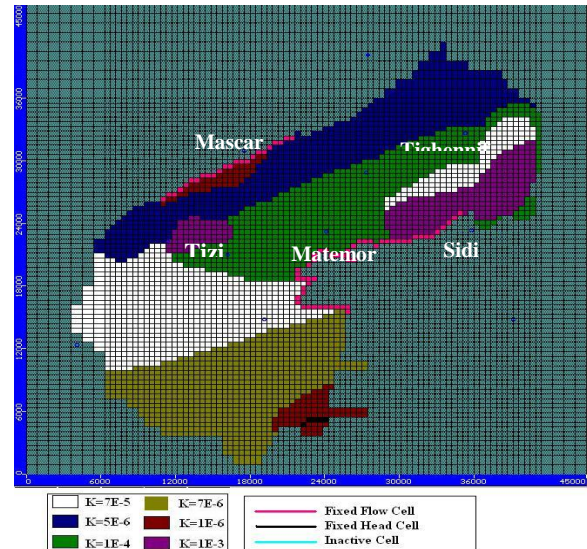


Figure: 3 Model Grid and Model Boundaries.

5. MODEL CALIBRATION

The purpose of calibrating the groundwater flow model of the Ghriss plio-quaternary Aquifer was to update the critical input parameters such that the simulated hydraulic head values are in close agreement with the calculated values.

The reference state for the calibration of the model should reflect a quasi permanent system. Stabilization of groundwater levels since 2000 can represent a steady state. Therefore, the steady-state calibration was performed by the restitution of the piezometric heads of January 2000.

Calculated vs. observed hydraulic head cross-plots (Figure 4) shows a good correlation between observed and simulated heads. The correlation coefficient is 0.98 and the RMS (*normalised root mean squared error*) average is 4.2 %. A RMS of 10% is considered acceptable in groundwater flow applications [1; 6], suggesting that the model adequately replicates groundwater conditions observed in the watershed.

6. SIMULATION RESULTS

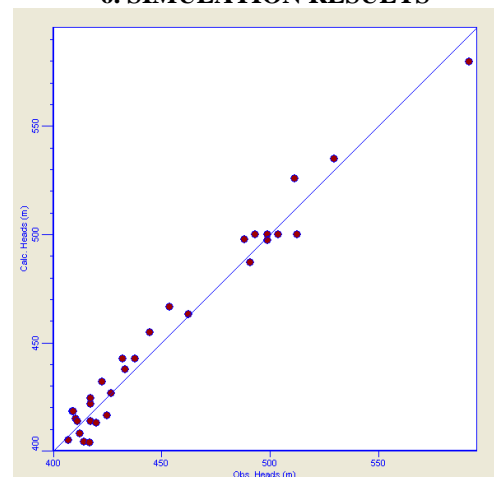


Figure 4: Calculated vs. Observed hydraulic heads for January 2000 (steady state).

Two simulations of the plio-quaternary aquifer in steady state were carried out to estimate firstly, the effects of future increase in groundwater extractions and secondly, the effects of decrease of precipitation recharge.

6.1. Simulation N°1

Agriculture is the largest consumer of water in the region with a volume of more than 52 million m³ per year [5]. In this simulation, we considered an increasing in the agricultural areas with 2000 ha. This will result in over-consumption of water estimated at 38.350 m³ per day. Additional groundwater extractions will be located in the central and northern plains, where are fertile agricultural lands.

This simulation indicates a drawdown in plio-quaternary aquifer of over -44 m located in southwest of Mascara city (Figure 5).

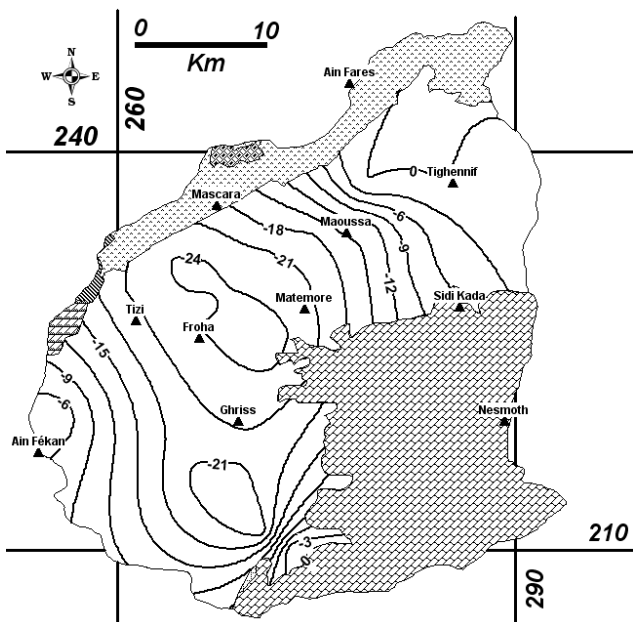


Figure 6: Drawdown in meters of the plio-quaternary water table for the simulation N°1.

6.2. Simulation N°2

This scenario prefigures a climate forcing affecting the region. Recharge applied to the model is reduced by 32%, equivalent to a decrease of 100 mm in the average annual precipitation.

This pessimistic scenario is not completely imaginary. Indeed, a difference of more than 100 mm was recorded for several pluviometric stations, particularly in the early 80's and 90 [8; 9].

The drawdowns vary between 0 and -24 m. This decrease in the groundwater resource was predictable.

7. CONCLUSION

Indeed, 75% of the plio-quaternary aquifer recharge comes from the infiltration of the precipitations. Maximum drawdown is recorded in the region between Matemore and Froha (Figure 6).

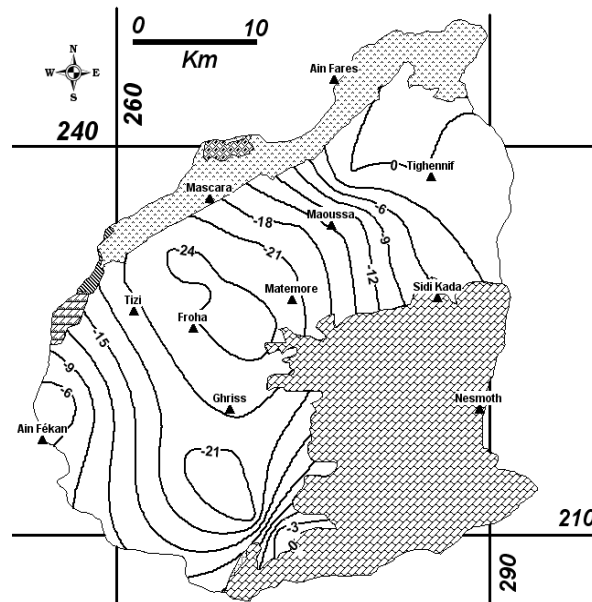


Figure 6: Drawdown in meters of the plio-quaternary water table for the simulation N°2.

The Ghriss plain is one of the most productive agricultural areas in northwestern Algeria. Modeling anthropic and climatic forcing on groundwater resource in the Ghriss plain indicates that:

- The most drawdown (-44 m) will be caused by the increase of agricultural areas (2000 Ha).
- The Froha region is the most sensitive to increased exploitation of the Plio-Quaternary groundwater resource.
- The north-east and far south of the plain are almost insensitive to the increase in groundwater pumping. This is mainly due to the inflow coming from the Jurassic aquifer.

The model and the obtained results can be an important tool for prediction and risk assessment. Future agricultural practice and subsurface water management can be forecasted and appropriate measures foreseen. Mitigating measures can be investigated, as artificial groundwater recharge in wet seasons.

REFERENCES

- [1] Anderson M., P & Woessner W., W, (1992) Applied groundwater modeling, simulation of flow and advective transport. Academic, San Diego, CA, 381 pp.
- [2] Assens, G., Besbes, M. & De Marsily, G., (1977). "Etude hydrogéologique de la plaine de Mascara sur modèle mathématique". Ecole nationale supérieure des mines de paris, Centre d'informatique Géologique, Paris, France (72 p).
- [3] Bekkoussa, B., Meddi, M. & Jourde, H., (2008). "Forçage climatique et anthropique sur la ressource en eau souterraine d'une région semi-aride : cas de la plaine de Ghriss, nord ouest algérien". *Revue sécheresse (2008), Vol. 19, n°3, 173-184.*
- [4] Bekkoussa B., (2009). "Modélisation du transport et de la propagation des nitrates dans les eaux souterraines de la plaine de Ghriss". *Thèse de doctorat, Université d'Oran, Algérie (190p).*
- [5] DPAT, (2005). "Rapport annuel de la direction de la planification et de l'aménagement du territoire de la Wilaya de Mascara". *Rapport interne DPAT, Mascara, Algérie, (131 p).*
- [6] Kahn K. G., Ge S., Caine J., S. & Manning A., (2008). "Characterization of the shallow groundwater system in an alpine watershed: Handcart Gulch, Colorado, USA", *Hydrogeology Journal (2008) 16: 103-121.*
- [7] McDonald, M.G. & Harbaugh, A.W., (1988). A Modular Three-Dimensional Finite-Difference Ground-Water Flow Model. Techniques of Water-Resources Investigations, United States Geological Survey, Washington, DC, USA.
- [8] Meddi H. & Meddi M. (2009). Variabilité des précipitations annuelles du Nord-Ouest de l'Algérie. *Sécheresse*, vol. 20, n° 1, p. 57-65.
- [9] Meddi, M. & Hubert, P., (2003). Impact de la modification du régime pluviométrique sur les ressources en eau du Nord Ouest de l'Algérie. Hydrology of mediterranean and semiarid regions. Proceeding of an international symposium held at Montpellier. IAHS Publication N° 278 April 2003 : 229-235.
- [10] ONM (2006). Données climatologiques ONM (office national de la météorologie) des stations de la plaine de Ghriss.
- [11] Sourisseau, B., (1972). Etude hydrogéologique de la plaine de Ghriss. Rapport Agence Nationale des Ressources Hydraulique, Alger, Algérie.

Investigating Geotourism Capabilities of the Gavkhoni Wetland According to the FAS model

Hamideh Beigi¹ & Fatemeh Hadimehr²

¹Ph.D student in Department of Geography Sciences and Planning, Isfahan University, Iran
(Beigi1982isfahan@yahoo.com)

²M.A Department of Geography, Najafabad Branch_Islamic Azad University, Iran
(f_amouhadi@yahoo.com)

ABSTRACT

Nowadays, sustainable tourism is a comprehensive achievement that has willing for long-lasting development of the tourism industry without destructive effects on natural habitat.

Geotourism as a new concept of the tourism that is based on special geographical Characteristics of one place that sustains and develops environment, inheritance, beautifulness, culture and welfare of the local people. One can play an effective role in the national development and national economy diversification of the area by planning and recognizing the opportunities as well as the limitation of Geotourism. Thus, there are two questions here:

1. What are the potentialities and limitations of Geotourism development?
2. Which strategies are required for developing this type of tourism and following national and regional development?

Using measurement and field studies methods and determination of the strengths, weaknesses, opportunities and threats by FAS model, the authors provide some strategies and suggestions for developing Geotourism in the Gavkhoni Wetland.

Experimental analysis about this area presents that although the Geotourism Investments in this area is very various, this area is confronted with serious transregional threats. We will have a powerful Geotourism pole in this region, if the tourism infrastructure policies minimize and review.

Keywords: Wetland, Geotourism, Geotourism investments, FAS model

1. INTRODUCTION

Nowadays, sustainable tourism is a comprehensive achievement that has willing for long-lasting development of the tourism industry without destructive effects on natural habitat [13]. Sustainable tourism considers tourism as frontier border which it is established triangular relationship between host society, its land and guest society or tourists in one hand, and on the other hand between host society ,its land and tourism. The concept of the sustainability in the tourism industry has different dimensions, which in this case developing general information in basis of protecting from natural resources could be effective. For achieving to the sustainable tourism development four subjects should be considered basically:

- Ecological sustainability: It presents that development is twin with survival of ecological procedures, habitat diversification and biological resources.
- Cultural sustainability: It means that development promotes the control of people to their lives and it needs coordination of the development procedures

with culture and human values and reinforcement of the local societies for preparing their needs from stabilizing and reinforcing partnership.

- Economical sustainability: Development is effective and useful because of comprehensive and proper management of the natural resources and production and distribution procedures economically. Therefore, the present usages of the development can be seen as supporters and proponents of the future generation.
- Local sustainability: The development is planned for making a profit to local society. Therefore, pay attention to the local people and Geotourism are considered by local societies [7].

Geotourism as a new concept of the tourism that is based on special geographic characteristics of one place, takes people's willing all over the world ever increasingly. We can describe Geotourism as bellow:

"A kind of tourism that sustains and enhances the geographical characteristics of one place (includes environment, inheritance, aesthetics, culture and wellbeing of residents)"[14].

Certainly Geotourism should be sustainable-it means that it shouldn't have destructive effect, moreover, it centralizes all of the natural and human characteristics that it can become visual worth of one place.

Iran has god-gifted valuable treasures, antecedent history and cultural civilization that always were considered by visitors. Because of having unique geological shapes, Iran has investigated for many years all over the world, and also has called "the heaven of the geologist" and "1.5 million square kilometers museum of the geologists"[1]. Islamic republic of Iran, because of possessing more than 40 worthy wetlands and being the birthplace of the Ramsar agreement, needs to discover and protected its natural Geotourists investments. Wetlands are the most biological spaces in the world because of having various unique biologics, several tourism recreation importances, innumerable scientific, investigation values and etc. They also have special situation in the international environmental protection system and biotravel accumulations [11].

The Gavkhoni Wetland, the ninth international wetland in Iran, with 47600 hectares extant in 145 kilometers is placed on south-east part of Isfahan. This wetland is located between 32°15' north and 32°22' north and 52°45' east and 52°59' east [10].

This wetland is natural, interior, free and has salt water which is settled in the list of Ramsar Convention with ZIR.18 code in 1975. The Gavkhoni Wetland is one of the unique and rare wetlands in the world because of having special geographical natural and habitat conditions and also ecological, biological and hydraulic factors, which is scientifically so important for the researchers [9]. Geotourism pays attention to this area because of its old residence with wealthy culture. Considering the mentioned matters and the importance of the potentialities and limitations of The Gavkhoni

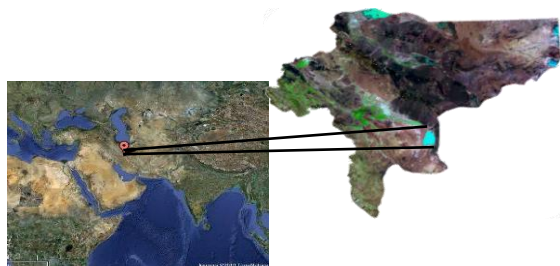


Figure 1: Gavkhoni Wetland position in south-east of Isfahan, Iran.

Wetland, it can affect the planning of the sustainable tourism and its problems in this area. The authors try to introduce both the Geotourists investments of The Gavkhoni Wetland and to investigate its strengths, weaknesses, opportunities and threats from professors, students, geologists and visitors perspective. Finally, according to these ideas and points, each interior and exterior factor which affects Geotourism of The

Gavkhoni Wetland is assessed and evaluated based on FAS model.

2. DISCUSSION

The strategic planning and evolution is one of the geographical science subjects which is used recently. Strategic planning tries to evaluate all dimensions of the projects and plans in order to select the best and the most strategic decision. Indeed, this planning is a systematic way in order to make decisions and to carry out activities for forming, guiding and achieving to its usage and results [8]. Strategic management is a process for analyzing and recognizing the interior environment (strengths and weaknesses points) and the exterior environment (opportunities and threats points) of the systems. Besides, using this strategic management, the systems are established their strategic way and created strategies to achieve their aims [3]. Experience has shown that wherever the tourism develops accidentally and without planning and strategy, several habitat and social problems emerge and in long-term its problems become more than its usages [2].

In order to collecting strategy and to evaluate interior and exterior environment of The Gavkhoni Wetland, each factor should investigate and study separately, and the results should show in the effective interior and exterior factors matrixes.

2.1. The Geotourism Strength Points of the Gavkhoni Wetland

The Gavkhoni Wetland as a huge and unique aquatic expanse has several important values such as; nourishment subterranean water, control of the flood, suitable wildlife habitat and biological diversification and etc. This wetland can be pronounced as valuable Geotourism inheritance at national and international level because of having beautiful characteristics and special microclimatic. This area has high protecting ability for many reasons such as; the existence of the habitat expanse, suitable biological conditions, wildlife and plant covering. This diversification have several usages such as; centralized and vast tourism, exercise investigation and education and also protecting the rare and animal species of this area. The most Geotourism strength of international The Gavkhoni Wetland is pointed below.

2.1.1 Geological investments of the Gavkhoni Wetland

Considering the tectonic situation, the Gavkhoni Wetland is created because of the subsidence [3]. Educational/ scientific tourism pays attention to this area for many reasons such as; placing in Sanandaj-Sirjan geological zone, having set of various sediments, emergence of the numerous phases of the mountain, desert and volcanic stones Fig.2. This area can become a Geopark for studying and investigating for the

researchers and students about the science of the earth and holding scientific tours.



Figure 2: Black mountain in north-east of Gavkhoni wetland

2.1.2 Geomorphologic Investments of the Gavkhoni Wetland

The Gavkhoni Wetland area attracts the fans of the Desert tourism, Sport tourism, Ecotourism and Health tourism because of having vast geomorphologic phenomenon such as; watery, winding and evaporative phenomenon Figure 3,4.



Figure 3: Salt Polygon in south part of Gavkhoni Wetland



Figure 4: The Taq coverage over western part of Gavkhoni wetland

About the Desert, we can point to the usage of the Geotourist capabilities of the windy sands in the west side of the Gavkhoni Wetland, holding the seminar about the sand painted and Art tourism, visiting salty

polygon, salt mine and also visiting different shapes of compressed sand like citadel, sandy hills, seif, barkhan, nebeka and etc.

About the Sport tourism, it can point to the usage of the Geotourist capabilities in order to establish the motorcycling lands to fly with glider, paraglider and kite.

Also about the Ecotourism, visiting the various geomorphic shapes like Zayanderood Delta, Shakh Kenar waterfall, river and Lake Terrace and visiting the Karsetik springs and Arzezin wells in this area are mentioned.

Finally about the Health tourism, we can mention; the usage of the cure property of the sands and calm, silent environment of the salt desert for resting and relaxing, the black mud of the Gavkhoni Wetland and the salt in this area. Achieving to this aim, the authores advises the establishment of the rooms for salt therapy near the borders of Khara mine.

2.1.3 Climatic Investments of the Gavkhoni Wetland

Since the Gavkhoni Wetland is located in the desert area of Iran, the desert tourism is considered more. The existence of the annually average of sunny days (268.5 hours), is caused that this area is proper for the usage of the solar generators [5]. This matter is also accounts for the Geotourist capabilities of this area for using the renewal energy sources. Besides, the starry nights of the desert are appropriate for observing and studying for the astronomy fans.

2.1.4 Herbaceous Investments of the Gavkhoni Wetland

Botanists can take advantage of the 50 species of plants which are classified in 12 family and 54 kinds [9]. One of the important issues about this area is the existence of the salty kinds such as Gas and Taq which is not only attract the salt of the soil but also prevents the spreading of the desert.

2.1.5 Animal Investments of the Gavkhoni Wetland

International Gavkhoni Wetland counts as the most important habitat of animals in central plateau of Iran. One of the Geotourist capabilities in this area is the existence of various species of amphibian, creeps, mammals, native and immigrant birds which immigrate to this area each year because of cold weather [6].we can take advantage of this property for bird watching via strong telescopes which are located on the black mountain. Although, in recent years we have observed the reduction of these species for many reasons such as drought and pollution, but with solving these problems, the wetland will experienced its gold days again.

2.1.6 Cultural-Historical Investments of the Gavkhoni Wetland area

Because of possessing ancient villages and wealthy culture, the Gavkhoni Wetland is figured as a powerful pole of the Geotourism. There are historical attractive such as; old mosques, bridges and historical bands, reservoirs, wind wards, caravansaries, pigeon houses and historical village "Qahi" which has several camel houses and historical houses.

This area is the center of the Historical tourism, the Art tourism, the Cultural tourism, and the Rural tourism for many reasons such as; traditional architecture, castle residence like "Qoortan Castle" which is the biggest bricked and mud place after the "Bam citadel" in Iran, unique handicrafts like karbafi, unique clothing of the women of Varzaneh (white veil), Dari dialect of the local people, and attractive customs like Zar-o-Zar Khak customs in Qoortan, Erpa and Barat in Varzaneh.

2.2. The Weaknesses of the Gavkhoni Wetland Geotourism

Although, the Gavkhoni Wetland has several various Geotourists investments but can't attract interior and exterior tourists because of some reasons which gathered bellow:

1. Undetermined and unconfirmed aims and policies of the tourism industry.
2. Dispersion of the area and the existence of the long distance between the tourism places which is caused the limitation plan and organization for attracting the tourists in this area.
3. Low investment by the private part in this area.
4. Lack of enough effort by the tourism designer and planner for introducing this area in Iran.
5. Lack of enough budget for executing tourism project and researches.
6. Lack of correct culture and insight about tourism attraction by the staffs and planner.
7. Lack of appropriate residential facilitations and hospitalities according to the tourists' requests in the urban and rural areas.
8. Inadequacy of trained experts and leaders in this area
9. Lack of rebuilding, renovating and protecting the Geotourism investment in this area

It should be mentioned that the above items, weaknesses points, can change to the golden opportunities with

proper planning managing in long term and attract a lot of tourists to this area.

2.3. FAS model (internal and external factors Analysis summary)

This model analyze and organized the external and internal factors of the systems according to the classification of the strategic factors such as; strengths, weaknesses, opportunities and threats points. To construct these tables, it is necessary to do the following processes step by step to analyze the system's situation:

- In the first column, there are 8 up to 10 important strengths, weaknesses, opportunities and threats points about the system.
- In the second column (weight), each factor weights from 1 (the most important) to 0 (the least important) based on its possible effect on the current strategic situation of its weight systems. The more weight the more effect on the current and future situation. Sum of the column (2) is (1) without considering the number of the factors.
- In the third column (classification), each factor is given a special score from 5(very good) to 1(poor) based on its current position and importance. This classification shows in what way the system respond to every factor.
- In the fourth column (weigh score), weight multiplies with the degree of each factor to reach the weight score for each factor (Column 2 * Column 3).
- In fifth column, the factors are graded based on their scores. At last, we can determine how system responds to the available and potential factors and forces. The weight score of the system is always 3.[4] .

2.4. Effective Internal and External Factors Analysis Summary on the Geotourism of the Gavkhoni Wetland through the perspective of the professors, students and tourists based on FAS model

In this section, you see the analysis and comparison of effective internal and external factors Analysis summary on the Geotourism of the Gavkhoni Wetland through the perspective of the author, professors, students and tourists based on FAS model. In total, 100 subjects from a range of 25 professors, 55 students and 20 regional tourists were participated in this study and answered the questionnaires.

According to the results, 3 tables for strengths and opportunities points and 3 tables for weaknesses and threats points were designed.

As you see in table (1), according to the data which are obtained from the responses of the professors of the geography and geology and analyzed by the IFAS model, the most important strength point of the Geotourism of the Gavkhoni Wetland is the existence of the beautiful and unique sights and the most important weakness is lack of appropriate residential facilitations and hospitalities for the tourists.

After classifying the answers in the range of 5 (very great) to 1 (very few), the answered were multiplied with proper number (very great=5, great=4, average=3, few=2, very few=1), then obtained numbers were plus with each other and multiplied with their weight in order to achieve the total score. At last, total score were divided by the total number of professors (25) to achieve average weight score.

Total number of all average scores of the effective internal factors which is **4.3**, shows their important role in the Geotourism of the Gavkhoni Wetland.

Table 1: Effective Internal Factors Analysis Summary on the Geotourism of The Gavkhoni Wetland through the perspective of the professors

Internal factors	weight	Grading					Total	Average
		1	2	3	4	5		
Strengths (S)								
S ₁ : The existence of the beautiful and unique sights	0.15	20	5				120	0.72
S ₂ : The existence of various and excellent historical attractions	0.15	15	9				114	0.68
S ₃ : Taking advantage of the sand and salty therapy	0.1	13	12	1			113	0.45
S ₄ : Taking advantage of the sport potential of the sandy hills	0.1	14	11				114	0.45
S ₅ : Taking advantage of the sandy hills for holding seminars	0.07	12	13				112	0.31
S ₆ : The high level of the knowledge, culture of the local people in this area	0.05	16	9				116	0.23
Weaknesses (W)								
W ₁ : Lack of appropriate residential facilitations and hospitalities	0.15	10	12	3			107	0.64
W ₂ : Lack of unified planning and policies	0.1	6	12	7			99	0.39
W ₃ : Low investment in the Geotourism part in this area	0.1	3	10	8	4		87	0.34
W ₄ : Lack of rebuilding, renovating and protecting the Geotourism investment in this area	0.03	5	7	7	6		86	0.1
Total	1							4.3

Comments: (1: Very Great, 2: Great, 3: average, 4: Few, 5: Very Few)

As you see in table (2), according to the data which are obtained from the responses of the professors of the geography and geology and analyzed by the EFAS model, the most important strength point of the Geotourism of the Gavkhoni Wetland is multidirectional Geotourism insight which covers all sides of it and the most important weakness is entering the rural, urban and industrial population, drained salty lands. Total number of all average scores of the effective external factors which is **3.94**, shows their important role in the Geotourism of the Gavkhoni Wetland.

As you see in table (3), according to the data which are obtained from the responses of the professors of the geography and geology and analyzed by the IFAS model, the most important strength point of the Geotourism of the Gavkhoni Wetland is the existence of the beautiful and unique sights and the most important weakness is lack of appropriate residential facilitations and hospitalities for the tourists. Total number of all average scores of the effective external factors which is

4.41, shows their important role in the Geotourism of the Gavkhoni Wetland.

Table 2: Effective External Factors Analysis Summary on the Geotourism of the Gavkhoni Wetland through the perspective of the professors

External factors	weight	Grading					Total	Average
		1	2	3	4	5		
Opportunities (O)								
O ₁ : Multidirectional Geotourism insight which covers all sides of tourism	0.15	2	11	12			90	0.54
O ₂ : Placing a crowded city (Isfahan), Varzaneh and other urban and rural centers next to the Gavkhoni Wetland	0.1	2	10	13			89	0.35
O ₃ : Paying more attention to the planning and investment in Geotourism part by the government	0.1	1	8	7	9		76	0.30
O ₄ : Rising the motivation of the private sector on the investment in this area	0.1	5	13	7			98	0.39
Threats (T)								
T ₁ : Entering the rural, urban and industrial population to Zayandehrood directly and indirectly	0.2	18	7				118	0.94
T ₂ : Decreasing the entrance water from Zayandeh Rood to the wetland	0.15	18	7				118	0.70
T ₃ : Establishing the connecting road between Varzaneh and Nodoushan near the wetland against the Ramsar agreement	0.1	10	15				110	0.44
T ₄ : The extension of the traditional and local culture because of coming large number of the tourists to this area	0.05	3	3	10	9		75	0.15
T ₅ : Cultural incompatibility among tourists and local people in this area	0.05	4	11	10			69	0.13
Total	1							3.94

Comments: (1: Very Great, 2: Great, 3: average, 4: Few, 5: Very Few)

Table 3: Effective Internal Factors Analysis Summary on the Geotourism of the Gavkhoni Wetland through the perspective of the students

Internal factors	weight	Grading					Total	Average
		1	2	3	4	5		
Strengths (S)								
S ₁ : The existence of the beautiful and unique sights	0.15	43	12				263	0.71
S ₂ : The existence of various and excellent historical attractions	0.15	40	12	3			257	0.70
S ₃ : Taking advantage of the sand and salty therapy	0.1	33	15	7			246	0.44
S ₄ : Taking advantage of the sport potential of the sandy hills	0.1	33	15	7			246	0.44
S ₅ : Taking advantage of the sandy hills for holding seminars	0.07	30	18	7			243	0.30
S ₆ : The high level of the knowledge, culture of the local people in this area	0.05	29	20	6			243	0.22
Weaknesses (W)								
W ₁ : Lack of appropriate residential facilitations and hospitalities	0.15	40	11	4			256	0.70
W ₂ : Lack of unified planning and policies	0.1	29	19	4	3		239	0.43
W ₃ : Low investment in the Geotourism part in this area	0.1	16	15	14	9	1	201	0.36
W ₄ : Lack of rebuilding, renovating and protecting the Geotourism investment in this area	0.03	14	22	12	5	2	206	0.11
Total	1							4.41

Comments: (1: Very Great, 2: Great, 3: average, 4: Few, 5: Very Few)

As you see in table (4), according to the data which are obtained from the responses of the professors of the geography and geology and analyzed by the EFAS model, the most important strength point of the Geotourism of the Gavkhoni Wetland is multidirectional Geotourism insight which covers all sides of it and the most important weakness is entering the rural, urban and industrial population, drained salty lands. Total number of all average scores of the effective external factors which is **4.27**, shows their important role in the Geotourism of the Gavkhoni Wetland.

Table 4: Effective External Factors Analysis Summary on the Geotourism of the Gavkhoni Wetland through the perspective of the students

External factors	weight	Grading					Total	Average
		1	2	3	4	5		
Opportunities (O)								
O ₁ : Multidirectional Geotourism insight which covers all sides of tourism	0.15	16	25	13	1		221	0.60
O ₂ : Placing a crowded city (Isfahan), Varzaneh and other urban and rural centers next to the Gavkhoni Wetland	0.1	23	17	10	3	2	221	0.40
O ₃ : Paying more attention to the planning and investment in Geotourism part by the government	0.1	21	19	13	2		224	0.40
O ₄ : Raising the motivation of the private sector on the investment in this area	0.1	21	20	8	6	1	222	0.40
Threats (T)								
T ₁ : Entering the rural, urban and industrial population to Zayandehood directly and indirectly	0.2	51	4				271	0.98
T ₂ : Decreasing the entrance water from Zayandeh Rood to the wetland	0.15	49	6				269	0.73
T ₃ : Establishing the connecting road between Varzaneh and Nodoushan near the wetland against the Ramsar agreement	0.1	34	18	3			251	0.45
T ₄ : The extension of the traditional and local culture because of coming large number of the tourists to this area	0.05	16	9	17	10	3	190	0.17
T ₅ : Cultural incompatibility among tourists and local people in this area	0.05	5	9	26	7	8	161	0.14
Total	1							4.27

Comments: (1: Very Great, 2: Great, 3: average, 4: Few, 5: Very Few)

Table 5: Effective Internal Factors Analysis Summary on the Geotourism of the Gavkhoni Wetland through the perspective of the Tourists

Internal factors	weight	Grading					Total	Average
		1	2	3	4	5		
Strengths (S)								
S ₁ : The existence of the beautiful and unique sights	0.15	16	4				96	0.72
S ₂ : The existence of various and excellent historical attractions	0.15	17	3				97	0.72
S ₃ : Taking advantage of the sand and salty therapy	0.1	9	11				89	0.44
S ₄ : Taking advantage of the sport potential of the sandy hills	0.1	13	7				93	0.46
S ₅ : Taking advantage of the sandy hills for holding seminars	0.07	9	9	2			87	0.30
S ₆ : The high level of the knowledge, culture of the local people in this area	0.05	12	6	2			90	0.22
Weaknesses (W)								
W ₁ : Lack of appropriate residential facilitations and hospitalities	0.15	17	3				97	0.72
W ₂ : Lack of unified planning and policies	0.1	9	8	3			86	0.43
W ₃ : Low investment in the Geotourism part in this area	0.1	6	8	4	1	1	77	0.38
W ₄ : Lack of rebuilding, renovating and protecting the Geotourism investment in this area	0.03	7	9	3	1		82	0.12
Total	1							4.51

Comments: (1: Very Great, 2: Great, 3: average, 4: Few, 5: Very Few)

As you see in table (5), according to the data which are obtained from the responses of the professors of the geography and geology and analyzed by the IFAS model, the most important strength point of the Geotourism of the Gavkhoni Wetland is the existence of the beautiful and unique sights and the most important weakness is Lack of appropriate residential facilitations and hospitalities. Total number of all average scores of the effective external factors which is **4.51**, shows their important role in the Geotourism of the Gavkhoni Wetland.

As you see in table (6), according to the data which are obtained from the responses of the professors of the geography and geology and analyzed by the EFAS model, the most important strength point of the Geotourism of the Gavkhoni Wetland is multidirectional Geotourism insight which covers all sides of it and the most important weakness is entering the rural, urban and industrial population, drained salty lands.

Total number of all average scores of the effective external factors which is **4.1**, shows their important role in the Geotourism of the Gavkhoni Wetland.

Table 6: Effective External Factors Analysis Summary on the Geotourism of the Gavkhoni Wetland through the perspective of the Tourists.

External factors	weight	Grading					Total	Average
		1	2	3	4	5		
Opportunities (O)								
O ₁ : Multidirectional Geotourism insight which covers all sides of tourism	0.15	8	7	4	1		82	0.61
O ₂ : Placing a crowded city (Isfahan), Varzaneh and other urban and rural centers next to the Gavkhoni Wetland	0.1	4	12	3	1		79	0.39
O ₃ : Paying more attention to the planning and investment in Geotourism part by the government	0.1		9	4	2		57	0.28
O ₄ : Raising the motivation of the private sector on the investment in this area	0.1	3	11	5	1	5	76	0.38
Threats (T)								
T ₁ : Entering the rural, urban and industrial population to Zayandehood directly and indirectly	0.2	18	2				98	0.98
T ₂ : Decreasing the entrance water from Zayandeh Rood to the wetland	0.15	16	4				96	0.72
T ₃ : Establishing the connecting road between Varzaneh and Nodoushan near the wetland against the Ramsar agreement	0.1	11	8	1			90	0.45
T ₄ : The extension of the traditional and local culture because of coming large number of the tourists to this area	0.05	3	6	9	1	1	69	0.17
T ₅ : Cultural incompatibility among tourists and local people in this area	0.05		4	8	3	5	51	0.12
Total	1							4.1

Comments: (1: Very Great, 2: Great, 3: average, 4: Few, 5: Very Few)

3. CONCLUSION

In this study, the authors investigated the strengths, weaknesses, opportunities and threats points of the Geotourism of the Gavkhoni Wetland based on FAS model. According to the data which are obtained from the responses of the professors of the geography and geology, students and tourists analyzed by the IFAS model, the most important strength point of the Geotourism of the Gavkhoni Wetland the existence of the numerous and excellent historical attractions and the most important weakness is Lack of appropriate residential facilitations and hospitalities. Although, this area has potential and powerful Geotourists investments but it faces with management weak points. We have a national and even international Geotourism pole if these weaknesses wipes out.

After analyzing the data by the EFAS model, the most important strength point of the Geotourism of the Gavkhoni Wetland is multidirectional Geotourism insight which covers all sides of it and the most important weakness is entering the rural, urban and industrial population, drained salty lands. Total number of all average scores of the effective external factors which is **4.27**, shows their important role in the Geotourism of the Gavkhoni Wetland. Entirely, the external environment is a threat to the Geotourism of the Gavkhoni Wetland. Therefore, its population should be decreased and also its required water should be prepared by the proper management.

REFERENCES

[1] Amrikazemi, A., Mehrpooya, A., ``Global Geotourism``, chapter 5, Geotourism resources of Iran``, Elsevier, 290, (2006).

- [2] Darvishzadeh, A. ``Iran geology``, Amir Kabir Pub, 902, (1991).
- [3] Harison. G, Karoon.G. `` Strategic management``, Translator: Qasemi.Behrooz, Heyat Pub, 289, (2003).
- [4] Hekmatnia. H, Mosavi.M. `` Usage of the model in the planning with emphasize on urban Geography and planning``, Novin Elm. Pub 320, (2006).
- [5] Iran Metrological organization, <http://www.weather.ir,n.d>.
- [6] Moinian.H. `` Investigation of the Ecology and quality of the Zayandeh Rood river``, MA Thesis, Islamic Azad Ahvaz University, (2000).
- [7] Maqsodi. T, Lashkar Ara.F. `` Tourism, development and village``, year 24, 264 number, (2004).
- [8] Moradimasahi.V. ``Strategic planning in huge cities``, urban planning and processing Pub, 252, (2002).
- [9] Najari.H. `` Gavkhoni international Wetland``, environmental protection Agency Pub, 164, (2003).
- [10] Noori.H`` Valued study of Isfahan tourism centers (The Gavkhoni Wetland)``, Isfahan culture, 15 number, (2000).
- [11] Papoliyazdi, M,`` Tourism (characters and concepts)``,Samt Publication, 284, 2006.
- [12] Ranjbarian .B, Zahedi. M. `` Tourism planning at the regional and national level``, Isfahan Jahad Daneshgahi, (1999).
- [13] Sharifzadeh . A , Moradnejad . H z. ``Sustainable development and rural tourism``, Jahad social economical monthly magazine, summer, (2002).
- [14] Tourtellot,J.,<http://www.nationalgeographic.com/travel/sustainable/>, n.d.

Optimization of Influential Parameter to Biodegrade the Phenol in Batch by Microbial Consortium

Hamitouche, A.^{1,2}, Bendjama, Z.¹, Amrane, A.^{3,4}, Chebout, M.¹, Habieb, F.¹, Kaouah, F.¹, Hamane, D.¹

¹ Laboratoire des Sciences du Génie des Procédés Industriels, Faculté de Génie Mécanique et de Génie des Procédés, Université des Sciences et de la Technologie Houari Boumediene, BP 32, El-Alia, 16111, Bab ezzouar, Alger, Algeria

² Centre de Recherche scientifique et technique en Analyses Physico-Chimiques, BP 248, CRAPC, Alger, Algeria

³ Ecole Nationale Supérieure de Chimie de Rennes, Université Rennes 1, CNRS, UMR 6226, Avenue du Général Leclerc, CS 50837, 35708 Rennes Cedex 7, France

⁴ Université européenne de Bretagne, 35000 Rennes, France

ABSTARCT

Phenol is a very toxic compound present at different concentrations caused by the development of industrialization, more and more industrial wastewater containing phenolic compounds are discharged from industrial processes such as oil refineries, chemical plants and coke ovens. A variety of techniques have been used for the remediation of phenol. Conventional methods of treatment are largely chemical or physical, but these processes lead to secondary effluent problems. Besides, biological treatment is an effective method which shows an increasing number of industrial applications, since a wide range of microorganisms can assimilate phenol as the sole source of carbon. In this purpose, phenol biodegradation was carried out in a batch reactor containing mixed bacteria; the temperature (30°C), the stirring velocity (200 r/min), initial concentration of NaH₂PO₄ (3 g/L), initial concentration of MgSO₄ (0,1 g/L) and the phenol concentration (100 mg/L) were kept constants. The initial pH was varied in the range 5 – 9 and the concentrations of other mineral components were tested in the following concentration ranges: 0 – 2 g/L for KNO₃, 0 – 4 g/L for KH₂PO₄.

Their effects on phenol biodegradation and specific growth rate were examined. All experiments were carried out at a given initial bacterial concentration of 0.08 g/L. The shorter biodegradation time of phenol was 18.58 h. Maximum specific growth rate (0.389 h⁻¹) and total phenol removal (99.99 %) were recorded for an optimal pH value equal 7 with optimal concentrations KNO₃ and KH₂PO₄ equal to 0.5 g/L.

Key words: Biodegradation, Phenol, Microbial consortium.

1. INTRODUCTION

Phenolic compounds and its derivatives are major environmental pollutants from industrial processes such as petroleum processing plants, oil refineries, coke oven and pharmaceutical industries (Abduli *et al.*, 2007; Onwurah, *et al* 2007; Dabhade *et al.*, 2009; Hassani *et al.*, 2009; Hamitouche *et al*, 2010; Hamitouche *et al*, 2011). The largest use of phenol is as an intermediate in the production of phenolic resins, synthetic fibers and for epoxy resin precursors. Besides, phenol is naturally present in some foods, in human and animal wastes, in decomposing organic material, and is produced endogenously from the metabolism of protein (USEPA, Toxicological Review of phenol).

The presence of phenols in the environment poses a significant risk to aquatic biota; phenol is lethal to fish at low concentrations of 5–25 mg.L⁻¹, for example. As environmental regulations become more restrictive, innovative treatments of wastewaters containing phenols must be considered. Phenols can be removed from industrial effluents by physicochemical methods such as ozonation, Fenton's reagent, UV or hydrogen peroxide (Gogate *et al*, 2004 a, b), but these treatments

are usually complex and expensive. For these reasons, the interest in the use of biological methods is increasing. Many aerobic bacteria are capable to use aromatic compounds as the sole carbon and energy source. Although both aerobic and anaerobic microorganisms are able to degrade phenol, aerobic processes are preferred.

A typical pathway for metabolizing phenol is to hydroxylate the ring to form catechol and then to open the ring through ortho or meta oxidation (Ellis *et al*, 2006). Batch and semicontinuous (Nuhoglu *et al* 2005; Yoong *et al*, 2000) processes employing both suspended and immobilized cultures (Orupold *et al*, 2001; Tziotzios *et al*, 2005; Karigar *et al*, 2006) were used to study the phenol degradation kinetics. Most of these studies were focused on the effect of the initial phenol concentration on the aerobic phenol degradation kinetics (Nuhoglu *et al*, 2005; Chen *et al*, 2004; Kumar *et al*, 2005; Arutchelvan *et al*, 2006). Only a few studies cover other environmental factors such as temperature, additional carbon sources, and salinity (Polymenakou *et al*, 2005; Peyton *et al*, 2002).

Since the aerobic phenol biodegradation is preferred to

the anaerobic pathway, the dissolved oxygen (DO) concentration may be a limiting factor of the treatment process (Etzensperger et al, 1989; Melo et al; 2005) studied the phenol degradation in an aerobic rotating biological contactor. Those authors found that the phenol degradation rate improved by increasing the rotation speed due to the increase of the oxygen mass transfer coefficient; thus, the process efficiency was limited by the DO availability. In addition, other environmental factors, such as pH, may decrease the efficiency of the biotreatment. For example, Alva and Peyton (2003) reported that although *Halomonas campisalis* can completely degrade phenol and catechol when the pH range between 8 and 11, the metabolic intermediates *cis,cis*-muconate and (+)- mucunolactone are accumulated at pH 8 and 9. Magbanua and Bowers (2006) studied the production of soluble microbial products (SMPs) by activated sludge receiving a mixed feed of phenol and glucose; those authors found that at pH ranging between 6.5 and 7.5, about 10–20% of the phenol carbon appeared in the SMPs.

The main goal of this paper was to investigate the biodegradation of phenol by mixed bacteria; the effect of pH, KH_2PO_4 and KNO_3 concentration were optimized to determine the best conditions for phenol removal.

2. MATERIALS & METHODS

The microbial consortium used in this work was obtained from activated sludge from the hazardous wastewater plant of Boumerdès (Algeria). The stock cultures were stored at 4 °C. The mixed bacteria were activated for 24 h at 30 °C in the nutrient medium (NB) containing (g/ L): peptone, 15, yeast extract, 3, sodium chloride, 6, and (D+)-glucose, 1.

After 24 h, when cells were grown, the biomass was harvested by centrifugation. The microorganisms collected after centrifugation (3000 r/min) for 30 min were suspended in NaCl 0.5 % and re-centrifuged. After the third washing, The microorganisms collected after centrifugation were re-suspended in NaCl 0.5 % to determine the concentration of the microbial consortium. This solution (microbial consortium and NaCl 0.5%) was analyzed by measuring OD at 600 nm using a Vis spectrophotometer (HACH DR 2800); the OD value was then converted to dry cell mass using a dry weight calibration curve. The dry cell mass density (g/ L) was found to follow the following regression equation $x \text{ (g/ L)} = 1.044 \times \text{OD}_{600}$.

Specific growth rate was determined in the exponential growth phase (Dagley & Gibson, 1965; Stanier et al., 1966; Chiam & Harris, 1982; Worden & Donaldson, 1987). For each flask, the specific growth value was determined from linear semi logarithmic plot of cell concentration versus time during the exponential growth phase, namely when specific growth rate became nearly

constant (D'Adamo et al., 1984).

As the OD value of adapted cells reached 2.7 – 2.9, an aliquot of the culture was centrifuged at 3000 rpm for 30 min. To wash the biomass, it was re-suspended in NaCl 0.5% and centrifuged. The cells (1 ml) were then transferred and inoculated in Erlenmeyer flasks (250 mL) to yield an initial OD of 0.078, and containing 100 mL of medium containing nitrogen source (KNO_3) and the following mineral salt supplementation (MSS), namely NaH_2PO_4 (3 g/L), KH_2PO_4 and MgSO_4 (0.1 g/L) at the required concentrations, and 100 mg/ L of phenol. The cells were cultivated at 30 °C and 200 rpm. Samples were withdrawn at suitable time-intervals and the concentration of cells was deduced from optical density measurement and phenol was measured as described below.

Phenol was colorimetrically estimated using a Vis spectrophotometer (HACH DR 2800) according to the method previously described by Yang & Humphrey (1975) and based on rapid condensation with 4-aminoantipyrine followed by oxidation with alkaline potassium ferricyanide and absorbance read at 510 nm.

3. RESULTS & DISCUSSION

To determine the optimal concentration of KH_2PO_4 , we varied the concentration of the salt from 0 to 4 g/L. The concentration of phenol (100 mg / L), stirring speed (200 r/min), the concentration of nitrogen sources namely KNO_3 (1 g/L), the initial pH of the solution (7) and temperature (30 C°) were kept constants. The results of measurements of biomass and the concentration of phenol versus time are shown in Figures 1 and 2.

The Figure 1, note that the phenol is totally degraded for a time ranging between 18.58 and 29.08 h.

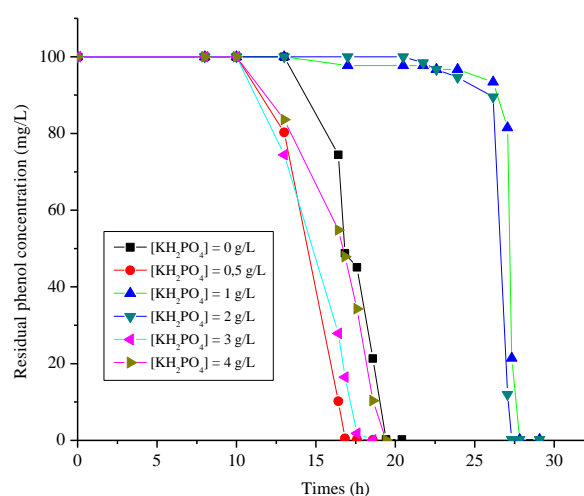


Figure 1: Evolution of residual phenol concentration versus times for different concentration of KH_2PO_4

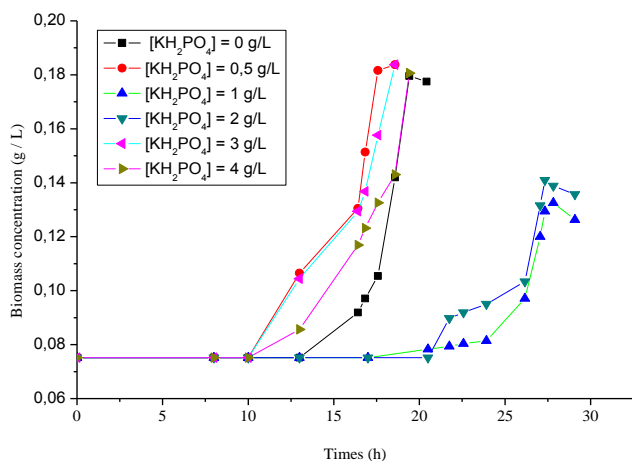


Figure 2: Evolution of biomass concentration versus the times for different concentrations de KH_2PO_4 .

Figure 2 shows that the latency period varies from 10 to 20.5 h.

The figures 1 and 2 show that increasing the concentration of bacteria promotes the removal of phenol.

The calculation of specific growth rates for each concentration of KH_2PO_4 shows (Table 1) that the maximum growth rate is obtained at a concentration of KH_2PO_4 equal to 0.5 g / L.

The work of Hamitouche et al, 2010 and 2011 shows that by using phenol as a carbon source with the salts $(\text{NH}_4)_2\text{SO}_4$ and NH_4Cl , the maximum of specific growth rate of the bacterial mixture is obtained at concentrations of KH_2PO_4 equal to 3 and 4 g / L , respectively.

For biodegradation of phenol by *Areobasidium pullulans* FE13 isolated from industrial effluent, Dos Santos et al (2009) added in saline 4.3 g/L KH_2PO_4

Table 1: Evolution of specific growth rate versus concentration of KH_2PO_4

KH_2PO_4 (g/L)	Specific growth rate (h^{-1})
0	0,297
0,5	0,358
1	0,279
2	0,267
3	0,189
4	0,126

To determine the optimal concentration of KNO_3 , the batch tests were conducted by maintaining constant the phenol concentration, (100 mg/L), stirring velocity (200 r/min), KH_2PO_4 concentration (0.5 g/L), initial pH of solution (7) and temperature (30 °C). We examine the effect of KNO_3 (0 – 2 g/L) on biodegradation.

The curves representing the biomass and the initial concentration of phenol versus time for different values

of initial concentration KNO_3 are plotted in figure 3 and 4.

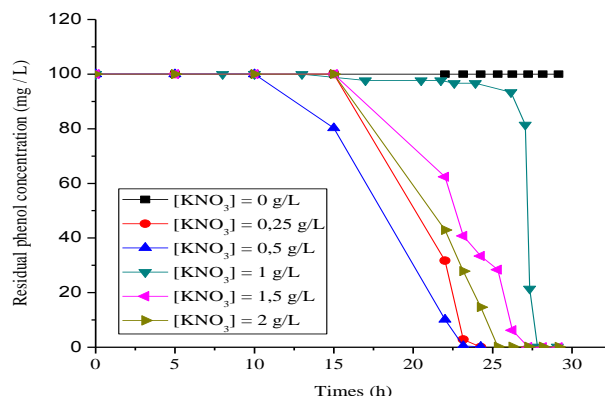


Figure 3: Evolution of residual phenol concentration versus times for different concentration of KNO_3

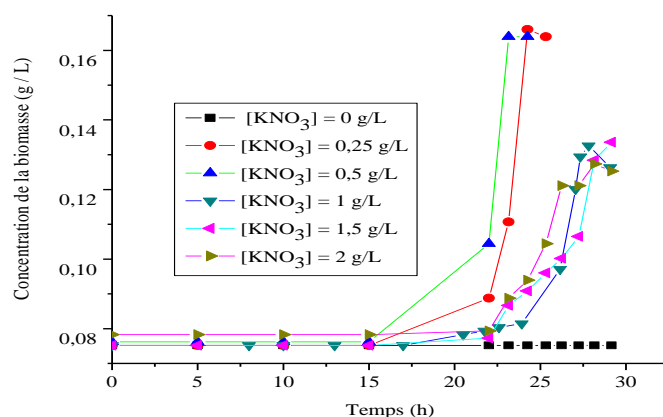


Figure 4: Evolution of biomass concentration versus the times for different concentrations de KNO_3

Table 2: Evolution of specific growth rate versus concentration of KNO_3

KNO_3 (g/L)	Specific growth rate (h^{-1})
0	0
0,25	0,372
0,5	0,389
1	0,358
1,5	0,206
2	0,161

It is found that the phenol is completely degraded by mixed culture after time varying from 24.25 to 27.83 h (figure 3). The figure 4 shows that the time of lag phase varies from 15 to 17 h.

The figures 3 and 4 shows the importance of nitrogen sources because in the absent of the bacteria stop to grow and to eliminate the phenol

In the table 2 we have grouped the values of the specific growth rate corresponding to a value of concentrations of KNO_3 . He shows that the maximum values of the

specific growth rate ($0,389 \text{ h}^{-1}$) is obtained at a concentration of KNO_3 equal to 0.5 g/L . In

The work of Hamitouche et al, 2010 and 2011 shows that by using phenol as a carbon source with the salts $(\text{NH}_4)_2\text{SO}_4$ and NH_4Cl , the maximum of specific growth rate of the bacterial mixture is obtained at concentrations of KNO_3 equal to 1 g/L .

The pH is a very important parameter since it influences the biodegradation process. The batch tests were conducted by maintaining constant the phenol concentration, (100 mg/L), stirring velocity (200 r/min), KH_2PO_4 concentration (0.5 g/L), KNO_3 concentration (0.5 g/L) and temperature ($30 \text{ }^\circ\text{C}$). We examine the effect of initial pH of solution (5 - 9).

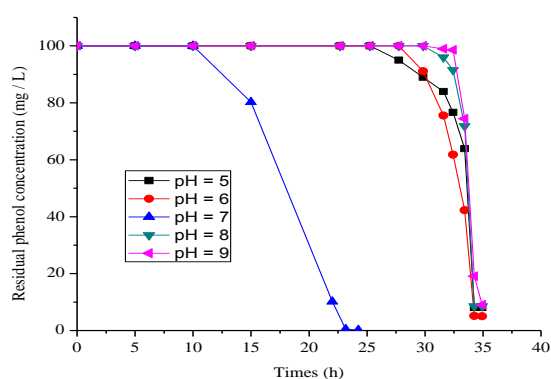


Figure 5: Evolution of residual phenol concentration versus times for different value of initial pH.

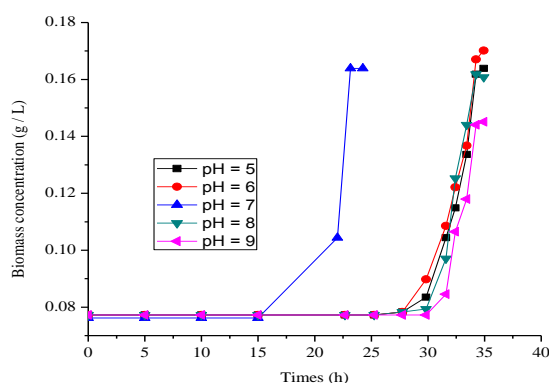


Figure 6: Evolution of biomass concentration versus the times for different value of initial pH.

Table 3: Evolution of specific growth rate versus initial pH of solution

pH	Specific growth rate (h^{-1})
5	0,23
6	0,24
7	0,389
8	0,303
9	0,274

An examination of figure 5 shows that phenol is

degraded from 98 to 100 % for the time ranging from 24.25 to 34.92h. The figure 6 shows that the time of lag phase varie from 15 to 25.25 h.

The table 3 indicate that the best specific growth rate corresponding to pH equal to 7.

4. CONCLUSION

Growth kinetics of the used microbial consortium and its potential for phenol assimilation were investigated leading to high biodegradation activity of the considered mixed culture, with an optimal maximum specific growth rate of 0.389 h^{-1} for a total phenol biodegradation time of 25.5 h. Irrespective of the culture conditions, total phenol biodegradation (100 mg/L) was achieved during times ranging from 20.6 to 33.2 h. The optimal conditions are 0.5 g/L of KH_2PO_4 , $0,5 \text{ g/L}$ of KNO_3 and the optimal pH value was 7.

REFERENCES

- [1] Abduli, M. A., Nabi Bidhendi, G. R., Nasrabadi, T. and Hoveidi, H. (2007).Evaluating the Reduction of Hazardous Waste Contact in Tabriz Petrochemical Complex, Focusing on Personal Protective Equipment Method. *Int. J. Environ. Res.*, 1(1), 14-18.
- [2] D'Adamo, P. D., Rozich, A. F. and Gaudy, A. F. Jr. (1984). Analysis of growth data with inhibitory carbon sources. *Biotechnol. Bioeng.*, 26 (4), 397-402.
- [3] Arutchelvan, V., Kanakasabai, V., Elangovan, R., Nagarajan, S., Muralikrishnan, V., (2006), Kinetics of high strength phenol degradation using *Bacillus brevis*, *J. Hazard. Mater.*, 129, 216–222.
- [4] Chen, W.M., Chang, J.S., Wu, C.H., Chang, S.C., (2004), Characterization of phenol and trichloroethene degradation by the rhizobium *Ralstonia taiwanensis*, *Res. Microbiol.*, 155, 672–680.
- [5] Dabhade, M. A., Saidutta, M.B. and Murthy, D.V.R. (2009). Adsorption of Phenol on Granular Activated Carbon from Nutrient Medium:Equilibrium and kinetic Study. *Int. J. Environ. Res.*, 3(4), 545-556.
- [6] Dagley, S. and Gibson, D. T. (1965). The bacterial degradation of catechol. *Biochem. J.*, 95 (2), 466-474.
- [7] Ellis, L.B.M., Roe, D., Wackett, L.P., (2006), The University of Minnesota biocatalysis/biodegradation database: the first decade, *Nucleic Acids Res.*, 34, D517–D521.

- [8] Etzensperger, M., Thoma, S., Petrozzi, S., Dunn, I.J., (1989), Phenol degradation in a three-phase biofilm fluidized sand bed reactor, *Bioproc. Biosys. Eng.*, 4, 175–181.
- [9] Gogate, P.R., Pandit, A., (2004), A review of imperative technologies for wastewater treatment I: oxidation technologies at ambient conditions, *Adv. Environ. Res.*, 8, 501–551.
- [10] Gogate, P.R., Pandit, A., (2004b), A review of imperative technologies for wastewater treatment II: hybrid methods, *Adv. Environ. Res.*, 8, 553–597.
- [11] Hamitouche. A, Amrane. A, Bendjama. Z, Kaouah. A, (2010), Effect of the ammonium chloride concentration on the mineral medium composition – biodegradation of phenol by a microbial consortium, *Int. J. Environ. Res.* 4(4): 849 – 854.
- [12] Hamitouche. A, Amrane. A, Bendjama. Z, Kaouah. A, (2011), Phenol biodegradation by mixed culture in batch reactor – Optimization of the mineral medium composition, *Desalination and Water Treatment.* 25, 20 – 24.
- [13] Hassani, A. H., Otadi, N., Javid, A.H., Khiabani, F.F. and Hoshyaripour, G. (2009). Improving the performance of Pars Oil Refinery Wastewater Treatment System. *Int. J. Environ. Res.*, 3(4), 653–662.
- [14] Karigar, C., Mahesh, A., Nagenahalli, M., Yun, D.J., (2006), Phenol degradation by immobilized cells of *Arthrobacter citreus*, *Biodegradation*, 17, 47–55.
- [15] Kumar, A., Kumar, S., Kumar, S., (2005), Biodegradation kinetics of phenol and catechol using *Pseudomonas putida* MTCC 1194, *Biochem. Eng. J.*, 22, 151–159.
- [16] Magbanua, B.S., Bowers, A.R., (2006), Characterization of soluble microbial products (SMP) derived from glucose and phenol in dual substrate activated sludge reactors, *Biotechnol. Bioeng.*, 93, 862–870.
- [17] Melo, J.S., Kholi, S., Patwardhan, A.W., D'Souza, S.F., (2005), Effect of oxygen transfer limitations in phenol biodegradation, *Process Biochem.*, 40, 625–628.
- [18] Nuhoglu, A., Yalcin, B., (2005), Modelling of phenol removal in a batch reactor, *Proc. Biochem.*, 40, 1233–1239.
- [19] Orupold, K., Masirin, A., Tenno, T., (2001), Estimation of biodegradation parameters of phenolic compounds on activated sludge by respirometry, *Chemosphere*, 44, 1273–1280.
- [20] Peyton, B., Wilson, T., Yonge, D.R., (2002), Kinetics of phenol biodegradation in high salt solutions, *Water Res.*, 36, 4811–4820.
- [21] Polymenakou, P.N., Stephanou, E.G., (2005), Effect of temperature and additional carbon sources on phenol degradation by an indigenous soil *Pseudomonad*, *Biodegradation*, 16, 403–413.
- [22] Stanier, R. Y., Palleroni, N. J. and Doudoroff, M. (1966). The aerobic *Pseudomonas* taxonomic study. *J. Gen. Microbiol.*, 43, 159-275.
- [23] dos Santos, V. L., de Souza Monteiro, A., Braga, D. T. and Santoro, M. M. (2009). Phenol degradation by *Aureobasidium pullulans* FE1 3 isolated from industrial effluents. *J. Hazard. Mater.*, 161 (2-3), 1413-1420.
- [24] Tziotziou, G., Teliou, M., Kaltsouni, V., Lyberatos, G., Vayenas, D.V., (2005), Biological phenol removal using suspended growth and packed bed reactors, *Biochem. Eng. J.*, 26, 65–70.
- [25] USEPA, Toxicological Review. Phenol. CAS No. 108-95-2, U.S. Environmental Protection Agency, Washington, DC, 2000.
- [26] Yoong, E.T., Lant, P.A., Greenfield, P.F. (2000), In situ respirometry in an SBR treating wastewater with high phenol concentrations, *Water Res.*, 34, 239–245.

The Impact of Wind Farms on the Stability of Electric Networks

I. Etier¹, M. Abderrazzaq²

¹The Hashemite University, Electrical Engineering Department, 13115 Zarqa, Jordan.

²Yarmouk University, Hijawi Faculty for Engineering Technology, Irbid, Jordan

Corresponding author: etier@hu.edu.jo

ABSTRACT

Wind energy integration into distribution networks is currently an international trend. The achieved high penetration level of wind energy has changed the conventional view of wind energy role. The exclusion of wind energy from the studies, concerning steady state and abnormal conditions, is no longer acceptable approach to the decision makers in energy industry. In this paper, the main issues, related to the role of wind energy in keeping the power systems running efficiently and securely in normal and abnormal conditions, will be highlighted. The impact of wind energy isolation during the fault is determined. The role of advanced wind turbines in enhancing the weak distribution networks is assessed. The significance of wind in deregulated systems and privatization schemes is discussed. Finally, the recent development in communication system and its role in improving the integration of wind energy into local distribution networks will be summarized.

Keywords: Wind Energy, Wind Turbine, Wind Farm, Grid connected.

1. INTRODUCTION

With increasing demand for clean energy, wind power seems to stand out as a global success story. On the other hand, the continuous fluctuation in oil prices in response to wars and political instabilities has made the Wind Turbines (WTs) the fastest growing energy source in the world. Wind power's dominance has been so significant that advocates are now gathering around an idea that would have seemed fantastic just a couple of years ago: that the wind would supply 12% of the world's electrical demand by 2020 [1]. The fear of high dependence on wind energy is no longer exists because the new systems are based on advanced power electronics and energy storage devices which assist in managing power flows from WTs. This arrangement enables the wind systems to contribute mightily to electricity grids without putting those grids at risk. The current technology improves the wind energy in two directions: firstly by making the wind power more portable to grid operators and by making it possible for engineers to exploit the wind resources in remote locations.

2. GENERAL REQUIREMENTS FOR GRID-CONNECTED WIND ENERGY

With the increase in number and size of WTs, wind farms have grown to include dozens of turbines and hundreds of megawatts- reaching the size of conventional power plants. To encourage the acceptance of installations like those, power system operators had to fight with the tendency of WTs to introduce voltage instability into electrical grids. That tendency follows from the intermittent nature of wind-generated

electricity, which directly affects the daily prediction and forecasting the consumer demand.

To understand the issues of the system's instability and the related solutions, one needs a few basics on the nature of power flows on utility grids. On the other hand, declining voltage on a network is a function of the consumption of both active and reactive power. This means that if a large load consumes significant amount of reactive power, it will cause the voltage to dip immediately unless the reactive load is adequately compensated for. The compensation can be achieved by supplying reactive power directly from the generators themselves or by installing banks of capacitors close to inductive loads. It is easy to understand the relationship of these issues to wind energy if we remember that most of the current WT generators are of induction type, which consumes a considerable amount of reactive power.

Generally, utilities require that wind farms should be able to provide dynamic reactive compensation, exactly as a conventional generator would be able to do. This means that these wind systems should be able to assist in restoring stability during a disturbance or some other crisis on the grid. In the past, when a generator failure or a momentary short-circuit occur, wind farms would automatically disconnect themselves. But now, most grid operators prefer keeping these WTs running during the disturbance events. As a response to this operational progress, wind farms and turbine developers must modify their designs and operating procedures to cope with these requirements, particularly for voltage faults.

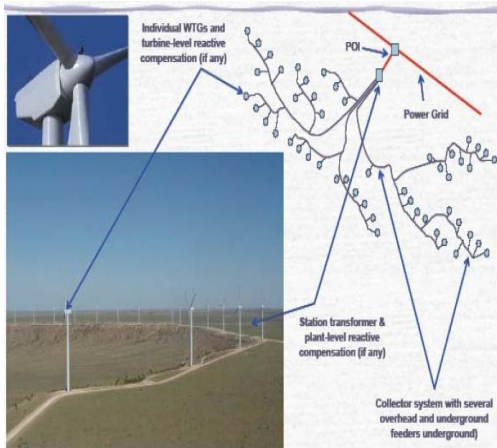


Figure 1: Typical wind farm layout

Concerning the power quality problems, it is worth mentioning that the new models of MW class WTGs have less effect on power quality issues such as harmonics, voltage flicker and voltage dip. The advanced technology, adopted for modern wind energy generation, has enabled the manufacturer to limit the power quality problems and to be in harmony with international standards and grid codes. The regular inspection and testing schemes of the wind-generated power give a chance to correct any deviation in the power supply.

3. SPECIFIC REQUIREMENTS FOR WIND ENERGY CONNECTION TO GRID

3.1 Behavior during the fault

In systems with significant wind energy resources, the nature and role of such energy has been changed in the last two decades. The power systems did not depend on the energy generated by WTGs, which were small in size and limited in contribution at that time. Under these circumstances, the behavior of WT at faults was not critical and the simple control systems, equipped with these turbines, were efficiently able to disconnect these machines from the network immediately when the fault occurs.

Currently, the WTGs are large in size and the capacity of new wind farms can attain hundreds of megawatts. They are distributed on large areas as shown in Figure 1.

The disconnection of WTGs due to a fault in nearby feeders is no longer preferred. It is desirable to keep the WTGs running during the faraway faults. This arrangement reduces the chance to cause consequential loss of generation, which might lead to a voltage collapse. This requirement implies that the new generation of WTGs should be able to keep running with voltage dips caused by faults in remote feeders. A series of load flow and short circuit calculations were made to study the impact of wind energy on the local distribution networks. Figures 2-4 show the dependence

of voltage dip on the distance of fault location in a typical radial distribution system. Figure 2 illustrates the disturbance effect when a fault on the same feeder connected to induction generators occurs, whereas Fig.3 shows a very slight voltage variation in a remote busbar due to a short circuit applied at different locations on the induction generator feeder.

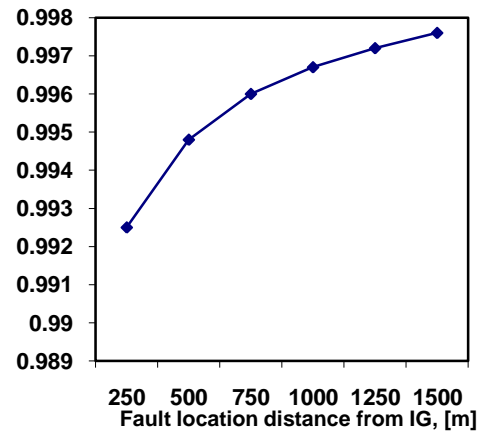


Figure 2: the impact of fault location on the voltage of the same feeder where the wind turbines are connected

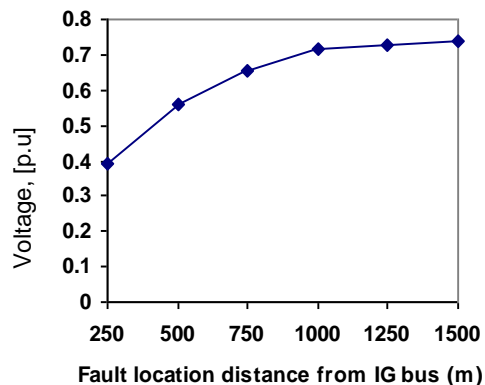


Figure 3: The impact of fault location on the voltage of a remote busbar (short circuit applied at different locations on the induction generator feeder).

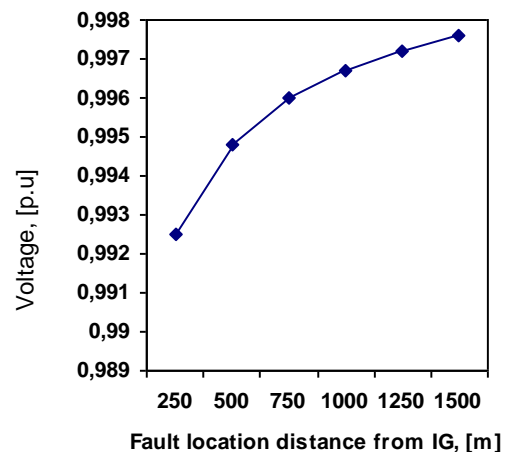


Figure 4: Recovery after the fault

Regarding the behavior during the short circuit, it is worth mentioning here that the induction generator characteristics are closely dependent on the deviation between the rotor speed and the synchronous speed. This leads to the fact the stator current increases very rapidly when the motor slip frequency increases.

3.2 Post fault behavior

Two important factors can affect the speed of recovery of wind machine after the fault; the demagnetization and the negative slip due the increase in rotor speed. The impact of the first factor depends on the strength of the electric network to which the WTs are connected. On the other hand, if the short circuit duration is relatively long and the magnetization process of the induction machine is slow, the generator speed increase becomes significant. Therefore, to improve the induction generator response to the system disturbances including short circuits and to successfully recover from the fault, it is necessary to build a fast process of magnetization so that it can produce torque and reduce the generator over speed.

3.3 Frequency and voltage control

Voltage and frequency control, during load variations, mainly depends on the behavior and the parameter adjustment of the voltage and speed regulators of the generation units. With the increase in the number of WTs, it becomes difficult to control the node voltages adequately by only using the synchronous generators in large-scale conventional power stations. Therefore, it is essential that all WTs also contribute to voltage control. The fact that the voltage is not the same throughout the system makes it a local quantity, as opposed to frequency, which is a global quantity, because it is identical in the whole system. Voltage problems must always be solved at or in the vicinity of the node at which the problem occurs, as opposed to frequency problems that can be solved everywhere, provided that no branch over loadings occur. The WTs distributed over a wide area and in different locations can be of great importance in this field [2]. On the other hand, the increasing of wind energy penetration can cause an overvoltage to some bus bars, if these turbines operate simultaneously. However, the probability of a simultaneous operation of WTs is very low even during the gust on a certain wind farm. When it is not possible to keep all node voltages in the system within the allowed deviation from their nominal values from the synchronous generators, other technologies must be used, such as capacitor banks, SVC's or STATCOMs.

Since the current power systems are still depending on massive generation units to produce the required electricity, the outage of these plants is usually associated with serious problems ranging from the usage of the expensive emergency reserve units to applying the load shedding scheme. The categories of

the load-shedding scheme are based on the importance of the load to be shed. Usually, the rural residential loads are classified in many countries as less important loads, which are switched off first in order to improve the frequency level. However, the presence of large-scale WTs can assist the frequency control in two ways. Firstly, wind energy can reduce the shortage in conventional generation and consequently lower the rate at which the frequency starts to decay. Secondly, WTs in windy sites can quickly restore the supply to the remote locations after load shedding. If the wind speed is increased by 2 folds the power generated from the wind turbine will increase by 8 folds according to the following equation

$$P = \frac{1}{2} \rho C_p A V^3 \quad (1)$$

Where, P is the output power in kW, ρ is the air density kg/m^3 , C_p is the power coefficient, A is the swept area in m^2 and V is the wind speed in m/s.

4. WIND TURBINES AND SYSTEM STABILITY

4.1 Dynamic behavior of wind turbines

Different models have been proposed to study the dynamic behavior of the WTs [3]. With the classical approach, the wind farm terminal voltages have recovered quickly, whereas with the physical model various oscillations were noticed in the terminal voltages. It is worth noting that the overspeed of WTs as a consequence of the fault was not high enough for the turbine to be disconnected and stopped by the protection system. The rotor speed was slightly decreased when subjected to the fault and thereafter increases in speed. If the overspeed is significantly low, the protection system of WTs does not react immediately. The presence of large-scale wind farms with high capacities in one location can have a bad effect on the system stability during the fault. Naturally, the windy sites are distributed in different locations in each country, which can be employed to enhance the system stability and prevent the voltage collapse.

4.2 Wind energy influence on voltage stability

Various studies have been performed to analyze the impact of wind energy on voltage stability [4,5]. The active and reactive powers are the main parameters used in the assessment of voltage stability limits. In all cases it has been concluded that voltage stability depends mainly on the network characteristics. Therefore, the distribution lines, known by their losses can be operated in more stable way with WTs. The later are characterized by their active power injected to the system and consequently an increase of system voltage at the terminals of these turbines. This voltage increase can compensate the reduction due to reactive power demanded. In the current work a typical radial distribution system was examined to assess the network

transient behavior when a three-phase fault is applied to an 11kV line. Figure 3 shows the voltage variation and the fast recovery after the transient.

5. WIND ENERGY AND DEREGULATION.

The tendency toward deregulation and privatization policies is gaining ground nowadays. This process goes in harmony with the distribution generation schemes, which consists of various sources generation including wind energy and other renewables. The companies operating these new plants try to limit the expenses on the engineering part and to run these plants as simple as possible. Therefore, the conventional power plants are not preferred choice for these new systems and many of them strongly support the installation of large-scale WTs. On the other hand, wind energy plants are easy to own, operate and maintain by small companies and local communities. In addition to the environmental considerations associated with wind energy, many small utilities and local communities have created new tariff schemes to encourage the customers to purchase the energy from WTs.

6. WIND ENERGY AND TECHNOLOGICAL DEVELOPMENTS

Advanced current design standards and certification rules have been positively reflected on wind energy development. Therefore, remarkable advances in wind power design have been achieved. One aspect of WTs that will increase rapidly is the use of information technology and sophisticated communication systems for the real time monitoring and control. No other commercial plant is operated remotely in this way [6]. This development will improve the protection and control systems of these turbines and consequently enhance the networks' stability. Moreover, the parallel progress in wind energy prediction will encourage the utilities to include more WTs in their local networks and enhance the weak grids significantly.

7. MAXIMIZING THE ROLE OF WIND FARMS

Wind resources must be adequate to be commercially viable. Moreover, the commercial outcome is very sensitive to wind speed, thus siting is important. The presence of strong transmission system is important to maximize the wind energy penetration. On the other hand, WT starting and stopping transients and power fluctuations during operation must not lead to unacceptable voltage or frequency fluctuations, excessive load-following costs or excessive wear and tear on turbine components. Wind farm designers and network service providers must avoid unsatisfactory network voltage profiles and protection problems due to either excessive or insufficient fault level.

The prediction of wind farm production must be sufficiently accurate to avoid unnecessary network

investment or generation reserve requirements and to satisfy wind farm investment risk management criteria. The new system operators try to benefit from installed wind turbines as much as possible by concentrating on improving the efficiency, reducing the losses and developing new models of wind speed prediction. The concentration is mainly on the short term prediction of wind energy to facilitate commercial tools for such energy. This trend is becoming more and more important with the continuous reduction and shortage of conventional resources.

Finally, the current developments in communications, information technology will enhance the new role of wind energy in electrical system stability. The data exchange and remote operation of wind farms become an easy task with the development of wireless communication system and fiber optics techniques.

8. CONCLUSIONS

The technical impact and stability issues concerning the connection of large-scale wind turbines to a typical network were discussed. The load flow and fault studies have illustrated that the voltage dip initiated by induction generators decreases significantly as the fault location distance increases. Regarding the dynamic response of the machine during transient conditions, it was shown that a complete recovery was achieved quickly. The distribution of WTs in different locations enhances the voltage and frequency stability of the system. The load shedding schemes in networks with high wind energy penetration must benefit from the existing WTs and modify these schemes accordingly. On the other hand, the trends of systems restructuring and deregulations give a potential to large scale wind energy schemes.

REFERENCES

- [1] P. Fairley, "steady as she blows", electric power, IEEE Spectrum, 2003.
- [2] T. Tomson, "Wind power grid matching problems. The Estonian case study", EWEC 2001, pp.1007-1009.
- [3] V.Akhmatov et al., Electrical Power and Energy Systems, 22 (2000), 421-434.
- [4] Popvic, Hiskins and Hill, "Stability of induction motors networks", Electrical power and energy, Vol. 20 No.7, 1998, pp. 475-487.
- [5] Andres Feijo and Jose Cidras, "Modeling of Wind Farms in the Load Flow Analysis", IEE Transactions on power systems, Vol. 15 No.1, 2000.
- [6] James and James, "Renewable energy world. Technology update, wind power". Science publishers, UK, Vol 2 No.1, January 1999, p 45.

New Public Management Reforms and Efficiency in Urban Water Service Delivery in Emerging Economies: Blessing or Curse?

M. M. N. Mukokoma¹ and M. P. Dijk Van²

¹Kyambogo University, Uganda; mmnalwoga@gmail.com

² UNESCO-IHE Institute for Water Education, Netherlands; mpvandijk@ese.eur.nl

ABSTRACT

Water utilities globally have been undergoing significant reforms since the 1990s. A common reform, particularly in emerging economies, known as New Public Management (NPM) is where ownership is retained by the public sector but private sector principles and practices are utilized. The theoretical and empirical debate on the effect of NPM on the performance of Public entities is still ongoing yet limited research has been conducted in the water sector in developing countries. In this paper we address the issue of whether adoption of NPM reform dimensions improves the technical efficiency of water utilities.

Using a ten year data (2000 – 2009) we computed technical efficiency scores for 30 Decision Making Units (DMUs); 18 for National Water and Sewerage Corporation (NWSC) in Uganda and 12 for Dar es Salaam Water and Sewerage Corporation (DAWASCO) / Dar es Salaam Water Authority (DAWASA) in Tanzania. Still over the same period we assessed NPM adoption levels that were categorized into three regions of before, transition and after NPM. Using a tobit regression model we found out that NPM adoption, particularly the dimensions of segregation of functions, managerial autonomy and accountability for results, significantly ($\chi^2(5) = 21.72$, $\text{Prob} > \chi^2 = 0.031$) contributes to technical efficiency.

Keywords: New Public Management, Data Envelopment Analysis (DEA), Efficiency, water reforms

1. INTRODUCTION

NPM is a common water reform paradigm in emerging economies (Manning [1]). This reform paradigm is where ownership is retained by the public sector but private sector principles and practices are utilized as described by Hood [2], Pollitt [3], and Walsh [4]. The debate on the effect of NPM on performance of public entities is still ongoing. Some researchers like Pollitt and Bouckaert [5] and Emile et al. [6] have concluded that NPM has led to performance improvements especially in terms of efficiency. Others have described the effect of NPM on efficiency as superficial (Ogawa and Tanahashi [7]), dismal, and mixed (Batley [8], Schwartz [9]).

In this paper we assess the effect of NPM reforms on the efficiency of urban water utilities in Uganda and Tanzania by analysing the technical efficiency levels of NWSC and DAWASA / DAWASCO over ten years; assessing the NPM reforms in terms of segregation of functions, managerial autonomy, market orientation, customer orientation, and accountability for results over ten years; and finally establishing the relationship between NPM reforms and the technical efficiency levels.

2. RELATED LITERATURE

NPM is founded on various theories that include; Weber's [10] bureaucratic theory; Taylor's [11] scientific management; Mueller's [12] public choice

theory and Tullock's [13] Principal – Agency theory. Due to the limitations in these theories NPM emerged.

Many authors like Hood [2], Pollitt [3], Walsh [4], Van Dijk [14], and Schwartz [15] have tried to characterize the NPM. There is no agreement on concrete characterization of NPM as argued by Groot and Budding [16]. The common ones that we have used in this paper are segregation of functions, managerial autonomy, and accountability for results, customer orientation, and market orientation.

Efficiency measurement is based on the production theory that views a firm as a production system where input resources utilized by the firm are translated into desirable outputs. Common tools used to measure efficiency are ratio analysis and frontier techniques. Ratio analysis involves a comparison between inputs and outputs. Simple ratios like staff per connection, water delivered per staff and operating cost per connection among others, are commonly used in the water sector as indicated by Tynan and Kingdom [17]. These are single – measure gap analysis that involve use of separate efficiency indicators like staff per 1000 connections, and expenditure as a percentage of revenue generated. Frontier analysis is a tool used to benchmark the relative performance of Decision Making Units [DMUs] by assessing how close the DMUs are to a “best practice” frontier as explained by Farrell [18]. A common method used is Data Envelopment Analysis [DEA].

DEA is a non-parametric method that was first

introduced in 1978 by Charnes et al. [19] as an empirically based methodology that eliminates the need for some of the assumptions and limitations of traditional efficiency measurement approaches. Many researchers like, Thanassoulis 2000 [20], Kirkpatrick et al. [21], Ogawa and Tanashi [8], and Ndandiko [22] have used DEA to assess efficiency of government service providers. Attractions to using DEA as a performance measurement models include the ability to handle multiple inputs and outputs, and ability to identify possible benchmarks.

3. APPROACH AND METHOD

Two typical cases of urban water utilities that have adopted NPM reforms in the great lakes region of Africa were selected. NWSC was also selected because it is being referred to as a high performing water utility in Sub-Saharan Africa (Schwartz [8], Muhairwe [23]). In contrast DAWASA / DAWASCO is commonly identified as a below average performing water utility (Mujwahuzi [24], Kjellen [25], Kiwanga [26]). A part from the contrast in performance, the two utilities have adopted different NPM reform routes. We analyse the 30 DMUs of the two utilities; 18 for NWSC and 12 for DAWASCO.

We used DEA to calculate the technical efficiency of the different DMUs. DEA calculates the relative efficiency of each DMU compared to other DMUs by using actual observed values for the inputs and outputs of each DMU. It also identifies the sources and level of inefficiency for each input and output (Charnes et al. [19]). Given a collection of $j=1,2,3,\dots,n$ DMUs, DEA attempts to maximize the ratio of outputs y to inputs x by attaching weights in order to assess each DMU relative to similar DMUs.

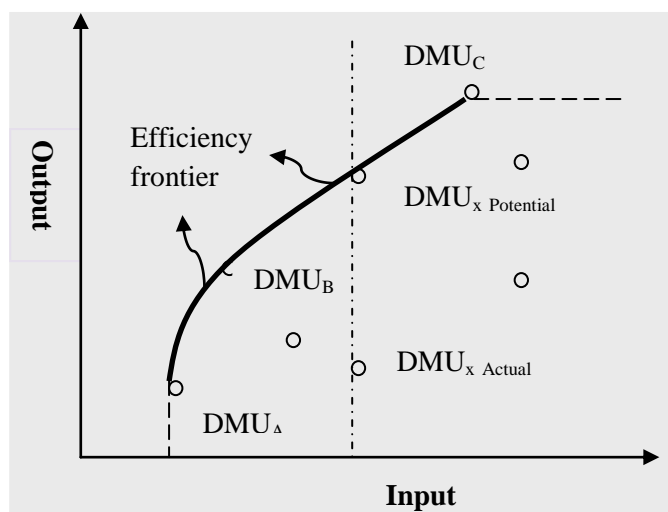


Figure 1: Data Envelopment Analysis. Source: Spottiswoode [27]

In figure 1, DMUs A, B, and C together define the efficiency frontier. By contrast, DMU_x clearly lies inside this frontier and its vertical distance (DMU_x

(potential) and DMU_x (actual) can be used to calculate its efficiency. DMU_s , B and C provide a reference 'peer group' that can be used to set output maximization or input minimisation for x .

We also used interviews (both formal and informal) with management and employees of NWSC and DAWASA / DAWASCO to ascertain the level of NPM reform adoption over the ten years. We analysed information from interviews and relevant documents using specific indicators to ascertain the level of NPM adoption of the different dimensions before and after NPM, and the association between NPM adoption and the efficiency levels. The formal interviews were semi-structured based on NPM characterization.

In a bid to assess whether the public sector reforms improve technical efficiency, it is common to regress the efficiency measures obtained from DEA against a series of explanatory variables as used by Coelli et al. [28] and Ndandiko [22]. Usually a two staged approach is followed where in the first instance the DEA efficiency scores are calculated and then in the second stage, a regression is run. While running the regression, we used DEA scores with censored data that cannot be higher than unity; hence the Tobit error term ε is assumed. This implies that the error term is distributed according to normal distribution but its likelihood function is bounded between 0 and 1. Various studies like; Coelli [28], Kirkpatrick [21], and Ndandiko [22]; have used a similar approach to assess efficiency in water utilities.

The general tobit model formulation with limited dependent variable as proposed by Greene [29] is given by in equation 1:

$$y_i^* = X_i \beta + \varepsilon_i \quad (1)$$

Where y_i^* is the latent variable; X_i represents the vector of explanatory variables; and β are the parameters to be estimated. It is assumed that the errors are normally distributed, with mean zero and variance σ^2 , $\varepsilon_i \sim N(0, \sigma^2)$.

Considering that in our study the efficiency scores were defined by DEA, where the limit for a unit to efficient is 1, the observed variables (y_i) are defined as in equation 2 follows:

$$y_i = \begin{cases} y_i^* & \text{if } y_i^* > 0, \\ 0 & \text{if } y_i^* \leq 0. \end{cases} \quad (2)$$

Initially we calculated the technical efficiency scores for 30 DMUs (18 for NWSC and 12 for DAWASCO) each year for 10 years using DEA. Measuring efficiency in this manner is consistent with both literature associated with the efficiency measurement of water service providers such as Moore [30], and Dewittee [31] and with past empirical approaches to efficiency

measurement in the water sector notably, Thanassoulis [20], Kirkpatric et al. [21] and Mugisha [32].

Banker et al. [33] suggests that as a way of balancing between the degrees of freedom and sample size; there should be three decision making units for every variable to ensure meaningful analysis. If x is the number of inputs and y the number of outputs, then the sample n should satisfy $n \geq 3(x + y)$. For this study we chose one input and two outputs $n \geq 9$; as shown in table 1.

Table 1: The DEA model used

Input	Outputs
Operating Expenses	Volume of water billed
	Non Revenue Water

There are two DEA model orientations; input and output orientation. The input orientation emphasizes input reduction to achieve a particular level of output. On the other hand, output orientation considers achieving more output with the present level of inputs. In this study we use output orientation because both corporations are public utilities and the arrangement between HO and DMUs is for the latter to maximize outputs given a particular level of inputs. Besides this, the water coverage in these areas is below 75% and Non Revenue Water is above 35%, hence increasing the amount of water billed is a key objective.

According to Charnes et al. [19] and Banker et al.[33], DEA orientation based on scale economies has two dimensions, variable and constant returns to scale. If one assumes that scale economies remain fixed even when the level of service delivery increases, then Constant Returns to Scale (CRS) type of DEA models is an appropriate choice. Conversely, if it is assumed that scale economies vary with the level of service delivery then Variable Returns to Scale (VRS) as developed by Banker et al. [33] would be desirable. In this study the different DMUs vary in terms of water billed, number of staff, and length of pipe network, hence we have chosen to use VRS because of the possibility of calculating technical efficiencies as different from scale efficiencies.

3. FINDINGS AND DISCUSSION

3.1 NPM reforms in NWSC and DAWASCO

The structural and legal reforms of NWSC date way back to 1995 when the utility was re-established as a corporation by the NWSC Act. However, despite the structural and legal reforms, water service delivery remained very poor characterized by unreliable water supply, low service coverage, inefficient billing and collection practices, inaccessibility of water especially in poor urban settings, aged and poorly maintained water infrastructure and generally very poor financial performance as shown in MWLE [34]. Because of

these water service delivery problems, government, together with donors were convinced that an international private operator was the solution. Consequently in 1999 government, through the Ministry of Water, told the management of the corporation that the later will be privatized if performance does not improve. The privatization threat triggered management of NWSC to adopt NPM reforms of segmentation of functions, autonomy of DMUs, market orientation, customer orientation, and accountability for results as highlighted by Mukokoma [35], Muhairwe [23].

For the case of DAWASCO the general NPM reforms date way back from 1997 with structural reforms that led to the formation of DAWASA. DAWASA was charged with the overall responsibility for water service delivery in Dar (Dar es Salaam) region. To segregate asset ownership functions from utilization, DAWASA in 2003 appointed City Water, a private operator, under a 10 year lease contract, but the latter’s services were terminated in 2005. In 2005, Dar es Salaam Water and Sewerage Corporation (DAWASCO), a public Corporation wholly owned by the Government of Tanzania was formed and took over from City Water. Since then it has been operating the water supply and sewerage system in Dar city to date following NPM principles.

3.2 Level of NPM adoption in NWSC and DAWASCO

Information from performance and management contracts, partnership deed agreements, water policy statements, and findings from 93 respondents was used to determine the level of NPM adoption. The scale for the level of adoption ranges from 0 (no adoption) to 100 (full adoption). The results in table 2 indicate the mean scores for the level of NPM adoption the two water utilities over ten years. The overall mean score was used to determine the three periods; before, transition to and after NPM. An overall mean score above 60% has been interpreted to mean that NPM has been adopted, between 60% and 50% as transition and below 50% NPM not adopted.

Table 2: Level of NPM adoption in NWSC & DAWASCO

REFORM	After NPM			Transition to NPM			Before NPM			
	2009	2008	2007	2006	2005	2004	2003	2002	2001	2000
NWSC	81	80	78	66	56	52	29	9	7	6
DAWASCO	55	51	42	31	18	43	29	4	4	4

The results in table 2 indicate that there is a steady increase in the level of adopting the NPM reforms in the two utilities. NWSC is higher on adopting the reforms that DAWASCO. Indeed while NWSC can be described as being in the after NPM period, DAWASCO can be described as being in the transition to NPM.

3.3 Mean technical efficiencies of NWSC and DAWASCO

We run the data for each year for each case study for 10 years to determine the efficiency scores. Table 3 shows the mean technical efficiency of the two utilities during the after, transition to and before NPM.

Table 3: Annual Technical efficiency for NWSC

REFORM	MEAN ANNUAL DEA EFFICIENCY SCORES FOR YEAR END 30 TH JUNE (VRS, output orientation)									
	After NPM			Transition to NPM			Before NPM			
	2009	2008	2007	2006	2005	2004	2003	2002	2001	2000
NWSC	93	85	87	82	78	64	80	73	68	60
DAWASCO	71	78	80	74	84	84	73	79	73	72

The mean efficiency level for the year end 30th June 2000 for NWSC was 60% while that of DAWASCO was 72%. This means that NWSC and DAWASA in 2000 would be able to increase their outputs by 40% and 28% respectively with the same level of inputs. Ten years later in 2009 the efficiency scores were 93% for NWSC and 71% for DAWASCO.

There was a sharp drop in the technical efficiencies between 2003 and 2004 for NWSC. This could be partially explained by the management contract between OSUL and NWSC that went sour. Interviews with management of Kampala water who were around during OSUL time indicated that the sour relationship between the two parties was caused by limited degree of delegation that was inherent in the management contract, low management incentives that dropped from 25% during the time of the previous operator (KRIP) to 10% with a 7% bonus upon full achievement of performance targets.

On the side of DAWASCO, there is an upward trend especially between 2003 and 2005. This is the period when City water was in charge of delivering water in the Dar region.

3.4 DEA efficiency scores in the before and after NPM situations

The researcher explored the significance of the differences in efficiency after/transition and before the introduction of NPM as indicated in the table 4.

Table 4: DEA mean efficiency scores before and after NPM

Utility	NO.	Mean		sd		t	p
		After/transition	before	after/transition	Before		
NWSC	18	80	64	13.4	26.5	3.16	0.04
DAWASCO	12	75.7	74.6	30.2	32.9	3.63	0.12

As indicated in the table 4, the mean efficiency score after NPM for NWSC was 80, [SD=13.] while the mean before was 64, [SD=26.5]. The difference was significant (t=3.16, p=0.04) at 0.05 level. With DAWASCO the mean score during transition period was 75.7, [SD=30.2], while the mean before was 74.6, [SD=32.9] and the difference was insignificant (t=3.16,p=0.12) at 0.05 level. This implies that NPM

produced significant changes in efficiency for NWSC while the case of DAWASCO, the efficiency difference are a result of other factors rather than NPM.

3.5 NPM dimensions that explain changes in efficiency

In order to obtain the overall contribution of NPM on the efficiency of NWSC and DAWASCO, a two-limit Tobit regression model was used (see Equations 1 and 2). Efficiency scores were regressed against five NPM variables. The variables were: segregation of functions, managerial autonomy, customer orientation, market orientation and accountability for results. Using data of the 30 DMUs a Tobit model was estimated and the results are as shown in the table 4.

Table showing a Tobit estimate of the contribution of NPM on the efficiency of water services

Table 5: Tobit estimate of the contribution of NPM on the efficiency of water services						
NWSC= 19 towns, DAWASCO=13 towns: Two limit Tobit estimate						
	ll(20)	ul(100)				
Log likelihood = 64.27			Number of observations = 32			
			LR chi2(5) = 21.72			
			Prob>chi2 = 0.031			
			Pseudo R2 = -0.24			
Ineff	Coeff	Std Err	t	P> t	[95% Conf Interval]	
Segregation of Functions	2.74	8.34	2.75*	0.00	-4.74 1.59	
Managerial Autonomy	234.23	24.73	2.53*	0.00	-2543 371.	
Customer orientation	4.65	8.43	-0.51	0.42	-32.6 40	18.3
Output orientation	1.67	10.47	3.29**	0.09	1.57 2.78	0.03
Accountability	0.04	0.045	2.44*	0.02	0.02 0.07	0.02
			Se	0.0654	0.0042	(Ancillary parameters)

*significant at 1% level, **significant at 5% level

The results indicate that segregation of functions of functions was significant (t= 0.2.75., p=0.00). This implies the as organisations increase segregation of functions, efficiency increases. Managerial autonomy was also significant (t= 2.52., p=0.00). This implies that as organisations increase managerial autonomy, efficiency increases. Customer orientation was negative and not significant (t= -0.51., p=0.40). This implies that as organisation increase customer orientation, efficiency may actually decrease, though not significantly. Output

orientation was positive but not significant ($t=3.29$, $p=0.09$). This implies that as output orientation increases, efficiency may increase though not significantly. Accountability was positive and significant ($t=2.44$, $p=0.02$). This implies that as accountability increases, efficiency increases, significantly. Generally, major NPM predictors of efficiency are, segregation of functions, managerial autonomy and accountability for results. The overall regression model indicated that NPM significantly ($\chi^2(5)=21.72$, $\text{Prob}>\chi^2 = 0.031$) contributes to efficiency.

5. CONCLUSION

These findings are in agreement with earlier conclusions that autonomy, and accountability for results improve efficiency. For example Emile et al. [6] found a positive relationship between autonomy and efficiency. Most studies at the beginning of the NPM reform were interested in whether increase competition especially in traditionally monopolistic industries would improve efficiency. Indeed the research results of Donahue [36], and Warner and Hedbon [37], confirmed that increased (market orientation) leads to improved service delivery through increased efficiency however, the results of this study have not confirmed this. On customer orientation Ogawa and Tanashi [7] found out that increased customer orientation may encourage inefficiency; this has been confirmed by this study. The overall conclusion is that adoption of NPM dimension of managerial autonomy, segregation of function and accountability for results are likely to improve water utility efficiency in Uganda and Tanzania.

REFERENCES

- [1] Manning N., "The Legacy of the New Public Management in developing countries"; *International Review of Administrative Sciences* Vol. 67, No.4, pp. 297- 312, 2001.
- [2] Hood, C., "A Public Management for All Seasons?" *Public Administration* Vol.69, No.1, 3–19, 1991.
- [3] Pollitt, C., *The Essential Public Manager*. Open University Press, Maidenhead, 2003.
- [4] Walsh, K., *Public Services and Market Mechanisms: Competition, Contracting and the New Public Management*. London: Macmillan, 1995.
- [5] Pollitt, C., and Bouckaert, G., *Public Management Reform: A Comparative Analysis*. Oxford: Oxford University Press, 2004.
- [6] Emile, K., Huberts, L., Hans Van Den Heuvel, *The ethics of New Public Management: is integrity at stake?* PAQ Winter, pp.400-439, 2007.
- [7] Ogawa H., Tanattashi K., "Effect of NPM: Data Envelopment Analysis". *Government Auditing Review* Vol.15, March, 2008.
- [8] Batley, R. *The role of Government in Adjusting Economies: An Overview of Findings*, Birmingham International Development Department, University of Birmingham, 1999.
- [9] Schwartz, K., "The New Public Management: The future for reforms in the African water supply and sanitation sector", *Utilities Policy* Vol.16, No.1, pp.49-58, 2008.
- [10] Weber, M. *From Max Weber*. Translated and edited by H. H. Gerth and C. Wright Mills. New York: Galaxy, 1946.
- [11] Taylor, F.W., *The Principles of Scientific Management*. New York: Harper, 1911.
- [12] Mueller, D. C., "Public choice: a survey" *Journal of Economic Literature* Vol. 14, No.2, pp.395-435, 1976.
- [13] Tullock, G., "The Welfare costs of Tariffs, monopolies & theft". *Western Economic Journal*, Vol. 5, June, pp. 224- 232, 1967.
- [14] Van Dijk M. P., *Managing Cities in Developing Countries; The theory and Practice of Urban Management*, Edward Elgar, Northampton USA, 2006.
- [15] Schwartz, K., "The New Public Management: The future for reforms in the African water supply and sanitation sector", *Utilities Policy*, Vol. 16: No. 1, pp. 49-58, 2008.
- [16] Groot, T., and Budding, T., "New Public Management's current issues and future prospects", *Financial Accountability and Management*, Vol. 24, No.1, pp. 1-13, 2008.
- [17] Tynan, N. and Kingdom, W., *Effective Water Service Provision*, Second Draft, Washington D.C.: World Bank, 2002.
- [18] Farrell, M., "The measurement of productive efficiency". *Journal of the Royal Statistical Society Series A (General)*, Vol. 120, No.3, pp.253–281, 1957.
- [19] Charnes, A., Cooper, W., Rhodes, E., "Measuring the efficiency of decision making units", *European Journal of Operational Research*, Vol. 2, No.6, pp. 429–444, 1978.
- [20] Thanassoulis, E., "The use of Data Envelopment

- Analysis in the Regulation of UK Water Utilities: Water Distribution”, *European Journal of Operations Research*, Vol.126, pp.436-453, 2000.
- [21] Kirpatrick, C., Parker, D., and Zhang, Y-F., (2004). “State versus Private Sector Provision of Water Services in Africa: An Empirical Analysis”, *Working Paper Series*, No.70. University of Manchester, 2006.
- [22] Ndandiko, C., *Private provision of Public services in developing countries?*, University of Twente, The Netherlands, 2010.
- [23] Muhairwe, W. T., *Making Public Enterprises Work: From Despair to Promise: A turn around account*, IWA Publishing, London, 2009.
- [24] Mujwahuzi, M. R., *Drawers of Water II. 30 Years of Change in Domestic Water Use & Environmental Health in East Africa. Tanzania Country Study*. London, IIED, 2002.
- [25] Kjellen, M., “From Public Pipes to Private Hands, water access and Distribution on Dar es Salaam Tanzania”, *PhD Thesis*; Stockholm University, Sweden, 2006.
- [26] Kiwanga, “Evaluation of water supply and sanitation delivery services in Tanzania” *World Water Week*, Peer reviewed workshop; February, 2008.
- [27] Spottiswoode, C., “Improving police performance A new approach to measuring police efficiency”, *Technical Annexes*, Public Service Productivity Panel, 2005.
- [28] Coelli, T.J., Rao, D.S.P., O’Donnell, C.J. and Battese, G.E., *An Introduction to Efficiency and Productivity Analysis*, 2nd ed. Springer, New York, 2005.
- [29] Green, W. H., *Econometric Analysis*, 5th Ed, Prentice Hall, New Jersey, 2003.
- [30] Moore, M., “Public Value as the Focus of Strategy”. *Australian Journal of Public Administration*, Vol. 53, No.3, pp.296–303, 1994.
- [31] De Witte, K., “How to stimulate natural monopolies? The drinking water experience”, *Service Public Federal Finances*, Vol.68, No.1, pp.255-264, 2008.
- [32] Mugisha, S., “Effects of incentive applications on technical efficiencies: Empirical Stance” *World Economic Forum*, 2007.
- [33] Banker, R.D. Charnes, A., & Cooper, W.W., “Some models for estimating technical and scale inefficiencies in data envelopment analysis”. *Management Science*, Vol.30, No.9, pp.1078–1092, 1984.
- [34] MWE - Ministry of Water, Lands and Environment, *Water and Sanitation Sector performance report*. GOU, 1998.
- [35] Mukokoma M.M.N., “Application and effectiveness of New Public Management in National Water and Sewerage Corporation”, *Journal of Science and Sustainable Development*, Vol. 2 No.1, pp.61 – 67, 2009.
- [36] Donahue, J. D., *The privatisation decision: Public ends, private means*. New York: Basic Books, 1989.
- [37] Warner, M., and Hedborn, R., “Local Government restructuring: Privatisation and its alternatives”, *Journal of Policy Analysis and Management*, Vol. 20, No.2, pp.315 – 336, 2001.

Effects of Skewed Bridge Crossing on Afflux

Serter Atabay¹, Kutsi S. Erduran^{1,2} and Galip Seckin³

¹The American University of Sharjah, UAE (satabay@aus.edu)

²University of Nigde, Turkey (kerduran@aus.edu)

³University of Cukurova, Turkey (gseckin@cu.edu.tr)

ABSTRACT

This paper presents the experimental results and findings from investigation of normal bridge crossing and skewed bridge crossing on the water surface elevation at upstream of bridge constriction for subcritical flow. Experiments were performed using a single opening straight deck bridge model with and without piers (DECK) in a two stage channel including various roughness conditions and different types of bridge crossings. Three different skew angles of $\phi = 0^\circ$, $\phi = 30^\circ$ and $\phi = 45^\circ$ were used in this investigation. Bridge crossing was classified as normal crossing when the skew angle is $\phi = 0^\circ$. Experimental investigation showed that the larger the skew of a structure relative to the direction of flow, the larger the backwater effect. It is also concluded that the effects of skewed crossing increase due to present of bridge piers.

Keywords: Bridge afflux, Skewed bridge crossing, Bridge waterways

1. INTRODUCTION

Constriction of the flow in waterways causes a loss of energy which is reflected in a rise in the water surface and in the energy line upstream of the bridge. Bridges can cause a significant obstruction to natural river flow and these results in an increase in backwater level well above the normal level and usually results in flooding. The increase in the water level with respect to the normal level is called the afflux (Figure 1). The afflux depends on many parameters including the bridge width, bridge piers, main channel friction coefficient, floodplain friction coefficient, bridge skew angle, eccentricity, and the flow discharge.

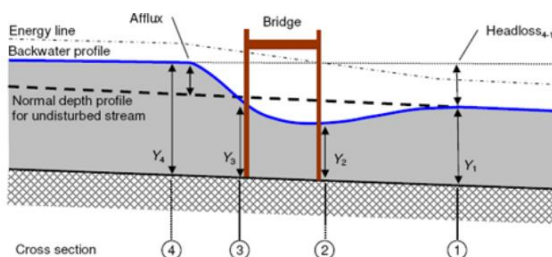


Figure 11: Typical representation of afflux due to bridge crossing [1]

The main purpose of this study is to investigate the effect of skewed bridge crossing on bridge afflux. Figure 12 shows a general layout of a bridge embankment with a skewed crossing and its effect on flood flow. The structure opening normal to flow is b_s , thus making the width normal to flow in the channel as $b = b_s \cos \phi$. The flow along the right hand floodplain or channel is trapped and a super-elevation is built up gradually. Due to this, one side of the opening is sometimes submerged while the other side operates with free flow conditions. In open channel, flow patterns are

not significantly affected by skews of up to 20 degrees [2]. In this study all the experiments were therefore carried out for the bridge models with skewed crossings of 0° , 30° and 45° .

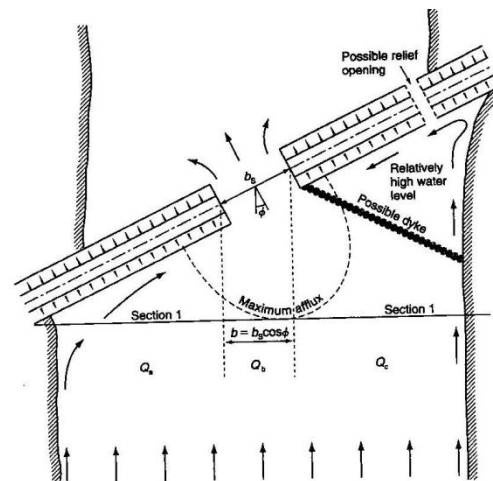


Figure 12: Skewed crossing plan view [3]

In this current study, the effects of skewed crossing on bridge afflux were investigated by comparing the experimental afflux values obtained using the normal bridge crossing ($\phi = 0^\circ$) with those obtained using the skewed crossings ($\phi = 30^\circ$ and $\phi = 45^\circ$).

2. LITERATURE REVIEW

The obstruction of bridge piers to the flow of water has been studied for over 150 years [3]. d'Aubuisson (1840) was one of the earliest researchers who investigate the effects of bridge piers on afflux [4]. This study was followed by Yarnell (1934) who carried out approximately a total of 2600 experiments in laboratory

related to bridge piers that were commonly used in USA [5].

In recent years many researchers investigated the backwater effects around arch and straight-deck bridges in the laboratory and the field [6]. The hydraulic performance of two-small arch bridges during floods at sites that are affected by a backwater from downstream was described by Hamill and McInally [7]. They obtained the coefficients of discharge and equations describing the stage-discharge relationship [6].

HR Wallingford presented reports including a backwater formula called HR arch bridge method based on laboratory experiments and verified with the field data [8]. Kaatz and James (1997) investigated the performance and reliability of different bridge methods [9].

Comprehensive laboratory experiments were recently conducted regarding to the measurement of flow characteristics around a bridge in a symmetrical rigid compound channel at the Hydraulic Laboratory of the University of Birmingham. This study presents the small part of these experimental data, the full description and methodology of which were given by two technical papers presented to JBA Consulting Engineers & Scientists and the Environment Agency (EA): as part of project titled "Scoping Study into Hydraulic Performance of Bridges and other Structures, including effects of blockages, at high flows [10,11]. These experimental data have extensively been used by different researchers [12,13,14].

The effect of skewness on bridge backwater prediction has recently been investigated by Seckin (2007) using the same flume having smooth or rough main channel and flood plains [14].

3. EXPERIMENTAL STUDY

The experiments were performed at the University of Birmingham, UK using a 22-m long, non-tilting compound channel. Channel slope is fixed at 2.024×10^{-3} and channel consists of a main channel and two symmetric floodplains. The flume was 1.213m wide, 0.400m deep and configured into a two-stage channel with a 0.398m wide rectangular main channel and two 0.4073m wide smooth floodplains at an elevation of $h=0.50$ m above the main channel bed [1,10,6].

Full details of the apparatus and experimental procedures are given by many researchers in related studies using the same flume [1,10,6,11]. The experimental apparatus and procedure are therefore only described briefly in this study.

The experiments were conducted in two different phases. During the first phase all the bridge models have a normal crossing ($\square \square \square$) whereas during the second phases all bridge models have skewed crossing ($\square \square \square$ and $\square \square \square$). Typical bridge model that was

used in Phase 1 for this study is shown in Figure 13. The flume has a recirculation system and flow rates were measured by an electro-magnetic flow meter. In order to obtain the backwater, the water surface profiles were firstly measured without any bridge model. The water surface profiles were later measured with the bridge model at the same flow rate. In order to investigate the effects of the bridge piers on afflux the same experiments were conducted with the same bridge model with piers.

Experiments were conducted for different flow discharges. However for each flow discharge the bridge model was replaced into the channel with normal crossing and two different skewed crossing. The water surface profiles were measured using a pointer gauge at 0.10m longitudinal intervals in the region where the bridge was placed. Outside the contraction and expansion length the water surface profiles were measured at 1.0m interval along the channel. The experimental afflux values were manually computed using the actual water surface elevations (with bridge) and normal water surface elevations (without bridge) at the same approach section. It should be noted that all experiments were carried out for low flow conditions (sub-soffit condition) and full details of the experimental results are given by many researchers [1,10,6,11].

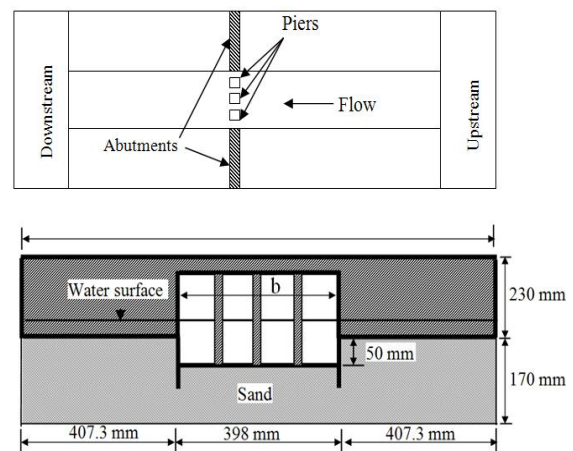


Figure 13: Experimental Bridge model a) Plan for normal crossing b) Cross-section [15]

4. EXPERIMENTAL RESULTS

Experimental results showed that both the skew angle and bridge piers affect the afflux values. Figure 14 clearly shows that the bridge model increases the water surface at the upstream of the bridge constriction. The bridge model with piers results in further increase in the water surface profile. This clearly shows the effect of the piers on the water surface profile. Figure 14 also shows that the flow becomes almost uniform at the downstream of the bridge at approximately 1m downstream of bridge model.

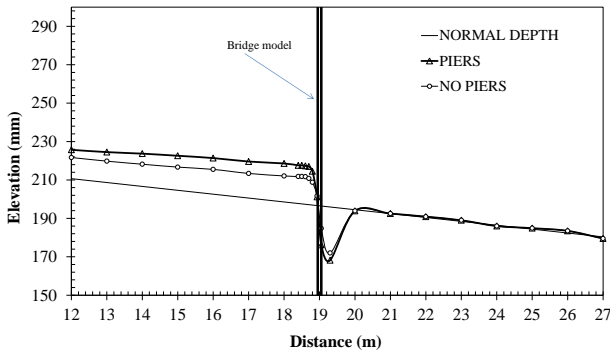


Figure 14: The effect of bridge constriction on water surface profile with and without bridge piers.

Figure 15: The effect of skew angle without bridge piers

Experimental results are also tabulated in Table 4 Table 5 and **Error! Reference source not found.**. The maximum water surface elevations, where the maximum afflux occurs, are shown in Table 4. The effects of bridge models having normal or skewed crossing with and without piers are clearly seen in this Table. It is clear that the bridge model without piers increases the water surface elevations between 16% and 19%. The bridge model with piers additionally increases the water surface elevations by 6% to 9%. Table 2 shows that when the skew angle increases the water surface elevation increases dramatically. The bridge model with the skew angle of 30o increases the water surface elevation by 35% to 43%, while the bridge model with the skew angle of 45o increases the water surface elevation by 43% to 57%. It can also be concluded that as the flow discharge increases the effects of piers and skew angle reduce.

Error! Reference source not found. shows the experimental afflux values which increase by the effects of piers and skew angle. The afflux values also increase by the flow discharges. As anticipated the maximum afflux occurs with the highest flow rate of 34 l/s for the bridge model having skewed angle of 45o.

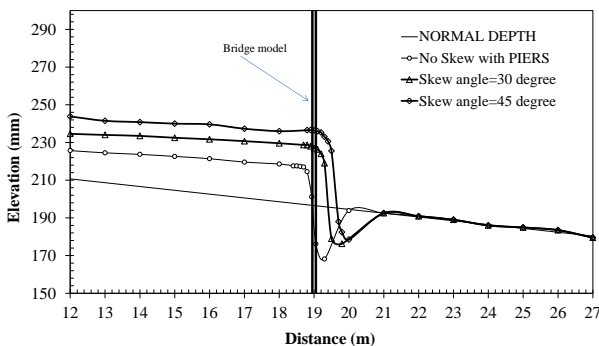


Figure 16: The effect of skew angle with bridge piers

The bridge model without piers increases the water surface elevations between 16% and 19%.

The bridge model with piers additionally increases the water surface elevations by 6% to 9%.

The skew angle increases the water surface elevation increases dramatically. In other word the larger the skew of a structure relative to the direction of flow, the larger the backwater effect.

The afflux values also increase by the flow discharges.

& Figure 16 clearly show that as the skew angle increases the water surface elevation at the upstream of the bridge dramatically increases. This obviously shows the effect of skewed crossing on the afflux values. It should be noted that the results shown in Figure 15: The effect of skew angle without bridge piers

Experimental results are also tabulated in Table 4 Table 5 and **Error! Reference source not found.**. The maximum water surface elevations, where the maximum afflux occurs, are shown in Table 4. The effects of bridge models having normal or skewed crossing with and without piers are clearly seen in this Table. It is clear that the bridge model without piers increases the water surface elevations between 16% and 19%. The bridge model with piers additionally increases the water surface elevations by 6% to 9%. Table 2 shows that when the skew angle increases the water surface elevation increases dramatically. The bridge model with the skew angle of 30o increases the water surface elevation by 35% to 43%, while the bridge model with the skew angle of 45o increases the water surface elevation by 43% to 57%. It can also be concluded that as the flow discharge increases the effects of piers and skew angle reduce.

Error! Reference source not found. shows the experimental afflux values which increase by the effects of piers and skew angle. The afflux values also increase by the flow discharges. As anticipated the maximum afflux occurs with the highest flow rate of 34 l/s for the bridge model having skewed angle of 45o.

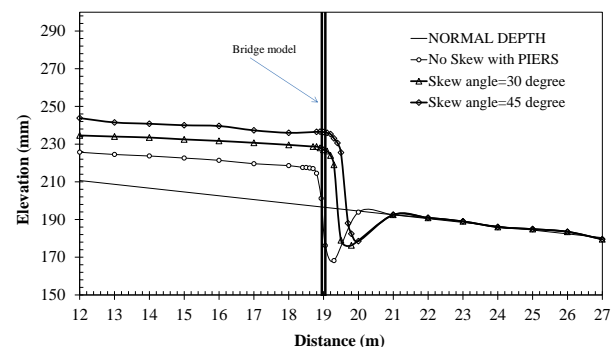


Figure 16: The effect of skew angle with bridge piers

5. CONCLUSION

6. CONCLUSION

The bridge model without piers increases the water surface elevations between 16% and 19%. The bridge model with piers additionally increases the water surface elevations by 6% to 9%. The skew angle increases the water surface elevation increases dramatically. In other word the larger the skew of a structure relative to the direction of flow, the larger the backwater effect. The afflux values also increase by the flow discharges.

are for the bridge model without piers whereas the results shown in Figure 16 are for the bridge model with piers.

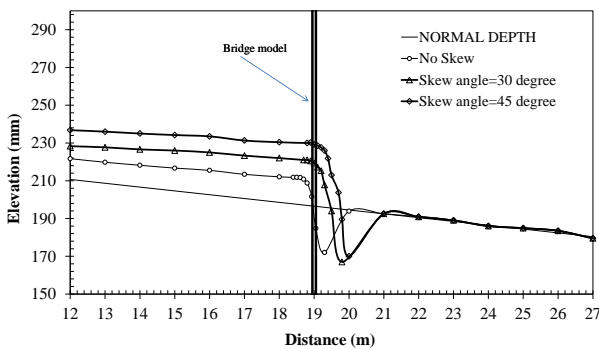


Figure 15: The effect of skew angle without bridge piers

Experimental results are also tabulated in Table 4 Table 5 and **Error! Reference source not found.** The maximum water surface elevations, where the maximum afflux occurs, are shown in Table 4. The effects of bridge models having normal or skewed crossing with and without piers are clearly seen in this Table. It is clear that the bridge model without piers increases the water surface elevations between 16% and 19%. The bridge model with piers additionally increases the water surface elevations by 6% to 9%. Table 2 shows that when the skew angle increases the water surface elevation increases dramatically. The bridge model with the skew angle of 30° increases the

water surface elevation by 35% to 43%, while the bridge model with the skew angle of 45° increases the water surface elevation by 43% to 57%. It can also be concluded that as the flow discharge increases the effects of piers and skew angle reduce.

Error! Reference source not found. shows the experimental afflux values which increase by the effects of piers and skew angle. The afflux values also increase by the flow discharges. As anticipated the maximum afflux occurs with the highest flow rate of 34 l/s for the bridge model having skewed angel of 45°.

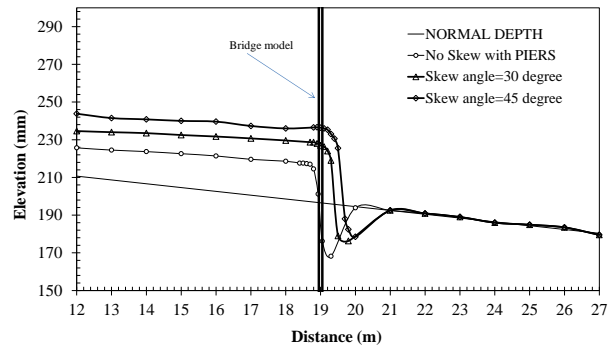


Figure 16: The effect of skew angle with bridge piers

7. CONCLUSION

The bridge model without piers increases the water surface elevations between 16% and 19%. The bridge model with piers additionally increases the water surface elevations by 6% to 9%. The skew angle increases the water surface elevation increases dramatically. In other word the larger the skew of a structure relative to the direction of flow, the larger the backwater effect. The afflux values also increase by the flow discharges.

Table 4: Water surface elevations where maximum afflux occurs

Discharge	Water Depth (in mm)						
	No Bridge	Normal Bridge Crossing		Skewed Bridge Crossing			
		No Piers	PIERS	30° No Piers	30° PIERS	45° No Piers	45° PIERS
18	69.75	83.20	89.10	93.50	102.90	100.70	109.30
21	78.93	93.28	98.98	102.98	112.39	110.68	118.79
24	86.93	103.22	108.73	114.02	122.93	121.62	128.91
30	103.97	122.20	127.70	134.70	143.40	142.30	150.40
34	114.86	133.59	139.89	147.19	154.79	153.69	163.89

Table 5: Percentage increase of water surface elevation

Discharge	Normal Bridge Crossing		Skewed Bridge Crossing			
	No PIERS	PIERS	30° No PIERS	30° PIERS	45° No PIERS	45° PIERS
18	19%	28%	34%	48%	44%	57%
21	18%	25%	30%	42%	40%	51%
24	19%	25%	31%	41%	40%	48%
30	18%	23%	30%	38%	37%	45%
34	16%	22%	28%	35%	34%	43%

Table 6: AFFLUX values (in mm)

Discharge	Normal Bridge Crossing		Skewed Bridge Crossing			
	No PIERS	PIERS	30° No PIERS	30° PIERS	45° No PIERS	45° PIERS
18	13.45	19.35	23.75	33.15	30.95	39.55
21	14.36	20.05	24.06	33.46	31.76	39.86
24	16.30	21.81	27.09	36.01	34.69	41.99
30	18.23	23.73	30.73	39.43	38.33	46.43
34	18.73	25.03	32.34	39.94	38.84	49.03

REFERENCES

- [1] S. Atabay, "Accuracy of the ISIS bridge methods for prediction of afflux at high flows.," *Water and Environment Journal*, pp. 22 (1), 64–73., 2008.
- [2] J. N. Bradley, "Hydraulics of bridge waterways: Hydraulic design," Office of Engrg U.S. Dept. of Transp., Federal Highway Administration, , Washington, D.C, Series no. 1. 2nd Ed., 1978.
- [3] Les Hamill, *Bridge Hydraulics*. London, UK: E & FN SPON, 1999.
- [4] Aubuisson de Voisins, J. F. D, *Traite d'hydraulique* ("Treatise on Hydraulics"), , 2nd ed., Levrault & Cie Pitois, Ed. Paris, 1840.
- [5] D. L. Yarnell, "Bridge piers as channel Obstructions.," U. S. Department of Agriculture, Washington D. C, Technical Bulletin 442, 1934.
- [6] Seckin, G., and Atabay, S., "Experimental backwater analysis around bridge waterways.," *Canadian Journal of Civil Engineering*, pp. 32 (6): 1015–1029, 2005.
- [7] Hamill L., and McNally G. A., "Hydraulic performance of two arch bridges during flood," *MUNIC ENG (INST CIV ENG)*., vol. Vol. 7, no. 5, pp. 241-256, 1990.
- [8] P. M. Brown, "Afflux at arch bridges," HR Wallingford, UK, Report SR 182, 1988.
- [9] Kaatz, K.J., and James, W.P., "Analysis of alternatives for computing backwater at bridges," *Journal of Hydraulic Engineering, ASCE*, vol. 123, pp. 784–792, 1997.
- [10] Atabay, S. and Knight, D.W., "Bridge afflux experiments in compound channels.," The School of Civil Engineering, The University of Birmingham, UK, Birmingham, UK, Report Supplied to JBA Consulting, , 2002.
- [11] Seckin, G., Knight, D.W., Atabay, S. and Seckin, N., "Bridge afflux experiments in compound channels.," The University of Birmingham, Birmingham, UK., Technical Paper Presented for JBA Consulting Engineers and Scientists and the Environment Agency, 2004.
- [12] AEHR, "Hydraulic performance of river bridges and other structures at high flows, Phase 2: Afflux Estimator Hydraulic Reference," JBA Consulting, Skipton, Environment Agency R&D Project W5A-065, 2006.
- [13] Mantz, P.A. and Benn, J.R, "Computation of afflux ratings and water surface profiles,"

Proceedings of the Institution of Civil Engineers, Water Management, vol. 162, no. 1, pp. 41-55, 2009.

- [14] G. Seckin, "The effect of skewness on bridge backwater," *Canadian Journal of Civil Engineering*, vol. 34, pp. 1371–1374, 2007.

- [15] Atabay S., Erduran K. S., and Seckin G., "Sustainable bridge pier shapes for flood management," in *International Symposium on Sustainable Systems and the Environment, ISSE'11*, Sharjah, UAE, 2011.

Assessment of Runoff Potential for Water Harvesting in Central Butana Rangeland, Sudan

Elsadig Ahmed Elfaki¹, A.M. Adeeb², Slim Saïdi³ & Alexandre Ickowicz³

¹Department of Agric. Engineering, Faculty of Agric. Sciences, University of Gezira, P. O. box 20, Wadmedani, Sudan. (sadigelfaki@hotmail.com).

²Water Management & Irrigation Institute, University of Gezira, P. O. box 20, Wadmedani, Sudan. (amadeeb@yahoo.com).

³Centre de coopération Internationale en Recherche Agronomique pour le Développement (CIRAD), Campus international de Baillarguet 34398, Montpellier, Cedex 5, France. (alexandre.ickowicz@cirad.fr), (slim.saidi@libertysurf.fr).

ABSTRACT

Global climate change and water shortage are just two looming threats to our way of life in the arid and semi-arid areas. Estimation of direct surface runoff in a watershed is necessary for planning, designing and environmental impact analysis of water resources management projects. The standard Soil Conservation Service – Curve Number is a versatile and widely used procedure for runoff estimation. This model computes direct runoff through empirical equations that requires rainfall and a watershed coefficient data. The watershed coefficient, known as the runoff curve number (CN), represents the runoff potential of the land cover soil complex. Butana rangeland is located in Eastern Sudan and considered as one of the best grazing areas. Due to rain variability and uneven distributions of rains, the area suffers from severe shortage of water which reflects on the quantity and quality of biomass production and drinking water. The runoff potential of the central Butana rangeland was evaluated and assessed through Curve Number model for better management of this rangeland which faces a severe water shortage problem during dry season. This potential of runoff water can be harvested either in the soil profile to improve biomass production or can be stored in artificial ponds for drinking water. Rainfall data, as input, was taken from six rain gauges installed in this area for the rainy season of 2006 and 2007. Landform, drainage pattern, slope, vegetation and land use/land cover were precisely mapped by the mean of perpendicular vegetation index (PVI), calculated from Spotview satellite scene and field survey data, and digital elevation model data. Soil units were digitized and saved in GIS database and intersected with other watershed characteristics. The model was run and the result shows big variation of runoff depths, but the average potential runoff depth in the study area, which covers 3600 km², was found 52 mm yr⁻¹. Hence, the total runoff volume was estimated for the whole study area as 187.2 x 10⁶ m³ annually.

Key words: Butana Rangeland, GIS, Hydrological Models, Curve Number Model

1. INTRODUCTION

Butana area lies in the central clay plains of Sudan. It is situated between the rivers of Rahad, Blue Nile, Nile and Atbara with approximate total area of 120 000 km². The area is located in the Sahel zone and determined by climatic and ecological transitions from the savannah in the south to the arid Sahara in the north (Akhtar, 1994). Based on long-term averages, the area is marked by annual precipitation from less than 50 mm in the North (Atbara) to 600 mm in the South (Gedarif) (Oliver, 1965). Generally rainfall is characterized by uneven distribution and long dry spells that affect crops and range vegetation at their critical growth and filling stages which leads immediately to a significant reduction in the total production and productivity of the area. There is a great potential of water harvesting as a methodology to overcome the problem of water shortage due to the long dry spells occurring from the high variability of rainfall in the arid regions of central Butana in Sudan. Water harvesting is one such technology and is based on the collection and concentration of surface runoff for cultivation before it reaches seasonal or perennial streams (Reij *et al.*, 1988). Surface runoff information is required for watershed management purpose. The *in situ* measurement of

runoff is considered more accurate but cannot be operated anytime and anywhere as required.

This conventional measurement is also expensive, time-consuming and difficult. Therefore, the accurate surface runoff modelling developed can serve this purpose with more convenient and less time consuming. With the advent of spatially distributed hydrologic models, it is possible to model hydrologic and related processes and their interactions with topography, vegetation, soils and climate to better model our environment. A hydrological model is a mathematical simulation of the complex hydrological cycle (Athanasios *et al.*, 2006), and is a powerful technique in hydrological system investigation for both research hydrologists and practicing water resources engineers involved in the planning and development of integrated approaches for the management of water resources (Webler and Tuler, 1999). Use of Remote Sensing (RS) and Geographic Information System (GIS) helps to spatially integrate all the parameters of the model (Gangodagamage and Agrarwal 2001).

Selection of a rainfall-runoff model is a compromise between model complexity and available input data. While more complex models should better represent the

physical processes, the assumption that they lead to more reliable results has been questioned (Loague and Freeze, 1985). The standard Soil Conservation Service – Curve Number model (SCS-CN) (USDASCS, 1972), also known as the hydrologic soil cover complex method, is a versatile and widely used procedure for runoff estimation and its one of the most widely used hydrological model. This method includes several important properties of watershed namely soil's permeability, land use and antecedent soil water conditions which are taken into consideration. No other rainfall runoff model has been used as successfully or as often on ungaged rangeland catchments as the CN (Graf, 1988). Tauer and Humborg (1992) used Remote Sensing (RS) data and a GIS to determine the potential sites for water harvesting, the surface runoff was estimated for the drainage basin during the wet season to determine the potential water harvesting areas using Landsat-TM and/or SPOT data combined with ground truth observations. A major limitation of the curve number method is that rainfall intensity and duration are not considered, only total rainfall volume.

The objective of this study is to simulate the surface runoff volume of central Butana watersheds using grid-based Curve Number (CN) method for better planning of water harvesting projects and to determine potential sites of water harvesting. In this method, watershed characteristics are considered to be spatial heterogeneity.

2. MATERIALS AND METHODS

2.1 Location

This study covers the central area of greater Butana in Sudan, which administratively belong to Gezira State and located between latitudes 14° 32' and 15° 17' N and longitudes 32° 21' and 34° 18' E as shown in figure (1).

2.2 Soil Map and Hydrological Soil Group (HSG)

The soil map of central Butana rangeland was acquired from Agricultural Research Station (ARC) and digitized in GIS and the Hydrological Soil Group (HSG) was determined according to soil characteristics. SCS has classified all soils into four hydrologic groups; these have been given symbols of A, B, C and D (Dingman, 1994). The classification is based on the infiltration rate which is obtained for a bare soil after prolonged wetting. The characteristics of these four groups are summarized in table (1).

2.3 Landuse and Vegetation Map

Remote sensing is a major source of information required for the study of landscape, landuse and vegetation development (Kumar, 2001). The Perpendicular Vegetation Index (PVI), proposed by Richardson and Wiegand (1977) is an efficient vegetation index for landuse discrimination in dry areas. Remote sensing data (SpotView), dated 5/10/2006, coupled with ground vegetation survey was used to determine the different classes of land use and land cover in central Butana. Spectral reflectance of different landuse and vegetation cover in eighteen field survey points covered by the satellite image was extracted from the image and groups the vegetation units by the mean of PVI.

2.4 Runoff Estimation

The standard Soil Conservation Service - Curve Number model (SCS-CN) (USDA-SCS, 1972) is based on the following relationship between rainfall depth, P , in millimetres, and runoff depth, Q , in millimetres as shown in equation (1).

$$Q = \frac{(P - 0.2S)^2}{(P + 0.8S)} \quad (1)$$

$$(Q = 0, IF, P < 0.2S)$$

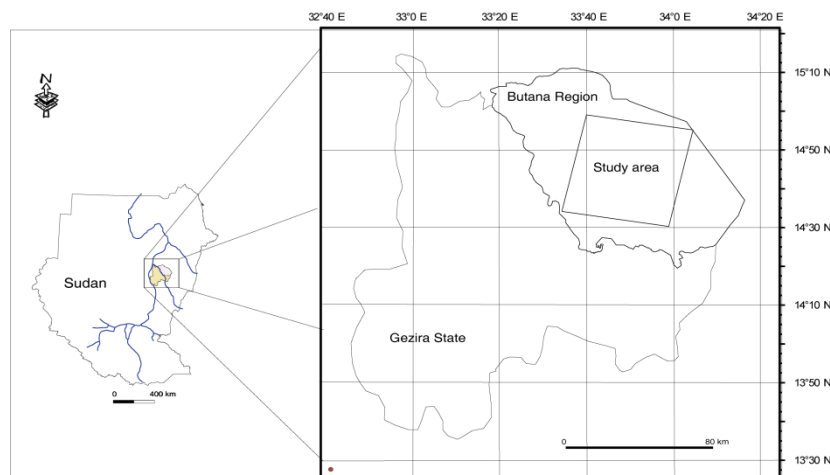


Figure 1: Location of Butana Area

The potential maximum retention, S , in millimetres, represents an upper limit of the amount of water that can be abstracted by the watershed through surface storage, infiltration, and other hydrologic abstractions. For convenience, S is expressed in terms of a curve number (CN) as shown in equation (2).

$$S = \frac{25400}{CN} - 254 \quad (2)$$

CN is a dimensionless watershed parameter ranging from 0 to 100. A CN of 100 represents a limiting condition of a perfectly impermeable watershed with zero retention and thus all the rainfall becoming runoff; on the other hand CN of zero conceptually represents the other extreme, with the watershed abstracting all rainfall with no runoff regardless of the rainfall amount.

Table 1: Hydrologic Soil Groups

Soil Group	Characteristics
A	Low overland flow potential, High minimum infiltration capacity even when thoroughly wetted (> 0.76 cm/h), Deep, well to excessively drained sands and gravel
B	Moderate minimum infiltration capacity when thoroughly wetted (0.13-0.76 cm/h) Moderately deep to deep, Moderately to well drained, Moderately fine to moderately coarse grained (e.g. sandy loam)
C	Low minimum infiltration capacity when thoroughly wetted (0.13-0.38 cm/h) Moderately fine to fine grained soils or soils with an impeding layer (fragipan)
D	High overland flow potential: Very low minimum infiltration capacity when thoroughly wetted (< 0.13cm/h) Clay soils with high swelling potential, Soils with permanent high water table, Soils with a clay layer near the surface, Shallow soils over impervious bedrock.

Source: (Dingman, 1993)

Table 2: Runoff Curve Numbers

Land Use, Crop, and Management	Hydrologic Soil Group			
	A	B	C	D
Row Crops, poor management	72	81	88	91
Row Crops, conservation management	65	75	82	86
Small Grains, poor management	65	76	84	88
Small Grains	61	73	81	84
Meadow	55	69	78	83
Pasture, permanent ,moderate grazing	39	61	74	80
Woods, permanent, mature, no grazing	25	55	70	77
Roads, hard surfaces and roof areas	74	84	90	92

Source: (USDA-SCS, 1972).

3. RESULTS AND DISCUSSION

3.1 Land use and Vegetation Pattern

One of the prime prerequisites for better use of land is information on existing land use patterns and changes in land use through time. Land use and land cover change has been recognized as an important driver of environmental change on all spatial and temporal scales, which contributes significantly to earth atmosphere interactions, forest fragmentation, and biodiversity loss (Turner *et al.*, 1994). It has become one of the major issues for environmental change monitoring and natural resource management.

A visual interpretation of PVI map was done to differentiate between different landuse type and vegetation units. Different values and classes of PVI represents different land use pattern. The lowest value of PVI was found in water bodies (haffirs), which cover approximately 0.01% of the total area and determined precisely by checking all the pixels cover all around haffirs. The next class to water is bare soil around water points and in the high pressure grazing areas. The third class is rangeland vegetation from which the extreme low value of PVI represents the degraded and poor condition of rangeland around water points and most of the high land and the high value is for good condition rangeland in water courses and adjacent to rainfed agriculture sector. The last PVI class represents the rainfed agriculture and reserved forests. The wide range of this class started from sparse sorghum fields to well mechanize and water managed fields. The reserved forest, which occupied the south western part of the study area, showed the same value of rainfed agriculture PVI and precise mapping of these forests was done by visual interpretation. Figure (2) explained that there are three main classes of land use in central Butana. Crop land, shown in green colour, comprises the large portion of the study area with the total area of 1695 km² (47.8%). The main crop grown in this area is sorghum, which constitute the main source of food for all people living in Butana. Beside that, the crop residue is kept as fodder for animals in the summer season. The second landuse type is rangeland which covers approximately 44.7% of the total area with a surface area of 1583 km². The last landuse type is forest, shown in brown and located in the south western side of the study area and covers an area of 264 km² (7.5%). The forests are dominant on red sandy clay soil (goz) and the dominant trees are Seyal (*Acacia tortilis*), while sparse trees of Kitr (*Acacia mellifera*) are found on clay soils.

3.2 Potential Runoff Estimation

Spatial information on runoff coefficient, slope and drainage plays a critical role in site selection for runoff harvesting/recharging structures. Satellite remote sensing techniques in conjunction with landform-soil vegetation relationships and ground truth are popular for locating suitable sites for the construction of water harvesting structures and soil and water conservation measures.

3.2.1 Hydrological Soil Group (HSG) and Curve Number (CN)

Hydrological soil groups (HSG) of central Butana were determined on the basis of information from the basic soil map of Butana. The soil map was digitized in GIS and HSG was determined according to soil characteristics in table (1). Four groups of HSG are found in Butana area, namely; A, B, C and D (Ramakrishnan *et al.*; 2008). The results of HSG of the Central Butana rangeland indicated that the HSG (C) occupied almost 60% of total area followed by HSG (D), which covers 30% and HSG (B) and HSG (A) are 9% and 1%, respectively. Information on land use and pattern of their spatial distribution is one of the criteria used for selecting a curve number (CN) (Ramakrishnan *et al.*; 2008). In the present study, the SpotView satellite data of the rainy season 2006 coupled with ground vegetation survey was used for the generation of land use categories. Spectral reflectance of the dominant vegetation species in the eighteen field survey points covered by the satellite image was extracted from the

image and grouped in the vegetation units. They are then evaluated to make sure that there is a suitable discrimination of individual classes. As the SCS-CN method is very sensitive to CN value, accurate determination of this parameter is very important (Ramakrishnan *et al.*; 2008). In each watershed, the combination or intersect between HSG and land use was assigned a special CN value, ranging from 0 to 100, extracted from table (2). The maximum value of CN was found to be 88, while the minimum was 25 and the average value was 75. The result of the CN showed that 31.5 % of the CN values in the study area are found within the range of 80 to 88, 52.6% in the range of 70 to 76, and only 0.1% are between 60 to 69 and the rest of the area is less than 60. Forty percent of the area is dominated by CN value of 74, which represents in most cases the rangeland area around and in between the rainfed agriculture, while 22.4% of the area was covered by CN value 84, which represent the high potential runoff area used in rainfed agriculture. The rest values of CN are less contributing and they are less than 10% of all values.

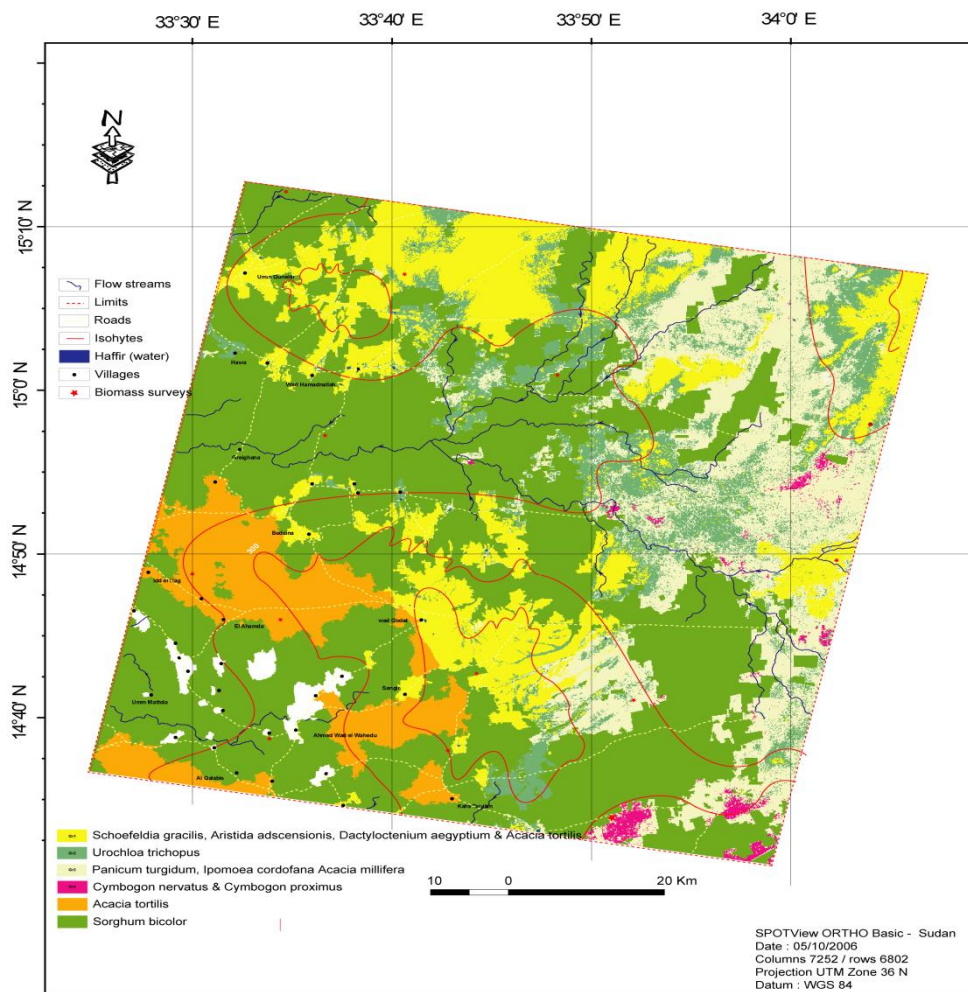


Figure 2: Land cover and Landuse Map of Central Butana

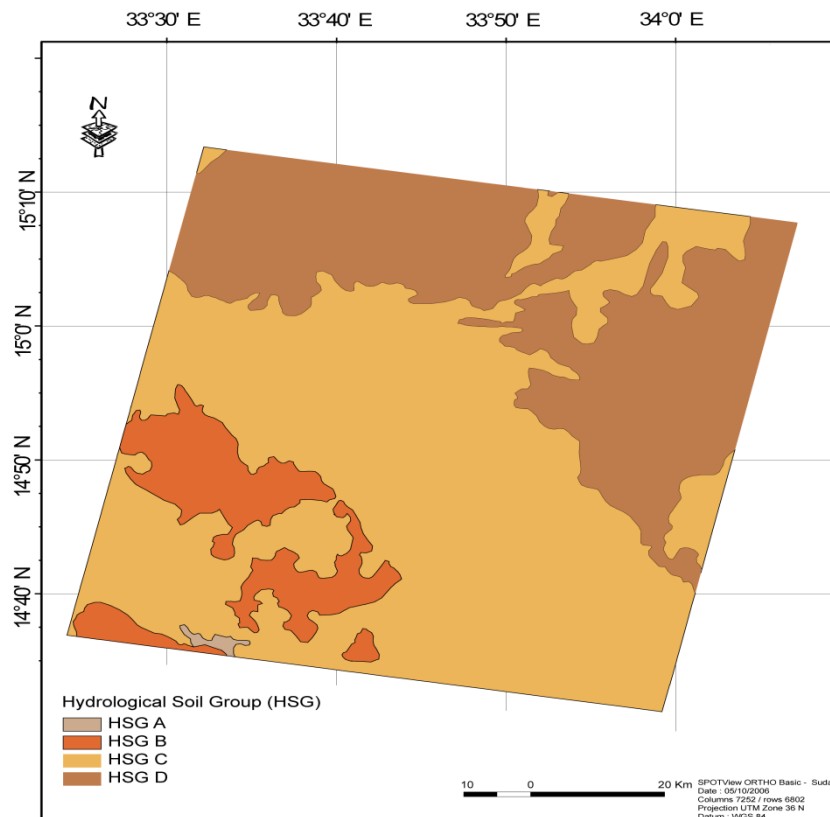


Figure 3: Hydrological Soil Group (HSG) of Central Butana Rangeland.

3.2.2 Annual Runoff Potential

The standard SCS-CN method is based on the relationship between rainfall depth, P , in millimetres, and runoff depth, Q , in millimetres as shown in equations (1). The result of potential runoff depends on CN values, which is a combination of land use and soil type. The high CN values produce high amount of runoff and vice versa. In addition to CN variation, spatial variability of rainfall over the area was incorporated for accurate runoff prediction. Woodward and Cronshey (1990) noted that the part of the drainage basin, which is represented by another rain gauge, significantly affects the runoff distribution under uniform rainfall conditions.

The spatial distribution of annual runoff depths was displayed in figure (4) which showed big variation from the minimum annual potential runoff of 13 mmyr^{-1} in the forest to the maximum amount of 64 mmyr^{-1} in some areas usually occupied by rainfed agricultural activities.

According to Blokhuis (1993), who noted that the reddish sandy clay soils (goz) showed an open growth of trees with much different types of *Acacia* species mainly seyal (*Acacia tortilis*) and sparse shrubs and grass covered surface, the lowest annual runoff potential was observed in the forest area which dominates the reddish sandy clay soils and produced the minimum potential of runoff (13 to 32 mmyr^{-1}) as shown in figure (4). This was due to the fact that the sandy soil shows

high infiltration rate values and also the dense canopy of trees increases the interception and water losses through evaporation. The rainfed agriculture areas in the central part and the open rangeland in the centre, north and east, dominated by clay soils, produce high to moderate runoff potential (61 to 64 mmyr^{-1}).

On the basis of runoff coefficient, which is a ratio between the rainfall and runoff (Ramakrishnan et al; 2008), the results showed these runoff coefficient classes and grouped them into three broad classes such as high ($>25\%$), moderate (20 to 25%) and low ($<20\%$). It is evident from these figures that only 16% of the study area falls under the high runoff potential class. The moderate and low runoff coefficient classes occupy 57% and 27% of the total area, respectively.

The average potential runoff depth in the study area, which covers 3600 km^2 , is 52 mm. Hence, the total runoff volume was estimated for the whole study area as $187.2 \times 10^6 \text{ m}^3$ annually. This water is sufficient to support 10 millions animal units and human for nine months at a consumption rate of 30 litres per individual per day and a loss of half the quantity by evaporation and deep percolation. If this water is captured it is sufficient to cause dramatic improvements in the livelihood of Butana people and the herder community. These results give positive indications to perfect and beneficial application of water harvesting techniques to maximize the use of scarce water resources. The high and moderate runoff coefficients areas were almost 73% of the total area and water harvesting application in

these areas can produce appreciable amount of stored water that can be used in either short term measures of drought mitigation for drinking water or improving pasture productivity or in long term measures in

planning and constructing small dams and reservoirs for supplementary irrigation.

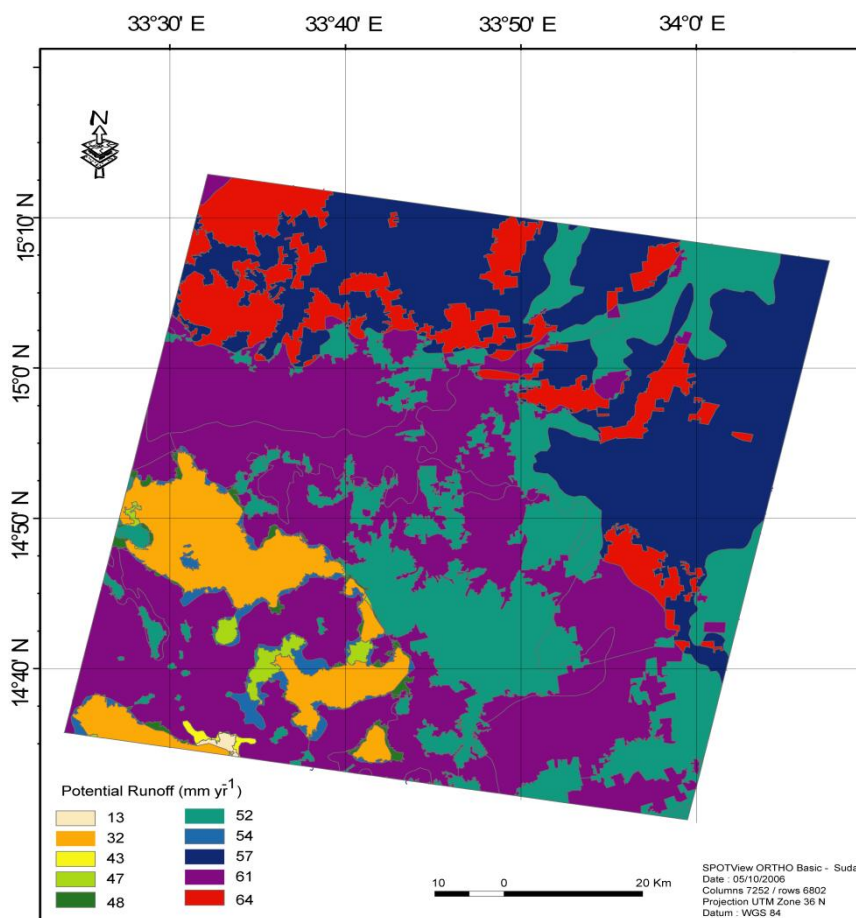


Figure 4: Runoff Potential of Central Butana Rangeland

REFERNCES

- [1] Akhtar, M. (1994). Geo-Ecosystems and Pastoral Degradation in the Butana. *Animal Research and Development*. (39): 17-26.
- [2] Athanassios, B., Evangelos, B. and Maria, M. (2006). Rainfall-Runoff Modelling For an Experimental Watershed of Western Greece Using Extended Time-Area Method and GIS. *Journal of Spatial Hydrology* (6): 93-104.
- [3] Blokhuis, W. A. (1993). Vertisols in the Central Clay Plains of Sudan / W. A. Blokhuis-Iii Thesis Wageningen, The Netherland.
- [4] Dingman, L. S. (1994). *Physical Hydrology*, Prentice-Hall, Inc, New Jersey, USA.
- [5] Gangodagamage, C., and Agrarwal, S. P. (2001) Hydrological Modelling Using Remote Sensing and GIS, 22nd *Asian Conference On Remote Sensing*, 5-9th November, Singapore, Organised By Centre For Remote Imaging, Sensing and Processing, National University Of Singapore.
- [6] Graf, W. L. (1988). *Fluvial Processes in Dryland Rivers*. New York, N. Y.: Springer Verlag.
- [7] Kumar, L. (2001). Imaging Spectrometry and Vegetation Science, in *Imaging Spectrometry. Basic Principles and Prospective Applications*, F. Van de Meer and S.M. de Jong, (Eds). Kluwer Academic Press: Dordrecht. pp. 111-155.
- [8] Loague, K. M., and Freeze R. A. (1985). A comparison of rainfall runoff modeling techniques on small upland catchments. *Water Resources Research* 21(2): 229-248.
- [9] Oliver, J. (1965). Evaporation Losses and Rainfall Regime in Central and Northern Sudan. *Weather* (20):58-64.
- [10] Ramakrishnan, D., Durgarao, H.V., Tiwari, K.C. (2008). Integrated approach of Remote sensing and GIS in delineation of sites for water harvesting

structures, Kali watershed, Dohad, Gujarat, India. *Geocarto International*. 23(2): 95–108.

- [11] Reij, C., Mulder, P. and Begemann, L. (1988). Water Harvesting For Plant Production. World Bank Technical Paper No. 91, Washington D.C., USA.
- [12] Richardson, A. J. and Wiegand C. L. (1977). Distinguishing Vegetation from Soil Background Information. *Photogrammetric Engineering and Remote Sensing*. (43): 1541-1552.
- [13] Schultz, G.A., and Engman, E. T. (2000). Remote Sensing In Hydrology and Water Management, Springer, Berlin, 483, Germany.
- [14] Tauer, W. and Humborg, G. (1992). Runoff Irrigation in the Sahel Zone: Remote sensing and GIS for Determining Potential Sites Technical Centre for Agric. and Rural Co-operation, the Netherland, GIS Publications.
- [15] Turner, B. L., Meyer, W. B. and Skole, D. L. (1994). Global Land-use/Land-cover Change: Towards an Integrated Study, *Ambio*, 23(1): 91-95.
- [16] USDA, SCS (United States Department of Agriculture, Soil Conservation Service). (1972). National Engineering Handbook. Hydrology Section 4. Chapters 4-10. Washington, D.C.: USDA.
- [17] Webler, T. and Tuler, S. (1999). Integrating Technical Analysis with Deliberation in Regional Watershed Management Planning, Applying the National Research Council approach. *Policy Studies Journal* 27(3):530-543.
- [18] White, Dale (1988). Grid-based Application of Runoff Curve Number. *Journal of Water Resources Planning and Management*, ASCE 114(6): 601-612.
- [19] Woodward, D. E. and Cronshey, R. D. (1990) Discussion of "Grid based application of runoff curve numbers" by D. White. *Journal of Water Resouces. Planning and Managment*. ASCE 116(6), 842

Effect of Alum Addition on the Treatment Efficiency of Cloth-Media Membrane Bioreactor

Saber A. El-Shafai*; Waleed M. Zahid

Prince Khalid Bin Sultan Chair for Water Research, Civil Engineering Department, College of Engineering, King Saud University, P.O. Box 800, Riyadh 11421, Saudi Arabia, E-mail: selshafai@ksu.edu.sa; wmezahid@ksu.edu.sa; pkc-wreuse@ksu.edu.sa

Oral presentation (Science in Water Reclamation and Reuse)

*Civil Engineering Department, College of Engineering, King Saud University, P.O. Box 800, Riyadh 11421, KSA

E-mail: selshafai@ksu.edu.sa; Tel: +966-1-4695261; Fax: +966-1-4695263

ABSTRACT

This research studied the effect of alum addition on the treatment efficiency of cloth-media membrane bioreactor treating municipal wastewater. Physico-chemical parameters of the treated effluents in the control reactor (R1) and reactors receiving 7.5 (R2) and 15 mg $Al_2(SO_4)_3/L$ (R3) meet Saudi and Egyptian water-reuse quality criteria for unrestricted irrigation. At Mixed Liquor Suspended Solids of 3.5 g/L and permeate flux of 16.3 L/m².h, the addition of alum enhances phosphorous removal from 45% in R1 to 58 and 69% in R2 and R3, respectively. The addition of alum did not affect the other treatment parameters which exceed 99% for turbidity, TSS and ammonia, and 97% for TKN in all reactors. Study of particle size and sludge volume index (SVI) indicates that the addition of alum may have indirect effect which inhibits or delays growth of filamentous bacteria in the reactors. The results show that the best range for the particle size which reflects mostly good settling properties is between 35-55 μm as minimum value and 240-290 μm as maximum value.

Keywords: alum, cloth-media, membrane bioreactor, municipal, wastewater, particle size, sludge volume index.

1. INTRODUCTION

Membrane bioreactor (MBR) is combination between biological activated sludge process and membrane filtration where membrane replaces the final clarifier for separation of active biomass from the treated effluent. The most promising advantages of MBR over the conventional activated sludge are small system footprint and reactor requirements, high effluent quality, good disinfection capability, higher volumetric loading rate and less sludge production (Scholz and Fuchs, 2000; Holler and Trösch, 2001; Massé et al., 2006; Guo et al., 2008; Yang et al., 2009). The cost of the membrane bioreactor and membrane fouling hinder the widespread application of the MBR in municipal wastewater treatment (Xu et al., 2003). Chemical coagulations have been used to enhance sludge characteristic and control membrane fouling (Song et al., 2008; Wu et al., 2006). For membrane materials, low cost cloth-media membranes have been evaluated and proposed for municipal wastewater treatment (Zahid and El-Shafai, 2010). The aim of this research is to study the effect of alum addition on the treatment efficiency of cloth-media membrane bioreactor. Effects of alum on sludge characteristics and membrane fouling were also investigated.

2. MATERIAL AND METHODS

Experiment was carried out at the wastewater treatment plant of King Saud University. The experiment extended for 30 days with intensive sampling and analysis program. Three cloth-media membrane bioreactors (R1, R2 and R3) were used. Each system consists of an aeration tank with float valve, membrane module connected with suction pump, aeration device, pressure gage and treated effluent receiving tank. In case of reactor 2 and reactor 3 there were a coagulation unit for each including storage tank with magnetic stirrer and coagulant dosing pump. Each reactor has 43.7 litre total working volume, 39.4 litre effective working volume and membrane module with 4.3 litre volume and 0.30 m² effective filtration area. At start-up, the reactors were fed with activated sludge at 3.5 g/L while estimated permeate flux was 16.3 L/m².h with 30 minutes relaxation period per day. The reactors were operated at 26.3 days sludge residence time. Air compressor was used to supply oxygen at the base of the membrane modules at 1.2 m³/m².h using air flow meters and control valves. R1 represents control without alum addition while R2 and R3 were supplied with 7.5 and 15 mg $Al_2(SO_4)_3/L$, respectively. All physico-chemical analyses were carried out according to APHA 2003 using HACH reagents. Particle size analysis of sludge was carried out using Microtrac S3500. One-way ANOVA was used for statistical analysis.

3. RESULTS AND DISCUSSION

Characteristics of the raw wastewater and treated effluents from the reactors are shown in Table 1 while percentages removal of main parameters, are depicted in Table 2. Physico-chemical parameters of the treated effluents meet Saudi and Egyptian water-reuse quality criteria for unrestricted irrigation. There are no

significant differences between the effluents except for COD and phosphorous. Addition of alum significantly reduces the phosphorous in the treated effluent of R2 and both phosphorous and COD in the treated effluent of R3. Statistically, the addition of alum significantly enhances phosphorous removal efficiency in R2 and R3 but did not affect the removal efficiency of COD, turbidity, TSS, ammonia and TKN.

Table 1: Characteristics of raw wastewater and effluents

Wastewater sample	Raw	Reactor1	Reactor 2	Reactor 3	
Parameter	Unit				
Temperature	°C	33-37	28-31	28-31	28-31
pH	-	7.61-8.38	7.15-7.70	7.13-7.52	7.14-7.49
Dissolved oxygen	mgO ₂ /L	0.32 ±0.21	4.18 ±0.96 ^a	4.15 ±0.79 ^a	3.69± 0.88 ^a
Chemical oxygen demand	mgO ₂ /L	377± 109	15.3 ±3.4 ^a	14.2 ±2.9 ^{ab}	12.9 ±2.4 ^b
Turbidity	NTU	115 ±119	0.44 ±0.18 ^a	0.86 ±0.65 ^b	0.42 ±0.22 ^a
Total suspended solids	mg/L	140 ±73	1.07± 0.36 ^a	1.76 ±1.02 ^b	1.03 ±0.45 ^a
Ammonia nitrogen	mgN/L	30.9 ±2.8	0.28 ±0.42 ^a	0.17 ±0.13 ^a	0.13 ±0.06 ^a
Nitrate nitrogen	mgN/L	0.17 ±0.03	7.9± 2.5 ^a	7.3 ±1.9 ^a	7.9 ±2.1 ^a
TKN	mgN/L	45.4 ±6.1	1.15 0.39 ^a	0.99 ±0.30 ^a	1.12 ±0.36 ^a
Total phosphorous	mgP/L	6.42 ±1.46	3.35 ±0.22 ^a	2.57 ±0.27 ^b	1.93 ±0.22 ^c
total alkalinity	mgCaCO ₃ /L	378 ±34	113± 15 ^a	106 ±16 ^{ab}	97 ±24 ^b

In the same row similar superscript letters for effluents of the reactors indicate there is no significant difference (p=0.05)

Table 2: Efficiency of the treatment reactors

Treatment parameter	Treatment reactor		
	Reactor 1	Reactor 2	Reactor 3
Chemical oxygen demand	95.6 ±1.2 ^a	96.1 ±1.1 ^a	96.4 ±1.0 ⁱ
Turbidity	99.4 ±0.6 ^a	99.1 ±1.0 ^a	99.6 ±0.5 ^a
Total suspended solids	99.1 ±0.6 ^a	98.5 ±1.1 ^a	99.1 ±0.5 ^a
Ammonia nitrogen	99.3 ±1.1 ^a	99.4 ±0.5 ^a	99.6 ±0.5 ^a
TKN	97.4 ±1.0 ^a	97.9 ±0.8 ^a	97.4 ±0.8 ^a
Total phosphorous	45.2 ±13.8 ⁱ	57.8 ±12.0 ^l	68.6 ±7.7 ^c

In the same row similar superscript letters indicate there is no significant difference (p=0.05)

The effect of alum on the sludge characteristics and membrane fouling is complex process. Indeed there was no significant difference between the transmembrane pressure of R1 and R3 while in case of R2 the addition of alum negatively affects the transmembrane pressure. The relation between the particles size and the settling properties of the sludge (SVI) is complex and particles size analysis alone could not be used as a tool to describe the settling properties of the sludge. But the parameter could be used with the SVI to study the factors affecting the sludge settling properties and the mechanism of action. The results show that the best

range for the particle size which reflects mostly good settling properties is between 35-55 as minimum value and 240-290 µm as maximum value. The effect of alum on particle size is indirect which may affect microbial population of the flocs. It was supposed that the alum would increase the particle size, but in reverse the particle size was reduced significantly in R3 with good settling properties (Table 3). In case of R2 the alum decreases the SVI but not significantly. This may be attributed to reduction or delay in the growth of filamentous bacteria in R3 with subsequent reduction in the floc size and good sludge volume index.

Table 3: Range of particles size (µm) and sludge volume index (SVI) in the treatment reactors

Date	R1		R2		R3	
	Particles size	SVI	Particles size	SVI	Particles size	SVI
14 July	47-289	53	51-291	52	37-253	50
18 July	51-285	75	55-303	61	33-245	56
21 July	52-277	94	57-294	83	34-240	56
24 July	75-320	277	70-313	190	33-245	157
28 July	69-319	300	70-311	210	50-285	103
1 August	70-319	244	70-307	190	53-289	98
4 August	79-376	244	81-369	190	61-308	98
8 August	70-334	217	72-328	190	53-297	177

In conclusion, the addition of alum in the aeration tank enhances phosphorous removal efficiency in the cloth-media membrane bioreactor without affecting the removal efficiency of the other treatment parameters. Addition of alum may have indirect effect on the sludge flocs and inhibits or delays the growth of filamentous bacteria in the reactors with subsequent better SVI. More research is required to better understand the relation between the sludge bulking problems and particles size of the sludge flocs.

REFERENCES

- [1] Zahid, W.M. and El-Shafai, S.A. (in press). Use of cloth-media filter for membrane bioreactor treating municipal wastewater. *Bioresource Technology* (in press).
- [2] Guo W., Vigneswaran S., Ngo H-H., Xing W., Goteti P. (2008). Comparison of the performance of submerged membrane bioreactor (SMBR) and submerged membrane adsorption bioreactor (SMABR). *Bioresource Technology*, **99**, 1012–1017
- [3] Holler S., Trösch W. (2001). Treatment of urban wastewater in a membrane bioreactor at high organic loading rates. *Journal of Biotechnology*, **92**, 95–101
- [4] Massé A., Spérandio M., Cabassud C. (2006). Comparison of sludge characteristics and performance of a submerged membrane bioreactor and an activated sludge process at high solids retention time. *Water Research*, **40**, 2405–2415
- [5] Scholz W., Fuchs W. (2000). Treatment of oil contaminated wastewater in a membrane bioreactor. *Water Research*, **34**(14), 3621–3629
- [6] Song, K-G., Kim, Y., Ahn, K-H., (2008). Effect of coagulant addition on membrane fouling and nutrient removal in a submerged membrane bioreactor. *Desalination* **221**, 467–474
- [7] Yang S., Yang F., Fu Z., Lei R. (2009). Comparison between a moving bed membrane bioreactor and a conventional membrane bioreactor on organic carbon and nitrogen removal. *Bioresource Technology*, **100**, 2369–2374
- [8] Wu, J., Chen, F., Huang, X., Geng, W., Wen, X., (2006). Using inorganic coagulants to control membrane fouling in a submerged membrane bioreactor. *Desalination* **197**, 124–136

The Use of Water Treatment Residuals in the Treatment of Textile Industry Wastewater

M. Mansoor Ahammed¹, Nevil J. Shakwala²

¹Civil Engineering Department, SV National Institute of Technology, Surat – 395007, India
(mansoorahammed@gmail.com)

²Civil Engineering Department, SV National Institute of Technology, Surat – 395007, India

ABSTRACT

Drinking water treatment residuals (WTR), often referred to as water works sludge, are waste products of the water treatment processes. An investigation was made to study the feasibility of reusing the sludge from a water treatment plant which uses poly aluminium chloride (PACl) as the coagulant in the treatment of real textile industry wastewater. Two different approaches were used for this. In the first approach, aluminium was first recovered from the sludge by acidification and then used as a coagulant, while in the second approach sludge itself was used as the coagulant. Optimum pH for aluminium recovery from the sludge was found to be 2. About 78% of the aluminium present in the sludge could be recovered under optimum conditions. Up to 60% COD removal from the textile wastewater could be observed by the recovered aluminium solution. The results from these tests demonstrate that water treatment sludge and aluminium recovered from water treatment sludge can be effectively used as a coagulant for treatment of wastewater from textile industries.

Keywords: aluminium sludge, water treatment residuals, textile industry wastewater, coagulation

1. INTRODUCTION

Enormous quantities of water treatment sludge are generated all over the world. On a global scale, available literature estimates that a whopping 10,000 tons of waterworks sludge is produced daily [1]. Due to regulatory changes in the recent past, WTR now have to be disposed of into landfills or through land application in many countries. In India, however, this sludge is still disposed of into water bodies [2]. However, with raising environmental concerns, it is likely that there will be stringent regulations on the disposal of this sludge in India also in the near future.

A number of research efforts have been made particularly in recent years to reuse waterworks sludge in many beneficial ways. These include use in building and construction materials, use in water and wastewater treatment and land based application for soil improvement. In water and wastewater treatment, beneficial reuses include the use of waterworks sludge as a coagulant or adsorbents for different contaminants like phosphates and heavy metals [3-7].

Resources recovery from WTR is an attractive proposition. Recovery of aluminium from water treatment sludge has been reported by many researchers [8]. Generally, four ways of coagulant recovery are employed for the water treatment sludge which includes acidification, basification, ion exchanging, and membranes. The effectiveness of the recovered coagulants has been generally varied, but nonetheless adjudged satisfactory in most cases. However, the purity of such recovered coagulants remains a contentious issue, just as the economy of the recovery process is still a subject of debate [9].

In the present study, an investigation was made to study the feasibility of reusing the sludge from a water treatment plant, which uses polyaluminium chloride (PACl) as the coagulant, in the treatment of a textile industry wastewater. Two different approaches were used for this. In the first approach, aluminium was first recovered from the sludge by acidification and then used as a coagulant; while in the second approach wet/dried sludge itself was used as the coagulant. Performance of the recovered coagulant and sludge was evaluated in terms of COD removal.

2. MATERIALS AND METHODS

2.1 Collection and Analysis of Water Treatment Plant Sludge

The water treatment sludge samples were collected from Katargam Drinking Water Treatment Plant in Surat, India, which has a capacity of 390 million litre per day. This plant uses PACl as the coagulant. Sludge was collected several times from the plant during the study period and was analysed for pH, water content, solids content, volatile solids, etc. Volatile solids content of the sludge was determined by calcinating the sludge at 500°C. Typical characteristics were: pH 6.9, TSS 44 g/L, volatile solids 650 mg/L and electrical conductivity 4.4 mS/cm.

To determine total content of different metals including aluminium in the sludge, acid digestion was used. For this, 2.5 g of dried and powdered sludge was digested for two hours at 140°C with 4 mL of concentrated nitric acid and 12 mL of concentrated hydrochloric acid. After cooling, 50 mL of distilled water was added and mixed thoroughly. The supernatant was separated

by centrifugation and was analysed for different metals. Concentrations of different metals are expressed as mg metal/g dry sludge.

2.2 Recovery of Aluminium from Sludge

Aluminium from the sludge can be recovered using both acidic and alkaline conditions and both the methods are attempted here. Aluminium recovery at different pHs were attempted. For this, 100 g of wet sludge was taken in an Erlenmeyer flask. The sludge suspension was stirred using a magnetic stirrer. It was dosed with 1 N sulphuric acid or 1 N sodium hydroxide till the desired pH was obtained, and the amount of acid/alkali required for achieving different final pH was noted. The acid or alkali was added while the sludge was mixed simultaneously and it was stopped as the pH of the solution reached at specified values. Aluminium recovery in the pH range of 1-12 was examined this way. For different pH values, supernatant was separated from the sludge by centrifugation and was analysed for aluminium to determine the efficiency of aluminium recovery at different pHs.

2.3 Wastewater

Wastewater from a dyeing and printing industry located in Udhna, Surat, India, was used in this study. Typical characteristics of the wastewater are presented in Table 1.

2.4 Coagulation Tests

Wastewater coagulation were performed with a jar test apparatus using 0.5 L samples in cylindrical beakers. In different jar tests, wastewater samples were rapidly mixed for 2 min at 100 rpm after addition of coagulant, followed by slow stirring for 20 min at 20 rpm. The flocs which had been formed were then allowed to settle for 1 hour. The supernatant was separated and was analysed for different parameters in different tests. In different tests, reuse of the aluminium as a coagulant was investigated in three different forms namely, (i) as aluminium recovered in the solution form from the sludge by the acidification at pH 2, (ii) as wet sludge obtained from the water treatment plant and (iii) as powdered dry sludge. Dry sludge was prepared by keeping the wet sludge in the oven 105°C till it is completely dry. PACl and alum ($\text{Al}_2\text{SO}_4 \cdot 18\text{H}_2\text{O}$) were also used in different tests for comparison of the efficiency of the recovered aluminium.

Table 1: Characteristics of the wastewater used

Parameter	Value
pH	5.0
COD (mg/ L)	1700
BOD (mg/ L)	180
TS (mg/ L)	3900
TDS (mg/ L)	3300
TSS (mg/ L)	1500
Temperature ($^{\circ}\text{C}$)	22

2.5 Analytical Methods

Analysis of different parameters was performed as per Standard Methods [10].

3. RESULTS AND DISCUSSION

3.1 Characteristics of the Sludge

Table 2 presents the amount of total recoverable metals in the sludge. These values were obtained after acid digestion of the sludge. The concentrations are expressed in mg metal/g dry weight of the sludge. It is seen that in addition to aluminium, the sludge also contains high amounts of iron and manganese. It is known that sediment particles which constitute turbidity contain these metals. It is also possible that some amount of iron is present in PACl. Low concentrations of heavy metals such as lead and zinc are also present in the sludge.

Table 2: Total recoverable metals in the sludge

Parameter	Concentration, mg metal/g dry weight of sludge
Aluminium	80
Iron	4.2
Manganese	2.1
Zinc	0.41
Lead	0.35

3.2 Optimum pH for Aluminium Recovery from Sludge

Aluminium recovery was attempted at both acidic and alkaline conditions in the range of pH 1-11. Figure 1 shows the percentage recovery of aluminium at different pH values. It can be seen that when the solution pH was reduced to 2 from 3, there was a rapid increase in recovery of aluminium. However, at pH 1, the recovery did not increase significantly compared to pH 2. This observation, together with the fact that large amount of acid was required for bringing the pH from 2 to 1 suggests that the optimum pH for aluminium extraction is 2. In all further studies, supernatant recovered at this pH was used. At this pH, the aluminium recovery was about 77.5%. Consequently, the recovered coagulant was prepared according to the following procedure. To 100 g of wet sludge, sulphuric acid was added to bring the pH to 2. The suspension was centrifuged to separate the solids, and the supernatant was stored for further use. The supernatant was analysed for different heavy metals and COD and the results are presented in Table 3.

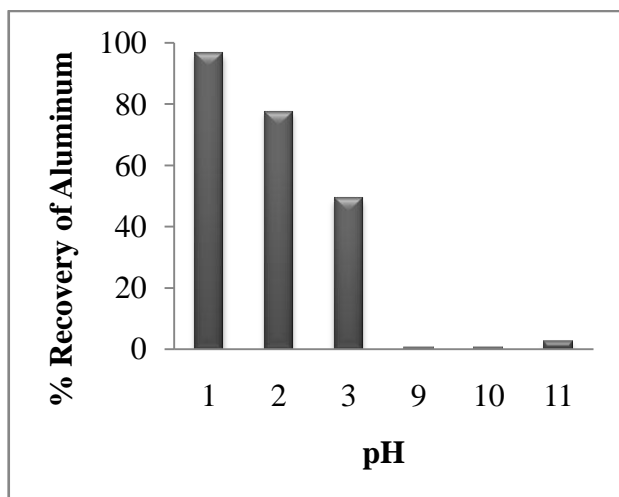


Figure 1: Percentage recovery of Al at different pHs

Table 3: Metals recovery at pH 2 from the sludge

Sl. No.	Parameter	Concentration, mg metal/g dry weight of sludge
1.	Aluminium	62
2.	Iron	3.3
3.	Manganese	1.6
4.	Zinc	0.21
5.	Lead	0.24
6.	COD	34

3.3 Tests with Textile Industry Wastewater

A preliminary jar test using recovered aluminium solution and PACl to determine the optimum dose of coagulant for COD removal indicated an aluminium dose of 60 mg/L. This dose was used in further studies.

Effect of pH on coagulation was investigated using the wastewater in the pH range of 4-9 and the results are presented in Figure 2. The results show that for all the coagulants used, the maximum COD and solids removal was obtained in the pH range of 6-7. While for fresh PACl and alum, maximum COD removal was 70-73%, it was lower with recovered aluminium solution (60%). Maximum removals of 50 and 45% were observed for wet sludge and dry sludge, respectively. The results of the test indicate the marked effect of pH on coagulation efficiency. It may be noted that in this test, a similar dose of 60 mg Al/L was used for all the coagulant. It is possible that with higher doses of recovered aluminium and sludge, the COD and solids removal could reach the level achieved by fresh PACl.

The tests conducted in this study are of preliminary nature. A large numbers of parameters affect the coagulation process. These include initial pH, dose of coagulant, characteristics of wastewater and type of coagulant. More tests should be conducted in order to

arrive at the suitable values for different parameters so as to optimise the removal efficiency. Overall, it may be said that this study shows potential of recovered reagent as a coagulant in wastewater treatment.

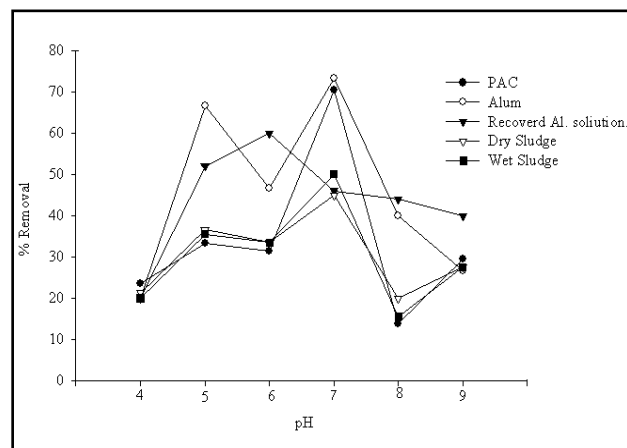


Figure 2: Effect of pH on COD removal with different coagulants

A preliminary cost analysis based on the cost of chemicals can be performed based on the chemical requirement for recovery of aluminium from water treatment plant sludge. However, a detailed economic analysis should include the sludge disposal costs and environmental benefits in addition to the cost of chemicals.

4. CONCLUSIONS

Based on the tests conducted in the present study, the following conclusions may be drawn:

It is possible to recover aluminium from water treatment sludge using acid extraction. The optimum pH for extraction was found to be 2 for the range of pH (1-11) studied. At this pH, about 78% of aluminium present in the sludge could be recovered. The recovered aluminium solution also had high iron and manganese content and low concentration of heavy metals, zinc and lead. About 60% removal of COD was obtained during coagulation of a textile industry wastewater with recovered coagulant, though this removal was relatively lower compared to PACl (70%) at a similar dose. pH had a significant effect on the coagulation with recovered as well as fresh coagulant. Maximum COD and solid removal was observed at pH 6-7.

REFERENCES

- [1] Dharmappa, H.B., Hasia, A. and Hagare, P. "Water treatment plant residuals management", *Water Sci. Technol.* Vol. 35, pp . 45-56, 1997.
- [2] Central Pollution Control Board, Ministry of Environment and Forests, Government of India. *Status of*

water treatment plants in India, New Delhi, India, 2009.

- [3] Chu, W. "Lead metal removal by recycled alum sludge", *Water Res.*, Vol. 33, pp. 3019–3025, 1999.
- [4] Basibuyuk. M., and Kalat, D. G. "The use of waterworks sludge for the treatment of vegetable oil refinery industry wastewater," *J. Environ. Technol.*, Vol. 25, pp. 373–380, 2004.
- [5] Guan, X. H., Chen, G.H., and Shang, C. "Reuse of water treatment works sludge to enhance particulate pollutant removal from sewage," *Water Res.*, Vol. 39, pp.3433–3440, 2005.
- [6] Zhao, Y.Q., Zhao, X.H. and Babatunde, A.O. "Use of dewatered alum sludge as main substrate in treatment reed bed receiving agricultural wastewater: long-term trial," *Bioresource Technology*, Vol. 100, pp. 644–648, 2009.
- [7] Moghaddama, S. S., Moghaddama, M. R. A. and Aramib, M. "Coagulation/flocculation process for dye removal using sludge from water treatment plant: Optimization through response surface methodology", *Journal of Hazardous Materials*, Vol. 175, pp. 651–657, 2010.
- [8] Ishikawa S, Ueda, N Okumura, Y, Iida Y and Baba K. "Recovery of coagulant from water supply plant sludge and its effect on clarification," *Journal of Material Cycles Waste Management*, Vol. 9, pp. 167–172, 2007
- [9] Babatunde, A. O., and Zhao, Y. Q. "Constructive approaches toward water treatment works sludge management: an international review of beneficial reuses", *Critical Reviews in Environmental Science and Technology*, Vol. 37, pp. 129–164, 2007.
- [10] APHA. *Standard Methods for the Examination of Water and Wastewater*, 20th Edition, American Public Health Association, New York, USA, 1998.

Nanofiltration Pretreatment of Desalination Seawater Feed for CO₂ Release Reduction in MSF Distillers

Aiman E. Al-Rawajfeh

Tafila Technical University (TTU), Department of Chemical Engineering,

P.O. Box 179, 66110 Tafila, Jordan.

Tel.: +962-3-22 50 034, Fax: +962-3-22 50 431, e-mail: aimanr@yahoo.com

ABSTRACT

The release of non-condensable (NC) gases, essentially carbon dioxide, oxygen and nitrogen, from the evaporating brine in desalination distillers notably affects the heat transfer for condensation, the energy consumption, the performance and the material lifetime of the distillers. Moreover, CO₂ release considerably influences the concentrations of HCO₃⁻, CO₃²⁻, CO₂, H⁺ and OH⁻ in the carbonate system of the brine and thus plays an important role in alkaline scale formation. The influence of nanofiltration on CO₂ release and scaling in MSF distillers has been investigated for different feed water composition from different intakes from the Arabian Gulf for once-through (OT) and brine recycle (BR) MSF distillers. The results were calculated using a previously developed verified model. The release rates decrease exponentially from the first stage to the last stage. The release rates, in the first stage, are reduced from 430 kg/h to 375, 320, 260, and 145 kg/h which correspond to 13, 26, 40, and 66% CO₂ release reduction when the feed is 20, 40, 60 and 100% pre-treated by NF, respectively.

Keywords: Nanofiltration, CO₂ release, Multi-stage flash (MSF) distillation, Heat transfer resistance.

1. INTRODUCTION

Multistage flash (MSF) distillation is a widespread desalination method with more than half of the desalination market. Plants, which use this process, are of complex, large-scale and costly. The major problems encountered in MSF distillers are the deposition of scale onto the heat transfer surfaces which results in a serious loss of efficiency and production, and corrosion [1]. In the MSF process, two different configurations can be differentiated. In once-through distillers, the concentrated brine from the last stage is discharged to the sea. In recycle distillers, a portion of the concentrated brine from the last stage is mixed with the feed water. When the brine enters the first flash chamber in MSF distillers, due to the sudden reduction of the CO₂ partial pressure, CO₂ is released into the vapour space. Consequently, scales (CaCO₃, Mg(OH)₂ and CaSO₄) precipitate in the bottom of the flash chamber and inside the tubes. On the basis of the reaction ($2\text{HCO}_3^- \leftrightarrow \text{CO}_2 + \text{CO}_3^{2-} + \text{H}_2\text{O}$), the total CO₂ release in the distiller is directly proportional to fraction of HCO₃⁻ decomposition at a certain top brine temperature (TBT) and the flow rate of the make-up.

The release of non-condensable (NC) gases, essentially carbon dioxide, oxygen and nitrogen, from the evaporating brine in desalination distillers notably affects the heat transfer for condensation, the energy consumption, the performance and the material lifetime of the distillers. Moreover, CO₂ release considerably influences the concentrations of HCO₃⁻, CO₃²⁻, CO₂, H⁺ and OH⁻ in the carbonate system of the brine and thus plays an important role in alkaline scale formation. Seawater is an aqueous mixed electrolyte. It attains its chemical composition through a variety of chemical

reactions and physicochemical processes. Among these are: acid–base reactions, gas absorption and desorption processes, precipitation and dissolution of solids and adsorption processes at interfaces. The pH of seawater is usually in the range from 7.7 to 8.3 in surface waters. The pH is buffered by a set of reactions that take place between carbon dioxide and water. Components of desalination feed waters can adversely impact the efficiency and/or useful life of desalination systems and their components.

In previous works, Al-Rawajfeh *et al.* [2-4] have modeled the CO₂ release rates in MED distillers. This model did not account for the deposition of alkaline scale and its effect on CO₂ release rates. Calcium carbonate and magnesium hydroxide were assumed to precipitate at negligible rates. Recently, Al-Rawajfeh [5,6] developed a model to simulate the simultaneous release of CO₂ with the deposition of CaCO₃ and investigated their mutual release-deposition relationship in MED [5] and MSF distillers [6]. The influence of CO₂ injection on the carbonate chemistry and the scale formation were also studied [7].

In this work, the influence of nanofiltration on CO₂ release and scaling in MSF distillers has been investigated for different feed water composition from different intakes from the Arabian Gulf for once-through (OT) and brine recycle (BR) MSF distillers. The results were calculated using a previously developed verified model.

2. RESULTS AND DISCUSSION

NF pre-treatment has a significant capability to lower the concentration of hard scale elements in seawater

especially Ca^{2+} , Mg^{2+} , SO_4^{2-} , and HCO_3^- . Hassan et al [8] have reported the following NF salts rejection values: Ca^{2+} 80.7%, Mg^{2+} 87.7%, total hardness 86.5%, SO_4^{2-} 93.3%, and HCO_3^- as CaCO_3 63.3%. In the same paper, the authors reported more than 26% rejection to monovalent ions such as Cl^- , Na^+ and K^+ by the NF membrane. The total seawater salinity was also decreased from 44,046 to 27,619 ppm after the NF treatment which is equivalent to 37% reduction in seawater total dissolved solids (TDS). The feed pH was also reduced from 8.2 to 7.85 after the NF pretreatment. As a result, it was able to increase the TBT of MSF to $>130^\circ\text{C}$. The recovery rate of MSF operating on NF permeate was found to reach 80% and 70% at TBT 130°C and 120°C respectively. Three different types of NF membrane were tested for salt rejection and permeate flux. For seawater softening, a special NF membrane was used which was characterized by an average rejection rate and permeate flow [8]. In a similarly related work, Awerbuch [9] presented the benefit of using NF membranes in the removal of scale elements from seawater. Awerbuch suggested using NF permeate-seawater mixture feed (partial feed pretreatment) to thermal process to reduce the cost of NF pretreatment. The study showed the feasibility to increase TBT in MSF up to 125°C with only 25% NF permeate mixture with seawater.

The CO_2 release rates decrease exponentially from the first stage to the last stage. This may be attributed to the drop in the concentration difference of CO_2 in the solution between the bulk and the phase interface because of the successive flow of the brine from the first stage to the last stage. The release of CO_2 in a stage reduces the total carbon dioxide (TC) in the next stage and so on. Additionally, the mass transfer coefficient and the phase interface area decrease. Because part of the brine blow-down is recycled and remixed with the make-up, the release rates in the recycle distiller are lower than those rates in the once-through distiller. Consequently, CaCO_3 deposition rates, in the flash chambers, notably decreases from the first to the last stage and this can be attributed to the following reasons [6]: (i) because of CaCO_3 precipitation in a certain stages, TA of solution entering the next stages becomes lower, and (ii) CO_2 release rate decreases, because the difference between the concentration of CO_2 in the bulk and at the phase interface, release driving force, decreases. This can be attributed to the increase in salinity with evaporation which causes the solubility of CO_2 to drop.

The effect of NF pretreatment on CO_2 release rates in a reference brine recirculation BR-MSF is shown in **Figure 1**. The release rates, in the first stage, are reduced from 430 kg/h to 375, 320, 260, and 145 kg/h which correspond to 13, 26, 40, and 66% CO_2 release reduction when the feed is 20, 40, 60 and 100% pretreated by NF, respectively.

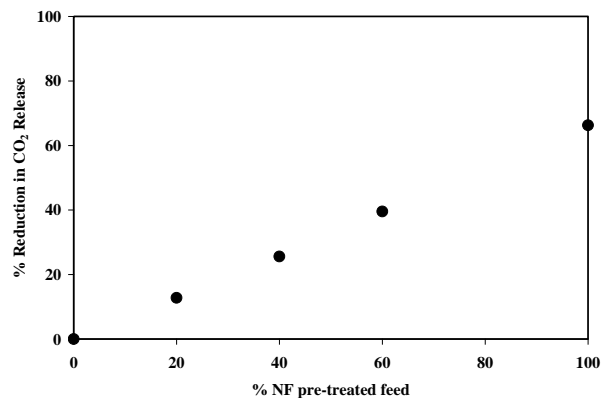


Figure 1: The effect of NF pretreatment on CO_2 release rates in a reference BR-MSF.

The effect of NF pretreatment on total CO_2 heat transfer resistance in reference brine recirculation BR-MSF and once-through OT-MSF is shown in **Figure 2**.

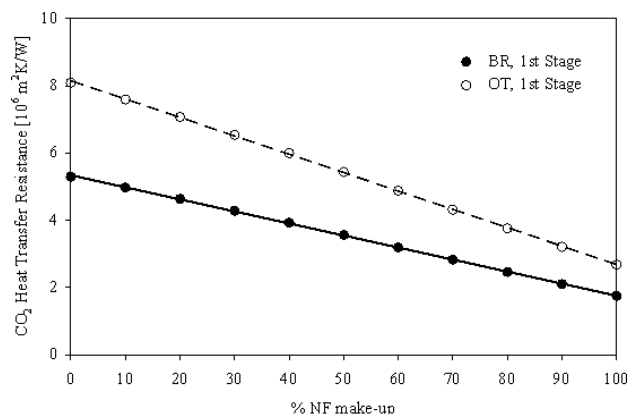


Figure 2: The effect of NF pretreatment on total CO_2 heat transfer resistance in reference brine recirculation BR-MSF and once-through OT-MSF.

3. CONCLUSION

CO_2 release can be reduced significantly by nanofiltration pretreatment of the feed seawater in thermal desalination plant. The study is applied to MSF two reference once-through and brine-recycle distillers. Consequently, the need of deaeration is reduced accordingly. Corrosion due to CO_2 is expected to decrease, as very large amounts of the gas are stop to release. The mentioned pretreatment, decreases the negative effect of CO_2 and non-condensable gases on heat transfer by reducing the CO_2 amount with the vapour produced.

REFERENCES

- [1] Patel, S.; Finan, M. A.; New antifoulants for deposit control in MSF and MED plants, *Desalination* 124 (1999) 63–74.
- [2] Al-Rawajfeh, A. E.; Glade, H.; Ulrich, J.; CO_2

- release in multiple-effect distillers Controlled by mass transfer with chemical reaction. *Desalination*, 156 (2003) 109-123.
- [3] Al-Rawajfeh, A. E.; Glade, H.; Qiblawey, H. M.; Ulrich, J.; Simulation of CO₂ release in multiple-effect distillers. *Desalination*, 166 (2004) 41-52.
- [4] Al-Rawajfeh, A. E.; Glade, H.; Ulrich, J.; Scaling in multiple-effect distillers: the role of CO₂ release. *Desalination*, 182 (2005) 209-219.
- [5] Al-Rawajfeh, A.E.; Modelling of Alkaline Scale Formation in Falling-Film Horizontal-Tubes Multiple-Effect Distillers. *Desalination*, 205 (2007) 124-139.
- [6] Al-Rawajfeh, A. E.; CaCO₃-CO₂-H₂O system in falling film on a bank of horizontal tubes: model verification. *J. Ind. Eng. Chem.*, 16 (2010) 1050-1058.
- [7] Al-Rawajfeh, A.E.; Simultaneous desorption-crystallization of CO₂- CaCO₃ in multistage flash (MSF) distillers. *Chem. Eng. Proc., Proc. Intens.*, 47 (2008) 2262-2269.
- [8] Al-Rawajfeh, A.E.; Al-Amaireh, M. N.; The influence of CO₂ injection on the carbonate chemistry and scaling in multiple-effect distillers. *Desalination and Water Treat.* 7 (2009) 191-197.
- [9] Hassan, A. M.; US Patent No. 0157410, 2006.
- [10] Awerbuch, L.; US patent No. 6998053B2, 2006.

Design Flow Factors for Sewerage Systems in Small Arid Communities

Emad Imam¹, Haitham Elnakar²

¹Professor, The American University in Cairo (eimam@aucegypt.edu)

²Graduate Research Assistant, The American University in Cairo (haitham.y@aucegypt.edu)

ABSTRACT

Reliable estimation of sewage flow rates is essential for the proper design of sewers, pumping stations, and treatment plants. The design of the various components of the sewerage system should be based on the most critical flow rates with a focus on extremely low and peak flow rates that would be sustained for a duration related to the acceptable limits of behaviour of the components under consideration. The extreme flow conditions and to what extent they differ from the average values are closely related to the size of the community or network, and the socio-economic conditions. A single pumping station is usually sufficient to pump flow from small communities in either flat or non-undulating topography. Therefore, the hydraulic loading on the wastewater treatment plant (WWTP) results from the pumped flow from the pumping station rather than the trunk sewer flow. The intermittent operation of the pumping units further accentuates the sewage hydrograph in the final trunk sewer. Accordingly, the design flow for the various components of the WWTP should be determined based on their relevant flow factors. In this study, analysis of one representative small community out of five monitored small communities in Egypt and the Kingdom of Saudi Arabia is presented. Pumped sewage flow rates were measured and the sewer incoming flows were hydraulically derived. The hourly and daily sewer and pumped flow records were analyzed to derive the relationship between the flow factors that would be sustained for various durations (instantaneously, one hour, two hours, etc) and their probability of non-exceedance. The resulting peaking factors with a consideration for their sustained flow duration and specified probability would permit the design of the various components of the treatment plant using more accurate critical flows.

Keywords: Peak Flow Factors, Sewers, Pumping stations, Wastewater treatment plants, Small Communities

1. INTRODUCTION

The efficient management of wastewater flow requires a realistic acquaintance with its characteristics. Thorough characterization data of these flows are necessary not only to enhance the progress of the efficient design of wastewater treatment and disposal systems, but also to facilitate the development and application of water preservation and waste load reduction strategies. Prediction of wastewater flow rates and its variation are both important at the stage of designing wastewater treatment plants (WWTPs) and during their operation. Small capacity WWTPs are seriously affected by flow rate variation. EPA (1976) reported that small communities will generally feed WWTPs with highly accentuated peaks and minimums ^[1]. Butler and Graham (1995) indicated that these flows are generally intermittent, of relatively short durations and are hydraulically non-steady ^[2].

Flow into the sewers of small community results from the quasi-random usage of a range of home appliances (with frequency of use being related to the time of day and living and work style of the residents), each with its own characteristics. At the outfall, the observed flow in the sewer is normally continuous and tends to have repetitive diurnal patterns, although it is still subject to variability. As the sewer network becomes larger, flows from the different branches join and tend to even out the

flow variation. Therefore, flow variability decreases as the population increases. The flow routing in the sewers further dampens these variations due to the in-sewer storage and subsequent release.

A Small community, due to its limited areal extent, is typically served by one pumping station to discharge the wastewater collected by the gravity sewer network to the treatment plant. The capacity of pumps, the hydraulic design of the sump, and the operation of the pumping station accentuate the inflow hydrograph reaching the treatment plant. Therefore, the peaking factors usually given by the design codes for sewer flow may not be applied identically in the design of the individual components of the treatment plant. The outflow of the pumping station should be equally considered. Sewage discharges from small communities flowing in the trunk sewer are highly variable, and there are uncertainties in the values of the maximum and average hourly and daily-sustained flows.

Peak and low flows are estimated as multiples of average wastewater flow. Several equations have been developed to estimate flow factors. The common variables that govern most of these equations are the population and the average daily flow. Table (1) summarizes some of the equations that estimate peaking factors.

Table 1: Some equations to estimate peak flow factors

Method	Peaking Factor Formula	Sustained Duration	Conditions of application
Babbitt and Baumann ^[3]	$\frac{5}{P^{0.2}}$	Instantaneous	$1 \leq P \leq 1000$, P in thousands
Harmon ^[4]	Lager of 2.5 or $1 + \frac{14}{4 + \sqrt{P}} \approx \frac{4.2}{P^{0.16}}$	Hourly	P in thousands
Munksgaard & Young ^[5]	$\frac{2.97}{Q_m^{0.0907}}$	Extreme Annual Peak 4 hours	Q_m , in m ³ /sec
	$\frac{2.9}{Q_m^{0.0902}}$	Extreme Annual Peak 8 hours	Q_m , in m ³ /sec
	$\frac{1.75}{Q_m^{0.036}}$	Extreme Annual Peak day	Q_m , in m ³ /sec

The probability of non exceedance is an important factor that should be considered in the estimation of the design flow factors. Gaines (1989) suggested that the engineering judgment should expect probabilities based on the function of sewers and the controlling agency permits^[6]. Zhang, Buchberger and van Zyl (2005) developed a theoretical peaking factor equation for water and domestic wastewater using Poisson rectangular pulse model^[7]. This equation relates the peaking flow factor with number of homes in the community and percentile of Gumbel distribution. They compared the results obtained by the rectangular pulse model at percentile 99.9 to some empirical methods like the Babbitt and Baumann and Harmon formulas at different population figures. The results from the rectangular pulse model gave values lower than those of Babbitt and Baumann equation, and higher than those of Harmon equation.

Moreover, various components of the WWTP should be designed based on relevant flow factors that account for their acceptable limits of behaviour. Metcalf and Eddy (1979) noted that the expected sustained flows that persist for various time durations (2 hours or longer) are on equal importance with the expected peak flows, especially in the design of wastewater treatment facilities^[8]. Young et al (1978) indicated that individual plant units are affected by different flow and load variations that require different peaking factors^[9].

The main objective of this study is to derive flow factors for the design of trunk sewers, pump stations and WWTP for typical small community accounting for their probability of non-exceedance and their variation with the duration of the sustained flow. Data of are presentative small community in Egypt called West of Golf is used to derive the peak factor which can be applied to other similar communities.

2. CASE STUDY- WEST OF GOLF (WG), CAIRO- EGYPT

West of Golf small community is a residential compound in New Cairo, Egypt with a saturated population equal to 22,000 capita. The current estimated population is about 6000 capita. The gross area of the community is 190 acres. The compound is located at high altitude far from the Nile, which makes the community a near-arid desert community. The community is composed of mostly luxury residential villas, green areas and more than 45 swimming pools. The average generated sewage from the community is 2200 m³/day.

The sewer system is a combined sewer system although it rarely rains. Gravity sewers collect the wastewater to a pumping station that discharges via a force main to a wastewater treatment plant serving this compound and other residential districts in the region. The pumping station has two duty submersible pumps with a capacity of 396 m³/hr each. Presently, only one duty pump is in operation automatically according to the set levels of water in the sump.

Sewage flows pumped to the treatment plant were measured by the station flow confirmed by a portable ultrasonic flow meter that was mounted on the discharge pipe of the pumping station. Hydraulic modeling of the sump and the pumps derived the incoming sewer flow hydrographs. Tracking of the water level variation in the sump was also used to verify the incoming sewer flow hydrograph.

Figure (1) shows a typical sewer flow hydrograph discharging into the sump of WG pumping station. It indicates that peak flow occurred near 4:00 pm on that day, while significantly lower flows took place late at night.

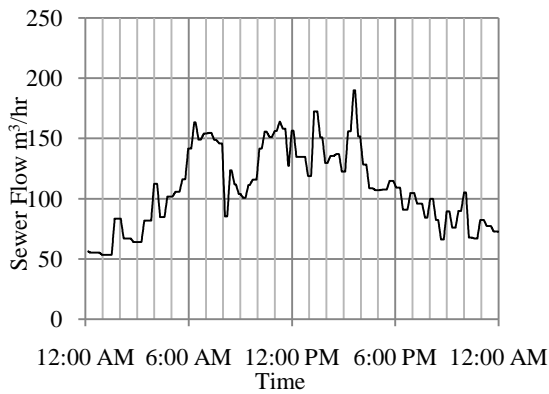


Figure 17: Sewer inflow hydrograph to WG Pumping Station (Saturday November 13, 2010- daily flow = 2290 m³/day)

Since the pumping capacity is 396 cubic meters per hour which is higher than the peak flow of 190 m³/hr and even much higher than the low night flow of 52 m³/hr., then the pumping station will operate intermittently with cycles of on- and off-periods. The intermittent flow and “surge-like” operation of WG pumping station, as shown in Figure (2), is the result of the oversized pump in relation to the present partial development of the community.

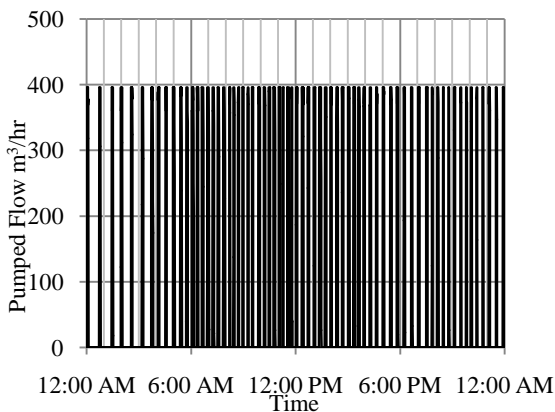


Figure 18: Intermittent Outflow of WG Pumping Station for (Saturday November 13, 2010- daily flow = 2290 m³/day)

Figure (3) shows the statistics of the durations of full pumping cycles (duration of a cycle = on-+ off- periods).

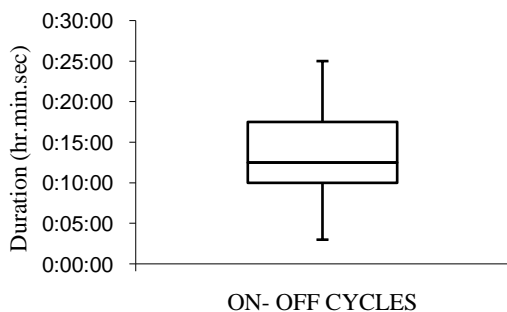


Figure 19: Statistics of the Durations of full pumping cycles West of Golf Pumping Station

3. Peak Flow Factors

Sewer flow varies with hour of the day, while the total daily flow varies with day of the year. Two peaking factors will be used to capture both variations: $P_{hr-t-avghr}$ to account for hourly variation within a given day, and $P_{i-avg d}$ to account for the variation of the daily flow within the year. Both factors may be combined to give peak flow factor ($P_{max/min.t}$) as:

$$P_{max/min.t} = (P_{max/min hr-t-avghr}) (P_{i-avg d}) \quad (1)$$

The $P_{max/min hr-t-avghr}$ is defined as:

$$P_{max/min hr-t-avghr} = \left(\frac{Q_{max/min hr-t}}{Q_{avg-hr}} \right) \quad (2)$$

Where ($Q_{max/min hr-t}$) = the average flow during a duration (t) hours when the sustained flow Q is either maximum or minimum. For every day of the record $Q_{max/min hr-t}$ is calculated for all durations t = (1, 2, ..., and 24); Q_{avg-hr} = the average hourly flow for that day of record.

The peaking factor given by Equation 2 is calculated for every day of the record and for every duration t. For every duration (t), there will be peaking factors equal to the number of days (N) for which hourly-flow record is available. All (N) peaking factors $P_{max/min hr-t-avghr}$ for the same (t) were sorted in a descending order. A factor with a rank (m) in the record is assigned a probability (p) of not being exceeded: $p = (m-0.5)/N$.

The $P_{i-avg d}$ is the factor that accounts for variation of daily flow (Q_i) during day (i) of the record with respect to the average daily flow ($Q_{avg-daily}$) of the record (N) as shown in equation 3.

$$P_{i-avg d} = \left(\frac{Q_i}{Q_{avg-daily}} \right) \quad (3)$$

The (N) values of the daily peaking factor ($P_{i-avg d}$) were sorted in a descending order. A factor with a rank (m) in the record is assigned a probability (p) of not being exceeded: $p = (m-0.5)/N$.

Several probability distributions were applied to the three-flow variation factors give by equations (1-3) and the Gumbel probability distribution was found to be the one that best fit the records.

Figures (4 and 5) describe the Gumbel distribution fit for selected maximum hourly and daily flow factors for West of Golf respectively.

Estimation of the extreme combined peak flow factors was based on the assumption that the proposed sewerage system will receive same peak hourly to average hourly flow ratio on the peak flow day, and same low hourly to average hourly ratio on the low flow day.

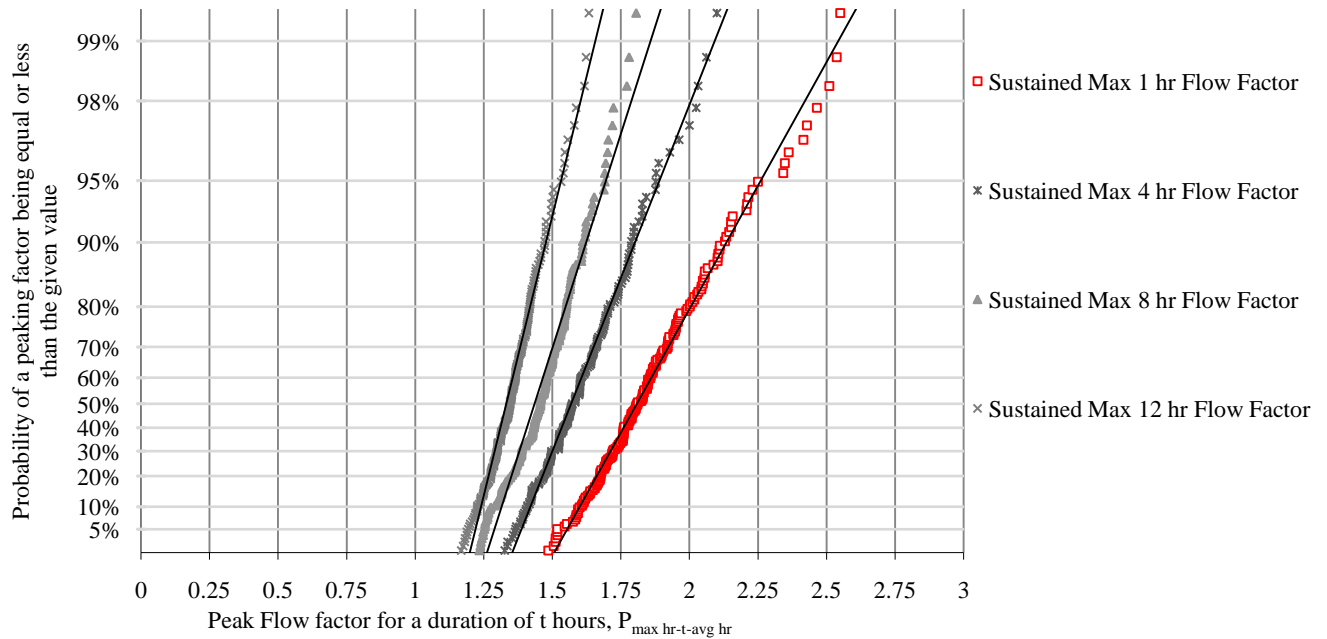


Figure 20: Probability of non-exceedance of the given peak flow factors for a duration of t-hours for WG sewage flows

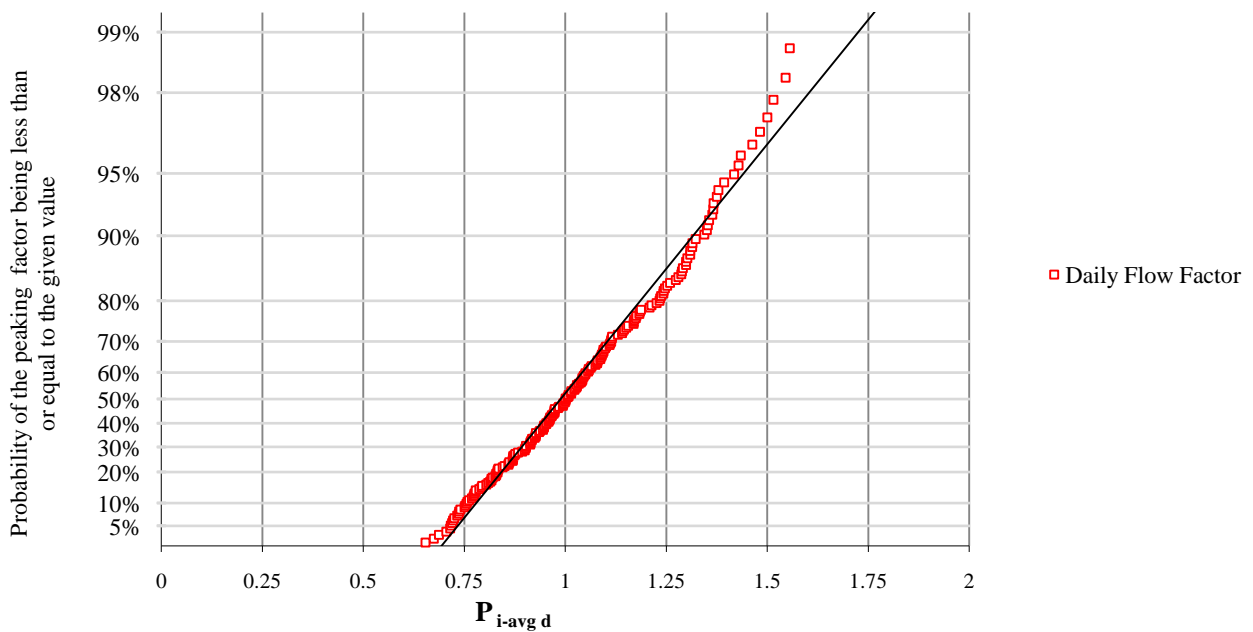


Figure 5: Probability of non-exceedance of the given peak daily flow factor ($P_{i-avg d}$) for WG sewage flows

4. RESULTS AND DISCUSSION

4.1 Pump and Sewer Flow Factors

The flow record for WG community comprised of 208 days of measured hourly flows and one year of measured total daily flows. Analyses of data collected from WG pumping station were carried out to estimate 1 hour, 2 hour, ...- 24 hours for the incoming and pumped sewage flow. Figure (6) gives the peak flow factor $P_{max.t-hr-avg.d}$ of the pumped and sewer flows for a 99 % probability of non-exceedance. The peak factor

for the maximum instantaneous flow ($t=0$) for the pumped flow is higher than the factor for the maximum sewer flow because of the over-sized pumps during the early stage of community development.

4.2 Extreme Design Hourly Flow Factors

The extreme sewer flow factors for selected probabilities for WG are shown in figure [7]. The 99% 1- hr sustained peak flow factor is 4.35 which means that the trunk sewer, treatment plant or pump station will receive this value or less at probability equal to 99

%. On the other hand, the 99% 1- hr sustained low flow factor) is 0.25 which means that the trunk sewer, treatment plant or pump station will receive this value or more at probability equal to 99 %. Values calculated from the derived extreme peaking factors and by different methods for different time setup are plotted on the same figure. It can be noted that values calculated from Babbit and Baumann and Harmon equations are within the envelope of probability curves between 50% to 95%. Values calculated from Muksgaard and Young 1980 are much higher than the derived values for all communities. This may be due to the arid communities' characteristics in this study and the different characteristics of the communities studied by Muksgaard and Young 1980.

4.3 Design Daily Flow Factors:

Figure (8) gives the results of design peak and low flow factors that are sustained for a given number of days for a probability non-exceedance of 99 % for WG. This graph is based on one year of consecutive daily flow monitoring. These daily flow factors for durations more than one day are in the design and operation of certain types of plants or components such as the sludge drying beds.

4.4 Effectiveness of Using Probability and Sustained Durations in Estimating Design Peaking Factors:

Figure (7) shows that the peak one hour-flow factor for a probability of non-exceedance of 99% is 4.45 while that for a 95% probability is 3.3; i.e. units based on the higher probability will be sized for a higher flow by nearly 1/3.

Therefore, the designer may opt to design the various plant components using different probabilities of non-exceedance to optimize on the size of the units. The main criterion for selecting the probability would be the consequences of subjecting the treatment unit to a higher flow, and the possibility of the entire plant not meeting its effluent standards.

In addition to estimating certain probability, different plant components should be designed according to their critical peak conditions. In Figures (7), and (8), the peak flow factors decrease as their sustained durations increase. Consequently, the use of the widely used instantaneous or hourly peaking factors in all treatment components is not the optimum factor. Pumps, screens, and grit chambers should be designed based on the extreme instantaneous peaking factor. Other units should be designed so that it can handle the flow within the average of its acceptable limits of behavior. Units can typically tolerate some flow variations occurring during their hydraulic residence or retention times.

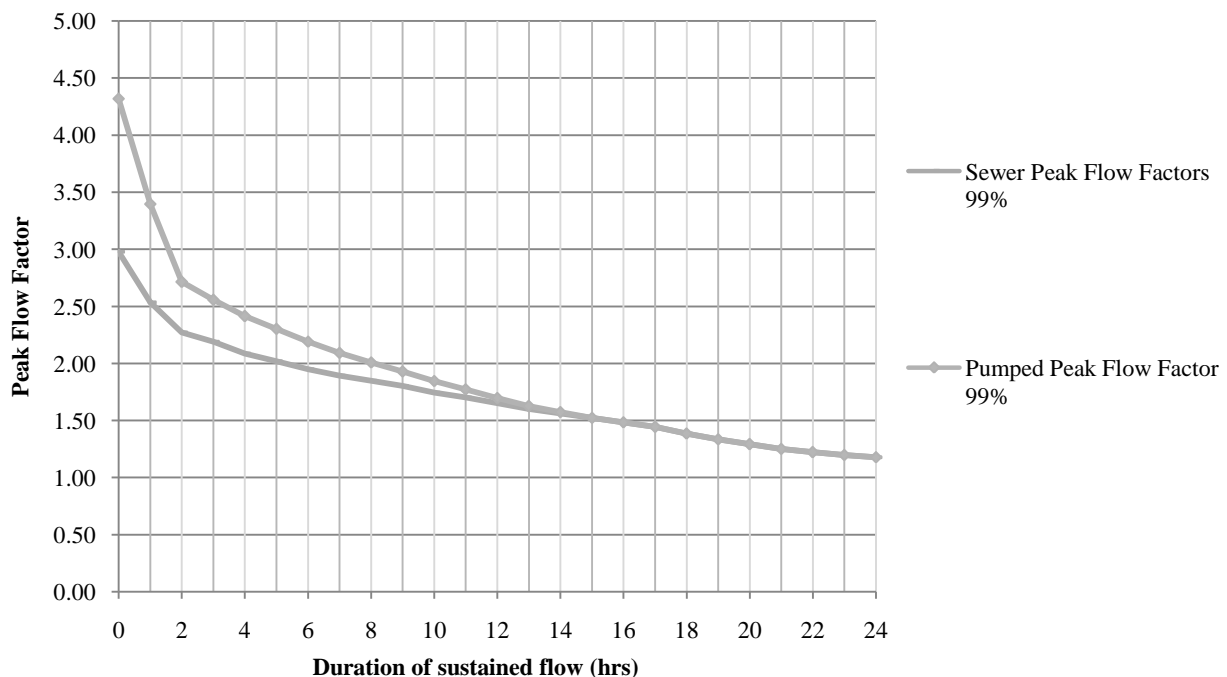


Figure 6: Sewer and pumped peak flow factors with probability 99% probability of non-exceedance.

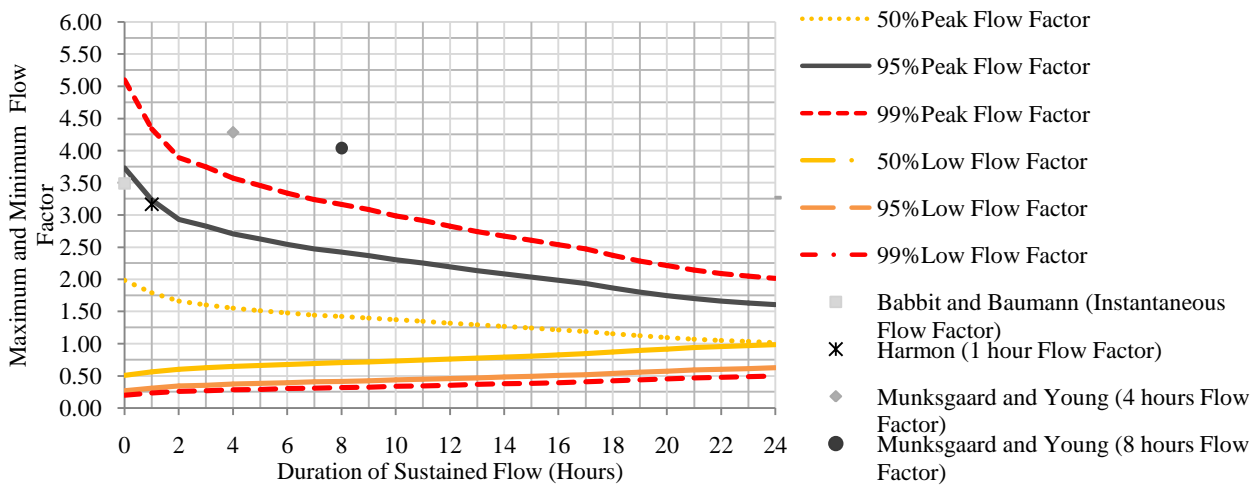


Figure 7: Maximum and Minimum flow factors for WG for sustained durations of t-hours and selected non-exceedance probability

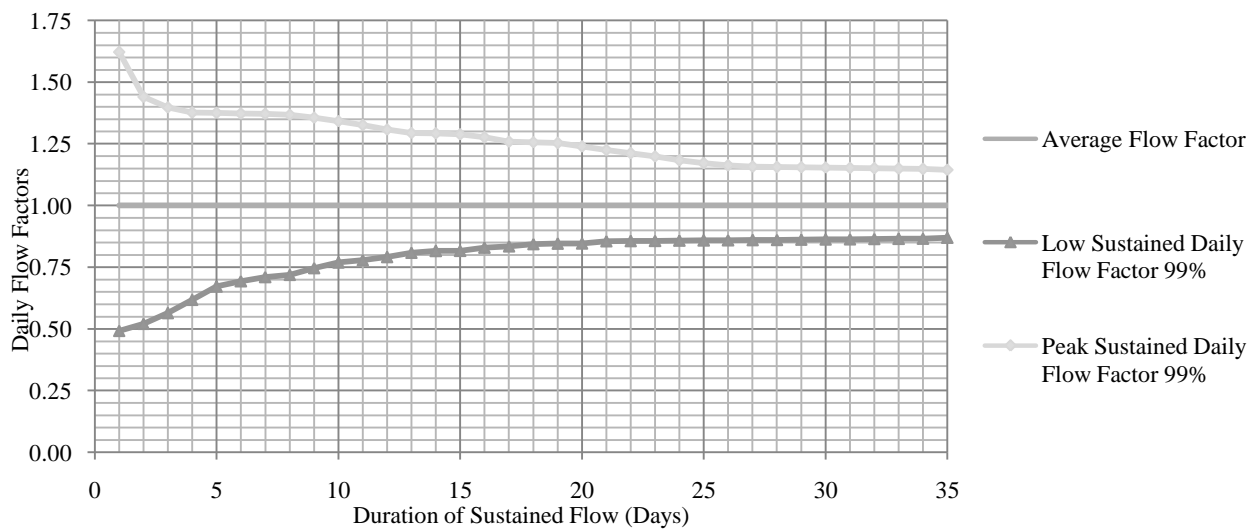


Figure 8: Design peak and low daily flow factors for probability equal to 99 % for WG.

5. CONCLUSIONS

A case study of West of Golf residential community has been investigated to derive probability based design maximum and minimum flow factors for the design of the sewerage system and the different components of the wastewater treatment plant. These flow factors are related to the duration during which these flows will be sustained, and to the probability that they are not exceeded. Each wastewater component of the waste water sewerage system should be designed with its own flow factor based on its acceptable limits of behavior. For small communities the sizing and operation of the pumping station accentuate the sewer hydraulic and results in a pulse-like pumped flow hydrograph that should be the basis for the design of the treatment plant.

ACKNOWLEDGMENTS

Credits:

This publication is based on a collaborative research project supported by Award No. C0015, from King Abdullah University of Science and Technology (KAUST), KSA.

Authors:

Emad Imam is a Professor at the department of Construction and Architectural Engineering at The American University in Cairo AUC. Haitham Elnakar is a Graduate Research Assistant at the same department.

REFERENCES

[1] Environmental Protection Agency, EPA, *Process Design Manual. Wastewater Treatment Facilities for Sewered Small Communities*, Cincinnati, Ohio, 1977.

- [2] Butler, D., and Graham N. J. D., "Modeling Dry Weather Wastewater Flow in Sewer Networks", *Journal of Environmental Engineering*, Vol. 121, No. 2, pp. 161-173, 1995.
- [3] Babbitt, H.E., and Baumann, E.R., *Sewerage and Sewage Treatment*, John Wiley and Sons, Inc, New York, 1958.
- [4] Alberta Environment, Environmental Assurance Division, Environmental Policy Branch, Drinking Water Branch, *Alberta Environmental Protection Standards and Guidelines*, Edmonton, 2006.
- [5] Munksgaard D. G. and Young J.C. "Flow and Load Variations at Wastewater Treatment Plants", *Water Pollution Control Federation*, Vol. 52, No. 8, pp. 2131-2144, 1980.
- [6] Gaines J.B. "Peak sewage flow rates prediction and probability", *Water Pollution Control Federation*, Vol. 61, No. 7, pp. 1241-1248, 1989.
- [7] Zhang, X, Buchberger S.G. and van Zyl J.E. "A Theoretical Explanation for Peaking Factors.", *ASCE EWRI Conferences*, Anchorage Alaska, May 15-19, 2005.
- [8] Metcalf, L., and Eddy, H. P., *Wastewater Engineering. Treatment, Disposal, Reuse*. Rev. by Tchobanoglous, G. McGraw-Hill, New York, 1979.
- [9] Young, J.C., et al., "Flow and Load Variations in Treatment Plant Design", *Journal of the Environmental Engineering Division*, Vol. 104, No. 2, pp. 289-303, 1978.

Hydro-meteorological Impacts of Climate Change in the Middle East: A Review

Abdullah Gokhan Yilmaz¹ and Monzur Alam Imteaz²

¹ Heriot-Watt University (a.g.yilmaz@hw.ac.uk)

² Swinburne University of Technology (mimteaz@swin.edu.au)

ABSTRACT

Hydrological cycle and water resources are influenced by climate change severely. Climate change induced temperature increase changes precipitation patterns over many regions in the world. Temperature and precipitation alterations affect hydrological cycle and water availability. Groundwater levels of aquifers have also been affected by climate change due to recharge variations. One of the most affected regions by climate change is the Middle East. Water availability per person per year is less than 1000 m³ in majority of the Middle East countries. Alteration in hydrological cycle due to climate change associated with population growth will affect the water availability & quality and will increase the intensity of water stress in this region. It is very likely to observe longer droughts due to temperature increase and more frequent and intense floods & desertification owing to change in variability and intensity of rainfall events. This paper aimed to review some of the available climate change impact studies on hydro-meteorology of the Middle East for the purpose of lighting the way for future studies for the region.

Keywords: Climate change, Middle East, Temperature, Precipitation, Hydro-meteorological

1. INTRODUCTION

Global surface temperatures have increased around 0.74°C during the last century due to human induced global warming [1]. Temperature increase is not uniform over the Earth and some parts of the Earth have been affected by climate change more than the others. Hydrology and water resources are severely suffered by climate change particularly in the regions in which experienced more warming than the others.

Precipitation patterns over many regions have been changed due to temperature increases. Joint effects of changes in temperature and precipitation patterns lead to alteration of hydrological cycles influencing streamflow regimes. Global warming motivated changes in globally averaged water vapour concentrations, evaporation, precipitation, humidity, wind speed and streamflow regimes have already been observed and very likely to be observed with increasing severity in the following years [2].

Water availability on the continents has a great importance for human health, economic development, food security, ecosystems and geophysical processes. Global warming has strongly affected the water availability due to firm relationship between saturation water pressure of water in air and temperature. Milly et al. (2005) projected 10–40% increases in runoff in eastern equatorial Africa, the La Plata basin and high latitude North America and Eurasia, and 10–30% decreases in runoff in southern Africa, southern Europe, the Middle East and mid-latitude western North America by the year 2050 based on 12 climate models.

The Middle East is mostly arid to semi-arid and water scarce in terms of water availability. Nine out of fourteen countries in the Middle East and North Africa have less than 1000 m³ per capita water availability, thereby; this part is the most water scarce part of the world [3,4]. Water shortage in the region is exacerbated by increasing population and water demand along with economic development. A rapid decrease in water availability, 667 m³ per capita, has been projected for the Middle East by 2025 [4]. When the figure is compared to projected water availability of world average, 4780 m³, by 2025; it is possible to have better understanding of the water shortage problem in the Middle East. Bou-Zeid and El-Fadel (2002) stated that only Iraq would have sufficient fresh water resources by 2025 (if not affected by water resources projects in the Turkey which is upstream of Euphrates and Tigris Basins).

Since the Middle East has already been experiencing water scarcity; even a small change in water availability may have significant consequences on many sectors including agriculture, hydro-power generation and water supply. Global warming has a potential to lead changes in climate variables and hydrological cycles as mentioned earlier. Therefore, it is vital to perform studies which are investigating hydrological impacts of climate change in global and regional scales. This study aimed to review the hydro-meteorological climate change impact studies for the different parts of the Middle East to provide better understanding of both existing and future hydro-meteorological effects of climate change in the Middle East.

2. CLIMATE CHANGE IMPACTS IN THE MIDDLE EAST

Some of the available studies which investigated hydro-meteorological impacts of climate change in the Middle East and Turkey due to its relationship with Syria and Iraq in terms of water resources in Euphrates and Tigris Basins were reviewed in this paper. Location map of the mentioned countries is shown in Figure 1.

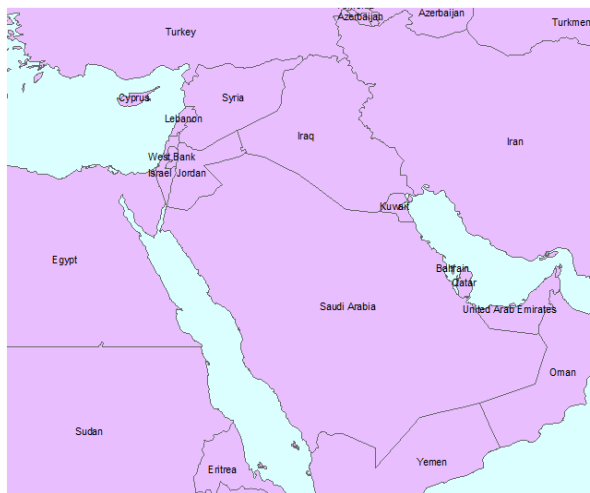


Figure 1: Location map of the region including Middle East countries

There is a common misunderstanding about the importance of climate change for the water potential of the region. It is assumed that since the region is already under water stress, changes in the climate variables will not have substantial influences on the water availability of the region. In opposite, temperature increases and possible precipitation decrease will significantly aggravate the existing water related problems. Thus, it is imperative to investigate future climate and water availability projections through climate change impacts studies.

The first step of climate change impact studies is to perform trend analysis tests for the historical hydro-climatology data to understand the finger prints of the climate change. The next step is to obtain future climate data via Global Climate Models (GCMs) and Regional Climate Models (RCMs). Although GCMs are very useful tool to project future climate, spatial resolution of GCMs is too coarse to use their outputs in hydrological impact studies. Thus, stochastic and dynamical approaches are used to downscale GCM outputs to finer spatial resolutions. RCMs are used to accomplish this task dynamically and they provide better representations of the basins through higher spatial resolutions. Then, outputs of the climate models are used in hydrological models which are calibrated by using historical hydro-meteorological data and prediction of future water potential/availability is achieved. In the following paragraphs, example studies examining for both existing

and future effects of climate change in the Middle East are shown.

Bou-Zeid and El-Fadel (2002) assessed the climate outcomes of the four GCMs including ECHAM4, HadCM2, CGCM1 and GFDL for the Middle East countries; Lebanon, Iraq, Israel, Jordan, Palestine and Syria. They reported temperature increases for all seasons and they underlined the significant increase in summer temperature between 0.8°C and 2.1°C. They explained that areas next to Mediterranean border (Lebanon, Israel, Palestine and costal Syria) will be least affected by temperature increases. However, these regions will be under risk of increased seawater intrusion due to sea level rise. Bou-Zeid and El-Fadel (2002) expressed that increasing mean temperatures will very likely lead increasing irrigation water demand. They also implied the desertification hazard owing to coupled effect of increased temperature and evapotranspiration. In addition, decrease in groundwater recharge due to higher winter temperatures based increased evapotranspiration was reported by Bou-Zeid and El-Fadel (2002). Bou-Zeid and El-Fadel (2002) selected Lebanon to investigate vulnerability of water resources to climate change in the Middle East. UNDP (1999) explained the fact that water resources in Lebanon particularly vulnerable to temperature increases and rainfall pattern changes. They implied the possibility of insufficiency to meet the water demands in 2025 in Lebanon, despite the fact that its current per capita water availability with 766- 1287 m³ which is relatively higher than the other countries in the region. They applied four GCMs outputs in Water Balance Model (WATBAL) for two representative regions (Ksara and Beirut) and reported decreases in surface water and groundwater resources between 5-15% by 2020 depending on the scenario.

Alkolibi (2002) investigated the effects of changes in climate on Saudi Arabia's agriculture and water supply. He explained that Saudi Arabia is very poor country in terms of water resources and agricultural potential. Thereby, projected increases in temperature and decrease in rainfall amount leading increase in evapotranspiration has a strong potential to affect water resources and agricultural activities in the region. He expressed a future decrease in water supply for Saudi Arabia according to common GCMs. Alkolibi (2002) also explained based on Liverman (1992) that the most significant rainfall decreases is expected to be observed in the regions in which already having less precipitation such as Saudi Arabia. Parry and Swaminathan (1992) explained that increase in temperature around 1.5°C will lead an increase in evapotranspiration between 5 and 15%. This amount of increase in evapotranspiration coupled with rainfall reduction will severely affect the crop yield of the region. He also added that the most affected crop by temperature increase will be winter wheat. Alkolibi (2002) expressed that water has been supplied through shallow and deep groundwater sources

and desalination in Saudi Arabia. Shallow and deep groundwater resources are under risk due to excessive use of them and low precipitation meaning low natural recharge of aquifers. Due to projected reduction in future rainfall amount and increasing population leading more withdrawal from groundwater aquifers, future of the groundwater in Saudi Arabia is precious. Alkolibi (2002) implied the importance of desalinated water (mostly sea water) in Saudi Arabia and he stated that major cities rely on desalinated water. He also investigated the trends in temperature and precipitation records of four oldest Saudi weather stations by using the data between 1961 and 1997 to understand the existing effects of climate change in the region. Trend analysis of historical precipitation data showed no clear evidence of climate change in Saudi Arabia. However, Alkolibi (2002) underlined that absence of climate change in climate records does not indicate that climate change will not affect the region in future. Projections of GCMs already demonstrated significant future changes in climate for the region including Saudi Arabia, thereby, very intensive water shortages, influencing especially agricultural production and water supply, can be expected in Saudi Arabia.

Kafle and Bruins (2009) examined the climate change impacts in Israel by performing trend analysis for average annual temperature, annual precipitation and annual aridity (humidity) index, P/PET (P= precipitation and PET=Potential Evapotranspiration). They selected 12 observation stations selected in specific spatial distribution patterns for the purpose of representing regional variations of the climate trend in Israel. They used climate data for the period of 1970-2002. They reported significant warming trends in all stations. They found an increasing trend in precipitation for the stations along or near the Mediterranean coast. However, stations in more inland or eastern part of Israel showed decreasing precipitation trends. Kafle and Bruins (2009) reported statistically insignificant increasing trend in aridity index for the most stations along the Mediterranean coast due to increasing trend in precipitation. However, all inland and the eastern stations showed decreasing trend in aridity reflecting clear increasing aridity. Some of the trends in inland stations are statistically significant suggesting tendency in climate to be more arid during the period 1970-2002 in the desert parts of the Israel.

Evans (2009) investigated possible future climate in the Middle East in the 21st century based on 18 GCMs participating in IPCC 4th Assessment Report. He predicted overall approximately 1.4 K temperature increase by mid-century and around 4 K by the late century based on the models under SRESA2 emissions scenario. In parallel to Kafle and Bruins (2009), he reported mild increases at locations close to water bodies such as Black Sea, Mediterranean Sea, Caspian sea, Red Sea and Persian Gulf (from smallest to largest) and large increases at inland areas far away from the

water bodies. Evans (2009) reported very mild increases in precipitation for the southernmost portion of the Middle East owing to Northward movement of Inter-tropical Convergence zone. However, he stated that largest change in precipitation is a decrease expected over an area including the Eastern Mediterranean, Turkey, Syria, Northern Iraq, Northeastern Iran and the Caucuses. He explained the largest decreases of over 125 mm annually for Southwestern part of Turkey. It means 25% reduction of current precipitation for this region. When it is considered that this region is one of the most important agricultural lands of Turkey, the effect of precipitation decrease will be very strong for the region in terms of agricultural production. Evans (2009) also reported over 170 000 km² land decrease in viable rainfed agriculture for an area including Israel, Lebanon, Syria, Iraq and Iran. He also explained the relationship between the timing of maximum precipitation in Iran and growing season of crops and he added that Northern Iranian agriculture can be forced to change cropping strategy/types.

As mentioned earlier in this paper, climate change effects have already been observed for many parts of the world. Sowers and Weinthal (2010) explained the observed effects of climate change in the Middle East with solid examples. They stated based on Altinbilek (2010) that there is a very significant increasing trend in temperatures, particularly for summer season, in the western Turkey for the last five decades and the hottest summer on record in 2007. They expressed the negative effect of climate change on dust storms which affect crops, human health, economic activity and tourism by referring to the study of El Raey (2008). They also presented studies showing changes in timing, form and intensity of rainfall and snowfall in Israel, Lebanon and Saudi Arabia. They expressed increasing intensity and frequency of drought for the area spreading of central Turkey, Syria and other countries of eastern Mediterranean based on Altinbilek (2010). They also reported severe and unprecedented floods and landslides in the Gaza Strip [5], in Saudi Arabia, in Turkey and along the Nile River [7]. Sowers and Weinthal (2010) also reported low and empty dams in Turkey due to decrease in surface water availability in Turkey [6].

Yilmaz et al. (2011) investigated the effects of climate change on water resources at one of the key basins of the Middle East, Euphrates Basin. They focused on the snow dominated headwater of the basin. They did streamflow forecasting by using RCM outputs in calibrated hydrological models and they attempted to estimate future surface water availability of the basin. They reported temperature increases for all seasons between 3°C and 5°C over the period of 2070-2100 based on RegCM outputs under A2 greenhouse gases emissions scenario. They stated the largest temperature increase in summer season and the lowest in winter season. They also projected precipitation decrease between 5 and 15% for the seasons except autumn in

which they expressed very mild precipitation increase. Yilmaz et al. (2011) also reported significant streamflow decreases up to 43% for the same time period. They stated reduction in streamflow for summer, spring and winter season, and increase in autumn season in accordance to precipitation predictions. They also estimated around one month shift in snow melting time due to temperature increases in the basin.

Wade et al. (2010) examined the effects of climate change in Jordan by the end of the 21st century by using RCM, HadRM3, outputs in hydrological models in a similar way to Yilmaz et al. (2011). They explained based on Oroud (2008) that up to 60% decrease can be observed in water yield in Jordan in response to 10% decrease in precipitation and 2°C increase in temperature. Also, Samuels et al. (2009) projected more frequent and intense floods in Jordan. Wade et al. (2010) expressed the largest reductions in precipitation, around 30% in the river Jordan region, for December and January months. They also projected a longer rainy season which compensated the rainfall amount decrease for the region. They explained decrease in mean annual rainfall in the headwaters of the River Jordan and the Wadi Faynan. They also predicted 2°C increase in temperature leading increased evaporation. Wade et al. (2010) projected no change in baseflows for the period of 2070-2100 in Upper River Jordan, on the other hand, they presented 12% reduction in baseflow in the Wadi Faynan for the same period. Suppan et al. (2008) predicted 23% decrease in the total runoff by the end of 21st century in parallel to findings of Samuels et al. (2009). Suppan et al. (2008) declared decrease in baseflow in Jordan due to reduction of groundwater recharge because of precipitation decrease. However, Samuels et al. (2009) predicted increased intensity in rainfall events, also increase in frequency of long lasting rainy spells resulting recharge for groundwater and offsetting effects of reduced rainfall in the region. Wade et al. (2010) predicted increase in irrigation demand due to decreased rainfall and increase near-surface temperature in Jordan. They presented irrigation water demand increase from 62 to 132 mm at Ramtha in the northwest Jordan over the period of 2071-2100 under the A2 emission scenario. They also declared 6% increase in agricultural water demand at Jordan valley and reduction in water availability in northwest Jordan, Israel and the West Bank for the period of 2021-2050 under A1B scenario.

Tayanc et al. (2009) investigated the effects of climate change in Turkey by using climate data (precipitation and temperature) between 1950 and 2005 from both urban and rural observation stations. They reported two different clear periods according to signal analysis of temperature data: 1) cooling period from 1960s till 1993, mostly with the lowest temperature values on 1992-1993 due to the eruption of Mount Pinatubo, 2) a significant warming trend for the last decade with the maximums in the record history in 2000-2002. They

also explained the importance of variability of urban precipitation series rather than rural series suggesting more frequent and intense flood and drought events in urban regions. Tayanc et al. (2009) found significant warming in southern and southeastern parts of the country according to spatial analysis. In particular, minimum temperatures showed very significant warming trends almost all locations owing to urbanization effect. According to seasonal analysis, summer, spring and autumn seasons showed significant warming trends in Turkey. Tayanc et al. (2009) showed that southeastern part of Turkey is under the risk of desertification because of significant warming in maximum and mean temperatures and significant decrease in precipitation. They also reported significant decreasing trends in precipitation in western parts of Turkey such as Aegean and Trachea regions and they linked this trend to positive trend of the North Atlantic Oscillation (NAO). However, some regions in northern Turkey showed increasing precipitation trends. Seasonal analysis showed significant decreasing precipitation trends in winter season which is the rainiest season in the majority of Turkey. They pointed in particular western Turkey as a risk zone due to significant precipitation decreases and increasing population, leading additional stress on already existing water resources problems.

Many studies showed reduction in precipitation of Middle East countries varying from 10% to 30% by the end of the current century [8]. These studies especially highlighted the strong influence of climate change on precipitation decrease in Mediterranean islands, southeastern Europe and the Turkish peninsula. Sowers et al. (2011) stated that Middle East region has experienced significant warming for the last five years. They also presented that the Levant (Syria, Lebanon, Palestine and Israel) will be the region most suffering from precipitation changes. Most climate models projected decreases in precipitation coupled with increasing temperatures leading water availability reduction and increasing water deficits in the Lower Jordan River basin including Israel, West Bank and Jordan. Suppan et al. (2008) reported mean annual temperature increase up to 4.5 °C coinciding 25% decrease in mean annual precipitation by the end of the century. Sowers et al. (2011) also explained that climate models outcome larger precipitation decreases in northern Levant. They reported significant decline in renewable water availability, around 50% by 2025 relative to 1997 levels by referring to 2007-2008 Human Development Report.

3. DISCUSSION ON ADAPTATION AND UNCERTAINTIES RELATED TO CLIMATE CHANGE STUDIES

As explained in the previous section, climate change and human induced other factors have important influences on water resources leading significant socio-

economic problems later. It is important to understand that effects of climate change on water availability are expected to be less than effects of population growth in the Middle East. Vorosmarty et al. (2000) has compared the possible global precipitation changes due to global warming and water demands due to population growth and they concluded that effects of demographic growth based water demand increase is larger than climate change on water availability. Conway (2005) also compared the effects of climate change and other anthropogenic factors including population increase, land use choices and development strategies and he ended up with the same conclusion of Vorosmarty et al. (2000). Although assumed no change in water availability due to climate change, water availability is expected to decline by 30% to 70% due to population increase in the Middle East and North Africa [9]. Decrease in water availability will affect all countries in the region, however, countries which rely on groundwater rather than surface water will be affected more severely.

The key solution for dealing with the problems associated with climate change and water demand increase owing to population growth is adaptation. Adaptation can be defined as developing institutional and political capacities for the purpose of ensuring sufficient water supply and water quality against the intensifying risks of climate change [9]. Most adaptation measures would be useful for the regions regardless of climate change impacts. This is called “no-regret” approach. Although climate change would not affect the regions, adaptation measures will be beneficial for the adaptability of water resources to the natural variability in climate patterns [3]. Main adaptation measures for water availability can be stated as follows: usage of surplus winter runoff, wastewater treatment and recycled water use, seawater/brackish water desalination, groundwater recharge, improved and efficient irrigation water management, adoption of a stricter water use policies, more research for better understanding of hydrological climate change effects.

Although hydrological impact studies provide an idea for the future climate and water availability, there are significant uncertainties of these studies. The most important ones are the selection of SRES scenario, the regional climate projections, uncertainties related to rainfall prediction of climate models, structure and calibration of hydrological models and finally errors in observed data.

4. CONCLUSION

Due to human induced greenhouse gases emissions, climate is changing in a way which can not be explained by natural variability. Increases in temperature due to climate change has been triggering changes in intense, frequency and variability of precipitation and finally affecting water resources and hydrological cycle. Middle East is one of the most water stressed part of the

world and it is very sensitive to even a small change in climate variables. Water shortage has already been exacerbated by rapid population growth and economic development in the region. Available climate change impact studies proposed that changes in climate variables in the Middle East will decrease water availability significantly in this century. Thereby, it is imperative to develop adaptation strategies to reduce the adverse effects of climate change on the water availability in the region.

Some of the available climate change impact studies for the Middle East were reviewed in this paper for the purpose of providing a useful literature for future climate change studies for the region. It is recommended to producing a more comprehensive review study by enlarging the number of climate change papers in the Middle East as a next step. Finally, it is very important to accomplish more research on climate change and water availability. Increasing number of studies will provide better understanding and clearer picture of future water potential of the countries in the Middle East. Thus, it will be possible to implement reasonable adaptation policies for the future of the water resources in the region.

REFERENCES

- [1] K.E. Trenberth, P.D. Jones, P. Ambenje, R. Bojariu, D. Easterling, A. Klein Tank, D. Parker, F. Rahimzadeh, J.A. Renwick, M. Rusticucci, B. Soden, and P. Zhai, “Observations: Surface and Atmospheric Climate Change”, in [S. Solomon, D. Qin, M. Manning, Z. Chen, M. Marquis, K.B. Averyt, M. Tignor, and H.L. Miller (eds) 2007, *Climate Change 2007: The Physical Science Basis. Contribution of Working Group I to the Fourth Assessment Report of the Intergovernmental Panel on Climate Change*, Cambridge University Press, Cambridge, United Kingdom and New York, NY, USA, 2007.
- [2] S. Beldring, T. Engen-Skaugen, E.J. Forland, and L.A. Roald, “Climate change impacts on hydrological processes in Norway based on two methods for transferring regional climate model results to meteorological station sites”, *Tellus*, vol. 60, no. 3, pp. 439–450, 2008.
- [3] E. Bou-Zeid, and M. El-Fadel, “Climate Change and Water Resources in Lebanon and the Middle East”, *Journal of Water Resources Planning and Management*, vol.128 (5), pp.343, 2002.
- [4] J. Berkoff, “A strategy for managing water in the Middle East and North Africa. Rep.” The International Bank for Reconstruction and Development, The World Bank, Washington, D.C., 1994.

- [5] Al Yaqoubi, "Gaza Strip: Sustainable Yield of the Coastal Aquifer". Unpublished report. Gaza City: Palestinian Water Authority, 2008.
- [6] D. Altinbilek, "Adaptation to Climate Change in Turkey: Floods and Droughts", *Climate Change Adaptation in the Middle East and North Africa: Challenges and Opportunities*, Dubai Initiative, 2010.
- [7] K. Abu Zeid, "The MENA Region Water Sector: From Politics in Climate Change to Hydro-Politics in Adaptation", *Climate Change Adaptation in the Middle East and North Africa: Challenges and Opportunities*, Dubai Initiative, 2010.
- [8] P.C.D. Milly, K.A. Dunne, and A.V. Vecchia, "Global pattern of trends in streamflow and water availability in a changing climate", *Nature*, doi:10.1038/nature04312, 2005.
- [9] J. Sowers, E. Weinthal, and A. Vengosh, "Climate change, water resources, and the politics of adaptation in the Middle East and North Africa", *Climatic Change*, vol. 104, pp.599–627, 2011.
- [10] F.M. Alkolibi, "Possible Effects of Global Warming on Agriculture and Water Resources in Saudi Arabia : Impacts and Responses", *Climatic Change*, vol.54, pp. 225–245, 2002.
- [11] D. Conway, "From headwater tributaries to international river: observing and adapting to climate variability and change in the Nile Basin", *Glob Environ Change*, vol.15 (2), pp.99–114, 2005.
- [12] M. El Raey, "Impact of climate change on the Nile Delta region", Paper presented at climate change in Egypt conference, Cairo, 11 November, 2008.
- [13] J.P. Evans, "21st century climate change in the Middle East", *Climatic Change*, vol. 92, pp.417–432, 2009.
- [14] H.K. Kafle, and H.J. Bruins, "Climatic trends in Israel 1970–2002: warmer and increasing aridity inland", *Climatic Change*, vol. 96, pp. 63–77, 2009.
- [15] D. Liverman, "The Regional Impact of Global Warming in Mexico: Uncertainty, Vulnerability, and Response", in *The Regions and Global Warming*, Chapter 4, Oxford University Press, 2002.
- [16] I.M. Oroud, "The impacts of climate change on water resources in Jordan". In *Climatic changes and water resources in the Middle East and North Africa* (eds F. Zereini & H. Hotzl), pp. 109– 123, Springer, 2008.
- [17] M.L. Parry, and M.S. Swaminathan, "Effect of Climatic Change on Food Production", in Mintzer, I. M. (ed.), *Confronting Climatic Change: Risks, Implications, and Responses*, Chapter 8, Cambridge University Press, 1993.
- [18] R. Samuels, A. Rimmer, and P. Alper, "Effect of extreme rainfall events on the water resources of the Jordan River", *J. Hydrol.*, vol. 375, pp. 513–523, 2009.
- [19] J. Sowers, and E. Weinthal, "Climate Change Adaptation in the Middle East and North Africa: Challenges and Opportunities", Working Paper 2, Dubai Initiative, 2010.
- [20] P. Suppan, H. Kunstmann, and A. Heckl, A. Rimmer, "Impact of climate change on water availability in the Near East". In *Climatic changes and water resources in the Middle East and North Africa* (eds F. Zereini & H. Hotzl), pp. 45–57. Springer, 2008.
- [21] M. Tayanc, U. Im, M. Dogruel, and M. Karaca, "Climate change in Turkey for the last half century", *Climatic Change*, vol. 94, pp. 483–502, 2009.
- [22] United Nations Development Program (UNDP), "The first national inventory of greenhouse gas emissions by sources and removals by sinks", Ministry of the Environment, United National Development Program, Beirut, Lebanon, 1999.
- [23] C.J. Vörösmarty, P. Green, J. Salisbury, R.B. Lammers, "Global water resources: vulnerability from climate change and population growth", *Science*, vol. 289, pp. 284–288, 2000.
- [24] J. Wade, E. C. L. Black, D. J. Brayshaw, M. El-Bastawesy, P. A. C. Holmes, D. Butterfield, S. Nuimat, K. Jamjoum, "A model-based assessment of the of projected climate change on the water resources of Jordan", *Philosophical Transactions of the Royal Society*, vol. 368, pp. 5151-5172, 2010.
- [25] A.G. Yilmaz, and M.A. Imteaz, "Impact of climate change on runoff in the upper part of the Euphrates Basin", *Hydrological Sciences Journal*, Accepted on 18 April 2011, In press.

Decentralized Sewage Reuse for Irrigation Purposes

Karl-Ulrich Rudolph¹, Tim Fuhrmann², Sandra Kreuter³, Stefania Paris⁴

¹⁻³ Institute of Environmental Engineering and Management at the University of Witten/Herdecke gGmbH (IEEM), Alfred-Herrhausen-Str. 44, 58455 Witten, Germany (E-mail: mail@uni-wh-utm.de)

⁴ HUBER SE, Industriepark Erasbach A1, 92334 Berching, Germany (E-mail: stefania.paris@huber.de)

ABSTRACT

Urban green areas are often irrigated by valuable drinking water from public supply. Especially in areas with water shortage or costly supply conditions it may be sensible to use wastewater for irrigation purposes. For direct utilization of raw wastewater from existing sewage systems near to the point of use (so called "sewage harvesting") decentralized treatment solutions are necessary. For the particular case of irrigation water, purification standards are lower than that for fully purified (potable) water, which offers potentials for specifically adopted treatment solutions. Within a current R&D project, a novel concept has been developed, focusing on only two main purification steps: a mechanical pre-treatment by screening and sedimentation and a subsequent disinfection by UV irradiation. The concept abandons biological treatment to keep the system manageable and allow non-continuous operation. Preparatory tests indicate that the disinfection of only mechanically purified wastewater by UV irradiation is a feasible solution with acceptable levels of UV doses and resulting power consumption. To minimize hygienic risks, the technical approach has to be integrated into a multi-barrier concept, taking into consideration the chosen way of water reuse and handling as well as the specific site conditions. The paper shows potentials as well as restrictions for the described reuse concept.

Keywords: compact wastewater treatment, decentralized, disinfection, irrigation, pilot plant, sewage reuse, UV irradiation

1. INTRODUCTION

Especially in arid regions, public green areas like parks or green stripes along traffic lines are essential for life in urban areas. To keep the green areas in a proper condition despite the arid climate conditions, they have to be irrigated intensively. But even in regions with scarce water resources, potable water from public water supply systems is often used for this purpose, resulting in an increasing lack of water for higher-valuable uses like water supply for the population or industrial purposes. On the other hand, particularly in arid developing countries, completely uncontrolled use of raw wastewater for irrigation purposes is widely spread often linked with significant hygienic problems. [35], [39]

Facing these challenges, within an ongoing research project a decentralized system for controlled utilization of sewage as irrigation water in public green areas has been developed to reduce the demand of water from public supply systems as well as to ensure reasonably secure conditions for the application of sewage for irrigation.

As part of a general multi-barrier concept, the objective of the project has not been to offer a costly full purification facility for sewage but to show a comparatively efficient system with partial clarification and disinfection of raw wastewater as far as it is necessary for the specific use in public green areas.

2. DEVELOPMENT OF A TECHNICAL CONCEPT

2.1 Wastewater disinfection as a key challenge for wastewater utilization

The complete reduction of organics and nutrients in wastewater is usually not required, if the treated water is used for irrigation purposes, as the contained nutrients can partly be used as valuable fertilizer (though salinization has to be taken into consideration). Therefore, when talking about wastewater reuse for irrigation of green areas, appropriate wastewater disinfection is a key issue.

Microbial pathogens have to be reduced to levels being suitable for irrigation applications. Seen from a strict technical point of view, purification of wastewater including disinfection can be performed to any wished level, up to a total sterilization of wastewater. But taking treatment costs and often limited competence of operational staff into consideration, performance of purification and disinfection systems should be limited only to the really required levels. However, it has to be pointed out that a merely partial purification of wastewater is only acceptable in combination with other hygienic safety measures like restricted irrigation, human exposure control, etc.

The design of site-specific concepts also has to reflect the relevant standards, regulations and guidelines existing for wastewater to be utilized for irrigation purposes, (compare for example [31], [38]).

2.2 Integration into a Multi-Barrier Strategy

In addition to the technological treatment concept, a multi-barrier strategy for hygienic risk management has to be outlined when using wastewater for irrigation in public areas (as described in the WHO guidelines [39]), taking into consideration three key issues:

- (1) Water reutilization suitable for site conditions (like geological situation, kind of plantings, etc.),
- (2) Way of handling suitable for water reutilization (e.g. distribution and application of the irrigation water),
- (3) Treatment suitable to the way of handling of raw sewage (especially regarding pathogen reduction).

These issues are dependent from each other in both ways, e.g. sewage treatment with only limited reduction of pathogens urgently requires suitable handling like drip irrigation instead of sprinkling and appropriate instructions for workers and operational staff. [30]

2.3 Requirements for a pilot treatment system

For decentralized production of irrigation water, the design of a suitable treatment system has to consider a compact construction and flexibility regarding different conditions at the application locality. As the removal of nutrients from the wastewater is of minor relevance in that case, the treatment concept can be focused on two main steps, which have been identified to be sufficient to produce irrigation water of the required quality:

- Mechanical/physical purification of the influent by fine screening and sedimentation/lamella separation (to remove grit and organic matter in order to avoid odorous and aesthetic problems with the irrigation and as pre-treatment for the subsequent disinfection),
- Adequate wastewater disinfection (to avoid health risk through pathogens contained in irrigation water).

In order to enhance the sedimentation process, dosing of flocculants has to be taken into consideration, too.

Funded by the German Federal Ministry of Research and Education (BMBF), a specific concept has been developed as displayed in figure 1. The idea is to create a system that allows a placement on or next to an existing manhole of the sewage system. The system combines partial removal of pathogens sticking to particles as well as helminthes by settlement with subsequent inactivation of pathogens contained in the effluent by UV irradiation. The physical treatment also results in a significant reduction of COD loads. [34], [37]

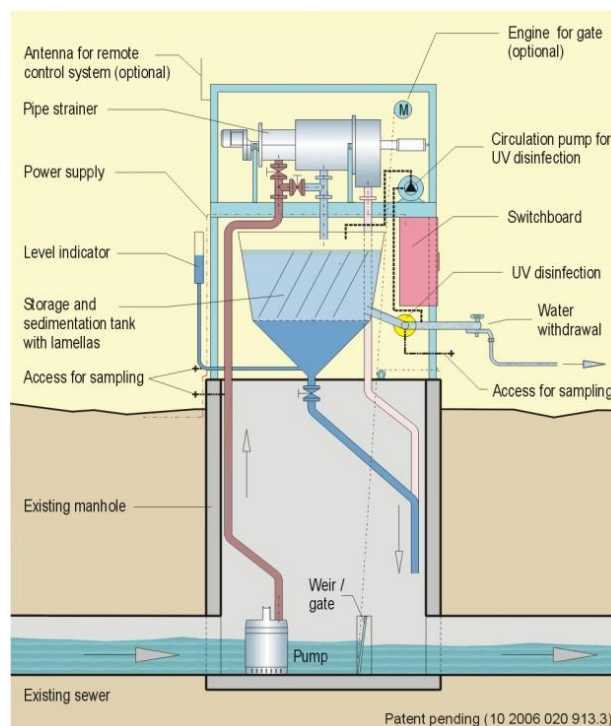


Figure 1: Schematic layout of the original concept [34], [37]

The concept has been realized by an upscaled containerized pilot system, which has been pre-tested in Germany and is currently operated in the UAE, accompanied by a measurement program to validate relevant operational data.

3. TECHNOLOGICAL BASE CONCEPT

3.1 Description

The pilot plant is mounted in a container and was designed for a flow rate of 5 l/s, equipped with a fine screen \varnothing 1 mm (Huber Pipestrainer), a buffer and sedimentation tank (1,000 l) and an UV disinfection unit with 4 lamps (0.33 kW, 50 - 100 % variable power, ITT Wedeco Spectrotherm) and sensor control, all equipment self-cleansing and fully automated. [36]

As described in table 1 and figures 1 and 2, a pump is directly lifting up the raw wastewater from the public sewer, feeding a pipestrainer (a high-tech, very fine screen). The wastewater is flowing from the outlet of the pipestrainer into a compact buffer and sedimentation tank. The clear water outlet from the sedimentation tank can further be treated by UV radiation, providing basic or full disinfection (depending on the specific needs, on-site). The residuals in form of grit from the pipestrainer and sediments from the tank are sent down the drain, directly back into the sewer line. [36]

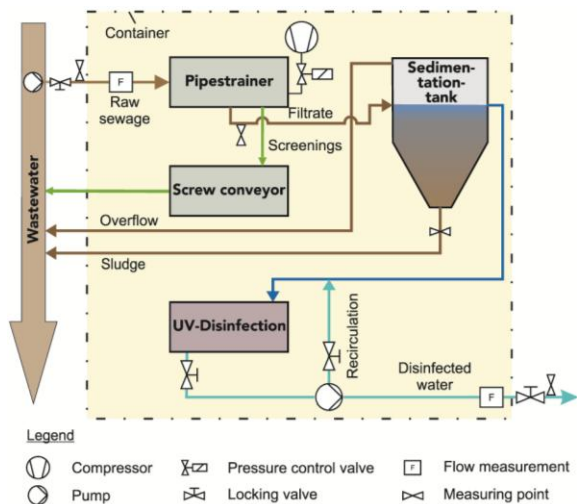


Figure 2: Flow chart of base concept

Table 1: Key parts of the pilot treatment system [36]

Part	Description
Feeding pump	A pump to feed the system with raw sewage from existing sewage systems, protected by a screen against coarse matter.
Pipe strainer	The mechanical separation of solid wastes and organic matter including removal of hair, fibres and fine suspended material is done by fine screening through a pipe strainer with a screen of 0.2 to 1.0 mm slot width. The pipe strainer consists of a horizontal screw which rotates inside a pipe-shaped screen basket and transports the solids retained on the screen surface up to the screenings' discharge. The wastewater to be treated flows through the screen from inside to outside and is then discharged vertically downwards through an outlet pipe connection (see Figure 1). The screen basket can be equipped with different screening elements and thus adapted to suit specific requirements, with the screen surface mechanically cleaned by brushes, which are fitted to the screw. Backwashing with water is not required.
Settlement tank	The sedimentation tank has two functions: settlement of suspended solids and buffer volume for flow variations and recirculation from the disinfection unit. Sediment can periodically be removed from the tank through valves back into sewage system.
UV irradiation reactor	Disinfection of the wastewater to the required level is ensured by a subsequent disinfection reactor with UV irradiation. By recirculation, the UV dose can be increased, resulting in higher disinfection efficiency.

3.2 Experiments

The first test phase has been realized at the wastewater treatment plant (WWTP) of Neumarkt, Germany, with about 130,000 PE. The wastewater is characterized by a high content of industrial pollution loads of approx. 67 % (mainly breweries, chemical industry), whereas the load originating from municipal wastewater is only

33 % of the total wastewater inflow load. In the first test series 12 random samples have been taken at the three following sampling points: (1) inflow, (2) after pipe strainer and (3) after UV-disinfection, over a period of 5 weeks. [29]

The flow in the pilot plant has been defined with 3 l/s and parameters TSS, turbidity and UV transmittance (UV-T) have been measured. These parameters provide information on sedimentation efficiency and conditions for UV disinfection, so that conclusions can be drawn in terms of possible impacts on UV disinfection [31]. 20 % UV-T at an UV dose of 500 J/m² has been defined as target value. Previous laboratory tests indicate that a sufficient bacterial reduction is achieved with an UV-T of 20 %. [29]

Table 2: Analytical Methods [29]

TSS	DIN 38 409 H2.
Turbidity	Hach Lange 2100 P ISO Portables measurement device
UV-Transmittance	WEDECO TUV.5

3.3 Results

As shown in Figure 3 there is a linear correlation between the parameters turbidity and TSS and an exponential correlation between turbidity and UV-T.

An increase in turbidity results in an increase in TSS or a decrease in UV-T. Consequently the objective is to keep turbidity as low as possible to avoid smaller suspended solids in the inflow to the UV disinfection unit. In order to reach this objective sufficient sedimentation has to be guaranteed.

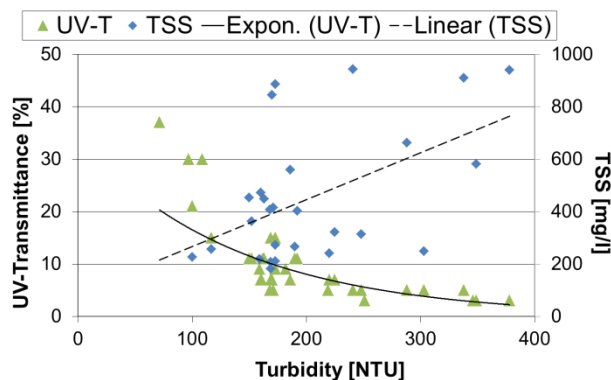


Figure 3: Correlation between turbidity, TSS and UV-T [29]

During the test phase it has been discovered that the sedimentation capacity has not been sufficient to achieve an adequate reduction of TSS and turbidity and thus an adequate UV-T (see figures 4 and 5).

At the measuring point “after pipestrainer” an average reduction of -14 % TSS (related to the inflow) has been measured but the operating state has been quite unstable

as TSS reduction ranges from - 63 % to even an increase of +37 %. After the pipestrainer the parameter turbidity has even been increased in average by 40 % in 11 of 12 samples. Although the pipestrainer took out load from the wastewater inflow, it caused on the other side an increase of turbidity. One possible reason is the comminution of organic substances by the brushes of the pipestrainer which results in an increase of TSS content.

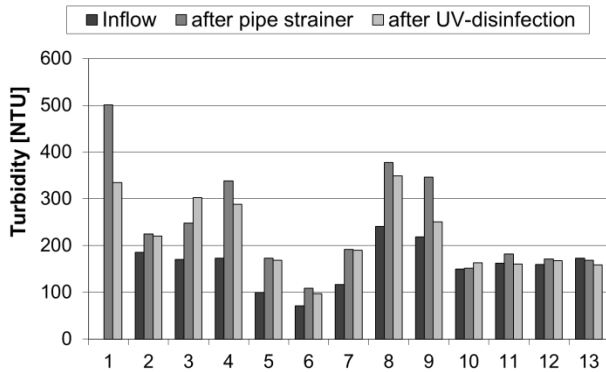


Figure 4: Turbidity measurement results [29]

The average reduction of TSS and turbidity after sedimentation and disinfection step has been measured with 19 % and 16 % respectively, related to TSS and turbidity values after pipestrainer measuring point.

The overall average increase of turbidity of 32 % and only minor decrease of TSS of 19% in the outflow in comparison to the inflow results from the hydraulic overload of the system, fluctuation of wastewater composition (discontinuous industrial inflow), a discontinuous operating state and an unstable inflow to the pilot plant.

The average UV-T amounts to 11 % in the inflow but fluctuated between 5 and 37 %. The average UV dose has been 317 J/m². After the pipe strainer there has not been an improvement of UV-T which is decreased in average by 27 % to 8 % and has not changed significantly after sedimentation and UV-disinfection treatment steps. It is assumed that due to the pipestrainer mainly the concentration of small, severely settleable particles has increased and therefore the dimensioning of the sedimentation tank and the defined inflow do not assure a sufficient retention time for the sedimentation and reduction of these particles. These results and further laboratory tests resulted in some changes of the technological concept (see below). [29]

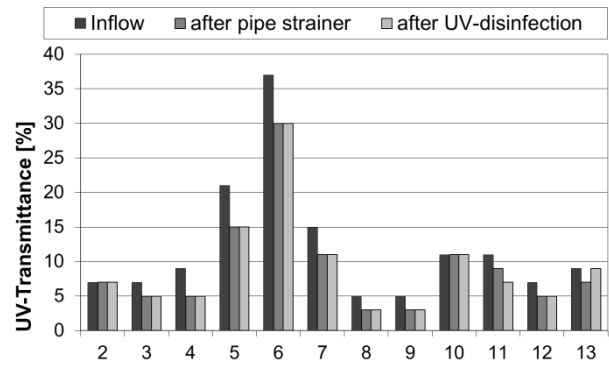


Figure 5: UV-Transmittance measurement results [29]

4. ADAPTED TECHNOLOGICAL CONCEPT

4.1 Description

Due to the results of the first test series the sedimentation tank (0.79 m²) has been replaced by a lamella clarifier resulting in an increase of sedimentation area to 6.3 m². Additionally, the sedimentation process is supported by a coagulation/flocculation process adding a 0.1 % polymer dispersion. [29]

Flocculation tests in laboratory scale have been conducted using Fe-III-chloride, poly aluminum chloride (PAC) and polymer dispersion Ashland Praestol K110L of which the latter has been selected for the pilot plant due to low costs and bigger floc formation resulting in lower sedimentation time. Additionally the addition of Fe-III-chloride and PAC leads to an unintended reduction of pH. [29]

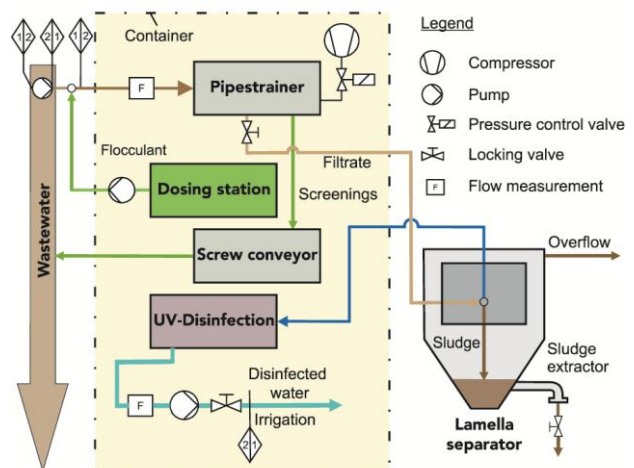


Figure 6: Flow chart of adapted concept

The updated technological concept shown in figure 6 consists of following components:

- (1) pipe strainer (unchanged),
- (2) lamella clarifier tank (GEA 2H with TUBEdek lamella, 2 m³),
- (3) polymer dosing station (ProMinent AF 400 RC) and,
- (4) UV-disinfection unit (unchanged).

4.2 Experiments

Investigations have been made in order to clarify whether the treatment capacity of the pilot plant is sufficient to meet the selected quality standards and reference parameters for effluent reuse (see table 2).

Table 3: Limit values for effluent reuse [29]

Parameter	Sharjah	Europe	US EPA
BOD [mg/l]	15	n/a	45
COD [mg/l]	100	n/a	90
TSS [mg/l]	15	100	30
TDS [mg/l]	1,500	2,000	450
pH [-]	6-9	6-8	6-9
Total-N [mg/l]	66.3	n/a	30
Total-P [mg/l]	30	n/a	20
E.coli [CFU/100ml]	100	2,000	1,000
Total coliform organ. [CFU/100ml]	n/a	n/a	200

Test series 2 have been executed in February/March 2010 at WWTP Neumarkt, Germany, by taking random samples over 21 days (sampling points see above). Due to the results from test series 1 the inflow to the pilot plant has been reduced to 1 l/s. [29]

Table 4: Further analytical methods [29]

COD	Hach-Lange cuvette tests LCK 514
TN	Hach-Lange cuvette tests LCK 338
TP	Hach-Lange cuvette tests LCK 349
E. coli, total coliforms	3M petrifilm count plates

Test series 3 have been executed in June/July 2011 at the American University of Sharjah (AUS) by taking random samples. The wastewater is originating from the AUS being mechanically pre-treated by a screen. The inflow was fluctuating about 1 - 1.5 l/s. Only the results of the microbiological analyzes are presented here. [33]

4.3 Results

4.3.1 Test Series 2: February/March 2010

During test series 2 dosing of 0.1 % polymer dispersion Ashland Praestol K110L has been varied between 10, 20, 30 and 40 ml/s.

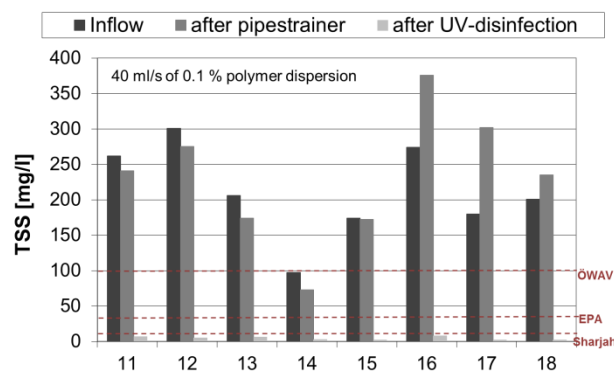


Figure 7: TSS measurement results [29]

The best treatment results of all analyzed parameters have been achieved with dosing of 40 ml/s, i.e. TSS limit values could only be met with 40 ml/s polymer dosing (average TSS content of 5 mg/l in outflow). In most cases, with lower polymer dosing, TSS limit values have been exceeded in the outflow (40 mg TSS/l on average). In some cases an increase of TSS after the pipestrainer was observed independent from the dosing amount. The average inflow TSS has been measured with 245 mg/l.

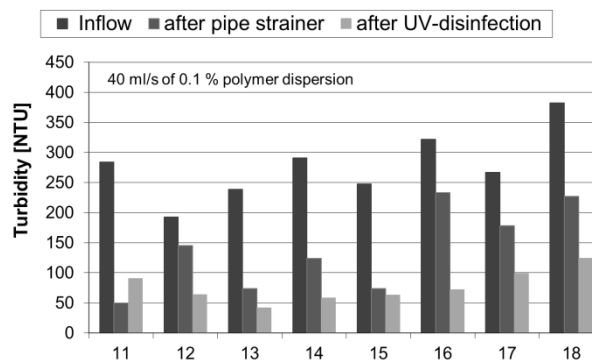


Figure 8: Turbidity measurement results [29]

Turbidity increases with increasing TSS content. The lowest turbidity values have been measured with 40 ml/s polymer dispersion dosing due to rapid flocculation and generation of bigger flocs (77 NTU on average). The US EPA limit value (30 NTU) could not be met. The average turbidity of the raw wastewater in the inflow of the pilot is 340 NTU.

By dosing of 40 ml/s of polymer dispersion the target value of 20% UV-T could be met on almost all measuring days (on average 25 % in the outflow). Less addition of polymer dispersion results in smaller flocs and therefore deteriorates the parameter UV-T and limit values could not be met anymore (e.g. only 9 % UV-T in the outflow for 10 and 20 mg/l of polymer dosing).

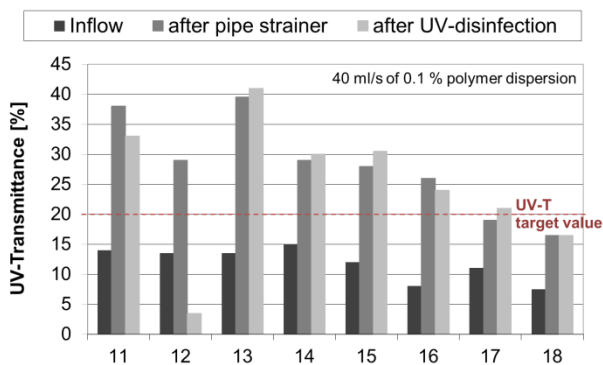


Figure 8: UV-Transmittance measurement results [29]

With 40 ml/s polymer dispersion dosing the best reduction rates of COD has been observed (in average 42 %). Anyway these reduction rates are not sufficient to meet the Sharjah limit value for CSB of 100 mg/l.

The limit value for TN in Sharjah (66 mg /l) could be met with polymer dispersion dosing of 30 and 40 ml/s for all samples. In general it must be stated that the increase of nitrogen-reduction due to mechanical treatment and polymer dispersion addition is not significant.

The limit values for TP are met in all samples.

4.3.2 Test Series 3: June/July 2011

On average the UV-T in the inflow has been measured with 16 %. Due to the mechanical and chemical treatment processes the UV-T value has increased on average to 37 % in the outflow of the pilot plant.

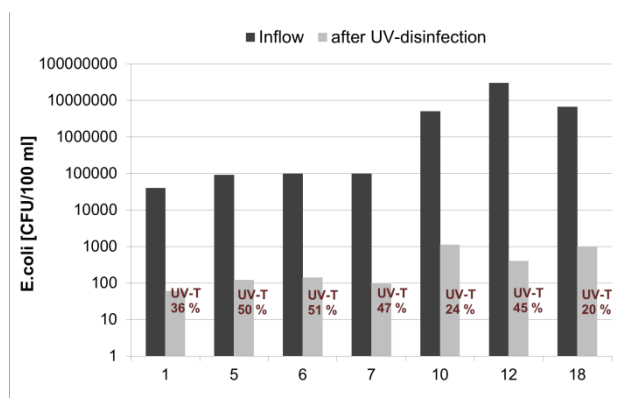


Figure 9: Reduction of Escherichia coli [33]

The reduction of parameter E. coli has been measured with 2.8 to 4.9 log units. The U.S. EPA limit value of 1000 CFU/100 ml could be met in most cases whereas the Sharjah limit value 100 KBE/100 ml could only be met in two cases (see Figure 9).

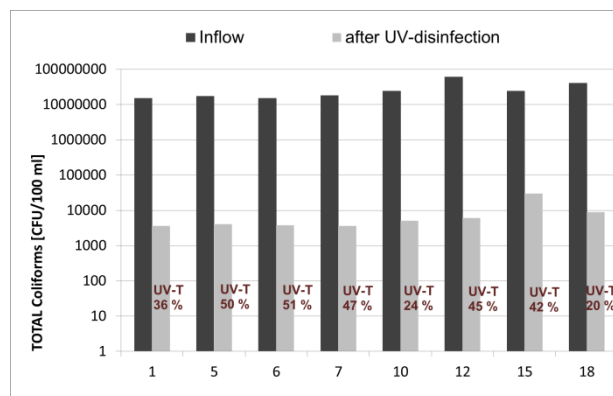


Figure 10: Reduction of total coliforms [33]

A 2.9 - 4.0 log reduction could be measured for total coliforms. The U.S. EPA limit value (220 CFU/100 ml) could not be met (see Figure 10).

Despite the target value of 20 % UV-T is considerably exceeded in most cases, the reduction rates of microbiological parameters have not increased simultaneously.

5. CONCLUSIONS

Within the described research project a compact treatment system has been developed for the efficient decentralized reuse of wastewater from existing sewage systems to be used for irrigation of public green areas like parks and green stripes along roads of cities in arid regions. The relatively simple and flexible system may be a component to reduce the use of valuable potable water for irrigation purposes in these regions.

The experiments show that with the help of the pilot plant wastewater can generally be treated to levels suitable for reuse purposes, with some exception for specific parameters. On average a target value for UV-T of 20 % could be met resulting in a significant log-reduction of E. coli (2.8 - 4.9) and total coliforms (2.9 - 4.0). On the other hand at the outflow of the pilot plant the limit values for these microbiological parameters could not be met. Likewise, limit values for TSS at the outflow could only be met in some cases.

Within this project further test series are planned to be carried out using a bigger mesh size for the pipestrainer (2 mm instead of 1 mm) in order to improve the flocculation process. It is assumed that the pipestrainer comminutes solid particles and destroys flocs which have already been formed resulting in an increase of turbidity and decrease of UV-T. In order to reach UV-T values of > 20 % especially fine and colloid particles have to be removed from the wastewater.

6. ACKNOWLEDGEMENTS

The pilot project described in this paper has been supported by the German Ministry of Education, Science and Research, BMBF (www.bmbf.de/en), project no. 02WD0757 and 02WD0759, under the umbrella of the sustainability and water research program [32]. The authors and all project stakeholders (www.uni-wh-utm.de, www.huber.com and www.wedeco.com) would like to express their thanks for the support.

REFERENCES

- [29] Aguilera, C. S.: *Optimierung und Betrieb einer Pilotanlage zur Rohabwasserbehandlung für Bewässerungszwecke in ariden Gebieten (Optimization and operation of a pilot plant for the treatment of raw sewage for irrigation purposes in arid regions)*, diplom thesis at FH Mainz, Mainz, 2010.
- [30] Cornel, P., Firmenich, E., Fuhrmann, T., et al.: *Assessment of Process Steps for the Treatment of Wastewater for Reuse*, Editor: DWA, Hennef, Germany, 2008.
- [31] Fuhrmann, T., Rudolph, K.-U.: "Wastewater ponds and subsequent UV disinfection - a lean cost option for agricultural wastewater reuse", *Proceedings of the 6th IWA Specialist Conference on Wastewater Reclamation and Reuse for Sustainability (WRRS)*, Antwerp, Belgium, 9-12. Oct. 2007.
- [32] Furrer, R.: "Übersicht über den BMBF Förderschwerpunkt dezentrale Wasserver- und -entsorgungssysteme", Presentation at IFAT Forum Water and Wastewater, Munich, 08. May 2008.
- [33] Grüner, S.; Jahn, L.: *Inbetriebnahme und Optimierung der Pilotanlage BMBF Sharjah zur Rohabwasserbehandlung für Bewässerungszwecke in ariden Gebieten (Implementation and optimization of the Sharjah pilot treatment system for sewage to be used for irrigation purposes in arid regions)*, project thesis at TU Dresden, under elaboration, to be released end of 2011.
- [34] IEEM, GTZ, HUBER: *Dezentrale Verwertung von Rohabwasser aus der Kanalisation zur Grünflächenentwicklung in ariden Stadtgebieten (Decentralized Utilization of wastewater taken from the sewage system for development of green areas in arid cities)*. Final Report of BMBF granted joint project no. 02WD0417 with GTZ GmbH and HUBER AG, Institute of Environmental Engineering and Management at the University of Witten/Herdecke gGmbH (IEEM), Witten, Germany, 2005.
- [35] Jiménez, B.; Asano, T.: *Water Reuse: An international survey, contrasts, issues and needs around the world*, Editors: Blanca Jiménez and Takashi Asano, IWA Publishing, London, 2008, ISBN: 1843390892.
- [36] Rudolph, K.-U.; Paris, S.: "Sewage Harvesting for Urban Green Irrigation". Presentation at 5th IWA Specialist Conference on Efficient Use and Management of Urban Water, Sydney, Australia, 25.-28. Oct. 2009.
- [37] Rudolph, K.-U.; Paris, S.; Heindl, F.: "Sewage Harvesting For Urban Green Irrigation". *Poster presentation at IWA Conference "Leading Edge Technology 2009"*, Singapore, 22.-26. June 2009.
- [38] U.S. EPA: *Guidelines for Water Reuse*, EPA/625/R-04/108, Produced by Camp Dresser & McKee Inc. for U.S. Environmental Protection Agency (U.S. EPA), Washington, USA, Sep. 2004.
- [39] World Health Organisation: *Guidelines for the safe use of wastewater, excreta and greywater, Vol. 2: Wastewater use in agriculture*, World Health Organisation (WHO), Geneva, Switzerland, 2006.

UV Disinfection of Only Partially Pre-clarified Wastewater for Irrigation Purposes

Tim Fuhrmann¹, Karl-Ulrich Rudolph²

¹⁻² Institute of Environmental Engineering and Management at the University of Witten/Herdecke gGmbH (IEEM), Alfred-Herrhausen-Str. 44, 58455 Witten, Germany (E-mail: mail@uni-wh-utm.de)

ABSTRACT

Within the context of wastewater utilization for irrigation purposes, one of the key issues is the appropriate disinfection of the water. Unlike nutrients, which can be used as fertilizer to some extent, microbial pathogens in raw sewage have definitely to be reduced to minimum levels being acceptable for irrigation applications with respect to the protection of people and environment. From a technical point of view, disinfection of wastewater can be performed to nearly any wished level, up to the total sterilization of wastewater. But taking into consideration treatment costs and necessary competence of operational staff, the performance of purification resp. disinfection systems should be limited to the concrete required levels, which often results into an only partially purification of the wastewater.

There exist a number of proven disinfection methods for wastewater, like chlorination, ozonization, membrane filtration and UV irradiation. Most of them require extensive pre-clarification of raw sewage prior to the disinfection process, to avoid an extremely ineffective performance or the production of harmful by-products. In this context UV disinfection has been identified as a feasible option for an application with only partially pre-clarification of wastewater. Laboratory scale tests with UV irradiation of only physically treated wastewater and effluents of waste stabilization ponds have shown that required disinfection levels can be reached with acceptable levels of UV doses and resulting power consumption. Especially according to the requirements for irrigation water, disinfection by UV light is an appropriate option for point-of-use systems, which makes it preferable for decentralized wastewater treatment systems and offers options for efficient combinations with manageable mechanical pre-treatment systems or natural methods like waste stabilization ponds.

Keywords: disinfection, irrigation, sewage, pathogens, reuse, UV irradiation, wastewater treatment

1. INTRODUCTION

If treated wastewater is used for irrigation purposes, appropriate wastewater disinfection is one of the overall key issues. The sanitary protection of workers conducting irrigation activities and population which comes in contact with irrigated areas or the harvested agricultural products as well as the conservation of the environment against possible contaminations requires a reduction of microbial pathogens in the water to levels being suitable for irrigation applications.

Technically seen, disinfection of wastewater could be performed to nearly any level up to a complete sterilization of the water. But if taking into consideration operational aspects like treatment costs and necessary competence of operational staff, a compromise should be found between desirable low levels of pathogens on the one hand and the limitations by site specific economical and knowledge resources on the other hand. This is also reflected by the various quality standards and guidelines for water to be utilized for irrigation purposes.

Compilations of typical quality standards for microbial constituents like bacteria, viruses, protozoans and helminth eggs in the context of water reuse are given for example by [40], the U.S. EPA [38] and the WHO [57].

Due to economic reasons the performance of disinfection systems should be limited to a level, that the concrete required water quality levels can be secured. It has to be taken into consideration that a not fully complete purification of wastewater is only acceptable in combination with a multi-barrier concept resp. other health protection measures like restricted irrigation or human exposure control etc. (as described in the WHO guidelines [57]).

2. COMPARISON OF DISINFECTION METHODS FOR ONLY PARTIALLY PURIFIED WASTEWATER

There exist a number of proven disinfection means for wastewater like chlorine, ozone, UV light and membrane filtration, as exemplarily compared in table 1. Most of them require extensive pre-clarification of raw sewage prior to the disinfection process, to avoid an extremely ineffective performance as well as the production of harmful by-products.

Carefully considering criterions relevant in the context of producing irrigation water, like performance, investment costs, operation and maintenance efforts, demanded staff competence etc., UV irradiation has been identified as a most promising option for the

Table 1: Comparison of disinfection methods ([40]; [41])

Criteria	Cl ₂ / ClO ₂	NaOCl	UV	Ozone	PAA	Membrane
Safety	Low	Moderate	High	Moderate	Low	High
Bactericidal action	High	High	High	High	High	High
Virucidal action	Moderate	Moderate	Moderate	Mod. - high	Moderate	Mod. - high
Protozoa removal	Low	Low	High	High	Low	High
Bacterial-regrowth	Low	Low	Mod. – high	Low	High	Low
Residual toxicity	High	High	Low	Moderate	Low	Low
By-products	High	High	None	Low	None	None
Operability	High	High	High	High	High	High
Full-scale experience	High	Moderate	High	Moderate	Low	High
Operating costs	Low	Low	Low	Moderate	Low	Mod. - high
Investment costs	Moderate	Moderate	Moderate	High	Moderate	High

application of only partially pre-clarified wastewater.

Because of the above mentioned advantages, nowadays the use of UV light as reclaimed water disinfectant has numerous applications, especially at small and medium scale facilities [40].

3. DISINFECTION BY ULTRAVIOLETT LIGHT

Ultraviolet (UV) light as an energy-rich light with a wavelength of about 200 to 400 nm has a germicidal effect on micro-organisms by damaging deoxyribonucleic acid (DNA) and ribonucleic acid (RNA). The effect is particularly efficient with a wavelength of about 254 nm (see efficiency curve in figure 1). This wavelength goes together with the emission maximum of low-pressure mercury lamps, often used as UV light source.

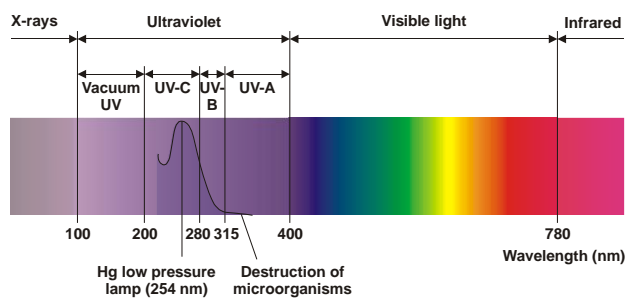


Figure 1: Identification of the UV radiation portion of the electromagnetic spectrum [56]

Like with all other disinfectants, the performance of the germicidal effect depends on the UV dose applied to the pathogens, which is limited by the output of the UV lamps (UV dose = lamp intensity x exposure time) and by the quality of the water to be disinfected.

4. DEPENDENCE OF UV DISINFECTION EFFICIENCY ON WATER QUALITY

In wastewater UV light interacts with the materials

contained in the irradiated liquid through absorption, reflection, refraction and scattering. Therefore the remaining UV dose available for pathogen inactivation is very much depending on the water constituents. There are three key parameters often used to describe the influence of water constituents on the disinfection efficiency of UV irradiation:

- turbidity, stated in nephelometric turbidity units (NTU),
- suspended solids content (SS) and
- UV transmittance (or vice versa the UV absorption), as the share of light passing through a water sample over a specified distance, e.g. 1 cm.

Usually, for optimal UV-dose efficacy suspended solids contents of 5 mg SS/l, turbidity levels of 5 NTU and transmittance values above 60 % are recommended [40].

To archive these values UV disinfection is typically applied after conventional biological treatment (secondary effluent), often followed by filtration prior to the UV irradiation unit, which might add on cost when reduction of suspended solids and turbidity is not required for other reasons.

Different authors researched the dependence between UV efficiency and turbidity respectively SS as well as particle size related aspects. In figures 2 and 3 examples of measurements with turbidity and SS are displayed. It is for sure that increased levels of turbidity and SS reduce the efficiency of UV light disinfection (a clear negative correlation, as shown in the figures), but no general mathematically describable dependence has been verified between UV efficiency and turbidity or SS so far, as the results were always been found to be highly site-specific.

Therefore, when assessing water quality in terms of disinfection efficiency, UV transmittance (or UV ab-

sorbance) is the preferable parameter to clearly describe the behavior of UV light in treated wastewater. [41]

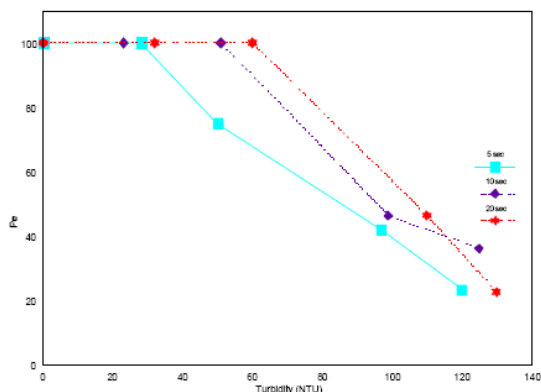


Figure 2: Example for site specific relationship between inactivation of *S. faecalis* with turbidity [44]

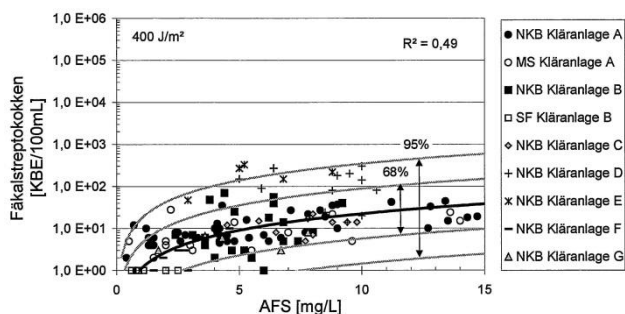


Figure 3: Site specific relationships between inactivation of *S. faecalis* with SS for different WWTPs [48]

5. EXPERIMENTAL VALIDATION OF THE EFFECT OF LOW UV TRANSMITTANCE

In contrast to fully clarified wastewater, literature review shows that there is still little knowledge about disinfection of only partially purified sewage (see for example [48], [42], [46], [43]). Most authors postulate that UV disinfection of sewage is feasible only after extended secondary treatment.

In contrast to this, own tests of the authors with UV disinfection at different water qualities obtained through limited pre-treatment by fine screening, sedimentation etc. as well as with effluent of different waste stabilization ponds indicate UV irradiation to be feasible for disinfection of only poorly purified sewage with acceptable levels of UV doses and resulting power consumption. The tests have been conducted on laboratory scale using a collimated beam device equipped with low pressure mercury lamps. The laboratory tests have been conducted according to the relevant U.S. EPA guideline [54].

UV transmittance of raw sewage is extremely low (often < 5%). Therefore the achievement of pathogens concentrations near zero by UV disinfection without any pre-treatment is economically not feasible, as necessary

UV doses are much too high for practical applications. For example, to secure a reduction of the indicator bacteria *Escherichia coli* from typical levels of about 10^7 cfu/100ml in raw sewage to values of about 10^1 cfu/100ml after irradiation, UV doses of several thousand J/m² are necessary, in comparison to only 300 to 500 J/m² (= 30 to 50 mJ/cm²) necessary for fully purified secondary effluent. [51]

Applying means of mechanical pre-treatment improves the disinfection efficiency significantly. In figure 4 typical results of laboratory scale tests for the inactivation of *E. coli* in screened (6 mm) sewage after different short-time sedimentation periods (15 to 90 min) are displayed. To reach for example a reduction of about three to four log units to levels of maximum 10^3 cfu/100ml (analogues to typical values of the former and the current WHO guideline for wastewater use in agriculture [57]), UV doses of 500 to about 1.500 J/m² (= 150 mJ/cm²) are necessary, depending on the settlement time. This shows that even with relatively small settlement times adequate disinfection efficiencies can be achieved with reasonable UV doses.

Similar results have been achieved with effluents of waste stabilization ponds, which have shown UV transmission values in a range of 30-70% when not affected by extensive algal concentrations.

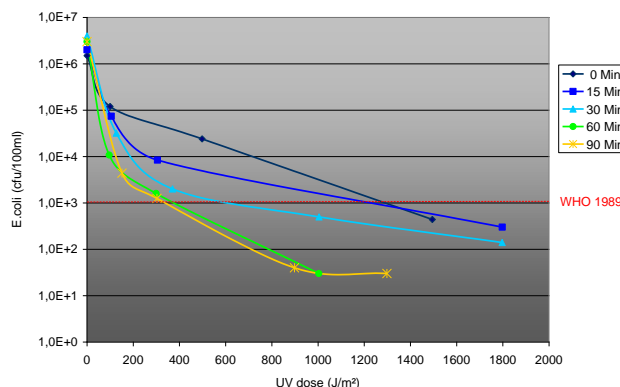


Figure 4: Example of dose-response curves for the inactivation of *Escherichia coli* by UV light in screened sewage after different settlement times [51]

Taking safety margins into consideration the results of several tests with different water qualities can be summarized as follows:

- Minimum treatment requirements for wastewater before UV disinfection comprise at least fine screening and sedimentation of minimum 30 min.
- The minimum UV dose to be applied to wastewater should be at least 1,000 - 2,000 J/m² (= 200 mJ/cm²).
- Reduction of bacterial indicators can be realized to levels which are in compliance with the WHO guideline to use the water for restricted irrigation.

6. NEW CONCEPT FOR DISINFECTION BY UV IRRADIATION

The results show that UV disinfection of sewage is feasible even without extended conventional purification means like secondary treatment combined with additional post filtration. This indicates the possibility of a different approach for treatment of wastewater to be used for agricultural purposes. If the objective of the treatment is focused on disinfection, the biological treatment and filtration as pre-treatment for the disinfection process can be reduced or eventually omitted and replaced by a 3-5 times more powerful UV irradiation unit, as schematically shown in figure 5 [50]. Without a biological step such a system is easier to manage and allows non-continuous operation. By this it could be applied as small, decentralized treatment units e.g. for urban irrigation purposes [52], [53].

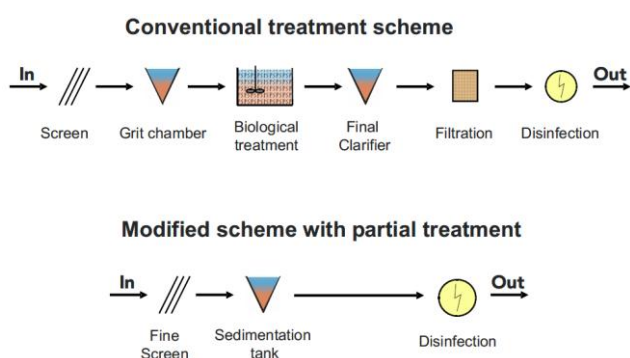


Figure 5: Schematic outline of a conventional wastewater pre-treatment followed by UV disinfection in comparison to an approach without pre-treatment and a larger UV unit instead [50]

It has to be considered that such an approach is not applicable for very strict disinfection requirements (for example *E. coli* contents $\ll 10^3$ cfu/100ml). Additionally, the system has always to be integrated in a multi-barrier concept with additional health protection measures.

7. REACTIVATION OF PATHOGENS

Differently to disinfection by chlorine, UV irradiation leaves no residual disinfection dose in the water passing the UV reactor. In addition, repair mechanisms like photo-reactivation and dark repair of UV irradiated cells may let the number of pathogens increase again after the application of UV light.

Photo-reactivation becomes significantly evident not before some hours of visible light exposure on disinfected water (when storing for a time longer than two days the number of bacterial pathogens will decline again). Data of different authors show a wide range of exposure time, e.g. varying for reactivation of coliforms of about 1.0 to 2.0 log units from 2 to 6 h light exposure (see for example collection of different authors in [46]). Photo-reactivation as well as dark repair effects are highly depending on site conditions (temperature, light exposure, surfaces etc.). The repair effects become more

evident when adequate UV doses cannot be ensured during the UV irradiation, which might be given with disinfection of not fully purified wastewater [44].

Therefore, when disinfecting wastewater by UV light, it has to be considered that the pathogen reduction can be reversed when storing the water for some time. So UV disinfection is preferably appropriate for point-of-use systems.

8. CONCLUSIONS

Treatment of sewage to be reused as irrigation water for green areas in arid urban regions is first of all a question of disinfection. UV irradiation has been identified as appropriate disinfection method for applications with not fully pre-clarified wastewater. Laboratory scale tests of the authors clearly indicate that even with only mechanical treatment of raw sewage the disinfection by UV light is reasonable according to irrigation requirements. The disinfection to usual microbiological standards for irrigation water demands levels of UV doses allowing economical applications for practical use.

Wastewater treatment concepts with less pre-treatment prior to the UV disinfection process in favor of more powerful UV irradiation units might be an interesting solution for specific applications.

Taking into consideration reactivation processes of wastewater, UV irradiation is preferably appropriate for point-of-use applications. Because of their limited demands regarding operational efforts and competence of operational staff, UV irradiation systems are especially applicable for decentralized and small scale wastewater treatment systems.

ACKNOWLEDGEMENTS

The research activities, on which this paper is based on, have been supported by the German Ministry of Education, Science and Research (BMBF, www.bmbf.de/en), project no. 02WA0543 and 02WD0757.

REFERENCES

- [40] Bixio, D.; Wintgens, T.: *Water reuse system management manual*, SQUAREC, EVK1-CT-2002-00130, May 2006, European Commission, Edited by Bixio, D. and Wintgens, T., European Communities Publishing Services, 2006, ISBN: 92-79-01934-1.
- [41] Fuhrmann, T.; Rudolph, K.-U.: "Wastewater ponds and subsequent UV disinfection - a lean cost option for agricultural wastewater reuse", *Proceedings of 6th IWA Specialist Conference on Wastewater Reclamation and Reuse for*

- Sustainability* (WRRS 2007), 9-12 Oct. 2007, Antwerp, Belgium.
- [42] Emerick R. W., Loge F., Thompson D., Darby J. L.: "Factors influencing ultraviolet disinfection performance, Part II: Association of coliform bacteria with wastewater particles", *Water Environ. Res.*, Vol. 71, No. 6, pp.1178-1187, 1999.
- [43] Frank J. L., Robert W. E., Tim R. G., Jeannie L. D.: "Association of coliform bacteria with wastewater particles: impact of operational parameters of the activated sludge process", *Water Research*, Vol. 36, pp. 41-48, 2002.
- [44] Lindenauer, K.G. and J.L. Darby: „Ultraviolet disinfection of wastewater: effect of dose on subsequent photoreactivation", *Water Research*, Vol. 28, No. 4, pp. 805-817, 1994.
- [45] Mbuya, O.S.; Mankazana, J.B.; Latinwo, L.K.; Gardner, C.S.: "The Use of Ultraviolet Light to Disinfect Drinking Water - An Alternative to Chlorination", Presentation, Center for Water Quality, Florida A&M University Tallahassee, 2003, http://www.usawater-quality.org/conferences/2003/presentations/Mbuya_UVLight.pdf.
- [46] Oberg, C.: „Desinfektion von biologisch gereinigtem Abwasser mit UV-Licht und Ozon und ihre Nebenwirkungen (Disinfection of biologically treated wastewater by UV light and ozon and their side effects)", *Schriftenreihe Umwelttechnik und Umweltmanagement*, Issue 13, Dep. of Environmental Engineering and Management, Private University of Witten / Herdecke, Witten, Germany, 1995.
- [47] Rott, U.; Schöler, A.: *Untersuchungen über den Einfluss von suspendierten Stoffen und deren Partikelgrößenverteilung auf die Desinfektionswirkung einer UV-Anlage (Investigations about the influence of the distribution of particle size on disinfection efficiency of UV systems)*, Final report 2001, BMBF granted project no. 02WA9742/1, Institute for Sanitary Engineering, Water Quality and Solid Waste Management, University of Stuttgart, Germany.
- [48] Schöler, A.: „Untersuchungen zum Einfluss der suspendierten Stoffe auf die UV-Desinfektion von Kläranlagenabläufen (Studies into the influence of suspended solids on UV disinfection of Sewage works effluents)", *KA*, Vol. 51, No. 4, pp. 382-389, April 2003.
- [49] Rudolph, K.-U.; Nelle, T.; Oberg, C.: "Disinfection of wastewater by ultraviolet-irradiation and ozonation", *Proceedings, Joint German-Israeli Workshop on Water Technology*, BMFT, Kernforschungszentrum Karlsruhe, 15.-16. Sept. 1992, Karlsruhe, Germany.
- [50] Rudolph, K.-U.: "Affordable Treatment and Disinfection Options for Agricultural Wastewater Reuse", Presentation at *21st Annual WateReuse Symposium*, organized by WateReuse Association, American Water Works Association, Water Environment Federation, 13. Sep. 2006, Hollywood, USA.
- [51] Rudolph, K.-U.; Fuhrmann, T.; Soud, R.: "Decentralized Raw Sewage Utilisation for Irrigation of Green Areas in Arid Cities", Presentation at *6th IWA Specialist Conference on Wastewater Reclamation and Reuse for Sustainability („WRRS 2007")*, 09.-12. Oct. 2007, Antwerp, Belgium.
- [52] Rudolph, K.-U.; Paris, S.: "Sewage Harvesting for Urban Green Irrigation", Presentation at *5th IWA Specialist Conference on Efficient Use and Management of Urban Water („Efficient 2009")*, 25.-28. Oct. 2009, Sydney, Australia.
- [53] Rudolph, K.-U.; Paris, S.; Heindl, F.: "Sewage Harvesting For Urban Green Irrigation", Poster presentation at *IWA Conference Leading Edge Technology 2009*, 22.-26.06.2009, Singapore.
- [54] U.S. EPA: *Ultraviolet Disinfection Guidance Manual*, Proposal Draft June 2003, EPA 815-D-03-007, United States Environmental Protection Agency (U.S. EPA), Washington, USA, 2002.
- [55] U.S. EPA: *Guidelines for Water Reuse*, EPA/625/R-04/108, Produced by Camp Dresser & McKee Inc. for U.S. Environmental Protection Agency (U.S. EPA), Washington, USA, Sep. 2004.
- [56] WEDECO: Product brochure, date unknown.
- [57] WHO: *Guidelines for the safe use of wastewater, excreta and greywater, Vol. 2: Wastewater use in agriculture*, World Health Organisation (WHO), Geneva, Switzerland, 2006.

Copper Cementation on Iron Using Copper Sulphate Solution with Different Organic Solvents

Muhammad Nazim¹, Priyabrata Pal^{1*}, Ahmed Al Sohaibi¹ & Binay K. Dutta²

¹Department of Chemical Engineering, The Petroleum Institute, Abu Dhabi

²West Bengal Pollution Control Board, West Bengal, India (binaykdutta@yahoo.com)

(*Email of corresponding author: ppriyabrata@pi.ac.ae)

ABSTRACT

Cementation is defined as an electrochemical reaction that involves the precipitation of noble metal ion from its solution by another more electropositive metal. It was found that the iron has a good potential to remove copper from aqueous solution by using cementation reaction. The objective of the research is to study and characterize the particles obtained during cementation reaction and also to determine purity of the particles by using different solvents. In order to observe the size of the particles and to investigate copper purity formed during the cementation, Scanning Electron Microscopy (SEM) and Energy Dispersive X-ray Spectroscopy (EDX) analysis were performed. In this study, 1-butanol, acetone, trichloroethylene and n-heptane were used with water as solvents. It was found that 1-butanol is the most suitable with respect to the smallest size of the particles having 93.78% (by weight) of copper. Except n-heptane all other solvents gave considerable purity of copper. The particle size varied from 1-butanol < n-heptane < trichloroethylene < acetone within the range 165.1 to 390.8 nm with largest size of 549 nm in aqueous solution. The nearly nano sized copper particles have potential applications as catalyst for organic reactions. It was found that solvents have considerable effect on the particle size and purity of the produced copper particles.

Keywords: Cementation, copper nanoparticles, effect of solvents, characterization of particles

1. INTRODUCTION

Cementation is defined as an electrochemical reaction that involves the precipitation of noble metal ion from its solution by another more electropositive metal. It has been used to recover metals from their solution for a long time. Copper is considered to be one of the most valuable metals used in the industry. A large number of investigations relating copper deposition on iron more specifically to study the preparation of the copper particles have been carried out. The purpose of present work is to study the reaction of copper cementation on iron metal and to investigate the produced size of the copper particles.

Various researchers have studied [1-17] the effects of various parameters on the size and morphology of produced copper particles.

An effort has been done [1] for the preparation of copper oxide nano particles by sonochemistry route from copper acetate and sodium hydroxide in polypropylene glycol, polyvinyl alcohol and polyethylene glycol. Morphology and size of particles have been studied by varying concentration of copper in different alcohols. It was observed that poly ethylene glycol and copper concentration of 0.05 M gave the best results. A research for the investigation of size of copper particles was carried out [2] under the effect of ultrasonics and in different concentrations of ethylene glycol (which acts as a capping agent). Copper particles were produced by the reduction of an aqueous copper sulphate solution by hydrazine. It was found that smaller spherical copper particles can be produced by

reduction with sonication with specific capping agent. A novel two step reduction method was developed [3] for preparation of copper nano particles from copper sulfate pentahydrate. Oleic acid was used as a surfactant and extractant to avoid oxidation. Dispersion and morphology were investigated at different temperatures, pH and ratio of Cu^{2+} to NaH_2PO_2 . Spherical copper particles with size of about 30 nm coated with oleic acid were obtained. Pure copper nano particles were prepared [4] by reduction of cupric chloride with hydrazine in CTAB solution. Ammonia solution was used for pH adjustment and with hydrazine being used as a reducing agent. It was found that the mean nano particles diameter first decreased and became constant with the increase of hydrazine concentration. CTAB was helpful to prevent particle agglomeration. Preparation of copper metal nano particles was carried out [5] by reducing $\text{CuSO}_4 \cdot 5\text{H}_2\text{O}$ with $\text{NaH}_2\text{PO}_2 \cdot \text{H}_2\text{O}$ in ethylene glycol in the presence of microwave irradiation. Size and agglomeration of copper nano particles were investigated by varying concentrations, time, and radiation intensity. It was observed that microwave irradiation accelerated the reaction rate and resulted in proper dispersion. Copper nano particles were prepared [6] by electron beam radiation method in water system using different surfactants such as polyvinyl alcohol, sodium dodecyl benzene sulfonate, gluten and polyethylene glycol. Results showed that almost pure copper particles were obtained with an average size of 20 nm, 40 nm and 20 nm in gluten, PEG and SDBS respectively. Another chemical reduction method was developed [7] to produce high dispersive copper nano particles using potassium boro hydride. The influence of different reaction parameters such as temperature,

copper concentration, dispersant on the size and conversion of product was studied. It was found that n-butanol was an effective dispersant and copper sulphate concentration of 0.4 mol/L gave good results. Copper particles in colloidal form were prepared [8] in aqueous solution by the reduction of copper dodecyl sulfate with sodium borohydrate. Spherical or elongated copper metallic particles were obtained above the critical micellar concentration. Below the critical micellar concentration isolated particles were formed with interconnected network of either oxide or pure copper. Copper nano particles with high purity were prepared [9] by reduction of copper salt by sodium citrate/sodium formaldehyde sulfoxylat and myristic acid/sodium formaldehyde sulfoxylat. Also, similar type of reaction between hydrazine with sodium formaldehyde sulfoxylate in polymer produced a mixture of Cu_2O and Cu. Another method has been described [10] for preparing copper nano particles in a protecting agent of poly vinyl pyrrolidone through a polyol method. We observed monodisperse spherical copper nano particles were formed having a size in the range of 45 nm. Effects of concentration of reducing agent, temperature, injection rate on the size of the particles were studied. It was found that copper surface was covered with copper oxide and poly vinyl pyrrolidone was chemisorbed on the surface of copper. In another work [11], copper nano particles were produced in organic phase stabilized by bis ethyl hexyl hydrogen phosphate. It was observed that copper was easily transformed into oxide in the presence of solvents with high dipole moments and in non-polar solvents, the copper nano particles were found to be stable in air. A method for producing [12] copper nano particles in a toluene-water two phase system was developed. The reaction involved movement of metal cations from the aqueous phase to the toluene phase with the help of a phase transfer reagent of tetra octyl ammonium bromide. Reduction was done by sodium boro hydride in oleylamine that acts as a stabilizing ligand. Spherical copper nano particles with an average size of 6.06 nm were produced. Thermal decomposition method was developed [13] to produce copper nano particles by copper oxalate. Copper nano particles having face centered cubic structure and size around 40 nm were synthesized. A method for the production of copper nano particles was developed [14] by reduction of copper nitrate through hydrazine monohydrate with the help of silver nano particles as catalysts. Nano particles in the size range of 5-50 nm were produced in less time and in highly disperse form due to catalytic effect of silver nano particles. Alumina supported copper nano particles were synthesized [15] from copper acetyl acetonate and aluminum isopropoxide precursors using aerogel. These alumina based copper nanoparticles were applied for the preparation of 1,2,3 triazoles to check their activity by the reaction of alkynes, sodium azide and alkyl halides. Copper nano particles were prepared [16] in cubic shape and in the size range of 75-250 nm from spherical copper particles in two steps. The first involved the

formation of spherical particles by reduction reaction of copper sulphate and borohydride and then cubic particles were mixed with a specific amount of copper sulphate and sodium ascorbate to form cubic copper nano particles. Synthesis of stable copper nano particles was done [17] by reduction of a complex of copper soyabean extract with sodium boro hydride. Spherical copper particles with average size of 20 nm were observed.

The present work was devoted to:

- (1) produce copper particles as low as nano range by the reduction of copper sulphate with elemental iron.
- (2) study of the particles obtained during cementation reaction to judge variation in the particle size and purity.

2. MATERIALS & METHODS

2.1 Chemicals Used

$\text{CuSO}_4 \cdot 5\text{H}_2\text{O}$ (S.d. fine-Chem Limited, India)
 H_2SO_4 (97% pure, J.T. Baker, Holland)
 NaOH (Scharlan Chemie S. A, Spain)
 Distilled Water

2.2 Instruments Used

Spectrophotometer (Agilent 8453 UV-Visible Spectrophotometer, Germany)
 Magnetic Stirring Hot Plate (Wise stir, MSH-20 D, Korea)
 pH Meter (Thermo electron corporation, U.S.A.)
 SEM & EDX
 Centrifuge (DYNAC, USA)

2.2 Methods

A long Iron wire of uniform diameter was obtained from the local market in Abu Dhabi. Sandpaper was used to scrub the rust off the wire. In each experimental run, a 80 ml solution of a given concentration of copper and 20 ml of respective solvent (n-butane, n-heptane, trichloroethylene and acetone) were prepared and iron wire of length 7 cm and diameter 0.27 cm was added with stirring being supported by a magnetic stirrer at 400 rpm. The solution was filtered after 35 minutes to remove the particles from the solution and was washed with distilled water. These collected particles were then dried in a vacuum oven for 2-3 hours and were then analyzed for particle size and composition by Energy Dispersive X-ray Analysis (EDX) and Scanning Electron Microscopy (SEM) respectively.

3. RESULTS & DISCUSSION

The cementation reaction was carried with copper sulphate solution and iron wire in the presence of different organic solvents to investigate their effect on the purity and size of the particles.

In this study, 1-butanol, acetone, trichloroethylene and n-heptane were used with water as solvents. The physical properties of these solvents are given in table 1.

Table 1: Physical properties of solvents

Properties	Solvent				
	Water	1-butanol	n-heptane	TCE	Acetone
Mol. Wt.	18	74	100	131	58
Density	1	0.81	0.68	1.46	0.79
Viscosity	1	3.0	0.38	0.53	0.30
Dipole moment	1.85	1.52	0	1.90	2.91
Dielectric Const.	80	17.8	1.9	3.39	20.7

In order to observe the size of the particles and to investigate the copper purity formed during the cementation, Scanning Electron Microscopy (SEM) and Energy Dispersive X-ray Spectroscopy (EDX) analysis were performed as shown in the figures 1-5 and table 2. It was found that 1-butanol is the most suitable with respect to the smallest size of the particles having 93.78% (by weight) of copper. Except n-heptane all other solvents are giving considerable purity of copper. The particle size varied from 1-butanol < n-heptane < trichloroethylene < acetone within the range 165.1 to 390.8 nm with largest size of 549 nm in aqueous solution. The results are summarized in table 2.

Table 2: Purity & sizes of different particles in the clusters for each sample

Sample ID	Sizes of Different Particles in the Clusters (nm)				Wt % Copper
	1	2	3	4	
1)	549.8	562	1230	1430	93.78
2)	390.8	409.8	507.7	702.0	94.38
3)	294.4	580.1	584.1	641.8	82.45
4)	186.4	201.1	258	--	63.38
5)	165.1	241.3	328.4	337.9	93.67

It was found that the solvents have considerable effect on the particle size and purity of the produced copper particles. Generally, organic solvents inhibit the cementation reaction as the reaction is slowed down due to the presence of foreign inert molecules. As the length of the hydrocarbon solvent increases, the molecules are hindered from the cementation reaction. Thus, with 1-

butanol and n-heptane, the particle size is less than the other solvents. The change in particle size from 186.4 nm to 165.1 nm is due to the larger dielectric constant of 1-butanol. Therefore, the particle size is smallest in 1-butanol.

Since acetone is completely miscible in water, the reaction is taking place throughout the volume of the solution. The molecular geometry of trichloroethylene and acetone is almost similar. But dielectric constant of trichloroethylene is very low compared to water and also its solubility is very low, therefore the agglomeration is reduced as compared with acetone. In acetone, agglomerations of the produced copper particles take place and cause a larger size of produced copper particles due to its complete miscibility in water. The solubility of 1-butanol and acetone are reasonably high in water, thus the reaction take place over the entire volume of the solution resulting in the production of particles with more than 90% copper purity. In n-heptane, the purity of produced copper particle is the lowest (63%) due to its immiscibility in water. As the reaction is hindered due to presence of immiscible n-heptane, the copper particle size produced is less in the presence of n-heptane. The produced copper particle is oxidized in the presence of dissolved oxygen which produces fewer amounts of pure copper particles.

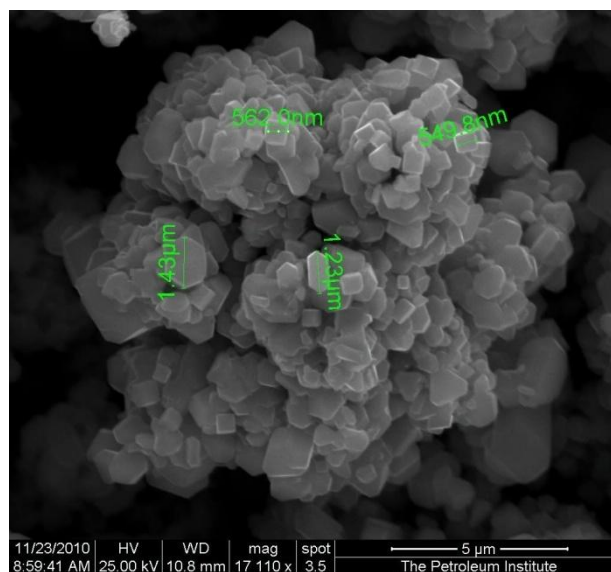


Figure 1: SEM image of particles produced in aqueous solution of copper sulphate

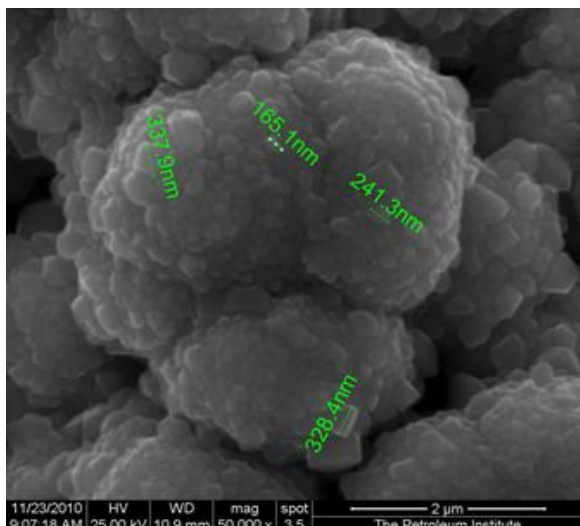


Figure 2: SEM image of particles produced in aqueous solution of copper sulphate & 1-butanol

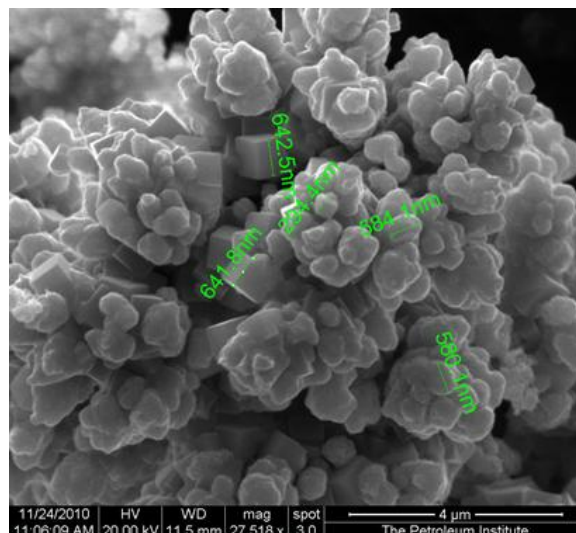


Figure 5: SEM image of particles produced in aqueous solution of copper sulphate & trichloroethylene

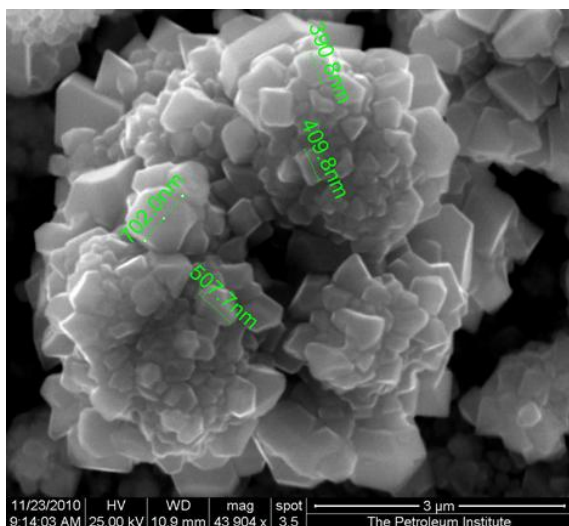


Figure 3: SEM image of particles produced in aqueous solution of copper sulphate & acetone

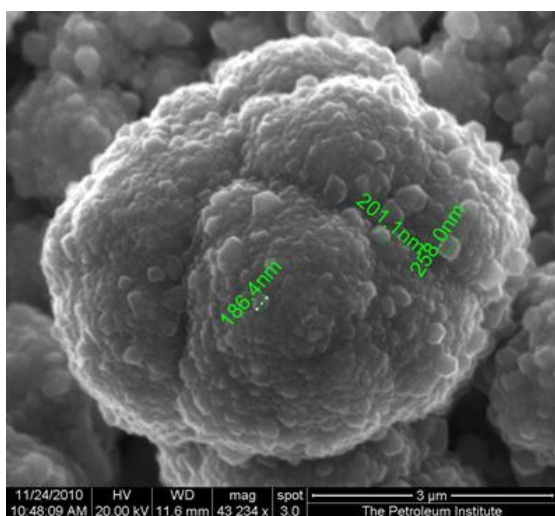


Figure 4: SEM image of particles produced in aqueous solution of copper sulphate & n-heptane

4. CONCLUSION

Organic solvents are likely to be effective in producing copper particles in nanometer range. Among the four solvents used, 1-butanol was found to be the most effective solvent to produce nearly nano sized copper particles. These particles have potential applications in catalysis.

REFERENCES

- [1] Ranjbar-Karimi, R., A. Bazmandegan-Shamili, "Sonochemical synthesis, characterization and thermal and optical analysis of CuO nanoparticles." *Physica B: Condensed Matter* 405(15): 3096-3100, 2010
- [2] Moghimi-Rad, J., F. Zabihi, "Effect of ultrasound radiation on the size and size distribution of synthesized copper particles." *Journal of materials science* 45(14): 3804-3811, 2010
- [3] Wen, J., J. Li, "Preparation of copper nanoparticles in a water/oleic acid mixed solvent via two-step reduction method." *Colloids and Surfaces A: Physicochemical and Engineering Aspects*, 2010
- [4] Wu, S. H. and D. H. Chen, "Synthesis of high-concentration Cu nanoparticles in aqueous CTAB solutions." *Journal of colloid and interface science* 273(1): 165-169, 2004
- [5] Zhu, H., C. Zhang, "Rapid synthesis of copper nanoparticles by sodium hypophosphite reduction in ethylene glycol under microwave irradiation." *Journal of crystal growth* 270(3-4): 722-728, 2004
- [6] Zhou, R., X. Wu, "Influences of surfactants on the preparation of copper nanoparticles by electron beam irradiation." *Nuclear Instruments and*

Methods in Physics Research Section B: Beam Interactions with Materials and Atoms 266(4): 599-603, 2008

- [7] Qiu-li, Z., Y. Zhi-mao, Y., Bing-jun, D., Xin-zhe, L., Ying-juan, G., "Preparation of copper nanoparticles by chemical reduction method using potassium borohydride." *Trans. Nonferrous Met. Soc. China* 20, 240-244, 2010
- [8] Lisiecki, I., F. Billoudet, "Control of the shape and the size of copper metallic particles." *The Journal of Physical Chemistry* 100(10): 4160-4166, 1996
- [9] Khanna, P., S. Gaikwad, "Synthesis and characterization of copper nanoparticles." *Materials Letters* 61(25): 4711-4714, 2007
- [10] Park, B. K., S. Jeong, "Synthesis and size control of monodisperse copper nanoparticles by polyol method." *Journal of colloid and interface science* 311(2): 417-424, 2007
- [11] Song, X., S. Sun, "A method for the synthesis of spherical copper nanoparticles in the organic phase." *Journal of colloid and interface science* 273(2): 463-469, 2004
- [12] Dadgostar, N., S. Ferdous, "Colloidal synthesis of copper nanoparticles in a two-phase liquid-liquid system." *Materials Letters* 64(1): 45-48, 2010
- [13] Salavati-Niasari, M., F. Davar, "Synthesis and characterization of metallic copper nanoparticles via thermal decomposition." *Polyhedron* 27(17): 3514-3518, 2008
- [14] Grouchko, M., A. Kamyshny, "Synthesis of copper nanoparticles catalyzed by pre-formed silver nanoparticles." *Journal of Nanoparticle Research* 11(3): 713-716, 2009
- [15] Kantam, M. L., V. S. Jaya, "Preparation of alumina supported copper nanoparticles and their application in the synthesis of 1, 2, 3-triazoles." *Journal of Molecular Catalysis A: Chemical* 256(1-2): 273-277, 2006
- [16] Jana, N. R., Z. L. Wang, "Seed-mediated growth method to prepare cubic copper nanoparticles." *Curr. Sci* 79(9): 1367-1370, 2000
- [17] Guajardo-Pacheco, M. J., J. Morales-Sánchez, "Synthesis of copper nanoparticles using soybeans as a chelant agent." *Materials Letters* 64(12): 1361-1364, 2010.

Conversion and Liquefaction of Petrochemical Sludge (Biological and Chemical) using Subcritical Water Technology

Omid Tavakoli^{1*}, Sara Modarres², Mohammad Hossein Sarrafzadeh³

¹ School of Chemical Engineering, College of Engineering, University of Tehran, 16 Azar Street, Tehran, Iran (otavakoli@ut.ac.ir)

² School of Chemical Engineering, College of Engineering, University of Tehran, 16 Azar Street, Tehran, Iran (saramodarress@yahoo.com)

³ School of Chemical Engineering, College of Engineering, University of Tehran, 16 Azar Street, Tehran, Iran (sarrafzdh@ut.ac.ir)

* Corresponding author

ABSTRACT

In this study, conversion of biological and chemical sludge from the wastewater treatment facility of a petrochemical plant to liquid hydrocarbons under subcritical conditions was investigated using water as solvent in temperature range of 200 – 350 °C and pressure of 1.5 to 10 MPa. The studies were performed with different solvent/sludge ratios (1.5, 1.3 and 1.1) for reaction time of 10, 20, 30 and 50 minutes. The results revealed that total product yield increased with increasing temperature. The yields of liquids and solid residue were determined for each extraction run. TOC and COD analysis was performed for liquid phase. In addition, ICP analysis was done for solid residue to determine the type and amount of heavy metals of the same phase.

Keywords: Petrochemical wastewater, Biological sludge, Chemical sludge, Heavy metals, Subcritical water technology

1. INTRODUCTION

The Sewage sludge including industrial and domestic sludge recently have gained special attention due to the huge amount of sludge produced from physical, chemical, or biological treatment. In this subject the industrial sludge and especially petrochemical sludge illustrated the high concentration of heavy metals and hazardous materials and according to the environmental regulations should meet certain metal and hazardous compounds concentrations before it can be safely discharged or used as a fertilizer. One of the conventional methods to treat such sludge is incineration process. The incineration process although reduces the sludge volume but the main drawbacks of incineration are first, the large energy consumption required for sludge evaporation due to the high water content and second, the formation of hazardous air pollutants such as polynuclear aromatic hydrocarbons (PAHs), dioxin-like compounds, polychlorinated biphenyls (PCBs), and so forth. The increase in cost of waste disposal and growth of environmental concerns attract attention to alternative technologies such as pyrolysis, gasification, and supercritical fluid extraction (SCFE) to obtain hydrocarbons as liquid fuel and chemical feedstock.

According to literature a synthetic crude oil could be produced by heating of sewage sludge at 300-350 °C in an oxygen-free environment. Kuriakose et al. reported the data obtained to utilize the waste sludge of a petroleum refinery and about the 17 wt % of a light oil fraction, that was recovered, could be used as diesel fuel by blending with other appropriate refinery streams. Many researchers have investigated the effect of operating parameters such as temperature and residence

time on product distribution. Shen et al. have investigated oil recovery from sewage sludge by low temperature pyrolysis in a fluidized bed reactor. Liquefaction of dewatered sewage sludge (150-350 °C) was examined to reduce nitrogen that needed to be removed from oil before use. Direct thermochemical liquefaction of sewage sludge for production of liquid fuels (heavy oil) and as a means of pollution control was studied by catalytic conversion using sodium carbonate at 250-340 °C. Xu et al. studied the effect of carbon catalyst on the gasification of some organic feedstock (glycerol, glucose, and sewage sludge) in supercritical water at 600 °C and 34.5 MPa.²⁰ In a similar work, they found that the product was composed mainly of hydrogen-rich gas at a higher operating temperature (650 °C).²¹ A large portion of sewage sludge includes high water content up to 95%.²² Unlike classical gasification and liquefaction processes, high drying costs can be avoided by using extraction with supercritical water. Many studies are present on sewage sludge utilization with thermal processes, but liquefaction of petrochemical sewage sludge by supercritical water extraction was not encountered in the literature.

In this paper, the near-critical water treatment of petrochemical sludge from a wastewater treatment facility of a petrochemical plant was performed in a batch reactor system. The aim of the study was to determine the product distribution evolved from near-critical extraction with water ($T_c = 374$ °C, $P_c = 220$ bar) under moderate temperatures (200-350 °C). The distribution of heavy metals in residual sludge and liquid phases was investigated to elucidate conversion and liquification efficiency of such sludge.

2. EXPERIMENTALS

2.1. Petrochemical Sludge Samples

The investigations were performed with sludge samples obtained from Mobin Petrochemical Company in Iran. In this experimental study, a mixture of effluents from a chemical sludge centrifuge (pH: 7, water content 72 wt %, ash content = 7 wt% and solid quality: colloidal flocs) and sludge discharged from a biological sludge centrifuge (pH: 7, water content: 83 wt %, ash content = 16 wt% and solid quality: biological flocs) was used. Properties of dewatered sewage sludge used in the experimental studies are given in Tables 1 and 2.

Table 1: Properties of dewatered chemical sludge used in the experimental studies

Element oxide	Wt %
L.O.I	50.21
Fe ₂ O ₃	33.1
MgO	1.36
CaO	1.24
ZnO	1.14
Al ₂ O ₃	0.84
TiO ₂	0.78
P ₂ O ₅	0.72

Table 2: Properties of dewatered biological sludge used in the experimental studies

Element oxide	Wt %
L.O.I	56.42
Fe ₂ O ₃	35.3
P ₂ O ₅	2.24
ZnO	1.19
MgO	0.71
Al ₂ O ₃	0.7
CaO	0.5
TiO ₂	0.48

2.2. Procedure for Extraction Studies

2.2.1. Sub-critical Fluid Extraction

The experiments were carried out in an SS 316 reactor having an internal volume of 35 cm³. The reactor was heated by electrical furnace and held at determined temperature for different interval times. The amount of dried sewage sludge and water used in experimental runs were prepared to give a mass ratio (water/sludge) of 1.5, 1.3, and 1.1. Experiments were conducted on the determination of the optimum water/sludge ratio at 4 different temperatures (200,250,300 and 350°C). Reaction conditions for sub-critical water treatment are given in Table 3.

Table 3: Reaction Conditions for sub-critical water Extraction in Different Solvent/Sludge Ratio

Variable	Level
Water/Sludge ratio	1.5, 1.3, 1.1
Reaction temperature (°C)	200-250-300-350
Reaction time (min)	10-20-30-50

2.3. Fractionation of the Products

At the end of each run, the reactor was cooled to ambient temperature in a short period of time. The amount of residual sludge was measured and collected by using 50cc flacons. The metal concentration of residual sludge was determined by ICP (Induced Coupled Plasma) analysis. The products remaining in the reactor were washed with 15cc pure water and 10cc n-hexane and filtered to separate solid residue and oil fractions. After completion of extraction, the residue was dried and subjected to ash analysis for determination of inorganic content. Liquid products that were obtained after filtration of reactor contents were combined in a flask to preparation for TOC (Total Organic Carbon) analysis. The mixture after precipitation was filtered to separate hexane-insoluble parts and hexane-soluble oil parts. In this study oil phase didn't observed.

3. RESULTS AND DISCUSSIONS

No significant effect of water/sludge ratios within the investigated range (in mass ratio of water/sludge as 1.5, 1.3, and 1.1) was observed on total product yield. The ratios of residual sludge/dry sludge were decreased by increasing of the temperature and time of reactions in this study (Figures 1-4)

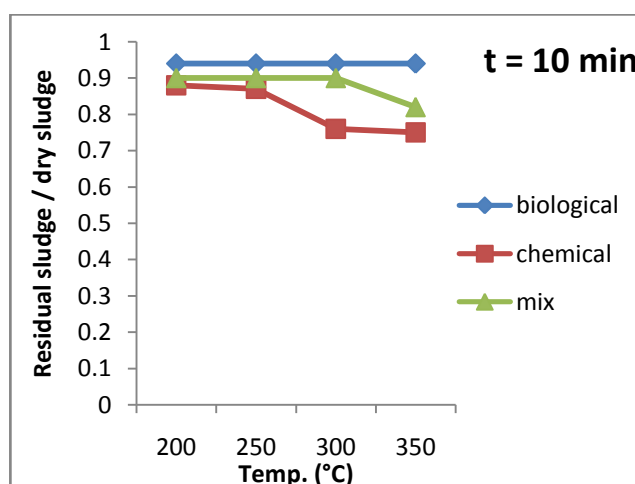


Figure 1: Yields of residual sludge/ dry sludge as a function of temperature (reaction time = 10 min)

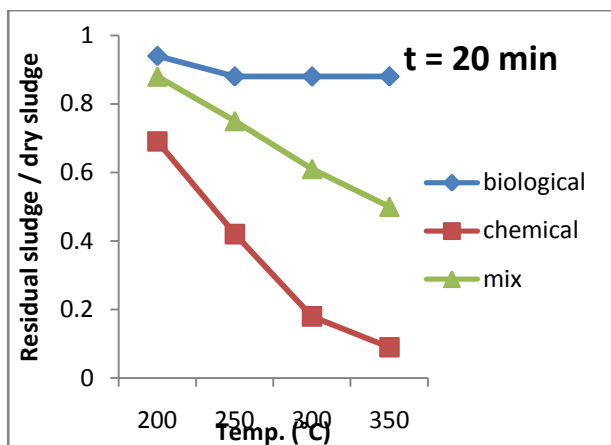


Figure 2: Yields of residual sludge/ dry sludge as a function of temperature (reaction time =20 min)

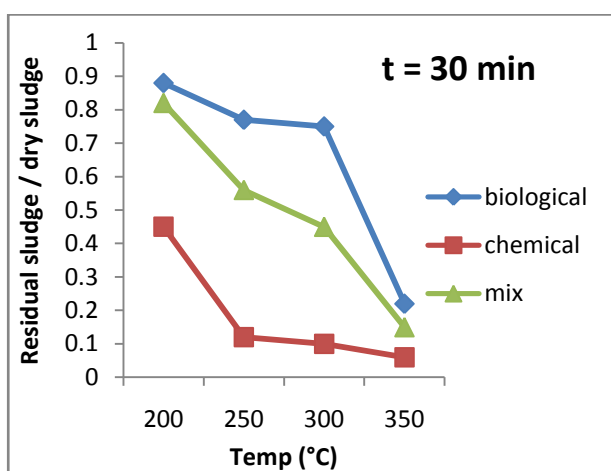


Figure 3: Yields of residual sludge/ dry sludge as a function of temperature (reaction time =30 min)

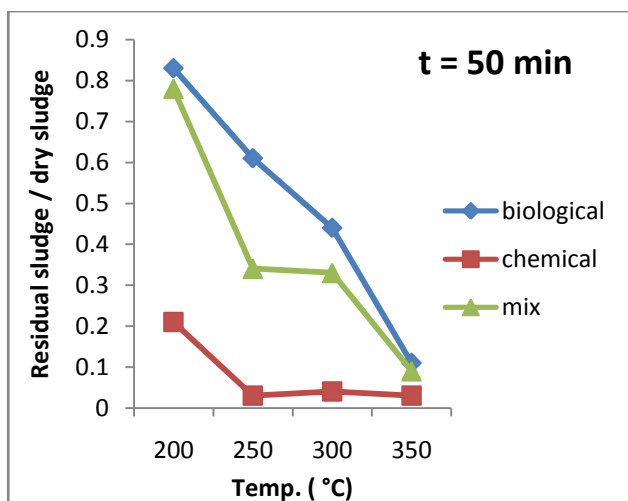


Figure 4: Yields of residual sludge/ dry sludge as a function of temperature (reaction time =50 min)

Besides the water/sludge ratio, the temperature of the system was an influence on product yield and distribution and the major component of the residual solid product was Fe at elevated temperatures (Table 4).

By increasing the temperature of water, Fe and Al yields increased in 50wt% mixture of both sludge (Table 5).

Table 4: Yield of the major compounds in residual sludge of chemical and biological sludge.

Kind of sludge metal	Biological sludge	Chemical sludge
Fe (ppm)	144236	155393
Al (ppm)	9712	6984
Zn (ppm)	7096	2670
Ca (ppm)	3855	1820
Mg (ppm)	1907	2875
Cu (ppm)	255	265
Cr (ppm)	224	326
Ni (ppm)	57	58
Co (ppm)	45	48

Table 5: Yield of the major compounds in residual sludge phase as a function of temperature for 50wt% mixture of chemical and biological sludge

Kind of sludge	Mixture (T=200 °C)	Mixture (T= 250°C)	Mixture (T= 300°C)	Mixture (T= 350°C)
Compounds				
Fe (ppm)	152545	155041	166565	168046
Al (ppm)	10516	10728	14182	17060
Zn (ppm)	4492	6397	7823	10235

In this research, the yield of total organic carbon (TOC) increased from 4.1 to 235 mg/LC with increasing temperature up to 250° C and then decreased to 155 mg/L C (Figure 5).

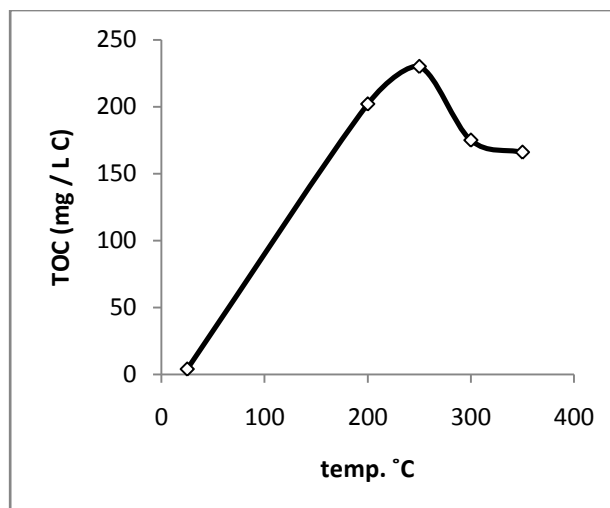


Figure 5: Yield of TOC as a function of temperature in liquid phase

5. CONCLUSION

Sub-critical water technology is an efficient, environmentally clean, and an attractive extraction/treatment technique due to its special properties of density, ion product of water, dielectric constant, etc. comparing to the conventional treatment methods. In addition to these, there are several other advantages such as rapid extraction, no organic solvent requirement, and higher efficiency, despite the investment and operating costs for this method.

In this study, water/sludge mass ratios (1.5, 1.3, and 1.1) were determined to be less effective on the total product yield, but the temperature has a great effect on the total product yield and the composition of residual sludge and liquid phase. The residual sludge compounds consisted mainly of Fe and Al. Water in the sub-critical state acts not only as a solvent but also reacts with the compounds in sludge leading to the dissolution of fragments. An increase in the yield as well as in the amount of Fe and Al and a decrease in a ratio of residual sludge/dry sludge were observed when the temperature was varied from 200 to 350 °C in sub-critical water treatment.

REFERENCES

- [1] Chung-Sun E. Road, Chungli, “*Sintering effect on cement bonded sewage sludge ash*”, *Cement & Concrete Composites*, 28, 26–32, 2006.
- [2] M. A. Abdul, M. Abbasi, T. Nasrabadi, H. Hoveidi, N. Razmkhah, “*Solid waste management in tabriz petrochemical complex*”, *Iran. J. Environ. Health. Sci. Eng.*, 3, 185-192, 2006.
- [3] M. Marcucci, L. Tognotti, “*Reuse of wastewater for industrial needs : the Pontedera case*”, *Resources Conservation and Recycling*, 34, 249-259, 2002.
- [4] Wiebusch, B., and Seyfried, C. F. “*Utilization of sewage sludge ashes in the brick and tile industry.*” *Water Sci. and Technol.*, 36, 251–258. 1977.
- [5] Deng-Fong Lin, Chih-Huang Weng, “*Use of sewage sludge ash as brick material*”, *Dept. of Civ. Eng.*, 2002.
- [6] J.H. Tay, K.Y. Show, D.J. Lee, S.Y. Hong, “*Reuse of wastewater sludge with marine clay as a new resource of construction aggregates*”, *Water Sci. Technol.*, 50, 189-196, 2004.
- [7] S. Barnabé, S.K. Brar, R.D. Tyagi, I. Beauchesne and R.Y. Surampalli, “*Pre-treatment and bioconversion of wastewater sludge to value-added products—Fate of endocrine disrupting compounds*”, *Science of The Total Environment*, 407, 1471-1488, 2009.
- [8] Mohammed H. Al Sayed , Ismail M. Madany, A. Rahman M. Buali, “*Use of sewage sludge ash in asphaltic paving mixes in hot regions*”, *Construction and Building Materials*, Vol. 9, 19-23, 1995.
- [9] Chih-Huang Weng, Deng-Fong Lin, Pen-Chi Chiang, “*Utilization of sludge as brick materials*”, *Advances in Environmental Research* , 7, 679–685, 2003.
- [10] Craig Cogger, Dan Sullivan, “*Recycling municipal wastewater sludge in washington*”, *Washington State University*, 1987.
- [11] Joo-Hwa Tay, Sze-Yunn Hong, and Kuan-Yeow Show, “*Reuse of industrial sludge as pelletized aggregate for concrete*”, *Journal of Environmental Engineering*, 126, Paper No. 20945, 2000.
- [12] J.H. Tay, K.Y. Show, D.J. Lee, S.Y. Hong, “*Reuse of wastewater sludge with marine clay as a new resource of construction aggregates*”, *Water Sci. Technol.*, 50, 189-196, 2004.
- [13] Joo-Hwa Tay, Woon-Kwong Yip, “*Sludge Ash as Lightweight Concrete Material*”, *Journal of Environmental Engineering*, 115, 56-64, 1989.
- [14] L.C. Wang, L.F. Lin, S.O. Lai, “*Emissions of polycyclic aromatic hydrocarbons from fluidized and fixed bed incinerators disposing petrochemical industrial biological sludge*”, *Journal of Hazardous Materials* 168, 438–444, 2009.
- [15] D. Abdessemed, G. Nezzal, “*Filterability of biological sludge on porous membranes*”, *Desalination* 245, 621-625, 2009.
- [16] T. Melin, B. Jefferson, S. Bixio, C. Theoye, W. De wilde, J. Vander Graaf and T. Wintgens, “*Membrane bioreactor technology for wastewater treatment and reuse*”, *Desalination*, 187, 271-282, 2006.
- [17] M. Marcucci, L. Tognotti, “*Reuse of wastewater for industrial needs: the Pontedera case*”, *Resources Conservation and Recycling*, 34, 249-259, 2002.
- [18] E. Vgetti, E. Llorens, A. Pedescoll, I. Ferrer, R. Castellnou, J. Garcia, “*Sludge dewatering and stabilization in three full-scale systems in Catalonia, Spain*”, *Bioresource Technology*, 100, 3882-3890, 2009.
- [19] J.H. Tay, W.K. Yip, “*Sludge Ash as Lightweight Concrete Material*”, *Journal of Environmental Engineering*, 115, 56-64, 1989.

- [20] M.J. Martin, A. Artola, M.D. Balaguer, M. Rigola, "Activated carbons developed from surplus sewage sludge for the removal of dyes from dilute aqueous solutions", *Chemical Engineering Journal*, 94, 231-239, 2003.
- [21] J.H. Tay, K.Y. Show, D.J. Lee, S.Y. Hong, "Reuse of wastewater sludge with marine clay as a new resource of construction aggregates", *Water Sci. Technol.*, 50, 189-196, 2004.
- [22] S. Barnabé, S.K. Brar, R.D. Tyagi, I. Beauchesne and R.Y. Surampalli, "Pre-treatment and bioconversion of wastewater sludge to value-added products—Fate of endocrine disrupting compounds", *Science of The Total Environment*, 407, 1471-1488, 2009.
- [23] L. Chu, S. Yan, X.H. Xing, X. Sun and B. Jurcik, "Progress and perspectives of sludge ozonation as a powerful pretreatment method for minimization of excess sludge production", *Water Research*, 43, 1811-1822, 2009.
- [24] M.J. Martin, E. Serra, A. Ros, M.D. Balaguer, M. Rigola, "Carbonaceous adsorbents from sewage sludge and their application in a combined activated sludge-powdered activated carbon (AS-PAC) treatment", *Carbon*, 42, 1389-1394, 2004.
- [25] G. Tulay, S. Mehmet, Y. Mithat, M. Hakan, I. Rahim, M. Ismail H., Ö. Ahmet R., B. Levent, "Near-Critical and Supercritical Fluid Extraction of Industrial Sewage Sludge", *Chemical Engineering Journal*, 46, 1051-1057, 2007.
- [26] J.M. Toledo, J. Corella, L.M. Corella, "The partitioning of heavy metals in incineration of sludges and waste in a bubbling fluidized bed: 2. Interpretation of results with a conceptual model", *Journal of Hazardous Materials*, 126, 158-168, 2005.
- [27] H.L. Chiang, C.G. Chao, C.Y. Chang, C.F. Wang, P.C. Chiang, "Residue characteristics and pore development of petrochemical industry sludge pyrolysis", *Water Research*, 35, 4331-4338, 2001.
- [28] J.H. Tay, S.Y. Hong, K.Y. Show, "Reuse of industrial sludge as pelletized aggregate for concrete", *Journal of Environmental Engineering*, 126, Paper No. 20945, 2000.
- [29] R.F. Susanti, B. Veriansyah, J.D. Kim, J. Kim, Y.W. Lee, "Continuous supercritical water gasification of isooctane: A promising reactor design", *International Journal of Hydrogen Energy*, 35, 1957-1970, 2010.
- [30] E.D. Lavric, H. Weyten, J.D. Ruyck, V. Plesu, V. Lavric, "Supercritical water oxidation improvements through chemical reactors energy integration", *Thermal Engineering*, 26, 1385-1392, 2006.
- [31] C.G. Chao, H.L. Chiang, C.Y. Chen, "Pyrolytic kinetics of sludge from a petrochemical factory wastewater treatment plant—a transition state theory approach", *Chemosphere*, 49, 431-437, 2002.
- [32] C. Cogger, D. Sullivan, "Recycling municipal wastewater sludge in Washington", Report, Washington State University, 1987.
- [33] G.R. Xu, J.L. Zou, G.B. Li, "Stabilization of heavy metals in sludge ceramsite", *Water Research*, 44, 2930-2938, 2010.
- [34] Q.Y. Chen, M. Tyrer, C.D. Hills, X.M. Yang, P. Carey, "Immobilisation of heavy metal in cement-based solidification/stabilisation: A review", *Waste Management*, 29, 390-403, 2009. Min K =

Plasma Assisted Decomposition of Gaseous Hydrocarbons to Produce CO_x Free Hydrogen

I. Aleknaviciute¹, T. G. Karayiannis, M. W. Collins and C. Xanthos

School of Engineering and Design, Brunel University, Uxbridge, Middlesex, UK

¹irma.aleknaviciute@brunel.ac.uk

ABSTRACT

Hydrogen production is currently achieved using well developed conventional methods, such as steam reforming. However, the necessity for catalysts in current processes results in the major disadvantage of catalyst deactivation. In this paper we survey the alternative approach of using plasma technology to produce CO_x free hydrogen. Plasma assisted hydrogen production systems eliminate the use of catalysts and have been successfully investigated for different types of plasmas. An important conclusion is that propane holds particular promise as an alternative feedstock. This formed the rationale for our experimental programme to investigate CO_x free hydrogen production from propane. In a corona discharge reactor operating at atmospheric pressure internally, electrons were energized by an electric field to ionize propane and induce chemical reactions. Argon was used to provide additional electrons and photons for higher reaction rates. A range of each test parameter was covered, namely, the effect of power input in the range of 4.5 – 105.15 W and residence time of 1, 2, 3, 4, 5 and 8.18 minutes. 19 % hydrogen content by volume was achieved at a power input of 102 W and residence time of 8.18 minutes.

Keywords: propane decomposition, hydrogen production, non-thermal plasma

1. INTRODUCTION

Hydrogen is a secondary form of energy and needs to be manufactured, just as electricity requires generation. The majority of experts agree that hydrogen has a great role to play in the future energy sector as an important energy carrier. Hydrogen and hydrogen rich gas generation already have a significant role in industrial processes such as natural gas liquefaction, ammonia synthesis, refining and desulphurization, hydrogenation of hazardous waste, chemical plants, synthesis of methanol and ethanol and is also used as a fuel for rocket, IC engine and high temperature industrial furnace [1]. Hydrogen production is especially significant for the anticipated use of fuel cells, which are considered as 'a key technology for future sustainable energy supply' [1]. Fuel cells are being developed for transportation as well as for stationary and portable power generation, with the aim of producing energy at improved efficiency, durability, and lower emissions of gaseous contaminants such as CO, CO_x, NO_x and SO_x. Stationary applications could vary from large central power stations to distributed-power generators for buildings, residences in urban areas and small systems located in remote areas. For central power stations applications, the use of phosphoric acid fuel cells (PAFCs), molten carbonate fuel cells (MCFCs) and solid oxide fuel cells (SOFCs) have been considered. Fuel cell use for residential and distributed power generation systems may present some advantages over conventional energy generation systems (burning of fossil fuels in power stations), such as the reduction of transmission and distribution costs, improved quality of power delivery and the possibility of providing combined heat and electricity. Polymer electrolyte fuel

cells (PEFCs) have been investigated for use in transportation and have also been recognised as having the best potential to replace the internal combustion engine for automotive propulsion power [2]. In addition to the above applications, hydrogen rich gas production may play an important role in the reduction of emissions from internal combustion engine vehicles. The addition to a fuel of light components, which have a low temperature of ignition, increases the speed of propagation of combustion. Hence, hydrogen rich gas combusted together with fuel in the engine would provide a very lean operation and reduce CO_x, NO_x and other hydrocarbon based emissions [3].

Up to the present day, hydrogen has been mainly produced from fossil fuels, through steam reforming of methane (SMR) or partial oxidation of hydrocarbon fuels [1]. SMR is the most popular route for hydrogen production from methane, contributing 48% of the world's hydrogen production [1]. In the US, the FreedomCar and the Hydrogen Fuel initiatives, launched in 2002 and 2003 respectively, are two complementary government-industry research and development policy actions that promote hydrogen fuel and fuel cell vehicles. Coordinated by the US Department of Energy (DOE), these initiatives aim to mass-market fuel cell and hydrogen combustion vehicles at an affordable cost within 10 to 15 years from the launch of the initiatives [3]. Experts believe that natural gas resources will be sufficient for several decades to expand hydrogen generation capacity to support these two incentives, which anticipate that by 2040 the use of hydrogen in fuel cell powered cars and light trucks could replace consumption of 18.3 million barrels of petroleum per day; for this 150 million tonnes

of annual hydrogen production will be needed [1]. Conventional thermo-catalytic technology for hydrogen and syngas (carbon monoxide and hydrogen) production has certain drawbacks including high economic investment cost, catalyst poisoning, decrease in catalyst efficiency or deactivation of catalyst by carbon deposition, high temperature requirement to activate catalytic sites, low flow rate of inlet gas injected [5] and equipment size [6]. An important application of plasma technology is in the production of hydrogen and syngas; plasma can eliminate or decrease problems associated with catalyst sensitivity and deterioration, achieve higher conversion efficiencies and increase specific productivity. Plasma technology offers fast response time, compactness and low weight, and can be operated over a broad range of fuels; all of these factors are very attractive for automotive applications [7]. Therefore, a significant amount of research has been directed towards hydrogen generation from methane employing the plasma approach.

Dufour et al. [8, 9] have used a Life Cycle Approach to compare conventional methods of hydrogen production from methane, namely steam reforming and pyrolysis. Their results show that even if carbon capture and storage technology are used, the most environmentally friendly method is pyrolysis, avoiding the generation of CO_x completely [9]. Hydrocarbon pyrolysis was also recognised as the most promising route for hydrogen production by Edwards et al. [10], with Abbas and Daud [11] concurring with Dufour et al. that the process is the best from the point of environmental pollution as it does not produce any CO_x . Pyrolysis is a more economical option when compared to SMR with carbon capture [12]. The process co-produces valuable carbon products in solid form such as carbon black or graphite [13], this being much easier to sequester than carbon compounds in gaseous form [11]. In the US, approximately 5 million tonnes/year of carbon is used in the production of electrolytes for aluminium (requiring 0.4-0.5 kg per kg of aluminium) and by the ferroalloy industries. If the production of carbon were to increase, it could be used in other potential applications such as carbon to carbon composite use as building and construction material, electricity generation via carbon fuel cells and soil amendment [14].

Hydrogen production from gaseous hydrocarbons, such as propane, would especially benefit oil refineries where demand for hydrocarbon feedstock varies with time, so that the industry gains more flexibility in the feedstock choice [15]. Propane is attracting considerable attention in hydrogen production studies primarily because it is a major constituent of liquefied petroleum gas [16]. In addition, propane is produced in relatively high amounts from natural gas and oil crude refining [17]. It is also attractive for on-board hydrogen generation, because of it being liquefiable and easy to store and transport [18]. Propane is an inexpensive fuel with a high energy density, and offers a new approach to more economical

hydrogen production [19].

Based on the above rationale, our present work is focused on achieving decomposition of propane to generate CO_x free hydrogen using the corona discharge non-thermal plasma method.

2. EXPERIMENTAL FACILITY AND METHODOLOGY

2.1 Design of the reforming unit

In order to investigate plasma-based pyrolysis of propane, the main apparatus is the corona discharge reforming unit itself. This is shown schematically in Fig 1 a) with Fig 1 b) as a photograph of the plasma chamber with major components indicated.

The plasma chamber consists of two 316 stainless steel disks (23 mm thickness, 142 mm diameter), a stainless steel pin electrode, borosilicate glass cylinder, C103 copper disc with integrated cartridge heater (max output 500 W, 30 mm thickness, 142 mm diameter), PID temperature control system built in house, high voltage power supply (Matsusada, max output = 30 kV, 5 mA), vacuum pump (Edwards) and pressure gauge. The glass cylinder is 150 mm in length, 100 mm in outer diameter and 5 mm in thickness; it is made of borosilicate glass and can sustain a maximum short term working temperature of 500 °C and a maximum pressure of 73.7 bars. The top and bottom discs are connected and stabilized by three metal support rods.

The bottom disc of stainless steel acts as a plate electrode. The chamber was designed to allow for tests with both liquids and gases, and in order to undertake tests involving liquid hydrocarbons it has an integrated well to position a measured amount of liquid. The active electrode is installed at the centre of the top disc and can be removed and changed to test different configurations. A glass rod serves as an insulator and for electrode stability purposes; it can be moved vertically to vary the inter-electrode distance. The outer end of the rod is connected to an extra high tension (EHT) lead at the inner end of the rod to provide the power supply for the active electrode. A positive direct current high voltage is applied to the active electrode from a HV generator through a 3.12 M Ω resistor, creating a positive corona discharge.

2.1 Experimental method

The propane (referred to as working gas) is subjected to a positive corona discharge with argon, total volume of 1 atmosphere and ratio 1:1. In experiments with methane, it has been shown that argon addition enhances the rate of methane conversion to its radicals in plasma assisted methane decomposition [20]. The amount of propane and argon entering the system is measured by volume, using a pressure gauge. The

chamber is first flushed with argon by exhausting to vacuum and then filling with argon (2 cycles) to ensure that there is no air in the system. Then the chamber is filled with 0.5 atmosphere argon and 0.5 atmosphere propane. High voltage direct current power is supplied to the pin electrode initiating electrical break down of the argon gas and hence generating active plasma species such as electrons and ions. Cracking of hydrocarbon molecules is achieved by plasma ionization of the hydrocarbon molecules by an impact of an energetic electron or photo-ionic decomposition (chemical reactions of ions induced by a photon) [21].

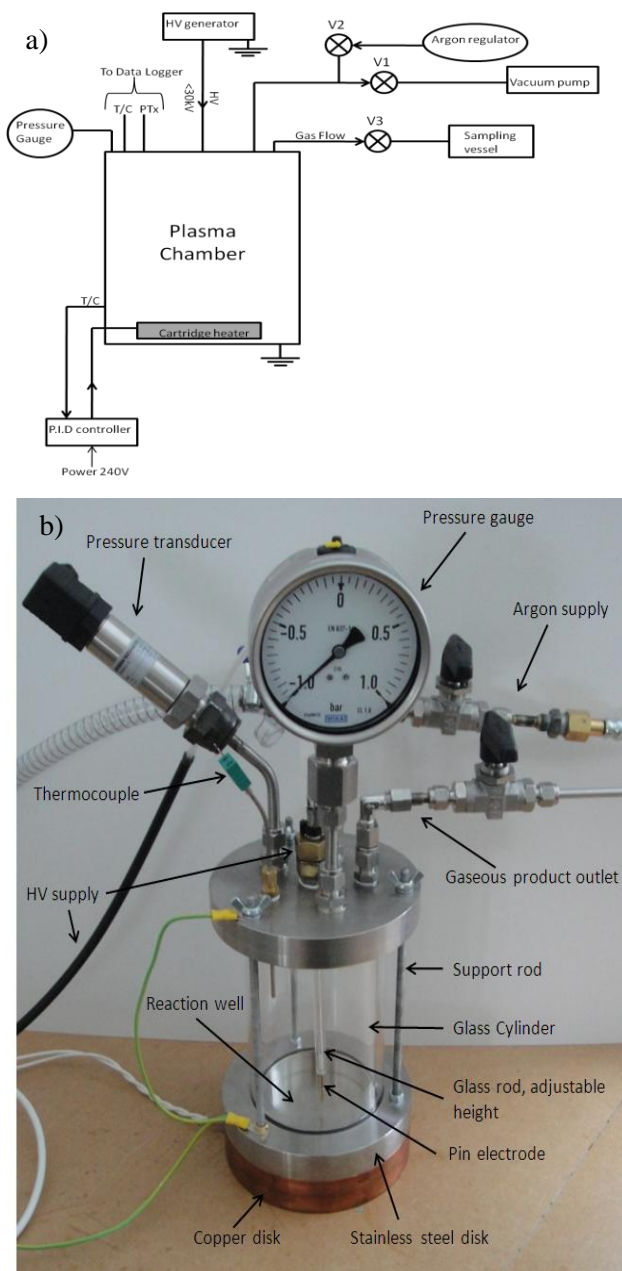


Figure 1: a) Corona discharge reactor schematic: V1-V3 - valves; T/C – thermocouple; PTx – pressure transducer; b) Plasma chamber design, showing all relevant components.

Gaseous samples are collected after each experiment and characterized by the GC-MS instrument comprised of a Hewlett Packard series 5890 Gas Chromatography instrument and a Trio-1000 Mass Spectrometer. Gaseous products do not need any treatment and can be analyzed by the GC-MS directly. The products will also be tested by a GC to measure accurately the concentrations of hydrogen present.

3. RESULTS AND DISCUSSION

3.1 Effects of power input and residence time on hydrogen production

A series of plasma decomposition tests were performed by varying the power input from 4.5 to 105.15 W, for each nominated residence time of 1, 2, 3, 4 and 5 minutes. The inter-electrode distance and gas composition are kept constant at 15 mm and 1:1 argon to propane respectively.

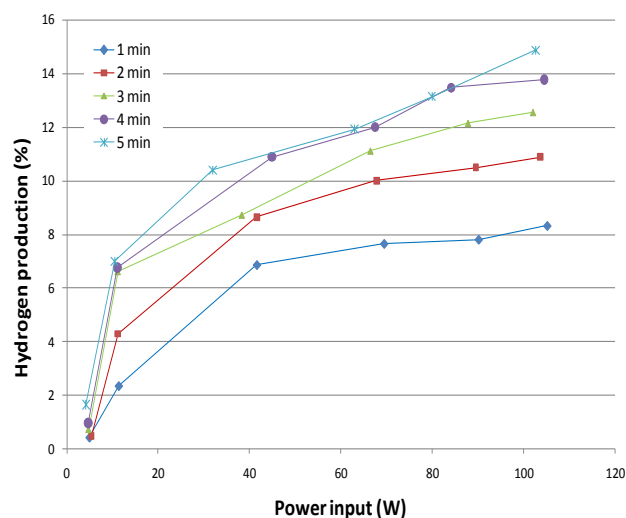


Figure 2: Effect of power input and residence time on hydrogen generation. Constant conditions: inter-electrode distance 15 mm. propane to argon ratio 1.

As shown in figure 2, at all residence times tested, an increase in power input leads to a higher hydrogen generation, because the energy deposited on the feed gas (argon and propane in this case) increases with increasing the power input. At residence time 5 minutes, increasing power input from 4.2 to 102.65 W leads to an increase of hydrogen generation from 1.6 to 14.8 % by volume.

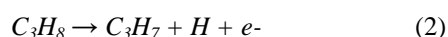
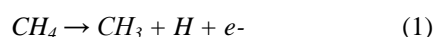
Hydrogen production increases with increasing residence time at all input power levels, as shown in figure 2. A similar trend has been observed in the pulsed corona discharge reforming of methane [20]. However, as shown in the figure, there is a diminishing effect with residence time, i.e. the increase from 4 min to 5 min is small. This will be investigated further. The longer residence time allows higher energy deposition on each molecule of the feed gas resulting in higher conversion

rates. At power inputs of just over 100 W, increasing the residence time from 1 to 5 minutes, leads in an increase of hydrogen production from 8.33 to 14.88 % by volume. A further increase to 8.18 minutes resulted in hydrogen content of 19 % at power input of 102.65 W, not shown in the graph.

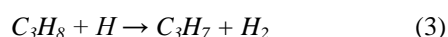
3.2 Decomposition mechanism and other compounds present

Mishra et al. [21] proposed a possible explanation for methane activation and conversion mechanisms under pyrolysis conditions in a pulse corona discharge as follows (equations 1 and 4 – 8 below):

Energetic electrons collide with methane molecules and hence radical H and CH₃ formation, i.e. a pure plasma process. This mechanism is adapted here for propane activation as follows:



The radical H may further react with another propane molecule to form an H₂ molecule and C₃H₇ radical:

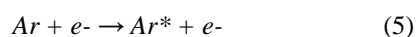


With the addition of argon to the system two extra processes may occur:

- (i) Release of extra electrons:



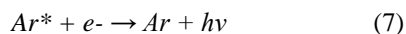
- (ii) Production of excited Ar* by reverse processes:



The latter accompanied by an emission of a photon, hv:



Or the direct capture of an electron by Ar* and emission of a photon:



Reaction (4) provides extra electrons for propane activation by an energetic electron, process described in equation 2, i.e. chemical reaction initiated via the collision with an electron, which is not consumed by the reaction. Reaction (7) generates photons assisting in photo-ionic decomposition of propane. A full decomposition of propane would result in generation of pure carbon in the solid state and pure hydrogen in a gaseous state:

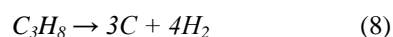
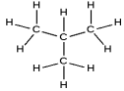
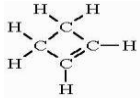
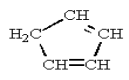
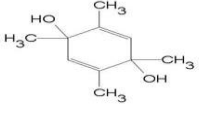
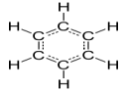


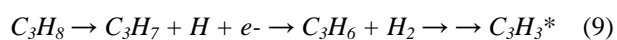
Table 1 shows the list of compounds, other than hydrogen, generated (recorded by the GC-MS) during corona discharge decomposition of propane. Production of methane, ethene and ethane can be explained by an incomplete propane decomposition and hence the generation of smaller molecules. However, from table 1 it can also be seen that larger molecules than the original have been generated.

Table 1: List of the compounds generated during plasma assisted decomposition of propane recorded by the GC-MS, and the corresponding chemical formulae.

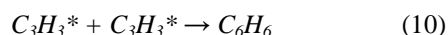
Compound	Formulae
Methane	CH ₄
Ethene	H ₂ C=CH ₂
Ethane	C ₂ H ₆
Propane	C ₃ H ₈
1 - Propene	H ₂ C=CH-CH ₃
Isobutane	
1 - Butene	H ₂ C=CH-CH ₂ -CH ₃
1 - Buten - 3 - yne	H ₂ C=CH-C≡C-H
Butane	C ₄ H ₁₀
Cyclobutene	
1,3 - Butadiyne	H-C≡C-C≡C-H
1,2 - Butadiene	H ₂ C=C=CH-CH ₃
Butyne	H-C≡C-CH ₂ -CH ₃
1 - Pentene - 3 - ene	H-C=C-CH=C-CH ₃
1,3, - Cyclopentadiene	
1,3 - Pentadiene	H-C=C-CH=C-CH ₃
3-Penten-1-yne	H-C≡C-C=CH-CH ₃
2,5 - Cyclohexadiene	
Benzene	

Kado et al. [22] concluded that in non-equilibrium pulsed discharges, methane first decomposes into atomic carbon in response to electron impact, then the atomic carbon combines with hydrogen or carbon to form CH or C₂. The authors postulate that the CH and C₂ are the precursors of C₂H₂. Lü and Li [23] and Cho et al. [24] also proposed methane coupling reactions to be a result of methane dehydrogenation followed by the coupling of radicals in plasma assisted methane decomposition.

The mechanisms proposed in [23] and [24] could explain the larger molecules generated during propane decomposition. Propane molecules are first dehydrogenated or partially dehydrogenated, generating reactive radicals, followed by recombination to generate larger molecules. This also explains generation of the cyclic molecules and compounds with either double or triple bonds, due to the loss of hydrogen. For example, the generation of the benzene molecule could occur due to the partial dehydrogenation of the propane molecule by the processes described in (2) and (3) subsequently leading to the formation of C₃H₃* radicals:



The recombination of these radicals would result in the formation of benzene:



4. CONCLUSIONS

In this paper we have presented a short review of the importance of hydrogen and the significance of the ability to reduce CO_x emissions during its production. Propane has been identified as a potentially useful feedstock.

The survey forms the background to reporting the development of a non-thermal plasma reforming unit operating at atmospheric pressure for converting gaseous hydrocarbons to CO_x free hydrogen. A series of experiments has been performed to investigate the effects of power input and residence time on hydrogen production by plasma decomposition of propane. We have shown that higher power inputs and longer residence time favors the production of hydrogen. A hydrogen concentration by volume of nearly 20 % has been achieved at power input of 102 W, residence time 8.18 minutes, inter-electrode distance 15 mm and argon to propane ratio 1:1.

Ongoing work includes further parametric studies of the effects of inter-electrode distance, gas composition and the polarity of corona discharge on hydrogen generation.

REFERENCES

- [1] Balat, M. "Potential importance of hydrogen as a future solution to environmental and transportation problems", *Int. J. Hydrogen Energy*, vol. 33, p. 4013, 2008.
- [2] Ahmed, S., Krumpelt, M. "Hydrogen from hydrocarbon fuels for fuel cells", *Int. J. Hydrogen Energy*, vol. 26, p. 291, 2001.
- [3] Brent, D., Y. "Hydrogen and Fuel Cell Vehicle R&D: FreedomCAR and the President's Hydrogen Fuel Initiative", *CRS Report for Congress*, 2007. Code: RS21442.
- [4] Cohn, D. R., Rabinovich, A., Titus, C. H., Bromberg, L. "Near-term possibilities for extremely low emission vehicles using onboard plasmatron generation of hydrogen", *Int. J. Hydrogen Energy*, vol. 22, p. 715, 1997.
- [5] Luche, J., Aubury, O., Khacef, A., Cormier, J-M. "Syngas production from methane oxidation using a non-thermal plasma: Experiments and kinetic modelling", *Chemical Engineering Journal*, vol. 149, p. 35, 2009.
- [6] Deminsky, M., Jivotov, V., Potapkin, B., Rusanov, Y. "Plasma Assisted Production of hydrogen from hydrocarbons", *Pure Appl. Chem.*, vol. 74 p. 413, 2002.
- [7] Holladay, J.D., Hu, J., King, D. L., Wang, W. "An overview of hydrogen production technologies", *Catalysis Today*, vol. 139, p 244, 2009.
- [8] Dufour, J., Serrano, D. P., Galvez, J. L., Moreno, J., Garcia, C. "Life Cycle Assessment of processes for hydrogen production. Environmental feasibility and reduction of greenhouse gas emissions", *Int. J. Hydrogen Energy*, vol. 34, p. 1370, 2009.
- [9] Dufour, J., Galvez, J. L., Serrano, D. P., Moreno, J., Martinez, G. "Life Cycle Assessment of hydrogen production by methane decomposition using carbonaceous catalysts", *Int. J. Hydrogen Energy*, vol. 35, p. 1205, 2010.
- [10] Edwards, P. P., Kuznetsov, V. L., David, W. I. F., Brandon, N. P. "Hydrogen and fuel cells: towards sustainable energy future", *Energy Policy*, vol. 36, p. 4356, 2008.
- [11] Abbas H. F., and Daud, W. M. A. W. "Hydrogen production by methane decomposition: A review", *Int. J. Hydrogen Energy*, vol. 35, p. 1160, 2010.
- [12] Bockris, J. O'M. "The origin of ideas on hydrogen economy and its solution to the decay of the environment", *Int. J. Hydrogen Energy*, vol. 27, p. 731, 2002.
- [13] Ahmed, S., Aitani, A., Rahman, F., Al-Dawood, A., Al-Muhaish, F. "Decomposition of hydrocarbons to hydrogen and carbon", *Appl. Catal. A: General*, vol. 359, p. 1, 2009.
- [14] Muradov, N. Z., Veziroğlu, T. N. "From hydrocarbon to hydrogen-carbon to hydrogen economy", *Int. J.*

Hydrogen Energy, vol. 30, p. 225, 2005.

- [15] Rakib, M. A., Grace, J. R., Lim, C. J., Elnashaie, S. S. E. H., Ghiashi, B. "Steam reforming of propane in a fluidized bed membrane reactor for hydrogen production", *Int. J. Hydrogen Energy*, vol. 35, p. 6276, 2010.
- [16] Wang, X., Wang, N., Wang L. "Hydrogen production by sorption enhanced steam reforming of propane: A thermodynamic investigation", *Int. J. Hydrogen Energy*, vol. 36, p. 466, 2011.
- [17] Wang, X., Wang, N., Zhao, J., Wang L. "Thermodynamic analysis of propane and steam reforming for synthesis gas or hydrogen production", *Int. J. Hydrogen Energy*, vol. 35, p. 12800, 2010.
- [18] Zeng, G., Tian, Y., Li, Y. "Thermodynamic analysis of hydrogen production for fuel cell via oxidative steam reforming of propane", *Int. J. Hydrogen Energy*, vol. 35, p. 6726, 2010.
- [19] Lejeff-Hey, K., Kalk, T., Mahlendorf, F., Niemzig, O., Trautman, A., Roes, J. "Portable PEFC generator with propane as fuel", *Journal of Power Sources*, vol. 86, p. 166, 2004.
- [20] Mishra, L. N., Shibata, K., Ito, H., Yugani ,N., Nishida, Y. "Characterization of methane destruction using pulsed corona discharge at atmospheric pressure", *J. Plasma Fusion Res.*, vol. 6, p. 760, 2004.
- [21] Mishra, L. N., Shibata, K., Ito, H., Yugani ,N., Nishida, Y. "Characterization of pulsed discharge plasma at atmospheric pressure", *Surface and Coatings Technol.*, vol. 201, p. 6101, 2007.
- [22] Kado, S., Urasaki, K., Skine, Y., Fujimoto, Y. "Direct Conversion of methane to acetylene or syngas at room temperature using non-equilibrium pulsed discharge", *Fuel*, vol. 82, p. 1377, 2003.
- [23] Lü, J., and Li, Z. "Conversion of natural gas to C₂ hydrocarbons via cold plasma technology", *Journal of Natural Gas Chemistry*, vol. 19, p. 375, 2010.
- [24] Cho, W., Kim, Y. C., Kim, S-S. "Conversion of natural gas to C₂ product, hydrogen and carbon black using a catalytic plasma reactions", *J. Ind. Eng. Chem.*, vol. 16, p. 20, 2010.

Colloid Particles Deposition in Porous Media: Role of Hydrodynamic and Electrolyte Concentration

A. Djehiche¹, V. Canseco², A. Omari³, H. Bertn², and M. Gafsi¹

¹ LRGC, University Amar Telidji Laghouat, ALGERIA (djehichea@yahoo.fr)

² Laboratoire TREFLE, UMR 8508, Université de Bordeaux,
33405 Talence Cedex France

³ Laboratoire des Milieux Dispersés Alimentaires, ISTAB, Avenue des Facultés,
33405 Talence Cedex France

ABSTRACT

This study deals with colloid transport in porous media which applications are found in subsurface water, petroleum engineering, hydraulic engineering, deep-bed filtration or civil engineering. An experimental study of colloidal polystyrene Latex particles deposition in a consolidated porous medium is presented. The influence of ionic strength of the colloid suspension and the flow rate on particle deposition is investigated. Results show that the rate of blocking and the maximum attainable surface coverage are determined by a unique interplay between solution ionic strength, and the number of Peclet (Pe) which is a ratio between convective and diffusive effects. In other respects, using a γ rays attenuation technique allows us to measure local porosity fluctuation due to particles deposition. By this way deposition kinetics may be followed locally and precisely. It has been shown that particles deposition depends strongly on the Peclet number. In the diffusive regime deposition has a plateau value while it decreases according to the power law, $Pe^{-1/3}$ in the convective regime. Nevertheless when considering the thickness of the adsorbed layer over large scales, obtained results using the γ rays attenuation technique are found in good agreement with those obtained by means of an usual technique especially at latest stages of adsorption process.

Keywords: Colloid; porous medium; Peclet number; permeability; γ -ray.

1. INTRODUCTION

In porous media the deposition of colloidal particles in flowing suspensions is a challenging problem of both scientific and industrial importance. Many applications can be found in fields such as of Petroleum, Hydraulic engineering, deep-bed filtration, a unit operation commonly used in water treatment to remove fine particles, pathogens and colloid-associated pollutants from dilute suspensions Yao *et al.* [1]; M. Elimelech [2]. The extent of migration of colloidal materials (e.g. viruses, bacteria, humic colloids and metal oxides) and colloid-bound pollutants in ground waters and soils is also controlled by the processes of colloid deposition. In all cases, colloid particles suspended in the flowing liquid can be captured by the surrounding solid walls of the pore space, with some deposits occurring gradually inside the porous medium. This deposit formation phenomenon creates two problems. First, it can drastically increase the local concentration of pollutant particles. Second, gradual fouling of the porous medium occurs in some regions, considerably reducing the permeability of the porous medium Gohr Pinheiro *et al.* [3]. These modifications have, on a large scale, an important consequences on the physical phenomena, thus it is necessary to characterize these conditions properly.

The deposit of particles depends mainly on the interactions particle-pore solid wall and particle-particle

as well as hydrodynamic conditions characterized by the number of Peclet ($Pe = \text{diffusion/convection}$). Experiments Verapeen *et al.* [4] and numerical simulations Lopez *et al.* [5] as well as what have been previously shown that the hydrodynamic thickness of deposit varied in $Pe^{-1/3}$ during a flow dominated by the convection.

In this study, we present an experimental study of transport and deposit of colloidal particles in a consolidated, homogeneous porous medium and initially saturated with water. The liquid injected into artificial consolidated porous medium is a suspension of latex particles whose dimension is known.

2. PHYSICAL PRINCIPLE OF γ -RAY ATTENUATION TECHNIQUE

The measurement technique that we adopted is the γ -spectrometry whose basic principle is the attenuation of X-rays or the γ -rays by a liquid or a solid Groenevelt *et al.* [6]; Gharbi *et al.* [7-9]. This attenuation obeys the exponential law of Beer-Lambert.

$$I_1 = I_0 e^{-\mu X} \quad (1)$$

where I_1 is the emergent intensity, I_0 is the incident intensity, X is the thickness of the medium and μ is the attenuation coefficient of the material

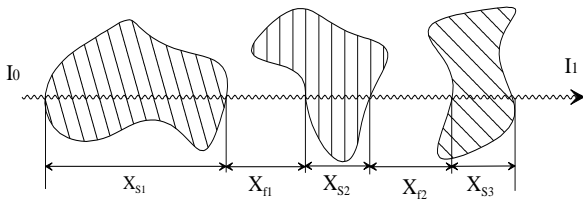


Figure 1: Porous saturated medium subjected to an incident γ radiation

Let us consider a porous medium saturated (solid, liquid) represented with 2D (Figure 1) and subjected to an incident radiation. The radiation is attenuated by the solid matter constituents and the liquid, its intensity transmitted is then given by;

$$I_1 = I_0 e^{-\mu_s X_s - \mu_f X_f} \quad (2)$$

where μ_s and μ_f are the solid and liquid attenuation coefficients, X_s and X_f are the solid and liquid equivalent thicknesses defined respectively by;

$$X_s = \sum_i X_{s_i} \text{ and } X_f = \sum_i X_{f_i}$$

When we carry out two photons counting at the same place of the dry medium then saturated medium by a liquid, we obtain for each case the two following attenuation equations;

$$N_1 = N_0 e^{-\mu_s X_s - \mu_g X_g} \quad (3)$$

$$N_2 = N_0 e^{-\mu_s X_s - \mu_f X_f} \quad (4)$$

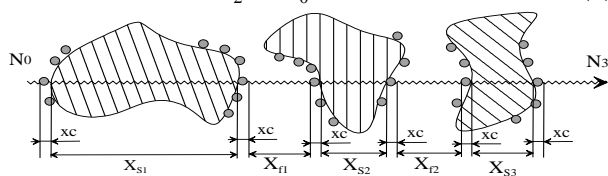


Figure 2: Damaged porous medium

where N_1 , N_2 and N_0 are the photons numbers of emergent and incident intensities, μ_g and μ_f are the gas and liquid attenuation coefficients. Considering that $\mu_g \ll \mu_f$, ratio between Eqs. 3 and 4 gives:

$$\text{Ln} \frac{N_1}{N_2} \approx \mu_f X_f \quad (5)$$

The porosity of a porous medium is defined by the ratio of the pores volume and the total volume of the medium. By analogy, along the radiation beam, porosity is equivalent to a length ratio, therefore;

$$\phi = \frac{1}{\mu_f X} \text{Ln} \frac{N_1}{N_2} \quad (6)$$

where X is the length of the porous medium and μ_f is a physical characteristic of the fluid of saturation. When the porous medium is locally damaged by particles deposition (Figure 2), the transmitted photon number, N_3 , is expressed by:

$$N_3 = N_0 e^{-\mu_s X_s - \mu_f X_f^e - \mu_c X_c} \quad (7)$$

where $X_f^e (= \sum_i X_{f_i}^e)$ Equivalent thickness of the liquid,

$X_c (= \sum_i X_{c_i})$ Total thickness of deposited colloids and μ_c is the colloidal attenuation coefficient.

The porosity of the damaged porous medium becomes:

$$\phi_d = \frac{1}{X(\mu_f - \mu_c)} \left[\text{Ln} \frac{N_1}{N_3} - \mu_c X \phi \right] \quad (8)$$

The total deposited particles thickness is then:

$$X_c = X(\phi - \phi_d) \quad (9)$$

The thickness of the local deposited layer was determined from this measurement by using a model of porous medium which will be described further.

3. EXPERIMENTAL SETUP

An artificial consolidated porous medium was used (Aerolith-10). Its initial porosity and permeability were 0.41 and $9.0 \cdot 10^{-12} \text{ m}^2$, respectively. The 0.15 m long sample was a cylindrical core of 0.05 m diameter. The colloidal suspension, which was used (averaged diameter of 780 nm), is a bi-disperse polystyrene latex particle suspension. The concentration of the colloidal suspension was settled to 200 ppm.

3.1 Experimental procedure

The porous medium was saturated with brine and the initial values of permeabilities and field of local porosity were measured. The colloidal suspension was then injected at a constant flow, corresponding to predetermined Peclet. A regular collection of the effluents was carried out, measurement results of the latex concentration by spectroscopy are presented in Figures 3 and 4. At different stage of the process, the injection of the suspension was stopped and was immediately followed by a brine injection to move the particles not deposited, which can allow us to measure the faded medium field local, porosity and permeability. These results are interpreted and the thicknesses of hydrodynamic layer is calculated, and presented in Figure 7.

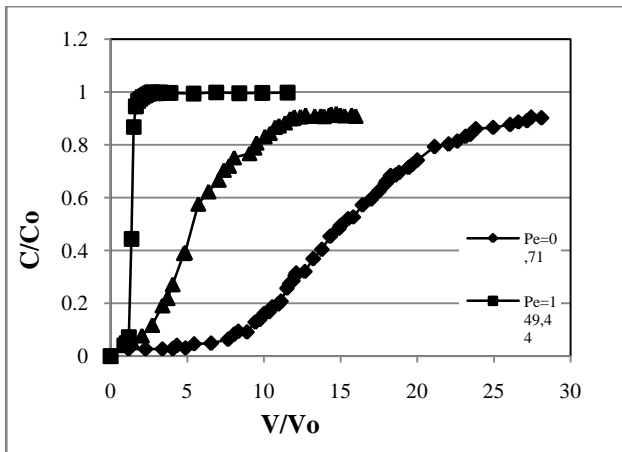


Figure 3: Latex concentration in the effluent as the function of the volume of suspension injected.

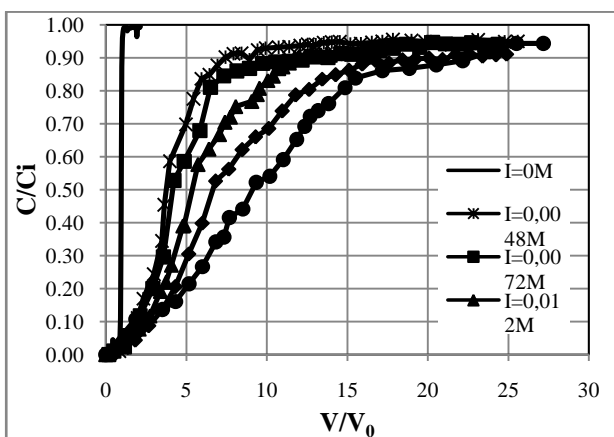


Figure 4: Colloidal suspension breakthrough curves obtained with different values of ionic strength.

4. RESULTS AND DISCUSSION

4.1 Permeability measurement

Initially, we consider that the global damage of the porous medium due to colloidal particle deposit, was determined by the permeability reduction. The Darcy's law Bear [10] is expressing the proportionality between the pressure drop ΔP and the flow rate Q of a viscous incompressible fluid is flowing in a 1D homogeneous porous medium:

$$\frac{Q}{A} = \frac{k\Delta P}{\eta L} \quad (10)$$

where A is the cross-section of the porous medium, L its length, η is the fluid dynamic viscosity and k the permeability.

k is an intrinsic property of the porous medium which can be determined in experiments from pressure drop for various values of the flow.

Figure 5 shows the reduction of the permeability with the increase of pore volumes injected into the medium, and which we have reduced the permeability progressively until 30 pore volumes (PV). This indicated that deposition is a progressive process.

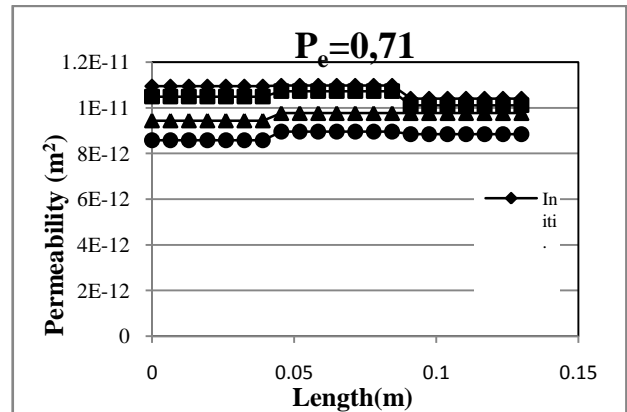


Figure 5: Permeability measurement along the porous medium (lozenge initial value, square after injection of 12 PV, triangle after injection of 17,5 PV, circle after injection of 30 PV)

4.2 Porosity measurement

Secondly, we determine the local damage of the porous medium by using the γ -ray attenuation technique. This is obtained starting from the local change of porosity as described previously. Figure 6 represents the local variation of porosity before and after injection of the colloidal suspension. However, one clearly observes a reduction of porosity measured after the injection of the colloidal suspension. We note also a progressive deposit of the particles along the porous medium which makes the average value of the porosity pass from 0.43 to approximately 0.40 after 30 PV of suspension have been injected.

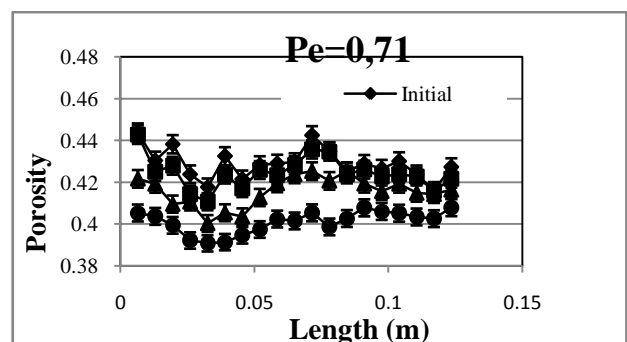


Figure 6: Porosity measurement along the porous medium (lozenge initial value, square after injection of 12 PV, triangle after injection of 17,5 PV, circle after injection of 30 PV)

4.3 Equivalent hydrodynamic thickness of deposited layer

Our fundamental objective is to determine the damage of the porous medium when a colloidal suspension flows through it. This damage is usually expressed by the measurement of the equivalent hydrodynamic

deposited layer thickness, called δ which can be defined in the following way:

The porous medium can be represented schematically by a beam of capillary tubes of the same radius R_p and the flow is assumed to be laminar. The flow rate is expressed using the Poiseuille law:

$$Q = \frac{\pi R_p^4}{8\eta} \frac{\Delta P}{L} \quad (11)$$

Equation of Darcy (eq. 10) and the equation of Poiseuille (eq. 11) Therefore;

$$R_p = \sqrt{\frac{8k}{\phi}} \quad (12)$$

The permeability reduction is deduced from Darcy's law which is expressed by:

$$R_k = \frac{k_i}{k_d} = \frac{\Delta P_i}{\Delta P_d} \quad (13)$$

Indices i and d correspond respectively to the initial and damaged medium. From (11) and (13), the hydrodynamic deposited layer thickness which is expressed by:

$$\delta = R_p (1 - R_k^{-1/4}) \quad (14)$$

In figure 6 we traced the calculated hydrodynamic layer thickness. After injection of 30 PV of the colloidal suspension, we see that the hydrodynamic layer thickness including between $0.55\mu\text{m}$ and $0.84\mu\text{m}$, is of the same order of magnitude as the particles diameter. This indicates that the deposit is mainly of a monolayer.

4.4 Effective deposited layer thickness

In order to compare the values obtained from equivalent hydrodynamic thickness and the effective thickness of the deposited layer, we use the relation given by Gharbi *et al.*, (2004) to determine this effective thickness:

$$e = \left(\frac{3}{4\pi} V_{c/g} + \frac{d_g^3}{8} \right)^{1/3} - \frac{d_g}{2} \quad (15)$$

where d_g is the diameter of the grains and $V_{c/g}$ is the volume of colloids deposited by grain. A comparison between the values of e and δ is presented in figure 7.

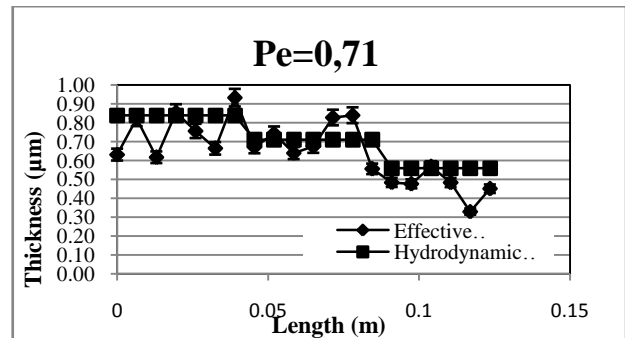


Figure 7: Thickness of the deposited layer (lozenge local measurement by γ , square global measurement by head loss).

4.5 Discussion

The results presented in figure 7 show that the local method of thickness determination of deposited layer and the global method giving the equivalent hydrodynamic thickness of deposited layer provide close results. The order of magnitude of the deposited layer is similar to the diameter of the particles, which confirms that the deposit is carried out in a monolayer. Several experiments with various flows rate were effected, and all show the dependence of the deposit of particles with respect to the number of Peclet. Defining the Peclet number Pe as the ratio of the mean velocity in a pore $Q/(A\phi)$ and the particle velocity of diffusion a/D_0 gives:

$$Pe = \frac{Qa}{D_0 A \phi} \quad (16)$$

where D_0 is the particle diffusivity in the bulk defined by:

$$D_0 = \frac{kT}{6\pi\eta a} \quad (17)$$

and kT , η and a stand for the Boltzmann factor, the viscosity of continuous phase (brine) and particle radius, respectively.

For low values of Pe , repulsive interactions particle/particle and attractive interactions solid/particle, we can observe a monolayer deposition of the particles covering the near total of the pore surface. When the value of Pe increases, the number of particles deposited per unit of area decreases. This can be explained by the phenomenon "hydrodynamic shadowing" which translates the influence of a particle deposited on the deposit of other particles in its vicinity.

5. CONCLUSION

In this study we show that non-destructive experimental technique used (attenuation of the gamma radiation) and the adopted methodology allow the space monolayer of

the deposited particle in any point of the porous medium. Moreover, the local character of measurement is an asset to appreciate the effective damage of the porous medium, whereas the usual methods are destructive or intrusive also give only indirect measurements of the global damage through the medium of permeability fall. We highlight that the deposit is carried out a progressive way along the porous medium until obtaining a monolayer deposit.

REFERENCES

- [1] Yao, K. M., Habibian, M. T. and O'Melia, C. R. "Water and wastewater filtration: concepts and applications", *Envir. Sci. Technol.* **5**, p. 1105, 1971.
- [2] Elimelech, M. "Predicting collision efficiencies of colloidal particles in porous media ", *Wat. Res.* **26** (1), p.1, 1992.
- [3] Gohr Pinheiro, I., Schmitz, P., Houi, D. "Particle capture in porous media when physico-chemical effects dominate", *Chemical Engineering Science*, **54**, p. 3801, 1999.
- [4] Verapeen, J-P., Nicot, B., Chauveteau, G. "In-depth permeability damage by particle deposition at high flow rates", *SPE 68962, European Formation Damage Conference*, The Hague, The Netherlands, 2001.
- [5] Lopez, P., Omari, A. and Chauveteau, G. "Simulation of Surface Deposition of Colloidal Spheres under Flow", *Colloids and Surfaces A: Physicochem. Eng. Aspects* **240**: p. 1, 2004.
- [6] Groenevelt, P.H., de Swart, J.G. and Cisler, J. "Water content measurement with 60 keV gamma ray attenuation", *Bull. Inst. Ass. Sci. Hydrology*, **14**(2), p. 67, 1969.
- [7] Gharbi, D., Bertin, H. and Omari, A. "Use of a gamma ray attenuation technique to study colloid deposition in porous media", *Experiments in Fluids*, **37**, p. 665, 2004.
- [8] Djehiche, A., Bertin, H., Omari, A. and Derriche, Z. "Experimental study of the deposit of colloidal particles in porous media ", *the 3st International Conference on Applications of Porous Media*, Marrakech, Morocco, 2006.
- [9] Canseco, V., Djehiche, A., Bertin, H., and Omari, A. "Experimental study of colloids transport in porous media" *the 12th International Conference on Surface and Colloid Science*, Beijing, China, 2006.
- [10] Bear, J. "*Dynamics of fluids in porous media*", American Elsevier Publishing Company, N.Y., USA, 1972.

A comparative Life Cycle Assessment (LCA) of Using Virgin Crushed Aggregate (VCA) and Recycled Waste Concrete Aggregate (RCA) in Road Construction

Sagar P. Parajuli¹, Mussie S. Naizghi¹, Brian Warshay¹, Hassan A. Arafat¹

¹Masdar Institute of Science and Technology
P.O. Box 54224, Abu Dhabi
Corresponding author, E-mail: harafat@masdar.ac.ae

ABSTRACT

Recycled concrete aggregate (RCA) materials have been applied in construction works such as road base construction. Depending upon the quality of RCA and intended application, RCA can yield acceptable strength and is being considered as a viable alternative to virgin crushed aggregates (VCA). This work has been carried out in the context of the recent establishment of concrete recycling facility at Al Dhafra Waste Facility (Abu Dhabi, UAE), by the center of waste management (CWM). The CWM is currently in the process of formulating and enforcing appropriate policies regarding the C&D waste handling. In this study, a comparative life cycle analysis (LCA) was conducted, in the context of Abu Dhabi, to compare the application of VCA and RCA in road base construction, in order to compare both options for their environmental impacts. The environmental impacts of the two construction materials, VCA and RCA, have been analyzed using specialized computer package (the SimaPro software) and available literature data pertaining to energy and emissions. It was found that the use of RCA was more appropriate in the construction applications for short-term roads, which have shorter life span, such as access roads and feeder roads. On the other hand, the use of VCA was found to be more environmentally appealing in long-lived strategic roads such as highways.

Keywords: life Cycle Analysis, solid waste, environmental impact, C&D waste

1. INTRODUCTION

Buildings and similar structures use a huge amount of concrete and its effective disposal is getting increasing attention as older structures are being dismantled and newer structures are being constructed to fit with the modern market. With the development of technology, the availability of recycling facilities for such dismantled materials is also spreading. Moreover, landfills are becoming increasingly difficult to find, are usually remote from demolition sites, or are too costly to maintain. All this has increased the necessity for C&D waste recycling. Dismantled concrete after crushing can yield good aggregates with acceptable strength and is being considered as a viable material in road base construction. In fact, it has been proved by different tests that the strength of recycled aggregates is comparable to that of crushed aggregate or natural gravel [1]. Both geotechnical and environmental properties of the crushed material indicate that the use of demolition waste in the form of RCA in road constructions is acceptable and can be recommended to replace landfilling of this material [2]. Besides course road base, recycled aggregates are used in many construction applications such as embankment filling, foundation soling, bank protection and drainage filters. In this study, the application of recycled concrete waste in the base course construction in the road will only be considered. Nowadays, C&D waste is becoming a major issue. However, it presents an opportunity, making this study especially relevant in developed cities because of

the rapid development in the recycling technology. Moreover, environmental concerns and recycling are increasingly being addressed by national policies [3].

2. GOAL/SCOPE DEFINITION

This work is being carried out to explore the viability of using recycled concrete aggregates in road base construction against conventional virgin crushed aggregates (VCA) in cities such as Abu Dhabi. The environmental impact of the two options will be analyzed in detail using SimaPro software and an appropriate recommendation will be made based on the results. This study is directed towards policy makers, contractors, consultants and the general public. The result of the LCA will help the audience increase their awareness and make them choose the option that has the least environmental impact for a given application.

In civil engineering works, roads are designed based on the maximum load per unit area expected along the road's life span. The section of road being considered for comparison is 1 km in length, 7 meter in width and has a specific thickness. It has been found that strength of recycled concrete can be 10-25% lower than that of normal concrete that use VCA [4]. Though the strength properties may differ when RCA and VCA are being used for road base construction and a detailed strength comparison was not available, it is assumed that use of RCA required 30% more thickness in course base layer

than using VCA to compensate for the strength difference.

It is exhausting to consider all the process components associated with aggregates production and hence the system boundaries have been assigned to simplify the life cycle emphasizing the major processes and components. The cradle of the VCA is the quarry site and that for RCA is the demolished concrete originating from construction and demolishing (C&D) waste. The grave for both cases is the road construction site. In general, roads serve for very long time and possible future intervention involves regular maintenance, upgrading, expansion and renovation. In no case, the base course is completely removed which renders waste scenario to be usually irrelevant when considered for the short term. As a result, time boundary is not considered in this case. In the long term, on the other hand, because production of RCA involves demolition and crushing, strength of RCA is less than that of VCA and may not be used again after the end of life of the road [5]. The conceptual boundary of different cases considered in this study has been depicted in Figure 1. The geographic boundary for this project has been set as the United Arab Emirates.

The process flow diagrams of VCA and RCA are shown in Figure 2 (a) and (b), respectively. Different scenarios have been considered to make a comparative study when the circumstance of use and end of life vary. In the first case, the grave of the aggregates has been considered as the construction site (i.e., road with no foreseeable end-of-life). In the second scenario, the grave has been considered as the constructed road and the effect of leaching has been included with the assumption that demolished C&D waste from RCA will be taken to the landfill and that from VCA will be reused after the end of its life.

3. FLOW PROCESSES

Most of the aggregates used in construction works in Abu Dhabi come from Ras al-Khaimah, Fujairah and Al Ain ranging from a distance of about 140-220 km. In this study, an average distance of 180 km has been adopted. After the end of the life of the constructed road, the road will be demolished and the C&D will be recycled.

In RCA production, except for the steel removal, the crushing and grading process of RCA is similar to that of VCA. The steel parts are removed (picked) by electromagnets which consume comparatively less energy than the crushers [6]. The transportation from the demolished structure to the C&D waste recycling facility will not be considered as the assumption is that the clients (Contractors) will bring the C&D waste themselves to the recycling plant to avoid the cost of conventional disposal. This is because the distance to the landfill site at 70 km (considering the largest landfill site in Abu Dhabi – Al Dhafra) is farther than that to the recycling facility at 50 km. After the process of grading, the RCA will be transported to the construction site which is assumed to be 50 km away from recycling facility where it will be used as sub base material for road construction. The transportation distance for RCA is assumed less than that for VCA because of the fact that the recycling facilities are closer to the city than the quarry site. At the end of the life of the road constructed from RCA, the road will be demolished. Since the quality of the recycled aggregate deteriorates after use, it will not be recycled and thus it will end up in the landfill at this point. Therefore, the VCA which will serve two life spans for the road (first as Virgin and second as a recycled) while the RCA will serve only for one life span of the road as it will not be reused again.

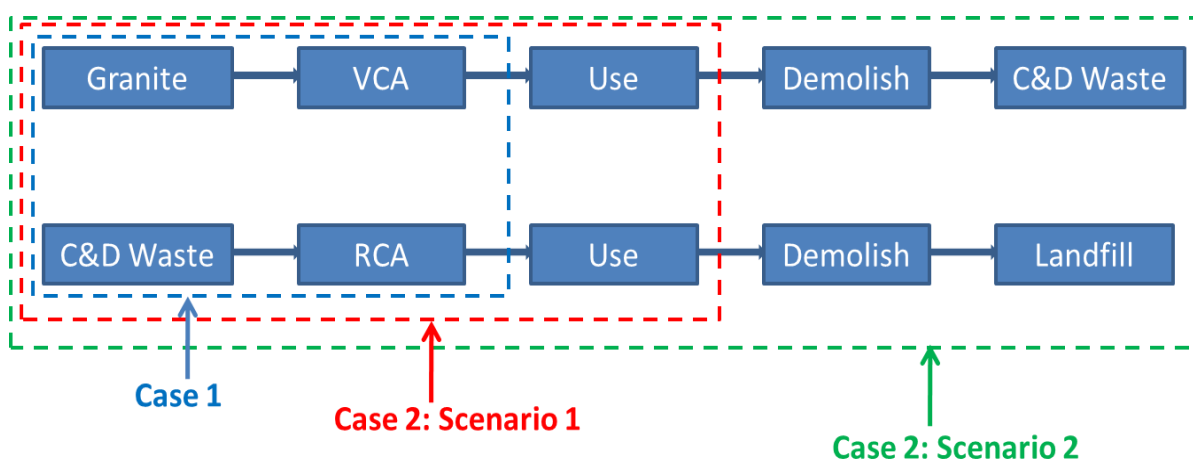


Figure 21: Conceptual boundary of the life cycle

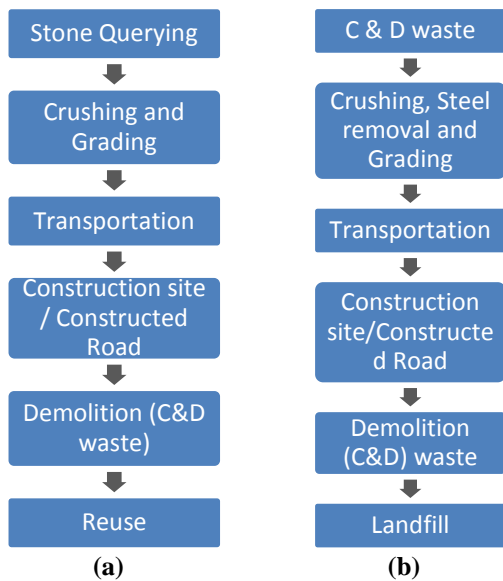


Figure 22: Process flow diagram of VCA (a) and RCA (b)

4. SIMAPRO DATABASE

In case 1, only SimaPro inventory data was available to be used to analyze the life cycle of VCA and RCA. In case 2, individual processes were built to represent the production processes of VCA and RCA based on literature data. Though the data available from past studies do not represent the exact geographic and environmental conditions of Abu Dhabi, an effort has been made to modify the processes in the context of Abu Dhabi. The energy consumption data (diesel and electricity consumption) for VCA production has been used from [7]. The emissions associated with VCA production were based on the previous study [8]. The energy consumption data associated with the production of RCA was taken from [9]. The leaching of chemicals to the groundwater from the constructed road was adapted from [10]. Since the avoidance of landfill of the

demolished C&D waste contributes positively to the environment, a positive credit has been given to the RCA process in terms of carbon dioxide (CO₂) being saved based on the previous study [11] in case 1. In case 2, because the C&D waste of VCA does not need to be taken to landfill as it will be recycled into RCA, avoided landfilling and avoided transportation involved were included as credit in the life cycle process of VCA. For consistency, only one type of truck is being used for all the transportation involved. In the production of VCA and RCA, 10% and 35% loss as fine powder has been considered for VCA and RCA, respectively, because more fine powder is produced in the process of demolition and crushing in the production of RCA [11].

4. RESULT AND DISCUSSION

The impact assessment results of VCA and RCA are depicted in Figures 3 and 4 for two scenarios: a scenario without RCA landfill and a scenario with RCA landfill. The idea behind the inclusion or exclusion of the landfill is the age of the road that will be constructed from the RCA. For the road built from VCA there is no question of landfill as it will be recycled both in the short term and long term [5]. For the RCA, if the road has not reached the end of its life span, there is a possibility of recycling and thus the demolished road will not end up in a landfill. However, once it reaches its end of its life it will end up in the landfill. In figures 5 and 6, the results of a comparison between the same scenarios when the RCA and VCA differs in proportions, has been depicted.

Both the RCA and VCA have been further divided into categories that include and exclude leaching. Two cases related to leaching are considered because leaching might not be important in places like Abu Dhabi where the rainfall is almost insignificant.

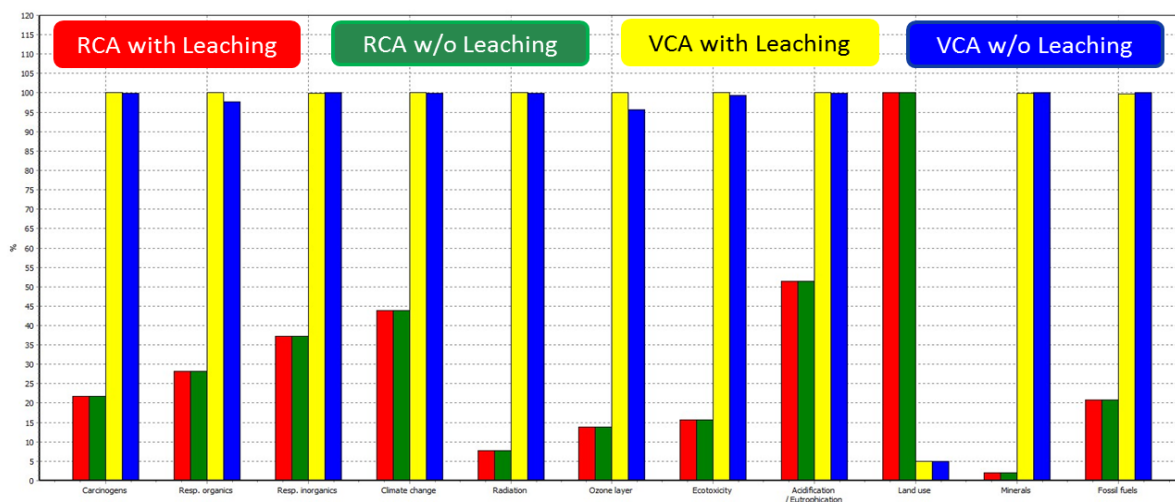


Figure 3: Impact assessment result without RCA landfill

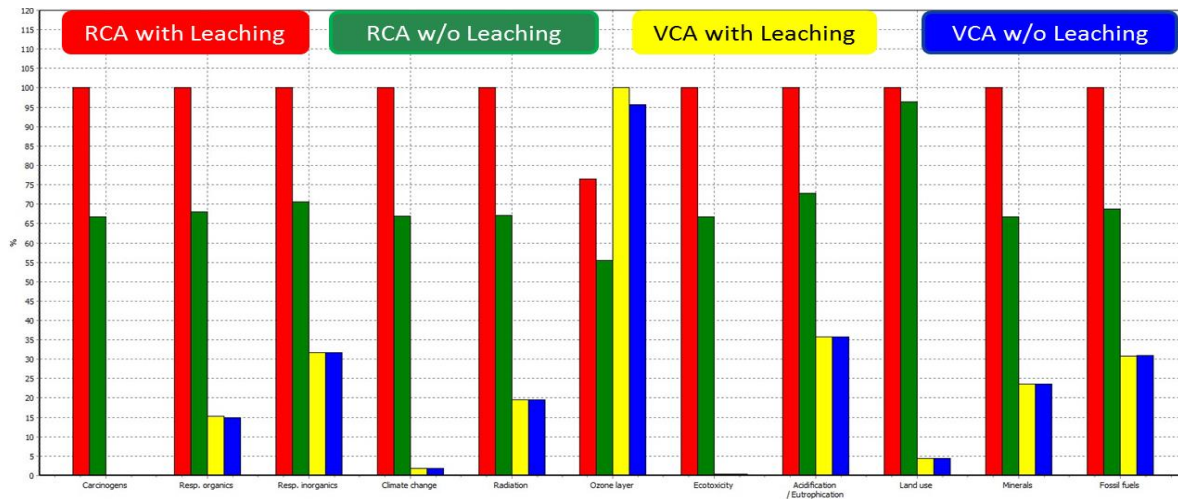


Figure 4: Impact assessment result with RCA landfill

Since there can be some precipitation events with torrential rainfall and in some places (especially close to the sea) where the ground water table is higher, consideration of leaching may become important.

In the scenario without RCA landfill, it can be seen (Figure 3) that the VCA causes more environmental damage than the RCA. This is primarily due to the fact that the process of VCA production involves more energy consumption and transportation than that of RCA. Both the energy consumption and transportation are associated with the use of fossil fuel which in turn is responsible for much of the damage assessment indicators shown in the figure. The only exception in the indicators is in land use; more land use is required in the case of RCA as compared to the VCA. The reason has to do with the relative location of the production of the RCA and VCA in Abu Dhabi. Because VCA production takes place in the desert uninhabitable area (an area which may not be used for some important purpose), the impact of land use is practically negligible, as shown by both Figures 3 and 4. However, the production of the RCA happens in the vicinity of the city area that impact the valuable land which would have been used for other beneficial purposes. Hence, the land use impact is significant in the case of RCA.

The inclusion of landfill for RCA (Figure 4) completely reverses the environmental impact. Now RCA has more of an environmental impact than VCA. The scenario in Figure 5 basically represents the case when the road has served its useful life and the RCA cannot be recycled because its quality has deteriorated and thus has to be destined to a landfill. Another interesting contrast when compared to Figure 4 is the effect of including or excluding leaching. It can now be seen that leaching can significantly affect the environmental indicators in the RCA. This is because RCA has more leachable chemicals associated with it than VCA, including cement and other construction material such as asphalt. However, because the constituent chemicals responsible for causing harm to the environment are less in VCA,

the inclusion and exclusion of leaching is not evidently as seen in both Figures 3 and 4.

5. POLICY ISSUES

Out of the total solid waste of Abu Dhabi, C&D waste accounts for about 60-70%. About 9000 tons of C&D waste per day is generated in Abu Dhabi [12] and about 80% of this is demolished concrete. Therefore, about 7200 tons of demolished concrete is produced per day. Considering 35% loss as fine powder in the RCA processing and production, about 4680 tons of RCA for aggregate use can be produced per day. This can effectively be used in the road base construction in Abu Dhabi. There are about 264 companies currently who have demolition permits [13].

Al Dhafra, Abu Dhabi's largest landfill site, spreads a large area of land about 16 square kilometers. The Center for Waste Management (CWM) is responsible for making regulations regarding the management of C&D waste. The objective of CWM is to avoid and minimize environmental and health pollution risks associated with the storage, collection, transport, handling, re-use, recycling and disposal of waste. CWM has developed regulations enforcing that all construction and demolition waste will have to be recycled. Further regulation will require that construction projects have to use a minimum of 40% of the recycled material in their construction whenever and wherever applicable. In 2010, for the first time, a concrete recycling facility at Al Dhafra, Abu Dhabi has been established. The capacity of the recycling facility is about 9000-16000 tons of C&D waste/day. Currently the produced RCA is being used at Al Gharbia road construction in the western part of Abu Dhabi which is an appreciable start. Though there is no requirement of demolished waste use, it is likely that some minimum requirements will be introduced in the future [14]. Around the world, practices of adopting RCA differ greatly. For example, in many states in the USA, there is a maximum limit on the percentage of RCA that can be used in road base

construction, which varies from 15–60% [3]. So, the policy regarding the use of RCA should be able to address the local conditions of Abu Dhabi in relation to the national state priorities.

6. LIMITATIONS OF STUDY

The energy and emissions data that have been used for the LCA are obtained from different sources and may not exactly represent the environmental, geographical and political context of Abu Dhabi. Although this may affect the results of the analysis, maximum effort has been exerted to adapt the database for the existing conditions here in Abu Dhabi.

7. RECOMMENDATIONS

Construction aggregates are, by weight, the largest component in the construction industry and proper use and reuse of these material is inevitable [15]. Therefore, based on the LCA analysis of the VCA and RCA presented here, it can be recommended that short term roads such as temporary feeder roads should be constructed with a higher proportion of RCA. On the other hand, long term roads such as highways and strategic roads are recommended to be constructed using base coarse with a higher proportion of VCA. Moreover, awareness among the stakeholders (the public and the construction company) towards the use of recycled C&D waste should be increased. The state should formulate engineering specifications regarding the strength of intended applications of RCA or VCA in construction. The proposed policies and regulations by CWM regarding C&D waste management should be expanded and made clear based on the production of C&D waste in Abu Dhabi and its potential application.

8. REFERENCES

- [1] J. G. Prokopy. (2011) Portland Cement Association. [Online]. http://www.cement.org/tech/cct_aggregates_recycled.asp
- [2] M. Wahlström, J. Laine-Ylijoki, A. Määttänen, T. Luotojärvi, and L. Kivekäs, "Environmental quality assurance system for use of crushed mineral demolition wastes in earth constructions," *Studies in Environmental Science*, vol. 97, pp. 725-734, 1997.
- [3] A. Horvath, "Life-cycle Environmental and Economic Assessment of Using Recycled Materials for Asphalt Pavements," University of California, 2003.
- [4] S. W. Tabsh and A. S. Abdelfatah, "Influence of recycled concrete aggregates on strength properties of concrete," *Construction and Building Materials*, vol. 23, pp. 1163-1167, 2009.
- [5] F. Collins, "Inclusion of carbonation during the life cycle of built and recycled concrete: influence on their carbon footprint," *International Journal of Life Cycle Assessment*, vol. 15, pp. 549-556, 2010.
- [6] US Department of Transportation, "Transportation applications of recycled concrete aggregate," 2004.
- [7] J. Sjunnesson, "Life cycle assessment of concrete," LUND University, 2005.
- [8] R. Wales and A. Desalvio, "Determination of emission from the mineral extraction industry," Mojave Desert Air Quality Management District.
- [9] K. M. Cochran, "Construction and demolition debris recycling: methods, market and policy," University of Florida, 2006.
- [10] R. Chowhury, D. Apul, and T. Fry, "A life cycle based environmental impacts assessment of construction materials used in road construction," *Resources, Conservation and Recycling*, vol. 54, pp. 250-255, 2010.
- [11] H. Shima, R. Tateyashiki, R. Matsusashi, and Y. Yoshida, "An advanced concrete recycling technology and its applicability assessment through input-output analysis," *Journal of Advanced Concrete Technology*, vol. 3, no. 1, pp. 53-67, 2005.
- [12] R. Absal. (2010) Gulf News.com. [Online]. <http://gulfnews.com/news/gulf/uae/environment/waste-recycling-facility-opens-in-abu-dhabi-1.625526>
- [13] Statistics Center - Abu Dhabi, "Statistical Yearbook of Abu Dhabi," 2010.
- [14] Center of Waste Management - Abu Dhabi. (2010) Center of Waste Management - Abu Dhabi. [Online]. <http://www.cwm.ae//index.php?page=debris>
- [15] T. Kelly, "rushed Cement Concrete Substitution for Construction Aggregates - A Material Flw Analysis," 2005.

Enhancing the Remediation Efficiency of Photo-Fenton Reaction by Oxygen and Humic Substances

Fawzy Ismail Eissa

Environment and Bio-agriculture Department, Faculty of Agriculture, Al-Azhar University, 11884, Nasr city, Cairo, Egypt. (fawzy.eissa@yahoo.com)

ABSTRACT

Removal of organic pollutants from water by Fenton reaction is most effective at pH 2.8. Thus, the necessity to acidify the reaction medium limits the applicability of this process. Consequently, the effect of oxygen and humic substances [Humic acid (HA), Suwannee River humic acid (SRHA) and Suwannee River fulvic acid (SRFA)] on the photo-Fenton ($Fe^{2+}/H_2O_2/UV-Vis$) treatment of diuron-contaminated water at pH 2.8 and 5.0 was studied to enhance the efficiency of this process and extend its optimum pH range towards neutral conditions. Results showed that the removal of diuron was faster in photo-Fenton/ O_2 system than photo-Fenton system without O_2 at pH 2.8 and 5. Likewise, addition of humic substances (HS) at a concentration of 10 mg L^{-1} greatly enhances the rate of diuron degradation in a catalytic photo-Fenton system at pH 2.8 and 5, indicating that the HS-modified photo-Fenton system is effective and applicable for degrading organic pollutants. Five intermediate products were identified by GC-MS analysis during the treatment of diuron-contaminated water. Based on these results, application of HS and O_2 would be a promising means for enhancing and extending the optimum pH of the catalytic photo-Fenton process towards neutral conditions.

Keywords: Fenton reaction, humic substances, herbicide, water treatment.

1. INTRODUCTION

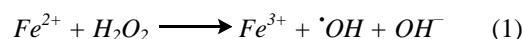
Pollution of surface waters and waste waters by pesticide residues mainly resulting from agriculture activities and pesticide manufacturing plants has strongly increased since several decades. Nowadays, it constitutes a very serious environmental problem for the human health and the ecosystems [1].

Since their discovery in 1950, Phenyl-urea compounds are the most widely used herbicides in agriculture for variety of purposes [2]. Diuron is a phenylurea herbicide that inhibits photosynthesis, thus impeding weed growth. It is toxic and non-biodegradable and mainly used for the control of germinating grass and broadleaved weeds in many crops, non-crop areas such as roads, garden paths and railway lines as well as its use as antifouling paint biocide [3, 4]. Diuron has been extensively used in agriculture and on non-crop areas. As a result, diuron is frequently detected in water bodies. In an EU-wide survey, diuron was detected in 70 % of European river samples [5]. Diuron is considered as a highly toxic, persistent priority substance by the EU [6] and has a half-life of 300 days when applied to the soil [7]. Diuron is also listed in the Contaminant Candidate List 3 of the US EPA [8] which identifies potential drinking water contaminants for regulation in the future.

Since herbicides, due to their biorecalcitrant and toxic properties, cannot be directly treated in conventional wastewater treatment plants based on the activity of a microbiological consortium, the development of new technologies aimed at the easy degradation of such substances is of practical interest [9].

One example of innovative technologies is the so-called advanced oxidation processes (AOPs), which consider an alternative to the conventional processes for the treatment of non-biodegradable and/or toxic compounds. Generally, non-biodegradable and/or toxic compounds lose their toxicity and increase their biodegradability upon oxidation treatment and before total mineralization can be achieved [10]. AOPs have been defined broadly as those aqueous phase oxidation processes which are based primarily on the intermediacy of the hydroxyl radical ($\cdot OH$) in the mechanism(s) resulting in the destruction of the target pollutant [11]. $\cdot OH$ is a nonselective oxidant that is able to oxidize a wide range of organic molecules.

Among all the AOPs, photo-Fenton reaction is frequently preferred because it achieves higher reactions yields with low treatment costs, mainly due to a more efficient use of solar light as photon source [12]. Furthermore, it uses non-toxic, easy-to-handle reagents. The Fenton reagent, consisting of H_2O_2 and ferrous iron, has been shown to be effective in the degradation of a wide spectrum of organic and inorganic pollutants [13]. The hypothesis of Haber and Weiss [14] that the Fenton reaction involves the formation of $\cdot OH$ radicals as the actual oxidants [Eq. (1)] is widely accepted.



The Fenton reagent has been known for more than a century but its application as an oxidizing process for destroying hazardous organics was not applied until the late 1960s [15]. The optimum pH for Fenton oxidations is usually reported in the acidic range near pH 3 [13]. However, water and soil may possess a high buffer

capacity. Therefore, the necessity to acidify the reaction medium limits the applicability of the Fenton process in environmental technology.

Thus, the main aim of the present work is to study the effect of oxygen and humic substances in enhancing the efficiency of photo-Fenton reaction and extending its optimum pH range towards neutral conditions. Degradation products formed during the remediation of diuron-contaminated water were identified as well by GC-MS. However, little has been reported on the degradation of pollutants by the photo-Fenton systems in the presence of humic substances.

2. MATERIALS AND METHODS

2.1. Chemicals

All chemicals and solvents used were of analytical reagent grade and were used as received. Diuron 99% and hydrogen peroxide (30%) were obtained from Cica-reagent, Kanto Chemical Co. Inc., Tokyo, Japan. Acetonitrile, dichloromethane and ethyl acetate were purchased from Nacalai Tesque Inc., Japan (HPLC grade, >99.5%). 3,4-Dichlorophenyl urea and 3,4-Dichlorophenyl isocyanate were purchased from Tokyo Chemical Industry Co., Ltd., Japan. Ferrous sulfate ($\text{FeSO}_4 \cdot 7\text{H}_2\text{O}$) (99%) and humic acid (HA) were obtained from Nacalai Tesque Inc., Japan. 2-nitrobenzaldehyde was purchased from Tokyo Kasei Kogyo. Suwannee River humic acid (SRHA) and Suwannee River fulvic acid (SRFA) were purchased from the International Humic Substance Society (IHSS). All solutions were prepared with ultra-pure water (Milli-Q water, $>18 \text{ M}\Omega \text{ cm}^{-1}$, Millipore Japan).

2.2. Herbicide removal experiments

A solution containing the initial concentration of diuron (42 mg/l) in MilliQ water was carefully agitated (This value corresponds to the maximum solubility of diuron in water at 25 °C). Then, freshly prepared ferrous sulfate ($\text{FeSO}_4 \cdot 7\text{H}_2\text{O}$) at Fe concentration of 0.2 mM was added, and H_2O_2 at a final concentration of 20 mM was finally added, to account the removal of diuron with photo-Fenton reaction ($\text{Fe}^{2+}/\text{H}_2\text{O}_2/\text{UV-Vis}$) in the presence and absence of oxygen. The pH of the reaction mixture was adjusted to 2.8 and 5.0 by adding a dilute aqueous solution of HCl or NaOH.

Other experiments were carried out using photo-Fenton reaction at the above-mentioned concentration of Fe and H_2O_2 plus Humic acid (HA) or Suwannee River humic acid (SRHA) or Suwannee River fulvic acid (SRFA) at a final concentration of 10 mg/l for treatment of diuron-contaminated water at pH 2.8 and 5. The solutions were continuously purged with molecular oxygen throughout each experiment.

A solar simulator (Oriel, Model 81160-1000) unit equipped with a 300 W Xenon lamp (ozone free, Oriel Model 81160) and special glass filters restricting the transmission of wavelengths below 300 nm was used for irradiation. This Xenon lamp has been demonstrated to be equivalent to natural sunlight. The wavelength range varies from 300 to 800 nm, which represents radiation very close to natural sunlight [16].

During irradiation, the solution in the quartz cell was well mixed with a stirring bar and the temperature was kept at 20 °C. The solution from the irradiated samples was removed at regular intervals and filtered through a 0.45 μm Ekicrodisc syringe filter for HPLC analysis. These experiments were conducted in triplicates and the results representing the mean values. The relative standard deviations ranged from 2 to 8%.

2.3. HPLC system

The progress in the removal of diuron was followed with HPLC system consisting of a PU-2089 plus pump (Jasco, Japan), a Rheodyne injection valve (Cotati, CA, USA) with a 50 μL sample loop and a UV-VIS detector (SPD-10A, Shimadzu) interfaced with a C-R6A Chromatopac integrator (Shimadzu, Japan) was used. The column was an Ultron VX-ODS (Suplecosil LC-18, particle size 5 μm ; Supelco) 250 mm \times 4.6 mm I.D. A guard column (Suplecosil LC-18, 5 μm , 10 mm \times 4.6 mm I.D.) was fitted in the front of the analytical column. A mixture of acetonitrile and MilliQ water (40/60, v/v) was used as a mobile phase at a flow rate of 1 mL min^{-1} . The UV detector wavelength was 254 nm for the diuron and 260 nm for 2-nitrobenzaldehyde which was used to normalize the results of the present study to a clear sky, noon conditions of Higashi-Hiroshima city (34°N) on 7th of October calculated by Takeda *et al* [17] because the power of the solar simulator is slightly changed by time. Under these conditions, the retention time for diuron was 7.1 min. Its calibration was calculated on the basis of the peak areas obtained with standardized samples analysed under the same HPLC conditions. The detection limit of diuron under these conditions was 3 $\mu\text{g L}^{-1}$.

2.3. Identification of diuron herbicide degradation products

In order to identify the photoproducts of diuron, MilliQ water samples were spiked at 42 mg/l levels of diuron and irradiated for 3 hours in the quartz glass cell, then subjected to solid phase extraction followed by GC-MS analysis. The intermediate products of the photodegradation of diuron were extracted by solid phase extraction (OASIS 60 mg Waters cartridges, Milford, MA, USA). The irradiated water samples were passed through the cartridges at a flow rate of about 10 ml/min. Air vacuum was employed to eliminate the water residues from the cartridges. A mixture of dichloromethane and ethyl acetate (1/1, v/v) was used to elute the intermediate products. This solution was

concentrated under nitrogen flow for the by-products analysis. The GC-MS was performed using a GC (HP 6890 series) equipped with a mass selective detector MSD (HP 5973). The system was equipped with a TC-5 capillary column (30m long \times 0.25mm i.d., film thickness 0.25 μ m), splitless injection, and used helium as carrier gas (1 ml/min). The GC oven temperature was programmed to initially hold at 50 $^{\circ}$ C for 3 min, to increase from 50 to 275 $^{\circ}$ C at a rate of 5 $^{\circ}$ C/min and to hold at 275 $^{\circ}$ C for 15 min. The injector and interface temperature were kept at 250 $^{\circ}$ C. Mass spectra were obtained by the electron-impact (EI) mode at 70 eV, using the full scan mode.

3. RESULTS AND DISCUSSION

3.1. Photo Fenton reaction with and without oxygen

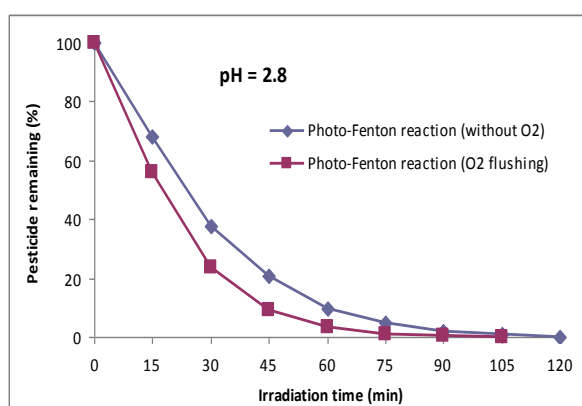


Figure 1: Effect of photo-Fenton/O₂ system [Fe 0.2 mM and H₂O₂ 20 mM] on the degradation of diuron at pH 2.8

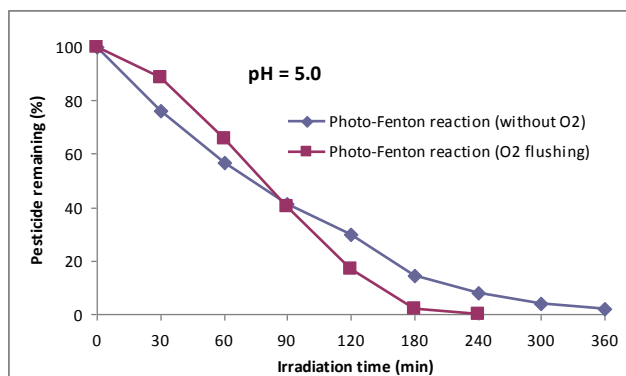
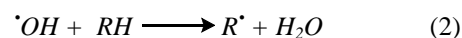


Figure 2: Effect of photo-Fenton/O₂ system [Fe 0.2 mM and H₂O₂ 20 mM] on the degradation of diuron at pH 5

As shown in Figures. 1 and 2, the degradation of diuron was faster when oxygen was used as carrier gas suggesting that oxygen played a positive role in the degradation of diuron. Oxygen leads to slower consumption of H₂O₂ [18] and generation of a peroxy-organic radical in Photo-Fenton/O₂ system, which leads therefore to the quicker degradation of diuron. A total oxidation of the organic pollutants is possible only at a sufficient concentration of oxygen. According to the mechanism of oxidation, the organic pollutants (RH) are first reduced to organic radicals in water by the OH

radicals formed from the photo-Fenton reaction (Eq.2) and this organic radical reacts instantaneously with dissolved oxygen to yield a peroxy-organic radical, thus initiating subsequent oxidation by chain reaction (Eq.3) [19].



The application of Fenton system to the treatment of real wastewater is limited due to its optimum pH and the high cost of H₂O₂. It is well known that oxygen is a cheap oxidant, but its oxidation potential is too low to oxidize the organics by it. The study of Kim *et al* [20] suggested that the degradation rate of the organic pollutants in landfill leachate depended on the concentration of dissolved oxygen. Molecular oxygen took part in the mineralization of aniline in Fenton or photo-Fenton reactions, acting as electron acceptor and partially replacing H₂O₂, thus the input of H₂O₂ was reduced [21].

3.2. Photo Fenton reaction in the presence and absence of humic substances

As it can be seen from Figs. 3 and 4, in the presence of HS, the removal of diuron at pH 2.8 and pH 5 was much faster than that for the Fenton reaction without HS. Humic substances are classified into humic and fulvic acid (HA and FA) as well as humin according to their solubility characteristics. Humic acids can be obtained at relatively low cost by alkaline extraction of peat, lignite or Leonardite and thus are commercially available on a large scale. Humic and fulvic acids are known to form complexes with metal ions by binding to carboxylate, polyphenolic and nitrogen-containing sites. Fe(III) and Cu(II) are the most preferentially bound metals [22]. In other words, Humic substances, a complex mixture of polymeric phenolic macromolecules, have the complex formation property to increase the solubilities, reactivities and mobilities of environmental chemicals and also the photosensitization ability to absorb solar energy and generate radical species which may attack chemicals in the environments and initiate their degradation [23,24]. HS can act as photocatalyst to pesticide photolysis in aqueous solution only within specific ranges of concentration, which depends on HS and pesticide chemical characteristics. Under UV-visible radiation, this photocatalysis is based on photogeneration of $\cdot OH$ radicals and susceptibility of pesticide molecules to $\cdot OH$ attacks define the photocatalysis efficiency. The $\cdot OH$ photogeneration process seems to be directly related to the phenolic group concentration in HS molecule [25].

It has been suggested that humic substances can act as sensitizers that produce reactive intermediates such as singlet oxygen, superoxide anion, hydrogen peroxide, solvated electrons or peroxy radicals of humic

substances in triplet states [26]. All these species may enhance the efficiency of the degradation process [27, 28]. The presence of humic acids enhanced the ability of Fenton process for pesticide degradation, and this is due to the protonation of humic acids which produce a locally acid environment favorable for Fenton reactions taking place [29]. Also, in the system containing humic substance, the oxidation intermediate may complex with $\text{Fe}^{2+}/\text{Fe}^{3+}$. The resulting complex products are able to reduce Fe^{2+} faster than H_2O_2 causing the enhancement of pesticide degradation [30, 22]. In the aquatic environment, natural organic matter, such as humic acid (HA), plays an important role in photo-Fenton systems, including the photosensitized generation of H_2O_2 and the photoreduction of Fe(III) to Fe(II) [31]. In these systems, the reducing and complexing abilities of HA to Fe(III) assist in the catalytic reactions of Fe(III)/Fe(II) redox cycles [32]. The light irradiation of *p*-quinone, which is known to be a structural part of HA, results in the production of $\cdot\text{OH}$. This reaction may contribute to the removal of organic pollutant [33].

In a study by Voelker and Sulzberger [34], an increase in the rate of H_2O_2 degradation by the Fenton reaction was observed at pH 5 when FA was added, whereas the effect was negligible at pH 3. The authors concluded that Fe(II)-fulvate complexes formed at pH 5 are able to react more rapidly with H_2O_2 than Fe(II)-aquo complexes, leading to a higher rate of $\cdot\text{OH}$ production.

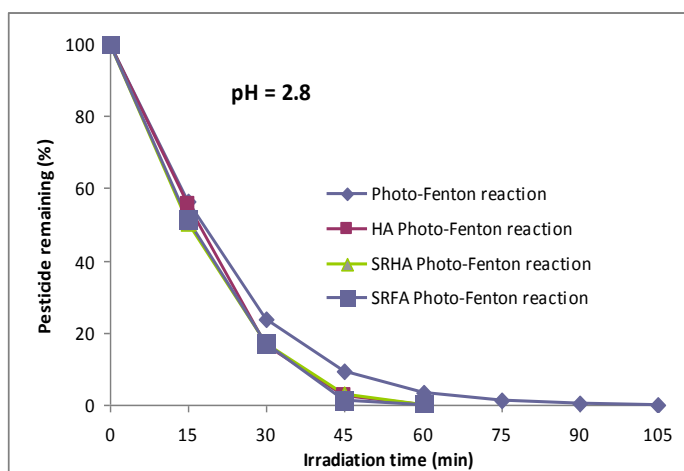


Figure 3: Effect of humic substances-modified photo-Fenton system [Fe 0.2 mM; H_2O_2 20 mM; Humic acid (HA), Suwannee River humic acid (SRHA), Suwannee River fulvic acid (SRFA) 10 mg/l] on the photodegradation of diuron at pH 2.8

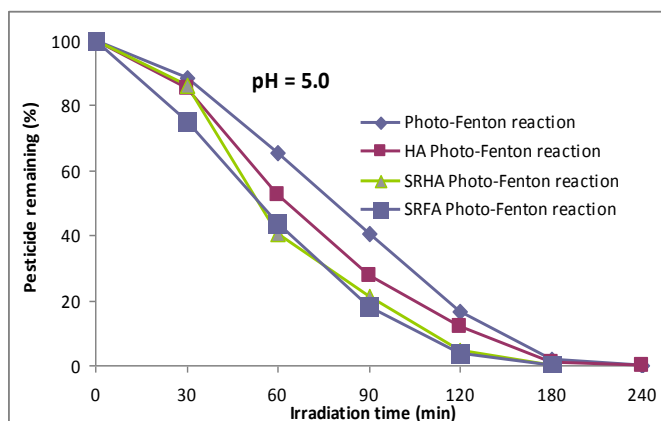


Figure 4: Effect of humic substances-modified photo-Fenton system [Fe 0.2 mM; H_2O_2 20 mM; Humic acid (HA), Suwannee River humic acid (SRHA), Suwannee River fulvic acid (SRFA) 10 mg/l] on the photodegradation of diuron at pH 5

3.3. Identification of diuron herbicide degradation products

Five products were identified by the molecular ion and mass fragmentation pattern and through comparison with NIST library data and also by comparing retention times and spectra with commercially available authentic standards. The structures of the main degradation products are represented in Fig. 5. The similarities of these compounds to the NIST library data were more than 85%. In addition to these five compounds, other degradation products would still possibly exist in the photocatalysis system but were not detected because of their low concentration, extraction efficiency and limited sensitivity in GC-MS. Based on the intermediate products listed in Fig. 5, it could be concluded that the first step in the degradation pathway of diuron was initiated by the attack on the aromatic ring by $\text{OH}\cdot$ radicals without dechlorination. The next step involved a series of oxidation processes that eliminated alkyl groups. The last step involved oxidative opening of the aromatic ring, leading to small organic ions and inorganic species [7, 35]. Moreover, during the photodegradation of diuron loss of the two methyl- and 3,4-dichlorophenyl groups are the dominant processes. 3,4-dichloroaniline and 3,4-dichlorophenyl isocyanate were proposed as the main diuron's degradation intermediates [36, 9]. *N, N'*-dimethylurea was also identified as the main degradation product of diuron [37]. 3,4-Dichlorophenylurea and *N*-(3,4-dichlorophenyl) formamide were also detected as diuron degradation products by Macounova *et al* [38] and Bouquet-Somrani *et al* [39], respectively.

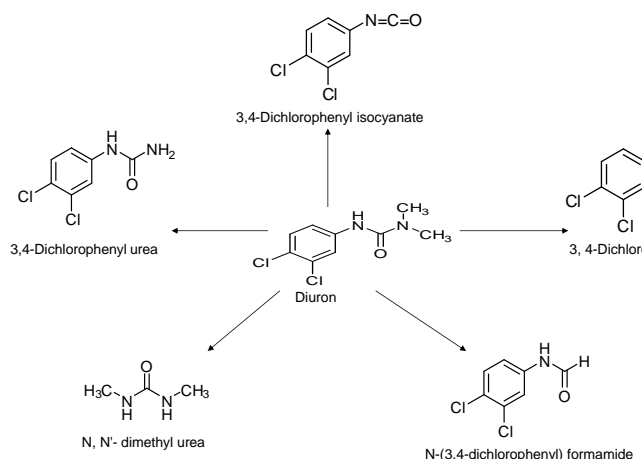


Figure 5: The main degradation products of diuron herbicide.

REFERENCES

- [1] Oturan M.A., Edelahi M.C., Oturan N., El kacemi K. and Aaron J. "Kinetics of oxidative degradation/mineralization pathways of the phenylurea herbicides diuron, monuron and fenuron in water during application of the electro-Fenton process", *Applied Catalysis B: Environmental*, 97: 82–89, 2010.
- [2] Barbash J.E., Thelin G.P., Kolpin D.W. and Gilliom R.J. "Major herbicides in ground water: results from the national water-quality assessment", *J. Environ. Qual.*, 30, 831–845, 2001.
- [3] Tixier C., Bogaerts P., Sancelme M., Bonnemoy F., Twagilimana L., Cuer A., Bohatier J. and Veschambre H. "Fungal biodegradation of phenylurea herbicide, Diuron: structure and toxicity of metabolites", *Pest Manage. Sci.*, 56, 455–462, 2000.
- [4] Giacomazzi S. and Cochet N. "Environmental impact of diuron transformation: a review", *Chemosphere*, 56, 1021–1032, 2004.
- [5] Loos R., Gawlik B., Locoro G., Rimaviciute E., Contini S. and Bidoglio G. "EU-wide survey of polar organic persistent pollutants in European river waters", *Environ. Pollut.*, 157, 561–568, 2009.
- [6] European Union "Decision No 2455/2001/EC of the European Parliament and of the Council of 20 November 2001 establishing the list of priority substances in the field of water policy and amending Directive 2000/60/EC", *Official Journal of the European Communities* (15/12/2001, pp. 331/1), 2001.
- [7] Malato S., Caceres J., Fernandez-Alba A.R., Piedra L., Hernando M.D., Aguera A. and Vial J. "Photocatalytic treatment of diuron by solar photocatalysis: evaluation of main intermediates and toxicity", *Environ. Sci. Technol.*, 37, 2516–2524, 2003.
- [8] [8] U.S. Environmental Protection Agency "Candidate Contaminant List 3, <http://www.epa.gov/safewater/ccl/ccl3.html>", (accessed on 25 September 2009), 2009.
- [9] Farre M.J., Domenech X. and Peral J. "Assessment of photo-Fenton and biological treatment coupling for Diuron and Linuron removal from water", *Water Research.*, 40, 2533–2540, 2006.
- [10] Scott J.P. and Ollis D.F. "Integration of chemical and biological oxidation processes for waste treatment: review and recommendations", *Environ. Prog.*, 14, 88–103, 1995.
- [11] Ollis D. Comparative aspects of advanced oxidation processes, *Emerging Technologies in Waste Management II*, ACS Symposium Series 518, Washington, DC, pp. 18–34, 1993.
- [12] Malato S., Blanco J., Alarcon D.C., Maldonado M.I., Fernandez-Ibanez P. and Gernjak, W. "Photocatalytic decontamination and disinfection of water with solar collectors", *Catal. Today*, 122, 137–149, 2007.
- [13] Pignatello J.J., Oliveros E. and MacKay A. "Advanced oxidation processes for organic contaminant destruction based on the Fenton reaction and related chemistry", *Crit. Rev. Environ. Sci. Technol.*, 36, 1–84, 2006.
- [14] Haber F. and Weiss J.J. "The catalytic decomposition of hydrogen peroxide by iron salts", *Proc. Royal Soc. Lond.*, 147: 332–351, 1934.
- [15] Neyens E. and Baeyens J. "A review of classic Fenton's peroxidation as an advanced oxidation technique", *J. Hazard. Mater.*, 98, 33–50, 2003.
- [16] Durand G., Mansour M. and Barcelo D. "Applications of thermosparry chromatography-mass spectrometry in photochemical studies of pesticides in water", *J. Chromato.*, 554, 233–250, 1991.
- [17] Takeda K., Shindo H., Nakatani N. and Sakugawa H. "Photochemical formation of hydroxyl radicals from chemical species dissolved in river water", *J. Jpn. Soc. Wat. Environ.*, 28: 509–513, 2005.
- [18] Du Y., Zhou M. and Lei L. "The role of oxygen in the degradation of *p*-chlorophenol by Fenton system", *Journal of Hazardous Materials*, B 139, 108–115, 2007.
- [19] Kim S.M. and Vogelpohl A. "Degradation of organic pollutants by the photo-Fenton-process", *Chemical Engineering & Technology*, 21, 187–191, 1998.
- [20] Kim S.M., Geissen S.U. and Vogelpohl, A. "Landfill leachate treatment by a photoassisted Fenton reaction", *Water Sci. Technol.*, 35, 239–248, 1997.
- [21] Utset B., Garcia J., Casado J., Domenech X. and Peral J. "Replacement of H₂O₂ by O₂ in Fenton and photo-Fenton reactions", *Chemosphere*, 41, 1187–1192, 2000.
- [22] Georgi A., Schierz A., Trommler U., Horwitz C.P., Collins T.J. and Kopinke, F.D. "Humic acid modified Fenton reagent for enhancement of the working pH range", *Appl. Catal. B: Environ.*, 72, 26–36, 2007.
- [23] Cooper W.J., Zika R.C., Petasne B.G. and Fisher A.Y. "Sunlight-induced photochemistry of humic substances in natural water, in "Aquatic humic substances:

- Influence on fate and treatment of pollutants”, Suffet I.H. and P. McCarthy, eds., PP. 333-362. American Chemical Society, Washington DC, 1989.
- [24] Frimmel F.H. “Photochemical aspects related to humic substances”, *Environ. Int.*, 20, 373-385, 1994.
- [25] Garbin J.R., Milori D.M.B.P., Simoes M.L., da Silva W.T.L. and Neto L.M. “Influence of humic substances on the photolysis of aqueous pesticide residues”, *Chemosphere*, 66, 1692–1698, 2007.
- [26] Aguer J.P., Richard C. and Andreux F. “Effect of light on humic substances: production of reactive species”, *Analisis*, 27, 387-390, 1999.
- [27] Beschkov V., Bardarska G., Gulyas H. and Sekoulov I. “Degradation of triethylene glycol dimethyl ether by ozonation combined with UV irradiation or hydrogen peroxide addition”, *Water Sci. Technol.*, 36, 131-138, 1997.
- [28] Konstantinou I.K., Zarkadis A.K., Albanis T.A. and Triantafyllos A. “Photodegradation of selected herbicides in various natural waters and soils under environmental conditions”, *J. Environ. Qual.*, 30, 121-130, 2001.
- [29] Fan C., Tsui L. and Liao M. “Parathion degradation and its intermediate formation by Fenton process in neutral environment”, *Chemosphere*, 82, 229–236, 2011.
- [30] Paciolla M.D., Kolla S. and Jansen, S.A. “The reduction of dissolved iron species by humic acid and subsequent production of reactive oxygen species”, *Adv. Environ. Res.*, 7, 169–178, 2002.
- [31] Voelker B.M., Morel, F.M.M. and Sulzberger B. “Iron cycling in surface waters: effects of humic substances and light”, *Environ. Sci. Technol.*, 31, 1004-1011, 1997.
- [32] Fukushima M. and Tatsumi K. “Degradation Pathways of Pentachlorophenol by Photo-Fenton Systems in the Presence of Iron(III), Humic Acid, and Hydrogen Peroxide”, *Environ. Sci. Technol.*, 35, 1771-1778, 2001.
- [33] Fukushima M., Tatsumi K. and Morimoto K. “The Fate of Aniline after a Photo-Fenton Reaction in an Aqueous System Containing Iron(III), Humic Acid, and Hydrogen Peroxide”, *Environ. Sci. Technol.*, 34, 2006-2013, 2000.
- [34] Voelker B.M. and Sulzberger B. “Effects of fulvic acid on Fe(II) oxidation by hydrogen peroxide. *Environ. Sci. Technol.*, 30, 1106–1114, 1996.
- [35] Mestankova H., Escher B., Schirmer K., Gunten U. and Canonica S. “Evolution of algal toxicity during (photo) oxidative degradation of diuron”, *Aquatic Toxicology*, 101: 466-473, 2011.
- [36] Salvestrini S., Di Cerbo P. and Capasso S. “Kinetics of the chemical degradation of diuron”, *Chemosphere*.48, 69–73, 2002.
- [37] Lanyi K. “Study of the Photodegradation of Urea-Type Herbicides by Capillary Gas Chromatography”, *Chromatographia Supplement*. 57, 235-241, 2003.
- [38] Macounova K., Krysova H., Ludvik J. and Jirkovsky J. “Kinetics of photocatalytic degradation of diuron in aqueous colloidal solutions of Q-TiO₂ particles”, *J. Photochem. Photobiol. A: Chem.*, 156, 273–282, 2003.
- [39] Bouquet-Somrani C., Fajula F., Finiels A., Graffin P., Geneste P. and Olive J. “Photocatalytic degradative oxidation of Diuron in organic and semi-aqueous systems over titanium dioxide catalyst”, *New J. Chem.*, 24, 999-1002, 2000.

The Role of the Dynamic Process of Aeration on the Evolution of Dissolved Oxygen and Phosphorus in Water Supplies

Gafsi Mostefa¹, Kettab Ahmed², Djehiche Abdelkader¹

¹Research Laboratory of Civil Engineering: RLCE, ResearchTeam
Water Resources, University of Ammar Telidji Laghouat, Laghouat , Algeria
Email: m.gafsi@mail.lagh-univ.dz; msgafsi@yahoo.fr;
a.djehiche@mail.lagh-univ.dz; djehichea@yahoo.fr

²LaboratoryResearch inWater Science:LRW-Water/ENP NationalPolytechnic
School ElHarrach, AvenueHassenBadi, Algiers, Algeria
Email: kettab@yahoo.fr; lrs-eau@netcourrier.com
Website: www.enp.edu.dz; www.lrs-eau-enp.dz

ABSTRACT

The very marked eutrophication of the lake was primarily due to exogenous compounds in extremely important nutrients largely dominated by phosphorus. Thus, long periods of stratification, associated with a significant amount of organic matter (mainly phosphorus), were the source of frequent anoxic layers deep. The main purpose of this study is to show the performance of hypolimnetic aeration process in increasing the amount of oxygen dissolved and decrease the amount of phosphorus in the deeper layers of the lake. The 10.3 km² of the water of Lake Hallwil are an important tourist center for the canton of Lucerne (Switzerland). In fact fishing and water sports are practiced. Before its restoration in the winter of the year 1985/1986, this lake eutrophication showed significant disruption of aquatic activities, and pollution damage to its various uses, and thus inhibited the development of tourism in the region. For this, EAWAG, to address the eutrophication of Hallwil lake, put into service in the winter of 1985/1986, an installation of a aeration system in two alternate modes of aeration namely by a aeration system in winter destratification and aeration hypolimnètic in summer (air / pure oxygen). The average values for oxygen and phosphorous concentrations, in the case of the hypolimnetic aeration, are both within the range of the allowed values:

- Summer season (30 m ≥ H ≥ 15 m): [O₂]min ≥ 4.5 g/m³ ; [P₂]max ≤ 0.20 g/m³

In the hypolimnetic aeration mode, the heating of the hypolimnion did not reach the thermocline and hence the thermal stratification is preserved. Finally, the restoration of the lake has greatly contributed to the increase of the amount of dissolved oxygen and decreases the amount of total phosphorus, especially in the deep layers of the hypolimnion, where a strong requirement in oxygen is needed for the oxidation of the phosphorus and nitrogenous compounds generated by the sediments.

Keywords: hypolimnetic aeration, dissolved oxygen, total phosphorus, thermal stratification, temperature, hypolimnion, lake

1. INTRODUCTION

The artificial mixing of stratified lakes with aerators may cause several changes; it prevents thermal stratification from becoming established and to increase the dissolved oxygen throughout the water column [1, 2]. As well it prevents surface river or lake parts from freezing over [3, 4], and make barriers against saltwater intrusion in rivers and lakes [3, 5], and delay ice formation in harbors and inland waterways [3, 4]. The artificial mixing help producing surface currents to protect harbor areas against high amplitude waves [4, 6, 7]; and avoids oil slicks from spreading after oil tanker accident, or protection of coastal habitats against damage from oil [3, 6, 7], also in the composition of the algal population, in the total possible number of algae, and in the algal growth rate [2, 6, 7], as well as bring about an almost complete compensation of the oxygen deficit resulting from metabolic activity [2, 6, 7].

The 10, 3 km² of the water plane of Hallwil Lake presents an important touristic pole for canton of Lucerne (Suisse). In fact fishing and many water sports are practiced. Before its restoration in the winter 1985/1986, this lake presents an important eutrophication that disturbs the aquatic activities, and a damaging nuisances to its different uses, and that boaters the touristic development of the region [8, 9].

For this fact, the Department of Surface Water, Research and Management Institute for Federal Planning, Treatment and the Protection of Waters (EAWAG) in Lucerne (Switzerland), in order to remediate to the eutrophication of the Hallwil lake, has implemented in the winter 1985/1986, an installation of alternate aeration system in two aeration modes [8,9]:

The main purpose of this study is to show the performance of hypolimnetic aeration process in increasing the amount of oxygen dissolved and decrease

the amount of phosphorus in the deeper layers of the lake.

2. MATERIALS AND METHODS

The Halwill Lake is eutrophic lake, phosphorous limited that has been experimented in the anaerobic middle during the summer season for the last century. In 1986, the system of the diffuser « Tanytarsus » (Figure 1) is installed as a final ultimate technique of restoration to fight the anaerobic middle found in the lake [8, 9]. This system is alternated between two modes of artificial aeration, the first is the aeration by the system of déstratification using big air bubbles; and the second is the hypolimnetic oxygenation, using respectively tiny bulls of air or oxygen.

The restoration in the Halwill lake uses a circular diffuser featherbubbles (Figure 1) and ejects air or oxygen. These systems are more suitable for deep lakes where the charge of dissolved bubbles in the hypolimnion and the momentum generated by the feathers are sufficiently weak to avoid a significant erosion of the thermocline.

The six (06) diffusers of figure 1, have a diameter of 6.5 m each, and are located in a circular configuration of 3.00 m diameter near the middle of the lake (Figure 1 and table 1). Every diffuser uses air or oxygen during summer season for the hypolimnetic aeration mode and air during the cold season for the destratification aeration mode [8, 9].

3. RESULTS AND DISCUSSION

3.1 Estimation of the warming rate in the Hypolimnion before and during the aeration

At a depth of 15 m, the sampled points of the annual average temperatures before and during the aeration are in the mean conserved (Fig. 2), which proves that the diffusion air/oxygen did not disturb this layer which is known as the base of the thermocline. That is, that the stratification is quite maintained after the action of the aerator.

In contrast, at the levels 30 and 45 m, the profiles coincide almost during all the time of the observation (1972-2002) and present a visible increase during the aeration. This explains that the aeration has created a small augmentation of the temperature of the two layers of the bottom. The average temperature of the deep two layers goes from the value 4.3 °C (before aeration) to 5.5 °C during the aeration.

3.2 Oxygenation

After the shift from the non aerated period to the aerated one, the depths 15 and 30 m of the bottom undergo an increase in the content in oxygen (Fig. 3), which is outstanding at the depth 30 m. this shows that the

system of aeration has fashionably contributed to the improvement of the content in oxygen in these three zones. The mean oxygen concentration in the layer of the hypolimnion shifts from the value 3 g/m³ (before the aeration) to 5 g/m³ (during the aeration).

The highest contents in oxygen are observed in the intermediary and superficial layers of the hypolimnion. We can as well note that the profiles of the extreme layers of the hypolimnion are closer during all the period of restoration, which confirms that a complete mixing of the content in oxygen has occurred between these two levels.

In the lower level, the oxygen concentrations were almost null before the restoration of the lake, to take a minimum average value over 2 g/m³.

Finally, the restoration of the lake has greatly contributed to the increase of the oxygen amount especially in the deep layers of the hypolimnion, where a strong requirement in oxygen is needed for the oxidation of the phosphorus and nitrogenous compounds generated by the sediments.

The figure 4 shows the evolution of the average concentration of dissolved oxygen from the surface, 15m, 30m and the bottom (45m) of the lake before and during the period of hypolimnetic aeration of May to September 82 and May to September 87.

In summer, the values of concentration of dissolved oxygen (before hypolimnetic aeration), are respectively, 4.21 g/m³, 1.6g/m³ and 1.05g/m³ in layers 15, 30 and 45m (bottom). But, we can appreciate one increase of this quantity during aeration, whose result are 7.2g/m³, 7.9g/m³ and 1.8 g/m³ in layers 15, 30 and 45 m respectively.

The increase in dissolved oxygen induces the reduction of eutrophication. During aeration, the amount of oxygen increased appreciably, especially at 15 and 30m, hence the smooth functioning of hypolimnetic aeration.

3.3 Total Phosphorous

The amount of phosphorus that the lake contained before the restoration has decreased in considerable way after the implementation of the aerator, for the three considered levels (Fig. 5). However, the diminution the most noted occurred at the level the most lower of the lake. Thus, the weakest concentrations of this component are observed in the depth 15 m; and the highest are those of the bottom layer. In the three levels, the maximum average contents of phosphorus before reach the values de 0.3 g/m³, 0.35 g/m³ and 0.62 g/m³ respectively, and then during the restoration take the values 0.18 g/m³, 0.20 g/m³ et 0.3 g/m³ in the levels 15, 30 and 45 m respectively. Consequently, the implementation of the aerator was too helpful for the diminution of the content in this component, which

when it is high leads to the increase of the trophic level of the lake.

The average value of the phosphorus amount of the hypolimnion before the aeration exceeds the value of 0.4 g/m^3 , while it is lower than 0.15 g/m^3 during the aeration.

The figure 6 shows the evolution of the average concentration of total phosphorus from the surface, 15m, 30m and the bottom (45m) of the lake before and during the period of hypolimnetic aeration of May to September 82 and from May to September 1987.

The evolution of the average concentration of total phosphorus before hypolimnetic aeration, are respectively 0.23 g/m^3 , 0.31 g/m^3 and 0.47 g/m^3 in the layers 15 m, 30 m and at the bottom. Maintaining an average concentration of total phosphorus during hypolimnetic aeration of 0.16 g/m^3 in 15m, 0.21 g/m^3 in 30 m and 0.35 g/m^3 in the lake bottom. So the average concentration of total phosphorus decreased during hypolimnetic aeration, leading to a decrease in the eutrophication of the lake; thus reducing the cost of processing and exploitation of raw water. Hence the proper functioning of the installation of hypolimnetic aeration.

4. FIGURES AND TABLES

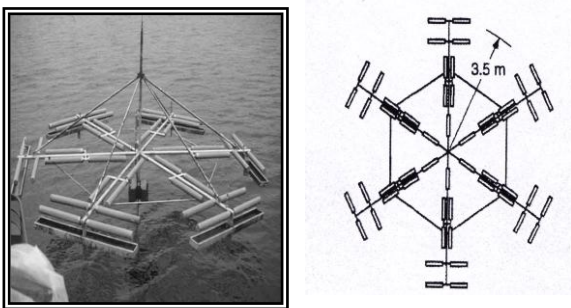


Figure 1: One of the six diffusers of Tanytarsus that has a diameter

6.5 meters [8, 9]. The system of the diffuser that has been installed in the Hallwil Lake, when the destratification and the aeration or the hypolimnetic oxygenation is set.

Table 1: Special characteristics of the Halwill lake and the system of the diffuser [8, 9]. The gas pressure is 1bar; temperature is 0°C.

Parameters	Value
Maximum depth (m)	46.5
Average depth (m)	28.9
Surface (106 m^2)	9.9
Total Volume of water (106 m^3)	285
Shape of the des diffusers	Circular
Number of the diffusers	6
Diameter of the diffuser (m)	6.5
Average depth of the diffusers (m)	46
Gas flow of all diffusers ($\text{Nm}^3 \cdot \text{h}^{-1}$)	46-148(O_2)

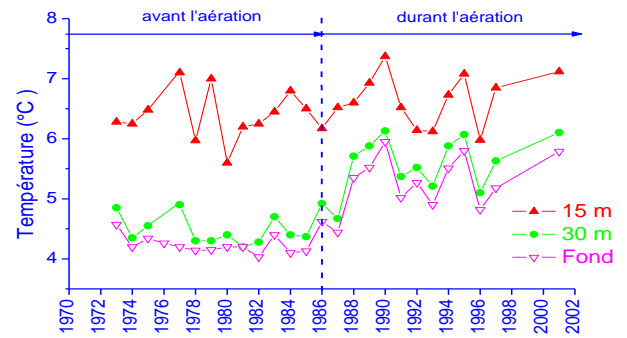


Figure 2: Chronological Evolution of the temperature between the levels 15 m, 30 m and the bottom before and during the hypolimnetic aeration [9].

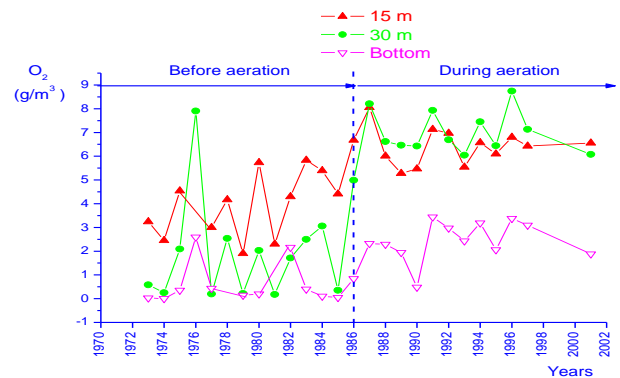


Figure 3: Chronological Evolution of the dissolved oxygen between the depths 15 m, 30 m and the bottom before and during the hypolimnetic aeration [9].

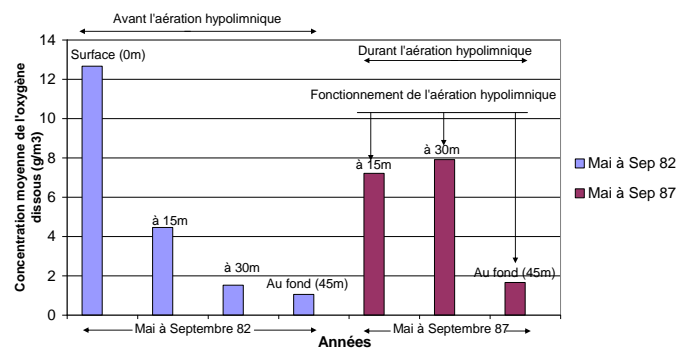


Figure 4: Evolution of the average concentration of dissolved oxygen from the surface, 15m, 30m and thoroughly before and during hypolimnetic aeration from May to September 82 and from May to September 87 [9, 10].

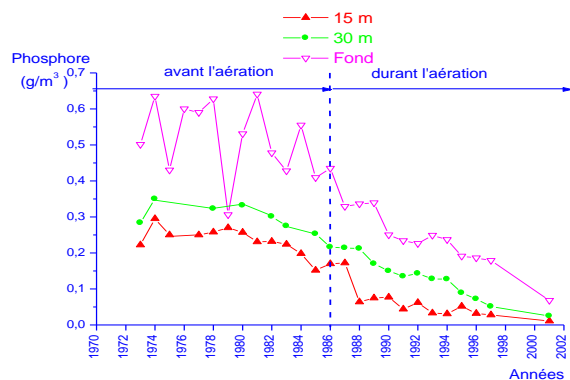


Figure 5: chronological Evolution of total phosphorus of levels 15 m, 30 m and the bottom before and during the hypolimnetic aeration [9].

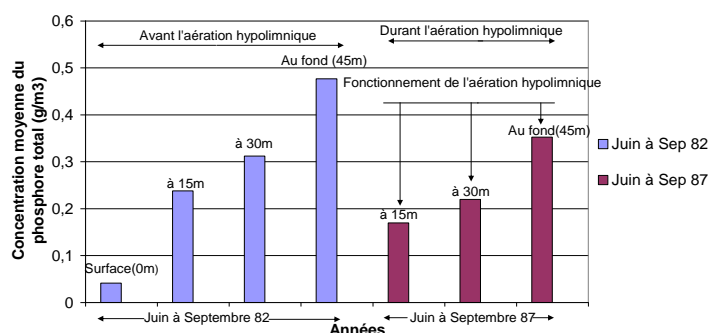


Figure 6: Evolution of the average concentration of total phosphorus from the surface (0m), 15m, 30m and thoroughly before and during hypolimnetic aeration from May to September 82 and from May to September 87 [9, 10].

5. CONCLUSIONS

The operation of the installation of hypolimnetic aeration system during the summer years of experimental records has yielded the following results:

During the restoration, the average minimum concentration of oxygen exceeds 4.5 g/m^3 in the summer season.

In the hypolimnetic aeration mode, the heating of the hypolimnion did not reach the thermocline and thus the thermal stratification is preserved.

The average values for oxygen and phosphorous concentrations are both within the range of the allowed values:

- Summer season ($30 \text{ m} \geq H \geq 15 \text{ m}$):
 $[\text{O}_2] \text{ min} \geq 4.5 \text{ g/m}^3$; $[\text{P}_2] \text{ max} \leq 0.20 \text{ g/m}^3$

This lets to conclude that the state of the lake is out of the stage of eutrophication.

In the aerated layer, the content in dissolved oxygen is maintained over a threshold that is necessary for the survival when the brewing is on. Moreover, the conservation of the thermal stratification creates a suitable habitat for the maintaining of a favorable

temperature for the cold water fishes. Accordingly, the temperature as well as the oxygen profiles confirms this fact.

The aeration hypolimnetic mode has significantly allowed the minimization of the phosphorus amount. The maximum content of this component dissolved in the lake is within the acceptance interval. This is being well validated for a long period by the evolution of phosphorus in this mode of aeration.

REFERENCES

- [1] Davis, J. M. Destratification of reservoirs- A design approach for perforated-pipe compressed-air systems. *Water Serv.*, 84, 497-505 (1980).
- [2] Bernhardt, H., and Clasen, J. Recent developments and perspectives of restoration for artificial basin used for water supply. *Intern Congr on Lake Pollution and Recovery*, 1985, 213-227 (1985).
- [3] Gafsi, M., Kettab, A., Benmamar, S., et Benziada, S. *International Journal of Food, Agriculture & Environment-JFAE.*, Vol 7. (2) 815-822. 2009.
- [4] Wilkinson, D.L. Two-dimensional bubble plumes. *Journal of Hydraulic Division ASCE*, 105(2), 139-154 (1979).
- [5] Kobus, H.E. Analysis of the Flow Induced by an Air-Bubble system. In *Proc. 11th Conf. Coastal Engng*, London, pp. 1016-1031. ASCE (1968).
- [6] Brevik, I., and Ø. Kristiansen. The flow in and around air-bubble plumes, *Int. J. Multiphase Flow*, 28(4), 617-634 (2002).
- [7] Gafsi, M., and Kettab, A. (2010). The Effect of the Hypolimnetic Aeration Technique in the Decrease of the Phosphorus Content at The Bottom of the water. The 5th International Conference Water Resources in Mediterranean Basin, Université Lille1, France, May 26-28, 2010. Abstract Volume, p 154.
- [8] McGinnis, D.F, A.Lorke, A.Wuest, A.Stockli, and J.C. Little. *Water Resources Research*, Vol.40, W10206, doi:10.1029/2004WR003038, 2004.
- [9] Gafsi, M., and Kettab, A. L'Eutrophisation dans les Eaux de Surface, Modélisation Physique. Thèse de Doctorat d'état en Hydraulique, Ecole Nationale Polytechnique (ENP) d'Alger, Algérie, Novembre 2009.
- [10] Semaoune, M, Kettab, A., and Gafsi, M. Etude Comparative de l'Aération par Destratification et de l'Aération Hypolimnetique, Application sur le Lac de Hallwil (Suisse), Thèse de Magister, ENP, Algérie, 2008.

Field Experiment and Numerical Simulation of Point Source Irrigation in Sandy Soil with Multiple Tracers

Tarek Selim^{1,2}, Yasser Hamed¹, Fethi Bouksila³, Ronny Berndtsson^{2,4}, Akissa Bahri⁵, and Magnus Persson²

¹Civil Engineering Department, Faculty of Engineering, Port Said University, Egypt

²Department of Water Resources Engineering, Lund University, Box 118, 221 00 Lund, Sweden

³INRGREF, B.P. 10, 2080 Ariana, Tunisia

⁴Center for Middle Eastern Studies, Lund University, Box 201, 221 00 Lund, Sweden

⁵African Water Facility, B.P. 323 – 1002 Tunis Belvédère, Tunisia

ABSTRACT

In this study, three plots in sandy soil in northern Tunisia were irrigated by a single irrigation dripper with a solution containing dye and bromide for three successive hours. Fifteen hours after ceasing of infiltration, horizontal 5 cm trenches were dug. Dye pattern, bromide concentration, and water content were recorded. Indication of preferential flow due to water repellency of initial dry soil was found during the early stages of infiltration. However no deep preferential flow occurred. This enables the use of drip irrigation to improve the sustainability of irrigation systems. Numerical simulation using Hydrus-2D was conducted for the field experiment. It was found that in both field experiments and numerical simulation the mobility of the bromide is different from the mobility of dye; the dye was retarded approximately twice by volume compared to bromide. The simulation results support the use of Hydrus-2D as a roughly, rapid and labor saving tool for investigation tracers' mobility in sandy soil under point source irrigation.

Keywords: *Drip irrigation, Dye, bromide, Preferential flow, Retardation factor, Hydrus-2D.*

1. INTRODUCTION

Improved irrigation efficiency can decrease irrigation amount in water scarce countries, especially the Middle East. Drip irrigation in general is a way to improve irrigation efficiency and reduce harmful effects of irrigated agriculture on the surrounding environment. It offers a high degree of control leading to adequate water and fertilizers application according to crop requirements, thereby reduce leaching. In addition, it minimizes salinity and matrix stress in the root zone, though salts accumulate in the periphery of the wetted area (Yurterren et al., 2005). Higher levels of salinity in the irrigation water can be tolerated with drip irrigation as compared to other irrigation methods (Rhoades et al., 1992). The distribution of soil water content is decreasing away from the point source. This results in a root distribution pattern in which most of the roots are typically found in the highly leached zone beneath the drippers (Shalhevet et al., 1983).

It is generally accepted that water may flow through the soil via preferential paths, bypassing large parts of the soil matrix (e.g., Gee et al., 1991). This reduces the availability of water and nutrients to plants, leaches chemicals such as pesticides from the vadose zone to the groundwater (Arias-Estevéz et al., 2008), and causes accelerated transport of pollutants (Bundt et al., 2000).

Since preferential flow is a three-dimensional process occurring at the scale of individual soil pores it is difficult to map this process in the field. Using dye and/or tracers is the most efficient way to reveal spatial

flow patterns though field soil. Many field studies using tracers have been conducted under high infiltration rates (Kung, 1990; Flury & Flühler, 1994; Lin & McInnes, 1995; Yasuda et al., 2001; Öhrström et al., 2004; Sander & Gerke, 2007; Nobles et al., 2010) and there is a lack of information for situations with lower infiltration rates.

Although, many studies (e.g., Kasteel et al., 2002; Nobles et al., 2004) indicated constrained mobility of Brilliant Blue (BB) and showed that BB has limited capacity to serve as tracer of water flow in soils due to its sorption characteristics. BB behaves like many important organic contaminants and provides information about concentration patterns at a much finer resolution as compared to other techniques (Kasteel et al., 2002). On the other hand, bromide (Br) is the most commonly used tracers to monitor water movement in soil. As a negatively charged, non-reactive anion, it does not adsorb to negatively charged soil constituents, and it can be quantified easily in soil samples. By using both BB and Br in the same solution, a complete image about water and solute transport can be captured (BB can demonstrate preferential flow along macropores and Br can demonstrate the flow through soil matrix primarily). Therefore, BB is believed to be a better alternate for movement of larger organic molecules, while Br is more appropriate for tracing water flow.

By combining dye with conservative tracers, e.g., bromide, the retardation of dye can be quantified. Zehe & Flühler (2001) combined BB and Br and found that the retardation factor ranges between 0.86 and 2.16.

Öhrström et al. (2004) found that in sandy soil (water content around 0.30 m³ m⁻³) the retardation factor ranges from 1.47 to 1.5. Kasteel et al. (2002) compared the mobility of BB in a field soil (Gleyic Luvisol) with that of bromide. They found that the BB does not follow the same flow paths as bromide, but they did not repeat their experiments in different types of soil in order to test the difference in dye adsorption from soil to soil.

Although, tracer experiments are an effective method for capturing the water and solute infiltration in unsaturated soil, it has both high time and labor demands and the experiments can only be done once at the same site. Furthermore, dye tracer experiments do not show the flow dynamics. In combination with numerical simulation, these shortcomings can be overcome. Numerical simulation is a fast and efficient approach for simulating water and solute transport. Although many researches have been carried out to simulate soil water distribution under surface point source irrigation (e.g., Skaggs et al., 2004; Ajdary, 2008), numerical simulations for the mobility of different tracers under drip irrigation does not appear to have caught researcher's attention so far. In view of the above, the aim of this study was to 1) investigate infiltration patterns with different tracers (bromide to mimic fertilizer and dye mimic an organic contaminant) under low infiltration rate in sandy soil, 2) study the potential preferential flow in dry sandy soil under point source irrigation, and 3) study the potential of using numerical model as a rapid tool for predicting the mobility of different tracers under drip irrigation.

2. MATERIALS AND METHODS

2.1 Area description

The experiments were carried out at the end of the dry season in August, 2003, in northern Tunisia. The experimental site was situated at Nabeul, which is located approximately 70 km southeast of Tunis. The soil is classified as loamy sand. The experimental plot was located at the first third of a 40 x 40m experimental field area. The water table is located at about 4 m depth. The field was tilled to a depth of 0.30- 0.40 m. Drip irrigation is commonly used to irrigate vegetables and other crops in the area. At this particular site, drip irrigation was used one year before the experiments to irrigate potatoes. Three plots (N1, N2, and N3) were chosen with an inter-plot distance of 2.5 m. The dimensions of each plot were 2m x 2m and the initial water content (before experiment) was 0.074-0.10m³m⁻³.

The climate at the field site is Mediterranean, characterized by mild winters receiving the major part of the annual precipitation (450 mm on average), and hot and dry summers. Total rainfall and distribution are highly variable from year to year. Average annual potential evapotranspiration is 1370 mm.

2.2 Field Experiments

Local irrigation water with an electrical conductivity (σ_{iw}) of 3.95 dS/m was used for the experiments. The irrigation water was mixed with BB dye (6 g/l) and potassium bromide (4 g/l), resulting in a total electrical conductivity (σ_p) of about 10.5 dS/m. The solute was applied through a single dripper with a constant average flux of 2.5 l/h. This flux is typically used in the area when irrigating vegetables, e.g., tomatoes or cucumbers. Approximately 7.5 l was discharged from a small tank through the single dripper and a constant pressure was maintained using a small battery-driven pump.

The dye tracer used was the food-grade dye pigment Vitasyn-Blau AE 85 (Swedish Hoechst Ltd.). This dye has been used in several studies due to its good visibility, low toxicity, and weak adsorption on soils (Flury et al., 1994; Aeby et al., 1997; Persson, 2005). The dye is readily soluble in water (solubility >50 kg m⁻³) and the water solution gives a clearly visible blue staining to the soil and its electric conductivity is very low. After infiltration, the plots were covered with plastic sheet to avoid evaporation and to protect from rain. Fifteen hours after the infiltration, horizontal soil surface sections were dug with 5 cm intervals at each plot. A scale within a 50 by 50 cm wooden frame with its origin coinciding with the position of the dripper was put on the soil surface before taking photos. The position of the frame was determined using two fixed points adjacent to each plot. Horizontal soil sections were photographed with a digital camera from 1.5 m height. The Sigma Probe (EC1 Sigma Probe, Delta-T Devices Ltd., Cambridge, UK) was used to measure soil solution electrical conductivity (σ_w) at 5 cm intervals in a spatial grid within the 50 by 50 cm scale. The Sigma Probe measures σ_w independent from both soil moisture content (θ) and the degree of contact between the probe and soil (Hilhorst, 2000; Hamed et al., 2003; 2006). The σ_w measurements were converted to relative electrical conductivity according to

$$\sigma_{rel} = \frac{\sigma_w - \sigma_{in}}{\sigma_p - \sigma_{in}} \quad (1)$$

where σ_{in} is the initial soil electrical conductivity and σ_p is the electrical conductivity of the applied pulse. Soil samples from different soil layers from surface till the depth of 60 cm in the three selected plots were collected to determine soil physical properties. Particle size distribution was determined by mean of sieve analysis and the hydrometer method. Initial and final soil moisture content values were calculated from the collected soil samples beneath the dripper till the depth of 60 cm before and after the infiltration experiment.

2.3 Image analysis

The digitized images were analyzed using Adobe Photoshop (Adobe Systems Inc.). The images were converted into the CMYK (Cyan, Magenta, Yellow, and Black) color space. The cyan channel was chosen for recognizing stained from unstained soil and the remaining channels were discarded. After that, the images were transferred into gray-scale. A histogram for each image was made to get a gray level threshold that discriminated the colored soil from non-colored soil. By using the image processing toolbox in Matlab (The Mathworks Inc.) the images were converted into black and white images with resolution of 0.3 x 0.3 cm and the dye covered area was calculated. For more details, see Öhrström et al. (2004). The dye covered area was calculated in order to estimate the bromide-dye volumetric retardation factor. In general, soil sections were excavated until no dye traces were seen. This meant in most cases down to a depth of 50 cm and an average of eleven images at each plot.

2.4 Numerical simulation

The mobility of different tracers, dye and bromide, under drip irrigation was simulated with two-dimensional numerical modeling using Hydrus-2D software package. The Hydrus software package simulates two and three-dimensional movement of water, heat and multiple solutes in variably saturated media based on finite-element numerical solutions of the flow equations (Simunek et al., 1999; see Gardenas et al., 2005 for a detailed description of the application of Hydrus-2D). Assuming a homogeneous and isotropic soil, the program uses the Galerkin finite-element method to solve the 2D Richards equation (Richard, 1931) for saturated-unsaturated water flow and solute transport with the convection-dispersion equation (e.g. Hillel, 1998).

The simulated domain was an axi-symmetrical domain, 100 cm width and 75 cm depth (one-half of the flow domain). Unstructured triangular mesh with 5617 2D elements was used to spatially discretize the flow domain. Triangular elements of smaller sizes were generated closer to the soil surface where rapid change in flux occurs. The simulation assumed no flux boundary conditions along the vertical sides of the soil domain. Bottom boundary was considered as free drainage boundary because the water table is situated far below the domain of interest (4 m below the soil surface). Because of covering the plots with plastic sheet during the field experiment, top boundary was assumed no flux throughout the simulation period except during the period of water application. It was constant flux of 7.95 cm h⁻¹ at the location of dripper. The flux radius was taken equal to 10 cm as neither ponding nor surface runoff was assumed to occur. Figure 1 shows the conceptualized simulated area and

the imposed boundary conditions. Longitudinal dispersivity (ϵ_L) was approximated to one-tenth of the profile depth for each soil layer (see e.g., Beven et al., 1993; Cote et al., 2001). The transversal dispersivity (ϵ_T) was set equal to 0.1 ϵ_L , dye adsorption isotherm coefficient was set equal to 0.10 dm³ kg⁻¹ (Öhrström et al., 2004), and molecular diffusion was neglected. The initial θ distribution within the flow domain was chosen related to the field measurements. The simulations were conducted for an 18 h period.

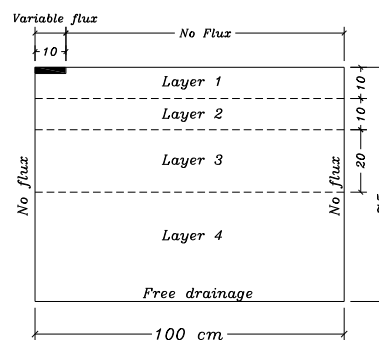


Figure 1: The conceptual diagram of simulated area.

2.5 Soil hydraulic parameters optimization by inverse modeling

Appropriate estimation of soil hydraulic parameters provides good simulation for the field data. Based on the measured water content within the soil profile before and after the infiltration experiment, inverse parameter estimation option (using Marquardt-Levenberg parameter optimization algorithm) in Hydrus-2D was used to identify soil hydraulic parameters. Initially, the soil hydraulic parameters (residual water content, Θ_r ; saturated water content, Θ_s ; saturated hydraulic conductivity, K_s ; shape parameters, α and n ; pore connectivity parameter, l) for different soil layers were assumed using ROSETTA pedotransfer function of Schaap et al. (2001), using textural percentages and bulk density, to execute the inverse solution. After that, predicted water content values were compared with measured values and the final soil hydraulic parameters values were selected from the run at which the predicted and the measured values were in close agreement.

3. RESULTS AND DISCUSSION

3.1 Dye and bromide analysis

Figure 2 shows the soil water content directly beneath the dripper before and after infiltration for the three plots. Fifteen h after ceasing the water application, θ was higher at the top 10 cm of the soil profile. This indicates that the redistribution process still continued. Due to the low initial θ value, the soil color was relatively light and the dyed areas were distinguished easily.

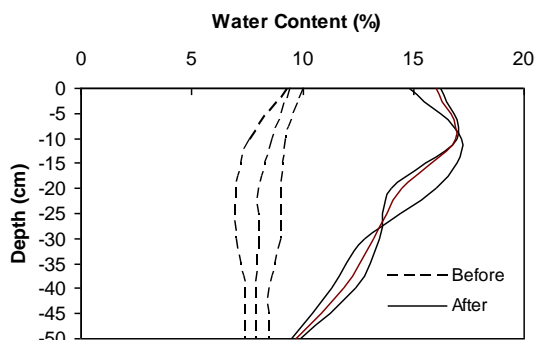


Figure 2: Soil water content before and after infiltration.

The dye patterns with depth at each of the three plots had approximately the same shape. The maximum dye penetration was 45 cm in plots N1 and N2. In plot N3 the maximum dye penetration was 50 cm. The greater dye penetration depth at plot N3 was probably caused by a higher percentage of coarse sand at deeper layer (70% at 40-60 cm, see table 1). Figure 3 shows the dye patterns with depth for plot N2. It was noted that, there is a probability of water repellency at the 20 cm depth as an area in the top right side was unstained. Water repellency may be cause for heterogeneous infiltration. In the other plots no visible indications of water repellency were observed. The dye pattern were in general homogenous and no evidence of deep preferential flow was observed, which is an advantage for using drip irrigation in this field.

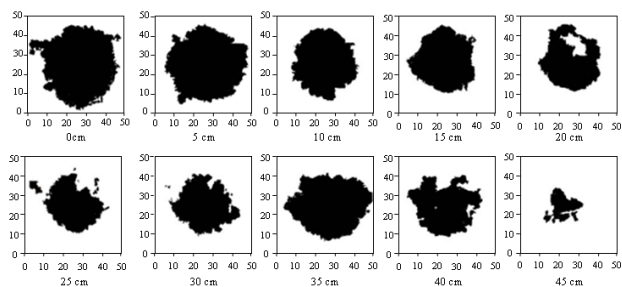


Figure 3: Dye patterns with depth in sandy soil (plot N2), no dye was observed at the 50 cm depth. H^{all} sections are 50 cm length and 50 cm width with dripper in the center.

Figure 4 shows the isolines of the relative bromide concentration in different horizontal sections (10 cm interval) for plot N2. The bromide was detected in an area lager than the 50 by 50 cm frame. Unfortunately, no measurements were taken outside the frame. However, a visual inspection revealed that the wetted area only extended slightly outside the frame at most depths, thus Fig. 4 gives an almost complete picture of the bromide distribution. The isolines of bromide represent detected bromide concentrations by the sigma probe. The isolines in the measured profiles were drawn using a kriging interpolation algorithm. Outside the outer isoline, the bromide concentration was too low or the soil was too dry to allow measurements by the sigma probe. The actual initial σ_w could not be measured because the sigma probe cannot measure it in a dry soil

($\theta < 0.10 \text{ m}^3\text{m}^{-3}$). When drawing the isolines, the relative bromide concentration was manually set equal to zero when the sigma probe gave the "too dry" error message.

According to the relative bromide concentration isolines at the 20 cm depth in plot N2, it was noted that the $\sigma_{rel} = 0$ coincides with the unstained patch in the dye pattern at the same depth which support the occurrence of water repellency at this location. In almost all horizontal sections for all plots, the maximum value of relative bromide concentration was detected beneath the dripper. Some higher relative bromide concentrations were detected far from the dripper that may be attributed to preferential flow in top tillage soil layer. This preferential flow could possibly be explained by water repellency at the early stages of infiltration. As infiltration continued the soil was wetted and no longer water repellent. From the relative bromide concentration isolines in all plots, it was observed that the concentration of bromide is less than the concentration of the applied pulse, which probably indicated that physical non-equilibrium flow occurred during the solute infiltration. It should be noted that the soil was initially dry, which means that no sigma probe readings could be taken. If there are available conductivity readings in unstained soil it means that the soil was wetted (water and bromide reached to these regions but not the dye). This is evidence that the bromide flow in different pathways as compared to the dye. Comparing the patterns of both relative bromide concentration and dye distribution, it was observed that the relative bromide concentration distribution had larger heterogeneity than dye. This can be explained by the water repellency at early stages of infiltration. Even after the soil was wetted and the water repellency disappeared, higher concentrations of bromide were found in the preferential flow paths in top tillage soil layer. Since the dye only was recorded as stained or unstained soil, the areas with higher dye concentration could not be identified.

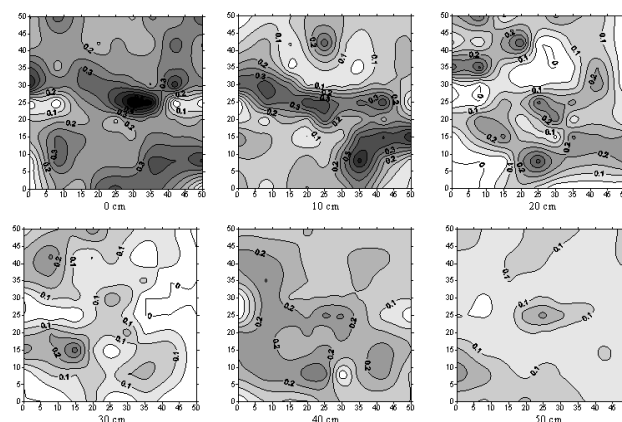


Figure 4: The isolines of relative bromide concentration in different horizontal sections (plot N2). H^{all} sections are 50 cm length and 50 cm width with dripper in the center.

Figure 5 shows the dye-bromide covered area with depth. From the dye coverage area curve, it can be noted that there are two peaks, one upper at the soil surface layer and a second at about 30-40 cm depth. The first upper peak is probably due to the hydrophobic properties of the dry top soil. This caused water and solutes to spread horizontally until gravitational forces of infiltrated solute overcame the hydrophobic strength. The second deeper peak demarks the tillage depth. The transition between the upper tilled and lower untilled soil layers caused horizontal flow. Comparing the impact of textural soil stratification on water flow, Hillel (1971) concluded that it is the soil layer with the lower hydraulic conductivity, which controls the process.

The area covered by bromide at different horizontal sections was estimated from the Sigma Probe readings corresponding to relative bromide concentration higher than 0.10. Öhrström et al. (2004) stated that the visible lower limit of dye in a loamy sand soil corresponded to a relative bromide concentration of 0.10 (using similar dye pulse concentration). Consequently, it is clearly seen how the dye was retarded in relation to bromide in both vertical and horizontal directions.

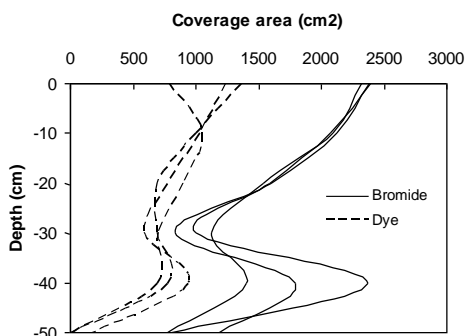


Figure 5: The coverage area for both dye and bromide with depth.

3.2 Retardation factors

The above results were used to estimate dye-bromide volumetric retardation factor. In general, BB has similar adsorptive behavior as some contaminant while bromide ion moves much like $\text{NO}_3\text{-N}$ (fertilizer) in soil. Consequently, we can have a rough but general idea about how fertilizers and other contaminant may be transported in the present initially low water content soil type. To quantify the retardation, the volumetric retardation factor (R_{vol}) regarding bromide as compared to dye was calculated by dividing the volume of soil with measurable bromide concentration by the volume of soil stained with dye

$$R_{\text{vol}} = \frac{\text{Volume of soil stained by bromide}}{\text{Volume of soil stained by dye}} \quad (2)$$

The volume of soil stained by both bromide and dye was calculated by integrating the area under bromide-

dye coverage area curve (Fig. 5). The retardation factor R is related to the adsorption k_d by

$$R = 1 + \frac{\rho_b}{\theta} k_d \quad (3)$$

There are different methods for calculating the adsorption coefficient (e.g. Flury & Flühler, 1995; Ketelsen & Meyer-Windel, 1999; Morris et al., 2008). In our study, R_{vol} was found to be 1.98, 2.04, and 1.95 at plot N1, N2, and N3 respectively. These results concur with results of previous studies for soils with similar texture. A retardation factor of 2.00 corresponds to k_d of $0.10 \text{ dm}^3 \text{ kg}^{-1}$ (for $\rho = 1.68 \text{ gm/cm}^3$, $\Theta = 0.17 \text{ m}^3 \text{ m}^{-3}$).

3.3 Numerical simulation analysis

3.3.1 Soil parameters optimization

Table 1 shows the soil hydraulic parameters for different soil layers used to simulate the tracers' mobility. These values were conducted from running the inverse parameter estimation option in Hydrus-2D depending on the water content measurements directly below the dripper by the end of infiltration experiment.

Table 1: Hydraulic parameters of simulated soil layers for plot N2.

Soil layer	Depth (cm)	Θ_r	Θ_s	α	n	k_s (cm/h)
1	0-10	0.01	0.325	0.049	1.365	32.76
2	10-20	0.026	0.491	0.054	1.516	18.83
3	20-40	0.013	0.508	0.052	1.64	35.30
4	40-75	0.028	0.375	0.059	1.66	21.31

Figure 6 shows the measured and simulated water content profile under the dripper for plot N2 after adjusting soil hydraulic parameters. It is obvious from the figure that the predicted pattern of water content distribution was in a good agreement with the measured data. The overestimated values of water content in the model is caused by the occurrence of a faster redistribution process in the field than the model due to tillage of the topsoil layer in the field, while the soil in the model was assumed homogenous. A value of $0.016 \text{ m}^3 \text{ m}^{-3}$ for the root mean square error (RMSE) and a value of 0.91 for correlation coefficient (R^2) were observed between the simulated and measured volumetric water content. These values support the goodness of fit between the field experiment and numerical simulation. Therefore, the obtainable soil hydraulic parameters can be staunchly used to execute Hydrus-2D for predicting the mobility of different tracers under drip irrigation.

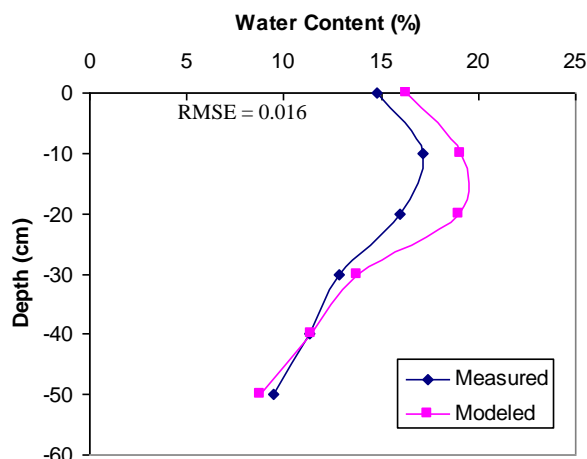


Figure 6: Comparison between the measured and simulated water content profile under the dripper (plot N2).

3.3.2 Tracers' mobility

Figure 7a shows the contour map for dye concentration larger than 0.2 g l^{-1} . Dye at concentration lower than 0.2 g l^{-1} could not be analyzed by the image processing tool (e.g., Ewing & Horton, 1999; Öhrström et al., 2004). Figure 7b shows contour maps for σ_{rel} larger than 0.10. From these maps, it is clear that the mobility of dye differs substantially from that of bromide. This difference is mainly due to the different adsorption characteristics of dye. The bromide-dye volumetric retardation factor was calculated using Eq. (2). The volume of soil stained by bromide was calculated based on the hypothesis that the bromide stains a soil volume equal to a half sphere with radius equal to the bromide infiltration depth beneath the dripper. The same calculations were carried out for the dye. The volumetric retardation factor was found to be 1.93, 1.85, and 1.80 for plots N1, N2, and N3 respectively. Comparing the results of the field experiments and the simulation, the calculated volumetric retardation factor was close to the one calculated based on the field measurements. It is worth noting that the difference between measured and simulated depth for both bromide and dye was due to the difference in nature of the soil layers between field experiments (heterogeneous due to land treatment) and the simulation (homogeneous). In addition, the assumed dispersivity values in the numerical model may be a source of error between the measured and simulated data. Although the bromide has the ability to describe the water movement in vadose zone, the simulated bromide penetration depth is less than the maximum simulated wetted depth. This is probably due to the diffusion and dispersion characteristics of bromide that leads to very low concentrations at the wetting front.

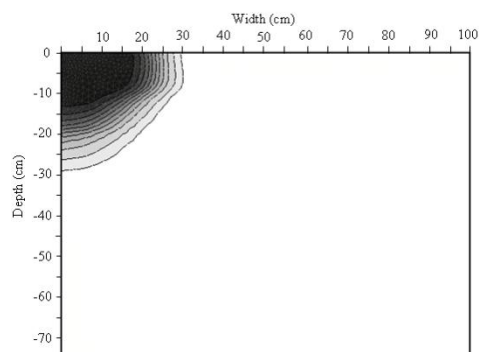


Figure 7a: Contour map for dye concentration (plot N2).

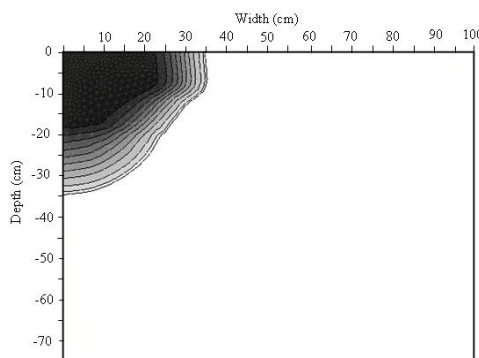


Figure 7b: Contour map for bromide concentration (plot N2).

4. SUMMARY AND CONCLUSIONS

Field experiment for a sandy soil was investigated in terms of solute transport patterns from a single dripper. At each plot about 7.5 l dye and bromide tagged irrigation water was infiltrated at a constant approximate rate of 2.5 l/h. This is a typical daily application rate in the area using drip irrigation. Preferential flow did not clearly appear even below the tillage depth. The coarse soil particle size and the almost absence of soil aggregation could explain that results. Consequently, the lack of preferential flow is an advantage for better water irrigation efficiency and soil leaching. Because of the coarse sandy soil, drip irrigation can be recommended to improve plant culture for a better water and soil nutrient absorption.

The obtainable electric conductivity readings by the sigma probe after infiltration in the soil unstained by dye mean that the soil was wetted (the sigma probe cannot measure it in a dry soil ($\theta < 0.10 \text{ m}^3 \text{ m}^{-3}$)). This is evidence that the bromide flow in different pathways compared to dye. The observed retardation for dye and bromide can be used as initial guess for retardation of fertilizers and organic pollutants, respectively. Numerical simulation with good estimation of soil hydraulic properties for the field experiment showed consistent results for the retardation factor.

In sum, the simulation results for tracers' mobility were in a good agreement with field data. Therefore, Hydrus-2D can be used as a roughly and rapid tool for

calculating the mobility of different tracers in sandy soil under point source irrigation. Nevertheless, it facilitates to identify the impact of contaminant transport on the surrounding environment. It is worth mentioning that a great care must be considered when using Hydrus-2D for simulation under high infiltration rate or infiltration in fine texture soils to avoid water ponding on the soil surface that has a quantified effect on the water flow and solute transport behavior.

5. ACKNOWLEDGMENTS

This work was financially supported by the Swedish Science Research Council. Equipment was funded by the Lundberg Foundation and the Royal Physiographic Society.

REFERENCES

- [1] Aeby, P., Forrer, J., Steinmeier, C. & Flühler, H. (1997) Image analysis for determination of dye tracer concentrations in sand columns. *Soil Sci. Soc. Am. J.* 61, 33-35.
- [2] Ajdary, K. (2008) Application of Hydrus-2D for simulation of water distribution in different types of soils. International meeting on soil fertility land management and agroclimatology. Turkey, 2008. 253-261.
- [3] Arias-Estrevez, M., Lopez-Periago, E., Martinez-Carballo, E., Simal-Gandara, J., Mejuto, J.C. & Garcia-Rio, L. (2008) The mobility and degradation of pesticides in soils and the pollution of groundwater resources. *Agric. Ecosyst. Environ.* 123, 247-260.
- [4] Beven, K., Henderson, D. & Reeves, A. (1993) Dispersion parameters for undisturbed partially saturated soil. *J. Hydrol.* 143, 19-43.
- [5] Bundt, M., Albrechta, A., Rroidevaux, P., Blaser, P. & Fluhler, H. (2000) Impact of preferential flow on radionuclide distribution in soil. *Environ. Sci. Technol.* 34, 3895-3899.
- [6] Cote, C., Bristow, K.L., Ford, E.J., Verburg, K. & Keating, B. (2001) Measurement of water and solute movement in large undisturbed soil cores: analysis of Macknade and Bundaderg data. CSIRO Land and Water, Technical Report 07/2001.
- [7] Ewing, R.P. & Horton, R. (1999) Discriminating dyes in soil with color image analysis. *Soil Sci. Soc. Am. J.* 63, 18-24.
- [8] Flury, M. & Flühler, H. (1994) Brilliant Blue FCF as a dye tracer for solute transport studies – A toxicological overview. *J. Environ. Qual.* 23, 1108-1112.
- [9] Flury, M. & Flühler, H. (1995) Tracer characteristics of Brilliant Blue FCF. *Soil Sci. Soc. Am. J.* 59, 22-27.
- [10] Gardenas, A., Hopmans, J.W., Hanson, B.R. & Simunek, J. (2005) Two-dimensional modeling of nitrate leaching for different fertilization scenarios under micro-irrigation. *Agric. Water Manage.* 74, 219-242.
- [11] Gee, G.W., Kincaid, T., Lenhard, R.J. & Simmons, C.S. (1991) Recent studies of flow and transport in the vadose zone, U.S. Natl. Rep. Int. Union Geod. Geod. Geophys., 1987-1990, Rev. Geophys. Vol. 29, 227-239.
- [12] Hamed, Y., Persson, M. & Berndtsson, R. (2003) Soil salinity measurements using different dielectric techniques. *Soil Sci. Soc. Am. J.* 67, 1071-1078.
- [13] Hamed, Y., Samy, G. & Persson, M. (2006) Evaluation of the WET-sensor compared to TDR. *Hydrol. Sci. J.* 51, 671-681.
- [14] Hilhorst, M.A. (2000) A pore water conductivity sensor. *Soil Sci. Soc. Am. J.* 64, 1922-1925.
- [15] Hillel, D. (1971) *Soil and Water: Physical Principles and Processes*. Academic Press, New York.
- [16] Hillel, D. (1998) *Environmental Soil Physics*. Academic press, Inc. 525 B Street, Suit 1900, San Diego, CA 92101-4495.
- [17] Kasteel, R., Vogel, H.J. & Roth, K. (2002) Effect of non-linear adsorption on the transport behaviour of Brilliant Blue in a field soil. *Eur. J. Soil Sci.* 53, 231-240.
- [18] Kasteel, R. & Meyer-Windel, S. (1999) Adsorption of Brilliant Blue FCF by soils. *Geoderma* 90, 131-145.
- [19] Kung, K.J.S. (1990) Preferential flow in a sandy vadose zone: 1. Field observation. *Geoderma* 46, 51-58.
- [20] Lin, H.S. & Mcinnes, K.J. (1995) Water flow in clay soil beneath a disc tension infiltrometer. *Soil Sci.* 159, 375-382.
- [21] Morris, C., Mooney, S.J. & Young, S.D. (2008) Sorption and desorption characteristics of the dye tracer, Brilliant Blue FCF, in sandy and clay soils. *Geoderma* 146, 434-438.

- [22] Nobles, M.M., Wilding, L.P. & Lin, H.S. (2010) Flow pathways of bromide and Brilliant Blue FCF tracers in caliche soils. *J. Hydrol.* 393, 114-122.
- [23] Nobles, M.M., Wilding, L.P. & McInnes, K.J. (2004) Submicroscopic measurements of tracer distribution related to surface features of soil aggregates. *Geoderma* 123, 83-97.
- [24] Öhrström, P., Hamed, Y., Persson, M. & Berndtsson, R. (2004) Characterizing unsaturated solute transport by simultaneous use of dye and bromide. *J. Hydrol.* 289, 23-35.
- [25] Persson, M. (2005) Accurate dye tracer concentration estimations using image analysis. *Soil Sci. Soc. Am. J.* 69, 967-975.
- [26] Rhoades, J.D., Kandiah, A. & Mashali, A.M. (1992) The use of saline waters for crop production. *FAO Irrigation and Drainage*, paper 48. Food and Agriculture Organization of the United Nations, Rome.
- [27] Richards, L.A. (1931) Capillary conduction of liquid in porous media. *Physics* 1, 318-333.
- [28] Sandar, T. & Gerke, H.H. (2007) Preferential flow patterns in paddy fields using a dye tracer. *Vadose Zone J.* 6, 105-115.
- [29] Schaap, M., Leij, F. & van Genuchten, M. (2001) ROSETTA: A computer program for estimating soil hydraulic properties with hierarchical pedotransfer functions. *J. Hydrol.* 251: 163-176.
- [30] Shalhevet, J., Hoffman, G.J., Meiri, A., Heuer, B. & Francois, L.E. (1983) Salinity tolerance of crops in irrigated agriculture dynamic conditions, Final Report to BARD.
- [31] Simunek, J., Sejna, M. & van Genuchten, M. Th. (1999) The Hydrus-2D software package for simulating the two-dimensional movement of water, heat, and multiple solutes in variably-saturated media. *IGWMC-TPS 53*, Version 2.0, International Ground Water Modeling Center, Colorado School of Mines, Golden, Colo.
- [32] Skaggs, T.H., Trout, T.J., Simunek, J. & Shouse, P.J. (2004) Comparison of Hydrus-2D simulations of drip irrigation with experimental observations. *J. Irrig. Drain. Engin.* 130 (4): 304-310.
- [33] Yasuda, H., Berndtsson, R., Persson, H., Bahri, A. & Takuma, K. (2001) Characterizing preferential transport during flood irrigation of a heavy clay soil using the dye Vitasyn Blau. *Geoderma* 100, 49-66.
- [34] Yurtseven, E., Kesmez, G.D. & Unlukara, A. (2005) The effects of water salinity and potassium levels on yield, fruit quality and water consumption of a native central Anatolian tomato species (*Lycopersicon esculantum*). *Agric. Water Manage.* 78, 128-135.
- [35] Zehe, E. & Flüher, H. (2001) Preferential transport of isoproturon at a plot scale and a field scale tile-drained site. *J. Hydrol.* 247, 100-111

Threats to Groundwater Resources due to Uncontrolled Land filling in Jordan: A Review with Some Remedial Measures Recommendations

Mohammad Aljaradin¹, Kenneth M. Persson¹

¹Lund University, Water Resources Engineering, P.O.Box: 118, 221 00 LUND, SWEDEN

ABSTRACT

Jordan is considered to be one of the ten most water-stressed countries in the world, with less than 150 cubic meters freshwater available per capita annually. Groundwater plays a central role in Jordan where it represents 55-60% of the available water resources, equaling 850 MCM/a (2006). With growing economical development, the solid waste production increases. Landfilling is the most common method to handle solid waste. The total estimated daily generation of municipal solid waste is about 3800 tons. The waste is disposed off at 21 landfill distributed all over the country. Most of these landfills are practicing open dumping. A number of landfills are expanding without proper control which represents one of the major threats to the important and vulnerable groundwater resource. With the current regulation and attention focused in many environmental aspects in the country, the risk of groundwater contamination is not fully acknowledged. The aim of this study is to review the present status of the landfills and the quality of the nearby groundwater. In addition long and short term remedial measures are also suggested to reduce and prevent further contamination.

Keywords: *Uncontrolled land filling, Groundwater contamination, Jordan.*

1. INTRODUCTION

Jordan has a total area of 90,000 km² and a population of 5.8 million (2005). The country lies in the dry and semi dry climatic zones which are characterized by their minimal rainfall and high percentage of evaporation. The climate is a mix of Mediterranean and dry desert, temperature varies from a few degrees below zero in the winter to around 46 degrees centigrade in the summer season. Annual precipitation ranges from 50 mm in the desert to 600 mm in the northwest highlands. Only nine percent of Jordan's area receives more than 200 mm of the rainfall annually (Al-Kharabsheh and Ta'any 2005). Approximately 92.2% of the rainfall evaporates, 5.4% recharges the groundwater and the rest, 2.4%, goes to the surface water. The generation of solid waste has become an growing environmental and public health problem everywhere in the world, so also in Middle East Countries (MEC). As in much of the developing countries, the fast expansion of urban, agricultural, and industrial activities in Jordan spurred by rapid population growth and the change in consumer habits has produced vast amounts of solid wastes. Landfills have been identified as one of the major threats to groundwater resources. Areas near landfills have a greater possibility of groundwater contamination because of the potential pollution source of leachate originating from the nearby site. Such contamination of groundwater resource poses a substantial risk to local resource user and to the natural environment (Mor, Ravindra et al. 2006).

2. LANDFILL SITUATION IN JORDAN

Landfills have been the most common and cheapest methods of waste disposal in many countries around the

world. Especially in developing countries, it is considered to be cost effective and reliable method if the land is available. However the inadequate management and operation of these landfills could pose serious environmental impact. Landfills have been identified as one of the major threats to groundwater resources. The placed waste in landfills is subjected to infiltration from precipitation or from co-disposal of liquid and sludge with MSW.

In Jordan, Sanitary landfilling of municipal solid waste has evolved over the past 15 years as the recommended method for the dispose of solid wastes. Previously since 1950, waste disposal was basically open dumping and burning without complying with the proper regulations, while in the beginning of 1980 the awareness increased for establishing sanitary landfills. Nowadays landfilling practiced in Jordan is simply dumping the waste in trenches with leveling and compacting by trash compactors to reduce the size and the thickness of the layers, and finally cover the waste with soil (Manoj Chopra 2001). Figure 1 illustrates landfilling practices in the country.

Landfills in Jordan are operated by common service council (CSCs) (which usually serve more than municipality in the same governate) with dual supervision of the Environment and Municipalities Ministries.

There are at present 21 landfills in Jordan listed in table 1, the location of these landfills was not chosen according to the international standards, it was chosen according to population density as to serve the largest possible number of municipalities. The exception is the Al-ghabawi landfill which receives more than 50% of

the volume of the generated solid waste in Jordan, The location of this landfill was selected after conducting an environmental impact assessment for best site selection (Al-Tarazi, Abu Rajab et al. 2008). It was also designed and engineered according to international standards

while constructed. The rest of the landfills that receives 40% -50% of the volume of waste in the country are not designed according to international standards for landfills in terms of health or environmental requirements.

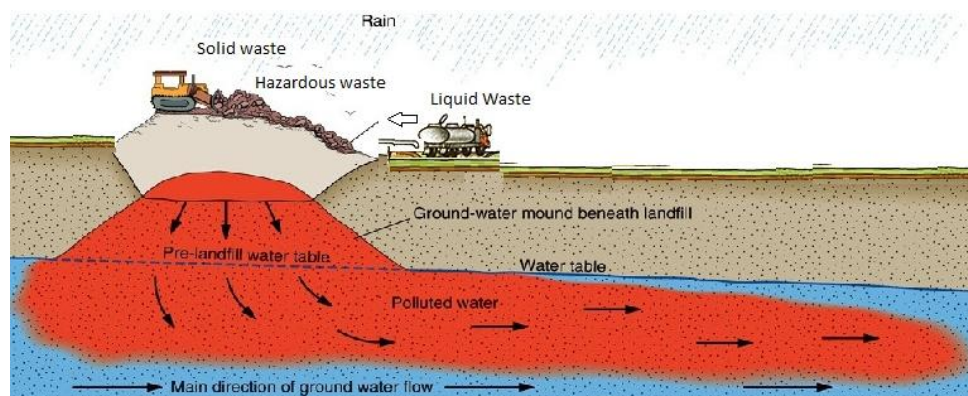


Figure 1: Land filling practice at Jordan

The methods of dumping practiced and the lack of lining could lead to contamination of groundwater, soil and air. For example, Al-Ekader landfill which is located near the Syrian borders and in the vicinity of Yarmouk river basin gives rise to some political tension with Syria, since effluents from the Al-Ekader landfill pose a threat to the Yarmouk basin. On the other hand,

Mafraq landfill was located on a geological fault and represents a threat to the groundwater aquifer. While, Al-Hamra is located in a bedrock area where no soil is available for daily covers, leachate produced is flowing out from the dump site threatening the public health and polluting the soil (Abu Qdais 2007).

Table 1: Domestic Landfills in Jordan - Source: (Environment 2009)

No	Site Name	Operating Date	Governate	Area in Dunm	Received Waste Tons / day
1	Al-Ekader	1980	Irbid	806	800
2	Husaineat	1986	Mafraq	180	170
3	North Badia	2003	Mafraq	360	43
4	Al-Ruasihed	2003	Mafraq	179	4
5	Al-Hamra	1990	Al-Salt	275	450
6	Al-ghabawi	2003	Amman	1947	2500
7	Madaba	1974	Madaba	87	500
8	Dhulil	1991	Zarqa	270	295
9	Dair alla	1998	Balqa	363	290
10	Azraq	1983	Zarqa	250	17
11	Noth shuneh	1983	Irbid	200	67
12	South shuneh	1988	Al-Balqa		55
13	Ghor Al-Mazra'a	1997	Karak	205	22
14	Lajoon	1995	Karak	485	190
15	Ghor Al-Safi	1997	Karak	153	25
16	Tafilah	1990	Tafilah	450	65
17	Al-shoubak	1983	Ma'an	26	45
18	Eyil Neimat	1984	Ma'an	274	42
19	Ma'an	1994	Ma'an	502	90
20	Al-Quaira	2000	Aqaba	270	25
21	Aqaba	2000	Aqaba	60	115

3. GROUNDWATER SITUATION IN JORDAN

Jordan is facing a future of very limited water resources, It has among the lowest renewable water resources in the world on a per capita basis (Abdel-Nabi Fardous 2004), A global comparison identifies Jordan as one of the ten countries with the lowest volumes of available renewable water resources per capita (Schmidt 2010) and they are projected to decline from more than 160 m³ per capita per year for all uses at present to only 91 m³ per capita per year by 2025, putting Jordan in the category of having an absolute water shortage (Al-Halasa and Ammary 2006; Al-Halasa and Ammary 2007; Jamal Radaideh^a 2009; Jamal Radaideh 2009). Groundwater plays a central role in Jordan where it represents 55-60% of the available water resources, equaling 850 million m³ annually (MCM/a) (2006). Groundwater in Jordan is of two types, renewable and non-renewable fossil water distributed among 12 basins as shown in figure 2. The safe yield of renewable groundwater basins is around 275 MCM. In the year 2000, the abstraction of groundwater resources was 473 MCM to meet the required demand in which 411 MCM was from renewable groundwater (150% of the safe yield) and 62 MCM from fossil water (Al-Halasa, 2003). The most important non-renewable groundwater resources is the Disi aquifers in southeastern Jordan. The utilizable fossil ground water is estimated at 90 MCM per year for a period of 100 years (Mohsen and Al-Jayyousi, 1999).



Figure 2: Groundwater basins in Jordan. Arrows represent the direction of flow

Ground water contamination is generally irreversible once it is contaminated; it is difficult to restore the original quality. In Jordan, ground water quality has been deteriorating by point and non point source including domestic agricultural and industrial uses and become an increasing problem in recent year.

4. GROUND WATER CONTAMINATION DUE TO UNCONTROLLED LANDFILLING

Leaching of pollutants from landfills may result in groundwater contamination, especially when it comes to uncontrolled landfills with the absence of lining and/or monitoring systems of the waste received. Areas near landfills have a greater possibility of groundwater contamination because of the potential pollution source of leachate originating from the nearby site (Mor, Ravindra et al. 2006). The generation and the chemical characteristics of leachate in arid climate countries depends upon the MSW characteristics, moisture content, capillary action, water content of subsurface soil and ambient temperature (Al-Yaqout and Hamoda 2003). Landfill leachate contains a variety of contaminants including heavy metals such as cadmium, nickel, zinc, copper, and lead. Usually these metals are found at moderate concentration levels in municipal landfill leachate. Typical values are in the range: Cd 5–10 µg l⁻¹, Ni 100–200 µg l⁻¹, Zn 500–2000 µg l⁻¹, Cu 50–100 µg l⁻¹, and Pb 50–100 µg l⁻¹ (Christensen 2004). Such contamination of groundwater resource poses a substantial risk to local resource user and to the natural environment. During the last 20 years, many evidences for ground water contamination has been occurred especially in northern part of Jordan (Ali El-Naqa 2006). In addition, it was proven that major cause of groundwater contamination for the most important aquifer in Jordan that is known as Amman- wadi sir (B₂/A₇) is the presence of Russeifa solid waste disposal site. Abu-Rukah (2001; 2005) stated that the Al-Ekader landfill leachate constitutes a serious threat to the local aquifers in the Yarmouk Basin (Table 2).

Jawad (1998) reported a gradual increase of element concentrations in the groundwater wells around the Al-Akader landfill starting from 1985. Nitrate concentrations rose dramatically, doubling more than ten times in ten years; this indicates that the previously unsaturated zone had become saturated with polluted water. Also (Mutewakil M. Obeidat, Fayez Y. Ahmad et al. 2008; Awawdeh 2009) insure that the Yarmouk basin is contaminated with high nitrate concentration; exceeding the maximum acceptable concentration for drinking water standard. This was identified previously by (Abu Rukah and Alsokhny 2004). In their study in northern Jordan, they found high concentration of HCO₃⁻ and NO₃⁻ of 307 and 51 mg/l, respectively, in groundwater. Another study by (Obeidat, Massadeh et al. 2007) showed high nitrate concentrations in groundwater at Amman-Zarqa basin; it ranged from 10 to 330 mg/l, and increased dramatically from the year 2001 to 2006. About 92% of the samples have NO₃⁻ concentration more than 20 mg/l.

Table 2: Characteristics of the leachate samples collected from Al-Ekader landfill site- Source: (Abu-Rukah 2001)

Parameters	L1	L2	L3	L4	L5	L6
pH	7.79	7.63	7.96	7.93	7.91	7.84
Temp. ^(c)	20	20	20	20	20	20
Turbidity (NTU)	40	40	150	160	130	110
EC	3.6	3.75	4.86	4.72	4.89	4.84
Alkalinity mg/l	670	665	2300	2400	2000	2700
Cations (mg/l)						
Fe	0.16	0.15	18.16	15.25	11.34	13.55
Mn	1.1	0.11	0.78	0.52	0.41	0.44
Ca	219	332	443	181	233	340
Na	556	538	485	778	735	256
K	65.2	61.6	1266	1273	1282	1371
Anions (mg/l)						
Cl	10.3	11.2	1996	2650	2170	2338
So ₄	73.0	82.5	1105	1088	1164	11065
Heavy Metals (mg/l)						
Cd	0.012	0.013	0.16	0.52	0.42	0.37
Zn	95	90	261	169	174	159
Cu	0.12	0.25	0.52	0.044	0.048	19.45
Pb	0.19	0.89	1.70	1.50	0.65	1.5

5. CONCLUSION

From the previous studies, it is clearly evident that the leachate generated from the landfill site is affecting the groundwater quality in the northern part of Jordan through percolation in the subsoil. Therefore, some remedial measures are required to prevent further contamination.

Since most of the current landfills have a poor landfilling practice, it is important for the authorities to improve the current state of landfilling practice to minimize the negative environmental and socio-economic impacts in long and short term. The improvement of the landfills has to be done gradually according to the country's condition and its financial and technical abilities.

Long term remedial measures required to improve landfills:

Engineered landfill sites are generally provided with impermeable liner and drainage system at the base of the landfill, which will not allow leachate to percolate into subsoil. All the leachate accumulated at the base of the landfill can be collected for recycling or treatment

(Fatta, Papadopoulos et al. 1999). In Jordan, landfills neither have any bottom liner nor any leachate collection and treatment system (Al-ghabawi landfill is an exception). Therefore, all the leachate generated finds its paths into the surrounding environment. In such conditions the only options that could be followed are:

1. Conducting feasibility studies for choosing the landfill site, because the improper location of some landfill sites, presently located above important groundwater basins sensitive to contamination, or an areas with rocky nature; this could be accomplished starting by a reduction of the number of landfill sites from 21 to the half at least.
2. Limiting the infiltration of the water through the landfill cover by providing impermeable clay cover and surface water diversion. Due to this, less water will enter and subsequently less leachate will be generated, thereby reducing the amount of leachate reaching the landfill base.
3. Extraction of the leachate collected at the base can be done and it can be recycled, so that less amount will enter the aquifer below. Also increasing the evapo-transpiration rate by providing vegetation cover over the landfill can also reduce leachate production.
4. Adopting Al-ghabawi experience, since it's considered to be the first sanitary landfill in the Middle East, to all landfills with construction of waste water treatment plant to handle the leachate generated and the septic waste water especially to the areas which are not covered with sewer system.

Short term remedial measures required to improve landfills:

The improvement of the landfills has to be done gradually according to the country's condition and its financial and technical abilities. The following improvement can be done to minimize the negative environmental and socio-economic impacts in short term:

1. Insure daily cover.
2. Improvement of access road.
3. Construction the basic infrastructure, fencing and weighbridge.
4. Stop open burning inside landfills.
5. Establishing surface drainage system.
6. Raise the awareness's and competences of the employees.
7. Construction of leachate collection and gas venting facilities.
8. Ensure no disposal of hazardous and medical waste.

Recommendation for further work:

Further studies needed to assess the groundwater water contamination through: 1. Experimental determination to estimate the extent of the leachate adverse impacts on the groundwater of the area, where the landfill is situated, and the pollution level of the aquifer. 2. Mathematical modeling to simulate leaching from solid waste landfills and the solute transport into the aquifers; these will be also the aim of our next articles.

REFERENCES

- [1] A. Jawad Ali, S. A. A. S., Y. Abu Rukah, and Kh. A-Qudah (1998). "Aquifer Ground Water Quality and Flow in the Yarmouk River Basin of Northern Jordan." *Journal of Environmental Systems* 26(3).
- [2] Abdel-Nabi Fardous, M. M., Mohammed Jitan, Ra'ed Badwan (2004). *Harnessing salty water to enhance sustainable livelihoods of the rural poor in four countries in west asia and north africa. Jordan National Report. Amman, Jordan, National Center for Agricultur Research and Technology, Ministry of Agriculture*
- [3] Abu-Rukah (2005). *Study of colloidal content and associated heavy metals in landfill leachate: a case study of El-Akader landfill site: Jordan. Geneva, SUISSE, Inderscience Enterprises.*
- [4] Abu-Rukah, Y. A.-K., O. (2001). "The assessment of the effect of landfill leachate on ground-water quality-a case study. El-Akader landfill site-north Jordan." *Journal of Arid Environments* 49(3): 615-630.
- [5] Abu Qdais, H. A. (2007). "Techno-economic assessment of municipal solid waste management in Jordan." *Waste Management* 27(11): 1666-1672.
- [6] Abu Rukah, Y. and K. Alsokhny (2004). "Geochemical assessment of groundwater contamination with special emphasis on fluoride concentration, North Jordan." *Chemie der Erde - Geochemistry* 64(2): 171-181.
- [7] Al-Halasa, N. and B. Ammary (2006). *WATER RESOURCES POLICY AND MANAGEMENT IN JORDAN. Integrated Urban Water Resources Management: 59-68.*
- [8] Al-Halasa, N. and B. Ammary (2007). *Pollution Potential of the Shallow Aquifers in Jordan. Wastewater Reuse-Risk Assessment, Decision-Making and Environmental Security: 169-174.*
- [9] Al-Kharabsheh, A. and R. Ta'any (2005). "Challenges of Water Demand Management in Jordan." *Water International* 30(2): 210 - 219.
- [10] Al-Tarazi, E., J. Abu Rajab, et al. (2008). "Detecting leachate plumes and groundwater pollution at Ruseifa municipal landfill utilizing VLF-EM method." *Journal of Applied Geophysics* 65(3-4): 121-131.
- [11] Al-Yaqout, A. F. and M. F. Hamoda (2003). "Evaluation of landfill leachate in arid climate--a case study." *Environment International* 29(5): 593-600.
- [12] Aldecy de Almeida, S., S. Shozo, et al. (2008). "Evaluation on Surface Water Quality of the Influence Area of the Sanitary Landfill " *Engenharia Ambiental : Pesquisa e Tecnologia* 5(2): 139-151.
- [13] Ali El-Naqa, N. H., Mustafa Kuisi (2006). "GIS-based evaluation of groundwater vulnerability in the Russeifa area, Jordan." *Revista Mexicana de Ciencias Geológicas* 23(3): 10.
- [14] Awawdeh, M., Jaradat, Rasheed (2009). "Evaluation of aquifers vulnerability to contamination in the Yarmouk River basin, Jordan, based on DRASTIC method." *Arabian Journal of Geosciences* 3(3): 273-282.
- [15] Christensen, D. L. B. a. T. H. (2004). "Speciation of Heavy Metals in Landfill Leachate: A Review." *Waste Management & Research* 22(3).
- [16] Environment, M. o. (2009). *Jordan's Second National Communication to the United Nations Framework Convention on Climate Change (UNFCCC). Amman. 2009/11/4731.*
- [17] Fatta, D., A. Papadopoulos, et al. (1999). "A study on the landfill leachate and its impact on the groundwater quality of the greater area." *Environmental Geochemistry and Health* 21(2): 175-190.
- [18] Jamal Radaideh a, K. A.-Z. b., *, Adnan Al-Harabsheh c, Rida Al-Adamat d (2009). "Quality Assessment of Harvested Rainwater for Domestic Uses " *Jordan Journal of Earth and Environmental Sciences* 2(1): 26 -31.
- [19] Jamal Radaideh, K. A.-Z., Adnan Al-Harabsheh, Rida Al-Adamat (2009). "Quality Assessment of Harvested Rainwater for Domestic Uses " *Jordan Journal of Earth and Environmental Sciences* 2(1): 26 -31.

- [20] Manoj Chopra, D. R., Wail Abu El-Shaar (2001). US-Jordan Municipal Solid Waste Management Collaborative Research. Arlington, The National Science Foundation, University of Central Florida. VA 22230.
- [21] Mor, S., K. Ravindra, et al. (2006). "Leachate Characterization and Assessment of Groundwater Pollution Near Municipal Solid Waste Landfill Site." *Environmental Monitoring and Assessment* 118(1): 435-456.
- [22] Mutewekil M. Obeidat, N. A. H. Fayez Y. Ahmad, et al. (2008). "Assessment of nitrate contamination of karst springs, Bani Kanana, northern Jordan." *Revista Mexicana de Ciencias Geológicas* 25(3): 426-437.
- [23] Obeidat, M., A. Massadeh, et al. (2007). "Analysis and evaluation of nitrate levels in groundwater at Al-Hashimiya area, Jordan." *Environmental Monitoring and Assessment* 135(1): 475-486.
- [24] Schmidt, G. (2010). "Jordan: The Nationwide Groundwater Simulation Model." Retrieved 29-04, 2010, from http://www.bgr.bund.de/nn_324630/EN/Themen/Wasser/Projekte/TZ/TZ__Jordanien/gw__modellierung__fb__en.html.

Water Scarcity and Solar Desalination Systems in the Eastern Mediterranean Region: A Case of Northern Cyprus

O. Phillips Agboola¹, F. Egelioglu²

¹Mechanical Engineering Department, Eastern Mediterranean University, Famagusta, TRNC, via Mersin 10, Turkey, (phillips.agboola@cc.emu.edu.tr)

²Mechanical Engineering Department, Eastern Mediterranean University, Famagusta, TRNC, via Mersin 10, Turkey, (Fuat.egelioglu@emu.edu.tr)

ABSTRACT

The constant decline of renewable water in the Middle East and North Africa (MENA) and the Mediterranean regions qualify these two regions the most water scarce in the world. Water scarcity can be defined as a situation where there is not enough water to meet all local demand. These demands may include water needed for ecosystems, agricultural and domestic use. Water is definitely physically scarce in the MENA and the Mediterranean regions with less than 1000 m³/capita/year and the scarcity is related to domestic water, fresh water for drinking and water for food production. Water scarcity in these regions is a function of both water supply and water demand as both applies in most of the countries. Using the Falkenmark indicator the Mediterranean regions will see increased deterioration in the availability of renewable water and more people will suffer the effects of water shortage. The area will face major constraints in meeting water requirements for agriculture in the coming decades. The severe impacts of the non-availability of renewable water in these regions are cushioned by the development of desalination technology that is at an advanced stage in most of the countries in the region. Water desalination technology provides unlimited and constant supply of high quality water, and reduces the pressure on freshwater ecosystems and groundwater resources. Selection of the appropriate desalination technology, use of renewable energy and a proper method of dealing with high salinity wastewater discharge are very important measures necessary to mitigate the negative impacts of desalination activity, reduce desalination costs and make desalination sustainable and reliable. This work reviews the nature of water scarcity in the Eastern Mediterranean region and advances in solar desalination using the Northern part of Cyprus as a case study

1. INTRODUCTION

The over-exploitation of non-renewable groundwater (aquifers) in the Middle East and North Africa region (MENA) and in Mediterranean countries has reached crisis levels. The acute water scarcity is arguably the most fundamental problem these regions are grappling with and attempting to solve in order to improve the region's potential for economic growth and reduce high levels of poverty in the region. The weak management of the available water resources, which has worsened an already grave situation of rapidly depleting aquifers, worsens the acute water scarcity and other renewable water resources (see Table 1). The crisis is most acute in MENA region close to the Mediterranean Sea where saline intrusion of coastal aquifers reduces domestic supplies and pollutes hinterland domestic and agricultural water. According to USAID, the world's "water crisis" is not so much an issue of scarcity as it is of poor management and inequitable distribution. This is true especially in the MENA/Mediterranean region where most of the countries are surrounded with seawater but these water sources are not consumable due to its high level of dissolved salt and minerals. For instance, in the Mediterranean Sea salinity is around 40,000 part per million (ppm) while acceptable drinking water salinity in Europe is 500 ppm. In overcoming this acute water scarcity, sea and brackish water desalination

by solar desalination technologies seem like a very attractive option. This technology delivers solutions on a long and short-term scale for reducing if not eradicating the water scarcity in the region. Indeed, with cheap energy resources like the sun, desalination technologies will provide a lasting solution in the region. This paper intends to review comprehensively the water scarcity in the Eastern part of the Mediterranean region with the advances in solar desalination technology employed by most of the MENA/Mediterranean member states to tackle and alleviate the freshwater scarcity crisis. The case study will be the northern part of Cyprus, a territory under isolation from the entire world except Turkey. This work also provides solar desalination innovations as seen in many of the countries in the Mediterranean and MENA region suffering from water crisis. In addition, the work accessed the framework of cooperation among the Mediterranean countries of the MENA and Mediterranean region in solving the water scarcity, using the example of Turkey and Northern Cyprus.

2. COUNTRIES IN MENA/MEDITERRANEAN REGION

The MENA region (Middle East and North Africa) is made up of different territories extending from Morocco in northwest Africa to Iran in southwest Asia. Its

member states include Algeria, Bahrain, Djibouti, Egypt, Iran, Iraq, Israel, Jordan, Kuwait, Lebanon, Libya, Morocco, Oman, Palestinian territories, Qatar, Mauritania, Saudi Arabia, Ethiopia, Sudan, Syria, Tunisia, United Arab Emirate and Yemen. Some of these countries are also located close to the Mediterranean Sea qualifying them as Mediterranean countries also. The MENA region citizens live under conditions of water stress and the condition is worsened with increase in population expected to grow from around 300 million today to around 500 million in 2025 and per capita availability of water is expected to be halved by 2050[1]. The source of water varies from country to country in the MENA region. For instance, Egypt and Iraq depend solely on surface water from large international rivers. Others, like Yemen, Djibouti and the Arab States of the Gulf Cooperation Council countries depend almost entirely on groundwater and desalination, while others use a mixture of surface and groundwater. The Mediterranean Sea divides two opposite demographic development (Africa and Europe/Asia) and it comprises of 25 countries divided into the North, East and South Mediterranean. The Northern part of the Mediterranean sea consist of countries like Portugal, Spain, France, Italy, Malta, Bosnia, Croatia, Slovenia, Yugoslavia, Albania, Greece and the Eastern part consist of countries like Turkey, Cyprus(South and North), Syria, Lebanon, Israel, Palestinian territories of Gaza and the West Bank, Jordan while the Southern part consist of Egypt, Libya, Tunisia, Algeria, Morocco. The Mediterranean water resources are limited and threatened especially in the Eastern and Southern parts of the region where water resources are characterized by drought and low levels of yearly rainfalls. This shortage of surface water had led to over withdrawal from the aquifers within the member countries. Table 1 shows the average precipitation and water resources in Southern Mediterranean. Turkey is one country in the Eastern part of the Mediterranean that has far more than 1000 m³/capita water resources, the remaining countries have water resources around 1000 m³/capita or below 500 m³/capita, an indicator of severe water scarcity [2,3].

3. CONTRIBUTIONS OF DESALINATION AND SOLAR DESALINATION IN MENA AND EASTERN EUROPE

The oil rich countries of the MENA region have constantly satisfied their water needs through desalination of seawater, a process that requires significant quantities of energy to achieve separation of salts from seawater. Using thermodynamics, it is possible to calculate the minimum energy to separate pure water from seawater. The agreed figure ranges from 0.7-0.9 kWh/m³. The energy consumption and environmental pollution caused by the use of fossil fuels to power these plants are of great concern. Majority of these plants across the Middle East region also produce electricity. Water is very important for survival and

worth every effort to make it available to the people. For instance, Saudi Arabia has 27 desalination plants in the Kingdom, supplying over 70% of the country's drinking water as well as more than 2.8 GW of electricity. The most recent of the desalination plants produced about 800,000 m³ as well as 2,750 megawatts of electricity at an investment cost of US\$ 3.8 billion. The UAE is another oil rich country in the MENA region with daily production of about 8,885,366 m³/d of contracted desalination capacity. The country spent about \$682.3 million in 2010 as cost of operating existing plants and adding the new plants. Algeria in the Northern part of Africa has a desalination plants with a daily production of 200,000 cubic meters of potable water with an investment cost of US\$ 250 million. The El-Hamma Seawater Desalination Plant in Algeria provides sufficient water for the country's capital and supplies excess water to some neighbourhoods around the capital. Other desalination plants include Jordan's 2,400 cubic metres per day plant that eases the water problem in Deir Alla in the Jordan Valley. Turkey has desalination plants that produce more than 500,000 m³ of fresh water daily to support its surface and underground water. All of the mentioned desalination plants use fossil fuel and given current understanding of the greenhouse effect and the importance of CO₂ levels, burning of fossil fuels (oil) on this large scale negatively affects the environment. Thus, apart from satisfying the additional energy demand (this may not be a problem to the oil rich countries), environmental pollution is a major concern. Therefore, alternative sources of energy like the Sun will be required to power these desalination plants. Fortunately, Countries of these regions (MENA & Eastern Europe) have exploitable renewable sources of energy that can drive desalination processes. Production of fresh water using desalination technologies driven by renewable energy systems is thought to be a viable solution to the water scarcity at remote areas characterized by lack of potable water and conventional energy sources like heat and electricity grid. The advance in solar desalination is still ongoing and renewable energy powered desalination systems cannot compete with conventional systems in terms of the cost of water produced, but will be better off if the environment is seen as a major factor for consideration. The Abu Dhabi solar desalination plant in the United Arab Emirates is an example of a working solar desalination plant in the region with capacity of 85 m³/day of fresh water using seawater with a salinity of 55,000 ppm. It was commissioned in 1984, it is still working until now, and the country plans to spend around \$600 million on a new solar desalination plant. Figure 1 shows the extensive use of desalination technology in the MENA/Mediterranean region.

4. WATER RESOURCES AND SCARCITY IN NORTH CYPRUS (N. CYPRUS)

N. Cyprus is at the hub of three continents (Africa, Asia and Europe) where the trade routes intersect, located at

35°N 33°E of the Greenwich meridian. The country is surrounded by the Mediterranean Sea, and it is characterized with the Mediterranean climate of hot and dry summer and mild winter. The de-facto population of N. Cyprus is 285,365 according to recent report by the Statistics and Research Department of the State Planning Organization 2009 [5]. The land distribution of N. Cyprus constitutes 56.7% for agricultural purposes (about 1870 km²), 19.5% for forestry (about 643 km³), 5.0% of grassing area (163km²), 10.7% is covered by towns, villages, rivers and reservoirs (386 km²) and nearly 8.2% is bare land (269 km²). It also has 87 km² of irrigable land [6]. There are no ever flowing or perennial streams in N. Cyprus. There are 38 streams in N. Cyprus, of which 10 originated from the southern part of the island, around the Trodos Mountains and are relatively rich in water when they flow but the construction of dams by the southern administration prevented the flow of the streams to the Northern part. Eight of these streams namely Yesilirmak, Kamburdere, Madendere, Lefke deres, Gamlidere, Taslidere, Dogance and Guzelyurt deres carry around 43 million m³ of water per year. Kanlidere and Ganlidere are quite large streams that start from the south and flow to the North but bring no water because the water flows into dams built in the Southern part of Cyprus. The remaining 30 Streams get their water from Besparmak Mountains and carry about 27 million m³ of water on the average per year [7]. A total of 70 million m³ of water flows in stream in N. Cyprus. Approximately 38 million m³ of this water feed the aquifers in the western part of the country. The remaining water is used in irrigation and some of it flows uncontrolled. There are about 40 dams and ponds built in N. Cyprus. The storage capacity of these dams and ponds vary between 2000 m³ to 4.5 million m³ and have a total storage capacity of 21 million m³ per year. The most important water resources in N. Cyprus are the groundwater sources. All the drinking water and most of the irrigation water came from the ground water reservoirs (aquifers).

The aquifers are characterized into 13 groups within 8 hydrological regions, which have variable capacities of water storage. The Guzelyurt aquifer is the most important and the largest of the aquifers in N. Cyprus. It is located in the Guzelyurt region with an area of 280 km² of which only 180 km² is in the northern part while the remaining 100km² extends to the Southern half of the island. It is estimated that the water holding capacity of the aquifers is about 920 million m³. Annual water inflow is about 37 million m³ and annual water outflow is about 57 million m³. About 92% of this water from Guzelyurt aquifer is used in irrigation and 8% is used for domestic purposes. Because of the excess water withdrawal from this aquifer, the water level has fallen

sharply and salt content of the water about 1km from the shore is around 2000 ppm NaCl.

Akdeniz aquifer is near the Akdeniz village, it has an area of 20 km². Its average thickness is about 30 m with annual water feed of about 2 million m³ of which the same amount of water is drawn annually from it. Lefke - Gemikonagu aquifer annual feeding is about 14 million m³, annual withdrawal is about 6 million m³, and the remaining water is directed to the Guzelyurt aquifer.

The Girne Coastal aquifer surface area is about 40 km² consisting of two small aquifers of 7 km² each. Annual replenishment of the aquifer on the average is about 10.5 million m³ which is also the amount withdrawn on a yearly basis. Gazimagusa Aquifer is no longer in active use due to the aquifer contamination by the seawater. It occupies 45 km³ of which 16 km³ is only the Northern part of the island; the remaining extends to the southern part of the island. The water withdrawal is much more than the water inflow to the aquifers and the quality of the water is growing worse (see Table 2). Theoretical water demand in N. Cyprus is about 123 million m³/year of which 93 million m³/ year is used for agriculture and 30 million m³ for domestic use. Actual water consumption in N. Cyprus is about 84 million m³ and 78 million m³ for agriculture while 16 million m³/ is used for domestic purposes yearly [8]. Table 3 shows the sector wise annual water withdrawals for Agricultural and domestic uses. Table 4 presents the water resources based on annual water extractions. The effect of the water shortage is more pronounced in the Agricultural sector. The sector used to contribute more than 30% of the GDP to the country's economy some decades ago. Citrus fruit occupies the greatest part of the production in agriculture with a yield of 12-16 tons/ha. However, the present water shortage (for irrigation purpose) and the salt-water intrusion into farmlands have rendered large portions of farmland non-productive for years. Owing to limited water resources and degradation of water quality, the yearly production of Citrus has decreased from 129,972 tons in 1999 to 90,083 tons presently according to North Cyprus's State Planning Organization Statistics and Research Department record. On the domestic water use, water rationing is a common thing with the water corporation supplying water to homes once or twice a week depending on the location. The supplied water quality (1000-2000 ppm) is very poor making it unsafe for drinking. Every home has to either provide its drinking water through rooftop Reverse Osmosis (energy intensive) or buy water from water vendors at a cost of \$0.14/liter. The cost of electricity (\$0.7/kW/h) in Northern part of Cyprus has made Reverse Osmosis (RO) un-attractive.

Table 1: Water resources, use in the Southern, and Eastern Mediterranean countries [4]

Country	Average precipitation 1961-1990 (km ³ /year)	Total renewable water resources (km ³ /year)	Total water use in 2000 (km ³ /year)	Per capita water resources (m ³ /capita, year)	Water use per capita in 2000 (m ³ /capita, year)	Percentage of water use as total water resources (%)	Ratio of irrigated area to total crop area (%)
Algeria	211.50	14.32	6.07	452	201	44.40	15.77
Cyprus	4.60	0.78	0.24	1009	311	30.86	33.37
Egypt	51.40	58.30	68.65	831	1011	121.72	100.00
Israel	9.20	1.67	1.62	265	287	108.30	57.87
Jordan	9.90	0.88	0.98	169	207	122.32	37.62
Lebanon	6.90	4.41	1.37	1122	392	34.98	40.21
Libya	98.50	0.60	4.81	108	870	805.56	64.59
Morocco	154.70	29.00	12.76	991	399	40.26	18.14
Syria	46.70	26.26	12.00	1514	844	55.74	26.98
Tunisia	33.90	5.00	2.73	517	312	60.38	13.37
Turkey	459.50	229.30	37.52	3280	563	17.16	21.08

Table 2: The aquifers capacities in N. Cyprus [DSI 2003]

Aquifers	Recharge (10 ⁶ m ³)	Safe Yield (10 ⁶ m ³)	Withdrawals (10 ⁶ m ³)
Guzelyurt	37	37	57
Akdeniz	15	1.5	1.5
Lefke -G. Konagi-Y. dalga	15.5	6	6
Yesilirmak	7	1.5	1.5
Girne Mountains	11.5	11.5	11.5
Gazimagusa	2	2	8.5
Beyarmudu	0.5	0.5	0.5
Cayonu-Guvercinlik-Turkmenkoy	2	2	2
Lefkosa-Serdarli	0.5	0.5	0.5
Yesilkoy	1.6	1.6	3
Girne Coast	5	5	5
Yedikonuk-Buyukkonuk	0.3	0.3	0.3
Dipkarpaz	1.5	1.5	1.5
Korucam	1.2	1.2	1.2
Others	2	2	2
Total	89.1	74.1	103

Table 3: Sector wise annual water withdrawals (m³)

	Agricultural use		Subtotal	Live stock	Hotels	Domestic use			Subtotal	Total
	Irrigation	Losses				Universities	Residents	Losses		
LMR										
C. Lefkosa 6,436,675	82,022	70,215	152,237	75,387	18,834	226,555	4,513,408	1,450,255	6,284,438	
Degirmenlik 2,467,483	575,349	513,982	1,089,331	165,500		0		0	1,732,564	569,419
Ercan 1,509,672	550,961	522,686	1,073,647	192,050	0	0	143,354	100,621	436,025	
Guzelyurt 69,012,219	37,812,296	21,863,489	59,675,785	248,173	2,774	0	6,930,926	2,154,562	9,336,434	
Lefke 6,646,557	3,170,069	2,490,606	5,660,675	30,746	5,256	40,184	682,185	227,511	985,882	
Sub-Total 87,161,937	42,190,697	25,460,978	67,651,675	711,856	26,864	266,738	14,002,437	4,502,368	19,510,262	
MMR										
Magosa A 7,799,141	1,824,077	1,673,518	3,497,595	118,877	125,414	359,211	2,705,380	992,664	4,301,546	
Magosa B 1,117,969	348,666	344,259	692,924	70,089	0	0	256,869	98,087	425,045	
Akdogan 3,527,190	1,335,133	1,103,063	2,438,196	177,768	0	0	659,920	251,30	1,088,994	
Y.Erenkoy 3,640,954	1,228,282	1,078,670	2,306,952	187,094	4,672	0	834,390	307,84	1,334,002	
Mehmetcik 2,069,512	686,154	673,919	1,360,073	92,392	0	0	453,330	163,717	709,439	
Y. Iskele 2,258,833	485,257	463,085	948,342	123,857	39,420	0	844,793	302,421	1,310,491	
Gonendere 1,153,454	212,983	212,984	425,967	72,330	0	0	487,275	167,882	727,487	
Gecitkale 1,082,355	373,223	360,357	33,579	136,433	0	0	131,856	80,487	348,776	
Sub-Total 22,649,409	6,493,774	5,909,854	12,403,628	978,841	169,506	359,211	6,373,813	2,364,411	10,245,781	
GMR										
Germe East 4,422,253	669,566	642,904	1,312,470	62,118	315,506	47,897	1,966,620	717,642	3,109,783	
Germe West 7,214,776	2,826,507	2,729,797	5,556,304	10,001	248,127	0	1,017,620	382,724	1,658,472	
Bogaz 2,266,669	374,485	369,072	743,557	139,131	0	0	1,032,494	351,487	1,523,112	
Camilibel 2,269,075	926,917	834,605	1,761,521	131,732	0	0	258,694	117,128	507,554	
Sub-Total 16,172,772	4,797,475	4,576,377	9,373,852	342,981	563,633	47,897	4,275,428	1,568,982	6,798,920	
North Cyprus 125,984,118	53,481,946	35,947,209	89,429,155	2,033,678	760,003	673,846	24,651,678	8,435,761	3	6,554,963

Note: Lefkosa Main Region (LMR), Magosa Main Region (MMR) & Germe Main Region (GMR) are major regions in North Cyprus

Table 4: Water resources based on annual water extractions (m³)

	Available resources		Dams	Transport	Desalinization	Ground water
	Springs	Sanitary				
LMR						
C. Lefkosa	0	3,445,840	152,237	0	0	0
Degirmenlik	19,751	0	318,009	0	0	3,219,054
Ercan	0	0	0	0	0	1,509,672
Guzelyurt	0	0	0	1,661,901	0	73,634,756
Lefke	0	0	1,490,806	0	0	5,155,751
Total	19,751	3,445,840	1,961,052	1,661,901	0	83,519,233
MMR						
Magosa A	0	36,870	0	0	0	7,762,272
Magosa B	0	0	0	0	0	1,117,969
Akdogan	0	0	0	0	0	3,527,190
Y.Erenkoy	0	0	0	0	0	3,640,954
Mehmetcik	4,179	0	0	0	0	2,065,333
Y. Iskele	40,898	5,422	97,737	0	0	2,114,776
Gonendere	12,665	0	425,967	0	0	714,822
Gecitkale	25,266	0	0	0	0	1,057,089
Total	83,008	42,292	523,704	0	0	22,000,405
GMR						
Germe East	11,654	41,026	474,620	0	109,500	3,785,453
Germe West	111,527	7,321	0	0	0	7,095,928
Bogaz	1,962	0	43,174	0	0	2,221,533
Camilibel	137,390	0	80,253	0	0	2,051,432
Total	262,533	48,347	598,047	0	109,500	15,154,346
North Cyprus	365,292	3,536,479	3,082,803	1,661,901	109,500	120,673,984

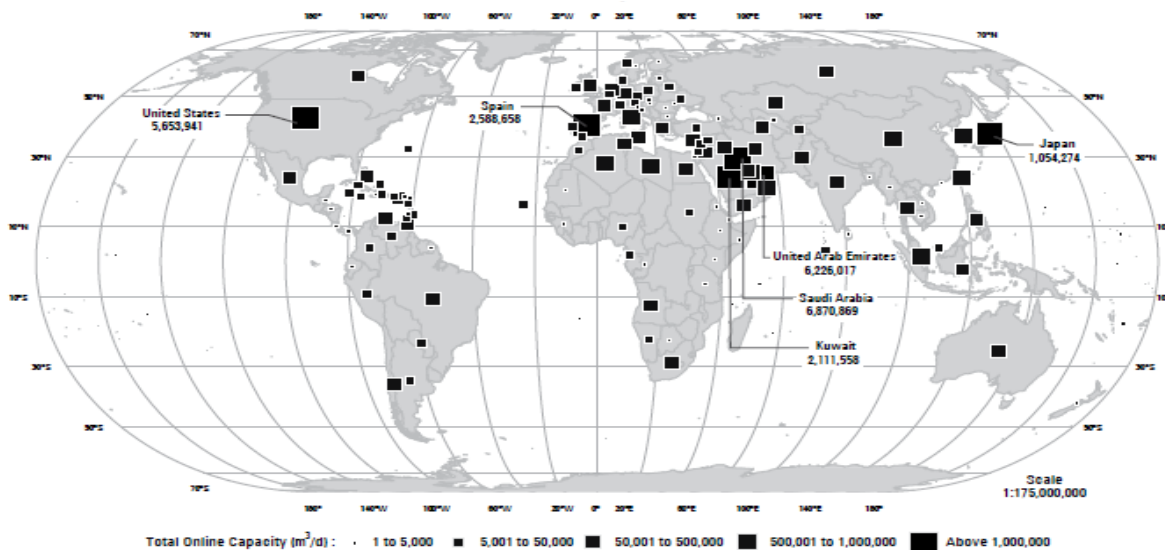


Figure 1: Total Desalination capacity by Countries

5. EFFORTS TO SOLVE N.CYPRUS WATER PROBLEM

The water shortage for both domestic and agriculture use in North Cyprus is quite evident. Various measures were planned and implemented to increase the supply of water. Projects have been proposed as to import water from Turkey by a tanker, or using large water bags and/or by pipeline. The first load of water was transported by water bags on 25th July 1998 [9]. Water bags of 10,000 m³ capacity with potential of bringing 3 million m³ of water in one year from Soguksu River of Anamur in Turkey were introduced. An increase in the capacity of the water bags to 30,000 m³ would enable 7 million m³ of water to be imported annually. This amount is the maximum that the system can permit to be pumped from Kumkoy to Serhatkoy and then on to Dikmen where the main reservoirs are situated and from where water is sent to Nicosia and Gazimagusa. The total investment cost (excluding the in-use values) was estimated at \$16,725,000 in 1997. This project was later abandoned due to water loss when the bags burst due to some sharp materials in the Mediterranean Sea as they were being transported. Another important project was for water conservation by converting traditional irrigation systems to modern irrigation methods in areas like Guzelyurt, the new irrigation equipment would have conserved water used for irrigation by 30%. However, this project was not fully implemented since most of the farmers stayed away due to the financial implication involved. The 30% of water to be saved would have relieved the over extraction of the Guzelyurt aquifer and prevented seawater intrusion, thus increasing the productivity and quality of agricultural output. One other project to ease the water shortage in

North Cyprus is by importing water by pipeline either from Anamur or from Manavgat in Turkey. Through this project 75 million m³ of water could be brought to Kumkoy of North Cyprus. The Council of Ministers of Turkey has taken the decision to implement the project with the Turkish firm ALARKO. The project is estimated to cost about \$450 million dollars and will require huge electricity (160 Mega watts) for the water pumps. The project might be feasible if some quantity of water could be sold to either South Cyprus or other Middle East countries [6]. This project is now postponed due to some conflicting views between the government and the local villagers that would be affected by this project. Another important project is the Rehabilitation of the Haspolat Sewage Treatment Plant sponsor by the European Union in a bid to unite the two communities on the Island; the project will cost 25 million Euro. This project will provide 3.5 million m³ of water to be used in agriculture.

Another project was the establishment of a 150m³/day capacity small RO desalination plant in Eastern Mediterranean University to supply potable water for the use of the campus, but due to ill management of the plant, the plant is not functioning again. There are other small RO rooftop units available in some homes in Famagusta and some few places in Lefkosa and Girne. Efforts are on to establish another RO plant in the hotel centre area on the Island.

6. SOLAR DESALINATION RESEARCH IN EASTERN AND SOUTHERN MEDITERRANEAN

The works of renowned author(s) like Tiwari et al and Delyannis have provided detailed historical review on

desalination and solar desalination units [10, 11]. A number of other author(s) have also performed experimental and analytical investigations on different solar desalinating units to increase efficiency, daily production and to optimize the use of alternative energy [12-19]. It was found out that the still productivity increased up to 51% when asphalt basin liner and sprinkler have been used. In addition, 16% of daily productivity occurred at night, this is due to the temperature difference between the glass cover and water in the basin. The major results of the study were increasing ambient temperature or solar radiation will increase the productivity, also the thinner the water depth in the basins, the higher the productivity of the system. In addition, a comparison study on the productivity of double-effect and single-effect solar still has been carried out by Al-Hinai [14]. The average annual productivities of single-effect and double-effect solar stills were 4.15 and 6 kg/m².day, respectively. Another experimental work by Nijmeh et.al [19] considered different salts as absorbing materials to increase the absorptivity of water and thereby increase the productivity of the solar still. The absorbing materials were charcoal 50%, violet dye, potassium permanganate (KMnO₄) and potassium dichromate (K₂Cr₂O₇). The highest productivity obtained by violet dye with an increase of about 29% in efficiency.

There are many research performed/ongoing on solar desalination in N. Cyprus, the department of Mechanical of Eastern Mediterranean University in Famagusta have continued to provide innovative research on solar desalination. Table 5 shows some selected research on solar desalination in the last five years. The solar energy can be maximized with external reflectors (mirrors) to enhance the solar radiation on the desalinating units. The effect of solar radiation, in feed flow rate, nozzles jets, bare plate and wick clothes are studied on daily production. The solar desalination technology has not attracted many to invest substantially in it. The poor investment, especially from government, was due to the low daily production of about 6.4kg/m² per day. There are other desalination systems across the region in terms of reverse osmosis, even the Eastern Mediterranean University used to have a functional unit of 1000 m³per day but membrane problems and ill management of the unit have wreck the system. There are more reverse osmosis plants in building stages in the Bafra region of the country to serve the consortia of five star hotels. The huge investment in reverse osmosis is because of its extensive use in most of the MENA regions.

7. CONCLUSION

Cyprus has been facing increasingly severe water scarcity, especially in the northern part of the country. The scarcity is characterized by insufficient rainfall and seawater intrusion into the aquifers thereby resulting into poor water quality. Effective water resource

management is a promising approach but will do little in the case of the water scarcity in the northern part of Cyprus. The natural condition of water resources represents the physical limit to which North Cyprus needs to adapt in its development. Addressing North Cyprus's water scarcity requires an integrated, scientific approach with long-term, coordinated efforts in desalination technology. According to the land distribution of Northern Cyprus, the country has a huge potential for solar desalination. The bare land is in excess of 269 km² of which about 15 km² of that land will produce 1 million m³ of water per year. The total bare land can produce around 18 million m³ of fresh water through solar desalination if it is fully use for that purpose. The potential to solve water crises in Northern part of Cyprus is huge and obtainable.

The solar desalination research going on have proved that with local materials and weather condition of the country a 6.41 liters/m³ is achievable in summer seasons and 3.21 liters/m³ in winter season. This paper also recommends other solutions to address the water scarcity issue while improving water resource management. The country needs to establish institutional systems that control and regulate water withdrawal as seen in most countries in the southern Mediterranean. The water withdrawal for agricultural purpose is left with the municipalities to manage, this should be given to the established institution to authorize and regulate water use within the entire state. The established institution should issue water withdrawal permits to farmers and should be consistent with water resource planning and allocation, and facilitate the use of modern irrigation and desalination systems in the country.

Table 5: Some selected Solar Desalination Research in N. Cyprus

No	Name of the System	Average solar Intensity (w/m ²)	Ambient mean Temp (°C)	Productivity (kg/m ² .day)	Reference
1.	IBSS with bare plate	450	30	1.29	20
2.	IBSS with black fleece	450	30	2.995	20
3.	IBSS with bare plate and Glass base without mirror	620	34	3.41	21
4.	IBSS with black wick and Glass base without mirror	620	34	4.21	21
5.	IBSS with bare plate and Glass base with mirror	710	34	5.13	21
6.	IBSS with black wick and Glass base with mirror	710	34	6.41	21
7.	IBSS with metal sheet plate	620	34	2.80	21
8.	IBSS with blue wick	620	34	3.61	21
9.	Single basin solar still	540	34	2.20	21

Note: Incline basin solar system (IBSS)

Table 6: Some selected Solar Desalination Research in Mediterranean countries

No Reference	Name of the System	Average solar Intensity (w/m ²)	Ambient mean Temp (°C)	Productivity (kg/m ² .day)	
1.	Double stepped plastic solar still (Italy) 22	625	30	1.800	
2.	Single basin solar with deep basin (Egypt)	605	28	2.045	23
3.	Single slope solar still, asphalt covered basin (Jordan) 24	525	29	4.120	
4.	Triple basin solar (Jordan)	740	27	4.896	25
5.	Single Slope solar still (Jordan) 26	710	25	3.560	
6.	Distiller with a film in capillary motion (Algeria) 27	650	40	5.190	
7.	Solar still coupled to an outside condenser (Turkey)	480	30	6.520	28
8.	Vertical Solar still oriented towards east (Algeria) 29	520	40	6.630	
9.	Asymmetrical green house type solar still (Jordan)	584	32	7.000	30

REFERENCES

- [1] World Bank on MENA region. <http://go.worldbank.org/JQVM8LMP70>
- [2] Falkenmark, M. Widstrand, C. 1992. Population and water resources: a delicate balance. Population Bulletin 47. Population Reference Bureau, UN, Washington, DC.
- [3] Yang, H., Reichert, P., Abbaspour, K., Zehnder, A.J.B., 2003. A water resources threshold and its implications for food security. Environmental Science and Technology 37, 3048–3053.
- [4] Food and Agriculture Organization of the United Nations (FAO), 2011a. FAOSTAT. Database, FAO. <www.fao.org>.
- [5] Turkish Republic of Northern Cyprus statistical Yearbook, 2009.State Planning organization, Statistical and Research Department
- [6] Bicak. H and Jenkins.G.P.2000, "Transporting water by tanker from Turkey to North Cyprus: cost and pricing related". Water balance in the Eastern Mediterranean, ICRC, Canada
- [7] Ozturk S., 1995: Up to date water potential on NC, Proc of the 2nd water Congress of Chamber of Engineers,(ed) Dortrenk Press Ltd., NC, pp 23-29
- [8] Elkiran .Gand Ergil .M."The assessment of water budget of North Cyprus" Building and Environment, 41 (2006), pp 1671-1677
- [9] Kibris Newspaper, 1998
- [10] G.N.Tiwari, H.N.Singh, R.Tripathi. Solar Energy 75 (2003) 367-373
- [11] E.Delyannis. Solar Energy 75 (2003) 357-366
- [12] K.K. Murugavel, K.S.K. Chokalingam, K. Srithar. Desalination 220 (2008) 687-693
- [13] O.O. Badran, Desalination 209 (2007) 136-143
- [14] H.Al-Hinai et al. Desalination 150 (2002) 75-83

- [15] G.M.Cappelletti. Desalination 142 (2002) 221-227
- [16] K.K. Murugavel, K. Chockalingam, K. Srihar, Desalination 220 (2008) 687–693
- [17] Al-Karaghoul, W.E.Al-naser. Applied Energy 78 (2004) 347-354
- [18] M.Ali Samee, U.K.Mirza, T.Majeed, N. Ahmad, Renewable and Sustainable Energy Reviews 11 (2007) 543-549
- [19] S.Nijmeh, S.Odeh, B.Akash. International Communications in Heat and Mass Transfer 32 (2005) 565-572
- [20] H.S. Aybar, F.Egelioglu and U. Atikol, An experimental study on an inclined solar distillation system, Desalination, 180 (2005) 285-289
- [21] O. Phillips Agboola and F. Egelioglu. Thermodynamics and economic analysis of Concentrating Solar Desalination System. Ongoing PhD Dissertation in Mechanical Engineering Department, Eastern Mediterranean University, 2010.
- [22] G.M Cappelletti. An experiment with plastic solar still. Desalination 142 (2002) 221-227
- [23] S. Aboul-Enein,A.A El-Sebaii,E. El-Bialy. Investigation of a Single basin solar still with deep basin. PII: S0960-1481 (98)
- [24] O.O Badran,Experimental study of the enhancement parameters on a single slope solar still productivity . Desalination 209 (2007) 136-143
- [25] M.A Hamdam,A.M. Musa,B.A Jubran. Performance of solar still under Jordanian climate. Energy Conversion&Management 40 (1999) 495-503
- [26] O.O Badran,M.M. Abu-Khader, Evaluating thermal performance of a single slope solar still. Heat Mass Transfer (2007) 43: 985-995.
- [27] B. Boucekima,B. Gros, R Ouahes, M. Diboun. Performance study of the capillary film solar distiller. Desalination 116 (1998) 185-192
- [28] A.El-Bahi,D. Inan. A solar still with minimum inclination, coupled to an outside condenser. Desalination 123 (1999) 79-83
- [29] M. Boukar,A Harmin, Parametric study of a vertical solar still under desert climatic condition. Desalination 168 (2004) 21-28
- [30] Al-Hayek,O.O. Badran. The effect of using different designs of solar stills on water distillation. Desalination 169(2004) 121-127

Study on Amorphous Ag-Doped Manganese Dioxide Electrodes for Electrochemical Supercapacitors Applications

Sameh Hassan¹, Ahmed Abd El-Moneim²

¹ Energy Resources and Environmental Engineering Department, Egypt-Japan University of Science and technology, New Borg El Arab City, Alexandria, Egypt, postal Code 21934.

² Material Science and Engineering Department, Egypt-Japan University of Science and technology, New Borg El Arab City, Alexandria, Egypt, postal Code 21934.

ABSTRACT

Amorphous MnO₂ and Ag-doped MnO₂ thin films were galvanostatically deposited on a polished stainless steel substrate from 20 mM KMnO₄ aqueous solutions without and with AgNO₃ additions at cathodic current density of 1 mA/cm² for the application in electrodes of electrochemical supercapacitors. The supercapacitive properties of the deposited thin films have been studied in 0.5 M Na₂SO₄ electrolyte by cyclic voltammetry, impedance spectroscopy and charge-discharge measurement techniques. The Ag-free MnO₂ film showed better capacitive behaviour and lower charge transfer resistance compared to the Ag-doped MnO₂ films. The specific capacitance and charge transfer resistance values for Ag-free MnO₂ films were 160 F/g at a scan rate 10 mV/s and 3.87Ω, respectively. Cyclic stability using charge-discharge measurement technique indicates the excellent stability of Ag-free MnO₂ films and its possible use as a low cost electrode for supercapacitor applications.

Keywords: Cyclic voltammetry, Manganese dioxide, Power density, Energy density, Cyclic stability.

1. INTRODUCTION

Several energy storage devices, such as compressed air, hydrogen, flywheels, batteries, capacitors, and fuel cells, have been developed for various practical applications. Among these devices, high performance batteries and capacitors have presented themselves as one of the achievable, economically feasible options for meeting today's severe energy demands. Supercapacitors have received a lot of attention as viable electrical energy storage devices owing to their ability to deliver high powers, excellent reversibility, and longer cycle life than batteries [1-3]. On the basis of the energy storage mechanism, supercapacitors can be classified into two categories [4-6], namely the electrical double-layer capacitor (EDLC) and the pseudo-capacitor. The capacitance of the former comes from the charge accumulation at the electrode-electrolyte interface (double-layer capacitance), therefore it strongly depend on the surface area of the electrode accessible to the electrolyte. The capacitance of the latter is due to the reversible faradic transfer of charge between electrode and electrolyte, such as surface functional groups and transition metal oxides. Supercapacitors fill the gap between batteries (low specific power and high specific energy) and conventional capacitors (high specific power and low specific energy), i.e. they have a specific power as high as conventional capacitors and a specific energy close to that of batteries. It is obvious that the electrode is the key in the development of supercapacitors.

MnO_x is a promising electrode material for electrochemical capacitors because of its the relatively low cost, excellent electrochemical performance, environmentally friendly character in comparison with the ruthenium oxides or other transition metal oxides [7-9]. Hydrus RuO₂ has been extensively studied [10, 11] as an active electrode material for supercapacitors with capacitance as high as 720 F/g in aqueous acidic electrolytes. Although RuO₂ gives high specific capacitance, its disadvantages of high cost and toxic nature limits its further commercial application. As an inexpensive alternate to RuO₂, hydrus manganese oxide prepared by both chemical and electrochemical methods was found to possess capacitive characteristics with acceptable values of specific capacitance [12-16]. A specific capacitance of 130 F/g was reported [16] at a scan rate of 5 mV/s, for MnO₂ synthesized by sol-gel method.

Recent investigations showed that 1–8 wt.% Ag addition to lithium manganese dioxide electrode can significantly improve battery performance due to the increase in conductivity [17]. In another investigation the increase in conductivity of Ag-doped RuO₂ compared to pure RuO₂ was reported [18]. As a result, Ag-doped RuO₂ showed much higher SC compared to the SC of undoped RuO₂ [18]. Therefore, it is important to fabricate and investigate the Ag-doped MnO₂ films. MnO₂ films for application in ES can be prepared by anodic or cathodic electrodeposition from aqueous solutions. However, anodic electrolytic deposition of MnO₂ on metallic current collectors presents difficulties

related to the anodic oxidation and dissolution of metals. In contrast, cathodic electrodeposition can be performed on various metallic substrates. It should be noted that cathodic electrodeposition is an important industrial technique for the deposition of metals. Therefore, cathodic electrodeposition is a promising method for the co-deposition of oxides and metals and the fabrication of doped films and composites.

The goal of the present study is to fabricate Ag-free MnO_2 and Ag-doped MnO_2 thin films by galvanostatically cathodic deposition on polished stainless steel substrate from KMnO_4 aqueous solutions without and with AgNO_3 additions for the application in electrodes of electrochemical supercapacitors.

2. EXPERIMENTAL

Stainless-steel (SS) sheet of grade 316 LN, thickness 0.25 mm and surface area of 60 mm \times 150 mm was used as current collector and substrate for the electrodeposition of the active materials. Prior to the electrodeposition experiments the substrate were mechanically polished with SiC papers down to 2000.

MnO_2 and Ag-doped MnO_2 thin films were galvanostatically deposited from 20 mM KMnO_4 solution without and with AgNO_3 additions (0.5, 2 and 4 mM) at cathodic current density of 1 mA/cm² onto SS substrate for 0.5 hour. The weight of the deposited films was measured by means of a Sartorius micro-balance (Model BP211D). The structure was characterized by means of X-ray diffractometer (Shimadzu, XRD-7000) using Cu K α radiation.

All electrochemical investigations were performed at 30 \pm 1.0°C using two compartment three electrodes electrochemical cell with platinum foil as an auxiliary electrode and a saturated Ag/AgCl reference electrode. The capacitive performance of the deposited films was examined in 0.5 M Na_2SO_4 electrolyte using the electrochemical impedance spectroscopy (EIS), cyclic voltammetry (CV) measurement techniques and galvanostatic charge–discharge. The cyclic voltammetry measurements were carried out at potential ranges of 0–0.9 V vs. Ag/AgCl (sat.) at scan rates of 10–90 mV/s. The excitation amplitude for impedance measurements was 10 mV root mean square (RMS) in a frequency domain of 10⁻¹ to 10⁵ Hz.

3. RESULTS AND DISCUSSION

3.1. Structure

Figure 1 shows XRD patterns of Ag-free MnO_2 and Ag-doped MnO_2 thin films prepared by galvanostatic cathodic deposition method on polished SS substrate from 20 mM KMnO_4 aqueous solutions without and with 2 mM AgNO_3 addition at 1mA/cm². As seen, the

XRD patterns show no reflection peaks typical characteristics of any crystalline or nanocrystalline MnO_2 -based oxide films. This indicates the formation of amorphous Ag-free MnO_2 and Ag-doped MnO_2 thin films with very high degree of structure disorder. Sharp reflection peaks from SS substrate are also detected in the diffraction patterns of both oxides referring to the formation of thin deposit films on the SS substrate. It's also worth noting that Ag-free MnO_2 and Ag-doped MnO_2 thin films show almost identical diffraction patterns.

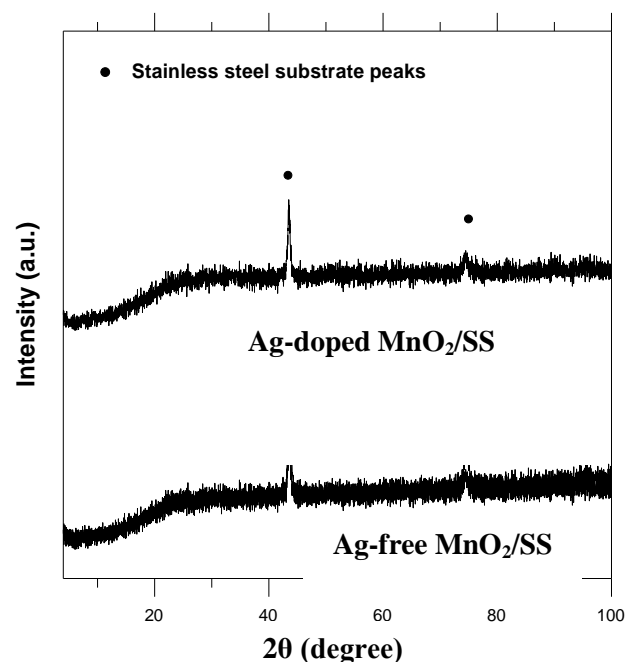


Figure 1: XRD patterns of Ag-free MnO_2 and Ag-doped MnO_2 (2 mM AgNO_3) films deposited on polished SS substrate.

3.2. Supercapacitive Properties of the Deposit Film

3.2.1. Cyclic Voltammetry

Figure 2 shows the CV curves of the Ag-free MnO_2 and Ag-doped MnO_2 films in the potential range of 0–0.9V (Ag/AgCl). All the curves are near-rectangular in shape and show symmetrical anodic and cathodic halves which indicate ideal capacitive behavior of the deposited films. As it can be seen in Fig. 2, the capacitive current density of Ag-free MnO_2 is higher than those of Ag-doped MnO_2 .

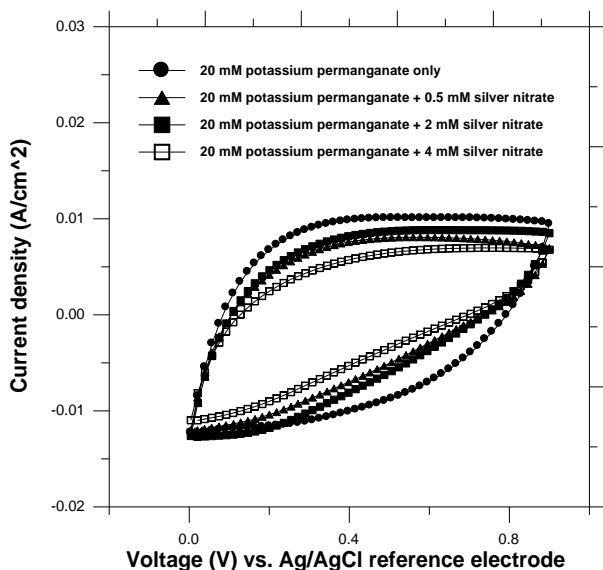


Figure 2: Cyclic voltammetric curves of Ag-free MnO₂ and Ag-doped MnO₂ films measured in 0.5 M Na₂SO₄ solution at scan rate of 90 mV/s.

For estimating the specific capacitance (SC) of the deposited oxide films, the amount of capacitive charge (Q) was obtained using half the integrated area of the CV curve presented in Fig.2, and then the SC was calculated from dividing the capacitive charge by the film mass (m) and the width of the potential window (ΔV) using equation (1).

$$SC = \frac{Q}{m \cdot \Delta V} \tag{1}$$

Figure 3 summarizes the dependence of the SC on the CV scan rate for Ag-free MnO₂ and Ag-doped MnO₂ films. In general, the specific capacitance decreases as the scan rate increases. This behavior can be attributed to the high probability of exposing both inner and outer surface of the deposited oxide to the ions with the decrease in the scan rate [19].

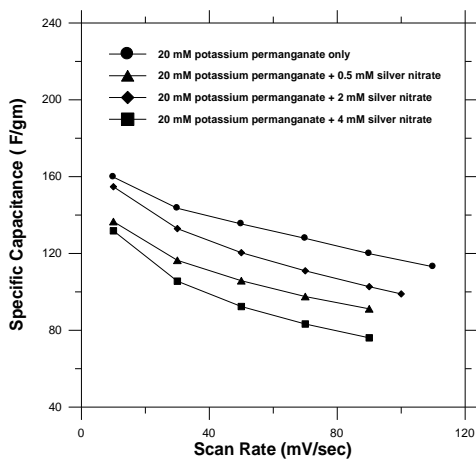


Figure 3: Variation of the specific capacitance with the scan rate of CV measurement for MnO₂ and Ag-doped MnO₂ films. Meanwhile, the maximum values of the specific capacitance for the films deposited from 20 mM KMnO₄ aqueous solutions with 0.0, 0.5, 2 and 4 mM AgNO₃ additions at scan rate of 10 mV/s are 160, 137, 155 and 132 F/g, respectively. This fact indicates that the introduction of Ag in the matrix of the deposited MnO₂ has no beneficial effect on its capacitive properties.

3.2.2. Electrochemical Impedance Spectroscopy Characterization

In principle, the power output capability of electrochemical supercapacitor depends strongly on not only the rates of ionic mass transport [20] but also the equivalent series resistance (ESR) [21]. The ESR is the sum of two major parts, an electronic resistance and an ionic one. EIS has been widely used to study the redox (charging/discharging) processes of electrode materials and to evaluate their electronic and ionic conductivities. Figure 4 shows the measured Nyquist plots of MnO₂ and Ag-doped MnO₂ electrodes in 0.5 M Na₂SO₄ electrolyte. The inset of Fig.4 represents the high frequency region of the recorded full impedance plots.

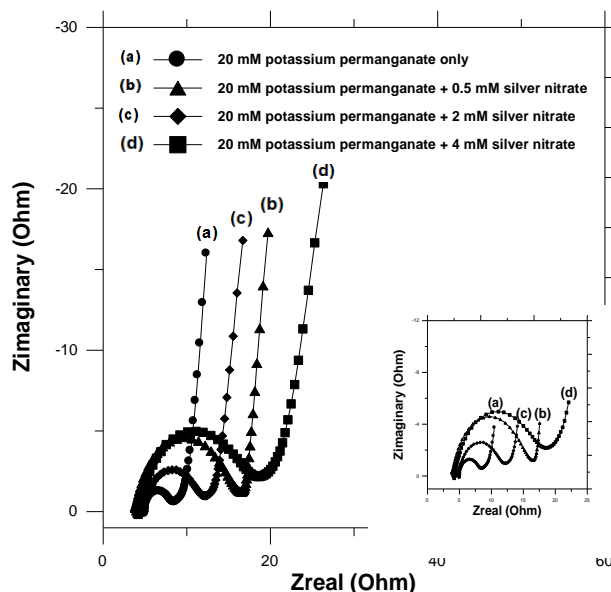


Figure 4: The Nyquist plots of MnO₂ and Ag-doped MnO₂ electrodes investigated in 0.5 M Na₂SO₄ electrolyte in the frequency range of 0.1 Hz–100 kHz at 5 mV amplitude.

In Fig. 4, two well-separated patterns are observed: an arc is obtained at frequencies high enough, which is related to interfacial processes; the low-frequency region of such plots indicated a capacitive behavior related to the film charging mechanism.

The initial non-zero intersect with the real impedance axis at the beginning of the semicircle indicates the typical ESR value of all system [19, 22]. The estimated ESR values for the films deposited from 20 mM

KMnO₄ aqueous solutions with 0.0, 0.5, 2 and 4 mM AgNO₃ additions are 5, 4.1, 4.85 and 4.17 Ω, respectively. These results indicate that the ESR value of MnO₂ deposited film has not been significantly affected by Ag doping.

On the other hand, all spectra showed a clear semi-circle at the high frequency region, which corresponds to the charge transfer resistance (R_{ct}). The magnitude of the charge transfer resistance can be derived from the difference in the real part of the impedance between low and high frequencies using fitting program provided with the electrochemical workstation [1, 23]. The estimated R_{ct} values for the films deposited from 20 mM KMnO₄ aqueous solutions with 0.0, 0.5, 2 and 4 mM AgNO₃ additions are 3.87, 12.79, 7.81 and 15.3 Ω, respectively. The increase in the R_{ct} value of MnO₂ with Ag addition may refer to the detrimental effect of Ag addition on the electronic transport properties of the deposited oxide.

On the other hand, a comparison of the imaginary impedance (Z imaginary) data at the same frequencies for all the deposited films indicates that the capacitance for Ag-free MnO₂ film is higher than those of Ag-doped MnO₂ films. This fact is in a good agreement with the SC data presented in Fig. 3

3.2.3. Galvanostatic Charge–Discharge

Figure 5 presents the charge–discharge curves for the films deposited from 20 mM KMnO₄ aqueous solutions with 0.0, 0.5, 2 and 4 mM AgNO₃ additions. The curves were measured in the potential range between 0 and +1 V at a discharge current density of 1.1 mA/cm². In Fig. 5, there is a linear variation of potential during charging process, indicating the capacitive behavior of MnO₂ and Ag-doped MnO₂ films. The discharge part of the curves consists of three segments: a resistive component from the sudden decrease of voltage (iR drop) related to the internal resistance of the deposit, the capacitance component which is related to the voltage change due to ions separation at electrode interface in the double layer region and the faradaic component which is attributed to charge transfer reaction of deposit. Detailed analysis of the results in Fig. 5 clearly shows that the Ag-free MnO₂ film has longer time for charging–discharging processes and lower iR drop value than those recorded for Ag-doped MnO₂ deposited films. These facts indicate the higher energy and power densities of Ag-free MnO₂ than those of Ag-doped MnO₂.

3.2.4. Cyclic Stability using Galvanostatic Charge–Discharge

The cycle stability test of Ag-free MnO₂ film was performed at discharge current density 5.5 mA/cm² and the results are presented in Fig. 6.

As it can be clearly seen in Fig. 6, there is a little decrease in the value of specific capacitance during the first 30 cycles and then the specific capacitance value remained almost constant.

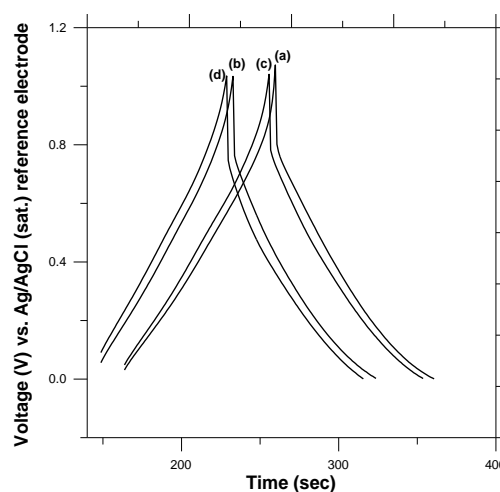


Figure 5: Charge–discharge curves in 0.5 M Na₂SO₄ electrolyte for thin films deposited from 20 mM KMnO₄ aqueous solutions with (a) 0.0 M AgNO₃, (b) 0.5 mM AgNO₃, (c) 2 mM AgNO₃ and (d) 4 mM AgNO₃

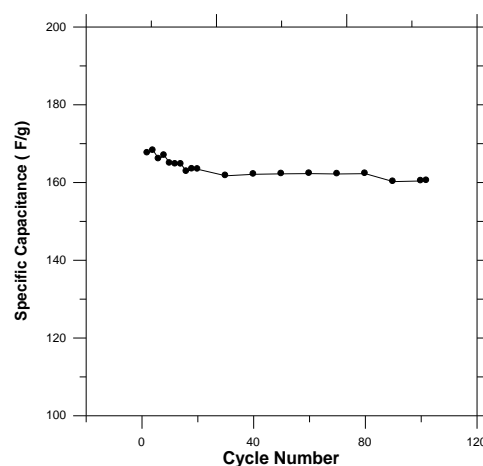


Figure 6: Cyclic-life data of the Ag-free MnO₂/SS electrode at discharge current density 5.5 mA/cm².

A decrease of about 4 % in the initial specific capacitance was observed after 100 cycles. This decrease in the value of specific capacitance is very less compared to the reported value in the literature [24] and indicates the high stability of the deposited film.

4. CONCLUSION

The results presented in this investigation indicated that amorphous Ag-free and Ag-doped manganese dioxide thin films were successfully prepared by galvanostatic cathodic deposition onto polished SS electrodes from KMnO₄ solution without and with AgNO₃ addition. The Ag-doped manganese MnO₂ films showed lower

capacitive behavior and higher charge transfer resistance compared with Ag-free MnO₂ deposited film. The specific capacitance and charge transfer resistance values for Ag-free MnO₂ films were 160 F/g at a scan rate 10 mV/s and 3.87Ω, respectively. The Ag-free MnO₂ film prepared by the cathodic electrolytic deposition on low cost stainless steel substrate can be considered as possible electrode materials for supercapacitor application.

5. ACKNOWLEDGEMENTS

This work was supported by Egypt Japan University of science and technology (E-just). The authors gratefully acknowledge Prof. Dr Masaaki Suzuki and Dr Tarek Naser for their honest supervision, continuous encouragement, helps and valuable advice during the achievement of this work.

REFERENCES

- [1] Conway B E, *Electrochemical Supercapacitors: Scientific Fundamentals and Technological Applications*, Kluwer Academic/Plenum, New York, 1999, p. 1.
- [2] Burke A F et al. *Materials for Energy Storage and Conversion: Batteries, Capacitors and Fuel Cells*, Materials Research Society, Pittsburgh, 1995, p. 375.
- [3] Lam L T, Louey R. Development of ultra-battery for hybrid-electric vehicle applications. *J. Power Sources*, 2006, 158:1140-1148.
- [4] Zhang Li Li et al. Manganese oxide-carbon composite as supercapacitor electrode materials. *Microporous and Mesoporous Materials*, 2009, 123:260-267.
- [5] Winter M, Brodd R J. What Are Batteries, Fuel Cells, and Supercapacitors. *Chem. Rev.*, 2004, 104:4245-4270.
- [6] Pandolfo A G, Hollenkamp A F. Carbon properties and their role in supercapacitors. *J. Power Sources*, 2006, 157: 11-27.
- [7] Dubal D P et al. Effect of different modes of electrodeposition on supercapacitive properties of MnO₂ thin films. *Applied Surface Science*, 2011, 257:3378-3382.
- [8] Pang S C, Anderson M A, Chapman T W. Novel Electrode Materials for Thin-Film Ultracapacitors: Comparison of Electrochemical Properties of Sol-Gel-Derived and Electrodeposited Manganese Dioxide. *J. Electrochem. Soc.*, 2000, 147:444.
- [9] Dan-Dan Zhao & Zhi Yang & Eric Siu-Wai Kong & Cai-Ling Xu & Ya-Fei Zhang. *J. Solid State Electrochem.* DOI 10.1007/s10008-010-1182-x.
- [10] Zheng, J. P. and T. R. Jow). A New Charge Storage Mechanism for Electrochemical Capacitors. *Journal of the Electrochemical Society*, 1995, 142(1): L6-L8.
- [11] Kim IH, Kim KB. Ruthenium oxide thin film electrodes for supercapacitors. *Electrochem Solid-State Lett.*, 2001(4):A62.
- [12] Chang J K, Tsai W T. Material Characterization and Electrochemical Performance of Hydrous Manganese Oxide Electrodes for Use in Electrochemical Pseudocapacitors. *J. Electrochem. Soc.*, 2003, 150:A1333.
- [13] Hu C C, Tsou T W. The optimization of specific capacitance of amorphous manganese oxide for electrochemical supercapacitors using experimental strategies. *J. Power Sources*, 2003, 115:179.
- [14] Long J W, Young A L, Rolison D R. Spectroelectrochemical Characterization of Nanostructured, Mesoporous Manganese Oxide in Aqueous Electrolytes *J. Electrochem. Soc.*, 2003, 150: A1161.
- [15] Kim H, Popov B N. Synthesis and Characterization of MnO₂-Based Mixed Oxides as Supercapacitors *J. Electrochem. Soc.*, 2003, 150:D56.
- [16] Reddy R N, Reddy R G. Sol-gel MnO₂ as an electrode material for electrochemical capacitors. *J. Power Sources*, 2003, 124:330.
- [17] Wu XM, He Z Q, Chen S, Ma M Y, Xiao Z B, Liu J B. Silver-doped lithium manganese oxide thin films prepared by solution deposition. *Mater Lett.*, 2006, 60:2497-2500.
- [18] Ahn H J, Sung Y E, Kim W B, Seong T Y. Crystalline Ag nanocluster-incorporated RuO₂ as an electrode material for thin film micropseudocapacitors. *Electrochem. Solid State Lett.* 2008, 11:A112-115.
- [19] Yong Zhang et al. Electrochemical investigation of MnO₂ electrode material for supercapacitors. *International Journal of Hydrogen Energy*, 2011, 36:II 760-II 766.
- [20] Izadi-Najafabadi A, Tan DTH, Madden J D. Towards high power polypyrrole/carbon capacitors. *Synth Met.*, 2005, 152:129-32.

- [21] Celzard A, Collas F, Mareche JF, Furdin G, Rey I. Porous electrodes-based double-layer supercapacitors: pore structure versus series resistance. *J Power Sources* 2002, 108:153–162.
- [22] Lu Q, Zhou Y. Synthesis of mesoporous polythiophene/MnO₂ nanocomposite and its enhanced pseudocapacitive properties. *J. Power Sources*, 2011, 196:4088-4094.
- [23] Tuken T, Yazici B, Erbil M. A new multilayer coating for mild steel protection. *Prog Org Coat*, 2004, 50:115–122.
- [24] Prasad K R, Miura N. Potentiodynamically deposited nanostructured manganese dioxide as electrode material for electrochemical redox supercapacitors. *Journal of Power Sources*, 2004, 135:354–360.

Effect of Deposition Current on the Capacitive Behavior of Manganese Dioxide/Stainless Steel electrodes

Sameh Hassan¹, Ahmed Abd El-Moneim²

¹Energy Resources and Environmental Engineering Department, Egypt-Japan University of Science and technology, New Borg El Arab City, Alexandria, Egypt, postal Code 21934.

²Material Science and Engineering Department, Egypt- Japan University of Science and technology, New Borg El Arab City, Alexandria, Egypt, postal Code 21934.

ABSTRACT

Amorphous manganese dioxide thin film was prepared by galvanostatic cathodic deposition at current densities of 0.5-1 mA/cm² on etched stainless-steel substrate from 20 mM KMnO₄ solution. The structure of the deposited oxides was investigated using X-ray diffraction analysis. The capacitive behavior of the manganese dioxide electrodes were characterized by cyclic voltammetry and electrochemical impedance spectroscopy in 0.5 M Na₂SO₄ electrolyte. The capacitance performance was found to increase with the increase in the deposition current density. The electrode deposited at current density of 1 mA/cm² showed specific capacitance of 174 F/g at scan rate of 10 mV/s, equivalent series resistance of 3.53Ω and charge transfer resistance of 1.39 Ω. The improvement in the capacitive behavior of the electrode with the increase in the deposition current density was attributed to the increase in the electronic properties of the deposited oxides.

Keywords: Manganese dioxide, Supercapacitor, Energy density, Electrodeposition.

1. INTRODUCTION

Energy storage devices have become more demanded due to the fast growing market of portable electronic devices and hybrid electric vehicles (HEVs) [1]. Supercapacitors, also known as electrochemical capacitors or ultracapacitors, are an energy storage devices capable of storing charges in the electrode/electrolyte interface, have received much attention due to their unique properties, such as pulse supply of high power, longer cycle life and higher energy density [2]. However, the energy density of supercapacitors (< 10 Wh /kg) is lower than that of batteries (> 100 Wh/ kg) but their power is significantly higher with lifetime longer [3]. On the basis of the energy storage mechanism, supercapacitors can be classified into two categories [4,5], namely the electrical double-layer capacitor (EDLC) and the pseudocapacitor. EDLCs store charge electrostatically through the charge accumulation at the electrode/electrolyte interface, therefore strongly depending on the surface area of the electrode accessible to the electrolyte. Pseudocapacitors store charge Faradaically through the transfer of charge between electrode and electrolyte. There are two electrode materials that are used to store charge in pseudocapacitors, conducting polymers and metal oxides [3, 6, 7]. The latter is of interest in our work.

Because of their high conductivity, metal oxides have also been explored as a possible electrode material for pseudocapacitors [8-12]. The most of relevant research concerns ruthenium oxide. This is because other metal oxides have yet to obtain comparable capacitances. A very high specific capacitance of up to 750 F/g was

reported for RuO₂ prepared at relatively low temperatures [2]. The capacitance of ruthenium oxide is achieved through the insertion and removal, or intercalation, of protons into its amorphous structure. Furthermore, the equivalent series resistance (ESR) of hydrous ruthenium oxide is lower than that of other electrode materials. As a result, ruthenium oxide pseudocapacitors may be able to achieve higher energy and power densities than similar EDLCs and conducting polymer pseudocapacitors.

However, the high cost of this noble metal material limits its further commercial application. Hence, much effort has been aimed at searching for alternative inexpensive electrode materials with good capacitive characteristics, e.g., transition metal oxides, such as MnO_x, NiO_x, CoO_x [2], etc. Thus, a major area of research is to utilize cheap metal oxide and/or the development of fabrication methods to reduce the cost of ruthenium oxide, without reducing the performance [8, 9]. MnO_x has been considered as a promising electrode material for electrochemical capacitors because of its low cost and excellent capacitive performance in the aqueous electrolytes. Manganese dioxide (MnO₂) is generally produced by anodic deposition at a high current density onto metallic conductive substrate using acidified MnSO₄ solution. However, this method usually leads to the dissolution of the conductive substrate and/or build up an insulating oxide layer at the interface of the active oxide and substrate, which negatively affect the value of specific capacitance as well as the resistance of developed manganese oxide electrodes. To improve the capacitive behavior and resistance of the deposited manganese

dioxide, the present study is undertaken to deposit manganese dioxide thin film onto stainless steel substrate from KMnO_4 aqueous solution using galvanostatic cathodic deposition technique. Special attention is given to study the effects of deposition cathodic current density on the structure properties as well as capacitive performance of MnO_2 thin film.

2. EXPERIMENTAL

Stainless-steel (SS) sheet of grade 316 LN, thickness 0.25 mm and surface area of 60 mm \times 150 mm was used as substrate material for the electrodeposition. The substrate was first etched in a mixture of hydrofluoric acid 40%: nitric acid 69%: distilled water with ratio 1:1:1 for 1 hour, then washed and dried in air.

MnO_2 thin films were galvanostatically deposited from 20 mM KMnO_4 solution at a cathodic current density of 0.5, 0.75 and 1 mA/cm² onto SS substrate for 0.5 hour. The weight of the deposited manganese dioxide film was measured by means of a Sartorius micro-balance (Model BP211D). The structure was characterized by means of X-ray diffractometer (Shimadzu, XRD-7000) using $\text{Cu K}\alpha$ radiation.

All electrochemical measurements were performed at $30 \pm 1.0^\circ\text{C}$ using two compartment three electrodes electrochemical cell with platinum foil as an auxiliary electrode and a saturated Ag/AgCl reference electrode. The electrochemical impedance investigations and the cyclic voltammetry (CV) polarisation measurements were carried out in 0.5 M Na_2SO_4 electrolyte using VersaSTAT4 potentiostat/galvanostat. The cyclic voltammetry (CV) measurements were carried out at potential ranges of 0–0.9 V (Ag/AgCl) at scan rates of 10–100 mV/s. The excitation amplitude for impedance measurements was 10 mV root mean square in a frequency domain of 10^{-1} to 10^5 Hz.

3. RESULTS AND DISCUSSION

3.1. Structure

Figure 1 shows typical X-ray diffraction pattern of MnO_2 film galvanostatically deposited onto etched SS substrate at 1 mA/cm². The XRD pattern shows sharp peaks corresponding to crystalline stainless steel substrate. No reflection peaks typical to the formation of crystalline or nanocrystalline MnO_2 , indicating to the formation of amorphous MnO_2 oxide film. It's worth mentioning that the amorphous phase of the oxide material is generally necessary to have an electrode with large surface area for supercapacitor applications [13]. Meanwhile XRD diffraction results revealed that the value of deposition current density has insignificant effect on the recorded XRD patterns of the deposited films.

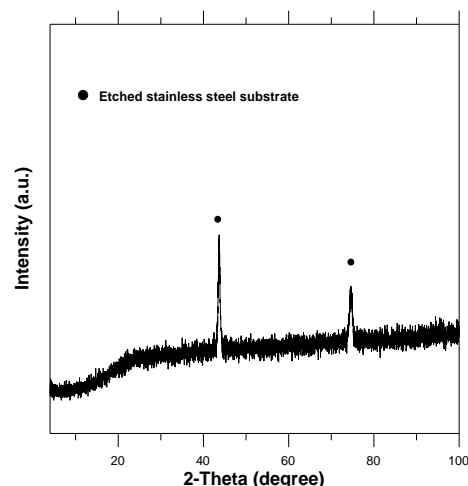


Figure 1: XRD pattern for MnO_2 film galvanostatically deposited at 1 mA/cm² on an etched stainless steel substrate.

3.2. Supercapacitive behaviour

3.2.1. Cyclic Voltammetry

Figure 2 shows the CV curves in 0.5 M Na_2SO_4 electrolyte for MnO_2 films obtained at different deposition current densities. It's clearly seen that all the curves are near-rectangular in shape and show symmetrical anodic and cathodic halves which indicate ideal capacitive behavior of the deposited manganese dioxide films. In addition, the capacitive current density tends to increase with the increase in the deposition current density.

For estimating the specific capacitance (SC) of the deposited oxide films, the amount of capacitive charge (Q) was obtained using half the integrated area of the CV curve presented in Fig.2, and then the SC was calculated from dividing the capacitive charge by the film mass (m) and the width of the potential window (ΔV) using equation (1).

$$SC = \frac{Q}{m \cdot \Delta V} \quad (1)$$

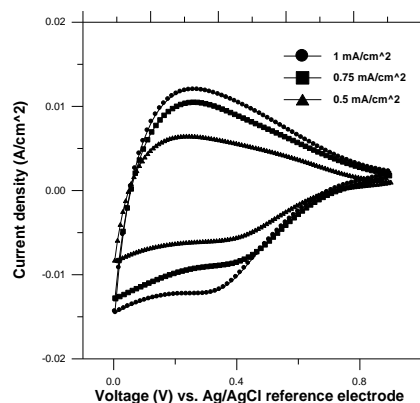


Figure 2: Cyclic voltammetric curves of MnO_2 films measured in 0.5 M Na_2SO_4 solution at scan rate 100 mV/sec as a function of deposition current density.

Figure 3 summarizes the dependence of the specific capacitance on the scan rate at CV measurement for MnO_2 films deposited at different deposition current densities. In general, the specific capacitance decreases as the scan rate increases. This behavior can be attributed to the high probability of exposing both inner and outer surface of the deposited oxide to the ions with the decrease in the scan rate [14]. Meanwhile, the maximum values of the specific capacitance at current densities of 1, 0.75 and 0.5 mA/cm^2 using scan rate of 10 mV/sec are 174, 140 and 97 F/g , respectively.

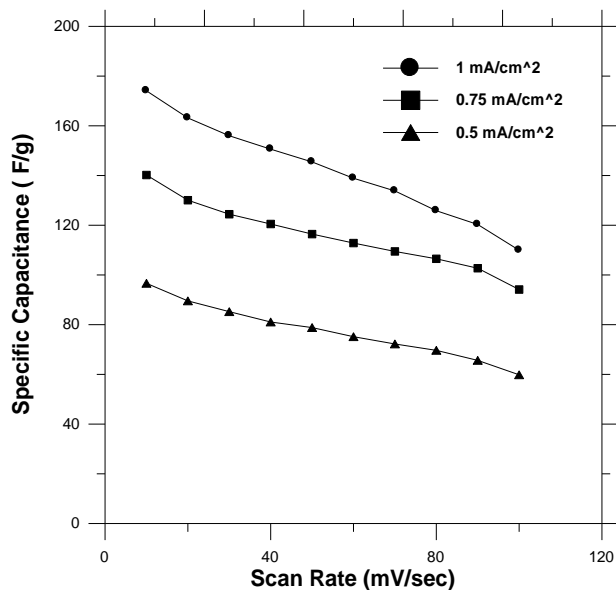


Figure 3: Dependence of the specific capacitance on the scan rate of CV measurement for MnO_2 films deposited at different deposition current densities.

3.2.2. Electrochemical Impedance Spectroscopy

In general, the power output capability of electrochemical supercapacitor depends strongly on not only the rates of ionic mass transport [15] but also the equivalent series resistance (ESR) [16]. The ESR is the sum of two major parts, an electronic resistance and an ionic one. EIS has been widely used to study the redox (charging/discharging) processes of electrode materials and to evaluate their electronic and ionic conductivities. Figure 4 shows the measured Nyquist plots in 0.5 M Na_2SO_4 electrolyte for MnO_2/SS electrodes prepared under the different deposition current densities. The inset of Fig.4 represents the high frequency region of the recorded full impedance plots.

As it can be seen in Fig. 4, two well-separated patterns are observed: an arc is obtained at frequencies high enough, which is related to interfacial processes; the low-frequency region of such plots indicated a capacitive behavior related to the film charging mechanism.

The initial non-zero intersect with the real impedance axis at the beginning of the semicircle indicates the

typical ESR value of all system [14, 17]. The estimated ESR values for the deposited oxide films at deposited current densities of 1, 0.75 and 0.5 mA/cm^2 are 3.53, 3.54 and 3.91 Ω , respectively. The results indicate that the variation in the ESR value with the deposition current density is insignificant.

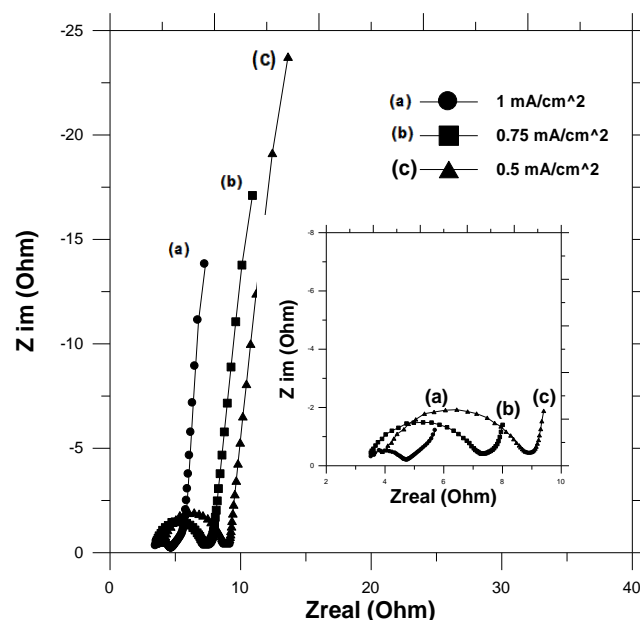


Figure 4: Nyquist plots of MnO_2/SS electrodes prepared under different deposition current densities.

On the other hand, all spectra showed a clear semi-circle at the high frequency region, which corresponds to the charge transfer resistance [3]. The magnitude of the charge transfer resistance can be derived from diameter of the semi-circle [18]. The estimated R_{ct} values of the MnO_2 films deposited at 1, 0.75 and 0.5 mA/cm^2 are 1.39, 4 and 5.28 Ω , respectively. The decrease in the R_{ct} value with increase in the deposition current density indicates that the enhancement in pseudocapacitive characteristics is mainly due to an improvement in the electronic properties of the deposited oxide by the deposition at high current density, such as 1 mA/cm^2 . Meanwhile, the comparison of imaginary impedance (Z_{im}) data at the same frequencies for all the deposited films confirms that the capacitive behaviour of the deposited film increases with the increase in the deposition current density. This fact is in a good agreement with the SC data presented in Fig. 2.

3.2.3. Cyclic Stability using Galvanostatic Charge–Discharge

The cycle-life test of the deposited MnO_2 film at 1 mA/cm^2 was performed at discharge current density 5.5 mA/cm^2 and the result is presented in Fig. 5.

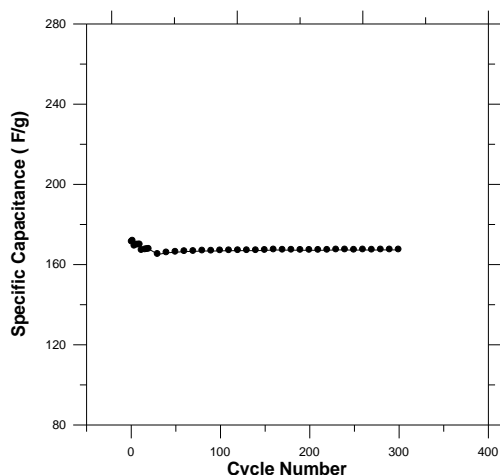


Figure 5: Cyclic-life data of MnO₂/SS electrode at discharge current 5.5 mA/cm².

4. CONCLUSION

In an attempt to develop a novel electrode with low cost, high capacitive performance and long cyclic stability, amorphous manganese dioxide thin films were galvanostatically deposited onto etched SS electrodes from KMnO₄ solution at different cathodic current densities in range of 0.5-1 mA/cm². The capacitive performance of the films was found to increase with the increase in deposition density. The MnO₂ film deposited at current density of 1 mA/cm² has the highest SC of 174 F/g at scan rate of 10 mV/s and the smallest charge transfer resistance of 1.39 Ω. The excellent capacitive performance suggests that the amorphous MnO₂ films obtained by cathodic deposition from KMnO₄ solution has the potential to be used as an electrode materials for high performance supercapacitor.

5. ACKNOWLEDGEMENTS

This work was supported by Egypt Japan University of science and technology (E-just). The authors gratefully acknowledge Prof. Dr Masaaki Suzuki and Dr Tarek Naser for their honest supervision, continuous encouragement, helps and valuable advice during the achievement of this work.

REFERENCES

- [1] Zhang Li Li, Tianxin Wei, Wenjuan Wang, X.S. Zhao. Manganese oxide-carbon composite as supercapacitor electrode materials. *Microporous and Mesoporous Materials*, 2009, 123:260-267.
- [2] Zhao Dan-Dan et al. Carbon nanotube arrays supported manganese oxide and its application in electrochemical capacitors. *J. Solid State Electrochem.* DOI 10.1007/s10008-010-1182-x.
- [3] Conway B E, *Electrochemical Supercapacitors: Scientific Fundamentals and Technological Applications*, Kluwer Academic/Plenum, New York, 1999.
- [4] Winter M, Brodd R J. What Are Batteries, Fuel Cells, and Supercapacitors. *Chem. Rev.*, 2004, 104:4245-4270.
- [5] Pandolfo A G, Hollenkamp A F. Carbon properties and their role in supercapacitors. *J. Power Sources*, 2006, 157:11-27.
- [6] Conway, B E. Transition from "supercapacitor" to "battery" behavior in electrochemical energy storage. *Journal of the Electrochemical Society*, 1991, 138(6):1539-1548.
- [7] Conway, B E, Birss V et al. The role and utilization of pseudocapacitance for energy storage by supercapacitors. *Journal of Power Sources*, 1997, 66(1-2):1-14.
- [8] Burke A. Ultracapacitors: why, how, and where is the technology, *Journal of Power Sources*. 2000, 91(1):3750.
- [9] Kotz R, Carlen M. Principles and applications of electrochemical capacitors. *Electrochimica Acta*, 2000, 45(15-16):2483-2498.
- [10] Kim, I H, Kim K B. Ruthenium oxide thin film electrodes for supercapacitors. *Electrochemical and Solid State Letters*, 2001, 4(5): A62-A64.
- [11] Zheng J P, Jow T R. A New Charge Storage Mechanism for Electrochemical Capacitors. *Journal of the Electrochemical Society*, 1995, 142(1): L6-L8.
- [12] Zheng, J P, Cygan P J et al. Hydrous Ruthenium Oxide as an Electrode Material for Electrochemical Capacitors. *Journal of the Electrochemical Society*, 1995, 142(8): 2699-2703.
- [13] Dubal D P et al. Effect of different modes of electrodeposition on supercapacitive properties of MnO₂ thin films. *Applied Surface Science*, 2011, 257:3378-3382.
- [14] Yong Zhang et al. Electrochemical investigation of MnO₂ electrode material for supercapacitors. *International Journal of Hydrogen Energy*, 2011, 36:II760-II766.
- [15] Izadi-Najafabadi A, Tan DTH, Madden J D. Towards high power polypyrrole/carbon capacitors. *Synth Met.*, 2005, 152:129-32.
- [16] Celzard A, Collas F, Mareche JF, Furdin G, Rey I. Porous electrodes-based double-layer

supercapacitors: pore structure versus series resistance. *J Power Sources* 2002, 108:153–162.

- [17] Lu Q, Zhou Y. Synthesis of mesoporous polythiophene/MnO₂ nanocomposite and its enhanced pseudocapacitive properties. *J. Power Sources*, 2011, 196:4088-4094.
- [18] Tuken T, Yazici B, Erbil M. A new multilayer coating for mild steel protection. *Prog Org Coat*, 2004, 50:115–122.
- [19] Prasad K R, Miura N. Potentiodynamically deposited nanostructured manganese dioxide as electrode material for electrochemical redox supercapacitors. *Journal of Power Sources*, 2004, 135:354–360.

Synthesis of Polymethylmethacrylate

Lakhdari Fatiha¹, Benharrats Nassira²

¹LAKHDARI Fatiha 1 flakdari@yahoo.fr

²BENHARRATS Nassira 2 nassira_benharrats@yahoo.fr

ABSTRACT

The objective of this work consists on synthesis of a bulk transparent polymer-inorganic nanocomposite and its photostabilization by addition of Zinc oxide. The poly methyl methacrylate (PMMA) is a thermoplastic and transparent plastic. Recycling of the PMMA is easy, the macromolecules of PMMA are depolymerised in methyl methacrylate molecules under the action of temperature. The zinc oxide (ZnO) is widely used as additive into several materials and products including plastics, ceramics, glass, etc. ZnO is in a natural product but most of time its synthetic version is used commercially. It is used for photostabilization of many polymers in transformation processes. In this study, we, first, prepare the polymer-inorganic nanocomposite by emulsion polymerization of Methyl Methacrylate (MMA) in the presence of zinc oxide particles. We have, initially, optimized the quantity of the additive which improves the UV resistance without decreasing the transparency of the polymer. In a second step the obtained materials are continuously exposed to UVB (280 nm) during various time (two to six months). The photodegraded nanocomposites are characterized by IR spectroscopy, thermal analysis ATD-ATG, and X-ray diffraction. The UV filtration effect of nanocomposites films is followed by UV spectroscopy. The results show a significant improvement of the thermal and optical properties of the PMMA.

Keywords: Polymers, photostabilisation, ZnO, PMMA.

1. INTRODUCTION

The polymeric materials have attracted much attention because of its uses in many fields. Moreover, the polymer play significant role in preparing solar cells,¹ gas sensors,^{2,3} varistors,^{4,5} catalysts,⁶⁻⁸ electrical and optical device⁹⁻¹¹ and electrostatic dissipative coatings.¹²

These applications gave been based on their strong sensitivity to natural ageing during their use under the atmospheric conditions, which required some changes in their properties such as: colouring, deformation and the cracking of surface, change in the breaking strength and to lengthening, etc. This led unrelentingly to the deterioration of the physical properties, mechanical and aesthetics of the polymeric materials which strongly reduces the lifespan of these materials.

As a continuation of our program on the development of novel nanostructured materials with enhanced functionality, we report herein the optimum conditions for the synthesis of news nanocomposites starting from polymethylmethacrylate (PMMA) and Zinc oxide (ZnO) as additive during the polymerization process in order to enhanced its photostabilisation and thermo stabilisation.

Artificially by exposure prolonged to UVB (280 Nm).

The identification and the characterizations of the various synthesized products are carried out by various methods of analyses such as the IR spectroscopy, the thermic analyses DTA-TGA. The filter effect is followed by spectroscopy UV.

2. EXPERIMENTAL METHODS

2.1. Polymerization of methyl methacrylate (MMA) in emulsion

An emulsifier solution of sodium dodecyle sulphates (SDS) (0.4 gr) in distilled water (200 ml) was heated under stirring (80 °C). Methyl methacrylate (MMA) (5 gr) was added drop-wise. The heating was continued for 5 min. Sodium persulphate was added with different percentages. The reaction mixture was heated for 4 hrs. The product was washed with water, dissolved in acetonitrile, precipitated from methanol and dried under vacuum.

2.1. Preparation of the PMMA grafted ZnO nanocomposites

ZnO sol is synthesized according to the method given by Znaidi et al. A typical sol preparation consist of

the following steps: Zn(II) solution (0.001-0.1 mol.L⁻¹) is prepared by refluxing zinc acetate dehydrate (ZAD, Kebo) in ethanol (Solveco) at 80°C for 2 hr under stirring. Distilled water is subsequently added to these solutions and thus transparent solutions are obtained. The ratio of distilled water to Zn, r (r = [H₂O]/ [Zn⁺²], is varied between 0-4.

ZnO sol was mixed with MMA monomer and several different wt% ZnO containing methyl methacrylate have been prepared. After the addition of the initiator, sodium persulphate (Na₂S₂O₈), the sol has been dispersed in the MMA matrix by using ultrasonification. The polymerization is completed after ethanol is evaporated, and the transparent PMMA-ZnO is obtained

2.2. Ageing of PMMA and the nanocomposites PMMA-ZnO

The photostabilisation of the synthesized materials PMMA and PMMA-ZnO have been studied by their exposures to UV-lamp (280nm) during 45-180days.

3. RESULTS AND DISCUSSION

3.1. Characterization by IR spectroscopy

Figure 1 is the Infra-Red absorption spectra of PMMA and photodegraded PMMA during 180 days using UV-lamp. These spectra show a typical band absorption which is in agreement of the literature.

Thus, their IR spectra showed a characteristic absorption bands at 1730 and 1250 cm⁻¹ for C=O and C-O bands, respectively, of the ester group of PMMA. In addition to the characteristic absorption bands of the aliphatic protons of the methyl and methylene groups which appears at 2950 and 1480cm⁻¹. An absorption band allotted to the elongations of the groupings ethylenes -CH₂- is located at 2950 cm⁻¹.

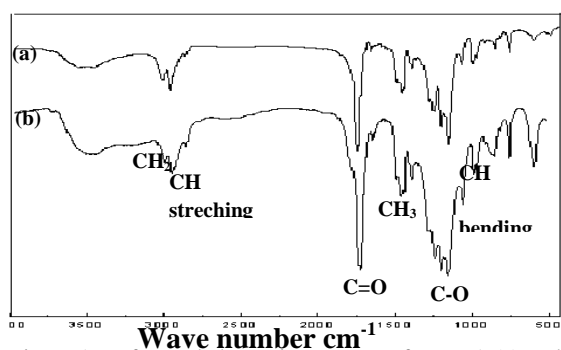


Figure 1: Infra-Red absorption spectra of PMMA (a) and photodegraded PMMA (b) by UV, ($\lambda = 280\text{nm}$ t=180jours)

Figure 2 is the Infra-Red absorption spectra of the PMMA and PMMA grafted ZnO (1% and 1.5%) nanocomposites degraded under UV during 180days under the same conditions.

The spectra show a difference in intensity of the absorption band corresponding to the carbonyl groups which is more intense for the degraded PMMA compared to the nanocomposites one. The intensity of the band decreases when the concentration of ZnO increases confirming the efficiency of the ZnO as like absorber UV.

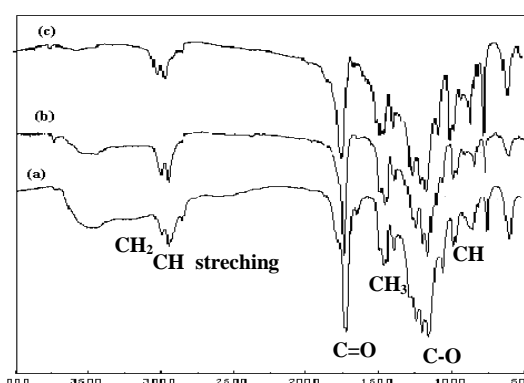


Figure 2: Spectrum IR of PMMA (a), and the degraded PMMA grafted ZnO (b and c) (1% and 1.5%), under UV, $\lambda = 280\text{nm}$ t=180days

3.2. Characterization by spectroscopy UV

Figure 3 is the UV spectra of the PMMA before and after its photodegradation under irradiation using UV lamp ($\lambda = 280\text{nm}$) during 180 days. The spectra show an intense absorption at 220 nm for the degraded PMMA, which is due the electronic transition from the groups strongly combined carbonyl resulted from the oxidation during the degradation. Thus, under the effect of UV-radiations, the increasing of the chromophores was occurred.

Figures 4 and 5 are the UV spectra of PMMA grafted ZnO (1%) and (1.5%) nanocomposites, respectively, degraded under UV during 180days, before and after photodegradation under UV, 180 days.

These spectra show an increasing in the absorption after the degradation with UV which is similar to the PMMA.

In the other hands, no difference in the absorption bands was observed in the change of the ration between wt/ratio (1 and 1.5%).

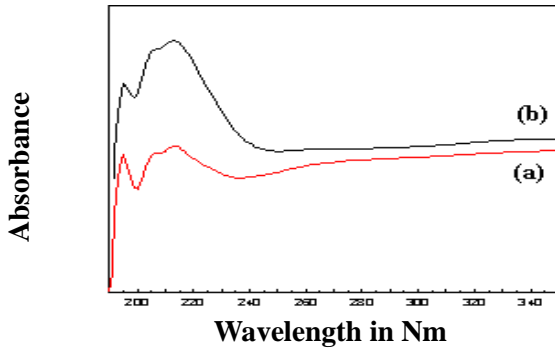


Figure 3: Spectrum UV of the PMMA (a) and Photodegraded PMMA (b) (UV, $\lambda = 280\text{nm}$ $t = 180\text{jours}$)

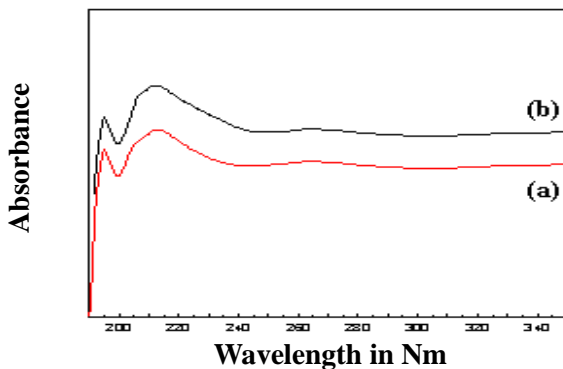


Figure 4: Spectrum UV of the nanocomposite with 1 % ZnO (a) and Photodegraded under (b) (UV, $\lambda = 280\text{nm}$ $t = 180\text{jours}$)

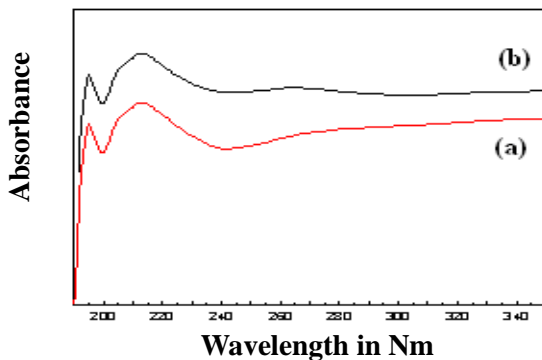


Figure 5: Spectrum UV of the Photodegraded nanocomposite with 1.5 % ZnO (b) under UV, ($\lambda = 280\text{nm}$ $t = 180\text{jours}$)

3.3. Characterization of the samples by DTA-TGA

Figures 6 and 7 represent the thermograms respective DTA and TGA of the PMMA and degraded PMMA under UV during 180 days. Figure 8 represents the thermograms DTA of the PMMA charged with 1.5% ZnO before and after photodegradation.

The results of the differential and gravimetric thermal analyses show that the PMMA stable until 325°C , once is thermally photodegraded, this

temperature decreases by 20°C and passes to 305°C .

This thermal stability is improved by the addition of oxide of Zinc (ZnO) with weak concentration (1.5 %) as shown in the figure 8. The initial temperature of degradation passes to 365°C is an improvement of 40°C .

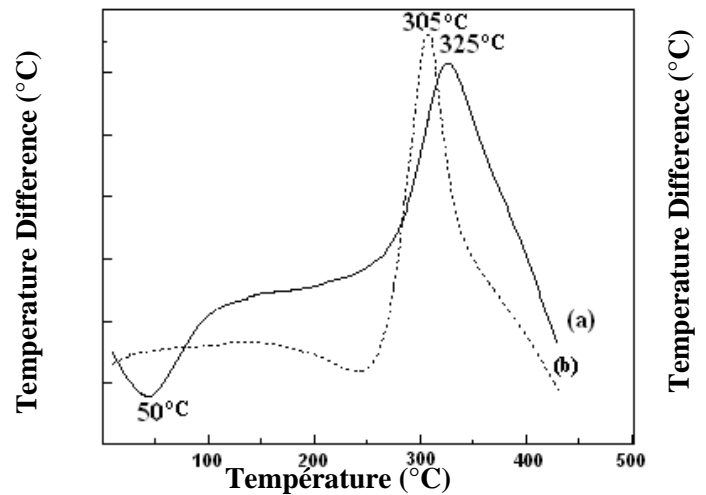


Figure 6: Thermograms DTA (a) of the PMMA and of the photodegraded PMMA (b) under UV, $\lambda = 280\text{nm}$, $T = 180\text{jours}$

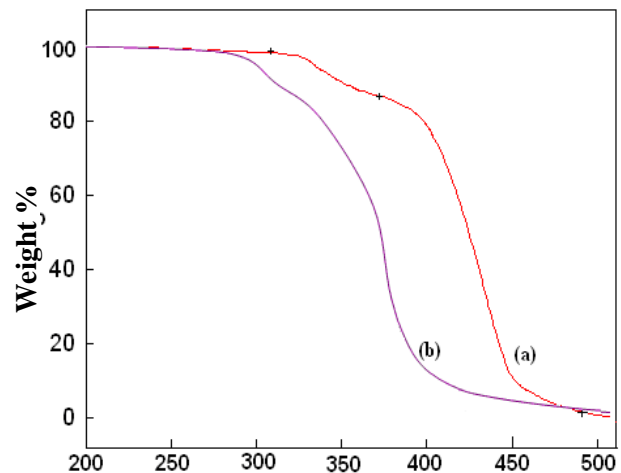


Figure 7: Thermograms TGA of PMMA (a) and of the photodegraded PMMA (b) under UV, $\lambda = 280\text{nm}$ $T = 180\text{jours}$

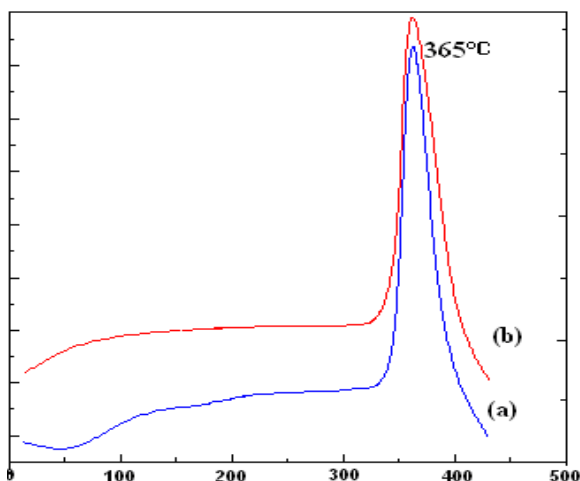


Figure 8: Thermograms DTA of the nanocomposite grafted with 1.5% ZnO (A) and photodegraded nanocomposite grafted with 1.5% ZnO (b) under UV, $\lambda= 280\text{nm}$ $t=180\text{jouis}$

4. CONCLUSION

The synthesis of PMMA grafted ZnO nanocomposites was successfully carried out by applying Znaidi method.

The spectroscopy study was in agreement with the literature data.

REFERENCES

- [1] Z.S. Wang, C.H. Huang, Y.Y. Huang, Y.J. Hou, P.H. Xie, B.W. Zhang, H. M. Cheng, A highly efficient solar cell made from a dye-modified ZnO covered TiO₂ nanoporous electrode, *Chem. Mater.* 13 (2001) 678–682.
- [2] H.M. Lin, S.J. Tzeng, P.J. Hsiau, W.L. Tsai, Electrode effects on gas sensing properties of nanocrystalline zinc oxide, *Nanostruct. Mater.* 10 (1998) 465–477.
- [3] J.Q. Xu, Q.Y. Pan, Y.A. Shun, Z.Z. Tian, Grain size control and gas sensing properties of ZnO gas sensor, *Sens. Actuators, B, Chem.* 66 (2000) 277–279.
- [4] J. Wu, C.S. Xie, Z.K. Bai, B.L. Zhu, K.J. Huang, R. Wu, Preparation of ZnO glass varistor from tetrapod ZnO nanopowders, *Mater. Sci. Eng., B, Solid State Mater. Adv. Technol.* 95 (2002) 157–161.
- [5] M. Singhal, V. Chhabra, P. Kang, D.O. Shah, Synthesis of ZnO nanoparticles for varistors application using Zn-substituted aerosol of microemulsion, *Mater. Res. Bull.* 32 (1997) 239–247.
- [6] M.L. Curridal, R. Comparelli, P.D. Cozzli, G. Mascolo, A. Agostiano, Colloidal oxide nanoparticles for the photocatalytic degradation of organic dye, *Mater. Sci. Eng., C, Biomim. Mater., Sens. Syst.* 23 (2003) 285–289.
- [7] V.P. Kamat, R. Huehn, R. Nicolaescu, A “sense and shoot” approach for photocatalytic degradation of organic contaminants in water, *J. Phys. Chem., B* 106 (2002) 788–794.
- [8] S.B. Park, Y.C. Kang, Photocatalytic activity of nanometer size ZnO particles prepared by spray pyrolysis, *J. Aerosol Sci.* 28 (1997) S473–S474 (Suppl.).
- [9] C. Feldmann, Polyol-mediated synthesis of nanoscale functional materials, *Adv. Funct. Mater.* 13 (2003) 101–107.
- [10] M.J. Zheng, L.D. Zhang, G.H. Li, W.Z. Shen, Fabrication and optical properties of large-scale uniform zinc oxide nanowire arrays by one-step electrochemical deposition technique, *Chem. Phys. Lett.* 363 (2002) 123–128.
- [11] R. Wu, C.S. Xie, Formation of tetrapod ZnO nanowhiskers and its optical properties, *Mater. Res. Bull.* 39 (2004) 637–645.
- [12] M. Kitano, M. Shiojiri, Benard convection ZnO/resin lacquer coating—a new approach to electrostatic dissipative coating, *Powder Technol.* 93 (1997) 267–273.

Induced Transboundary Waterborne Emission Savings as Result of National Environmental Policies: the Case of the Danish Packaging Taxation Policy

Enian Cela¹, Shinji Kaneko²

¹Hiroshima University, Japan (eniancela@hiroshima-u.ac.jp)

²Hiroshima University, Japan (kshinji@hiroshima-u.ac.jp)

ABSTRACT

The application of national environmental policies is bound to produce environmental consequences beneficiary to the regulation country. However, the benefits could spread to through various channels (like the trade channel) to partner countries as well. In this paper, we show how the paper/paperboard packaging taxation policy applied in Denmark induced waterborne emission savings in six partner countries: Germany, Norway, the Netherlands, Sweden, Finland and France. In the methodology, we combine econometrical modeling of Danish packaging imports and econometrical simulation of imports under “business as usual” scenario. Specific emission factors for BOD and COD are then applied to calculate the emission savings for each pollutant. Results reveal combined saving for the six countries in the amount of 12 thousand kg for BOD and 63 thousand kg in the case of COD for the period 2001-2007.

Keywords: packaging taxation, waterborne emissions, econometrical model.

1. INTRODUCTION

Water pollution remedy is considered as a critical issue in the European Union and member states. As a reflection of the Union’s seriousness to come to terms with water pollution and improved water quality stands the Water Framework Directive (EU WFD). According to this directive, the member states are to attain appropriate conditions for water resources by year 2015. Several national plans and measurement programs have taken place in the recent years until 2009 symbolizing an action towards the fulfillment of the directive (Kunkel et al., 2010) [1]. Another example is the Nitrate Directive which aims toward the prevention of water pollution from agricultural sources (Goodchild, 1998) [2].

In this paper, another point of view is analyzed. What we want to show is that also non-water pollution prevention measures could produce environmental benefits in the form of reduced waterborne emission. The benefits are not confined solely to the regulating country, but would spread through the trade channel to associated commercial partners as well. In this analysis, we are going to introduce the case of the Danish paper/paperboard packaging taxation policy intended to decrease the demand for

packaging which was enacted in 1999. By means of econometrical modeling, the study will show how the taxation policy affected the Danish imports of paper/paperboard packaging coming from Germany, Norway, the Netherlands, Sweden, Finland and France in the period 2001-2007. In the next step, applying emission factors for two waterborne pollutants namely BOD and COD, the saved emissions as a result of reduced exports from the six Danish partners are going to be commuted.

2. THE DANISH PACKAGING TAXATION POLICY

Denmark is one of the first countries to apply eco-taxation on packaging (Brisson,1992) [3]. The first taxes were applied as early as 1978 on the purchases of beverage containers (for both alcoholic and non-alcoholic). Later on, the taxation law was extended to include milk cartons. The major step however, was taken in year 1999 when the Danish government enacted policies to enable eco-taxation to cover the whole range of packaging. Taxation is applied in the form of product charges burdened on the packaging users with the purpose of reducing the demand for virgin packaging. Although taxation is set to cover all packaging categories for the precise purpose of preventing possible substitution manifestations, the charge rates vary

across the packaging groups. Life-cycle considerations were taken into account when choosing the different rates (ECOTEC, 2001) [4].

In the case of paper/paperboard packaging, an effective taxation policy would also produce positive environmental outcomes in the form of reduced waterborne emissions related to the production of paper and paperboard. Furthermore, should the policy affect Danish imports of paper/paperboard packaging (Denmark represents a predominant importer of the commodity), the benefits would spread to the exporting partners. The mechanism is quite simple: smaller Danish imports mean smaller exports from the trade partner, smaller exports mean reduced production; reduced production means smaller emissions of waterborne pollutants. In the next section, we are going to explain the applied methodology in our analysis.

3. POLICY ANNUAL IMPACT

In our former paper (Cela and Kaneko, 2011) [5], the effectiveness of the Danish taxation policy in the case of paper/paperboard packaging was confirmed by means of panel data econometrical modeling. A dummy variable capturing the taxation effect was included amongst the explanatory variables in a panel data explaining Danish imports of paper/paperboard packaging. The panel data included 13 cross-sections (exporting countries) and was conducted for the period 1994-2007 assuming taxation policy began application from 2001. The applied equation with obtained coefficients (all coefficients were statistically significant) is:

$$LNIMP = 1.30*lnSFBT - 0.93*lnRPRI - 2.18*lnDIST - 2.15*TI + 0.77*BOR - 0.54*TAX \quad (1)$$

IMP_{jt} – quantity imports from partner country j into Denmark in period t in kg;
 $SFBT_t$ – sales of the Danish Food, Beverage and Tobacco sector in real 2005 DKr and seasonally adjusted in period t ;
 $RPRI_t$ – price of paper and paperboard packaging imports in real 2005 DKr in period t ;
 $DIST_j$ – distance in km between Copenhagen and the partner country j capital;
 TI_{jt} – Denmark Trade Integration with partner country j at period t (dummy);
 BOR_j – common border between Denmark and partner country j (dummy);
 TAX_t – tax application on paper and paperboard packaging purchases in period t (dummy).

Now, we apply the equation results obtained to simulate annual exports from Germany, Norway, the Netherlands, Sweden, Finland and France (countries included in the panel data amongst the whole 13 cross-sections) assuming that Denmark never applied the taxation policy. These calculations were carried out for the period 2001-2007 when the taxation policy was in effect in Denmark. Furthermore we commute the differences between the actual annual import figures from each country and the simulated ones we obtained. These differences are shown in Table 1:

In the next section, we calculate the saved annual emission of BOD and COD in the case of each partner country.

Table 1: Annual differences between actual and simulated Danish imports by country (in kg)

Country/year	2001	2002	2003	2004	2005	2006	2007
Germany	-299,710	-420,026	-465,177	-391,313	-300,167	-308,371	-259,987
Norway	-307,426	-413,236	-504,210	-290,010	-95,005	-196,966	-142,649
Netherlands	-223,045	-290,336	-350,725	-442,731	-19,521	-171,797	-152,159
Sweden	-198,882	-45,412	-135,534	-177,992	-302,434	-197,217	-227,906
Finland	-18,619	-26,094	-28,899	-24,310	-18,648	-19,157	-16,151
France	-13,381	-18,753	-20,769	-17,471	-13,401	-13,768	-11,607

Note: negative sign shows that the actual imports were smaller compared to the simulated ones

4. SAVED WATERBORNE EMISSIONS

The Confederation of European Paper Industries provides each year the sustainability report

regarding pulp and paper production amongst the members of this establishment (the six countries subject of our analysis are member states). Reported data include information regarding the situation of

the paper economy, competitiveness, social affairs and environment (CEPI, 2009) [6]. In the section related to environment are reported data on the pollutants associated with pulp and paper production. The pollutants are divided into

waterborne and airborne. In the first category are included BOD, COD and AOX. Figures regarding specific emissions for each pollutant across the years are reported in table 2:

Table 2: Specific emissions related to pulp and paper production (kg per ton of paper produced)

Pollutant/year	2001	2005	2006	2007
BOD	1.68	1.03	0.99	0.93
COD	9.08	6.65	6.69	6.57
AOX	0.048	0.031	0.032	0.03

Source: CEPI, 2009.

From table 2, it can be observed that emissions of COD are more intensive compared to the other two pollutants. BOD is in second place, whilst pulp and paper production is comparatively non-intensive in terms of AOX pollution. For this reason, we decided to calculate saved emissions belonging to BOD and COD only. AOX was not included in the analysis.

We would remind that our economical analysis includes the period from 2001 until 2007 (the years when the Danish policy was applied). The differences between the actual and simulated import quantities for calculated for this period (Table 1). On the other hand, from Table 2 we can observe that specific emissions are not available for the years 2002, 2003 and 2004. In order to fill the gap,

we decided to apply the specific emissions of year 2001 for the period 2002-2004 in order to obtain the saved emissions figures.

For the calculation of the saved emissions we assumed that the quantities of paper and paperboard that “were not” exported as a result of the policy in Denmark, “were not” produced. Trade diversion possibilities are not taken under consideration. The annual saved emissions for each exporting country are commuted by simply multiplying the difference of exports (exhibited in table 1) with the specific emission factor of the pollutant in the respective year. The figures are reported in Table 3 with totals for each country:

Table 3: Annual saved emissions by country (in kg)

Country/year	2001	2002	2003	2004	2005	2006	2007	Total
BOD								
Germany	503	705	781	657	309	305	241	3,501
Norway	516	694	847	487	97	194	132	2,967
Netherlands	374	487	589	743	201	170	141	2,705
Sweden	334	762	227	299	311	195	211	2,339
Finland	31	43	48	40	19	18	15	214
France	22	31	34	29	13	13	10	152
Total	1,780	2,722	2,526	2,255	950	895	750	11,878
COD								
Germany	2,721	3,813	4,223	3,553	1,996	2,063	1,708	20,077
Norway	2,791	37,52	4,578	2,633	631	1,317	937	16,639
Netherlands	2,025	2,636	3,184	4,019	129	1,149	1,000	14,142
Sweden	1,805	412	1,230	1,616	2,011	1,319	1,497	9,890
Finland	169	236	262	220	124	128	106	1,245
France	121	170	188	158	89	92	76	894
Total	9,632	11,019	13,665	12,199	4,980	6,068	5,324	62,887

Source: Author calculations

Results from table 3 show that nearly 12 thousand kg of BOD and 63 thousand kg of COD pollution were saved in the combined six exporting countries as a result of the Danish policy. The bulk of emission saving was realized in the major exporting partners i.e. Germany, Norway, Netherlands and

Sweden with minor figures in the case of Finland and France.

5. CONCLUSIONS AND DISCUSSIONS

This paper represents an attempt to identify the impact that the Danish taxation policy on

paper/paperboard packaging had in terms of reducing waterborne pollution related to pulp and paper production on six trade partner countries. In the analysis, we took an import focused approach considering that country predominantly imports paper/paperboard packaging. Results revealed that an aggregate of 12 thousand kg of BOD and 63 thousand kg of COD were saved in Germany, Norway, the Netherlands, Sweden, Finland and France.

An important limitation to our analysis is the fact that this research was conducted for the first years when the Danish policy was applied (2001-2007). However, the policy impact could change in the further future. Determining the impact in the longer run could be an important next step of research. Nevertheless, the policy was effective in the short-run as we demonstrated. An additional important future aspect would be expressing emission savings in monetarized pattern.

REFERENCES

- [1] Kunkel, R., Kreins, P., Tetzlaff, B., Wendland, F. "Forecasting the effects of EU policy measures on the nitrate pollution of groundwater and surface waters", *Journal of Environmental Sciences*, 22,6, pp. 872-877, 2010.
- [2] Goodchild, R.G. "EU policies for the reduction of nitrogen in water: the example of the Nitrates Directive", *Environmental Pollution*, 102, S1, pp. 737-740, 1998.
- [3] Brisson, I. "Packaging waste and the environment: economics and policy", *Resources, Conservation and Recycling*, 8, pp. 183-292, 1993.
- [4] ECOTEC. "Study on the economic and environmental implications of the use of environmental taxes and charges in the European Union and its member states", Brussels: ECOTEC, 2001.
- [5] Cela, E., Kaneko, S. "Determining the effectiveness of the Danish packaging tax policy: The case of paper and paperboard packaging imports", *Resources, Conservation and Recycling*, 55, pp. 836-841, 2011.
- [6] CEPI. "Sustainability Report", 2009.

The Impact of Wind Farms on the Stability of Electric Networks

Issa Etier¹, Mohammad Abderrazzaq²

¹The Hashemite University, Electrical Engineering Department, 13115 Zarqa, Jordan.

²Yarmouk University, Hijawi Faculty for Engineering Technology, Irbid, Jordan

Corresponding author: etier@hu.edu.jo

ABSTRACT

Wind energy integration into distribution networks is currently an international trend. The achieved high penetration level of wind energy has changed the conventional view of wind energy role. The exclusion of wind energy from the studies, concerning steady state and abnormal conditions, is no longer acceptable approach to the decision makers in energy industry. In this paper, the main issues, related to the role of wind energy in keeping the power systems running efficiently and securely in normal and abnormal conditions, will be highlighted. The impact of wind energy isolation during the fault is determined. The role of advanced wind turbines in enhancing the weak distribution networks is assessed. The significance of wind in deregulated systems and privatization schemes is discussed. Finally, the recent development in communication system and its role in improving the integration of wind energy into local distribution networks will be summarized.

Keywords: *Wind Energy, Wind Turbine, Wind Farm, Grid connected.*

1. INTRODUCTION

With increasing demand for clean energy, wind power seems to stand out as a global success story. On the other hand, the continuous fluctuation in oil prices in response to wars and political instabilities has made the Wind Turbines (WTs) the fastest growing energy source in the world. Wind power's dominance has been so significant that advocates are now gathering around an idea that would have seemed fantastic just a couple of years ago: that the wind would supply 12% of the world's electrical demand by 2020 [1]. The fear of high dependence on wind energy is no longer exists because the new systems are based on advanced power electronics and energy storage devices which assist in managing power flows from WTs. This arrangement enables the wind systems to contribute mightily to electricity grids without putting those grids at risk. The current technology improves the wind energy in two directions: firstly by making the wind power more portable to grid operators and by making it possible for engineers to exploit the wind resources in remote locations.

2. GENERAL REQUIREMENTS FOR GRID-CONNECTED WIND ENERGY SYSTEM

With the increase in number and size of WTs, wind farms have grown to include dozens of turbines and hundreds of megawatts- reaching the size of conventional power plants. To encourage the acceptance of installations like those, power system operators had to fight with the tendency of WTs to introduce voltage instability into electrical grids. That tendency follows from the intermittent nature of wind-generated electricity, which directly affects the daily prediction and forecasting the consumer demand.

To understand the issues of the system's instability and the related solutions, one needs a few basics on the nature of power flows on utility grids. On the other hand, declining voltage on a network is a function of the consumption of both active and reactive power. This means that if a large load consumes significant amount of reactive power, it will cause the voltage to dip immediately unless the reactive load is adequately compensated for. The compensation can be achieved by supplying reactive power directly from the generators themselves or by installing banks of capacitors close to inductive loads. It is easy to understand the relationship of these issues to wind energy if we remember that most of the current WT generators are of induction type, which consumes a considerable amount of reactive power.

Generally, utilities require that wind farms should be able to provide dynamic reactive compensation, exactly as a conventional generator would be able to do. This means that these wind systems should be able to assist in restoring stability during a disturbance or some other crisis on the grid. In the past, when a generator failure or a momentary short-circuit occur, wind farms would automatically disconnect themselves. But now, most grid operators prefer keeping these WTs running during the disturbance events. As a response to this operational progress, wind farms and turbine developers must modify their designs and operating procedures to cope with these requirements, particularly for voltage faults.

Concerning the power quality problems, it is worth mentioning that the new models of MW class WTs have less effect on power quality issues such as harmonics, voltage flicker and voltage dip. The advanced technology, adopted for modern wind energy generation, has enabled the manufacturer to limit the

power quality problems and to be in harmony with international standards and grid codes. The regular inspection and testing schemes of the wind-generated power give a chance to correct any deviation in the power supply.

3. SPECIFIC REQUIREMENTS FOR WIND ENERGY CONNECTION TO GRID

3.1 Behavior during the fault

In systems with significant wind energy resources, the nature and role of such energy has been changed in the last two decades. The power systems did not depend on the energy generated by WTs, which were small in size and limited in contribution at that time. Under these circumstances, the behavior of WT at faults was not critical and the simple control systems, equipped with these turbines, were efficiently able to disconnect these machines from the network immediately when the fault occurs.

Currently, the WTs are large in size and the capacity of new wind farms can attain hundreds of megawatts. They are distributed on large areas as shown in Figure 1.

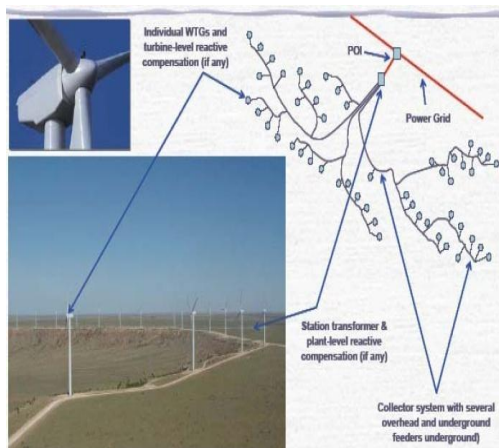


Figure 1: Typical wind farm layout

The disconnection of WTs due to a fault in nearby feeders is no longer preferred. It is desirable to keep the WTs running during the faraway faults. This arrangement reduces the chance to cause consequential loss of generation, which might lead to a voltage collapse. This requirement implies that the new generation of WTs should be able to keep running with voltage dips caused by faults in remote feeders. A series of load flow and short circuit calculations were made to study the impact of wind energy on the local distribution networks. Figures 2-4 show the dependence of voltage dip on the distance of fault location in a typical radial distribution system. Figure 2 illustrates the disturbance effect when a fault on the same feeder connected to induction generators occurs, whereas Fig.3 shows a very slight voltage variation in a remote busbar

due to a short circuit applied at different locations on the induction generator feeder.

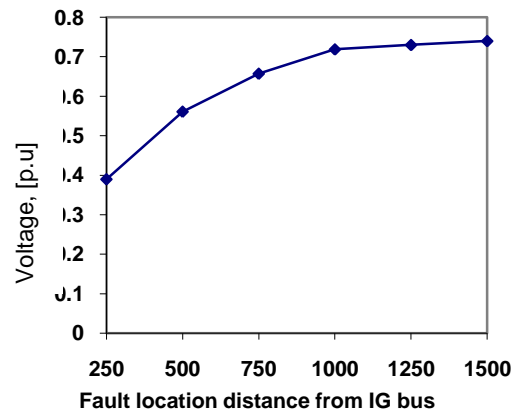


Figure 2: the impact of fault location on the voltage of the same feeder where the wind turbines are connected

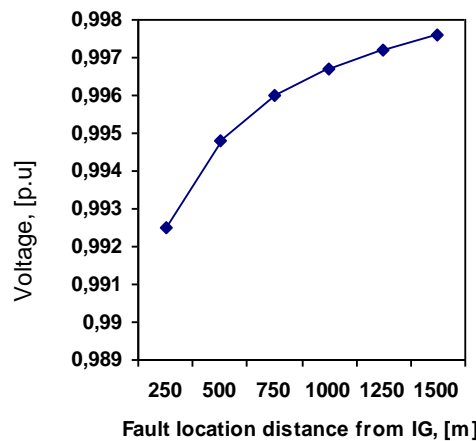


Figure 3: The impact of fault location on the voltage of a remote busbar (short circuit applied at different locations on the induction generator feeder).

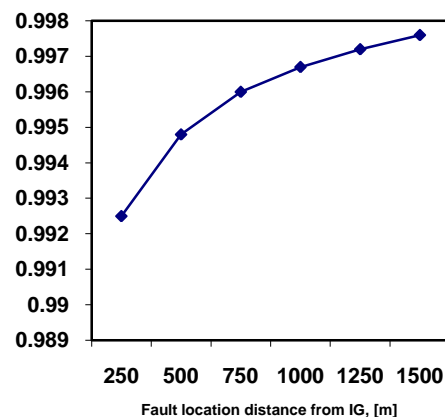


Figure 4: Recovery after the fault

Regarding the behavior during the short circuit, it is worth mentioning here that the induction generator characteristics are closely dependent on the deviation between the rotor speed and the synchronous speed.

This leads to the fact the stator current increases very rapidly when the motor slip frequency increases.

3.2 Post fault behavior

Two important factors can affect the speed of recovery of wind machine after the fault; the demagnetization and the negative slip due the increase in rotor speed. The impact of the first factor depends on the strength of the electric network to which the WT's are connected. On the other hand, if the short circuit duration is relatively long and the magnetization process of the induction machine is slow, the generator speed increase becomes significant. Therefore, to improve the induction generator response to the system disturbances including short circuits and to successfully recover from the fault, it is necessary to build a fast process of magnetization so that it can produce torque and reduce the generator over speed.

3.3 Frequency and voltage control

Voltage and frequency control, during load variations, mainly depends on the behavior and the parameter adjustment of the voltage and speed regulators of the generation units. With the increase in the number of WT's, it becomes difficult to control the node voltages adequately by only using the synchronous generators in large-scale conventional power stations. Therefore, it is essential that all WT's also contribute to voltage control. The fact that the voltage is not the same throughout the system makes it a local quantity, as opposed to frequency, which is a global quantity, because it is identical in the whole system. Voltage problems must always be solved at or in the vicinity of the node at which the problem occurs, as opposed to frequency problems that can be solved everywhere, provided that no branch over loadings occur. The WT's distributed over a wide area and in different locations can be of great importance in this field [2]. On the other hand, the increasing of wind energy penetration can cause an overvoltage to some bus bars, if these turbines operate simultaneously. However, the probability of a simultaneous operation of WT's is very low even during the gust on a certain wind farm. When it is not possible to keep all node voltages in the system within the allowed deviation from their nominal values from the synchronous generators, other technologies must be used, such as capacitor banks, SVC's or STATCOMs.

Since the current power systems are still depending on massive generation units to produce the required electricity, the outage of these plants is usually associated with serious problems ranging from the usage of the expensive emergency reserve units to applying the load shedding scheme. The categories of the load-shedding scheme are based on the importance of the load to be shed. Usually, the rural residential loads are classified in many countries as less important loads, which are switched off first in order to improve

the frequency level. However, the presence of large-scale WT's can assist the frequency control in two ways. Firstly, wind energy can reduce the shortage in conventional generation and consequently lower the rate at which the frequency starts to decay. Secondly, WT's in windy sites can quickly restore the supply to the remote locations after load shedding. If the wind speed is increased by 2 folds the power generated from the wind turbine will increase by 8 folds according to the following equation

$$P = \frac{1}{2} \rho C_p A V^3 \quad (1)$$

Where, P is the output power in kW, ρ is the air density kg/m^3 , C_p is the power coefficient, A is the swept area in m^2 and V is the wind speed in m/s.

4. WIND TURBINES AND SYSTEM STABILITY

4.1 Dynamic behavior of wind turbines

Different models have been proposed to study the dynamic behavior of the WT's [3]. With the classical approach, the wind farm terminal voltages have recovered quickly, whereas with the physical model various oscillations were noticed in the terminal voltages. It is worth noting that the overspeed of WT's as a consequence of the fault was not high enough for the turbine to be disconnected and stopped by the protection system. The rotor speed was slightly decreased when subjected to the fault and thereafter increases in speed. If the overspeed is significantly low, the protection system of WT's does not react immediately. The presence of large-scale wind farms with high capacities in one location can have a bad effect on the system stability during the fault. Naturally, the windy sites are distributed in different locations in each country, which can be employed to enhance the system stability and prevent the voltage collapse.

4.2 Wind energy influence on voltage stability

Various studies have been performed to analyze the impact of wind energy on voltage stability [4,5]. The active and reactive powers are the main parameters used in the assessment of voltage stability limits. In all cases it has been concluded that voltage stability depends mainly on the network characteristics. Therefore, the distribution lines, known by their losses can be operated in more stable way with WT's. The later are characterized by their active power injected to the system and consequently an increase of system voltage at the terminals of these turbines. This voltage increase can compensate the reduction due to reactive power demanded. In the current work a typical radial distribution system was examined to assess the network transient behavior when a three-phase fault is applied to

an 11kV line. Figure 3 shows the voltage variation and the fast recovery after the transient.

5. WIND ENERGY AND DEREGULATION

The tendency toward deregulation and privatization policies is gaining ground nowadays. This process goes in harmony with the distribution generation schemes, which consists of various sources generation including wind energy and other renewables. The companies operating these new plants try to limit the expenses on the engineering part and to run these plants as simple as possible. Therefore, the conventional power plants are not preferred choice for these new systems and many of them strongly support the installation of large-scale WTs. On the other hand, wind energy plants are easy to own, operate and maintain by small companies and local communities. In addition to the environmental considerations associated with wind energy, many small utilities and local communities have created new tariff schemes to encourage the customers to purchase the energy from WTs.

6. WIND ENERGY AND TECHNOLOGICAL DEVELOPMENTS

Advanced current design standards and certification rules have been positively reflected on wind energy development. Therefore, remarkable advances in wind power design have been achieved. One aspect of WTs that will increase rapidly is the use of information technology and sophisticated communication systems for the real time monitoring and control. No other commercial plant is operated remotely in this way [6]. This development will improve the protection and control systems of these turbines and consequently enhance the networks' stability. Moreover, the parallel progress in wind energy prediction will encourage the utilities to include more WTs in their local networks and enhance the weak grids significantly.

7. MAXIMIZING THE ROLE OF WIND FARMS

Wind resources must be adequate to be commercially viable. Moreover, the commercial outcome is very sensitive to wind speed, thus siting is important. The presence of strong transmission system is important to maximize the wind energy penetration. On the other hand, WT starting and stopping transients and power fluctuations during operation must not lead to unacceptable voltage or frequency fluctuations, excessive load-following costs or excessive wear and tear on turbine components. Wind farm designers and network service providers must avoid unsatisfactory network voltage profiles and protection problems due to either excessive or insufficient fault level. The prediction of wind farm production must be sufficiently accurate to avoid unnecessary network investment or generation reserve requirements and to satisfy wind farm investment risk management criteria. The new

system operators try to benefit from installed wind turbines as much as possible by concentrating on improving the efficiency, reducing the losses and developing new models of wind speed prediction. The concentration is mainly on the short term prediction of wind energy to facilitate commercial tools for such energy. This trend is becoming more and more important with the continuous reduction and shortage of conventional resources.

Finally, the current developments in communications, information technology will enhance the new role of wind energy in electrical system stability. The data exchange and remote operation of wind farms become an easy task with the development of wireless communication system and fiber optics techniques.

8. CONCLUSION

The technical impact and stability issues concerning the connection of large-scale wind turbines to a typical network were discussed. The load flow and fault studies have illustrated that the voltage dip initiated by induction generators decreases significantly as the fault location distance increases. Regarding the dynamic response of the machine during transient conditions, it was shown that a complete recovery was achieved quickly. The distribution of WTs in different locations enhances the voltage and frequency stability of the system. The load shedding schemes in networks with high wind energy penetration must benefit from the existing WTs and modify these schemes accordingly. On the other hand, the trends of systems restructuring and deregulations give a potential to large scale wind energy schemes.

REFERENCES

- [1] P. Fairley, "steady as she blows", electric power, IEEE Spectrum, 2003.
- [2] T. Tomson, "Wind power grid matching problems. The Estonian case study", EWEC 2001, pp.1007-1009.
- [3] V.Akhmatov et al., Electrical Power and Energy Systems, 22 (2000), 421-434.
- [4] Popvic, Hiskins and Hill, "Stability of induction motors networks", Electrical power and energy, Vol. 20 No.7, 1998, pp. 475-487.
- [5] Andres Feijo and Jose Cidras, "Modeling of Wind Farms in the Load Flow Analysis", IEE Transactions on power systems, Vol. 15 No.1, 2000.
- [6] James and James, "Renewable energy world. Technology update, wind power". Science publishers, UK, Vol 2 No.1, January 1999, p 45.

A Comparative Study of Vapour Compression Refrigeration Systems under Air to Air and Air to Water Mode

Kemal Çomaklı¹ and Uğur Çakır²

¹ Atatürk University, Eng. Faculty, Mechanical Eng. Dep. Erzurum/TÜRKİYE kcomakli@atauni.edu.tr

² Bayburt University, Eng. Faculty, Mechanical Eng. Bayburt/TÜRKİYE ucakir@bayburt.edu.tr

ABSTRACT

The use of energy in the buildings for heating and cooling is nearly one third of the total energy consumed on the World. As there is growing concern it the use of fossil fuels that is being depleted soon and because of sustainability issue an alternative energy source must be found to meet the heating/cooling energy need of buildings. This situation made the researchers to study on the systems those use the energy more efficiently, more economically and decrease the cost of energy like heat pump system. In this paper an experimental performance study was made on a traditional vapor compressed refrigeration system that can be run air to air mode and air to water mode by help of a valve. The experiments made under different thermal conditions. Thermodynamic performance of systems are presented and compared with each other for different working conditions.

Keywords: Heat Pump, Energy Analysis, Air source heat pump

1. INTRODUCTION

Heat pump systems are used for heating or cooling applications in buildings due to their high energy effectiveness and reliability. The technical and thermo physical characteristics of heat source or heat sink used directly have a big important role on the technical and economical performance of heat pumps. The heat sources and heat sinks which are commonly used or preferred in practical applications are ambient air, lake water, river water, soil, rock, and wastewater, affluent and exhaust air.

The heat pumps which use water as heat source are have attractive performance characteristics when designed and installed properly. Additionally those systems are considered a viable alternative to conventional cooling and heating systems. They offer many performance advantages over air-source heat pumps due to outstanding heat transfer properties of water and much more favorable temperatures of river or lake water. The advantages and disadvantages of water-source heat pump systems are discussed previously by several researchers [1-5].

The most common used heat source for heat pumps is ambient air. Ambient air is free, widely available and can be found in everywhere. However, the capacity and performance of air-source heat pumps decrease rapidly with decreasing ambient temperature during heating season, and with increasing ambient temperature during cooling season.

Although, a simple heat pump system consists of four main components, which are compressor, two heat exchangers (condenser and evaporator) and expansion valve, many auxiliary components may be used on heat pumps such as valves, thermostats, some measurement

tools, pumps, fans, or extra heaters. The main structure and the type of new heat pumps have changed very much due to the improving technology and changing thermal demands all over the world. The properties of the components used on heat pumps are affective on the performance and on the thermodynamic behavior of heat pumps. In addition, the thermal characteristics and types of the heat sources and heat sinks are very important for the performance of heat pumps.

Heat Pump systems are available in array of types and combinations that can suit almost any application. For heating purposes, they can be divided into basic types, determined by the source and the destination of the heat and the medium that the heat pump uses to either absorb or reject the heat in each of these locations. At either of the heat exchangers the heat transfer media can be either liquid (water, or often a glycol mixture) or air; sometimes it is a combination of the two. In describing the type of heat pump, generally the heat source is generally provided first, followed by the destination or heat sink. The main variants in common use are; air to air, water to water, water to air, air to water, ground to water, ground to air types.

Efficient energy utilization is one of the foremost issues on the world for the environmental and ecological protection at these days. It has become a concern because of environmental and energy problems like global warming, the depletion of conventional energy sources like fossil fuels and the increasing cost of energy. Additionally; the big portion of energy used on the world is consumed at heating and cooling applications in the residential and other buildings or in industrial plants. According to the recent studies, the energy used for residential and construction activities make up about 40% of the world's total energy consumption and heating and cooling applications have

a key role in it [1-3]. Efficient energy use, including waste heat recovery and applications of renewable energy can reduce carbon dioxide emission and global warming. One of the heating setups which offer more economic and more efficiently heating applications is heat pump system which is promising means of reducing the consumption of fossil energy resources, and hopefully the cost of delivered energy for residential heating/cooling. Heat pumps are advantageous and widely used systems in many applications due to their high utilization efficiencies compared to conventional heating and cooling systems. Those systems first emerged in 1940-1950s and have some advantages when compared with conventional or traditional heating systems. Heat pump systems do not produce exhaust gases while heating any space and use less energy than other systems. In addition, heat pumps are capable to use the abundant natural resources such as air source, geothermal source, waste heat and the heat of the soil.

However, a simple heat pump system consists of four main components, which are compressor, two heat exchangers (condenser and evaporator) and expansion valve, many auxiliary components may be used on heat pumps such as valves, thermostats, some measurement tools, pumps, fans, or extra heaters. The main structure and the type of new heat pumps has changed very much due to the improving technology and changing thermal demands all over the world. The properties of the components used on heat pumps are effective on the performance and on the thermodynamic behavior of heat pumps. In addition, thermal characteristics and the types of the heat sources and heat sinks are very important for the performance of heat pumps. Commonly used heat sources and heat sinks are ambient air, exhaust air, lake water, river water, ground water, earth, rock, wastewater and effluent. Most used heat sources and heat sinks on heat pump systems are ambient air and water around the world.

Ambient air is a widely available and a free heat source for heat pumps. However, the thermodynamic performance of air source heat pump systems decrease depend on the decreasing the temperature of air in the heating seasons and increasing the temperature of air in cooling seasons. Because of the heat transfer properties of water, water source heat pump systems offer some performance advantages over heat pump systems which use air as heat source. Heat Pump systems are available in array of types and combinations that can suit almost any application. For heating purposes, they can be divided into basic types, determined by the source and the destination of the heat and the medium that the heat pump uses to either absorb or reject the heat in each of these locations. At either of the heat exchangers the heat transfer media can be either liquid (water, or often a glycol mixture) or air; sometimes it is a combination of the two. In describing the type of heat pump, generally the heat source is generally provided first, followed by

the destination or heat sink. The main variants in common use are; air to air, water to water, water to air, air to water, ground to water, ground to air types.

Because of the fact that; utilization of heat pump has been is spread over the world as a result of the improvements and developments on it, the structure of heat pumps, types and the sizes of the components used on heat pump systems has changed very much and in the light of these developments, modern and more complicated heat pump systems have been came out at the last years. For that reason, it is necessary to make a comprehensive thermodynamic performance and economic comparison among different types of heat pumps to determine which of them is better in which case according to their heat sources and sinks as water or air.

Many studies and investigations have reported in the open literature on different types of heat pumps and on comparison of them experimentally or by simulations, according to their heat sources, heat sinks, and the place they are being used, the refrigerant used as working fluid, structures and capacities of components i.e. [6-12]. For example; Swardt and Meyer [6] made a study on that, the performance of a reversible ground-source heat pump coupled to a municipality water reticulation system was compared experimentally and with simulations to a conventional air-source heat pump for space cooling and heating. The experimental and simulated comparisons of the ground source system to the air source system were conducted in both the cooling and heating cycles. The results showed that, the utilization of municipality water reticulation system a heat source/sink is a viable method of optimizing energy usage in the air conditioning industry, especially when used in the heating mode.

Bakırcı et al. [7] made a study in order to investigate the performance of the solar-ground source heat pump system in the province of Erzurum having cold climate. The COP of the heat pump and the system were found to be in range of 3.0-3.4 and 2.7 to 3.0, respectively. It is also claimed that; the system investigated could be used for residential heating in the province of Erzurum being a cold climate region of Turkey. Urchueguia et al. [8] made an experimental comparison between a ground coupled heat pump system and a conventional air to water heat pump system, focusing at the heating and cooling energy performance. For whole climatic season the results obtained demonstrated that, a ground source heat pump system is viable and energy efficient alternative to conventional systems for heating and cooling applications in the South European regions. Heat pumps systems are compared according to their thermodynamic performances depend on the used refrigerant type in most of the comparative studies. Venkataramanmurthy and Kumar [9] made a study which presents an experimental comparison of energy, exergy flow, and second law efficiency of R22 and is

substitute R436b (hydrocarbon mixture of 52% of propane (R290) 48% of isobutene (R600a)), vapor compression refrigeration cycles. The energy flow of various points on refrigeration cycle, efficiency and second law efficiency for both R22 and R436b refrigeration cycles were compared. The results were presented graphically that shows the location of in efficiencies. Petit and Meyer [10] made a comparison of the economical viability in South Africa of horizontal-ground source systems and air-source systems. In order to realize this aim, monthly heating and cooling capacities and coefficients of performance for both systems were determined. The payback period, net present value, and internal rate of return of systems were calculated. It was concluded that, ground source systems are more viable than air source systems.

In this paper an experimental performance study was made on a traditional vapor compressed refrigeration system that can be run air to air mode and air to water mode by help of some valves. The experiments made under different thermal conditions. Thermodynamic performance of systems are presented and compared with each other for different working conditions. In order to achieve this aim, the multifunctional heat pump experimental setup, which can be operated in two different modes, including air to air, air to water, modes, was installed in the laboratories of Mechanical Engineering Department of Atatürk University in Erzurum, Turkey. The direction of refrigerant fluid used in the system can be easily changed between the condensers and evaporators with the help of valves. In this way the designed heat pump experimental setup can be operated in different modes.

2. EXPERIMENTAL SET UP AND ANALYSIS

Fig 1 shows the schematic diagram of the experimental apparatus. The system was originally designed for operating with R22. The main components of the system are a scroll compressor, an air cooled evaporator, an air cooled condenser, a water cooled condenser, thermostatic expansion valve, and the other elements like measurement and control equipments. In addition electrical air and water heaters are used in order to keep the temperature of air and water passing into the evaporator and condensers at the desired levels. Two electrical fans are used to circulate the air on the evaporator and condenser which is air cooled.

First, the system was charged with 15 Bar R22 while all the valves were in opened position under the temperature of outdoor air and then system was run in wanted heat pump mode by closing interested valves. When the running mode wanted to be changed, all of the valves were opened and waited for one day to obtain equal spreading of refrigerant in the system for every mode. Temperature and pressure values in the key-point of the plant, as shown in Fig. 1, were continuously monitored in order to check the achievement of steady-

state conditions. Usually, the start-up time required about 1 hour. After each experimental run, the raw data which consist of temperatures from the thermocouples, pressures from the manometers, air flow rates from the anemometer, and refrigerant flow rate from the flow meters, water flow rates from the rotameters, compressor input current and voltage from the ampermeter were recorded.

The tests were performed under laboratory conditions, during the air temperature was about 20-22°C, and the relative humidity was about 40-60%. The tests were made under the following order for four running mode; first air to air mode, secondly air to water mode, tests were completed. Each experiment was repeated at least three times under same conditions at different times. When all tests were made and completed for each running mode, the experimental setup was closed and waited about two days with opening all valves on it before starting the tests for another running mode.

First, the temperature degree and flow rate of the condenser fluid were fixed to the constant values; 20°C-1.2 kg/s for air, 20°C-0.15kg/s for water. And then the experiments were performed at five different temperature levels for five different flow rate values of evaporator fluid. For example first, the flow rate of evaporator air adjusted to a constant value and the tests were performed for five different evaporator fluid temperatures and then the same procedure was applied for other experiments. The numerical values of the evaporator air temperatures and flow rates are presented in Table 1 for two heat pump tests.

All of the measured values which consist of temperatures from the thermocouples, pressures from the manometers, compressor input power from the wattmeter, and flow rates of the fluids used on the system from the flow meters, rotameters and anemometers were used for determining the thermodynamics performances of two heat pump modes to achieve the aim mentioned previously.

Mass and energy balances are employed to determine the heat input, and energy efficiencies. From the measured parameters; the heat delivered by the condenser to the air or water is calculated by

$$\dot{Q}_{\text{con-air}} = \dot{m}_a C_a (T_{\text{ca out}} - T_{\text{ca in}}) \quad (1)$$

$$\dot{Q}_{\text{con-water}} = \dot{m}_w C_{cw} (T_{\text{cw out}} - T_{\text{cw in}}) \quad (2)$$

The heat extracted by the evaporator from the air is calculated by

$$\dot{Q}_{\text{evap-air}} = \dot{m}_a C_a (T_{\text{ea in}} - T_{\text{ea out}}) \quad (3)$$

The power input to the compressor is calculated by

$$\dot{W}_{\text{Comp elec}} = \sqrt{3} \cdot \text{Cos}(\phi) \cdot U \cdot I \cdot W \quad (4)$$

Where U, I and Cos (φ) are voltage (V), current (A) and power factor, respectively. The coefficient of performance (COP) for any heat pump and system

$$COP_{HP} = \frac{\dot{Q}_c}{\dot{W}_{comp,elec}} \quad (5)$$

$$COP_{sys} = \frac{\dot{Q}_c}{\dot{W}_{comp,elec} + \dot{W}_{Fan}} \quad (6)$$

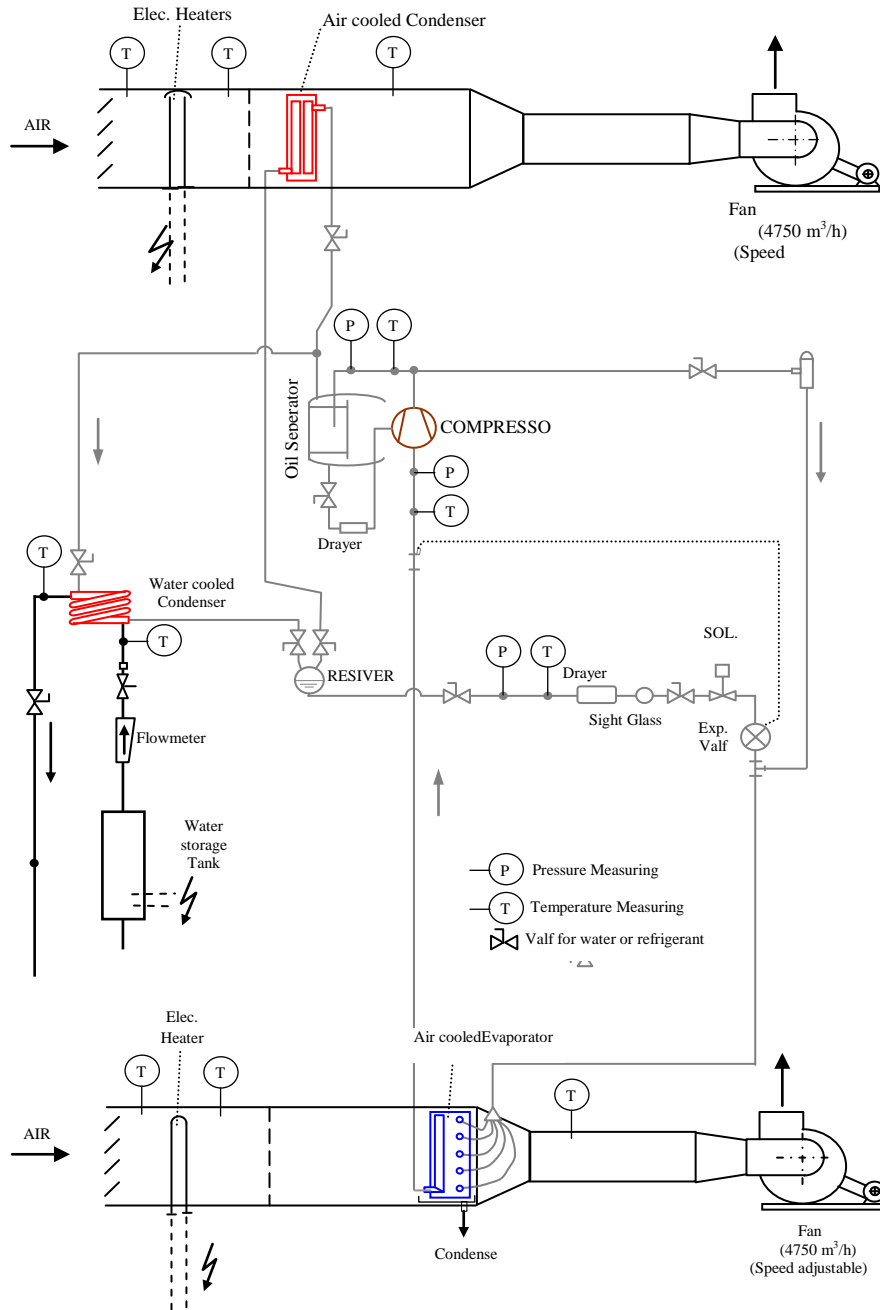


Figure 23: Experimental system

Table 1: Levels of parameters

Parameter	Fluid	Level 1	Level 2	Level 3	Level 4	Level 5	Level 6
Mass flow rate (kg/s)	Cond/ Evap. Air	0.41	0.71	0.83	1.1	1.2	---
	Cond. Water	0.100	0.110	0.125	0.139	0.15	----
Temperature (°C)	Evap. Air	20	22	26	28	30	32

3. RESULTS

Two different heat pump systems those run on the same experimental setup, have same heating capacity, use just one compressor, controlled by the same control equipments and the same measurement system are analyzed and compared experimentally. They are compared with each other by using energy balances-first law of thermodynamics in this study. All of the experiments were performed under the same conditions as the air temperature and air humidity ratio in the laboratory. Within the scope of the study presented here; COP of heat pump types are evaluated, discussed and compared as the results of this paper. Differences of energetic performance of two different heat pump types according to the increasing rate of temperature and flow rate of the fluid used as heat source is expressed and compared.

Figure 2 and 3 shows the change of COP values of two heat pump units and systems according to the increasing rate of temperature of the air as heat source. As seen on the Figure 2, the heat pump unit which has the maximum COP value is air to air type. It is known that COP of heat pumps increases when the temperature of heat source increases. As seen on the related figures, performances of the two heat pumps increase when the evaporator air temperature increase.

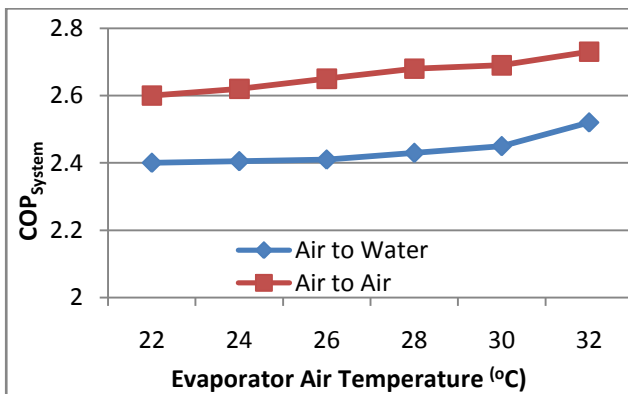


Figure 2: COP change of heat pumps versus increasing of evaporator fluid temperature

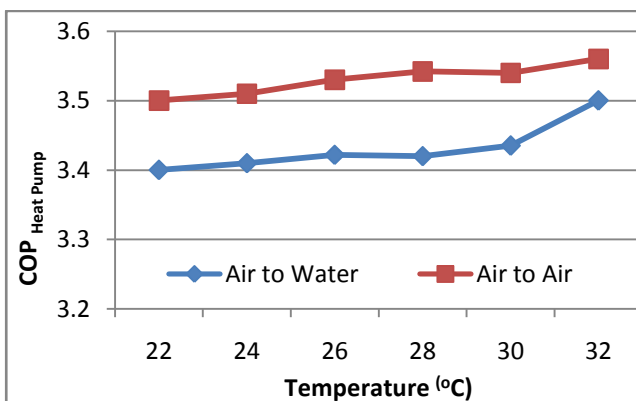


Figure 3: COP change of systems versus increasing of evaporator fluid temperature

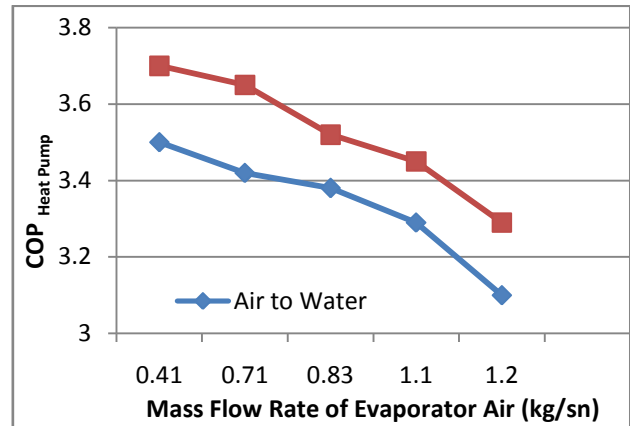


Figure 4: COP change of heat pumps versus increasing of mass flow rate of evaporator fluid

Mass flow rate of the fluid used as heat source has a big importance for the performance of heat pumps. It is understood from the Figure 4 that, COP of the heat pumps which use air as evaporator fluid (air to air and air to water) are decreasing with the increasing of the mass flow rates of the fluid used as heat source. Experimental uncertainties were calculated by using the estimation method of Kline and McClintock [13], maximum uncertainties of the COP is found as 3.53%. The individual contributions to the uncertainties of the COP for each of the measured physical properties are summarized in Table 2.

Table 2: Uncertainties in the values of the relevant variables.

Variables	Uncertainty (%)
Temperature (T)	2.5
Pressure (P)	1.6
Voltage (U)	1.7
Current (I)	1.7
Power factor (Cosφ)	1.7
Mass flow rate (m _r)	1,3

4. CONCLUSION

There are various studies on comparison of different heat pump types. The comparisons made between the systems, installed at different places, used for different aims, use different refrigerants as working fluid, run and tested under different conditions, have different heating capacities or have different specifications. In this study, an experimental multifunctional heat pump setup was designed to make a comprehensive comparative investigation for two different heat pump types; they have same heating capacity and same specifications. The direction of refrigerant fluid used in the system can be easily changed between the condensers and evaporator with the help of valves. In this way the designed heat pump experimental setup can be operated in different modes. Heating capacity of each heat pump mode is equal under the same conditions and can be adjusted by changing the flow rate and temperature

levels of the fluid used as heat source and sink. Only one measurement system was used to get data for all heat pump types and all experiments.

The temperature degree of heat source has a big importance for using heat pumps efficiently. The heat pump units are designed for the various thermal applications have specific properties in general and therefore they are unique setups. In summary, they provide high levels for comfort, make significant reductions in electrical energy consuming and they are friendly systems for the nature. As seen on the figures in the results previously, COP of the air to air heat pump is higher than COP of the air to water heat pump in generally. The COP values of two heat pumps are affected from the increasing of evaporator air temperature. COP of the heat pumps decrease, when the mass flow rate of the evaporator air increases.

REFERENCES

- [1] Büyükalaca O, Ekinci F, Yılmaz T. Experimental investigation of Seyhan River and Dam Lake as heat source-sink for a heat pump. *Energy* 2003;28(2): 157-69
- [2] S.P. Kavanaugh, Design considerations for ground and water source heat pumps in southern climates. *ASHRAE Trans*, **95** 1 (1989), pp. 1139-1149.
- [3] S.P. Kavanaugh, J.G. Woodhouse and J.R. Carter, Test results of water-to-air heat pumps with high cooling efficiency for ground-coupled applications. *ASHRAE Trans*, **97** (1991), pp. 895-901.
- [4] S.P. Kavanaugh and M.C. Pezent, Lakewater applications of water-to-air heat pumps. *ASHRAE Trans*, **96**1 (1990), pp. 813-820.
- [5] ASHRAE systems and equipment handbook (SI); 1992[chapter 47].
- [6] De Swardt C A, Meyer J. P.A. Performance comparison between an air-source and a ground-source reversible heat pump. *Fuel and Energy Abstr* 2002;43(4): 285
- [7] Bakirci K, Ozyurt O, Comakli K, Comakli O. Energy analysis of a solar ground source heat pump system with vertical closed loop for heating applications. *Energy* 2011;36(5): 3224-32
- [8] Urchueguía JF, Zacarés M, Corberán MÁ, Martos J, Witte H. Comparison between the energy performance of a ground coupled water to water heat pump system and air to water heat pump system for heating and cooling in typical conditions of the European Mediterranean coast. *Energy Conve and Manag* 2008;49(10): 2917-23
- [9] Venkataramanmurthy VP, Kumar Senthil P. Experimental comparative energy, exergy flow and second law efficiency analysis of R22, R 436b vapour compression refrigeration cycles. *Int J Eng. Sci* 2010;2(5): 1399-1412
- [10] Petit PJ, Meyer JP. A techno-economic analytical comparison of the performance of air source and horizontal-ground-source air-conditioners in South Africa. *Int J Energy Res* 1999;21(11): 1011-21.
- [11] Çakır U. Exergetic comparison of heat pumps according to fluids used in the condenser and evaporator. 2011. Ph. D. Thesis, Atatürk University Graduate School of Natural and Appl Sci Dep of Mechanical Eng.
- [12] Comakli K, Simsek F, Comakli O, Sahin B. Determination of optimum working conditions R2 and R404A refrigerant mixtures in heat-pumps using Taguchi method. *Appl Energy* 2009;86(5): 2451-58
- [13] Kline SJ, McClintock FA. Describing uncertainties in single-sample experiments. *Mech Eng* 1953;75:3-8

Energetic and Exergetic Comparison of Water-Water and Water-Air Heat Pumps

Uğur Çakır¹ and Kemal Çomaklı²

¹ Bayburt University, Eng. Faculty, Mechanical Eng. Bayburt/Türkiye (ucakir@bayburt.edu.tr)

² Atatürk University, Eng. Faculty, Mechanical Eng. Dep. Erzurum/Türkiye (kcomakli@atauni.edu.tr)

ABSTRACT

Heat pumps have been widely used for years in developed countries due to their higher energy utilization efficiencies than those of both conventional heating and cooling systems. In this study an experimental energetic and exergetic comparison of a heat pump system that can be run in different modes as water-water and water-air was made. System components do not change when the running mode changes except evaporator. That means some external and internal effects (like compressor type, pipe lines) can affect the system performance will be same for each running mode. That situation gives us an opportunity to have more real and more reliable thermodynamic comparison of those systems. The aim of this comparison is to demonstrate that; which system leads to more efficient energy conversion and supply of energy and exergy. In the analysis four balance (mass, energy, entropy and exergy) equations are applied to the system for two modes. Exergy and energy efficiency values for both systems are given, while exergy destructions in each of the system are determined and presented.

Keywords: Energy analysis, Exergy analysis, Heat pump, Water source heat pump

1. INTRODUCTION

Using energy more efficiently has become an important concern due to environmental and energy problems, such as global warming and the depletion of fossil fuels. That means, energy supply of the world must become more sustainable. This can be achieved by two ways. First one of them is to improve conventional energy conversion systems or to bring in to new systems to use existing energy sources more effectively. Cogeneration system is an example for that way. The second way is to find out new or alternative energy sources, or new systems using clean and renewable energy sources like wind and solar energy, and spread usage of those systems over the world. Heat pump systems are the systems which can be a renewable energy conversion system sometimes and a common energy conversion system which use the fossil energy sources more efficiently than others.

The big portion of energy used on the world is consumed at heating and cooling applications in the residential or other buildings or in industrial plants. According to the studies, the energy used for residential and construction activities make up about 40% of the world's total energy consumption and heating applications have a key role in it [1-3]. Heat pumps are promising means of reducing the consumption of fossil energy resources, and hopefully, the cost of delivered energy for residential heating. An intelligent extension is to try to combine the two to further reduce the cost of delivered energy. In general, it is widely believed that combined systems will save energy, but what is not often known is the magnitude of the possible energy saving and the value of those savings relative to the additional expense [4].

Heat pumps offer the most energy-efficient way to provide heating and cooling in many applications, as they can use renewable heat sources in our surroundings. Even at temperatures we consider to be cold, air, ground and water contain useful heat that is continuously replenished by the sun. However, heat pumps consume less primary energy than conventional heating systems and, they are an important technology for reducing emissions of gases that harm the environment [5,6].

A simple heat pump system consists of four main components, which are compressor, two heat exchangers (condenser and evaporator) and expansion valve, in addition to these components, many auxiliary components may be used on heat pumps such as valves, thermostats, some measurement tools, pumps, fans, or extra heaters. For heating purposes, they can be divided into basic types, determined by the source and the destination of the heat and the medium that the heat pump uses to either absorb or reject the heat in each of these locations. At either of the heat exchangers the heat transfer media can be either liquid (water, or often a glycol mixture) or air; sometimes it is a combination of the two. In describing the type of heat pump, generally the heat source is generally provided first, followed by the destination or heat sink. The main variants in common use are; air to air, water to water, water to air, air to water, ground to water, ground to air types.

Thermal characteristics and the types of the used heat sources and heat sinks are very important for the performance of heat pumps. Commonly used heat sources and heat sinks are ambient air, exhaust air, lake water, river water, ground water, earth, rock, wastewater

and effluent. Most used heat sources and heat sinks on heat pump systems are ambient air and water around the world. Ambient air is a widely available and a free heat source for heat pumps. However, the thermodynamic performance of air source heat pump systems decrease depend on the decreasing the temperature of air in the heating seasons and increasing the temperature of air in cooling seasons. Because of the heat transfer properties of water, water source heat pump systems offer some performance advantages over heat pump systems which use air as heat source [7].

The common method to examine the energy conversion systems is first law of thermodynamics in general. However that method cannot perfectly describe the performance of those systems since the essence of energy utilization is to extract available energy as much as possible [8]. That means common method of energy accounting ignores completely the quality of energy. It only tracks the quantity which according to the first law of thermodynamics will never change. In addition an energy balance provides no information on the degradation of energy or resources during a process and does not quantify the usefulness or quality of the various energy and material streams flowing through a system and exiting as products and wastes.

A better method for energy accounting could be based on both first and second law of thermodynamic, which asserts that work, is the highest. In short we named that analyze method with exergy analyze. The exergy method of analysis overcomes the limitations of the first law of thermodynamics. Exergy analysis clearly indicates the locations of energy degradation in a process and can therefore led to improved operation and technology.

The exergy of an energy form or substance is a measure of its usefulness or quality or potential to cause change [9]. Exergy is defined as the maximum work which can be produced by a system or a flow of matter or energy and it comes to equilibrium with a specified reference environment (dead state) [10].

Many studies and investigations have reported in the open literature on different types of heat pumps and on comparison of them experimentally or by simulations, according to their heat sources, heat sinks, and the place they are being used, the refrigerant used as working fluid, structures and capacities of components i.e. [11-21]. For example; Petit and Meyer [11] made a comparison of the economical viability in South Africa of horizontal-ground source systems and air-source systems. In order to realize this aim, monthly heating and cooling capacities and coefficients of performance for both systems were determined. Urchueguia et al. [12] made an experimental comparison between a ground coupled heat pump system and a conventional air to water heat pump system, focusing at the heating and cooling energy performance. The results demonstrated that, a ground source heat pump system is

viable and energy efficient alternative to conventional systems for heating and cooling applications in the South European regions. Kavak Akpınar and Hepbaşlı [13] reported that; they made a comparative study on exergetic assessment of two ground-source (geothermal) heat pump systems for residential applications. The study dealt with the exergetic performance evaluation of two types of ground source heat pump systems installed in Turkey based on the actual operational data. The first one is a ground source heat pump system designed and constructed for investigating geothermal resources with low temperatures, while the other one is a ground source heat pump with a vertical ground heat exchanger. Esen et al. [14] made a study which reported a techno-economic comparison between a ground-couple heat pumps system (GCHP) and air coupled heat pump (ACHP) system. The experimental results were obtained from June to September in cooling season in 2004. The test results indicated that system parameters can have an important effect on performance and that GCHP systems are economically preferable to ACHP systems for the purpose of space cooling. Sopha [15] et al. studied on factors that influence the choice of heating system based on Norwegian households' perceptions. Electric heating, heat pump and wood pellet heating were compared with a special focus on wood pellet heating. The results showed that socio-demographic factors, communications among household, the perceived importance of heating system attributes and the applied decision strategy all influence the Norwegian homeowners.

The study in this paper makes energetic and exergetic analyze of two heat pump systems which are water to water and water to air experimentally to make a comprehensive. An experimental multifunctional heat pump setup was designed to make a comprehensive exergetic comparative investigation for two different heat pump types; they have same heating capacity and same specifications. Experimental system consists of, two condensers and one evaporator, one expansion valve and one compressor. The direction of refrigerant fluid used in the system can be easily changed between the condensers and evaporators with the help of valves. In this way the designed heat pump experimental setup can be operated in different modes. Heating capacity of each heat pump mode is equal under the same conditions and can be adjusted by changing the flow rate and temperature levels of the fluid used as heat source and sink.

2. MATERIALS AND METHODS

A schematic diagram of the experimental apparatus is shown in Fig.1. system was originally designed for operating with R22 but it is able to be operated with some other refrigerants or refrigerant mixtures like R407C or R134a. The main components of the system are a scroll compressor, a water cooled evaporator, an air cooled condenser, a water cooled condenser, one

thermostatic expansion valve, and the other auxiliary elements like measurement and control equipments. In addition, electrical air and water heaters are used in order to keep the temperature of air and water passing into the evaporator and condensers at the desired levels. Two electrical speed adjustable fans are used to circulate the air on the evaporator and condenser which are air cooled and tap water is used directly for the water cooled evaporator and condenser by using no pump. The tests were performed under laboratory conditions, during the air temperature was about 20-22°C. A lot of tests were made by changing the temperature and mass flow rates of the cooling fluid of evaporator, under constant temperature and constant flow rate levels for condenser cooling fluid for each one of the four heat pump modes.

The main components of the system are a scroll compressor, a water cooled evaporator, an air cooled condenser, a water cooled condenser, one thermostatic expansion valve, and the other auxiliary elements like

measurement and control equipments. In addition, electrical air and water heaters are used in order to keep the temperature of air and water passing into the evaporator and condensers at the desired levels. Two electrical speed adjustable fans are used to circulate the air on the evaporator and condenser which are air cooled and tap water is used directly for the water cooled evaporator and condenser by using no pump. The tests were performed under laboratory conditions, during the air temperature was about 20-22°C. A lot of tests were made by changing the temperature and mass flow rates of the cooling fluid of evaporator, under constant temperature and constant flow rate levels for condenser cooling fluid for each one of the four heat pump modes.

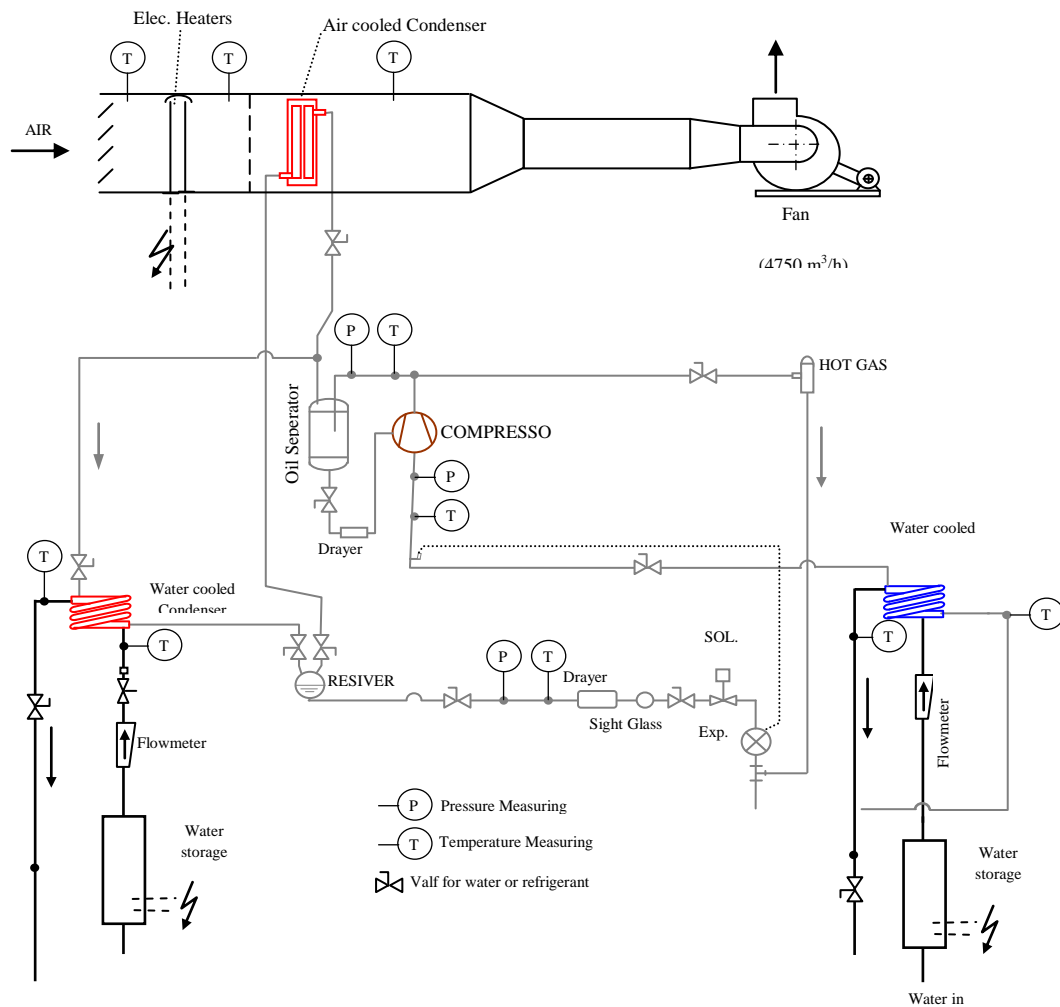


Figure 1: Schematic view of the experimental setup

Table 1: Levels of parameters

Parameter	Fluid	Level 1	Level 2	Level 3	Level 4	Level 5	Level 5
Mass flow rate (kg/s)	Evap. Air	0,41	0.71	0.83	1.1	1.2	---
	Evap./Cond. Water	0.100	0.110	0.125	0.139	0.15	---
Temperature (°C)	Evap. Water	12	14	16	18	20	22

2.1. Determination of heat-pump characteristics

All of the measured values which consist of temperatures from the thermocouples, pressures from the manometers, compressor input power from the wattmeter, and flow rates of the fluids used on the system from the flow meters, rotameters and anemometers were used to determine the exergetic performances of four heat pump modes to achieve the aim mentioned above. It is needed to make energy analysis to make a healthy exergy analysis. Mass, energy and exergy balances are employed to determine the heat input, the rate of exergy destruction, and energy and exergy efficiencies. From the measured parameters: The heat delivered by the condenser to the air or water is calculated by;

$$\dot{Q}_{\text{con-air}} = \dot{m}_a C_a (T_{\text{ca out}} - T_{\text{ca in}}) \quad (4)$$

$$\dot{Q}_{\text{con-water}} = \dot{m}_w C_w (T_{\text{cw out}} - T_{\text{cw in}}) \quad (5)$$

The heat extracted by the evaporator from the air or water is calculated by

$$\dot{Q}_{\text{evap-water}} = \dot{m}_w C_w (T_{\text{ew in}} - T_{\text{ew out}}) \quad (6)$$

$$\dot{W}_{\text{Comp}} = \sqrt{3} \cdot \text{Cos}(\varphi) \cdot U \cdot I \quad (7)$$

The power input to the compressor is calculated by

$$\text{COP}_{\text{HP}} = \frac{\dot{Q}_c}{\dot{W}_{\text{comp,elec}}} \quad (8)$$

Where U, I and Cos (φ) are voltage (V), current (A) and power factor, respectively. The coefficient of performance (COP) for any heat pump;

$$\dot{E}_{\text{in}} - \dot{E}_{\text{out}} = \dot{E}_{\text{dest}} \quad (6)$$

2.2. System exergy analysis

Energy and exergy balances can be written as;

$$\dot{E}x = \dot{m} \cdot ex \quad (7)$$

$$\dot{E}x_{\text{in}} - \dot{E}x_{\text{out}} = \dot{E}x_{\text{dest}} \quad (8)$$

$$\boxed{\phantom{\dot{E}x_{\text{in}} - \dot{E}x_{\text{out}} = \dot{E}x_{\text{dest}}}} \quad (9)$$

The specific flow exergy of the refrigerant and water is evaluated as [22]:

$$\begin{aligned} ex_{\text{air}} = & (C_a + \omega C_{\text{vapor}}) T_0 \left[\left(\frac{T}{T_0} \right) - 1 - \ln \left(\frac{T}{T_0} \right) \right] \\ & + (1 + 1.6078 \omega) R_{\text{air}} T_0 \ln \left(\frac{P}{P_0} \right) \pi \\ & + R_{\text{air}} T_0 \left\{ \begin{aligned} & (1 + 1.6078 \omega) \ln \left[\frac{(1 + 1.6078 \omega_0)'}{(1 + 1.6078 \omega)} \right] \\ & + 1.6078 \omega \ln \left(\frac{\omega}{\omega_0} \right) \end{aligned} \right\} \end{aligned} \quad (10)$$

Where h is enthalpy, s is entropy and the subscript zero indicates properties at the reference (dead) state. The total flow exergy of air is determined as [22];

$$\omega = \frac{\dot{m}_{\text{vapor}}}{\dot{m}_{\text{air}}} \quad (11)$$

Where the specific humidity ratio is;

$$\eta_{\text{ex,HP}} = \frac{\dot{E}x_{\text{heat}}}{\dot{W}_{\text{comp,elec}}} = \frac{\dot{E}x_{\text{in cond}} - \dot{E}x_{\text{out cond}}}{I \cdot V \cdot \text{Cos}(\varphi) \cdot \sqrt{3}} \quad (12)$$

Exergy efficiency and exergy destruction of the heat pumps is as follow;

$$\dot{E}_{\text{dest HP}} = \sum \dot{E}_{\text{in HP}} - \sum \dot{E}_{\text{out HP}} \quad (13)$$

By using the estimation method of Kline and McClintock [23], maximum uncertainties of the COP and exergy efficiency are found as follows: COP, 3.53%; exergy efficiency, 3.53%. The individual contributions to the uncertainties of the COP and exergy efficiency for each of the measured physical properties are summarized in Table 2.

Table 2: Uncertainties in the values of the relevant variables.

Variables	Uncertainty (%)
Temperature (T)	2.5
Pressure (P)	1.6
Voltage (U)	1.7
Current (I)	1.7
Power factor (Cos φ)	1.7
Mass flow rate (m_r)	1,3

3. RESULTS

Two different heat pump systems those run on the same experimental setup, have same heating capacity, use just one compressor, controlled by the same control equipments and the same measurement system are analyzed and compared experimentally and exergetically with each other by using second law of

thermodynamics in this study. Within the scope of the study presented here; COP, exergy efficiency and rate of exergy destruction of heat pump types are evaluated, discussed and compared as the results of this paper. Differences of energetic and exergetic performance of two different heat pump types according to the increasing rate of temperature and flow rate of the fluid used as heat source is expressed and compared.

Figure 2 and 3 shows the change of COP values of two heat pump units according to the increasing rate of temperature and mass flow rate levels of the fluid as heat source. As seen on the Figure 2, the heat pump unit which has the higher COP value is water to air type. It is known that COP of heat pumps increase depends on increasing of heat source temperature. Mass flow rate of the fluid used as heat source has a big importance for the performance of heat pumps. Figure shows the change of COP values of the heat pumps according to the mass flow rate changes of evaporator water. Higher increasing rate is actualized on the COP of the water to water heat pump with the increasing of mass flow rate of the evaporator water.

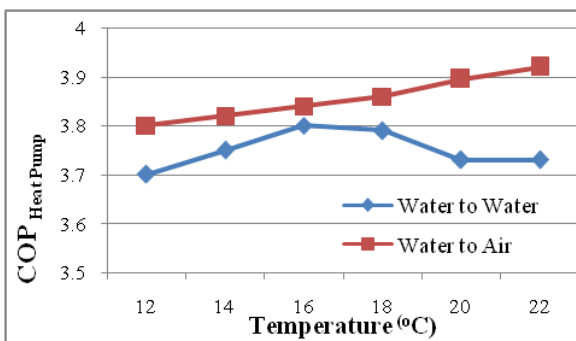


Figure 2: COP change of heat pumps versus evaporator water temperature increasing

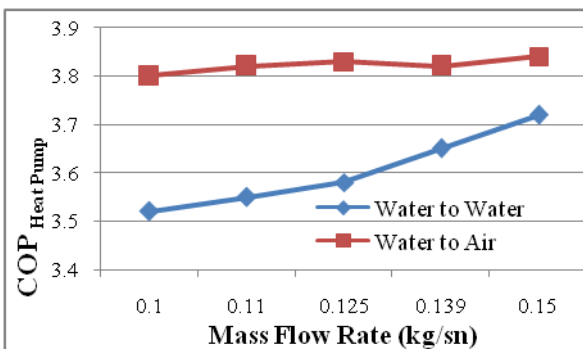


Figure 3: COP change of heat pumps versus mass flow rate increasing of evaporator water

Exergy efficiency change of the heat pumps according to the evaporator temperature and according to mass flow rate of evaporator water can be seen on Figure 4. As seen on the figure exergetic efficiency of the water to air heat pumps is higher than the exergy efficiency of water to water heat pump. Both of the exergy efficiencies of two heat pump systems are increase when the temperature of evaporator water increases.

Rates of exergy efficiency increases of two systems are nearly equal to each others. When the temperature of the evaporator water increase from 12°C to 22°C, exergy efficiency of water to water heat pump increases from 23% to 25,9%, and exergy efficiency of water to air heat pump increase from 29% to 31,3%. Effects of the mass flow rate changes of evaporator water on the exergetic efficiencies of heat pumps can be seen on the Figure 5.

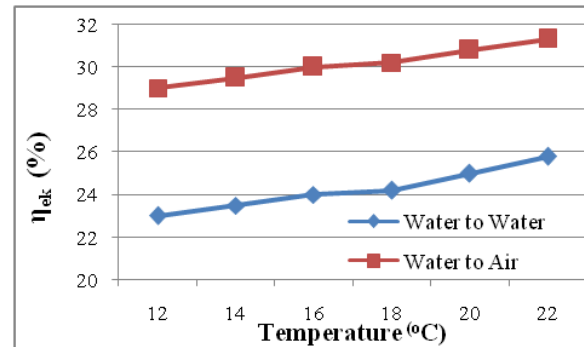


Figure 4: Exergy efficiency of heat pumps versus evaporator water temperature increasing

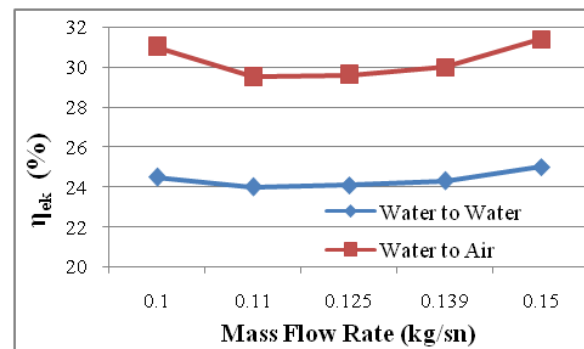


Figure 5: Exergy efficiency change of heat pumps versus mass flow rate increasing of evaporator water

Figure 6 and Figure 7 shows the exergy destructions of two heat pumps according to heat source (water) temperature changes. As understood from the figures, more exergy is dissipated on the water to air heat pump than water to water heat pump. When the evaporator water temperature increases, exergy destruction of the water to water heat pump increases more than the exergy destruction of the water to air heat pump.

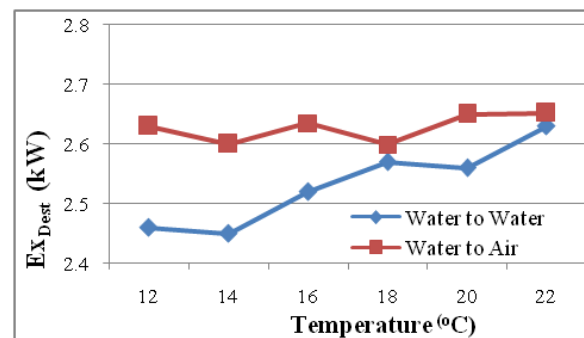


Figure 6: Exergy destruction change of heat pumps versus evaporator water temperature increasing

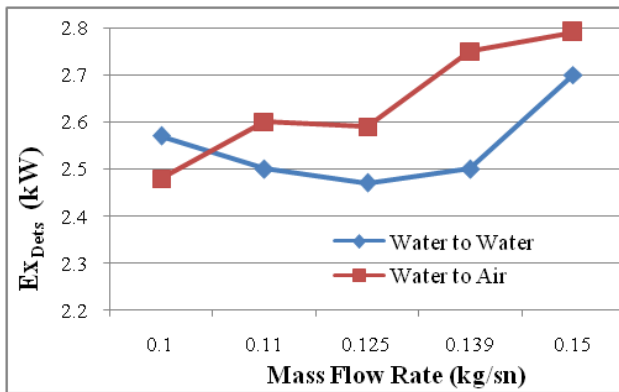


Figure 7: Exergy destruction change of heat pumps versus mass flow rate increasing of evaporator water

4. CONCLUSION

In this paper, energy and exergy analysis of two different heat pump types (water to water and water to air) have been investigated; regarding temperature and mass flow rate changes of the evaporator fluid use as heat source. The coefficient of performance of heat pumps is primarily depending on the temperature of heat source. In addition, it depends on the mass flow rate of the heat source fluid. This analysis shows that; the heat pump unit which has the higher COP value is water to air type, other one is water to water type.

REFERENCES

- [1] Pei G, Li G, Jie J. Comparative study of air source heat pump water heater systems using the instantaneous heating and cyclic heating modes. *Appl Therm Eng* 2011;31(2-3): 342-47
- [2] Çakır U. Exergetic comparison of heat pumps according to fluids used in the condenser and evaporator. 2011. Ph. D. Thesis, Atatürk University Graduate School of Natural and Appl Sci Dep of Mechanical Eng.
- [3] Dalkılıç A, Wongwises S. A performance comparison of vapor compression refrigeration system using various alternative refrigerants. *Int Commun Heat Mass Transfer* 2006;37(9): 1340-49
- [4] Kaygusuz K., Experimental and theoretical investigation of a solar heating system with heat pump. *Renewable Energy* 2000;21:79e102.
- [5] OmerAM. Ground-source heat pumps systems and applications. *Renewable and Sustainable Energy Reviews* 2008;12:344e71.
- [6] Bakirci K, Ozyurt O, Comakli K, Comakli O. Energy analysis of a solar ground source heat pump system with vertical closed loop for heating applications. *Energy* 2011;36(5): 3224-32
- [7] Büyükalaca O, Ekinci F, Yılmaz T. Experimental investigation of Seyhan River and Dam Lake as heat source-sink for a heat pump. *Energy* 2003;28(2): 157-69
- [8] Xiaowu W, Ben H.2 2005. Exergy analyses of domestic solar water heaters. *Renewable and sustainable energy reviews*, 90(2005), 638-645
- [9] Rosen MA., Dincer I., ON exergy and environmental impact.,*Int. J Energy Res.* 1997;21;643-645
- [10] Utlu Z., Hepbaşlı A., Parametrical investigation of the effect of dead (reference) state on energy and exergy utilization efficiencies of residential - commercial sectors: A review and an application, *Renewable and sustainable energy reviews*, 11 (2007) 603 – 634
- [11] Petit PJ, Meyer JP. A techno-economic analytical comparison of the performance of air source and horizontal-ground-source air-conditioners in South Africa. *Int J Energy Res* 1999;21(11): 1011-21.
- [12] Urchueguía JF, Zacarés M, Corberán MÁ, Martos J, Witte H. Comparison between the energy performance of a ground coupled water to water heat pump system and air to water heat pump system for heating and cooling in typical conditions of the European Mediterranean coast. *Energy Conve and Manag* 2008;49(10): 2917-23
- [13] Kavak Akpınar E, Hepbaşlı A. A comparative study on exergetic assessment of two ground-source (geothermal) heat pump systems for residential applications *Build Environ* 2007;42(5): 2004-13.
- [14] Esen H, İnallı M, Esen M. A techno-economic comparison of ground-coupled and air-coupled heat pump system for space cooling. *Build Environ* 2007;42(5): 1955-65
- [15] Sophia BM, Klöckner CA, Skjevraak G, Hertwich EG. Norwegian households' perception of wood pellet stove compared to air to air heat pump and electric heating. *Energy Policy* 2010;38(7): 3744-54
- [16] Çakır U. Exergetic comparison of heat pumps according to fluids used in the condenser and evaporator. 2011. Ph. D. Thesis, Atatürk University Graduate School of Natural and Appl Sci Dep of Mechanical Eng.
- [17] Comakli K, Simsek F, Comakli O, Sahin B. Determination of optimum working conditions

- R22 and R404A refrigerant mixtures in heat-pumps using Taguchi method. *Appl Energy* 2009;86(5): 2451-58
- [18] Bakirci K, Ozyurt O, Comakli K, Comakli O. Energy analysis of a solar ground source heat pump system with vertical closed loop for heating applications. *Energy* 2011;36(5): 3224-32
- [19] Park K, Seo T, Jung D. Performance of alternative refrigerants for residential air-conditioning applications. *Appl Energy* 2007;84(10): 985-91.
- [20] Nanxi L, Shi L, Lihong H, Mingshan Z. Moderately high temperature water source heat-pumps using an ear-azeotropic refrigerant mixture. *Appl Energy* 2005;80(4): 435-47.
- [21] GeY, Cropper R. Air-cooled condensers in retail systems using R22 and R404A refrigerants. *Appl Energy* 2004;78(1): 95-110.
- [22] Rosen MA, Dinçer İ. Effect of varying dead-state properties on energy end exergy analyses of thermal systems. *Int J Thermal Sci* 2004;43(2): 121-133
- [23] Kline SJ, McClintock FA. Describing uncertainties in single-sample experiments. *Mech Eng* 1953;75:3-8

A Simulation Study on Determining the Position and Orientation of a Classic Rectangle-Lengthwise Type Greenhouse System to Have More Benefit from Solar Radiation

Murat BALCI¹, Uğur ÇAKIR¹ and Kemal ÇOMAKLI²

¹Mechanical Eng. Dep./ Eng. Faculty/ Bayburt University/ Bayburt / TÜRKİYE (ucakir@bayburt.edu.tr, mbalci@bayburt.edu.tr)

²Mechanical Eng. Dep./ Eng./ Atatürk University/ Erzurum / TÜRKİYE (kcomakli@atauni.edu.tr)

ABSTRACT

Green housing has become a sector which is growing and spreading rapidly in Türkiye and on the World. The main purpose of green housing is to keep the temperature level in the green house to product the plants under desired climatic conditions. In this way, agricultural growing can be made at any season more efficiently and easily. Solar energy is used in the best part of common greenhouse systems because of that, sun is everywhere and sun is the cheapest energy source on the world. Solar energy can be used directly or with an auxiliary system in the greenhouses. Most of the greenhouse systems in Türkiye have a classical rectangle shape and use the solar energy directly by creating greenhouse effect in. So that positioning and orientation of lengthwise type greenhouse systems is very important to get more radiation and more benefit from sun in a day, month and year.

In this study a simulation program is written to determine the optimum position, direction and orientation of classic rectangle-lengthwise type greenhouse in Erzurum, Türkiye ($39,6^{\circ}$ North and 41° east, altitude 1853m) by using MATLAB. The simulation is run and some results were obtained for daily, monthly and annually by using the solar energy use and thermodynamic principles. At the end of the study we present the determined the optimum position of systems according to global location of the situation, dimensions of the system and climatic conditions of the place.

Keywords: Greenhouse, solar energy, solar radiation

1. INTRODUCTION

Greenhouses are the structures used for providing the most suitable microclimate for the best conditions for the maximum plant growth during off-season. One of the most dominant parameters which affect the plant growth is air temperature. Short solar radiation is allowed to enter in to the microclimatic space by transparent covering of the greenhouse. But the covering is partially opaque to the long wave radiation resulting in the greenhouse effect.

In cold climates, higher inside air temperature is desirable during all hours for maximum plant growth that can be achieved by keeping the greenhouse closed for maximum greenhouse effect or by using any suitable heating system Whereas, in a composite climate, greenhouse effect is desirable only for a brief winter period (2–3 months) but for rest of the months, excess heat from the greenhouse must be removed by using any suitable cooling system [1].

One of the most energy consuming activities is heating of greenhouse especially in winter periods. Lack of heating has adverse effects on the yield, cultivation time, quality and quantity of the products in the greenhouse. Due to high relative cost of energy, only a small number of greenhouse owners can afford to the use of auxiliary heating systems. The use of low-cost and alternative heating system is therefore of primary

importance for a greenhouse to provide optimum indoor conditions during winter months.

The researchers and green house designers make many studies to reduce the consumption of auxiliary energy and to increase the using rate of solar energy. Efforts to decrease energy consumption have directed the researchers to use alternative energy sources for heating of greenhouse or to design the new types of greenhouses. Several types of passive solar systems and techniques have been proposed and used for the substitution of conventional fuels with solar energy as a low cost technology as solar energy is the ideal source of energy for space heating, particularly in northern hemisphere where it is sufficiently available [2–5].

The shape and the orientation is very important for providing the adequate temperature level of greenhouse. Total solar radiation received by a greenhouse at a particular time and location also depends upon its shape as well as orientation, which ultimately determines the inside air temperature. Various researchers have used different greenhouse shapes at different latitudes for raising off-season vegetables and ornamental plants around the world.

It is already established that inside air temperature of a passive greenhouse directly depends upon the ambient air temperature, the solar radiation intensity, the overall heat transfer coefficient, the cover material and the wind velocity. Most of the investigations and studies

which in progress or which have been made recently, intend to get more benefit from the energy of sun [1-12]. For example, in the study made by V.P. Sethi [1] the length, width and height (at the center) are kept same for all the selected shapes. A mathematical model for computing transmitted total solar radiation (beam, diffused and ground reflected) at each hour, for each month and at any latitude for the selected geometry greenhouses (through each wall, inclined surfaces and roofs) is developed for both east-west and north-south orientation. Results show that uneven-span shape greenhouse receives the maximum and quonset shape receives the minimum solar radiation during each month of the year at all latitudes. East-west orientation is the best suited for year round greenhouse applications at all latitudes as this orientation receives greater total radiation in winter and less in summer except near the equator. M.K. Ghosal, G.N. Tiwari, D.K. Das, K.P. Pandey [2] made a study on Modeling and comparative thermal performance of ground air collector and earth air heat exchanger for heating of greenhouse.

In the study made by V.P. Sethi and R.K. Dubey [6] upper space inside an east-west oriented greenhouse (where the micro-climate is also under control) is optimized for producing maximum number of nursery plants by developing a multi-rack tray system (MRTS). The MRTS is designed in such a way that the vertical distance between the two consecutive trays (H) and width of the tray (W) is optimized for different months of the year at different latitudes so that the shadow of the upper tray does not fall on the lower one. The number of stacks in a greenhouse of fixed height (say 4 m) is a direct function of the maximum altitude angle of the sun at noon (as) at particular latitude. It is observed that at 10°N and 20°N latitudes as remains greater than 45_ ($H/W > 1$) even during the winter months. It means not more than two stacks are possible inside a 4 m high greenhouse during December and January. The computations show that at 30°N , 40°N and 50°N latitude, the number of stacks inside a greenhouse can be five, seven and twelve, respectively during the winter months of December and January. A transient thermal model coupled with MRTS is also developed to predict the soil, plant and air temperature inside the greenhouse. It is observed that the predicted and measured values are in close agreement. It is also observed that due to the increased mass of soil (in the trays) inside the greenhouse and due to reduced conduction losses to the ground beneath, MRTS also acted as a soil heat storage system before germination of the plants which stored heat during the sun-shine hours and released the same during the off-shine hours and resulted in $5-2^\circ\text{C}$ higher inside air temperature till the early night hours as compared to ambient air temperature. Nursery of marigold (ornamental plant) is successfully raised using the MRTS inside a 3 m high greenhouse having three stacks at 30°N latitude.

Experiments showed that there was almost uniform growth of plants in all the three trays.

In the paper presented here, a simulation study on determining optimum orientation of a classic rectangle-lengthwise type greenhouse system which has the sizes $L=10\text{m}$ and $W=5\text{m}$ to have more benefit from solar radiation. A computer modeling program was developed by using MATLAB to calculate the incoming radiation energy to the greenhouse at any orientation and then changing of the solar energy gathered by the greenhouse according to the direction of it is determined for twelve months and for whole year.

2. DESCRIPTION – VALIDATION OF THE MODEL

In this study it is investigated that; when a rectangular shaped green house like in Figure 1; $L=10\text{m}$, $W=5\text{m}$ and $H=3\text{m}$, gathers the most solar energy according to the direction of it.

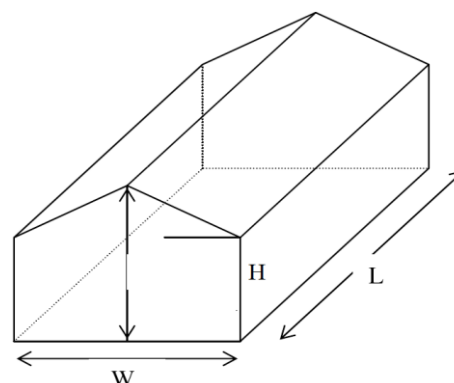


Figure 1: The analyzed greenhouse and sizes of it

Azimuth is the angle of sun in the east-west direction. Geographic south is defined as azimuth= 0° . Angles to the east of due south are negative, with due east having azimuth= -90° . Angles to the west of due south are positive, with due west having an azimuth= 90° . In the temperate latitudes of the northern hemisphere, the sun tracks an arc across the horizon as seen on Figure 2, change of azimuth.

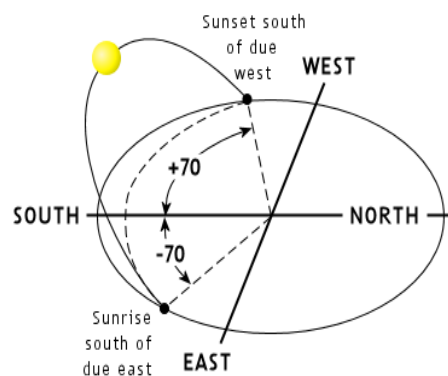


Figure 2: Azimuth angle

2.1 Calculations

The solar radiation coming on the unit area of a slope surface at the outside of the atmosphere in space; Q_{oe} is defined as [13];

$$Q_{oe} = \frac{12}{\pi} I_{gs} \cdot f \cdot \left\{ \begin{array}{l} \frac{\pi}{180} (H_2 - H_1) \sin d \left(\begin{array}{l} \sin e \cdot \cos s \\ -\cos e \cdot \sin s \cdot \cos a \end{array} \right) \\ + (\sin H_2 - \sin H_1) \cdot \cos d \cdot \left(\begin{array}{l} \cos e \cdot \cos s \cdot \sin e \\ \sin s \cdot \cos a \end{array} \right) \\ - (\cos H_2 - \cos H_1) \cos d \cdot \sin s \cdot \sin a \end{array} \right\} \quad (1)$$

where d is declination angle, e is latitude angle of related region, s is the slope angle of any surface, a is azimuth angle of surface, I_{gs} is the instant radiation that comes to the unit area of an horizontal surface at the outside of the atmosphere, f is the coefficient of the correction factor for solar constant which is 1370 W/m^2 , H_2 and H_1 are the first and last solar radiation coming angles to the surfaces.

The *declination* is the angular position of the sun at solar noon, with respect to the plane of the equator. Its value in degrees is given by Cooper's equation:

$$d = 23.45 \cdot \sin \left(360 \frac{n + 284}{365} \right) \quad (2)$$

$n = 1$ for January 1, $n = 32$ for February 1, etc.). Declination varies between -23.45° on December 21 and $+23.45^\circ$ on June 21. Slope angles of the wall surfaces of greenhouse are 90° , and 45° for roof walls. f is calculated as follows ;

$$f = 1 + 0.033 \cos \left(360 \frac{n}{365} \right) \quad (3)$$

Values of the H_1 and H_2 can be calculated by using the following equations;

$$\cos H = - \frac{\sin d \cdot \sin e}{\cos d \cdot \cos e} = - \tan d \cdot \tan e \quad (4)$$

$$C_1 = \sin a \cdot \cos d \cdot \sin s \quad (5)$$

$$C_2 = \cos d \cdot (\cos e \cdot \cos s + \cos a \cdot \sin e \cdot \sin s) \quad (6)$$

$$C_3 = \sin d (\sin e \cdot \cos s - \cos a \cdot \cos e \cdot \sin s) \quad (7)$$

$$D^2 = C_1^2 + C_2^2 + C_3^2 \quad (8)$$

$$H_{1p} = 2 \arctan \frac{C_1 - D}{C_2 - C_3} \quad (9)$$

$$H_{2p} = 2 \arctan \frac{C_1 + D}{C_2 - C_3} \quad (10)$$

$$\cos g_0 = C_2 + C_3 \quad (11)$$

After using the equations previously presented, H_1 and H_2 can be determined by using the table is shown below.

		First radiation coming hour angle, H_1	Last radiation coming hour angle, H_2
$\cos g_0 > 0$ ($g_0 < 90^\circ$)	$D^2 > 0$ $D^2 < 0$	Max (H_{1p} , $-H$) $-H$	Min (H_{2p} , H) H
$\cos g_0 < 0$ ($g_0 > 90^\circ$)	$D^2 > 0$ $D^2 < 0$	Max (H_{2p} , $-H$) no solar radiation	Min (H_{2p} , $-H$) no solar radiation

2.2 Scope of the study

This study investigates the importance of the position and direction of a rectangular lengthwise greenhouse to get the more solar energy it can get from the sun. We calculated the change of the solar energy gathered by greenhouse to determine the position of system which the greenhouse can have maximum solar radiation. As seen in the Figure 3, firstly azimuth angle of the short edge of greenhouse is $a_2, 0^\circ$ and the long edge's is $a_1; -90^\circ$. We determined the change of solar energy that gathered by greenhouse in a day for every month and for whole year to identify the optimum position.

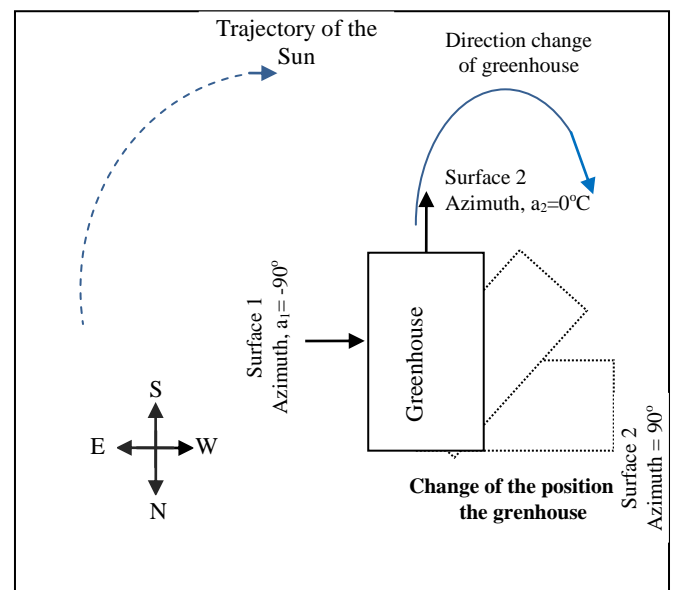


Figure 3: Scope of the study

3. RESULTS

The solar energy incomes to the greenhouse from the sun for the azimuth angles of short edge from $a_2=0^\circ$ to $a_2=90^\circ$ and graphicated by help of the computer modeling program developed by using MATLAB. The results obtained from the program are presented in the graphics below. The figures between from 4 to 15 show us the gathered amount of gathered solar energy by greenhouse versus change of a_2 in any month of the year.



Figure 4: Amount of gathered solar energy by greenhouse versus change of a_2 in January

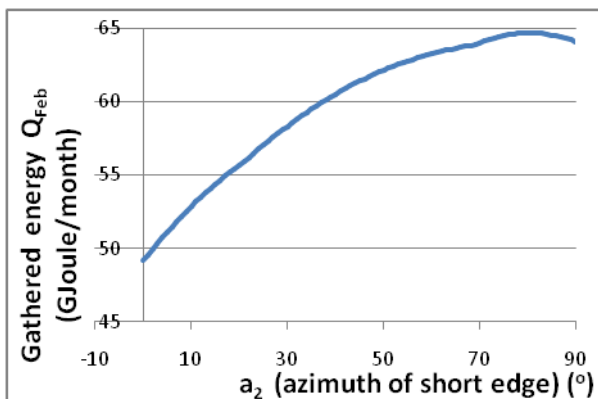


Figure 5: Amount of gathered solar energy by greenhouse versus change of a_2 in February

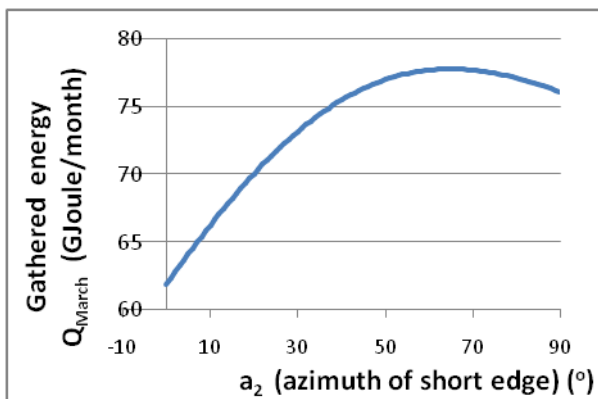


Figure 6: Amount of gathered solar energy by greenhouse versus change of a_2 in March

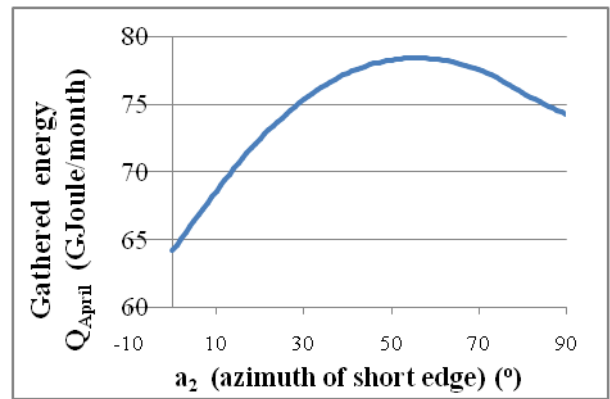


Figure 7: Amount of gathered solar energy by greenhouse versus change of a_2 in April

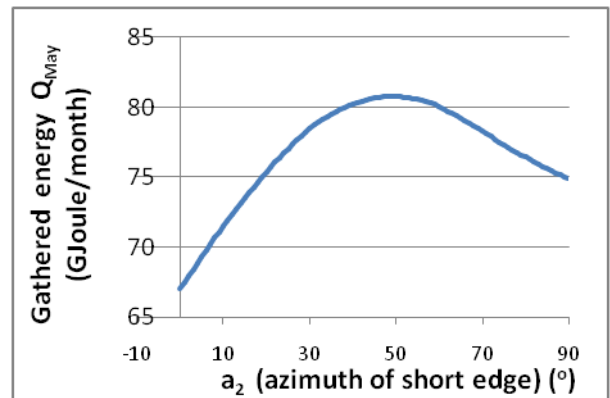


Figure 8: Amount of gathered solar energy by greenhouse versus change of a_2 in May

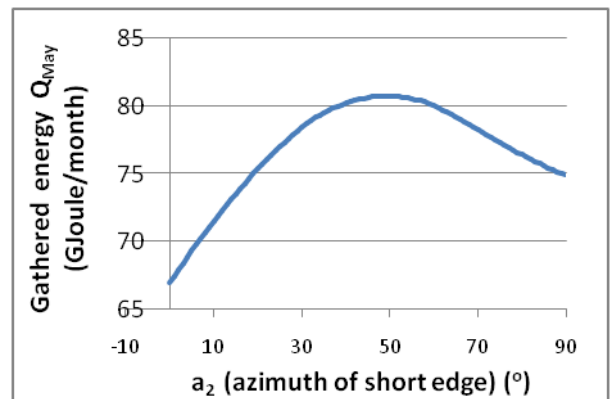


Figure 9: Amount of gathered solar energy by greenhouse versus change of a_2 in June

When the azimuth angle of surface 2 which is the short edge of the green house is zero ($a_2=0$), collected energy by greenhouse becomes minimum for all months of a year.

The angle which makes the gathered energy maximum differs according to months. The azimuth angel, a_2 which makes the gathered energy maximum for January is nearly 80° , but for the month of June is nearly 50° .

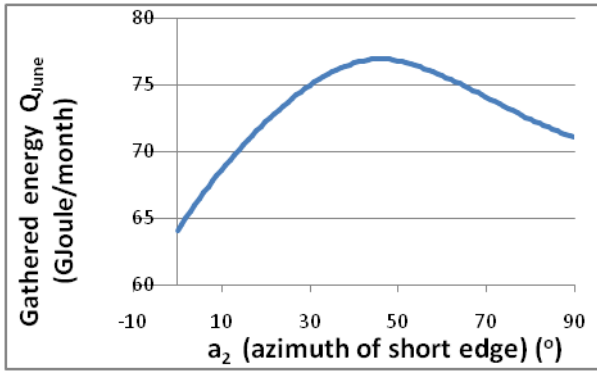


Figure 10: Amount of gathered solar energy by greenhouse versus change of a_2 in July

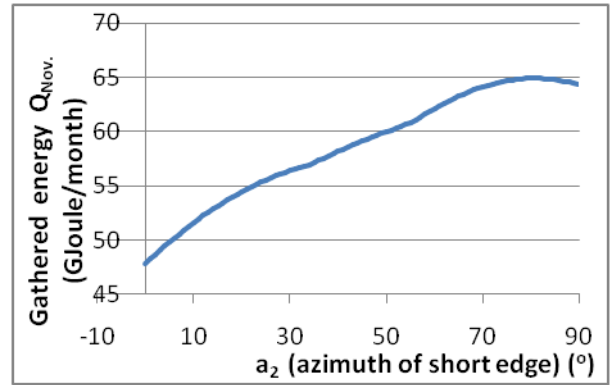


Figure 14: Amount of gathered solar energy by greenhouse versus change of a_2 in November

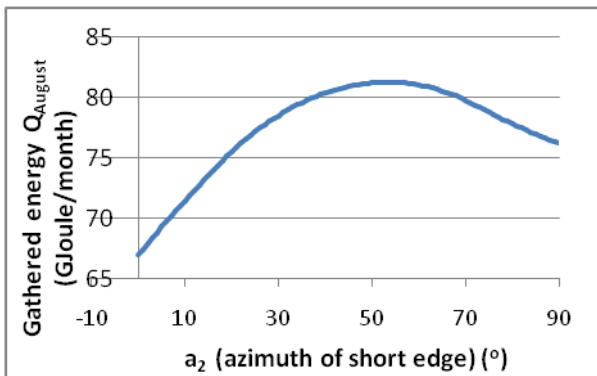


Figure 11: Amount of gathered solar energy by greenhouse versus change of a_2 in August

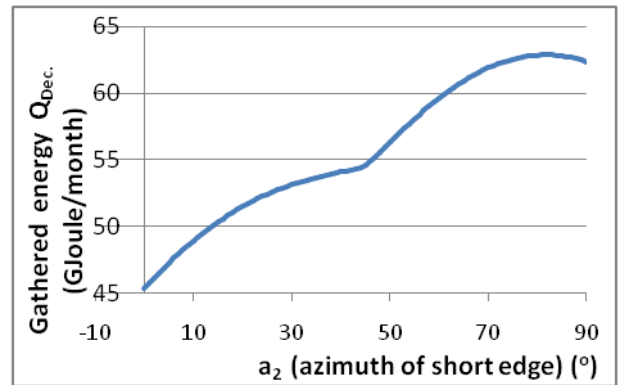


Figure 15: Amount of gathered solar energy by greenhouse versus change of a_2 in December

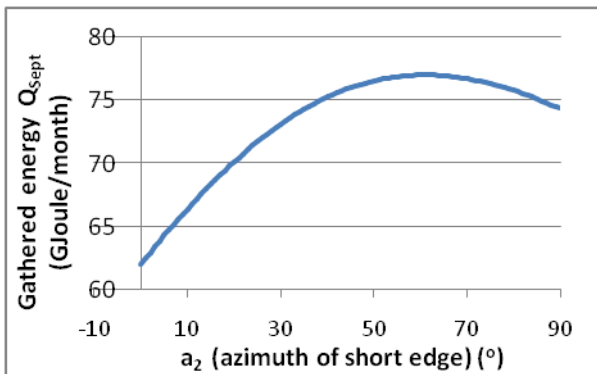


Figure 12: Amount of gathered solar energy by greenhouse versus change of a_2 in September

As seen on the figures 4-15, the optimum azimuth angle for short angle to make the total gathering energy by system, differs from 45° to 82° .

The angle when the total energy collected by greenhouse in whole year becomes highest is the optimum azimuth angle. Figure 16 presented to show the change of the total energy collected by greenhouse according to a_2 .



Figure 13: Amount of gathered solar energy by greenhouse versus change of a_2 in October

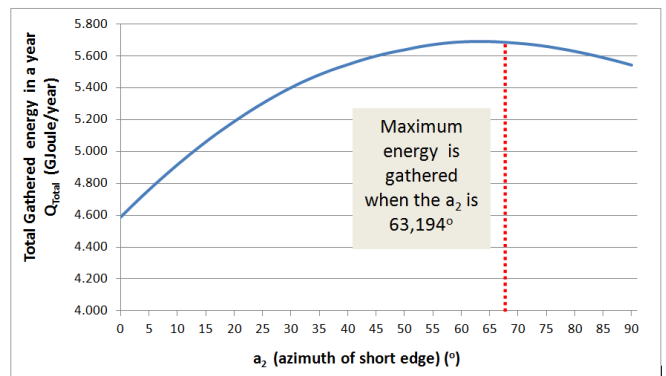


Figure 16: Amount of gathered solar energy in a year by greenhouse versus change of a_2

The optimum a_2 angle is defined as $63,194^\circ$, for the greenhouse which is installed in Erzurum, 39.6° north and 41° east, altitude 1853m and which has the layouts as $L=10m$, $H=3m$ and $W=5m$. It is showed on the Figure 17 shows us the amounts of gathered solar

energy in different months when a_2 is optimum, as $63,194^\circ$. When a_2 is optimum, December and January are the months the gathered energy becomes minimum and August is the month the solar radiation energy coming on the greenhouse becomes maximum.

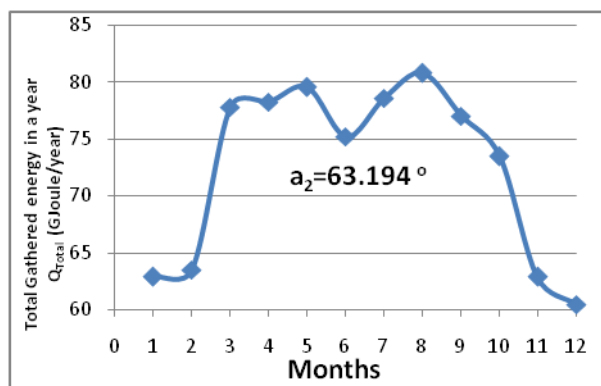


Figure 17: Amounts of gathered solar energy in different months when a_2 is optimum

4. CONCLUSION

Greenhouse systems in Türkiye have a classical rectangle shape and use the solar energy directly by creating greenhouse effect in generally. Positioning and orientation of lengthwise type greenhouse systems is very important to get more radiation and more benefit from sun in a day, month and year. This study optimizes the direction of a sample greenhouse system under the geographical conditions of Erzurum, ($39,6^\circ$ North and 41° east, altitude 1853m) by using MATLAB. The simulation is run and some results were obtained for, monthly and annually by using the solar energy use and thermodynamic principles. At the end of the study we identified the optimum azimuth angle for short edge is as $63,194^\circ$. When the a_2 is $63,194^\circ$, total gathered solar energy by greenhouse reaches the maximum value.

REFERENCES

- [1] V.P. Sethi. On the selection of shape and orientation of a greenhouse: Thermal modeling and experimental validation, *Solar Energy* 83 (2009) 21–38
- [2] M.K. Ghosal, G.N. Tiwari, D.K. Das, K.P. Pandey. Modeling and comparative thermal performance of ground air collector and earth air heat exchanger for heating of greenhouse. *Energy and Buildings* 37 (2005) 613–621
- [3] M. Santamouris, G. Mihalakakou, C.A. Balaras, J.O. Lewis, M. Vallindras, A. Argiriou, Energy conservation in greenhouses with buried pipes, *Energy* 21 (5) (1996) 353–360.
- [4] J.R. Barral, P.D. Galimberti, A. Barone, A.L. Miguel, Integrated thermal improvements for greenhouse cultivation in the central part of Argentina, *Solar Energy* 67 (1–3) (1999) 111–118.
- [5] M.N. Bargach, R. Tadili, A.S. Dahman, M. Boukallouch, Survey of thermal performances of a solar system used for the heating of agricultural greenhouses in Morocco, *Renewable Energy* 20 (2000) 415–433.
- [6] V.P. Sethi, R.K. Dubey Optimal space utilization of a greenhouse using multi-rack tray system: Thermal modeling and experimental validation. *Energy Conversion and Management* 49 (2008) 2890–2899
- [7] N.L. Panwara, S.C. Kaushik, Surendra Kothari. Solar greenhouse an option for renewable and sustainable farming. *Renewable and Sustainable Energy Reviews* 15 (2011) 3934–3945
- [8] Esquira I. In: Von Zabeltitz C, editor. *Greenhouse heating with solar energy*. FAO; 1987.
- [8] Ozturk, H.H., 2005. Experimental evaluation of energy and exergy efficiency of a seasonal latent heat storage system for greenhouse heating. *Energ. Convers. Manage.* 46, 1523–1542.
- [9] Jolliet, O., Danloy, L., Gay, J.B., Munday, G.L., Reist, A. HORTICERN, an improved static model for predicting the energy consumption of a greenhouse. *Agric. For. Meteorol.* 55, 265–294.
- [10] Sethi, V.P., Sharma, S.K., 2007. Survey of cooling technologies for worldwide agricultural greenhouse applications. *Sol. Energ.* 81 (12), 1447–1459.
- [11] S. Zhu a., J. Deltour, S. Wang. Modeling the thermal characteristics of greenhouse pond Systems. *Aquacultural Engineering* 18 (1998) 201–217
- [12] Efrén Fitz-Rodríguez, Chieri Kubota, Gene A. Giacomellia, Milton E. Tignor, Sandra B. Wilson, Margaret McMahon. Dynamic modeling and simulation of greenhouse environments under several scenarios: A web-based application. *Computers and Electronics in Agriculture* 70 (2010) 105–116
- [13] Kılıç A. Ve Öztürk A., *Güneş Enerjisi (Solar energy book, in Turkish)*, Kiptaş Dağıtımçılık, 1983

Evaluation of Different Substrate Material of Constructed Wetlands for Bioremediation of Household Sewage

Maryam Bibi ^a, Tahira Sultana ^{a*}, Iftikhar Ahmad ^b

^a Department of Environmental Sciences, International Islamic University, Islamabad, Pakistan

^b Pakistan Agriculture Research Council, Islamabad, Pakistan

ABSTRACT

This research evaluated the performance of different byproducts which can be considered as wastes of environment, to enhance pollutant bioremediation in constructed wetland and use the treated water for purpose of green revolution. Four month experiment was conducted at research facility of National Agriculture Research Center (NARC) Islamabad, using four containers as a constructed wetland with application of sewage water from Shehzad town nearby to NARC. This study aims to explore a novel application of different agricultural byproducts/wastes (sugar bagasse, rice husk, leaves, rice straw, Typha, cobs wastes), brick byproducts (over burn bricks) and coal with different combination of sand, gravel and boulders as a medium in a vertical down flow subsurface wetland (DFCW) to treat household sewage water in prevailing climate. Constructed wetlands were operated with hydraulic retention time of 3 days. Results have demonstrated the average removal efficiencies of all the mixtures of 4 constructed wetlands with seasonal temperature change i.e. system M-01 (rice husk, straw, leaves), system M-02 (typha, sugar bagasse, cobs wastes), system M-03 (coal) and system M-04 (over burn bricks) were as follows: Chemical oxygen demand (COD), Biological Oxygen Demand (BOD), Phosphates, Total Dissolved Solid (TDS), Electrical conductivity (EC), Bicarbonates, Chlorides, Hardness, Oil and grease with slightly alkaline pH. The wastewater treatment performances of the agricultural byproducts as compared to coal as a substrate material for constructed wetland were more efficient in remediation of pollutant of wastewater than other substrates. Since this study is a pioneer for implementation of vertical subsurface constructed wetland using locally available sources, it has proved that this eco technology is potentially economical, suitable for bioremediation and could also be used for water quality enhancement.

Keywords: *Bioremediation, Constructed wetlands, Biological Oxygen Demand.*

1. INTRODUCTION

Wastewater treatment is a problem that has plagued man ever since he discovered that discharging wastes into water resources can lead to many additional environmental problems. Water covers 70% of the earth with only 3% of fresh water resources only a small percentage (0.01%) of this freshwater is available for human use [1]. Urbanization, motorization and industrialization are the major contributors of pollution in natural environment [2, 3]. Over-exploiting water resources has led to serious environmental consequences, such as ground subsidence, salinity intrusion, and ecosystem deterioration [4-10]. Globally about 2 million tons of sewage per day is discharged into world's water reservoirs, but in developing countries the condition is worse where 90% of raw sewage are dumped into surface water bodies [11]. Estimated quantity of 2000 million gallons of sewage is discharged to fresh water bodies in Pakistan and only 10% of the wastewater is treated [12-14]. In 2004 population growth rate of Pakistan was 1.9% and it is projected that this figure will be 173 million by 2010 and 221 million by 2050. The per capita water availability has dropped from 5,600 m³ to 1,000 m³ [15]. Water shortage in agriculture sector of Pakistan is estimated 29% by 2010 and 33% by 2025 will pose severe food shortage in agriculture dependent country

[16], [17]. During the past 40 years, considerable interest has been expressed in the potential use of a variety of natural biological systems to restore and maintain the chemical, physical, and biological integrity of the nation's waters. The operational experience and research results reported in the available literature suggest that use of constructed wetlands as a part of water treatment offers considerable opportunity for future savings in wastewater treatment costs for small communities and for upgrading even large treatment facilities. Constructed wetlands also known as treatment wetlands are basically engineered systems designed to remediate pollutants from the contaminated water [18,19]. A lot of works have been done on constructed wetland and its substrate efficiency for the treatment of municipal and agriculture effluents. The studies have been well covered in scientific and engineering literature for finer porous media i.e. zeolites, anthracite, shale, vermiculite, ceramic filter media, gravel, steel slag and bio-ceramic Filtralite and manganese ore gravel showed high removal efficiencies of pollutants [19-33]. In Pakistan limited studies are conducted on the treatment performances of different substrates e.g. compost and gravel, peat and mixtures of sand, peat, blast furnace slag and Polonite [34-36]. Current trend of water deficiency due to climate change, precipitation pattern and population increases etc. to mitigate this impact used, water should be recycled and

reuse. In the study different by-products and wastes materials are used as useful products for wastewater treatment, without reprocessing thus reducing waste burden over the earth. Objective of the study is to evaluate and to compare the performance of four laboratory scale DFVCW with different substrate material for sewage wastewater treatment.

2. MATERIALS AND METHODS

2.1. Site Description

Islamabad the Federal Capital Territory of Pakistan is a planned city constructed at the foot hills of Himalayas at the edge of Pothohar Plateau in north of the country at an elevation of 558 meter Above Sea level (ASL). The total area covered by the city is 8010 km² (33° 43' 09.6" N; and 73° 03' 23.3" E). Experimental site of the study is located at National Agriculture Research Centre (NARC) Islamabad. A part of the organization assigned to the experiments is National Institute of Bioremediation (NIB) orchards at NARC. Ex situ experiment site located on wastewater canal that supplied wastewater from Shehzad town to orchard (NIB).

2.2. Experimental Design

Four pilot scale Sub Surface Down-flow lab-scale constructed wetlands employed to investigate pollutant removal receiving sewage

2.2.1. Size and Configurations

water contaminated by confined housing operations in Shehzad town Islamabad. Site was cleared for experimental setup, followed by excavation up to eight feet to take flow from sewage channel without requirement of an electric motor. Plastic containers of an area 2.638 f² (7.475 f³), were used for experimental purpose. The diameter of each wetland reactor was 55 cm and the height was 85 cm. Four DFVCW were named as M-01, M-02, M-03 and M-04 with different substrate composition.

2.2.2 Substrata

Each unit was filled with different substrates media, the substrates percentage composition and arrangement of constructed wetlands were as follows;

2.2.2.1 Substrate composition and layering of M-01

Constructed wetland (M-01) unit was filled with media consisted of 28.4 cm layer of over burn bricks (12.7-25.4 mm) at base, 28.44 cm layer of gravel (8-16 mm) and sand (1/2-1 mm) at the middle and 17.78 cm Agriculture waste (1 kg Typha leaves, 3 kg corn cobs wastes, 2 kg sugar bagasse) on the top as the supporting

layer. The free board of 10.5 cm was allowed for dried sludge accumulation.

2.2.2.2 Substrate composition and layering of M-02

Constructed wetland (M-02) unit was filled with media consisted of 28.4 cm layer of over burn bricks (12.7-25.4 mm) at base, 28.44 cm layer of gravel (8-16 mm) and sand (1/2-1 mm) at the middle and 17.78 cm Agriculture waste (Agriculture wastes (2Kg of rice husk, 1 Kg maize straw, ½ Kg Bhang, 1/2 Kg Neem (Azadirachta indica) on the top as the supporting layer. The free board of 10.5 cm was allowed for dried sludge accumulation.

2.2.2.3 Substrate composition and layering of M-03

Constructed wetland (M-03) unit was filled with media consisted of 28.4 cm layer of over burn bricks (12.7-25.4 mm) at base, 17.78 cm coal (16-21 mm) layer at the middle and, 28.44 cm mixture of gravel (8-16 mm) and sand (1/2-1 mm) on the top as the supporting layer. The free board of 10.5 cm was allowed for dried sludge accumulation.

2.2.2.4 Substrate composition and layering of M-04

Constructed wetland (M-04) unit was filled with media consisted of 21.3 cm layer of large pieces of over burn bricks (12.7-25.4 mm) at base, 21.33 cm layer small pieces of over burn bricks (16-22 mm) at the middle and, 33.68 cm mixture of gravel (16-21 mm) and sand (1/2-1 mm) on the top as the supporting layer. The free board of 10.5 cm was allowed for dried sludge accumulation.

2.2.3 Ventilation and drainage systems

To reduce anoxic condition in the area, one vertical pipe, having diameter of 100 mm, was installed in the middle of each constructed wetland units. The inflow system consisted of chemically inert plastic pipe which directly fed into each plastic drum with inlet flow of 260ml/ 20 min individually from sewage canal. Three days of hydraulic retention time was achieved by the experiment. Operating conditions in the four constructed wetlands were the same.

2.2.4 Sample preparation and Analysis

Samples of wastewater were collected from main in-let, four out-let of each CW, in polyethylene bottles properly washed and properly rinsed 3-4 times with de-ionized water. Sealed BOD and COD plastic bottles wrapped with black electrical tape were used for BOD & COD sampling. Samples were collected every 1.5 week at each DFVCW inlet and four outlets. Sampling was done at 11 am and then after 3-4 hour composite sampling was done. Each aliquot of composite samples

were packed in ice-filled esky before dispatch to the NIB Labs, NARC, Islamabad, at the time of collection. Sampling was performed for a period of four months from 22th December to 25th April. JENWAY 3510 pH meter was used for pH analysis. EUTECH (cyber scan series 600) was used for Total Dissolved Solids (TDS) and Electrical Conductivity (EC). Bicarbonates (HCO_3), Phosphates, Chlorides, Hardness, Oil and grease was analyzed by APHA, 2002 [37,38]. Biological Oxygen Demand (BOD) and Chemical Oxygen Demand (COD) by EPA, 2000 [39].

2.2.5 Data Analysis

Statistical significance was computed by analysis of variance (ANOVA) at $P < 0.05$ using STATISTICA 7.0 [40]. Treatment efficiency for removal of various CWs was determined by the percentage equation using EXCEL, 2010.

3. RESULTS AND DISCUSSION

One-way ANOVA between each DFVCW bioreactors (M-01, M-02, M-03 and M-04) for all the included physico-chemical variables yielded no significant difference in their means as (mentioned in Table-4) which indicates that all these experimental design with different substrate as a media of constructed wetlands contribute equally to the reduction physico-chemical concentrations in the in-fluent sewage stream. While every DFVCW with different substrate division in comparison with In-let for all the included variables shows significant difference p values in Table-1. In all cases, the treatment efficiency obtained in the novel systems was comparable to, or higher than, the performances obtained in conventional and other similar wetland systems [41].

3.1 pH

pH values for In-let and constructed wetlands (M-01, M-02, M-03 and M-04) was in optimum range of pH (6.5-9.5) according to [42]. In-let samples were described as neutral water (Mean 7.5). Samples (M-01,) represent slightly acidic water on neutrality scale (Min.6.50-Max.7.9). Slight variation of pH was because of detergents and different chemicals in household effluents. The Samples (M-02, M-03 and M-04) represent neutral water (Min.7.10-Max.7.80). Effluent pH mean values showed almost no difference among the experimental units as table 1 [43]. In season (March and April) pH is relatively high as compared to (Jan and Feb) because of rainfall there is excess of HCO_3 due to reaction between water and carbon dioxide.

3.2 Temperature

There is no abnormal temperature values recorded in In-let and out-lets samples from experimental setup of

constructed wetlands. Differences in temperature of all the samples are related to the time of sample collection (low temperature in winter and relatively high temperature in spring). Temperature of each experimental set (M-01, M-02, M-03 and M-04) is significantly different ($p < 0.02$) from In-let sample representing percent change of Min.20.5-Max.27.8 as Table 2.

3.3 Biological oxygen demand (BOD)

BOD is used to assess the water quality regarding organic matter present in both suspended and dissolved form [44]. Samples from constructed wetlands (M-01, M-02, M-03 and M-04) are categorized in the range of very clean to fairly clean waters [45]. The average removal efficiencies of

BOD in the DFVCW (M-01, M-02, M-03 and M-02) were 98, 97.8, 98.1 and 98.2%, respectively. As mentioned in table 3, each experimental set have significant difference with p value (0.00) showing 99.9 percent decrease of BOD concentration than In-let (sewage) point of the setup.

3.4 Chemical oxygen demand (COD)

COD is higher than BOD values, because more compounds can be chemically oxidized than can be biologically oxidized [46]. According to Swedish EPA, In-let (raw sewage) samples are categorized as very high level contaminated waters [47]. Samples from constructed wetlands (M-01, M-02, M-03 and M-04) are categorized in the range of very clean to fairly clean waters. According to irrigation standards the COD after treatments of CW's is very lower than the permissible limits (Table 4). The average removal efficiencies of COD in the DFVCW's (M-01, M-02, M-03 and M-02) were 92.4, 92.7, 92.4 and 92.1%, respectively.

3.5 Total dissolved solids (TDS)

Total dissolved solids or Salinity represents the total amount of solids remaining when a water sample evaporates to dryness [48]. Sewage wastewater samples (In-let) record a high TDS concentration comparing with typical value of sewage wastewater (500 ppm) according to [49], especially samples analyze in the month of March and April which shows high TDS concentration. Results of the all four treatment constructed wetlands (M-01, M-02, M-03 and M-04) shows that the TDS are in ranges of palatable water (600 ppm) according to [50-51]. The average removal efficiencies of Phosphates in the DFVCW's (M-01, M-02, M-03 and M-04) were 39.5, 40.2, 39.9 and 41.2%, respectively. Concentration of TDS in the treatment constructed wetlands (M-01, M-02, M-03 and M-04) samples as well as of In-let (raw sewage) samples are

lower than the permissible values for irrigation water (see Table 5).

3.6 Electrical Conductivity (EC)

Conductivity is the ability of a substance to conduct electricity. Increase in conductivity indicates that there is a source of dissolved ions and salts in the vicinity which may be sewage wastewater or urban runoff from roads. The unit of measurement for electrical conductivity is expressed in either micro Siemens per centimeter ($\mu\text{S/cm}$) or milli Siemens per centimeter (mS/cm). It is also effectively a surrogate for Electric Conductivity (EC) and is important for irrigation because it is a measure of the salinity of the water [52]. The average removal efficiencies of electrical conductivity in the DFVCW's (M-01, M-02, M-03 and M-02) were 48.5, 67.4, 59.4 and 61.7%, respectively. As mentioned in table 6, each experimental set have

significant difference with *p* value (0.00) showing 99.9 percent decrease of Electrical conductivity concentration than In-let (sewage) point of the setup.

3.7 Bicarbonates (HCO_3^-)

Bicarbonates, Hydroxide and carbonates represent the main contributor to alkalinity in all natural waters [53-54]. Bicarbonates are positively co related to Free CO_2 . Carbonates of all the samples were zero, this means that pH below 8.5 all the carbonates converted into bicarbonates [55]. Excess of bicarbonates in In-let samples results due to domestic sewage, decomposition of Sulphates and Denitrification of organic matter and bacteria [55-56]. The average removal efficiencies of bicarbonates in the DFVCW's (M-01, M-02, M-03 and M-02) were 21.1, 22.5, 19 and 20.1%, respectively.

Table 1: Descriptive statistics of pH

Variables	Samples	Valid N	Mean	Minimum	Maximum	Range	Variance	Std.Dev	Skewness	Kurtosis	P Value*	NEQ's
pH	Inlet	13.00	14.22	6.70	101.00	94.30	624.04	24.98	3.74	13.99		6-10
	M-01	13	7.18	6.40	7.50	1.10	0.13	0.36	-0.97	0.07	0.04	
	M-02	13	7.35	7.10	7.80	0.70	0.03	0.18	1.10	3.28	0.17	
	M-03	13	7.33	6.40	7.90	1.50	0.13	0.37	-1.13	3.13	0.17	
	M-04	13	7.31	7.10	7.50	0.40	0.02	0.13	-0.47	-0.76	0.17	

Table 2: Descriptive statistics of Temperature

Variables	Samples	Valid N	Mean	Minimum	Maximum	Range	Variance	Std.Dev	Skewness	Kurtosis	P Value*	NEQ's
Temperature	Inlet	13.00	18.88	12.00	35.00	23.00	45.66	6.76	1.66	2.29		
	M-01	13	14.08	12.00	19.00	7.00	6.08	2.47	0.92	-0.33	0.02	
	M-02	13	14.15	11.00	21.00	10.00	9.47	3.08	0.80	0.31	0.02	
	M-03	13	14.38	11.00	20.00	9.00	10.42	3.23	0.78	-0.99	0.02	
	M-04	13	15.00	11.00	24.00	13.00	16.33	4.04	1.07	0.39	0.02	

Table 3: Descriptive statistics of BOD

Variables	Samples	Valid N	Mean	Minimum	Maximum	Range	Variance	Std.Dev	Skewness	Kurtosis	P Value*	NEQ's
BOD	Inlet	13.00	128.54	88.00	198.00	110.00	996.94	31.57	0.99	0.94		80 mg/l
	M-01	13	2.47	1.00	3.20	2.20	0.51	0.72	-0.75	-0.44	0.00	
	M-02	13	2.80	1.60	3.90	2.30	0.46	0.68	0.39	-0.11	0.00	
	M-03	13	2.41	1.60	3.10	1.50	0.28	0.53	-0.25	-1.56	0.00	
	M-04	13	2.29	1.46	3.40	1.94	0.45	0.67	0.10	-1.41	0.00	

Table 4: Descriptive statistics of COD

Variables	Samples	Valid N	Mean	Minimum	Maximum	Range	Variance	Std.Dev	Skewness	Kurtosis	P Value*	NEQ's
COD	Inlet	13.00	163.69	110	300	190.00	3536.40	59.47	1.73	1.95		150 mg/l
	M-01	13	12.42	11.34	13.69	2.35	0.40	0.63	-0.23	0.64	0.00	
	M-02	13	11.86	10.09	14.54	4.45	1.22	1.11	0.95	1.99	0.00	
	M-03	13	12.30	11.02	14.78	3.76	0.88	0.94	1.44	3.47	0.00	
	M-04	13	12.80	11.33	15.73	4.40	1.07	1.04	1.91	5.61	0.00	

Table 5: Descriptive statistics of TDS

Variables	Samples	Valid N	Mean	Minimum	Maximum	Range	Variance	Std.Dev	Skewness	Kurtosis	P Value*	NEQ's
TDS	Inlet	13.00	682.92	505.00	1198.00	693.00	36442.24	190.90	1.92	3.85		3550 mg/l
	M-01	13	412.85	323.00	528.00	205.00	4383.81	66.21	0.28	-0.72	0.00	
	M-02	13	407.77	318.00	548.00	230.00	5483.03	74.05	0.61	-0.74	0.00	
	M-03	13	410.31	324.00	554.00	230.00	5460.40	73.89	0.81	-0.62	0.00	
	M-04	13	401.31	311.00	538.00	227.00	5053.06	71.08	0.67	-0.43	0.00	

Table 6: Descriptive statistics of EC

Variables	Samples	Valid N	Mean	Minimum	Maximum	Range	Variance	Std.Dev	Skewness	Kurtosis	P Value*	NEQ's
EC	Inlet	13.00	2.12	1.40	2.90	1.50	0.17	0.41	-0.29	0.66		
	M-01	13	1.09	0.11	1.27	1.16	0.09	0.31	-3.23	11.10	0.00	
	M-02	13	0.69	0.01	1.32	1.31	0.31	0.56	-0.23	-2.16	0.00	
	M-03	13	0.86	0.01	1.24	1.23	0.22	0.47	-1.12	-0.46	0.00	
	M-04	13	0.82	0.01	1.32	1.31	0.25	0.50	-0.86	-1.11	0.00	

Table 7: Descriptive statistics of HCO_3^-

Variables	Samples	Valid N	Mean	Minimum	Maximum	Range	Variance	Std.Dev	Skewness	Kurtosis	P Value*	NEQ's
HCO_3^-	Inlet	13.00	564.62	490.00	658.00	168.00	3165.59	56.26	0.54	-1.19		
	M-01	13	445.46	401.00	630.00	229.00	3952.10	62.87	2.48	6.56	0.00	
	M-02	13	437.38	400.00	600.00	200.00	3444.42	58.69	2.16	4.56	0.00	
	M-03	13	456.92	411.00	600.00	189.00	4046.24	63.61	1.87	2.38	0.00	
	M-04	13	450.77	405.00	600.00	195.00	3671.86	60.60	1.68	2.09	0.00	

Table 8: Descriptive statistics of Phosphates

Variables	Samples	Valid N	Mean	Minimum	Maximum	Range	Variance	Std.Dev	Skewness	Kurtosis	P Value*	NEQ's
Phosphates	Inlet	13.00	57.63	40.20	75.00	34.80	100.51	10.03	-0.06	-0.53		
	M-01	13	1.15	0.01	3.40	3.39	1.13	1.06	0.99	0.21	0.00	
	M-02	13	1.10	0.02	3.70	3.68	1.22	1.11	1.10	0.99	0.00	
	M-03	13	1.13	0.01	3.10	3.09	0.90	0.95	0.74	0.20	0.00	
	M-04	13	1.15	0.10	3.10	3.00	0.86	0.93	1.15	1.05	0.00	

Table 9: Descriptive statistics of Chlorides

Variables	Samples	Valid N	Mean	Minimum	Maximum	Range	Variance	Std.Dev	Skewness	Kurtosis	P Value*	NEQ's
Chlorides	Inlet	13.00	67.46	52.00	79.40	27.40	55.89	7.48	-0.39	0.53		
	M-01	13	39.42	30.00	52.00	22.00	53.61	7.32	0.48	-0.82	0.00	
	M-02	13	42.02	31.00	57.60	26.60	76.83	8.77	0.52	-0.97	0.00	
	M-03	13	42.10	31.00	56.00	25.00	62.43	7.90	0.12	-1.24	0.00	
	M-04	13	42.24	32.00	57.60	25.00	68.78	8.29	0.62	-0.74	0.00	

Table 10: Descriptive statistics of Hardness

Variables	Samples	Valid N	Mean	Minimum	Maximum	Range	Variance	Std.Dev	Skewness	Kurtosis	P Value*	NEQ's
Hardness	Inlet	13.00	462.15	417.00	550.00	133.00	1864.97	43.19	1.18	0.29		
	M-01	13	290.08	217.00	370.00	153.00	2557.91	50.58	-0.11	-1.49	0.00	
	M-02	13	280.31	214.00	343.00	129.00	2022.90	44.98	-0.19	-1.61	0.00	
	M-03	13	279.92	218.00	357.00	139.00	2219.08	47.11	0.25	-1.38	0.00	
	M-04	13	268.23	203.00	313.00	110.00	1681.19	41.00	-0.24	-1.74	0.00	

Table 11: Descriptive statistics of Oil and Grease

Variables	Samples	Valid N	Mean	Minimum	Maximum	Range	Variance	Std.Dev	Skewness	Kurtosis	P Value*	NEQ's
Oil & Grease	Inlet	13.00	384.00	114.00	858.00	744.00	56944.67	238.63	1.10	0.07		15 mg/l
	M-01	13	43.46	19.20	89.00	69.80	606.50	24.63	0.77	-1.43	0.00	
	M-02	13	46.79	20.60	99.00	78.40	773.25	27.81	1.01	-0.19	0.00	
	M-03	13	48.10	19.90	78.00	58.10	518.11	22.76	0.00	-1.86	0.00	
	M-04	13	47.45	20.20	78.00	57.80	518.89	22.78	0.00	-1.90	0.00	

3.8 Phosphates

Several studies have been conducted on the potential use of constructed wetlands in the removal of phosphorus from wastewaters [57]. The average removal efficiencies of Phosphates in the DFCW bioreactors M-01, M-02, M-03 and M-04 were 98, 98, 98 and 98%, respectively.

Phosphates removal in constructed wetlands may take place due to microbial immobilization retention by the substrate and precipitation in the water column [58]. As mentioned in table 8, each experimental set have significant difference with p value (0.00) showing 99.9 percent decrease of phosphates concentration than In-let (sewage) point of the setup.

3.9 Chlorides

Chlorides ion is most abundant in nature. It originates from natural sources, domestic sewage, industrial effluents and urban runoff containing de-icing salts (16, 59). Chlorides are troublesome in irrigation water and also harmful to aquatic life [60]. High chloride content impacts taste and could cause corrosion [61]. Inlet (raw sewage) show chlorides concentration below the permissible limits of (1000 mg/l) according to PAK-NEQ's 2000. But it exceeds the recommended value of wastewater (50 ppm) according to [48]. As mentioned in table 9, each experimental set have significant difference with p value (0.00) showing 99.9 percent decrease of chlorides concentration than In-let (sewage) point of the setup. The average removal efficiencies of chlorides in the DFCW bioreactors M-01, M-02, M-03 and M-04 were 41.5, 37.7, 37.5 and 37.3%, respectively.

3.10 Hardness

Hardness of water is equivalent to concentration of total inorganic salts (Calcium and Magnesium) which are to precipitate when it is heated and negatively affects the solubility of soap in the water [62][59]. Inlet (raw sewage) show hardness concentration to the limits of (500 ppm) represent a tolerate hardness according to [59] [63]. The average removal efficiencies of hardness in the DFCW bioreactors M-01, M-02, M-03 and M-04 were 37.2, 39.3, 39.4 and 41.9%, respectively. As mentioned in table-10, each experimental set have

significant difference with p value (0.00) showing 99.9 percent decrease of hardness than In-let (sewage) point of the setup.

3.11 Oil and Grease

Oil and Grease is a mixture of chemical species consist of compounds (esters) of alcohol or glycerol (glycerin) with fatty acids. The term covers fats, oils, waxes and other related constituents of wastewater. The glycerides of fatty acids that are liquids at ordinary temperatures are called oils and those that are solids are called fats. They can arise from all sources including meats and meat processing, butter, margarine, cooking oil and vehicle oils. Oil and grease interfere with biological life at the water surface and also cause unsightly films [52]. There are no existing or proposed standards for oil and grease for irrigation and agriculture in Pakistan, although for aquatic life and general waters the oil and grease maximum permissible levels are 5 mg/l and 15 mg/l respectively. All the samples tested exceeded these limits but the tolerance limit for sewage effluent discharged on land for irrigation of 50 mg/l was not exceeded in treatment wetlands samples. The farmers using wastewater for irrigation are in contact with the wastewater and the oil and grease is undesirable for agriculture as well as for aquaculture. As mentioned in table 11, each experimental set have significant difference with p value (0.00) showing 99.9 percent decrease of hardness than In-let (sewage) point of the setup.

4. CONCLUSION

This study has shown that the entire treated water sample meets the WHO limits for the physico-chemical properties. COD and Phosphates removal efficacy was found to be higher with agriculture wastes and over burn bricks (M-01, M-02 and M-04) as substrate in experiments. Over burn bricks are believed to favor adsorption/crystallization due to intrinsic characteristics, notably their internal porosity. The presence of agriculture wastes associated to sand and gravel would be beneficial by contributing to a source of food for microbial development, which enhance bioremediation. Neutral pH conditions and temperature fluctuations would favor adsorption and bioremediation of sewage wastewater. In small scale wastewater treatment plants,

increase in HRT (Hydraulic Retention Time) may be important thus reducing pollutants load in sewage. The differences in the removal performances have resulted from the physical structures and the chemical compositions of the substrate mediums, as well as the differences of the aerobic and anaerobic environments within the wetlands. These results indicated that the properly designed and operated constructed wetlands could also be used for wastewater treatment all over the world, successfully. Further studies should be conducted with regards to the conditions associated to HRT, waste as a substrate, metals concentrations and microbial fauna in wastewater treatment systems.

REFERENCES

- [1] Hinrichsen, D; Tacio, H. The coming freshwater crisis is already here: The linkages between population and water, DC: Woodrow Wilson International Center for Scholars, Washington, 2002.
- [2] Liu and Diamond, 2005 J. Liu and J. Diamond, China's environment in a globalizing world. *Nature*, 435 (2005), pp. 1179–1186.
- [3] Shalizi, 2006 Z. Shalizi, Addressing China's Growing Water Shortages and Associated Social and Environmental Consequences, World Bank, Washington D.C., USA (2006).
- [4] Liu and Yu, 2001 C.M. Liu and J.J. Yu, Groundwater exploitation and its impact on the environment in the North China Plain. *Water International*, 26 (2001), pp. 265–272.
- [5] Han, 2003 Z.S. Han, Groundwater resources protection and aquifer recovery in China. *Environmental Geology*, 44 (2003), pp. 106–111.
- [6] Foster et al., 2004 S. Foster, H. Garduño, R. Evans, D. Olson, Y. Tian, W. Zhang and Z. Han, Quaternary aquifer of the North China Plain—assessing and achieving groundwater resource sustainability. *Hydrogeology Journal*, 12 (2004), pp. 81–93.
- [7] Liu and Xia, 2004 C.M. Liu and J. Xia, Water problems and hydrological research in the Yellow River and the Huai and Hai River Basins of China. *Hydrological Processes*, 18 (2004), pp. 2197–2210.
- [8] Fan et al., 2006 H. Fan, H. Huang and T. Zeng, Impacts of anthropogenic activity on the recent evolution of the Huang (Yellow) River Delta. *Journal of Coastal Research*, 22 (2006), pp. 919–929.
- [9] Cai and Ringler, 2007 X.M. Cai and C. Ringler, Balancing agriculture and environmental water needs in China: alternative scenarios and policy options. *Water Policy*, 9 (2007), pp. 95–108.
- [10] Xia et al., 2007 J. Xia, L. Zhang, C.M. Liu and J.J. Yu, Towards better water security in North China. *Water Resource Management*, 21 (2007), pp. 233–247.
- [11] Anonymous. World Water Day. 22-03-2010; info, United Nations, 2010.
- [12] WB-SCEA. Pakistan Strategic Country Environmental Assessment. Main report, Report no. 36946-PK World Bank; 2006. p. 1-66.
- [13] WB-CWRAS. Pakistan country water resources assistance strategy water economy; Running dry', 34081-PK, Agriculture and Rural Development Unit, World Bank, 2005.
- [14] WWF. Pakistan's waters at risk; Water and health related issues in Pakistan and key recommendations, Lahore — 54600, Pakistan, 2007, 1-33.
- [15] National Water Policy (Draft) 2005, Ministry of Environment, Government of Pakistan
- [16] Hussain M, Rasool SA, Khan MT, Wajid A. Enterococci vs coliforms as a possible fecal contamination indicator: baseline data for Karachi. *Pak J Pharm Sci* 2007;20: 107–11.
- [17] PAK-EPA. State of Environment Report 2005. Pakistan Environmental Protection Agency (Pak-EPA). Govt. of Pakistan, Islamabad, Pakistan: Ministry of Environment; 2005.
- [18] Deuren, V.J; Lloyd, T; Chhetry, S; Liou, R; Peck, J. Remediation technologies screening matrix and reference guide, Report by Platinum International, Inc. Report No. SFIM-AEC-ET-CR-97053, 2002, 4th Edition.
- [19] Kadlec, R.H; Knight, R.L. Treatment Wetlands. Lewis Publishers, Boca Raton, 1996, 893.
- [20] Belmont, M.A; Ikonomou, M; Metcalfe, C.D, Presence of nonylphenolethoxy-late surfactants in a watershed in central Mexico and removal from domestic sewage in a treatment wetland. *Environ. Toxicol. Chem*, 2006, 25, 29–35.
- [21] Hedstrom, A. Reactive filter material for ammonium and phosphorus sorption in small scale wastewater treatment. 2006. 17/ ISSN:1402-1544/ISRN:LTU-DT—06/17—SE.

- [22] Vohlaa, C; Kõiva, H; Bavorb, J; Chazarenc, F; Mandera, U; Filter materials for phosphorus removal from wastewater in treatment wetlands, *Ecological Engineering*, 2011, 37, 70–8.
- [23] Brix, H. Do macrophytes play a role in constructed treatment wetlands? *Water Sci. Technol*, 1997, 35, 11–17.
- [24] Tanner, C.C; Sukias, J.P.S; Upsdell, M.P. Organic matter accumulation during maturation of gravel-bed constructed wetlands treating farm dairy wastewater. *Water Res.* 1998, 10, 3046–3054.
- [25] Tanner, C.C.; Sukias, J.P.S.; Upsdell, M.P.; Substratum phosphorus accumulation during maturation of gravel-bed constructed wetlands. *Water Sci. Technol*, 1999, 40, 147–154.
- [26] Kadlec, R.H; Reddy, K.R. Temperature effects in treatment wetlands. *Water Environ*, 2001, 3, 543–557.
- [27] Sundaravadivel, M.; Vingesvaran, S. Constructed wetlands for wastewater treatment. *Crit. Rev. Environ. Sci. Technol*, 2001, 31, 351–409.
- [28] Kadlec, R.H; Tanner, C.C; Hally, V.M; Gibbs, M.M. Nitrogen spiraling in subsurface-flow constructed wetlands: implications for treatment response. *Ecol. Eng.* 25, 365–381.
- [29] Garcia, J; Aguirre, P; Barragan, J; Mujeriego, R; Matomoros, V; Bayona, J.M. Effect of key design parameters on the efficiency of horizontal subsurface flow constructed wetlands. *Ecol. Eng.* 2005, 25, 405–418.
- [30] Akrotos, C.S; Tsihrintzis, V.A. Effect of temperature, HRT, vegetation and porous media on removal efficiency of pilot-scale horizontal subsurface flow constructed wetlands. *Ecol. Eng.* 2007, 29, 173–191.
- [31] Zhang X.L. Studies on performance of purification and influence on clogging of vertical flow constructed wetlands with different filter media, Ph.D Thesis, Graduate School of the Chinese Academy of Sciences, 2007.
- [32] Albuquerque. Oliveira, J; Semitela, S; Amaral, L. Influence of bed media characteristics on ammonia and nitrate removal in shallow horizontal subsurface flow constructed wetlands. *Bioresource Technology* 100, 2009, 6269–6277.
- [33] Cheng X.J; Chen, G; Huang, F. Ming, L.G; Liu, J; Yang, n; Nan, G, S. Iron and manganese removal by using manganese ore constructed wetlands in the reclamation of steel wastewater, *Journal of Hazardous Materials* 169, 2009, 309–317.
- [34] Aslama, M.M; Malik, M; Baiga M.A; Qazia, I.A; Iqbal, J. Treatment performances of compost-based and gravel-based vertical flow wetlands operated identically for refinery wastewater treatment in Pakistan. *ecological engineering* 30, 2007, 34–42.
- [35] Kietlin'ska, A; Renman, G. An evaluation of reactive filter media for treating landfill leachate. *Chemosphere* 61 (2005) 933–940.
- [36] Xiong J.B; Mahmood, Q. Adsorptive removal of phosphate from aqueous media by peat. *Desalination*, 259, 2010, 59–64.
- [37] APHA (1998) Standard methods for the examination of water and wastewater, 20th ed. Washington, DC, American Public Health Association.
- [38] APHA, Standard Methods for the Examination of Water and Wastewater, 21st Edition –Method, (titration).
- [39] EPA. Manual of Methods Analysis of Water and Wastes, 2000.
- [40] Nyquist, O; Greger, M. A field study of constructed wetlands for preventing and treating acid mine drainage *ecological engineering*, 35, 2009, 630–642.
- [41] Sun, S; Bleck, R; Rooth, C; Dukowicz, J; Chassignet, E and Killworth, P. Inclusion of thermobaricity in isopycnal-coordinate ocean models, *J. phys. oceanog.* 1999. 29, 2719–2729.
- [42] Drinking Water Analysis and Action Plan For State Reported Public Water System Data In the EPA Safe Drinking Water Information System / Federal Version (WHO/SDWIS/FED) Office of Water (4606M) EPA, 2006, 816-R-07-010.
- [43] Irini P; Kotti; Georgios, D; Gikas and Vassilios, Tsihrintzis, A. Effect of operational and design parameters on removal efficiency of pilot-scale FWS constructed wetlands and comparison with HSF systems, *Ecological Engineering*, 36, 2010, 862–875.
- [44] Ahipathy and Puttaiah. Toxicity of vries habhavathy river water and sediment the growth of *Phaseolus vulgaris* (French bean), *J. Appl. Sci. Environ. Manage.* March, 2007, 11, 17–26.

- [45] Williams, D.D; Williams, N.E; Hynes, H.B.N. Observations on the life history and burrow construction of the crayfish *Cambarus fodiens* (Cottle) in a temporary stream in southern Ontario, *Canadian Journal of Zoology*, 1974, 52:365-370, 10.1139/z74-044
- [46] Bartram, J. and Ballance, R. Water quality monitoring United Nations Environment Programme, World Health Organization E and FN Spon, London. 1996. 383.
- [47] Phyllis, K; Scannell, W and Lawrence, Duffy, K. Effects of Total Dissolved Solids on Aquatic Organisms: A Review of Literature and Recommendation for Salmonid Species, *American Journal of Environmental Sciences* 3 (1): 1-6, 2007 ISSN 1553-345X.
- [48] Pescod, M. B. Wastewater treatment and use in agriculture, FAO, Irrigation and Drainage, 1992, Paper, No. 47, 118.
- [49] CCME Canadian Council of Ministers of the Environment. Canadian Environmental Quality Guidelines, Update 5.0. Canadian Council of Ministers of the Environment, Winnipeg, Manitoba, 2005.
- [50] European standards for drinking water, World Health Organization, 2004, second edition.
- [51] Barnes, B; K.H; Meyer, J.L and Freeman, B.J. Sedimentation and Georgia's Fishes: An analysis of existing information and future research, Georgia Water Resources Conference, the University of Georgia, Athens Georgia. March 1997, 20-22.
- [52] Metcalf and Eddie. 2003. Wastewater Engineering Treatment and Reuse, Forth Edition. New York, USA: McGraw Hill.
- [53] Pelham, H; Holmbeck, S.A. and Rasmussen, T.C. Characterization of temporal and spatial variability of turbidity in the Upper Chattahoochee River. K.J. Hatcher, ed. Georgia Water Resources Conference. Athens, Georgia, March 20-22, 1997
- [54] Manmi, A.M. water resources management in Rania area sulaimaniyah, NE-Iraq march 2008.
- [55] Appelo, C.A.J. and Postma, D. Variable dispersivity in a column experiment containing MnO₂ and FeOOH coated sand, *J. Contam. Hydrol*, 1999. 40, 95-106.
- [56] Molle, P.; Lienard, A; Grasmick, A; Iwema, A. Phosphorous retention in subsurface constructed wetlands: investigations focused on calcareous materials and their chemical interactions, *Water Sci. Technol.* 48, 2003, 77-83.
- [57] Reddy, K.R; D'Angelo, E.M. Biogeochemical indicators to evaluate pollutant removal efficiency in constructed wetlands, *Water Sci. Technol.* 35 (1997) 1-10.
- [58] Gray, S; Kinross, J; Read, P; Marland, A. The nutrient capacity of maerl as a substrate in constructed wetland systems for waste treatment, *Water Res.* 34, 2000, 2183-2190.
- [59] WHO (2006) Guidelines for drinking-water quality, 3rd ed. Vol. 1. incorporating first and second addenda. Geneva, World Health Organization.
- [60] Rajkumar, S., Velmurugan, P., Shanthi, K., Ayyasamy, P.M., and Lakshmanaperumalasamy, P. 2004. Water Quality of Kodaikanal lake, Tamilnadu in Relation to Physico-Chemical and Bacteriological Characteristics, Capital Publishing Company, Lake 2004, pp. 339-346.
- [61] WHO (1990). Guidelines for drinking water quality, Vol.2. Health Criteria and other supporting information, Geneva; WHO.
- [62] Al-Manharawi, S. and Hafiz, A. 1997. Fresh water, Resources and quality. Arabic press. Cairo, 181 p.
- [63] European standards for drinking water, World Health Organization, 2004, second edition.

Mitigating the Impacts of Animal Production on Surface Water Quality in Grassland Ecosystem: Techniques and Measures

¹Majid Ajorlo, ²Mahboubeh Ebrahimian

¹ Faculty of Natural Resources, University of Zabol, 98615, Zabol, Iran (ajorlo_m54@yahoo.com)

²Faculty of Forestry, Universiti Putra Malaysia, 43400, Serdang, Malaysia (m_ebrahimian81@yahoo.com)

ABSTRACT

The impacts of livestock production system on the environmental resources e.g. soil, water bodies and biodiversity are considered to be the biggest threat to their sustainability. In this paper, the Best Management Practices (BMPs) both structural and managerial that are widely used to alleviate the influence of animal production activities on stream water quality in grassland ecosystem were discussed. Riparian buffers, exclusion fencing, off-stream water, alternate shade, geotextile and gravel pads and installation of subsurface drainage were introduced as structural measures for mitigating animal influences on surface water. Furthermore, waste management, stocking density, vegetation reestablishment and regular movement of drinking and feeding troughs were discussed as managerial techniques for reducing the negative impact of grazing on surface water. Development of grazing management strategies with particular reference to the conservation of riparian areas and limiting cattle direct access to streams can be highly recommended to protect water quality in grassland ecosystem particularly in areas with steep sloping and hilly terrains.

Keywords: Best Management Practices, Environmental resources, Grazing, Grassland, Water quality

1. INTRODUCTION

Demand for livestock products in the last decades has increased in Asia and the production has increasingly moved from small-scale farms to large-scale commercial units. The rising demand in livestock products can considerably contribute to environmental degradation. The key environmental impacts of livestock production are their effects on the vegetation cover, soil properties, surface water quality, riparian area, wildlife habitat and biodiversity in grassland ecosystem.

Most of environmental concerns in grassland appear at high stocking rate. High stocking rate results in the deposition of large quantities of urine and faeces on pastures and increase the probability of nutrients and pathogens being transported to surface water. Thus, water quality degradation related with livestock production will be most serious when stocking rate exceeds the carrying capacity of grassland. Therefore, degradation of water bodies in livestock production system is of growing environmental concern [7]. Animal production units can contribute to nonpoint or diffuse source pollution through free grazing of animal on grassland[15] and point sources of pollution due to poor storage of slurry, silage effluents, milk parlour and shed washings, and midden drainage in animal production units [10]. The environmental impacts of animal activities can be prevented, mitigated and ameliorated by proper management practices. The aim of this article was to elaborate the impacts of animal production on surface water quality and introduce key Best Management Practices (BMPs) that can be used for mitigation and

amelioration of those negative impacts by animal production activities.

2. SURFACE WATER QUALITY OF GRASSLAND

Quality of water from grassland is a function of precipitation (interval, duration, and intensity), landscape characteristics (slope, gradient, terrain), soil characteristics (depth, texture, moisture content), vegetation cover (species composition, basal density, canopy cover, plant litter) and grazing management.[21, 5] concluded that the main water quality contaminants of concern in grassland are sediment due to soil erosion, nitrogen, phosphorus, pathogens, and suspended solids which are classified as non-point source pollutants [13]. Water quality from grazing land is degraded when suspended solids, nutrients, and pathogens exceed the standard limits for specific uses. Pollutants enter the surface water through overland and subsurface flows either in the form of suspended materials or dissolved substances. Both surface and subsurface flows will carry both dissolved and suspended materials [8].

3. IMPACT OF ANIMAL ON SURFACE WATER QUALITY

The impact of animal on surface water can vary by management strategies and depends on changes in land use (e.g. conversion of forest to pasture), differences in catchment attributes (e.g. topography, drainage system, geology, soil type), grazing management practices (e.g. stocking rate, grazing period, access of livestock to watercourses), and the availability of off-stream water

supplies, salt and mineral block licks [9]. Animal can negatively affect water quality by direct deposition of faeces and urine into the water bodies [8, 6], aggregation in specific locations such as bedding ground near to water bodies, over-grazing, untimely defoliation (relative to rainfall events and soil wetness) [8], and through fertilizers application associated with production of high productive pasture [7]. Grazing animal can also adversely affect surface water through increasing soil erosion and sediment export into water bodies [6]. Water quality degradation with micro-organisms such as various types of bacteria is another major concern associated with grazing animal. Bacteria can be transferred from the animal waste into surface water bodies.

4. MITIGATION MEASURES AND TECHNIQUES

Point sources of pollution in animal production system are easy to identify and can be effectively controlled by following Codes of Good Agricultural Practices [22]. However, the diffuse sources of pollution such as loss of nutrients through leaching in surface runoff are difficult to assess and control. Any practices that reduce the amount of the time that cattle spend in stream, and hence reduce the manure loading, will decrease the potential for adverse impact of water pollution from grazing animal.

Best Management Practices (BMPs) refer to a combination of practices determined to be effective economical approaches for preventing or reducing pollution generated by nonpoint sources. Best management practices include managerial and structural practices [12, 5]. Managerial practices such as proper stocking rate and rotational grazing are designed to minimize pollutant inputs to waterways through land management practices; whereas structural measures such as riparian buffers and vegetative filter strips, portable water supply, portable shade source and fencing riparian areas modify the transport of the pollutants to waterways [5].

To reduce the influence of animal grazing on stream water quality, several BMPs are currently recommended by the Natural Resources Conservation Service (NRCS). These BMPs include livestock riparian buffers, exclusion fencing, offstream water source, alternate shade, and waste management. Proper stocking rate, rotational grazing, location of feeding troughs and watering points, portable water supply, portable shade source, fencing riparian areas from animal access are some appropriate practices to mitigate adverse impact of grazing on surface water quality [14].

4.1 Structural Measures

4.1.1 Riparian Buffers

Animal congregate in riparian areas in catchment for available forage and water, cooler temperature, and shade from riparian trees particularly during hot hours. Congregation in riparian areas is harmful for stream water quality. Riparian buffers are vegetal structure establish on stream banks to reduce contaminant transportation to surface water. Riparian buffers assist in the stabilization of stream banks, the filtering of runoff and the enhancement of habitat by controlling water temperature and providing shelter to wildlife. Riparian buffers consisting mainly of trees and shrubs are highly effective at stabilizing stream banks and are moderately effective at filtering dissolved pollutants such as nitrate and orthophosphates. Those buffers consisting mainly of grass provide a high level of sediment filtration with a moderate level of dissolved nutrient filtration [16]. Several studies have reported the effectiveness of grass buffer strips (18, 4) at controlling non-point sources of pollution from agriculture. It has been reported that forested vegetated riparian strips reduced the concentration of nitrogen in groundwater by 68–100 % and in surface runoff by 78–98 % [20]. [19] reported that vegetated riparian buffers consisting of grass or forest reduced concentrations of nitrate in shallow groundwater by up to 90%.

4.1.2 Exclusion Fencing

Exclusion fencing is another measure of protecting riparian areas and streams through the installation of fence to exclude cattle from streams [9, 5]. Streambank fencing and total cattle exclusion from riparian areas is generally only recommended practice for severely degraded streambanks [1]. However, there are some difficulties associated with exclusion fencing such as economic constraints, removing a stream from use as a drinking water source, installing alternate water sources, additional fencing expenditures, and permanently removing a portion of the pastures from production [5]. [11] evaluated the effects of excluding dairy cows from streams along with planting trees in stream banks and observed 33, 78, 76, and 82% reductions in weekly nitrate + nitrite, total Kjeldahl nitrogen (TKN), total phosphorus (TP), and sediment loads, respectively, from the 14.9 ha pasture area adjacent to the fenced section of stream.

4.1.3. Alternate Water Source

Streams, springs and water troughs provide water requirements of animal in grassland. Animal unrestricted access to these water sources can cause a reduction in water quality. The development of off-stream water and placement of salt and mineral lick blocks at sites located away from streams will enhance surface water quality [9]. When given a choice, cattle will usually drink from the closest source of water. Therefore, alternate water sources reduce the total amount of time animal spend in the stream water and travelling to and from the water. Installation of new

removable water troughs can be recommended in many types of grassland. Installing the sufficient numbers of removable water troughs with respect to distance, slope and topography should be conducted urgently in overgrazed grasslands. [17] showed that stream bank erosion was reduced by 77% due to installation of the alternative water source. Concentrations of total suspended solids, total nitrogen, and total phosphorus reduced by 90, 54, and 81%, respectively. Similar reductions were observed in concentrations of fecal coliform and fecal streptococcus.

4.1.4 Alternate Shade Source

Naturally, tree and shrub canopy is major shade source for animal in grassland. These areas suffer from heavy deposition of animal wastes, soil compaction and erosion. Unfortunately, in many cases such shade sources have been located on stream banks and negatively influence the riparian area and streams in many ways. Animal access restriction to shade sources on riparian areas should be done prior to other mitigation practices. Alternate shades can be provided using both natural and constructed shade, as a BMP to improve stream quality and animal grazing performance. [5] noticed that steers in pastures without shade loafed around the water trough at the majority hours of a day. By providing an alternate method for cooling, the amount of time cattle loaf in streamside areas may be reduced.

4.1.5 Geotextile and Gravel Pads

Heavily used areas such as feeding area, watering area, bed ground and sheds gateway in animal production units can become muddy during wet condition, which limits equipment mobility, affects animal performance and contributes to erosion and reduced environmental quality [2]. These areas usually have high animal densities and can be a source of surface and groundwater contamination. Geotextile and gravel pads offer a low-cost alternative to concrete for providing all-weather surfaces for cattle and vehicle traffic, and are used in many livestock facilities to minimize mud, surface runoff, erosion of heavy traffic areas. Producers have willingly adopted pads for heavy use areas of pasture farms, and cost share programs have enhanced the rapidness of adoption. Geotextile fabric improves stability, load bearing capacity, filtration and drainage of the site. This technique can be utilized in front of cattle shed gateway as well as at the centre of farm where all paddocks gateway meet. [2] reported the effect of geotextile pad treatment was significant on the reduction of surface runoff EC, TS, COD, NO₂-N, TN and TP values in cattle feeding and loafing areas.

4.1.6 Installation of Subsurface Drainage System

This technique is practical and useful in areas with high annual rainfall and low groundwater level. This

technique may not be applicable in grasslands where land type is rolling and hilly as well as high content of clay in soil. The installation of subsurface drainage leads to a lowering of the water table level and decrease moisture content of the surface soil, thus increasing the shear strength of the soil and its resistance to damage. However, there is uncertainty over how the installation of subsurface drainage influences sediment and nutrient transfers from land to surface waters and there is evidence to suggest that subsurface drains may, in some cases, act as preferential pathways for runoff and provide a direct canal to watercourses.

4.2 Managerial Techniques

4.2.1 Waste Management

Animal can produce large quantities of waste (urine and faeces) while are housed indoors. Animal waste is stored in the form of slurry (a liquid mix of urine and faeces) or manure (a heap of solid dung and bedding material). Poor management of stored wastes can present a threat to environmental quality. Major factor contributing to poor waste management is related to the storage capacity of farm waste facilities, leakage of the storage system, overspill of storage reservoirs and being located adjacent to surface water. In grassland where pasture-based livestock production system is practiced, there is no serious problem regarding waste storage. Nonetheless, milk parlour washing and shed washing are two serious problems in relation to waste management in such system. Waste water of such construction directly flows to adjacent stream in the catchment. A simple remediation measure for this issue would be installation of waste storage facility.

4.2.2 Stocking Density

Stocking density of a farm can be one of the most important factors controlling the magnitude and extent of environmental degradation. Although animal grazing can be beneficial to the environment and enhancing soil condition at moderate stocking densities, heavy stocking density can damage soil, vegetation and water quality and threatening the sustainability of livestock production system. Optimum stocking density in terms of minimal environmental degradation and economical viability depends on factors such as soil texture, soil wetness, topography, pasture grazing capacity, animal species, proper utilization and farmer income. Stocking density also fluctuate by the conditionality of rainfall, plant growth, soil moisture content. For example, it is speculated that 1 and 2.5-3 AU/ha are environmentally optimum stocking densities in tropical native and improved pastures, respectively [3].

4.2.3 Vegetation Reestablishment in Compacted Area

This practice aims to be implemented over small areas such as old sites of drinking/feeding troughs, paddock gateways, bedding grounds, shelterbelts, paddock gateways, animal traffic paths and anywhere which have been compacted severely due to daily animal traffic and the soil requires loosening and rejuvenating. This process breaks up layers of compacted soil and removes deep hoof prints, allowing vegetation to re-establish in the absence of animal.

4.2.4 Regular Movement of Drinking and Feeding Troughs

The soil and vegetation around these facilities tend to receive the greatest damage by grazing animals because animals tend to congregate around them. These areas can then become source for sediment, nutrients and pathogens, threatening water quality in surface waters. Regular moving of troughs to new points before significant visible degradation occurs can reduce damage to vegetation cover and soil and minimize environmental negative consequences at these areas.

REFERENCES

- [1] Miller, J., Chanasyk, D., Curtis, T., Entz, T., and Willms, W. "Influence of stream bank fencing with a cattle crossing on riparian health and water quality of the Lower Little Bow River in Southern Alberta, Canada", *Agricultural Water Management*, No. 97, pp. 247–258, 2010.
- [2] Singh, A., Bicudo, J.R., and Workman, S.R. "Runoff and drainage water quality from geotextile and gravel pads used in livestock feeding and loafing areas", *Bioresource Technology*, No.99, pp. 3224–3232, 2008.
- [3] Ajorlo, M. "Effect of distance from critical points on the soil and vegetation characteristics of rangelands", *Pazuhesh & Sazandegi Journal*, No. 74, pp. 170-174, 2007. (In Persian)
- [4] Blanco-Canqui, H., Gantzer, C.J., and Anderson, S.H. "Performance of grass barriers and filter strips under interrill and concentrated flow", *Journal of Environmental Quality*, No. 35, pp. 1969–1974, 2006.
- [5] Agouridis, T.C., Workman, S.R., Warner, R.C., and Jennings, G.D. "Livestock grazing management impacts on stream water quality: a review", *Journal of American Water Resources Association*, pp. 591-606, 2005.
- [6] Lowrance, R., and Sheridan, J.M. "Surface runoff water quality in a managed three zone riparian buffer", *Journal of Environmental Quality*, No. 34, pp. 1851–1859, 2005.
- [7] Hubbard, R.K., Newton, G.L., and Hill, G.M. "Water quality and the grazing animal", *Journal of Animal Sciences*, No. 82, pp. 255–263, 2004.
- [8] Ohlenbusch, P., Jones, R., Boyer, W., May, G., and Huber, L. *Understanding grazing land and water quality*. Kansas State University. <http://www.oznet.ksu.edu/glwq>. 2002.
- [9] Scrimgeour, G.J., and Kendall, S. "Consequences of Livestock Grazing on Water Quality and Benthic Algal Biomass in a Canadian Natural Grassland Plateau", *Environmental Management*, Vol. 29, No. 6, pp. 824–844, 2002.
- [10] Hooda, P.S., Edwards, A.C., Anderson, H.A., and Miller A. "A review of water quality concerns in livestock farming Areas", *Science of Total Environment*, No. 250, pp. 143-167, 2000.
- [11] Line, D.E., Harman, W.A., Jennings, G.D., Thompson, E.J., and Osmond, D.L. "Nonpoint-source pollutant load reductions associated with livestock exclusion", *Journal of Environmental Quality*, No. 29, pp. 1882-1890, 2000.
- [12] Ohlenbusch, P.D., Jones, R.D., Boyer, W., Huber, L., and May, G., *Grazing Land Water Quality Education Program: Part 4*. Kansas Department of Health and Environment. Bureau of Water. 2000
- [13] Risse, L. M., *Maintaining Water Quality in Grazing Systems*. Grazing Management Training School Workbook, Berry College, pp. 65-79, 1999.

5. CONCLUSIONS

By quantifying the impacts of animal production on environmental resources in grassland ecosystem, valuable information can be provided for the relevant authorities in livestock production sector e.g. livestock keepers and farm managers for better knowledge and understanding of livestock-environment interaction and for preventing or mitigating environmental degradation in grassland ecosystem. The main processes that contribute to animal-induced water quality pollution of streams in grassland are direct defecation and urination into streams, runoff of fecal material from the adjacent land to stream, increased erosion of stream banks by cattle traffic and unrestricted cattle access to streams. Consequently, any structural or managerial practices that include total exclusion of animal from streams particularly in severely degraded stream banks are good mitigation measures for reducing the negative impact of animal on surface water.

- [14] FCA (Florida Cattlemen's Association). *Water quality best management practices for cow/calf operations in Florida*. Kissimmee, FL: Florida Cattlemen's Association. 64 p.1999.
- [15] Royce. E.L., *Manure Loading into Streams from Direct Fecal Deposits*, Fact Sheet No. 25. Cooperative Extension, University of California, 1999.
- [16] Dosskey, M.G. "Viewpoint: Applying Riparian Buffers to Great Plains Rangelands ",*Journal of Range Management*, Vol. 51, No. 4, pp. 428-431. 1998.
- [17] Sheffield, R.E., Mostaghimi, S., Vaughan, D.H., Collins, E.R., and Allen, V.G. "Off-stream water sources for grazing cattle as a stream bank stabilization and water quality BMP", *Transaction of ASAE. (American Society of Agriculture Biological Engineering Transaction)*, Vol. 40, No. 3, pp. 595-604, 1997.
- [18] Daniels, R.B., and Gilliam, J.W. "Sediment and chemical load reduction by grass and riparian filter", *SoilScience Society of American Journal*, NO. 60, pp. 246–251, 1996.
- [19] Osborne, L.L., and Kovacic,D.A. "Riparian vegetated buffer strips in water-quality restoration and stream management", *Freshwater Biology*,, No. 29, pp. 243–258, 1993.
- [20] Petersen, R., Petersen, B., Lacoursiere, J., *A Building-block Model for Stream Restoration*. In *River Conservation and management*, J. Wiley, New York, 1992.
- [21] Tiedemann,A.R., and Higgins,D.A.,*Effects of management strategies on water resources*. In: Quigley, T.M., Sanderson, H.R., Tiedemann, A.R. *Managing interior Northwest rangelands: The Oregon Range Evaluation Project*, USDA Forest Service,1989.
- [22] MAFF (Ministry of Agriculture, Fisheries, and Food),*The Analysis of Agricultural Materials*. 3rd ed. Her Majesty's Stationery Office, London, 1986.

Energy Efficiency in Spanish Wastewater Treatment Plants: The Role of the Internal and External Factors

María Molinos-Senante¹, Francesc Hernández-Sancho², Ramón Sala-Garrido³

¹Department of Applied Economics II. University of Valencia, Spain (maria.molinos@uv.es)

²Department of Applied Economics II. University of Valencia, Spain (francesc.hernandez@uv.es)

³Department of Mathematics for Economy. University of Valencia, Spain (ramon.sala@uv.es)

ABSTRACT

Wastewater treatment plants (WWTPs) are energy-intensive facilities. Thus, reducing their carbon footprint is particularly important, both economically and environmentally. Knowing the real operating energy efficiency of WWTPs is the starting point for any energy-saving initiative. In this article, we applied a non-radial Data Envelopment Analysis (DEA) methodology to calculate energy efficiency indices for sampling of WWTPs located in Spain. In a second stage analysis, we examined the operating variables contributing to differences in energy efficiency among plants. It is verified that energy efficiencies of the analyzed WWTPs were quite low, with only 10% of them being efficient. We found that plant size, quantity of organic matter removed, and type of bioreactor aeration were significant variables in explaining energy efficiency differences. In contrast, age of the plant was not a determining factor in energy consumption. Lastly, we quantified the potential savings, both in economic terms and in terms of CO₂ emissions, that could be expected from an improvement in energy efficiency of WWTPs.

Keywords: energy efficiency, non-radial DEA, wastewater treatment, CO₂ emissions, energy saving.

1. INTRODUCTION

It is well known that water and energy are closely linked. Every step in the integrated water cycle—drinking water treatment and supply, wastewater collection, and purification—requires energy, and water is used in the generation of hydroelectric energy and in the operation of most thermal power plants [1]. At the same time, there is a strong scientific consensus that climate change may affect both the quantity and quality of available water and energy resources in light of predictions of more frequent extreme weather phenomena such as heat waves and intense rainfall in the coming years [2]. Alteration of the water cycle due to climate change may greatly affect water supplies and wastewater treatment infrastructures [3].

The UN's Intergovernmental Panel on Climate Change (IPCC) estimates that for 2030 a 60% reduction in greenhouse gas emissions is needed to achieve a goal of no more than a 3 °C increase in the earth's global temperature level [4]. The wastewater treatment industry will play an important role in achieving this ambitious objective, since in the last several decades energy consumption has grown considerably, both through increases in treated volume and the implementation of new technologies aimed at achieving higher effluent qualities [5].

However, we should not forget that reducing the WWTP carbon footprint is not just an environmental issue; there are also important economic repercussions [6]. In the last few years, we have seen a continual rise in energy costs, from an average of 0.0756 €/kWh in the EU-27 in 2005 to 0.1023 €/kWh in 2009 [7]. Thus, energy

becomes an important cost factor in wastewater treatment, generally second only to personnel costs [8].

The amount of energy needed for operations varies widely among individual WWTPs depending on effluent characteristics, treatment technology, required effluent quality, and plant size [9]. Studies conducted by the Electric Power Research Institute [10] and the Institute for Diversification and Energy Saving of Spain [11] have shown that plants with a lower treatment capacity use more energy than larger plants. Additionally, for all WWTP sizes, most of the energy is consumed in biological treatment. In fact, several other studies [12] indicate that bioreactor aeration comprises between 50% and 60% of total WWTP energy consumption.

We must also keep in mind that energy demand in this industry will grow with time due to a number of factors, such as population growth and the corresponding growth in the contaminant load to be treated, as well as increasingly stringent regulatory and environmental protection standards for effluent quality and residual water reuse. These changes are expected to result in more energy intensive processes [13]. Thus, optimization of energy consumption, efficiency of design and of equipment and technology operations, energy recovery processes, and good management of energy pricing are being increasingly considered in the field of water treatment. Obviously, higher energy efficiency means lower energy consumption, lower greenhouse gas emissions, and lower operating costs for WWTPs [14].

Given the economic and environmental importance of energy consumption in the water treatment industry, and

the usefulness of efficiency measurements for finding energy savings opportunities, the primary goal of our study was to contribute an analysis tool for measuring the energy efficiency of wastewater treatment processes and their economic and environmental consequences. Using a non-radial DEA model, a set of scores of energetic efficiency is computed at plant-level for a sample of WWTPs located in the Valencia region (on the Mediterranean coast of Spain). As a second step, we applied a non-parametric test to determine whether there are statistically significant differences in energy efficiency between WWTPs categorized in terms of their different operating variables. Finally, we defined a Total Improvement Index and a Relative Improvement Index to quantify both the potential economic savings and potential reduction in CO₂ emissions whether improvements in energy efficiency are achieved.

2. MATERIAL AND METHODS

2.1 Non-radial Data Envelopment Analysis.

In the field of production economics, the term efficiency denotes the rational use of available resources, such that all production inputs are employed optimally based on the available technology. Farrell [15] pioneered the study of frontier functions as reference points in measuring efficiency for each production units. This analysis method was the starting point for the so-called DEA models in the economics literature.

Basically, DEA is a mathematical programming technique that based on available data of all Units under study allows build an envelopment surface of efficient production frontier. Thus, those Units that establish the envelopment surface are considered efficient Units, and those that do not rest on the surface are considered inefficient Units. Thus, if a production Unit produces the maximum output for a given input vector (output-oriented DEA) or utilizes the minimum inputs to produce a given output (input-oriented DEA), it is said to be at the production frontier. In both cases, a Unit is considered to be efficient if and only if it is not possible to increase its output quantities while its input quantities are fixed, and it is not possible to decrease its input quantities without altering the resulting output quantities [16].

DEA measures global efficiency for each Unit studied. That is, it measures the maximum radial (proportional) reduction in all Inputs (increment in all outputs) that would raise the Unit's efficiency to the level of the most efficient Units in the study set [17]. However, considering that most production processes have multiple inputs and outputs, radial DEA modeling does not provide information on the efficiency of specific inputs or outputs (depending on the model's orientation) that intervene in the process. To solve this problem, Färe, Grosskopf, and Lovell [18] developed a series of non-radial DEA models where individual inputs reductions (increase of outputs) are measured. In other

words, this type of model provides an efficiency indicator for each of the variables in the process. The great advantage of this type of indicators is that it enables us to identify the specific inputs on which to act in order to increase the efficiency of the Unit being studied. In this context, we set out to evaluate the efficiency of a sampling of WWTPs, using a non-radial DEA model defined by Färe et al. [18] to obtain a specific indicator of energy efficiency for WWTPs.

Given $K = 1, 2, \dots, k, \dots, K$ processes, each one utilizing a vector $x^k = (x_1^k, x_2^k, \dots, x_N^k)_{(N \times 1)}$ to produce a vector of outputs $y^k = (y_1^k, y_2^k, \dots, y_M^k)_{(M \times 1)}$, and with intensity vector λ for variables $(K \times 1)$, the global efficiency index (known as the Russell measure) is calculated with the following expression, where the arithmetic mean of the efficiency indices of each input is minimized:

$$MR(y, x) = \min \left\{ \sum_{n=1}^N \theta_n / N : (\theta_1 x_1, \theta_2 x_2, \dots, \theta_N x_N) \in L(y), 0 \leq \theta_n \leq 1 \right\} \quad (1)$$

That is, the various inputs are minimized by different proportions, unlike with the radial measure, where all inputs are minimized by the same proportion.

For each process k , we can obtain values for the previous Russell measure by solving the following linear programming optimization:

$$\begin{aligned} RM(y^k, x^k) &= \frac{1}{N} \min \sum_{n=1}^N \theta_n \\ \text{s.t.} & \\ \sum_{k=1}^K \lambda_k y_{km} &\geq y_{k^m}, \quad m = 1, \dots, M \\ \sum_{k=1}^K \lambda_k x_{kn} &\leq \theta_n x_{k^n}, \quad n = 1, \dots, N \\ \lambda_k &\geq 0, \quad k = 1, \dots, K \\ 0 \leq \theta_n &\leq 1, \quad n = 1, \dots, N \end{aligned} \quad (2)$$

where RM is the Russell measure while each θ_n obtained provides an efficiency indicator for each of the inputs considered.

2.2 External or Operating Variables.

We proceeded to apply a second stage of analysis to determine which variables explained the efficiency indices just obtained. For this second step, two approximation methods can be used. The most common approach involves the use of regression analysis, for example, censored Tobit regression or ordinary least squares after transforming estimates of efficiency. Nonetheless, this procedure suffers important shortcomings [19]. From a conceptual viewpoint, Grosskopf [20] notes that if the variables selected for the second analysis step are expected to affect

efficiency, they should have been included in the first modeling step to obtain efficiency scores. An alternative approach involves grouping the units (i.e., WWTPs) according to certain specific characteristics or operating variables that appear to be related to efficiency, and then verifying whether there are statistically significant differences between the groups' efficiency scores using, for example, non-parametric hypothesis tests. We chose this second approach, using the Kruskal-Wallis non-parametric test.

2.3 Total and Relative Improvement Index

Finally, assessing the efficiency indexes of unit level, allows quantify the potential savings from an increase in Unit efficiency. This calculation involves using the group of less energy-efficient plants as a reference, and measuring the level of improvement, either in energy cost or consumption, that could be expected if the plants were being operated efficiently (TII – Total Improvement Index). Also, using the variables identified previously as explaining energy efficiency differences, we can quantify the relative savings that could be expected for the less efficient WWTPs if they behaved like the more efficient group of plants (RII – Relative Improvement Index). The following expressions can be used:

$$TII = (1 - E^{ew})RV_{mean}^{ew} \quad (3)$$

$$RII = (E^{eb} - E^{ew})RV_{mean}^{ew} \quad (4)$$

where, TII = Total Improvement Index; E^{ew} = Mean efficiency index for the less efficient group of processes; RV^{ew} = Representative variable for the less efficient group; RII = Relative Improvement Index; E^{eb} : Mean efficiency index for the more efficient group of processes.

3. SAMPLE DATA

For the present empirical study, we used a sample of 177 WWTPs located in the Valencia region of Eastern Spain. To ensure a comparable energy efficiency index for each of the WWTPs, it was necessary to include plants that use the same treatment technology and eliminate the same kinds of contaminants. All of the plants examined in our study utilize prolonged aeration without elimination of nutrients. The treatment process in the analyzed WWTPs consisted of eliminating two contaminants: suspended solids (SS) and organic matter measured as chemical oxygen demand (COD). The inputs required were energy, staff, reagents, maintenance, waste management, and other. The statistical data were from 2009 and were provided by the Regional Administration responsible for the management of WWTPs (EPSAR).

Table 2: Sample Description. Source: EPSAR.

		MEAN	STD. DEVIATION
INPUTS (€/m ³)	Energy	0.223	0.285
	Staff	0.499	0.364
	Reagents	0.021	0.038
	Maintenance	0.119	0.136
	Waste Management	0.044	0.048
	Other	0.020	0.024
OUTPUTS (mg/L)	SS eliminated	281	190
	COD eliminated	609	353

4. RESULTS AND DISCUSSION

We used a non-radial DEA model which enabled us to obtain the global efficiency index of each plant as an average of the indices of the individual inputs. Table 3 shows the mean values for our WWTPs sample. It can be seen that the efficiency levels for each input, and therefore the global efficiency for the whole group, are low. The average global efficiency index was 0.29, indicating that there is substantial improvement potential for the group of WWTPs. If we consider that a Unit is efficient when its score is 1, the WWTPs studied could save about 70% of their inputs (costs) if they operated at the efficiency frontier. The data shown in Table 3 are very relevant, showing that among all the line items considered, the highest efficiency indices were the ones for staff and energy.

Energy	Staff	Reagents	Maintenance	Waste	Other	Global
0.310	0.316	0.229	0.243	0.218	0.301	0.288

Table 3: Mean efficiency index for each input type and global efficiency index.

Using equation (3), we can quantify the energy savings that would be possible if the plants operated at the efficiency frontier, that is, if their energy efficiency index values were 1. Knowing the mean energy efficiency (0.3093), the total annual energy consumption of the plants (19,225,285 kWh) and the total treated wastewater volume (31,697,347 m³/year), we can estimate that if all of the plants were efficient, the energy saved would be 13,279,865 kWh/year,

which is equivalent to 4,781 annual metric tons of CO₂ emissions¹ or 0.15 Kg CO₂/m³, and, in economic terms², 3,487,293 €/year or 0.11 €/m³.

Having obtained plant level efficiency index values, we can now evaluate if the operational and structural

¹ Kg of CO₂ emissions per kWh used by the national electrical production grid is 0.36. Source: 2009 Spain Energy White Book

² Average energy cost for the WWTPs studied was 0.263 €/kWh.

variables of the plants affect their energy efficiency. That is, we can now study behavioral differences in the plants through a set of representative variables. Based on previous studies [21; 22], we assumed that energy efficiency may be affected by the following factors: (i) plant size expressed as wastewater flow rate; (ii) age of plant, or years since plant was built or refurbished; (iii) characteristics of influent water and effluent expressed as grams of COD per m³ of treated water; and (iv) type of aeration in the bioreactor.

First, we used plant size as a reference. To find out how this variable affects energy efficiency, we classified the WWTPs into three groups based on annual volume of treated wastewater, and calculated mean energy efficiency index for each group (see Table 4). In accordance with [23], we found that smaller plants are less efficient than larger ones. We found that, only 3% of the smaller plants operate efficiently in terms of energy, as compared to 32% of the larger plants. The Kruskal-Wallis test results confirm significant differences in energy efficiency among the plant size three groups in our study. The small and medium plants were found to consume 98% and 46% more energy, respectively, than the larger ones.

Table 4: Mean energy efficiency index by size intervals, expressed in (thousands of m³/year); energy consumptions in (kWh/m³), and Kruskal-Wallis test result.

Size (10 ³ m ³ /year)	<100	100-250	>250
Number of plants	107	35	34
Mean energy efficiency	0.226	0.319	0.561
% efficient plants	2.8	11.4	32.4
Energy consumption (kWh/m ³)	0.963	0.708	0.486
Kruskal-Wallis test	0.000		

Having obtained mean energy efficiency and energy consumption values for each group of WWTPs, we then quantified the environmental and economic costs associated with the lower efficiency of the small and medium plants. Thus we estimated that if small plants operated at the same energy efficiency as larger plants, their energy consumption would drop by 0.322 kWh/m³, avoiding emission of 116 g of CO₂/m³ and saving 0.085 €/m³. For medium plants, energy savings would be 0.171 kWh/m³, equivalent to emission of 62 g CO₂/m³ and a cost savings of 0.045 €/m³.

Another potentially significant variable in explaining efficiency differences is plant age, defined as the time that has past since the plant's initial construction or refurbishing. We grouped the plants into three time intervals. Results in Table 5 show that plant age appears not to be a determining factor of energy efficiency.

Surprisingly, we observed that the older plants were better both in terms of efficiency and in terms of energy consumption per m³ of treated water. However, a greater percentage of efficient plants were evident in the group

newer than 8 years, which tells us that in this group, efficiency differences between plants are considerable. In contrast, the results also show that despite the fact that, on average, plants of medium age are the most inefficient, their mean energy consumption is 30% lower than that of the newer plants. The fact that efficiency does not depend on plant age tells us that proper equipment maintenance as well as optimum process operation are extremely important for achieving energy efficiency.

Table 5: Mean energy efficiency index by age interval expressed in (years since construction), energy consumption in (kWh/m³) and Kruskal-Wallis test.

Age (years old)	<8	8-18	>18
Number of plants	31	127	18
Mean energy efficiency	0.336	0.297	0.352
% efficient plants	16.1	9.5	5.6
Energy consumption (kWh/m ³)	1.015	0.783	0.751
Kruskal-Wallis test	0.428		

Since most WWTP energy is consumed by the bioreactor [24], we proceeded to analyze the amount of eliminated organic matter as a variable affecting efficiency. We formed three groups based on COD eliminated in g/m³.

Table 6: Mean energy efficiency by COD removal interval as (g/m³), energy consumption in (kWh/m³) and Kruskal-Wallis test.

COD removal (g/m ³)	<400	400-800	>800
Number of plants	50	87	39
Mean energy efficiency	0.223	0.327	0.380
% efficient plants	4.0	11.5	15.4
Energy consumption (kWh/m ³)	0.612	0.685	1.119
Kruskal-Wallis test	0.017		

One result, surprising at first glance, was that the plants with the highest energy consumption were at the same time the most efficient. However, if we analyze the numbers more deeply and we remember the basic definition of efficiency, we see that in quantifying this indicator we not only take into account the volume of treated water but also the amount of contaminants eliminated, another critical parameter. We can say that, in spite of consuming more total energy, the plants which eliminate more organic matter are more efficient, either because of incoming water differences or because of operating differences, than those which eliminate less COD per m³ of treated water. This interpretation was confirmed by the Kruskal-Wallis test, which yielded a value showing that efficiency differences between the three groups of WWTPs are statistically significant.

Lastly, following the reasoning that the biological process is the primary consumer of energy, we analyzed whether using diffusers or turbines for aeration affects WWTP efficiency. With turbines, water is mixed vigorously, creating turbulence and allowing air to be introduced, increasing specific surface area. In contrast,

diffusers are designed to produce a great deal of bubbles by forcing air through porous media or special nozzles.

The results shown in Table 7 indicate that type of aeration is one of the factors that determining plant efficiency. Thus WWTPs that use diffusers are, on average, 28% more efficient than WWTPs that use turbines. Also, 14.3% of the WWTPs in the diffuser group are efficient plants, whereas efficient plants constitute only 6.5% of the WWTPs in the turbine group. We should point out, however, that in this case, similar to the COD elimination variable, greater efficiency does not imply lower energy consumption per unit of treated water. The fact that diffuser plants are more efficient but also more energy-consuming than turbine plants indicates that in diffuser plants the concentration of organic matter eliminated is greater.

Table 7: Mean energy efficiency index as a function of aeration system (turbine or diffuser), energy consumption (kWh/m³) and Kruskal-Wallis test result

Aeration system	Turbine	Diffuser
Number of plants	92	84
Mean energy efficiency	0.273	0.349
% efficient plants	6.5	14.3
Energy consumption (kWh/m ³)	0.799	0.843
Kruskal-Wallis test	0.091	

Having shown the relationship between efficiency and aeration type, the next step was to quantify the savings in energy, CO₂ emissions and costs that turbine plants could obtain if they operated at the same efficiency as diffuser plants. We calculated savings of 0.06 kWh/m³, 22 g CO₂ emissions per m³ of treated water, and 0.016 €/m³.

The methodology described above enabled us to determine the efficiency of each input required to operate a WWTP, especially energy, which has particular environmental and economic importance. We can also analyze the relationship between energy efficiency and any representative process variable based on available statistical data. In this study, we utilized those variables that we considered to be the most relevant both for their explanatory power and for the availability and access to the data.

5. CONCLUSIONS

WWTPs are energy-intensive facilities contributing in some measure to climate change (Piósz et al. 2009). In the near future, this energy consumption is expected to grow considerably due to a higher expected volume of water being treated, as well as to the adoption of new technologies aimed at yielding higher quality effluents.

By analyzing energy efficiency of WWTPs we can identify which measures have the highest potential of reducing energy consumption and consequently greenhouse gas emissions, as well as improving

production costs for such facilities, making them more competitive. With these objectives in mind, we analyzed the efficiency behavior of a sample of WWTPs located in the Valencia Region of Spain, and we identified several variables that can explain differences between the plants. We also quantified the savings in CO₂ emissions and economic costs that could be obtained if plant efficiencies were improved.

Our study confirmed that efficiency levels for the studied sample of WWTPs as a whole were low and that the number of plants operating efficiently was very small. There is tremendous opportunity for improvement in energy management that could result in considerable reductions in CO₂ emission as well as in economic operating costs.

We also showed that plant size, quantity of eliminated organic matter, and bioreactor aeration type are significant variables affecting energy efficiency of WWTPs. In contrast, plant age is not a determining factor in energy consumption, which implies that proper equipment maintenance, optimal operation, and good resource management are critical factors in achieving energy efficiency. The finding that WWTPs' efficiency is affected by economies of scale suggest, from a policy perspective, that there are a larger number of sub-optimal facilities. Finally, given the growing importance of environmental and economic consequences of energy consumption, we want to emphasize that the wastewater treatment sector has a responsibility to contribute to reduction of greenhouse gas emissions and overall energy consumption. To achieve this objective, good analysis tools are necessary so that private companies and the relevant regulatory agencies can better meet the challenge of reducing the industry's carbon footprint improving environmental and economic sustainability.

ACKNOWLEDGEMENTS

The authors acknowledge the statistical assistance from the *Entitat de Sanejament d'Aigües (EPSAR)* and the financial aid received from the Spanish government through the NOVEDAR-Consolider Project (CSD2007-00055) and FPU program (AP2007-03483) and the Generalitat Valenciana government (ACOMP/2010/138).

REFERENCES

- [1] GWRC (Global Water Research Coalition). An energy and carbon footprint neutral urban water cycle by 2030. Workshop on Water and Energy. Available from: www.globalwaterresearchcoalition.net
- [2] Rahmstor S and Schellnhuber HJ. *Der Klimawandel (Climate change)*. Verlag CH and Beck editors. Muenchen; Wissen: 2009.
- [3] Cromwell JE, Smith JB and Rauche RS. No doubt

about climate change and its implications for water suppliers. In: Howe C, Smith JB & Henderson J, editors. *Climate Change and Water: International Perspectives on Mitigation and Adaption*. London: IWA Publishing; 2010. P. 5-11.

- [4] IPCC. Summary for Policy Makers. In *Climate Change 2007: The Physical Science Basis. Contribution of Working Group I to the Fourth Assessment Report of the Intergovernmental Panel on Climate Change*. Solomon S, Qin D, Manning M, Chen Z, Marquis M, Averyt K B, Tignor M & Miller HL, editors. Cambridge: Cambridge University Press; 2009.
- [5] Nakagawa N, Otaki M, Miura S, Hamasuna H and Ishizaki K. Field survey of a sustainable sanitation system in a residential house. *Journal of Environmental Science* 2006; 18 (6): 1088-93.
- [6] Gill ZM, Tierney MJ, Pegs IM and Allan N. Measured energy and water performance of an aspiring low energy/carbon affordable housing site in the UK. *Energy and building* 2010.
- [7] EUROSTAT 2010. Available from: <http://epp.eurostat.ec.europa.eu/portal/page/portal/statistics/themes>
- [8] Molinos-Senante M, Hernández-Sancho F and Sala-Garrido R. Economic feasibility study for wastewater treatment: A cost benefit analysis. *Science of the Total Environment* 2010; 408 (20): 4396-4402.
- [9] Guimet V, Kelly R, Doung F, Rosina M, Audic JM and Terry JM. Green energy resource: research and learning experiences from wastewater treatment plants. *Proceedings of IWA World Water Congress, Montreal (Canada) 2010*.
- [10] EPRI (Electric Power Research Institute). *Water and Sustainability: U.S. Electricity Consumption for Water Supply & Treatment- The Next Half Century*. *Water & Sustainability* 2002; 4: EPRI report 1006787.
- [11] IDAE (Institute for Diversification and Energy Saving). *Water and Energy: The complex interplay of two scarce resources. The energy footprint of the water. A first estimate of energy consumption of desalination and urban wastewater treatment*. (In Spanish). IDAE e-newsletter 2010; number 50, July.
- [12] Malcolm B, Middleton R, Wheale G and Schulting F. *Energy Efficiency in the Water Industry, a Global Research Project*. *Proceedings of IWA World Water Congress, Montreal (Canada) 2010*.
- [13] Schosseler P, Lohmann T, Schmitt B, Perbal S, Dubois C and Saverborn K. Implementing Sustainable Sanitation concepts in Luxembourg – methodological approach and outcomes. *Water Science Technology* 2007; 56 (5): 33-41.
- [14] Zhou P, Ang BW and Poh KL. Measuring environmental performance under different environmental DEA technologies. *Energy Economics* 2008; 30: 1-14.
- [15] Farrell MJ. The Measurement of Productive Efficiency. *Journal of the Royal Statistical Society A* 1957; 120: 253 – 281.
- [16] Charnes A, Cooper WW, Lewin AY and Seiford LM. *Data envelopment analysis: theory, methodology and application*. Boston; Kluwer Academic Publishers: 1996.
- [17] Sueyoshi T and Goto M. DEA approach for unified efficiency measurement: Assessment of Japanese fossil fuel power generation. *Energy Economics* 2010; (In Press)
- [18] Färe R, Grosskopf S, and Lovell CAK. *Production frontiers*. Cambridge; Cambridge University Press: 1994.
- [19] Picazo-Tadeo AJ, Sáez-Fernández F. and González-Gómez F. The role of environmental factors in water utilities' technical efficiency. Empirical evidence from Spanish companies. *Applied Economics* 2009; 41 (5): 615 – 628.
- [20] Grosskopf S. Statistical inference and nonparametric efficiency: a selective survey. *Journal of Productivity Analysis* 1996; 7: 161 – 176
- [21] Benett A. *Energy efficiency: Wastewater treatment and energy production*. Filt + Sepa 2007; December: 16-19.
- [22] Terrazas E, Vázquez A, Briones R, Lázaro I and Rodríguez I. EC treatment for reuse of tissue paper wastewater: Aspects that affect energy consumption. *Journal of Hazardous Materials* 2010; 181: 809-816.
- [23] Hernández-Sancho F. and Sala-Garrido R. Technical efficiency and cost analysis in wastewater treatment processes: A DEA approach. *Desalination* 2009; 249 (1): 230-234.
- [24] Sun, Y. and Li, YW. The technology of wastewater treatment and energy recovery based on UASB reactor. *International Conference on Mechanic Automation and Control Engineering. MACE2010; 2010; art 5535519; 4310-43*.

Vortex Ring Buoyant Plume on Porous Body in Thermal Non-Equilibrium

Carmine Golia¹, Bernardo Buonomo², Antonio Viviani³, Michele Di Natale⁴

^{1,2,3}Department of Aerospace and Mechanical Engineering (carmine.golia@unina2.it);
(bernardo.buonomo@unina2.it); (antonio.viviani@unina2.it)

⁴Department of Civil Engineering Second University of Naples 29, via Roma, 81031 Aversa (CE), Italy
(michele.dinatale@unina2.it)

ABSTRACT

The rising of a thermal buoyant vortex ring within a viscous fluid impinging on a porous body (still or rotating) is numerically simulated with an unsteady Lagrangian Thermal-Vortex Blob Method in terms of a vorticity-velocity-temperature formulation that integrates the complete Helmholtz equation coupled with the Energy equation under Oberbeck-Boussinesq hypothesis. The code results to be fully mesh less since vortex and thermal blobs move naturally where they are needed. In occasion of the re-meshing, the computational field is automatically adapted to the regions which are really interested by the dynamic of the phenomenon. The two phases problem is solved using a dynamic mask technique for a Brinkman-Forchheimer porous phase. The fluid/solid phases of the porous body are considered in local thermal non-equilibrium. Simulations of a buoyant thermal plume rising against a circular cylinder are presented for several settings, with the plume vertically aligned with a still or rotating cylinder.

Keywords: Mesh-less Lagrangian Method, Buoyant Plume Impingement, Porous Media, Thermal non-Equilibrium.

1. INTRODUCTION

Scope of the work is to investigate the rising of a buoyant vortex ring plume within a viscous fluid impinging on a porous Body (still or rotating). Such phenomena are important in a wide variety of application, including, among others: secondary and tertiary oil recovery, fixed bed regeneration in chemical processing, hydrology, filtration, combustors, thermal and sound insulators, transport and store of thermal energy, fuel cells.

Common examples of industrial applications include: management of geo thermal systems, heat pipes, phase change applications, transpiration cooling, and oil recovery with injection of solvent into oil field to drive oil to pumping spots. In addition new technologies are thriving on utilizing porous layers to serve as a heat sink medium. Such applications are quoted in Tien and Vafai [1] and in Amiri, Vafai and Kuzay [2].

It must be emphasized that suitable models of turbulent flow in porous media are essential for further analysis to achieve more efficient designs.

This work presents a novel approach that is equivalent to DNS simulation and is capable to deal easily with complex geometry with operating conditions of real engineering interest. The method is based on a Lagrangian formulation of the physical phenomenon and the solution method result to be completely mesh less.

The focus is on the study of large-scale vortical structures, such as vortex rings. This is motivated by the fact that in such case local transport behaviors depend on the characteristics of the porous media.

In particular here we want explore if the combination of a grid free Lagrangian Blob method with a Fluid/Porous/Solid domain embedding approach can be useful for the preliminary analysis of heterogeneous unsteady thermal buoyant problems in heterogeneous media (fluid flow/porous media) with complex geometries and with generalized forcing parameters of real engineering interests, where easiness, readiness, short computational times, good qualitative and sufficient quantitative accuracy are the most important aspects.

2. MECHANICS OF POROUS FLOW

The porosity ϕ of a medium is defined as the fraction of the fluid over the total volume of the medium. Thus $(1-\phi)$ is the fraction occupied by solid.

The fluid velocity can be obtained as averaged over the total elementary volume to get the ‘‘Darcy velocity, \underline{v} ’’; this velocity is related to the fluid velocity ‘‘ \underline{V} ’’, averaged over the fluid elementary volume, by the Dupuit-Forchheimer relationship $\underline{v} = \phi \underline{V}$, with ϕ the porosity.

In 1856 Henry Darcy [3] found a proportionality between flow rate and pressure gradient that is given by the ratio of the fluid dynamic viscosity and a dimensional coefficient called ‘‘permeability, K ’’ that depends only on the geometrical characteristics of the medium. For isotropic medium:

$$\underline{\nabla} p = -\frac{\mu}{K} \underline{v}$$

2.1 Extensions of the Darcy's law

By averaging the Navier-Stokes equation according to the Darcy principle it is possible to include the (small) inertial effects and to impose no slip conditions on the walls to get the Darcy-Brinkman equation:

$$\frac{1}{\varphi} \frac{\partial \underline{v}}{\partial t} + \frac{1}{\varphi^2} \underline{v} \bullet \nabla \underline{v} = -\frac{1}{\rho_f} \nabla p - \frac{\nu}{K} \underline{v} + \tilde{\nu} \nabla^2 \underline{v} \quad (1)$$

where $\tilde{\nu}$, the effective viscosity, is originally put equal to the dynamic viscosity of the fluid ν . [In general this is not true since the ratio $\tilde{\nu}/\nu$ depends on the geometry of the medium, but for high porosity cases $\tilde{\nu}$ is usually taken equal to ν]

For high enough speed, the effects of turbulences must be taken into account, and by a formal averaging it is possible to derive the Brinkman-Forchheimer equation as:

$$\begin{aligned} \frac{1}{\varphi} \frac{\partial \underline{v}}{\partial t} + \frac{1}{\varphi^2} \underline{v} \bullet \nabla \underline{v} = & -\frac{1}{\rho_f} \nabla p + \frac{\nu}{\varphi} \nabla^2 \underline{v} + \\ & -\frac{\nu}{K} \underline{v} - \frac{C_f}{\sqrt{K}} |\underline{v}| \underline{v} \end{aligned} \quad (2)$$

Here C_f is a geometric coefficient that may be expressed in function of the porosity φ as: $C_f = 1.75/\sqrt{150 \varphi^3}$.

For porous media composed by spheres of average diameter d_p , the permeability can be related to the porosity as:

$$K = (d_p \varphi^3) / [150(1-\varphi)^2] \quad (3)$$

2.2 Forms of the energy equation for local thermal non-equilibrium

In general, for an isotropic medium, without radiation effects and viscous dissipation, by taking averages over an elemental volume, we can derive:

solid phase

$$\begin{aligned} (\rho c)_{solid} \frac{\partial T_{solid}}{\partial t} = & \nabla \bullet (k_{solid} \nabla T_{solid}) + q_{solid}^{vol} + \\ & + \frac{h}{(1-\varphi)} (T_{fluid} - T_{solid}) \end{aligned} \quad (4)$$

fluid phase

$$\begin{aligned} (\rho c_p)_{fluid} \left[\varphi \frac{\partial T_{fluid}}{\partial t} + \underline{v} \bullet \nabla T_{fluid} \right] = & \varphi \nabla \bullet (k_{fluid} \nabla T_{fluid}) + \\ & + \varphi q_{fluid}^{vol} + h (T_{solid} - T_{fluid}) \end{aligned} \quad (5)$$

where: ρ is the density, c is the specific heat of the solid, c_p the specific heat at constant pressure of the fluid, k the thermal conductivity and q^{vol} the specific volumetric heat production (if any), h is a heat transfer coefficient.

2.3 Form of the momentum equation in case of natural convection

For temperature and species concentration gradients small enough, the variations of density can be considered only in the gravitational term at the right-hand of the momentum equation (2) [Oberbeck-Boussineq approximation]. For natural thermal convection the simplest linearized equation of state is:

$$\rho_{fluid} = \rho_{ref} [1 - \beta (T_{fluid} - T_{ref})] \quad (6)$$

with β the coefficient of (volumetric) thermal expansion of the fluid and ρ_{ref} the reference density at T_{ref} . In such case the momentum equation can be expressed as:

$$\begin{aligned} \frac{1}{\varphi} \frac{\partial \underline{v}}{\partial t} + \frac{1}{\varphi^2} \underline{v} \bullet \nabla \underline{v} = & -\frac{1}{\rho_f} \nabla p + \frac{\nu}{\varphi} \nabla^2 \underline{v} + \\ & -\frac{\nu}{K} \underline{v} - \frac{C_f}{\sqrt{K}} |\underline{v}| \underline{v} - \beta (T - T_{ref}) \underline{g} \end{aligned} \quad (7)$$

and the thermal energy equation remains unchanged.

3. THE FORMULATION

In this work we couple a grid free unsteady Lagrangian Thermal-Vortex Blob method with a penalization method that considers a base fluid phase with over imposed porous bodies described by Brinkman-Forchheimer model. The boundary layers around solid bodies are simulated by a porous layer.

3.1 Lagrangian Blob method

The blob concept [4] is based on the tentative to make discrete the free space Dirac representation of a generic function "f(x, t)" at the location x, and time t as the convolution:

$$f(\underline{x}, t) = \int f(\underline{x}', t) \delta(\underline{x} - \underline{x}') d\underline{x}' \quad (8)$$

This representation is made discrete, in a Lagrangian formulation, as follows:

$$\begin{aligned} f_p(\underline{r}_p, t) = & \sum_{\substack{q \in \text{Cluster} \\ \text{around } p}} \frac{1}{\sigma^d} W\left(\frac{\underline{r}_p - \underline{r}_q}{\sigma}, h\right) \{f_q(\underline{r}_q, t) \Delta \text{Vol}_q\} \\ = & \sum_{\substack{q \in \text{Cluster} \\ \text{around } p}} \frac{1}{\sigma^d} W\left(\frac{\underline{r}_p - \underline{r}_q}{\sigma}, h\right) F_q(\underline{r}_q, t) \end{aligned} \quad (9)$$

where:

- h is the reference grid space;
- the kernel function $W(r, h)$ must satisfy given properties in order that, in the limit $h \rightarrow 0$, the two representations coincides (h can be regarded as equivalent grid size);
- ΔVol_q is the *finitesimal* elementary volume associated with the q -th particle;
- d is the dimension of the filed space;
- " $\sigma = h \gamma$ " is defined as the **blob's radius** , " γ " is a parameter ($1 \div 1.45$) to allow a duly overlapping;
- $F_q(r_q, t) = f_q \Delta Vol_p$ is considered as the "field intensity" of the variable " f_q " over the finite volume $dVol_p$.

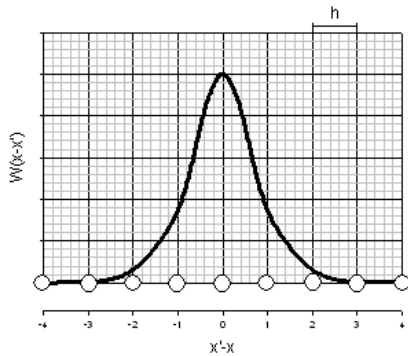


Figure 24: Kernel function for the blob representation

Note that the blob representation is defined as a **space average** (i.e. it is an implicit sub-scale model).

The Lagrangian blob method represents the space averaged equivalent for the Helmholtz formulation of the complete Navier-Stokes equations. So that, if the "h" parameter and the time integration step are small enough with respect to turbulent scale, the Lagrangian Blob method does not need any turbulent stress term, and it can be considered to represent a DNS method.

Blobs are "Dirac particles" that directly translate with flow and transport extensive properties. They move according to velocity field, and exchange momentum and energy with neighborhood blob particles according to diffusive processes.

Blob methods differ from classical grid techniques since they do not involve projection of the equation in a finite dimensional space.

Obviously the Lagrangian Blob formulation of a differential problem needs the representation of all the differential operators in the problems, namely divergence, gradient and Laplacian. This may be a problem that can be solved in various manners, as it will be reported later.

3.2 The formulation of the code

The Code Algorithm uses a blob representation of the complete Helmholtz equation coupled with Energy

equation under Boussinesq hypothesis. It derives that the continuity equation is satisfied by definition, and that the pressure disappears from the momentum equation. In 2D case it results for the vorticity (a pseudo vector normal to the plane of the flow, automatically solenoidal) the equation (eulerian representation):

$$\varphi \frac{\partial \omega}{\partial t} + \underline{v} \cdot \nabla \omega = \varphi \nu \nabla^2 \omega - \varphi^2 \frac{\nu}{K} \omega + -\varphi^2 \frac{C_f}{\sqrt{K}} \left[|\nabla \underline{v}| \wedge \underline{v} + |\underline{v}| \nabla \wedge \underline{v} \right] - \varphi^2 \beta \left[\underline{g} \wedge \nabla T \right] \quad (10)$$

The blob representation of this advection/diffusion problem is formulated with the use of a splitting technique [5]-[6] that separates explicitly convective and diffusive steps, recasting the problem in a coupled hyperbolic one for the particle blob paths, and in a parabolic problems for the diffusive and source phenomena occurring along the trajectory for each particle. It results:

- **Convective steps** (trajectory of the p -th particle):

$$\frac{d \underline{r}_p}{dt} = \underline{v}(\underline{r}_p, t) \quad (11)$$

- **Diffusive Step** (variations of the field properties of the p -th particle along its trajectory)

Momentum:

$$\frac{d \underline{\omega}_p}{dt} = \begin{cases} \nu \nabla^2 \omega_p - \beta \left[\underline{g} \wedge \nabla T_p \right] & \text{fluid phase} \\ \nu \nabla^2 \omega_p - \varphi \frac{\nu}{K} \omega_p - \varphi \frac{C_f}{\sqrt{K}} \left[|\nabla \underline{v}_p| \wedge \underline{v}_p + |\underline{v}_p| \nabla \wedge \underline{v}_p \right] & \\ -\varphi \beta \left[\underline{g} \wedge \nabla T_p \right] & \text{porous phase} \end{cases} + \quad (12)$$

Energy: Solid phase

$$\begin{aligned} (\rho c)_{solid} \frac{dT_{solid}}{dt} &= \nabla \cdot (k_{solid} \nabla T_{solid}) + \\ + q_{solid}^{vol} &+ \frac{h}{(1-\varphi)} (T_{fluid} - T_{solid}) \end{aligned} \quad (13a)$$

Energy: Fluid phase

$$\begin{aligned} (\rho c_p)_{fluid} \varphi \frac{dT_{fluid}}{dt} &= \varphi \nabla \cdot (k_{fluid} \nabla T_{fluid}) + \\ + (1-\varphi) q_{fluid}^{vol} &+ h (T_{solid} - T_{fluid}) \end{aligned} \quad (13b)$$

Note that we have not considered the dissipative term in the energy equation since it is very small and it is usually discarded in case of buoyancy.

The Blob representation of the above eqns. (detailed elsewhere by Golia et alia [7- 12]) considers as field unknowns for each p -th particle: the local "Vortex intensity" $\Gamma_p = \omega_p \Delta V_p$ (i.e. local velocity circulation) and the local "Thermal intensity" $\Theta_p = T_p \Delta V_p$. The blob representations of the Laplacian diffusive terms and of the Gradient terms present in (23) and (24) are performed according to the Particle Strength Exchange (PSE) method proposed by Degond & Mas-Gallic [13] and expressed as:

$$\nabla^2 \Gamma_p = \sum_{q=1}^N (\Gamma_p - \Gamma_q) \text{Lapl}(r_p - r_q, h) \quad (14)$$

$$\nabla \Theta_p = \sum_{q=1}^N (r_p - r_q) (\Theta_p + \Theta_q) \text{Grd}(r_p - r_q, h) \quad (15)$$

The kernel used in (14) and (15) are the high order ones according to Eldredge et alia [14].

The velocity field needed in (11) and (12) is computed as sum of a potential velocity field (if any) and a vortical velocity field computed from the vorticity field with a generalized Biot-Savart law.

This represents a classical N-Body problem that require $O(N^2)$ calculations. To overcome this computational burden we use an "in house" Adaptive Fast Multipole Method (FMM) that results a $O(N)$ algorithm [15]. This FFM was devised to be capable of self organize in order to reach optimal computation conditions when N is varying and able to warrant an imposed error level on the calculation of the velocity field induced by the vortex blobs.

The resultant problem is a IVP to be time integrated for particles located in particular volume phase. For fluid particle we use a 3rd order Adams-Bashforth method that computes the "n+1 time step" values using the old values at the "n time step" and at the "n-1 time step"., for particles undergoing Brinkmann penalization we use an implicit time integration method.

Usually, after a number of integration steps, to avoid inaccuracy due to the typical Lagrangian distortion of particle field, a regrid process is performed to project the field on a regular mesh. New particles are allocated on the new mesh points and their values are interpolated from the cluster of the neighborhood ones, on the old disordered lattice, with a suitable kernel function:

$$F_p^{new} = \sum_{q=1}^{Neighborhood} F_q^{old} W_{regrid} \left[(r_p^{new} - r_q^{old}), h \right] \quad (16)$$

The kernel $W_{regrid}(\bullet, \bullet)$ used here is compact over $r/h=2.5$ and is third order accurate according to [16]. It results a real grid free method capable of automatically self adapt to compute only part of the field that is really involved by the thermo-fluid phenomena.

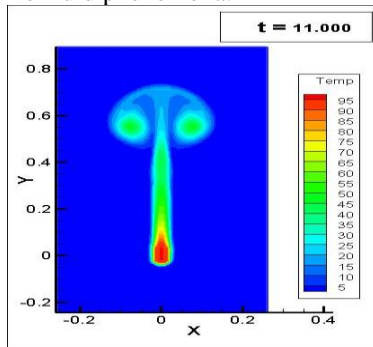


Figure 2: Thermal plume in free space

4. THE PROBLEM SOLVED

As stated before, we want mainly verify the capability of our code to simulate a buoyant plume rising toward a circular cylinder (still or rotating) vertically aligned. First of all we simulate the rising in free space (Fig. 2).

The plume is generated by a cluster of fixed blob kept at constant temperature. In this figure, as in all the others, isothermal contours are visualized, for temperature rise above the environment. The most important parameters of the simulation are reported in Table I (all in S.I. units).

Table 1: Main parameters used in the simulations

Fluid parameters		
$\rho_{fluid} = 900$	$\nu = 0.5 \cdot 10^{-6}$	$Pr = 2.5$
$\beta = 0.0002$	$c_{fluid} = 3000$	$\lambda_{fluid} = 0.6$
Porous material		
$\phi = 0.4$	$K = 1 \cdot 10^{-8}$	$D_{ps} = 0.00158$
$\rho_{solid} = 1700$	$c_{solid} = 800$	$\lambda_{solid} = 2.4$
Generalized force:		
Cluster of blobs at constant temperature		
fixed elliptical cluster: semi-axis $a=0.021$, $b=0.042$		
at 80°C constant temperature rise in standard gravity		
Computational parameters		
$h = 0.01$	$dt = 0.0025$	
Regrid: every 20 time step		$Grashoff = 0.46 \cdot 10^9$

All the results are obtained as unsteady evolution starting from still field. Unfortunately the still figures presented in this paper are not able to demonstrate the dynamic development of the thermal field. The presentation of the paper at the Congress will reproduce the relative movies

In the following we will consider a plume impinging on a porous still cylinder (vertically aligned), and afterwards the same for a cylinder rotating counter clock-wise.

For all the above cases, we shall report the fluid/solid temperatures as well as their isothermals.

Moreover, the heating curves for the rise of enthalpy for the fluid and solid phases in the porous cylinder, and their relative ratio, versus time are also reported.

4.1 Still porous cylinder

This is the master case which Fig. 3 refers to in the case of vertical alignment of the plume with the cylinder.

It is evident that the solid phase will start to be heated when the plume reaches the bottom side of the cylinder (at about $t=2.59$) as can be noted in Fig. 3.

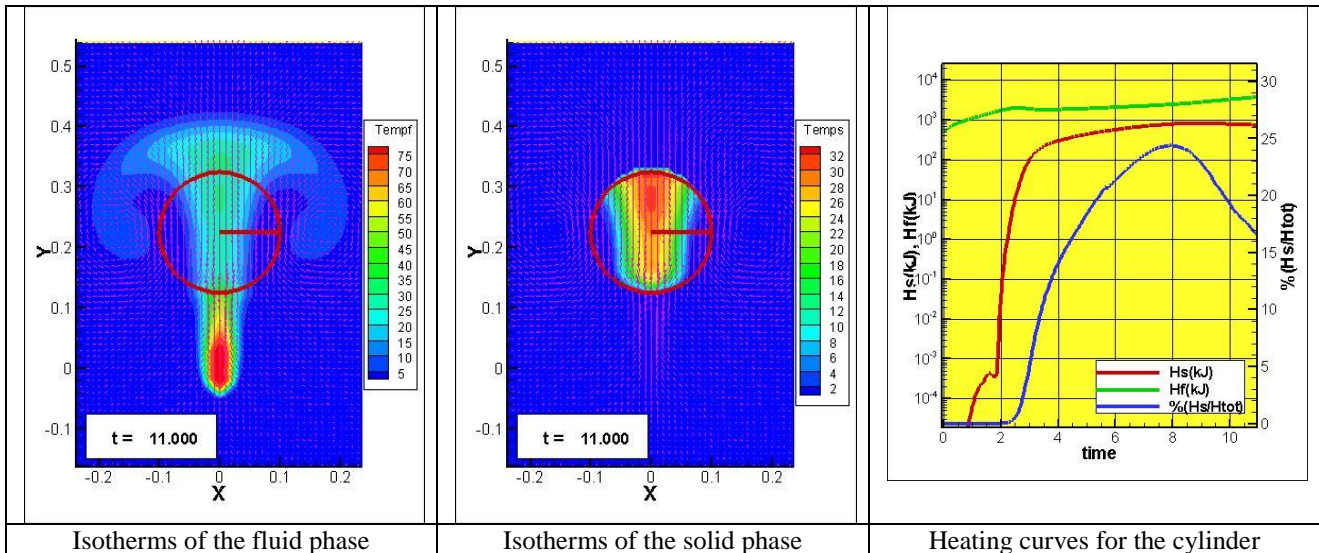


Figure 3: Thermal buoyant plume over a porous cylinder (vertically aligned)

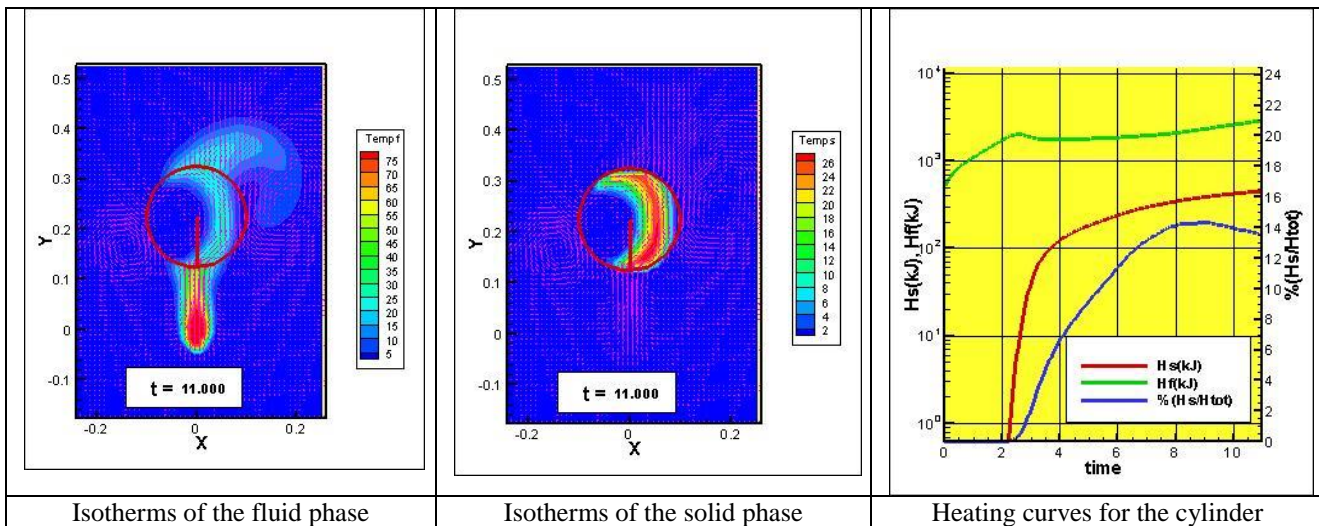


Figure 4: Rotating porous cylinder (vertically aligned)

The trend of the rise for the H_{solid} depends strongly on the fact that the vortex ring cup touches the cylinder after the pinch-off (i.e. when the rising sting separates from the cup and is no longer able to energize the vortex ring that will go toward dissipation). The ripple around $t=1.8$ refers to the rising cup touching the cylinder. The movie will highlight such facts. It derives then that the trespassing of the residual cup through the porous body will give more energy to the solid phase with respect to the later times when solely the sting will be present in the porous body. In Fig. 3 the red line will then tend to flatten the curve growth and the “efficiency ratio” (blue line) will decrease after its maximum at about $t=8$.

4.2 Rotating porous cylinder

Fig.4 reports the case of a porous cylinder rotating steadily counter clock-wise. The dynamics of this field is quite interesting and obviously depends on the angular speed of the cylinder.

The vortex cup touches the base of the cylinder at about $t=2.8$. In this point the surface velocity of the cylinder is rightward; the velocity of the left vortex of the cup is leftward whereas the velocity of the right vortex of the cup is rightward.

It derives then the left vortex is slowed down and remains in the left neighborhoods going decaying, in contrast the right vortex is accelerated rising along the right side of the cylinder.

It derives then also the energy exchange within the porous phase is enhanced in favor of the right side. The dynamics of the heating curves follow the same trends as per the previous case (still cylinder) but the values of the enthalpy decrease.

5. CONCLUSIONS

The modeling of complicate phenomena involving interaction of a thermal rising plume with a porous layer is analyzed quite well with a simulation algorithm that uses an unsteady Lagrangian Thermal and Vortical Blob formulation.

One of the most interesting aspect is that the model is completely mesh free, and capable to self-adjust to the instantaneous state of the physics (with no numerical viscosity due to Lagrangian formulation), and, since blobs will move where they are needed, with the insurance of good local description of the phenomena involved.

Future actions are planned to:

- Perform a complete parametric analysis of the interaction plume porous cylinder, rotations and lateral settings.
- Consider packs of plumes and cylinders.
- Consider the local variation of the fluid parameters with temperature (most important for liquids). and/or of a second scalar property (such as the solute concentration).
- improve the time integration in the code. This is a must since, when the porous/solid regions are considered, the equations are quite "stiff" because (cases of real interest). This penalization action cause the description to be almost of order one.

REFERENCES

- [1] C. L. Tien, K. Vafai "Convective and radiative heat transfer in porous media", *Advances in Appl. Mech.* 1989; 27: 225 - 281.
- [2] A.Amiri, K.Vafai, T.M. Kuzay "Effects of boundary conditions on non-Darcy heat transfer through porous media and experimental comparisons" *Num. Heat Transfer* 1995; 27(6): 651- 664.
- [3] D.A.Nield, A.Bejan, *Convection in Porous Media*, 2006, Springer.
- [4] G.H.Cottet, P.D.Koumoutsakos, *Vortex Methods: Theory and Practice*, 2000, Cambridge Univ. Press.
- [5] A. J .Chorin, "Numerical Study of Slightly Viscous Flow" *J. Fluid Mech.* 1973; 57 (4): 785-796.
- [6] A. J. Chorin, "Vortex sheet approximation" *J. Comp. Phys.* 1978; 27: 428-442.
- [7] C.Golia, B.Buonomo, O.Manca, A.Viviani, "A Vortex-Thermal Blobs Method for Unsteady Buoyancy Driven Flows" *ASME-IMECE, Anaheim CA (USA)* 2004.
- [8] C.Golia, B.Buonomo, "An Effective Blob Approach to Unsteady Thermal Buoyant Flow" *CMEM, Malta*, 2005.
- [9] C.Golia, B.Buonomo, "Numerical Simulation of Unsteady Natural Convection by Blobs Methods" *60th ATI Congress, Roma*, 2005.
- [10] C. Golia, B. Buonomo, "On the accuracy of integral representation of differential operators in meshless Lagrangian blob method" *CMEM, Praga*, 2007.
- [11] C. Golia, B. Buonomo, A.Viviani, "A corrected vortex method for 3D thermal buoyant flows", *Energy Conversion and Management* 2008; 49 (11): 3243-3252.
- [12] C.Golia, B. Buonomo, A.Viviani, "Grid Free Lagrangian Blobs method with Brinkman layer Domain Embedding Approach for heterogeneous Unsteady Thermo Fluid Dynamics Problems", *International Journal of Engineering* 2009; 3(3): 313-328.
- [13] P.Degond, S.Mas-Gallic, "The weighted Particle method for Convection-Diffusion Equations, part.1: the case of an isotropic viscosity" *Math.s of Computation* 1989; 53 (188) : 485-507.
- [14] J. D. Eldredge, A. Leonard, T. Colonius, "A General Deterministic Treatment of Derivatives in Particle Methods" *J. Comp. Phys.* 2002; 180: 686-709.
- [15] V. Rokhlin, L. Greengard, "A fast algorithm for particle simulation" *J. Comp. Phys.* 1987; 73: 325-348.
- [16] E.Meijering, M.Unser, "A Note on Cubic Convolution Interpolation" *IEEE Trans. Image Process.* 2003; 12 (4): 477-479.

Study on Amorphous Ag-Doped Manganese Dioxide Electrodes for Electrochemical Supercapacitors Applications

Sameh Hassan¹, Tarek Naser¹, Masaaki Suzuki², Ahmed Abd El-Moneim³

¹Energy Resources and Environmental Engineering Department, Egypt-Japan University of Science and technology, New Borg El Arab City, Alexandria, Egypt, 21934 (phy_2008@yahoo.com, tarek.naser@ejust.edu.eg)

²Department of Chemical Engineering, Tokyo Institute of Technology, 2-12-1 O-okayama, Meguro-ku, Tokyo, Japan, 152-8552 (masaaki@chemeng.titech.ac.jp)

³Material Science and Engineering Department, Egypt- Japan University of Science and technology, New Borg El Arab City, Alexandria, Egypt, 21934 (ahmed.abdelmoneim@ejust.edu.eg)

ABSTRACT

Amorphous MnO₂ and Ag-doped MnO₂ thin films were galvanostatically deposited on a polished stainless steel substrate from 20 mM KMnO₄ aqueous solutions without and with AgNO₃ additions at cathodic current density of 1 mA/cm² for the application in electrodes of electrochemical supercapacitors. The supercapacitive properties of the deposited thin films have been studied in 0.5 M Na₂SO₄ electrolyte by cyclic voltammetry, impedance spectroscopy, and charge-discharge measurement techniques. The Ag-free MnO₂ film showed better capacitive behavior and lower charge transfer resistance compared to the Ag-doped MnO₂ films. The specific capacitance and charge transfer resistance values for Ag-free MnO₂ films were 160 F/g at a scan rate 10 mV/s and 3.87 Ω, respectively. Cyclic stability using charge-discharge measurement technique indicates the excellent stability of Ag-free MnO₂ films and its possible use as a low cost electrode for supercapacitor applications.

Keywords: Cyclic voltammetry, Manganese dioxide, Power density, Energy density, Cyclic stability.

1. INTRODUCTION

Several energy storage devices, such as compressed air, hydrogen, flywheels, batteries, capacitors, and fuel cells, have been developed for various practical applications. Among these devices, high performance batteries and capacitors have presented themselves as one of the achievable, economically feasible options for meeting today's severe energy demands. Supercapacitors have received a lot of attention as viable electrical energy storage devices owing to their ability to deliver high powers, excellent reversibility, and longer cycle life than batteries [1-3]. On the basis of the energy storage mechanism, supercapacitors can be classified into two categories [4-6], namely the electrical double-layer capacitor (EDLC) and the pseudo-capacitor. The capacitance of the former comes from the charge accumulation at the electrode/electrolyte interface (double-layer capacitance), therefore it strongly depend on the surface area of the electrode accessible to the electrolyte. The capacitance of the latter is due to the reversible faradic transfer of charge between electrode and electrolyte, such as surface functional groups and transition metal oxides. Supercapacitors fill the gap between batteries (low specific power and high specific energy) and conventional capacitors (high specific power and low specific energy), i.e. they have a specific power as high as conventional capacitors and a specific energy close to that of batteries. It is obvious that the electrode is the key in the development of supercapacitors.

MnO_x is a promising electrode material for electrochemical capacitors because of its the relatively low cost, excellent electrochemical performance, environmentally friendly character in comparison with the ruthenium oxides or other transition metal oxides [7-9]. Hydrous ruthenium oxide has been extensively studied [10,11] as an active electrode material for supercapacitors with capacitance as high as 720 F/g in aqueous acidic electrolytes. Although RuO₂ gives high specific capacitance, its disadvantages of high cost and toxic nature limit its further commercial application. As an inexpensive alternate to RuO₂, hydrous manganese oxide prepared by both chemical and electrochemical methods was found to possess capacitive characteristics with acceptable values of specific capacitance [12-16]. A specific capacitance of 130 F/g was reported [16] at a scan rate of 5 mV/s, for manganese dioxide synthesized by sol-gel method.

Recent investigations showed that 1–8 wt.% Ag addition to lithium manganese dioxide electrode can significantly improve battery performance due to the increase in conductivity [17]. In another investigation the increase in conductivity of Ag-doped RuO₂ compared to pure RuO₂ was reported [18]. As a result, Ag-doped RuO₂ showed much higher SC compared to the SC of undoped RuO₂ [18]. Therefore, it is important to fabricate and investigate the Ag-doped MnO₂ films. MnO₂ films for application in electrochemical supercapacitors (ES) can be prepared by anodic or

cathodic electrodeposition from aqueous solutions. However, anodic electrolytic deposition of MnO_2 on metallic current collectors presents difficulties related to the anodic oxidation and dissolution of metals. In contrast, cathodic electrodeposition can be performed on various metallic substrates. It should be noted that cathodic electrodeposition is an important industrial technique for the deposition of metals. Therefore, cathodic electrodeposition is a promising method for the co-deposition of oxides and metals and the fabrication of doped films and composites.

The goal of the present study is to fabricate Ag-free MnO_2 and Ag-doped MnO_2 thin films by galvanostatically cathodic deposition on polished stainless steel substrate from KMnO_4 aqueous solutions without and with AgNO_3 additions for the application in electrodes of ES.

2. EXPERIMENTAL

Stainless-steel (SS) sheet of grade 316 LN, thickness 0.25 mm and surface area of 6 mm \times 15 mm was used as current collector and substrate for the electrodeposition of the active materials. Prior to the electrodeposition experiments, the substrate were mechanically polished with SiC papers down to 2000.

MnO_2 and Ag-doped MnO_2 thin films were galvanostatically deposited from 20 mM KMnO_4 solution without and with AgNO_3 additions (0.5, 2, and 4 mM) at cathodic current density of 1 mA/cm² onto SS substrate for 0.5 hour. The weight of the deposited films was measured by means of a Sartorius micro-balance (Model BP211D). The structure was characterized by means of X-ray diffractometer (Shimadzu, XRD-7000) using Cu K α radiation.

All electrochemical investigations were performed at 30 \pm 1.0 $^\circ$ C using two compartment three electrodes electrochemical cell with platinum foil as an auxiliary electrode and a saturated Ag/AgCl reference electrode. The capacitive performance of the deposited films was examined in 0.5 M Na_2SO_4 electrolyte using the electrochemical impedance spectroscopy (EIS), cyclic voltammetry (CV) measurement techniques, and galvanostatic charge–discharge. The CV measurements were carried out at potential ranges of 0–0.9 V vs. Ag/AgCl (sat.) at scan rates of 10–90 mV/s. The excitation amplitude for impedance measurements was 10 mV root mean square (RMS) in a frequency domain of 10¹ to 10⁵ Hz.

5. RESULTS AND DISCUSSION

5.1. Structure

Figure 1 shows XRD patterns of Ag-free MnO_2 and Ag-doped MnO_2 thin films prepared by galvanostatic cathodic deposition method on polished SS substrate from 20 mM KMnO_4 aqueous solutions without and

with 2 mM AgNO_3 addition at 1 mA/cm². As seen, the XRD patterns show no reflection peaks typical characteristics of any crystalline or nanocrystalline MnO_2 -based oxide films. This indicates the formation of amorphous Ag-free MnO_2 and Ag-doped MnO_2 thin films with very high degree of structure disorder. Sharp reflection peaks from SS substrate are also detected in the diffraction patterns of both oxides referring to the formation of thin deposit films on the SS substrate. It's also worth noting that Ag-free MnO_2 and Ag-doped MnO_2 thin films show almost identical diffraction patterns.

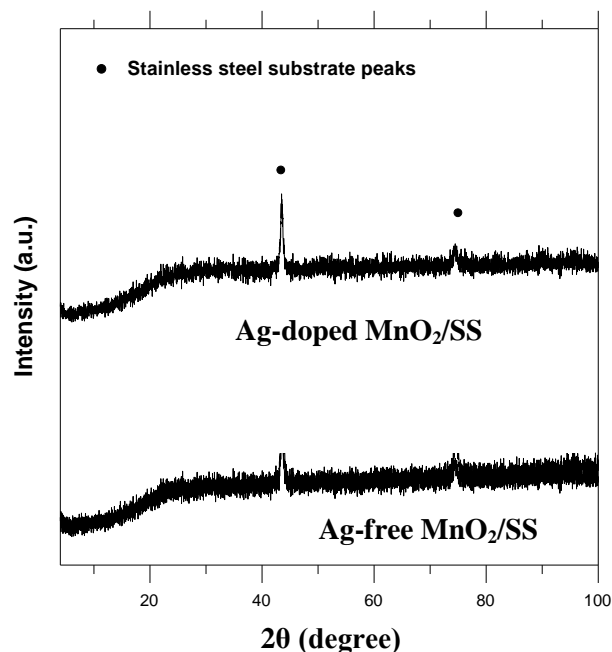


Figure 1: XRD patterns for Ag-free MnO_2 and Ag-doped MnO_2 (2 mM AgNO_3) films deposited on polished SS substrate.

3.2. Supercapacitive Properties of the Deposit Film

3.2.1. Cyclic Voltammetry

Figure 2 shows the CV curves of the Ag-free MnO_2 and Ag-doped MnO_2 films in the potential range of 0–0.9V vs. Ag/AgCl (sat.). All the curves are near-rectangular in shape and show symmetrical anodic and cathodic halves which indicate ideal capacitive behavior of the deposited films. As it can be seen in Fig. 2, the capacitive current density of Ag-free MnO_2 is higher than those of Ag-doped MnO_2 .

For estimating the specific capacitance (SC) of the deposited oxide films, the amount of capacitive charge (Q) was obtained using half the integrated area of the CV curve presented in Fig. 2, and then the SC was calculated from dividing the capacitive charge by the film mass (m) and the width of the potential window (ΔV) using equation (1).

$$SC = \frac{Q}{m \cdot \Delta V} \quad (1)$$

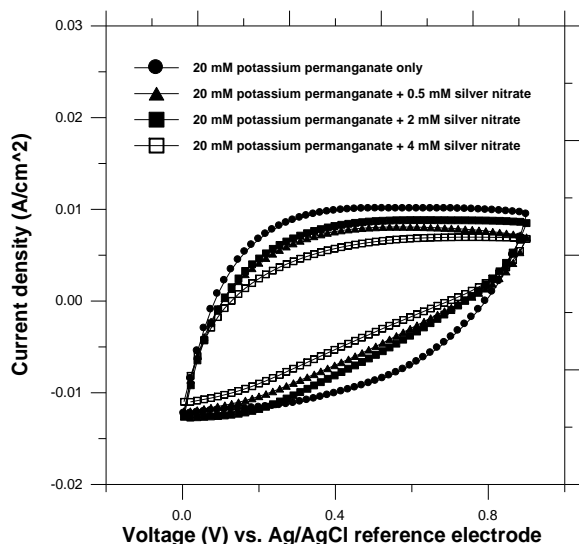


Figure 2: Cyclic voltammetric curves of Ag-free MnO_2 and Ag-doped MnO_2 films measured in 0.5 M Na_2SO_4 solution at a scan rate of 90 mV/s.

Figure 3 summarizes the dependence of the SC on the CV scan rate for Ag-free MnO_2 and Ag-doped MnO_2 films. In general, the specific capacitance decreases as the scan rate increases. This behavior can be attributed to the high probability of exposing both inner and outer surface of the deposited oxide to the ions with the decrease in the scan rate [19].

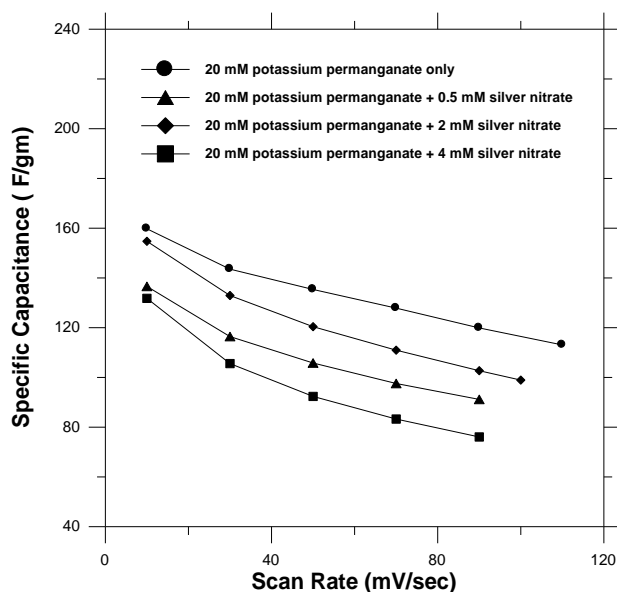


Figure 3: Variation of the specific capacitance with the scan rate of CV measurement for MnO_2 and Ag-doped MnO_2 films.

Meanwhile, the maximum values of the specific capacitance for the films deposited from 20 mM KMnO_4 aqueous solutions with 0.0, 0.5, 2, and 4 mM AgNO_3 additions at a scan rate of 10 mV/s are 160, 137, 155, and 132 F/g, respectively. This fact indicates that the introduction of Ag in the matrix of the deposited

MnO_2 has no beneficial effect on its capacitive properties.

3.2.2. Electrochemical Impedance Spectroscopy Characterization

In principle, the power output capability of electrochemical supercapacitor depends strongly on not only the rates of ionic mass transport [20] but also the equivalent series resistance (ESR) [21]. The ESR is the sum of two major parts, an electronic resistance and an ionic one. EIS has been widely used to study the redox (charging/discharging) processes of electrode materials and to evaluate their electronic and ionic conductivities.

Figure 4 shows the measured Nyquist plots of MnO_2 and Ag-doped MnO_2 electrodes in 0.5 M Na_2SO_4 electrolyte. The inset of Fig. 4 represents the high frequency region of the recorded full impedance plots.

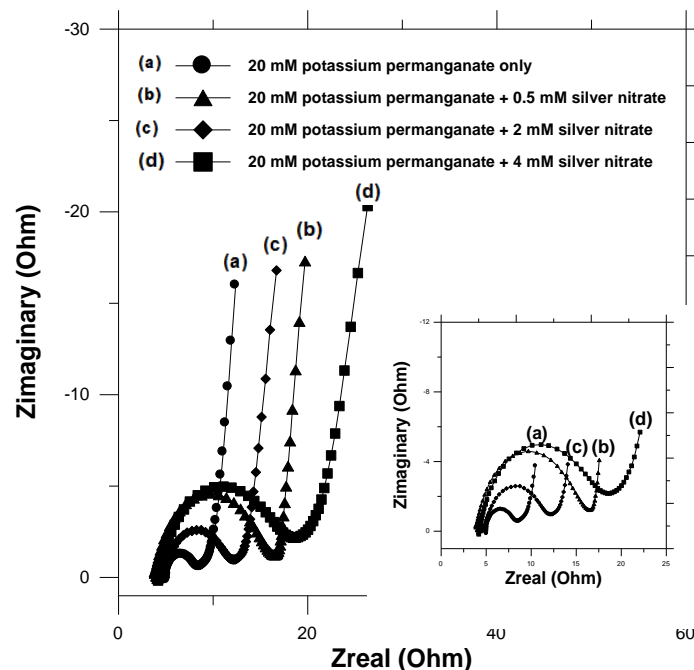


Figure 4: The Nyquist plots of MnO_2 and Ag-doped MnO_2 electrodes investigated in 0.5 M Na_2SO_4 electrolyte in the frequency range of 0.1 Hz–100 kHz at 10 mV amplitude.

In figure 4, two well-separated patterns are observed: an arc is obtained at frequencies high enough, which is related to interfacial processes; the low-frequency region of such plots indicated a capacitive behavior related to the film charging mechanism.

The initial non-zero intersect with the real impedance axis at the beginning of the semicircle indicates the typical ESR value of all system [19,22]. The estimated ESR values for the films deposited from 20 mM KMnO_4 aqueous solutions with 0.0, 0.5, 2, and 4 mM AgNO_3 additions are 5, 4.1, 4.85, and 4.17 Ω , respectively. These results indicate that the ESR value

of MnO₂ deposited film has not been significantly affected by Ag doping.

On the other hand, all spectra showed a clear semi-circle at the high frequency region, which corresponds to the charge transfer resistance (R_{ct}). The magnitude of the R_{ct} can be derived from the difference in the real part of the impedance between low and high frequencies [1,23] using fitting program provided with the electrochemical workstation. The estimated R_{ct} values for the films deposited from 20 mM KMnO₄ aqueous solutions with 0.0, 0.5, 2, and 4 mM AgNO₃ additions are 3.87, 12.79, 7.81, and 15.3 Ω , respectively. The increase in the R_{ct} value of MnO₂ with Ag addition may refer to the detrimental effect of Ag addition on the electronic transport properties of the deposited oxide.

Meanwhile, a comparison of the imaginary impedance (Zimaginary) data at the same frequencies for all the deposited films indicates that the capacitance for Ag-free MnO₂ film is higher than those of Ag-doped MnO₂ films. This fact is in a good agreement with the SC data presented in Fig. 3.

3.2.3. Galvanostatic Charge–Discharge

Figure 5 presents the charge–discharge curves for the films deposited from 20 mM KMnO₄ aqueous solutions with 0.0, 0.5, 2, and 4 mM AgNO₃ additions. The curves were measured in the potential range between 0 and +1 V at a discharge current density of 1.1 mA/cm².

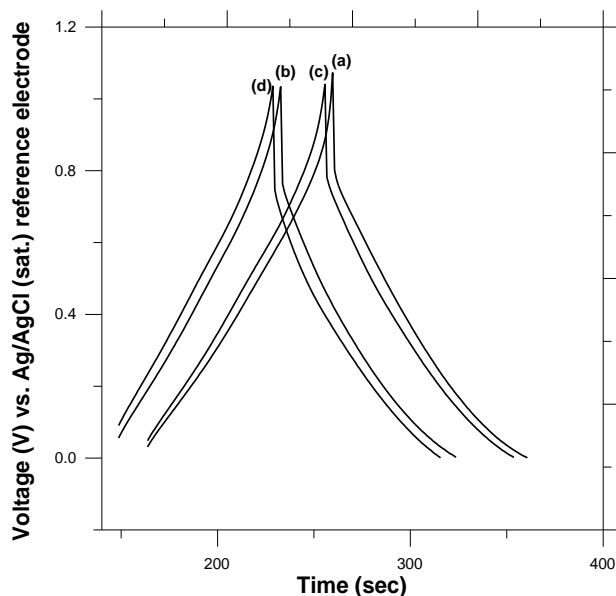


Figure 5: Charge–discharge curves in 0.5 M Na₂SO₄ electrolyte for thin films deposited from 20 mM KMnO₄ aqueous solutions with (a) 0.0 M AgNO₃, (b) 0.5 mM AgNO₃, (c) 2 mM AgNO₃, and (d) 4 mM AgNO₃

In figure 5, there is a linear variation of potential during charging process, indicating the capacitive behavior of MnO₂ and Ag-doped MnO₂ films. The discharge part of

the curves consists of three segments: a resistive component from the sudden decrease of voltage (iR drop) related to the internal resistance of the deposit, the capacitance component which is related to the voltage change due to ions separation at electrode interface in the double layer region and the faradaic component which is attributed to charge transfer reaction of deposit. Detailed analysis of the results in Fig. 5 clearly shows that the Ag-free MnO₂ film has longer time for charging-discharging processes and lower iR drop value than those recorded for Ag-doped MnO₂ deposited films. These facts indicate the higher energy and power densities of Ag-free MnO₂ than those of Ag-doped MnO₂.

3.2.4. Cyclic Stability using Galvanostatic Charge–Discharge

The cyclic stability test of Ag-free MnO₂ film was performed at discharge current density 5.5 mA/cm² and the results are presented in Figure 6.

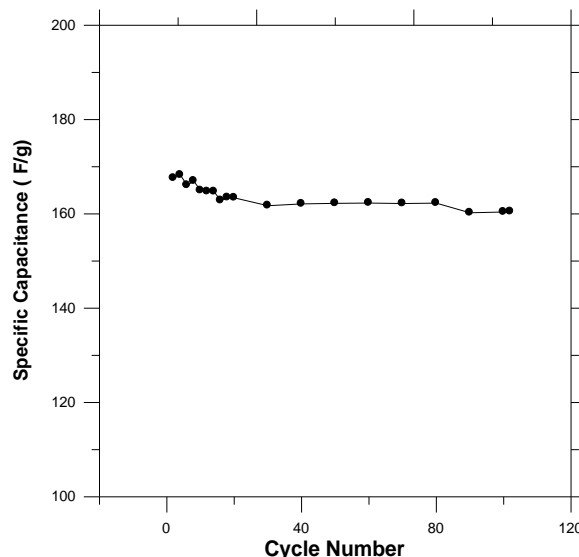


Figure 6: Life-cycle data of the Ag-free MnO₂/SS electrode at discharge current density 5.5 mA/cm².

As it can be clearly seen in figure 6, there is a little decrease in the value of specific capacitance during the first 30 cycles and then the specific capacitance value remained almost constant. A decrease of about 4 % in the initial specific capacitance was observed after 100 cycles. This decrease in the value of specific capacitance is very less compared to the reported value in the literature [24] and indicates the high stability of the deposited film.

4. CONCLUSIONS

The results presented in this investigation indicated that amorphous Ag-free and Ag-doped manganese dioxide thin films were successfully prepared by galvanostatic cathodic deposition onto polished SS electrodes from KMnO₄ solution without and with AgNO₃ addition. The

Ag-doped manganese MnO₂ films showed lower capacitive behavior and higher charge transfer resistance compared with Ag-free MnO₂ deposited film. The specific capacitance and charge transfer resistance values for Ag-free MnO₂ films were 160 F/g at a scan rate 10 mV/s and 3.87 Ω, respectively. The Ag-free MnO₂ film prepared by the cathodic electrolytic deposition on low cost stainless steel substrate can be considered as possible electrode materials for supercapacitor application.

ACKNOWLEDGEMENTS

This work was supported by Egypt Japan University of Science and Technology (E-just).

REFERENCES

- [1] Conway, B.E., *Electrochemical Supercapacitors: Scientific Fundamentals and Technological Applications*, Kluwer Academic/Plenum, New York, 1999, p. 1.
- [2] Burke, A.F., Murphy, T.C., in: Goughly, D.H., Vyas, B., Takamura, T., and Huff, J.R. (Eds.), *Materials for Energy Storage and Conversion: Batteries, Capacitors and Fuel Cells*, Materials Research Society, Pittsburgh, 1995, p. 375.
- [3] Lam, L.T., and Louey, R. "Development of ultra-battery for hybrid-electric vehicle applications", *J. Power Sources*, Vol. 158, pp. 1140-1148, 2006.
- [4] Zhang, L.L., Tianxin, W., Wenjuan, W., and Zhao X.S. "Manganese oxide-carbon composite as supercapacitor electrode materials", *Microporous and Mesoporous Materials*, Vol. 123, pp. 260-267, 2009.
- [5] Winter, M., and Brodd, R.J., "What Are Batteries, Fuel Cells, and Supercapacitors", *Chem. Rev.*, Vol. 104, pp. 4245-4270, 2004.
- [6] Pandolfo, A.G., and Hollenkamp, A.F. "Carbon properties and their role in supercapacitors", *J. Power Sources*, Vol. 157, pp. 11-27, 2006.
- [7] Dubal, D.P., Dhawale, D.S., Gujar, T.P., and Lokhande, C.D. "Effect of different modes of electrodeposition on supercapacitive properties of MnO₂ thin films", *Applied Surface Science*, Vol. 257, pp. 3378-3382, 2011.
- [8] Pang, S.C., Anderson, M.A., and Chapman, T.W. "Novel Electrode Materials for Thin-Film Ultracapacitors: Comparison of Electrochemical Properties of Sol-Gel-Derived and Electrodeposited Manganese Dioxide", *J. Electrochem. Soc.*, Vol. 147, pp. 444, 2000.
- [9] Zhao, D., Yang, Z., Kong, E.S., Xu, C., and Zhang, Y. "Carbon nanotube arrays supported manganese oxide and its application in electrochemical capacitors", *J. Solid State Electrochem.* DOI 10.1007/s10008-010-1182-x.
- [10] Zheng, J.P., and Jow, T.R. "A New Charge Storage Mechanism for Electrochemical Capacitors", *Journal of the Electrochemical Society*, Vol. 142, No. 1, pp. L6-L8, 1995.
- [11] Kim, I.H., and Kim, K.B. "Ruthenium oxide thin film electrodes for supercapacitors", *Electrochemical and Solid State Letters*, Vol. 4, No. 5, pp. A62-A64, 2001.
- [12] Chang, J.K., and Tsai, W.T. "Material Characterization and Electrochemical Performance of Hydrous Manganese Oxide Electrodes for Use in Electrochemical Pseudocapacitors", *J. Electrochem. Soc.*, Vol. 150, pp. A1333, 2003.
- [13] Hu, C.C., and Tsou, T.W. "The optimization of specific capacitance of amorphous manganese oxide for electrochemical supercapacitors using experimental strategies", *J. Power Sources*, Vol. 115, pp. 179, 2003.
- [14] Long, J.W., Young, A.L., and Rolison, D.R. "Spectroelectrochemical Characterization of Nanostructured, Mesoporous Manganese Oxide in Aqueous Electrolytes", *J. Electrochem. Soc.*, Vol. 150, pp. A1161, 2003.
- [15] Kim, H., and Popov, B.N. "Synthesis and Characterization of MnO₂-Based Mixed Oxides as Supercapacitors", *J. Electrochem. Soc.*, Vol. 150, pp. D56, 2003.
- [16] Reddy, R.N., Reddy, R.G. "Sol-gel MnO₂ as an electrode material for electrochemical capacitors", *J. Power Sources*, Vol. 124, pp. 330, 2003.
- [17] Wu, X.M., He, Z.Q., Chen, S., Ma, M.Y., Xiao, Z.B., and Liu, J.B. "Silver-doped lithium manganese oxide thin films prepared by solution deposition", *Mater. Lett.*, Vol. 60, pp. 2497-2500, 2006.
- [18] Ahn, H.J., Sung, Y.E., Kim, W.B., and Seong, T.Y. "Crystalline Ag nanocluster-incorporated RuO₂ as an electrode material for thin film micropseudocapacitors", *Electrochem. Solid State Lett.*, Vol. 11, pp. A112-115, 2008.
- [19] Zhang, Y., Li, G., Lv, Y., Wang, L., Zhang, A., Song, Y., and Huang, B. "Electrochemical investigation of MnO₂ electrode material for supercapacitors", *International Journal of Hydrogen Energy*, Vol. 36, pp. II760-II766, 2011.

- [20] Izadi-Najafabadi, A., Tand, T.H., and Madden, J.D. "Towards high power polypyrrole/carbon capacitors", *Synth Met.*, Vol. 152, pp. 129–132, 2005.
- [21] Celzard, A., Collas, F., Mareche, J.F., Furdin, G., and Rey, I. "Porous electrodes-based double-layer supercapacitors: pore structure versus series resistance", *J Power Sources*, Vol. 108, pp. 153–162, 2002.
- [22] Lu, Q., and Zhou, Y. "Synthesis of mesoporous polythiophene/MnO₂ nanocomposite and its enhanced pseudocapacitive properties", *J. Power Sources*, Vol. 196, pp. 4088-4094, 2011.
- [23] Tuken, T., Yazici, B., and Erbil, M. "A new multilayer coating for mild steel protection", *Prog. Org. Coat.*, Vol. 50, pp. 115–122, 2004.
- [24] Prasad, K.R., and Miura, N. "Potentiodynamically deposited nanostructured manganese dioxide as electrode material for electrochemical redox supercapacitors". *Journal of Power Sources*, Vol. 135, pp. 354–360, 2004.

Adsorption of Dye Pollutants on Hydrothermally Synthesized Mesoporous Copper Phosphate Materials

Abdmeziem Kaïssa¹, Roumila Yasmina², Bagtache Radia^{1,2}.

¹Laboratoire d'Electrochimie-corrosion, Métallurgie, Chimie Minérale; Equipe de chimie inorganique.

Faculté de chimie, USTHB, BP 32 El Alia, Alger, Algérie :

(abdmeziemk@gmail.com; roumila.yasmina@yahoo.fr)

²C.R.A.P.C. BP n°248 Alger, 16004, RP Alger, Algérie: (rbagtache@usthb.dz)

ABSTRACT

Porous inorganic framework materials have attracted considerable interest due to their countless applications in different areas. A strong research effort and increasing emphasis have been devoted to the development of new materials. This paper deals with the synthesis and characterization of copper phosphate materials prepared under hydrothermal conditions, in the presence of a cationic surfactant. Depending on the composition and parameters of the starting reaction mixture, various phases, exhibiting different structural and textural features were obtained. In this work, we report on the synthesis of two phases, one of them has fixed the surfactant and was denoted Cu-P-CTAB and the other one was free of it (denoted Cu-P). The as made materials have been characterized from the structural viewpoint by means of several physicochemical techniques. Both materials were tested in the adsorption of acid orange 10, an azo anionic dye, presenting two sulfonate acid groups and a rather high size, making its removal from wastewater difficult. The adsorption experiments revealed that the surfactant free copper phosphate was more efficient. Pseudo-first-order, pseudo-second-order and intraparticle diffusion models were applied to kinetic experimental data that fitted best with the pseudo-second-order model. As for equilibrium experiments, they were more in accord with the Freundlich isotherm model. Thermodynamic parameters such as change in free energy ΔG^0 , enthalpie ΔH^0 and entropie ΔS^0 were evaluated. The negative charge of free energy change indicated that the adsorption process was spontaneous.

Keywords: Copper phosphate, hydrothermal synthesis, surfactant, dye pollutant

1. INTRODUCTION

Since the first discovery of mesoporous molecular sieves (denoted M41S) [1], the synthetic approach to mesoporous materials has also been extended to non-silicious mesoporous materials, using various pathways. Much work has been devoted to the synthesis of metal oxides [2,3] and metal phosphates [4-6] due to their wide applications in various fields. Titanium, zirconium, niobium and tin phosphates have been extensively reported and mainly applied as heterogeneous acid catalysts or for photocatalytic and photovoltaic processes. Unlike silicious mesoporous materials, non-siliceous ones have been rarely used for adsorption.

This paper deals with the hydrothermal synthesis and characterization of mesoporous copper phosphate materials that were applied in the adsorption of dye pollutants.

2. EXPERIMENTAL

2.1 Synthesis

The copper phosphate materials were obtained hydrothermally from a reaction mixture containing H_3PO_4 (85 wt% aqueous solution), $CuCl_2$, $2H_2O$, cetyltrimethylammonium bromid (CTAB) and water, in the following molar ratios.

- For Cu-P-CTAB compound: 1 $CuCl_2$, 2 H_2O ; 1 CTAB ; 5 H_3PO_4 ; 300 H_2O (crystallization temperature: 60°C)
- For Cu-P compound : 1 $CuCl_2$, 2 H_2O ; 0,4 CTAB : 3,7 H_3PO_4 ; 300 H_2O (crystallization temperature: 90 °C)

2.2 characterizations

N_2 adsorption-desorption isotherms were carried out at liquid nitrogen temperature using an ASAP 2010 analyser from Micromeritics. Prior to each measurement, the samples were outgassed at 200°C until a residual pressure of 2×10^{-3} Torr was reached. The specific surface areas were determined by using the Brunauer-Emmett-Teller (BET) procedure.

TG and DTG analyses were carried out using a SDT Q600 thermoanalyzer. The Infrared (FTIR) spectra were recorded as KBr pellets on a Bruker Vector 22 FTIR spectrometer, within the 400-4000 cm^{-1} region. The crystals morphology was visualized by scanning electron microscopy using a Jeol J.S.M. 6360 LV microscope with EDX equipment.

The adsorption kinetic experiments were performed at original pH of 6.5, by batch procedures. Equilibrium isotherm studies were carried out with different initial concentrations of the dye (10–60 mg/L). The adsorbent was compressed into disc pellets of about 1cm diameter. The concentration of the dye was determined by UV-Visible absorption spectroscopy using a VARIAN

GARY 50 Con spectrometer. The dye concentrations were calibrated with the Beer-Lambert's law at λ max value of 484 nm.

3. RESULTS AND DISCUSSIONS

3.1. Characterization of the phosphate materials

The S.E.M micrographs of the as-synthesized materials are shown on Fig.1.

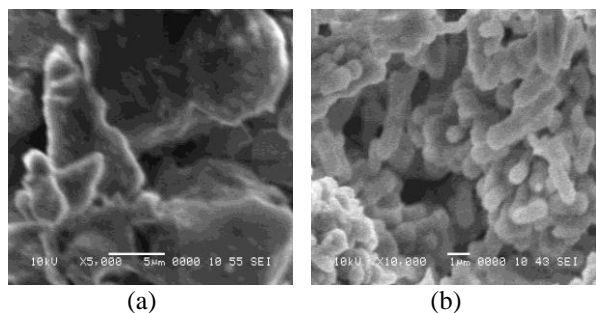


Figure 1: Scanning electron micrographs
(a) Cu-P-CTAB (b) Cu-P

EDX data (Fig.2), FTIR analysis (Fig.3) and thermal curves (Fig.4) confirmed the presence of the surfactant in the Cu-P-CTAB product, despite intensive washing.

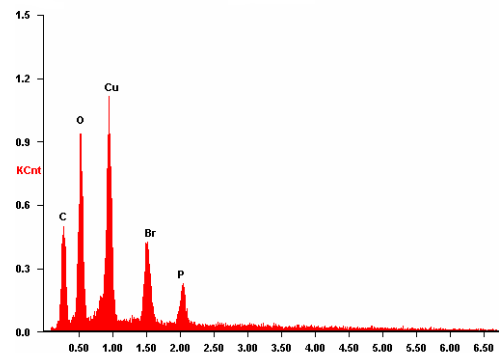
Indeed, unlike Cu-P infrared spectrum (not shown), the Cu-P-CTAB one exhibited the well known sharp bands at 2920 and 2850 cm^{-1} corresponding to asymmetric and symmetric C-H stretching, respectively.

Moreover, thermal analysis (Fig.4) showed the decomposition of organic matter from about 280°C, as confirmed by mass spectrometry curves (not shown).

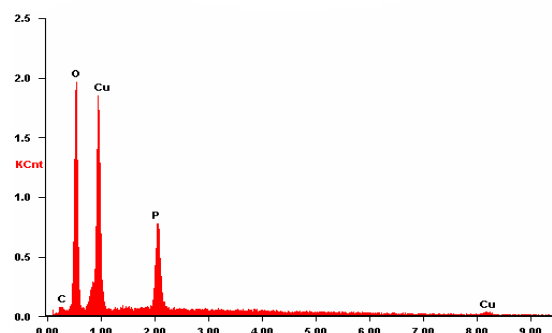
As for the textural studies, the nitrogen adsorption/desorption isotherms (Fig.5) revealed that Cu-P-CTAB compound presented a lower porosity. It might be explained by the presence of occluded surfactant molecules occupying the pore openings.

3.2. Adsorption of dye pollutant

Various kinds of dyestuffs appear in the effluents of wastewaters in various industries such as textiles, leather, paper etc. A very small amount of dye in water is highly visible and may be toxic to human and environment. Due to their mainly synthetic origin and aromatic structures, they are biologically non-degradable.



(a)



(b)

Figure 2: EDX patterns of the as-synthesized materials (a) Cu-P-CTAB (b) Cu-P

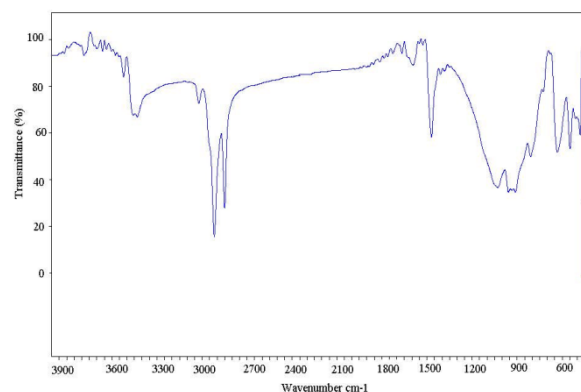
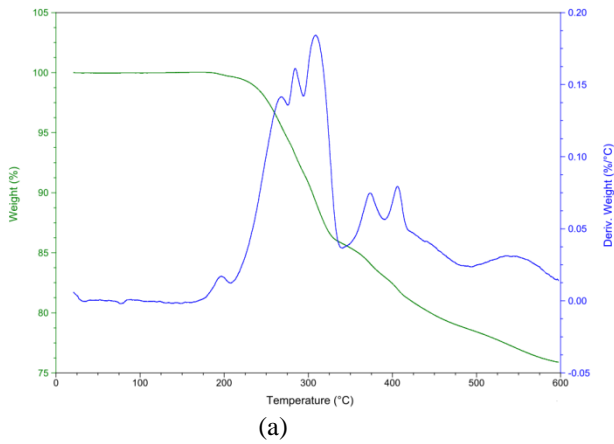
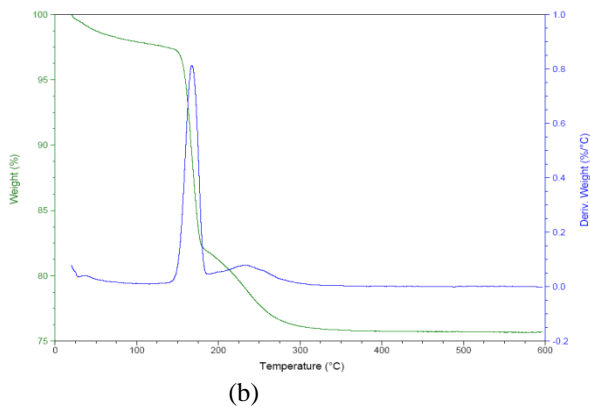


Figure 3: FT-IR spectrum of Cu-P-CTAB



(a)



(b)

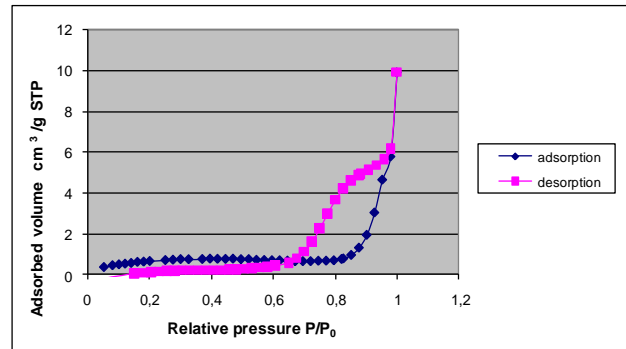
Figure 4: TG and DTG curves
(a) Cu-P-CTAB (b) Cu-P

Among the major technologies that are used for wastewater treatment, adsorption is more and more becoming a prominent effective and feasible method.

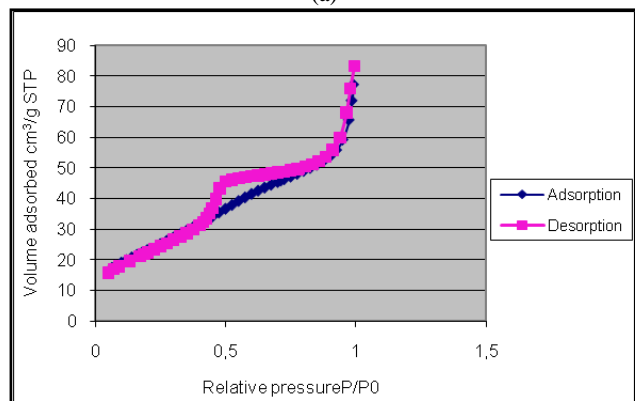
Both synthesized materials were tested for acid orange 10 adsorption but Cu-P-CTAB showed very low affinity at the original pH of 6.5. This same compound was previously used in phenol removal [8] in which it was very efficient. These observations suggested that the adsorption processes were different for the two pollutants. Work is in progress to find the best adsorption conditions for acid orange 10 onto Cu-P-CTAB phase.

The adsorption kinetics of the acid dye on the Cu-P compound are presented in Fig 6. The contact time was extended to 48h. The results fitted well with the pseudo-second-order model (Table1).

The parameters were obtained from the (t/q_t) versus t curves that are not reported here.



(a)



(b)

Figure 5: N₂ adsorption-desorption isotherms
(a) Cu-P-CTAB (b) Cu-P

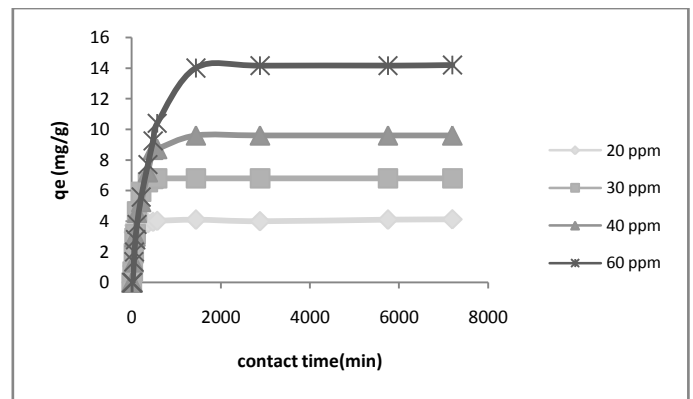


Figure 6: Adsorption kinetics on Cu-P compound
(pH 6.5, T= 20°C, adsorbent amount: 2,5g/L)

Table 1: Pseudo-second-order model parameters

Initial concentration (ppm)	K_2 (g/mg.min)	q_e (mg/g)	R^2
20	7,84	4,82	1
30	5,31	6,88	0,99
40	6,90	9,84	0,98
50	7,58	15,72	0,99
60	10,58	14,99	0,93

In this table, q_e (mg/g) represents the amount of adsorbed dye per gram of adsorbent; K_2 is the rate constant of the pseudo-second order and R^2 the fitness coefficient.

The intraparticle diffusion model study suggested that multiple stages were involved in the adsorption process. Indeed, the plots are not linear over the whole time range (plots not reported in this abstract).

The Freundlich isotherms led to good results (curves not shown), implying that the sites of adsorption on the surface of the adsorbent are more likely heterogeneous.

The effect of temperature on the adsorption of the dye was studied by carrying out a series of experiments at 20, 28, 35 and 45 °C. The equilibrium adsorption percentages (% removal) as a function of the equilibrium concentration of dye in the solution C_e (mg/L) are shown in Figure 7.

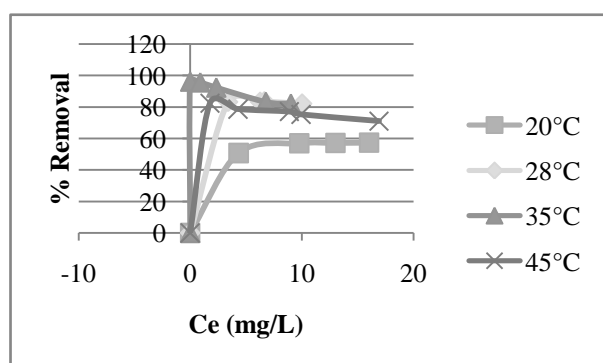


Figure 7: Effect of temperature on the % adsorption (pH 6.5, adsorbent amount: 2,5g/L)

As can be seen from the curves, the adsorption increased with temperature, from 20 to 35°C.

However, at 45°C, the adsorption decreased again, probably due to some desorption of the adsorbate.

The thermodynamic parameters were calculated for each initial concentration and each temperature. We give, as examples the values obtained at 35°C and $C_0 = 40$ ppm: ΔG^0 (- 7. 02 kJ/mol), enthalpie ΔH^0 (148. 77 kJ/mol) and entropie ΔS^0 (507 J/mol).

4. CONCLUSION

In this study, the hydrothermal synthesis of copper phosphates was reported. The compounds were characterized by several physico-chemical techniques which revealed that one of them included the surfactant in its structure while the other one did not. The latter compound was favourable for the adsorption of acid orange 10, an azo dye pollutant. The results of the studies indicated that the adsorption process was spontaneous and endothermic. Isotherm modelling showed that Freundlich model had better performance for representation of the experimental data

Work is in progress with varying the conditions of pH and ionic strength. These parameters seem to influence favourably the adsorption of the dye onto the surfactant loading phosphate material.

REFERENCES

- [1] Beck, J.S., Vartuli, J.C., Roth, W.J., Leonowicz, M.E., Kresge, C. T., Schmitt, K. D., Chu, C. T-W., Olson, D. H., Sheppard E. W., McCullen, S.B., Higgins, J.B., Schlenker J. L. "A New Family of Mesoporous Molecular Sieves Prepared with Liquid Crystal Templates", J.Am.Chem.Soc, vol.114, pp.10834-10843, 1992.
- [2] Liu, X.M., Yan, Z.F., Lu, M.G.Q. "Solid- state synthesis and characterisation of mesoporous zirconia with lamellar and wormhole-like mesostructures", J. Porous Mater, Vol.15, pp.237-244, 2008.
- [3] Zhu, J., Tay, B.Y., Ma, J. "Hydrothermal synthesis and characterization of mesoporous SnO₂/SnO₂-SiO₂ on neutral template", Journal of Materials Processing Technology , vol 192-193, pp 561-566, 2007.
- [4] Sarkar, K., Yokoi, T., Tatsumi, T., Bhaumik, A. "Mesoporous hybrid zirconium oxophenylphosphate synthesized in absence of any structure directing agent", Microporous and Mesoporous Materials, Vol.110, pp.405-412, 2008.
- [5] Sarkar, A., Pramanik, P. "Synthesis of mesoporous niobium oxophosphate using niobium tartrate precursor by soft templating method", Microporous and Mesoporous Materials, Vol.117, pp.580-585, 2009.
- [6] Pan, C., Yuan, S., Zhang, W. "A neutral templating route to mesoporous titanium phosphate molecular sieves with enhanced thermal stability". Applied Catalysis A: General, Vol.312, pp.186-193, 2006.
- [7] Mal, N.K., Bhaumik, A., Fujiwara, M., Matsukata, M. "Novel organic- inorganic hybrid and organic-free mesoporous niobium oxophosphate synthesized in the presence of an anionic surfactant", Microporous and Mesoporous Materials, Vol.93, pp.40-45, 2006.
- [8] Abdmeziem, K., Roumila, Y., Bagtache, R., Mekhezoumi, D., Couchot, P. "Adsorption of phenolic pollutants on porous copper materials: a comparative study", Proceeding: Global Conference on Global warming 2009, 05-09 July 2009 Istanbul Turkey.

Nonlinear Modeling of River Flow

Esmail Amiri¹

¹Department of Statistics, Imam Khomeini International University, Ghazvin, Iran (e_amiri@ikiu.ac.ir)

ABSTRACT

In the hydrology studies, it is well known that the time series associated with river flow are the consequence of various influencing factors, and therefore are complicated and have nonlinear behaviors. In an empirical study, we investigate the capability of three classes of nonlinear models namely Threshold Autoregressive (TAR), Smooth Transition Autoregressive (STAR) and Markov Switching Autoregressive (MSAR) to capture stochastic dynamics of Colorado River discharge time series. Least square (LS) and Maximum likelihood (ML) method is employed to estimate parameters of the models. For model comparison three criteria, namely Likelihood, AIC and BIC are calculated. The results show that the TAR models perform better than other two competing models. To forecast future river discharge values an iterative method is applied. Moreover, a Monte Carlo method is used to build forecasting river discharge confidence intervals.

Keywords: Hydrology, River flow, Non-linear, Autoregressive, Markov switching, likelihood, AIC, BIC.

1. INTRODUCTION

The inherent nonlinear nature of hydrologic systems and the associated processes has been known for long (e.g. [8]; [2]; [3]). River flow can be characterized by several general features. As a result of the periodicity in precipitation, river flow has also strong seasonal periodicity. The seasonal cycle of river flow is asymmetric; i.e., river flow increases rapidly (usually during late winter and spring) and decreases gradually (toward the end of the autumn). The fluctuations in river flow are large for large river flow and small for small river flow. It is important to note that unlike other climate components, river flow may have a direct impact of human activity, like damming, use of river water for agriculture, etc., a fact which makes the river flow data more difficult to study. The fluctuations in river flow are of special interest since they are directly linked to floods and droughts. There are several interesting characteristics of river flow fluctuations: (i) the river flow fluctuations have power law tails in the probability distribution (e.g. [12]; [11]), (ii) the river flow fluctuations are long-term correlated (e.g. [7]; [14]), and (iii) river flow fluctuations are multifractal (e.g. [18]; [13]; [10]). These scaling laws may improve the statistical prediction of extreme changes in river flow (e.g. [4]).

Reference [22] analyze river flow using a two-state regime switching autoregressive model, [15] and [1] also apply regime switching models to river flow time series. Reference [9] fit a mixed threshold autoregressive model to a river flow data set. Our aim is to compare performance of three classes of nonlinear models, namely Threshold Autoregressive (TAR), Smooth Transition Autoregressive (STAR) and Markov Switching Autoregressive (MSAR) to capture stochastic dynamics of Colorado river discharge time series. Least square (LS) and Maximum likelihood (ML) method is employed to estimate parameters of the models. For model comparison three criteria namely loglikelihood, AIC and BIC are calculated.

Sections 2 to 4 illustrate TAR, STAR and MSAR models respectively, section 5 describes data, section 6 presents empirical results and final section is devoted to the conclusion.

2. THRESHOLD AUTOREGRESSIVE

One popular class of nonlinear time series models is the threshold autoregressive (TAR) models, which is probably first proposed by [19] and discussed in detail in [20]. The TAR models are simple and easy to understand, but rich enough to generate complex nonlinear dynamics. For example, it can be shown that the TAR models can have limit cycles and thus be used to model periodic time series, or produce asymmetries and jump phenomena that cannot be captured by a linear time series model. In spite of the simplicity of the TAR model form, there are many free parameters to estimate and variables to choose when building a TAR model, and this has hindered its early use. A special class of TAR model is called self-exiting TAR (SETAR).

2.1 TAR and SETAR Models

Consider a simple AR(p) model for a time series $\{y_t\}$

$$y_t = \mu + \alpha_1 y_{t-1} + \alpha_2 y_{t-2} + \dots + \alpha_p y_{t-p} + \varepsilon_t \quad (1)$$

where μ and $\alpha_i (i = 1, 2, \dots, p)$ are the AR coefficients, $\varepsilon_t \sim N(0, 1)$ and $\sigma > 0$ is the standard deviation of disturbance term. The model parameters $\alpha = (\mu, \alpha_1, \alpha_2, \dots, \alpha_p)$ and σ are independent of time t and remain constant. To capture nonlinear dynamics, TAR models allow the model parameters to change according to the value of a weakly exogenous threshold variable z_t :

$$y_t = \mu^{(j)} + \alpha_1^{(j)} y_{t-1} + \alpha_2^{(j)} y_{t-2} + \dots + \alpha_p^{(j)} y_{t-p} + \sigma^{(j)} \varepsilon_t, \quad \text{if } r_{j-1} < z_t \leq r_j \quad (2)$$

where $j = 1, 2, \dots, k$, and

$-\infty = r_0 < r_1 < \dots < r_k = \infty$. In essence, the $k - 1$ non-trivial thresholds $(r_1, r_2, \dots, r_{k-1})$ divide the domain of the threshold variable z_t into k different regimes. In each different regime, the time series y_t follows a different AR(p) model. When the threshold variable $z_t = y_{t-d}$, with the delay parameter d being a positive integer, the dynamics or regime of y_t is determined by its own lagged value y_{t-d} and the TAR model is called a self-exciting TAR or SETAR model. For the ease of notation, let SETAR(1) denote the one-regime linear AR model with $k = 1$, SETAR(2) denote the two-regime TAR model with $k = 2$, etc.

3.SMOOTH TRANSITION AUTOREGRESSIVE

In the TAR models, a regime switch happens when the threshold variable crosses a certain threshold. Instead, in some cases it is reasonable to assume that the regime switch happens gradually in a smooth fashion. If the discontinuity of the thresholds is replaced by a smooth transition function, TAR models can be generalized to smooth transition autoregressive (STAR) models. A systematic modeling cycle approach for STAR models is proposed by [17], and [21] provides a survey of recent development for STAR models. If the binary indicator function is replaced by a smooth transition function $0 < G(z_t) < 1$ which depends on a transition variable z_t (like the threshold variable in TAR models), the model becomes a smooth transition autoregressive (STAR) model :

$$y_t = X_t \alpha^{(1)} (1 - G(z_t)) + X_t \alpha^{(2)} G(z_t) + \sigma \varepsilon_t \quad (3)$$

where $X_t = (1, y_{t-1}, \dots, y_{t-p})$ and

$$\alpha^{(j)} = (\mu^{(j)}, \alpha_1^{(j)}, \dots, \alpha_p^{(j)}), j = 1, 2. \text{ Now the}$$

observations y_t switch between two regimes smoothly in the sense that the dynamics of y_t may be determined by both regimes. Two popular choices for $G(z_t)$ are the logistic function and the exponential function. Using the logistic function, the transition function can be specified as:

$$G(z_t; \gamma, c) = \frac{1}{1 + e^{-\gamma(z_t - c)}}, \quad \gamma > 0 \quad (4)$$

and the resulting model is referred to as logistic STAR or LSTAR model. Using the exponential function, the transition function can be specified as:

$$G(z_t; \gamma, c) = 1 - e^{-\gamma(z_t - c)^2}, \quad \gamma > 0 \quad (5)$$

and the resulting model is referred to as exponential

STAR or ESTAR model. In equations (4) and (5) the parameter c can be interpreted as the threshold, as in TAR models, and γ determines the speed and smoothness of transition.

4. MARKOV SWITCHING AUTOREGRESSIVE

If the model parameters in the simple AR(p) model in (1) are relaxed to be dependent on a latent or hidden state variable $S_t = \{1, \dots, k\}$, it becomes:

$$y_t = \mu_{S_t} + \alpha_{1S_t} y_{t-1} + \alpha_{2S_t} y_{t-2} + \dots + \alpha_{pS_t} y_{t-p} + \sigma_{S_t} \varepsilon_t \quad (6)$$

where the hidden state variable S_t follows a k-regime ergodic Markov chain with a finite number of states defined by the transition probabilities:

$$Pr(S_t = j | S_{t-1} = i) = p_{ij}, \quad \sum_{j=1}^k p_{ij} = 1, \forall i, j \in \{1, \dots, k\} \quad (7)$$

This is usually referred to as the Markov switching AR(p) process(MSAR). The MSAR model has proved to be effective at modeling nonlinear dynamics usually observed in economic and financial time series. For example, [6] uses a two-state Markov switching AR(4) model with constant σ^2 to capture the different dynamics observed in the U.S. real GNP during economic recessions and expansions. Markov switching time series models have seen extraordinary growth and become extremely popular for modeling economic and financial time series. They have been applied to model and forecast business cycles, the term structure of interest rates, volatility in economic and financial variables, foreign exchange rate dynamics, inflation rate dynamics, etc(e.g [24]).

In this study we assume only μ is dependent on S_t and μ_{S_t} is defined as

$$\mu_{S_t} = \mu_1 + \sum_{j=1}^k \mu_j I_{jt}, \quad \mu_j > 0 \quad (8)$$

where I_{jt} is an indicator variable that is equal to 1 when $S_t \geq j$ and k is the number of states.

5. DATA

We analyze a ten-year long daily mean water discharge series measured at Colorado(River Colorado) in U.S.A, from 1/01/2000 to 12/31/2009. The data is downloadable from <http://waterdata.usgs.gov/co/nwis/>. Our data set thus consists of 3653 daily mean discharge observations measured in cubic feet/s . Figures 1 and 2 show the plot of the time series and its highly skewed marginal distribution. A very important feature of the series is that short and steep rising periods are followed

by longer, gradually falling ones. This phenomenon is called the “asymmetric shape of the hydro-graph” in hydrology. The hydro-graph is a graphical representation which shows how discharge of a river varies over time. The series is very persistent, the one-lag and two-lag autocorrelation being around 0.9826 and 0.9562, respectively. This suggests that an AR model with order 2 could be considered as a starting point for modeling the Colorado river time series.

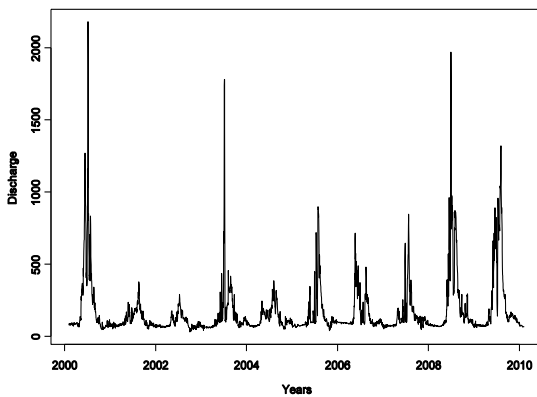


Figure 1: Plot of the daily Colorado discharge

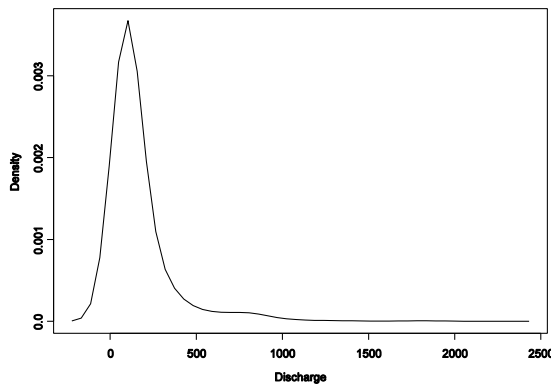


Figure 2: Plot of the daily Colorado discharge marginal distribution

6. EMPIRICAL RESULTS

Four class of models are fitted to the Colorado time series using S+FinMetrics software. To estimate the model parameters Least square (LS) and Maximum likelihood (ML) methods are applied. The computational result of parameter estimation and model fit criterion are presented in the following subsections.

6.1 AR models

Two AR models namely, AR(1) and AR(2) are fitted to the Colorado River time series, the value of the estimated parameters are presented in the Table 1. In Table 1, third and fifth rows present standard error (S.E) of the estimated parameters. Comparing AIC values,

Table 6 shows that AR(2) performs better than AR(1). Thus AR(2) is a good choice as a starting point.

Table 1: Estimates of AR(1) and AR(2) parameters

		μ	α_1	α_2	σ^2
AR(1)		166.3533	0.9701	-	2193
	S.E.	(25.6934)	(0.0040)	-	
AR(2)		166.3538	1.4201	-0.4638	1721
	S.E.	(15.6564)	(0.0147)	(0.0147)	

6.2 SETAR model

It is preferred to test for the existence of threshold-type nonlinearity in the time series first. Reference [16] proposes a conventional F test based on an auxiliary regression which is named Tsay’s approach. Tsay’s approach centers on the use of an arranged auto-regression with recursive least squares (RLS) estimation. Null Hypothesis is that no threshold nonlinearity. For assumed AR(2) model, the values of F statistic with 33281 degree of freedom are 48.4582 and 38.9696 for $d = 1$ and $d = 2$, respectively. P-value is close to 0 in both cases. Thus Null Hypotheses is rejected and threshold nonlinearity is present. Tsay suggests to choose the delay parameter d with greater F statistic, therefore we choose $d = 1$.

6.2.1 Threshold values

Tsay [16] also proposes to use two graphical tools for identifying the threshold values: (1) the scatter plot of standardized predictive residuals from the arranged auto-regression versus the ordered threshold variable; (2) the scatter plot of the t-statistics of the RLS estimates of parameters from the arranged auto-regression versus the ordered threshold variable. Both plots may exhibit structural breaks at the threshold values. The plots in Figure 3 show that both estimates are significant with t-statistics greater than 2 in absolute values in most cases. In addition, the trend in the t-statistics seems to have more than one breaks. Since we compare the performance of SETAR or MSAR model to STAR model, and STAR model in this study has two regimes, therefore we look for a SETAR model with only one threshold value. To identify the optimum threshold value we use TSB R package and apply the method described in [5]. Based on Minimum AIC fit with thresholds searched from the 10 percentile to the 90 percentile of all data. The estimated threshold is the 52 percentile of all data which is around 100.

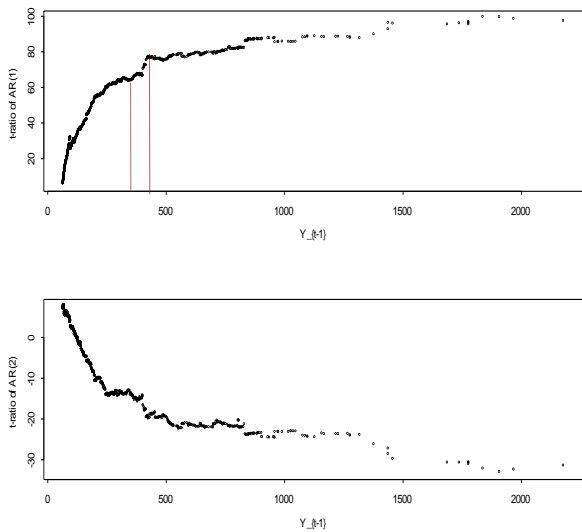


Figure 3: Scatter plot of t-statistics of RLS estimates of AR coefficients versus ordered threshold variable.

This suggests a SETAR(2) model with one threshold value $r = 100$. We follow [16] and use least squares (LS) to estimate the unknown parameters in (2) with given values of d and threshold. As long as there are enough observations in each regime, the LS estimates are consistent.

Table 2 presents the estimated parameter values of SETAR(2) fitted to Colorado river time series. Columns 1, 6 and 7 of Table 2 present regime, standard error of residuals (S.E. Res) and number of observations (No. Obs.) in each regime, respectively. In Table 2 standard errors of parameters (S.E.) and t-statistics (T) for each estimated parameter are presented.

Table 2: Estimates of SETAR(2) parameters

		μ	α_1	α_2	S.E. Res.	No. Obs.
Reg. 1		3.935	0.892	0.0725	11.41	1922
	S.E.	(1.682)	(0.035)	(0.03)		
	T	2.339	25.177	2.4299		
Reg. 2		11.687	1.425	-0.476	58.78	1731
	S.E.	(2.087)	(0.021)	(0.021)		
	T	5.600	67.714	-22.71		

6.3 STAR Model

6.3.1 Smooth transition values

In this study we concentrate on LSTAR models and choose logistic smooth transition function. We follow [24] and estimate the parameters of model (3) by nonlinear least squares (NLS). Under the additional assumption that the errors are normally distributed, NLS is equivalent to maximum likelihood estimation. Otherwise, the NLS estimates can be interpreted as quasi maximum likelihood estimates.

Parameters of logistic smooth transition function are estimated, Table 3 presents the values of γ , c , standard error of estimated (S.E) parameters and heteroskedastic standard errors (S.E.W) of estimated parameters using White[23] corrections.

Table 3: Estimates of Smooth transition parameters

	Values	S.E.	S.E.W
γ	0.340	0.169	0.526
c	349.775	569.175	1714.880

Based on estimates of smooth transition function, the parameters of STAR(2) model is estimated. Table 4 displays the estimated values of the parameters. Table 4 shows standard error and heteroskedastic standard error of estimated parameters using White's corrections. There is a significant difference between heteroscedastic and homoscedastic standard errors.

Table 4: Estimates of STAR(2) parameters

		μ	α_1	α_2	S.E. Res.
Lower regime		-519.179	-0.043	0.339	39.298
	S.E.	(1104.25)	(1.654)	(0.691)	
	S.E.W.	3361.760	4.934	2.010	
Upper regime		979.605	1.295	-0.917	39.298
	S.E.	(835.678)	(0.227)	(0.111)	
	S.E.W.	2596.653	0.716	0.329	

6.4 MSAR model

To estimate parameters of model (6) and hidden states (7) we follow[5] and take the maximum likelihood estimate(MLE) approach.

Table 5 shows the estimated parameters of the MSAR(2) model.

Table 5: Estimates of MSAR(2) parameters

Parameters	Value	Parameters	Value
μ_1	8.139904	α_{22}	-0.9681845
μ_2	8.140394	σ	1095.603
α_{11}	0.9421819	p_{11}	0.7533865
α_{12}	-0.02253395	p_{22}	0.4020307
α_{21}	1.967952		

6.5 Model Comparison

Model comparison criteria for five models are calculated. Table 6 shows that the fitted SETAR model has the lowest AIC.

Table 6: Model comparison criterion

	Log likelihood	AIC	BIC	Rank
AR(1)	-19236.35	38478.7		5
AR(2)	-18793.6	37595.2		4
SETAR	-16902.51	33817.02	33854.24	1
STAR	-18581.03	37174.06	37211.28	3
MSAR	-18135	36290	36321	2

6.6 Prediction

A more important task is to generate forecasts of future values of the time series that is of interest. Due to the well performance of SETAR models we only consider predictions from these models. Prediction from SETAR models can be easily computed using Monte Carlo simulations. Forecasting from a SETAR model is similar to forecasting from a univariate AR model. Since the forecast errors are asymptotically normally distributed, the h step ahead forecast can be simulated by generating normal random variables.

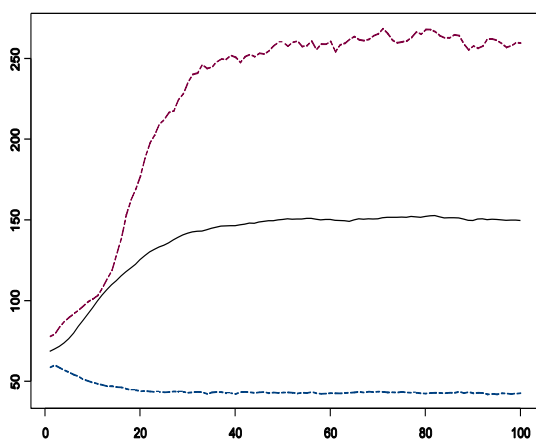


Figure 3: Plot of the Predicted confidence intervals from SETAR model fitted to daily Colorado discharge.

Fig. 3 shows the plot of 60% point-wise confidence intervals for the 100 steps ahead forecasts based on 10000 Monte Carlo simulations. The plot indicates that after less than 40 steps, the forecasts settle down to the asymptotic mean of the SETAR process.

7. CONCLUSION

In an empirical study we compare performance of three classes of nonlinear models, namely Threshold Autoregressive (TAR), Smooth Transition Autoregressive (STAR) and Markov Switching Autoregressive (MSAR) to capture stochastic dynamics of Colorado river discharge time series. Least square (LS) and Maximum likelihood (ML) method are employed to estimate parameters of the models. For model comparison three criteria namely loglikelihood, AIC and

BIC are calculated. Model comparison criteria indicate well performance of SETAR models. Monte Carlo simulation is used to produce forecast confidence intervals. The confidence intervals indicate that after less than 40 steps, the forecasts settle down to the asymptotic mean of the SETAR process.

We propose the following future research directions :

- 1- Looking for the parsimonious SETAR models by considering more than 1 threshold values.
- 2- Investigating new automatic methods to estimate more than 1 threshold values.

REFERENCES

- [58] Aksoy, H. "Markov-chain based modeling techniques for stochastic generation of daily intermittent streamflows", *Adv. Water Resour.*, Vol. 26, pp. 663-671, 2003.
- [59] Amorocho, J. "The nonlinear prediction problems in the study of the runoff cycle", *Water Resources Research*, Vol.3, No. 3, pp. 861-880, 1967.
- [60] Amorocho, J. and Brandstetter, A. "Determination of nonlinear functional response functions in rainfall-runoff processes", *Water Resources Research*, Vol. 7, No. 5, pp. 1087-1101, 1971.
- [61] Bunde, A., Eichner, J.F., Havlin, S., Koscielny-Bunde, E., Schellnhuber, H. J. and Vyushin, D. "Scaling of atmosphere and ocean temperature correlations in observations and climate models", *Phys. Rev. Lett.* Vol. 92, 039801, 2004.
- [62] Cryer, J.D. and Chan, K.S. *Time Series Analysis With Applications in R*, Springer 2nd Edition, 2008.
- [63] Hamilton, J.D. "A New Approach to the Economic Analysis of Nonstationary Time Series Subject to Changes in Regime", *Econometrica*, Vol. 57, pp. 357-384, 1989.
- [64] Hurst, H.E. "Long-term storage capacity of reservoirs" *Trans Am Soc Civil Engineers*, Vol. 116, pp. 770-799, 1951.
- [65] Izzard, C.F., "A mathematical model for nonlinear hydrologic systems", *Journal of Geophysical Research*, Vol. 71, No. 20, pp. 4811-4824, 1966.
- [66] Jian, W.B., Yao, H., Wen, X.H. and Chen, B.R. "A nonlinear Time series model for spring flow: An example from Shaxi province China", *Journal of Ground Water*, Vol. 36, No. 1, pp. 147-150, 1998.
- [67] Kantelhardt, J.W., Rybski, D., Zschiegner, S.A., Braun, P., Koscielny-Bunde, E., Livina, V., Havlin, S. and Bunde, A.

- “Multifractality of river runoff and precipitation: comparison of fluctuation analysis and wavelet methods” *Physica A*, Vol. 330, pp. 240-245, 2003 .
- [68] Kroll, C.N. and Vogel, R.M. “The Probability Distribution of Low Streamflow Series in the United States”, *Journal of Hydrologic Eng*
- [69] *ineering, ASCE*, Vol. 7, No. 2, pp. 137-146, 2002 .
- [70] Murdock, R. U. and Gulliver, J. S. “Prediction of river discharge at ungauged sites with analysis of uncertainty”, *J. Water Resour. Pl-Asce*, Vol. 119, pp. 473-487, 1993 .
- [71] Pandey, G., Lovejoy, S. and Schertzer, D. “Multifractal analysis including extremes of daily river flow series for basin five to two million square kilometres, one day to 75 years”, *J. Hydrol.*, Vol. 208, pp. 62-81, 1998.
- [72] Pelletier, J. D., and Turcotte D. L. “Long-range persistence in climatological and hydrological time series: Analysis, modeling and application to drought hazard assessment”, *J. Hydrol.*, Vol. 203. No. 1-4, 198-208, 1997.
- [73] Szilagyi, J., Balint, G. and Csik, A. “ A hybrid, Markov-chain based model for daily streamflow generation at multiple catchment sites”, *Journal of Hydrologic Engineering*, Vol. 11, No. 3, pp. 245-256, 2006.
- [74] Tsay, R.S. “Testing and Modeling Threshold Autoregressive Processes”, *Journal of the American Statistical Association*, Vol. 84. No. 405, 231-240, 1989.
- [75] Teräsvirta, T. “Specification, Estimation, and Evaluation of Smooth Transition Autoregressive Models”, *Journal of the American Statistical Association*, Vol. 89, 208-218, 1994 .
- [76] Tessier, Y., S. Lovejoy, Hubert, P., Schertzer, D., and Pecknold, S. “Multifractal analysis and modeling of rainfall and river flows and scaling, causal transfer functions”. *J. Geophys. Res.*, Vol. 101, No. 21, 26427-26440, 1996.
- [77] Tong, H. “On a Threshold Model”, in C.H. Chen (ed.), *Pattern Recognition and Signal Processing*, Amsterdam: Sijhoff & Noordhoff, 1978 .
- [78] Tong, H. *Non-Linear Time Series: A Dynamical System Approach*, Oxford University Press, 1990.
- [79] Van Dijk, D., Teräsvirta, T. and Franses, P.H. “Smooth Transition Autoregressive Models — A Survey of Recent Developments”, *Econometric Reviews*, Vol. 21, No. 1, pp. 1-47, 2002.
- [80] Vasas ,K., Elek, P., and Markus, L. “A two-state regime switching autoregressive model with an application to river flow analysis”, *Journal of Statistical Planning and Inference* Vol. 137, pp. 3113-3126, 2007.
- [81] White, H. “A Heteroskedasticity Consistent Covariance Matrix Estimator and a Direct Test for Heteroskedasticity”, *Econometrica*, Vol. 48, 817-838, 1980.
- [82] Zivot, E., WANG Jia-hui. *Modeling Financial Time Series with S-Plus*, Springer-Verlag, , 2006 .

The Impacts of Wastewaters Discharges on the Quality of Littoral Case of the Coastal Region *Ain Temouchent* (West Algeria)

Noria Kada Benabdallah¹, DJamila Harrache²

¹Department of Chemistry, Biotoxicological laboratory– Unit of Chemistry and Environment – Faculty of Science – University of Djillali Liabès – SIDI BEL ABBES – ALGERIA(noria20042003@yahoo.fr)

²Department of Chemistry, Biotoxicological laboratory– Unit of Chemistry and Environment – Faculty of Science – University of Djillali Liabès – SIDI BEL ABBES – ALGERIA (djharrache@yahoo.fr)

ABSTRACT

The evaluation of the quality of coastal waters is a means to prevent any risk to human health. It identifies the potential impacts of various effluents. The objective of this work, which is a preliminary approach, characterize and evaluate the impact of discharge of effluents on the marine environment, and especially on aquatic life. The sampling sites of seawater are located on the coastal region of *Ain Temouchent* (west Algeria), cover four tracks: *Terga*, *Sidi Djalloul*, *Beni saf*, *Rachgoun* and four wastewater collectors. The determination of the impact of these releases is required to evaluate their consequences on the Wildlife and the flora. For this purpose, the physico-chemical parameters evaluated are: pH, T, C.E., Cl⁻, P₂O₅, SO₄²⁻, NO₃⁻, and NO₂⁻. The aim of the characterization of the seawater quality is to prevent risks to the aquatic ecosystem. Tests were conducted during wet period, the results show that the concentrations of nutrients from different seawaters analyzed vary very little from one station to another, except the site *Terga* which marks a significant value to nitrite (higher than 300µg/l) and significant enrichment in orthophosphate (higher than 1.3 mg/l). Indeed, this site receives a significant input of wastewater. Finally, the estimation of other parameters is underway to estimate the degree of pollution caused by improper management of wastewater.

Keywords: pollution, Environmental impact, physicochemical analysis, wastewaters discharges, coastal *Ain Temouchent*, Algeria.

1. INTRODUCTION

The urbanization and industrial and agricultural development have led to environmental problems dangerous, Designed by a major anthropogenic pollution which in turn leads to degradation of the quality of the aquatic environment, terrestrial or sailor. Currently, marine pollution is a basis of many discussions, and has always been a major concern. This problem is most acute in the world, where the sewage will remain the main source of contamination, by volume, the environment, marine and coastal environment (GESAMP, 2001a).

Although the wastewater management in Algeria is governed by a set of texts, laws and regulations which states the need to link any dwelling or company rejecting polluted water to networks sanitation (Kerfouf et al, 2010).

One of the major causes of marine pollution is represented by the discharge of wastewater, which can create many difficulties for both flora and fauna, as for human health.

In this context, to estimate the quality of the coastal environment of the region of *Ain Temouchent* (northwest Algeria), it is important to evaluate qualitatively and quantitatively the pollution load of effluents from various nature and origin that are released in sea level of the wilaya.

This work consists initially to identify these effluents,

to conduct physical and chemical analysis by the determination of some pollution parameters and then evaluate the risks associated with sea water and their impact on ecosystems.

Finally, accordance with the accelerated deterioration of our environment, it is important to implement various programs to address the problems of pollution caused by waste water causing degradation of the quality of coastal environments.

It should also therefore to design the measures to be implemented to clean, maintain and better protect the aquatic environment.

2. DESCRIPTION OF THE STUDY AREA

In order to assess the impact of wastewater discharges on the receiving marine environment, two rounds of sampling were carried out:

The first series concerns the evaluation of the quality of water discharged to the sea, while the latter aims to control the spatial and temporal variation of marine water quality depending on the type of effluent discharged that may be subject to serious pollution. Eight sampling stations were chosen to cover both superficial sea water, the urban and industrial discharges, four of the middle receiver and four others are chosen for the water discharged. The choice of these stations, based on their accessibility, representativeness sources of pollution, and their situation in relation to population centers.

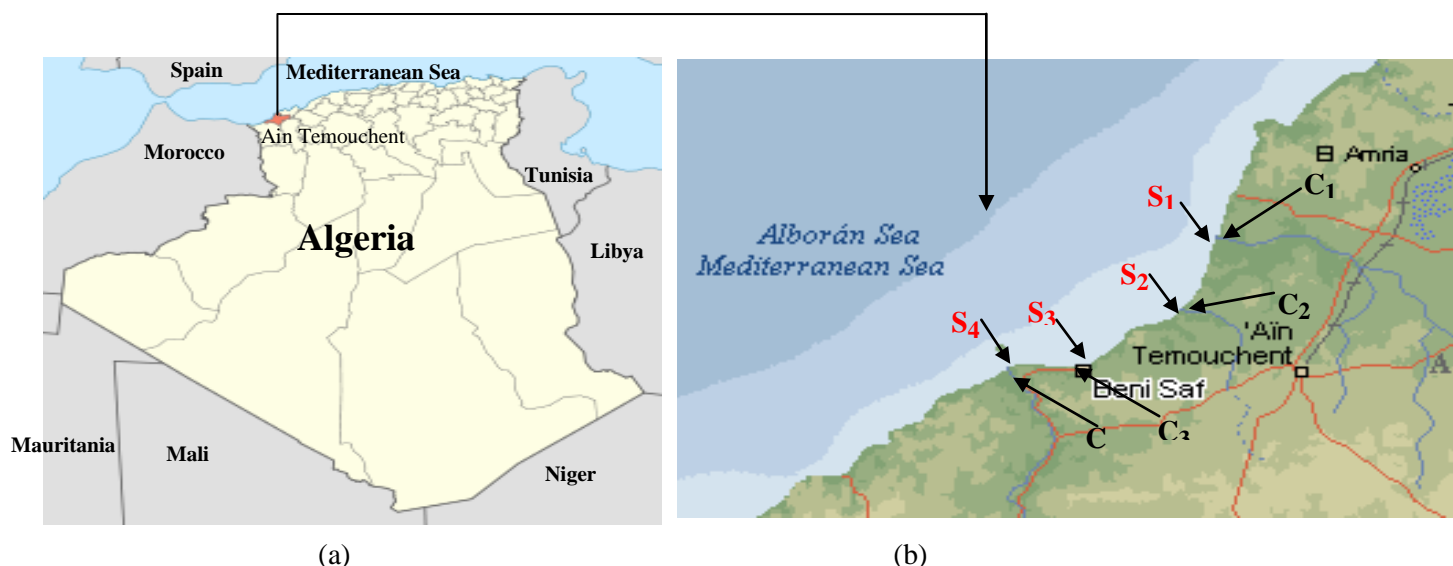


Figure 1: (a)localisation de la zone d'étude, (b)localisation des sites d'échantillonnages

Four companies of samples were carried out in wet period: in November, January, March and May. The sampling sites selected for this study at the Coastal *Ain Temouchent* are: (see Figure 1 (a) and (b)).

S1 (Terga Beach): Located near the mouth of the Oued El Maleh.

S2 (Sidi Djelloul Beach): Located near a resort area, receives the discharge of low river flow Sidi Djelloul.

S3 (FERPHOS): located inside the port, is located at the discharge point C3, which collects domestic wastewater from the city of Beni-Saf, with a capacity of 45 200 inhabitants (wikipedia.2011), discharged directly to sea.

S4 (Rechgoun) located 8 km from the city of Beni Saf, this area is characterized by the existence of agricultural land could produce an agricultural pollution through leaching and runoff.

On the other hand, the points of discharge to have been an assessment of the degree of pollution effluents are:

C1: Oued El Maleh, which drains a catchment area of about 873.50 km, with a length of the main stream of about 72.14 km and a maximum altitude of 800 m, according to direction of Hydraulics of the wilaya (DHW, 2011). It collects sewage mixed rainwater, domestic sewage and industries sewage from the complex detergent ENAD / HENKEL of Chaābat El Ham, sometimes discharged without any treatment. That effluent flows directly out to sea at the beach Terga. The flow is estimated at 75.80 m³/s (Qmin) and 379 m³/s (Qmax) (DHW, 2011).

C2: This is the Oued Sidi Djelloul which opens into the sea at the beach of Sidi Djelloul, draining a watershed

of approximately 186.54 km² and a maximum altitude of about 674 m (DHW, 2011). Other storm water, the river receives domestic waste some extending over a length of 36.19 km and a speed not exceeding 282.22 m³/s. This river is dry in summer.

C3: is cloaca of the domestic sewage of the city of Beni-Saf, with a capacity of 45 200 inhabitants discharged directly to sea.

C4: Oued Tafna which opens into the sea at the beach Rechgoun. It collects all the sewage of Commons Oulhaça and Rechgoune. In addition, the wastewater discharged without treatment into the river that are already polluted by releases of contaminated water from the dam Boughrara to 60 km in lower, are far from negligible. (Tarik Ghodbani 2008)

3. MATERIALS AND METHODS

3.1 Sampling

For our study, water samples were carried out every two months in the wet season from November 2010 to May 2011. Water samples for physico-chemical analysis were collected with plastic bottles, for filling sub-surface, rinsed with water of the sampling point. After labeled samples carefully kept in a cooler at low temperature and then transported to the laboratory for analysis. During the sampling of wastewater, it must take into account the difficulties of access during sampling.

3.2 Physicochemical parameters

Analyses of liquid effluents, focused on 10 physico-chemical (pH, T, EC, TDS, salinity, Cl⁻, P2O5, SO4⁻², NO3⁻, NO2⁻). Also, the quality assessment of marine waters was carried out by determining the following

physical and chemical parameters (pH, T, EC, salinity, Cl⁻, P₂O₅, NO₂⁻). These parameters were determined following the methods described by RODIER.(Rodier , 1984). The pH and temperature were measured in situ both for sea water or to sewage.

3.3 Materials and methods of analysis

- The pH measurement was made using a portable pH meter, while the temperature was determined using a mercury thermometer graduated in 1 / 10 in ° C.

- The conductivity, salinity and TDS were measured in the laboratory with an electric conductivity of type: inoLab Cond Level 1 (graphite measuring cell constant 0475 cm⁻¹ ± 1.5%). Nutrients, nitrates, nitrites and orthophosphates were determined by the colorimetric method using UV-Vis spectroscopy (2401pc SCIMADZU).

- Nitrates: the method used to determine nitrate is the method in "sodium salicylate" in the presence of sodium salicylate, nitrate-paranitro give the sodium salicylate, colored in yellow for a colorimetric assay to a length of wavelength of 420 nm.

- Nitrites: is the method to sulfanilamide, diazotization is carried out of sulfanilamide under acidic conditions and in the presence of N-[1 naphthyl] ethylene diamine, there is a coupling reaction leading to the formation of a purple colored complex capable of a colorimetric assay at 543 nm.

- The orthophosphates: orthophosphate ions, in acidic and in the presence of ammonium molybdate, phosphomolybdic complex, which give after reduction by ascorbic acid, may develop a blue coloration of a colorimetric assay at 690 nm.

- Sulfates: the determination of sulfates was performed by the method néophéliométrique, these ions are precipitated in a hydrochloric acid medium in the form of sulfates barryum. The precipitate obtained is stabilized by a solution of polyvinylpyrrolidone. The homogeneous suspensions were measured with a spectrophotometer at a wavelength of 650 nm.

- Chlorides: the analysis is done by the method of Mohr and are dosed with a solution of silver nitrate in the presence of potassium chromate.

4. RESULTS AND DISCUSSION

Table 1: characteristic physicochemical liquids discharged into the sea in the region of Ain Temouchent:

	Oued El Maleh			Oued Sidi jalloul			Site de Ferphos (Beni saf)			Oued Tafna		
	Max	Min	Med	Max	Min	Med	Max	Min	Med	Max	Min	Med
T(°C)	23	14	18	23	13	19	23	20	21,25	26	16	20
pH	8,2	7,6	7,95	8,7	8,1	8,27	8,1	7,6	7,8	9,1	8,4	8,77
CE(μs/cm) à 25°C	8620	7280	7890	5500	4230	4750	2120	143,6	173,9	24700	2630	9765
salinité	4,8	4,0	4,37	2,9	2,2	2,5	0,9	0,5	0,67	15,0	1,2	5,65
T.D.S(mg/l)	3696	3436	3588,6 7	2522	1864	2127	931	6,47	764,75	3070	1151	2183,67
Cl ⁻ (mg/l)	2520,5	2094,5	2277,3	1491	1065	1244,27	461,5	62,125	288,88	8662	589,3	3096,49
P ₂ O ₅ (mg/l)	2,842	1,3698	1,83	0,043	<0,06	0,086	4,8094	1,9018	3,62	0,2094	0,1013	0,135
NO ₃ ⁻ (mg/l)	46,37	0	11,84	2,5299	<0,5	1,52	0,7205	0,0531	0,38	24,5	0,0624	12,47
NO ₂ ⁻ (mg/l)	0,321	0,0194	0,173	0,0374	0,0094	0,024	0,0956	0,018	0,052	0,309	0,0039	0,211
SO ₄ ⁻² (mg/l)	264,7	128,8	175,65	198,32	103,2	124,91	144,19	6,588	71,06	615,57	124,69	274,64

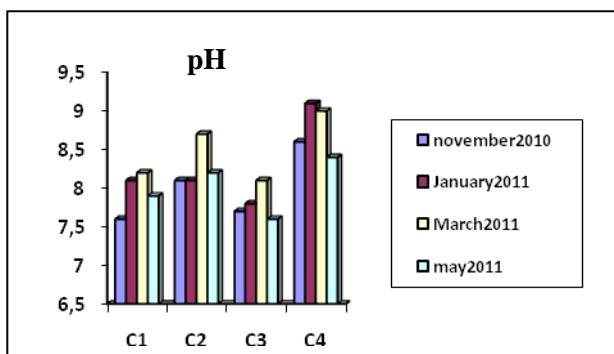


Figure 2: pH of wastewater

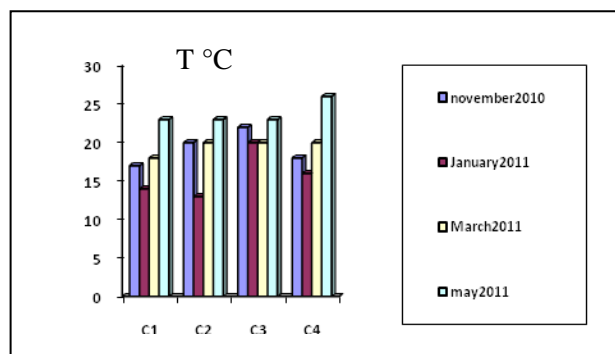


Figure 3: Temperature of wastewater

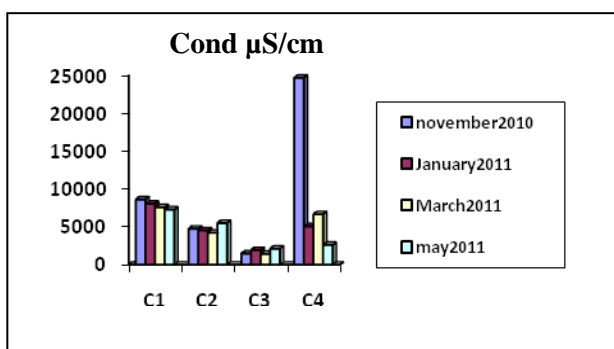


Figure 4: Conductivity of the wastewater

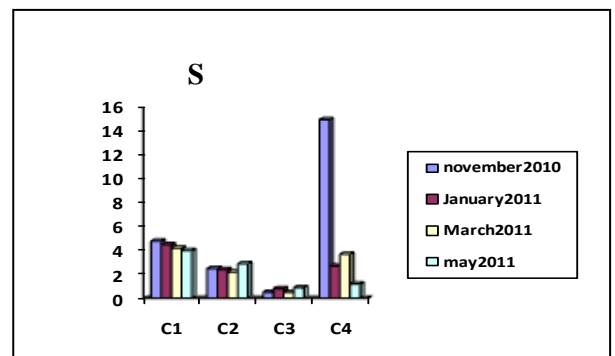


Figure 5: Salinity wastewater

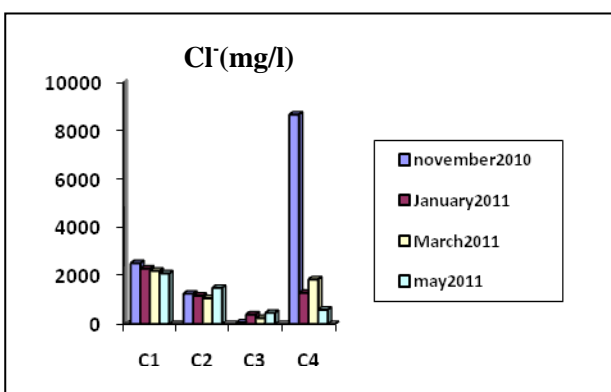


Figure 6: Rates of chloride wastewater

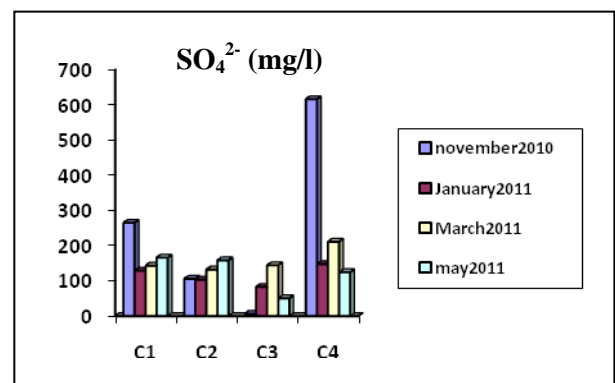


Figure 7: Rates of sulfate wastewater

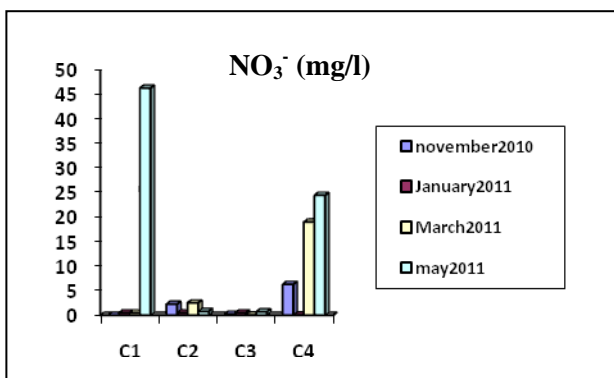


Figure 8: Rates of nitrate wastewater

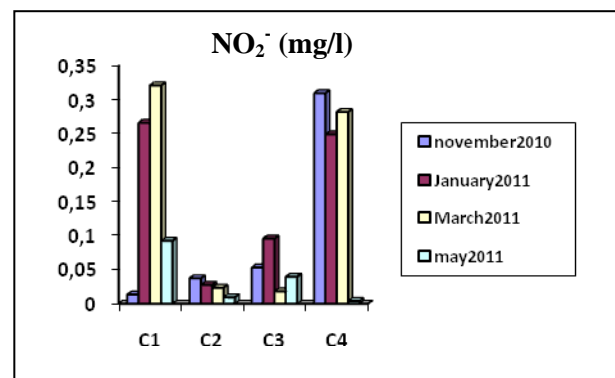


Figure 9: Rates of nitrite wastewater

PO₄³⁻ (mg/l)

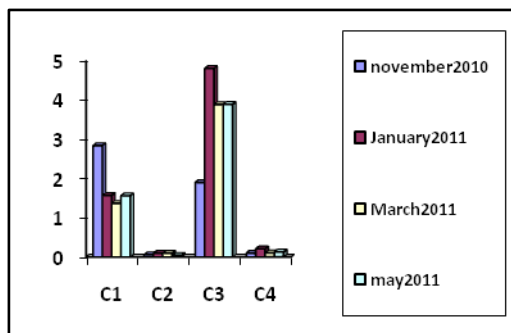


Figure 10: Rates of orthophosphates wastewater

The pH of the medium can be a good indicator of biological activity. Also, its influence is felt by the role it has on the increase or decrease the toxicity of several elements in governing many chemical reactions. The pH at all sites is greater than 7 with a maximum of 9,1 and 8.6 noted in levels of C4 discharges (river Tafna) and C2 (Oued Sidi Djelloul), respectively.

Temperature: The average temperature of the effluent between 18 ° C and 24.5 ° C. The maximum value (26 ° C) was recorded at site C4 (Oued Tafna) in May. Generally, the average values of this parameter are less than 30 ° C.

Electrical conductivity: the conductivity measurement gives a good indication of overall concentrations of dissolved salts, it can quickly assess the degree of mineralization of water. Referring to Table 1, it appears that all samples have high values of conductivity with the exception of the C3 (FERPHOS). The maximum value was recorded at the level of river Tafna (C4) is the order of 24700 μ s/cm. This is probably due to the excessive influence of seawater flow in the Oued.

Chlorides: there are high concentrations of chlorides for all sites. The maximum value was recorded at site C4 (OuedTafna) which is represented by a concentration of about 8662 mg / l. This result may be related to the invasion of sea water or chloride is present, on the one hand, and on the other hand, it should be noted that the chlorides can be from agriculture (for the site of OuedTafna C4), industrial (complex detergent ENAD / Henkel), urban (domestic waste in urban areas) or natural.

The high **salinity** and **TDS**, are related to the predominant contribution of marine waters. It is important to note that these contributions are more important than the distance to the sea is low.

Sulfates: They are of the multiple original, natural, industrial and agricultural runoff. Sulfate can be attacked by bacteria that reduces the hydrogen sulfide (H₂S) which can easily be transformed into sulfuric acid corrosive to sewer.

Surface waters contain highly variable levels of sulfates. Their concentration is generally between 2.2 and 58 mg / l (Meybeck et al., 1996). In light of the results, we find that monthly concentrations of sulphates in the different sites vary for some sites, confined between 6.588 mg / l and 615.575 mg / l considered as minimum and maximum values recorded at the C3 and C4 respectively. The highest content was recorded in November (C4) may be due to agricultural activities adopted at the perimeters of neighboring Oued Tafna.

Nitrate: nitrate levels generally have considerable variations both in space and in time range from 0 to 46.37 mg / l and are due to the importance of human activities in the study area.

The highest nitrate levels are marked at oued El Maleh (46.371 mg / l) and oued Tafna (24.500 mg / l) (see Figure of the nitrate) the latter site is the richest in nitrates (value NO₃-average = 12.47 mg / l, while that recorded at Oued el Maleh, it does not exceed 11.84 mg / l. this wealth can be explained by municipal effluents on the one hand and the leaching agricultural land on the other.

The waters of other sites C2 (sidi Jaloul) and C3 (Ferphos) are characterized by a slight fluctuation in nitrate during the sampling cycle. Their concentrations are between 2.5299 mg / l maximum considered value recorded in the waters of the C2 site (Sidi Jaloul), and 0.0531 mg / l considered significant minimum value at C3 (Ferphos).

Nitrite: They are the intermediate stage between the ammonium ion (NH₄⁺) and nitrate. Nitrites are unstable and are rapidly transformed into nitrates.

The analysis of the results indicates that the levels of nitrites are highly variable during the study period, and they range from a maximum of about 0.321 mg / l that was recorded in March at Oued El Maleh and a minimum of 0.00399 mg / l observed in May at Oued Tafna. The highest values are observed in the waters of exceptional sites C1 (Oued el Maleh) and C4 (Oued Tafna). (Table 1). Other sites display low levels.

Low concentrations are recorded at sewage-to-some sites could be explained by the fact that the nitrite ion (NO₂⁻) is an unstable compound in the presence of oxygen, whose concentration is usually much lower that of the two forms that are linked, ammonium and nitrate ions. (Thomas, 1985)

Orthophosphates: phosphate is an essential mineral nutrient for plants, but it is important to note that the increase in content can contribute to accelerated eutrophication, that is to say the growth of some types of algae in surface waters which causes a decrease in the proportion of oxygen dissolved in water. Indeed,

the release of phosphorus in aquatic ecosystems is one of the most serious environmental problems, because depending on the concentration of this element, you can see the

Quality physicochemical of sea water and impacts of effluent discharged:

eutrophication of the environment, more or less important. During the sampling cycle, levels of orthophosphate recorded at the various sites are low. Vary between 0.06 and 4.8094 mg / l. From Table No. 1, the highest values were recorded at sites C1 (Oued El Maleh) and C3 (FERPHOS) which are respectively 2.842 mg / l and 4.8094 mg / l. the other concentrations show a variation in 0043 C2 (Sidi Jaloul) and C3 1.9018 (FERPHOS).

The physicochemical analysis for samples collected in the receiving environment, lead us to the following results:

Temperature: Temperature affects the development and reproduction of aquatic organisms. The values of the marine surface water temperatures vary depending on the thermal regime of the Mediterranean climate, namely the highest in May (20°C-23°C) and lowest in winter (16° C). These values are recorded in the interim period of the study (November to May). The temperatures recorded in November (18-20 ° C) are slightly lower than those recorded in May (20-23 ° C).

PH: Outside the station S2 (Sidi Djelloul), the minimum values of all the stations are less than 8 (Table 2) indicate a slight acidification, while the maximum values tend to a basic medium close to 8.2. The lowest values are between 7.8 and 7.9, and the highest values are between 8.0 and 8.3.

Chlorides, conductivity and salinity: outside the stations S1 (Terga) and S2 (Sidi Jaloul), no significant variation of chlorides, salinity and conductivity were recorded.

Nitrites and orthophosphates: The impact of a spill industrial wastewater and domestic on the quality of the sea water, was felt by the rate of nitrite and orthophosphate content in the receiving environment. For ions NO₂-and P₂O₅, maximum concentrations were recorded at site S1 (Table No. 2) which are respectively 335,025 mg / l and 1.3772 mg / l.

Nitrite is toxic, it oxidizes hemoglobin to methemoglobin, and therefore impairs the ability of the blood of marine animals to carry oxygen (Russo, 1985)

A phosphate content superior to 0.025-0.05 mg / l, accelerate the eutrophication process that is characterized by the proliferation of microalgae phytoplankton or benthic macroalgae (Menesguen, 1991; Chocat, 1997).

In sum, the impact of the massive introduction of nutrients in surface waters of the receiving environment is diverse and multifaceted;

For example, eutrophication (nutrient enrichment) encourages the growth of phytoplankton and promotes the growth of toxic species, the decomposition of plankton biomass in excess increases the consumption of dissolved oxygen and causes the decrease in periodic or permanent oxygen leading to a mass mortality of fish and other organisms. "The outbreak involving species of algae toxin production is the common cause of human health problems very seriously, especially when toxins are ingested through contaminated seafood" (GESAMP 2000).

Table 2. Characteristic physicochemical of sea water in the region of Ain Temouchent

	Terga			Sidi jalloul			Beni saf			Rechgoune		
	Max	Min	Med	Max	Min	Med	Max	Min	Med	Max	Min	Med
T(°C)	20,3	16	17,8	17	17,12		21	16	18,25	21	17	18,5
pH	8,0	7,8	7,9	8,3	8,0	8,2	8,3	7,8	8,02	8,3	7,9	8,15
CE(ms/cm) at 25°C	56,0	32,8	47,72	56,2	49,3	52,55	56,3	55,2	55,87	56,5	55,4	56,1
salinity	37,2	20,5	31,17	37,3	32,2	34,6	37,4	36,6	36,85	37,5	36,7	37,25
Cl ⁻ (mg/l)	20,91	11,34	17,49	20,99	18,08	19,46	21,06	20,56	20,76	21,16	20,67	20,95
NO ₂ ⁻ (µg/l)	335,025	7,208	178,87	07,43	0,3498	03,12	223,59	5,9139	62,12	4,29	0,0175	1,64
P ₂ O ₅ (mg/l)	1,3772	0,0508	0,426	<0,1	0,0145	0,066	0,1723	<0,05	0,1121	<0,05	<0,05	<0,05

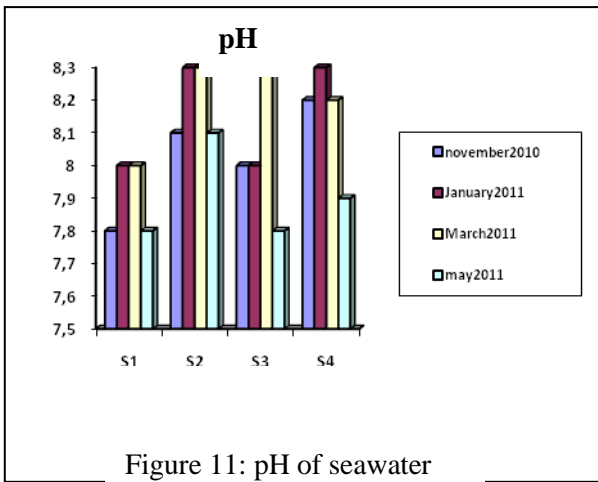


Figure 11: pH of seawater

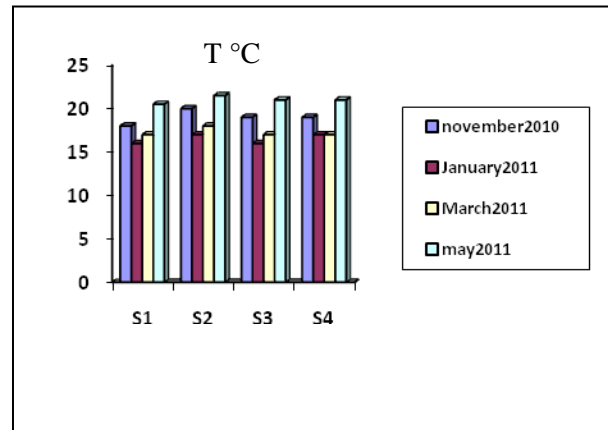


Figure 12: Temperature of seawater

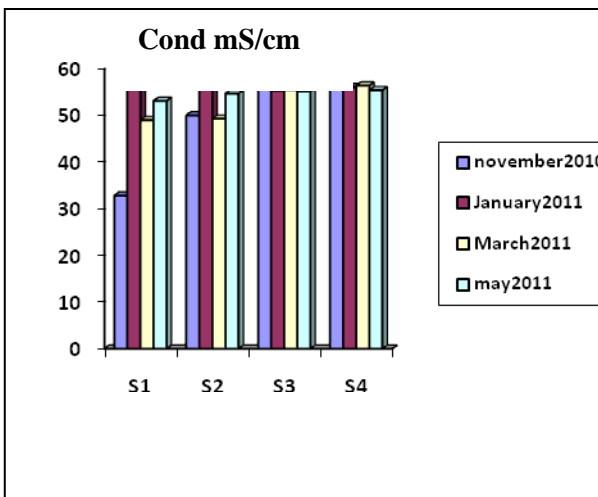


Figure 13: Conductivity of the seawater

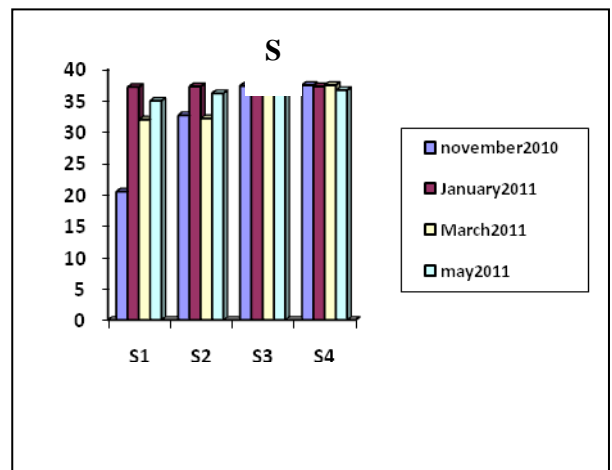


Figure 14: Salinity seawater

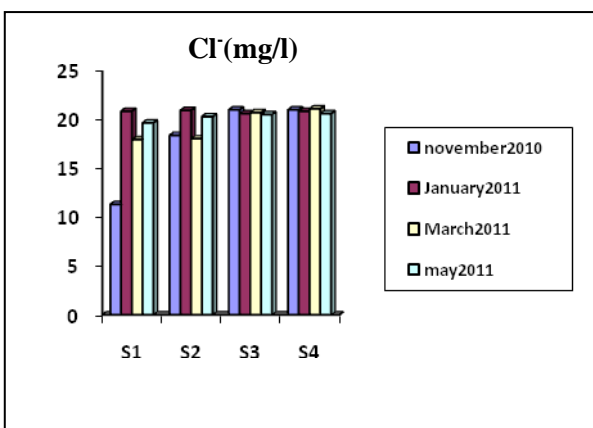


Figure 15: Rates of chloride seawater

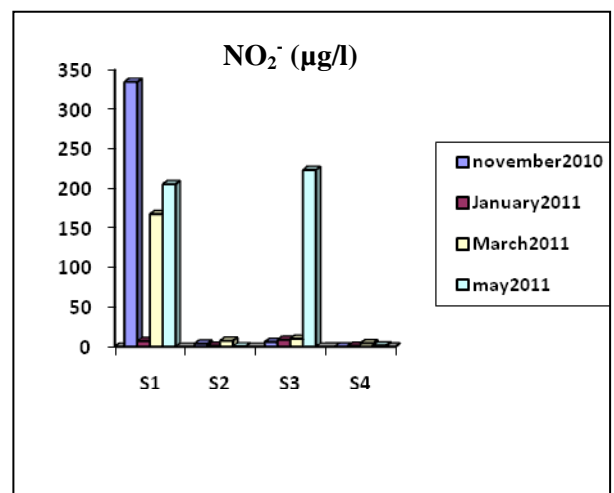


Figure 16: Rates of nitrite seawater

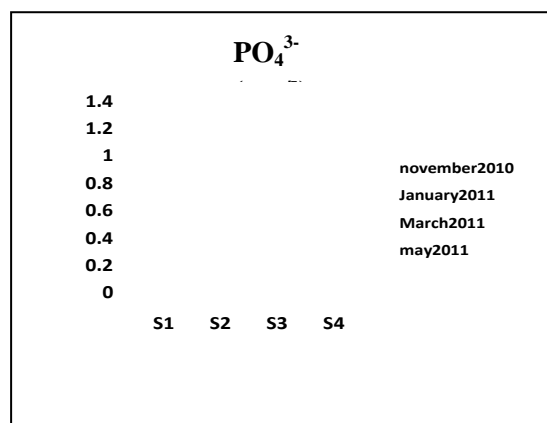


Figure 17: Rates of orthophosphates seawater

5. CONCLUSION

The present study has established a comprehensive diagnosis of the state of pollution for each study site. The results of the quality parameters of surface seawater have shown that the receiving environment is under the influence of wastewater discharges, which was verified by a slight acidification of the medium for some sites ($\text{pH} < 8$), a decrease in salinity more or less significant and the presence of high levels of nitrites and orthophosphates.

Indeed, the maximum values were marked at the beach Terga (S1), which receives input water from a complex of detergent, which are respectively of about 335.025 g/l (NO_2^-) and 1.3772 g/l (P_2O_5).

In addition, levels of nutrients are found significant at the (S3) who suffers domestic wastewater discharges and is characterized by a concentration of nitrite that does not exceed 223.59 mg/l and a value that orthophosphates is the order of 0.1723 g/l.

From this fact, the presence of certain levels of nutrients (nitrogen and phosphorus) in the receiving marine environment that are closely related to the loading of wastewater discharged, can lead to a proliferation of plants and types of harmful algae that disrupt the ecological balance of aquatic life and reduce the proportion of oxygen dissolved in water and consequently, cause an increased risk of mortality in some aquatic organisms.

To this end, pre-treatment of liquid effluents before discharge into a receiving water is needed to maintain and ensure a good ecological balance of the aquatic ecosystem.

In addition, it is important to set standards to reduce or

limit the harmful consequences caused by direct discharges of effluents (domestic, industrial or agricultural) in nature, which may have adverse effects on the environment.

4. REFERENCES

- [1] GESAMP (2001a). Protecting the Oceans from Land- Based Activities. Land-based Sources and Activities Affecting the Quality and Uses of the Marine, Coastal and Associated Freshwater Environment. GESAMP Reports and Studies No. 71. Nairobi (Kenya), Programme des Nations Unies pour l'environnement <http://gesamp.imo.org/no71/index.htm> [Geo-2-238]
- [2] Kerfouf A., la qualité bactériologique du golf d'Oran (Algérie occidentale) rev. Microbiol. Ind. San et environ. Vol 4, N°1, p : 22-31 (2010).
- [3] Wikipedia. Villes d'Algérie http://fr.wikipedia.org/wiki/Villes_d'Alg%C3%A9rie
- [4] DHW « Estimation du débit max et min des oueds en utilisant des formules empiriques ». Direction d'hydraulique de la wilaya de Ain Temouchent.(2011).
- [5] Tarik Ghodbani, « Rechgoun, un espace à protéger sur le littoral ouest de l'Algérie », *Méditerranée*[En ligne], 105 | 2005, mis en ligne le 03 septembre 2008. URL : <http://mediterranee.revues.org/index350.html>
- [6] [6] RODIER.J L'analyse de l'eau, 8^{ème} éd. Paris : Bordas, (1984)
- [7] Meybeck M., Friedrich G., Thomas R., Chapman D. Rivers. Water quality assessments: a guide to the use of biota, sediments and water in environment monitoring, Chapman edition, 2nd ed. E & FN Spon, London, pp. 59-126. (1996)
- [8] O. Thomas. « Métrologie des eaux résiduaire ». Ed. Cebedoc / Tec. et Doc. 11,Liège -75384. Paris, (1985)
- [9] Russo R.C., Ammonia, Nitrite and Nitrate dans *fundamentals of aquatic toxicology*. Petrocelli Sam R., Rand Gary M (editeurs). (1985).
- [10] Chocat B., *Eycyclopédie de l'hydrologie urbaine et de l'assainissement*. Technique et Documentation, Londres, New York, Paris. (1997).

Treatment of Oilfield Produced Water through NF/RO Membranes: Generating a Sustainable Drinking Water Resource by Reusing a Pollution Source

Salem Alzahrani¹, A. W. Mohammad², Pauzi Abdullah³, Othman Jaafar¹

¹Department of Civil and Structural Engineering, Universiti Kebangsaan Malaysia, 43600 UKM Bangi, Selangor, Malaysia (salem@eng.ukm.my)

²Department of Chemical and Process Engineering, Universiti Kebangsaan Malaysia, 43600 UKM Bangi, Selangor, Malaysia

³School of Chemical Sciences and Food Technology, Universiti Kebangsaan Malaysia, 43600 UKM Bangi, Selangor, Malaysia

ABSTRACT

Produced water is generated as a by-product of oil production in the petroleum industry, at rate of more than 23.46 million-m³ per day. Currently, 99% of all produced water is disposed to the environment, which implies a significant depletion of natural water resources in the future. Consequently, water resource sustainability concerns suggest exploring the potential of reusing treated produced water (viz., treated up to disposal standards) as a promising source of water for beneficial reuse. To that end, this study aimed to assess the quality of produced water obtained after filtration with Nanofiltration (NF) and Reverse Osmosis (RO) membranes, and to compare the quality of water obtained through these filtration mechanisms against the quality standards of drinking water and livestock water. In course of experiments, real samples of produced water were filtered using a dead-end stirred cell. Thereafter, an assessment was conducted with respect to more than 25 water quality parameters, using standard methods. The results of the study revealed that the treated produced water successfully meets the regulatory quality standards of drinking water and livestock water. The study concluded that treated produced water has the potential for beneficial reuse, and that NF/RO membranes are highly suited for treating produced water to yield a promising source of water supply.

Keywords: Produced Water, Treatment, NF/RO Membrane, Reuse, Drinking Water

1. INTRODUCTION

Produced water is generated in the petroleum industry as a by-product of various oil production processes, such as drilling, stimulation, enhanced recovery and refining [1]. Although the origin of produced water varies from field to field, depending on geological and operational conditions [2], the bulk of produced water is mostly derived from formation waters in oil reservoirs.

Currently, 2.5 barrels of produced water are generated for every corresponding barrel of oil produced, per day [3] implying that the current global oil production rate of 80 million barrels of oil per day [4] simultaneously generates more than 200 million barrels of produced water per day. Consequently, an increasing demand for oil due to economic and population growth foretells of an increasing amount of produced water generation in the petroleum industry. Additionally, the generation of produced water increases in time, as an oil well matures [1]. Thus, by the year 2025, produced water generation is estimated to reach up to 5 barrels of produced water for each barrel of oil produced [3], which would amount to more than 400 million barrels of produced water per day. Currently, 99% of all produced water is disposed to the environment [3], rendering this water only as a source of pollution, especially due to the absence of effective technology for its complete treatment. These statistics warn of a significant depletion of natural water resources in the future.

Produced water contains a multitude and diversity of constituents ranging from complex organic and inorganic chemical species to suspended solids [5]. Traditional methods of produced water treatment have been costly and ineffective particularly in removing its dissolved content, and especially as standalone methods [6]. The large numbers of inorganic and organic species that characterize the composition of produced water create unique challenges in treatment. For instance, a particularly unresolved issue is that of elevated levels of soluble organics in produced water those accumulate from oil and grease tests, appear in small percentages in discharge streams, and cannot be effectively removed by existing treatment technologies [5].

So far, endeavors in produced water treatment have not attained optimal reuse of produced water, especially as a strategic option based on the principle of sustainable development, to preserve this resource that is being wasted in much larger quantities than what is being generated from the desalination of seawater and groundwater. Current scientific efforts towards the management and disposal of untreated produced water amount to a spending of more than \$ 40 billion every year [7], and remain focused largely on developing the most economical as well as environmentally compliant solutions. Plausibly, such a focus stems from regulations governing the discharge of treated produced water into the environment, wherein the allowable limit

for the oil content of produced water varies by country (generally $\sim < 30$ mg/L). This challenge of treating produced water to comply with discharge regulations can be met effectively by the promising and demonstrated capability of membrane technology. Further, water resource sustainability concerns suggest exploring the potential of reusing treated produced water (viz., treated up to disposal standards) as a promising source of water for beneficial reuse. In light of these premises, this study aimed to assess the quality of produced water obtained after filtration with Nanofiltration (NF) and Reverse Osmosis (RO) membranes, and to compare the quality of water obtained through these filtration mechanisms against the quality standards of drinking water and livestock water.

2. MATERIAL AND METHODS

2.1 Representative Membranes: NF and RO

Two new hydrophilic commercial membranes supplied by AMFOR INC® (China) were used in produced water filtration processes, namely the BW30 RO and the NF. Both membranes were manufactured from polyethersulfon.

2.2 Produced Water Samples

Produced water samples were obtained from the produced water treatment plant attached to a petroleum refinery in Malaysia. Due to confidentiality, the name of the company cannot be disclosed in this paper. The collected samples were either in the last stage of treatment or just prior to being discharged to the sea.

2.3 Produced Water Treatment Through NF/RO Membranes

The treatment of produced water processes were carried out using a dead-end stirred cell (Sterlitech, Model HP4750), with a diameter of 47 mm and an effective membrane area of 14.6 cm^2 , at a pressure level of 6 bars. The stirred cell was operated by pressurizing the head space in the stirred cell with nitrogen from a gas cylinder. The new membrane was mounted at the bottom of the stirred cell and then compacted at an elevated pressure until a steady state flux was reached. The flux was equilibrated for the passage of the first 20 ml of permeate, and the following 20 ml permeate was collected for concentration analysis. In the course of experiments, various produced water samples were used, each stirred at a speed of 400 rpm.

2.4 Analytical Methods of Produced Water Quality

Laboratory analysis for the produced water quality was conducted according to APHA standard methods [8]. The physico-chemical and biological parameters in the analysis were classified into the following five categories:

- 1- Anions: chloride (Cl^-), fluoride (F^-), nitrate (NO_3^-), nitrite (NO_2^-), sulfate (SO_4^{2-}) and sulfide (S^{2-}).
- 2- Cations: barium (Ba^{2+}), manganese (Mn^{2+}), iron (Fe^{2+}) and sodium (Na^+).
- 3- Heavy Metals: arsenic (As), cadmium (Cd), chromium (Cr), copper (Cu), lead (Pb), nickel (Ni), mercury (Hg), selenium (Se), silver (Ag) and zinc (Zn).
- 4- Physico-Chemical Parameters: ammonia, pH, total dissolved solids (TDS) and turbidity.
- 5- Bacterial and Microbial Content: fecal coliform and coliform.

3. RESULTS AND DISCUSSION

An assessment of produced water quality, with respect to twenty six parameters, was conducted through experiments of filtration with NF and RO membranes, using standard methods. It was apparent that the quality of produced water before filtration was quite enabling towards attaining potable water standards upon filtration. Additionally, the obtained results demonstrated how NF and RO membranes differed greatly in the quality of water they filtered.

3.1 Comparison of Produced Water Quality vs. WHO and USEPA Drinking Water Quality Standards

Two regulatory quality standards for drinking water were used in this assessment, namely: World Health Organization (WHO) and U.S. Environmental Protection Agency (USEPA) standards [9, 10]. Table 1 presents the data for produced water quality assessment against each one of these standards, before and after filtration with NF and RO membranes, at pressure level of six bars. The various constituents of produced water that sum up to the 26 parameters of this assessment are categorized below:

Anions: six parameters were analyzed, namely: chloride, fluoride, nitrate, nitrite, sulfate and sulfide. The concentrations of these parameters in produced water samples before filtration were lower than the allowable limit for WHO and USEPA drinking water standards, as seen in Table 1, implying a high potential for recycling such water for beneficial reuse even without the use of advanced treatment technology. Only sulfate (285 mg/L) and sulfide (0.17 mg/L) concentrations were higher than the permissible limits set by WHO and USEPA, and were reduced after filtration with NF and RO membranes to successfully meet the allowable limit (250 mg/L) set by WHO and USEPA, wherein that the sulfate concentration was reduced from 285 mg/L to 66 mg/L through NF membrane and to 54 mg/L by RO membrane. As for sulfide concentration in produced water, the pre-filtration concentration (0.17 mg/L) was higher than

allowable limit (0.05 mg/L) of the WHO standard, and it was reduced by filtration to 0.04 mg/L with NF membrane, and to < 0.01 mg/L with RO membrane.

Cations: four parameters were measured, namely: barium, iron, manganese and sodium. It was observed that, prior to filtration, the concentration of barium was already lower than the permissible WHO and USEPA limits, and that of manganese (0.086 mg/L) was lower

than the WHO limit but higher than the USEPA limit (0.05 mg/L). Also, pre-filtration concentrations of sodium and iron in produced water were 262 mg/L and 0.54 mg/L, respectively, which exceeded the allowable limits, set by WHO and USEPA. Post-filtration, however, the assessment of produced water quality revealed that sodium, iron and manganese concentrations were reduced to values well below the allowable WHO and USEPA standards.

Table 7: Data from produced water quality assessment vs. WHO and USEPA water quality standards

No.	Test Parameter	Units	Raw Produced Water	Treated Water		WHO	USEPA
				NF	RO		
Anions							
1	Cl ⁻	mg/L	230	223	53	250	250
2	F ⁻	mg/L	0.3	0.2	< 0.1	1.5	2
3	NO ₃ ⁻	mg/L	< 0.01	< 0.01	< 0.01	50	10
4	NO ₂ ⁻	mg/L	< 0.01	< 0.01	< 0.01	3	1
5	SO ₄ ⁻	mg/L	285	66	54	250	250
6	S ⁻²	mg/L	0.17	0.04	< 0.01	0.05	-
Cations							
7	Ba ²⁺	mg/L	0.24	0.08	0.02	0.7	2
8	Fe ²⁺	mg/L	0.54	0.03	0.11	0.3	0.3
9	Mn ²⁺	mg/L	0.086	0.035	0.01	0.4	0.05
10	Na ⁺	mg/L	262	177	64.8	200	200
Heavy Metals							
11	As	mg/L	0.014	ND	ND	0.01	0.01
12	Cd	mg/L	0.0006	0.0003	0.0003	0.003	0.005
13	Cr	mg/L	0.0011	0.0009	0.0007	0.05	1
14	Cu	mg/L	ND	ND	ND	2	1
15	Pb	mg/L	0.006	0.003	0.001	-	0.01
16	Ni	mg/L	0.002	0.012	0.02	0.02	-
17	Hg	mg/L	< 0.001	< 0.001	< 0.001	0.001	0.002
18	Se	mg/L	0.008	0.001	ND	0.01	0.05
19	Ag	mg/L	ND	ND	ND	0.1	0.1
20	Zn	mg/L	0.04	0.02	0.04	5	5
Physico-chemical Parameters							
21	Ammonia	mg/L	21.9	11.6	6.01	1.5	-
22	pH	-	7.5	7.8	7.6	6.5 – 8.5	-
23	TDS	mg/L	854	520	244	1200	500
24	Turbidity	NTU	21	< 1	< 1	0.1	-
Bacterial and microbial Content							
25	Coliform	cfu/100ml	402	ND	ND	-	0
26	Fecal Coliform	cfu/100ml	20	ND	ND	-	0

ND = Not Detected

Heavy Metals: 10 out of the 13 toxic metals from USEPA's Priority Pollutant Metals list were selected and analyzed in this study, namely: arsenic, cadmium, chromium, copper, lead, mercury, nickel, selenium, silver and zinc. Generally, the pre-filtration concentrations of heavy metals in produced water were

in trace amounts and lower than the allowable limits set by WHO and USEPA, which was most likely due to the effect of discharge regulations. However, the single exception was the pre-filtration arsenic concentration (0.014 mg/L), which was higher than allowable limits of WHO and USEPA (0.01 mg/L). However, post-filtration concentrations of arsenic were diminished to

non-detectable values. It should be noted that there occurred an unexpected increase in the concentration of nickel (up from the pre-filtration 0.002 mg/L) during the treatment process, although not exceeding the permissible limits of WHO and USEPA standards. Such an increase could be explained by the type of filtration cell used, which is often made from stainless steel and could be considered an external source for this increment in nickel concentration.

Physico-Chemical Parameters: four parameters were measured for this category, namely: pH, total dissolved solids, turbidity and ammonia. The value of pH for produced water was found to be within the WHO and USEPA allowable range of 6.5 to 8.5, both before and after treatment process. The most notable of all tested parameters was TDS. A high TDS concentration implies a high concentration of dissolved salts. As seen from the results, filtration by the NF membrane reduced the TDS in produced water from 854 mg/L to 520 mg/L, while the RO membrane yielded an even greater TDS reduction to below 244 mg/L, which implied a 71% reduction in TDS. Conclusively, both membranes achieved a final TDS that did not exceed the maximum allowable USEPA limit of 500 mg/L or the WHO limit of 1200 mg/L. The pre-filtration sample’s turbidity value of 21 NTU was effectively reduced to non-detectable levels by both the membranes. These results are well below the threshold limits of 0.1 NTU set by the USEPA for drinking water standards. Incidentally, out of all the produced water quality parameters analyzed, ammonia exceeded the threshold concentration (1.5 mg/L) set by WHO’s drinking water standard. The pre-filtration ammonia concentration of 21.9 mg/L was reduced to 11.6 mg/L by NF membrane and to 6.01 mg/L by RO membrane. However, the effectiveness of the membranes in removing ammonia content from produced water was essentially limited by the applied pressure of 6 bars. In this context, applying higher pressures is anticipated to enhance membrane performance, especially for the RO membrane, in removing ammonia. However, it must be noted that the WHO guidelines for drinking water proposed 1.5 mg/L as the threshold odor concentration of ammonia at high levels of alkalinity. Since the pH values of the produced water samples were in low levels of alkalinity, it is believed that an increase in pH will aid a further reduction of ammonia content.

Bacterial and Microbial Content: Two parameters were selected to examine the efficiency of the selected membranes in removing bacterial populations from produced water and thereby enabling its beneficial reuse as potable water. The analyzed parameters were: fecal coliforms and coliforms, whose levels in produced

water samples before filtration were found to be very high. Pre-filtration, coliforms were detected at 402 cfu/100ml and total coliforms were found to be 20 cfu/100 ml. Such concentrations will lower the recycling potential of any water for beneficial reuse. The emergence of membrane technology in its effective treatment of bacterial contamination, without the addition of chemicals additives or water disinfectants, derives its success from factors such as the pore size of membranes (e.g., less than 1 µm), which ensures the removal of all types of bacteria and microbes to zero levels as substantiated by the results of this study.

Table 8: Water quality guide for livestock use

TDS (mg/L)	Conductivity (mmhos/cm)	Livestock Watering Comments	This Study
Less than 1,000	< 1.5	Excellent for all classes of livestock.	√
1,000 to 2,999	1.5-5	Very satisfactory for all classes of livestock. May cause temporary and mild diarrhea in livestock not accustomed to them.	-
3,000 to 4,999	5-8	Satisfactory for livestock, but may cause temporary diarrhea or be refused at first by animals not accustomed to them.	-
5,000 to 6,999	8-11	Can be used with reasonable safety for dairy and beef cattle, sheep, swine, and horses. Avoid use for pregnant or lactating animals.	-
7,000 to 10,000	11-16	Considerable risk in using for pregnant or lactating cows, horses or sheep, or for the young of these species. In general, use should be avoided although older ruminants, horses, poultry, and swine may subsist on them under certain conditions.	-
Over 10,000	16	This water is considered unsatisfactory for all classes of livestock.	-

3.2 Comparison of Produced Water Quality vs. Water Quality Guide for Livestock Use

Based on the water quality guide for livestock use [11], the quality of produced water obtained after filtration through NF and RO membranes was found to be compatible for all classes of livestock standards, as shown in Table 2.

4. CONCLUSION

The results of this study revealed that treated (viz., membrane filtered) produced water successfully meets

the regulatory quality standards of drinking water and livestock water. Thus, the study concluded that treated produced water has the potential for beneficial reuse, and that NF/RO membranes are highly suited for treating produced water to yield a promising source of water supply. Further, the experimental results indicate that, in treating produced water towards drinking water standards, the RO membrane is far more effective than the NF membrane in rejecting salts or inorganic content and bacteria. However, despite this study's discovery of the high degree of effectiveness in the use of membranes to remove small dissolved molecules in produced water, further work is necessary to establish the same effectiveness with respect to the each organic species in the dissolved content of produced water. To this end, experiments are underway to extract hydrocarbons compounds from produced water in order to compare their respective concentrations with those of drinking water quality standards, and also to identify the potential of NF and RO membranes technology in meeting such standards by removing all the small organic molecules.

REFERENCES

- [1] Collins, A.G. *Geochemistry of Oilfield Waters*. Elsevier Science Publishers, Amsterdam, 1975.
- [2] Pillard, D., Tietge, J and Evans, J. Estimating the acute toxicity of produced waters to marine organisms using predictive toxicity models, in: Reed, M and Johnsen, S. (Eds), *Produced Water 2: Environmental Issues and Mitigation Technologies*. Plenum Publishing Corp, 1996, pp. 49-60.
- [3] Global Water Intelligence. *Produced Water Market: Opportunities in the Oil, Shale and Gas Sectors in North America*. 1 ed., Media Analytics Ltd, New York, 2011.
- [4] Ferro, B.D and Smith, M. Global Onshore and Offshore Water Production. in, <http://www.touchoilandgas.com/global-onshore-offshore-water-a7137-1.html>. 2007.
- [5] Stephenson, M.T. Components of Produced Water: A Compilation of Industry Studies. *Journal of Petroleum Technology*, Vol. 44, pp. 548-603, 1992.
- [6] Veil, J.A., Puder, M.G., Elcock, D and Redweik, R.J. A White Paper Describing Produced Water from Production of Crude Oil, Natural Gas, and Coal Bed Methane. Tech Report W-31-109-Eng-38, January 2004.
- [7] Bailey, B., Crabtree, M., Tyrie, J., Elphick, J., Kuchuk, F., Romano, C and Roodhart, L. Water Control. *Oilfield Review*, Vol. 1, pp. 30-51, 2000.
- [8] American Public Health Association (APHA). *Standard Methods for the Examination of Water and Wastewater*. 21 ed., Washington, DC, 2005.
- [9] World Health Organization (WHO). *Guidelines for Drinking-Water Quality*. 3 ed., World Health Organization, Geneva, 2008.
- [10] U.S. Environmental Protection Agency (USEPA), National Primary and Secondary Drinking Water Regulation. Available: <http://water.epa.gov/drink/contaminants/upload/mc1-2.pdf>. 2009.
- [11] ALL Consulting. Coal Bed Methane Produced Water: Management and Beneficial Use Alternatives. Oklahoma Tech Report, July 2003.

An Integrated Neural Network-Fuzzy Mathematical Programming for Optimum Long-Term Electricity Price Forecasting in Noisy and Complex Environments

A. Azadeh*, S.F. Ghaderi, M. Moghaddam, S.H. Seyedmahmoudi, M. Mahdi

Department of Industrial Engineering and Center of Excellence for Intelligent Based Experimental Mechanics,
University College of Engineering, University of Tehran, Tehran, Iran

*Corresponding Author, Tel: +98 21 88021067, Fax: +98 21 82084194. (aazadeh@ut.ac.ir or ali@azadeh.com)

ABSTRACT

This paper presents an integrated algorithm consisting of artificial neural network (ANN), fuzzy linear regression (FLR), and conventional linear regression (CLR) for optimum long-term electricity price forecasting. Three ANN models and seven well-known FLR models as well as CLR model are considered simultaneously to provide a robust framework for electricity price forecasting. Thus, it can be easily applied to uncertain and complex environments due to its flexibility. The proposed algorithm is applied to forecast long-term electricity price regarding to a real data set. The analysis of variance for a randomized complete block design (ANOVA-RCBD) and Fisher least significant difference (LSD) test are performed on the forecasting results of the ANN, FLR, and CLR models and the actual values of electricity price. The results indicate that there is a significant difference between the performance of ANN and FLR models in terms of mean absolute percentage error (MAPE). Moreover, it is shown that the CLR and FLR models, in general, considerably outperform the ANN models in this case. The proposed integrated ANN-FLR-CLR algorithm may be easily applied to other data sets by a minor modification.

Keywords: Electricity Price Forecasting; Artificial Neural Network (ANN); Fuzzy Linear Regression (FLR); Optimization

1. INTRODUCTION

The variations of electricity price can unfortunately involve utilities incomes and consumers costs. Therefore it is very imperative to make some tools in order to forecast electricity prices and minimize costs or maximize benefits [1]. Forecasting electricity consumption is a relatively difficult task. Electricity consumption represents two essential attributes, on a one hand it shows the strong annual changes and on the other hand it clearly shows the increasing trend. Moreover, the time series forecasting method is affected by other variations that make the problem harder to create a model. There are three types of load forecasting including short-term, middle-term, and long-term load forecasting [2-10]. In addition fuzzy regression has been used for load forecasting [11-23]. Several studies in literature have been involved in the field of electricity price forecasting (either short-term or long-term) and proposed different methodologies and algorithms to deal with this problem [24-54]. All stated studies proposed a forecasting method as the most superior method based on their findings. However, adopting a forecasting method without regarding to the case conditions can make distortion in results. Therefore, in this paper an integrated algorithm is proposed for optimum long-term forecasting of the electricity price. The unique nature of the proposed algorithm lies in the integration of ANN, FLR, and CLR methods. So, it can be applied to certain, uncertain, and/or complex environments due to utilizing ANNs,

FLR, and CLR. To the best of our knowledge, this is the first study in literature which proposes such integrated algorithm based on ANNs, FLR, and CLR for long-term forecasting of the electricity price. The proposed algorithm facilitates the decision-making process in different case conditions and therefore provides a comprehensive framework for long-term forecasting of the electricity price. In following section the ANNs and FLR models are introduced.

2. THE INTEGRATED ANN-FLR-CLR ALGORITHM

In this study, an integrated algorithm based on ANNs and FLR methods is proposed to deal with the long-term forecasting of electricity price inspired by a real data set from 1972 to 2007. Different well-known FLR models have been compared to identify the best FLR method with respect to the MAPE. On the other hand, ANNs are used for forecasting according to the real data set. The main idea of the proposed integrated algorithm is based on using ANNs and FLR methods in situations of having potentially complex, non-linear, and inconsistent data, and potentially uncertain data, respectively. After running both FLR and ANN models, the best approach is identified according to their related MAPE. Figure 1 schematically presents the proposed integrated ANN-FLR-CLR algorithm.

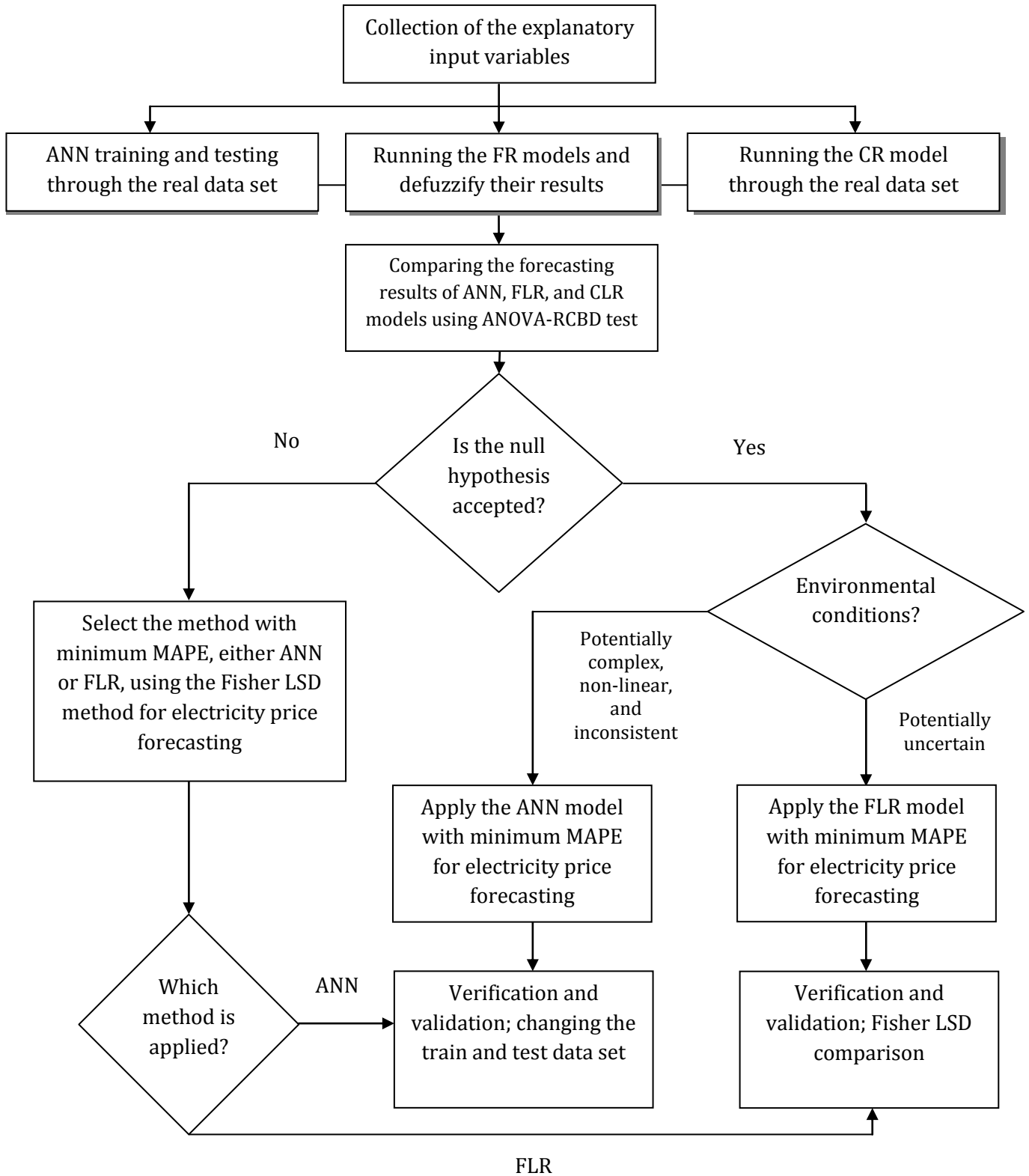


Figure 1: The proposed integrated ANN-FLR-CLR algorithm for electricity price forecasting

3. EXPERIMENT: THE ALGORITHM IMPLEMENTATION

The proposed integrated ANN-FLR-CLR algorithm is applied to a case study of electricity price forecasting with respect to a data set from 1972 to 2007 in Iran. As mentioned in previous sections, the economic indicators considered in this paper are the electricity consumption, powerhouses efficiency, inflation, and fuel price. In order to estimate the annual electricity price, the fuzzy linear relationship can be taken into consideration, where A_j ($j=0,1,2,3,4,5$) are the fuzzy coefficients, Y indicates the forecasted electricity price, X_0 is equals to one, X_{EC} represents electricity consumption, X_{PE} is powerhouses efficiency, X_{In} indicates inflation, and X_{FP} represents fuel price.

For each ANN, FLR, and CLR model, the input data set is divided into train and test data. The obtained results for different FLR models are fuzzy numbers which should be converted into crisp scalars through a proper defuzzification method. In this study, the center of area defuzzification method is applied. In order to calculate the MAPE, the estimated values are compared with their corresponding actual values in test data set. Lingo software is used for solving the FLR models. The Lingo programming codes of the FR models are presented in Appendix A. Moreover, MATLAB software is used for developing the ANN model. Furthermore, a sensitivity analysis is performed on the number of periods dedicated for testing the developed models. In order to do this, in 12 different alternatives (i.e. ANOVA-RCBD blocks), the number of test periods has been considered from 7 to 18 years, respectively.

Table 1 presents the results of ANOVA-RCBD for comparison of the ANN, FLR, and CLR models with respect to their MAPE values. Thus, it can be concluded that there are significant differences between the performances of the models with respect to the number of periods. In other words, as the number of test periods increases, the MAPE value accordingly encounter a considerable change. As the results show, increasing the number of test periods (i.e. decreasing the number of train periods) significantly reduces the precision of the ANN, FLR, and CLR models and so, in general, increases the related MAPE values.

The Fisher LSD test is used to verify and validate the results obtained by the ANN, FLR, and CLR models. The Fisher LSD test compares the means of two variables, computes the difference between the two variables for each case, and tests to see if the average difference is significantly different from zero. At significance level of $\alpha=0.05$, the Fisher LSD test performed on classification accuracy rate showed that

the proposed FLR models (except Sakawa and Yano [48] (Eq. (2.1))) and CLR reveal approximately equal performances in terms of forecasting the electricity price.

It can be concluded that there are significant differences between all pairs of ANN and FLR models. All ANN models significantly differ with the CLR model in this case. From Fisher LSD results, it is deduced that, in general, all ANN models and Sakawa and Yano [48] (Eq. (2.1)) (i.e. treatments 9 to 13) yield approximately similar solutions at significance level of $\alpha=0.05$, and on the other hand, the FLR and CLR models (except Sakawa and Yano [48]; Eq. (2.1)) have similar performance at significance level of $\alpha=0.05$. It can also be concluded that the CLR model has the minimum MAPE value (with 7 number of test periods) among all the methods used for forecasting the electricity price. Accordingly, each of the CLR and FLR models (except Sakawa and Yano [48]; Eq. (2.1)) can be recommended as the preferred method for this purpose.

4. CONCLUSION

In this study, the most well-known ANN and FLR models as well as the CLR models have been used for forecasting the electricity price in Iran. The economic indicators considered in this study are inflation rate, electricity consumption, the efficiency of powerhouses, and fuel price. In order to show the applicability and superiority of the proposed algorithm, the data for electricity price in Iran from 1972 to 2007 have been used. The input data is divided into train and test data. According to the train data, the ANN, FLR, and CLR models have been tuned for all their parameters and the best coefficients are identified. For determining the rate of error related to each of the ANN, FLR, and CLR models estimations and selecting the most preferred model(s), the rate of forecasted output of each model is compared with its actual data to calculate the MAPE. The MAPE values have been compared via the ANOVA-RCBD. Results show that all three methods are different from each other. By considering of the Fisher LSD results, it shows that FLR models (except Sakawa and Yano [48] (Eq. (2.1))) outperform is rival (i.e. ANN) for long-term forecasting of electricity price. By applying Fisher LSD method, it is concluded that the proposed FLR models by Ozelkan et al. [50], Tanaka et al. [49], Hojati et al. [46] (Eq. (8)), Hojati et al. [46] (Eq. (7)), and Sakawa and Yano [48] (Eq. (2.2)) are respectively recommended for electricity price in Iran due to having higher precisions compared to the other methods.

Table 1: ANOVA-RCBD table for comparison of the MAPE results obtained by the ANN, FLR and CLR models

Source of Variation	Sum of Squares	Degrees of Freedom	Mean Square	F_0
Between treatments	0.390181	10	0.039018	5.208783
Between blocks	6.382729	11	0.580248	77.45935
Error (within treatment)	0.823991	110	0.007491	
Total	7.596901	131		

Table 2: The features of the integrated ANN-FLR-CLR algorithm versus other methods

Method	Features									
	Long-term forecasting	Multiple outputs	Multiple inputs	Dealing uncertain, limited, and non-crisp data	Intelligent modeling	High forecasting capability and reliability	Dealing environment complexity and non-linearity	Dealing ambiguity	Flexibility	Robustness against noisy and inconsistent data
The integrated ANN-FLR-CLR algorithm	✓	✓	✓	✓	✓	✓	✓	✓	✓	✓
ANN	✓	✓	✓		✓		✓			✓
FLR	✓			✓				✓		
CLR	✓									
Azadeh et al. [8]	✓	✓	✓		✓		✓			✓
Bigdeli et al. [35]	✓	✓	✓		✓		✓			✓
Vahidinasab et al. [33]	✓	✓	✓		✓		✓			✓
Gareta et al. [1]	✓	✓	✓		✓		✓			✓
Hong and Lee [27]	✓			✓				✓		

Nomenclature

FLR	Fuzzy Linear Regression
CLR	Conventional Linear Regression
LP	Linear Programming
ANN	Artificial Neural Network
LMB	Levenberg–Marquardt Backpropagation
BFGSB	Broyden Fletcher Goldfarb Shanno Quasi-Newton Backpropagation
CGB	Conjugate Gradient Backpropagation
SSE	Sum Squared Error
ANOVA	Analysis of Variance
RCBD	Randomized Complete Block Design
MAPE	Mean Absolute Percentage Error
LSD	Least Significant Difference
SS	Sum of Squares
MS	Mean Square
EC	Electricity Consumption
PE	Powerhouse's Efficiency
In	Inflation
FP	Fuel Price

Table 2 shows the superiorities of the proposed integrated ANN-FLR-CLR algorithm over several previous studies/methods. The proposed algorithm is applicable to complex, non-linear and/or ambiguous environments due to utilizing ANN and FLR mechanisms. It is robust against inconsistency and noise in data as well as high dimensionality and collinearity. Besides, it provides higher generalization capability and precision via eliminating possible noise in the data set. Dealing with uncertain, limited, and non-crisp data is caused the proposed integrated ANN-FLR algorithm to have preference over conventional approaches such as regressions. Moreover, the flexible algorithm is capable of switching between different ANN and FLR models due to utilizing statistical tests such as ANOVA and Fisher LSD for determining the most appropriate forecasting model for different cases. Consequently, the proposed integrated ANN-FLR-CLR algorithm of this study, as a preferred approach, can be a good alternative for electricity price forecasting in most cases.

REFERENCES

- [1] Gareta, R., Romeo, L.M., Gil, A. Forecasting of electricity prices with neural networks. *ENERG CONVERS MANAGE*, Vol.47, Issues 13-14, (2006), pp. 1770-1778.
- [2] Filik, U.B., Kurban, M. A New Approach for the Short-Term Load Forecasting with Autoregressive and Artificial Neural Network Models. *INT J COMPUT INTEL RES*, Vol.3, Issue 1, (2007), pp. 66-71.
- [3] Fesharaki, F. Oil prices in the short, medium and long-term. *ENERG POLICY*, Vol.18, Issues 1, (1990), pp. 66-71.
- [4] Malik, F., Nasereddin, M. Forecasting output using oil prices: A cascaded artificial neural network approach. *J ECON BUS*, Vol.58, Issues 2, (2006), pp. 168-180.
- [5] Chen, S.S., Chen, H.C. Oil prices and real exchange rates. *ENERG ECON*, Vol.29, Issues 3, (2007), pp. 390-404.
- [6] Sharda, R. Neural networks for the MS/OR analyst: An application bibliography. *INTERFACES*, Vol.24, Issues 2, (1994), pp. 116-130.
- [7] Zhang, G., Patuwo, B.E., Hu, M.Y. Forecasting with artificial neural networks: The state of the art. *INT J FORECAST*, Vol.14, Issues 1, (1998), pp. 35-62.
- [8] Azadeh, A., Saberi, M., Ghaderi, S.F., Gitiforouz, A., Ebrahimipour, V.. Improved estimation of electricity demand function by integration of fuzzy system and data mining approach. *ENERG CONVERS MANAGE*, Vol.49, Issues 8, (2008a), pp. 2165-2177.
- [9] Azadeh, A., Ghaderi, S.F., Sohrabkhani, S.. A simulated-based neural network algorithm for forecasting electrical energy consumption in Iran. *ENERGY POLICY*, Vol.36, Issues 7, (2008b), pp. 2637-2644.
- [10] Hong, D.H., Yi, H.C.. A note on fuzzy regression model with fuzzy input and output data for manpower forecasting. *FUZZY SET SYST*, Vol.138, Issues 2, (2003), pp. 301-305.
- [11] Ross, T.J. *Fuzzy Logic with Engineering Applications*. McGraw-Hill, New York, (1995).
- [12] Wang, H.F., Tsaur, R.C. Resolution of fuzzy regression model. *EUR J OPER RES*, Vol.126, (2000), pp. 637-650.
- [13] Chang, P.T., Konz, S.A., Lee, E.S. Applying fuzzy linear regression to VDT legibility. *FUZZY SET SYST*, Vol.80, (1996), pp. 197-204.
- [14] Azadeh, A., Saberi, M., Ghorbani, S. An ANFIS algorithm for improved forecasting of oil consumption: a case study of USA, Russia, India and Brazil *Journal of Scientific and Industrial Research* Vol. 69(03) (2010) pp. 194-203
- [15] Peters, G.. Fuzzy linear regression with fuzzy intervals. *FUZZY SET SYST*, Vol.63, (1994), pp. 45-55.
- [16] Tanaka, H., Uejima, S., Asia, K.. Linear regression analysis with fuzzy model. *IEEE Trans. Sys Man Cybernet*, Vol.12, (1982), pp. 903-907.
- [17] Azadeh, A., Saberi, M., Anvari, M., Moghaddam, M. An integrated ANN-K-Means algorithm for improved performance assessment of electricity distribution units, *Journal of Scientific and Industrial Research* Vol. 69(09) (2010) pp. 672-679
- [18] Wang, H.F., Tsaur, R.C. Insight of a fuzzy regression model. *FUZZY SET SYST*, Vol.112, (2000), pp. 355-369.
- [19] Chang, Y.H.O., Ayyub, B.M.. Fuzzy regression methods- a comparative assessment. *FUZZY SET SYST*, Vol.119, (2001), pp. 187-203.
- [20] Azadeh, A., Ghaderi, F., Anvari, M. Izadbakhsh, H., Dehghan, S. Performance assessment and optimization of thermal power plants by DEA BCC and multivariate analysis, *Journal of*

- Scientific and Industrial Research Vol. 66(10) (2007) pp. 860-872.
- [21] Celmins, A. Multidimensional least-squares model fitting of fuzzy models. *MATH COMPUT MODEL*, Vol.9, (1987), pp. 669-690.
- [22] Diamond, P. Fuzzy least squares. *INFORM SCIENCES*, Vol.46, (1988), pp. 141-157.
- [23] Savic, D., Pedrycz, W. Evaluation of fuzzy regression models. *FUZZY SET SYST*, Vol.39, (1991), pp. 51-63.
- [24] Lee, T.S., Chiu, C.C. Neural network forecasting of an opening cash price index. *INT J SYS SCIENCE*, Vol.33, Issue 3, (2002), pp. 229 – 237.
- [25] Bao, Y., Lu, Y., Zhang, J. Forecasting Stock Price by SVMs Regression. *LEC NOTE COMPUT SCIENCE*, Vol.3192, (2004), pp.295-303.
- [26] Leigh, W., Hightower, R., Modani, N. Forecasting the New York stock exchange composite index with past price and interest rate on condition of volume spike. *EXPERT SYST APPL*. Vol.28, Issue 1, (2005), pp.1-8.
- [27] Hong, Y.Y., Lee, C.F. A neuro-fuzzy price forecasting approach in deregulated electricity markets. *ELECTR POW SYST RES*, Vol.73, Issue 2, (2005), pp. 151-157.
- [28] Li, C., Wang, S.. Next-Day Power Market Clearing Price Forecasting Using Artificial Fish-Swarm Based Neural Network. *LEC NOTE COMPUT SCIENCE*, Vol.3972, (2006), pp. 1290-1295.
- [29] Azadeh, A., Ghaderi, S.F., Sohrabkhani, S. Forecasting electrical consumption by integration of Neural Network, time series and ANOVA. *APPL MATH COMPUT*, Vol.186, Issue 2, (2007), pp.1753-1761.
- [30] Tsang, P.M., Kwok, C., Choy, S.O., Kwan, R., Ng, S.C., Mak, J., Tsang, J., Koong, K., Wong, T.L. Design and implementation of NN5 for Hong Kong stock price forecasting. *ENG APPL ARTIF INTEL*. Vol. 20, Issue 4, (2007), pp.453-461.
- [31] Georgilakis, P.S. Artificial Intelligence Solution to Electricity Price Forecasting. *APP ARTIF INTELL: INT J*, Vol. 21, Issue 8, (2007), pp. 707-727.
- [32] Anderson, E.J. and Xu H., Nash, equilibria in electricity markets with discrete prices, *Mathematical Methods of Operations Research*, 2004, Vol. 60, Number 2, pp.215-238.
- [33] Niu, D-xiao, Liu, D., and Xing, M., Electricity price forecasting using generalized regression neural network based on principal components analysis, *Journal of Central South University of Technology*, 2008, Vol. 15, Supplement 2, pp. 316-320.
- [34] Doorman, G. and Nygreen, B., Market Price Calculations in Restructured Electricity Markets, *Annals of Operations Research*, 2003, Vol. 124, Numbers 1-4, pp. 49-67.
- [35] Bigdeli, N., Afshar, K., Amjady, N. Market data analysis and short-term price forecasting in the Iran electricity market with pay-as-bid payment mechanism. *ELECTR POW SYST RES*, Vol.79, Issue 6, (2009), pp.888-898.
- [36] Hsu, S.H., Hsieh, J.P.A., Chih, T.C., Hsu, K.C. A two-stage architecture for stock price forecasting by integrating self-organizing map and support vector regression. *EXPERT SYST APPL*. Vol. 36, Issue 4, (2009), pp.7947-7951.
- [37] Lackes, R., Börgermann, C., Dirkmorfeld, M.. Forecasting the Price Development of Crude Oil with Artificial Neural Networks. *LEC NOTE COMPUT SCIENCE*, Vol.5518, (2009), pp.248-255.
- [38] Zhou, H., Chen, B. Han., Z.X and Zhang, F.Q Study on probability distribution of prices in electricity market: A case study of Zhejiang Province, China. *COMMUN NONLIN SCIENCE NUMER SIMUL*, Vol. 14, Issue 5, (2009), pp. 2255-2265.
- [39] Cui, B., Han, R.. Modeling of dimensional errors in slender bar turning using artificial neural networks, *INTELL CONTROL AUTOM*, 2008. *WCICA 2008. 7th World Congress on*, China, Vol.25, Issues27, (2008), pp. 6053–6056.
- [40] Zhang, G.P., Qi, M. Neural network forecasting for seasonal and trend time series. *EUR J OPER RES*, Vol.160, Issues 2, (2005), pp. 501–514.
- [41] Kröse, B., Smagt, P.V.D. An introduction to Neural Networks; The University of Amsterdam: Amsterdam, (1996).
- [42] Haykin, S. *Neural Networks: A Comprehensive Foundation* (2nd ed.); Prentice-Hall: Englewood Cliffs, NJ, (1999).
- [43] Christodoulou, C.G. and Georgiopoulos, M. *Application of Neural Networks in Electromagnetics*; Artech House: MA, USA, (2001).

- [44] Anderson, E.J. and Xu, H. Supply Function Equilibrium in Electricity Spot Markets with Contracts and Price Caps , *Journal of Optimization Theory and Applications*, 2005, Vol. 124, Number 2, pp. 257-283.
- [45] Weron, R., Heavy-tails and regime-switching in electricity prices, *Mathematical Methods of Operations Research* , 2009, Vol. 69, Number 3, pp. 457-473.
- [46] Hojati, M., Bector, C.R., Smimou, K. A simple method for computation of fuzzy linear regression. *EUR J OPER RES*, Vol.166, (2005), pp. 172-184.
- [47] Jozsef, S. On the effect of linear data transformations in possibilistic fuzzy linear regression. *FUZZY SET SYST*, Vol.45, (1992), pp. 185-188.
- [48] Sakawa, M., Yano, H.. Multi-objective fuzzy linear regression analysis for fuzzy input-output data. *FUZZY SET SYST*, Vol.47, (1992), pp. 173-181.
- [49] Tanaka, H., Hayashi, I., Watada, J. Possibilistic linear regression analysis for fuzzy data. *EUR J OPER RES*, Vol.40, (1989), pp. 389-396.
- [50] Ozelkan, E.C., Duckstein, L. Multi-objective fuzzy regression: A general framework. *COMPUT OPER RES*, Vol.27, (2000), pp. 635–652.
- [51] Montgomery, D.C.. *Design and Analysis of Experiments*, 5th Edition, John Wiley & Sons, Inc., New York, NY. (2001), PP. 60–125.
- [52] Min-xiang, H., Xiao-hu, T. and Zhen-xiang, H., An electricity price model with consideration to load and gas price effects, *Journal of Zhejiang University - Science A*, 2003, Vol. 4, Number 6, pp. 666-671.
- [53] Bhole, B. and Surana, S., Electricity Prices and state commitment to energy efficiency in the U.S., *Energy Efficiency*, 2011, Vol. 4, Number 1, pp. 9-16.
- [54] Genc, T.S., Discriminatory Versus Uniform-Price Electricity Auctions with Supply Function Equilibrium, *Journal of Optimization Theory and Applications*, 2009, Vol. 140, Number 1, pp. 9-31.

An Intelligent Approach for Improvement of Short Term Water Consumption Forecasting in a Large and Complex Metropolitan City

F. Rouhollah¹, A. Azadeh², N. Neshat³, and H. Hamidipour²

¹*Faculty of Medicine, Tehran Medical Branch, Islamic Azad University, Tehran, Iran*

²*Department of Industrial Engineering and Center of Excellence for Intelligent Based Mechanical Experiments, College of Engineering, University of Tehran, P.O. Box 11365-4563, Iran*

³*Department of Industrial Engineering, Tarbiat Modares University, Tehran, Iran*

ABSTRACT

This study presents a hybrid approach consisting of Artificial Neural Network (ANN), Fuzzy Linear Regression (FLR), and analysis of variance (ANOVA) for improvement of water consumption forecasting. Hence, it can be easily applied to uncertain or certain, and/or complex environments due to its flexibility. The proposed hybrid approach is applied to forecast short-term water consumption in Tehran, Iran from 5 April 2004 to 21 March 2009. In this study, daily water consumption is viewed as the resultant of future and historical meteorological data. Implementation of the hybrid approach in a large metropolitan city such as Tehran seems to be ideal because of potential non-linearity and uncertainty in water consumption function of Tehran, Iran. The results of Mean Absolute Percentage Error (MAPE) indicate that selected ANN outperforms selected FLR in warm days. However, both ANN and FLR are ideal for cold days. In order to verify and validate the results, a sensitivity analysis is carried out by changing the train and test data sets. Finally, the comparison of the MAPE results of the hybrid approach with conventional linear regression confirms its considerable superiority for both warm and cold days.

Keywords: Forecasting; Water Consumption; Artificial Neural Network (ANN); Fuzzy Linear Regression (FLR); Complexity; Uncertainty

1. INTRODUCTION

Forecasting urban water consumption plays a key role in planning and management of urban water resources. In particular, facing the threat of urban water scarcity, some policies and strategies are required and these need to be on precise water consumption forecasts.

Most studies dealing with forecasting urban water demand have considered annual or monthly data and few have addressed daily water consumption. Liu and Zhang (2006) adopted a combined forecast model using wavelet decomposition and Artificial Neural Networks (ANNs) to forecast short-term urban water consumption. It was found that the combined forecast method is reasonable, and can rapidly and accurately forecast the water consumption.

A non-homogeneous Poisson Rectangular Pulse (PRP) system that provides a platform for simulating stochastic water consumption was developed by Steven et al. (2007). The results demonstrated that simulated PRP model is a powerful tool for forecasting urban water demand.

Wang et al. (2007) developed neural network model based on Particle Swarm Optimization (PSO) to forecast daily water consumption. The optimized neural network model has advantageous properties such as high generalization performance and accuracy.

An ensemble model to forecast water demand was developed considering the warm season with a three-day lead-time for the Louisville Water Company water supply system, Louisville, Kentucky. In this ensemble model, the uncertainty associated with explanatory meteorological data is integrated into regression model (Zhang et al. 2007).

Oliveira et al. (2009) identified the influencing factors on potable water consumption in the State of Parana-Brazil using a neural representation structure.

Pulido-Calvo et al. (2003) found ANN model outperforms regression and time series for total daily water demand of Fuente Palmera, Spain. The ANFIS (Adaptive Neuro-fuzzy Inferences System), autoregressive (AR) and autoregressive integrated moving average (ARIMA) based models for forecasting urban water consumption were also adopted and compared (Altunkaynak et al. 2005; Atsalakis and Ucenic 2005).

Ghiassi et al. (2008) provided urban water demand forecasts using a time series and an autoregressive integrated moving average model. Comparison results showed dynamic neural network presents more accurate and precise forecast rather than times series forecasts in this study.

Linear regression, growth curve, and grey markov models were adopted to forecast urban water demand of

2010, 2015 and 2020 in Qingdao by Juan et al. (2008). By analyzing and comparing the forecasts of these models, the growth curve model was introduced as superior model to forecast urban water demands of 2010, 2015, and 2020 in Qingdao.

An integrated neural network and Genetic Algorithm was applied and compared with Grey Markov approach for forecasting water consumption by Ma et al (2004). The results showed the integrated approach outperforms grey theory approach for forecasting water consumption of Benxi Iron-steel Company. Two grey Markov models were combined to forecast water consumption of a farmland in Liao River area (Qiaona 2007).

Briefly, previous literature in the field of water consumption modeling has categorized into studies related to the parametric modeling and intelligent modeling. The parametric methods of forecasting are appropriate to a straightforward estimation of the relationship between the estimated variable and the explanatory variables. However, they are bounded by some strict assumptions about the given data. Hence, forecasting by parametric methods in complex and ambiguous environments leads to search for intelligent solutions such as Artificial Neural Networks (ANNs).

Consequently, in this study we proposed an integrated approach for improved water consumption forecasting. The unique nature of this approach lies in the integration of the Artificial Neural Network (ANN), Fuzzy Linear Regression (FLR), and Conventional Regression (CR) approaches. Hence, it can be applied to certain, uncertain, and/or complex environments due to its flexibility. The proposed approach is applied for the daily water consumption forecasting in a metropolis like Tehran with potential uncertainty and complexity in its environment.

2. MATERIAL AND METHODS

Forecasting the future water consumption in Tehran, where the typology of water consumptions changes very rapidly and ambiguity is particularly challenging. Therefore, forecasting process requires methods that work efficiently with complex, noisy, and/or uncertain data. This capability is very important, because we seldom have complete, crisp, and consistent data to forecast water consumption in cities of developing countries. Thus, we propose a hybrid approach consisting of ANN, FLR, ANOVA and MAPE for improved water consumption forecasting (according to Fig. 1). The proposed approach is capable of handling both complexity and uncertainty. Several notes should be considered while using this approach:

- 1) As the water consumption volume is hardly estimated in terms of its determinants and their relationships are complex, the environmental condition is considered to be potentially complex and inconsistent. Moreover, it is implied to be

potentially uncertain when there are biases in data collection process due to lack of adequate data, human or measurement errors.

- 2) ANOVA, F-test defines whether the means of forecasted values and actual values are all equal. Hence, the null and alternative hypotheses are:
- 3)

$$\begin{aligned} H_0: \mu_1 = \mu_2 = \mu_3 \\ H_1: \mu_i \neq \mu_j \quad i, j = 1, 2, 3, i \neq j \end{aligned} \quad (4)$$

Where μ_1, μ_2 are the means of the forecasted values by selected ANN and FLR, respectively, and μ_3 is the means of the actual data.

- 4) All error estimation methods except MAPE have scaled output. As input data used for the model estimation have different scales, MAPE method is the preferred method to estimate relative errors.

$$\text{Mean Absolute Percentage Error} = \frac{\sum_{t=1}^n \left| \frac{x_t - \hat{x}_t}{x_t} \right|}{n} \quad (5)$$

Where x_t is the actual value and \hat{x}_t is the estimated value and n is number of observations (test data).

- 5) In this paper, we aim at developing the eight well-known FLR models (Tanaka et al. (1982), Sakawa and Yano (1992), Peters (1994), Ozelkan and Duckstein (2000), Hojati et al. (2005)). For more detailed information refer to (Azadeh et al. 2008b, c).

2.1 Experiment

Tehran, Iran is a densely populated city with a population of 14 Millions. Taking into consideration the potential uncertainties in natural phenomena and nonlinearity in Tehran water consumption function, the hybrid ANN-FLR is applied to Tehran to forecast daily water consumption.

The components of water consumption profile of Tehran according to the typical classification include residential, industrial, commercial, institutional, municipal and government water consumptions (Hall and Watson 2000). Note that consumptions relevant to fire services are not taken into account in this study.

In the light of reviewed literature, factors that need to be considered in forecasting of urban water consumption include: climatic factors such as meteorological data, air temperature, precipitation, and humidity as well as socio-economic factors such as household income, holidays, water price, and population. Socio-economic factors are postulated to impose long-term changes on water use patterns; while climatic factors induce short-term variations of water consumptions (Yu et al. 2002).

Management of short-term water consumption considers a period of one hour to a few days for forecasting. Short-term forecasting is useful in efficient operation and management of an existing water system.

The selection of the determinants to forecast short-term water consumption in Tehran was taken from the articles available in the literature (Maximum daily temperature, forecasted maximum temperature of following day, and Antecedent Precipitation Index (API) are used to account for daily water consumption in Tehran and relevant data was provided from database of Metrology Organization of Tehran.

Note that API is calculated by $API_j = k.API_{j-1} + P_j$ where P_j is the precipitation in millimetre on day j and the value of k is dependent on the potential loss of

moisture and varies seasonally but a constant value of 0.85 was adopted as being representative of the previous day's rainfall (Bruse and Clark, 1966).

In this study, the daily water consumptions in Tehran from 5 April 2004 to 21 March 2009 were considered. The studied period was divided into warm days (6 May to 7 October) and cold days (5 April to 5 May and 8 October to 6 March). Note that 7 March to 4 April for each year are excluded in studied period with regard to the excessive fluctuation in water consumption due to holidays and house cleaning. Daily water consumption data of Tehran within studied period was determined by sewage system. In order to adopt the FLR and ANN models for warm and cold days, separately, daily water consumption data within 5 April to 31 December 2004 is considered as test data and the rest as train data.

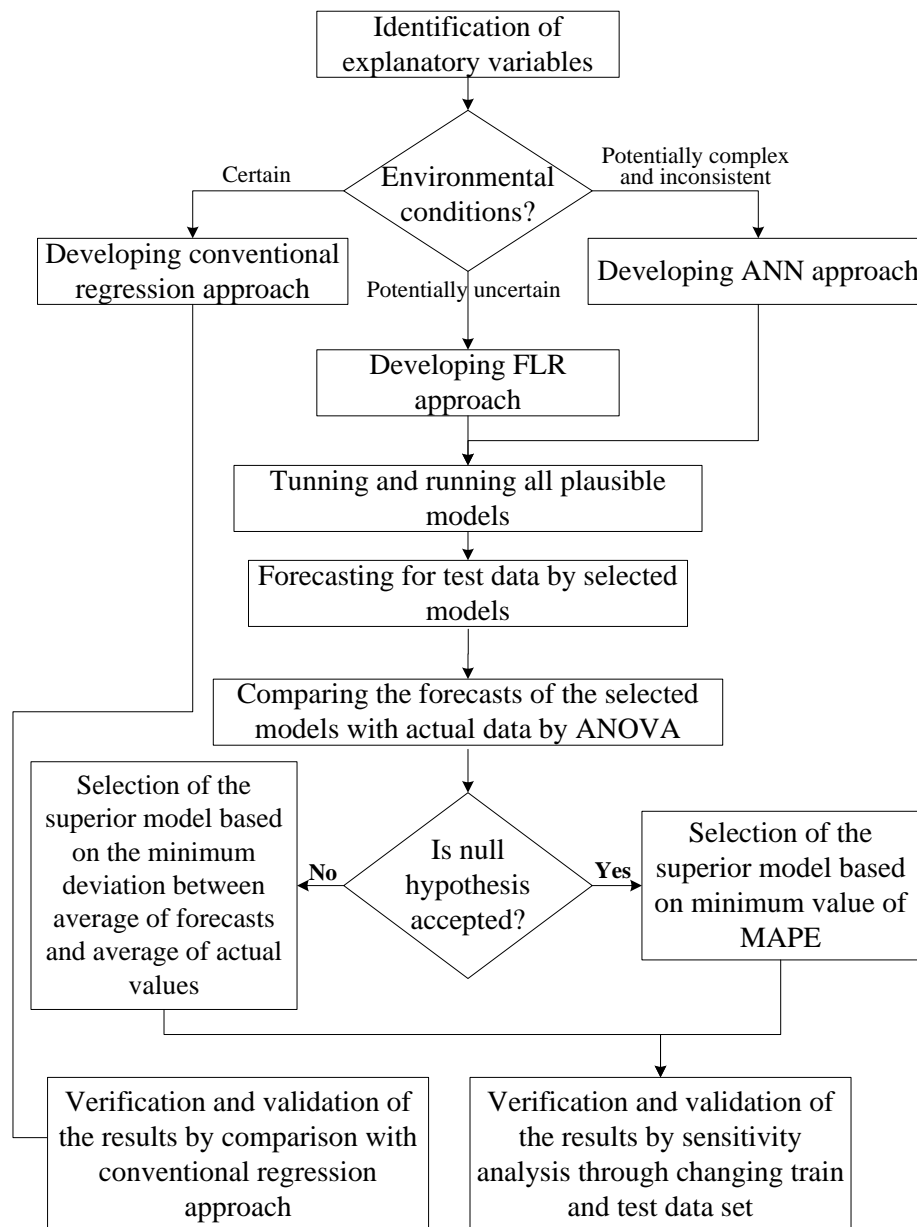


Figure 1: The proposed ANN-FLR approach for optimum water consumption forecasting

For choosing the optimal network of the ANN models of warm and cold days, a number of different network configurations, consisting of one hidden layer and different number of neurons in hidden layers with various transfer functions were considered. The training process was run under the MATLAB environment and a minimum value of user-specified error function. Moreover, minimum mean square error (MSE) is reached while the number of epochs is less than 10000 epochs.

Eight distinct FLR models so called, TNK_1 (Tanaka et al., 1982), TNK_2 (Tanaka et al., 1989), SAK_1 (Sakawa et al., 1992), SAK_2 (Sakawa et al., 1992), PTR_1 (Peters, 1994), OZK (Ozelkan et al., 2000), HJT_1 (Hojati et al., 2005), HJT_2 (Hojati et al., 2005) were constructed according to the states FLR approaches in section 1.2.

2.2 Computational Results

The MAPE results of eight FLR model forecasts for test data were obtained according to the Tables 2 for cold and warm days. As results show, the OZK (Ozelkan et al., 2000) and HJT_2 (Hojati et al., 2005) models with an MAPE of 0.0414 and 0.0455 give the best and most accurate results among all other models for cold and warm days, respectively.

Moreover, different network configurations of ANN models for warm and cold days were developed, separately. According to the Fig.s 2 and 3, the minimum values of MAPE for test data were obtained while numbers of neurons in hidden layer were 40 and 15 for warm and cold days, respectively.

The analysis of variance (ANOVA) was performed on the forecasts of selected FLR and ANN as well as actual values for warm and cold days, separately. The null hypothesis in ANOVA F-test was accepted and the minimum value of MAPE was used to identify the superior model for daily water consumption forecasting accordingly.

2.3 Sensitivity Analysis

As mentioned, the train and test data were originally considered 1710 and 270 days, respectively. However, to perform a comprehensive sensitivity analysis, the train and test data were step-by-step moved through these days. The results of Table 3 show that categorizing data of 8 October 2007 to 31 December 2007 as test data and the rest as train data results in the minimum value of MAPE function (3.78 %) for selected ANN relating to cold days. Similarity, considering data of 6 Jun 2007 to 7 October 2007 as test data and the rest as train data results in the minimum value of MAPE function (3.81%) for selected ANN model relating to warm days (See Table 4).

According to the results of Tables 3 and 4, the minimum values of MAPE are resultant in considering 5 February to 6 March and 5 April to 5 May and 8 October to 31 December 2007 as test duration for the selected FLR: OZK (Ozelkan et al., 2000) for cold days and 23 July to 7 October 2007 for selected FLR: HJT_2 (Hojati et al., 2005) for warm days.

Tables 5 and 6 are presented in order to add up the findings of this section. For comparison purpose, the MAPE results of the Conventional Linear Regression (CLR) are provided as well. As seen, the selected ANN outperforms the selected FLR for cold days considering its capability of dealing with complexity and nonlinearity in collected data. However, both ANN and FLR are ideal for cold days. Furthermore, this is an indication of suitability of the hybrid approach over conventional and non-flexible approaches. Moreover, comparison of the MAPE values confirms the superiority of selected ANN and FLR over CLR for warm and cold days.

3. CONCLUSION

This study has undertaken to present a hybrid approach consisting of ANN, FLR, MAPE and ANOVA for improved water consumption forecasting. We applied the hybrid approach to forecast daily water consumption in Tehran with regard to the potential complexity and uncertainty in its environment. Eight distinct models based on well-known FLR approaches were adopted to forecast daily water consumption for warm and cold days, separately. Because of potential non-linearity and complexity in consumption function, ANN approach was also applied to this model. Next, the analysis of variance (ANOVA) was performed on the forecasts of the selected FLR and ANN models and actual values for warm and cold days, separately.

The ANOVA and MAPE results indicated that ANN outperforms its rivals for water consumption forecasting in warm days because of its capability of dealing with complexity and nonlinearity. However, both ANN and FLR are suitable for cold days. In order to verify and validate the results, a sensitivity analysis was carried out by changing the train and test data sets. Finally, the superiority of the hybrid approach was also shown over the conventional regression approach.

According to the mentioned features in Table 1, this hybrid approach is applicable to complex, non-linear and/or ambiguous environments due to ANN and FLR mechanisms. It is robust against inconsistency and noise in data as well as high dimensionality and co-linearity.

Table 1: The features of the integrated ANN-FLR approach versus studies

Feature Approach	Short-Term Forecasting	Multiple Outputs capability	Dealing Environment Complexity and Non-Linearity	Dealing Uncertain, Limited and Non- Crisp Data	Intelligent Modeling	Multiple Inputs	Dealing Ambiguity	Influencing Factor Determining	Robustness against Noisy and Inconsistent Data
The ANN- FLR Approach	√	√	√	√	√	√	√	√	√
Yu et al. (2002)	√	√				√			√
Ma et al (2004)	√	√				√			√
Atsalakis & Ucenic, (2005)	√			√					
Liu & Zhang (2006)		√				√			√
Steven et al. (2007)							√		
Wang et al. (2007)	√	√				√			√
Zhang et al. 2007				√					
Juan et al. (2008)									√
Oliveira et al. (2009)	√	√							√

REFERENCES

- [1] Altunkaynak, A., Özger, M. and Çakmakci, M. (2005). "Water consumption prediction of Istanbul city by using fuzzy logic approach." *Water Resour. Manag.*, 19(2), 641–654.
- [2] Atsalakis, G. and Ucenic, C. (2005). "Time series prediction of water consumption using neuro-fuzzy (ANFIS) approach." *IWA Int. Conf. on Water Econ., Stat. and Financ.*, Rethymno, Greece.
- [3] An, A., Chan, C., Shan N., Cercone N., and Ziarko, W. (1997). "Applying knowledge discovery to predict water-supply consumption." *IEEE Expert*, 72-78.
- [4] Azadeh, A., Saberi, M., Ghaderi, S.F., Gitiforouz, A. and Ebrahimipour, V. (2008a). "Improved estimation of electricity demand function by integration of fuzzy system and data mining approach." *Energy Conversat. Manag.*, 49(8), 2165-2177.
- [5] Azadeh, A., Ghaderi, S.F. and Sohrabkhani, S. (2008b). "A simulated-based neural network algorithm for forecasting electrical energy consumption in Iran." *Energy Policy*, 36(7), 2637-2644.
- [6] Bruse, J.P. and Clark, R.H. (1966). "Introduction to Hydrometeorology." 1st ed, Pergamon Press, Oxford, U.K, 319.
- [7] Buchberger, S.G., and Li, Z. (2007). "A modeling system for simulation of stochastic water demands." *Proc. World Environ. On Water Resour. Congr.* Tampa, Florida.
- [8] Ghiassi, M., Zimbra, D.K., and Saidane, H. (2008). "Urban water demand forecasting with a dynamic artificial neural network model." *J. Water Resour. Plan. Manag.*, 134(2), 138-146.
- [9] Hall, E. and Watson, M. (2000). "Urban Water Consumption." *Water sew. effl.*, 31, 1-10.
- [10] Hojati, M., Bector, C.R. and Smimou, K. (2005). "A simple method for computation of fuzzy linear regression." *Eur. J. Operation Research*, 166(1), 172–184.
- [11] Jozsef, S. (1992) "On the effect of linear data transformations in possibilistic fuzzy linear regression." *Fuzzy Sets Syst.*, 45, 185-188.
- [12] Hong, D.H. and Yi, H.C. (2003). "A note on fuzzy regression model with fuzzy input and output data for manpower forecasting." *Fuzzy Sets Syst.*, 138(2), 301–305.
- [13] Huijen, N. and Gollard, A.A. (1994). "Using a system dynamic simulation model to forecast long term urban water demand." *Int. System Dyn. Conf.*, 76-88.

- [14] Juan, C., Zhou-hu, W.U. and Yao, J. (2008). "Forecast of urban domestic water demand in Qingdao." *J. Qingdao Technol. Univ.*
- [15] Liu, H.B., and Zhang, H.W. (2006). "Short-term water consumption forecast in municipal water supply networks based on wavelet decomposition." *Water Resour.*, 22(17), 60-73.
- [16] Ma, F.H., Yang, W., Yang, F., and Yu, X.X. (2004). "Forecast water consumption with improved BP neural network." *J. Liaoning Technol. Univ.*, 23(2), 191-193.
- [17] Oliveira, D.M., Oliveira, A.L., Neri Nobre, C., and Zarate, L.E. (2009). "The usage of Artificial Neural Networks in the classification and forecast of potable water consumption." *Int. Jt. Conf. on Neural Netw.*, Atlanta, Georgia, USA, 2331-2338.
- [18] Ozelkan, E.C. and Duckstein, L. (2000). "Multi-objective fuzzy regression: A general framework.", *Comput. Operation Research*, 27(1), 635-652.
- [19] Pulido-Calvo, I., Roldan, J., Lopez-Luque, R. and Gutierrez-Estrada, J. (2003). "Demand forecasting for irrigation water distribution systems." *J. Irrig. Drain. Eng.*, 129(6), 422-431.
- [20] Rumelhart, D.E. and McClelland, J.L. (1986). "Parallel distributed processing: Explorations in the microstructure of cognition." *Found.*, MIT Press, Cambridge, MA.
- [21] Sakawa, M., Yano, H. (1992). "Multi-objective fuzzy linear regression analysis for fuzzy input-output data." *Fuzzy Sets Syst.*, 47(2), 173-181.
- [22] Peters, G. (1994). "Fuzzy linear regression with fuzzy intervals." *Fuzzy Sets Syst.*, 63(1), 45-55.
- [23] Tanaka, H., Uejima, S. and Asia, K. (1982). "Linear regression analysis with fuzzy model." *IEEE Trans., System Man Cybern.*, 12, 903-907.
- [24] Tanaka, H., Hayashi, I., Watada, J. (1989). "Possibilistic linear regression analysis for fuzzy data." *Eur. J. Operation Research*, 40(3), 389-396.
- [25] Qiaona, S. (2007). "Forecast of the water consumption in agriculture based on grey Markova model." *J. Anhui Agric. Sci.*, 35(6), 1788-1803.
- [26] Werbos, P.I. (1974). "Beyond Regression: new tools for prediction and analysis in the behavior sciences." PhD Thesis, Harvard University, Cambridge, MA.
- [27] Wang, H.F. and Tsaur, R.C. (2000). "Resolution of fuzzy regression model." *Eur. J. Operational Research*, 126, pp.637-650.
- [28] Wang, L., Wang, Z. and Yue, L. (2007). "Forecast model of urban daily water consumption based on particle swarm optimization." *China Water Wastewater*, 23(7), 89-93.
- [29] Yu, M.J., Joo, C.N. and Koo, J.Y. (2002). "Application of Short-term water demand prediction model to Seoul." *J. Water Sci. Technol.*, 46(6-7), 255-261.
- [30] Zhang, G.P. and Qi. M. (2005). "Neural network forecasting for seasonal and trend time series." *Eur. J. Operation Research*, 160(2), 501-514.

A Greedy Randomized Adaptive Search Procedure-Genetic Algorithm for Electricity Consumption Estimation and Optimization in Agriculture Sector

S.F. Ghaderi, A. Azadeh¹, S.M. Asadzadeh, R. Jalali, S. Hemmati

Department of Industrial Engineering and Center of Excellence for Intelligent Based Experimental Mechanics, University College of Engineering, University of Tehran, Iran

¹Corresponding Author: Department of Industrial Engineering, College of Engineering, University of Tehran, Iran aazadeh@ut.ac.ir

ABSTRACT

This study presents a flexible algorithm for electricity energy consumption estimation and optimization in agriculture sector based on Greedy Randomized Adaptive Search Procedure (GRASP) and Genetic Algorithm (GA) with variable parameters using stochastic procedures. The standard economic indicators used in this paper are price, value added, number of customers and electricity consumption in the previous period. The proposed algorithm may be used to estimate energy demand in the future by optimizing parameter values. The proposed algorithm uses analysis of variance (ANOVA) to select from GA, GRASP or conventional regression for future demand estimation. Furthermore, if the null hypothesis in ANOVA F-test is rejected, the least significant difference (LSD) method is used to identify which model is closer to actual data at α level of significance. To show the applicability and superiority of the proposed algorithm the data for electricity consumption in Iranian agriculture sector from 1979 to 1999 is used and applied to the proposed algorithm. This is the first study that introduces and uses an integrated GRASP-GA-Regression for electricity consumption estimation and optimization in agriculture sector.

Keywords: Greedy Randomized Adaptive Search Procedure; Genetic Algorithm; Electricity Consumption; Analysis of Variance; Conventional Regression

1. INTRODUCTION

According to the increasing demand of electricity, demand function estimation is really essential. The estimation of electrical energy demand based on economic indicators may be done with different kinds of mathematical models. These equations might be linear or non-linear. Al-Shobaki et al. (2008) developed forecasting models to predict future generation and electrical power consumption in Jordan. The proposed time-series models account for trend, monthly seasonality, and cycle dynamics. Bianco et al. (2009) investigated the influence of economic and demographic variables on the annual electricity consumption in Italy with the intention to develop a long-term consumption forecasting model. Chui et al. (2009) focused on the long-term forecasting of electricity demand using autoregressive, simple linear and multiple linear regression models.

Due to the fluctuations of economic indicators, the non-linear forms of the equations can estimate electrical energy demand more effectively. The non-linearity of economical indicators and electrical energy demand has lead to search for different solution methods such as genetic algorithm and GRASP. Genetic algorithm and GRASP are optimizing and stochastic search techniques which possess vast and powerful applications.

Electrical energy consumption has been studied widely in the literature and several soft computing methods are employed to forecast electricity consumption in short

term as well as long term. The estimation of Turkey's energy demand based on economic indicators using genetic algorithm was performed by Ceylan and Ozturk (2004). Various studies on estimation of electricity demand using GA have been reported in the literature. For example, see Canyurt et al. (2004); Ozturk et al. (2003a) and Ozturk et al. (2003b) for some recent advances in this area. Hashemini & Niaki (2006) have introduced a new type of genetic algorithm to find the best regression model among several alternatives and have assessed its performance by an economical case study. The empirical results of the study by Karabulut et al. (2008) in Turkey demonstrate successful electrical load forecast with a low error rate using genetic programming. Azadeh et al. (2008) develop a simulated-based neural network algorithm for forecasting electrical energy consumption in Iran.

Cheng and Wei (2009) proposed a new model, which incorporates one step-ahead concept into adaptive-network-based fuzzy inference system (ANFIS) to build a fusion ANFIS model and enhances forecasting for electricity loads by adaptive forecasting equation. By developing a new training or identification stage in a nonlinear chaotic dynamic based predictor, Unsihuay-Vila et al. (2009) proposed a new hybrid approach based on nonlinear chaotic dynamics and evolutionary strategy to forecast electricity loads and prices. Wang et al (2008) proposed an optimal model which integrates a traditional Support Vector Machines (SVM) forecasting technique with the reduction attributes of Rough Sets (RS) based on Immune Genetic Algorithm (IGA) to

form a new forecasting model. Pai and Hong (2005) proposed a recurrent support vector machines with genetic algorithms (RSVMG) to forecast electricity load. Genetic algorithms (GAs) are used to determine free parameters of support vector machines.

In spite of some similarities, the proposed soft computing approaches are different in some modeling features. Table 1 gives a comparison between the existing algorithms in the literature and the proposed GRASP-GA-Regression algorithm of this study. Clearly, it is capable of handling data non-linearity and linearity for consumption estimation and optimization.

It is also flexible and integrated in which GA, GRASP, or Regression may be selected as the best performer.

The proposed algorithm which is based on GA, GRASP, conventional regression and ANOVA is discussed in the next section. The input variable used to estimate the best conventional regression model and consequently GA and GRASP model is the function of independent variables; price, value added, number of customers, and electricity consumption in the previous period.

Table 9: comparison between the existing algorithms in the literature and the proposed GRASP-GA algorithm of this study

Study	Algorithm	Features				
		Optimality	Flexibility	Integration mechanism	Linearity	Non-linearity
Azadeh et al. (2007a)	ANN-GA	✓		✓	✓	✓
Bao (2002)	ANN				✓	✓
Darbellay (2000)	ANN				✓	✓
Haldenbilen (2004)	GA	✓			✓	✓
Park et al. (1995)	Adaptive ANN				✓	✓
Zhang and Oi (2005)	ANN				✓	✓
Canyurt et al. (2004)	GA	✓			✓	✓
Ceylan and Ozturk (2004)	GA	✓			✓	✓
Ghaderi et al. (2006)	Econometric Modeling				✓	✓
Ozturk et al. (2003a)	GA	✓			✓	✓
Ozturk et al. (2003a)	GA	✓			✓	✓
Sadeghi (2003)	Econometric Modeling				✓	
This study	GRASP-GA-OLS	✓	✓	✓	✓	✓

2. THE INTEGRATED GRASP-GA ALGORITHM

The economic indicators used in this paper are price, value added, number of customers and electricity consumption in the last periods. The proposed algorithm may be used to estimate energy demand in the future by optimizing parameter values. The proposed algorithm uses ANOVA to select either GA or conventional regression for future demand estimation. Furthermore, if the null hypothesis in ANOVA F-test is rejected, the least significant difference (LSD) method is used to identify which model is closer to actual data at α level of significance. The significance of the proposed algorithm is twofold. *First, it is flexible and identifies the best model based on the results of ANOVA, whereas previous studies consider the best*

fitted GA model based on MAPE or relative error results. Second, the proposed algorithm may identify conventional regression as the best model for future electricity consumption forecasting because of its dynamic structure, whereas previous studies assume that GA always provide the best solutions and estimation. Figure 1 depicts the proposed algorithm of this study. The reader should note all steps of the integrated algorithm are based on standard and scientific methodologies which are GA, GRASP, conventional regression, ANOVA and least significant differences (LSD). Furthermore, the GA and GRASP modeling is based on which regression model is selected for the data set. The best model is distinguished by modeling, running and testing various regression models and selecting the model with lowest error.

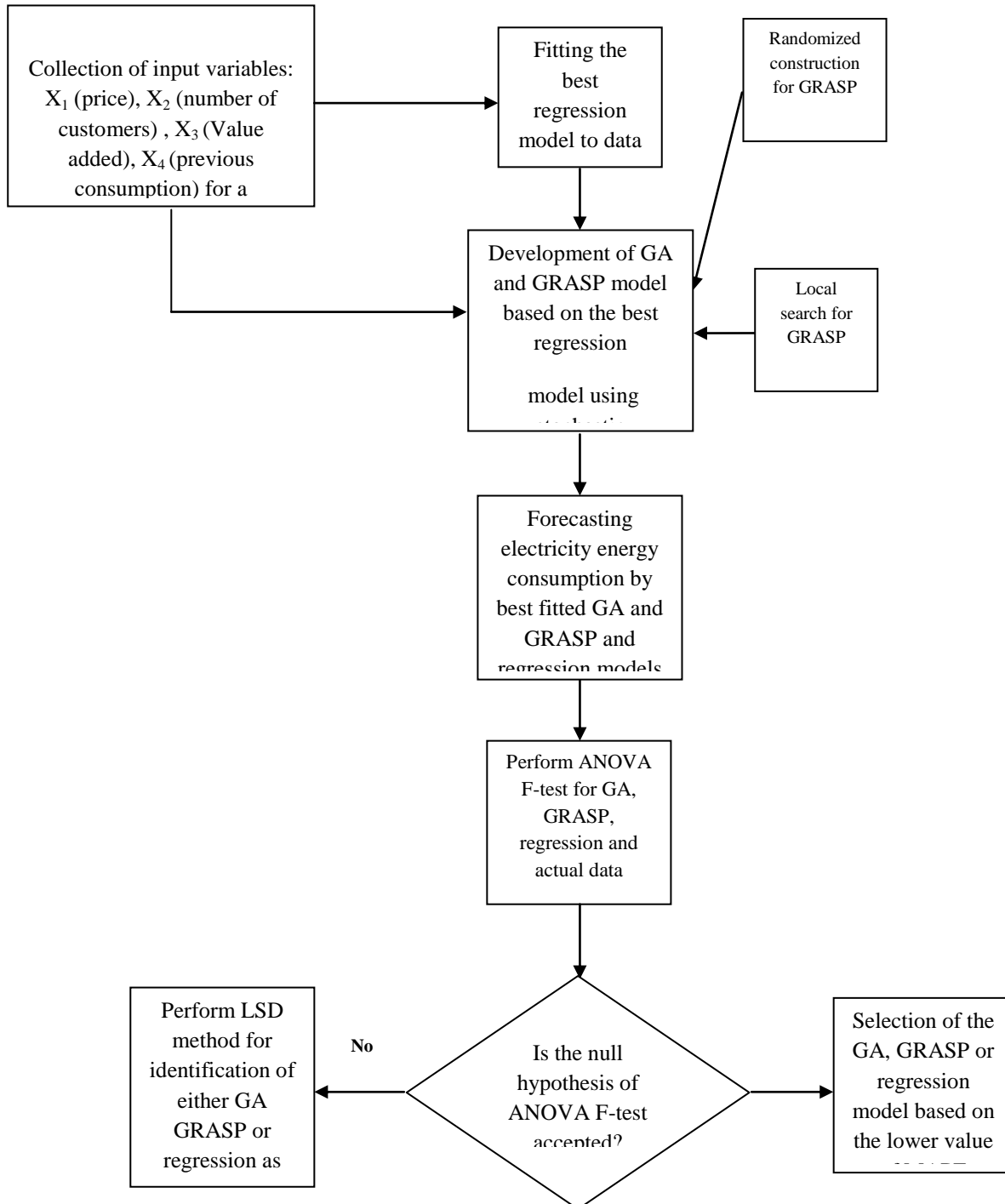


Figure 1: The flexible GRASP-GA, regression algorithm for electricity energy forecasting in agriculture sector

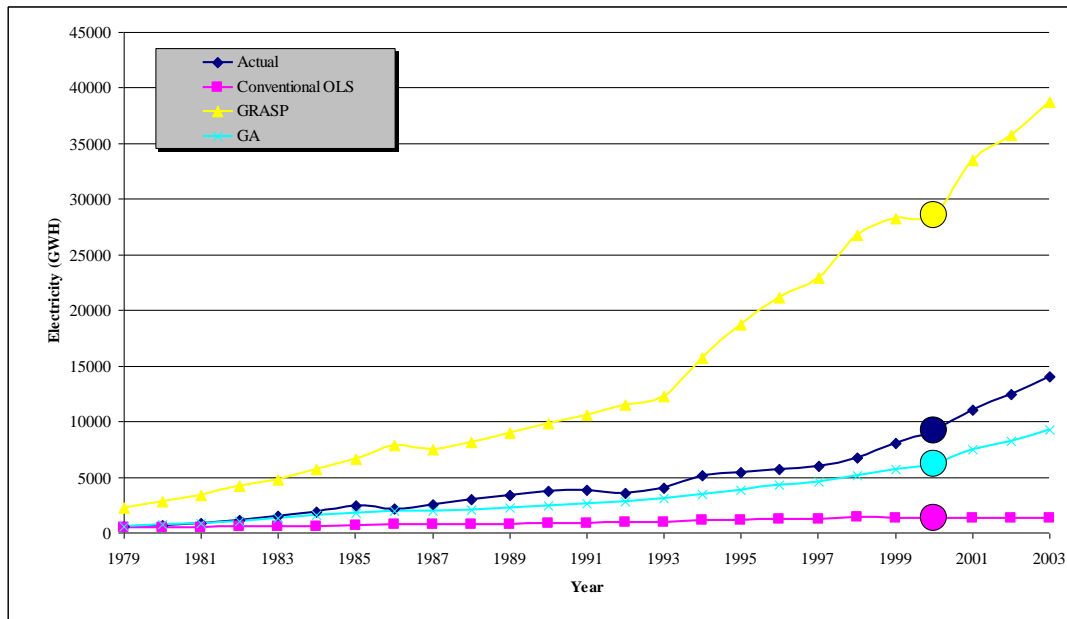


Figure 2: The results of estimating electricity consumption by GA, GRASP and conventional OLS method

3. EXPERIMENTS AND RESULTS

The proposed algorithm is applied to electricity consumption estimation and forecasting in agricultural sector of Iran from 1979 to 2003. It is furthermore used to identify the preferred model to forecast and estimate electricity consumption in the agricultural sector of Iran by the integrated mechanism of the flexible approach. The best fitted regression model was identified as a linear-logarithmic model which is the function of independent variable. This is achieved through ordinary least square (OLS) method (retrieved by SPSS). As shown in Figure 2, the estimated values by GRASP are less fitted than OLS and GA.

The estimated results of GA, GRASP and OLS are compared with actual data by ANOVA F-test (Montgomery, 2001). The results are shown in Table 1. According to ANOVA results in Table 1, with $\alpha = 0.05$ the null hypothesis is rejected and therefore, further analysis needs to be performed to foresee which treatment pairs caused the rejection of null hypothesis. Furthermore, LSD was used to compare treatment means. There are 12 degrees of freedom for error and at $\alpha = 0.05$ and Equation (7) is used to estimate LSD = 1.13 with $t_{0.025, 9} = 2.621$.

Table 1: ANOVA for GRASP, regression, GA, and actual data

Source of variation	Sum square	Degrees of freedom	Mean square	F _o	F _{$\alpha = 0.05$}
Between groups	8.82	3	2.94	7.9	5.14
Between blocks	61.43	3	20.47	55.01	4.76
Within groups	3.35	9	0.37		
Total	73.6	15			

We observed from LSD that regression average value and actual average value are considerably different and GA and GRASP average values and actual average value do not differ significantly. Furthermore, the flexible algorithm prescribe that we stop at this stage and both GA and GRASP are superior to linear-logarithmic model. To select one of the methods, the MAPE analysis is performed and the results are shown in Table 2. As shown, GA provides much better estimate than GRASP for this case study. Moreover, GRASP does not provide good estimate for the case of this study. Also, the MAPE estimation of regression is even worse than GRASP. One implication is that GRASP is not an ideal candidate for regression problem of this study. Therefore, it may be concluded that for chaotic data such as the case our study, GA provides better estimations with respect to electricity consumption. It should be noted that intelligent methods and meta-heuristics such as GA and GRASP are used as power optimization (local) tool when the sample space is limited. Developing countries are usually faced with data limitations. This is why we were able to access to 25 sets of data (21 of which is selected for training GA, GRASP and regression). It was shown that GA was a better estimate than GRASP and conventional regression. The reader should note that utilization of OLS or conventional regression would have resulted in huge error and imprecision in future forecasting. This would result in incorrect strategic planning with respect to electricity consumption in agricultural sector of Iran. The integrated GRASP-GA-OLS was able to reduce this error considerably (about 55 percent in comparison with OLS).

Table 2: The MAPE estimation of the proposed algorithm

	GA	Regression	GRASP
MAPE	0.33	0.88	1.94

4. CONCLUSION

This study presented an integrated algorithm for forecasting electricity energy consumption in agriculture sector of Iran based on GA and GRASP with variable parameters using stochastic procedures. The economic indicators used in this paper were price, value added, number of customers and electricity consumption in the previous period. The proposed algorithm may be used to estimate energy demand in the future by optimizing parameter values. The GA and GRASP applied in this study has been tuned for all its parameters and the best coefficients with minimum error are identified, while all parameter values are tested concurrently. The proposed algorithm first identifies the best regression model with lowest possible relative error. It then uses the type of model selected by regression for GA and GRASP modeling and estimation. Third, it uses ANOVA F-test to select either GA or GRASP or conventional regression for future demand estimation based on the test data. Furthermore, if the null hypothesis in ANOVA F-test is rejected, the LSD experiment is used to identify which model is closer to actual data at α level of significance. The significance of the proposed algorithm is two fold. First, it is flexible and identifies the best model based on the results of ANOVA, whereas previous studies consider the best fitted GA model based on MAPE or relative error results. Second, the proposed algorithm may identify conventional regression as the best model for future electricity consumption forecasting because of its dynamic structure, whereas previous studies assume that GA always provide the best solutions and estimation. To show the applicability and superiority of the proposed algorithm the data for electricity consumption in Iranian agriculture sector from 1979 to 1999 was used and applied to the proposed algorithm. The results showed that GA and GRASP are superior to conventional best fit linear-logarithmic regression according to ANOVA F-test and LSD experiment. However, it is argued that the utilization of GA, GRASP and conventional regression assures that for a given data set either one may be selected. This is turn minimizes the bias of utilizing only one approach like previous studies and enhances the overall performance of future forecasting and estimation in agriculture sector of Iran. The reader should note that utilization of OLS or conventional regression would have resulted in huge error and imprecision in future forecasting. This would result in incorrect strategic planning with respect to electricity consumption in agricultural sector of Iran. The integrated GRASP-GA-OLS was able to reduce this error considerably.

In general, meta-heuristics methods such as GRASP and GA are used when the sample space is limited or small in comparison to exact or conventional methods.

Second, if the relative error (MAPE) reported by GA or GRASP is relatively small, it is the indication of its acceptability and reasonability. The integrated approach of this study is flexible and uses GA, GRASP or conventional regression approach to identify the best fitted model. Moreover, in the actual case of this study (25 sets of data for annual energy consumption in agriculture sector of Iran), a very small value of MAPE is reported in comparison with conventional regression. Third, the selection of 25 sets of data is due to lack of data from standard sources for the case of this study. It should be noted that both GA and GRASP are capable of dealing with local optimization search. In addition, they are capable of dealing with both data complexity and small sample space due to their intelligent mechanisms. This is of great importance in developing countries such as Iran where there is shortage of data and conventional methods may not provide accurate forecasting. Due to small sample space, both GA and GRASP are used to insure local optimal solution. In addition, an actual case study was used to show the applicability of the integrated approach.

REFERENCES

- [1] Al-Shobaki, S., Mohsen, M., Modeling and forecasting of electrical power demands for capacity planning, *Energy Conversion and Management* 2008, 49 (11), 3367-3375
- [2] Azadeh, A., Ghaderi, S.F. and Tarverdian, S., Electrical energy consumption estimation by genetic algorithm. *Proceedings of IEEE Conference on Industrial Electronics*, 2006, 9-13 July, Montreal, Canada.
- [3] Azadeh, A., Ghaderi, S.F., Sohrabkhani, S., A simulated-based neural network algorithm for forecasting electrical energy consumption in Iran, *Energy Policy* 2008, 36 (7), 2637-2644
- [4] Azadeh, A., Ghaderi, S.F., Sohrabkhani, S., Forecasting electrical consumption by integration of neural network, time series and ANOVA, *Applied Mathematics and Computation*, 2007b, 186: 1753-1761.
- [5] Azadeh, A., Ghaderi, S.F., Tarverdian, S. Saberi, M., Integration of artificial neural networks and genetic algorithm to predict electrical energy consumption, *Applied Mathematics and Computation*, 2007a, 186: 1731-1741.
- [6] Azadeh, A., Tarverdian, S., Integration of Genetic Algorithm, *Computer Simulation and Design of experiment for Forecasting Electrical Consumption*. *Energy Policy*. 2007c, 35(10): 5229-5241.
- [7] Bao, J., Short-term load forecasting based on neural network and moving average, *Technical*

- Report, Department of Computer Science, Iowa State University, 2002
- [8] Bianco, V., Manca, O., Nardini, S., Electricity consumption forecasting in Italy using linear regression models, *Energy* 2009, 34 (9), 1413-1421
- [9] Canyurt, O.E., Ozturk, H. and Hepbasli, A. Energy demand estimation based on two-different genetic algorithm approaches. *Energy Sources*, 2004, 26 (14) 1313-1320.
- [10] Ceylan, H. and Ozturk, H., Estimating energy demand of Turkey based on economic indicators using genetic algorithm approach. *Energy Conversion and Management*, 2004, 45, 2525–2537.
- [11] Cheng, C.-H., Wei, L.-Y., One step-ahead ANFIS time series model for forecasting electricity loads, *International Journal of Electrical Power and Energy Systems*, 2009, in Press
- [12] Chui, F., Elkamel, A., Surit, R., Croiset, E., Douglas, P.L., Long-term electricity demand forecasting for power system planning using economic, demographic and climatic variables, *European Journal of Industrial Engineering* 2009, 3 (3), 277-304
- [13] Darbellay, M. S., Forecasting the short-term demand for electricity, Do Neural Networks stand a better chance? *International Journal of Forecasting*, 2000, 16: 71- 83
- [14] Energy Balance 2004, Energy balance, published by Ministry of Energy, Iran, 2004.
- [15] Ghaderi, S.F., Azadeh, A. and Mohammadzadeh, S., Modeling and forecasting electricity demand for major economic sectors in Iran. *Information Technology Journal* 2006, 5(2), 260-266.
- [16] Goldberg, D.E, Genetic algorithm in search, optimization and machine learning. Harlow, England: Addison-Wesley, 1989.
- [17] Haldenbilen, H. Ceylan, Genetic algorithm approach to estimate transport energy demand in Turkey. *Energy Policy*, 2004, 11, 89-98
- [18] Hasheminia, H. and Akhavan Niaki, S.T., A genetic algorithm approach to fit the best regression/econometric model among the candidates. *Applied Mathematics & Computation*, 2006, in press.
- [19] Holland. J.H., Adoption in Neural and Artificial Systems, The University of Michigan Press, Ann Arbor, MI, USA, 1975.
- [20] Karabulut, K., Alkan, A., Yilmaz, A.S., Long term energy consumption forecasting using genetic programming *Mathematical and Computational Applications*, 2008, 13 (2), 71-80
- [21] Montgomery, D.C. Design & Analyze of Experiments, Jhon Wiley & Sons, New York, 2001.
- [22] Ozturk, H., Canyurt, H., Hepbasli, A. and Utlu, Z., Three different genetic algorithm approaches to the estimation of residential energy input/output values. *Building and Environment* 2003a, (39), 807-816.
- [23] Ozturk, H., Ceylan, H., Canyurt, O.E. and Hepbasli, A., Electricity estimation using genetic algorithm approach: a case study of Turkey. *Energy* 2003b, (30), 1003–1012.
- [24] Pai, P.-F., Hong, W.-C., Forecasting regional electricity load based on recurrent support vector machines with genetic algorithms, *Electric Power Systems Research* 2005, 74 (3), 417-425
- [25] Park, M.D., Merchant, R., Dinh, T., Tong, C., AzeemFarah, A. J., Drake, C., Practical experiences with an adaptive Neural Network short-term load forecasting system", *IEEE Transactions on Power Systems*, 10, 1995, No. 1, 254-265
- [26] Sadeghi, M. Demand stability for energy in Iran. PhD Dissertation, Faculty of Economics, University of Tehran, Iran, 1999.
- [27] Sadeghi, N. Forecasting and modeling electricity demand by an econometric model. MS Thesis, Faculty of Economics, University of Tehran, Iran, 2003.
- [28] Unsihuay-Vila, C., Zambroni de Souza, A.C., Marangon-Lima, J.W., Balestrassi, P.P., Electricity demand and spot price forecasting using evolutionary computation combined with chaotic nonlinear dynamic model, *Optimization and Engineering*, 2009, in Press
- [29] Wang, J., Liu, Z., Lu, P., Electricity load forecasting using rough set attribute reduction algorithm based on immune genetic algorithm and support vector machines, *Proceedings of International Conference on Risk Management and Engineering Management*, 2008, art. no. 4673233, 239-244
- [30] Zhang, G. P., Oi, M., Neural networks forecasting for seasonal & trend time series. *Journal of Operational Research*, 2005, 160, 501-514.

Application of Principal Component Analysis to the Study of Trace Metals in Sediment from Sulaibikhat Bay, Kuwait

Hassan Alshemmari

Environmental Science Department, Kuwait Institute for Scientific research. (hshamari@kisir.edu.kw)

ABSTRACT

Surface sediment samples were collected from 35 locations in Sulaibikhat Bay, Kuwait. As, Cd, Co, Cr, Cu, Hg, Ni, Pb, Zn and Hg concentrations were determined. Grain sizes, total organic carbon (TOC), carbonate and mineralogical data were determined. The abundance of the trace metals, their geographical distribution, and their relationships with each other and with sediment and environmental parameters are described. Principal component analysis (PCA) were applied to the data matrix to identify the possible pollution sources. Six principal components were extracted. They covered 84.2% of the variance and the scatter plot of scores on the first two principal components PC1 and PC2 shows a separation between the stations, influenced by the Ghazalli outfall waste discharge. PC1 loads highly against TOC, calcium carbonate (negatively), Hg, Cu, Pb, Zn and pyrite, with an explained 38.7% of the variance. PC2 loads against sand (negatively), Co, Ni, silt and aragonite (negatively), with an explained 15.0% of the variance. The statistical techniques applied in this study proved to be useful tools for interpreting the environmental data in Sulaibikhat Bay.

Keywords: Principal component analysis, Grain sizes, Sediment, Aragonite

1. INTRODUCTION

Urbanization and industrial expansion have put remarkable ecological stress on the Kuwaiti environment. There are serious concerns, not only for the integrity and productivity of the coastal ecosystem, but also for the safety of potable water produced by coastal desalination plants (Khan et al., 1999; Alshemmari, 2009; Alshemmari et al., 2010). The Kuwaiti marine environment is exposed to a range of polluting discharges, including industrial and municipal wastewaters, desalination and power plant effluents, and urban runoff (Al-Muzaini, 2002). Al-Muzaini (2000) also considered municipal sewage to be an important source of pollution in Kuwait's marine environment.

The behaviour and fate of elements in the environment is governed by a range of factors which affect their availability and mobility. This wide range of sedimentary physical, and chemical measurements (geochemical factors) such as grain size, minerals, surface area, surface charge, cation exchange capacity, organic and carbonate contents. Sediment is a significant part of the marine ecosystem and constitutes a major reservoir for trace species entering the aquatic environment from natural and anthropogenic sources. Sediments are usually regarded as the ultimate sink for some pollutants from water (e.g. trace metals) (Tack and Verloo, 1995; Shuttleworth et al., 1999; Hlavay et al., 2004; Alshemmari, 2009). Marine sediments are heterogeneous mixtures of components of different origins and chemical behaviours. Trace metals are present, at low concentrations, throughout the natural environment. They may be present in many different forms and in different environmental compartments (e.g. in water, sediment, and biota). They generally have numerous sources, and these can be natural (e.g. rock

weathering) or anthropogenic (e.g. sewage discharges). Anthropogenic activity may elevate their environmental concentrations far beyond natural levels (Yuan et al., 2004; Cuong and Obbard, 2006). Trace metals entering the marine environment are distributed in surface waters by physical (i.e. water movement) or chemical and biological (scavenging) processes and accumulate in the sediment in a variety of forms.

Statistical treatments of physical, chemical and mineralogical data range from the calculation of relatively simple correlation coefficients through highly complex multivariate techniques (e.g. principal component analysis). In this study principal component analysis (PCA) is used to extract components as function variables in the data set, thus determining the influence of hidden or unmeasured or unmeasurable effects on the data distribution. PCA outputs simplify the identification of the key controls on trace metal in Sulaibikhat Bay. Further, the results of the PCA detect the latent or theoretical factors of the data set and reduce its dimensionality to allow exploration of the correlations between trace metals and different controlling factors.

2. METHODOLOGY

2.1 Sampling and sample analysis

Sediment samples were taken from 35 different sampling sites from Sulaibikhat Bay. The surface sediment samples (~0.3g dry) were digested in Teflon reaction vessels for total trace metals extraction according to the modified MOOPAM, (1999) (ROPME). The grain sizes, TOC, carbonate and mineralogical data were determined. Sample collection and analysis were described in details in (Alshemmari et al., 2010).

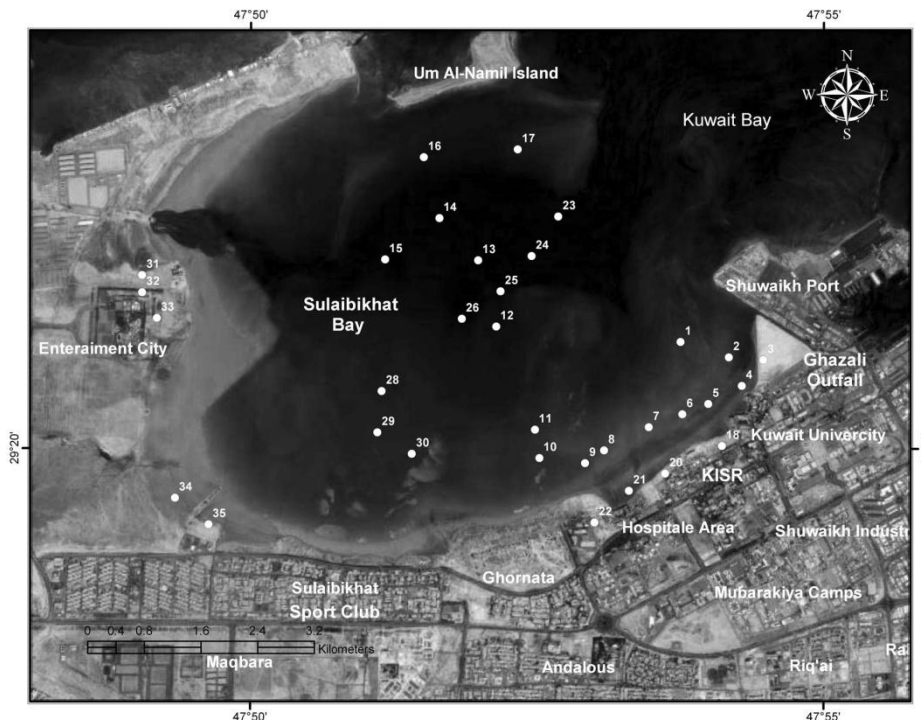


Figure 1. Location of sampling site in the Sulaibikhat Bay

2.2 Statistical analysis

The principles of PCA, and the way in which it can be applied to reduce the number of variables in a data set and detect structure in the relationships between those variables. There are many publications that deal with PCA; some of these are included in the reference list (e.g., Kinneer and Gray, 1994; Fabrigar et al., 1999; O'Connor, 2000; Harris, 2001). For PCA, the following assumptions are made about the data (Kinneer and Gray, 1994; Harris, 2001). For a satisfactory PCA, the variables should not exhibit multicollinearity; that is, the variables should not be highly intercorrelated. If intercorrelations are too high, collinear terms should be combined or otherwise eliminated before PCA. The Kaiser-Mayer-Olkin (KMO) test may be used to assess multicollinearity in PCA (Kinneer and Gray, 1994). Assumption of adequate sample size as a minimum, there must be more cases (samples) than components. It is essential to ensure sample adequacy before PCA is undertaken.

The KMO test and Bartlett's test of sphericity can be used to achieve this. PCA requires that the KMO index of sampling adequacy is greater than 0.50. In addition, the probability associated with Bartlett's test should be less than the level of significance, which is 0.001 (Kinneer and Gray, 1994). Using the variables of all the trace metals with grain size, mineralogy, TOC and calcium carbonate content produced a KMO value of 0.57, which exceeds the minimum requirement of 0.50 and confirms the suitability of the data for principal component analysis (Table 1). Moreover, the results of

Bartlett's test for sphericity were less than the level of significance. Thus, both tests indicated the suitability of the sample data for PCA.

Table 1: KMO and Bartlett's Test

Kaiser-Meyer-Olkin Measure of Sampling Adequacy.		.571
Bartlett's Test of Sphericity	Approx. Chi-Square	1325.496
	Df	276
	Sig.	.001

From a set of p variables, p components can be extracted. The variance in the correlation matrix is converted into p eigenvalues. Each eigenvalue represents the quantity of variance measured by one component. The first component represents the largest possible variance. The second component accounts for the second largest amount of variance, and so on. The eigenvalue of each component may be compared to 1 to observe how much more or less variance it represents than does a single variable (Kinneer and Gray, 1994; Harris, 2001). Generally, an initial judgment can be made about how many components to retain on the basis of an initial unrotated extraction. The major justification for the rotation method is to decrease the complexity of the components by making large loadings larger and small loadings smaller within each

component. Rotation involves maximizing the relationships between the variables and some of the components; it helps to produce a more understandable output. The sums of eigenvalues are not affected by rotation. Varimax rotation is an orthogonal rotation of the component axes yielding results that simplify the identification of each variable with a single component by maximizing the variance of the squared loadings of a component in a component matrix. The Varimax rotation results of each component will tend to have either large or small loadings for a particular variable (Kinnear and Gray, 1994; Harris, 2001).

3. RESULTS AND DISCUSSION

Table 2 shows the components extractable from the analysis with their eigenvalues, the percent of variance attributable to each component, and the cumulative

variance of the component. Six principal components (PC1–PC6) describe almost 84% of the total variance of the system. All the remaining components are insignificant. PC1 loads highly against TOC, calcium carbonate (negatively), Hg, Cu, Pb, Zn and pyrite, with an explained 38.7% of the variance (Table 2 and 3). PC2 loads against sand (negatively), Co, Ni, silt and aragonite (negatively), with an explained 15.0% of the variance, whereas PC3 loads against alkali feldspar, gypsum and calcite, with an explained 11.2% of variance (Table 2 and 3). PC4 includes clay, As, chlorite and illite, with an explained variance of 8.39%. PC5 includes Cr, plagioclase feldspar and dolomite, with an explained variance of 6.54%. PC6 includes muscovite and kaolinite, with an explained variance of 4.36% (Tables 2 and 3).

Table 2: Eigenvalues and Percentage Variance Explained for the Varimax Rotated Principal Components

Component	Initial Eigenvalues			Rotation Sums of Squared Loadings		
	Total	% of Variance	Cumulative %	Total	% of Variance	Cumulative %
1	9.30	38.74	38.74	5.63	23.46	23.46
2	3.59	14.97	53.70	4.68	19.50	42.96
3	2.68	11.17	64.87	3.15	13.12	56.07
4	2.01	8.39	73.26	2.46	10.27	66.34
5	1.57	6.54	79.80	2.43	10.12	76.46
6	1.05	4.36	84.17	1.85	7.71	84.17

Table 3: Varimax Rotated Loadings (only those greater than 0.1 are shown, irrespective of sign)

Variables	Principal Component					
	1	2	3	4	5	6
Clay	0.15	0.33	-0.26	0.63	0.29	-0.11
Sand	-0.25	-0.86	-0.27	-0.23	-0.12	
TOC	0.90	0.13	0.18	0.23	-0.13	0.14
CaCO ₃	-0.61	-0.43		-0.48		-0.26
Hg	0.95					
As	0.23	0.21		0.72		
Co	0.38	0.81	0.18	0.37		
Cr	-0.12	0.58	-0.12		0.66	
Cu	0.91	0.29	0.15	0.19		
Ni	0.34	0.81	0.22	0.36		
Pb	0.85	0.32		0.18		
Zn	0.91	0.30	0.11	0.21		
Silt	0.22	0.83	0.41			
Chlorite		0.24	0.55	0.59		0.39
Illite	0.35	0.23	0.49	0.52	-0.25	0.23
Muscovite		-0.15			0.14	0.90
Alkali feldspar			0.82	-0.13	0.17	-0.22
Plagioclase feldspar	-0.14	-0.15		0.11	0.90	
Gypsum	0.17	0.18	0.84	0.15	-0.16	
Calcite		0.34	0.80	-0.13		0.23
Dolomite					0.91	
Aragonite		-0.79		-0.19	0.15	0.20
Pyrite	0.61	-0.21	-0.28	-0.30	-0.17	0.35
Kaolinite	0.38			0.17	-0.14	0.65
Explained Variance (%)	38.74	14.97	11.17	8.39	6.54	4.36

Of these six components of the system, the first three account for 64.8% of the total variance of the system. The 2-D loading plots (Figure 2) show the relationships between the variables. PC1 shows Hg, Cu, Pb, Zn and pyrite grouped together with TOC. Concentrations of Hg, Cu, Pb, Zn and pyrite are influenced by variations of TOC and the amount of carbonate. Organic carbon shows a significant positive correlation with Hg, Cu, Pb, Zn and pyrite, whereas calcium carbonate shows a significant negative correlation with Hg, Cu, Pb and Zn. Previous geochemical studies have demonstrated that TOC plays an important role in determining trace-metal concentrations in sediments (Förstner and Wittmann, 1979; Salomons and Förstner, 1980; Horowitz et al., 1989; Rasmussen et al., 1998).

positively with Co, Ni and silt; however, these two groups are negatively correlated with each other. The 2-D loading plots (Figure 2) show the variables of PC2 in two separate locations at the top and bottom of the two plots. PC3 is loaded positively with a group of variables that includes only minerals (alkali feldspar, gypsum and calcite). In this study, PC1 and PC2 were used to interpret the relationships between trace metals and other variables. Sediments with high TOC contain high concentrations of trace metals such as Hg, Cu, Pb and Zn. Sediments of silt grain size contain high concentrations of trace metals such as Co and Ni. In addition, sediments with high calcium carbonate or sand contents contain low concentrations of trace metals such as Hg, Cu, Pb, Zn, Co and Ni.

PC2, is loaded highly negatively with a group of variables including sand and aragonite and loaded

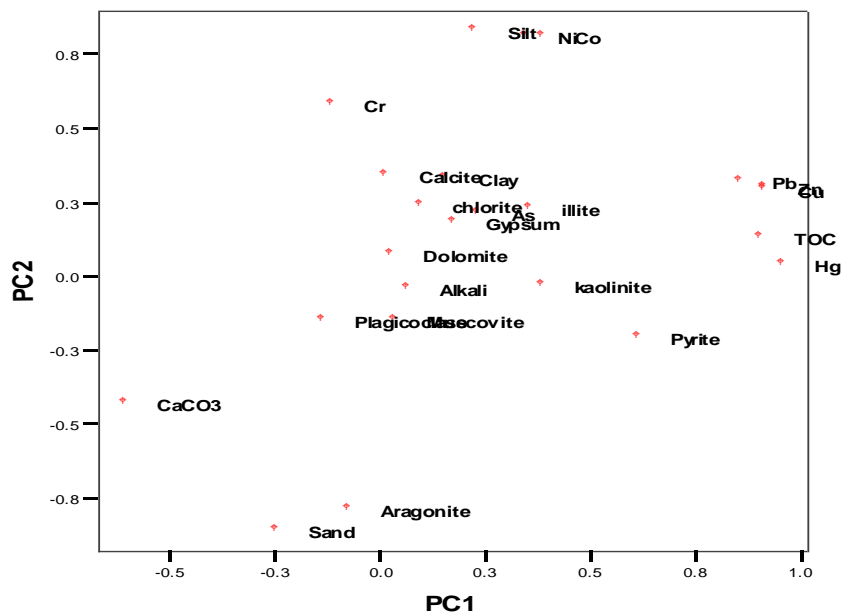


Figure 2: PCA loading 2-D plot (PC1 vs. PC2) for TOC, calcium carbonate, total trace metals, grain size and minerals

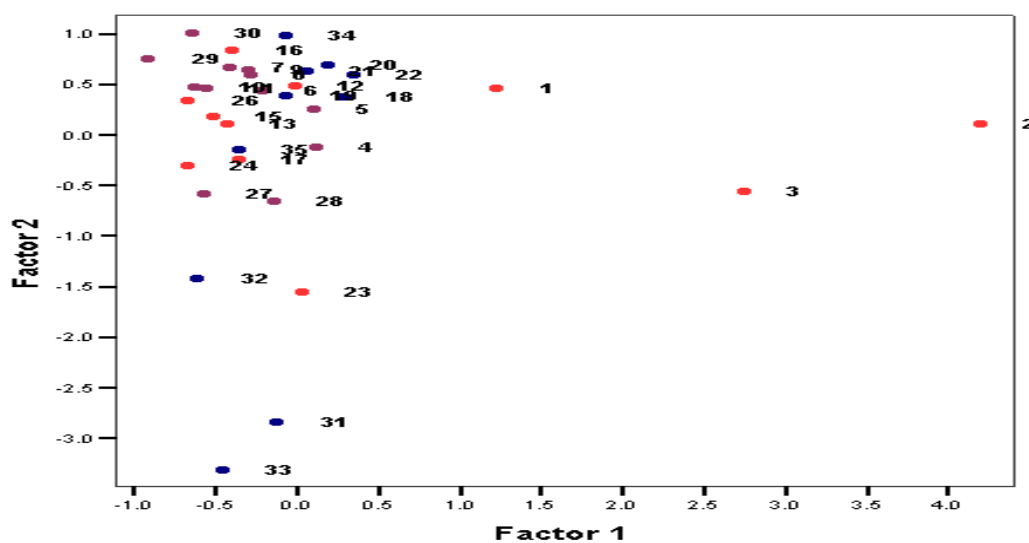


Figure 3: Component score plot showing sampling stations in 2-D for the first two factors

The PCA results using plots of component scores for sampling sites as objects are shown in (Figure 3). From these, three groups are identified. The first contains the heavily polluted sites located near the Ghazali outfall (sites 1, 2, 3). The second group includes moderately polluted sites located in either the central channel or the upper tidal flat (sites 4, 5, 6, 7, 9, 10, 11, 12, 13, 14, 15, 16, 17, 18, 19, 20, 21, 22, 24, 25, 26, 28, 29, 30, 34). The third group contains unpolluted sites (sites 8, 23, 27, 31, 32, 33, 35) where sediments with high calcium carbonate or sand contents predominate.

4. CONCLUSION

Multivariate statistical techniques were used in this study to assess the degree to which mineralogical and sedimentological factors in sediments from Sulaibikhat Bay control trace-metal abundances in geochemical extracted. The relationships between variables were described. The analysis shows that grain size, TOC, calcium carbonate and minerals clearly influence trace-metal concentrations. principal component analysis was applied to the data matrix to identify environmental factors and possible pollution sources. Six components that account for almost 84% of the total variance of the system were extracted. PC1 contains predominantly sediments that have high TOC and are rich in trace metals, whereas PC2 includes coarse aragonite. The 2-D loading plots show the relationships between these variables. Scatter plots of scores for the first two components (PC1 and PC2) show a differentiation of the stations influenced by waste discharge from the Ghazali outfall. The statistical technique of principal component analysis applied in this study proved to be useful tools for interpretation of environmental data in Sulaibikhat Bay.

ACKNOWLEDGEMENTS

The authors would like to thank Dr. A. N. Al-Ghadban, Head of the Environmental Science Department at Kuwait Institute for Scientific Research (KISR) for his encouragement and support. KISR is greatly appreciated for its financial support.

REFERENCES

- [1] Al-Muzaini, S. (2002) Sewage discharge impact on the development of the Shuwaikh. *Technology* 8, 51-54.
- [2] Alshemmari, H. (2009). Prediction of element speciation in sediments from Sulaibikhat Bay, Kuwait. Ph.D. Thesis, Newcastle University.
- [3] Alshemmari, H., Alotaibi, Y., Owens, R. (2010). Trace metal concentrations in the surface sediments of Sulaibikhat Bay, Kuwait. *Kuwait Journal of Science and Engineering* 37 (2A), 87-110.
- [4] Cuong, D. T. & Obbard, J. P. (2006) Metal speciation in coastal marine sediments from Singapore using a modified BCR sequential extraction procedure. *Applied Geochemistry* 21, 1335-1346.
- [5] Fabrigar, L. R., Wegener, D. T., MacCallum, R. C. & Strahan, E. J. (1999) Evaluating the use of exploratory factor analysis in psychological research. *Psychological Methods* 4, 272-299.
- [6] Förstner, U. & Wittmann, G. (1979) Metal Pollution in the Aquatic Environment, Springer, New York.
- [7] Harris, R. J. (2001) A Primer of Multivariate Statistics (3rd Edition), Lawrence Erlbaum Associates, London.
- [8] Hlavay, J., Prohaska, T., Weisz, M., Wenzel, W. W. & Stingeder, G. J. (2004) Determination of trace elements bound to soil and sediment fractions. *Pure and Applied Chemistry* 76(2), 415-442.
- [9] Horowitz, A. J. (1991) A Primer on Sediment-Trace Element Chemistry. Lewis Publishers, Michigan, USA.
- [10] Khan, N. Y., Saeed, T., Al-Ghadban, A. N., Beg, M. U., Jacob, P. G., Al-Dousari, A. M., Al-Shemmari, H., Al-Mutari, M., Al-Obaid, T. & Al-Matrouk, K. (1999) Assessment of sediment quality in Kuwait's Territorial Waters. *Phase I: Kuwait Bay*. Kuwait Institute for Scientific Research.
- [11] Kinnear, P. R. & Gray, C. D. (1994) SPSS for Windows Made Simple. Lawrence Erlbaum Associates, Hove, U.K.
- [12] MOOPAM (Manual of Oceanographic Observations and Pollutant Analyses Methods) 1999. Third Edition. ROPME (Regional Organization for the Protection of the Marine Environment), Kuwait.
- [13] O'Connor, B. P. (2000) SPSS and SAS programs for determining the number of components using parallel analysis and Velicer's MAP test. *Behavior Research Methods, Instrumentation, and Computers* 32, 396-402.
- [14] Rasmussen, P. E., Villard, D. J., Gardner, H. D., Fortescue, J. A. C., Schiff, S. L. & Shilts, W. W. (1998) Mercury in lake sediments of the

Precambrian Shield near Huntsville, Ontario, Canada. *Environmental Geology* 33, 170–181.

- [15] Salomons, W. & Förstner, U. (1980) Trace metal analysis on polluted sediments-Part II. Evaluation of environmental impact. *Environmental Technology Letters* 1, 506-517.
- [16] Shuttleworth, S. M., Davison, W. & Hamilton-Taylor, J. (1999) Two-dimensional and fine structure in the concentrations of iron and manganese in sediment pore-waters. *Environment Science and Technology* 33, 4169-4175.
- [17] Tack, F. M. G. & Verloo, M. G. (1995) Chemical speciation and fractionation in soil and sediment heavy metals analysis. *International Journal of Environmental Analytical Chemistry* 59, 225-228.
- [18] Yuan, C., Shi, J., He, B., Liu, J., Liang, L. & Jiang, G. (2004). Speciation of heavy metals in marine sediments from the East China Sea by ICP-MS with sequential extraction. *Environment International* 30, 769-783.

Concentrations of natural and manmade radioactive nuclides for Wadi Al-Numan area in Makkah Al-Mukarramah Province

Safiah Q. Hamidalddin¹, Afaf A. Fakeha², Zaina Suleiman Mohammad Al-Garni³, Nagdy M. Ibraheim⁴

¹Department of Physics, Faculty of Science for Girls, King Abdulaziz University, Jeddah, Saudi Arabia, Tel.:

+966503670645, (safiahqh@yahoo.co)

²(afafageha@yahoo.com),

³(sky1401@hotmail.com)

⁴(Nuclear Safety Centre) EAEA

ABSTRACT

Fifteen surface soil samples were sampled for analysis. In situ a gamma-ray spectrometer based on NaI(Tl) crystal was applied for the determination of the ²²⁶Ra and ²³²Th series and ⁴⁰K concentrations. Also a gamma-ray Scout system was used to give the dose rate μ Sv/h at each point. Samples were analyzed by a gamma-ray spectrometer based on HPGe crystal detector, for the concentrations in Bq/kg dry weight for the ²²⁶Ra and ²³²Th series and ⁴⁰K. Also concentrations of K, Al, Bi, Pb, & Th in ppm and in percent were measured by an ICP- atomic absorption spectrometer. An XR-diffraction spectrometer was used for the mineral compositions.

Two underground water samples from the study area Wady Alhusienieh and Wady Abu Dieh (Western province of Saudi Arabia) were analyzed by both an atomic absorption spectrometer for the; Ca, Na, Mg, K, Fe, Al, Cs, Hg, Bi, Pb and U concentrations, and a HPGe gamma-ray spectrometer system for the concentrations of radioactive nuclides of the ²²⁶Ra and ²³²Th series and ⁴⁰K from the absorbed dose which calculated for the age categories ; <1y, 1-2y, 2-7 y, 7-10y and > 17y.

Key words: atomic absorption, gamma-ray spectrometry, natural radioactivity, absorbed dose.

1. INTRODUCTION

Umm al Qura university buildings are situated in Wadi Al Numan area in Makkah Al-Mukarramah province so a detailed study of this area, surface soil and water, is of great importance. The study area was divided to 15 parts. Fifteen surface soil and two underground water samples. A global positioning system (GPS) was used to point the sampling axes, (longitude, latitude, altitude). The area has a commercial value for the huge building materials found in this area.

Study of radioactivity levels and concentrations of natural and man-made radionuclides have been done all over the world. In Egypt (Ibrahiem et al 1993) gave a base map for the radioactivity in the Delta and middle Egypt, by a HPGe gamma-ray system they measured the absorbed dose one meter above the ground in each point. Also (Ibrahiem et al 1995) studied sediments and surface area of Naser lake area by both neutron activation analysis and gamma-ray spectroscopy techniques. Amaral, 2000, in Portugal studied gamma-ray spectrum and dose rate. In Situ, also studied the type and composition of the different rocks, as well as the mechanical, chemical and biological properties for each type of soil. Morton et al, 2006, measured the natural radioactivity concentrations of ²³²Th, ²³⁸U, ²²⁶Ra series and ⁴⁰K, as well as the man made ¹³⁷Cs. Also they studied the salinity level in the

soil from the series of the black plateau resulting from the flood of Virgin River, south-east of Nevada State USA. Also they analyzed the samples by EDS electron dispersion spectrometer in addition XRD diffraction spectrometer for the soil composition. Wu, 2006 studied the accumulation of radioactive concentrations owing to the long period of irrigation according to the Yucca Mountain program of Nevada State USA to point out, time needed to reach equilibrium, the suitable time for irrigation, study of agricultural areas irrigated for long time and the change of concentrations of radioactive nuclides in water.

The aim of this work is to make base line map for the study area, to be compared with future studies for any environmental or geological changes. Study of the relation between type of soil and the radioactivity level, measurements of dose rate for population in this area, also relation between the geological composition of the soil and the dose rate.

2. GEOLOGY OF THE STUDY AREA

It lies east of the Red sea between 21 15 00 and 21 30 00 latitude north, 39 45 00 and 40 00 00 longitude east and elevation between 281 and 326 m above the sea level. Rate of rain between 28 mm to 273.9 mm per year, average of 115.6 mm (from the year 1980 to 1995), (Saudi Geological Survey, 2010).

Four types of rocks are found in the study area:

- 1- Metamorphic rocks.
- 2- Mafic rocks.
- 3- Felsic rocks.
- 4- Quaternary deposits.

3. SAMPLING AND SAMPLE PREPARATION

The study area was divided to 15 part, a sample was collected from each part.

Sampling was done from 0-5 cm by a template 25x25x5cm. Samples were collected in a polyethylene bags, then labeled. Remains of plants, weeds and rocks were removed, soil samples were grinded, sieved with a 1mmx1mm mesh sieve, mixed for homogeneity. Samples were dried to 80 °C not to lose the volatile of ^{137}Cs , or the natural polonium. A 640 cc sample was weighed then stored for one month in a polyethylene Marinelli beaker, for gamma-ray spectrometry, to reach secular equilibrium between ^{226}Ra and ^{232}Th and their progeny, also 10 gm of the dried sample was used for the analysis by atomic absorption for the K, Al, Bi, Pb and Th concentrations. Also 10 gm for XRD for the chemical and mineral composition. Also samples were mechanically analyzed for the type of soil, clay, sandy, loamy, etc. During the sampling a Global Positioning System model GARMIN GPS 45 was used to point latitude, longitude and altitude of each point.

Also two underground water samples from two wells in the study area, about five liters were collected in polyethylene beakers, then acidified with concentrated nitric acid to prevent the adsorption of the radioactive nuclides on the bottle surface, which may change their concentrations.

Sampling was done obeying methods adopted by (RADREM, 1980).

4. MEASUREMENTS

In Situ NaI(Tl) detector model GR-320 was used during the sampling to measure the concentrations of ^{226}Ra and ^{232}Th series as well as ^{40}K concentrations from the gamma-ray transitions 1764, 2615 and 1460 keV respectively. In the same time a GAMMA-SCOUT dose meter was applied for the dose rate nGy/h in every sampling point.

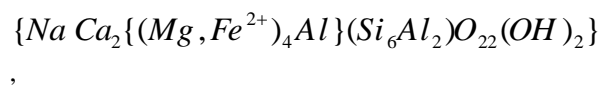
An X-ray diffraction spectrometer model Burker XRD D8 Advance was applied for the chemical and mineral composition. Also an inductively coupled plasma atomic absorption spectrometer of A-Analyst 700 model Perkin Elmer OPTIMA 4000 DV series, for the concentrations of Th, Pb and Bi ppm and K and Al %.

A gamma-ray spectrometer based on a HP Ge crystal of the vertical type Tennelec model number CPVDS 530-15200 was applied for the concentrations of ^{226}Ra and ^{232}Th series and ^{40}K as well as the manmade ^{137}Cs . Energies in keV of 295.2 (20.1) and 351.9 (38.3) ^{214}Pb and 609.3 (49.9), 1120.3 (16.2) and 1764.5 (16.0) ^{214}Bi were used for the ^{226}Ra series. 338.4(13), 911.16 (30.3) and 968.97 (18.3) ^{228}Ac and 727.25 (8.1) ^{212}Bi , also 583.02(33.2) and 2614.48 (35.9) ^{208}Tl for the ^{232}Th series (Saito and Moriuchi; 1985). 1460.8(10.7) for the ^{40}K and 661.65 (89.9) for the ^{137}Cs (Holden; 2003).

5. RESULTS AND DISCUSSION

The mechanical analysis for the soil classification shows that soil type are two categories silty sand and sand clay mixture.

Table (1) represents XRD analysis results it shows the major and minor minerals. The major mineral is the quartz $\{\text{SiO}_2\}$, the next are albite $\{\text{Na Al Si}_3 \text{O}_8\}$, pargasite



and microline $\{\text{K Al Si}_3 \text{O}_8\}$

Table (2) gives concentrations of Al and K in percent (%), Bi, Pb and Th in ppm by atomic absorption analysis. Thorium concentrations range from <DL to 5.55 ppm an average of 3.0 ppm. The stable lead (^{206}Pb , ^{207}Pb and ^{208}Pb) from 12.4 to 25.9 ppm with an average 18.4 ppm. Bismuth (^{209}Bi) from <DL (<10 ppm) to 21.8 ppm. Potassium from 1.4 to 2.8 % with an average of 2%. Aluminum from 7.7 to 8.2 %.

Table (3) shows the results of the In Situ measurements. ^{226}Ra , ^{232}Th and ^{40}K as well as the dose rate $\mu\text{Sv/h}$ which can't be considered accurate results because of the interference of the background of the surroundings of soil and rocks. ^{226}Ra series concentrations ranged from ND to 2.4 ppm with an average 1.1 ppm. ^{232}Th series concentrations ranged from 1.4 ppm to 6.9 ppm with an average of 4.0 ppm. ^{40}K concentrations ranged from 1.7% to 3% with an average of 2.3%. The dose rate above the earth surface directly was from 0.08 $\mu\text{Sv/h}$ to 0.22 $\mu\text{Sv/h}$.

The results of gamma-ray spectrum by the HPGe system in Bq/kg dry weight for the silty sand show that, for ^{226}Ra series concentrations ranged from 9.2 to 11.6 with an average of 11.6, it is lower than the average 35 Bq/kg, given by UNSCEAR 2000.

²³²Thseries concentrations ranged, in Bq/kg dry weight, from 9.5 to 15.2 with an average of 12.5, which is lower than that, 35 Bq/kg, given by UNSCEAR 2000.

⁴⁰K concentrations, in Bq/kg dry weight, ranged from 378.2 = 1.3% to 557.8 =1.9% with an average of 481.3 =1.6%, which is lower than the average given by UNSCEAR 2000.

¹³⁷Cs (fallout) concentrations, in Bq/m², ranged from LDL to 31.4 with an average of 26.9.

For sand clay mixture, the ²²⁶Ra series concentrations, in Bq/kg dry weight, ranged from 10.1 to 18.1 with an average of 13.3. Which is lower than that given by UNSCEAR 2000.

²³²Thseries concentrations, in Bq/kg dry weight, ranged from 11.1 to 22.6, with an average 15.6 less than 35 given by UNSCEAR 2000.

⁴⁰K concentrations ranged from 454 =1.5% to 592.6=2.0% less than the value given by UNSCEAR 2000, 370.

¹³⁷Cs concentrations, in Bq/m², ranged from LDL to 164.1 with an average of 83.3.

Table (4) represents a comparison between the soil type and concentrations Bq/kg dry weight for ²²⁶Ra, ²³²Thseries and ⁴⁰K (range) average.

Radium equivalent is calculated from the equation (1), (Kumer et al, 2003)

$$Ra_{eq} = A_{Ra} + (A_{Th} \times 1.43) + (A_K \times 0.077) \quad (1)$$

Where: A_{Ra}, A_{Th} and A_K are concentrations Bq/kg for the ²²⁶Ra, ²³²Thseries and ⁴⁰K respectively.

Equation (2) was applied to convert concentrations Bq/kg to absorbed dose, using factors given by (Quidos et al, 2004).

$$D = C_{Re} A_{Re} + C_{Th} A_{Th} + C_K A_K \quad (2)$$

Where: D is the absorbed dose one meter above the earth nGy/h,

C_{Ra}, C_{Th} and C_K are conversion factors Bq/kg to nGy/h for radium, thorium series and K respectively,

While: A_{Ra}, A_{Th} and A_K are concentrations Bq/kg for Ra-226, Th-232 series and ⁴⁰K respectively.

Table (5) represents comparison between ²²⁶Ra, ²³²Th and ⁴⁰K concentrations and the calculated absorbed dose measured by gamma-ray spectrometry, In Situ and laboratory.

The results do not match in both techniques, because

of the interference of the back ground of the surroundings of soil and rocks in situ and there is a shield radiation surrounding the detector in the laboratory to overcome the background radiation. In situ, the measurements were calculated at the surface of the earth directly and the measurements of the annual doses were calculated at one meter from the surface of the earth. In addition, the samples at in situ contain various percentages of moisture, which affects the concentration measurements, while the samples were measured in the laboratory were sifted, dried and stirred.

Table (6) gives Conversion factors nGy/h per Bq/kg used in the present work and that used by (Amaral , 2000).

Table (7) gives a comparison between concentrations of isotopes in Bq/ kg dry weight in the present work and other publication of the same types of soil.

For the underground water Which is used for drinking and irrigation purposes, two samples (1) and (2) respectively were collected from Wady Alhusienieh and Wady Abu Dieh, the concentrations ppm and ppb were given ; for Ca, Na, Mg, K, Fe, Al, Cs, Hg, Bi, Pb and U respectively.

Concentrations in Bq/l for ²³⁸U (considering that ²³⁸U abundance is around 100%), ²²⁶Ra, ²³²Thseries and ⁴⁰K were calculated respectively.

Dose was calculated from the equation given by, (Desideri et al, 2007) :

$$E = KGCT \quad (3)$$

6. TABLES

Where: E is the dose Sv/y from drinking
 K is the conversion factor Sv/Bq
 G the rate of drinking water/ day for each age category, it were taken 0.7, 1, 1, 1 and 2 liters /day for <1 y, 1-2y, 2-7y, 7-10 y and > 17y respectively
 C is the concentration of the specific radionuclide (Bq/l)
 T is the duration of consumption, taken 365 days.

From the EU treaty the permissible (Total Inductive Dose) TID in drinking water is 0.1 mSv/y excluding the tritium and ⁴⁰K, which are distributed uniformly in the body. Also radon and its progeny was excluded, so the dose were calculated from uranium and radium only (Wisser, 2003).

Table (8) represents elemental concentrations in ppm or ppb measured by ICP-Atomic Absorption spectrometer from Wady Alhusienieh and Wady Abu Dieh samples (1), (2) respectively.

For Ca, the concentrations in ppm of both samples are in the accepted range. For Na, results show that both samples have concentrations in ppm higher than the guideline value set by EPA, and need chemical treatment before using for drinking purposes. For K, the concentrations in ppm of both samples are less than the acceptable values per a day per person. For Fe, the concentrations in ppm are <0.1. For Al, the concentrations in ppb of both samples are in the accepted range. For Cs, Hg and Bi, the concentrations in ppb are <0.1. For Pb, the concentrations in ppb are less than the guideline value set by EPA. For U, the concentrate

ions in ppb of both samples are in the accepted range. Table (9) Shows Concentration of radioactive nuclides in water samples (1) and (2) in Bq/l measured by HPGe.

The measured concentrations are 0.098 and 0.168 for ²³⁸U and LDL and 1.2 for ²²⁶Ra series and LDL for ²³²Thseries(²²⁸Ra), ⁴⁰K and ¹³⁷Cs.

Table (10) represents dose conversion factors for ²³⁸U, ²²⁶Ra and ²²⁸Ra in SvBq⁻¹.

Table (11) represents the annual dose measured from ²³⁸U, ²²⁶Ra and ²²⁸Ra in mSv/y for age class ≤ 1 y (infants) to class >17 y (adults).

The results show that the samples exceeded the annual limit of dose allowed by WHO (0.1 mSv/y) for all radioactive nuclides in drinking water, so samples need chemical treatment

Table 1: The mineral contents by XRD Spectrometer

Sample code	Type	Major	
Makk-1	Silty sand	QUARTZ,ALBITE, PARGASITE,	
Makk-3		QUARTZ,ALBITE,PARGASITE,	
Makk-4		QUARTZ,ALBITE,PARGASITE,	
Makk-6		QUARTZ,ALBITE, RICHTERITE	
Makk-9		QUARTZ,ALBITE, PARGASITE, MICROCLINE	
Makk-11		QUARTZ,ALBITE , PARGASITE, MICROCLINE	
Makk-2	Silty sand	QUARTZ, ALBITE, PARGASITE, MICROCLINE	
Makk-5		QUARTZ,ALBITE,PARGASITE,	
Makk-7		QUARTZ,ALBITE, PARGASITE, MICROCLINE	
Makk-8		QUARTZ,ALBITE, PARGASITE, MICROCLINE	
Makk-10		QUARTZ,ALBITE, PARGASITE, MICROCLINE	
Makk-12		QUARTZ,ALBITE, PARGASITE, MICROCLINE	
Makk-13		QUARTZ,ALBITE, PARGASITE	
Makk-14		QUARTZ,ALBITE, PARGASITE, MICROCLINE	
Makk-15		QUARTZ,ALBITE, PARGASITE, MICROCLINE	
		sand-clay mixture	

Table 1 Continued

Sample code	Type	Minor	Trace
Makk -1	Silty sand	MICROCLIN E	
Makk -3		MICROCLIN E	
Makk -4		MIOCROCLI NE	
Makk -6		MICROCLIN E	BIOTITE
Makk -9			VERMICULITE
Makk -11			CLINOCHLORE
Makk -2			AUGITE
Makk -5	sand-clay mixture	GYPSUM, MIOCROCLI NE	VERMICULITE, BIOTITE
Makk -7		CLINOCHLORE	BIOTITE
Makk -8			VERMICULITE, CLINOCHLORE
Makk -10		CLINOCHLORE	BIOTITE
Makk -12			CLINOCHLORE, BIOTITE
Makk -13		MICROCLIN E	CLINOCHLORE, MUSCOVITE
Makk -14			CLINOCHLORE, BIOTITE
Makk -15			CLINOCHLORE, BIOTITE

Table 2: Concentrations of Al, K, Bi, Pb and Th measured by Atomic Absorption Analyzer

Elements Units	Th ppm	Pb ppm	Bi ppm	K%	Al%
DL.*	1.00	7.50	10.00	0.05	0.05
Sample no.	Concentrations				
Mak 1	1.97	19.52	<10.0	2.00	8.48
Mak 2	3.09	17.13	<10.0	2.10	8.31
Mak3	1.89	21.11	<10.0	1.99	8.49
Mak 4	2.98	18.72	<10.0	1.77	8.24
Mak 5	2.75	15.54	<10.0	1.42	7.97
Mak 6	2.82	17.13	<10.0	1.96	8.21
Mak 7	<1.00	20.31	<10.0	1.82	8.72
Mak 8	2.57	18.72	<10.0	1.90	8.28
Mak 9	2.76	18.72	<10.0	2.21	8.08
Mak 10	2.85	21.11	21.81	2.15	7.90
Mak 11	2.26	12.35	10.18	2.81	7.66
Mak 12	2.50	14.74	19.95	1.94	8.06
Mak 13	3.55	15.54	19.27	1.97	8.28
Mak 14	4.42	25.88	12.03	2.02	8.08
Mak 15	5.55	19.52	16.49	1.94	7.89

*DL.:Detection Limit

Table 3: In Situ sample axes (latitude, longitude and elevation and concentrations of K %, ^{226}Ra , ^{232}Th series ppm, in addition to the dose $\mu\text{Sv/h}$

Sample code	Elevation (m)	Longitude (E)	Latitude (N)
Mak001	292	39.93548	21.326
Mak002	288	39.93095	21.32307
Mak003	284	39.92477	21.32058
Mak004	281	39.92545	21.32442
Mak005	286	39.92826	21.32742
Mak006	291	39.93428	21.32854
Mak007	291	39.93874	21.31957
Mak008	306	39.94633	21.31961
Mak009	305	39.95486	21.32035
Mak010	319	39.96634	21.32485
Mak011	308	39.95832	21.32571
Mak012	293	39.94696	21.3317
Mak013	326	39.98647	21.32631
Mak014	319	39.98235	21.31875
Mak015	311	39.97542	21.32312

Table 3 continued

Sample code	^{226}Ra (ppm)	^{232}Th (ppm)	K %	Dose rate $\mu\text{sv/h}$
Mak001	1.8	6.9	1.9	0.08
Mak002	1.7	2.1	2.6	0.11
Mak003	0.3	3.1	2.1	0.13
Mak004	1.5	2.9	1.9	0.13
Mak005	1.1	4.5	1.7	0.15
Mak006	1.2	1.4	2.2	0.12
Mak007	1.4	2.2	1.7	0.15
Mak008	2.4	2.8	2.4	0.15
Mak009	0.5	6.1	2	0.13
Mak010	1.9	3.6	2.8	0.15
Mak011	0.6	1.5	3	0.22
Mak012	0.1	2.3	2.2	0.13
Mak013	1.5	6.7	2.2	0.15
Mak014	N D	6.9	2.7	0.19
Mak015	0.3	6.9	2.6	0.18

Table 4a: Comparison between the soil type and concentrations in Bq/kg dry weight for ^{226}Ra , ^{232}Th series and ^{40}K and ^{137}Cs in Bq/m² (range) average.

Classification	NO. of sample	Concentrations	^{226}Ra series
		DL	0.68 ± 0.16
sand-clay mixture	9	(Range)	$(10.1 \pm 0.56 - 18.1 \pm 0.39)$
		(average) in Bq/kg and Bq/m ²	(13.3 ± 0.18)
silty sand	6	(Range)	$(9.2 \pm 0.66 - 14.1 \pm 0.64)$
		(average) in Bq/kg and Bq/m ²	(11.6 ± 0.25)

Table 4b

Classification	NO. of sample	Concentrations	^{232}Th series
		DL	0.53 ± 0.16
sand-clay mixture	9	(Range)	$(11.1 \pm 0.65 - 22.6 \pm 1.18)$
		(average) in Bq/kg and Bq/m ²	(15.6 ± 0.44)
silty sand	6	(Range)	$(9.5 \pm 1.1 - 15.2 \pm 0.95)$
		(average) in Bq/kg and Bq/m ²	(12.5 ± 0.44)

Table 4c

Classification	NO. of sample	Concentrations	⁴⁰ K
		DL	7.84 ± 1.10
sand-clay mixture	9	(Range)	(454.0 ± 4.31 - 592.6±3.92)
		(average) in Bq/kg andBq/m ²	(514.9 ± 1.48)
silty sand	6	(Range)	(378.2 ± 4.83 - 557.8 ± 4.14)
		(average) in Bq/kg andBq/m ²	(481.3 ± 1.9)

LDL: Lower than Detection Limit

Table 4d

Classification	NO. of sample	Concentrations	¹³⁷ Cs
		DL	0.11 ± 0.06
sand-clay mixture	9	(Range)	(LDL- 164.1 ± 22.67)
		(average) in Bq/kg andBq/m ²	(83.3 ± 7.57)
silty sand	6	(Range)	(LDL- 31.4 ± 17.16)
		(average) in Bq/kg andBq/m ²	(26.9 ± 9.7)

Table 5 continued

Series , Nuclei	Th-232	Ra-226	K-40	Dose at distance 1m
Unit	Bq/kg	Bq/kg	%	µSv/h
No. of sample				
Mak1	9.5	10.7	1.7	0.023
Mak2	14.4	13.1	1.8	0.023
Mak3	10.5	12	1.7	0.023
Mak4	15.2	12.6	1.5	0.023
Mak5	12.9	12.3	1.5	0.023
Mak6	14.4	14.1	1.7	0.026
Mak7	11.1	10.1	1.6	0.022
Mak8	14.1	12.8	1.70	0.025
Mak9	10.1	9.2	1.3	0.018
Mak10	15.1	12.5	2.0	0.028
Mak11	15	11.1	1.9	0.026
Mak12	16.1	11.9	1.7	0.025
Mak13	16.4	14.5	1.9	0.028
Mak14	17.4	14.5	1.8	0.028
Mak15	22.6	18.1	1.8	0.031

Table 5: comparison between ²³²Th, ²²⁶Ra and ⁴⁰K concentrations and dose measured, by gamma-ray spectrometry, in Situ and in laboratory

Series , Nuclei	Th- 232	Ra-226	K-40	Dose on the surface
Unit	Bq/kg	Bq/kg	%	µSv/h
No. of sample				
Mak1	28.1	22.2	1.9	0.08
Mak2	8.5	21.0	2.6	0.11
Mak3	12.6	3.7	2.1	0.13
Mak4	11.8	18.5	1.9	0.13
Mak5	18.3	13.6	1.7	0.15
Mak6	5.7	14.8	2.2	0.12
Mak7	9.0	17.3	1.7	0.15
Mak8	11.4	29.6	2.4	0.15
Mak9	24.8	6.2	2.0	0.13
Mak10	14.7	23.4	2.8	0.15
Mak11	6.1	7.4	3.0	0.22
Mak12	9.4	1.2	2.2	0.13
Mak13	27.3	18.5	2.2	0.15
Mak14	28.1	ND	2.7	0.19
Mak15	28.1	3.7	2.6	0.18

Table 6: Conversion factors nGy/h per Bq/kg used in the present work and that is used by (Amaral, 2000)

Dose rate (nGy/h per Bq/kg)	Amaral, 2000	Qunidos et al, 2004
Ra-226 series	0.4500	0.4551
Th-232 series	0.6680	0.5835
K -40	0.0424	0.0429

Table 7: Comparison between concentration of isotopes Bq/kg dry weight in the present work and other publication of the same types of soil

Nuclide Or series	Soil origin	Ra-226 series	Th-232 series	K-40
References				
(Ibrahim et al., 1993)	clay loam, silty Clay loam, silty loam (1)	15.5	17.9	317
	sandy loam, sandy clay loam, sand clay (2)	14.8	15.5	228.6
Present work	sand-clay mixture	13.3	15.6	514.9
	silty sand	11.6	12.5	481.3

Table 8: Element concentrations in ppm or ppb measured by ICP-Atomic Absorption Analyzer in water samples 1 and 2 respectively

Elements	DL	Units	Sample-1	Sample-2
Ca	0.2	ppm	120.2	228.7
Na	0.2	ppm	115.3	135.7
Mg	0.2	ppm	25.6	53.6
K	0.2	ppm	3.9	4.6
Fe	0.1	ppm	<0.1	<0.1
Al	0.1	ppb	41.81	51.43
Cs	0.1	ppb	<0.1	<0.1
Hg	0.1	ppb	<0.1	<0.1
Bi	0.1	ppb	<0.1	<0.1
Pb	0.1	ppb	0.7	1.68
U	0.1	ppb	7.89	13.51

Table 9: Concentration of radionuclides in water samples in Bq/l measured by HPGe

LDL: Lower than Detection Limit.

Sample Code	Concentration in Bq/l			
	U-238 *	Ra-226 Series	Ra-228	K-40
DL.	0.001	0.40 ± 0.07	0.30 ± 0.07	4.6 ± 0.5
Sample - 1 Sample - 2	0.098 0.168	LDL 1.2 ± 0.1	LDL LDL	LDL LDL

*U-238 is measured as total uranium by atomic absorption spectrometry.

Table 10: Dose conversion factors for ^{238}U , ^{226}Ra , ^{228}Ra in SvBq^{-1}

Rad io-nuclide	Dose conversion factors (K)				
	≤ 1 y	1-2 y	2-7 y	7-10 y	> 17 y
^{238}U	3.4×10^{-7}	1.2×10^{-7}	8.0×10^{-8}	6.8×10^{-8}	4.5×10^{-8}
^{226}Ra	4.7×10^{-6}	9.6×10^{-7}	6.2×10^{-7}	8.0×10^{-7}	2.8×10^{-7}
^{228}Ra	3.0×10^{-5}	5.7×10^{-6}	3.4×10^{-6}	3.9×10^{-6}	6.9×10^{-7}

Table 11a: The annual dose measured from ^{238}U , ^{226}Ra , ^{228}Ra in mSv/y for age class ≤ 1 y to 1-2y

Doses in mSv/y	Age Class <1y		Age Class 1-2y	
	Sample 1	Sample 2	Sample 1	Sample 2
^{238}U Dose	0.0085	0.0146	0.0043	0.0073
^{226}Ra Dose	<0.5	1.4	<0.1	0.4
^{228}Ra Dose	<2.3	<2.3	0.6	0.6
Annual Dose $^{238}\text{U} + ^{226}\text{R} + ^{228}\text{R}$	<2.8	<3.8	<0.8	<1.1

Table 11b: The annual dose measured from ²³⁸U, ²²⁶Ra, ²²⁸Ra in mSv/y for age class 2-7 y to 7-10y

Doses in mSv/y	Age Class2-7y		Age Class7-10	
	Sample 1	Sample 2	Sample 1	Sample 2
²³⁸ U Dose	0.0029	0.0049	0.0024	0.0042
²²⁶ Ra Dose	<0.1	0.3	<0.1	0.4
²²⁸ Ra Dose	<0.4	<0.4	<0.4	<0.4
Annual Dose ²³⁸ U+ ²²⁶ R+ ²²⁸ R	<0.5	<0.6	<0.5	<0.8

Table 11c: The annual dose measured from ²³⁸U, ²²⁶Ra, ²²⁸Ra in mSv/y for age class >17y

Doses in mSv/y	Age Class>17y	
	Sample 1	Sample 2
²³⁸ U Dose	0.0032	0.0055
²²⁶ Ra Dose	<0.1	<0.2
²²⁸ Ra Dose	<0.2	<0.2
Annual Dose ²³⁸ U+ ²²⁶ R+ ²²⁸ R	<0.2	<0.4

REFERENCES

[83] Abulfaraj, W. & Abdul-Majid, S. (1991) Tevels of ¹³⁷Cs & Natural Radioactivity in Saudi Arabian Soil, *Transactions of the American Nuclear Society* 63 :58-59.

[84] Ahmad, N., Matiullh., Hussein, A.J.A.(1998) Natural Radioactivity in Jordanian soil & Building Materials and the Associated Radiation Hazards, *J. Environ Radioactivity* 39(1):9-22.

[85] Alencar, A. S. & Freitas, A.C. (2005) Reference levels of natural radioactivity for the beach Sands in a Brazilian south-eastern coastal region, *Radiation Measurements* 40 : 76- 83

[86] Amaral, E.M.(2000) Natural gamma radiation in air versus soil natural in Portugal, The 10th International Congress of the International Radiation Protection Association (IRPA), May14-19, Hiroshima.

[87] Bowles, J.E. (1978) Engineering Properties of Soils &their Measurement, McGraw-Hill Book

Company, New York.

[88] Debertin, K. & Helmer, R. (1988) Gamma and X-ray spectrometry with semiconductor detectors, Amsterdam North-Holland

[89] Desideri, D., Meli M.A., Feduzi,L., Roselli, C, Rongoni,A and Saetta, D. (2007),²³⁸U,²³⁴U ²²⁶Ra & ²¹⁰Po concentrations of bottled Mineral Waters in Italy and their Dose contribution, *Journal of Environmental Radioactivity*, 94 (2) :86- 97.

[90] Ibrahiem, N.M., Abd El Ghani, A.H., Shawky, S.M., Ashraf, E.M., & Farouk, M.A. (1993) Measurement of Radioactivity levels in soil in the Nile delta & middle Egypt, *Health Phys* 64 (6) : 620-627.

[91] Ibrahiem, N.M., Shawky, S.M. & Amer, H.A. (1995) Radioactivity levels in lake Nasser sediments, *Appl. Radial. Isot.* 46 (5):297-299.

[92] Ibrahiem, N.M. (2003) Radioactive disequilibrium in different rock types in Wadi Wizr, the Eastern desert of Egypt, *Applied Radiation and Isotopes* 58:385-392.

[93] Kumar, A., Kumar, M., Singh, B.& Singh, S.(2003) Natural activities of ²³⁸U , ²³²Th & ⁴⁰K in some Indian building materials, *Radiation Measurements* 36:465-469.

[94] Lederer, C.M. and Shirley, V.S. (1978) Table of Isotopes, 7th Edition, New York: John Wiley & Sons.Lederer, C.M. and Shirley, V.S. (1978) Table of Isotopes, 7th Edition, New York: John Wiley & Sons.

[95] Leet, I., & Judson, S. (1965). Physical Geology, 3rd edition, Englewood cliffs, New Jersey : Prentice-Hall, Inc.

[96] Melo,D. Lipsztein, J. L., Juliao, L., Lauria, D., Hacon, S., Dias da Cunha, K. & Cristina Lourenco, M. (2000) Internal chronic exposure to natural radionuclides, The 10th International Congress of the International Radiation Protection Association (IRPA),May14-19, Hiroshima, Japan: P-1a-24

[97] Morton, J., Buck, B., Merkler, D. & Wu, D. (2006) ²³⁸U, ²³²Th, ⁴⁰K & ¹³⁷Cs activity & salt mineralogy in the black butite soil series of the virin river flood plain NV,USA, *Health Phys* 90 (6) TAM-A.4.

[98] Saito, K. and Moriuchi, S. (1985) Development of a Monte Carlo Code for the Calculation of

Gamma Ray Transport in the Natural Environment, *Radiation Protection Dosimetry* 12 (1): 21-28.

- [99] Saudi Geological Survey & King Abdulaziz University Radiation Safety Committee, Faculty Of Engineering (2005) Environmental Radiation Study for The Holy City of Makkah Al Mukarramah, Report, SGS-CR-2005-1
- [100] Seelman-Eggebert, W., Pfennig, G. and Munzel, H. (1968) *Nuclearkarte*, 3rd Edition, Germany: Kernforschungszentrum Karlsruhe
- [101] Semkow, T.M., Parekh, P.P., Schwenker, C.D., Khan, A.J., Bari A., Colaresi, J.F., Tench O.K., David G. and Guryn, W. (2002) Low-Background Gamma Spectrometry for Environmental Radioactivity, *Applied Radiation and Isotopes* 57: 213-223.
- [102] Tufail, M., Nasim Akhtar., & Waqas, M. (2006) Measurement of terrestrial radiation for assessment of gamma dose from cultivated & barren saline soils of Faisalabad in Pakistan, *Radiation Measurements* 41 :443-451.
- [103] Tyler, A.N. (2004) High accuracy in situ radiometric mapping, *Journal of Environmental Radioactivity* 72 : 195-202.
- [104] UNSCEAR, United Nations Scientific Committee on the Effects of Atomic Radiation (2000) Report to the General Assembly with Scientific Annexes.
- [105] Wisser, S (2003) Balancing natural radionuclides in drinking water supply –an investigation in German Ref and Canada with respect to geology, radiometry and legislation Ph.D. Thesis Gutenberg- University, Mainz, Germany.

Effect of The Type of Water on Leaching of Aluminum Utensils During Food Preparation

Fathia S. Mohammad¹, Essam A. H. Al Zubaidy¹ and Ghada Bassioni²

1 Chemical Engineering Department, American University of Sharjah, UAE
(fmohammed@aus.edu) (izubaidy@aus.edu)

2 Chemical Engineering Department, the Petroleum Institute, Abu Dhabi, UAE; on leave from Faculty of Engineering, Ain Shams University, Cairo, Egypt (gbassioni@pi.ac.ae)

ABSTRACT

The intake of aluminum from cooking utensil is of growing concern to the health of the community. In the present work, leaching of aluminum from aluminum utensils using different water in food preparation was investigated. The effects of pH, salt concentration, temperature, and cooking time using tap and drinking water with Indian and Egyptian utensils which are available in local market are used in this work.

For Indian utensils, the Aluminum intake/ person were 100.75 using drinking water and 301.93 (mg/person) using tap water alone at boiling temperature. The type of food had a significant effect of increasing Aluminum intake using drinking water and this value increased to 181.17 (mg / person) using 40% meat extract with tomato juice, citric acid and salt. While using the tap water, the type of food was believed to make a passive layer which reduces the Aluminum intake to lower values ranging from 42.65 to 148.8 (mg/person) for different types of foods.

For Egyptian utensils, the Aluminum intake/ person were 21.39 using drinking water and 403.8 (mg/person) using tap water alone at boiling temperature. The type of food had a significant effect on increasing Aluminum intake using drinking water and this value increased to 100.63 and 120.77 (mg / person) using 40% meat extract with tomato juice, citric acid and salt. While using the tap water food solution, the aluminum intake reduces to lower values ranging from 42.63 to 127.62(mg/person).

Keyword: *aluminum cookware, water, leaching process, aluminum intake*

1. INTRODUCTION

Human bodies can excrete small amount of aluminum very efficiently; an aluminum tolerable daily intake of 1 mg/kg body weight /day has been established by the World Health Organization (WHO) of the United Nation (UN) [1]. But unfortunately due to many reasons, most of us expose to and ingest more than what our bodies can handle [2]. Various reports suggest that high aluminum intakes may be harmful to some patients with bone diseases or renal impairments. The aluminum health effects are far too vast to even being summarized [3]. Aluminum reduces

the growth rate of human brain cells. Growth rate decrease becomes more pronounced at higher aluminum concentration [4]. The cause of Alzheimer disease is still unknown, but aluminum might play a major role for the cause of the disease. It is possible to control aluminum intake from six main sources; food, packaging, medicines, pots, water, and air [5].

Most foods contain some aluminum; for example, tea, some herbs and some spices contain particularly high aluminum levels. Aluminum often binds strongly with other substances in food such as fluoride and phosphate, which may make it less absorbable. Studies have found that

beverages (tea, coffee and soft drinks) and cereals (cakes, puddings, biscuits, breakfast cereals, bread, flour, oatmeal and rice) are the main sources of aluminum from food. Aluminum can be naturally present in food, but some aluminum salts are added as food additives. Aluminum-based additives are widely used in bleaching, preserving and pickling processes and in powdered foods such as instant coffee, dried milk and table salt. Bread, cake, biscuits and baking powders may have high aluminum levels if they contain aluminum food additives. Food may come into contact with aluminum from packaging, foil trays, foil lined cartons, and aluminum cans. In order to reduce the amount of unwanted aluminum intake from cookware, cooking acidic foods in uncoated aluminum pans must be avoided. Many antacids used for treating indigestion and ulcers contain large amounts of aluminum compounds, but little of the aluminum is normally absorbed. Antacids make the stomach more alkaline which prevent the absorption of most of the aluminum. Aluminum absorption is higher if antacids are taken with orange juice instead of water. Table (1) shows the estimated aluminum concentration of selected food [6].

Table (1): Estimated aluminum concentration in some selected food

Food	Aluminum Content (mg/100g)	Food	Aluminum Content (mg/100g)
Meat, poultry, & fish*	0.02 – 0.12	Peanut butter	0.2
Cheese, natural*	1.57	Walnut	0.2
Cheese, processed	29.7	Vegetables	0.01 – 0.44
Fruits	0.01 – 0.04	Spinach	2.52
Bran, wheat	1.28	Baking powder	2,300
Bread, white	0.3	Cocoa	4.5
Bread, whole wheat	0.54	Pickles, with aluminum additives	3.92
Herbs & spices	8.2 – 75.0	Tea, dry bag	128
Salt, with aluminum additives	16.4	Tea, steeped	0.46

* Food not cooked or stored in aluminum pans, trays or foil.

2. MATERIAL AND METHOD

2.1. MATERIAL

Two kinds of aluminum cookware, from different origins, are chosen from the local market. The cookware origins are India and Egypt. The cookware are cut into small rectangular shapes with dimensions of 1x1.2 cm and each has a small hole of 1 mm diameter at one end in order to hang them in the water sample .

2.2. METHOD

2.2.1. WEIGH LOSS METHOD

In the present work, the weight loss method (W_L) at room and different temperatures is used to study the aluminum leaching into different food solution samples. The aluminum specimens are cleaned by distilled water and acetone, dried, and weighed using a four-digit sensitive balance. After the test, aluminum samples are cleaned by distilled water followed by acetone and reweighed again. The pH values of the solution are also measured before and after the experiment. The corrosion rate and aluminum intake per person calculations is done by previous work [7]. To assure consistency, all the experiments are performed in duplicates.

2.2.2. Environmental scanning electron microscopy (ESEM) test

The samples are analyzed, before and after the experiment, using the environmental scanning electron microscopy (ESEM) which is connected with an energy dispersive x-ray (EDX). This test will give indications about the leaching of the metals from the initial condition. Also the picture will show the damage of the aluminum surface.

3. RESULT AND CONCLUSION

Three food solutions are used to immerse the aluminum samples from different origins of cook wares.

Solution # 1: 250 ml of 40% meat extract+ 250 ml tomato juice

Solution # 2: 250 ml of 40% meat extract+ 250 ml tomato juice+ 3 g citric acid

Solution # 3: 250 ml of 40% meat extract+ 250 ml tomato juice+ 3 g citric acid + 5 g salt

The aluminum intake per person in drinking water

and tap water are shown in Figure (1) and (2) for Indian and Egyptian cookware samples after two hours of immersing the aluminum sample at boiling temperature.

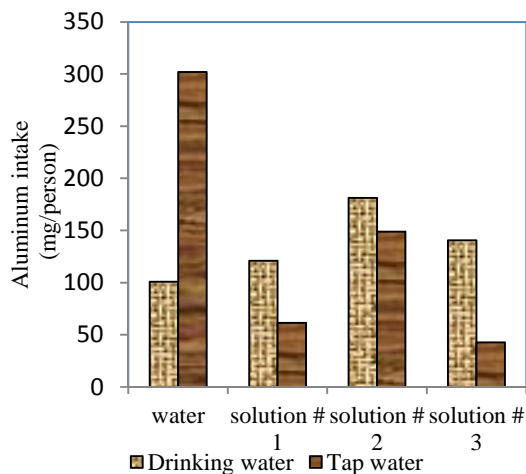


Figure (1): Aluminum intake in mg/person for Indian cookware sample using tap and drinking water in different food solutions

From this figure it can be seen that the aluminum intake using drinking water alone show a value of 100.75 (mg/person) while using tap water alone is 301.93 (mg/person). The addition of meat extract increases the corrosion rate with solution # 1 using drinking water to 140.62 (mg/person) and show a decrease using tap water to 42.65 (mg/person). The addition of table salt and citric acid cause a sharp increase in the corrosion rate to 181.17 (mg/ person) using drinking water and 148.8 (mg/person) using tap water.

From this figure it can be seen that the aluminum intake using drinking water alone shows a value of 21.39 (mg/person) while using tap water alone is 403.8 (mg/person). The addition of meat extract increases the corrosion rate with solution # 1 using drinking water to 65.5 mg/person and shows a decrease using tap water to 42.65 (mg/person). The addition of table salt and citric acid causes a sharp increase in the corrosion rate to 120.77 (mg/ person) using drinking water and 127.62 (mg/person) using tap water.

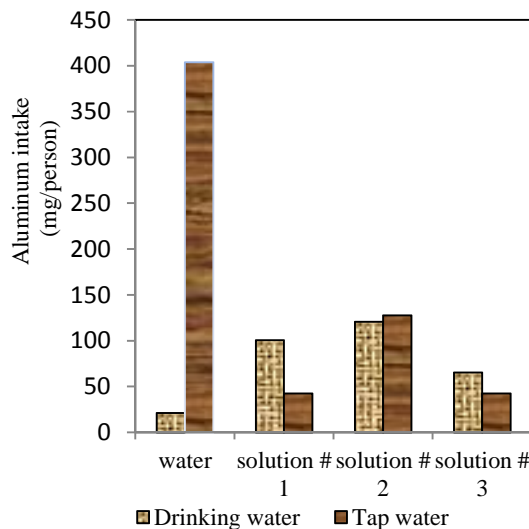
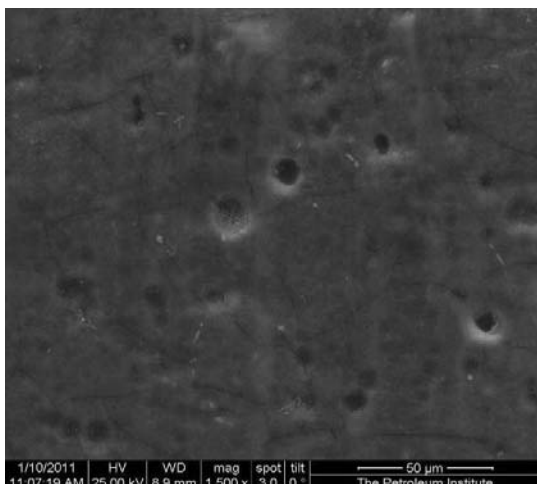


Figure (2): Aluminum intake in mg/person for Egyptian cookware sample using tap and drinking water in different food solutions

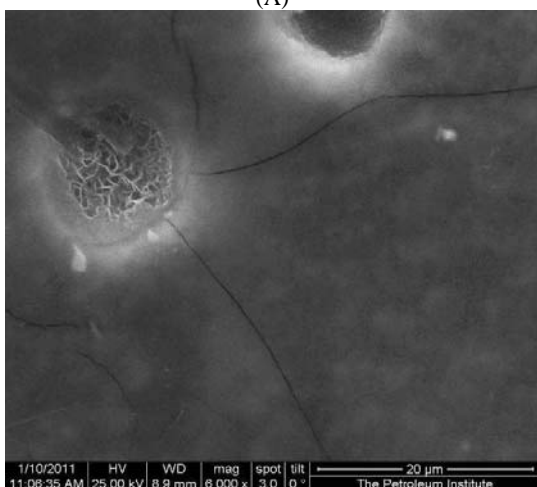
The above results show that the leaching of aluminum using drinking water alone is less than the one in tap water. The leaching is increased in the food solution prepared by drinking water while it is reduced in food solution prepared by tap water. This decrease in tap water solution is either because of the formation of passive layer or the change in the mode of reaction from uniform to localized one.

The drinking water solution shows an increase in the leaching value as the salt and citric acid concentrations increase (Solutions (1), (2), & (3)). The pH values of the solutions are 3.3, 3.0 and 2.8, respectively. This variation in the pH value seems to be the reason for such behavior with the increase of citric acid concentration.

Figures (3-A) & (3-B) and Figure (4) show the damage on the Indian sample that is exposed to drinking water and solution (1) at boiling point for two hours, respectively. Figure (3) clearly show the severe localized attack which explains the lower leaching value of drinking water compared to tap water.



(A)



(B)

Figures (3-A) & (3-B): ESEM image of the Indian sample after two hours of exposure to boiling drinking water

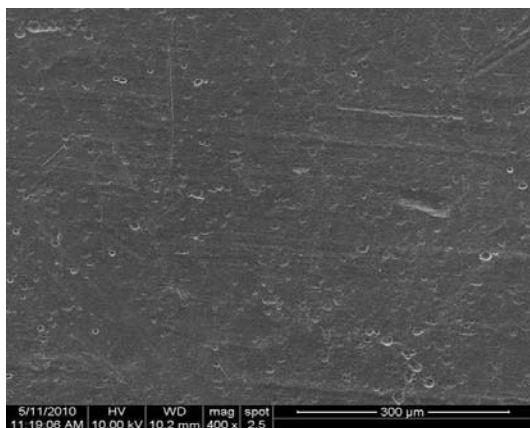


Figure (4): ESEM image of Indian sample after two hours of exposure in solution #1 using tap water

The effect of temperature on the Indian aluminum cookware sample is studied using drinking water after two hours of exposure. The aluminum intake increases with temperature as shown in Figure (5).

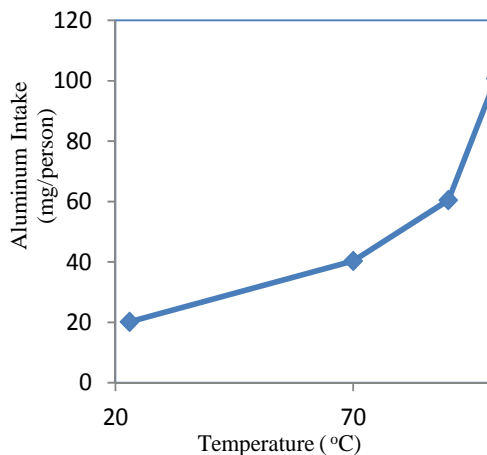


Figure (5): Effect of temperature on the Aluminum intake of Indian cookware sample at two hours of exposure in drinking water

The aluminum leaching is five times higher at 100°C than at ambient temperature. At 185°C (oven) the leaching is even more and the corrosion rate is more than eight times than that at 100°C. As the temperature increases, the kinetic energy will be higher and the movement of molecules becomes faster and therefore the aluminum contaminates food more frequently. The effect of temperature on the Indian aluminum sample using tap water after two hours of exposure is shown in Figure (6).

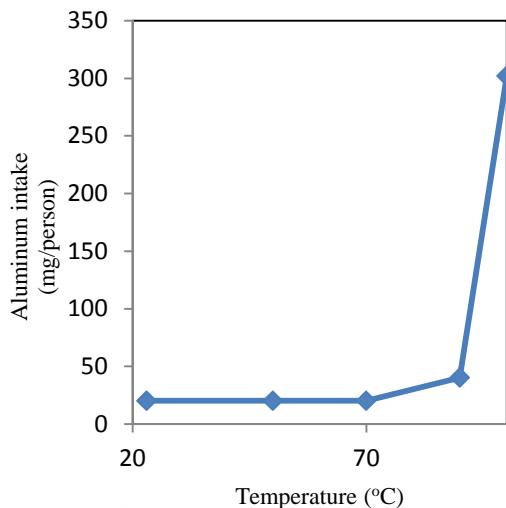
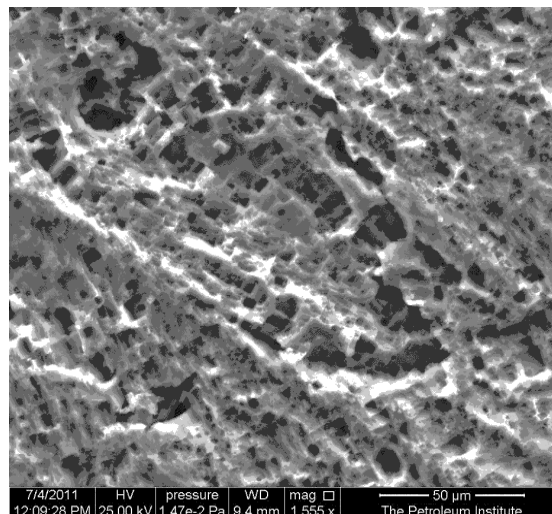


Figure (6): Effect of temperature on the aluminum intake for Indian cook ware in tap water

The corrosion rates at temperatures below 100°C are less than that in drinking water, while at 100°C the corrosion rate is three times more than that in drinking water.

The pH values of the food solution have also a significant effect on aluminum leaching; at pH values of 2, 2.4 and 3.1 the localized attack is clearly noticed (Figures (7)). While at pH value of 6.7, there is very low uniform corrosion rate (Figure (8)). Increasing the pH to 10 shows very severe local attack (Figure (9)); i.e. pitting is filling the whole surface of the sample. Previous work [8] reports that aluminum usually develops a protective surface of oxide film upon exposure to the atmospheric or aqueous solution. This film is responsible for the corrosion resistance of aluminum in most environments when aluminum is exposed to high concentration of acids or bases. This solution causes pitting corrosion to the aluminum in the presence of chloride ions.



Figures (7): ESEM images of the Egyptian sample after 14 days of exposure to 3.5% NaCl solution in drinking water (pH= 2) at room temperature

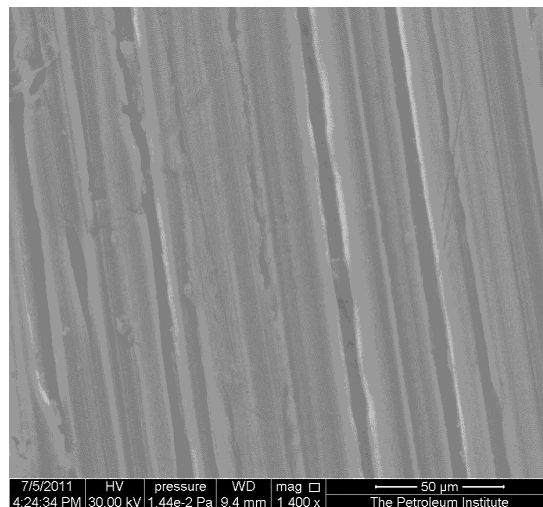
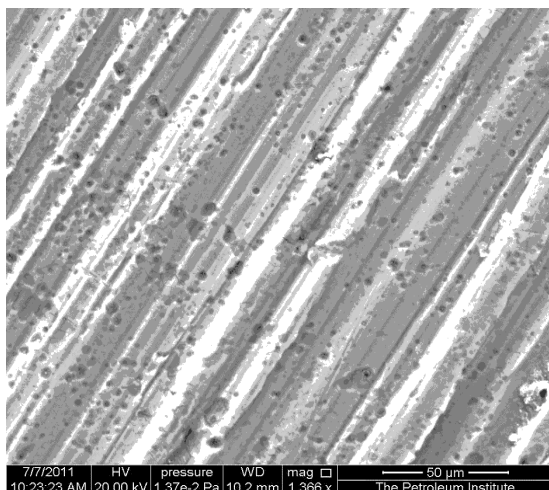


Figure (8): ESEM image of the Egyptian sample after 14 days of exposure to 3.5% NaCl solution in drinking water (pH = 6.7) at room temperature



Figures (9): ESEM images of the Egyptian sample after 14 days of exposure to 3.5% NaCl solution in drinking water (pH= 10) at room temperature

4. Conclusion

The aluminum intake using two different samples of cookware, one of Egyptian origin and the other of Indian origin is studied. It is shown that the type of water has a significant effect on the aluminum intake. The Egyptian sample shows lower aluminum intake using drinking water alone and higher value using tap water alone. The addition of food solution and especially citric acid and table salt increase the aluminum intake. The cooking time and temperature has also a significant effect on aluminum leaching from the cookware to the food solution. As the cooking temperature increases, the aluminum intake increases accordingly.

Acknowledgement

The authors thank the American University of Sharjah and The Petroleum Institute in Abu Dhabi for financial support.

References

1. WHO (World Health Organization), "Safety evaluation of certain food additives and contaminants", WHO Food additives Series 46. Joint FAO/WHO Expert Committee on Food Additives, 2001
2. Jack Damond, "A report on Alzheimer's disease and current research", Alzheimer Society of Canada, 2005
3. Gitelman, H., , "Aluminum and health critical review", Marcel Dekker, Inc. New York, N.Y., 1989
4. Min Sook Kim, "Aluminum exposure: a study of an effect on cellular growth rate", The Science of Total Environment, issue 278, p. 127-135, 2001
5. Aluminum and Alzheimer's disease, Information Sheet, Al Zeheimer Scotland Action on Dementia, Oct. 4, 2003.
6. Peter O. Snyder, 2008, "The effect of aluminum and iron cooking utensils on food", Hospitality Institute of Technology and Management, retrieved on Aug. 8, 2011 from: <http://www.hi-tm.com>
7. Fathia S. Mohammed, Essam Al Zubaidy, and Ghada Bassioni, "Effect of aluminum leaching process of cooking wares on food", International Journal of Electrochemical Science, issue 6, p. 222-230, 2011.
8. A. Y. El-Etre, "Inhibition of aluminum corrosion using opuntia extract", Corrosion Science, Vol. 45, Issue 11, p. 2485, 2003

Optimal Observer Driven Controller with Disturbance Rejection for a Natural Gas Hydrogen Producing Reformer

V. Radisavljevic^{1,2}, Member of ASME, A. Muhammad³, S. Hoda³, M. Ghattas³

¹California State University Los Angeles, Department of Mechanical Engineering
5151 State University Drive, Los Angeles, California 90032-8153, (vradisa@calstatela.edu)

²American University of Sharjah, Department of Mechanical Engineering,
PO. Box 26666, Sharjah, United Arab Emirates (vgajic@aus.edu)

³American University of Sharjah, Department of Electrical Engineering,
P.O. Box 26666, Sharjah, United Arab Emirates
(b00032400@aus.edu); (b00027356@aus.edu); (b00025580@aus.edu)

ABSTRACT

In this paper we present an optimal observer driven controller design for a linearized model of a fuel cell reformer, which produces hydrogen from natural gas. To solve this control problem we first design an observer to estimate all state variables at all times. Then, we design two feedback control loops, one of them with an integrator (integral control) and another one with proportional feedback from the estimated state trajectories (obtained from the observer output). In the third step, we design a feed-forward controller whose role is to off-set for the impact of the disturbance at steady state. According to the presented simulation results, the proposed controller clearly copes well with the disturbance and reduces its impact within a few seconds from the time when the disturbance occurs, despite large jumps in the fuel cell current (disturbance).

Keywords: hydrogen, disturbance rejection control, optimal observer

1. INTRODUCTION

In this paper we present an optimal observer driven controller design for a fuel cell reformer, which produces hydrogen from natural gas. The hydrogen obtained is then pumped to the anode side of the PEM (proton exchange membrane (also known as polymer electrolyte membrane)) fuel cell.

The reformer mathematical model and its controller/observer design techniques are considered in [1]-[3]. In addition, in this paper, we include the integrator loop with a piecewise constant disturbance rejection feature and a feed-forward controller. This helps to regulate temperature of the catalytic partial oxidation process and the anode hydrogen mole fraction at the desired values. The corresponding 10th-order nonlinear model and its state space variables are

$$\frac{dx(t)}{dt} = f(x(t), u(t), w(t))$$

$$x = [x_1 \ x_2 \ x_3 \ x_4 \ x_5 \ x_6 \ x_7 \ x_8 \ x_9 \ x_{10}]^T$$

$$= [T_{cpox} \ p_{H_2} \ p^{an} \ p^{hex} \ \omega^{bl} \ p^{hds} \ p_{CH_4}^{mix} \ p_{air}^{mix} \ p_{H_2}^{wrox} \ p^{wrox}]^T \quad (1)$$

$\omega_{cp}(t)$ is the compressor (that blows air for fuel (natural gas) oxidation) angular velocity. $w(t)$ is the disturbance and it represents the stack current, $w(t) = I_{st}(t)$. The control variables operate the blower's angular velocity and the fuel (natural gas) tank valve, that is

$$u(t) = \begin{bmatrix} u_{blower}(t) \\ u_{valve}(t) \end{bmatrix} \quad (3)$$

The measured output $y(t)$ serves at the same time as the controlled variable. It is defined by

$$y(t) = z(t) = [T_{cpox}(t) \ y_{H_2}^{an}(t)]^T \quad (4)$$

where $y_{H_2}^{an}$ is the anode hydrogen mole fraction. The goal is to regulate the catalytic partial oxidation temperature and the anode hydrogen mole fraction at the desired values at steady state, $T_{cpox} = 972$ K and $y_{H_2}^{an} = 0.088$ (8.8%).

The linearized system matrices at steady state are given in page 147 of [1]. The linearized system is represented by

$$\begin{aligned} \frac{\delta x(t)}{dt} &= A\delta x(t) + B\delta u(t) + G\delta w(t) \\ \delta y(t) &= \delta z(t) = C\delta x(t) \\ z &= z_{ss} + \delta z, \quad x = x_{ss} + \delta x, \\ u &= u_{ss} + \delta u, \quad w = w_{ss} + \delta w \end{aligned} \quad (5)$$

where the introduced state space matrices are given by

$$A = \begin{bmatrix} A_1 & A_2 \end{bmatrix}$$

$$A_1 = \begin{bmatrix} -0.074 & 0 & 0 & 0 & 0 \\ 0 & -1.468 & -25.3 & 0 & 0 \\ 0 & 0 & -156 & 0 & 0 \\ 0 & 0 & 0 & -124.5 & 212.63 \\ 0 & 0 & 0 & 0 & -3.333 \\ 0 & 0 & 0 & 0 & 0 \\ 0 & 0 & 0 & 0 & 0 \\ 0 & 0 & 0 & 221.97 & 0 \\ 0 & 0 & 2.0354 & 0 & 0 \\ 0.0188 & 0 & 8.1642 & 0 & 0 \end{bmatrix}$$

$$A_2 = \begin{bmatrix} -0.074 & -3.53 & 1.0748 & 0 & 10^{-6} \\ 0 & 0 & 0 & 2.5582 & 13.911 \\ 0 & 0 & 0 & 0 & 33.586 \\ 0 & 112.69 & 112.69 & 0 & 0 \\ 0 & 0 & 0 & 0 & 0 \\ -32.43 & 32.304 & 32.304 & 0 & 0 \\ 331.8 & -334 & -341 & 0 & 9.9042 \\ 0 & -253.2 & -254.9 & 0 & 32.526 \\ 0 & 1.8331 & 1.214 & -0.358 & -3.304 \\ 0 & 5.6043 & 5.3994 & 0 & -13.61 \end{bmatrix} \quad (6.a)$$

$$B = \begin{bmatrix} 0 & 0 & 0 & 0 & 0.12 & 0 & 0 & 0 & 0 & 0 \\ 0 & 0 & 0 & 0 & 0 & 0.1834 & 0 & 0 & 0 & 0 \end{bmatrix}^T \quad (6.b)$$

$$G = \begin{bmatrix} 0 & -0.328 & -0.024 & 0 & 0.0265 \\ & 0.0504 & 0 & 0 & 0 & 0 \end{bmatrix}^T \quad (6.c)$$

$$C = \begin{bmatrix} 1 & 0 & 0 & 0 & 0 & 0 & 0 & 0 & 0 & 0 \\ 0 & 0.994 & -0.088 & 0 & 0 & 0 & 0 & 0 & 0 & 0 \end{bmatrix} \quad (6.d)$$

2. OBSERVER AND CONTROLLER DESIGNS

The goal is to design the linear-quadratic optimal observer driven controller that will maintain

$T_{cprox} = 972$ K and $y_{H_2}^{an} = 0.08$ (8.8%) at steady state despite the constant disturbance coming from the changes of the fuel cell stack current (due to the fact that the fuel cell load changes as $I_{st} = V_{st} / R_L$, where the load R_L represents the load of all users that turn on and off at random time instants).

2.1 Observer Design

It is known, see for example [5], that the observer for (5) has the following form

$$\begin{aligned} \frac{\delta \hat{x}(t)}{dt} &= A\delta \hat{x}(t) + B\delta u(t) + Gw(t) + K(y(t) - \hat{y}(t)) \\ &= (A - KC)\delta \hat{x}(t) + B\delta u(t) + Gw(t) + Ky(t) \\ \hat{y}(t) &= \delta \hat{z}(t) = C\delta \hat{x}(t) \end{aligned} \quad (7)$$

The observer gain K has to be chosen such that the observer feedback matrix $A - KC$ is asymptotically stable. That can be achieved by choosing any desired location of the observer eigenvalues, and with a help from the MATLAB function “place” find the observer gain K such that the eigenvalues are placed in that desired location ($K = \text{place}(A, C, \text{desired_eigenvalues})$). Note that the location of the system eigenvalues should be chosen such that the closed-loop observer is much faster than the closed-loop system (determined by system closed loop matrix $A - BF$, where F is a linear proportional full-state feedback gain).

2.2 Integral Feedback Controller Design

Since the disturbance is a piecewise constant (see Figure 2), we design a feedback loop with an integrator in it [4]. The integrator is placed such that it fed with the error term that represents the difference between the desired and actual system output values. Assuming that the system is asymptotically stable, the error input into integrator must be equal to zero (otherwise the integrator will be producing huge feedback signals that will eventually destabilize the system). Introducing new variables that are in fact integrals of the error terms, that is

$$\begin{aligned} \frac{d\sigma_1(t)}{dt} &= T_{cprox}^{desired} - T_{cprox} \\ \frac{d\sigma_2(t)}{dt} &= y_{H_2}^{desired} - y_{H_2} \end{aligned} \quad (8)$$

we form the augmented system

$$\begin{aligned} \begin{bmatrix} \frac{d\delta x(t)}{dt} \\ \frac{d\sigma}{dt} \end{bmatrix} &= \begin{bmatrix} A & 0 \\ C & 0 \end{bmatrix} \begin{bmatrix} \delta x(t) \\ \sigma(t) \end{bmatrix} + \begin{bmatrix} B \\ 0 \end{bmatrix} \delta u(t) \\ &= A_{aug} x_{aug}(t) + B_{aug} \delta u(t), \\ \sigma(t) &= \begin{bmatrix} \sigma_1(t) \\ \sigma_2(t) \end{bmatrix}, \quad x_{aug}(t) = \begin{bmatrix} \delta x(t) \\ \sigma(t) \end{bmatrix} \\ A_{aug} &= \begin{bmatrix} A & 0 \\ C & 0 \end{bmatrix}, \quad B_{aug} = \begin{bmatrix} B \\ 0 \end{bmatrix}, \end{aligned} \quad (9)$$

The control signal is obtained via proportional feedback from the state variables coming from the augmented system, that is

$$\delta u(t) = -F \begin{bmatrix} \delta x(t) \\ \sigma(t) \end{bmatrix} = -F_x \delta x(t) - F_\sigma \sigma(t) \quad (10)$$

2.3 Optimal Linear-Quadratic Feedback Controller

The feedback control law defined in (10) can be implemented in an optimal way by minimizing a quadratic performance criterion that carries information about the “squares” of the tracking errors and the “square” of the control input deviation from its nominal steady state operating points. With feedback gains obtained through optimization (minimization) of the quadratic performance criterion defined by

$$J = \int_0^\infty \left[\delta x^T(t) C^T Q_z C \delta x(t) + \sigma^T(t) Q_\sigma \sigma(t) + \delta u^T(t) R \delta u(t) \right] dt \quad (11)$$

The values for the weighted matrices can be found in [1], formula (7.14). They are given by

$$Q_z = \begin{bmatrix} 80 & 0 \\ 0 & 1100 \end{bmatrix}, \quad Q_\sigma = \begin{bmatrix} 150 & 0 \\ 0 & 100 \end{bmatrix} \quad (12)$$

$$R = \begin{bmatrix} 100 & 0 \\ 0 & 120 \end{bmatrix}$$

The corresponding optimal feedback gain can be found by using the MATLAB function “lqr” (linear-quadratic regulator (controller)) as follows $F=lqr(Aug,Baug,Q,R)$, where the matrix Q is the block diagonal matrix: $Q=[C^*Q_z^*C \text{ zeros}(10,2); \text{zeros}(2,10) Q_\sigma]$.

2.4 Feed-forward Controller Design

In addition to feedback controller defined by (10), we will use the feed-forward controller to off-set for the impact of the disturbance at the steady state (after some long enough period of time). Namely, at steady state, we have from (5)

$$0 = A \delta x_{ss} + B \delta u + G \delta w \quad (13)$$

which under the assumption that matrix A is invertible (which holds in this case), produces the following feed-forward term

$$\delta x_{ss} = -A^{-1} B \delta u - A^{-1} G \delta w \quad (14)$$

With this modification, the feedback controller applied to the system is implemented as follows (which modifies the controller defined in (10))

$$\delta u(t) = -F_x (\delta x(t) - \delta x_{ss}) - F_\sigma \sigma(t) \quad (15)$$

Hence, the actually implemented controller has two components: the full-state feedback component and the integral control component.

3. SIMULATION RESULTS

In this section we demonstrate the efficiency of the observer and controller designs considered in Section 2. We assume that the initial disturbance (current) value is 100 A and that at 30 s the disturbance jumps to 150 A, and at 60 s it jumps to 300 A (you will need to use two step inputs).

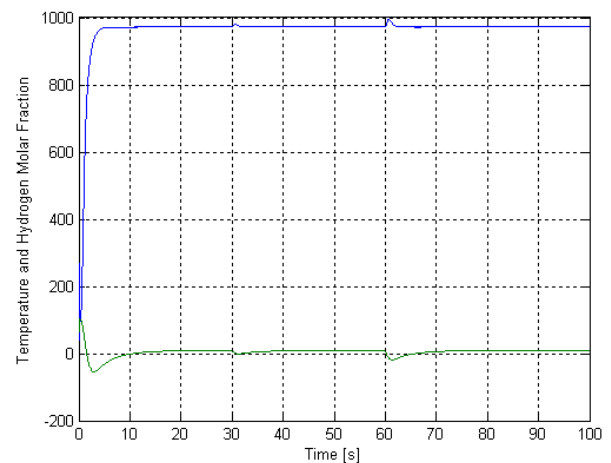


Figure 1: Obtained simulation results for the temperature (top curve) and the hydrogen molar fraction (bottom curve)

The obtained results using the proposed controller defined in (15) are presented in Figure 1, and the waveform of the disturbance current is presented in Figure 2. The simulation results obtained for the temperature (upper curve) and hydrogen molar fraction (lower curve) are presented in Figure 1, and the variations of the fuel stack current are presented in Figure 2. It can be seen from these figures that despite of large variations in the stack current (a jump from 100 A to 150 A at 30 s, and another jump from 150 A

to 300 A at 60 s), the output (controlled) variables are only slightly changed at these time instances, and the corresponding ripples disappear very quickly, within a few seconds.

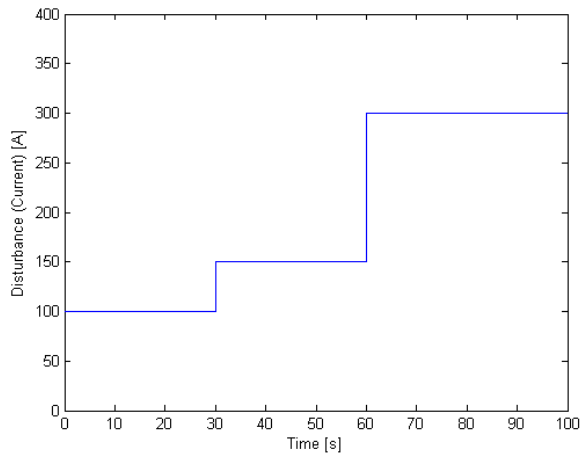


Figure 2: Variations of the fuel cell disturbance

Comment 1: We have observe that very good results can be obtained also by removing the feed-forward controller loop. Namely, it was proposed in [1] to use this feedforward controller, but seems that the integral controller is sufficient to successfully rejects constant disturbances and regulates the system output at the desired values. However, if we cut the integral control loop and keep the feed-forward controller the results become unacceptable.

4. EXTENSION TO THE NONLINEAR MODEL

As documented in [4], the integral feedback controller could be also used for rejection of constant disturbances of a nonlinear systems as long as the closed-loop system is asymptotically stable. In addition, a nonlinear observer could be designed using the corresponding nonlinear system model. One possible and simple choice of a nonlinear observer design can be found in [6]. For the model given in (1), this nonlinear observer is given by

$$\begin{aligned} \frac{d\hat{x}(t)}{dt} &= f(\hat{x}(t), u(t), w(t)) + K(y(t) - \hat{y}(t)) \\ \hat{y}(t) &= C\hat{x}(t) \end{aligned} \quad (16)$$

This will be our future research topic and it is out of the scope of this paper.

5. CONCLUSIONS

We have designed an observer based controller with both full-state and integral feedback that provides excellent features for the considered linearized system.

The study is underway to extend the results obtained to the corresponding nonlinear model of the gas reformer (used in fuel cells to generate hydrogen). It has been observed that the full-state and integral loops regulate successfully the system output at the desired values and that the feed-forward controller appears to be redundant in this application.

REFERENCES

- [1] J. Pukrushpan, A. Stefanopoulou, and H. Peng, *Control of Fuel Cell Power Systems: Principles, Modeling, Analysis, and Feedback Design*, Springer, 2004.
- [2] J. Pukrushpan, A. Stefanopoulou, and S. Varigonda, "Control-oriented model of fuel processor for hydrogen generation in fuel cell applications," *Control Engineering Practice*, Vol. 14, 277-293, 2006.
- [3] V. Tsourapas, A. Stefanopoulou, and J. Sun, "Model-based control of an integrated fuel cell processor with exhaust heat regulation," *IEEE Transactions on control Systems Technology*, Vol. 15, 233-244, 2007.
- [4] H. Khalil, *Nonlinear Systems*, 3rd edition, Prentice Hall, Upper Saddle River, New Jersey, 2003.
- [5] Z. Gajic and M. Lelic, *Modern Control Systems Engineering*, Prentice Hall, 1996, also Dover Publications, 2012.
- [6] B. Friedland, *Control System Design*, Prentice Hall, 1996.

Reduced-Order Observer and Optimal Controller Designs for the Air Flow of a Linearized Model of a 75kW PEM Fuel Cell for Electric Cars

Z. Gajic², H. Al Samhouri², Z. Al-Jarrah², O. Odeh²,

¹Rutgers University, Department of Electrical and Computer Engineering
94 Brett Road, Piscataway, New Jersey 08854
gajic@ece.rutgers.edu

²American University of Sharjah, Department of Mechanical Engineering,
P.O. Box 26666, Sharjah, United Arab Emirates
b00024156@aus.edu; b00025259@aus.edu; b00028784@aus.edu

ABSTRACT

In this paper we show that the results of a well-known paper on the observer design and the optimal observer driven controller for a 75 kW polymer electrolyte membrane fuel cell used to power electric cars can be significantly improved by implementing the reduced-order observer instead of the full-order observer. For the same initial conditions, the magnitude of the observation error has been drastically reduced from $O(10^2)$ to $O(10^{-13})$ when the reduced-order observer is implemented. Even more, we point out that the same paper uses a superficial method based on the system observability measure alone to reduce the original system order from nine to eight, and present the correct way to perform system order reduction by using balancing order-reduction technique by examining both the system controllability and observability measures.

Keywords: optimal controller design, Fuel cells for electric cars

1. INTRODUCTION

The polymer electrolyte membrane (PEM, also known as the proton exchange membrane) fuel cell model has been developed by the University of Michigan researchers and considered in detail in a series of journal papers, see for example [1]-[2] and the book [3]. The corresponding 9th-order nonlinear model and the state space variables are given by

$$\begin{aligned} \frac{dx(t)}{dt} &= f(x(t), u(t), w(t)) \\ x &= [x_1 \quad x_2 \quad x_3 \quad x_4 \quad x_5 \quad x_6 \quad x_7 \quad x_8 \quad x_9]^T \\ &= [m_{O_2} \quad m_{H_2} \quad m_{N_2} \quad \omega_{cp} \quad p_{sm} \\ &\quad m_{sm} \quad m_{H_2O_A} \quad m_{H_2O_C} \quad p_{rm}]^T \end{aligned} \quad (1)$$

where subscripts cp, sm, rm stand respectively for the compressor, supply manifold, and return manifold. $O_2, H_2, N_2, H_2O_A, H_2O_C$, respectively stand for oxygen, hydrogen, nitrogen, anode water and cathode water. $\omega_{cp}(t)$ is the compressor (that blows air (oxygen) on the cathode side) angular velocity. The control variable is the compressor motor voltage, $u(t) = v_{cm}(t)$. $w(t)$ is the disturbance and it represents the stack current, that is, $w(t) = I_{st}(t)$. It is assumed

that the hydrogen comes from a pressurized tank, so that a simple proportional controller for the anode hydrogen molar flow rate can be used as $W_{H_2}^{in} = K_1(K_2 p_{sm} - p_{anode})$. Hence, the main task in this model is to determine the cathode air molar flow rate, or more precisely the compressor angular velocity that determines the compressor molar flow rate (equal to the cathode molar flow rate).

The output (measured) variables are given by

$$y(t) = [W_{cp} \quad p_{sm} \quad v_{st}]^T = h_y(x, u, w) \quad (2)$$

where $W_{cp} = W_{cp}(x_4, x_5)$ is the compressor air molar flow rate, $p_{sm} = x_5$, and v_{st} is the fuel cell stack voltage. In addition to the measured output $y(t)$, the controlled output is given by

$$z(t) = [e_{Pnet} \quad \lambda_{O_2}]^T = h_z(x, u, w) \quad (3)$$

where $e_{Pnet} = P_{net}^{ref} - P_{net}$ (the difference between the desired $P_{net} = 40$ kW and actual net power), and $\lambda_{O_2} = W_{O_2}^{in} / W_{O_2}^{reacted}$. The objective is to have $e_{Pnet} = 0$ and $\lambda_{O_2} = 2$ (to avoid fuel cell oxygen starvation (lack of oxygen can considerably degrade

the cell V-I characteristic and even damage the cell membrane)).

The linearized system matrices at steady state (corresponding to the following steady state quantities:

$P_{net}^{ss} = 40$ kW, $I^{ss} = 191$ A, $v_{cm}^{ss} = 164$ V, $\lambda_{O_2}^{ss} = 2$) can

be found in [1], p. 145. The data in [1] are represented by matrices A, B_u, C_y, D_{yu} , respectively corresponding to the standard state space matrices A, B, C, D , that is

$$\begin{aligned} \frac{\delta x(t)}{dt} &= A \delta x(t) + B_u \delta u(t) + B_w \delta w(t) \\ \delta y(t) &= C_y \delta x(t) + D_{yu} \delta u(t) + D_{yw} \delta w(t) \\ \delta z(t) &= C_z \delta x(t) + D_{zu} \delta u(t) + D_{zw} \delta w(t) \end{aligned} \quad (4)$$

$$\begin{aligned} z &= z_{ss} + \delta z, & x &= x_{ss} + \delta x, & u &= u_{ss} + \delta u, \\ y &= y_{ss} + \delta y, & w &= w_{ss} + \delta w \end{aligned}$$

where $\delta z = [\delta e_{P_{net}} \quad \delta \lambda_{O_2}]^T$. It is assumed in [1]-[3], for the reason of design simplicity that $\delta w(t) = 0$.

It is interesting to observe that the linearized model of [1]-[3] is of order eight. Namely, the state variable corresponding to the mass of water in the cathode is removed since it is “weakly observable”. This is a superficial conclusion, it is known from the balancing transformation [4]-[5] that the state space variables that are *both* weakly controllable and weakly observable have small impact on the system output response, and hence they can be appropriately removed from the system model.

Using the observer obtained state estimates $\delta \hat{x}(t) \approx \delta x(t)$, the optimal observer driven controller is designed as

$$\delta u_{opt}(t) = -F \delta \hat{x}(t) \quad (5)$$

where the gain F optimizes (minimizes) the following quadratic performance criterion

$$\begin{aligned} \min_F \left\{ \int_0^\infty [\delta z^T \delta z] dt \right\} &= \min_F \left\{ \int_0^\infty (\delta x^T C_z^T C_z \delta x \right. \\ &\quad \left. + \delta u^T D_{zu}^T D_{zu} \delta u + 2 \delta x^T C_z^T D_{zu} \delta u) dt \right\} \end{aligned} \quad (6)$$

with the goal to bring the state space variables to their steady state values.

In the next section we present the simulation results for the state space matrices of the considered fuel cell using the data obtained from [1]-[3].

2. SIMULATION RESULTS WITH FULL- AND REDUCED-ORDER OBSERVERS

Full-Order Observer Simulation Results

The state space system matrices, corresponding to the notation used in (4), are given by [1]-[3]

$$A = [A_1 \quad A_2]$$

$$A_1 = \begin{bmatrix} -6.30908 & 0 & -10.9544 & 0 \\ 0 & -161.083 & 0 & 0 \\ -18.7858 & 0 & -46.3136 & 0 \\ 0 & 0 & 0 & -17.3506 \\ 1.299576 & 0 & 2.969317 & 0.3977 \\ 16.64244 & 0 & 38.02522 & 5.066579 \\ 0 & -450.386 & 0 & 0 \\ 2.02257 & 0 & 4.621237 & 0 \end{bmatrix}$$

$$A_2 = \begin{bmatrix} 83.74458 & 0 & 0 & 24.05866 \\ 51.52923 & 0 & -18.0261 & 0 \\ 275.6592 & 0 & 0 & 158.3741 \\ 193.9373 & 0 & 0 & 0 \\ -38.7024 & 0.105748 & 0 & 0 \\ -479.384 & 0 & 0 & 0 \\ 142.2084 & 0 & -80.9472 & 0 \\ 0 & 0 & 0 & -51.2108 \end{bmatrix}$$

$$B_u^T = [0 \quad 0 \quad 0 \quad 3.946683 \quad 0 \quad 0 \quad 0 \quad 0]$$

$$C_y = [C_{1y} \quad C_{2y}]$$

$$C_{1y} = \begin{bmatrix} 0 & 0 & 0 \\ 0 & 0 & 0 \\ 12.96989 & 10.32532 & -0.56926 \end{bmatrix}$$

$$C_{2y} = \begin{bmatrix} 5.066579 & -116.446 & 0 & 0 & 0 \\ 0 & 0 & 0 & 0 & 0 \\ 0 & 0 & 0 & 0 & 0 \end{bmatrix}$$

$$C_z = [C_{1z} \quad C_{2z}]$$

$$C_{1z} = \begin{bmatrix} -2.4837 & -1.9773 & 0.109013 \\ -0.63477 & 0 & -1.45035 \end{bmatrix}$$

$$C_{2z} = \begin{bmatrix} -0.21897 & 0 & 0 & 0 & 0 \\ 0 & 13.84308 & 0 & 0 & 0 \end{bmatrix}$$

$$D_{zu} = \begin{bmatrix} 0.169141 \\ 0 \end{bmatrix}$$

The observer designed in [1]-[3] for $\delta\hat{x}(t)$ is of the full-order, equal to the order of the linearized system, that is equal to eight. The full-order observer is given by [6]

$$\frac{d\tilde{x}(t)}{dt} = (A - KC_y)\tilde{x}(t) + B_u\delta u(t) + K\delta y(t) \quad (7)$$

The full-order observer gain K was chosen via the eigenvalue (pole) placement technique such that closed-loop full-order observer eigenvalues were placed far to the left at the following locations

$$\begin{aligned} \lambda(A - KC_y) = \\ = (-1) \times [18 \ 17 \ 25 \ 20 \ 24 \ 20 \ 22 \ 19] \end{aligned} \quad (8)$$

so that the full-order observer is very fast. This has been achieved using the MATLAB function “place” as

```
KT=place(A',Cy',lambda)
K=KT'
```

The corresponding estimation error for this observer, equal to $e(t) = \delta x(t) - \delta\hat{x}(t)$ is presented in Figure 1. More precisely, Figure 1 represents the difference between the system and observer outputs, that is,

$$\delta y(t) - \delta\hat{y}(t) = C(\delta x(t) - \delta\hat{x}(t)) = Ce(t) \quad (9)$$

It can be seen that despite the fact that the observation error goes quickly to zero, in less than 0.6s it has a huge magnitude around 0.1s of the order of $O(10^2)$. It should be pointed out that the system initial conditions are kept the same in both cases (full- and reduced-order observers), and that the observer choice of the initial conditions was hardly affected the magnitude of the observation errors in both cases: the full- and reduced-order observer designs. In simulation, the system initial condition was taken as

$$x(0) = [2 \ 2 \ 2 \ 2 \ 2 \ 2 \ 2 \ 2]^T \quad (10)$$

and the full-order observer initial conditions were relatively close to $x(0)$

$$\hat{x}(0) = [1 \ 3 \ 2 \ 3 \ 1 \ 4 \ 2 \ 1]^T \quad (11)$$

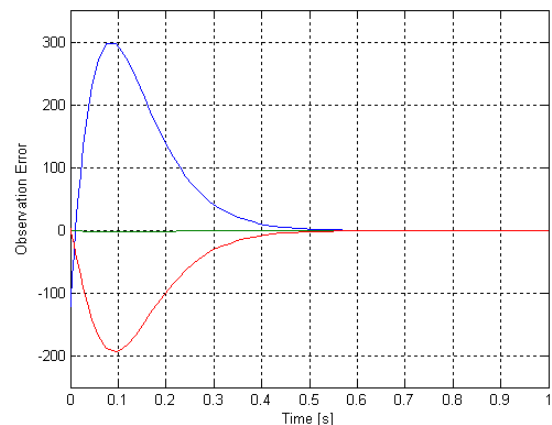


Figure 1: Observation Error for the Full-Order Observer

Reduced-Order Observer Simulation Results

If we exploit the fact that the measurement formula for $\delta y(t)$ gives at all times three instantaneous (algebraic) equations for eight state variables, we can design a reduced-order observer of dimension five for the remaining five state variables [6]. According to [6], the reduced order observer (whose dimension is equal to five) has the form

$$\frac{d\tilde{q}(t)}{dt} = A_q\tilde{q}(t) + B_q\delta u(t) + K_q\delta y(t) \quad (12)$$

where

$$A_q = C_1AL_2 - K_1C_yAL_2$$

$$B_q = C_1B_u - K_1C_yB_u$$

$$K_q = C_1AL_2K_1 + C_1AL_1 - K_1C_yAL_1 - K_1C_yAL_2K_1$$

The matrix C_1 needed for the design of the reduced-order observer [6], is chosen to make the rank of the augmented matrix given below equal to eight, and it was chosen as

$$\text{rank} \begin{bmatrix} C_y \\ C_1 \end{bmatrix} = 8 \quad (13)$$

$$C_1 = \begin{bmatrix} 2 & 3 & 1 & 1 & 0 & 0 & 0 & 0 \\ 4 & 7 & 9 & 0 & 1 & 0 & 0 & 0 \\ 0 & 1 & 2 & 0 & 0 & 1 & 0 & 0 \\ 2 & 3 & 4 & 0 & 0 & 0 & 1 & 0 \\ 7 & 9 & 10 & 0 & 0 & 0 & 0 & 1 \end{bmatrix}$$

The matrices L_1 and L_2 are compatibly partitioned matrices of the augmented matrix defined in (13), that is

$$\begin{bmatrix} L_1 & L_2 \end{bmatrix} = \begin{bmatrix} C_y \\ C_1 \end{bmatrix}^{-1} \quad (14)$$

The matrix K_1 is chosen to place the closed-loop eigenvalues of the reduced-order observer, the eigenvalues of the matrix A_q in the desired locations. It can be shown, [6], if the original system is observable, that is, the pair (A, C_y) is observable, then, the pair $(C_1 A L_2, C_y A L_2)$ is also observable, so that the matrix K_1 can be found to place the closed loop eigenvalues of A_q in the desired locations. The reduced-order observer closed-loop eigenvalues were placed at

$$\lambda_{reduced} = [-25 \quad -27 \quad -28 \quad -30 \quad -31] \quad (15)$$

which gives to the reduced-order observer relatively the same speed as for the full order observer (see (8)). The reduced-order observer gain can be obtained using MATLAB as follows

```
K1T=place((C1*A*L2)',(C*A*L2)',lambda_reduced);
K1=K1T'
```

The reduced-order observer initial conditions were chosen as

$$\begin{bmatrix} 1 & 2 & 3 & 2 & 1 \end{bmatrix} \quad (16)$$

Using the fifth-order reduced-order observer, the optimal estimates of the original variables are given by

$$\delta\hat{x}(t) = L_2 \delta\hat{q}(t) + (L_1 + L_2 K_1) \delta y(t) \quad (17)$$

Finally the optimal feedback gain (defined in (5) and obtained through minimization of (6)) is identical for both the system-full-order-observer and system-reduced-order-observer configurations. It does not impact neither the full-order observer nor the reduced-order observer, due to the well known separation principle, [6], that states that the closed-loop system eigenvalues (defined by $\lambda(A - B_u F)$) and the closed-loop observer eigenvalues are independent. It can be obtained via MATLAB using the following statement

```
F=lqr(A,Bu,Cz'*Cz,Dzu'*Dzu,Cz'*Dzu)
```

The corresponding simulation results for the observation error (the deference between the system and observer outputs) are presented in Figure 2. It can

be seen from Figure 2 that we have a drastic improvement for the observation error that is bounded at all times by $O(10^{-13})$.

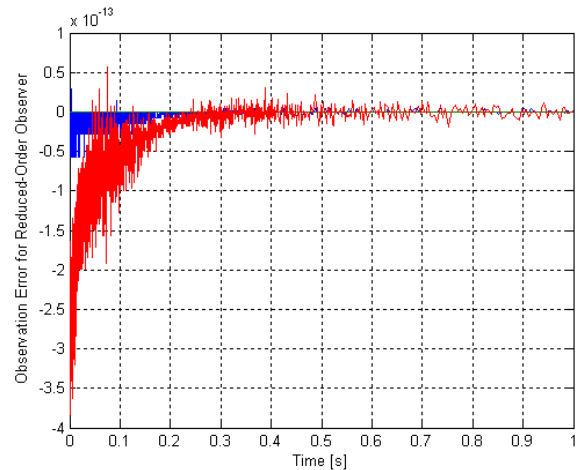


Figure 2: Observation Error for the Reduced-Order Observer

3. CONCLUSIONS

We have shown that the reduced-order observer performs much better than the full-order observer. In addition, the proposed reduced-order observer is a dynamic system of order five which is much simpler for implementation than the original full-order observer, whose order is equal to eight (the order of the system under consideration).

REFERENCES

- [1] J. Pukrushpan, H. Peng, and A. Stefanopoulou, "Control oriented modeling and analysis for automotive fuel cell systems," *Transactions of ASME Journal of Dynamic Systems, Measurements, and Control*, Vol. 126, 14-25, 2004.
- [2] J. Pukrushpan, A. Stefanopoulou, and H. Peng, Control of fuel cell breathing," *IEEE Control Systems Magazine*, 30-46, 2004.
- [3] J. Pukrushpan, A. Stefanopoulou, and H. Peng, *Control of Fuel Cell Power Systems: Principles, Modeling, Analysis, and Feedback Design*, Springer, New York, 2004.
- [4] J. Moore, "Principal component analysis of linear systems: controllability, observability, and model reduction," Vol. 26, 17-32, 1981.
- [5] K. Zhou and J. Doyle, *Essential of Robust Control*, Prentice Hall, Upper Saddle River, New Jersey, 1998.
- [6] Z. Gajic and M. Lelic, *Modern Control Systems Engineering*, Prentice Hall, London, 1996.

THE EFFECTS OF CLIMATE CHANGE: HOW CAN ALGERIA DEAL WITH IT

M. BOUGHEDAOU

Département de chimie industrielle, Université Saad Dahlab of Blida, Algeria
boughedaoui@wissal.dz

R. KERBACHI

Laboratory of Science and Technology for the Environment, ENP, Algiers, Algeria
r_kerbachi@yahoo.fr

ABSTRACT

With a rate of 0.4% of global GHG emissions, the contribution of Algeria on global warming is minimal. However, it suffers from its geographical location and climatic characteristics, all adverse effects that would induce even a small rise in temperature. The models predict that rainfall events are less frequent but more intense, while droughts are more common and longer. The spatial and temporal distribution of rainfall will also change. The analysis of climate data from 1931 to 1990 in northern Algeria reveals a rise in temperature of 0.5 ° C would reach an increase of 1 ° C by 2020. The decrease of water resources, declining agricultural yields, encroaching desert, the challenge of planning, the energy consumption for air conditioning, etc. are only the initial impacts that Algeria must find ways to fight. These problems are in addition to those already existing and related to the high population growth, extreme urbanization of the country, the environmental degradation and the imperatives of economic development.

The question everyone asks of us today is that Algeria may be to adapt to climate change or reduce its vulnerability, what are the measures to be taken at different levels to implement or improve response actions and adaptation, which means she must mobilize and what are its chances of success. We present in this study an analysis of the current situation, trends in emissions of CO₂ in Algeria, mitigation and adaptation strategy Algeria and especially what the impact of the new national plan for promoting renewable energy adopted in 2011 and expects to produce 40% of electricity needs from solar. We will develop avenues of thought that are able to mitigate induced impacts in the medium term by the climate change.

Key words : Climate change, GHG, vulnerability, mitigation, adaptation, Algeria

1. Introduction:

Algeria is the three-story climate is affected by climate change both natural and socio-economic development. Since joining the United Nations Framework Convention on Climate Change (UNFCCC), Algeria has developed an initial strategy against climate change and developed numerous projects for adaptation and mitigation of changes climate (MATE, 2011). The national strategy is based primarily on the development of four components: institutional strengthening to support climate change awareness and education; mitigation of emissions of greenhouse gases, adaptation to climate change. Sectors of energy, industry, transport, waste, and those water resources, agriculture and forestry are expected to gradually integrate climate change aspects in sectoral policies and programs activities for research and development of means of adaptation and mitigation respectively. In this paper, we present the most important elements of the fight against climate change in Algeria with a critical analysis of different perspectives and actions to

achieve the objectives of the Convention and the national strategy.

2. GHG emission inventory

Algeria has conducted two national emission inventories of greenhouse gas (GHG) emissions for the years 1994 and 2000. The methodology used is that of the 1996 IPCC, IPCC and IPCC GPG 2006. The inventory covered the direct six greenhouse gases (CO₂, CH₄, N₂O, SF₆, CFCs, PFCs) and indirect greenhouse gas precursors (NO_x, CO, NMVOC and SO₂). The overall GHG emissions in direct totaling 117.31 Mt eq CO₂ in 2000, with an amount of CO₂ absorbed by forests estimated at 14.16 Mt CO₂, or net emissions in eq CO₂ in the amount of 103.14 Mt (Table 1). Considering the estimated Algerian population of 29.7 million inhabitants in 2000, per capita emissions are 3.95 t eqCO₂/hab/an. By comparing the emission per habitant, Algeria is among important emitters from developing countries (Table 2).

Table 1: Emissions of direct greenhouse gas emissions

Sectors	Emissions	Absorptions
	Gg eqCO ₂	Gg CO ₂
Energy	87 597	0
Industrial Processes	5463	0
Agriculture and Forestry	12 822	14 167
Agriculture	6535	0
Forests	6287	14 167
Waste	11 428	0
Total	117 310	14 167

Table 2: Comparison of emissions per capita among other countries

Country	USA	France	Algeria	Tunisia	India	Morocco	Lebanon	World average
Emissions (tCO ₂ / cap / year)	19.85	6.15	3.95	1.92	1.4	1.27	3.50	4.68

By activity, the energy sector (production and consumption) which is the source of highest emissions, about ¾ of the total (Figure 1) and this sector has the most important potential for mitigation measures.

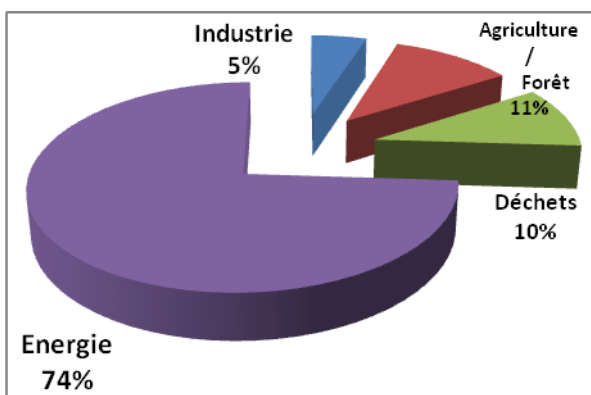


Figure 1: Total GHG emissions by sector

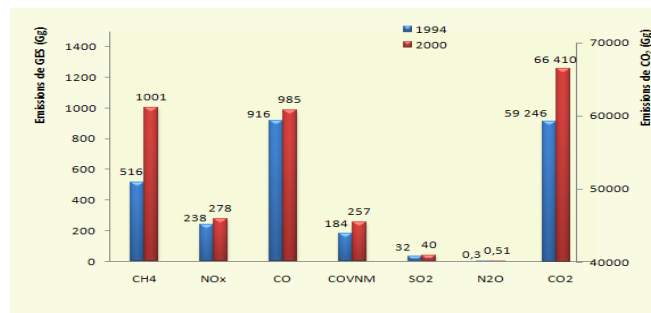


Figure 2: GHG emissions from the energy sector in 1994 and 2000

CO₂ emissions due to energy consumption are estimated at 59, 246 Mt CO₂ in 1994 while in 2000 they amounted to 66.410 Mt (Figure 2). The annual average growth of 2.0% seems to be in line with the increase of the average annual consumption of energy during this period. Thus, with this growth, emissions will increase by 2020 of 40% over the year 2000. The Global Atmospheric Watch station in Assekrem, Tamanrasset, where the atmospheric content of CO₂ is measured growing steadily from 360 ppm in 1995 to 385 ppm in 2008 (ONM, 2010), an annual increase of about 2 ppm / year is calculated (Figure 3). The trend growth levels of CO₂ (Mauna Loa) is also observed at the urban background station of Assekrem measuring three greenhouse gases (CO₂, CH₄, N₂O) since 1995. (www.onm.dz)

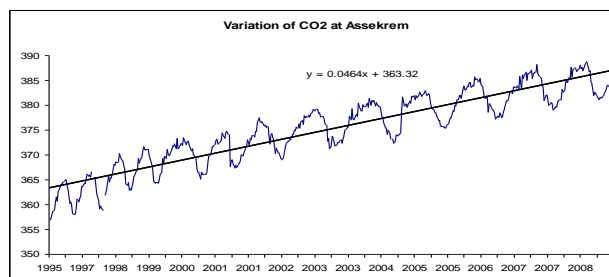


Figure 3: Evolution of CO₂ Station Assekrem (ONM, 2009)

3. Climate Change

In its 2007 report, the IPCC has combined 25 global climate models to assess the impacts of climate change in 2050 and 2100. In the Mediterranean region, there provided a temperature rise of 2-3 ° C by 2050, and 3-5 ° C by 2100. The rain events are less frequent but more intense, while droughts are more common and longer. The spatial and temporal distribution of precipitation would change, which directly affect and agriculture and water resources. Regional models with the IPCC scenarios applied

to Algeria for the period 1990-2020 forecast growth of the average temperature of 0.8 °C to 1.1 °C, and reduced precipitation 10% (Figures 4, 5) with an increase in the sea level of 5 to 10 cm. Increased evaporation due to the temperature increase in addition to decreased precipitation will accentuate the decrease in the amount of water mobilized in dams and groundwater.

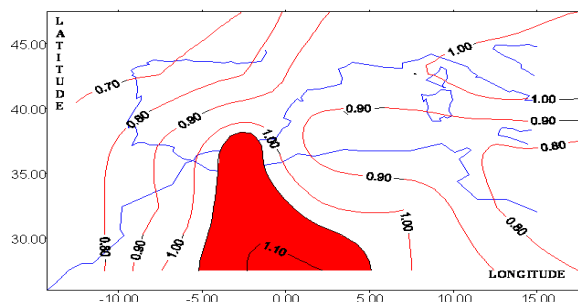


Figure 4: Projected Temperature (°C) to 2020 (Fall)

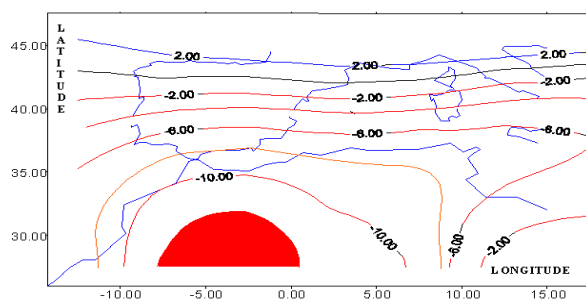


Figure 5: Change in precipitation (in%) to 2020 (winter)

4. Vulnerability

The major vulnerability of the country is observed in the areas of water and agriculture. Algeria is a semi arid to arid north to south. Water availability per capita is 600 m³/hab./an, placing Algeria in the category of poor countries in water resources under the shortage threshold set by the UNDP or the scarcity set by the World Bank in 1000 m³/hab./year. The rate of groundwater exploitation in the north of the country reached about 90%, nearly 2 billion m³/year. Some aquifers are already overexploited. To ensure that consumption needs, the country of use in recent years desalination of sea water with a production capacity of about 2 million m³/day.

Land used by agriculture, which occupy nearly 21% of the total land area, are estimated at 49 million ha distributed as follows: 8.4 million ha of agricultural area, 33 million ha used as routes, 6.6 million ha of forests and steppes of alfa. Irrigated land accounts for 11% of the agricultural area, an area of 929,000

ha. Algeria therefore has only 3.5% of the total area of the country as arable land and irrigated. The report "availability / capita" agricultural land rose from 0.75 ha / capita in 1962 to 0.24 ha / cap in 2008. This enormous loss of farmland is not only the result of human pressures (industrial, construction, pollution ...) but also the result of desertification, soil erosion, the vegetation cover loss. Climate change will degrade biodiversity and contribute to the weakening of the soil and reduced vegetation cover resulting in a gradual desertification. In the steppe, the effect of climate change is reflected by the change in the cyclical nature of drought from one year to three years in the 60 to two years out of five in the 70s and 80s for seven out of ten years now.

Vulnerability to climate change is a vital issue for the protection of natural resources and human health and the environment protection, developing the strategic development of the country. There are many research projects underway that examine the effects of climate change.

5. Strategy

The national strategy against the CC is essentially based on components: climate change adaptation, mitigation of GHG emissions, institutional strengthening for mainstreaming of climate change at all levels and in all sectors such as the energy, industry, transport, waste, water resources, agriculture and forests. For this purpose, a legal and regulatory framework is developed to ensure the implementation of this strategy. A program of public awareness, training of operators socioeconomic and education of children in school is run from 2000 to date. In the industrial sector and energy legislation is reinforced by texts of laws on energy conservation, development land, waste management, electricity and gas distribution, protection of the environment in the context of sustainable development of renewable energy, water, energy efficient audits. The inter-sectoral committee of energy management is created and was able to develop a national energy management plan and has at its disposal the national fund of energy management for its implementation. Another national fund for renewable energy is created for the promotion of renewable energy through the diversification of energy resources within the country. Many industrial initiatives are developed to either mitigate or adapt to climate change. The analysis of the current state with a future projection highlights some strength of the actions undertaken to date and the barriers that stand against the outcome of this strategy.

Benefits:

- Legislative and regulatory framework well-developed
- Comprehensive strategy to promote renewable energy
- Availability of financial resources (funds, budgets)

Barriers:

- Low technical inter-sectoral coordination
- Weakness of new technologies transfer
- Insufficient technological mastery
- Insufficient qualified human resources
- Limited availability of national expertise
- Difficulties in applying existing regulations
- Low ownership of areas of CC local and regional
- No program of scientific research and development related to CC

However, despite all these measures already taken, it appears the need for coordination at the national level and especially inter-sectoral lacking to date. The creation of the National Agency on Climate Change (NACC) could achieve this coordination at the national level and capitalize on the experiences and replicate best practices across the country. It will also run multi-sectoral projects ensuring proper coordination and reconciliation of areas around the theme of climate change. The agency created in 2005 has not a great development in spite of the strategic role it is supposed to play in this area in the country. The implementation of the government strategy should be based in part on such an agency for successful policy and action plans provided. It is urgent to analyze the course of this agency in order to propel to the forefront and allow it to play its role at a time when this problem is growing both at the domestic level and worldwide.

6. Mitigation

When looking at the national inventory of greenhouse gas emissions, one can observe that the sectors most emitters are: the energy industry, transport and housing. These sectors are a major source for mitigation.

The main mitigation measures implemented or being implemented to reduce emissions of pollutants and greenhouse gases are:

- Recovery of associated gas from oil wells (90% in 2020)
- The widespread use of gas in oil refineries

- The widespread use of natural gas for domestic
- The renewal of power plants by introducing the combined cycle
- Development of hybrid plants (natural gas-solar)
- The development of the use of LPG and CNG as vehicle fuel,
- The reduction of gas flaring in energy industries,
- Introduction of energy efficiency in buildings,
- Solar energy development

However all these measures do not allow substantially reduction of the current level of GHG emissions. The estimated reduction impacted by these measures account for 10 to 12%. The new development plan for renewable energy announced in early 2011 provides for the production of 20 000 MW of electricity from solar by 2030, half of which is for the local market and the other part will be exported to other markets in Europe. This project will impact on GHG mitigation in Algeria and Europe. The estimated reduction of at least 40% CO₂ emissions by 2030 compared to the scenario without the solar plan.

7. Conclusion

Algeria, which is part of Mediterranean hot spot is very vulnerable to climate change. Experts predict at the medium term an increase in temperature of 2 °C, a decrease in rainfall of 10 to 15% and more frequent droughts and more intensive. Facing this situation, and to ensure the availability of water resources, curbing soil erosion and sustainable development, the country has implemented a strategy for adapting to climate and GHG mitigation. It covers all sectors, especially the energy sector which is responsible for the largest share of GHG emissions (74%). Much progress has been made in the mobilization of water resources for drinking and irrigation, and much remains to be done in agriculture. In the field of energy, the final development plan for Renewable Energy is undoubtedly a big challenge for the country. Overall the strategy will reduce up to 60% of GHG emissions. Algeria has a good chance of a successful struggle against the CC, if certain conditions are met such as the formation of qualified human capabilities, the integration of all the possibilities, good coordination and good governance.

SIMULATION OF BLUE NILE RIVER USING A DISTRIBUTED HYDROLOGICAL MODEL AND GLOBAL DATA SET

OSAMA R. ABD EL-AZIZ^a, OLIVER CRISTIAN SAAVEDRA VALERIANO^{b,c}

^aPhD Student, Researcher, Department of Energy Resources and Environmental Engineering, Egypt-Japan University for science and technology E-JUST (Borg El-Arab, Alexandria, Egypt, 21934)

^bDr. of Eng., Adjunct Professor, Department of Energy Resources and Environmental Engineering, Egypt-Japan University for science and technology E-JUST (Borg El-Arab, Alexandria, Egypt, 21934)

^cDr. of Eng., Associate Professor, Department of Civil and Environmental Engineering, Tokyo Institute of Technology (Meguro-ku, Tokyo, Japan)

Abstract

Model-based decision support tools based on hydrological models can be useful for the management of water resources. However, in developing countries, there might be a lack of local data (ground measurements) to set-up, calibrate and validate hydrological models for water assessment. Then, as complementary source, remote sensing data at global scale can be used for this purpose. Nowadays, there are available global datasets that could be useful to prepare and force hydrological models. They range from topographical data (Hydro 1k), soil data (FAO soil maps) and land use characteristics (NASA's Terra Satellite) as well as meteorological data. For example, one of the most attractive might be the satellite-based precipitation and temperature. Some data have been collected by different satellites such as Tropical rainfall measuring mission (TRMM), national center for environmental prediction (NCEP) and national center for atmospheric research (NCAR). On the other hand, others provide statistical data such as the climatic research unit (CRU) monthly datasets for rainfall, temperature and number of wet days per month that can produce daily data using the Daily Weather Generator Algorithm (DWGA). In this research, remote sensed data have been examined to set-up a distributed hydrological model for the Blue Nile River to assess water resources in the catchment useful to support decision making. This basin is one of the head streams of the Nile River and source of almost 70 percent of its floodwater at Khartoum. It rises as the Abbay from a spring 1,800 above sea level, near Lake Tana in northwestern Ethiopia. It flows through a deep canyon southeast and west around the Choke mountains and then turns northwest to join White Nile at Khartoum. Its length is about 1,450 kilometers and the Basin area is almost 325,000 Km². The Distributed Hydrological model (DHM) which was employed in this study is a grid-based geomorphology-based hydrological model (GBHM). This model use governing equations to describe hydrological processes. Global datasets were used to generate the inputs for simulating daily and monthly stream flows. The model set up was carried out using precipitation data sets, first with few ground stations. The simulated discharge was examined at Khartoum gauging stations. A semiautomatic calibration of model parameters was possible using an optimization algorithm. NCEP/NCAR data was used showing acceptable results at Khartoum gauge station. The NCEP/NCAR Reanalysis temperature data gave a higher performance than weather generated temperature time series, though it has coarse spatial resolution. Even though physical based models require more ground data to be combined with remote sensing to improve simulation of hydrological processes, at the moment global data set seem acceptable to support decision making.

Keyword: Remote sensing; global data; Blue Nile River; Distributed hydrological modeling; Tropical rainfall measuring mission

1. Introduction

Implementation of water management policies requires decision support tools. Modeling is one of these decision support tools. However, in developing countries, they do not lack only appropriate tools and personnel to develop and maintain water resources model, but they do not have sufficient data to build, calibrate and validate models. For instance, rain gauge network is too sparse to produce reliable areal rainfall estimation. We should use different sources other than ground collected data.

Remote sensing is used in hydrology to estimate rainfall, surface temperature and soil moisture from satellite imagery, which can be used to determine other hydrological processes such as evapo-transpiration. Rainfall estimation from satellite imagery has been used for more than two decades (Engman, 1995). A number of algorithms have been developed based

imaged from the infrared sensors. These images give a measure of cloud top temperature that can be used to identify convective storms and deduce rainfall rate (Levizzani et al., 2002). The latest technology is precipitation Radar on broad TRMM satellite, which can measure vertical structure of troposphere precipitation (Kawanishi et al, 2000). Most of these satellite data are available online and free of charge, including precipitation, surface temperature, soil moisture, radiation, relative humidity, wind speed, etc. In most cases, these data are used for climatic change models.

In this study remote sensed data were analyzed and used to develop a hydrologic model. The precipitation data sets used are two satellites data sets TRMM and NCEP/NCAR Reanalysis, a global database CRU TS 2.1 (Mitchell et al., 2005) and ground stations rainfall data. The temporal resolution was day, except that of CRU which is month. Thus, a weather generator was used to convert monthly statistics back to daily.

*Osama Ragab . Tel.: +127610234

In present practical application, Distributed Hydrological model (Dawn Yang, 2000), a physically based model with daily time step was used as It is effective for simulation of large basins. On the other hand, distributed models incorporate the temporal and spatial variability of catchment conditions and meteorological inputs and allow for a better representation of the hydrological processes than other model types (Yang et al., 2002). Developments in distributed hydrological models emphasize the capturing of the local unique contributions due to different land cover, soil properties and topography (Yang et al., 2001a). The importance of the spatial variability of precipitation using the distributed hydrological modeling approach has not been fully investigated, due to lack of precipitation data of high spatial resolution.

The main objective of the present study is to develop a hydrologic model of Blue Nile basin, which is distributed in Ethiopia and Sudan countries using readily available remote sensed data.

2. Study area

The Nile River encompasses ten countries. The Blue Nile basin, which has been selected as the study area, is located in the high steep mountainous region of the upper Nile River (Fig. 1) on the Ethiopian plateau, which is concentrated at elevations of 2000-3000m, with several peaks up to 4000 m or more. The plateau country is not flat but very broken and hilly, with grassy uplands, swamp valleys and scattered trees. There are occasional rocky peaks, some of which are of volcanic origin. The curious course of the river may follow the original drainage pattern radiating from such volcanic centers. The basin is cut by deep ravines or canyons in which the Blue Nile and other rivers flow. The valley of Blue Nile is 1300 m deep in places, and the course of the river is often difficult to cross. The whole area is intersected by streams, most of which are perennial through highly seasonal in their flow. The catchment area of the Blue Nile basin lying upstream of the Khartoum hydrological station is 325000 Km². There are two reservoirs located in this basin (see Figure 1), which play an important role in flood regulation during the flood season (July, august and September). The average annual rainfall over the Blue Nile basin is about 1600 mm. It increases from about 1000mm near the Sudan border to about 1400-1800 mm over parts of the upper basin, in particular in the loop of the Blue Nile below Lake Tana, and above 1800 mm in the south within the Didessa basin.

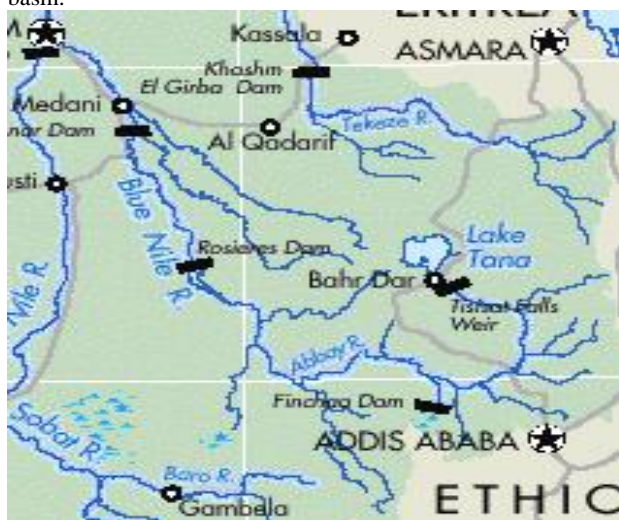


Fig. 1 Study area

3. Methodology

The development of a distributed hydrological model starts with the collection of digital geographic information related to the study area for building a digital representation of the basin. This is the basis for making a distributed hydrological model. A digital elevation model (DEM) is used to define the target area, and the target basin is subdivided into a number of fundamental units for hydrological simulation. The catchment parameters related to topography, land use and soil are then calculated for each simulation unit. As shown in Figure 2, geographical information system (GIS) defines the general structure of the hydrological model. The study basin is divided into a discrete grid system, and the grid is represented by a number of geometrically symmetrical hill slopes. The river network is divided into sub catchments of an appropriate size. The components of the hydrological model include the data input, the hydrological simulation and the resulting output. The hydrological simulation part includes runoff generation from the hill slope and the flow routing in the river network.

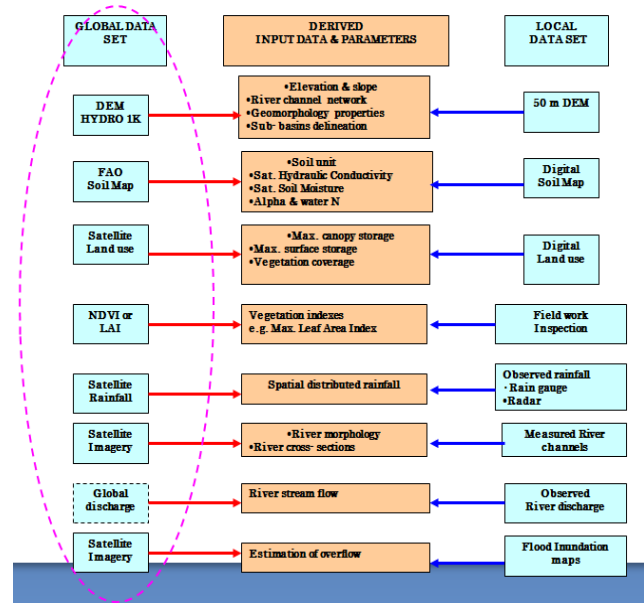


Figure 2.General structure of the hydrological model

3.1. Data Preparation

The geographic information used for the construction of a distributed hydrological model includes the topography, the land cover, the soil, and geological maps. The digital data of elevation, land use and geological conditions were obtained from satellite data.

3.1.1. Topography

The topography data used for building model is from HYDRO1K. HYDRO1k is a geographic database developed to provide comprehensive and consistent global coverage of topographically derived data sets, including streams, drainage basins and ancillary layers derived from the USGS' 30 arc-second digital elevation model of the world (GTOPO30). HYDRO1k provides a suite of geo-referenced data sets, both raster and vector, which will be of value for all users who need to organize, evaluate, or process hydrologic information on a

continental scale. It has a spatial resolution approximately 1000 meters. Fig. 3 shows the elevation map for Blue Nile river Basin.

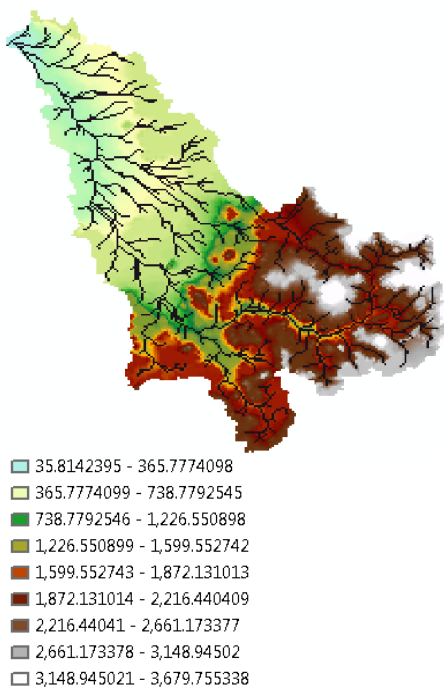


Figure 3. Elevation map

area. This data set was generated from average areal monthly grids of 0.5x0.5 degree resolution from CRU TS2.1 data set to daily time series using a weather generator algorithm (DWGA).

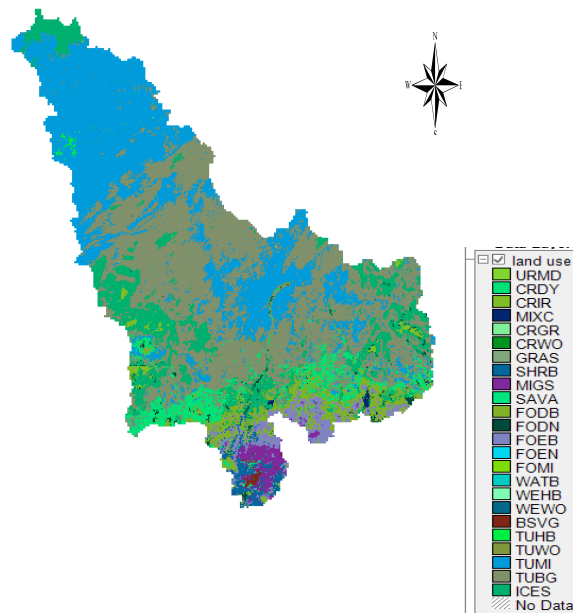


Figure 4. Land use types

3.1.2. Land use

A digital land-use map is available at a 1 Km resolution and 24 different types of land cover. Land use in Blue Nile basin is dominated by Savanna which covers 38.7%. Other important land use types are BAREN OR SPARSLY VEGETATED and DRYLAND CROPLAND AND PASTURE with 30.7% and 12.2% respectively. Water bodies cover 5.15% of the total area of the watershed. Fig. 4 shows different types of land use in Blue Nile Basin.

3.1.3. Soil

The soil map used is from FAO world soil classification has a scale of 1:2, 500, 00. The FAO soil classification defines 31 major soil groups, and their physical and chemical properties, texture and slope. The vertical distribution of the saturated hydraulic conductivity of the topsoil is assumed to decrease exponentially from K_{s1} near the soil surface to K_{sg} for groundwater at the bottom of the topsoil. K_{s1} and K_{sg} are parameters that require calibration. Table II shows the soil-water parameters used in the hydrological simulations for some soils. Fig. 5 shows different types of soil in Blue Nile River Basin.

3.1.4. Precipitation

There are 4 data sets of rainfall used in this study: rain gauge data, CRU/DWGA, TRMM and NCEP/NCAR Reanalysis. The simulation period is July 2001 and 2002 for calibration and validation respectively. There is one ground station available (Khartoum station) at the outlet of the watershed with daily data.

The CRU/DWGA data set consists of 137 stations of precipitation and maximum-minimum temperature. These stations correspond to centroids of each sub basin of study

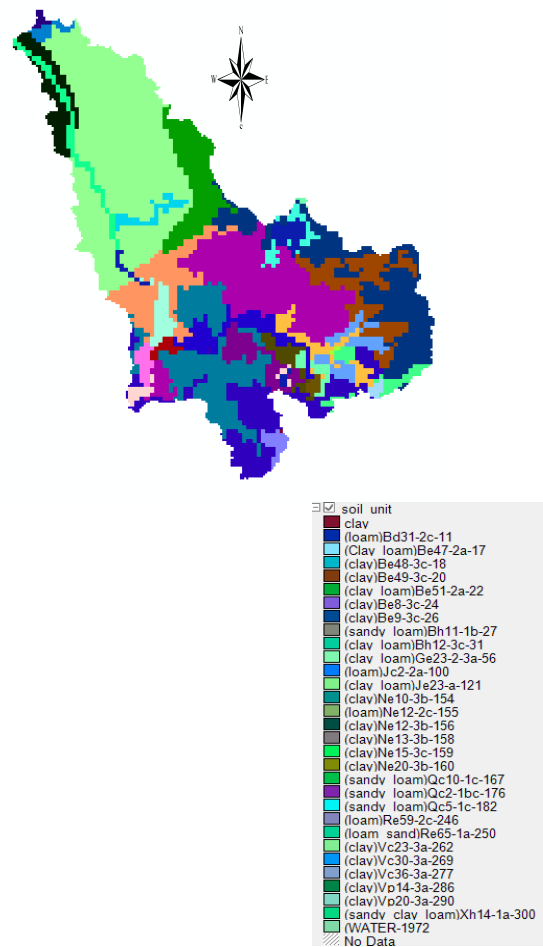


Figure 5. Soil map

The TRMM data sets have also 134 stations which are the centroids of the study area sub basin. Average accumulated rainfall time series data set downloaded from TRMM web site with a spatial resolution of 0.5x0.5 degree. The period of interest is 2001 to 2002.

The NCEP/NCAR Reanalysis precipitation data set comprises 192x94 points at global scale where precipitation rate is given. Only 130 points were used in this study. The selected periods are 2001 to 2002. Fig.6 (a, b) show the locations of stations for global data set and ground data respectively.

3.1.5. Temperature

Minimum, maximum monthly temperature for different weather stations has been provided. The data come from NCEP/NCAR data set.

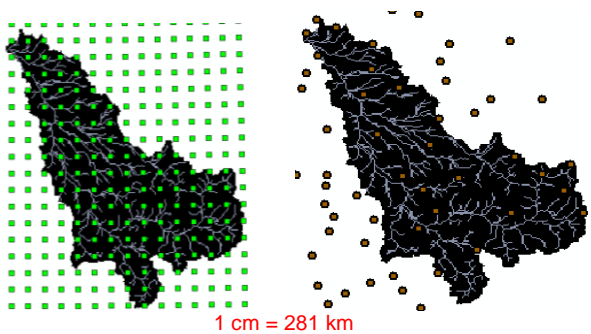


Figure 6. (a) Global data stations

Figure 6. (b) Ground data stations

3.1.6. Climate data

The solar radiation data, wind speed data, and relative humidity data have been generated by WXGEN, because measured data were not available.

3.2. Running Distributed Hydrological Model

In order to use satellite rainfall data, a grid-based hydrological model is used in this study, which is modified from the geomorphology-based hydrological model (GBHM) (Yang et al., 2002). As mentioned above, the finest DEM is available at 1000 m spatial resolution. In order to represent the topography accurately, the hydrological model should also use the same grid size. Unfortunately, grid-based distributed hydrological models usually cannot run at high resolution for practical applications due to their heavy computational requirement. A realistic resolution is required for producing a discrete catchment on which the hydrological simulation can be carried out. Aggregation from a fine DEM to a coarse DEM decreases the gradient and increases the length of the hillslope. Besides the topography, the heterogeneity of the vegetation and soil within computational grids also needs to be considered. Therefore, a sub grid parameterization scheme is necessary when a hydrological model uses a large-sized computational grid. However, the soil type is treated as uniform within grids due to the spatial resolution of the soil data.

3.2.1. Sub grid parameterization

In this study, the grid size in the hydrological model is 4000 m. The spatial heterogeneity inside a 4000 m grid is considered in the hydrological model. Figure 7 shows the concept of the sub

grid parameterization used in the grid-based distributed hydrological model. The distinguishing characteristic of the methodology on the sub grid parameterization is the representation of the sub grid variability of topography in terms of geomorphologic properties. In the GBHM developed by Yang et al.(2002), the geomorphologic property of the river-hill slope formation is used to represent the catchment topography. In a similar way, it is assumed that a large grid is comprised of a set of hill slopes located along the streams. Within a computational grid, all hill slopes are viewed as being geometrically similar. A hill slope of unit width is called a hill slope element, which is represented by a rectangular inclined plane (Figure 3). The length of a hill slope element is calculated from the 1000 m DEM as

$$\ell = a(i, j) / 2 \sum L \tag{1}$$

Where a (i, j) is the area of the grid at location (i, j), which is 1 km² here, but can also be a variable area if it is in a geographic (longitude/latitude) coordinate system; $\sum L$ is the total length of streams extracted from the 1000 m DEM. The slope angle is taken to be the mean slope of all subgrids in the 1000 m DEM. Considering the sub grid heterogeneity of vegetation, the hillslopes within a computational grid are grouped into different vegetation categories. The area fraction of each uniform vegetation class is calculated from the land-use map. Therefore, the fundamental unit for the hydrological simulation is the hillslope with uniform soil and vegetation types. The hydrological response from computational grids is the total of the responses from all hillslopes within the same grid. The streams located inside a grid (see Figure 3) are lumped into a single channel which flows along the main flow direction of this grid. The hydrological responses from hillslopes are assumed to distribute uniformly along the single lumped channel. In the discrete computational grid system of a study catchment, the river network links all of the grids and the catchment hydrological response are obtained by solving flow routing in the river network.

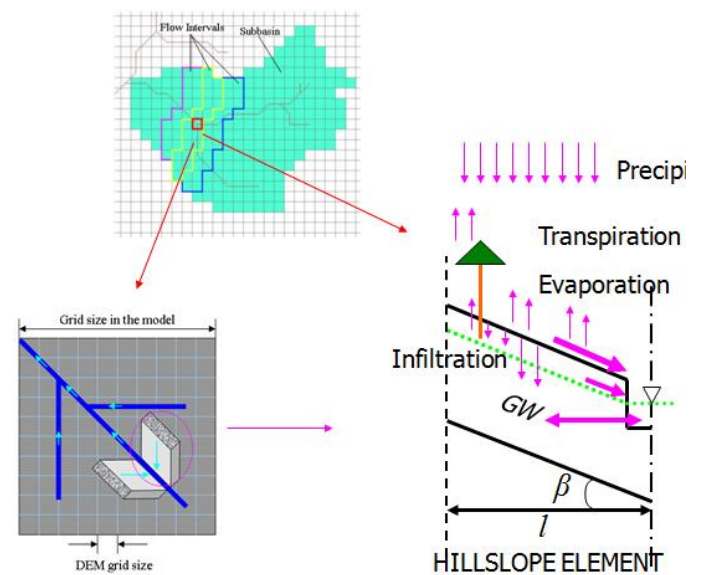


Figure 7. Concept of the grid-based hydrological model

3.2.2. Hill slope hydrological model

A physically based model is used to simulate the hydrological response from hill slopes. The hydrological processes included in this model are the canopy interception, evapotranspiration, surface flow, subsurface flow and the exchange between groundwater and the river (Yang et al., 2002). The canopy interception ability S_{c0} is described using a linear function of the leaf-area index (LAI; Sellers et al., 1996) as

$$S_{c0}(mm) = 0.2LAI \quad (2)$$

The LAI differs between vegetation species. The actual interception is determined by the rainfall intensity and deficit of the canopy storage (Yang et al., 2002). Water can evaporate from the canopy-intercepted water and soil surface, and can transpire by vegetation taken from the root zone. The actual evapotranspiration is estimated from the potential evaporation. The potential evaporation is estimated using temperature, wind speed and sunshine hours from that are generated by WXGEN. The infiltration and water flow in the subsurface in the vertical direction and along the hill slope are described in the quasi-two-dimensional subsurface model. The vertical water flow in the topsoil is represented by the Richards equation and solved by an implicit numerical solution scheme. In this scheme, the topsoil is divided into multiple layers. The depth of the first layer is 5 cm, and the remaining layers increase in depth to two times that of the upper layer, which must be less than the maximum of 50 cm. The first layer is upper boundary condition is given as the saturation of soil moisture for the rainfall cases. During non-rainfall periods, the upper boundary condition is given as the evaporation flux. The transpiration flux is treated as a sink in the soil layers within the root zone. The lower boundary condition is given as saturated because the groundwater reaches very high levels during the flood season. The precipitation and hydrological characteristics along the hill slope are uniform in the present model. The soil water distribution along the hill slope is treated as uniform. The depth of the surface water due to infiltration and saturation excess is calculated by solving for the vertical one-dimensional soil water movement using the Richards equation. In the subsurface of the topsoil, the soil water moves due to gravity along the hill slope towards the stream when the moisture content is more than the field capacity. The subsurface flow process is described by

$$q_{sub} = K(\theta) \sin \beta \quad (3)$$

Where q_{sub} is the flow rate, $K(\theta)$ is the hydraulic conductivity and β is the slope. The soil water content θ should be larger than the field capacity in this case. The surface runoff is the discharge that flows through the hill slope into the stream, which is treated as sheet flow and solved using Manning's equation. Groundwater aquifers are treated as individual storages corresponding to each grid. The exchange between the groundwater and the river water is considered as steady flow and is calculated using Darcy's law (Yang et al., 2002). The runoff generated from a grid is the sum of the hill slope responses, including both the surface and subsurface runoff. State variables, such as the soil moisture content of a grid, are output as the average value for the grid. The vertical flux, the actual evapotranspiration of a grid, is the total flux simulated from all hill slopes in the same grid.

3.2.3. Flow routing in the river network

In order to simulate flow routing in the river network, the number of river segments (links) and the flow sequences need to be defined. Here, the Pfafstetter scheme (Yang et al., 2000; Yang and Musika, 2003b) is applied for subdividing the catchment and for numbering the flow sequences among the sub catchments. The catchment is divided into nine sub catchments systematically using this scheme. If a sub catchment is still sufficiently large, then it is subdivided again using the same method. By repeating the same procedure, the catchment is finally divided into number of sub catchments with a limited drainage area. The drainage area of the sub catchment that is divided using the Pfafstetter scheme depends on the requirement of the hydrological simulation and the DEM resolution. In the present study of the Blue Nile basin, the average drainage area of the sub catchment is about 3000 Km². As mentioned above, streams located in a single grid are lumped into a single channel. It is practically difficult to identify and represent all of the river channels in a grid-based hydrological model. Therefore, the river networks of a sub catchment are simplified such that only the main river is considered. The lateral inflow into the main river is the total runoff generated from all of the grids at the same flow distance in the same sub catchment. The flow sequences among these simplified main rivers are defined by the codes of the divided sub catchments. The flow routing of all river networks in the catchment is modeled using the kinematic wave approach.

4. Results and discussion

In this section results of model simulating are presented. Before model simulation, global data sets were compared to ground station precipitation in the same periods of simulation and at the same location.

During the calibration process, the model was calibrated with ground station data to serve as a comparison bench mark for the different data set. In addition to that calibration was also done with every single data set to evaluate model performance.

4.1 Rainfall data analysis

A comparison of precipitation data sets used is needed to understand model behavior and help in calibration processes as they come from different places with different measuring systems and estimation algorithms.

The comparison of estimation methods requires the definition of a set of reference values of error criteria in order to evaluate the agreement between the estimates and the reference values. The reference data set was rain gauge data. Moreover, remote sensed data are space-average rainfall values, while ground stations measurements are point rainfall. The rainfall was estimate for each sub basin of the study area for all data sets, using Thiessen polygon method as shown in Fig.5.

4.1.1 Rainfall estimation error

The visual interpretation of global data was complemented by statistical analysis. Error (residual) and absolute error between global data sets and rain gauge precipitation data for simulation period are calculated. We consider rain gauge values $Z(t)$, and estimate value data as $\hat{Z}(t)$. The error is calculate as $e(t) = Z(t) - \hat{Z}(t)$, and the absolute errors is $|e(t)|$. For each of these quantities, the minimum, the maximum, the mean, the median

and the standard deviation was compared. The results are presented in Table 1-1, 1-2 and 1-3.

	CRU/DWGA	Gauge	Error	Absolute error
Mean	9.523355	14.71912	-5.196	16.5397
Minimum	0	0	-62.82	0
Maximum	58.242	64.456	42.792	62.817
Median	0	4.563	-4.563	32.145
Standard deviation	14.67409	16.79224	23.31522	23.01314

	NCEP/NCAR	Gauge	Error	Absolute error
Mean	11.17768	14.7912	-3.541	15.35053
Minimum	0	0	-37.83	0
Maximum	61.056	64.456	51.479	51.479
Median	0	4.563	-4.563	32.145
Standard deviation	15.637	16.79224	21.48488	20.72738

	CRU/DWGA	Gauge	Error	Absolute error
Mean	1.499052	14.71912	-13.22	13.22006
Minimum	0	0	-58.01	0
Maximum	6.445	64.456	0	58.011
Median	0	4.563	-4.563	32,145
Standard deviation	1.757	16.79924	20.73088	20.02756

4.2 Comparison Model Results

In this section, the results of the model simulation are presented. The model setup and calibration were done for all precipitation data sets, first with ground stations data, which served as bench mark to assess model performance of other precipitation data sets. Calibration with rain gauge data also helped to identify what are hydrological processes that most influence the hydrology cycle of the study area such as wetlands, and ground water flow.

A semi-automatic model calibration and validation were carried out at Khartoum flow gauging stations (Figure 1). A semi-automatic calibration involves calibration of a variable (for instance flow) at one site by defining an objective function for this site. Thus it is a multi objective function optimization task. This was done in order to ensure a good calibration for the whole study area which is a vast watershed, because calibration at downstream gauging station (Khartoum) gave good results at that particular site in 2001 and 2002 in validation. The results are presented for each precipitation data set separately. The criteria for model performance was checked with the Nash-Sutcliffe's model efficiency (Ns) and coefficient of determination (R^2) and root-mean-square error (RMSE) base on the observed and simulated monthly stream flows over the calibration and validation periods. The calibration and validation period are from 1 July to 31 July 2001 and 2002

respectively, for CRU/DWGA, NCEP/NCAR Reanalysis and TRMM data set.

4.2.1 Ground station data results

The hydrograph of observed and simulated at Khartoum gauging station are shown in Figure 8-1 and 8-2. The Nash-Sutcliff's model efficiency (Ns) was 0.93 and 0.76 for calibration and validation respectively. Other performance criteria are given in Table 2.

	Calibration	Validation
Ns	0.93	0.76
R2	0.92	0.82
RMSE	428.187	221.449

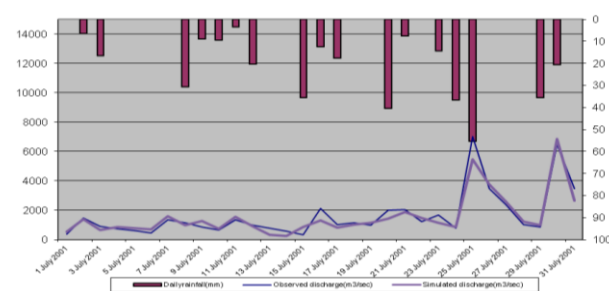


Figure 8.1 Rain gauge Calibration at Khartoum station

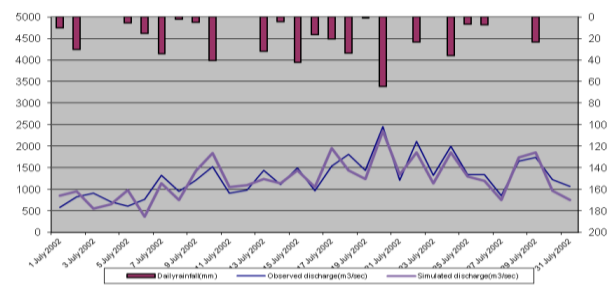


Figure 8.2 Rain gauge Validation at Khartoum station

4.2.2 CRU/DWGA

A semi automatic calibration was also performed at Khartoum station using CRU/DWGA precipitation data set. The calibration at Khartoum gave Nash-Sutcliff's model efficiency of -0.29 and R^2 of 0.2. The validation of the model was better. It gave Nash-Sutcliff's model efficiency of 0.12. Table 3 gives performance of the model. Figure 9-1 and 9-2 show hydrographs of calibration and validation respectively. The base flow prediction is reasonable, but peaks are either underestimated, or overestimated which give the overall model performance low.

	Calibration	Validation
Ns	-0.29	0.12
R2	0.20	0.35

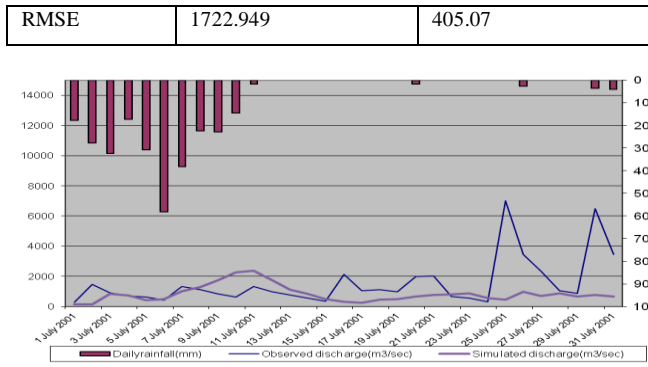


Figure 9.1 CRU/DWGA Calibration at Khartoum station

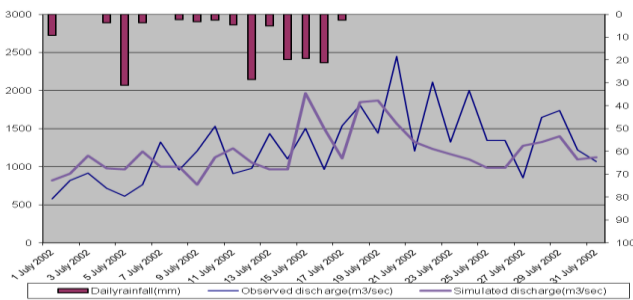


Figure 9.2 CRU/DWGA Validation at Khartoum station

4.2.3 NCEP/NCAR Reanalysis

The Distributed Hydrological model was calibrated and validated at Khartoum station (Figure 10-1 and 10-2). Table 4 gives performance of the model. The Nash-Sutcliffe's coefficient at Khartoum is 0.79 in calibration and 0.68 in validation. This means that NCEP/NCAR Reanalysis data set is better than other data set in this study area.

	Calibration	Validation
Ns	0.79	0.68
R2	0.74	0.70
RMSE	712.259	238.872

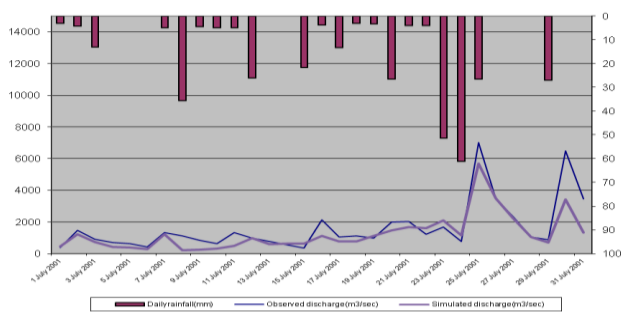


Figure 10.1 NCEP/NCAR Calibration at Khartoum station

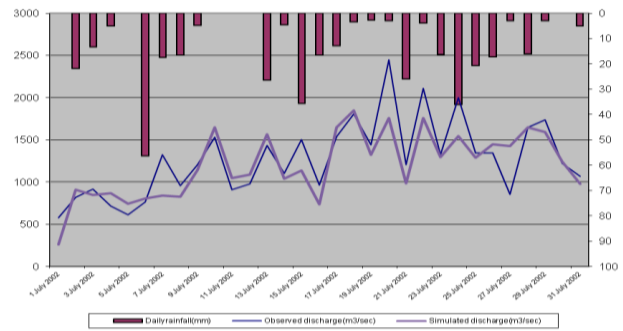


Figure 10.2 NCEP/NCAR Validation at Khartoum station

4.2.4 TRMM

The simulated stream flow using TRMM data set was compared to observed flow at Khartoum station. Due to underestimation of precipitation, the simulated stream flow was very low so that no calibration was done, except manual adjustment of ground water parameters.

Fig. 11 shows hydrographs of both simulated and observed stream flow at Khartoum station.

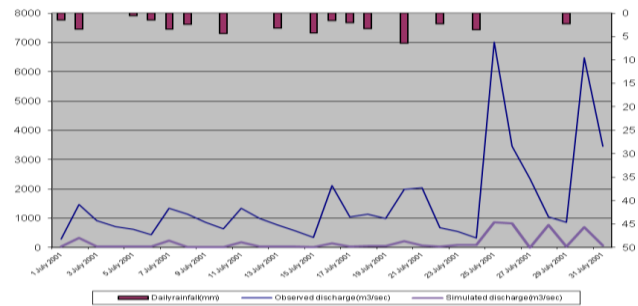


Figure 11 Hydrographs of measured and simulated discharge using TRMM data at Khartoum station

4.2.5 Discussion

Besides general problem related to flow gauging stations, modeling approach, each precipitation data sets has its own demerits. CRU/DWGA data set has underestimates precipitation which results in low model performance. The model predicted well base flow, but failed to predict peaks. The NCDP/NCAR simulation results show that underestimation of rainfall could give good model performance. However, this data gave relatively good results compared to other global data sets. The simulated hydrograph of TRMM data set shows under prediction of stream flow. The model performance was very low since there is no enough water in order to simulate observed stream flow. Nevertheless, observed and simulated hydrographs have same trend. This is to say the TRMM satellite captured rainfall events but failed to estimate the right amount. In addition, rainfall data used were taken at the beginning of the satellite mission (2001-2002), which could explain low data quality. Unfortunate, it was not possible to recent data because of limited stream flow data.

5. REFERENCES

[1] Tessema R., "Agricultural Drought Assessment for Upper Blue Nile Basin, Ethiopia" using SWAT, MSc. Thesis, Master of Water Science and Engineering, UNESCO-IHE, 2007.

- [2] Schuol, J., Abbaspour, K.C., 2007. "Using monthly weather statistics to generate daily data in a SWAT model application to West Africa". *Ecol. Model.* 201, 301-311.
- [3] Billi, P., el Badri Ali, O., "Sediment Transport of the Blue Nile at Khartoum". *Quaternary International* (2010), doi:10.1016/j.quaint.2009.11.041
- [4] Tarek Mohamed (2009). "Water and Sediment Management for the Blue Nile Basin". Thirteen International Water Technology Conference, IWTC 13 2009, Hurghada, Egypt
- [5] Nile Research Institute, National Water Research Center of Water and Ministry for Water and Agricultural, Egypt.

Experimental Testing of the Water Saving Potential of Different Faucet Aerators and their Performance over Time

Mahmoud F. Bader¹ and Bassam Abu-Hijleh²

¹ Sustainable Design of the Built Environment MSc Programme, The British University in Dubai
(ref_1277@hotmail.com)

² Sustainable Design of the Built Environment MSc Programme, The British University in Dubai
(bassam.abuhijleh@buid.ac.ae)

ABSTRACT

This research aimed at identifying the water saving potential of four different types of aerators including changes in their efficiency over a six month period. The study was conducted in Dubai International Academic City (DIAC) over six cycles. In each cycle the water flow rate from 16 faucet aerators and 3 control points were measured. Three different water pressures of 2.5, 2 and 1.5 bar were also used. The results revealed that the water flow rate from all faucets under 1.5 bar and 2 bar including the control points met the feature of the green building requirements of maximum water flow rate less than 6 L/min. On the other hand the water flow rate from aerators under a pressure of 2.5 bar were below 4.7 L/min. The water flow rate from faucet control point was 9.6 L/min. Furthermore, it was noted that, the water flow rates from faucet aerators under 1.5 and 2 bar decreased over subsequent cycles due to accumulation of sediments on the internal surfaces of the aerators. This was not the case for faucets under 2.5 bar of pressure. The water savings due to the installation of the aerators ranged between 20 % to 80 % compared to the control points depending on the different water pressure and types of aerators.

1. INTRODUCTION

1.1 Water Scarcity

Water is considered one of the most valuable resources. The demand for water is expected to increase rapidly in the future due to population increase and urbanization expands. According to United Nation (U.N) population division 2008: the current number of population is six billion and this number was expected increase to eight billion in 2025 [1].

Water consumption rate depends on many factors such as income rate and weather condition. Gulf countries are one of the areas where the gap between supply and demand is highest. Accordingly these countries are trying to bridge the gap by depending on water desalination which is associated with many negative environmental impacts in addition to high cost of the water production. In the U.A.E the average water consumption was 550 L/C/d in 2008 which is one of the highest rate in the world [2]. Table 1 shows the water consumption for different sectors in Dubai [3].

In U.S.A 16% of water consumption is in the building sector. Using large quantities of water in buildings has also cost impact on the operation and maintenance. Thus using efficient water fixtures can reduce the utility bills [4].

Table 1 water consumption in Dubai per sector [3]

Sector	Percentage of water consumption
Residential	60.61
Commercial	24.9
Industrial	3.7
Others	10.79

1.2 Needs for Water Consumption

There is a significant relationship between water consumption and energy demand, as water needs energy to be pumped through the water supply system. Additionally, energy is required for heating or cooling the water during different seasons which is proportionally relies on water quantity. Furthermore energy is required for treatment of the waste water. All these process require significant amounts of energy which in turn increase the production of green houses gases responsible for the global warming and climate change. Thus conserving water also save energy and protect the environment and future generation which is the main aim of the sustainability.

Haung et al. [5] conducted an experiment in hospital in Taiwan to investigate the effect of aerators and laminar on the promotion of Legionella species they built a model

plumbing system consisted from six faucets; two faucets with aerators, two with laminars and two as a control points. The researchers had also checked the water flow rates from such devices. They found: the water flow rate of 6 L/min for faucets with aerators, 1.2 L/min for faucets with laminars and 11 L/min for the control points [5].

1.3 History of the aerator

In the middle of the last century Elie P. Aghnides, a Greek inventor noted that, the water flowed from mountain streams is more effectively than the water flowed from normal water pipe due to aeration of the water during falling thus, breaking it in to bubbles foam, as a result he provided a set of metal screens in water pipe. He found that, the water outflow from the water pipe is bubbly, clean and soft [6].

Between the 1950's and 1980's, many changes have been integrated to original aerators in order to decrease the cost, improve the appearance of the aerator and to protect the aerator from becoming damaged, therefore in 1981 the aerator became concealed in the faucet [7]. By 1992 many modifications had been adapted to the aerator to comply with the requirements of the U.S Environmental protection Agency (EPA) and other standards to achieve the maximum water flow quantity of 2.5 GPM [8].

1.4 Principal function of the faucet aerator

The main function of the aerator is to drive air into the water flow thus produce considerable and whiter stream [9]. It consists of perimeter metal frame (housing) insert which may be P.V.C or wire mesh and a washer, Fig. 1.



Figure 1 Major components of an aerator [9]

1.5 Rational for the study

Many building assessment systems such as LEED, BREEAM and ESTIDAMA have emerged to character the green building. One of green buildings features is water conservation by using efficient plumbing fixtures such as faucet aerators. In this study different types of faucet aerators were used under different water pressures to evaluate the water saving using such fixtures also, to investigate the performance deterioration of the aerator over the time.

2. METHODOLOGY

2.1 Aerators used in the current experiment

In the conducted experiment four types of the aerators were chosen from the local market in the U.A.E they are described as below:

2.1.1 RST long life aerators

Referred to as (R) in the experiment; this aerator consists of a double inlet filter made of stainless and PVC. The outlet made of stainless steel mesh and there are many layers of mesh filters between the inlet and the outlet, Fig. 2.



Figure 2 Aerator type R

According to RST's manufacturer it "can save 40% to 60% of water and energy. It has a sensitive membrane which can diminish the water flow according to pressure" [10].

2.1.2 Neoperl type (N)

According to the manufacturer this aerator is in compliances with ASTM B456 corrosion prevention specifications. It also complies with ANS/NSF 61 against toxicity evaluation. Furthermore the water flow via aerators in sink faucets is 2.2 GPM maximum at 60 PSI, this means that it can save 20% to 30% of water use, i.e. using it can provide two LEED points when certifying a building [10]. Figure 3 shows aerator type N which consist of three major parts, Stainless steel casing, PVC casket and the inner par which has many PVC mesh layers.



Figure 3 Aerator type N

2.1.3 Kistenmacher (K)

Some parts of this type of aerator are made from PVC and other parts made of stainless steel, Figure 4. The casing inlet mesh and washer are made from rubber while the outlet mesh and casing are made from stainless steel [11].



Figure 4 Aerator type K

2.1.4 Pressure Compensating aerator (PCA) spray (P)

According to its manufacturer, this type is recommended in locations with low flow conditions. It is unbreakable single piece insert which provided non-splashing and non-aerated spray, Figure 5 The inlet and outlet mesh are made from plastic while the casing is made from stainless steel. Spray Faucets are suitable for hand washing and their uses is restricted to small domestic hand basins since its flows best at about 1.8 Liters/ Min [9]. This type is currently installed in Dubai International Academic City (DIAC) washrooms. The Advantage of this type is that, it has a potential to produce a constant water flow rate regardless of pressure fluctuations, Fig. 6.



Figure 5 Aerator type P [9]

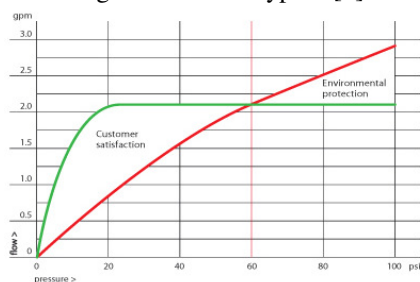


Figure 6 Pressure Compensating aerator [9]

2.2 Description of DIAC washrooms

Dubai International Academic City (DIAC) was established in 2007 and is located on 18 million square feet of land situated near Oasis City in Dubai. Currently it comprises three phases; each phase contains four academic buildings. Phase three which comprises buildings 9, 10, 11 and 12 was certified as LEED silver [12].

The DIAC water supply system consists of reinforced underground water tanks which receive water from Dubai

Electricity and Water Authority (DEWA). The water is pumped from the tanks through 150 mm PVC pipe into 100 mm PR. PVC pipes are located inside shafts then the pipes branched in to the washrooms. The branch pipes made from PR. PVC pipe of 16 mm to 25 mm for cold water and 20 mm PRP pipe for hot water. The washrooms are located on each floor between the buildings. Some washrooms have five washbasins and other have seven.

2.3 Experimental procedures

The most important feature of the experimental method, is finding the relationship between independent and dependent variables in order to prove the hypothesis. In this study water pressure and aerator types are considered as independent variables while water flow is considered to be dependent variables.

A request through British University in Dubai (BUiD) was sent to DIAC management to get permission to conduct the experiment. A meeting with the facility management department was conducted to understand their practice in the maintenance of the water supply systems during the meeting they revealed that; usually every six month there is maintenance for the existing aerators. Accordingly the next maintenance will be conducted after six months thus the experiment results would not be compromised. In addition they mentioned that no treatment could be carried out on DIAC campus. Furthermore, water tank location and water supply pipe type and size were obtained.

The washrooms under study were chosen on a condition that they should be used regularly by most consumers in order to avoid any bias which could result from stagnation of the water in the aerators. The old plumbing fixtures of the washbasins were dismantled and four different types of the aerators (total 16 no.) were labeled and sterilized using Alcohol and installed. Three different water pressure were set; 1.5, 2 and 2.5 bar (the maximum recommended by the DIAC management).

A stopwatch and a graduate cylinder were used for the field experiment, Fig. 7. In order to record the effect of the faucet aerators on the water flow rate, three control faucets (without aerators) were assigned in the three different pressure areas. The water flow rate tests were conducted every four weeks (October 2010 until March 2011).

In the first cycle, the old aerators were dismantled, sterilized by emerging them in hydroxide alcohol and replaced by the cleaned one. All water valves related to faucets aerators under the study were checked that they were fully opened. Water flow was tested by filling up graded bottle to 1000 ml: the time it took for this to happen was recorded. The flow test was repeated three times for each faucet then, the average was computed. The aforementioned steps were repeated for all cycles.



Figure 7 Tools used in Field Measurements

3. RESULTS

Table 2 illustrates the water flow rates expressed in liters per minute, of the different types of aerators as well as the control point, all which were under two Bar water pressure. In cycle one the flow varied from 1.81 L/min for aerator type P, 4.66 L/min for type N, 3.32 L/min for type K, 4.42 L/min for type R, and 5.5 L/min for the control point. It was noted that the flow rate slightly decreased over the cycles. These variations in the flow rates are presented in Fig. 8.

Table 2 Water flow rate (L/min) of different type of aerators under 2 bar water pressure

Cycle No	Q(P)	Q(N)	Q(K)	Q(R)	Q(C1)
1	1.81	4.66	3.32	4.42	5.55
2	1.8	4.55	3.38	4.4	5.57
3	1.85	4.7	3.42	4.53	5.86
4	1.79	4.61	3.34	4.36	5.92
5	1.74	4.52	3.4	4.41	5.95
6	1.73	4.53	3.29	4.29	5.92

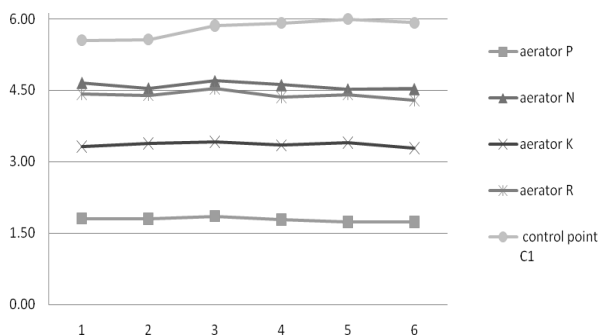


Figure 8 Water flow rate of different type of aerators and control point under 2 bar water pressure.

Table 3 presents the percentage of the water flow rate of the different types of aerators relative to the control point under 2 bar water pressure. It showed that in cycle one the

percentage of the flow rate for aerator type P compromised 32.55 % of the water flow relative to the control point, in aerator type N the flow rate was 83.97%, in aerator type K the flow rate was 59.82%, and in aerator type R the flow compromised 79.69 %. In the next cycles, the aerators flow rate percentage almost decreased in all faucets except for the control point which almost remained the same. Figure 9 presents the percentage of the water flow rate of faucets aerator relative to the control point all under 2 bar water pressure.

Table 3 percentage of water flow rate relative to control point under 2 bar water pressure

Cycle no.	% of Aerator P	% of Aerator N	% of Aerator K	% of Aerator R
1	32.55	83.97	59.82	79.69
2	32.25	81.62	60.69	78.94
3	31.67	80.19	58.36	77.41
4	30.18	78	56.52	73.67
5	28.94	74.62	56.71	73.58
6	29.2	75.29	55.94	72.51

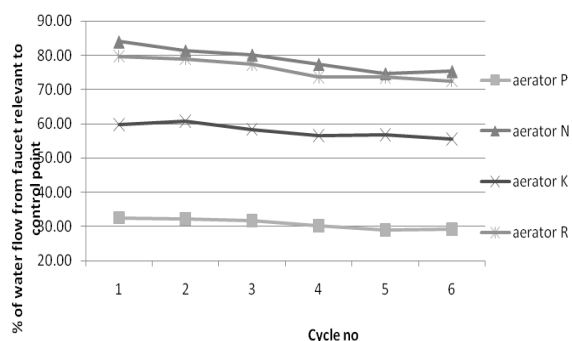


Figure 9 percentage of the water flow rate of faucet aerators relative to control point under 2 bar water pressure.

Table 4 illustrates the flow rate of different type of aerators and control point under water pressure of 2.5 bar. In cycle one; the flow rate was 1.67 L/min, 4.57 L/min 3.46 L/min, 3.94 L/min and 9.54 L/min for aerators P, N, K, R and C2 respectively. For the next cycles the flow rate slightly varied in each aerator despite the flow rate increased in the control point. At the end of the study the flow rates in all faucets almost the same in respect to first cycle however; the control point the flow rate was slightly increased. Figure 10 presents the variation in water flow from cycle to cycle under 2.5 water bar.

Table 4 Water flow rate (L/min) of different type of aerators under 2.5 bar water pressure

Cycle No	Q(P)	Q(N)	Q(K)	Q(R)	Q(C1)
1	1.67	4.57	3.46	3.94	9.54
2	1.74	4.65	3.49	4.11	10.6
3	1.69	4.09	3.41	4.17	9.67
4	1.66	4.17	3.41	3.98	10.27
5	1.82	4.58	3.46	4.19	9.83
6	1.82	4.58	3.4	4.11	9.87

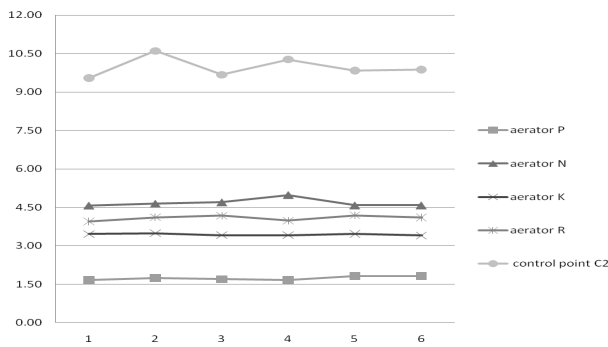


Figure 10 Water flow rate of different type of aerators and control point under 2.5 bar water pressure.

Table 5 shows the percentage of the water flow rates from the different types of aerators in respect to the control point under water pressure of 2.5 bar. In cycle one the percentage of the water flow rate from aerator type P comprised 17.49 % of the control point flow rate, 47.92% for aerator type N, 36.24 % for aerator type K and 41.35 % for aerator type R. In the following cycles the percentage almost decreased. Figure 11 presents the percentage of water flow rate from faucets aerators relative to control point under 2,5 bar water pressure.

Table 6 displays the water flow rates of the different types of aerators and control point under water pressure of 1.5 bar. In cycle one the flow rate was 2.03 L/min, 3.23 L/min, 2.62 L/min and 2.91 L/min for aerators P, N, K, and R respectively. On the other hand the flow rate of the control point was 4.33 L/min. Figure 12 presents the changes in flow rate of the aerators over the cycle period. It shows a decrease in the flow rate from cycle to cycle although the flow rate from the control point is increased.

Table 5 percentage of water flow rate relative to control point under 2.5 bar water pressure

Cycle no.	% of Aerator P	% of Aerator N	% of Aerator K	% of Aerator R
1	17.49	47.92	36.24	41.35
2	16.4	43.82	32.93	38.79
3	17.51	48.56	35.29	43.15
4	16.18	48.52	33.25	38.76
5	18.51	46.57	35.21	42.6
6	18.48	46.4	34.44	41.62

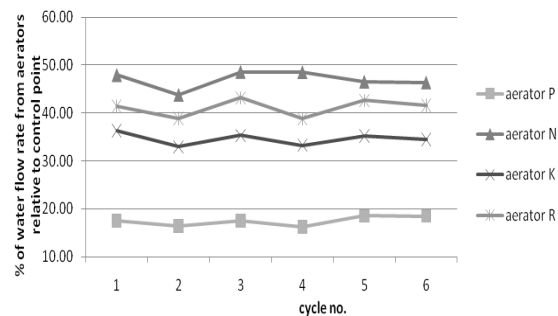


Figure 11 Percentage of water flow rate of faucet aerators relative to control point under 2.5 water bar

Table 6 Water flow rate (L/min) of different type of aerators under 1.5 bar water pressure

Cycle No	Q(P)	Q(N)	Q(K)	Q(R)	Q(C1)
1	2.03	3.23	2.62	2.91	4.33
2	1.88	3.16	2.63	2.92	4.4
3	1.95	3.05	2.63	2.88	4.6
4	1.84	3.09	2.66	2.93	4.48
5	1.83	3.08	2.6	2.94	4.53
6	1.76	2.95	2.56	2.84	4.48

Table 7 displays the percentage of the water flow rate from different aerators relative to control point under 1.5 bar of water pressure. In cycle one The flow rate from aerator type P presented 47.01% in comparison to control point and 74.64 %, 50.47% and 67.22% for aerators N, K and R respectively. The table shows the variations in flow rate percentages in the next cycles. Figure 13 shows the

percentage of water flow rate from faucet aerators relative to control point all under 1.5 water bar.

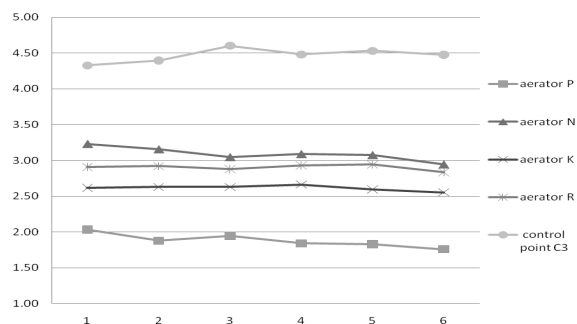


Figure 12 Water flow rate of different type of aerators and control point under 1.5 bar water pressure.

Table 7 percentage of water flow rate relative to control point under 1.5 bar water pressure

Cycle no.	% of Aerator P	% of Aerator N	% of Aerator K	% of Aerator R
1	47.01	74.64	60.47	67.22
2	42.73	71.8	59.82	66.42
3	42.32	66.21	57.12	62.59
4	41.09	68.94	59.46	65.36
5	39.3	65.78	57.06	63.33
6	42.13	69.21	58.53	64.97

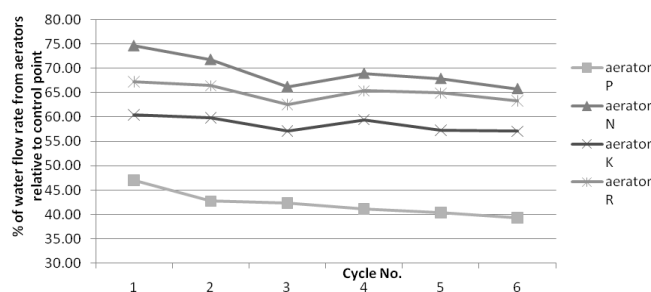


Figure 13 The percentage of water flow rate from faucet aerators relative to control point all under 1.5 water bar.

At the end of the study the all aerators were dismantled. It was observed that sediments clogged part of the aerators. The sediments seemed to be more in aerators under 1.5 bar and 2 bar, Fig. 14.



Figure 14 accumulated sediments on internal surface of aerator

4. DISCUSSION

The aerator works as obstacle for the sediment and inhibit it to flow with water which could has two effects. The first effect is that, the sediments may contain biodegradable organic matter which setup foundation for the forming of biofilm. The second effect is deterioration of the efficiency of the aerators by reducing the water flow rate over time; thus regular maintenance and cleaning is required to avoid deterioration.

It was noted that, flow rate from all faucets under 1.5 bar and 2 bar water pressure both with and without aerators, have a flow rate that complies with green building features that maximum flow rate is 6 L/min. Additionally, the water flow rate from aerator type P confirm the manufacturer claim that it has potential to keep a constant water flow regardless of the water pressure as seen in Tables (2-7). Additionally it offered higher water saving than the other types with an average saving of 58% to 83% in comparison to the control point. This type was closely followed by types K, R and N. with saving 41% to 65%, 24% to 59% and 21% to 53%, respectively. Although there is higher water saving with type P, it may also cause inconvenience to the end user due to slow rate.

Moreover, as seen in Tables 2 and 6, a decrease in the flow rates from aerators under 1.5 bar and 2 bar were noted over the cycles despite the flow rate in the control points under the same pressure being slightly increased. This was due to the accumulation of sediments in the aerators which may have compromised their efficiency. On the other hand, it was noted that all faucets under 2.5 pressure of water bar excluding the control point (the faucet without aerator) complied with the green building features proposed by DEWA. The flow rate in the control point was above 9 L/min and the flow rate in type P was the least followed by types K, R and N respectively however, a gain the flow rate in Type P might caused inconvenience to the end users. It was obvious that type P saved about 83 % of the water relative to the control point followed by 66% in type K then 65 % in type R and 53% in type N.

Additionally, the efficiency of the aerators reduced over the time due to accumulation of sediment on the inlet of the

aerator consequently it is advised to conduct maintenance to the aerators every three months to avoid such accumulation

5. CONCLUSIONS

All aerators have the potential to conserve water however; the water saving depends on the aerator types and water pressure. In this study the water saving ranged from 20 % to 80%. Aerator type P was the premium saver. Additionally, it confirmed the manufacturer claimed that aerator type P has a potential to keep constant water flow rate regardless of the water pressure variations, since this type can compensate the water pressure. On the other hand, this type has the potential disadvantage that it may compromise the end users due to its low flow rate.

It is worthy to mention that the water flow rate from faucets (pressure ≤ 2 bar) whether they have aerator or not met the green building requirements, i.e. that the maximum water flow rate is ≤ 6 L/ min. Using the aerator under water pressure ≤ 2 bar has two impacts: 1) A positive as it reduced the water splash and produces a fine stream flow. 2) A negative impact in that it was susceptible to sediment accumulation on its internal surface which may affected the water quality and reduce its water saving efficiency.

Furthermore, the water flow rates from faucet aerators' under 2.5 bar varied based on the type of the aerator. In this research aerator type P was the premium water saver followed by aerator types K, R and N respectively.

Finally, it is recommended to maintain the aerators every three months in order to avoid accumulation of sediments on the internal surface of the aerator.

REFERENCE

- [1] Wright, R. & Boorse, D. *Environmental Science Toward A Sustainable Future*. San Francisco: Pearson, 2011.
- [2] Absel, R. "Free Water-Saving Devices for UAE Homes" *Gulf news* [online] 13 January, 2010 [Accessed 15 August 2010]
- [3] Dubai Electricity and Water Authority (2009). *Water Statistics*
- [4] LEED *Reference Guide for Green Building Design and Construction*. Washington: Green Building Council, 2009.
- [5] Huang, W. and Lin, Y. "A controlled Study of Legionella concentration in Water from Faucets with Aerators or Laminar Water Flow Devices," *Infection Control and Hospital Epidemiology*, Vol.28, No. 6, pp 765-766, 2007.
- [6] Juror, J. *Waterfall Faucet*, Life Magazine, 1946.
- [7] Elie, A. *Concealed Liquid Flow Aerator*, 1992.
- [8] EPA *Water Sense*, 2010.
- [9] Neoperl 2010. [online]. [Accessed 15 September 2010].available at: <http://www.neoperl.net/en/oem/products/aerators/pressurecompensating.html>
- [10] RST ,Water saving system, 2010. [Online]. [Accessed 6 Oct. 2010] Available at:http://www.rst.co.za/index.php?option=com_content&view=article&id=47&Itemid=54
- [11] Kistenmacher [online]. Accessed 15 October 2010] Available at: http://www.kistenmacher.de/about_us.htm
- [12] Al Mashni, DIAC phase-III becomes Middle East's first and largest LEED certified academic facility, AMEinf.com, 2009. [Online] 23 June [Accessed 15 January 2011] available at: <http://www.ameinfo.com/201501.html>

The First Water Quality Model From the Arabian Gulf and a New Endogenous Development Capacity in the Region

Johannes Lawen¹, Ahmed Abdel-Wahab²

¹ Texas A&M University at Qatar, Texas A&M Engineering Building, Education City, 23874 Doha, Qatar
(johannes.lawen@qatar.tamu.edu)

² Texas A&M University at Qatar, Texas A&M Engineering Building, Education City, 23874 Doha, Qatar
(ahmed-abdel-wahab@qatar.tamu.edu)

ABSTRACT

A new water quality model has been developed within the Qatar sustainable Water and Energy utilization initiative (QWE). The model includes beside species transport also volatilization and conversion. The unstructured mesh type model follows a modular approach in order to focus on constituent conversion and mass-exchange with the atmosphere while being able to work with different separate hydrodynamic models. Nonlinear and spline approximations of kinetics, byproduct formation and joint atmosphere simulation have been embedded. The tool has been programmed as windows application with a graphical user interface and integrated error analysis concerning mesh dependency and system approximation. In this work industrial cooling water discharge and biocide plume simulations are presented. Model-, simulation-, graphical user interface- and visualization development have been carried out in Qatar. The work elaborates the advantage of local model development for a reliable engineering and environmental impact assessment consultancy service and reports on studies for which the model has been utilized.

Keywords: Water quality model, Finite Volume method, parabolic transport PDE, adaptive upwind method, matrix reordering

1. INTRODUCTION

Computer fluid dynamics are an indispensable part of science and engineering. Plant and chemical reactor design, cooling circuit heat transfer and environmental impact assessments rely on computer fluid dynamics. A new computer fluid dynamics software has been developed within the Qatar sustainable Water and Energy utilization imitative (QWE). This model has mainly been used for environmental impact assessment (EIA). Appliances in chemical reaction engineering are also possible. EIAs utilized the new model for water quality simulations along the eastern coast of Qatar and its cooling water discharge outfalls. Environmental Discharges of cooling water into receiving water bodies are an environmental concern [1] since discharged biocides, such as residual chlorine, are often harmful to aquatic life [2]. Therefore, many of cooling water discharge constituents are regulated [3]. In order to assess their environmental impact, cooling water plumes can be simulated. Coastal transport simulations and plume prediction models are often discussed in scientific articles [4, 5] and constitute a significant consultancy sector [6] in environmental impact assessment. Besides advective transport and dispersion, the development of hypochlorous and hypobromous acid as well as halogenated matter plumes depend on reactive consumption or accumulation and oxidants mass-exchange with the atmosphere. The accurate approximation of the coastal water body, the

incorporation of shoreline geometry, is important for a representative depiction of the simulated domain. Unstructured meshes are very suitable for complex domain shape approximation. The unstructured mesh allows an increased resolution at areas of importance, such as shorelines and surrounding discharge outfalls, while the cell size can be inflated for bulky areas of less importance; thus, saving computational time. The simulation software can be applied to depict environmental domains such as air and water bodies, species transport phenomena in chemical reaction engineering, or biocide conversion in cooling circuits. Concerning water quality simulations in the Arabian Gulf, several solely structured mesh and even closed form models, such as GEMSS [7] and Cormix [8], are often used in regional EIAs. Heretofore, these models neither allowed incorporating generalized kinetic models beyond first order decay nor generalized modeling of plume constituent mass-exchange with the atmosphere. The model introduced in this publication utilizes unstructured meshes which allow a smooth increase of the cell density (the resolution) in areas of importance, thus achieving a better approximation of shorelines, channels and industrial outfalls. Nonlinear conversion models or spline approximations of laboratory measurement time series can be employed. Therefore, nonlinear byproduct formation and fate can be simulated. Mass-exchange with the atmosphere has been embedded via Henry equilibrium coefficients. If the simulated species occurs naturally in the atmosphere (e.g. oxygen

or carbon-dioxide), then a corresponding equilibrium concentration can be set in the top layer of the water domain. If the simulated species does not constitute an air-fraction (e.g. biocides such as chlorine), then calculating species dependent equilibrium based mass-exchange at the sea-atmosphere interface requires simulating the species distribution in the surface-near atmosphere. Otherwise, neglecting minor species accumulation (due to volatilization) in the surface-near atmosphere and assuming an atmospheric species concentration of zero (for e.g. chlorine) would correspond to a sea top-layer equilibrium concentration of zero. This would result in solely dispersion dependent volatilization regardless of component specific volatilization behavior. Species volatilization requires therefore the simulation of its distribution throughout the near-sea-surface atmosphere. The developed water quality model can simulate the coastal water body's residual chlorine concentration coupled with the atmosphere. Options have been integrated for error analysis concerning the mesh dependency of results and allow a comparison between explicit and implicit solution approaches. Algorithms have been developed [9] which are optimized for flow field superimposed water quality simulations. With the available flow field information, the transport simulation's solver uses the phenomenological approach of fluid flow guided matrix reordering, allowing the explicit calculation of stable implicit approximations.

The model design approach is focused on water quality simulation including contaminant/species specific driving forces such as conversion and mass exchange with the atmosphere within a modular structure, with a separate hydrodynamic simulation. The tool has been programmed as a Windows application in FORTRAN 90 with graphical user interface and result plotting functions including interpolation. The developed tool furthers the establishment of unstructured meshes in water quality simulations. Complex kinetics beyond 1st order decay terms can be depicted based on an automatic spline approximation of laboratory measured oxidants decay and halogenated compound formation. If measurement distributions include all dependencies, all relevant parameters (e.g. temperature or salinity), then utilizing spline approximations might relieve the engineer or consultant from developing a kinetic model. The simulation of excess oxidants mainly considers the fate of hypobromous acid, since under seawater conditions residual chlorine quickly converts to chloride while producing hypobromous acid [10]. The simulation of the species distribution is split into a hydrodynamic and a superimposed reaction and flow field driven advection simulation – a strategy relying on the prerequisite that changes of hydrodynamic properties due to reactions are negligible [11]. This prerequisite is certainly fulfilled for the biocide concentration ranges operated at cooling

circuits. The coastal flow field computation in this work has been carried out with the unstructured grid Finite Volume Coastal Ocean Model [12-14]. The developed tool allows systematic analyzing of errors based on both horizontal unstructured mesh and vertical layer-grid resolution. Horizontal as well as vertical meshing can be split into triangle sub-meshes and sub-layers respectively in order to obtain a comparable accurate reference solution to quantify errors based on the finite volume domain approximation. Also, the developed tool's implicit matrix reordering-based solver can produce reference solutions to allow estimating error contribution of usual explicit (time-wise) approximations.

2. METHODOLOGY

The structure of the modules is depicted in figure 1. The developed tool is suggested to be intertwined in a structure which contains a water and air quality model, atmospheric flow and dispersion, as well as a hydrodynamic model. All receive the same unstructured horizontal mesh, as shown in figure 1, from a meshing tool like the Surface Modeling System (SMS) from Aquaveo. Based on this mesh a hydrodynamic tool such as the FVCOM is used to compute for each time-step flow, dispersion, salinity, temperature and surface elevation fields. Likewise the atmospheric model, such as a k - ϵ model [15] in Fluent, simulates velocity and dispersion fields for the atmosphere. Flow, dispersion, and surface elevation fields are fed into the water quality model. If necessary, for kinetic or marine life models, temperature and salinity fields are transferred to the water quality model as well, in order to set individual reaction rates in each finite volume cell. The coastal hydrodynamic and water quality simulation receive their source terms from a plant cooling circuit model. A cooling circuit mesh is generated with Fluent related meshing modules, the flow field inside the circuit is simulated with Fluent and then fed into the cooling circuit water quality model. This procedure has been examined by exporting the flow field from Fluent to the water quality model with Techplot. The advantage of this strategy is that all models which consider biocide and byproduct fate are integrated in one water quality model which receives flow fields from three different fluid dynamic simulations: cooling circuit, coastal water body and near-surface atmosphere.

2. METHODOLOGY

The structure of the modules is depicted in figure 1.

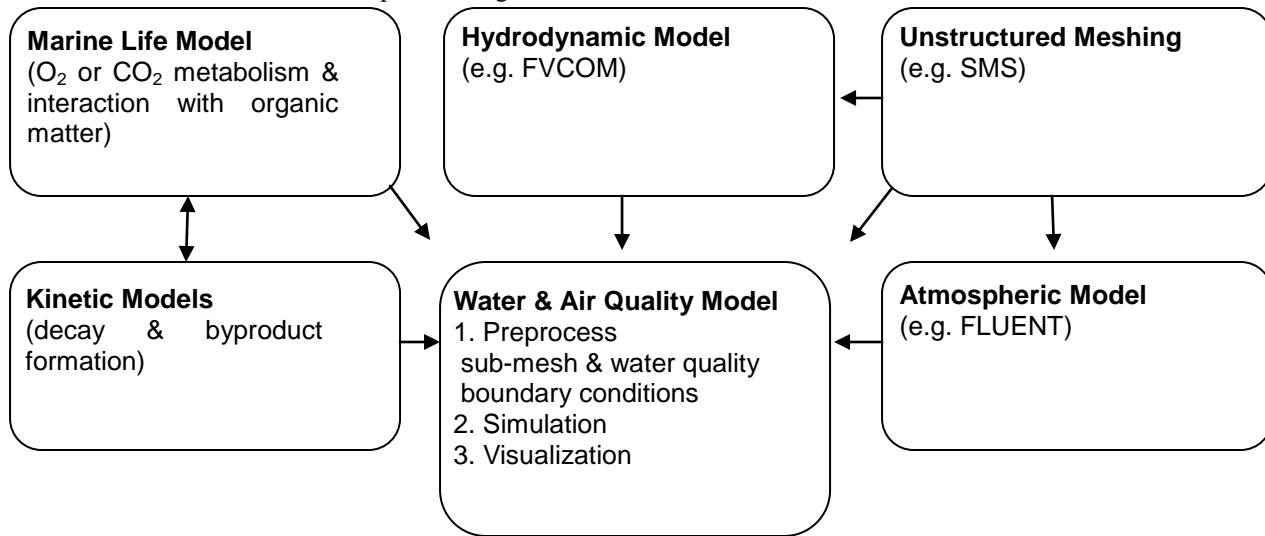


Fig. 1. Modular model structure of meshing, computer fluid dynamics, air and water quality model. The hydrodynamic and the atmospheric models compute flow, dispersion, and temperature fields for the water and air quality model. All 3 simulations utilize the same horizontal triangle-mesh generated by the unstructured meshing tool.

The developed tool is suggested to be intertwined in a structure which contains a water and air quality model, atmospheric flow and dispersion, as well as a hydrodynamic model. All receive the same unstructured horizontal mesh, as shown in figure 1, from a meshing tool like the Surface Modeling System (SMS) from Aquaveo. Based on this mesh a hydrodynamic tool such as the FVCOM is used to compute for each time-step flow, dispersion, salinity, temperature and surface elevation fields. Likewise the atmospheric model, such as a k - ϵ model (Launder et al., 1972) in Fluent, simulates velocity and dispersion fields for the atmosphere. Flow, dispersion, and surface elevation fields are fed into the water quality model. If necessary, for kinetic or marine life models, temperature and salinity fields are transferred to the water quality model as well, in order to set individual reaction rates in each finite volume cell. The water quality tool's transport model is a set of Finite Volume Equations (FVE). The FVE can either be derived from an advection, dispersion, and reaction partial differential equation (PDE) or by balancing directly mass flow through the Finite Volumes. The PDE is a balance of molar in and outflow of a species, j , along an infinitely small control volume. Terms for dispersive mass flow, conversion and convection are taken into account. In and outflows at $r_i + dr_i$ are

written at r_i , the cell centre, by substituting $\dot{n}(r_i + dr_i)$ with $\dot{n}(r_i) + \partial\dot{n}(r_i)/\partial r_i dr_i$. Linearized reactions l for each species j are notated with stoichiometric, σ_{jl} , and kinetic matrix, k_{jl} .

$$\begin{aligned} & \frac{\partial c_j(\mathbf{r}, \tau)}{\partial \tau} \\ &= \sum_i \frac{\partial}{\partial r_i} \left(D(\mathbf{r}, \tau) \frac{\partial c_j(\mathbf{r}, \tau)}{\partial r_i} - u_i(\mathbf{r}, \tau) c_j(\mathbf{r}, \tau) \right) \\ &+ \sum_l \sigma_{jl} k_{jl} (c_j(\mathbf{r}, \tau)) c_j(\mathbf{r}, \tau) \end{aligned} \quad (1)$$

$(c_j(\mathbf{s}))$ is a kinetic rate dependent on the component concentration. If the dependency of the rate on the concentration is given in the form of discretized data, then the conversion can be depicted with linear splines. The rate is updated dependent on the time and space wise local concentration.

3 WATER QUALITY MODEL

The developed water and air model solves the transport PDE for the water and air phase including exchange at the sea-atmosphere interface, species decay, and byproduct formation. New functions supporting error analysis are described in section 3.4 and an implicit solver optimized for flow field superimposed water quality computations is explained in section 3.2. The explicit and implicit form of the adaptive upwind finite volume equation, for all $c_{ih}^t \in \mathbf{c}_h^t$ cells $i_y \in \mathbf{I}$ in a layer h , can both be expressed with:

$$\begin{aligned}
\frac{\partial u}{\partial t} + u \frac{\partial u}{\partial x} + v \frac{\partial u}{\partial y} + w \frac{\partial u}{\partial z} - f v &= -\frac{1}{\rho_0} \frac{\partial P}{\partial x} \\
&+ \frac{\partial}{\partial z} \left(K_m \frac{\partial u}{\partial z} \right) + F_u \\
\frac{\partial v}{\partial t} + u \frac{\partial v}{\partial x} + v \frac{\partial v}{\partial y} + w \frac{\partial v}{\partial z} - f u &= -\frac{1}{\rho_0} \frac{\partial P}{\partial y} \\
&+ \frac{\partial}{\partial z} \left(K_m \frac{\partial v}{\partial z} \right) + F_v \\
\frac{\partial P}{\partial z} = -\rho g \text{ and } \frac{\partial u}{\partial x} + \frac{\partial v}{\partial y} + \frac{\partial w}{\partial z} &= 0.
\end{aligned} \tag{3}$$

where x , y and z are the east, north, and vertical axes. The FVCOM furthermore uses a heat and salinity balance and computes the density ρ as a function of temperature and salinity. P is the pressure; f the Coriolis parameter; g is the gravitational acceleration; K_m is the vertical eddy viscosity; F_u and F_v represent the horizontal momentum diffusion terms [18].

3 SPECIES TRANSPORT MODEL

The developed water and air model solves the transport PDE for the water and air phase including exchange at the sea-atmosphere interface, hypobromous acid decay, and halogenated compound formation. New functions supporting error analysis are described in section 3.5 and an implicit solver optimized for flow field superimposed water quality computations is explained in section 3.2. The explicit and implicit form of the adaptive upwind finite volume equation, for all $c_{ih}^t \in c_h^t$ cells $i_y \in I$ in a layer h , can both be expressed with:

$$\begin{aligned}
\frac{c_h^{t+\Delta} - c_h^t}{\Delta t} &= - \sum_s \left(g_{hs}^t (c_{nl(I,s)h}^t - c_h^t) \right. \\
&+ \dot{v}_{hs}^t v_h^{t-1} \left(\epsilon_{hs}^t \left((1 - \pi_{hs}^t) c_h^t \right. \right. \\
&+ \pi_{hs}^t c_{nl(I,s)h}^t \left. \left. \right) \right. \\
&+ \left. \left((1 - \pi_{hs}^t) c_h^{t+\Delta} \right. \right. \\
&+ \left. \left. \pi_{hs}^t c_{nl(I,s)h}^{t+\Delta} \right) (1 - \epsilon_{hs}^t) \right) \\
&+ k_h^t (c_h^t + c_h^{t+\Delta}) / 2
\end{aligned} \tag{4}$$

The logical control bit $\epsilon_{ih_s}^t \in \epsilon_{hs}^t$ regulates whether advective flows through side s of triangle ih is approximated explicit or implicit. Dispersion through the 5 surfaces of one of the unstructured mesh's triangle prism is quantified by $g_{hs}^t = \Delta a_{hs}^t \delta_{hs}^t / (\Delta r_s v_h^t)$ where $\delta_{hs}^t \in \delta_{hs}^t$ is the dispersion coefficient vector of cell ih at surface s ; $\Delta a_{ih_s}^t \in \Delta a_{hs}^t$ is the finite volume cell surface vector; $\Delta r_{ih_s}^t \in \Delta r_{hs}^t$ the inter-centroid distance vector and $v_{ih}^t \in v_h^t$ contains all cell volumes for a layer h . $\dot{v}_{ih_s}^t \in \dot{v}_{hs}^t$ is the volume flow vector for cell ih with respect to side s . The closed form kinetic model-based constant, or spline constant, $k_{ih}^t \in k_h^t$ corresponds to a certain concentration level and, as the case may be, to further parameters, such as temperature, which are

assigned to cell i and time level t . $\pi_{ih_s} \in \pi_{hs}$ regulates to what percentage a concentration value of a certain centroid (the concentration of cell i itself or of its neighbor) factors into the flow approximation. π_{ih_s} is the adaptive upwind control bit which functions to approximate flow calculation to 0% based on the mass-receiving centroid and to 100% based on the donating centroid (except at open boundaries). The first row in equation 3 represents dispersive exchange. The remainder of the equation contains the approximation of horizontal advection and conversion. Flow field, dispersion, surface elevation, salinity, and temperature arrays can be fed to the program by any hydrodynamic simulation which stores data either on the triangle centroids, nodes, or centers of the finite volume surfaces. For the error analysis in section 4, data from the FVCOM have been fed into the water quality model.

3.1 Boundary conditions

Ten boundary conditions have been embedded into the new water and air quality model. The horizontal open boundary condition $0 = \partial c / \partial n|_{n=0}$ with $\mathbf{n} \perp \partial \Omega$ defines the gradient at the boundary to be zero for both water and air. This suppresses dispersion but permits advection through the open boundary. The no-flux boundary condition $0 = \mathbf{u}c - D\partial c \partial n|_{n=0}$ assures that neither dispersive nor advective flux passes through a solid boundary. At the sea and air boundary layer, dispersion is replaced with the Henry coefficient equilibrium assumption $c_w = c_{at} / k_{eq}$. This requires that hypobromous acid is simulated throughout the near-surface atmosphere. If the species occurs in the atmosphere (e.g. O_2 or CO_2) then the corresponding equilibrium concentration (depending on salinity and temperature) is set in the entire top-layer of the water body and the simulation of the near-surface atmosphere can be omitted. The vertical open boundary condition for the atmosphere extrapolates the vertical gradient to the other side of the boundary. This type of open boundary condition permits dispersion and has been chosen to avoid an insulating functioning of the condition since dispersion is the dominating transport mechanism along the vertical extension. Intakes can be approximated by two different boundary conditions. 1) Mass conservation between intake inflow and the flow advected through the surfaces of the cell is assumed. Approximated for finite volumes, this is equivalent to setting all volume flows through the cell surfaces to zero. This has the effect that the concentration of the cell will be evened by dispersion to the levels of the surrounding cells. 2) Alternatively the intake cell can be set to a constant value which has been measured. This boundary condition can also be utilized when measurements have been taken at some locations and the ensuing plume is of interest. Therefore this boundary condition can be used for discharges, intakes

and calibrations with measurement values. Also source term boundary condition can be used for discharges as an alternative to setting a constant value. Contrary to the adaptive upwind principle, advection through the open boundaries is always calculated based on the cells which are located at the boundary. This is embedded by including the boundary condition information in the adaptive upwind control bit π_{ihs} .

3.2 The semi-implicit fluid flow adaptive matrix reordering solver

The developed software can simulate species distributions based on time wise explicit or implicit finite volume equations. The fluid flow adaptive solver allows solving a semi-implicit adaptive upwind system solely by means of matrix reordering. ε_{ihs} is the logical bit which sets the implicit partition of time wise species concentration approximation and is usually at 0.5 to assure an even averaging between explicit and implicit approximation. Assuming implicit or partially implicit approximation, the finite volume equation system (FVES) corresponds to a matrix form $\mathbf{M}\mathbf{c}^{t+\Delta} = \mathbf{b}$ with \mathbf{M} containing the coefficients of concentrations at subsequent time level $c_{ih}^{t+\Delta}$. This system could be solved entirely by matrix reordering under the condition that no circulations are given in the flow field. Unfortunately, coastal simulations contain circulations. Therefore, approximation and solver have been integrated, as published in a separate work [9], to generate a partially explicit and partially implicit approximated FVES. This is solvable by matrix reordering but keeps the most volume flows (and relatively stability affecting flows) in implicit approximation. The matrix reordering is carried out by calculating cells sequentially along the direction of the fluid flow. Due to the adaptive upwind principle, implicit approximated concentration values, $c_{ih}^{t+\Delta}$, can be isolated and calculated during fluid flow direction adaptive ordered computation. In case of circulations, relatively slow flows between relatively large cells are approximated explicit and ε_{ihs} is equal to zero. For the explicit solver ε_{ihs} is always equal to 1.

3.3 Hydrodynamic field interpolation

Hydrodynamic field data, velocity components, dispersion coefficient and, surface elevation and if necessary for the calculation of Henry equilibrium coefficients and kinetics models or spline kinetics also temperature and salinity fields are transmitted from the hydrodynamic simulation to the water quality model. Ideally velocity component field data are stored at the center of triangle prism surfaces, since the simulation relies on the balance of mass flow through the volume surfaces. Preferable velocity components at the surfaces are volume and mass flow conserving for each cell and

between neighboring cells. However, velocity component field data from the FVCOM model are generated at the triangle centroids (surface elevations are stored at triangle nodes). Therefore, the velocity components at the cell surfaces must be interpolated. The FVCOM flow field is furthermore not volume flow and mass flow conservative for a single cell. Three interpolation procedures have been embedded: 1) Taking the velocity components of a triangle centroid for each surface of the cell. 2) Linear weighted interpolation between two neighboring cell centroids. 3) Averaging the velocity values corresponding to the two triangle nodes which form a triangle side; velocity values at triangle nodes are calculated by averaging the values of all triangles which share the considered node.

The first procedure is the most primitive, it assures full mass flow conservation for a certain cell (except for cells at a solid boundary), inflow equals outflow, while mass flow conservation is not achieved considering inter-cell mass exchange (flow leaving a donating does not equal the inflow into the neighboring receiving cell). The second assures mass conservation between neighboring cells but does not achieve mass conservation considering the in and outflow balance of a cell.

Again, ideally fully mass flow conserving hydrodynamic field data corresponding to the center of cell surfaces are utilized. But this is a challenging prerequisite considering available 3D unstructured mesh dynamic coastal ocean models.

3.4 Atmospheric flow field model

The atmospheric or planetary boundary layer (PBL) is defined as the layer in which Earth's surface affects the atmosphere through momentum, heat, and moisture exchange occurring over time scales of a few hours to less than a day [19]. In general, in the top of the PBL turbulent motion is not significant whereas, the lowest part of the PBL, roughly 10%, (surface layer) in which momentum, heat, and moisture vertical fluxes do not vary by more than 10% [20]. Where similarity theories such as the Monin–Obukhov scaling theory provide the flux relations for velocity, potential temperature, and specific humidity (for oceanic environments where it is important to account for transfer of water vapor). These flux relations generate velocity, temperature and humidity profiles that provide boundary and initial conditions in atmospheric boundary layer (CFD) model. The k– ε turbulence model (or its variations e.g. RNG k– ε), based on the Reynolds Averaged Navier–Stokes (RANS) equations, can resolve the atmospheric boundary layer. Density variations are introduced into the momentum equation using the Boussinesq approximation, and appropriate buoyancy terms included in the k and ε equations. Such turbulence models have been successfully used for atmospheric flows but, as

mentioned above it requires modification of the form or values of the coefficients [21-23]. Further one should also include modify momentum equations by the addition of the Coriolis and centrifugal forces. Modified k and ϵ equations simulate velocity and dispersion fields for the atmospheric boundary layer under stable, neutral, or unstable thermal stratifications.

3.5 Investigating result dependency on horizontal, time wise and vertical meshing

An error analysis can be carried out by comparing more accurate system approximations with less accurate reference approximations. Within this regard it shall be differentiated between error analysis, sensitivity analysis (comparing disturbance of input and output) and uncertainty analysis (when different system properties appear to not be preferable among each other).

In figure 3 each triangle of figure 2 has been split into 16 sub-triangles. A triangle can be split into 4^n sub-triangles with the computational load increasing analogously with the factor 4^n . To achieve an error estimate for solution Y_i it can be compared with a solution of a higher order of accuracy with $Error_i \approx |(Y_{accurate} - Y_i)/Y_{accurate}|$ [24] if $|Y_{accurate} - Y_{true}| \ll |Y_i - Y_{true}|$. Simulation parameters such as the horizontal mesh resolution, number of vertical layers, time step and differential equation approximation are considered to fall under the category of error analysis in this work. The accuracy depending on the horizontal resolution can be evaluated by splitting triangles of a mesh shown in figure 2 into sub-triangles as shown in figure 3.

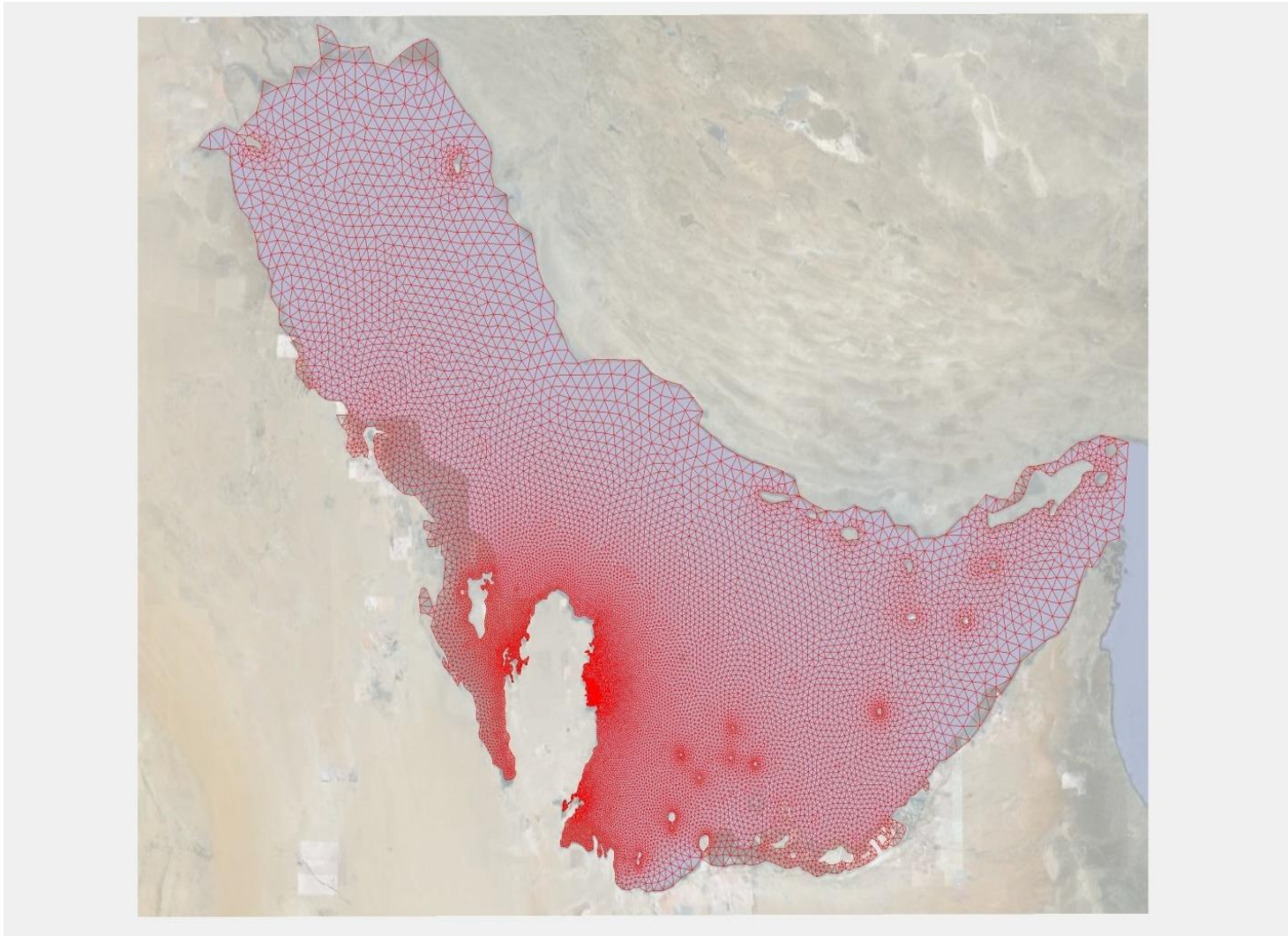


Figure 2: Unstructured triangle 3D Finite Volume mesh. Numerous triangle mesh layer extend the mesh along the vertical direction.

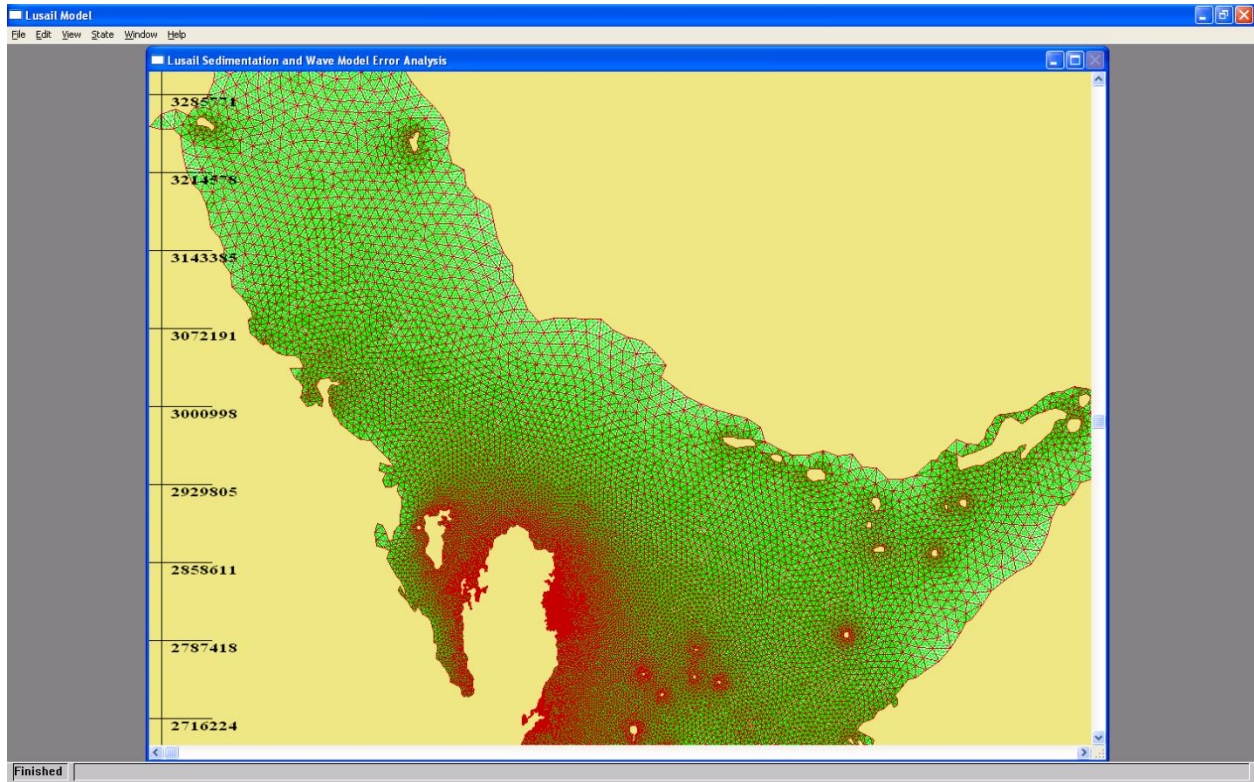


Figure 3: Triangle mesh within the new developed simulation software. Triangles of the mesh can be split for error analysis. In this case each triangle of the mesh from figure 2 has been split into 16 sub-triangles.

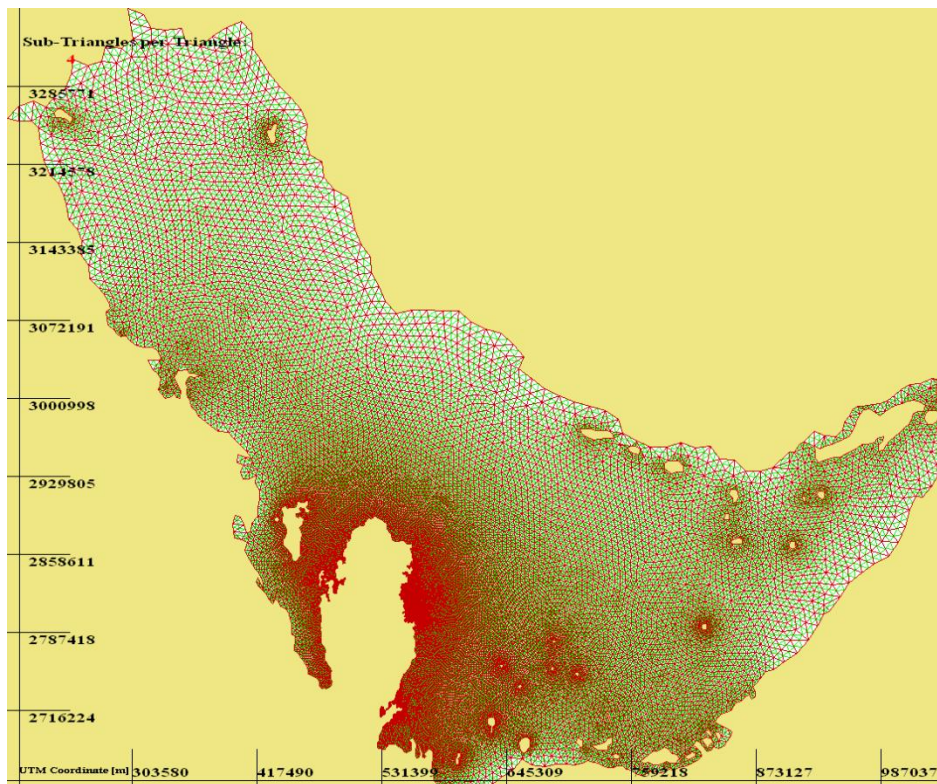


Figure 4: Splitting the mesh triangles into sub-triangles is also used to minimize interpolation. Prior to result output the resolution is increased to reduce the required interpolation.

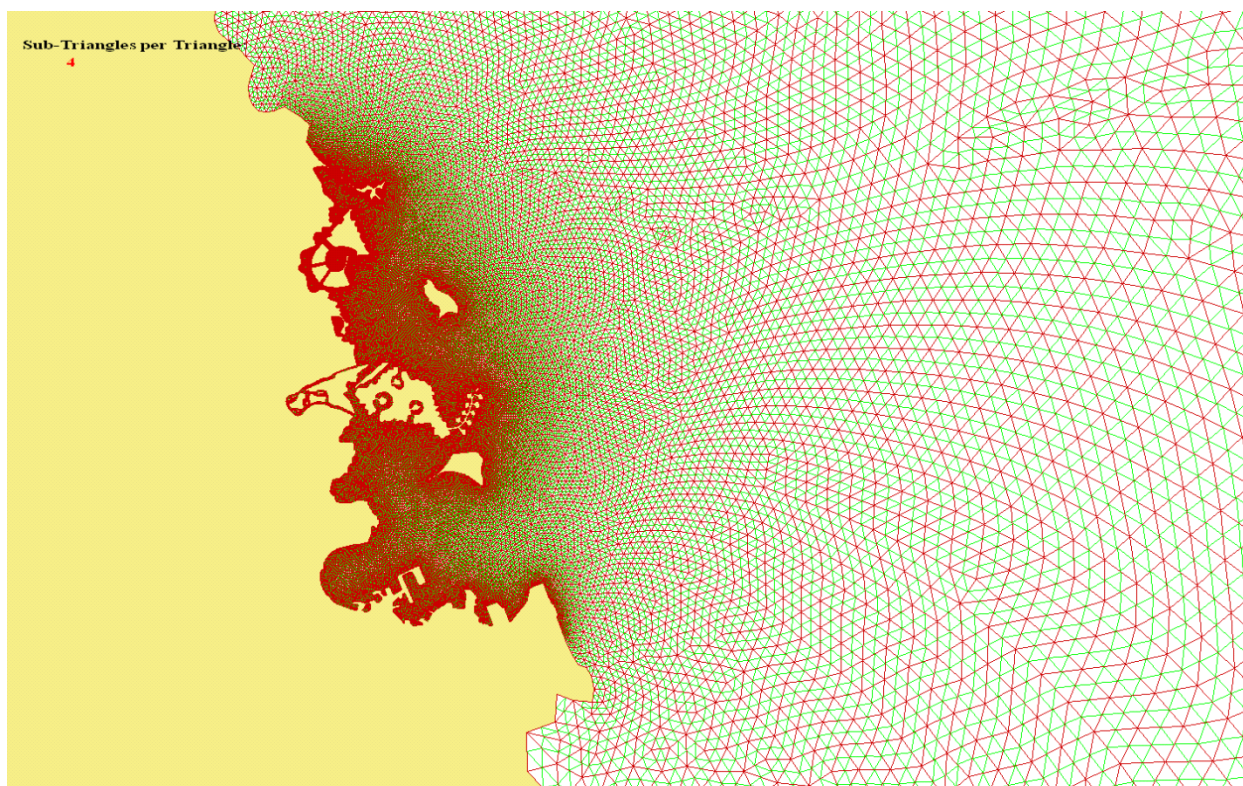


Figure 5: The Doha bay region. Doha undergoes extensive shoreline developments. Besides industrial environmental impact assessment sedimentation and erosion effects on new islands have to be simulated.

Figure 4 shows the developed Arabian Gulf mesh with 4 sub-triangles per triangle. The meshes shown in figure 1 to 4 can be used as comparison to validate the accuracy of the Finite Volume simulation. The mesh is centered on Qatar, the most resolution is spent on the Qatari east coast and especially the Doha bay region. This has been necessary to adapt to the complex shoreline geometries which result out of current developments. Artificial islands have been created such as The Pearl Qatar. Besides horizontal also vertical resolution can be varied systematically to validate the model accuracy. The vertical layer thickness and number can be varied by splitting a layer into sub-layers, as in figures 4 and 5, to investigate its influence on vertical dispersion. The developed water quality model allows effectively generating reference solutions for the following model parameter:

1. Horizontal meshing – the triangles of the horizontal triangle mesh can be split into sub-triangles for comparative simulations;
2. Vertical meshing – vertical layer can be split into sub-layer for comparative simulations or to increase the resolution;
3. And the time step can be varied.

The model has been used for industrial cooling water discharge simulations, biocide distribution simulations and byproduct formation simulations. The model has been applied to the Qatari coast as well as to Halul island in the Arabian Gulf. The vertical sub-meshing capability has been tested and has been utilized to conduct ongoing error analysis studies.

3.6 Integrated cooling circuit simulation

Biocide conversion and byproduct formation occurs already in the cooling circuit. The practicability of an integrated plume fate and cooling circuit simulation has been examined by utilizing the water quality model on heat exchanger type geometry. Both, unstructured and structured type meshes are possible. Whereas unstructured meshing has been utilized for the water quality model, a structured mesh has been utilized for the heat exchange simulation. The model structure has been successfully validated by exporting the Fluent hydrodynamic field data to the water quality model via Techplot. The data transmission is less complicated for the cooling circuit than for the coastal water body due to two aspects: 1) Due to the simpler physics Fluent can produce mass conserving flow fields compared to the mass conservation violating flow fields of the FVCOM. 2) Simple steady state hydrodynamic simulations can be meaningful for the cooling circuit whereas coastal simulations must be transient due to tidal dynamics. Flow field superimposed species transport is simulated within heat exchanger type geometries. Dynamic biocide conversion in case of unsteady biocide dosing can be simulated superimposed on a steady state flow field.

3.7 Kinetics and mass-exchange with the atmosphere

The nonlinear Hypobromous acid reaction with organic matter (to products such as TBM) can be

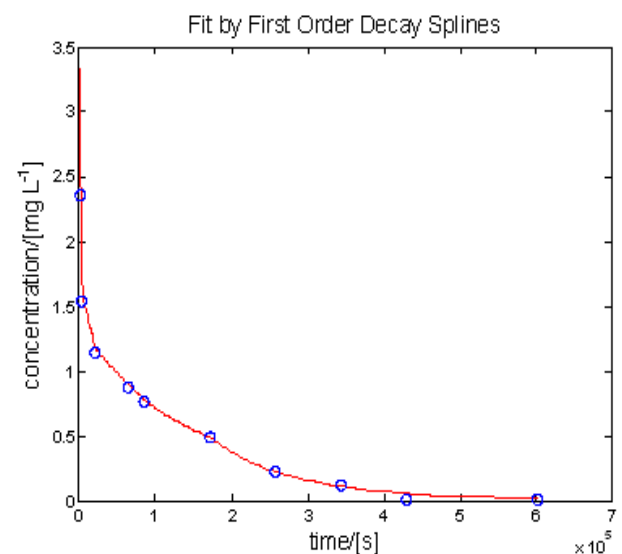


Figure 7: Decay of residual chlorine according to laboratory measurements (blue points) and simulation (red line).



Figure 6: A high triangle density has been dedicated to the Doha bay region.

simulated by closed form nonlinear models or a spline approximation which fits itself to laboratory measurements.

Table 1

Example for laboratory measurements for kinetic data to which the simulation creates a spline approximation.

<i>Time</i>	<i>Residual Chlorine</i>	<i>TBM</i>
[minutes]	[g/m ³]	[Mol/m ³]
0	3.345	6.750E-06
0.5	2.352	5.395E-04
1	1.53	6.780E-04
6	1.13	7.317E-04
18	0.868	7.396E-04
24	0.753	7.714E-04
48	0.474	7.921E-04
72	0.211	8.009E-04
96	0.103	7.999E-04
120	0	8.013E-04
168	0	8.019E-04

An individual first order decay constant corresponding to a certain concentration interval is selected for each cell for each time step. If no suitable closed form conversion model is available, a spline approximation which fits itself to laboratory measurements can be employed. This may be presented for the example of TBM in table 1. The spline fitting (fig. 7) can be made dependent on a variety of factors including temperature – otherwise it is run with data which have been taken at a temperature range which corresponds to the simulated case. Interaction with the atmosphere is taken into account based on Henry coefficients. If the constituent is present in the atmosphere, e.g. oxygen or carbon dioxide, (and sink or source function of the sea is negligible for the atmosphere), then a temperature and salinity field dependent equilibrium concentration distribution is assumed in the water boundary layer at the water-air interface. If the constituent is not present in the atmosphere, e.g. free residual chlorine in case of biocide discharge, then simulating the surface-near atmosphere is necessary. At the bromide rich seawater conditions in the Arabian Gulf free residual chlorine will form hypochlorous acid which will react further to a chloride and hypobromous acid [10]. The simulation will therefore consider excess oxidants (hypobromous acid). Hypobromous acid has according to Sander [25], who cites Batchley et al. [26], a Henry coefficient of $k_{H,inv}^{px} = 0.0295 \pm 0.0051$ atm which is equivalent to $k_{H,inv}^{px} = p_g/x_a = \rho_{H_2O}/(M_{H_2O}k_H)$ which yields at $T = 298.15$ K $k_H = 1932 \pm 334$ [M/atm]. Since hypobromous acid volatilization reduces the plume size it is safer to overestimate the solubility. Hence $k_H = 1932 + 334 =$

2266 [M/atm] shall be assumed which is in the dimensionless ratio of air and gas concentrations $k_{eq} = c_w/c_{at} = k_H RT = 55403$ where R is the ideal gas constant. Temperature and salinity dependencies of the equilibrium coefficient are taken into account with

$$k_{eq} = k_{eq}^* e^{\frac{\Delta_{solv} H}{R} \left(\frac{1}{T} - \frac{1}{T^*} \right)} \quad (5)$$

[25] where $\Delta_{solv} H$ is the enthalpy of solution. Dewulf et al. [27] identified that, in general, volatility increases with an increase in salinity:

$$\ln(c_{at}/c_w) = \frac{a}{T} + bc_{salin} + c \quad (6)$$

a is a negative constant whereas b and c are positive constants and c_{salin} is the salt concentration in g/L. Since, as stated above, mixing zone evaluation shall tend to underestimate volatilization, it is safer to use equilibrium data originating from low salinity conditions [26].

3. ARABIAN GULF MODEL

The Arabian Gulf has been created to overcome the previous practise of nested and weakly coupled models. Many EIAs simulate solely the study area with a coarse approximation of the boundary conditions considering currents and other hydrodynamic properties. In other cases Arabian Gulf models are fully omitted by calibrating the local model with tidal and current measurement data. The new Arabian Gulf model allows to refine the mesh at areas of interest and simulate an integrated system covering the entire Arabian Gulf and study area (e.g. plant cooling water outfall at the Qatari coast). The computational mesh has 3 spatial dimensions and 1 time dimension. The mesh is transient in shape. The surface can undergo tidal and wave elevations and changes with time. The vertical underwater terrain approximation can occur with σ or z -coordinates. σ -coordinates allow the vertical displacement of triangle nodes in order to follow the bathymetry and involve a coordinate transformation. Z -coordinates approximate terrain by setting bottom cells “wet” or “dry” depending on a terrain discretization. Both approaches have advantages and disadvantages, e.g. σ -coordinates allow a smooth terrain approximation. The developed model allows the mixed utilization of σ and z -coordinates in order to combine the benefits of both approaches.

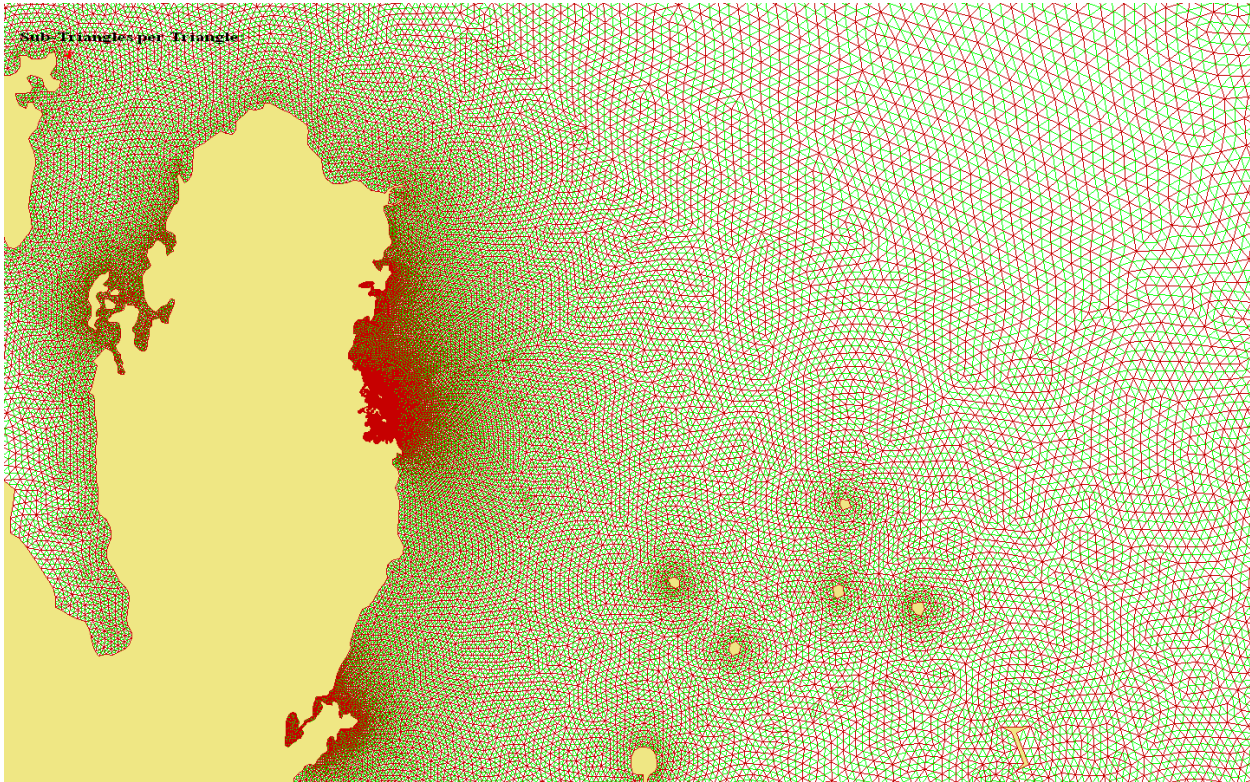


Figure 8: Arabian Gulf mesh around Qatar in the new programmed water quality model.

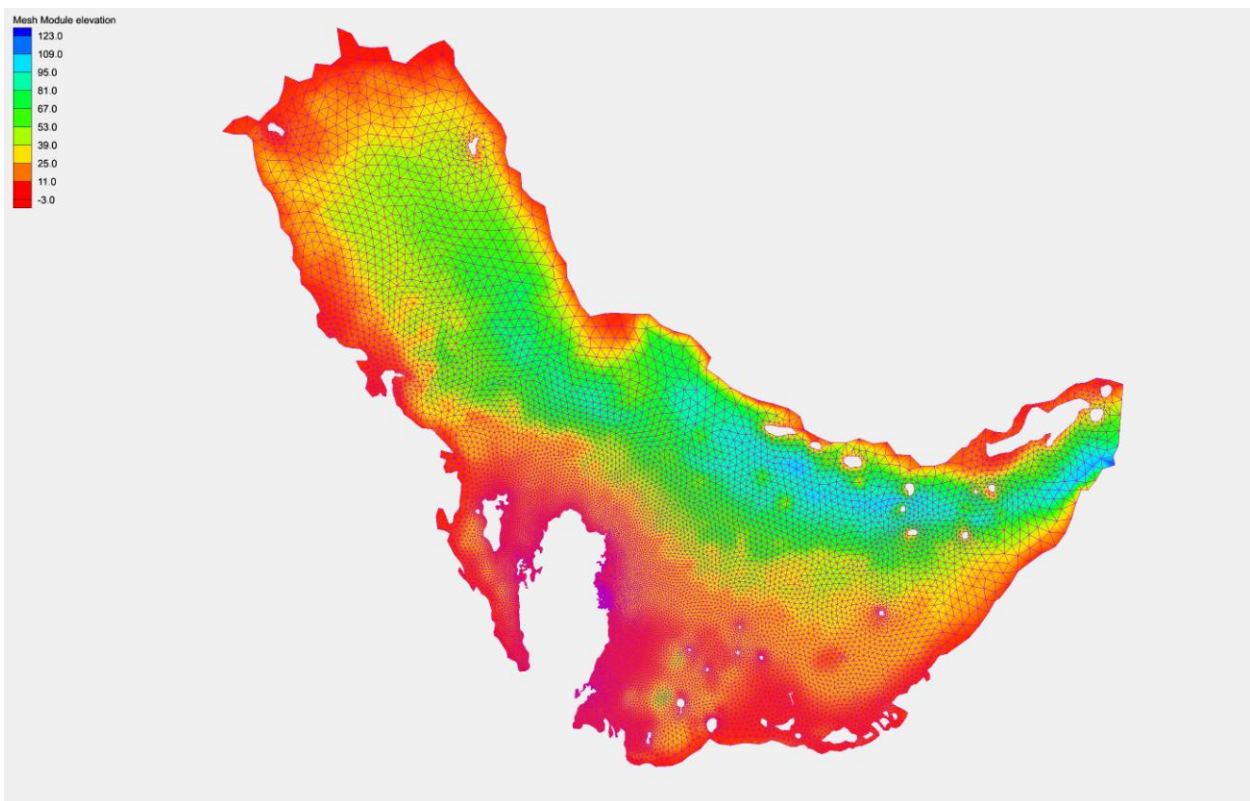


Figure 9: The mesh has also a vertical component. Bathymetry data from the Arabian Gulf have been interpolated to the triangle nodes. The vertical layer distributions approximate the terrain.

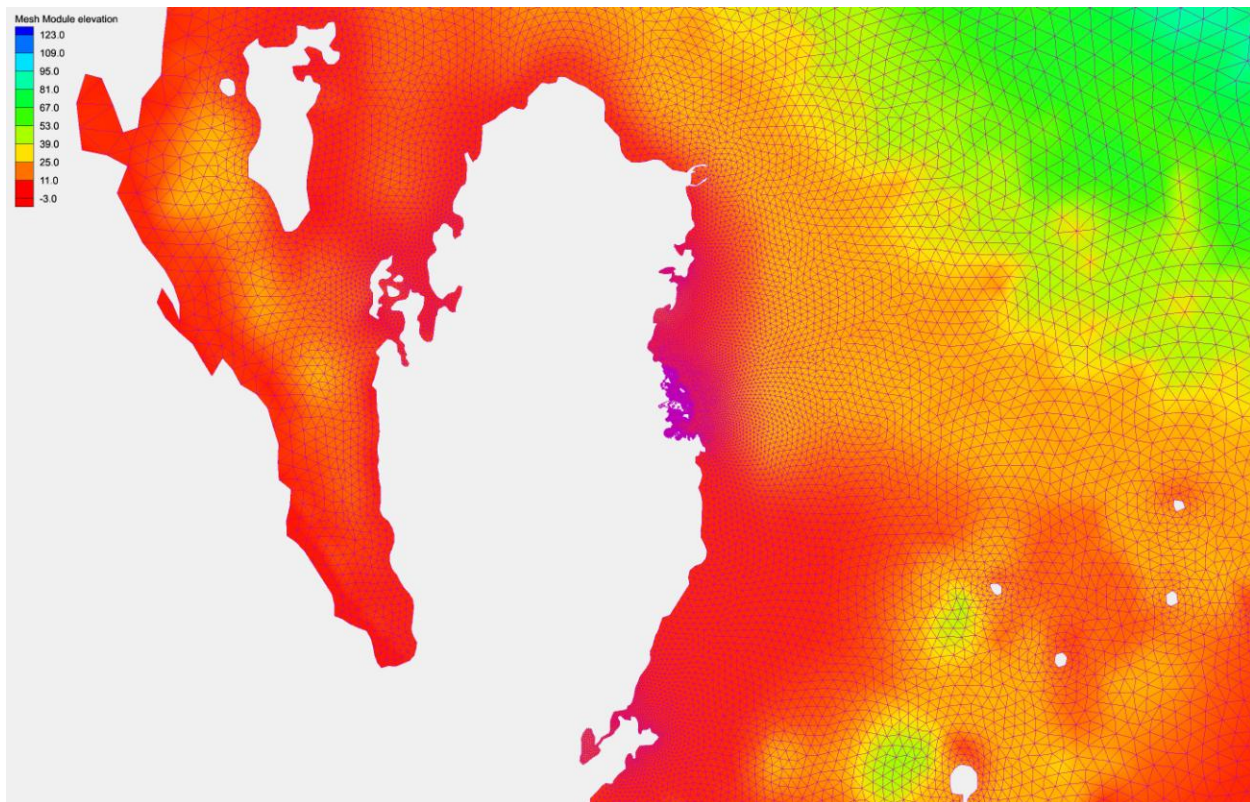


Figure 10: Arabian Gulf mesh surrounding Qatar including bathymetry visualization.

5 DISCUSSION

The Arabian Gulf Model introduces the integrated simulation of study areas and the rest of the Arabian Gulf. The model includes substantial endogenous CFD components which allow nonlinear conversion and byproduct formation. Local CFD capabilities support the validation and model transparency which is vital for reliable environmental impact assessments. Innovative features have been included such as integrated error analysis options for horizontal and vertical sub-meshing. Sub-meshing as an alternative to interpolation is featured too. The mesh allows the local refinement in order to suit the model to short-dated consulting requests. The modular approach allows conducting integrated plant and discharge simulations for cooling circuits. Marine life models can be imported in the water quality model. The separate species transport model is suitable to include complex kinetics and byproduct simulations.

Appendix A

Table A.1

Symbols for the partial differential equation and boundary conditions

Symbol	Description	Unit
\dot{n}	Molar mass flow	mol/s
$c_j(\mathbf{r}, t)$	Concentration of species j at \mathbf{r} and t	mol/m ³
j	Species index	-
$\mathbf{r}_i \in \mathbf{r}$	Spatial location vector	m
τ	Time	s
$D(\mathbf{r}, \tau)$	Dispersion coefficient	m ² /s
$\mathbf{u}_i(\mathbf{r}, \tau)$	Velocity component vector	m/s
$\in \mathbf{u}(\mathbf{r}, \tau)$		
l	Reaction index	-
$\sigma_{jl} \in \Sigma$	Stoichiometric coefficient matrix for species j and reaction l	-
$k_{jl}(c_j(\mathbf{r}, \tau)) \in \mathbf{K}$	Kinetic coefficient matrix dependent on $c_j(\mathbf{r}, \tau)$	1/s
c_w	Equilibrium concentration in water	mol/m ³
c_{at}	Equilibrium concentration in air	mol/m ³
k_{eq}	Henry coefficient	-

Table A.2

Symbols for the finite volume equation and approximated boundary conditions

Symbol	Description	Unit
$\mathbf{c}_{ih}^t \in \mathbf{c}_h^t$	Concentration vector for a layer h at time level t containing values for all cells listed in \mathbf{I}	mol/m ³
$s = [1, 2, 3]$	Side of a triangle	-
t	Time level	-
Δ	Time wise increment, time-step	s
$nl(\mathbf{I}, s)$	Neighbor list returning the index for the cell which neighbors to the cells \mathbf{I} at the side s	-
$\mathbf{v}_{ih}^t \in \mathbf{v}_h^t$	Finite volume vector for a layer h at time level t containing values for all cells listed in \mathbf{I} (the cell volume is dynamic due to varying surface elevation)	m ³
$g_{ihs} \in \mathbf{g}_{hs}$	$g_{hs} = \frac{\Delta \mathbf{a}_{hs}^t \delta_{hs}^t}{\Delta \mathbf{r}_s \mathbf{v}_h^t}$	1/s
$\Delta r_{is} \in \Delta \mathbf{r}_s$	Inter-triangle-center distance to side s	m
$\Delta a_{ihs}^t \in \Delta \mathbf{a}_{hs}^t$	Surface area of one surface of the finite volume	m ²
$\delta_{ihs}^t \in \delta_{hs}^t$	Dispersion coefficient vector at the center of the surface at side s	m ² /s
$\dot{v}_{ihs}^t \in \dot{\mathbf{v}}_{hs}^t$	Volume flow	m ³ /s
$\varepsilon_{ihs} \in \boldsymbol{\varepsilon}_{hs}$	Logical control bit array determining the ratio between explicit and implicit approximation.	-
$\pi_{ihs} \in \boldsymbol{\pi}_{hs}$	Adaptive upwind control bit array	-

Table A.3

Further utilized symbols

Symbol	Description	Unit
Y	Solution distribution	mol/m ³
\mathbf{M}	Matrix the coefficients of concentrations at subsequent time level	X
\mathbf{b}	Vector containing terms approximated at preceding time level and independent boundary conditions	X
$k_{H,inv}^{px}$	Inverted Henry coefficient, volatility instead of solubility, as ratio of partial pressure and mass fraction	atm
p_g	Partial pressure	atm
x_a	Mass fraction	-
ρ_{H_2O}	Density of water	kg/l
k_H	Henry coefficient at ratio of molar mass and partial pressure	M/atm
$\Delta_{soln} H$	Enthalpy of solution	1 atm mol ⁻¹
R	Ideal gas constant	1 atm mol ⁻¹ K ⁻¹
a	Temperature coefficient	K
b	Salinity coefficient	mol/l
c	Constant	-
T and T^*	Temperature and reference temperature	K
c_{salin}	Salinity, salt concentration	mol/l

References

- [1] Abarnou, A., Miossec, L., 1992, Chlorinated waters discharged to the marine environment chemistry and environmental impact. An overview, The Science of the Total Environment, 126, 173-197.
- [2] Taylor, C., 2006. The effects of biological fouling control at coastal and estuarine power stations. Marine Pollution Bulletin 53, 30-48.
- [3] EPA, 1980. Clean Water Act, Section 403, Ocean Discharge Criteria.
- [4] Abdel-Wahab, A., Linke, P., Alfadala, H.E., El-Halwagi, M.M., Batchelor, B., 2009. Towards a Holistic Approach to the Sustainable Use of Seawater for Process Cooling. Advances in Gas Processing: Proceedings of the 1st Annual Gas Processing Symposium. 332-340.
- [5] Lawen, J., Huaming, Y., Linke, P., Abdel-Wahab, A., 2010. Industrial Water Discharge and Biocide Fate Simulations with Nonlinear Conversion. Proceedings of the 2nd Annual Gas Processing Symposium. 99-106.
- [6] Adenekan, A.E., Kolluru, V. S., Smith, J. P., 2009. Transport and Fate of Chlorinated By-Products Associated with Cooling Water Discharges, Advances in Gas Processing: Proceedings of the 1st Annual Gas Processing Symposium. 341-353.
- [7] Kolluru, V.S., Edinger, J. E., Buchak, E. M., Brinkmann, P., 2003. Hydrodynamic Modeling of Coastal LNG Cooling Water Discharge. J Energ Eng. 129, No. 1, 16 – 31.
- [8] Jirka, G.H., 2008. Improved Discharge Configurations for Brine Effluents from Desalination Plants. J Hydr Eng, ASCE, 134, No. 1, 116-129.
- [9] Lawen, J., Linke, P., Abdel-Wahab, A., Bhatelia, T., Fieg, G., submitted 2010. Fluid Flow Direction Guided Solution of

an Implicit Adaptive Upwind Approximation for Advection Simulations. *J Comp & Fluids*.

[10] Abdel-Wahab, A., Khodary, A., Bensalah, N., Formation of Trihalomethanes (THMs) during Seawater chlorination, *Journal of Environmental Protection*, in press, 2010.

[11] Versteeg, H., 2007, The finite volume method for convection-diffusion problems, *Introduction to Computational Fluid Dynamics: The Finite Volume Method*.

[12] Chen, C.S., Liu, H.D., Beardsey, R.C., 2003. An Unstructured Grid, Finite-Volume, Three-Dimensional, Primitive Equations Ocean Model: Application to Coastal Ocean and Estuaries. *Journal of Atmospheric and Oceanic Technology* 20, 159-186.

[13] Lai, Z., Chen, C., Cowles, G., Beardsley, R.C., 2010. A non-hydrostatic version of FVCOM-validation experiment I: surface standing and solitary waves, *Journal of Geophysical Research* 115, C11010.

[14] Huaming, Y., 2008, 利用有限体积模型对狭长海湾填海优选方案的研究 (A Study on Optimum Schemes for Reclamation in a Narrow Bay using the Finite Volume Method), China Academic Journal Electronic Publishing House.

[15] Launder, B.E., Spalding, D.B., 1972, *Lectures in Mathematical Models of Turbulence*. Academic Press, London, England.

[16] Gour-Tsyh, Y., 2002, Fluid Flows and Reactive Chemical Transport in Variable Saturated Subsurface Media, *Environmental Fluid Mechanics Theories and Applications*, 207-255.

[17] Haidvogel, D., 1999, The hydrostatic Primitive Equations, *Numerical Ocean Circulation Modeling*, 19-21.

[18] Chen, C., Beardsley, R.C., Cowles, G., 2006, An Unstructured Grid, Finite-Volume Coastal Ocean Model FVCOM User Manual

[19] S.P. Arya, *Micrometeorology and atmospheric boundary layer*, *Pure Appl. Geophys.* 162 (2005) 1721–1745.

[20] H.A. Panofsky, J.A. Dutton, *Atmospheric Turbulence: Models and Methods for Engineering Applications*, John Wiley & Sons, Inc., Canada, 1984.

[21] C. Alinot, C. Masson, $k-\epsilon$ model for the atmospheric boundary layer under various thermal stratifications, *J. Solar Eng.* 127 (November) (2005) 438–443.

[22] A. Huser, P.J. Nilsen, H. Skatun, Applications of $k-\epsilon$ model to the stable ABL: pollution in complex terrain, *J. Wind Eng. Ind. Aero.* 67–68 (1997) 425–436.

[23] R. Morel, A. Laassibi, E. Alcaraz, R. Zegadi, G. Brun, D. Jeandel, Validation of a $k-\epsilon$ model based on experimental results in a thermally stable stratified turbulent boundary layer, *Int. J. Heat Mass Transfer* 35 (1992) 2717–2724.

[24] Lapidus, L., Pinder, G.F., 1999. *Numerical Solution of Partial Differential Equations*.

[25] Sander, R., 1999. *Compilation of Henry's Law Constants for Inorganic and Organic Species of Potential Importance in Environmental Chemistry*; <http://www.henrys-law.org>

[26] Dewulf, A., M. Craps, R. Bouwen, T. Taillieu, C. Pahl-Wostl, 2005. Integrated management of natural resources: dealing with ambiguous issues, multiple actors and diverging frames. *Water, Science and Technology* 52:115–124.

[27] Cressman, G.P., 1959. An Operational Objective Analysis System. *Mon. Wea. Rev.*, 87, 367–374.

[28] Barnes, S.L., 1964. A technique for maximizing details in numerical weather map analysis. *J. Appl. Meteor.*, 3, 396–409.

Anoxic Water Simulations and Vertical Sub-Meshing to Depict Strong Gradients

Johannes Lawen¹, Ahmed Abdel-Wahab²

¹ Texas A&M University at Qatar, Texas A&M Engineering Building, Education City, 23874 Doha, Qatar
(johannes.lawen@qatar.tamu.edu)

² Texas A&M University at Qatar, Texas A&M Engineering Building, Education City, 23874 Doha, Qatar
(ahmed-abdel-wahab@qatar.tamu.edu)

ABSTRACT

Coastal simulations of anoxic waters involve near-equilibrium oxygen loaded water close to the surface due to oxygen exchange with the atmosphere. Hence substantial vertical gradients of dissolved oxygen (DO) concentration are possible along the water column. Depicting substantial vertical gradients adds importance to the relevance of vertical resolution in a water quality model. Hydrodynamic coastal simulations require a relatively high computational effort and a practicable computational time often limits vertical resolution, the number of layers. This work demonstrates sub-layering in a DO water quality model, superimposed onto the hydrodynamic model, to increase the vertical resolution. Tidal movements, surface elevations, are evenly partitioned onto all sub-layer. The approach is demonstrated within a new unstructured mesh coastal water and air quality model has been developed that includes species transport, nonlinear decay, byproduct formation and mass-exchange between sea and atmosphere. The model has been programmed with a graphical user interface and is applicable to coastal seawater, lakes and rivers. Focused on species conversion and interaction with the atmosphere, the water and air quality model follows a modular approach. It is a compatible module which simulates distributions based on fluid dynamic field data of underlying existing hydrodynamic and atmospheric simulations. An error analysis concerning the vertical layer resolution has been carried out for different levels of DO concentration. In this work the developed dissolved oxygen model demonstrates its ability to accurately simulate also complex structures of anoxic water discharges.

Keywords: Water quality model, Finite Volume method, parabolic transport PDE, Anoxic Water

1. INTRODUCTION

Discharges of waste- and cooling water into receiving water bodies are an environmental concern (Abarnou et al., 1992) since discharged contaminants, such as biocides, chemical oxygen demand or excess temperature are often harmful to aquatic life (Tanaka et al., 1985; Taylor, 2006). Therefore, many of the discharge constituents are regulated (EPA, 1980). In order to assess their environmental impact, process-water plumes can be simulated. Coastal transport simulations and plume prediction models are often discussed in scientific articles (Abdel-Wahab et al., 2009; Lawen et al., 2010) and constitute a significant consultancy sector (Adenekan et al, 2009) in environmental impact assessment. Besides advective transport and dispersion, the development of a species plume depends on reactive consumption or accumulation – byproduct formation – and possibly mass-exchange with the atmosphere depending on the species. The accurate approximation of the coastal water body, the incorporation of shoreline geometry, is important for a representative depiction of the simulated domain. Unstructured meshes are very suitable for complex domain shape approximation. The unstructured mesh allows an increased resolution at areas of importance, such as shorelines and surrounding discharge outfalls, while the cell size can be inflated for bulky areas of less importance; thus, saving computational time.

Several solely structured mesh and even closed form models, such as GEMSS (Kolluru et al., 2003) and Cormix (Jirka, 2008), are often used in environmental impact assessment. Heretofore, these models neither allowed incorporating generalized kinetic models beyond first order decay nor generalized modeling of plume constituent mass-exchange with the atmosphere. The new water quality model utilizes unstructured meshes which allow a smooth increase of the cell density in areas of importance, thus achieving a better approximation of shorelines, channels and industrial outfalls. Nonlinear conversion models or spline approximations of laboratory measurement time series can be employed. Therefore, nonlinear byproduct formation and fate can be simulated. Mass-exchange with the atmosphere has been embedded via Henry equilibrium coefficients. If the simulated species occurs naturally in the atmosphere (e.g. oxygen or carbon-dioxide), then a corresponding equilibrium concentration can be set in the top layer of the water domain. If the simulated species does not constitute an air-fraction (e.g. biocides such as chlorine), then calculating species dependent equilibrium based mass-exchange at the sea-atmosphere interface requires simulating the species distribution in the surface-near atmosphere. Otherwise, neglecting minor species accumulation (due to volatilization) in the surface-near atmosphere and assuming an atmospheric species concentration of zero (for e.g. chlorine) would

correspond to a sea top-layer equilibrium concentration of zero. This would result in solely dispersion dependent volatilization regardless of component specific volatilization behavior. The developed water quality model can therefore extend the simulated domain onto the atmosphere. Options have been integrated for error analysis concerning the mesh dependency of results and allow a comparison between explicit and implicit solution approaches. Algorithms have been developed (Lawen et al., submitted 2010) which are optimized for flow field superimposed water quality simulations. With the available flow field information, the transport simulation's solver uses the phenomenological approach of fluid flow guided matrix reordering, allowing the explicit calculation of stable implicit approximations.

The water quality model allows vertical sub-meshing to accurately resolve water quality parameters which are influenced by the atmosphere. Hydrodynamic coastal simulations require a relatively high computational effort and a practicable computational time often limits vertical resolution, the number of layers. This work demonstrates sub-layering in a DO water quality model, superimposed onto the hydrodynamic model, to increase the vertical resolution. Tidal movements, surface elevations, are evenly partitioned onto all sub-layer.

The model design approach is focused on water quality simulation including contaminant/species specific driving forces such as conversion and mass exchange with the atmosphere within a modular structure, with a separate hydrodynamic simulation. The tool has been programmed as a Windows application in FORTRAN 90 with graphical user interface and result plotting functions including interpolation. The developed tool furthers the establishment of unstructured meshes in water quality simulations. Complex kinetics beyond 1st order decay terms can be depicted based on an automatic spline approximation of laboratory measured species decay or byproduct formation. If measurement value distributions include all dependencies, all relevant parameters (e.g. temperature or salinity), then utilizing spline approximations might relieve the engineer or consultant from developing a kinetic model. The simulation of the species distribution is split into a hydrodynamic and a superimposed reaction and flow field driven advection simulation – a strategy relying on the prerequisite that changes of hydrodynamic properties due to oxygen reactions, such as chemical oxygen demand or biota driven reactions, are negligible (Versteeg, 2007). The flow field computation in this work has been carried out with the unstructured grid Finite Volume Coastal Ocean Model (FVCOM; Chen et al., 2003; Huaming, 2008; Lai et al., 2010).

1.2. Vertical sub-meshing

The study illustrates the possibility of increasing the vertical resolution of a water quality simulation compared to the underlying hydrodynamic simulation by means of vertical sub-layering. This is relevant for constituents which exhibit substantial vertical gradients such as volatile chlorine or dissolved oxygen in anoxic waters. Considering dissolved oxygen, near-equilibrium conditions close to the surface will involve substantial vertical gradients in case of anoxic waters in deeper layers. Other coastal ocean studies concerning volatile species, such as free residual chlorine, did not utilize small boundary layers in the surface region (Kolluru et al., 2003). The new water quality model described herein can add several sub-layers in the surface region in order to accurately approximate the near surface concentration profile.

1.3. Error analysis concerning vertical sub-meshing

In this work, an error analysis has been carried out, described in detail in section 4, to identify error contribution estimates for vertical layer resolutions. A submerged anoxic discharge has been simulated with and without vertical sub-meshing. The developed tool allows systematic analyzing of errors based on both horizontal unstructured mesh and vertical layer-grid resolution. Horizontal as well as vertical meshing can be split into triangle sub-meshes and sub-layers respectively in order to obtain a comparable accurate reference solution to quantify errors based on the finite volume domain approximation. Also, the developed tool's implicit matrix reordering-based solver can produce reference solutions to allow estimating error contribution of usual explicit (time-wise) approximations.

2. METHODOLOGY

The structure of the modules is depicted in figure 1.

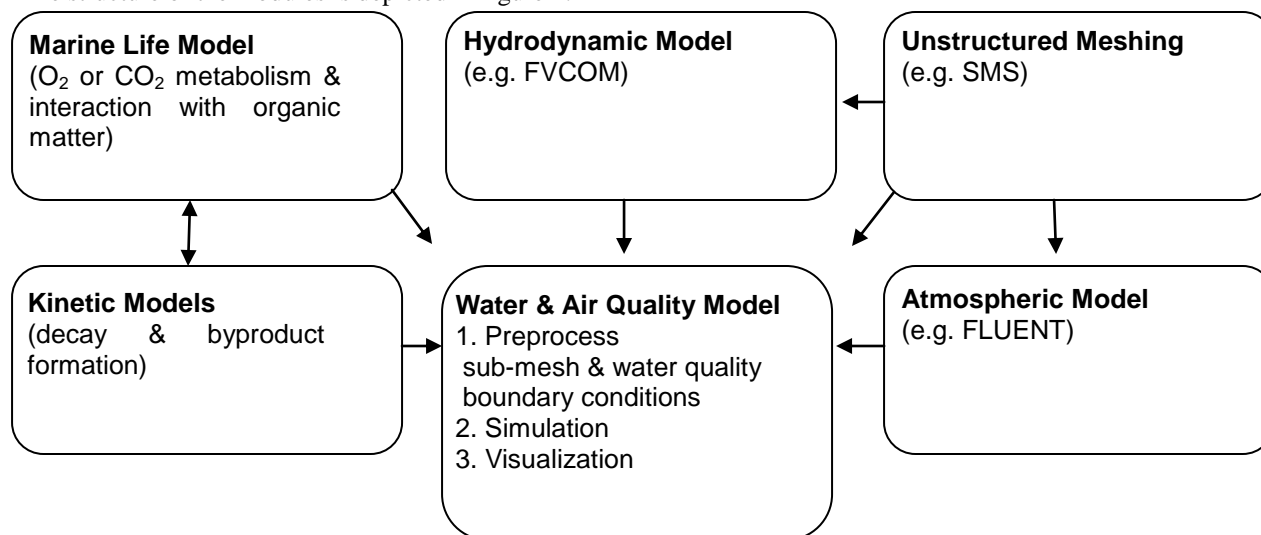


Fig. 1. Modular model structure of meshing, computer fluid dynamics, air and water quality model. The hydrodynamic and the atmospheric models compute flow, dispersion, and temperature fields for the water and air quality model. All 3 simulations utilize the same horizontal triangle-mesh generated by the unstructured meshing tool.

The developed tool is suggested to be intertwined in a structure which contains a water and air quality model, atmospheric flow and dispersion, as well as a hydrodynamic model. All receive the same unstructured horizontal mesh, as shown in figure 1, from a meshing tool like the Surface Modeling System (SMS) from Aquaveo. Based on this mesh a hydrodynamic tool such as the FVCOM is used to compute for each time-step flow, dispersion, salinity, temperature and surface elevation fields. Likewise the atmospheric model, such as a k - ϵ model (Launder et al., 1972) in Fluent, simulates velocity and dispersion fields for the atmosphere. Flow, dispersion, and surface elevation fields are fed into the water quality model. If necessary, for kinetic or marine life models, temperature and salinity fields are transferred to the water quality model as well, in order to set individual reaction rates in each finite volume cell. The water quality tool's transport model is a set of Finite Volume Equations (FVE). The FVE can either be derived from an advection, dispersion, and reaction partial differential equation (PDE) or by balancing directly mass flow through the Finite Volumes. The PDE is a balance of molar in and outflow of a species, j , along an infinitely small control volume. Terms for dispersive mass flow, conversion and convection are taken into account. In and outflows at $r_i + dr_i$ are

written at r_i , the cell centre, by substituting $\dot{n}(r_i + dr_i)$ with $\dot{n}(r_i) + \partial\dot{n}(r_i)/\partial r_i dr_i$. Linearized reactions l for each species j are notated with stoichiometric, σ_{jl} , and kinetic matrix, k_{jl} .

$$\begin{aligned} & \frac{\partial c_j(\mathbf{r}, \tau)}{\partial \tau} \\ &= \sum_i \frac{\partial}{\partial r_i} \left(D(\mathbf{r}, \tau) \frac{\partial c_j(\mathbf{r}, \tau)}{\partial r_i} - u_i(\mathbf{r}, \tau) c_j(\mathbf{r}, \tau) \right) \\ &+ \sum_l \sigma_{jl} k_{jl} (c_j(\mathbf{r}, \tau)) c_j(\mathbf{r}, \tau) \end{aligned} \quad (1)$$

$(c_j(\mathbf{s}))$ is a kinetic rate dependent on the component concentration. If the dependency of the rate on the concentration is given in the form of discretized data, then the conversion can be depicted with linear splines. The rate is updated dependent on the time and space wise local concentration.

3 WATER QUALITY MODEL

The developed water and air model solves the transport PDE for the water and air phase including exchange at the sea-atmosphere interface, species decay, and byproduct formation. New functions supporting error analysis are described in section 3.4 and an implicit solver optimized for flow field superimposed water quality computations is explained in section 3.2. The explicit and implicit form of the adaptive upwind finite volume equation, for all $c_{ih}^t \in \mathbf{c}_h^t$ cells $i_y \in \mathbf{I}$ in a layer h , can both be expressed with:

$$\begin{aligned}
\frac{c_h^{t+\Delta} - c_h^t}{\Delta t} = & \sum_{s=1}^5 g_{hs}^t (c_{nl(I,s)h}^t - c_h^t) \\
& - \sum_{s=1}^3 \frac{\dot{v}_{hs}^t}{v_h^t} \left(\varepsilon_{hs}^t \left((1 - \pi_{hs}^t) c_h^t \right. \right. \\
& + \pi_{hs}^t c_{nl(I,s)h}^t \left. \left. + \left((1 - \pi_{hs}^t) c_h^{t+\Delta} \right. \right. \right. \\
& + \pi_{hs}^t c_{nl(I,s)h}^{t+\Delta} \left. \left. \left. \right) (1 - \varepsilon_{hs}^t) \right) \right) \\
& + \frac{k_h^t}{2} (c_h^t + c_h^{t+\Delta})
\end{aligned} \quad (2)$$

The logical control bit $\varepsilon_{ihs}^t \in \varepsilon_{hs}^t$ regulates whether advective flows through side s of triangle ih is approximated explicit or implicit. Dispersion through the 5 surfaces of one of the unstructured mesh's triangle prism is quantified by $g_{hs}^t = \Delta a_{ihs}^t \delta_{hs}^t / (\Delta r_s v_h^t)$ where $\delta_{ihs}^t \in \delta_{hs}^t$ is the dispersion coefficient vector of cell ih at surface s ; $\Delta a_{ihs}^t \in \Delta a_{hs}^t$ is the finite volume cell surface vector; $\Delta r_{ihs}^t \in \Delta r_{hs}^t$ the inter-centroid distance vector and $v_{ih}^t \in v_h^t$ contains all cell volumes for a layer h . $\dot{v}_{ihs}^t \in \dot{v}_{hs}^t$ is the volume flow vector for cell ih with respect to side s . The closed form kinetic model-based constant, or spline constant, $k_{ih}^t \in k_h^t$ corresponds to a certain concentration level and, as the case may be, to further parameters, such as temperature, which are assigned to cell i and time level t . $\pi_{ihs} \in \pi_{hs}$ regulates to what percentage a concentration value of a certain centroid (the concentration of cell i itself or of its neighbor) factors into the flow approximation. π_{ihs} is the adaptive upwind control bit which functions to approximate flow calculation to 0% based on the mass-receiving centroid and to 100% based on the donating centroid (except at open boundaries). The first row in equation 3 represents dispersive exchange. The remainder of the equation contains the approximation of horizontal advection and conversion. Flow field, dispersion, surface elevation, salinity, and temperature arrays can be fed to the program by any hydrodynamic simulation which stores data either on the triangle centroids, nodes, or centers of the finite volume surfaces. For the error analysis in section 4, data from the FVCOM have been fed into the water quality model.

3.1 Boundary Conditions

Ten boundary conditions have been embedded into the new water and air quality model. The horizontal open boundary condition $0 = \partial c / \partial n|_{n=0}$ with $\mathbf{n} \perp \partial \Omega$ defines the gradient at the boundary to be zero for both water and air. This suppresses dispersion but permits advection through the open boundary. The no-flux boundary condition $0 = \mathbf{u}c - D\partial c \partial n|_{n=0}$ assures that neither dispersive nor advective flux passes through a

solid boundary. At the sea and air boundary layer, dispersion is replaced with the Henry coefficient equilibrium assumption $c_w = c_{at} / k_{eq}$. This requires that hypobromous acid is simulated throughout the near-surface atmosphere. If the species occurs in the atmosphere (e.g. O₂ or CO₂) then the corresponding equilibrium concentration (depending on salinity and temperature) is set in the entire top-layer of the water body and the simulation of the near-surface atmosphere can be omitted. The vertical open boundary condition for the atmosphere extrapolates the vertical gradient to the other side of the boundary. This type of open boundary condition permits dispersion and has been chosen to avoid an insulating functioning of the condition since dispersion is the dominating transport mechanism along the vertical extension. Intakes can be approximated by two different boundary conditions. 1) Mass conservation between intake inflow and the flow advected through the surfaces of the cell is assumed. Approximated for finite volumes, this is equivalent to setting all volume flows through the cell surfaces to zero. This has the effect that the concentration of the cell will be evened by dispersion to the levels of the surrounding cells. 2) Alternatively the intake cell can be set to a constant value which has been measured. This boundary condition can also be utilized when measurements have been taken at some locations and the ensuing plume is of interest. Therefore this boundary condition can be used for discharges, intakes and calibrations with measurement values. Also source term boundary condition can be used for discharges as an alternative to setting a constant value. Contrary to the adaptive upwind principle, advection through the open boundaries is always calculated based on the cells which are located at the boundary. This is embedded by including the boundary condition information in the adaptive upwind control bit π_{ihs} .

3.2 Kinetics and Mass-Exchange with the Atmosphere

If pollutants react, then conversion and byproduct formation can be simulated by nonlinear conversion terms or a spline approximation which fits itself to laboratory measurements. An individual first order decay constant corresponding to a certain concentration interval is selected for each cell for each time step. Interaction with the atmosphere is taken into account based on Henry coefficients. If the constituent is present in the atmosphere, e.g. oxygen or carbon dioxide, (and sink or source function of the sea is negligible for the atmosphere), then a temperature and salinity field dependent equilibrium concentration distribution is assumed in the water boundary layer at the water-air interface.

If the constituent is not present in the atmosphere, e.g. free residual chlorine in case of biocide discharge, then simulating the surface-near atmosphere is necessary. In

section 4 an error analysis is carried out for dissolved oxygen transport including a Henry equilibrium boundary condition at the sea-atmosphere interface.

3.3 Investigating Result Dependency on Vertical Meshing

An error analysis can be carried out by comparing more accurate system approximations with less accurate reference approximations. The developed water quality model allows effectively generating reference solutions for the vertical meshing – vertical layer can be split into sub-layer for comparative simulations or to increase the resolution.

al. 1999) if $|Y_{accurate} - Y_{true}| \ll |Y_i - Y_{true}|$. Simulation parameters such as the horizontal mesh resolution, number of vertical layers, time step and differential equation approximation are considered to fall under the category of error analysis in this work.

The vertical layer thickness and number can be varied by splitting a layer into sub-layers, as in figures 2 and 3, to investigate its influence on vertical dispersion. An error analysis has been carried out and is described in detail in section 4.

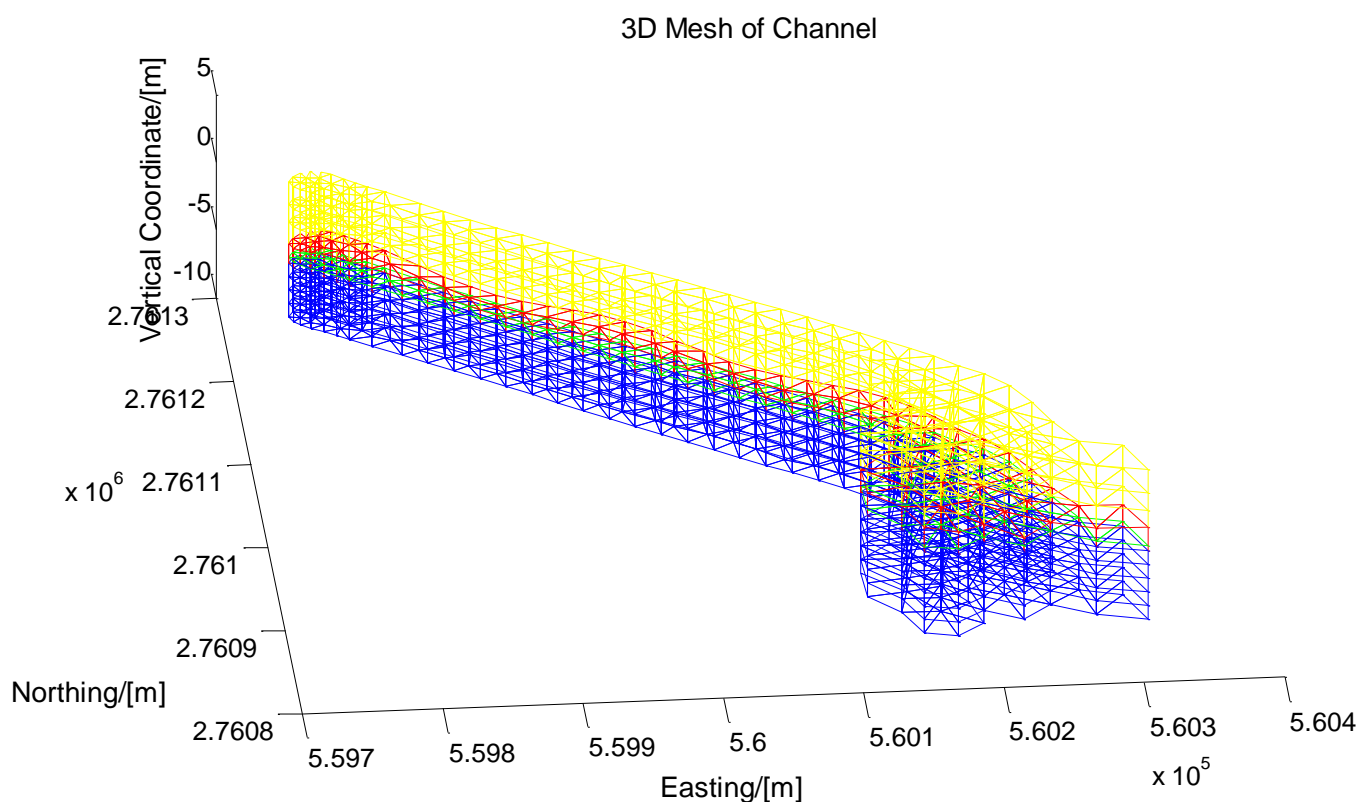


Figure 2: The channel depicted in figures 2 and 3 in a 3D view. Blue triangle prisms represent water. The green triangle mesh layer emphasizes the splitting of a layer into two sub-layers. The red triangle mesh layer is the surface between sea and air which adapts to surface elevation due to tidal movements. This has been graphically emphasized by superimposing a sinusoidal surface elevation onto the red surface mesh. The yellow layers represent the atmosphere.

Within this regard it shall be differentiated between error analysis, sensitivity analysis (comparing disturbance of input and output) and uncertainty analysis (when different system properties appear to not be preferable among each other).

To achieve an error estimate for solution Y_i it can be compared with a solution of a higher order of accuracy with $Error_i \approx |(Y_{accurate} - Y_i)/Y_{accurate}|$ (Lapidus et

In figure 3, investigating solution accuracy depending on the number of layers may be illustrated. Considering only vertical dispersion along z , biological sink, source (or reactions due to other reactants), and hypothetical quasi steady state, the simplified differential relation $D_{disp} d^2 c_{O_2}(z)/dz^2 = -k_{bio} c_{O_2}(z)$ has been solved numerically for various layering configurations.

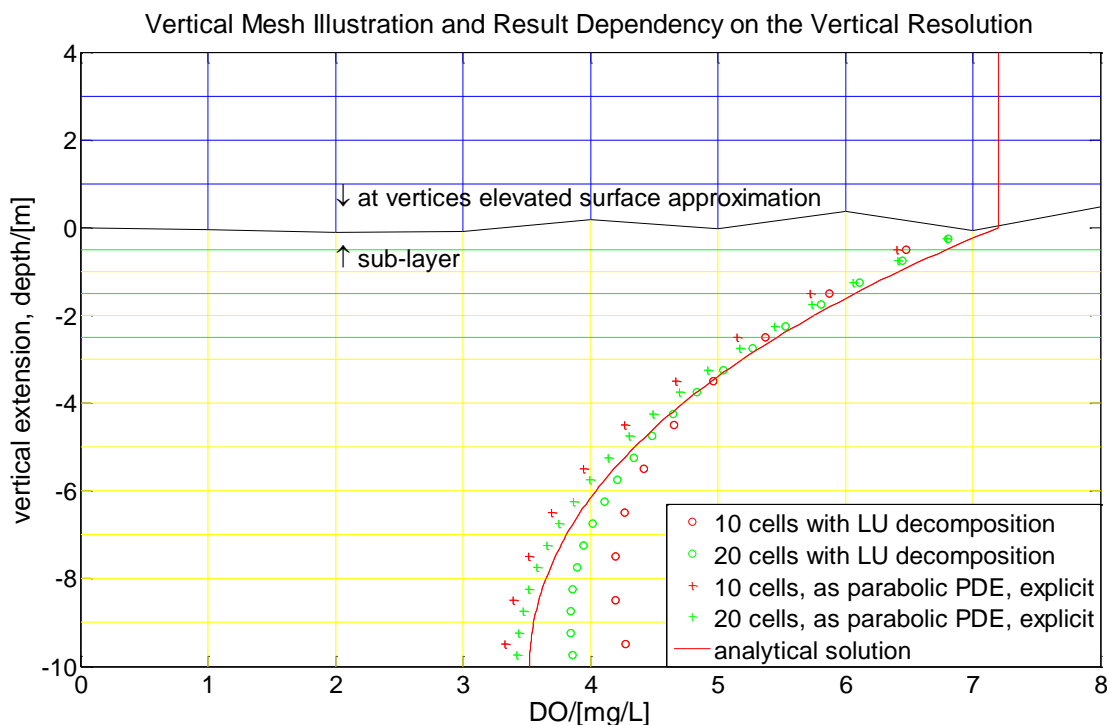


Figure 3: A 2D view showing the scheme of examining the influence of the vertical meshing onto a vertical result distribution. + and \circ show results for a vertical resolution of 0.5 m whereas + and \circ correspond to 1 m. The green layers emphasize sub-layers in the model which allow examining the result dependency on the vertical resolution.

3.5 Interface, Visualization and Result Analysis

The software has been programmed in FORTRAN 90 including Windows application user interface and visualization. Distributions can be visualized for single layer or average concentrations of a number of layers. Distributions can be shown in tripaving without interpolation, like in figure 7, or with interpolation like in figures 6, 8, and 9. The type of interpolation can be chosen among: linear triangle interpolation, where the triangle centers are Delaunay assembled to a complementary triangle mesh, followed by linear interpolation inside the triangle, or different types of inverse distance interpolations (Cressman, 1959; Barnes, 1964; Segal et al., 1981). Different color scales ranging from 512 to 1664 colors can be employed. Three different color scales have been utilized in figures 6, 7 and 8. Geographical UTM coordinates are indicated as abscissa and ordinate axes. Governmentally regulated mixing zones can be depicted as circles around the discharge, as shown in figures 6, 7, 8, and 9. The radius of a mixing zone can be set individually for each discharge. Zones where boundary values are exceeded can be visualized by an isoline plot to mark the border of a critical zone. The user can therefore easily identify whether the zone where the boundary concentration is exceeded lies only within the mixing zone or extends beyond the border of the mixing zone, violating regulations. The maximum concentration at the boundary of the mixing zone is indicated in the left upper corner as shown in figure 6.

4 CASE AND ERROR ANALYSIS

A dissolved oxygen distribution surrounding a process water outfall discharging anoxic water has been simulated to carry out an error analysis concerning vertical meshing, time-step, and explicit approximation. A coastal section at the shores of the Arabian Gulf, as shown in figure 4, has been approximated with a horizontally unstructured mesh with vertically structured layers. The mesh has 15 layers of 1 m and 2 m thickness, dependent on the water depth. The layers vary in thickness to adapt to tidal movements. Horizontally, 12,784 triangles assemble one layer. Cells in deeper regions are inactive in order to adapt to the bathymetry. For the cases depicted in figures 6 to 9, an anoxic discharge with a concentration of 0 mg/L dissolved oxygen has been set. Oxygen exchange with the atmosphere has been taken into account by setting a Henry equilibrium-based concentration in the top-layer. Further dissolved oxygen consumption due to chemical oxygen demand (COD) has not been taken into account for this error analysis. Several simulations with different settings concerning vertical mesh, time-step, and approximation have been carried out for the error analysis. The ambient concentration has been set to an equilibrium corresponding to the atmospheric oxygen concentration and has been normalized to 1 (100%) for the error analysis.

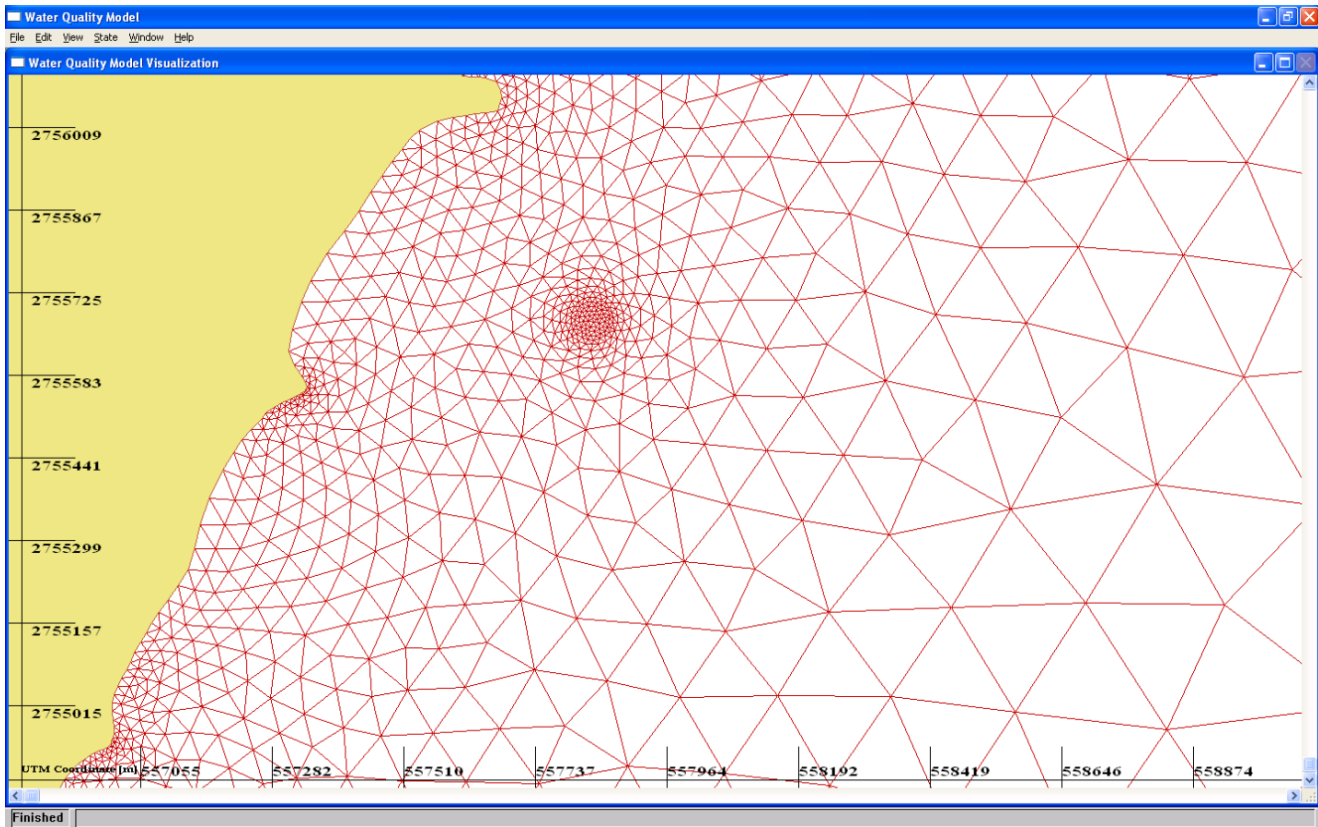


Figure 4: Water quality model interface showing a section of the mesh corresponding to the simulated area. The submerged discharge can be recognized in an area of high resolution.

3D Triangle Mesh Centered on a Submerged Discharge

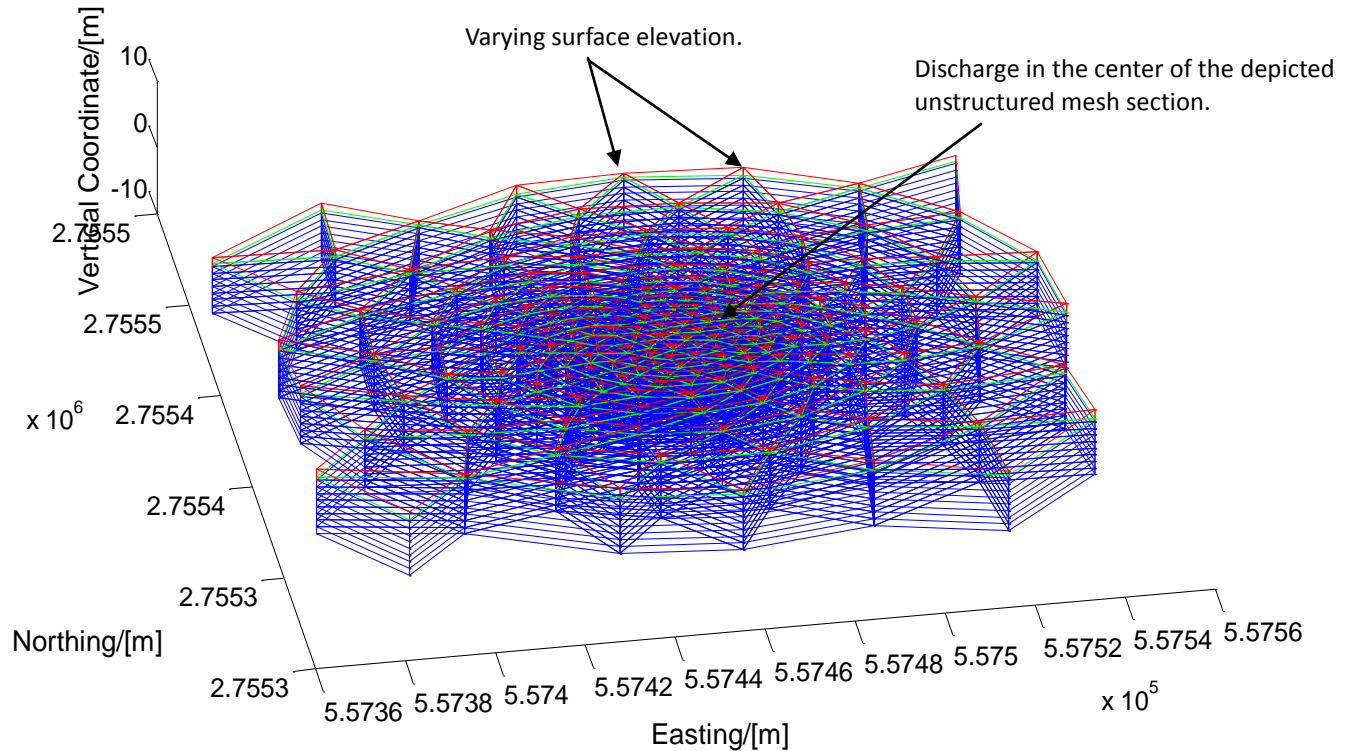


Figure 5: 3D view of the triangle prism, stacked in layers, and horizontally assembled to the computational domain. The green layer shows the utilized sub-layer. Centered on the discharge high resolution decreases with increasing distance from the discharge. Vertices of the red triangle layer are individually elevated depending on tidal elevation. In this figure a sinusoidal surface elevation has been added to emphasize the elevation adaption of the surface layer. The changing elevation is recognizable in the upper boundary of the depicted circular section.

The vertical resolution has been varied; the top-layer has been split into two sub-layers. The discharge is submerged to a depth of 8 meters. The discharge temperature is 41°C with an ambient temperature of 34°C. The water quality model and the FVCOM hydrodynamic model, which provided flow field and other hydrodynamic field data, used the same mesh. The cell size is reduced in areas of importance to accurately depict coastal and outfall geometries (figure 5). Close to the anoxic discharge the horizontal cell size is only 1 meter.

4.1 Test Results

Figure 6 shows the results for a domain approximation with 16 layers with a 1664 color scale.

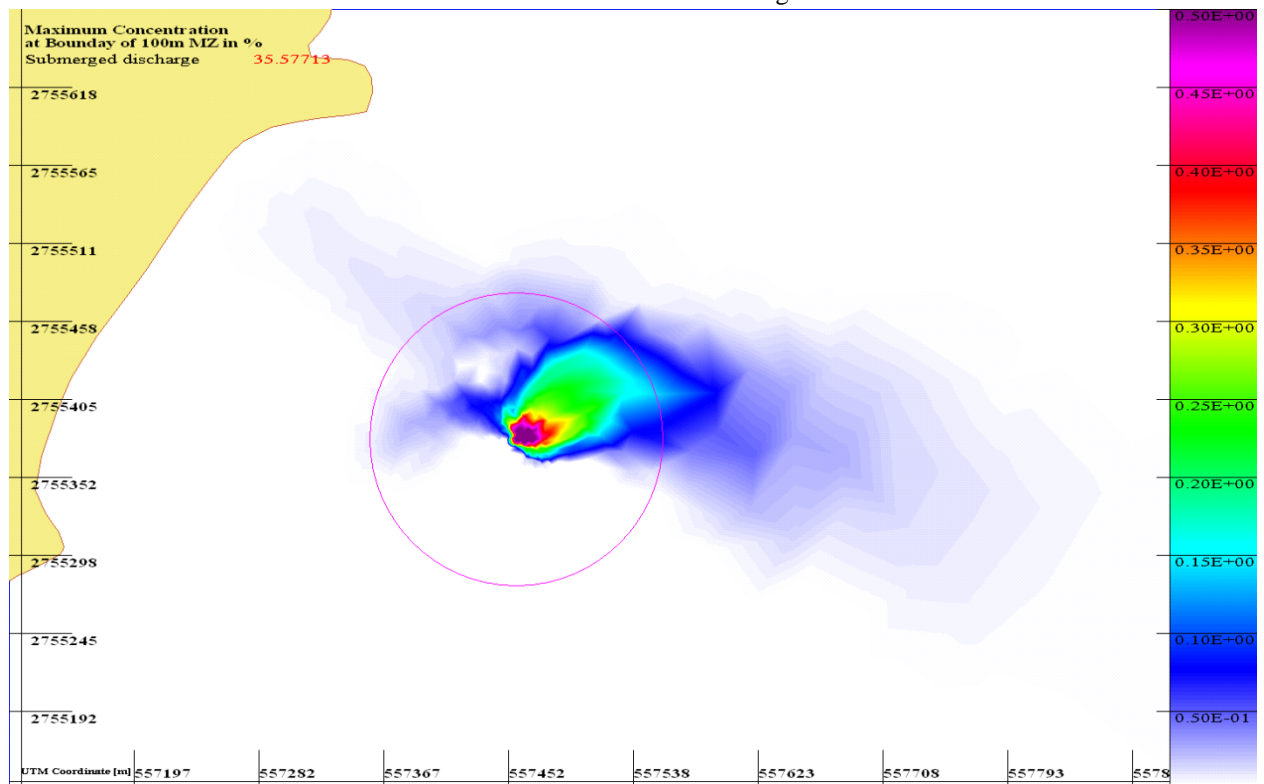


Figure 6: Plume after 2 h with 16 layers, a time step of 1 sec., and using a semi-implicit approximation (in 1664 colours).

The distribution corresponds to a vertical average along the water column. The concentration values correspond spatially to triangle centers which have been assembled to a complementary triangle mesh by Delaunay triangulation. Within these triangles linear interpolation is carried out for each pixel. The results of the different

cases are compared in table 2. Figure 7 shows the approximation using 16 layers with a 1152 color scale and tripping without interpolation. Figure 8 shows the simulation with 15 layers with interpolation and 1408 colors. Figure 9 shows the difference between the average concentration of the simulations with 15 and 16 layers, the distributions shown in figures 6 and 7 or 8, with 1664 colors. The hydrodynamic simulation has been calibrated with tidal data obtained from the Environmental Study Center of the State of Qatar. Tidal dynamics have a significant effect on the plume direction. Tidal effects are taken into account in the simulation. However, the smaller the scope of consideration the smaller is the influence of tidal dynamics. The considered mixing zone of 100 m is therefore mainly governed by currents induced by the discharged flow while the tidal influence is small at this

scale. The vertical size of the domain is adapting itself to the tidal surface elevation. The layer thickness in the mesh is smoothly varying and incrementally changed. Also the horizontal velocity components (u and v) have been calibrated to measurement values from stations located within the simulated domain.

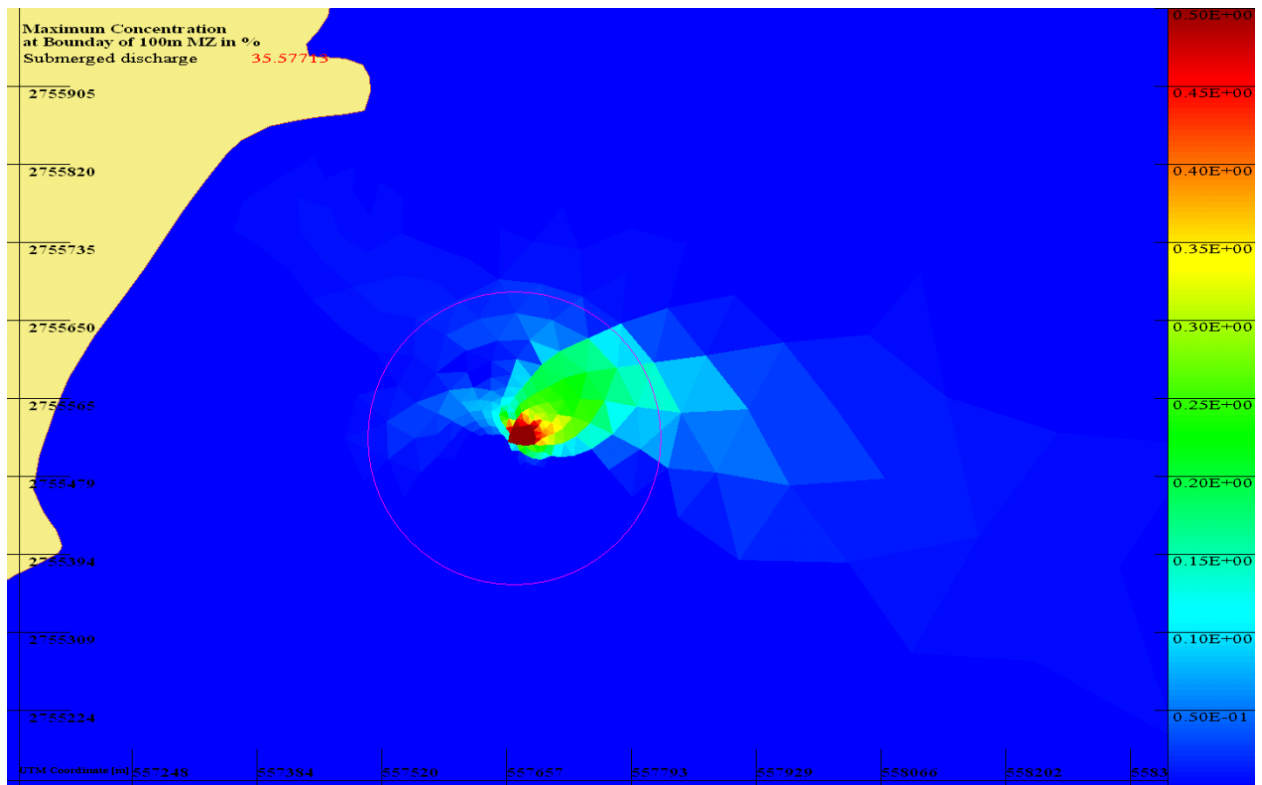


Figure 7: Plume of figure 8 with tripaving, 1152 colours, and without interpolation.

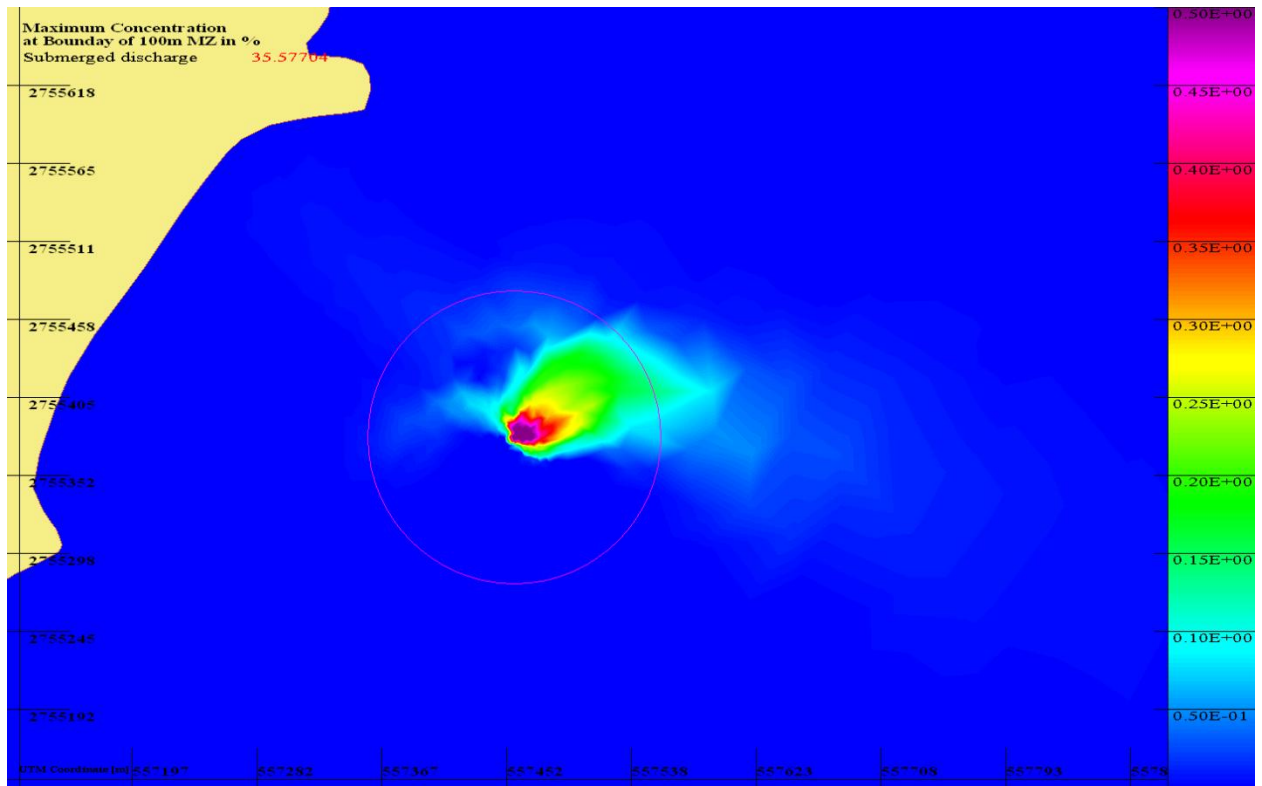


Figure 8: Plume after 2 h with 15 layers, a time step of 1 sec., and using a semi-implicit approximation (in 1408 colours).

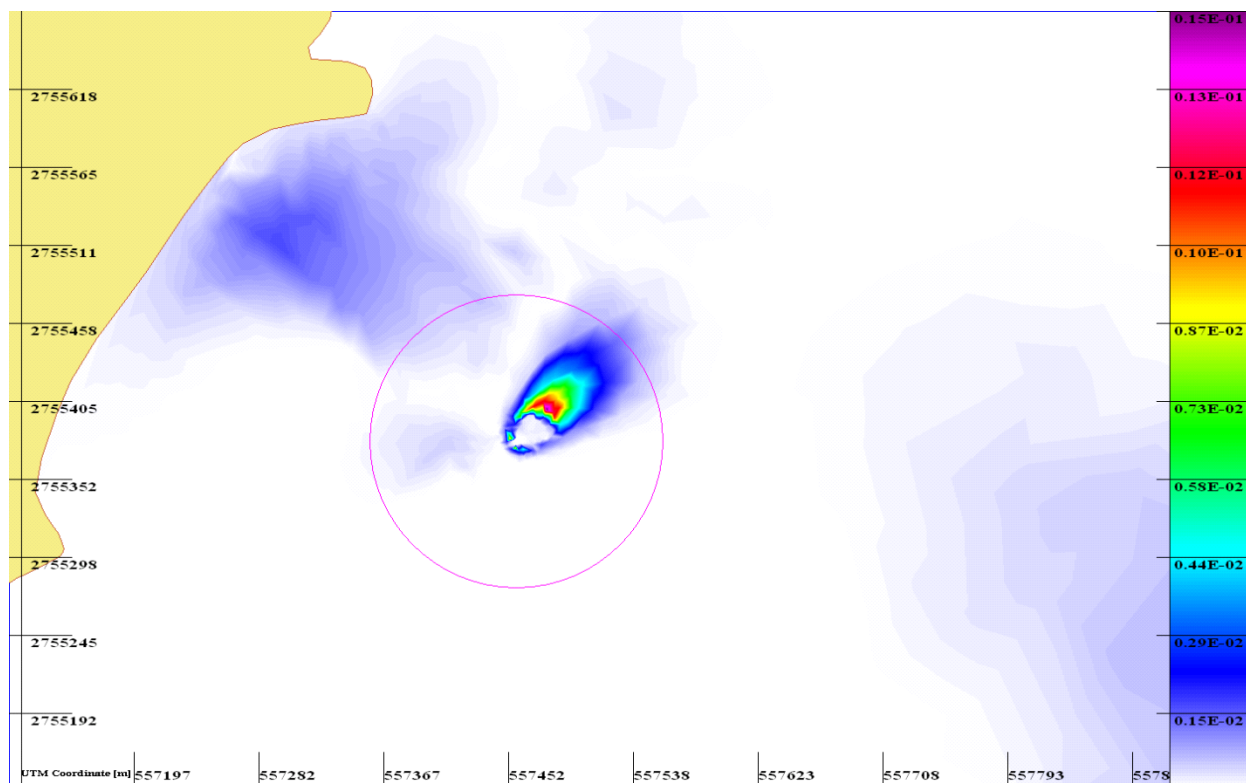


Figure 9: Showing the difference between the 15 and 16 layer simulation. The maximum difference is 0.0147=1.47%.

Table 2

Maximum concentration at the mixing zone boundary				
Time step/[s]	Explicit, 15 layer	Explicit, 16 layer	Semi-implicit, 15 layer	Semi-implicit, 16 layer
0.1	35.57906	35.57917	35.57729	35.57738
0.3	35.57720	35.57729	35.57910	35.57919
0.4	35.57598	35.57607	35.57911	35.57919
1.0	2.265563	32.52173	35.57704	35.57713

The difference between a 15 and a 16 layer approximation has been visualized in figure 9 which can function as a spatial and dynamic absolute error estimate distribution. The tool is able to plot the difference between two simulations, depending on the context, the error, the uncertainty, and the sensitivity. In table 3, the error estimate is shown for the maximum concentration at the boundary of the mixing zone, shown in table 2.

Table 3

Error estimates related to the mixing zone boundary.	
Model parameter	Error estimate in %,
Error, $\Delta = 0.1$ sec., explicit approximated	$3.09 \cdot 10^{-4}$
Error, $\Delta = 0.4$ sec., explicit approximated	$2.53 \cdot 10^{-4}$
Error, $\Delta = 0.3$ sec., semi-implicit approximated	$2.53 \cdot 10^{-4}$

Error estimate due to finite layer size in the approximation of near surface waters; Δ , time step size.

The error estimate concerning the layer resolution close to the surface has been calculated by comparing the 15 layer simulation with the simulation including two sub-layers in the top-layer. Table 3 shows selected examples for Error C, for the explicit solver with a time step of 0.1 and 0.4 seconds, and for the semi-implicit solver for a time step of 0.3 seconds.

5 DISCUSSION OF THE ERROR ANALYSIS

Table 3 shows estimates for error contribution due to vertical meshing. A trend can be observed by comparing the simulations with 15 or 16 layers. Having a smaller increment at the surface yielded a slightly bigger dissolved oxygen deficiency which indicates a slightly slower adaption to the surface equilibrium. However, the cases show just a small difference in results between the 15 or 16 layer approximation. Figure 9 illustrates a spatial and dynamic error distribution. The distribution shows that only the error at the location of the highest constituent concentration at the boundary of the mixing zone might be relevant when identifying whether mixing zone regulations are met. Taking this into account might allow indicating lower error estimates since the absolute error at one location will most probably be substantially lower than the highest error of the entire distribution.

6 CONCLUSION

Vertical sub-layering is suitable to function as comparisons in an error analysis within the validation process. Validating the sufficiency of a vertical layer resolution is especially valuable in case of anoxic discharges where substantial vertical gradients occur. If required substantial vertical sub-meshing can assure the accurate representation of volatile components. The visualization allows several different interpolation techniques and color scales. Plots allow superimposing, subtracting and visualizing the results of different scenarios to analyze errors, uncertainties or sensitivity. The tool visualization is optimized on the analysis of water quality results concerning their compliance with regulated boundary values and mixing zone sizes. Within this regard it has been illustrated that indicating the maximum of a dynamic absolute error estimate distribution (figure 9) might not be necessary. Only the maximum error at the boundary of the mixing zone is relevant when considering compliance with mixing zone regulations.

APPENDIX A

Table A.1

Symbols for the partial differential equation and boundary conditions

Symbol	Description	Unit
\dot{n}	Molar mass flow	mol/s
$c_j(\mathbf{r}, t)$	Concentration of species j at \mathbf{r} and t	mol/m ³
j	Species index	-
$\mathbf{r}_i \in \mathbf{r}$	Spatial location vector	m
τ	Time	s
$D(\mathbf{r}, \tau)$	Dispersion coefficient	m ² /s
$\mathbf{u}_i(\mathbf{r}, \tau)$	Velocity component vector	m/s
l	Reaction index	-
$\sigma_{jl} \in \Sigma$	Stoichiometric coefficient matrix for species j and reaction l	-
$k_{jl}(c_j(\mathbf{r}, \tau)) \in K$	Kinetic coefficient matrix dependent on $c_j(\mathbf{r}, \tau)$	1/s
c_w	Equilibrium concentration in water	mol/m ³
c_{at}	Equilibrium concentration in air	mol/m ³
k_{eq}	Henry coefficient	-

Table A.2

Symbols for the finite volume equation and approximated boundary conditions

Symbol	Description	Unit
$\mathbf{c}_{ih}^t \in \mathbf{c}_h^t$	Concentration vector for a layer h at time level t containing values for all cells listed in \mathbf{I}	mol/m ³
$s = [1 \ 2 \ 3]$	Side of a triangle	-
t	Time level	-
Δ	Time wise increment, time-step	s
$nl(\mathbf{I}, s)$	Neighbor list returning the index for the cell which neighbors to the cells \mathbf{I} at the side s	-
$\mathbf{v}_{ih}^t \in \mathbf{v}_h^t$	Finite volume vector for a layer h at time level t containing values for all cells listed in \mathbf{I} (the cell volume is dynamic due to varying surface elevation)	m ³
$\mathbf{g}_{hs} \in \mathbf{g}_{hs}$	$\mathbf{g}_{hs} = \frac{\Delta \mathbf{a}_{hs}^t \delta_{hs}^t}{\Delta \mathbf{r}_s \mathbf{v}_h^t}$	1/s
$\Delta \mathbf{r}_{is} \in \Delta \mathbf{r}_s$	Inter-triangle-center distance to side s	m
$\Delta \mathbf{a}_{ihs}^t \in \Delta \mathbf{a}_{hs}^t$	Surface area of one surface of the finite volume	m ²
$\delta_{ihs}^t \in \delta_{hs}^t$	Dispersion coefficient vector at the center of the surface at side s	m ² /s
$\dot{\mathbf{v}}_{ihs}^t \in \dot{\mathbf{v}}_{hs}^t$	Volume flow	m ³ /s
$\varepsilon_{ihs} \in \varepsilon_{hs}$	Logical control bit array determining the ratio between explicit and implicit approximation.	-
$\pi_{ihs} \in \pi_{hs}$	Adaptive upwind control bit array	-

REFERENCES

- [1] Abarnou, A., Miossec, L., 1992, Chlorinated waters discharged to the marine environment chemistry and environmental impact. An overview, The Science of the Total Environment, 126, 173-197.
- [2] Taylor, C., 2006. The effects of biological fouling control at coastal and estuarine power stations. Marine Pollution Bulletin 53, 30-48.
- [3] EPA, 1980. Clean Water Act, Section 403, Ocean Discharge Criteria.
- [4] Abdel-Wahab, A., Linke, P., Alfadala, H.E., El-Halwagi, M.M., Batchelor, B., 2009. Towards a Holistic Approach to the Sustainable Use of Seawater for Process Cooling. Advances in Gas Processing: Proceedings of the 1st Annual Gas Processing Symposium. 332-340.
- [5] Lawen, J., Huaming, Y., Linke, P., Abdel-Wahab, A., 2010. Industrial Water Discharge and Biocide Fate Simulations with Nonlinear Conversion. Proceedings of the 2nd Annual Gas Processing Symposium. 99-106.
- [6] Adenekan, A.E., Kolluru, V. S., Smith, J. P., 2009. Transport and Fate of Chlorinated By-Products Associated with Cooling Water Discharges, Advances in Gas Processing: Proceedings of the 1st Annual Gas Processing Symposium. 341-353.
- [7] Kolluru, V.S., Edinger, J. E., Buchak, E. M., Brinkmann, P., 2003. Hydrodynamic Modeling of Coastal LNG Cooling Water

- Discharge. *J Energ Eng.* 129, No. 1, 16 – 31.
- [8] Jirka, G.H., 2008. Improved Discharge Configurations for Brine Effluents from Desalination Plants. *J Hydr Eng, ASCE*, 134, No. 1, 116-129.
- [9] Lawen, J., Linke, P., Abdel-Wahab, A., Bhatelia, T., Fieg, G., submitted 2010. Fluid Flow Direction Guided Solution of an Implicit Adaptive Upwind Approximation for Advection Simulations. *J Comp & Fluids*.
- [10] Abdel-Wahab, A., Khodary, A., Bensalah, N., Formation of Trihalomethanes (THMs) during Seawater chlorination, *Journal of Environmental Protection*, in press, 2010.
- [11] Versteeg, H., 2007, The finite volume method for convection-diffusion problems, *Introduction to Computational Fluid Dynamics: The Finite Volume Method*.
- [12] Chen, C.S., Liu, H.D., Beardsey, R.C., 2003. An Unstructured Grid, Finite-Volume, Three-Dimensional, Primitive Equations Ocean Model: Application to Coastal Ocean and Estuaries. *Journal of Atmospheric and Oceanic Technology* 20, 159-186.
- [13] Lai, Z., Chen, C., Cowles, G., Beardsley, R.C., 2010. A non-hydrostatic version of FVCOM-validation experiment I: surface standing and solitary waves, *Journal of Geophysical Research* 115, C11010.
- [14] Huaming, Y., 2008, 利用有限体积模型对狭长海湾填海优选方案的研究 (A Study on Optimum Schemes for Reclamation in a Narrow Bay using the Finite Volume Method), China Academic Journal Electronic Publishing House.
- [15] Launder, B.E., Spalding, D.B., 1972, *Lectures in Mathematical Models of Turbulence*. Academic Press, London, England.
- [16] Gour-Tsyh, Y., 2002, Fluid Flows and Reactive Chemical Transport in Variable Saturated Subsurface Media, *Environmental Fluid Mechanics Theories and Applications*, 207-255.
- [17] Haidvogel, D., 1999, The hydrostatic Primitive Equations, *Numerical Ocean Circulation Modeling*, 19-21.
- [18] Chen, C., Beardsley, R.C., Cowles, G., 2006, *An Unstructured Grid, Finite-Volume Coastal Ocean Model FVCOM User Manual*
- [19] S.P. Arya, Micrometeorology and atmospheric boundary layer, *Pure Appl. Geophys.* 162 (2005) 1721–1745.
- [20] H.A. Panofsky, J.A. Dutton, *Atmospheric Turbulence: Models and Methods for Engineering Applications*, John Wiley & Sons, Inc., Canada, 1984.
- [21] C. Alinot, C. Masson, $k-\epsilon$ model for the atmospheric boundary layer under various thermal stratifications, *J. Solar Eng.* 127 (November) (2005) 438–443.
- [22] A. Huser, P.J. Nilsen, H. Skatun, Applications of $k-\epsilon$ model to the stable ABL: pollution in complex terrain, *J. Wind Eng. Ind. Aero.* 67–68 (1997) 425–436.
- [23] R. Morel, A. Laassibi, E. Alcaraz, R. Zegadi, G. Brun, D. Jeandel, Validation of a $k-\epsilon$ model based on experimental results in a thermally stable stratified turbulent boundary layer, *Int. J. Heat Mass Transfer* 35 (1992) 2717–2724.
- [24] Lapidus, L., Pinder, G.F., 1999. *Numerical Solution of Partial Differential Equations*.

Steady-State Quartz Formation in terms of Water Migration through Nanopores

K. Sato¹

¹Department of Environmental Sciences, Tokyo Gakugei University, Koganei, Tokyo 184-8501, Japan
(sato-k@u-gakugei.ac.jp)

ABSTRACT

Steady-state quartz formation in geological environment is an important phenomenon that can address the global environmental issues as diagenetic evolution, biogeochemical cycling, and reservoir formation, but the mechanism is not fully understood. Here, we discuss the steady-state quartz formation on the basis of our recent findings on water migration through nano-scale pores (nanopores). Water molecules diffuse through 2 Å nanopores in amorphous silica with an activation energy of 2.3 eV. They react with highly reactive nanopore surfaces involving an energy cost of 1.9 eV triggering off the quartz formation. We show experimentally that diffusion and reactions of water molecules in nanopores underlie the formation mechanism of silica quartz.

Keywords: steady-state quartz formation¹, geological environment², water migration³, nano-scale pore⁴

1. INTRODUCTION

Silica is one of the most important materials with respect to advanced nanotechnology as well as earth science. Amorphous silica transforms to crystalline quartz via metastable silica polymorphs, which has stimulated a long history of experimental and theoretical investigations [1]. In spite of efforts devoted over the last semi-century, the mechanism of long-term low-temperature quartz formation still remains puzzle. Empirically, the following facts have been shown relevant to the quartz formation [2-4]. 1. The transformation of amorphous silica to crystalline quartz is induced by the interaction between silica surfaces and water molecules. 2. The transformation to crystalline quartz undergoes thermally activated reaction. 3. Diffusion and reactions of water molecules are the rate-limiting step for the transformation to crystalline quartz at low temperature below 573 K.

Earlier tracer diffusion experiments for amorphous silica with tritiated water have suggested that water molecules diffuse with a considerably low activation energy of ~ 0.7 eV [5]. On the contrary, recent first principle calculation predicts more complex diffusion mechanism that an activation energy of water diffusion ranges from 0.8 to 2.2 eV depending on the sizes of nanopores [6-7]. The calculation further predicts that local chemical environments of nanopore surfaces cause different possible reactions with water molecules ranging activation energies from 0.3 to 5.9 eV. In this study, we discuss the steady-state quartz formation on the basis of our recent findings on water migration through nano-scale pores [8].

2. EXPERIMENTS

The cell wall of diatom is known to contain silica. We thus employed amorphous silica originated from diatom

frustules corrected from Mariana Trench, as starting materials. Hydrothermal synthesis on a 70-days time scale was performed in the temperature range from 383 K to 443 K in a cylindrical Teflon vessel. Silica products and oxygen bonding energies were examined by x-ray diffraction (XRD) and x-ray photoelectron spectroscopy (XPS), respectively.

Nanopore sizes and their intensities were investigated by positron lifetime spectroscopy. The positron source (²²Na), sealed in a thin foil of Kapton, was mounted in a sample-source-sample sandwich. Positron lifetime spectra were numerically analyzed using the POSITRONFIT code [9]. Nanopore surfaces were examined by the recently discovered phenomenon of *ortho*-Positronium (*o*-Ps) specific to light elements as, e.g., oxygen [10-11]. *o*-Ps picks off the electrons at nanopore surfaces, providing the information on electronic states of nanopore surfaces. The momentum distribution of *o*-Ps pick-off annihilation was extracted by means of positron-age-momentum correlation (AMOC) spectroscopy [12]. AMOC spectra were analyzed as the momentum *S* parameter (*S*(t)), which was determined as the ratio of the central area over (-3.6 to +3.6) × 10⁻³ m₀c to the total area of the momentum spectrum [13].

3. RESULTS AND DISCUSSION

Figure 1 shows XRD patterns observed for synthesized at 423 K for 336 h, 672 h, 1176 h, and 1680 h. Structural evolution toward crystalline quartz with increasing the synthesized time can be seen in the variation. The diffraction pattern at 336 h is of typical amorphous structure, which maintains up to 672 h. XRD peaks arising from the quartz phase begin to appear together with those from the cristobalite phase at 1176 h. The peaks of cristobalite phase disappear at 1680 h and the quartz phase is dominantly formed.

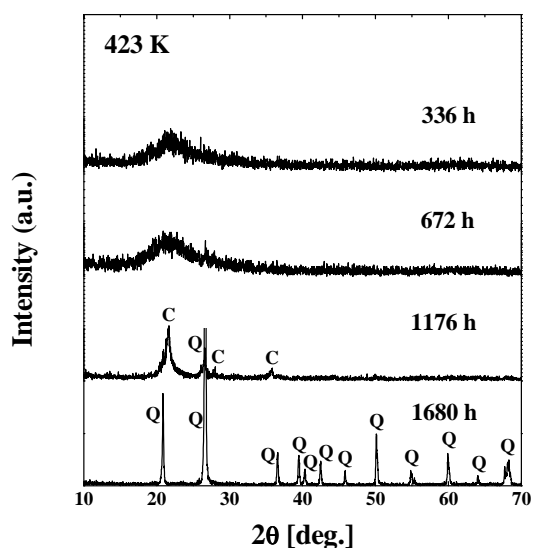


Figure 1. X-ray diffraction patterns observed for hydrothermally synthesized at 423 K for 336 h, 672 h, 1176 h, and 1680 h. XRD peaks indexed to the cristobalite and quartz are marked with C and Q, respectively.

Figure 2 shows oxygen 1s XPS spectra observed for synthesized at 423 K for 0 h, 336 h, 672 h, 1176 h, and 1680 h. All the oxygen 1s peaks are largely shifted toward the lower binding energy than of typical SiO₂ glass (~ 531.9 eV), signifying the presence of non-bridging oxygen bonds more than SiO₂ glass. At 336 h, FWHM of the spectrum increases by ~ 15 % whereas no chemical shift is observed. This demonstrates the formation of a variety of oxygen chemical bonds, as e.g., silanol group. Though no significant change is observed in XRD patterns, oxygen 1s peak is slightly shifted toward higher binding energy FWHM being constant at 672 h. The chemical shift becomes more prominent with the reduction of FWHM by ~ 10 % at 1176 h, where XRD peaks of quartz and cristobalite appear. It is known that the angle of Si-O-Si in cristobalite is larger than in amorphous silica at low temperature. The larger angle causes the lower electron density around oxygen atoms, leading to the chemical shift toward the higher binding energy. The chemical shifts observed with increasing synthesized time to 1176 h are thus attributable to the formation of cristobalite. The decrease of FWHM is due to dissociation of instantaneous bonds to form cristobalite and quartz. It is of interest that XPS sensitively detects the formation of cristobalite earlier than XRD. At 1680 h, oxygen 1s peak is shifted back to the lower binding energy with a slight reduction of FWHM due to the disappearance of cristobalite with larger Si-O-Si angle, in agreement with XRD.

Positron lifetime spectroscopy for amorphous silica yields three components, of which the longest-lived component τ_3 of ~ 1.6 ns is attributable to pick-off annihilation of *o*-Ps localized in nanopores of amorphous

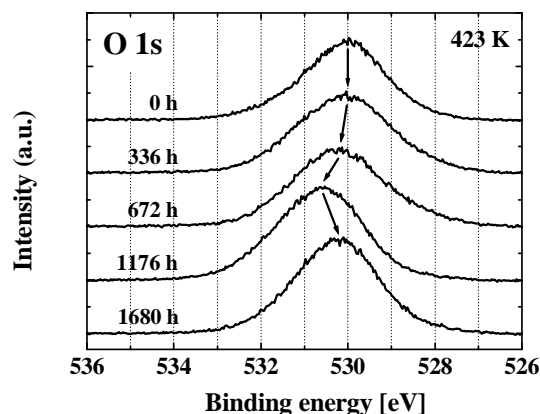


Figure 2. Oxygen 1s XPS spectra observed for hydrothermally synthesized at 423 K for 0 h, 336 h, 672 h, 1176 h, and 1680 h. Arrows are drawn for guiding the eye.

matrix. The size of nanopores is evaluated to be ~ 2 Å through the lifetime component τ_3 based on the Tao-Eldrup model:

$$\tau_3 = 0.5 \left[1 - \frac{R}{R_0} + \frac{1}{2\pi} \sin\left(\frac{2\pi R}{R_0}\right) \right]^{-1} \quad (1)$$

where $R_0 = R + \Delta R$, and $\Delta R = 0.166$ nm is the thickness of homogeneous electron layer in which the positron in *o*-Ps annihilates [14-15]. No systematic changes are observed in the lifetime τ_3 when the quartz formation proceeds at longer synthesized time. In light of the fact that no long lifetime component τ_3 is observed in silica polymorphs with high crystallinity, as e.g., crystalline quartz [16], nanopores are located not in the quartz phase but in the intergranular amorphous regions.

Figure 3 (a) shows synthesized-time variations of nanopore intensities I_3 at 383 K, 403 K, 423 K, and 443 K. Nanopore intensities decrease with increasing the synthesized time up to 1680 h (70 days) at the lower temperature of 383 K. The decreasing tendency with the synthesized time becomes increasingly prominent when the temperature is raised up to 443 K. The formation of quartz in the amorphous matrix creates the intergranular amorphous regions and its growth reduces the volume fraction of intergranular amorphous regions. It is thus reasonable that nanopores in the intergranular amorphous regions decrease together with the quartz formation. Good fits of isotherms are obtained by an exponential with a decay constant k_f , as indicated with solid lines. In Figure 3 (b), the logarithms of decay constants are plotted as a function of inverse temperature. It follows the Arrhenius law demonstrating that the quartz formation is governed by the thermally activated reaction. From temperature variation the activation energy of quartz formation is derived to be 4.2 eV.

Figure 4 shows the results of AMOC spectroscopy for synthesized at 423 K for 0 h, 168 h, 336 h, 672 h, 1176 h, and 1680 h, in which momentum $S(t)$ parameters are

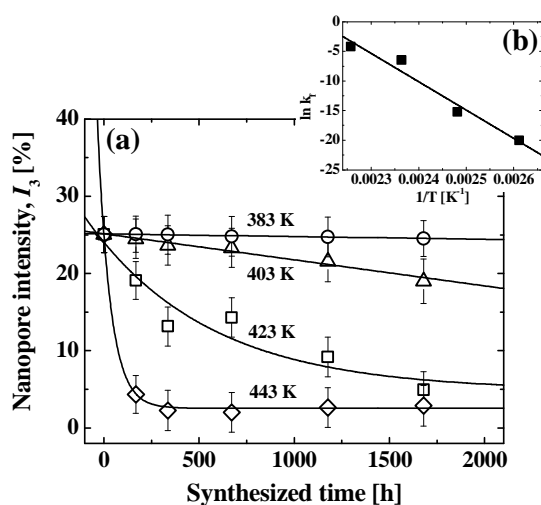


Figure 3. (a) Synthesized-time variations of nanopore intensities I_3 at 383 K (open circles), 403 K (open triangles), 423 K (open squares), and 443 K (open diamonds). Solid lines denote the results of the fits by an exponential with a decay constant k_f . (b) Logarithms of decay constants as a function of inverse temperature.

plotted as a function of positron age. Positron-age variations of $S(t)$ parameters are typical for Ps-forming materials as, e.g., glass and polymer [12]. The $S(t)$ parameters indicate high values around $t = 0$ ns arising from self annihilation of *para*-Ps (*p*-Ps). They rapidly decrease in the positron age from 0 to 0.8 ns due to the disappearance of *p*-Ps. Above the positron age of 2.0 ns the $S(t)$ parameters are saturated, where *o*-Ps pick-off annihilation is exclusively occurs. It should be noted in Figure 4 that the $S(t)$ parameters of *o*-Ps pick-off annihilation (*o*-Ps momentum parameter) are gradually deviated below, as marked with a thick circle. As is detailed in our former paper [12], the downward deviation of *o*-Ps momentum parameter is a consequence resultant from increased oxygen atoms incorporated with nanopore surfaces. We reasonably infer that reactions of water molecules cause chemical variations at nanopore surfaces.

The *o*-Ps momentum parameters at 383 K, 403 K, 423 K, and 443 K numerically determined by fitting the rate equation model [17] to the experimental AMOC data are shown in Figure 5 (a) as a function of synthesized time. Thermally activated reactions of water molecules at nanopore surfaces can be well seen similarly to that of quartz formation (see Figure 3 (a)). The logarithms of decay constants obtained from an exponential fit are plotted as a function of inverse temperature in Figure 5 (b). From the temperature variation the activation energy of reaction between water molecules and nanopore surface is derived to be 1.9 eV, which is lower than that of quartz formation.

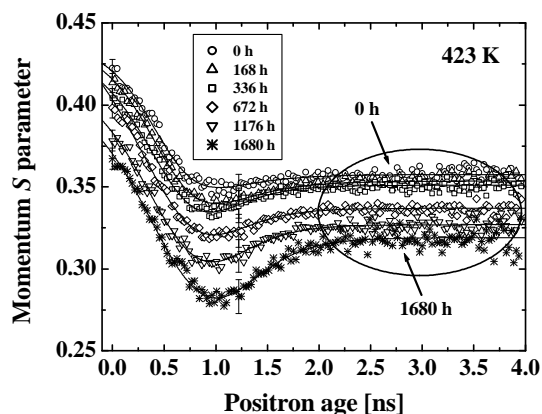


Figure 4. Results of AMOC spectroscopy for hydrothermally synthesized at 423 K for 0 h (open circles), 168 h (open triangles), 336 h (open squares), 672 h (open diamonds), 1176 h (open inverse triangles), and 1680 h (stars). Solid lines denote model fits to the experimental data (see text).

Based on the present observation of thermally activated quartz formation, temperature-dependent quartz formation rate J is modeled as

$$J(T) = A \exp\left(-\frac{E_f}{kT}\right) \quad (2)$$

where A , T , E_f , and k are pre-exponential factor, temperature, activation energy of quartz formation, and Boltzmann constant, respectively. Since reactions of water molecules at nanopore surfaces and diffusion of water molecules through nanopores are involved in the quartz formation, equation (2) is rewritten as

$$J(T) = A \exp\left(-\frac{E_d}{kT}\right) \exp\left(-\frac{E_r}{kT}\right) \quad (3)$$

where E_r and E_d are activation energies of water reaction at nanopore surfaces and water diffusion through nanopores, respectively. Applying equations (2) and (3) to the Arrhenius plots in Figures 3 (b) and 5 (b), E_r , E_d , and E_f are determined to be 1.9 eV, 2.3 eV, and 4.2 eV, respectively.

Here, we compare above activation energies with theoretical prediction for lack of experimental data. According to first principle calculations [6-7], the activation energy of water reaction at nanopore surfaces is variable ranging 0.3-5.9 eV with possible chemical environment of nanopore surfaces. The obtained activation energy E_r is relatively low while it is within the calculated range. As is already mentioned, XPS suggests that there exist non-bridging oxygen bonds for the present samples more than typical SiO₂ glass. It is thus anticipated that oxygen atoms incorporated with nanopore surfaces are highly reactive with dangling bonds and water molecules can easily form other bonds

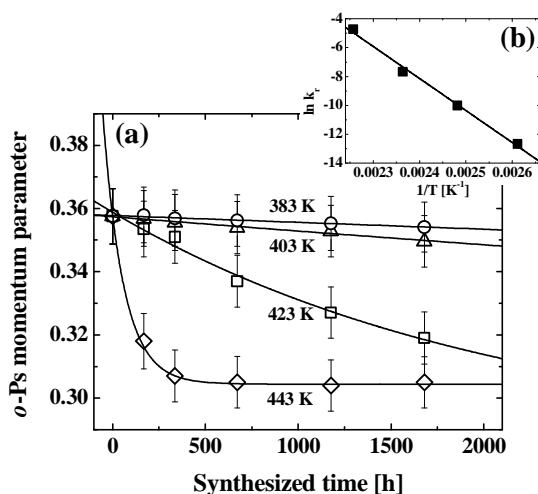


Figure 5. (a) Synthesized-time variations of *o*-Ps momentum parameter at 383 K (open circles), 403 K (open triangles), 423 K (open squares), and 443 K (open diamonds). Solid lines denote the results of the fits by an exponential with a decay constant k_r . (b) Logarithms of decay constants as a function of inverse temperature.

as, e.g., silanol. This is further supported by the increase of FWHM of XPS spectrum by $\sim 15\%$ at the synthesized time of 336 h without any chemical shift. The activation energy of water reaction at nanopore surfaces evaluated here is therefore concluded to be reasonable. The calculated activation energy of water diffusion through interconnected nanopores begins to increase rapidly at the nanopore radius of 3 \AA and reaches as high as 2.2 eV at the radius of 2 \AA . The activation energy of water diffusion E_d evaluated from E_r and E_f is in excellent agreement with the above calculation, confirming the validity of the present model.

Combining the results of XRD, XPS, and nanopore analysis, the following quartz formation mechanism can be drawn. There exist highly reactive nanopores with the size of 2 \AA in the present amorphous silica. Water molecules diffuse through the nanopores in the amorphous matrix with the activation energy of 2.3 eV . Nanopores surfaces are immediately hydroxylated by water molecules, in which silanol groups are dominant. The silanol groups are ionized producing mobile protons that associate/dissociate with the nanopore surfaces. Resultantly the electrical double layer is formed inducing reorientation of water molecules due to ionic conductivities. The formation of electrical double layer is evidenced by the data of sum frequency generation infrared (SFG-IR) spectroscopy [18]. The directional water molecules affect reactions at nanopore surfaces, triggering off the nucleation of crystalline quartz with the activation energy of 1.9 eV . Water molecules initially form a variety of instantaneous bonds relevant to oxygen at nanopore surface s. The oxygen chemical bonds

partially transform to that of cristobalite with larger Si-O-Si angle and then to that of quartz. The cristobalite phase disappears presumably to be closely packed structure for stabilization and, finally, the quartz phase becomes dominant involving the total energy cost of 4.2 eV .

4. ACKNOWLEDGEMENT

The authors are indebted to Drs. Ikehara (AIST) and Hatta (JIRCAS) for supplying starting materials and technical support for XPS experiments. Discussion with Profs. Fujimoto (Tokyo Gakugei University), Nakata (Tokyo Gakugei University), and Shikazono (Keio University) is gratefully appreciated. This work was partially supported by a Grant-in-Aid of the Japanese Ministry of Education, Science, Sports and Culture (Grant Nos. 21540317 and 23740234).

REFERENCES

- [1] for example, Liang, Y., Miranda, C.R., and Scandolo, S. "Tuning oxygen packing in silica by nonhydrostatic pressure", *Phys. Rev. Lett.*, Vol. 99, pp. 2155041-2155044, 2007.
- [2] Parks, G.A. "Surface and interfacial free energies of quartz", *J of Geophys Res.*, Vol. 89: pp. 3997-4008, 1984.
- [3] Marzer, J.J., and Walther, J.V. "Dissolution kinetics of silica glass as a function of pH between 40 and $85 \text{ }^\circ\text{C}$ ", *J of Non-Cryst Solids*, Vol. 170, pp. 32-45, 1994.
- [4] Dove, P.M., Han, N., Wallace, A.F., and De Yoreo, J.J. "Kinetics of amorphous silica dissolution and the paradox of the silica polymorphs", *Proc Natl Acad Sci USA*, Vol. 105, pp. 9903-9908, 2008.
- [5] Burn, I., and Roberts, J.P. "Influence of hydroxyl content on the diffusion of water in silica glass", *Phys Chem Glasses*, Vol. 11, pp. 106-114, 1970.
- [6] Bakos, T., Rashkeev, S.N., and Pantelides, S.T. "Reactions and diffusion of water and oxygen molecules in amorphous SiO_2 ", *Phys. Rev. Lett.*, Vol. 88, pp. 0555081-0555084, 2002.
- [7] Bakos, T., Rashkeev, S.N., and Pantelides, S.T. " H_2O and O_2 molecules in amorphous SiO_2 : defect formation and annihilation mechanisms", *Phys. Rev. B*, Vol. 69, pp. 1952061-1952069 2004.
- [8] Sato, K., Fujimoto, K., Nakata, M., and Hatta, T. "Diffusion-Reaction of Water Molecules in Angstrom Pores as Basic Mechanism of Biogenic Quartz Formation", *J. of Phys. Chem. C*, Vol. 115, pp. 18131-18135, 2011.
- [9] Kirkegaard, P., and Eldrup, M. "Positronfit extended: A new version of a program for analysing position lifetime spectra", *Comput. Phys. Commun.* Vol. 7, pp. 401-409, 1974.
- [10] Sato, K., Ito, K., Hirata, K., Yu, R.S., and Kobayashi, Y. "Intrinsic momentum distributions of positron and

- positronium annihilation in polymers", *Phys. Rev. B*, Vol. 71, pp. 0122011-0122014 2005.
- [11] Sato, K., Shanai, D., Hotani, Y., Ougizawa, T., Ito, K., Hirata, K., and Kobayashi, Y. "Positronium formed by recombination of positron-Electron pairs in polymers", *Phys. Rev. Lett.*, Vol. 96, pp. 2283021-2283024 2006.
- [12] Sato, K., Murakami, H., Ito, K., Hirata, K., and Kobayashi, Y. "Probing the elemental environment around the free volume in polymers with positron annihilation age-momentum correlation spectroscopy", *Macromolecules* Vol. 42, pp. 4853-4857 2009.
- [13] Sato, K., Baier, F., Sprengel, W., Würschum, R., and Schaefer, H.-E. "Study of an order-disorder phase transition on an atomic scale: the example of decagonal Al-Ni-Co quasicrystals", *Phys. Rev. Lett.* Vol. 92, pp. 1274031-1274034 2004.
- [14] Tao, S.J. "Positronium annihilation in molecular substances", *J. Chem. Phys.* Vol. 56, pp. 5499-5510 1972.
- [15] Eldrup, M., Lightbody, D., and Sherwood, J.N. "The temperature dependence of positron lifetimes in solid pivalic acid", *Chem. Phys.* Vol. 63, pp. 51-58, 1981.
- [16] Yoshizawa, K., Sato, K., Murakami, H., Shikazono, N., Fujimoto, K., and Nakata, M. "Open-nano pores in natural minerals studied by positron lifetime spectroscopy", *Materials Science Forum*, Vol. 607, pp. 189-191, 2009.
- [17] Castellaz, P., Major, J., Mujica, C., Schneider, H., Seeger, A., Siegle, A., Stoll, H., and Billard, I., "Chemical reactions of positronium studied by age-momentum correlation (AMOC) using a relativistic positron beam", *J. of Rad. and Nucl. Chem.* Vol. 210, pp. 457-467, 1996.
- [18] Du, Q., Freysz, E., and Shen, Y.R. "Vibrational spectra of water molecules at quartz/water interfaces", *Phys. Rev. Lett.*, Vol. 72, pp. 238-241, 1994.

On the Control Requirements of Heaving Wave Energy Converters

Mohammed Jama, Ali Assi*, and Hassan Noura

Electrical Engineering Department – UAE University

*Corresponding author: ali.assi@uaeu.ac.ae

ABSTRACT

Heaving point absorbers are semi-submerged Wave Energy Converters (WECs), which convert the incident wave energy into electricity directly through the Permanent Magnet Linear Generator (PMLG). The motion of WEC in real sea state is highly nonlinear; however linear model can be used sufficiently, when small constrained excursions are allowed. Control strategies are used to control the motion of the WEC floater to absorb as much energy as possible. This paper examines heaving WEC as a control problem and discusses the corresponding control components and requirements.

Keywords: Wave energy converter, heave, power take-off, optimal control.

1. INTRODUCTION

Wave energy is considered one of the most untapped renewable energy resources in the world, with an estimated power of 2 TW worldwide [1]. The waves are produced by wind action and are therefore an indirect form of solar energy. WECs are devices used to extract the mechanical energy of the wave and convert it to electrical power. Thousands of patents have been registered in the field of WECs since 1980 [2], but very few have reached to the demonstration and commercialization phase. Different devices use different working principles (oscillating water columns, overtopping devices, floating bodies, oscillating bodies) and are designed for different location (on-shore, near-shore, and off-shore). The power take-off (PTO) mechanism (electric or hydraulic generators, air or water turbines) may vary from one WEC to another [3, 4, and 5]. The amount of power that can be extracted from waves depends on the wave climate of a certain location and the efficiency of the used WEC, which in turn is a function of WEC geometry and the adopted PTO [6]. This paper discusses the linear model of heaving point absorbers, and the control strategies utilized to maximize the captured energy from the waves. The paper is organized as follows: Section 2 describes the principle of heaving WECs. Section 3 highlights the linear model of a heaving point absorber. In section 4, the WEC linear control strategies are discussed. Short-term forecasting algorithms and their contribution to the control law is examined in section 5. Finally section 6 describes the overall control architecture and its main components.

2. HEAVING WAVE ENERGY CONVERTER

One of the simplest oscillating –body devices is the heaving buoy or the heaving WEC, which oscillates against a fixed point of reaction (i.e. seabed) [2].

Sometimes these devices are conceived to be point absorbers due to the fact that their physical horizontal dimension is relatively small compared to the wavelength of the incident waves [7]. As shown in Fig. 1, the device is an axisymmetric heaving system, which consists of a floating body (buoy) connected to a PMLG through a rod. The vertical motion of the floating body due to wave excitation is utilized to generate electricity through PMLG. The merit of the PMLG is that it doesn't require any mechanical interface or intermediate energy conversion stages to convert the energy enclosed in waves into electrical energy [8]. However, several engineering challenges arise with the utilization of linear generators, such as: the need for more robust mechanical structure of the generator since several points of fixation is required for the reciprocating translator to have a fixed total air-gap area [9]. Also, unlike rotary machines, the output of the linear generator can't be connected directly to the grid due to the continuously varying frequency of the captured wave. Fortunately, the output signal quality can be significantly enhanced by utilizing power electronics based converters [9].

Conventionally, the PMLG is composed of a translator that moves in one degree of freedom, on which an alternating polarity permanent magnet is mounted. According to Faraday's law, the linear motion of the translator surrounded with a fixed stator windings, will induce voltage on the armature windings. Apart from electricity generation, the PMLG is utilized to damp the oscillation of the buoy in a controlled manner; hence the energy absorption of the WEC depends on the damping capabilities of the PMLG [10]. Besides, controlled excursions are applied on the floater by the PMLG to limit the damage that could occur due to extreme height waves.

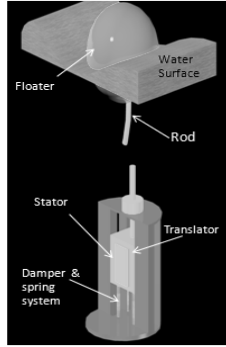


Fig. 1: Heaving point absorber structure.

3. DYNAMICS OF LINEAR WAVE ENERGY CONVERTER

In this section, the dynamic model of the WEC is discussed. This model will be derived by examining the dynamic interaction between water waves and oscillating bodies. WECs are generally highly non-linear systems, due to the non-linear nature of incident waves and the non-linearity that could be presented in the PTO and the used control circuit [5]. However, for the sake of simplicity, a linear model can be effectively used to adequately describe the motion of the WEC, if it is operating in the linear region, where only small motion (excursion) is allowed. There is an array of forces that is experienced by the oscillating body and an equal number of reaction forces as stated in Newton's third law [11]. Nevertheless, forces acting on the floating body are the one of interest when modeling the motion of WECs. Since this paper is only discussing point absorbers WECs, only one degree of freedom of motion (heave) will be considered. Like any equation of motion, the mathematical model of the heaving WEC begins with Newton's second law as

$$f_e - f_r - f_b - f_l - f_u = ma \quad (1)$$

Where m is the floater mass, a is the gravitational acceleration of the floater and f_e is the excitation force, which is the force exerted by the fluid on the WEC floater when it is held motionless due to the incident waves. The linearized excitation force in the frequency (ω) domain can be related to the incident wave elevation ($H(\omega)$) through a transfer function called the excitation coefficient ($W(\omega)$), that is

$$F_e(\omega) = W(\omega) H(\omega) \quad (2)$$

Due to the incident wave, the oscillating body and the surrounding fluid exert a force on each other called the radiation force (f_r). In the frequency domain

representation, the linearized part of the radiation force can be written as a function of the velocity ($V(\omega)$) as follows:

$$F_r(\omega) = Z_r(\omega) U(\omega) \quad (3)$$

$Z_r(\omega)$ is a frequency dependent complex function. Like the electrical impedance, $Z_r(\omega)$ is decomposed into real and imaginary parts as shown in Eq. (4).

$$Z_r(\omega) = B_r(\omega) + i\omega M_r(\omega) \quad (4)$$

Here $B_r(\omega)$ is known as the radiation damping, and $M_r(\omega)$ is the radiation added mass. In contrast to the electrical analogy, the radiation damping depends on the frequency and independent of the instantaneous velocity of the floater. The work done by the radiation damping effect dissipates part of the energy contained in the incident wave away from the WEC. Likewise, the radiation added mass is not a true physical mass, but it causes a hydrodynamic force that affects the motion of the WEC. Another force included in Eq. (1) is the spring buoyancy force (f_b), which results from the imbalance between the floater weight and the weight of the displaced fluid during oscillation. The weight of the displaced water is a function of the water density, the gravitational acceleration, and the volume of the displaced water (the volume of the submerged body). The frequency representation of the net buoyancy force (Eq. (5)) shows that it is linearly proportional to the floater displacement $X(\omega)$ (note that x has been used throughout the article to represent the vertical (heave) displacement).

$$F_b(\omega) = \rho g a_w X(\omega) \quad (5)$$

Where a_w represents the submerged water surface area, while ρ and g represent water density and the gravitational acceleration, respectively. It is important to mention here that buoyancy force is categorized to be an internal spring force that could also include other forces that oppose the motion of the body apart from the PTO spring force, which is described to be an external force. There are other types of dynamic forces that have damping (b_l) and spring (c_m) effects such as the fluid viscosity force, which is included in the net energy losses force, f_l shown in Eq. (1). All the previously discussed forces and impedances relate to the motion of the body (floater) in the absence of the PTO (control) force, which is the force applied by the PTO system on the WEC [11]. The mass-spring-damper linear representation of the PTO force can be written as follows:

$$F_c(\omega) = B_c(\omega) V(\omega) + i \left(\omega M_c(\omega) - \frac{c_c(\omega)}{\omega} \right) V(\omega) \quad (6)$$

$$Z_c(\omega) = B_c(\omega) + i X_c(\omega) \quad (7)$$

Where $M_c(\omega)$, $C_c(\omega)$, and $B_c(\omega)$ are the mass, spring, and damping control coefficients, respectively. As can be inferred from Eq. (6), the PTO impedance ($Z_c(\omega)$) has both real and imaginary parts (Eq. (7)). However, the PTO impedance at each instant could be only real or reactive or both, since it depends upon the frequency of the incident wave. Analogous to the electric circuits, if there is no reactance of the PTO impedance ($X_c(\omega) = 0$), the PTO force and the WEC velocity will be in phase and there is no instantaneous power reversal. While, in the presence of reactive impedance, the PTO force and the WEC velocity will not be in phase at any frequency and the instantaneous power will be oscillating between positive and negative [10]. Re-writing Eq. (1) in the frequency domain as a function of velocity, we obtain

$$F_e(\omega) = i\omega[m + M_r(\omega)]V(\omega) + [b_i + B_r(\omega)]V(\omega) + \left[\frac{c_b + c_m}{i\omega}\right]V(\omega) + Z_c(\omega)V(\omega) \quad (8)$$

Note that Eq. (8) depicts two types of impedances, one is the internal impedance that is associated with the floating body in the absence of the PTO mechanism, and the other impedance is associated with the PTO force (the last term in Eq. (8)). It is convenient to represent the motion of the WEC in the electrical analogy as shown in Fig. 2, which is used to realize the principle of optimizing (maximizing) the captured wave energy[11].

4. WEC LINEAR CONTROL STRATEGIES

This section discusses the control theory of the WEC. Most of the control techniques enclosed in this paper can be applied to WECs regardless of their degree of freedom of motion. Generally, there are two main control schemes to control the operation of the WEC. The first is the geometry control which acts on the WEC floating body to determine how much of the incident power is intercepted, which is beyond the scope of this paper. The second control scheme is the PTO control, which determines how much of the intercepted power is captured through linear generator in the case of point absorbers. As shown earlier, a heaving body produces waves that are radiated away from the floating body. In order to absorb the energy content in the incident waves, the heaving body should be able to generate waves that destructively interfere with them [11]. The PTO control task is to maximize the captured energy by optimizing the WEC oscillation. It is not possible to capture all of the intercepted energy. The radiated wave with half the incident wave's amplitude transports away 50% of the intercepted energy, since the wave energy is directly proportional to the square of the wave's amplitude [12]. The average power of the excitation wave and average radiated power are given by Eq. (9) and Eq. (10), respectively.

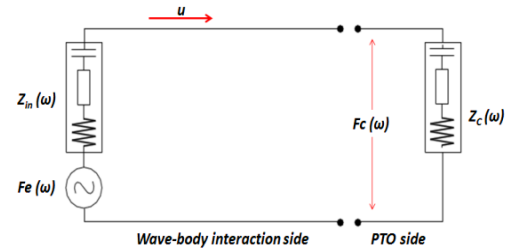


Fig. 2: The electrical analogy of the WEC.

$$P_e = \frac{1}{2} |F_e| |v| \cos(\varphi_F - \varphi_v) \quad (9)$$

$$P_r = \frac{1}{2} B_r |v|^2 \quad (10)$$

Where φ_F and φ_v are the phase angles of the excitation force and the velocity, respectively. The time average intercepted power (P_{int}) can be found by subtracting the radiated power (Eq. (10)) from the excitation wave power (Eq. (9)). P_{int} depends on the floater velocity amplitude in a parabolic manner, so the optimum velocity amplitude (u_{op}) can be found by maximizing P_{int} ($dP_{int}/du = 0$), as depicted in Eq. (11).

$$v_{op} = \frac{|F_e|}{2B_r} \cos(\varphi_F - \varphi_v) \quad (11)$$

By using Eqs. (9) - (11), the corresponding optimum (maximum) intercepted power can be found as follows:

$$P_{int-op} = \frac{|F_e|^2}{8B_r} \cos^2(\varphi_F - \varphi_v) \quad (12)$$

As described in Eq. (12), the optimum intercepted power is theoretically half of the power content in the excitation wave, while the other half is radiated away from the submerged heaving body. Eq. (11) insures picking up the optimum amplitude of the heaving velocity. However, if both the velocity and the excitation force have the same phase ($\cos(\varphi_F - \varphi_v) = 1$), an optimum phase condition can be also fulfilled [13].

4.1 Linear PTO Control

The intercepted power is captured through the PTO and control mechanism that can be considered as the electrical interface of the WEC. Linear PTO control means that the PTO (control) force has a linear relationship with the WEC floating body velocity [5]. Using the electrical analogy of the WEC shown in Fig. 2, the PTO impedance is considered as an electrical load that is supplied by a voltage source, which is in our case the excitation force exerted by the incident waves. Moreover, as mentioned in the previous section, all the

system impedances presented in the absence of the PTO force are grouped to form the internal impedance (Z_{in}). Thus the velocity amplitude (u) in the presence of the PTO mechanism can be described as follows:

$$v = \frac{F_e}{[Z_{in}(\omega) - Z_c(\omega)]} \quad (13)$$

While the captured time-averaged real power by the PTO (P_c) is

$$P_c = \frac{1}{2} B_c(\omega) |v|^2 \quad (14)$$

Where B_c is the load resistance Substituting Eq. (13) into Eq. (14) will lead to the following:

$$P_c = \frac{1}{2} \frac{B_c(\omega) F_e^2}{[Z_{in}(\omega) + Z_c(\omega)]^2} \quad (15)$$

Referring to the maximum power theory in linear electrical circuits, maximum real power can be transmitted to a load, if the load impedance is a complex conjugate of the source impedance. That is, both internal impedance and load impedances have equal real parts ($B_{in} = B_c$) and zero imaginary part. The useful captured power can be maximized by controlling the PTO impedance to be a complex conjugate of the system internal impedance, that is $Z_c = Z_{in}^*$. Hence, the maximum average captured power can be written as follows:

$$P_c = \frac{|F_e|^2}{8 B_{in}} \quad (16)$$

Where B_{in} is the damping coefficient of the system's internal impedance. Note that the maximum average captured power is less than the maximum average intercepted power (Eq. (12)), due to the higher damping imposed on the system. The previous discussion lays the foundation for examining different types of linear PTO control mechanisms based on the theory of maximum power transfer or equivalently, impedance matching.

4.1.1 Optimal Control

Referring to Eq. (16), the maximum average captured power is independent of the frequency (ω). In other words, this equation can only be used in the case of monochromatic motion of the WEC, where impedance matching is performed at single frequency at a time [5]. For example, if the excitation wave is a sinusoid with frequency (ω_1), the control impedance is adjusted to be equal to the complex conjugate of the system's internal impedance at that frequency [$Z_c(\omega_1) = Z_{in}^*(\omega_1)$], hence the maximum captured power in Eq. (16) would be re-written as:

$$P_c = \frac{|F_e(\omega_1)|^2}{8 B_{in}(\omega_1)} \quad (17)$$

In the case of monochromatic excitation, which leads to a motion at one frequency, a causal controller that doesn't require any future information is used. Moreover, the PTO impedance coefficients (mass, spring, and damping) are estimated once due to the excitation force monochromatic feature. Theoretically, using this type of control allows the absorption of 100% of the incident wave energy; hence it is called an optimal control. Real sea waves exhibit a polychromatic behavior, where the PTO control impedance coefficients vary with frequency at each instant [11]. This makes the causal optimal control un-realizable practically. In order to optimally absorb all the incident energy, the PTO controller have to predict the excitation velocity some time into the future, alongside with the instantaneous measured velocity, but this type of control strategy is also difficult to implement due to the fact that practically a pre-determined bandwidth of wave frequencies where most of the wave energy is concentrated at is required. Hence, predicting wave potential at all frequency components has no sufficient benefits, since at irregular sea state; most of the wave energy is concentrated at waves with low frequency (swells) [14].

4.1.2 Sub-Optimal Control

Using constant PTO impedance coefficients in a polychromatic sea environment will significantly deteriorate the energy capture. This type of control is called sub-optimal PTO control. Mainly, the velocity power spectrum is used to determine the operational frequency component, which represents the frequency at which the peak wave energy can be extracted. Since the PTO coefficients are constant, the equation of motion of this controller includes only causal terms (no premonition terms). More energy can be absorbed, if the controller is designed to have the capability to predict the excitation force (premonition term) for a band of frequencies around the operation frequency ($\omega_1 < \omega < \omega_2$). Outside the specified band, the PTO controller would operate in the causal sub-optimal control scheme [14].

5. WAVE FORECASTING TECHNIQUES

One of the first attempts to introduce forecasting into the WEC control law was proposed by Falnes [15], where the hydrostatic pressure acting on a heaving point absorber was predicted sometime in the future using the Kalman filter. The predicted pressure was utilized to determine the excitation force and hence an optimum phase control was achieved using latching mechanism.

Another wave forecasting method was introduced by Belmont [16], which is called Deterministic Sea Wave Prediction (DSWP). In this technique, the wave elevation is first measured at a point distant from the WEC, and then this measured data is used to build a model that estimates the sea shape when the wave has propagated downstream to the prediction site. This technique is suitable to predict moderate to long wavelength swell waves, because they have less high frequency components compared to wind waves. Thus the size of the floating body and the distance between the measurement and the prediction sites play an important role to reduce wave nonlinearities, hence less computation time and power is required to build the prediction model within the prediction time horizon (few to tens of seconds) [16]. DSWP model is realized by a combination of N one dimensional fixed point linear filters, each representing long crested seas with orientation angles θ_i ($i = 1, 2, 3, \dots, N$). Good prediction accuracy is obtained by this method when multi-directionality is omitted, however the complexity and computation time will significantly increase if multi-directional swells are considered, as a consequence, on-line control becomes difficult to implement.

Another model is the cyclic model, which is derived from the linear wave theory, as it says that irregular sea state can be modeled as a linear superposition of waves with different frequencies and directions. A discretized cyclical model to forecast the wave elevation can be written as:

$$\eta(k) = \sum_{i=0}^n A_i \cos(\omega_i k) + B_i \sin(\omega_i k) + \psi(k) \quad (18)$$

Parameters A_i and B_i comprise the amplitude and phase information of each wave frequency component (ω_i) and $\psi(k)$ is the model error. The model is nonlinear due to the spectral variations in the sea state (amplitude and phase). To linearize the model in the parameters A_i and B_i , a preliminary frequency selection procedure is adopted, so that the frequency is kept constant during the on-line estimation procedure [17]. Harvey's model [18] is utilized to adaptively model the amplitude variations.

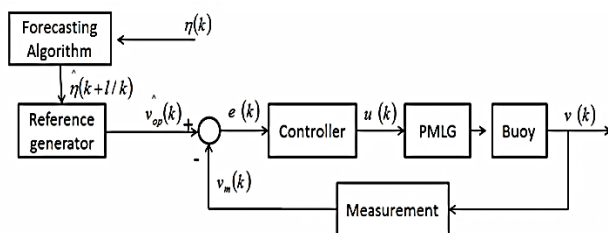


Fig. 3: General point absorber control architecture.

There are other classes of short-term prediction techniques which are based on the time series theory, a good example is Auto-Regression (AR) model. In this model, the wave elevation $\eta(k)$ is considered to be a weighted sum of n previously observed values of $\eta(k)$.

$$\eta(k) = \sum_{i=1}^n a_i \eta(k-1) + \psi(k) \quad (19)$$

The AR model parameters a_i can be estimated off-line for each batch of previously observed wave elevation values using a classical least squares method. One more degree of freedom can be added to the estimation process by estimating the model parameters online using Kalman filter or a recursive least squares with forgotten factor algorithm [17].

6. WEC CONTROL SYSTEM ARCHITECTURE

In this section, a simplified heaving WEC control regime is discussed. As mentioned in the previous section, the most suitable control strategy that can be adopted to effectively optimize the energy capture of point absorbers is an acausal sub-optimal control strategy. As depicted in Fig. 3, the PMLG is utilized as the control system actuator. By controlling the PMLG's armature current, the damping enforced by the PTO mechanism is controlled [19]. Power electronics converters are used to interface the WEC to the grid and do two main functions: 1) control the power flow from the WEC to the grid 2) control the damping action of the PMLG according to the principle of impedance matching (resonance) that has been discussed earlier [19]. Voltage sourced converters (VSC) are usually employed in this application. Current sourced converters (CSC) are a valid alternative as well, however, for the sake of achieving higher power factor and better conversion efficiency; VSCs are favorites over CSC's [20].

The voltage sourced back-to-back converter consists of a rectification side connected to the PMLG and an inversion side connected to the grid. Both converter sides are coupled via a capacitor bank (DC link). The coupling DC link is the back bone of the VSC based converters, where the difference between the instantaneous energy between the generator side and the grid side is stored in the DC link; hence, an inner control loop is dedicated to maintain the instantaneous energy balance and regular the DC voltage at the DC link. Many control laws have been proposed in literature to control both converter sides and the DC link [21]. The decoupled d-q vector control is usually adopted to generate the PWM gating signals for the converters switches as shown in Fig. 4. At every sampling instant, the optimum velocity (reference) signal is computed using the concept of impedance matching described in section 4.

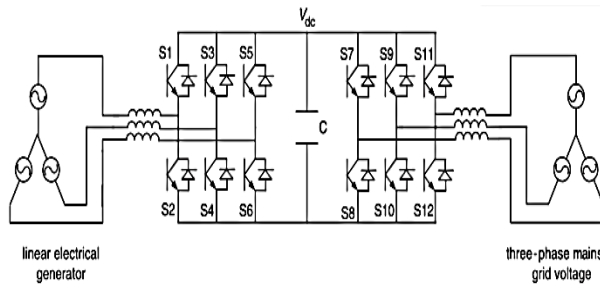


Fig. 4: Three phase diagram of the WEC system including the back-to-back converter.

7. CONCLUSION

Several PTO control techniques have been proposed in literature; however few of them offered acceptable performance. Some of these techniques showed good performance during simulation and then suffered from severe deterioration during experimentation. Switching control techniques are mainly used to overcome the variations in the wave environment throughout the year, however, switching from control law to another may in some cases jeopardize the controller stability. This paper serves as a background to carryout future research work to test several control laws and compare between their performances. This will include feedback control, impedance matching control, and artificial intelligence techniques.

REFERENCES

- [1] Valerio, D, Beirao, P, Mendes, M, Da Costa, J. "Comparison of control strategies performance for a wave energy converter". Proceedings of the Congress Centre, Ajaccio, France. pp. 773-778. June 25-27, 2008.
- [2] Falcao, O. "Wave energy utilization: a review of the technologies", *Journal of Renewable and Sustainable Energy Reviews* 14, pp.899-918, 2010.
- [3] Thorpe T. An overview of wave energy technologies—status, performance and costs. In: *Wave power: moving towards commercial viability*. London: Professional Engineering Publishing; 2000, p. 13–30.
- [4] Clément A, McCullen P, Falcao A, Fiorentino A, Gardner F, Hammarlund K, et al. Wave energy in Europe: current status and perspectives. *Renew Sustain Energy Rev* 2002;6:405–31.
- [5] Price. A (2009), "New Perspectives on Wave Energy Converter Control", Published PhD thesis, University of Edinburgh.
- [6] Valerio, D, Beirao, P, Mendes, M, Da Costa, J. "Identification and control of the AWS using neural network models". *Journal of Applied Ocean Research*. 30, pp: 178-188, 2008.

- [7] Valerio, D, Mendes, M, Beirao, Jose, "Identification and Control of the AWS using Neural Network Models". *Applied ocean research* 30 (2008) 178-188.
- [8] Rhinefrank K, Agamloh EB, von Jouanne A, Wallace AK, Prudell J, Kimble K, et al. Novel ocean energy permanent magnet linear generator buoy. *Renewable Energy* 2006;31:1279–98.
- [9] Danielsson O (2006) *Wave Energy Conversion-Linear Synchronous Permanent Magnet Generator*. Ph.D. thesis, Acta Universitatis Upsaliensis Uppsala.
- [10] Cruz, J (editor), "Ocean Wave Energy, Current status and future perspectives", Springer series un green energy and technology, Berlin, 2010.
- [11] J. Falnes, "Ocean Waves and Oscillating Systems", Cambridge University Press, UK, 2002. (ISBN 0-521-78211-2).
- [12] Falnes, J, "Principles for capture of energy of ocean from ocean waves. Phase control and optimum oscillation". *Norwegian Maritime Research*, Vol.6, No.4, pp.11-19.
- [13] Budal K, Falnes J. Interacting point absorber with controlled motion, in the *Power from Sea Waves*, BM Count: Academic Press; 1980.
- [14] Anne, A., & Price, E. (2009). *New Perspectives on Wave Energy Converter Control*. Engineering, Ph.D, thesis. University of Edinburgh.
- [15] K. Budal, J. Falnes, et al., "The norwegian wave-power buoy project," *The Second International Symposium on Wave Energy Utilization*, Trondheim, June 1982.
- [16] M. R. Belmont et al., "Filters for linear sea-wave prediction," *Ocean Engineering*, vol. 33, pp. 2332–2351, 2006.
- [17] Fusco, F and Ringwood, J (2010). Short-Term Wave Forecasting for Real-Time Control of Wave Energy Converters. *IEEE Transactions on Sustainable Energy*, vol. 1, 99-106.
- [18] G. S. Maddala, C. R. Rao and H. D. Vinod, eds., *Handbook of Statistics*, Elsevier Science Publishers B.Y, Vo/. 11. 1993.
- [19] Sterling, M. J. H. (2009). *Optimal Control for AWS-Based Wave Energy Conversion System*. *IEEE Transactions on Power Systems*, 24(4), 1747-1755.
- [20] Polinder, H.; Damen, M.E.C.; Gardner, F.; "Linear PM Generator system for wave energy conversion in the AWS," *Energy Conversion*, *IEEE Transactions on*, vol.19, no.3, pp. 583- 589, Sept. 2004.
- [21] Ottersten, R. (2003). *On Control of Back-to-Back Converters and Sensorless Induction Machine Drives*, Ph.D thesis, Chalmers University Of Technology.

Adsorption Of Cobalt Ions Onto Immobilized And Non-Immobilized Jordanian Low Grade Phosphate

Munther Kandah¹, Fahmi Abu Al-Rub² and Dalia Al-Shareef³

^{1,2,3} Jordan University of Science and Technology

Chemical Engineering Department

mkandah@just.edu.jo

ABSTRACT

The technical feasibility of using Non-immobilized Jordanian Low-Grade Phosphate (NIJLGP) and Immobilized Jordanian Low Grade Phosphate (IJLPG) as adsorbents for cobalt ions from water was investigated in this project. The effects of pH, agitation time, adsorbent mass, cobalt ions concentration, and adsorbent particle size on the adsorption efficiency were studied. Results showed that the optimum adsorption capacity for cobalt ions onto NIJLGP was found at 0.07 g NIJLGP, 0.063 mm NIJLGP, 5.7 for the water pH. The adsorption uptake was found to increase with the increase in the initial cobalt ions concentration and the equilibrium time was achieved after 30 minutes. The adsorption of cobalt ions onto NIJLGP was found to fit with Langmuir, Freundlich, and Tempkin adsorption isotherm models very well. A comparison between the adsorption capacity of the non-immobilized JLGP and the immobilized JLGP was also investigated in this project. The IJLGP showed higher adsorption efficiency than NIJLGP for cobalt ions due to the increase in the surface area of the immobilized JLGP compared with the NIJLGP.

Keywords; Immobilization, JLGP, Adsorption, Cobalt

1. INTRODUCTION

The presence of heavy metals in environment is a major concern because of their extreme toxicity and tendency for bioaccumulation in the food chain even in relatively low concentrations. Heavy metals pollute the environment from various industries such as metal plating, electroplating, mining and metallurgical process, ceramic, batteries, pigment manufacturing, plastic manufacturing, and textile [1].

Due to their health and toxicological effects, environmental agencies and authorities have set strict regulations to maintain the limit of heavy metals in wastewater below the maximum acceptable concentration levels. These strict regulations accelerated the research for new technologies which are environment-friendly and can reduce heavy metals concentrations in the discharged wastewaters to be below the maximum allowable limits. The conventional methods used to remove heavy metals from wastewaters include chemical solvent extraction [2], chemical precipitation [3], membrane filtration [4], ion exchange [5], and adsorption [6]. For dilute metal concentration, ion exchange, reverse osmosis and adsorption can be applied. However ion exchange and reverse osmosis have high operating cost, which makes adsorption a better alternative for heavy metals removal [7].

Activated carbon is the most widely and effectively used adsorbent but it suffers from a number of disadvantages such as its high manufacturing and

regenerating cost. Thus, the research has been active to find alternative and yet efficient adsorbents. These adsorbents should have the following properties: the ability to reduce the concentration of pollutants below the acceptable limits, high adsorption capacity and long lifetime. Jordanian Low-Grade Phosphate has proved to be good adsorbent for many different pollutants [8].

Cobalt is an element that occurs naturally in the environment in air, water, soil, rocks, plants and animals. It may also enter air and water and settle on land through wind-blown dust and enter surface water through run-off when rainwater runs through soil and rock containing cobalt. Demirbas [9] used activated carbon prepared from hazelnut shells to remove Co (II) from aqueous solution by adsorption. Batch-mode adsorption experiments were carried out to study varying parameters such as the initial metal ions concentration (13.3-45.55 mg/L), agitation speed (50-200 rpm), pH (2-8), temperature (293-323 K) and particle size (0.80-1.60 mm). The adsorption capacity calculated from Langmuir isotherm was 13.88 mg Co (II)/g carbon at 303 K employing a pH value of 6 and a particle size of 1.00-1.20 mm.

Hashem et. al., [10] used groundnut hulls which were chemically modified via esterification with citric acid under conditions which yield groundnut hulls rich in carboxyl content. The adsorption capacity of cobalt on groundnut hulls citrate increases with increasing the extent of esterification. The maximum values of

adsorption capacity were 28.7 and 270.3 mg/g on native and groundnut hulls citrate, respectively.

The objective of this work is to investigate the technical feasibility of using Immobilized and Non-immobilized Jordanian low grade phosphate for the removal of cobalt ions from aqueous solutions. The effects of different parameters, such as equilibrium pH, shaking time, amount of adsorbent and metal concentration on the adsorption capacity will be investigated. Adsorption equilibrium isotherms will be analyzed using different models.

2. Adsorption Models

The adsorption isotherm represents the relationship between the amount adsorbed by a unit weight of solid sorbent and the amount of solute remaining in the solution at equilibrium. Different isotherm models can be used to describe the sorption of a solute on solid sorbent.

2.1. Henry's Law

The simplest adsorption isotherm, in which the amount adsorbed varies directly with equilibrium concentration of the adsorbent, is often referred to as Henry's law, which is simply given by the equation:

$$q_e = K C_e^n \quad (1)$$

Where K (L/g) is the Henry's isotherm constant, C_e (mg/L) is the equilibrium concentration, and q_e (mg/g) is the equilibrium adsorbed amount on the adsorbent, also called uptake, which is calculated using the equation

$$q_e = \frac{(C_i - C_e)V}{w} \quad (2)$$

Where V (L) is the volume of the sorbate-bearing solution contacted (batch) with the sorbent; C_i and C_e (mg/L) are the initial and equilibrium concentrations of the sorbate in the solution, respectively, and w (g) is the mass of sorbent.

2.2. Langmuir Model

Langmuir isotherm model is based on the assumption that binding sites are homogeneously distributed over the adsorbent surface. These binding sites have the same affinity for adsorption of a single molecular layer. This model assumes that there is no interaction between adsorbed molecules. The mathematical representation of this model is:

$$q_e = \frac{q_m b C_e}{1 + b C_e} \quad (3)$$

Where q_m (mg/g) and b (L/mg), are the saturated monolayer sorption capacity, and the sorption equilibrium constant, respectively. The constant b is related to the affinity between the sorbent and sorbate

and it is related to the energy of adsorption through Arrhenius equation. Equation 3 can be rewritten in the linearized form given by eq. 4.

$$\frac{C_e}{q_e} = \frac{1}{q_m b} + \frac{C_e}{q_m} \quad (4)$$

2.3. Freundlich Model

The Freundlich model considers monomolecular layer coverage of solute by the sorbent. Moreover, it assumes that the sorbent has heterogeneous valance distribution and then has different affinity for adsorption. This model takes the following form:

$$q_e = K C_e^{1/n} \quad (5)$$

Where K and 1/n are the Freundlich constants related to the sorption capacity and sorption intensity of the sorbent, respectively.

2.4. Tempkin Isotherm Model

Tempkin considered the effects of some indirect adsorbent/adsorbate interactions on adsorption isotherms and suggested that because the heat of adsorption of all the molecules in the layer would decrease linearly with coverage. The Tempkin isotherm has been used in the following form:

$$q_e = \frac{RT}{b} (\ln A C_e) \quad (6)$$

Equation 6 can be expressed in its linear form as:

$$q_e = B \ln A + B \ln C_e \quad (7)$$

$$\text{Where } B = \frac{RT}{b}$$

A plot of q_e versus $\ln C_e$ enables the determination of the isotherm constants A and B, where the constant B is related to the heat of adsorption.

3. EXPERIMENTAL SETUP AND PROCEDURE

The rejected Jordanian low-grade phosphate samples used in this study were collected from the rejected waste area in the Jordan Phosphate Mines at Rusaifa. The phosphate samples were washed by distilled water to get rid of any non-adhesive impurities, dried at 105 °C to remove moisture, ground and sieved to different particle sizes (i.e., from 0.063 μm to 1mm) before use. This phosphate as a sedimentary phosphate contains calcite, organic matter, quartz and clays (illite, montmorillonite). Table 1 shows the chemical and physical analysis of such phosphate. The analysis has been carried out by Jordan Phosphate Mines Co. LTD/Fertilizer Complex laboratories.

Cobalt ion solutions with different concentrations (from 20 to 200 mg/L) were obtained by diluting the prepared 1000 mg/L stock cobalt solution from $C_4H_6CoO_4 \cdot 4H_2O$. The pH of the solution was adjusted by using diluted hydrochloric acid or diluted sodium hydroxide.

Table 1: Chemical and physical analysis of low-grade phosphate.

Chemical Analysis		Physical Analysis	
Analysis	Result %	Analysis	Result
P ₂ O ₅	26.35	Moisture	1.32%
CaO	48.13	Bulk density	1.067 g/ml
SiO ₂	10.04		
Cl	360 mg/L		
CO ₂	8.64		
Organic carbon	0.17		

* Note: Results are on dry basis.

Immobilized Jordanian Low-Grade Phosphate (IJLGP) was prepared by entrapping powder of JLGP with 0.063 mm diameter in an alginate matrix produced by ionic polymerization in calcium chloride solution, according to the following procedures [7], the powder of JLGP was suspended in a 2% sodium alginate solution kept at a temperature of 60°C. The mixture was then dropped into a 2% chloride solution using a peristaltic pump. The drops of Na-alginate solution gelled into 3.5±0.1 mm diameter beads upon contact with calcium chloride solution (Figure.1). The beads were washed well and then rinsed in deionized water and stored at 4°C.

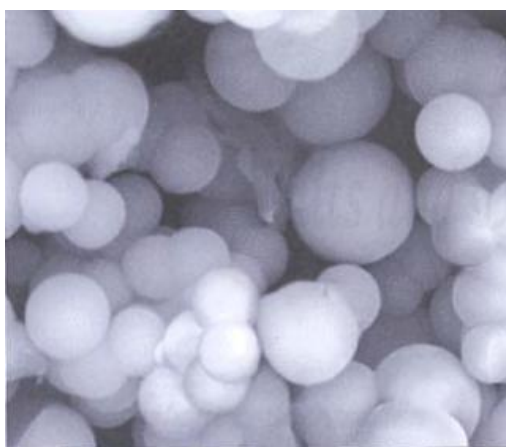


Figure 1: Immobilized Jordanian Low Grade Phosphate (IJLGP)

In all the experiments, 50 ml of Co²⁺ at constant pH was added into 100 ml bottle containing certain weight of low-grade phosphate. The bottles were introduced into a reciprocating shaker at 25 °C for predetermined time intervals. At the end of the experimental time, the low-grade phosphate was separated by centrifugation and the supernatant was analyzed for residual Co²⁺ concentration using atomic absorption spectrophotometer. The reported experimental values are the average of two or three measurements.

4. RESULTS AND DISCUSSION

4.1. Effect of pH

The effect of equilibrium pH on the percentage removal of Co²⁺ from 100 mg/L adsorbate solution was investigated at constant temperature (25 °C) using 0.07 g of 0.063 mm diameter NIJLGP.

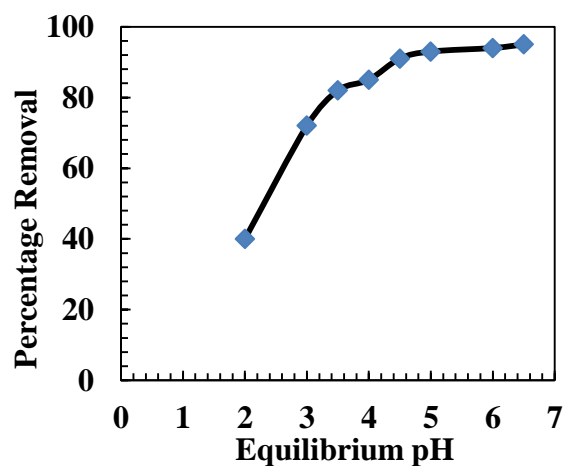


Figure 2: Effect of *pH* on the equilibrium uptake of cobalt ions using NIJLGP at temperature = 25 °C; NIJLGP mass = 0.07 g; NIJLGP particle size = 0.063 mm, shaking time = 6 h; initial cobalt concentration = 100 mg/L.

Experiments were carried out to examine the effect of pH on the adsorption of cobalt ions at 25 °C and an initial cobalt ions concentration of 100 mg/L. The results indicated that the percentage removal of cobalt ions was significantly affected by solution pH and that the percentage removal of NIJLGP increased with increasing pH as shown in Figure 2. At pH values of less than 3, there seemed to be negligible removal of cobalt. It is believed that hydrogen ions compete with cobalt ions for the same adsorption sites at low pH as proposed by many researches. The rise in cobalt removal with increasing pH can be explained by a strong relation between adsorption and the number of negatively charged sites, which is highly dependent on the dissociation of functional groups. Most of these functional groups are expected to be dissociated at high pH. Based on the experimental results presented in Figure 2, an optimum pH of 5.7 was selected for the rest of the experimental work. Although no cobalt

precipitation was observed at a pH of 6.5, a lower pH value was selected to rule out the possibility of cobalt precipitation.

4.2. Effect of Adsorbent Mass

The effect of adsorbent mass on the percentage removal and equilibrium uptake of Co^{2+} from 100 mg/L adsorbate solution was investigated at equilibrium pH of 4. Figure 3 shows that the amount of cobalt adsorbed increases with the increase in the adsorbent mass from 0.05 to 0.6 g. The percentage removal of cobalt was increased from 31.83% to 97.41% for an increase in NIJLGP mass from 0.05 to 0.6 g at initial cobalt ions concentration of 100 mg/L while the equilibrium uptake decreased from 56.39 mg/g to 7.91 mg/g. The increase in the adsorption of the amount of solute is obvious due to the increase in the adsorbent surface area. The percentage removal curve intersects with the equilibrium uptake curve at one point which represents the optimum weight equal to 0.07 g.

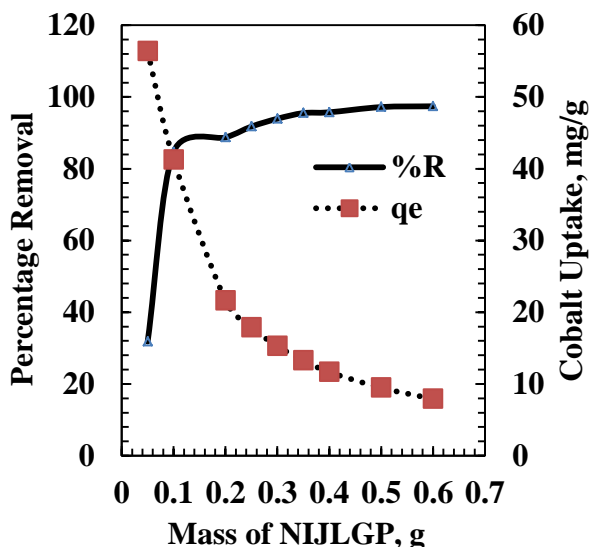


Figure 3: Effect of NIJLGP mass on the percentage removal and equilibrium uptake of cobalt ions at initial Co^{2+} concentration=100 mg/L; temperature=25°C; pH=4; NIJLGP particle size=0.063 mm; shaking time=6h.

4.3 Effect of Particle Size

The effect of different NIJLGP particle sizes on cobalt ions uptake and percentage removal were investigated as shown in Figure 4. It reveals that the metal uptake and percentage removal of cobalt on NIJLGP decreased from 41.98 mg/g to 20.13 mg/g and from 86.15% to 41.32% with the increase in the particle size from 0.063 to 2 mm for initial concentration of 100 mg/L. The smallest size obtained was 0.063 mm due to the limitation of available grinder configuration. It is well known that decreasing the average particle size of the adsorbent increases the surface area, thereby providing

more adsorption sites which in turn increase the adsorption capacity.

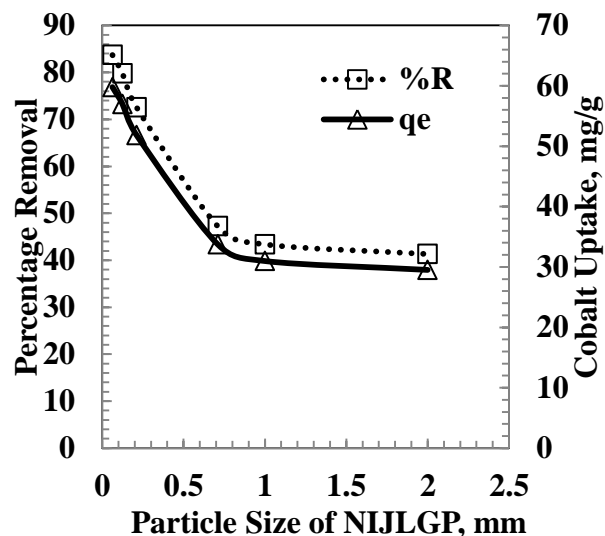


Figure 4: Effect of NIJLGP particle size on the percentage removal and equilibrium uptake of cobalt ions at initial Co^{2+} concentration = 100 mg/L; temperature= 25°C; pH=4; NIJLGP mass= 0.07 g; shaking time = 6h.

4.4 Effect of Adsorbate Concentration

The effect of adsorbate concentration on the percentage removal and equilibrium uptake of Co^{2+} from varying concentrations (20-200 mg/L) adsorbate solution was investigated at equilibrium pH of 4.

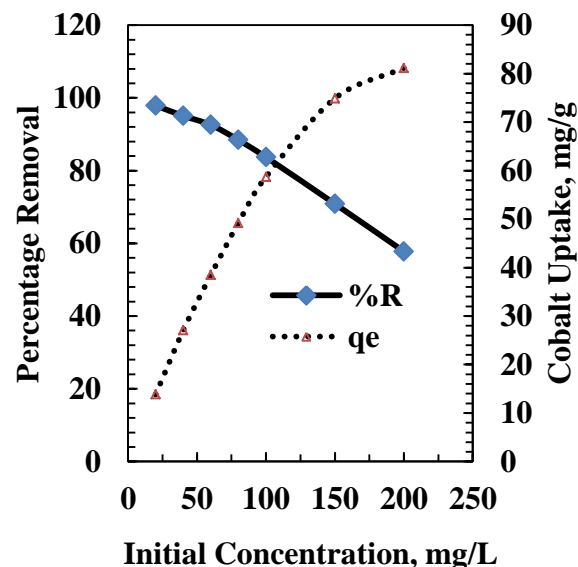


Figure 5: Effect of initial concentration of cobalt on the percentage removal and equilibrium uptake of cobalt ions at temperature =25°C; pH=4; NIJLGP mass =0.07 g; NIJLGP particle size =0.063 mm; shaking time = 6h.

Figure 5 shows the effect of the adsorption of cobalt ions concentration onto NIJLGP. It is clear that the cobalt uptake increases and the percentage removal of Co^{2+} decreases with the increase in cobalt ions concentration. The increase from 13.84 to 81.15 mg/g is a result of the increase in the driving forces, i.e. concentration gradient. However, the percentage removal of Co^{2+} onto NIJLGP was decreased from 97.87% to 57.77%. Though an increase in the cobalt uptake was observed, the decrease in the percentage removal may be attributed to the lack of sufficient surface area to accommodate much more cobalt ions available in the solution. The percentage removal at higher concentration levels shows a decreasing trend whereas the equilibrium uptake of cobalt displays an opposite trend. At lower concentrations, all cobalt ions present in the solution could interact with the binding sites and thus the percentage adsorption was higher than those at higher cobalt ions concentration.

At higher concentrations, the lower adsorption yield is due to the saturation of adsorption sites. As a result, the purification yield can be increased by diluting the waste waters containing high cobalt ions concentration. From the figure the optimum value of initial ions concentration was 143.7 mg/L.

4.5 Effect of Contact Time

The data obtained from the adsorption of Co^{2+} onto the NIJLGP shows that a contact time of 30 min was sufficient to achieve equilibrium and the adsorption did not change significantly with further increase in contact time. It is clear from figure 6 that there is no effect for the increase in the initial concentration of cobalt ions on the equilibrium time.

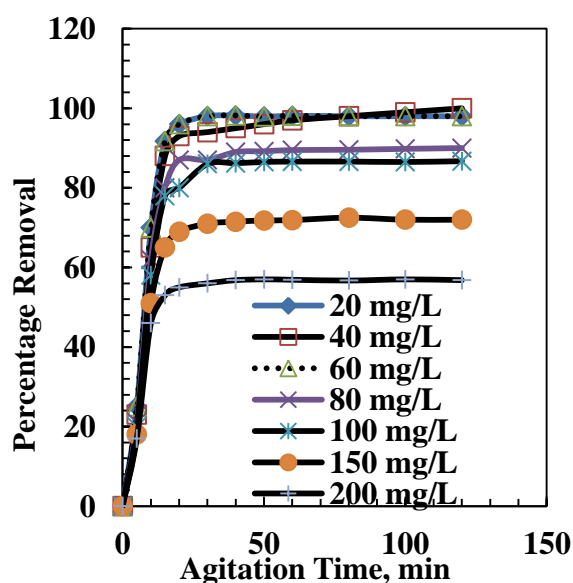


Figure 6: Effect of contact time on the percentage removal of cobalt ions at temperature =25 °C; pH = 4 ; NIJLGP mass = 0.07 g ; NIJLGP particle size = 0.063 mm.

4.6. Effect of Percentage Removal of Co^{2+} Onto IJLGP

In the present work, Ca-alginate in the bead form was used as an adsorbent and a support material for entrapment of JLGP and used for the removal of Co^{2+} ions from aqueous solution. Alginate beads were prepared by cross-linking with divalent calcium ions, and alginate droplets were precipitated in the bead form (diameter about 3.5 ± 0.1 mm) in calcium chloride solution. The effect of using these beads in adsorption process when the initial cobalt ions equal 100 mg/L was studied. The results from figure 7 showed that the percentage removal of Co^{2+} ions onto IJLGP is greater than those onto NIJLGP and the equilibrium time is the same. This might be due to the increase in the surface area of the IJLGP compared to that for NIJLGP.

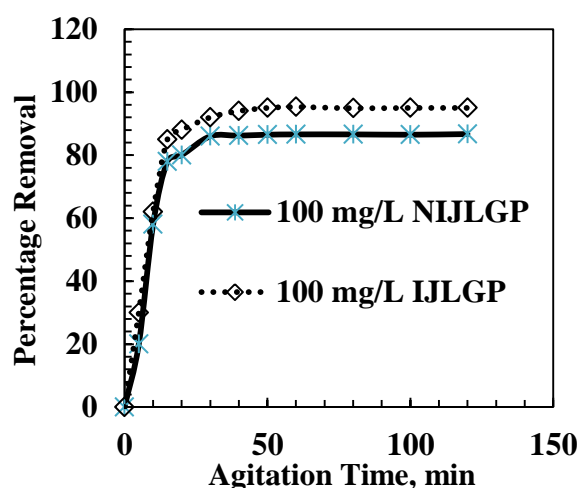


Figure 7: Effect of contact time on the percentage removal of cobalt ions from aqueous solution by IJLGP and NIJLGP at temperature=25°C; mass=0.07 g; particle size=0.063 mm; initial cobalt concentration=100 mg/L; pH=4.

4.7. Adsorption Isotherms

The equilibrium adsorption isotherms are considered very important data to understand the mechanism of adsorption. Langmuir, Freundlich, and Tempkin isotherm models were applied to the experimental data obtained from batch system in this study. The adsorption isotherm for Co^{2+} onto NIJLGP is shown in figures (8, 9, and 10).

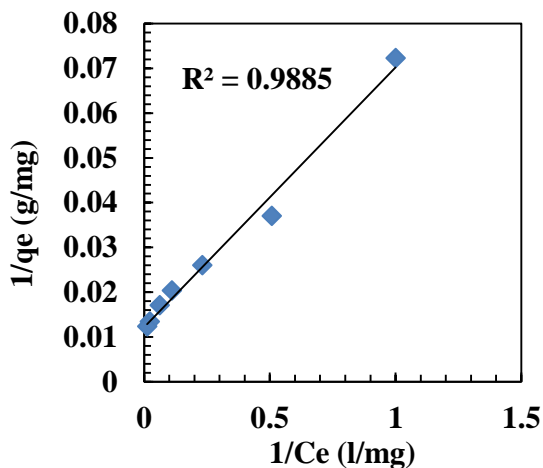


Figure 8: Langmuir adsorption isotherm at temperature = 25 °C; pH=4; NIJLGP mass = 0.07 g ; NIJLGP particle size = 0.063 mm.

The Langmuir isotherm model assumes a monolayer sorption which takes place at specific homogeneous sites within the adsorbent. As may be noted the value of q_m on NIJLGP is somewhat larger than that on many other adsorbents, thereby demonstrating the technical feasibility of using NIJLGP for the removal of cobalt ions from aqueous solutions.

The Freundlich is an empirical equation employed to describe heterogeneous system where K (L/g) and n are Freundlich isotherm constants, being indicative of the extent of the adsorption and the degree of nonlinearity between solution concentration and adsorption, respectively.

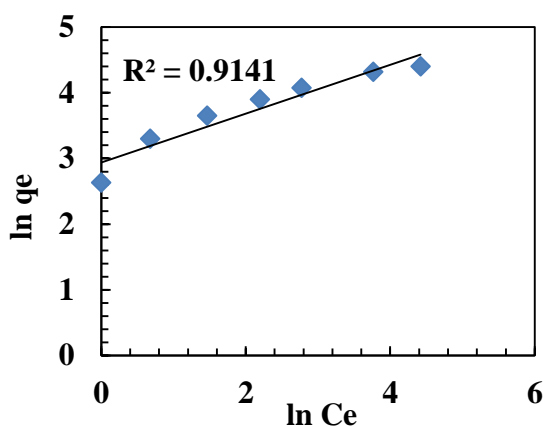


Figure 9: Freundlich adsorption isotherm at temperature = 25 °C; pH=4; NIJLGP mass = 0.07 g ; NIJLGP particle size = 0.063 mm.

Tempkin considered the effects of some indirect adsorbent/ adsorbate interactions on adsorption isotherms where the heat of adsorption of all the molecules in the layer would decrease linearly with coverage due to these interactions.

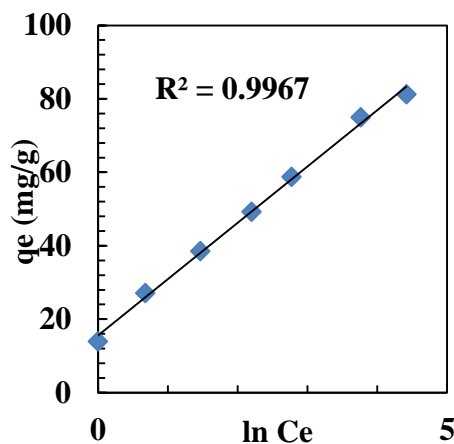


Figure 10: Tempkin adsorption isotherm at temperature = 25 °C; pH=4; NIJLGP mass = 0.07 g ; NIJLGP particle size = 0.063 mm.

The Langmuir, Freundlich, and Tempkin parameters for the adsorption of Co^{2+} onto NIJLGP are listed in table 2. Results are indicated that the adsorption of cobalt onto NIJLGP was correlated well with the Langmuir, Freundlich and Tempkin equations.

Table 2: Isotherm parameters for the adsorption of Co^{2+} onto NIJLGP

Model	Parameter	Value
Langmuir	q_m (mg/g)	62.5
	B (L/mg)	0.53
	R^2	0.99
	R_L	0.01
Freundlich	K (mg/mg)(L/mg) ^{1/n}	27.11
	N	4.54
	R^2	0.97
Tempkin	A (mL/mol)	11.02
	b (J.g/mol ²)	247.89
	R^2	0.98

The essential feature of the Langmuir isotherm can be expressed by means of a separation factor or equilibrium parameter, R_L which is calculated using the following equation:

$$R_L = 1 / (1 + bC_o) \tag{7}$$

where C_o is the highest initial Co^{2+} concentration (mg/L). As the R_L values lie between 0 and 1, the adsorption process is favorable. The R_L value for this study was 0.01, therefore, adsorption of Co^{2+} was favorable.

The Freundlich constants K and n indicate the adsorption capacity of the adsorbent and a measure of the deviation from linearity of the adsorption, respectively. The values of K and n at equilibrium were 27.11 g/L and 4.54, respectively. The value of n is

greater than unity, indicating that Co^{2+} exhibited increased adsorption on NIJLGP at higher concentrations. The well description of the experimental results with both Langmuir and Freundlich isotherm models implies that the surface of NIJLGP is made up of homogeneous and heterogeneous adsorption patches.

5. CONCLUSIONS

In this study; it has been shown that IJLGP has higher adsorption capacity towards the removal of cobalt ions from aqueous solution than NIJLGP. Results also showed that the highest adsorption of cobalt ions onto NIJLGP was achieved at a mass of 0.07 g, particle size of 0.063 mm, and equilibrium pH of 5.7. The adsorption of cobalt ions was found to fit the Langmuir, Freundlich, and Tempkin adsorption isotherm models. The time required to reach equilibrium was not significantly changing with the initial cobalt ion concentration and achieved after 30 minutes.

REFERENCES

1. Dean, J.G., Bosqui, F.L., and Lannouette, K.L. "Removing of heavy metals from wastewaters", *Environ. Sci. Technol.*, Vol. 6, pp. 518-524, 1977.
2. Nan, J., Han, D., and Zuo, X., "Recovery of metal values from spent lithium-ion batteries with chemical deposition and solvent extraction", *Journal of Power Sources*, Vol. 152, pp. 278-284, 2005.
3. Veeken, H.M., Akoto, L., Hulshof, W., and Weijma, J., "Control of the sulfide(S^{2-}) concentration for optimal zinc removal by sulfide precipitation in a continuously stirred tank reactor", *Water Research*, Vol. 37 pp. 3709-3717, 2003.
4. Bessbousse, H., Rhlalou, T., Verchère, J.-F., and Lebrun, L., "Removal of heavy metal ions from aqueous solutions by filtration with a novel complexing membrane containing poly(ethyleneimine) in a poly(vinyl alcohol) matrix", *Journal of Membrane Science*, Vol. 307, No. 2, pp. 249-259, 2008.
5. Lee, I-H., Kuan, Y-C., and Chern, J-M., "Equilibrium and kinetics of heavy metal ion exchange", *Journal of the Chinese Institute of Chemical Engineers*, Vol. 38, No. 1, pp. 71-84, 2007.
6. Gurgel, L., and Gil, L., "Adsorption of Cu(II), Cd(II) and Pb(II) from aqueous single metal solutions by succinylated twice-mercerized sugarcane bagasse functionalized with triethylenetetramine", *Water Research*, Vol. 43, No. 18, pp. 4479-4488, 2009.
7. Abu Al-Rub, F., El-Naas, M., Benyahia F., and Ashour, I., "Biosorption of nickel on black alginate beads, free and immobilized algal cells", *Process Biochemistry*, Vol. 39, pp. 1767-1773, 2004.
8. Kandah, M.I. "Zinc and cadmium adsorption on low-grade phosphate," *Sep. Purif. Technol.*, Vol. 35, pp. 61-70, 2004.
9. Demirbas E., "Adsorption of cobalt (II) ions from aqueous solution onto activated carbon prepared from hazelnut shells", *Adsorption Science and Technology*, Vol. 21, No. 10, pp. 951-963, 2003.
10. Hashem, A., Hebeish, A., Abdel-Halim, E., and El-Tahlawy, K.F., "Enhancement of Co(II) and Ni(II) adsorption from aqueous solutions on peanut hulls through esterification using citric acid", *National Research Centre, Dokki, Cairo, Egypt, Egyptian Journal of Chemistry*, pp. 29-45, 2004.

Sorption Capacity of Poly-tetra-fluoro-ethylene Sorbent for the Remediation of Oil Polluted Water

Essam Al Zubaidy* and Taleb Ibrahim

Chemical Engineering Department, American University of Sharjah, UAE
(izubaidy@aus.edu), (italeb@aus.edu)

ABSTRACT

Oil absorption capacity of Teflon (Poly-tetra-fluoro-ethylene) (PTFE) dust was used as synthetic sorbent to recover spilled crude oil from fresh and artificial seawater. The standard method of ASTM F 726-99 was used to evaluate oil adsorbing capacity of this sorbent using short, medium, and long term static sorption tests for 15 minutes, 1 hr, and 24 hours. The water uptake and the oil retention of this sorbent were measured. It was found that the PTFE oil sorption capacity was 3.167 g of oil adsorbed/g of sorbent using artificial seawater. The oil retention showed that within 30 seconds 50.53% of the oil was drained from the sorbent. This material can be reused for more than 20 times with slightly reduction of its oil sorption capacity

Keywords: *sorption; synthetic sorbent; oil spill to water; oil recovery*

***Corresponding author**

1. INTRODUCTION

Oil spills in marine environment is one of the most important issue in this area of the world because most of the world exporting crude oil is passing through this area and especially with the growth of the off-shore petroleum industry and the necessity of marine oil transportation and it will not only cause property loss, but it could also have a strong negative impact on the entire ecosystem. Wei et al., 2003 showed that polypropylene is an ideal sorbent for oil spill due to its low density, low water uptake, and excellent physical and chemical resistance, and the fiber diameter, sorbent porosity, and oil property are the most important factors in the oil-sorption performance of polypropylene nonwoven sorbents. Bayat et al., 2005 compared three sorbents in order to determine their potential for oil spill cleanup. Polypropylene nonwoven web, rice hull, and bagasse with two different particle sizes were used. Polypropylene can sorb almost 7 to 9 times its weight from different oils. Bagasse, 18 to 45 mesh size, follows polypropylene as the second sorbent in oil

spill cleanup. Bagasse, 14 to 18 mesh size, and rice hull have comparable oil sorption capacities, which are lower than those of the two former sorbents. The oil viscosity plays an important role in oil sorption by sorbents. Deniz et al., 2009, used butyl rubber, the sorption capacity for crude oil and petroleum products was $15\text{-}23\text{gg}^{-1}$ comparing with $10\text{-}16\text{gg}^{-1}$ for a nonwoven polypropylene. BR sorbent is reusable after simple squeezing and its continuous sorption capacity for crude oil is 7.6gg^{-1} in each cycle, and about three times the capacity of the PP sorbent. BR also removes efficiently polycyclic aromatic hydrocarbons such as acenaphthene and pyrene from sea water.

2. MATERIAL AND WORK

2.1 Materials

Crude oil from local resource was used in all sorption experiments. The main properties of crude oil used for this work were summarized in (Table 1).

Table 1: Characteristic of investigated oils

Properties	Crude oil
Specific gravity@15.6 °C	0.80846
API gravity	42.55
Viscosity @40 °C, cst	5.749
Water content, vol. %	0.0625
Water and sediment, vol%	0.0625
Carbon residue, wt%	0.453
Ash content, wt%	0.0558
Asphaltene content, wt%	0.274

2.2 Experimental work

The physical properties of crude oil as well as the recovered oil were performed according to the standard method of ASTM. These includes viscosities in centi-stock (cst) at 40 °C using U tube viscometer(ASTM D 445), the ash content in wt% according to ASTM D 582, the Conradson carbon residue in wt% according to ASTM D 189, the asphaltene content as heptanes insolubles in wt% according to ASTM D 3279 , the specific gravity according to ASTM D 1298 , salt content in PPM according to ASTM D 3230 , the water content according to ASTM D 95, the water and sediment according to ASTM D 4007 , the sulfur content in wt% according to ASTM D 4294.

The oil sorption capacity of synthetic sorbent in water medium was determined by taking specific quantity of crude oil which was added to salty water or artificial seawater (3.5% NaCl) as described in Technical Manual of the American Association of Textile Chemists and Colorists AATCC (Choi and Cloud, 1992). 1-6 grams of dry sorbent was then placed on the top of the oil surface a laboratory shaker at a frequency of 110 cycle's min⁻¹ for 30 sec. The short and medium term static sorption tests were achieved using a contact time of 15 minutes and 1 hour respectively. All the tests were operated in batch process and room temperature. The wet sorbent was then removed, let to drain for 30 seconds and re-weighed.

Water content in the removed wet sorbent was determined by centrifuge after adding toluene – xylene mixture of (20/80, v/v) as solvent and squeezing the sorbent to remove all the oil and water from it.

Reusability of the material was studied only for the case of sorption in oil medium by the above explained procedure. Twenty cycles of the sorption process were performed. Between each cycle, the

material was squeezed and weighed again. The mass of the squeezed material was the initial mass of the material in each subsequent sorption cycle.

3. RESULT AND DISCUSSION

Sorption capacity - Sorption capacity of PTFE in, oil without water, with fresh and artificial seawater, and water uptake in static state were measured. It is found that the PTFE passed the bouncy test after leaving it on the de-ionized and artificial seawater for 1 day. The water uptake was very low in both types of water (Figure 1).

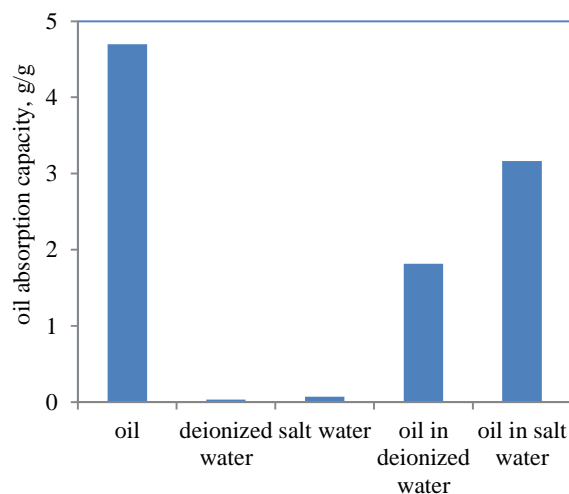


Figure 1: oil sorption capacity in oil and water, with water uptake using deionized and salt water

The oil sorption capacity using only crude oil was 4.698 g of oil sorbed per g of sorbent. The oil sorption capacity using short term static condition was 3.167 and 1.8821 g/g for both sorption in de-ionized water and artificial seawater respectively.

The sorption capacity was measured using short and medium term static test after 15 min, 60 min. by dipping of PTFE in crude oil in the presence of de-ionized water and artificial seawater. The amount adsorbed oil on PTFE with mass of sorbent showed that the amount of adsorbed oil increased with increasing the amount of PTFE. The sorption capacity of PTFE with mass of sorbent showed almost constant value for de-ionized water and artificial seawater. The oil sorption capacity was equal to 3.2g/g for salt water and 1.82 g/g for de-ionized water. These relations can be shown in (Figures 2) for short term sorption and (Figures 3) for medium term sorption.

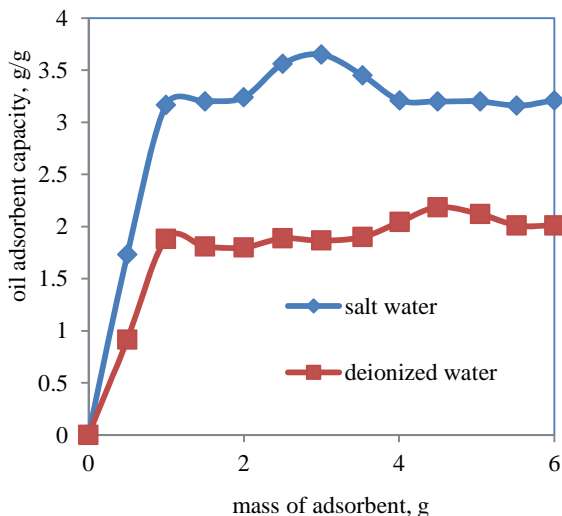


Figure 2 : Short term oil sorption capacity of PTFE using de-ionized water and artificial seawater

Oil retention test- The oil retention means the ability of adsorbent to keep the oil with time. The PTFE lost high quantity of oil in short time. It was shown that within draining time of 30 sec, the PTFE lost 50.53 mass % of the total adsorbed oil and can lose 70.3 mass % of its oil quantity within 2 minutes as shown in (Figure 4) and (Figure 5).

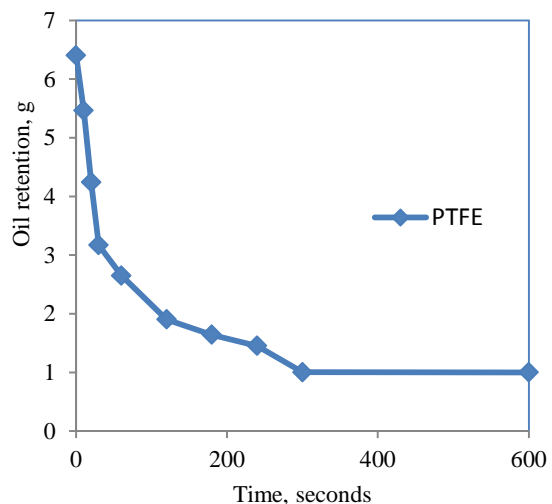


Figure 4: Oil retention for synthetic sorbents

These numbers were compared with polypropylene yarn. It was shown that this sorbent loss 29.3 mass % in 30 seconds and 38.1 mass % in two minutes. This is an important property and the evaluation of sorbent must not be evaluated by the amount of oil adsorbed but with the time of de-oiling from the sorbent.

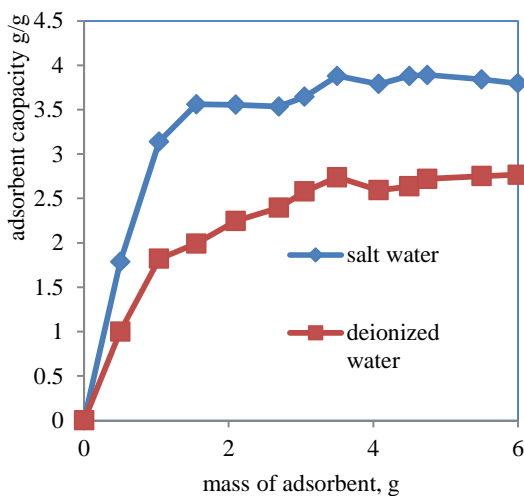


Figure 3: Medium term oil sorption capacity of PTFE using de-ionized water and artificial seawater

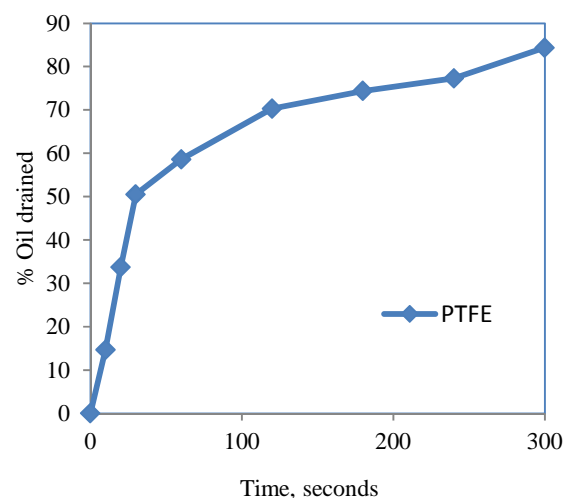


Figure 5: % oil drained from total amount of oil adsorbed with time

Sorbent reusability-The reusability of Teflon sorbent and its capacity of sorbent crude oil is shown in (Figure 6).

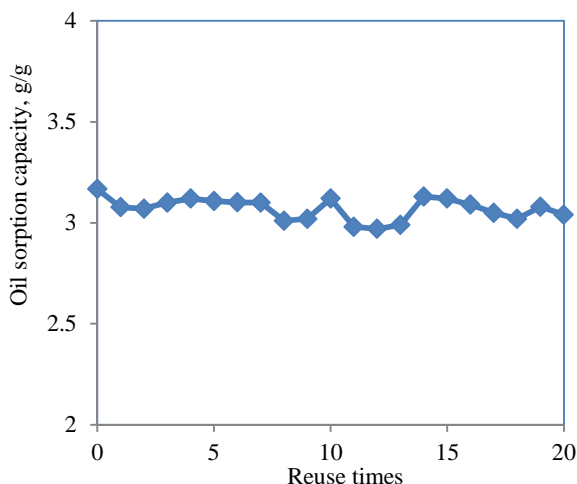


Figure 6: Reusable test for PTFE as oil absorption capacity g/g using artificial seawater

The oil sorbent capacity is decreased from 3.167 to 3.07 for the second cycle and 3.12 for the 10th cycle and 3.04 for the 20th cycle. This means that the PTFE synthetic sorbent is an elastic material that can adsorb almost same quantity after squeezing the sorbent. This reusability means that there is no need to replace it.

CONCLUSION

Evaluation of sorbents was studied and the oil retention showed a very important property of the sorbent because it is related to the time required to remove these sorbent from the surface of the oil polluted water. If the oil retention is slow, this means that most of the oil would be drained from the sorbent which subsequently affect its performance in oil spill oil recovery. The other important factor is its water uptake and bouncy factor if it passes or fail. The other factor is the oil quality of the recovered oil and if it can be used again and the effect of sorbent on the living organisms in the marine environment.

ACKNOWLEDGEMENT

The authors would like to thank the American University of Sharjah for their financial grant for this work.

REFERENCES

1. Bayat A., S. F. Aghamiri, A. Moheb, G. R. Vakili-Nezhaad, "Oil Spill Cleanup from Sea Water by Sorbent Materials", Chemical Engineering & Technology Volume 28, Issue 12, pp 1525–1528, 2005

2. Choi H. and Cloud R.M. "Natural sorbents in oil spill cleanup", Environmental Science and Technology, **26**(4), 772–776, 1992
3. Deniz Ceylan, Saadet Dogu, Burak Karacik, Sevil D. Yakan, Oya S Okay, and Oguz Okay "Evaluation of Butyl Rubber as sorbent material for the removal of oil and polycyclic aromatic hydrocarbon from sea water", Environ. Sci. Technol. 43, pp 3846-3852, 2009
4. Wei, Q.F; R.R. Mather, A.F. Fotheringham, and R.D. Yang, "Evaluation of nonwoven polypropylene oil sorbents in marine oil-spill recovery", Marine Pollution Bulletin 46, pp 780-783, 2003

Paper or Plastic? Clearing Misconceptions on Environmental Impacts of Coffee Cups Using Life Cycle Assessment (LCA)

Lee Won Jung, Maryam R. Al-Shehhi, Rasha Saffarini, Brian Warshay, Hassan A. Arafat*

Masdar Institute of Science and Technology
P.O. Box 54224, Abu Dhabi

*Corresponding author, E-mail: harafat@masdar.ac.ae

ABSTRACT

The making, use, and final disposal of coffee cups, widely used in coffee shops around the world, are major contributors to pollution. In this study, an environmental Life Cycle Assessment (LCA) of various coffee cup designs for a specific international chain, operating in the UAE, was carried out. The objectives of the work were to compare the environmental impacts of using paper cup with a sleeve, double paper cup, foam cup and reusable ceramic cup in the mentioned coffee shops, propose the best eco-friendly cup, and study how the geographical location and disposal scenarios can affect the environmental impacts of the various options. The system investigated includes raw materials production, processing of materials, energy and transportation of raw and finished product. It was concluded that, reusable ceramic cups have the minimum environmental impact in comparison to others. If disposable cups are a necessity, then foam cups are a better alternative than paper cups. Based on the influence of the geographical boundaries, if the coffee cups are manufactured locally, their environmental damage will be significantly lower than manufacturing them abroad (USA). In addition, it was found that shop policy has a significant impact on customer's decisions, which was proved by applying a discounted price for customers who bring their own reusable coffee mugs or use the ceramic mugs available in store instead of using paper cups. As a result, the consumption of disposable coffee cups is reduced. The main problem with foam cups is the consumers' perception. So, there is a need for awareness regarding the misconception that foam cups are more damaging environmentally than paper cups.

Keywords: Life Cycle Assessment (LCA), environmental impact, recycled paper

1. INTRODUCTION

With the growth of the coffee shop business, there has been a lot of damage and impact on the environment. From growing coffee in rainforests to the construction and operation of coffee bars and stores, environmental challenges and opportunities can be found throughout the coffee supply chain. One of the factors that have an impact on the environment is the use of disposable coffee cups. For this study, Caribou coffee shop in Masdar UAE was chosen, and an LCA was done to determine the possible alternatives of Caribou Coffee paper cups in this part of the world. The main reason behind selecting Caribou coffee shop is that its owners are interested in the use of eco-friendly and recyclable packages for its cups. With Caribou coffee shop's cooperation, LCA was performed to compare the existing sleeves coffee paper cup used in Caribou coffee shop against foam cup, double paper cup and reusable ceramic cup which is available in store. Also, to suggest the appropriate policy to reduce the environmental impacts of the coffee cups, we investigated several coffee shops' policies to cut down on their disposable cup consumption as part of their environmental stewardship. One of these policies is providing a discount to those who bring their own

reusable coffee mugs or use the ceramic mugs available in store instead of using paper cups. Leading coffee shop chains in the USA like Starbucks and Caribou coffee provide its customers with a 10-50 cent discounts for customers who don't take their coffee in a disposable cup. Thousands of tons of carbon dioxide are reduced by applying this policy in the coffee shops.

2. MATERIALS AND METHODS

2.1 Goal definition

- i) To compare the environmental impacts of using paper cup with a sleeve, double paper cup, foam cup and reusable ceramic cup.
- ii) To suggest the most eco-friendly coffee cup among the four alternatives.
- iii) To make a business decision based on environmental aspect. .

2.2 The existing product system

Currently, the coffee cup with a sleeve used in Caribou coffee shop in Masdar City in Abu Dhabi, UAE is manufactured in USA. Then, the cups and sleeves are

delivered from USA to UAE by airplane. The paper cups and sleeves are landfilled and incinerated in UAE.

2.3 The alternative product system

Considering that the present coffee cup is made of paper and needs a sleeve, three alternative cups will be compared with different scenarios. Firstly, based on Masdar disposal plan, 100 % of the paper will be recycled though Masdar disposal policy has not been implemented yet. The recycling company will be taking care of recycling Masdar's paper waste is Union Paper Mills Company which is located in Dubai. The Masdar's potential disposal plan is compared to the conventional disposal methods land filling in Al Dhafra landfill site near to Masdar city. Secondly, manufacturing location is assumed to be local, that is, Mussafah industrial zone in Abu Dhabi. The result from local manufacturing location will be compared to the one manufactured from USA by LCA.

The most representative materials for the three cups types were selected from SimaPro for different libraries as shown in Table 1.

Table1: Raw materials required for each product.

Product	Weight(g)	Raw Material	Library
Paper Cup	14.1	Liquid Packaging Board, at plant/RER S	Ecoinvent system processes
Sleeve	5.2	Corr, Cardboard Rec,1	DUWAL250
Double Cup	28.2	Liquid Packaging Board, at plant/RER S	Ecoinvent system processes
Foam Cup	4.8	Polystyrene, Extruded(XPS), at plant/RER S	Ecoinvent system processes
Petrol (For Foam Cup)	3.8	Petrol Unleaded Stock CH S	ETS-ESU 96 system processes
Ceramic Cup	585 [1]	Ceramics ETH S	ETS-ESU 96 system processes
Water (Washing Ceramic)	0.005	Tap Water at User CH/S	Ecoinvent system processes

The sources of energy that are required for producing the

paper cup and the sleeve were extracted from Franklin Associates [4]. According to the foam cup and the ceramic cup, the total required energies for manufacturing them are 0.04217 [5] and 28.05 MJ [9], respectively. Additional energy is required in the ceramic cup which is the washing energy and it has a value of 0.0885 MJ [9] per one ceramic cup. Data on the sources of energy required for generating the electricity needed for the manufacturing of the foam and ceramic cups were not specified, so the typical energy resources for the generated electricity in USA were used.

According to different scenarios, the transportation used is described in Table 2.

Table 2: Transportation methods used in different scenarios.

Manufacturing Transport(USA)	Places	Distance(km)	Library
Air traffic intercontinental	USA to Dubai	13197	IDEMAT
Truck 16t B250	Dubai to Abu Dhabi	113	BUWAL 250
Manufacturing Transport(locally)	Places	Distance(km)	Library
Truck 16t B250	Mussafah to Masdar	35	BUWAL 250
Landfill Transport	Places	Distance(km)	Library
Truck 16t B250	Masdar city to Al Dhafra	60	BUWAL 250
Recycling Transport(Masdar plan)	Places	Distance(km)	Library
Truck 16t B250	Masdar city to Dubai	113	BUWAL 250

In addition to these different scenarios, a survey was conducted with the help of Caribou coffee shop during the earth week to record the number of consumed paper cups during this period. During the earth week, caribou coffee shop in Masdar provided a discount of AED 3 on all Medium and large sized beverages for customer who used their own mugs or had their coffee in-house. The aim of this survey was to determine the effectiveness of such a policy in the region (Abu Dhabi, UAE). The results of the statistical survey during the Earth week are shown in Table 3.

2.4 The functional unit and the system boundaries

The LCA's functional unit is a 16 ounce coffee cup. The geographical boundary is USA and UAE depending on scenarios designed in the LCA. Time horizon is considered as one time use of a cup. It includes raw materials production, processing of materials, energy and transportation of raw and finished product. The excluded

components are capital equipment and maintenance, human labor and collection.

Table 3: Consumption of paper cups of Caribou coffee shop during earth week 21-28 March 2011.

Cup Type	No of paper cups consumed on each day								Total No.
Small Paper	54	43	45	26	8	24	44	57	301
Small Ceramic	2	2	1	2	1	2	4	4	18
Medium Paper	29	32	24	31	7	7	13	21	164
Medium Ceramic	7	6	6	5	8	5	6	8	51
Large Paper	3	7	1	7	1	4	3	5	31
Large Ceramic	1	2	0	1	0	0	1		5

2.5 The Inventory analysis

The network diagrams obtained from SimaPro for each of the four types of cups manufactured from USA and transported by airplane from USA to UAE and then landfilled; show that the biggest contributor to

environmental impacts is transportation. One example of the network diagram from SimaPro is shown in Figure 1. However, when the transportation means were changed from air shipment to sea shipment from USA to UAE keeping the disposal scenario (land filling) the same, the biggest contributors came from the raw materials from which the coffee cups were made.

When the results of manufacturing the coffee cups locally in Mussafah industrial zone, transported by truck to Caribou shop at Masdar and keeping the disposal scenario as land filling in UAE, it was found that the largest contributors to the environmental impacts still came from the raw material used in each type of cups as when the cups were shipped by sea which meant that the manufacturing process now had a greater environmental effect than the transportation means. However the magnitude of the environmental load from the contributors from these two different scenarios is different being of course larger in the first.

All three types of cups were assumed to keep the heat of the coffee for the same period of time, though in reality the different insulation period varies slightly from one material to another. Moreover, the collection of recycled corrugated cardboard of the sleeve was not included due to data gaps. The databases behind the tools used are

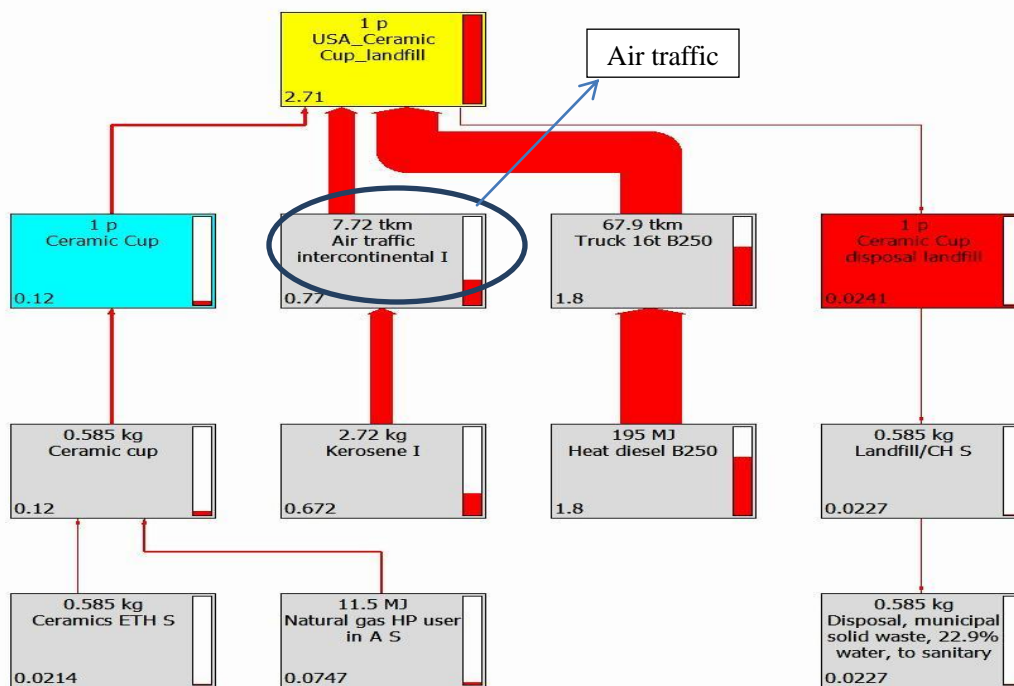


Figure 1: Ceramic cup manufactured in USA, transported by airplane and land filled in UAE network

mostly European. In washing the ceramic cup, the soap that should be associated with the water in the cup washing process was not considered.

The method that was selected for the Life cycle impact assessment was “Eco-indicator 99” because this indicator was developed for designers and design engineers to work with environmental information in a simple format and it is intended for internal use of companies. Furthermore, it averages European change instead of looking at specific conditions. There are three different cultural values under the Eco-indicator 99 which are Eco-indicator Individualist (I), Eco indicator Hierarchic (H), and the Eco-indicator Egalitarian (E) which were all considered.

3. RESULTS AND DISCUSSION

Different Scenarios were analyzed to know the environmental impacts of them and to know the most eco friendly scenario by comparing them with each other.

3.1 The Scenarios analysis

3.1.1 Scenario 1: manufacturing location is in USA and land filling disposal scenario

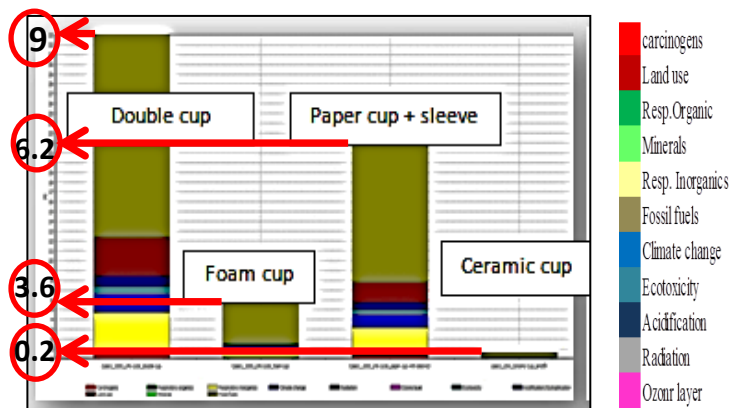


Figure 2: Single score-Eco indicator (E).

In this scenario (figure 2), the ceramic cup had the lowest environmental impact because it can be used for 1000 times (lower overall energy per use). Foam cup has the minimum environmental impact among the disposable cups because it requires low energy and low amount of raw material. On the other hand, the double cup had the biggest impact on the environment because it requires the highest manufacturing energy and the highest quantity of raw material. For the double cup, the environmental impact of these of (H) eco-indicator (46 pt) is higher than (E) eco-indicator (33 pt), but the categories of the

environmental impact are close. However, when individualist (I) eco-indicator is applied for the double cup, the overall single score points becomes lower (13 pt). In general, fossil fuel, inorganic and land use have significant environmental impact.

3.1.2 Scenario 2: manufacturing location is in UAE and Masdar disposal plan Scenario

Double cup was excluded in this scenario because it showed the highest environmental impact in comparison to other coffee cups in Scenario 1. In Scenario 2, the single paper cup with sleeve is recycled, but ceramic and foam cups are land filled. Figure 3 shows the single score results from which are obvious that the ceramic cup has the lowest environmental impact even though it is land filled while the paper cup is recycled.

For the paper cup with sleeve, the environmental impact of (H) eco-indicator (5.4 pt) is higher than (E) eco-indicator (4.8 pt), but the categories of the environmental impact are approximately the same. But, when eco-indicator (I) is applied (2.3 pt), the climate change is mainly affected, as well as, acidification, inorganic and minerals and land use. In comparing scenarios 1 and 2, it is clear that, the environmental impact of scenario 2 is because of the smaller transportation distance and the better disposal scenario.

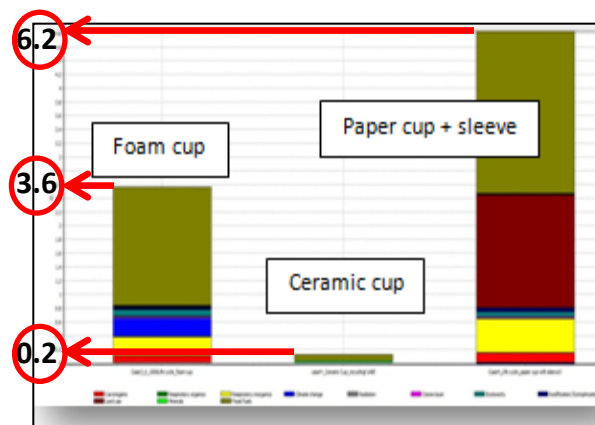


Figure 3: Single score-Eco indicator (E).

much lower than the environmental impact of scenario 1

3.1.3 Scenario 3: manufacturing location is in UAE and Masdar disposal plan and reusing the sleeve.

In this case, foam and ceramic cups are land filled .But, the paper cups with sleeve are recycled and it is compared with recycling the paper cup and reusing the sleeve. Reusing the sleeve has a positive impact on the environment because it reduces the consumption of fossil

fuel and land use, but although, it is reused, the ceramic cup and the foam cup have lower impact on the environment than it. In comparing the methods, the trend was the same as the previous scenarios; (H) eco-indicator has the highest environmental impact among other eco-indicators. Fossil fuels are mainly affected in all the cups in both eco-indicator (E) and (H) Minor effect was on respiratory organics and climate change. But, when eco-indicator (I) is applied, the biggest impact came from climate change, as well as, acidification, inorganic and minerals and land use. Land use is mostly affected in the case of paper cup with sleeve, while, in foam cup with the climate change is the most effecting category.

3.2 The sensitivity analysis

3.2.1 Sensitivity to manufacturing distance

In order to study the environmental footprint of importing the cups from a place as far as the U.S versus if the cups were manufactured somewhere closer, varying the manufacturing distance of the cups was examined. This sensitivity analysis was important because the light weight of the foam had contributed greatly in the relatively lower environmental impact of foam in our initial LCA when the cups were manufactured in US. However, even at the extreme case where cups were manufactured locally, foam cups remained to have a lower impact. The sensitivity analysis results single score showed that the smaller the manufacturing distance is the smaller the gap between the foam and paper cups became. When we compared the two extreme cases in our analysis where cups are manufactured locally (in Mussafah industrial zone) versus the current cases where cups are imported from the U.S we found that local manufacturing can result in 75% reduction in climate change, 75% reduction in fossil fuel consumption and 85% reduction in released respiratory organics. Furthermore, we found the breakeven distance at which the environmental impact of foam cups would be as large as that of paper cups. This was done by fixing paper cups distance to be manufactured locally, while varying the manufacturing distance of foam cups. It was found that the breakeven point happens when foam cups are transported from a manufacturing site 6,500 km away. However, we are aware that this is not an applicable scenario to the UAE since it not likely for paper cups to be manufactured locally due to the lack of trees in the region. (Figure 4)

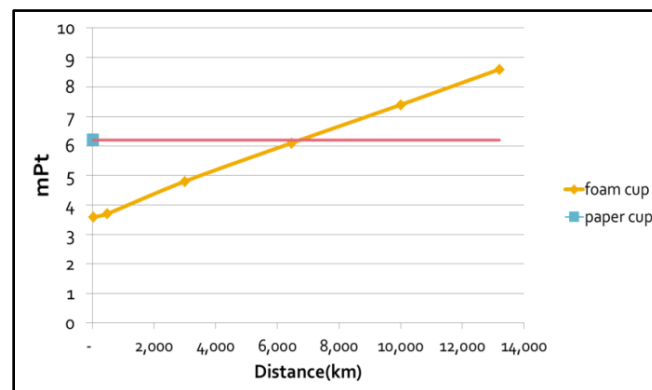


Figure 4: Variations of the environmental impact of foam cup vs. the distance.

3.2.2 Sensitivity to number of time the reusable ceramic cup is used

The manufacturing energy and the environmental impact of one ceramic cup are much higher than that of disposable cups. However, in order for a ceramic cup to become a better alternative to disposable cups it has to be used multiple times (which the real life scenario). The washing water and dishwashing energy associated with ceramic cup were incorporated in the LCA model each time the ceramic cup is used. A ceramic is used around 1,000 times [7] which was used as the baseline for this modeling. Then, a sensitivity analysis was conducted to see how many times the ceramic cup can be used to have the same impact as foam cups and paper cups. It was found that, the ceramic cup can be used more than 25 times to breakeven with paper cups and more than 30 times to breakeven with foam cups as illustrated in figure 5. However, in situations where ceramic cups are likely to be broken, disposable cups are the preferred option.

3.2.3 Sensitivity to land filling vs. recycling

When this sensitivity analysis was conducted, it was found that paper cups are more sensitive to recycling than foam cups. Therefore, the higher the recycling ratio is the smaller the differences in the environmental impact between the paper and foam cups became. Recycling paper plays a significant role in reducing the overall fossil fuel consumption, produced carcinogens, and Eco-toxicity associated with paper cups. However, even when considering 100% recycling, foam cups remain to be the most eco-friendly product.

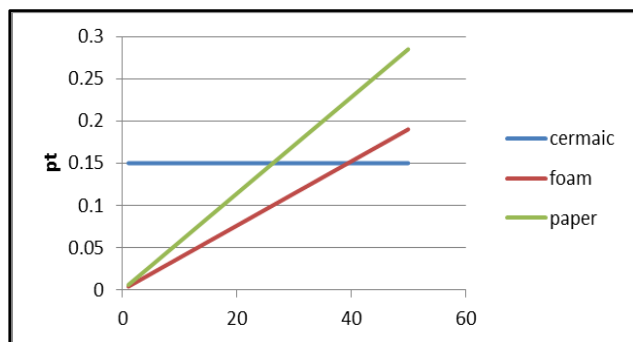


Figure 5: Variations of the environmental impact of foam cup and paper cup vs. number of time the reusable ceramic cup is used

3.2.4 Sensitivity to land filling vs. incineration

In case of not recycling, the effect of land filling to incineration was compared to see which a better option is in case no recycling can be done. Moreover, this was done to find out if disposal choices are better for some types of cups than for others. However, we found that incineration was a slightly better option for all cups compared to land filling.

3.2.5 Sensitivity to different eco indicators

The Eco-indicators (I) and (H) gave similar LCA results while the eco-indicator (I) gave less conservative results (i.e. lower single score points). Same pattern of results was observed; ceramic cup used a 1000 times was better than foam, and foam cup remained better than paper cups in all methods. Eco indicators (E) and (H) gave more values to fossil fuels, while the (I) gave more value to land use and climate change. This was observed in all scenarios considered. However, in this report eco-indicator (H) was mostly applied because it is more conservative.

3.2.6 Sensitivity to different types of fuels and electricity mixes

Throughout our LCA we tried to vary the electricity mixes and the sources and types of fuels used in the manufacturing process. This was done especially, when the electricity and fuels environmental impact for a certain product were significant. However, no significant difference was observed in the overall results. No sensitivity analysis was conducted on the actual raw material used in manufacturing the cups; this is because of limited alternatives in the industry and in the SimaPro database.

3.2.7 Sensitivity to different methods of transportation

Air traffic was the original method of transporting the cups from the manufacturing site in US. In the previous sensitivity analysis, of varying the manufacturing distance of air transportation resulted in significantly higher environmental impact. However, when the transportation method was changed to sea shipping, the emissions were significantly reduced.

4. CONCLUDING REMARKS

In summary and based on the LCA, the best choice of the coffee cups is the ceramic cup which has the least environmental impact comparing to paper and foam cups. Selling coffee in disposable cups at a relatively higher cost than using reusable cups can highly reduce the consumption of disposable cups. This policy had been already implemented in the U.S by several leading coffee shops. Earth Week Survey proves the affectivity of this policy also in Masdar-Abu Dhabi. If disposable cups are a necessity, though, then foam cups are more eco-friendly alternative to paper cups.

Regarding the functionality of foam cup, leading disposable packaging companies such as “Dart Design G” designs foam cups up to 24 oz. which proves that foam cups are rigid enough to withstand large volumes of hot liquid [8]. The main problem with foam cups is the consumers’ perception. Many people believe that paper cups as more eco-friendly, more sophisticated and safer to use. Therefore, after carrying out this study we recommend the use of Styrofoam cups due to their significant advantages.

To spread the awareness among consumers on the environmental and economic benefits of foam several actions can be taken. For example, coffee shops that choose to start using the more eco-friendly alternative of disposable cups can hang posters on their doors and windows explaining their new choice of cups. These posters can contain scientific facts on relative benefits of using foam cups with reference to credible sources. Governments can also help by giving lower advertising cost to coffee shops that want to advertise their coffee and new choice of cups on local TV. Added to this is the cost savings the coffee shop owners will make since foam cups in the market are six times cheaper than paper cups of the same size[2] [6]. Regarding the littering concern, although foam is not degradable, it has recently been discovered that usually landfill are air-tight and prevent even biodegradable items from decomposing. Since foam products are inert, they do not release any polluting gases or substances into the air, ground or water. A recent study that spanned 21 years, of landfill

contents revealed that foam cups and containers contribute less than 1/3 of 1% of the total landfill waste. Foam cups can also be safely incinerated in trash-to-energy programs like those used in Rochester [3].

REFERENCES

- [1] 16 oz Pot Belly Ceramic Mug - Matte Blue | Promotional Coffee Mug. (n.d.). Retrieved May 1, 2011, from <http://www.inkhead.com/pot-belly-ceramic-mug/14429/>
- [2] Dart Styrofoam Cup 16 oz Designer Print 16X16G. (n.d.). Retrieved May 1, 2011, from <http://www.supplyways.com/Dart-Styrofoam-Cup-16-oz-Designer-Print-16X16G-p/d16x16g.htm>
- [3] Europe, I. (2002). Packaging Materials 2. Polystyrene FOR Food Packaging Applications.
- [4] Foam, L. C. (2006). Final Peer-Reviewed Report Life Cycle Inventory of Polystyrene Foam, Bleached Paperboard, and Corrugated Paperboard Foodservice Products.
- [5] Hocking, M. B. (1991). Relative merits of polystyrene foam and paper in hot drink cups: Implications for packaging. *Environmental Management*, 15(6), 731–747.
- [6] Paper Cups. (n.d.). Retrieved May 1, 2011, from <http://plasticdrinkcups.com/paper-cups.html>
- [7] Paper Cups vs Ceramic Mugs. (n.d.). Retrieved April 28, 2011, from <http://www.articlesbase.com/recycling-articles/paper-cups-vs-ceramic-mugs-977165.html>
- [8] US - Stock Prints - Café G. (n.d.). Retrieved April 3, 2011, from <http://www.dartcontainer.com/web/products.nsf/pages/StockCafeGUS>
- [9] Ziada, H. (2009). Disposable Coffee Cup Waste Reduction Study.

Modeling Thermal Degradation in Geothermal Reservoirs Due to ReInjection

Ibrahim Kocabas

Chemical Engineering Department, AUS (ikocabas@aus.edu)

ABSTRACT

Reinjection of produced brines back into the geothermal reservoirs is a commonly practiced operation as a means of pressure maintenance and/or heat depleted water disposal. In a poorly designed reinjection scheme premature breakthrough of the injected cold water at the production well constitutes a major economic and environmental problem.

Geothermal reservoirs with a single faults zone located in a virtually immobile matrix block leads to an interesting heat extraction system. A horizontal reservoir confined by two impermeable bounding layers also leads to similar system of heat extraction. As the fault zone width (or reservoir thickness) in such systems may not be small compared to the longitudinal flow distance, the heat flow perpendicular to the flow direction within the fault zone (or horizontal reservoir) can no longer be represented by an infinite conductivity.

Thus one needs to consider a perpendicular finite conductive transport term in the governing equations. One can infer that a finite conductivity heat transfer will lead to slower heating of the reinjected waters than an infinite conductivity transfer. This in turns leads to a faster thermal degradation of the geothermal reservoir.

An interesting solution to such a system has been presented by Avdonin in 1959 for heating an oil reservoir as an enhanced oil recovery technique. In this work, we also develop analytical solutions to a similar system of thermal degradation in geothermal reservoirs closely following the work of Avdonin who used a double Laplace transform and obtain real space closed form functions using iterated Laplace transform technique.

We have also employed the developed solutions as design tools of the reinjection operations. For given set of the design parameters of heat transport, the design variables of injection rate, injection/production pair distance and injection patterns have been proposed for several scenarios.

Keywords: thermal transients, reinjection in geothermal reservoirs, thermal front, geothermal reservoir

1. INTRODUCTION

Reinjection of produced brines back into the geothermal reservoirs is a commonly practiced operation as a means of pressure maintenance as well as disposal of heat depleted water. Due to a poor design of a reinjection scheme the injected cold water may appear prematurely at the production wells leading to economic as well as environmental problems. Thus a thorough understanding of the theory thermal transients during reinjection is of vital importance.

Analytical models of transport in porous media are quite instructive in understanding the basic mechanisms of transport. Also, they are valuable in determining the collective role of transport parameters as well as carrying out sensitivity analysis for parameters. Finally, analytical models can serve as benchmarks for numerical models.

Many analytical models of heat[1,2,3,4,5] in porous media are restricted to one dimensional systems and limited to representation of a dominant mechanism of the tracer transport. Avdonin [11] has developed a two dimensional model of hot fluid injection into a layer but

he was able to use it only after reducing it to one dimensional average temperature distribution function due to limitation of computational tools at that time. Today the increasing computational powers provided by the modern computers have allowed development and implementation of sophisticated analytical models as well. In that respect, Sauty [12], Leij and Dane [13], Chrysikopoulos et.al.[14], and Sim and Chrysikopoulos [15] presented two and three dimensional solutions for homogeneous infinite media. In addition, Kocabas [16, 17] has recently applied the method iterated Laplace Transform to various problems to develop one and two dimensional solutions to a composite media consisting of a high conductivity zone located in an infinite matrix. Thus, the development of advanced analytical models besides numerical models has preserved its importance.

In this work, we have developed novel solutions to (1) Avdonin heat transfer problem which considers an infinite confining layer and (2) to a modified Avdonin system which assumes a finite confining layer. The double Laplace transform technique is utilized to develop two dimensional Laplace space solutions which closely follows the technique of Avdonin, Lauwerier and Kocabas and Onur. Only, for inverting the Laplace

space solutions into real space we have employed a slightly different approach than Avdonin in both systems. We have found that our solution is a simpler expression than that presented by Avdonin for the infinite confining layer case. The solution for the finite confining layer system was developed and presented for the first time as a novel solution in this work.

2. THEORETICAL DEVELOPMENT

The conceptual model employed here assumes a composite system consisting of a high conductivity zone, which will be referred to as the flowing layer, confined by two virtually impermeable layers of infinite or finite extent. In the flowing zone, both advection and transverse conduction of heat are assumed to take place, while only transverse conduction is assumed to occur in the confining layers.

2.1 Mathematical Model

For an incompressible fluid flowing in a linear system with a zero longitudinal thermal dispersion and a constant transverse heat conduction/thermal dispersion coefficient in the flowing part and a constant conduction coefficient in the confining layers, the governing equations posed are as follows. In order to facilitate the mathematical procedures we assume two different coordinate variables in the transverse direction. The two coordinates are collinear and simultaneous use of them greatly facilitates solution procedures, and of course, the final solutions will be the same. The governing equation in the flowing and the confining layers are given by Eq. 1 and eq.2 respectively.

$$\rho_r c_r \frac{\partial T}{\partial t} + \rho_w c_w \phi u \frac{\partial T}{\partial x} - k_t \frac{\partial^2 T}{\partial y^2} = 0 \quad (1)$$

$$\rho_m c_m \frac{\partial T_m}{\partial t} - k_m \frac{\partial^2 T_m}{\partial z^2} = 0 \quad (2)$$

The initial and boundary conditions are specified as follows

$$T = T_m = T_0 \quad \text{at} \quad t = 0 \quad (3)$$

$$T = T_i \quad \text{at} \quad x = 0 \quad (4)$$

$$k_t \frac{\partial T}{\partial y} = 0 \quad \text{at} \quad z = 0 \quad (5)$$

$$T_m = T \quad \text{at} \quad y = b \quad z = 0 \quad (6)$$

$$k_t \frac{\partial T}{\partial y} = k_m \frac{\partial T_m}{\partial z} \quad \text{at} \quad y = b \quad z = 0 \quad (7)$$

$$T_m \rightarrow 0 \quad \text{as} \quad z \rightarrow \infty \quad (8)$$

The dimensionless variables are very useful for they simplify mathematical formulation greatly. Considering many alternatives, we content that the following dimensionless variables set not only simplify the mathematics but also provide better insight into the physics.

$$T_D = \frac{T_o - T}{T_o - T_i}, \quad T_{mD} = \frac{T_o - T_m}{T_o - T_i} \quad (9)$$

$$t_D = \left(t - \frac{\rho_r c_r}{\rho_w c_w \phi u} x \right) \frac{k_m}{\rho_m c_m a^2}, \quad y_D = \frac{z}{b} \quad (10)$$

$$x_D = \frac{k_m x}{\rho_w c_w \phi u b^2}, \quad z_D = \frac{z}{a}, \quad \lambda = \frac{k_m}{k_t} \quad (11)$$

Using the above dimensionless variables Eq. 1 and Eq. reduce to Eq. 12 and Eq13 respectively.

$$\frac{\partial^2 T_D}{\partial z_D^2} - \lambda \frac{\partial T_D}{\partial x_D} = 0 \quad (12)$$

$$\frac{\partial^2 T_{mD}}{\partial z_D^2} - \frac{\partial T_{mD}}{\partial t_D} = 0 \quad (13)$$

The corresponding dimensionless initial and boundary conditions become:

$$T_D = T_{mD} = 0 \quad \text{at} \quad t_D = 0 \quad (14)$$

$$T_D = 1 \quad \text{at} \quad x_D = 0 \quad (15)$$

$$\frac{\partial T_D}{\partial z_D} = 0 \quad \text{at} \quad z = 0 \quad (16)$$

$$T_{mD} = T_D \quad \text{at} \quad y_D = 1, \quad z_D = 0 \quad (17)$$

$$\frac{\partial T_D}{\partial y_D} = \lambda \frac{\partial T_{mD}}{\partial z_D} \quad \text{at} \quad y_D = 1, \quad z_D = 0 \quad (18)$$

$$T_{mD} \rightarrow 0 \quad \text{as} \quad z_D \rightarrow \infty \quad (19)$$

2.1 Analytical Solution for An Infinite Confining Layer

The solutions of equations 12 through 19 are derived by employing the double Laplace transform technique (see Appendix A). The resultant solution for continuous injection of constant temperature fluid is:

$$T_D = 1 - \sum_{n=0}^{\infty} \sum_{m=0}^n \frac{(-1)^m}{m!} \binom{n}{m} \frac{2^{m+1}}{\sqrt{\pi}} F(\omega) \quad (20)$$

Where

$$F(\omega) = \int_0^\infty f(\omega) \omega^m \exp(-\omega^2) H_m(\omega) d\omega \quad (21)$$

$$f(\omega) = \operatorname{erfc}\left(\frac{2\sqrt{t_D} \omega + \lambda\alpha_1}{2\sqrt{\lambda x_D}}\right) + \operatorname{erfc}\left(\frac{2\sqrt{t_D} \omega + \lambda\alpha_2}{2\sqrt{\lambda x_D}}\right) \quad (22)$$

and

$$H_m(\omega) = m! \sum_{i=0}^{m/2} (-1)^i \frac{(2\omega)^{m-2i}}{i!(m-2i)!} \quad (23)$$

Eq. 20 is different than the solution provided by Avdonin even though both equations would yield the same numerical values for the same set of parameter values. However, Eq. 20 is simpler and more suitable for computational purposes than the form provided by Avdonin.

2.2 Analytical Solution for A Finite Confining Layer

The finite confining layer case has not been considered in previous studies and will be dealt with for the first time in this work. The finite confining case may be of greater importance for tracer transport in a fracture network separated by thin matrix blocks. However, as temperature is a special type of tracer and as we may sometimes encounter high permeability streaks of significant thickness and/or width separated by low permeability matrix slabs of similar size to that of high permeability layer a finite confining layer solution will also be presented. The governing equations, initial conditions and three of four boundary conditions are the same for this system as those for an infinite confining layer system. In other words Equations 1 through 7 in the preceding section also govern the finite matrix system. Only instead of Eq.8, the following relation is substituted.

$$\frac{\partial T_m}{\partial z} = 0 \quad \text{at} \quad z = 1 \quad (25)$$

Similarly Eq. 26 is employed instead of Eq.19.

$$\frac{\partial T_{mD}}{\partial z_D} = 0 \quad \text{at} \quad z_D = 1 \quad (26)$$

In order to derive the solutions for the finite matrix system, in addition to a double Laplace transform an iterated Laplace transform inversion has been utilized.

The solution for a finite confining layer is given by Eq.27.

$$T_D = 1 - \sum_{n=0}^\infty \sum_{m=0}^n \frac{(-1)^m}{m!} \binom{n}{m} \frac{2^{3/2}}{\sqrt{\pi}} B(\eta) \quad (27)$$

$$B(\eta) = \frac{2^m \eta^m}{m! \sqrt{\pi}} \int_{\alpha/(2\sqrt{x_D})}^\infty \left\{ \begin{array}{l} \exp\left(-\frac{(2\eta\sqrt{x_D} + \alpha)^2}{8x_D}\right) \\ D_{m-1}\left(\frac{2\eta\sqrt{x_D} + \alpha}{2\sqrt{x_D}}\right) S(\tau) \end{array} \right\} d\eta \quad (28)$$

$$S(\tau) = \int_0^{t_D} \frac{1 + 2 \sum_{k=1}^\infty (-1)^k \exp\left(\frac{-k^2}{\tau}\right)}{\sqrt{\pi\tau}} W(t_D) d\tau \quad (29)$$

$$W(t_D) = \int_0^\infty \omega e^{-\lambda R} \cos\left(\frac{\omega^2 2\eta\sqrt{x_D}\lambda(t_D - \tau)}{2} - \lambda_I\right) d\omega$$

3. TEMPERATURE DISTRIBUTION PROFILES

The temperature profiles are the temperature values plotted as a function of x_D for a fixed t_D , which affectively represent the temperature distributions in space at a given instant.

In this work, two profiles, one for a large t_D and one for a small t_D value are plotted in the Figures 2 to 3. Fig. 2 shows the characteristic effects of the physical processes modeled. The dimensionless concentration decreases from the centerline towards the interface of the two media (i.e. $y_D=1$ and $z_D=0$). Also, as there is only convective transport along the flow direction, the sharp convective front is distinctly visible. The concentration gradient along the flow direction is relatively small but still easily distinguishable.

As the t_D value increases (See Fig. 3) while the depletion of heat along the flow direction increases, the temperature gradient across the flowing zone is much less pronounced than that for a small t_D . The dimensionless time t_D is inversely proportional to the characteristic time of transverse dispersion t_d . The characteristic time of a process is an measure of the effectiveness of the process such that the smaller the characteristic time, the greater the speed of the process. A small t_D corresponds to either small advection time or large transverse dispersion characteristic time.

Figures Fig.6 shows the profile for a slug injection

mode. A very interesting feature is apparent in this figure. Notice that while the general shape shows that the concentrations are greater along the centerline of injection than those towards the interface, the region of $0 < x_D < 0.4$ shows exactly the reverse of that situation. The apparently contradictory case of a the positive gradient along z_D may be better explained as follows.

As the slug travels with convective flow, it is depleted of its tracer to the adjacent matrix. At early times, since transverse dispersion does not affect the part along the centerline of injection, the fluid will travel convectively without any loss of heat or smearing of temperature near the centerline. Once the slug passes a point, then the heat lost into the adjacent matrix will reenter the heat free flowing zone giving rise to the development of a positive smooth concentration gradient along z_D in the flow region the behind the rear end of the slug. Note for a spike injection model which more convenient for chemical tracers, since a spike injection has a zero thickness mathematically, the positive concentration gradients along z_D will be observed in the whole transport domain for the spike injection case for small t_D values. The case of large t_D values correspond to highly effective transverse dispersion and hence the fast depletion capacity into the matrix quickly regenerates the negative gradients anew.

3. TEMPERATURE RETURN PROFILES

Fig.10 show the tracer return profile across the half production plane at the outlet end of the system as a function of shifted time. The most prominent feature of this profiles is that they it exhibits a long tailing, which is an indication of the effect of heat conduction/dispersion into the confining layer.

4. AVERAGE TEMPERATURES

The average temperatures across the high conductivity zone serves as an accurate one-dimensional solution. Thus, we can infer the collective roles of parameters and geometric dimensions on the heat transport mechanisms along the flow direction. The average temperature across the half width of the high conductivity zone (which is also equal to the average temperature distribution across the whole width) is found using the following relation:

$$\bar{T}_D = \frac{1}{z_{Db}} \int_0^{z_{Db}} T_D(z_D) dz_D \tag{34}$$

Applying this relation to the solution [see appendix B] one obtains:

$$\bar{C}_D = 1 - \sum_{n=0}^{\infty} \sum_{m=0}^n \frac{(-1)^m}{m!} \binom{n}{m} \frac{2^{m+1}}{\sqrt{\pi}} \int_0^{\infty} \omega^m e^{-\omega^2} H_m(\omega) \int_0^{x_D} \frac{F(\omega, \eta)}{\sqrt{\pi \eta}} d\eta d\omega \tag{39}$$

Where

$$F(\omega, \eta) = \exp\left(-\frac{(n + 2\sqrt{t_D/\theta} \omega)^2}{\eta}\right) + \exp\left(-\frac{(n + 1 + 2\sqrt{t_D/\theta} \omega)^2}{\eta}\right) \tag{35}$$

The average temperature values are used to study the effect of dimensions and roles of parameters on transport. Equation 35 shows that the average concentration depends on two parameter groups, t_D/θ and x_D . In order to study the effect of collective roles of parameters use characteristic times of each process is more practical. The characteristic times for convection, transverse dispersion within the high conductivity zone and diffusion within the confining matrix are defined as follows:

$$t_w = \frac{x}{u} \quad t_t = \frac{b^2}{D_t} \quad t_m = \frac{\phi b^2}{\phi_m D_m}$$

Additionally, the pore volume injection is defined as:

$$PV = \frac{ut}{x}$$

The transverse Peclet number Pt in the high conductivity zone and Peclet number in the matrix are defined as:

$$P_t = \frac{t_t}{t_w} \quad P_m = \frac{t_m}{t_w}$$

The original parameters and the new parameters are related as follows:

$$\eta = \frac{1}{P_t}, \quad \tau = \frac{PV - 1}{P_t} \quad \text{and} \quad \theta = \sqrt{\frac{P_m}{P_t}}$$

For a unit value of θ , the average return profiles as function of Pt and pore volume injection are plotted in Fig xx. Similarly for unit value of Pt , the average return profiles as a function of θ and pore volume injection are plotted in Fig. xxx.

3. CONCLUSIONS

A set of new solutions to a two dimensional composite transport model have been developed by using a double and iterated Laplace transform techniques. The solutions are plotted as two dimensional concentrations distributions in space (distribution profiles) and time (return profiles). The solutions are found to be a function of three group of variables, namely, t_D/θ and x_D and z_D . The temperature distribution profiles along the dimensionless distance, x_D , show that the depletion heat from the flowing layer increases with increasing t_D/θ values. This increased mixing eliminates the distinctive curvatures of the solutions. Similarly, the temperature return profiles show that as the value of x_D increases, which is directly proportional to sampling distance, the mixing of heat also increases eliminating the profiles' distinctive curvatures. Since the profiles without distinctive curvatures are difficult to interpret, the sampling distance and the dimensionless effective time, t_D/θ , for the dispersion process become critical parameters.

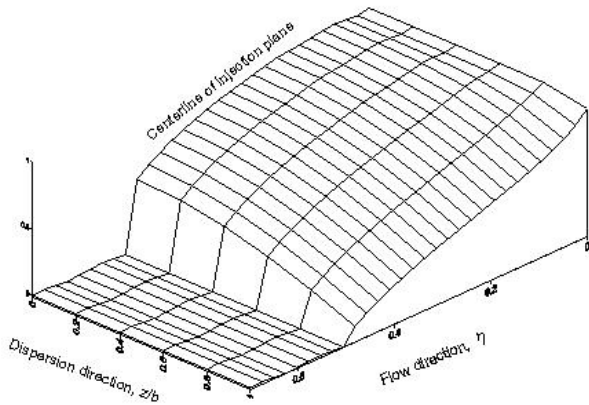


Fig. 1 Continuous injection solution, tracer distribution profile for $\tau=0.5$

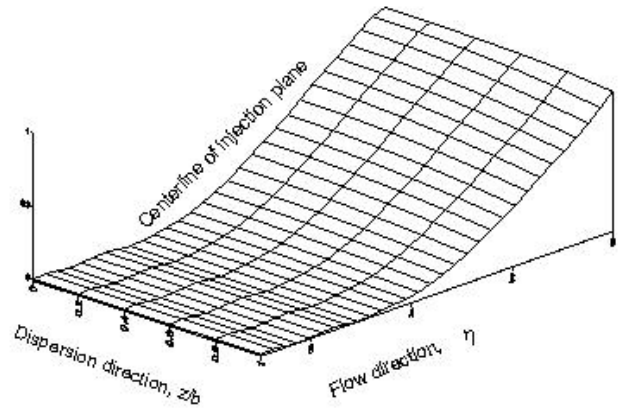


Fig. 2 Continuous injection solution, tracer distribution profile for $\tau=5$

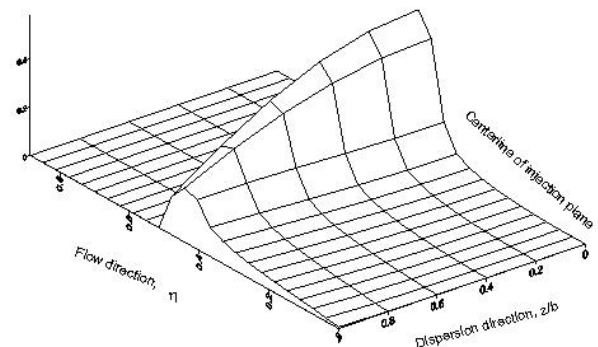


Fig. 3 Slug injection solution, tracer distribution profile for $\tau=0.5$

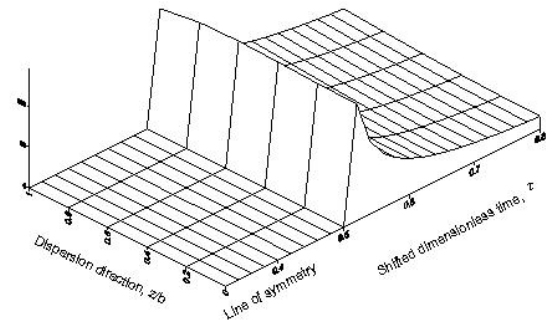


Fig. 4 Spike injection solution, tracer return profile across the half production plane for $\eta=0.5$

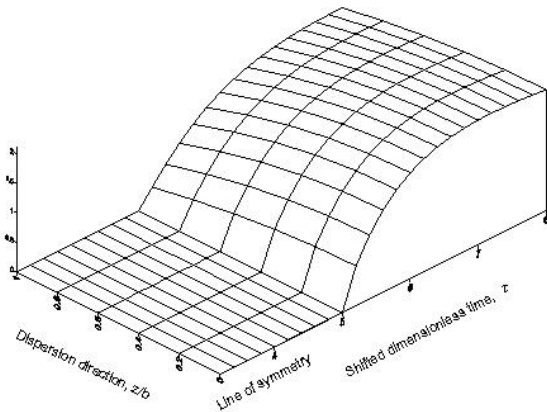


Fig. 5 . Spike injection solution, tracer return profile across the half production plane for $\eta=5$

REFERENCES

- [1] Taylor, A.B., Jackson, C.D., and Chopra, E.F. "Article Title", *Journal title*, Vol. 30, No. 2, pp. 1-20, 2010.
- [2] Avdonin, N.A., "Some formulas for calculating the temperature field of a stratum subject to thermal injection." *Neft'i Gaz*, Vol. 7 No. 3, pp.37-43, 1964. (in Russian).
- [3] Spillette, A.G., "Heat transfer during hot fluid injection into an oil reservoir." In: *D.N. Dietz (Ed.), Thermal Recovery Techniques, SPE Reprint Series 10*, pp. 21-26, 1965.
- [4] Cendejas, F. A., Rodriguez, H. R., "Heat transfer processes during low or high enthalpy fluid injection into naturally fractured reservoirs." *Proc. Nineteenth Workshop on Geothermal Engineering*, Stanford University, Stanford CA. 1994.
- [5] Kocabas, I., Islam M. R., Concentration and temperature transients in heterogeneous porous media, Part I: Linear Transport. *J. Pet. Sci. and Eng.* (2000a), 26, pp. 211-220.
- [6] Kocabas, I. "Thermal Transients During Nonisothermal Fluid Injection into Oil Reservoirs", *J. Petroleum Science and Engineering*, Vol. 42, pp. 121-133, 2004.
- [7] Stehfest, H., Numerical inversion of Laplace transforms," *Com. ACM* 13, (1970), pp. 144-49.
- [8] Davies, B. and Brian, M., Numerical inversion of Laplace transforms: A survey and comparison of methods," *J Comput. Phys.* (1979), 33, pp.1-32.
- [9] Sauty, J. P, Gringarten, A. C, Menjoz, A., Landel, P.A., 1982. Sensible energy storage in aquifers 1. Theoretical study. *Water Res. Res.*, 18 (2) pp.245-252.
- [10] Sauty, J. P, Gringarten, A., Landel, P.A., 1978. The effect of thermal dispersion on injection of hot water in aquifers. *Proc. The Second Invitational Well Testing Symposium, Div. Of Geothermal Energy, U.S. Dept. of Energy. Berkeley CA.*, pp. 122-131.
- [11] Kocabas, I. Application of iterated Laplace transformation to tracer transients in heterogeneous porous media, *J. Franklin Institute*, Volume 48, Issue 7, Sept. 2011, pp. 1339-136, (on line since April, 22, 2010), doi:10.1016/j.jfranklin.2010.04.002
- [12] Kocabas, I. "An Analytical Model of Temperature and Stress Fields During Cold Water Injection", *SPE Production and Operations*, May 2006, p.282-292

APPENDIX A : DERIVATION OF INFINITE CONFINING LAYER SOLUTION

The double Laplace transform used in this work is defined as follows [8]:

$$\begin{aligned} \ddot{T}_D &= T_D(s, p) \\ &= \int_0^\infty \int_0^\infty \begin{bmatrix} \exp(-px_D) \\ \exp(-st_D) \\ T_D(t_D, x_D) \end{bmatrix} dt_D dx_D \end{aligned} \quad (A1)$$

Note in A1 the real space variables t_D and x_D corresponds to Laplace space variables s and p respectively. The double Laplace transforms of Eq. 12 and Eq. 13 with respect to x_D and t_D are given by A2 and A3 respectively.

$$\frac{\partial^2 \ddot{T}_D}{\partial y_D^2} - \lambda p \ddot{T}_D = -\frac{\lambda}{s} \quad (A2)$$

$$\frac{\partial^2 \ddot{T}_{mD}}{\partial z_D^2} - s \ddot{T}_{mD} = 0 \quad (A3)$$

Solving these two equations we would obtain the general solutions:

$$\ddot{T}_D = C_1 e^{-\sqrt{\lambda p} y_D} + C_2 e^{\sqrt{\lambda p} y_D} + \frac{1}{ps} \quad (A4)$$

$$\ddot{T}_{mD} = C_3 \exp(-\sqrt{s} z_D) + C_4 \exp(\sqrt{s} z_D) \quad (A5)$$

Applying boundary condition given by Eq 17 leads to C_4 equal to zero and boundary condition given by Eq. 16 requires C_1 to be equal to C_2 .

$$\ddot{T}_D = C_1 \left[e^{-\sqrt{\lambda p} y_D} + e^{\sqrt{\lambda p} y_D} \right] + \frac{1}{ps} \tag{A6}$$

$$\ddot{T}_{mD} = C_3 \exp(-\sqrt{s} z_D) \tag{A7}$$

Applying the boundary conditions given by Eq.14 and Eq.15 and solving the resultant two algebraic equations for C1 we obtain:

$$C_1 = \frac{1}{ps} \left\{ \frac{\frac{\sqrt{\lambda s} e^{-\sqrt{\lambda p}}}{\sqrt{p} + \sqrt{\lambda s}}}{1 - \frac{\sqrt{p} - \sqrt{\lambda s}}{\sqrt{p} + \sqrt{\lambda s}} e^{-2\sqrt{\lambda p}}} \right\} \tag{A8}$$

Further manipulating the expressions in A8 using binomial expansion relations we may write:

$$C_1 = - \sum_{n=0}^{\infty} \sum_{m=0}^n \left\{ \frac{\left(e^{-(2n+1)\sqrt{\lambda p}} + e^{-(2n+1)\sqrt{\lambda p}} \right)}{\binom{n}{m} p (\sqrt{s} + \sqrt{p/\lambda})^{m+1}} \right\} \tag{A9}$$

Then A4 becomes:

$$\ddot{T}_D = \frac{1}{ps} - \sum_{n=0}^{\infty} \sum_{m=0}^n (-1)^m \binom{n}{m} 2^m G \tag{A10}$$

$$G = \frac{s^{(m-1)/2} (e^{-\alpha_1 \sqrt{\lambda p}} + e^{-\alpha_2 \sqrt{\lambda p}})}{p (\sqrt{p} + \sqrt{\lambda s})^{m+1}} \tag{A11}$$

Where

$$\alpha_1 = (1 - y_D + 2n) \text{ and } \alpha_2 = (1 + y_D + 2n)$$

Using the following Laplace inversion formulae, for the Laplace parameter s and p consecutively we arrive at the final solution:

$$L^{-1}(s^{(m-1)/2} f(\sqrt{s})) = \frac{1}{2^m \sqrt{\pi t_D^{m+1}}} \int_0^{\infty} \exp\left(-\frac{u^2}{4t_D}\right) H_m\left(\frac{u}{2\sqrt{t_D}}\right) f(u) du \tag{A12}$$

$$L^{-1}\left(\frac{1}{(s+a)^{m+1}}\right) = \frac{t_D^m e^{-at_D}}{m!} \quad m = 0,1,2,3... \tag{A13}$$

$$L^{-1}\left(\frac{1}{p} \exp(-k\sqrt{p})\right) = \text{erfc}\left(\frac{k}{2\sqrt{x_D}}\right) \tag{A14}$$

$$T_D = 1 - \sum_{n=0}^{\infty} \sum_{m=0}^n \frac{(-1)^m}{m!} \binom{n}{m} \frac{1}{\sqrt{\pi t_D^{m+1}}} \int_0^{\infty} \exp\left(-\frac{u^2}{4t_D}\right) H_m\left(\frac{u}{2\sqrt{t_D}}\right) \frac{u^m}{m!} (F(u, \alpha_1) + F(u, \alpha_2)) du \tag{A15}$$

Where

$$F(u, \alpha) = \text{erfc}\left(\frac{u + \lambda \alpha}{2\sqrt{\lambda x_D}}\right) \tag{A16}$$

Defining the following variable: $\omega = \frac{u}{2\sqrt{t_D}}$, results in Eq. 20 through 24.

The same technique may be used to solve the confining layer equation to obtain:

$$\ddot{T}_{Dm} = \left[\frac{e^{-\sqrt{s}(1-z_D)}}{p} - \frac{1}{p} \frac{e^{-\sqrt{s}(1-z_D)} G_m}{\left(1 - \frac{\sqrt{p} - \sqrt{\lambda s}}{\sqrt{p} + \sqrt{\lambda s}} e^{-2\sqrt{\lambda p}}\right)} \right] \tag{A14}$$

Where

$$G_m = \left(e^{-2\sqrt{\lambda p}} + 1 \right) \frac{\sqrt{\lambda s}}{(\sqrt{p} + \sqrt{\lambda s})} \tag{A15}$$

And the same approach as above is used to arrive at the final forms.

APPENDIX B : DERIVATION OF FINITE CONFINING LAYER SOLUTION

As the governing equations, initial conditions and most of the boundary conditions are the same as those of infinite confining layer system the general solutions will be the same for both cases. Thus, A8 and A10 will hold for this system as well. However, since confining layer has an impenetrable outer boundary the following form of the confining layer solution may be more useful than A9.

$$\ddot{T}_{mD} = C_3 \text{Sinh}(-\sqrt{s} z_D) + C_4 \text{Cosh}(\sqrt{s} z_D) \tag{B1}$$

applying boundary condition at $z_D = 1$ namely Eq.26 requires that:

$$C_3 = -C_4 \tanh(\sqrt{s}) \tag{B2}$$

Thus B1 reduces B1 to

$$\ddot{T}_{mD} = -C_4 \text{Tanh}(\sqrt{s}) \text{ Sinh}(\sqrt{s} z_D) + C_4 \text{Cosh}(\sqrt{s} z_D) \tag{B3}$$

Applying the other two boundary conditions at $y_D = 1$ and $z_D = 0$ given by Eq.14 and Eq.15 allows us to determine the two constants C1 and C3. Substituting the resultant expression of C1 into A6, we obtain:

$$\ddot{T}_D = \frac{1}{ps} - \frac{1}{ps} \frac{G}{\left(1 - \frac{\sqrt{p} - \sqrt{\lambda s} \tanh(\sqrt{s})}{\sqrt{p} + \sqrt{\lambda s} \tanh(\sqrt{s})} e^{-2\sqrt{\lambda p}}\right)} \tag{B4}$$

Where

$$G = \left(\frac{\sqrt{\lambda s} \tanh(\sqrt{s})}{(\sqrt{p} + \sqrt{\lambda s} \tanh(\sqrt{s}))} \right) \left(e^{-(1+y_D)\sqrt{\lambda p}} + e^{-(1-y_D)\sqrt{\lambda p}} \right) \tag{B5}$$

Substituting C3 into B3 we obtain:

$$\ddot{T}_{Dm} = \left[\frac{e^{-\sqrt{s}(1-z_D)}}{p} - \frac{1}{p} \frac{e^{-\sqrt{s}(1-z_D)} G_m}{\left(1 - \frac{\sqrt{p} - \sqrt{\lambda s} \tanh(\sqrt{s})}{\sqrt{p} + \sqrt{\lambda s} \tanh(\sqrt{s})} e^{-2\sqrt{\lambda p}}\right)} \right] \tag{B6}$$

Where

$$G_m = \left(e^{-2\sqrt{\lambda p}} + 1 \right) \frac{\sqrt{\lambda s} \tanh(\sqrt{s})}{(\sqrt{p} + \sqrt{\lambda s} \tanh(\sqrt{s}))} \tag{B7}$$

Then we use the following binomial expansion:

$$\left(\frac{\sqrt{p} - \sqrt{\lambda s} \tanh(\sqrt{s})}{\sqrt{p} + \sqrt{\lambda s} \tanh(\sqrt{s})} \right)^n = (-1)^n \sum_{m=0}^n (-1)^m \binom{n}{m} \frac{(2\sqrt{p})^m}{(\sqrt{p} + \sqrt{\lambda s} \tanh(\sqrt{s}))^m} \tag{B8}$$

Then A6 may be written as:

$$\ddot{T}_D = \frac{1}{ps} - \sum_{n=0}^{\infty} (-1)^n \sum_{m=0}^n \frac{(-1)^m \binom{n}{m} 2^m \frac{\sqrt{\lambda} \tanh(\sqrt{s})}{\sqrt{s}} p^{m/2-1} (e^{-\alpha_1 \sqrt{\lambda p}} + e^{-\alpha_2 \sqrt{\lambda p}})}{(\sqrt{p} + \sqrt{\lambda s} \tanh(\sqrt{s}))^{m+1}} \tag{B9}$$

In order to invert B(9) we use the following Laplace transform relations consecutively:

$$L^{-1} \left(p^{m/2-1} F(\sqrt{p}) \right) = \frac{1}{2^{m-1/2}} \frac{1}{\sqrt{\pi x_D^m}} \tag{B10}$$

$$\int_0^{\infty} \exp\left(-\frac{u^2}{8x_D}\right) D_{m-1}\left(\frac{u}{2\sqrt{x_D}}\right) F(u) du$$

$$F(u) = L^{-1}(f(p))$$

and hence

$$F(u) = H(u - \alpha) \frac{(u - \alpha)^m}{m!} \tag{B11}$$

$$\exp(-(u - \alpha)\sqrt{\lambda s} \tanh(\sqrt{s})) L^{-1} \frac{\tanh(\sqrt{s})}{\sqrt{s}} = \left\{ \frac{1}{\sqrt{\pi \tau}} + \frac{2}{2} \sum_{k=1}^{\infty} (-1)^k \exp\left(-\frac{k^2}{\tau}\right) \right\} \tag{B12}$$

$$L^{-1} e^{-(u-\alpha)\sqrt{\lambda s} \tanh(\sqrt{s})} = \int_0^{\infty} e^{-\lambda R} \cos\left(\frac{\omega^2 (u - \alpha)\sqrt{\lambda t}}{2} - \lambda_I\right) d\omega \tag{B13}$$

$$T_D = 1 - \sum_{n=0}^{\infty} \sum_{m=0}^n \frac{(-1)^m}{m!} \binom{n}{m} \frac{2^{3/2}}{\sqrt{\pi}} B(u) \tag{B14}$$

$$B(u) = \frac{1}{\sqrt{\pi x_D^m}} \tag{B15}$$

$$\int_{\alpha}^{\infty} \exp\left(-\frac{(u + \alpha)^2}{8x_D}\right) D_{m-1}\left(\frac{u + \alpha}{2\sqrt{x_D}}\right) F(u) du$$

$$F(u) = \frac{u^m}{m!} S(\tau) \tag{B16}$$

$$S(\tau) = \int_0^{t_D} \left\{ \frac{1}{\sqrt{\pi\tau}} + \frac{2}{\sqrt{\pi\tau}} \sum_{k=1}^{\infty} (-1)^k \exp\left(\frac{-k^2}{\tau}\right) \right\} W(t_D) d\tau \quad (\text{B17})$$

$$W(t_D) = \int_0^{\infty} \left\{ e^{-\lambda R} \cos\left(\frac{\omega^2 u \sqrt{\lambda} (t_D - \tau)}{2} - \lambda_I\right) d\omega \right\} \quad (\text{B18})$$

Africa Energization: Alternative Energy Capacity Building Strategies and Policies

O. Phillips Agboola¹, O. Mary Agboola²

¹Mechanical Engineering Department, Eastern Mediterranean University, Famagusta, TRNC, via Mersin 10, Turkey
(phillips.agboola@cc.emu.edu.tr),

²Economics Department, Eastern Mediterranean University, Famagusta, TRNC, via Mersin 10, Turkey,
(oluwatoyin.agboola@emu.edu.tr)

ABSTRACT

African Energization is long due; this problem has lingered for a long time without a comprehensive solution. Efforts to resolve this problem have met with both technical and political obstacles rendering them ineffective. Currently only a few African countries pursue the renewable energy alternative for electricity generation, the most common alternative source is hydropower; however, bio-fuel, solar photovoltaic's (PVs), geothermal and wind are more efficient alternatives fit for use, in both the rural and the urban areas of African countries. This paper presents the range of economic and political issues that constitute major obstacles to the realization of sustainable Africa electrification. One major observation in this work is that with the renewable endowments of most African countries, the continent should be generating an income from electricity while providing enough electricity for its citizenry. The work also provides some capacity building strategies and policies to help sustain the energy to be generated for electricity purposes.

1. INTRODUCTION

In recent years African electrification has topped the list of the continent's needs. Most discussions on Africa, within and outside her coast, have stressed the need for her to energize herself to meet the targeted economic and social development expected of her. The reality of the poor use of the rich energy generation potential of Africa only reveals that an adequate solution is still missing. The solution to this problem will require identifying the root causes and efforts to effectively tackle them. In mid 2009, Africa's population was estimated to be 999 million people [1, 2], accounting for 14.67% of the World's population. Meanwhile, the economic output of the Continent is only around 3.6% of the World's total. Africa's GNI (using purchasing power parities) is averaged \$2660 billion compared with the world GNI of \$10,090 [3]. In landmass Africa's land area covers just over 30.3 million km² in 53 countries of diverse culture, colors, sizes and languages. Africa as a continent consumes the least when it comes to World energy despite being the second largest continent in the world; this is especially true with fewer than 25 percent of Africans having access to electricity. In Uganda, only 5 percent of the population has access to electricity; in Kenya, 15 percent; in Congo, 6 percent. In the oil-rich Nigeria less than 40% have access to electricity, 25 of the 44 sub-Saharan nations face crippling electricity shortages. Electricity failure (blackouts) and rationing are common practice in most African countries to ensure that most urban areas have electricity at one time or the other. The poor electricity supply is more evident considering how big the market for standby generator set is, in most African countries, where individual and most firms (Public & Private) have to generate their own electricity at a very high cost. In Nigeria, the Manufacturers Association of Nigeria (MAN) and the National Association of Small Scale Industrialists had estimated that the sum of N1.8 billion on the average goes into standby power generation weekly. The increase in standby generation by individual house will increase Africa carbon emission contribution; which at the moment is the lowest in the world. Currently only a few Africa countries

pursue renewable energy alternative for electricity generation, the most common source is hydropower; however, solar photovoltaic's (PVs), bio-fuel, geothermal and wind are more efficient to use in both the rural and the urban areas of African countries. Most of these energy resources are yet to be fully exploited, which is a contributing factor in making the continent the lowest consumer of energy.

Table 1: Total Electricity Net Consumption (Billion Kilowatt hours) between 2005- 2008 [4]

	2005	2006	2007	2008
World	15738.65	16396.73	17138.89	17444.76
Africa	472.9185	490.0437	520.7385	525.1716
Algeria	27.516	26.911	28.335	30.5
Egypt	89.424	96.203	104.092	109.0874
Libya	18.353	20.833	22.341	22.886
Morocco	19.6557	19.2969	20.6421	21.4731
Mozambique	9.109	9.528	10.157	10.175
Nigeria	16.763	14.855	19.261	18.141
South Africa	205.0233	210.6084	219.6408	212.2418
Tunisia	11.2639	11.5171	11.8809	12.4901
Zambia	8.589	8.802	8.001	7.614
Zimbabwe	12.18	12.205	12.443	12.473

There is an urgent need for substantial increases in energy consumption in Africa as a whole if Africa is to be competitive with other developing regions of the world. The problems facing the development of energy in Africa appear to be overwhelming ranging from technical to political. A closer look into this issue in Africa will demonstrate that the energy sector in Africa provides enormous opportunities for formulating and implementing ambitious renewable energy programmes that will bring an environmentally sound and secure energy future [1]. Table 1 shows total net electricity consumption in some selected African countries compared with the total net electricity in Africa and the World

2. AFRICA ENERGY CAPACITY: RENEWABLE AND NON RENEWABLE

When it comes to natural endowments, Africa is a continent to be reckoned with due to her huge natural resources. In 2010, oil reserves in Africa were estimated at 119.114 billion barrels, around 8.8% of the World's total; three countries concentrated 78.64% and five countries concentrated 89.74 % of these reserves (Libya 37.17%, Nigeria 31.23%, Algeria 10.24%, Angola 8%, and Egypt 3.1%) [4,5]. The proven natural gas reserves were estimated at 495.25 trillion cubic feet, 7.5 % of the World's total; three countries concentrated 81.32% and five countries concentrated 94.24% of these reserves, (the same as above: Nigeria 37.41%, Algeria 32.10%, Egypt 11.81%, Libya 10.98%, and Angola 1.94%) [5]. Africa's coal reserves are estimated at 36 Gtoe, around 5.7% of the World's total; 90% of these coal reserves are concentrated in South Africa, and over 97% of Africa's coal is also produced in South Africa. In 2010, Oil & dry natural Gas productions were estimated respectively at 10.69 million b/d (barrels a day) and 202.30 billion cubic meters (around 12.66% and 6.71% of the World total, respectively). Moreover, recently, new oil and gas reserves are being discovered in several African countries and regions (Ghana, Mauritania, Uganda, Tanzania, Zambia, the Gulf of Guinea, etc.). The African natural energy resources are unevenly distributed rather they are more concentrated in a few countries (Nigeria, Algeria, South Africa, Angola and Libya). There is no doubt that African countries have abundant fossil fuel, though highly concentrated in some few countries, but this fuel are non-renewable sources of energy with limited period of exploitation. The renewable energy sources are equally available in Africa and more evenly distributed among the member countries than the fossil fuel. Hydropower potential in Africa can greatly contribute to its energization. Large hydropower potentials is present in the East, West and Central African countries with gross theoretical potentials of about 3892 TWh/year, technical exploitable potentials of about 1917 TWh/year and economic exploitable at 1096 TWh/year. This amount (1096 TWh/year) doubled the current electricity demand of the Africa continent. Nigeria produced more than 70% of its electricity generation from Hydropower systems. The continent can explore about 9000 Megawatt of geothermal potential and abundant biomass, solar and significant wind potential [6]. The potential in Nuclear energy is been exploited by South Africa, Egypt and Nigeria.

Biomass offers an attractive opportunity in Africa electrification, the abundant of biomass as estimated by Deepchand (2001) indicated that a significant proportion of current electricity generation in 16 Eastern and Southern African countries could be met by bagasse-based cogeneration in the region's sugar industry. About 20% of Mauritius electricity is been generated from cogeneration [7]. There is enormous exploitable hydropower capacity in African countries, but just only 7% has been harnessed—one of the world's lowest figures. Africa has an estimated proven geothermal potential of 9000MW but only 45MW (in Kenya) is currently in use. Solar power is another advantage in Africa for electricity generation, the average solar radiation (insolation) is between 5–6 kWh/m², solar energy technology offers huge advantage not only in electricity production but also in drying agricultural products. Some encouraging results with PV systems have been registered in Libya, South Africa, Kenya, Namibia, Nigeria and Zimbabwe; but these initiatives largely serve the high-income rural households. A number of innovative low-cost renewable energy technologies suitable for the rural and urban poor have been developed and are beginning to demonstrate encouraging levels of success. Notable examples include improved biofuel stoves; low-cost solar pasteurizing units; ram pumps for irrigation; pico and micro-hydro technologies suitable for agro-processing; and, efficient manually operated water pumping and agro-processing technologies. Figure 1&2 shows the crude oil distillation capacity and the crude oil proved reserves in sub region in the world. The African continent has the least distillation capacity despite her huge reserves an indication that technology that improves living standard and economy are lacking. Asia and Oceania, Europe and Eurasia have less crude oil reserves but have advance in the crude oil distillation. One will expect that the crude oil resources in Africa should motivate high crude oil distillation but this is not the case. Figure 3 also shows the coal overview (2009) of the sub region of the world with Africa having not the least but that does not transcend into coal power generation like the China. According to Figure 4, the enormous potential in gas production in Africa should position the continent among high energy user. In Nigeria for instance, less than 10% of the household uses gas for cooking while majority rely on kerosene and firewood. Yet gas flaring (associated gas from crude oil) is flare on daily bases, it was estimated that Nigeria loss around \$2.5 billion yearly on flare gas.

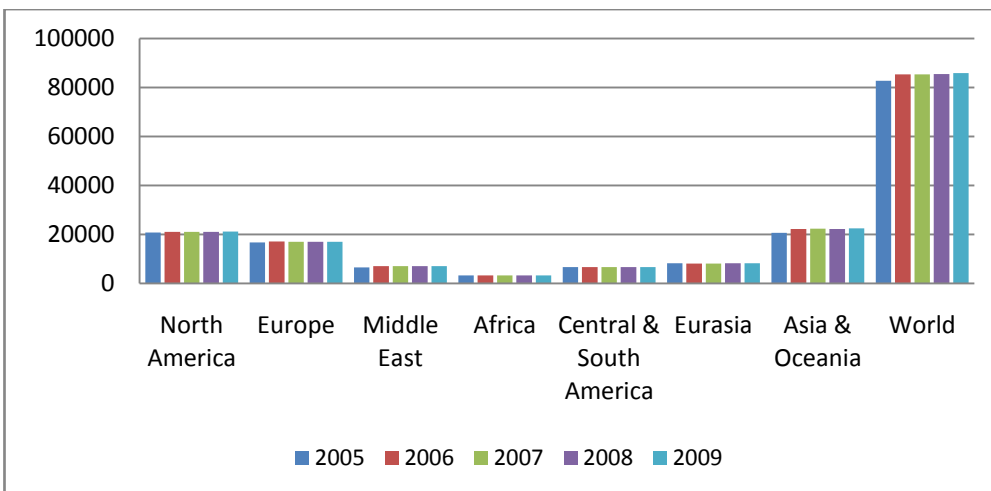


Figure 1: Crude Oil Distillation Capacity (Thousand Barrels Per Cal Day) [8]

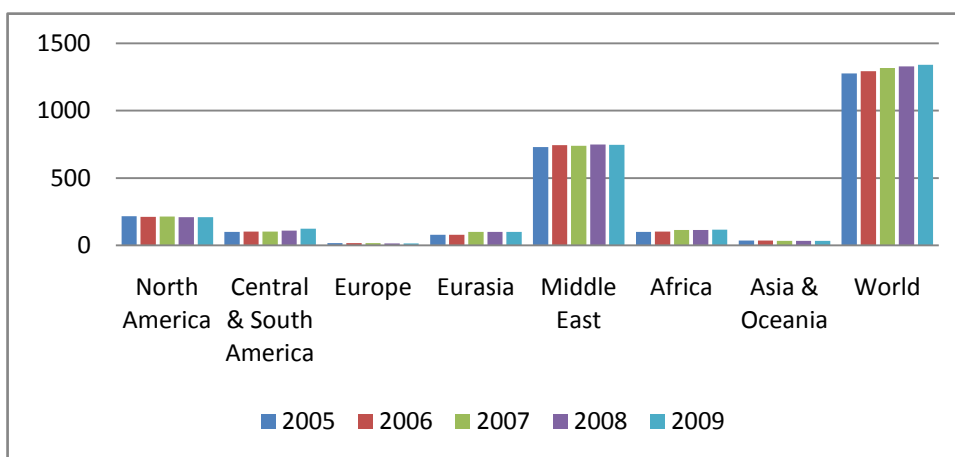


Figure 2: Crude Oil Proved Reserves (Billion Barrels) [8]

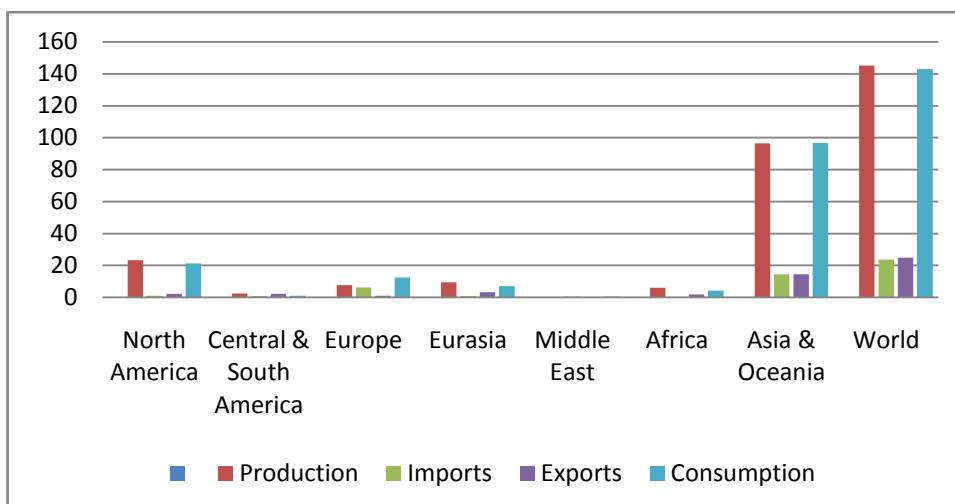


Figure 3: Coal Overview 2009 (Quadrillion Btu) [8]

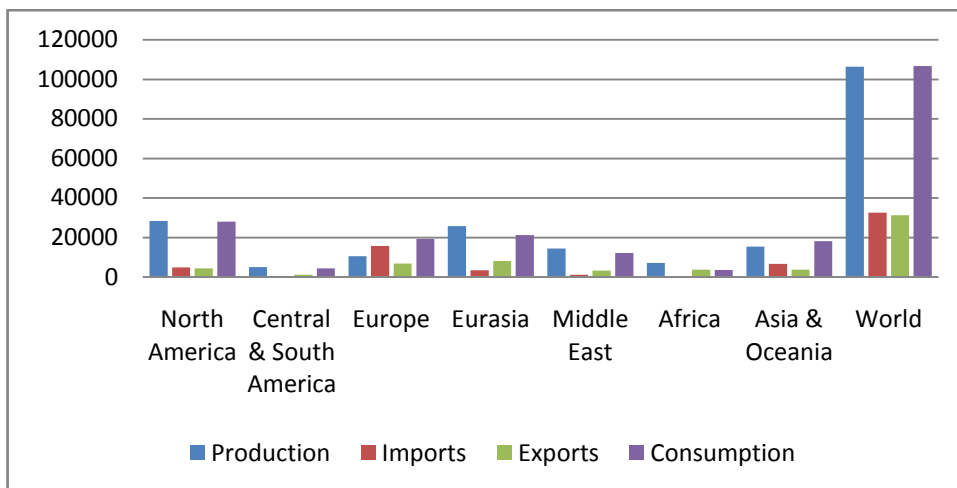


Figure 4: Natural Gas Overview 2009 (Billion Cubic Feet) [8]

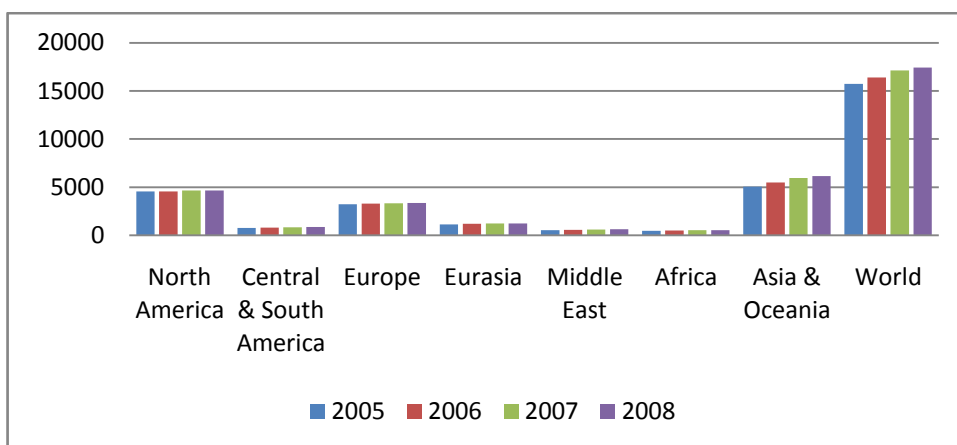


Figure 5: Total Electricity Net Consumption (Billion Kilowatt-hours) [8]

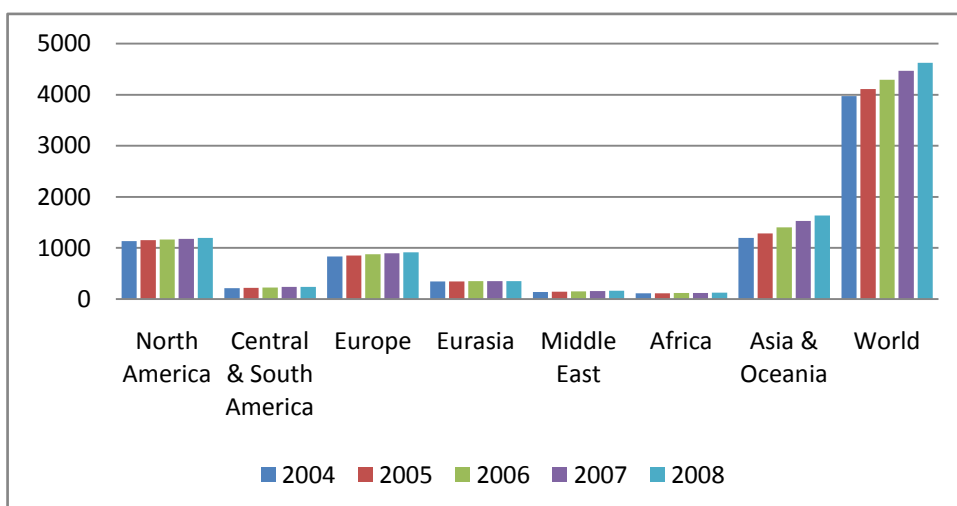


Figure 6: Total Electricity Installed Capacity (Million Kilowatts) [8]

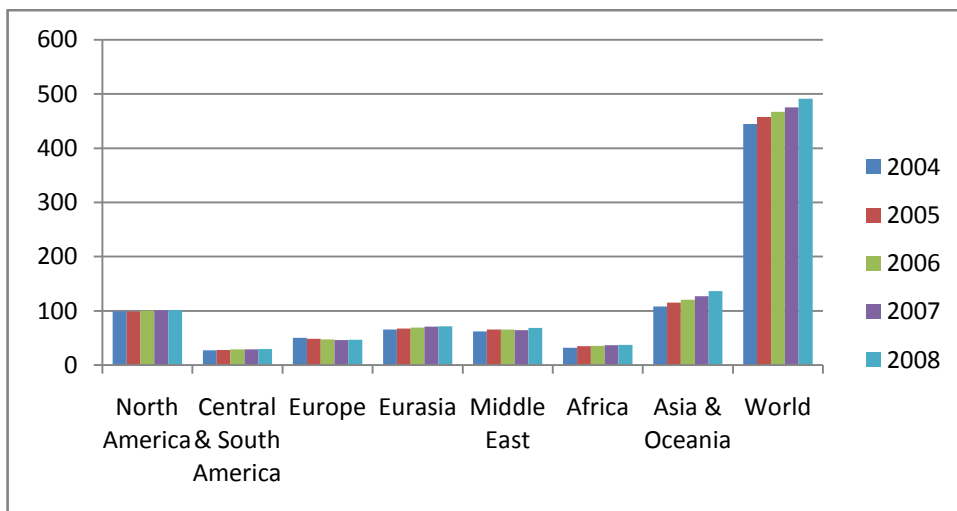


Figure 7: Total Primary Energy Production (Quadrillion Btu) [8]

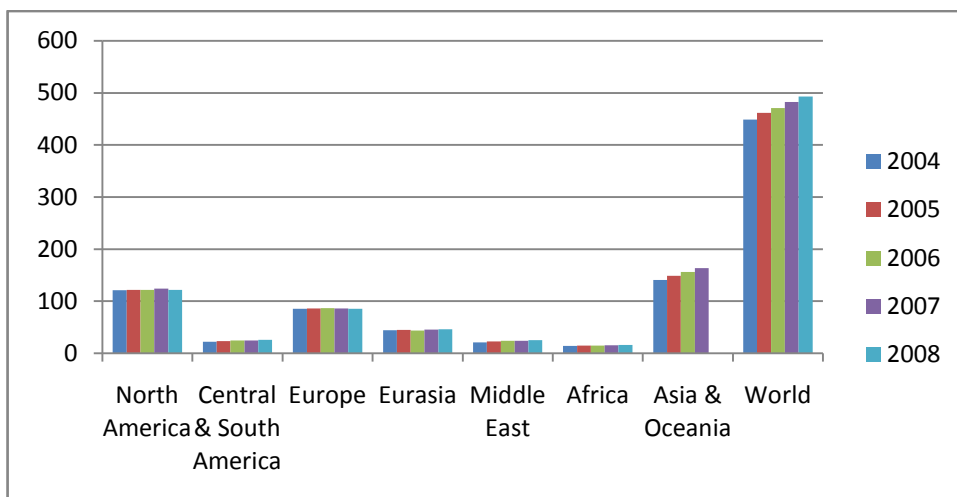


Figure 8: Total Primary Energy Consumption (Quadrillion Btu) [8]

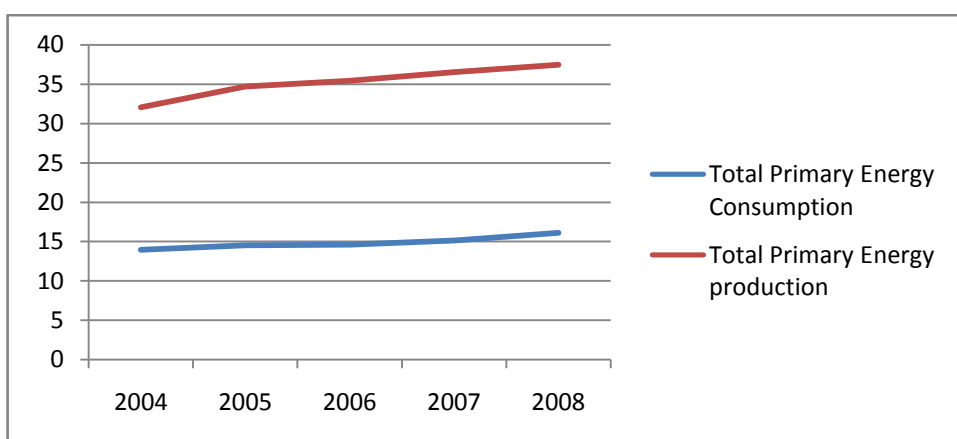


Figure 9: Total primary Energy Consumption/Production in Africa between 2004-2008[8]

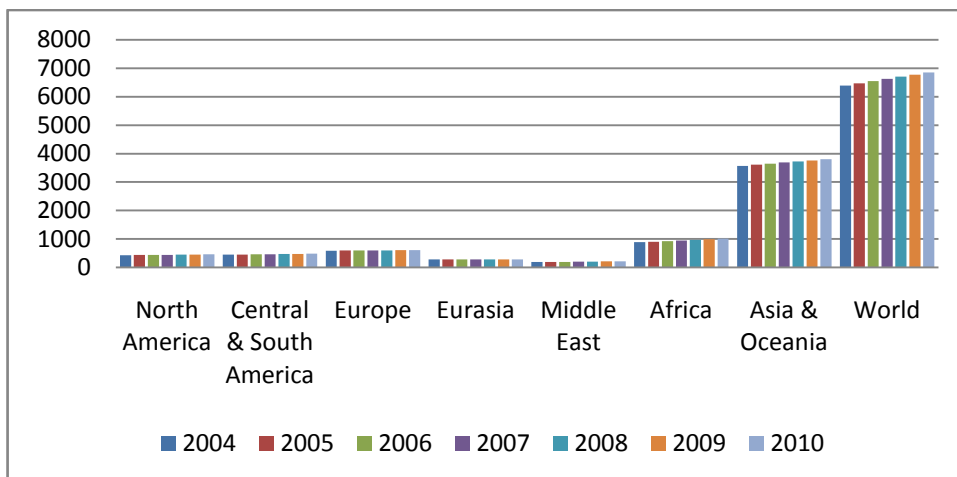


Figure 10: Population (Millions) [8]

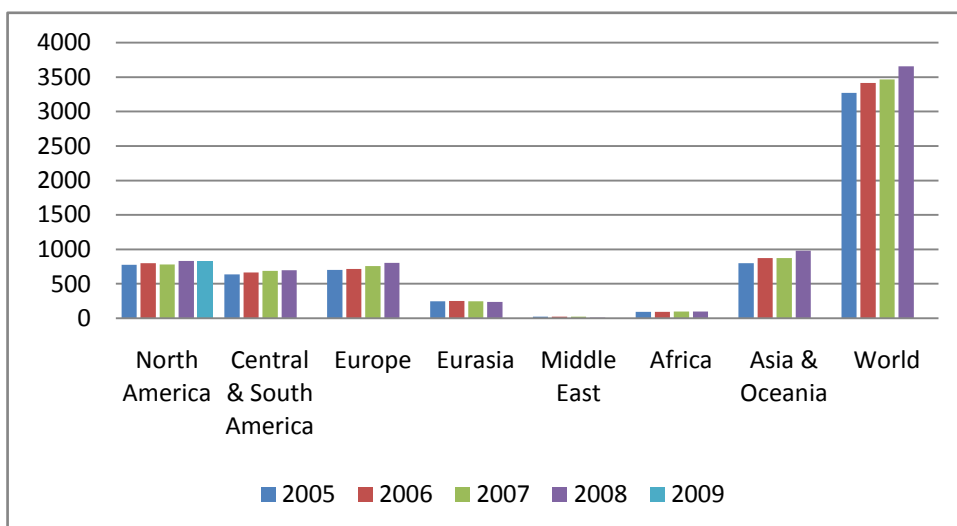


Figure 11: Total Renewable Electricity Net Generation (Billion Kilowatthours) [8]

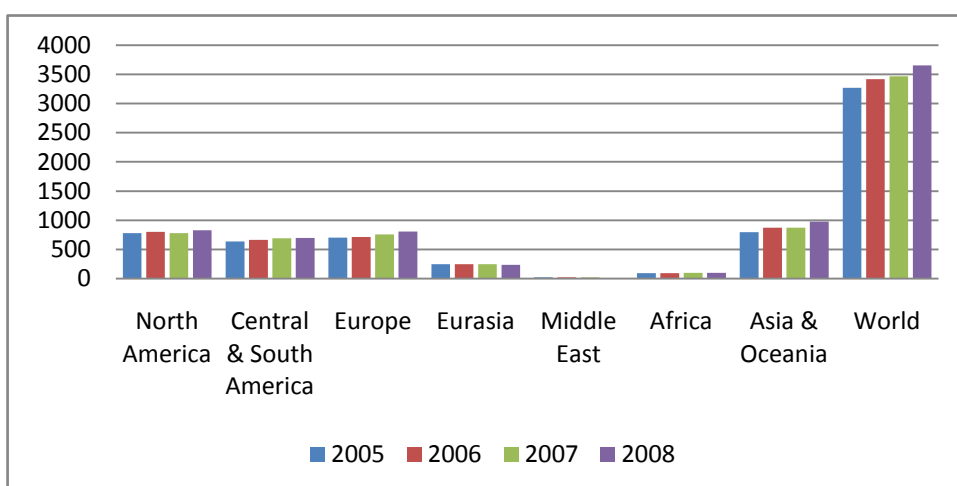


Figure 12: Total Renewable Electricity Net Consumption (Billion Kilowatthours) [8]

3. WHY THE POOR AFRICAN ENERGIZATION

With the energy capacity of Africa the continent can not still meet its electricity demand. There are numerous proven technologies for electricity generation in the world as seen in Europe and North America yet Africa can not adequately convert her energy sources to meet her energy requirement. Many African countries are significantly endowed in fossil fuels and renewable energy that can translate into economic development that will position the continent in the right direction. Sebitosi et al (2004) has identified the root problems as Policy issues, issues of social equity and environment, impact of rural administration and politics. This list ignores major factors like low per capita income in most of the African countries, low level of industrialisation, poor maintenance culture, technical inadequacy, lack of suitable personnel, huge migration of working age to Europe and North America and weak penetration of household appliances. For instance in Africa countries, the percentage of technical and economic hydropower potential currently exploited is around 7%, making it the lowest in the world when compared with 75% in Western Europe and about 22% in Middle East [8]. Leadership problem is evident in most African countries a factor that contributes to poor policy implementation. Policies implementation in Africa goes with the game of politics and bad governance. For instance, the Nigerian government initiative to generate 10,000MW of electricity before 2010 was seen as an improvement on the part of the government and a sum of \$3-\$16 billion was committed to the initiative that produced nothing, up till now Nigeria generates less than 6,000MW. The fabrics of most Africa governments have been laced with corruption allegations but none have been convicted in the real sense of it. Africa Development Bank (AfDB) estimated that the continent is losing in excess of US\$300 billion annually through corruption, an amount higher than donor and aid inflows to Africa yearly. Corruption diverts funds intended for development and undermines government's ability to provide basic services and discourage foreign investment. Other factors include capital requirements of Electricity generation for the small Africa countries, persistent civil wars and unrest in most part of the continent. Another important factor that is underlining poor energy utilization in Africa is the variance in energy data in Africa. When it comes to Africa data collation issues are a source of conflict, for instance the World Bank records 12% access level for Zambia while IEA records 19% this discrepancy in data collection/record show that true situation in most Africa countries are not transparent. Figure 5&6 represent Total Electricity Net Consumption and the Total install capacity, it will be observed clearly that Africa can not compare with the other region in the world. The consumption is equal to the install capacity while the likes of the North America are producing more than their consumption. In fact, the true consumption of electricity in Africa is actually thrice what was shown on the figure, majority of business operate on stand alone generators to meet there electricity need. If the Total Electricity Net Consumption as seen in Figure 5 is compare with Figure 10 which shows population, it will shows that the consumption does not truly represent the

population. Figure 7&8 shows basic comparison between Africa, North America, Central and South America, Europe, Eurasia, Asia and Oceania and the world in Total Primary Energy Consumption and Total Electricity Net Generation. Africa produces more primary energy but consume less of it, a trend we saw earlier too. This shows that the problem of Africa energization is not of resources but more politically and technical. Figure 9 show the wide gap between Africa primary energy production and consumption. If Africa will be energized herself, there is a need to reduce the gap between its primary energy consumption and production. The revenue generated from exporting primary energy to other continents has not transcended into cutting technology to harness its own resources. Figure 11&12 shows Total Renewable Electricity Net Generation and Total Renewable Electricity Net Consumption, few countries are taking the advantage of the renewable energy for electricity generation. Africa have land mass for biomass that can make her the leading producer of biomass. The current fear on Africa biomass is the issue of food insecurity.

4. RENEWABLE ENERGY CAPACITY BUILDING STRATEGIES

The challenges facing the development of a viable energy sector in Africa need to be properly addressed. Most African countries depend on traditional biomass to meet their basic energy needs due to corruption which resulted into high level of poverty and uneven wealth distribution. There is need for a huge development of energy infrastructure to improve the current per capital energy consumption in Africa. A sustainable energy in Africa will equally address the challenges of poor economic and social development and will ensure access to secure, affordable and reliable energy. Capacity building strategies in the following areas will enhance the development of secure energy in Africa.

- A mandatory renewable energy sources development across Africa through the auspices of Africa Union (AU).
- Development of Agricultural, Engineering and entrepreneurship projects that can reduce the migration of youth to Europe and North America.
- Private led financing mechanisms that can support the integration of renewable energy into the existing convectional energy sources.
- Incentives to attract Independent power producer to utilise renewable energy sources
- Creating atmosphere that reduce investments risks e.g solving ethnic wars
- Allowing the Africa Development Bank to play more in financing trans- countries energy projects
- Collaborating with the developed countries to increase the Hydropower utilisation
- Solving the gas flaring in Africa
- Establishing Africa energy policies that will involve all the Africa countries
- Creating an Africa energy information centre that will help to manage data and information on Africa energy

5. POLICY, REGULATORY, AND DEVELOPMENTAL FRAMEWORKS

Finances for most energy projects in Africa comes from oversea donors and investors, huge government mismanagement coupled with corruption have left most of the reserve of Africa countries empty. A high Priority should be given to sustainable financing programmes for renewable energy technologies projects. Nigeria for instance can use her Petroleum Trust Fund (PTF) for the integration of renewable energy into the national electricity grid. In Ghana, a national energy fund has been successfully utilized to finance renewable energy projects and energy efficiency activities on a sustainable basis. According to Africa Development Bank an estimate of US\$ 547 billion will be required to power African countries by 2030, this on yearly average will require over US\$ 27 billion per year from Sub- Sahara region but total funding to the energy sector in Sub-Saharan African is just about US\$ 2 billion every year. This difficulty in financing the energy sector in Africa will require external investments from the developed economy interested in the energy market in Africa. The new financing options should include mobilizing local and foreign financing, aid and grants; foreign direct investments; carbon financing. The private led local participation investment in Africa can only meet the financial demand of small-scale renewable energy systems as can be seen in some Africa countries like Nigeria and south Africa but the bulk finances needed to energize Africa will require huge investment from international financing organizations that will need guaranty from beneficiary government. Foreign investor participation will be attracted if ADB can create a section that operates as an insurance and broker body for the foreign investors interested in Africa market.

6. CAPACITY BUILDING IN TECHNOLOGIES ACQUISITION

The Africa continents need to move from being a technology user to technology producer like the Asian tigers countries. The African countries need to develop sub-regional, regional and continental research and development (R&D) capacity, technology manufacturing skills and good technology transfer adaptation strategies. It is not enough for Africa countries to be receivers when it comes to the state of art technology. The continent will do well if they can develop their own domestic technology capacities to than accommodate technology transfer adaption, and improve the technology through domestic innovation. Technology relationships in Africa with the developed world have mainly been one-way but the continent need to enter into two-way relationships with the develop countries to help build his own domestic capacity. Improving domestic innovate technology require financial and human resource in all the Africa countries. The Continent will have to initiate energy policies that will foster technology transfer and also assist in building its own technology. The need to invest in energy facilities and human personal is very crucial to the development of technology in Africa and the continent will need to strategies ways to stop his vibrant youth from migrating to the

developed world by providing adequate facilities and projects that will put into use their skills. The Africa continents is blessed with great minds that can do well in Science, Engineering and Medicines as can be seen from their contribution in the developed world. The brain drain systems like skilled immigrant to the developed countries need to be tackled by providing an environment that support good thinking and innovation. This will also promote and strengthen the domestic knowledge base, stimulate learning and innovation, and create the support structures to sustain energizing the Africa continent. Although most African countries do have operating skills and some modification skills, they will need both productive and innovative skills to scale up. If Africa countries will step up energy market they will need to enlarge there research base and thread the path of cutting-edge R&D as seen in Europe and America. Also the continent will need to consider technological maturity, reliability and financial feasibility to develop into the world technology hub. Africa will be better off committing itself into developing renewable energy technology like the Hydropower, Solar and Wind energy that will have immediate effects on its energy situation.

7. CONCLUSION

There are significant renewable and non-renewable energy sources in Africa which if fully exploited can energize the continent. Exploiting these resources face a number of challenges in most Africa countries, the most important being its ability to optimize the use of these resources in providing for its own use. The Africa continent needs to improve its economic and social development in order to compete favorably with other continents. The current advance in the use of renewable energy in generating electricity presents the continent with a unique opportunity to develop effective and contextualized strategies that would promote the dissemination of renewable energy technologies so as to address existing energy needs. This work recommended capacity building strategies in finance mobilization and policies to scale up renewable energy technologies in African energization. However, these capacity building strategies will not effectively assist in increasing the energy consumption in Africa if the business as usual scenario continues. The need for policy makers to adopt modest policies that will integrate renewable energy to the continent's energy mix and invite all development partners to assist the continent should be encouraged.

REFERENCES

- [1] Abeeku Brew-Hammond. Energy access in Africa: Challenges ahead. Energy Policy 38 (2010) 2291–2301
- [2] World Population Prospects: The 2006 Revision" United Nations (Department of Economic and Social Affairs, population division)
- [3] Population reference bureau. 2009 world population data sheet. www.prb.org

- [4] U.S Energy information Administration. Independent Statistical and Analysis. www.tonto.eia.doe.gov
- [5] International Energy Agency, IEA – “Energy Balances for Non-OECD Countries”, 2006 Edition, IEA, Paris, 2006.
- [6] Karekezi, S., and Ranja, T. 1997. Renewable Energy Technologies in Africa. ZED Books and AFREPREN. Oxford U.K
- [7] World Population Prospects: The 2006 Revision" United Nations (Department of Economic and Social Affairs, population division)
- [8] IAE – Electricity Information, 2006.

Concentrations of Natural and Man-Made Radioactivity Soil and Ground Water in Al-Madinah Al-Monawarah

Afaf A. Fakeha^{1,2}, Safiah Q. Hamidalddin^{1,3} Nuha Abdul-Hameed Al-Turkestany^{1,4}, Ahlam M.A. Al-Amri^{1,5} and Nagdya M.Ibraheim⁶

¹Department of Physics, Faculty of Science for Girls, King Abdulaziz university, Jeddah, Saudi

²Corresponding author. Tel.: +966505546949 (sabrytaha2000@yahoo.com)

^{3,4,5}(safiahqh@yahoo.com); (alturki28@hotmail); (ahlam1403@hotmail.com)

⁶Nuclear Safety Centre (EAEA)

ABSTRACT

Al-Madinah Al-Monawarah lies around latitude 39°36'00", longitude 24°28'00", altitude 624 m. Ten surface soil samples were collected from Al-Madinah Al-Monawarah province with a template 30×30×15 cm. Samples were analyzed by atomic absorption spectrometer for Aluminum (Al), Iron (Fe) and Calcium (Ca) concentrations in percent, Lead (Pb) and Arsenic (As) in ppm. The concentrations range for Al from (4.48 -7.65%), Fe from (3.08 -4.92 5%), Ca from (1.66 -10.60 %), Pb from (14 -27 ppm) and As from (10.5 -30.7 ppm). Also XRD spectrometry was applied for the chemical and mineral composition, the major and minor composition is ALBITE, CALCITE, CLINOCHLORE, MICROCLINE, QUARTZ. Gamma- ray spectrometer based on HPGe crystal was applied for the concentrations in Bq/kg dry weight, for (²³⁸U and ²²⁶Ra series) from 7.01 to 15.55 Bq/kg, (²³²Th and ²²⁸Ra series) from 5.23 to 21.8Bq/kg, ⁴⁰K concentrations range from (64.6 to 754.2 Bq/kg). The man-made ¹³⁷Cs was observed in some samples. The radium equivalent Bq/kg was calculated, and the absorbed dose rate nGy/h for each sample was calculated one meter above the earth. It is found that the values of the absorbed dose are in the accepted range put by EPA (Environmental Protection Association). Four underground water samples from the study area Al-Khief (Western province of Saudi Arabia) were analyzed by both an atomic absorption spectrometer for the; Ca, Na, Mg, K, Fe, Al, Cs, Hg, Bi, Pb and U concentrations, and a HPGe gamma-ray spectrometer system for the concentrations of radioactive nuclides of the ²²⁶Ra and ²³²Th series and ⁴⁰K from the absorbed dose which calculated for the age categories; <1y, 1-2y, 2-7 y, 7-10y and > 17y.

Keywords: atomic absorption, gamma-ray spectrometry, natural radioactivity, absorbed dose.

1. INTRODUCTION

Study of radioactivity levels and concentrations of natural and man-made radionuclides have been done all over the world. In Egypt (Ibrahiem et al 1993) gave a base map for the radioactivity in the Delta and middle Egypt, by HPGe gamma-ray system they measured the absorbed dose one meter above the ground in each point. Also (Ibrahiem et al 1995) studied sediments and surface area of Naser lake area by both neutron activation analysis and gamma-ray spectroscopy techniques. Amaral, 2000, in Portugal studied gamma-ray spectrum and dose rate In Situ, also studied the type and composition of the different rocks, as well as the mechanical, chemical and biological properties for each type of soil. Melo et al 2000; studied the severe internal dose in Brazil from the high radioactivity concentrations due to the concentrations of uranium and thorium in this area. Morton et al, 2006, measured the natural radioactivity concentrations ²³²Th, ²³⁸U and ²²⁶Ra series and ⁴⁰K, as well as the man made ¹³⁷Cs. Also they studied the salinity level in the soil from the series of the black plateau resulting from the flood of Virgin River, south-east of Nevada state USA. They analyzed the samples by EDS electron dispersion spectrometer in addition XRD diffraction spectrometer for the soil composition. Wu, 2006 studied the accumulation of radioactive concentrations owing to the long period of

irrigation according to the Yucca Mountain program of Nevada state USA to point out, time needed to reach equilibrium, the suitable time for irrigation, study of agricultural areas irrigated for long time and the change of concentrations of radioactive nuclides in water.

Flrou et al, 2007; studied the effect of the external dose intake for areas of high radioactivity levels in three islands from Greece of volcanic origin. In these areas many geothermal springs gives gases as carbon monoxide, carbon dioxide as well as radon. Study was done by In Situ NaI(Tl) spectrometer, concentrations of natural radionuclides in soil, spring water, sea water and sediments, they calculated the dose rate and the external risk also the quality assurance of the ecosystem. Baykara and Dogru, 2008, studied 72 soil samples from the northern and eastern regions of Anadool of Turkey, by NaI(Tl) for the concentrations of radioactivity and dose rate. Santos et al 2009 analyzed 78 soil samples by HPGe gamma-ray system for the concentrations of ²²⁶Ra and ²²⁸Ra. Jankovic Mandic et al studied the distribution of natural radionuclides in Belgrad province, Serbia, they compared the results with some published work. Saidou et al, 2011 studied site for uranium mining in Cameron to plot a base line map for Poli province, they found that the concentrations of radionuclides and the absorbed dose are slightly higher the world average.

The aim of this work is to make base line map for the study area, to be compared with future studies for any environmental or geological changes. Study of the relation between type of soil and the radioactivity level, measurements of dose rate for population in this area, also *relation* between the geological composition of the soil and the dose rate.

2. GEOLOGY OF THE STUDY AREA

The study area lies east of the Red sea between 24° 22' 27" and 24° 32' 16" latitude north and 39° 31' 36" and 39° 43' 11" longitude east and elevation 625m above the sea level. 430km from Mekka, 220km from Yanboa the nearest port to Al-Madina Almonawra, 150km from the Red Sea, and 980km from Al-Reyad. Mountain Ohod from the north, mountain Salaa north- west, Harrat Waqem and Wabara from the south. (Badr, 1993). Rock types in the study area are :

- 1-Volcanic rocks, Silicic volcanic rocks, pyroclastic rocks and rhyolitic tuff.
 - 2-Sandy rocks.
 - 3-Sedimentary rocks, from the erosion of volcanic rocks.
 - 4-Breccia Andesitic. 5-Basalt. 6-Sandy regions. 7- Sandstone.
 - 8-Harrat areas, Harrat Khyber and Harrat Hirmah.
- Al-Madina also contains vales from sand and clay, and sediments from granite, (Saudi Geological Survey, 2010).
- 9-Felsic rocks. 10-Quaternary deposits.

3. SAMPLING AND SAMPLE PREPARATION

The study area was divided to 10 parts, a sample was collected from each part. Sampling were done from 0 to 15 cm by a template 30x30x15 cm. Samples were collected in a polyethylene bags, then labeled. Remains of plants, weeds and rocks were removed, then soil samples were grinded, sieved with a 1mmx1mm mesh sieve, mixed for homogeneity. Samples were dried to 80 °C not to lose the volatile ¹³⁷Cs or the natural polonium. A 640 cc of the dried sample were weighed then stored for one month in a polyethylene Marinelli beaker, for gamma-ray spectrometry, to reach secular equilibrium between ²²⁶Ra and ²²⁶Th and their progeny. A 10 gm of the dried sample were used for the analysis by atomic absorption for the K, Al, Bi, Pb and Th concentrations. Also 10 gm for XRD for the chemical and mineral composition.

Sampling was done obeying methods adopted by Her Majesty's Office, the UK Atomic Energy Authority and UK Nirex Ltd, (RADREM, 1980).

4. MEASUREMENTS

An X-ray diffraction spectrometer model Burker XRD D8 Advance was applied for the chemical and mineral

composition. Also an inductively coupled plasma atomic absorption spectrometer of A-Analyst 700 model Perkin Elmer OPTIMA 4000 DV series, was used for the concentrations of Pb and As ppm and Al, Fe and Ca %.

A gamma ray spectrometer based on a HP Ge crystal of the vertical type Canberra model number GC2520, cryostat Canberra model 7500SL, FWHM 1.06 keV for the transition 122 keV ⁵⁷Co and 2.0 keV for the transition 1332.5 keV of ⁶⁰Co, peak to Compton ratio 53:1, relative efficiency 27.1%, were applied for the concentrations of the natural ²³²Th and ²²⁶Ra series and ⁴⁰K and the manmade ¹³⁷Cs.

Multichannel analyzer of 8K ADC (analogue to digital converter), Genie 2000 program, were used for spectrum analysis. ¹⁵²Eu in 640cc Marinelli beaker, the same type, volume and material of these used for measurements, were used for absolute calibration, and natural KCl with three different concentrations, as well as ²²⁶Ra point source normalized to the same configuration.

Energies (keV) of 295.2 (20.1) and 351.9 (38.3) ²¹⁴Pb and 609.3 (49.9), 1120.3 (16.2) and 1764.5 (16.0) ²¹⁴Bi were used for the ²²⁶Ra series. 338.4(13), 911.16(30.3) and 968.97(18.3) ²²⁸Ac and 727.25 (8.1) ²¹²Bi, also 583.02(33.2) and 2614.48(35.9) ²⁰⁸Tl for the ²³²Th series (Saito & Moriuchi;1985). 1460.8(10.7) for the ⁴⁰K and 661.65(89.9) for the ¹³⁷Cs (Holden;2003).

5. RESULTS AND DISCUSSION

Table (1) represents XRD analysis results it shows the major and minor minerals. The major mineral is the quartz (SiO₂), the next is albite (NaAlSi₃O₈), then calcite (CaCO₃). The minor minerals are clinocllore (MgFe²⁺17Si₂₀ O₅₄(OH)₆], and microline (KAlSi₃O₈).

Table (2) gives concentrations of Al, Fe and Ca % and Pb and As ppm by atomic absorption analysis. The stable lead (²⁰⁸Pb, ²⁰⁶Pb and ²⁰⁷Pb) ranged from 14.00 to 27.00 ppm. Calcium, (⁴⁰Ca, ⁴²Ca, ⁴³Ca, ⁴⁴Ca, ⁴⁶Ca and ⁴⁸Ca), they are all stable, ranged from 1.66 to 10.60%. Arsenic (⁷⁵As) ranged from 10.50 to 30.70 ppm. Aluminum (²⁷Al) ranged from 4.5 to 7.7%. Iron (⁵⁴Fe, ⁵⁶Fe, ⁵⁷Fe and ⁵⁸Fe), ranged from 3.08 to 4.92%.

Table (3) represents concentrations of radionuclides for the natural ²³⁸U – ²²⁶Ra series and ²³²Th – ²²⁸Ra series and ⁴⁰K and the manmade ¹³⁷Cs, Bq/kg dry weight.

For the ²³⁸U – ²²⁶Ra series concentrations protactinium-234m (^{234m}Pa) ranged from LDL to 12.3, and the ²²⁶Ra series from 7.01 to 1555. This shows disequilibrium in the series. For the ²³²Th – ²²⁸Ra series concentrations ranged from 5.23 to 21.8,

disequilibrium can't be observed in the series. The main reasons for disequilibrium the difference in chemical and physical properties of the elements in the series, weathering, radon as a gas can escape from the sample, also the emission of beta or alpha particles may led the residual nucleus leaving the crystal. ⁴⁰K concentrations ranged from 62.6 (2.2%) to 754.2 (25.5%) this sample contains microlene (KAl Si₃O₈).

Figures (1,2 and3) show the relations between ²²⁶Ra and ²²⁸Ra, ⁴⁰K and ²²⁶Ra and ⁴⁰K and ²²⁸Ra. ¹³⁷Cs were found in four samples concentrations around 3.0 Bq/kg dry weight. The Ra_{eq} is calculated from the equation (1) (Tufail et al 2006) :

$$Ra_{eq} = A_{Ra} + (A_{Th} \times 1.43) + (A_K \times 0.077) \quad (1)$$

Where; A_{Ra}, A_{Th} and A_K are concentrations Bq/kg for radium, thorium and potassium respectively.

The absorbed dose nGy/ h is given by the equation (2) (Quindos et al, 2004):

$$D = C_{Ra} A_{Ra} + C_{Th} A_{Th} + C_K A_K \quad (2)$$

Where: C_{Ra}, C_{Th} and C_K are the conversion factors Bq/kg to nGy/h for radium, thorium and potassium (Quindos et al 2004).

Table (4) represents the values of the Ra_{eq} and the absorbed dose. The Ra_{eq} Bq/kg dry weight ranged from 22 to 104.9, less than 370 adopted by EPA for the permissible value. Using the conversion factors from Bq/kg to nGy/y (Quindos et al,2004) the adsorbed dose one meter above the ground, ranged from 10 nGy/h (>1mmGy/y) to 52.2 nGy/h (0.46 mGy/y), it is within the permissible value given by EPA and UNSCEAR.

As a conclusion the collected samples show that the study area is safe for the radiological levels, for either to live or to cultivate if the type of soil is suitable.

Table (5) gives a comparison of the activity concentrations in the present work and some published values. Table (6) represents elemental concentrations in ppm or ppb measured by ICP-Atomic Absorption spectrometer for four samples from AL-Khief.

For Ca, the concentrations in ppm of the samples are in the accepted range. For Na, results show that samples have concentrations in ppm higher than the guideline value set by EPA, and need chemical treatment before using for drinking purposes. For K, the concentrations in ppm of the samples are less than the acceptable values per a day per person. For Fe, the concentrations in ppm are ranged from <0.1 to 3.08. For Al, the concentrations in ppb of the samples ranged from 33.53 to 2268.17. For Cs, the concentrations in ppb of the samples ranged from <0.1 to 0.39, Hg and Bi, the concentrations in ppb are <0.1. For Pb, the

concentrations in ppb are less than the guideline value set by EPA. For U, the concentrations in ppb of the samples are in the accepted range.

Table (7) Shows Concentration of radioactive nuclides in water for four samples in Bq/l measured by HPGe. The measured concentrations ranged from 0.001 to 0.016 for ²³⁸U and from 1.4±0.2 to 11.0±0.6 for ²²⁶Ra series and from LDL to 8.5±0.6 for ²³²Th series (²²⁸Ra) and from LDL to 339.2±3.0 and LDL for ³⁷Cs. Table (8) represents dose conversion factors for ²³⁸U, ²²⁶Ra and ²²⁸Ra in SvBq⁻¹.

Table (9) represents the annual dose measured from ²³⁸U, ²²⁶Ra and ²²⁸Ra in mSv/y for age class ≤ 1 y (infants) to class >17 y (adults).

The results show that the samples exceeded the annual limit of dose allowed by WHO (0.1 mSv/y) for all radioactive nuclides in drinking water, so samples need chemical treatment.

4. TABLES

Table 1: XRD analysis results

Sample No.	Major	Minor	Trace
SU-1	Quartz, Albite	Microcline, Cliniochlor, Calcite	Ludlokite, Biotite Augite, Magnetite
SU-2	Quartz, Albite	Calcite, Clinochlore	Geigerite, Microcline, Reevesite, Biotite, Magnetite
SU-3	Calcite, Quartz	Albite, Clinochlore	Magnetite, Tinaksite, Dundasite, Geigerite
SU-4	Quartz, Albite	Microcline, Calcite, Kaolinite Faujasite, Augite, Magnetite
SU-5	Quartz, Albite, Microcline	Clinochlore	Calcite, Volkovskite, Magnetite
SU-6	Quartz, Albite	Clinochlore	Calcite, Augite, Magnetite, Pargasite, Biotite, Ludlokite
SU-7	Quartz, Albite	Calcite, Clinochlore	Reevesite, Biotite, Magnetite, Pargasite
SU-8	Quartz, Albite	Clinochlore, Calcite	Pargasite, Augite, Biotite, Magnetite
SU-9	Quartz, Albite	Calcite, Clinochlore	Biotite, Augite, Pargasite, Microcline
SU-10	Quartz, Calcite, Albite	Clinochlore	Pargasite, Biotite, Tunisite, Offretite, Magnetite

Table 2: Results of the atomic absorption analysis

Elements	Al	Fe	Ca	Pb	As
DL.	0.25	0.05	0.05	1.00	5.50
Units	%	%	%	ppm	ppm
SU - 1	6.98	4.72	3.75	19.00	10.50
SU - 2	7.65	4.68	4.98	18.00	12.30
SU - 3	4.48	3.08	10.60	14.00	29.10
SU - 4	6.18	4.60	2.78	16.00	30.70
SU - 5	6.84	3.08	1.60	16.00	17.26
SU - 6	6.61	4.60	3.48	16.00	17.30
SU - 7	6.79	4.68	3.51	19.00	13.41
SU - 8	6.73	4.92	3.28	15.00	12.20
SU - 9	6.80	4.32	5.04	27.00	15.70
SU - 10	6.04	4.14	8.00	25.00	28.60

Table 3 continued

Sample code.	Concentration Bq/kg dry weight		Concentration %
	K-40	Cs-137	Natural-K
SU-1	262.69 ±1.42	0.94 ±0.078	8.875 ±0.048
SU-2	255.30 ±0.95	3.09 ±0.099	8.63 ±0.032
SU-3	64.64 ±0.033	3.6 ±0.16	2.183 ±0.011
SU-4	301.32 ±1.14	2.51 ±0.085	10.18 ±0.039
SU-5	754.21±2.31	1.7 ±0.06	25.48 ±0.078
SU-6	328.36 ±1.22	3.13 ±0.095	11.093 ±0.041
SU-7	312.40 ±1.57	3.181 ±0.133	10.554 ±0.053
SU-8	409.74 ±2.28	1.484 ±0.102	13.842 ±0.077
SU-9	265.92 ±1.42	0.91 ±0.071	8.984 ±0.048
SU-10	209.38 ±1.09	LDL	7.074 ±0.037

LDL : Lower than Detection Limit

Table 3: Represents concentrations of radionuclides for the natural $^{238}\text{U} - ^{226}\text{Ra}$ series and $^{232}\text{Th} - ^{228}\text{Ra}$ series and ^{40}K and the manmade ^{137}Cs , Bq/kg dry weight

Sample code.	Concentration Bq/kg dry weight		
	U-Ra series		Th series
	$^{214\text{m}}\text{Pa}$	Ra-226	Ra-228
SU-1	LDL	7.75 ±0.057	6.84 ±0.078
SU-2	12.1±0.56	10.54 ±0.051	13.95 ±0.09
SU-3	4.6±0.51	7.71±0.05	6.46 ±0.055
SU-4	3.56±0.29	10.08 ±0.044	18.79 ±0.13
SU-5	LDL	15.55 ±0.064	21.84 ±0.13
SU-6	11.42 ±0.52	7.01 ±0.037	8.21±0.054
SU-7	12.3±0.75	10.21 ±0.066	14.86 ±0.13
SU-8	LDL	8.45±0.063	8.02 ±0.099
SU-9	4.8±0.47	8.72±0.062	5.23 ±0.054
SU-10	9.7±0.7	7.60±0.045	6.16 ±0.058

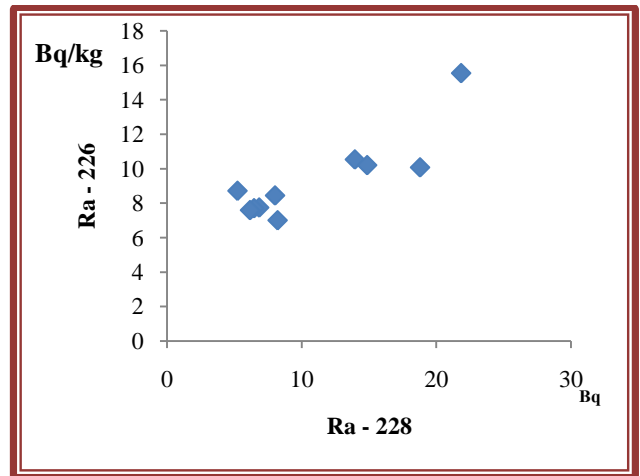


Figure 1: Relative between ^{228}Ra and ^{226}Ra per Bq/kg

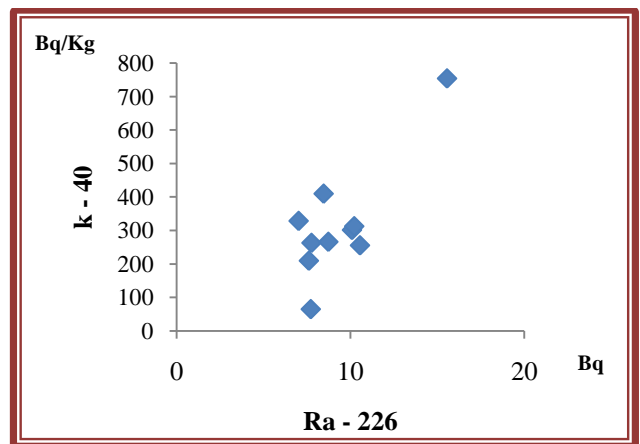


Figure 2: Relative between ^{226}Ra & ^{40}K per Bq/kg

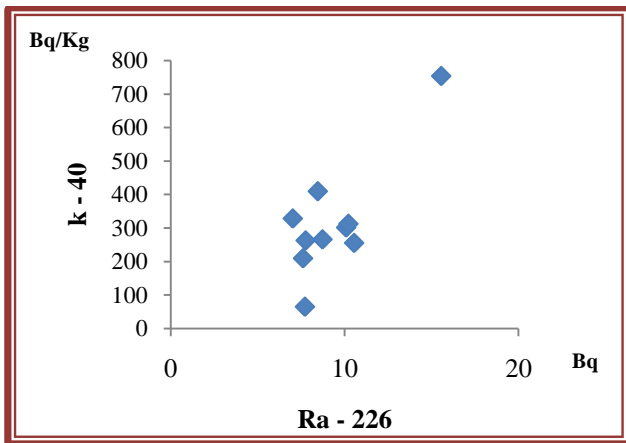


Figure 2: Relative between ²²⁶Ra & ⁴⁰K per Bq/kg

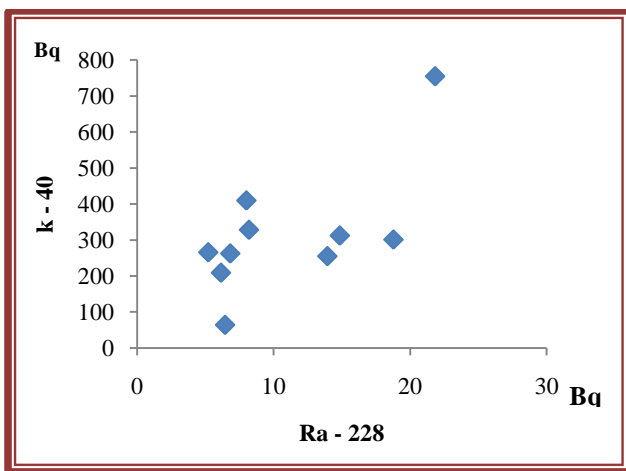


Figure 3: Relative between ²²⁸Ra & ⁴⁰K per Bq/kg

Table 5: Comparison of isotopes concentrations in Bq/kg dry weight concentrations in the present work and some published results

Reference	Present work	Ibrahiem <i>etal.</i> 1993	Ibrahiem <i>etal.</i> , 2003	Al-Garni Z., 2008
U-238-Ra-226	7.01-15.55	5.2-63.7	31-55	9.2-18.1
Th-232-Ra-228	5.23-21.8	2.5-95.6	2.4-3.2	9.5-22.6
K-40	64.6-754.2	29-653	65-1046	378.2-592.6

Table 6: Element concentrations in ppm or ppb measured by ICP-Atomic Absorption Analyzer in water samples

Elements	DL	Sample-1	Sample-2	Sample-3	Sample-4
Ca(ppm)	0.2	72.1	152.6	78	180.5
Na(ppm)	0.2	28.4	96.1	254	171.7
Mg(ppm)	0.2	15.3	36.5	28.5	53.7
K(ppm)	0.2	5.9	10.2	3.4	6.2
Fe(ppm)	0.1	0.31	0.13	<0.1	3.08
Al(ppb)	0.1	296.07	111.68	33.53	2268.17
Cs(ppb)	0.1	<0.1	<0.1	0.39	0.1
Hg(ppb)	0.1	<0.1	<0.1	<0.1	<0.1
Bi(ppb)	0.1	0.15	<0.1	<0.1	<0.1
Pb(ppb)	0.1	1.66	0.98	1.33	3.36
U(ppb)	0.1	0.1	1.24	1.25	1.14

Table 4: The radium equivalent Bq/kg and the absorbed dose nGy/h.

Sample Code	Ra _{eq} Bk/kg	Absorbed dose nGy/h
SU-1	37.76	18.79
SU-2	50.15	23.89
SU-3	21.93	10.05
SU-4	60.15	28.49
SU-5	104.86	52.17
SU-6	44.03	22.07
SU-7	55.53	26.72
SU-8	51.47	26.10
SU-9	36.67	18.43
SU-10	32.53	16.04

Table 7: Concentration of radionuclides in water samples in Bq/l measured by HPGe

Sample Code	Concentration in Bq/l			
	U-238 *	Ra-226 Series	Ra-228	K-40
DL.	0.001	0.40 ± 0.07	0.30 ± 0.07	4.6 ± 0.5
Sample – 1	0.001	2.02±0.2	LDL	13.6±0.2
Sample – 2	0.015	1.5±0.1	2.2±0.2	33.8±0.4
Sample – 3	0.016	11.0±0.6	8.5±0.6	339.2±3.0
Sample – 4	0.014	1.4±0.2	LDL	LDL

LDL: Lower than Detection Limit

*U-238 is measured as total uranium by atomic absorption spectrometry

Table 8: conversion dose Sv/Bq

Radio-nuclide	Dose conversion factors (K)				
	Sv/Bq				
	≤ 1 y	1-2 y	2-7 y	7-10 y	> 17 y
²³⁸ U	3.4×10 ⁻⁷	1.2×10 ⁻⁷	8.0×10 ⁻⁸	6.8×10 ⁻⁸	4.5×10 ⁻⁸
²²⁶ Ra	4.7×10 ⁻⁶	9.6×10 ⁻⁷	6.2×10 ⁻⁷	8.0×10 ⁻⁷	2.8×10 ⁻⁷
²²⁸ Ra	3.0×10 ⁻⁵	5.7×10 ⁻⁶	3.4×10 ⁻⁶	3.9×10 ⁻⁶	6.9×10 ⁻⁷

Table 9a: The annual dose measured from ²³⁸U, ²²⁶Ra, ²²⁸Ra in mSv/y for age class ≤ 1y

Doses in mSv/y	Age Class <1y			
	Sample 1	Sample 2	Sample 3	Sample 4
²³⁸ U Dose	0.0001	0.0013	0.0013	0.0012
²²⁶ Ra Dose	2.4	1.8	13.2	1.7
²²⁸ Ra Dose	<2.3	16.9	65.2	<2.3
Annual Dose ²³⁸ U+ ²²⁶ R+ ²²⁸ R	<4.7	18.7	78.4	<4.0

Table 9b: The annual dose measured from ²³⁸U, ²²⁶Ra, ²²⁸Ra in mSv/y for age class 1-2y

Doses in mSv/y	Age Class 1-2y			
	Sample 1	Sample 2	Sample 3	Sample 4
²³⁸ U Dose	0.00005	0.0007	0.0007	0.0006
²²⁶ Ra Dose	0.7	0.5	3.9	0.5
²²⁸ Ra Dose	0.6	4.6	17.7	0.6
Annual Dose ²³⁸ U+ ²²⁶ R+ ²²⁸ R	<1.3	5.1	21.5	<1.1

Table 9c: The annual dose measured from ²³⁸U, ²²⁶Ra, ²²⁸Ra in mSv/y for age class 2-7y

Doses in mSv/y	Age Class 2-7			
	Sample 1	Sample 2	Sample 3	Sample 4
²³⁸ U Dose	0.00004	0.0004	0.0005	0.0004
²²⁶ Ra Dose	0.5	0.3	2.5	0.3
²²⁸ Ra Dose	<0.4	2.7	10.5	<0.4
Annual Dose ²³⁸ U+ ²²⁶ R+ ²²⁸ R	<0.8	3.1	13.0	<0.7

Table 9d: The annual dose measured from ²³⁸U, ²²⁶Ra, ²²⁸Ra in mSv/y for age class 7-10y

Doses in mSv/y	Age Class 7-10			
	Sample 1	Sample 2	Sample 3	Sample 4
²³⁸ U Dose	0.00003	0.00038	0.00038	0.00035
²²⁶ Ra Dose	0.6	0.4	3.2	0.4
²²⁸ Ra Dose	<0.4	3.1	12.1	<0.4
Annual Dose ²³⁸ U+ ²²⁶ R+ ²²⁸ R	<1.0	3.6	15.3	<0.8

Table 9e: The annual dose measured from ²³⁸U, ²²⁶Ra, ²²⁸Ra in mSv/y for age class >17y

Doses in mSv/y	Age Class >17y			
	Sample 1	Sample 2	Sample 3	Sample 4
²³⁸ U Dose	0.00003	0.00038	0.00038	0.00035
²²⁶ Ra Dose	0.6	0.4	3.2	0.4
²²⁸ Ra Dose	<0.4	3.1	12.1	<0.4
Annual Dose ²³⁸ U+ ²²⁶ R+ ²²⁸ R	<1.0	3.6	15.3	<0.8

REFERENCES

- [1] Al-Garni, Z. S. M. (2008). Detailed study about the concentrations of natural and man-made radioactivity for Wadi Al-Numan Area in Makkah Al-Mukarramah Province, M. Sc., King Abdul Aziz University.
- [2] Amaral, E. M. (2000). Natural gamma radiation in air versus soil natural in Portugal, The 10th International Congress of the International Radiation Protection Association (IRPA), May 14-19, Hiroshima, Japan: P-1a-12.
- [3] Badr, Abd-Elbaset (1993); History of Al-Madinah Al-Monawarah (1st ed), Al-Madina Al-Monawarah.
- [4] Baykara, O. and Dogru M. (2000). Determination of terrestrial gamma, U, Th and K in soil fracture zones, Radia. Meas., vol. 44no.(1), pp. 116-121.
- [5] Beck, H.L. (1980). Exposure rate conversion factors for radionuclides deposited on the ground. US Department of energy, EMI-378, New York.

- [6] Clouvas, A., Xanthos, S., Antonopoulos-Domis, M., Silva, J., (2000). Montecarlo calculation of dose rate conversion factors for external exposure to photon emitters in soils. *Health physics*, 78, pp. 295-302.
- [7] Florou, H., Trabidou, G., Nicolaou, G. (2007). An assessment of the external radiological impact in areas of Greece with elevated natural radioactivity, *Journal of Environmental Radioactivity*, 93, pp. 74-83.
- [8] Holden Norman, E. (2003). *Table of the Isotopes (Revised 2002)*, BNL-71000-2003-BC.
- [9] Ibrahiem, N.M., Abd El Ghani, A.H., Shawky, S.M., Ashraf, E.M., & Farouk, M.A. (1993). Measurement of Radioactivity levels in soil in the Nile delta & middle Egypt, *Health Phys.*, 64 (6), pp. 620- 627.
- [10] Ibrahiem, N. M., Shawky, S. M. & Amer, H.A. (1995). Radioactivity levels in Lake Nasser sediments, *Appl. Radial. Isot.*, 46 (5), pp.297-299.
- [11] Ibrahiem, N. M. (2003). Radioactive disequilibrium in different rock types in Wadi Wizr, the Eastern desert of Egypt, *Applied Radiation and Isotopes*, 58, pp. 385-392.
- [12] Melo D. Lipsztein, J. L., Juliao, L., Lauria, D., Hacon, S., Dias da Cunha, K. & Cristina Lourenco, M. (2000). Internal chronic exposure to natural radionuclides, The 10th International Congress of the International Radiation Protection Association (IRPA), May 14-19, Hiroshima, Japan: P-1a-24.
- [13] Morton, J., Buck, B., Merkler, D. & Wu, D. (2006). ²³⁸U, ²³²Th, ⁴⁰K, ¹³⁷Cs activity & salt mineralogy in the black butite soil series of the virin river flood plain NV, USA, *Health Phys.*, 90 (6), TAM-A.4.
- [14] Quindos, L. S., Fernandez, P. L., Rodenas, C. Gomez- Arozamena, J. & Arteché, J. (2004). Conversion factors for external gamma dose derived from natural radionuclides in soils, *Jour. Environ. Radioactivity*, 71, pp. 139-145.
- [15] RADREM (1980). *Sampling and Measurement of Radionuclides in the Environment*, A Report by the Methodology Sub-Group to the Radioactivity Research and Environmental Monitoring Committee (RADREM), HER MAJESTY'S OFFICE, the UK Atomic Energy Authority and UK Nirex Ltd.
- [16] Saito, K. and Moriuchi, S. (1985). Development of a Monte Carlo Code for the Calculation of Gamma Ray Transport in the Natural Environment, *Radiation Protection Dosimetry*, 12 (1), pp. 21-2
- [17] Saidou, ; Bochud, Francois O. ; Baechler, Sebastien ; Moise, Kwato Njock ; Merlin, Ngachin and Pascal, (2011). Natural radioactivity measurements dose calculations to the public: Case of the uranium bearing region of Poil in Cameroon, *Radiation Measurements*, vol.46 Iss.2, pp. 254-260.
- [18] Santor Junior, J. A., Amaral, R. S., Silva C. M., Menezes R. S. C. and Bezera J. D. (2009). Radium 228 as indicator of Thorium 232 presence in a soil in pernambuco Brazil, *Bull. Of environ., Contamination & Toxicology*, vol. 82 no. (1-6), pp. 650-652.
- [19] Saudi Geological Survey, (2010). *Regional Geology and Local Geology*.
- [20] Tufail, M., Nasim Akhtar., & Waqas, M. (2006). Measurement of terrestrial radiation for assessment of gamma dose from cultivated & barren saline soils of Faisalabad in Pakistan, *Radiation Measurements*, 41, pp. 443-451.
- [21] UNSCEAR United Nations Scientific Committee on the Effects of Atomic Radiation (2000). *Report to the General Assembly with Scientific Annexes*.
- [22] Wu, D. (2006). Evaluation of radionuclide accumulation in soil, due to long term irrigation, *Health Phys.*, 90(6), TAM-A.5.

Analysis of the Water Evaporation and Drift Losses during Irrigation in Semi-arid Areas

Daniel Simonet¹ and Raafat Alnaizy² (AUS)

¹American Univeristy of Sharjah (dsimonet@aus.edu)

²American Univeristy of Sharjah (alnaizy@aus.edu)

ABSTRACT

Water evaporation and wind drift losses mainly depend on air relative humidity, air and water temperature, drop size, and wind speed. Evaporation and drift loss during water application by means of sprinkle irrigation was studied in the Emirate of Sharjah, United Arab Emirates (UAE) and Riyadh, Saudi Arabia. Results for both cities did not vary substantially due to high relative humidity even under high air temperature. Results indicated that evaporation losses are usually less than 5% under any climatological conditions in the two gulf cities. For nighttime watering to be considered, extra-costs (e.g. electricity, manpower) should not exceed potential savings.

Keywords: evaporation, irrigation, wind drift, humidity, watering, timing

1. INTRODUCTION

The climate in the Arab countries of the Arabian Gulf is generally an arid, subtropical desert. The characteristic features of the climate are intense summer heat with frequent strong winds – rainfall is sparse. Normally, rainfall does not occur during the summer months of May through October. The "rainy season" typically extends from November to April and is characterized by sporadically occurring showers of short (20-30 minutes) duration. The average annual rainfall in the UAE during the period from 1934 to 2004 is 110 mm with a recorded maximum of 344 mm in 1957 and a minimum of 7 mm in 1946 (1). Wind speed is generally high; it averages 6 km/hr, at 2m above ground level. The average open-pan evaporation rate is very high, with a daily average of approximately 8 mm per day (1). Table 1 shows Climatological data for Sharjah International Airport, UAE from 1977 to 2004 inclusive (2). Riyadh, the capital and largest city of Saudi Arabia, is situated in the center of the Arabian Peninsula on a large plateau, 600 m above sea level, 530 miles from Jeddah on the Red Sea and 240 miles from Dammam on the Arabian Gulf (3,4). It has a population of approximately five million people in the city, and seven million in the region, sprawling across 600 square miles (1,600 square kilometers). To the south, about 50 miles from Riyadh, lies Al Kharj, an extensively irrigated area with much agriculture. In 2009, the temperature in Riyadh reached 48°C in mid-June and included occasional gusts of hot winds that intensified a haze of sand that often covers the city. Winters are generally mild, but winter temperatures may fall below zero. The lowest monthly average temperature is 3 °C (37 °F) in January and December. There is a large contrast between daytime and nighttime temperatures, which yield an average temperature range of 19 °C (5), Table 2. As a result, water is a scarce and valuable resource in many Arabian Gulf countries (i.e. UAE and Saudi Arabia). For example, brackish groundwater and seawater

desalination are the Emirate of Sharjah major water sources. There are no permanent surface water sources. Typical to most cities in the Kingdom of Saudi Arabia, Riyadh was built in an area that used to have large natural water supplies (hence, its name, which in Arabic means the place of gardens). The three main sources of water are (6):

1. Wadi Hanifa and Wadi Nisa: rainwater to Wadi Hanifa is estimated to be 15 million cubic meter per year (most of this water comes from the Al-Hair area with wells producing about 18 thousand cubic feet per day); Wadi Nisah produces approximately 54 cubic meter/day.
2. Al Manjour Formation (this layer retains a considerable amount of water reaching up to 750 billion cubic meters) and Al Waseea (water volume is estimated to be around 57 billion cubic meters while the annual recharge is approximately 420 million cubic meters). Water is drawn from this formation through the two fields of Bowaib and Salboukh which have 108 thousand and 86 thousand cubic meter respectively. Al Manjour water is highly saline with salinity estimated at 1500mg/L which requires treatment prior to beneficial consumption. Five water treatment plants were established in Malaz, Shumaisi and Manfouha, and two in Bowaib and Salboukh.
3. Desalination of seawater is the most important water source in Riyadh, providing around 830 thousand cubic meters per day based on estimates. However, with the expansion of the city, Riyadh which has officially been the capital of Saudi Arabia since 1932 and is the most populous city of the Kingdom of Saudi Arabia, those water supplies have shrunk dramatically.

Due to its distance from alternatives major water reserves and the general scarcity of precipitation in the city, the relative humidity in Riyadh remains low throughout the year: Riyadh's climate receives an average of 106.5 mm (4.2 in) of rainfall per year, or 9 mm (0.3 in) per month. On average, there are 17 days per year with more than 0.1 mm of rainfall. The average annual relative humidity is 24.5% (7). Hence, evaporation is likely to be higher than in its more humid neighbors, e.g. UAE). Riyadh averages relative humidity value ranges from 14 % in June to 50 % in January (8). In contrast, the average relative humidity value of the Sharjah Emirate ranges from 51 % in May to 69 % in December and January (9), Table 1 and 2, and Abu Dhabi from 55 % in May to 68 % in January and December (10).

Irrigation in the semiarid state extensively uses precious desalinated water. The abundance of sports stadiums, parks and golf courses requires a huge demand for natural grass in the UAE. The Emirate of Sharjah covers about 2,600 square kilometers. Approximately seven million square meters of natural lawn and landscape, including golf courses, commercial landscapes, and home lawns in the Emirate of Sharjah are irrigated with precious potable water (11). The citizens understand that it is important to save water and are willing to pay high fees to maintain the natural grass facilities. Natural grass requires around 25 liters per square meter of water, which is a considerable amount. Government authorities are constantly advocating towards preserving the scarce natural resources.

When irrigation is applied by the sprinkler method, water is distributed over the irrigated area by spraying it through the air. During sprinkler operation, a stream of water is discharged into the air at high velocity. Many factors can affect the evaporation loss during sprinkler irrigation, including, nozzle design, any associated stream breakup mechanisms, the sprinkler's operating pressure, the height of the sprinkler's above ground surface, and wind speed and direction (3). Wind is a large factor in Riyadh with dominant wind direction blowing from the north, northeast, and northwest sides. Average wind speed is around 5 knots/hour (approximately 8 miles/hour), while the highest speed is about 25 knots/hour. The lowest rate of wind speed is 1.6 knots/hour, and the lowest wind speed on record is 0.8 knots/hour, Table 2.

Wind is a significant determinant of water evaporation. Wind leads to the loss of a percentage of the water by driving it away from the intended target, either in the air or on unintended surfaces, such as roadways and walkways. Also, the wind distorts the spray pattern, thus reduce coverage. Losses due to evaporation may increase by using small nozzles and operating sprinklers at high pressures to produce small water droplets and by operating systems when climate demand is undesirable (4). The maximum climate demand is normally during

the early afternoon, when relative humidity is lowest and air temperature and wind speed are highest (12). The amount of evaporation mainly depends on three factors: 1) the climate demand; 2) the time available for evaporation to occur; and 3) the surface area of the water droplets.

The objective of this study is to estimate evaporation and drift losses in sprinkler irrigation under semiarid conditions as efficiency improvement is thought to result from reducing the amount of water lost through evaporation and wind drift. Specifically, to estimate the cost savings in minimizing direct evaporation during irrigation by avoiding midday sprinkling. Particular interest in our study is that the Emirate of Sharjah and Riyadh are very green and boast many parks. Riyadh has dozens of open green spaces, such as Murabba Park, Prince Fahd al-Faisal Park, Jabal Abu Makhrouq Park, and Al Maktaba Park. The park surfaces of Riyadh are in the region of 700 thousand m².

Evaporation loss can potentially be reduced by changing irrigation-scheduled time. Climate demand is low at night and during early morning and early evening hours. There are several incentives to opt for nighttime watering rather than midday watering. Day watering is relatively inefficient due to substantial evaporation losses. In contrast, nighttime watering minimizes evaporation; and, without the sun and warmth of daytime, water soaks into the soil before it evaporates at a slower pace. An aggravating factor to consider is that watering plants during the day while they are exposed to bright sunlight can actually harm them due to the lens effect caused by water drop. In some experiments, it has been shown that watering at night can generate significant savings by reducing the evaporation rate 15 to 20 percent (13). Since it takes 640 gallons of water to irrigate 1,000 square feet with one inch of water, late nighttime watering gives potentially substantial savings in the amount of water used which transmutes into significant cost reductions (12). In addition, watering at night consumes water and electricity when these are at a minimum use (non-peak hours), thus when their costs are lower. Some municipalities (14) already offer a multi-layered user fee schedule; whereas lower fees apply during nighttime when consumption is at its lowest and higher fees apply during peak hours. In addition, water usage during non-peak times may put less strain on electric systems, a concern in areas that are often subjected to power shortcuts due to high demands, especially during the summer months when air-conditioning system are in full use. Some localities have already declared a preference for nighttime watering and only non-peak time watering is allowed.

2. GEOMETRIC AND THEORETICAL APPROACH

2.1 Water losses

The mathematical modeling of water evaporation and drift losses during irrigation is complex because it is affected by a large number of factors, e.g. temperature, relative humidity, drop size, working pressure, wind velocity, sprinkler head, nozzles, etc.. Thus, several simplifications are assumed. The analyses that follow are based on simple equations in order to determine the evaporation rates accurately. Many studies of evaporation loss during sprinkler irrigation were conducted (3, 4, 12, and 14-17). Evaporation loss may be accurately estimated using three climate factors: air temperature, relative humidity, and wind speed (15). The percentage of water evaporation losses during sprinkler irrigation was estimated for high and low temperature mean daily values as a function of climate factors (i.e. relative humidity and wind speed). Yazar (16) measured water evaporation and drift losses in open-field and obtained the following model:

$$E = 0.389 \exp(0.18W)(p_s - p_a)^{0.7} \quad (1)$$

Where E is the total percentage of water losses during irrigation due to evaporation and drift, W is the windspeed (m/s), and $(p_s - p_a)$ is the vapor pressure deficit where p_s and p_a are the saturation vapor pressure and the actual vapor pressure of the air (kPa). The Bolton (17) empirical formula to calculate the saturation vapor pressure (p_s) was used:

$$p_s = 6.112 \exp\left(\frac{17.67T}{T+243.5}\right) \quad (2)$$

Where T is the air temperature ($^{\circ}\text{C}$). The errors in the Bolton (17) empirical formula were reported to be less than 0.1% within a temperature range of $-30 \leq T \leq 35$ $^{\circ}\text{C}$. The actual vapor pressure may be also obtained as follows:

$$p_a = p_s \frac{Rh}{100} \quad (3)$$

where Rh is the percentage of relative humidity.

2.2 Cost

Water tariffs have been kept low since the 1990s through heavy subsidies. The government of Sharjah subsidizes 70% of the cost of water. We have made several assumptions in our model:

- a) Water use is constant and stands at about 25 liters per square meter; however, there might be monthly variations in water consumption. In addition, water usage shall match the season (high during summer months, low during winter months)

- b) The cost of water for commercial purpose is US\$0.00264 per liter (US\$0.01/gallon); the cost of water may be less since water used for gardening may be recycled water, which is cheaper.

- c) Humidity rate is the same during night and day. For nighttime watering, there are many costs to take into consideration such as electricity (e.g. additional lighting) and manpower costs. Additional incentives may be required to entice people to work during the night shift. Other costs might be harder to quantify, such as noise, health, and environmental problems. Noise is the most difficult cost to quantify. It would be none if we are considering watering a golf course at night (we assume there is no one there at night). However, it could also be an issue if sprinklers and energy generators operate near apartment windows in residential areas. This cost is also harder to quantify because of its subjective nature. Nighttime watering is potentially a health hazard, as it allows water to stagnate which invites insects and fungus. Fungus will spread across the lawn, killing the new grass as it grows, and more water only increases the fungus. Stagnant water can become a breeding ground for diseases: the duration of leaf wetness (the number of hours that the leaf blade is actually wet) has a greater impact on disease incidence than nighttime watering; hence, watering during early evening or late morning (prior to or following dew formation) would prolong leaf wetness, thus encouraging disease outbreak. In humid areas, with abundant fungal diseases (e.g. mildew, especially downy mildew), this would affect both the health of the lawn (thus necessitate the use of foliar spray) and the people because stagnant waters might breed insects, and this is conducive to disease outbreak. Thus, nighttime watering should be avoided when fungal grass disease is already present. This issue is still largely debated: according to Koski (13), nighttime watering does not encourage disease development. Health issues are less of a concern during the cooler season. There are fewer disease problems in the winter (December to February). Overall, there is a consensus that watering at night is better suited for areas with low humidity, dry weather and cooler nights, e.g. Saudi Arabia, California, and Mexico. Nocturnal watering in an arid area is less likely to lead to insects, fungus, or disease than nocturnal watering in a humid area. To mitigate health problems, one shall also ensure a proper drainage system: pools of standing water can become very hot and result in turf death due to scalding. There are additional costs to consider: rust on iron fences, gates, etc., will rise as a result of excessive nighttime watering. Such considerations are harder to quantify but can be controlled by using smaller quantities of water.

2.3 Discounted Value of Future Streams of Money

We calculate the Present Discounted Value (PDV) (i.e. takes all future streams of money such as cost of water loss and convert them in today's terms). The future

streams of money are discounted by the interest rate that could be earned between the present and the future period. If the future streams of money in each future period are B , and the interest rate is r , then the Present Discounted Value (PDV) is:

$$PDV = B_0 + \frac{B_1}{(1+r)} + \frac{B_2}{(1+r)^2} + \dots + \frac{B_t}{(1+r)^t} \quad (4)$$

If future streams of money B are constant (we assume a stable climate and water consumption for the next 50 years) and over a long period in the future (above 50 years), then $PDV = B / r$.

2.4 Choosing a discount rate

Cost-benefit decision making requires present value calculations. In our example, selecting a discount rate is problematic. Theoretically, the government opportunity cost of funds is the discount rate r and shall reflect the rate of return available on alternative investments, i.e. what else the government could accomplish with those same funds. In practice, choosing a discount rate is difficult; hence, the federal government often uses different discount rates, which depends on the public agency, the nature of the project, and the class of assets concerned. In the United States, the Office of Management and Budget (OMB) guidelines (2003) stipulate that government agencies must do two separate analyses when evaluating a project. One utilizes a real discount rate of 7 %, which is likened to the rate of return of private investment. The second apply the social discount rate (3 %), which is used to compute the present discounted value of social investment (18) and is lower than the market rate of return. The latter measures the valuation society places on consumption that is sacrificed in the present; and, an appropriate rate of return for projects that use resources from private consumption (19). Another discount rate would be based on the rate of return of a similar class of assets. In the UAE however, there is no such dual analysis (private investment rate of return and social discount rate). The selected discount rate was 2.50% (20).

3. RESULTS AND DISCUSSION

3.1 Water losses amount

Water evaporation losses may be a significant water sink in sprinkler irrigation, particularly in areas with strong winds, high temperatures, and low relative humidity. The results of the above models are presented in Tables 3 - 8, and Figures 1 - 6. The tables and figures show the total water losses as a function of relative humidity, air temperature, and wind speed. In the semi-arid meteorological conditions of Sharjah and Riyadh, the average maximum evaporation losses were 4.6 and 4.9% during day irrigations, respectively (Tables 6 and 8).

The mean minimum evaporation losses amounted to 0.2% for Sharjah and 0.3% for Riyadh during the month of January (Tables 3 and 7). Long-term daily and daytime wind speeds (average and highest) in Sharjah also are listed in Table 3 - 6. Daytime averages are shown because most evaporation takes place during daylight hours, when wind speeds and temperatures are highest and relative humidity values are lowest. Daytime wind speeds were collected from the Sharjah International Airport for the period of 1977 to 2004 inclusive (2). The wind speeds are highest (24 km/h) during April through August and lowest (18 km/h) in December (2). Figure 1 shows the relationships among air temperature, relative humidity, and evaporation rate during the entire year. This figure illustrates that the evaporation rate will be highest when temperatures are high and the relative humidity is low. Note that when temperatures are low, the evaporation rate will be low, despite the humidity level. Also, when the relative humidity is high, the evaporation rate will be low, despite the temperatures. Wind drift loss increases as wind speeds increase and as droplet sizes decrease. Figure 2 illustrates the effect of the wind speed on the rate of water losses during irrigation in Sharjah. The higher wind speeds, the larger droplets can be transported by the wind, and droplets can be transported greater distances.

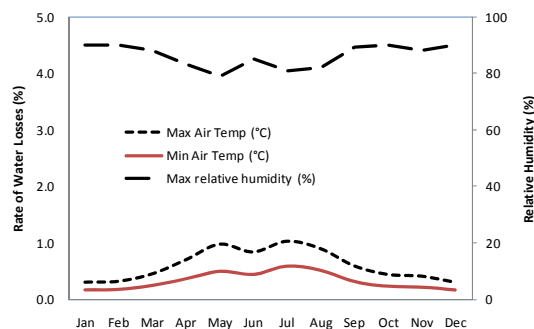


Figure 1: Total percentage of water losses during irrigation due to evaporation and drift at maximum relative humidity and Monthly mean Wind speed in the Emirate of Sharjah, UAE

Due to high humidity levels that are typical in the Arabian Gulf States, the evaporation rate is generally low despite the high temperatures. Table 6 and Figure 4 show the maximum possible monthly evaporation rate for Sharjah of 4.6%. These were calculated from the temperature and relative humidity data in Table 1 using the method discussed earlier. The maximum values were calculated from the maximum temperature, highest monthly mean wind speed, and minimum relative humidity data. These values would be expected to represent peak vapor pressure deficits occurring during the early afternoon, when temperatures are highest and humidity is lowest. The average values were calculated from average temperatures and average relative humidity readings. These values would be expected to represent average daily vapor pressure deficits, the

average of both daytime and nighttime conditions. In Sharjah, average daily vapor pressure deficits are low, ranging from 0.1 kPa in January to 0.7 kPa in July and August, Table 3. Maximum daily vapor pressure deficits are larger and more variable, ranging from 1.8 kPa in January to 6.1 kPa in July, Table 6. Monthly evaporation percentages for Sharjah were calculated using the wind speed data and the vapor pressure deficit data, Table 3 - 6. Figure 1 - 4 shows the monthly distribution of average and maximum daily evaporation percentages. The average daily values were low and uniform at about 1.5 percent throughout the year. The maximum (early afternoon) values were more variable, ranging from 1.6 percent in January and December to 4.6 percent in July, Table 6 and Figure 4. As projected, notwithstanding high temperatures, the estimated amounts of water losses are very little because the relative humidity in the Emirate of Sharjah is very high. Water irrigation can be applied at any time during the day or night.

In the same approach and methods, the total percentage of water losses during irrigation due to evaporation and drift in Riyadh were calculated. As expected, they were only slightly higher because of higher temperatures and lower humidity. Losses ranged from 1% to 4.9%, Table 7 and 8 and Figures 5 and 6. The figures justify the selection of the adequate irrigation time (day or night).

3.2 Water losses cost

Water loss in Sharjah due to an evaporation range from 0.33 % (at a cost of \$18,196 per year, and \$606,548 over infinity) (Table 3) with maximum relative humidity and monthly mean wind speed (and with minimum temperature mean daily) to 3.17 % (at a cost of \$173,321 per year, and \$5,777,373 over infinity) (Table 6) with minimum relative humidity and highest monthly mean wind speed and maximum temperature mean daily (a summary of water loss costs are contained in Table 9).

Overall, nighttime watering (done at minimum temperature daily) would reduce water losses by more than half with water losses falling from 0.59 % (day watering) to 0.33 % (nighttime watering) under maximum relative humidity and monthly mean wind speed (Table 9); from 1.05% to 0.58% under maximum relative humidity and highest monthly mean wind speed (Table 9); from 1.80 % to 0.98 % under minimum relative humidity and monthly mean wind speed (Table 9).

The greatest saving would be obtained under minimum relative humidity and highest monthly mean wind speed with water losses falling from 3.17% (daytime watering) to 1.73% (nighttime watering), representing annual savings of \$78,700 (\$173,321 - \$94,621) and future discounted savings of \$2,623,322 (\$5,777,373 - \$3,154,051). For nighttime watering to meet a costs/benefits analysis, extra-cost (manpower, fungi...)

should not exceed the aforementioned savings. Automation of sprinklers and other watering devices would be key factors.

In Riyadh, we found that water loss costs due to evaporation would range from 0.93% when relative humidity is maximum and temperature mean daily is minimum to 2.86% (Table 10) when relative humidity is minimum and mean daily temperature maximum based on a water cost of \$0.0016 per liter and a discount rate of 2.50% (20). Assuming constant conditions of low-level humidity throughout the year, and temperature reaching minima during nighttime (with minimum mean temperature daily serving as a proxy), the cost of evaporation falls from 2.86% during daytime watering with maximum temperature daily to 1.1%. Changing to nighttime watering will reduce wastage by 61.5% $((9,138-3,517)/9138)$, and translates into a savings of \$224,876 $(\$365,557 - \$140,681)$ over an infinite time (Table 10). These benefits/savings must be contrasted with the extra costs associated with nighttime watering as mentioned above. In contrast, when relative humidity is high, daytime watering during maximum daily temperatures led to a 2.47 % loss caused by evaporation as opposed to watering during nighttime applying minimum mean temperature daily as a proxy and leads to 0.93 % only in wastage. Thus changing to nighttime watering will reduce wastage by 62.5 % $((7,886-2,957)/7,886)$, and generate a savings of \$197,166 $(\$315,466 - \$118,300)$ (Table 10). For nighttime watering to be considered, extra-costs (e.g. electricity, manpower) should not exceed these savings.

4. CONCLUSIONS AND RECOMMENDATIONS

The total percentage of water losses during irrigation due to evaporation and drift in the Emirate of Sharjah and Riyadh city were calculated. The relative humidity in of Sharjah is very high; consequently, due to high temperatures, the expected amount of water evaporation loss would be low. Also, as expected, water evaporation loss in Riyadh was only slightly higher because of higher temperatures and lower humidity. Evaporation losses were less than 5% under any Climatological conditions in the two places. For nighttime watering to meet a costs/benefits analysis, extra-cost (manpower, fungi...) should not exceed potential savings: automation of sprinklers and other watering devices would be key factors. Evaporation may take place from exposed bodies of water in the case of surface irrigation, or from wind-drift and intercepted water in the case of sprinkler irrigation. An accurate knowledge of drop size distributions in the sprinkling irrigation equipment is not important because evaporation is controlled by the extreme relative humidity of the Arabian Gulf countries.

REFERENCES

- [1] The United Arab Emirates Ministry of Environment & Water.

- [2] Gary R. Feulner "Historical data for the study of recent climatic periodicity in the U.A.E.", Tribulus 16.1 Spring/Summer 2006
- [3] Myers, J.M., C.D. Baird and R.E. Choate. 1970. Evaporation losses in sprinkler irrigation. Florida Water Resources Research Center Publication No. 12. University of Florida, Gainesville. 41 pp.
- [4] Frost, K.R. and H.C. Schwalen. 1955. Sprinkler evaporation losses. *Agricultural Engineering* 36: 526-528.
- [5] <http://www.climate-temp.info/saudi-arabia/riyadh.html>
- [6] http://www.arriyadh.com/Eng/Ab-Arriyadh/Left/History/getdocument.aspx?f=/openshare/Eng/Ab-Arriyadh/Left/History/ArRiyadh-Geography.doc_cvt.htm
- [7] <http://www.climate-temp.info/saudi-arabia/riyadh.html>
- [8] <http://www.climate-charts.com/Locations/s/SD40438.php>
- [9] <http://www.climate-charts.com/Locations/u/UE41196.php>
- [10] <http://www.climate-charts.com/Locations/u/UE41216.php>
- [11] Total area of greenery in Sharjah:
<http://www.shjmun.gov.ae/v2/english/parks/statistics/total.asp>
- [12] Seginer, I. 1971. "Water losses during sprinkling." *Transactions of the ASAE* 14: 656-659, 664.
- [13] Koski T. Skinner V. YARD. **Lawn Care no. 7.202.** 1 (12/03)
- [14] <http://www.clemson.edu/hort/Drought1.php>
- [15] J.M. Tarjuelo, J.F. Ortega, J. Montero, J.A. de Juan "Modelling evaporation and drift losses in irrigation with medium size impact sprinklers under semi-arid conditions" *Agricultural Water Management* 43 (2000) 263-284.
- [16] Bavi, A., H.A. Kashkuli, S. Boroomand, A. Naseri and M. Albaji, 2009. Evaporation losses from sprinkler irrigation systems under various operating conditions. *J. Applied Sci.*, 9: 597-600.
- [17] Yazar, A., 1984. Evaporation and drift losses from sprinkler irrigation systems under various operating conditions. *Agric. Water Manage.* 8: 439-449.
- [18] DAVID BOLTON "The Computation of Equivalent Potential Temperature", *MONTHLY WEATHER REVIEW*, VOLUME 108, July 1980, pp 1046-1053
- [19] Jonathan Gruber. *Public Finance and Public Policy*. Second Edition. Worth Publisher. 2007.
- [20] Rosen HS. Gayer T. *Public Finance*. 9/e by, Princeton University, Georgetown University. McGraw Hill. 2010.
- [21] CIA Fact Book

Table 1: Climatological Data for the Emirate of Sharjah International Airport, UAE - 1977 to 2004 inclusive (Feulner 2006)

	JA	FE	MA	AP	MA	JU	JU	AU	SE	OC	NO	DE	Ye
	N	B	R	R	Y	NE	LY	G	P	T	V	C	ar
<u>Dry bulb Temp (°C)</u>													
Mean daily max.	24. 4	25. 7	29. 0	34. 2	39. 1	41.3	42.4	42. 2	40. 1	36. 3	31. 1	26. 5	34. 4
Mean daily min.	12. 1	13. 0	15. 5	18. 4	22. 2	25.0	27.9	27. 8	24. 6	21. 0	16. 9	13. 8	19. 9
Extreme max.	32. 5	35. 4	42. 5	44. 6	46. 4	49.2	47.8	48. 2	46. 7	43. 0	37. 3	33. 9	49. 2
Extreme min.	3.4	2.5	5.8	10. 9	13. 0	17.8	21.7	22. 2	18. 4	12. 3	8.1	4.9	2.5
<u>Wet bulb Temp (°C)</u>													
Mean daily max.	14. 4	15. 1	16. 9	19. 1	21. 6	24.5	26.1	26. 4	24. 9	22. 3	18. 5	16. 0	20. 5
Extreme max.	22. 0	23. 1	25. 0	26. 7	30. 2	32.1	33.0	33. 5	31. 5	32. 1	27. 2	24. 1	33. 5
Mean daily max.	90	90	88	82	76	82	80	80	87	89	87	90	85
Mean daily min.	41	38	33	25	21	23	26	27	26	28	33	40	30
<u>Sunshine (hours)</u>													
Mean total hours	23 4	225	251	29 3	340	337	320	317	30 0	294	265	234	284
Percentage of possible	73	74	70	80	85	85	79	82	85	86	84	75	80
<u>Rainfall (mm)</u>													
Mean daily hours	7.4	8.0	8.1	9.8	11. 0	11.3	10.3	10. 2	10. 0	9.5	8.8	7.6	9.3
Monthly mean	17. 9	31. 9	38. 0	7.9	1.0	0.0	3.5	0.0	0.4	2.6	4.9	21. 0	10. 8
Monthly extreme	97. 8	142 .9	156 .4	43. 7	20. 6	TR	53.1	0.6	9.2	63. 4	41. 6	146 .5	156 .4
Highest 24 hr. max.	62. 7	115 .5	76. 7	36. 6	14. 4	TR	35.2	0.6	5.5	62. 6	41. 6	60. 7	115 .5
Mean no. of rain days	6.0	5.9	8.1	2.5	0.4	0.1	0.7	0.4	0.1	0.2	1.3	4.6	2.5
<u>Atmospheric pressure (hPa)</u>													
Mean sea level pressure (MSLP)	10 18	101 6	101 4	10 10	100 6	100 0	997	999	10 05	101 2	101 6	101 8	100 9
<u>Weather - Mean no. of days</u>													
Fog - visibility less than 1 km	1.7	2.3	3.6	2.5	1.9	3.1	1.0	1.1	3.3	3.8	1.3	1.3	2.2
Dust/haze - visibility less than 1 km	0.2	0.1	0.5	0.1	0.0	0.1	0.2	0.1	0.1	0.1	0.1	0.1	0.1
Thunder	0.5	1.4	2.3	0.9	0.1	0.0	0.3	0.3	0.1	0.2	0.8	0.8	0.6
Hail	0.0	0.1	0.1	0.0	0.0	0.0	0.0	0.0	0.0	0.1	0.1	0.1	0.0
<u>Wind speed (km/h)</u>													
Monthly mean	11. 1	11. 1	13. 0	13. 0	13. 0	13.0	13.0	11. 1	11. 1	9.3	9.3	9.3	11. 1
Highest monthly mean	20. 4	22. 2	24. 1	24. 1	24. 1	24.1	24.1	24. 1	22. 2	22. 2	20. 4	18. 5	22. 2

Monthly extreme	74	61	78	67	63	59	76	54	52	46	59	52	78
<u>Gust (km/hr)</u>													
Monthly extreme	11	130	113	10	83	83	133	72	70	72	83	80	133
	3			7									

Table 2: Climatologically Data for Riyadh Saudi Arabia (3, 4)

	Jan	Feb	Mar	Apr	May	Jun	Jul	Aug	Sep	Oct	Nov	Dec
Average Maximum Temperature (°C)	28.0	30.0	35.0	38.0	42.0	44.0	45.0	45.0	43.0	38.0	33.0	28.0
Average Minimum Temperatures (°C)	3.0	4.0	8.0	12.0	18.0	21.0	23.0	24.0	19.0	14.0	9.0	3.0
Average Mean Temp (°F)	58	62	70	80	90	94	97	96	91	82	71	62
Average Dew Point (°C)	1.1	0.6	2.2	4.4	3.9	-0.6	-0.6	1.1	0.6	1.1	2.8	3.3
Average Wind speed (m/s)	3.58	4.02	4.02	4.47	4.47	5.81	4.92	4.92	4.47	3.13	3.13	3.58
Average Wind Direction	S	S	S	N	N	N	N	N	N	S	S	S
Days With Precipitation	4	3	6	7	4	N/A	N/A	1	N/A	1	1	4
Average Morning Relative Humidity (%)	60	52	47	43	29	19	16	18	21	31	46	60
Average Afternoon Relative Humidity (%)	32	27	24	19	13	8	8	8	9	13	22	33
Days With Lows Below Freezing	10	4	1	0	0	0	0	0	0	0	0	6
Days above 32.2° C	0	1	6	18	30	30	31	31	30	26	4	0

Table 3: Total percentage of water losses during irrigation due to evaporation and drift at maximum relative humidity and Monthly mean Wind speed in the Emirate of Sharjah, UAE.

	Monthly Mean												A v g
	Jan	Feb	Mar	Apr	May	Jun	Jul	Aug	Sep	Oct	Nov	Dec	
Relative Humidity (%)	90	90	88	83	79	85	81	82	89	90	88	90	86
Monthly mean Wind speed (m/s)	3.1	3.1	3.6	3.6	3.6	3.6	3.6	3.1	3.1	2.6	2.6	2.6	3.1
I. Maximum temperature mean daily													
Dry Bulb Temp (°C)	24.4	25.7	29	34.2	39.1	41.3	42.4	42.2	40.1	36.3	31.1	26.5	34.4
Saturation vapor pressure of air (mbar)	30.6	33.0	40.1	53.9	70.5	79.3	84.0	83.1	74.3	60.5	45.2	34.6	54.5
Actual vapor pressure of air (mbar)	27.5	29.7	35.3	44.7	55.7	67.4	68.0	68.2	66.2	54.5	39.8	31.2	47.0
($p_s - p_a$) (kPa)	0.3	0.3	0.5	0.9	1.5	1.2	1.6	1.5	0.8	0.6	0.5	0.3	0.7
Evaporation loss (%)	0.3	0.3	0.4	0.7	1.0	0.8	1.0	0.9	0.6	0.4	0.4	0.3	0.6
Water Loss due to evaporation (Thousands liters per month)	517	517	689	1,206	1,723	1,379	1,723	1,551	1,034	689	689	517	
Costs of Water Loss (\$)	1,365	1,365	1,820	3,184	4,549	3,639	4,549	4,094	2,729	1,820	1,820	1,365	
Costs of Water Loss Over Time (\$)	45,491	45,491	60,655	106,146	151,637	121,310	151,637	136,473	90,982	60,655	60,655	45,491	
Annual Costs of Water Loss (B)								\$32,299					
Costs of Water Loss Over Time (B/r)								\$1,076,623					
Annual Water Costs (A)								\$5,458,935					
Loss in % (B/A)								0.59					
II. Minimum temperature mean daily													
Dry Bulb Temp (°C)	12.1	13	15.5	18.4	22.2	25	27.9	27.8	24.6	21	16.9	13.8	19.9
Saturation vapor pressure of air (mbar)	14.1	15.0	17.6	21.2	26.8	31.7	37.6	37.4	30.9	24.9	19.2	15.8	23.2
Actual vapor pressure of air (mbar)	12.7	13.5	15.5	17.6	21.1	26.9	30.4	30.6	27.5	22.4	16.9	14.2	20.0
($p_s - p_a$) (kPa)	0.1	0.1	0.2	0.4	0.6	0.5	0.7	0.7	0.3	0.2	0.2	0.2	0.3
Evaporation loss (%)	0.2	0.2	0.3	0.4	0.5	0.4	0.6	0.5	0.3	0.2	0.2	0.2	0.3
Water Loss due to evaporation (Thousands liters per month)	345	345	517	689	862	689	1,034	862	517	345	345	345	
Costs of Water Loss (\$)	910	910	1,365	1,820	2,275	1,820	2,729	2,275	1,365	910	910	910	
Costs of Water Loss Over Time (\$)	30,327	30,327	45,491	60,655	75,819	60,655	90,982	75,819	45,491	30,327	30,327	30,327	
Annual Costs of Water Loss (B)								\$18,196					
Costs of Water Loss Over Time (B/r)								\$606,548					
Annual Water Costs (A)								\$5,458,935					
Loss in % (B/A)								0.33					

Table 4: Total percentage of water losses during irrigation due to evaporation and drift at maximum relative humidity and highest monthly mean wind speed in the Emirate of Sharjah, UAE.

	Monthly Mean												Avg
	Jan	Feb	Mar	Apr	May	Jun	Jul	Aug	Sep	Oct	Nov	Dec	
Relative Humidity (%)	90	90	88	83	79	85	81	82	89	90	88	90	86
Highest Monthly mean Wind speed (m/s)	5.7	6.2	6.7	6.7	6.7	6.7	6.7	6.7	6.2	6.2	5.7	5.1	6.2
III. Maximum temperature mean daily													
Dry Bulb Temp (°C)	24.4	25.7	29	34.2	39.1	41.3	42.4	42.2	40.1	36.3	31.1	26.5	34.4
Saturation vapor pressure of air (mbar)	30.6	33.0	40.1	53.9	70.5	79.3	84.0	83.1	74.3	60.5	45.2	34.6	54.5
Actual vapor pressure of air (mbar)	27.5	29.7	35.3	44.7	55.7	67.4	68.0	68.2	66.2	54.5	39.8	31.2	47.0
($p_s - p_a$) (kPa)	0.3	0.3	0.5	0.9	1.5	1.2	1.6	1.5	0.8	0.6	0.5	0.3	0.7
Evaporation loss (%)	0.5	0.5	0.8	1.2	1.7	1.5	1.8	1.7	1.0	0.8	0.7	0.5	1.0
Water Loss due to evaporation (Thousands liters per month)	862	862	1,379	2,068	2,929	2,585	3,102	2,929	1,723	1,379	1,206	862	
Costs of Water Loss (\$)	2,275	2,275	3,639	5,459	7,733	6,824	8,183	7,733	4,548	3,639	3,184	2,275	
Costs of Water Loss Over Time (\$)	75,819	75,819	121,310	181,965	257,783	227,456	272,947	257,783	151,637	121,310	106,146	75,819	
Annual Costs of Water Loss (B)								\$57,774					
Costs of Water Loss Over Time (B/r)								\$1,925,791					
Annual Water Costs (A)								\$5,458,935					
Loss in % (B/A)								1.05					
. Minimum temperature mean daily													
Dry Bulb Temp (°C)	12.1	13	15.5	18.4	22.2	25	27.9	27.8	24.6	21	16.9	13.8	19.9
Saturation vapor pressure of air (mbar)	14.1	15.0	17.6	21.2	26.8	31.7	37.6	37.4	30.9	24.9	19.2	15.8	23.2
Actual vapor pressure of air (mbar)	12.7	13.5	15.5	17.6	21.1	26.9	30.4	30.6	27.5	22.4	16.9	14.2	20.0
($p_s - p_a$) (kPa)	0.1	0.1	0.2	0.4	0.6	0.5	0.7	0.7	0.3	0.2	0.2	0.2	0.3
Evaporation loss (%)	0.3	0.3	0.4	0.6	0.9	0.8	1.0	1.0	0.6	0.4	0.4	0.3	0.5
Water Loss due to evaporation (Thousands liters per month)	517	517	862	862	1,379	2,068	2,929	2,585	3,102	2,929	1,723	1,379	1,206
Costs of Water Loss (\$)	1,365	1,365	2,275	2,275	3,639	5,459	7,733	6,824	8,183	7,733	4,548	3,639	3,184
Costs of Water Loss Over Time (\$)	45,491	45,491	75,819	75,819	121,310	181,965	257,783	227,456	272,947	257,783	151,637	121,310	106,146
Annual Costs of Water Loss (B)								\$31,844					
Costs of Water Loss Over Time (B/r)								\$1,061,460					
Annual Water Costs (A)								\$5,458,935					
Loss in % (B/A)								0.58					

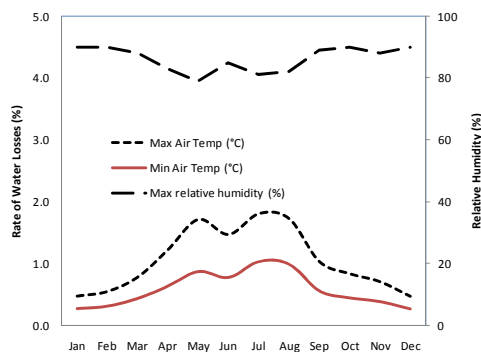


Figure 2: Total percentage of water losses during irrigation due to evaporation and drift at maximum relative humidity and highest monthly mean wind speed in the Emirate of Sharjah, UAE.

Table 5: Total percentage of water losses during irrigation due to evaporation and drift at minimum relative humidity and Monthly mean Wind speed in the Emirate of Sharjah, UAE.

	Monthly Mean												Av g
	Jan	Feb	Mar	Apr	May	Ju n	Jul	Aug	Se p	Oct	No v	Dec	
Relative Humidity (%)	42	40	34	27	24	26	27	30	28	31	35	42	32. 17
Monthly mean Wind speed (m/s)	3.1	3.1	3.6	3.6	3.6	3.6	3.6	3.1	3.1	2.6	2.6	2.6	3.1
Maximum temperature mean daily													
Dry Bulb Temp (°C)	24. 4	25.7	29	34.2	39.1	41. 3	42. 4	42.2	40. 1	36.3	31. 1	26.5	34. 4
Saturation vapor pressure of air (mbar)	30. 6	33.0	40.1	53.9	70.5	79. 3	84. 0	83.1	74. 3	60.5	45. 2	34.6	54. 5
Actual vapor pressure of air (mbar)	12. 8	13.2	13.6	14.5	16.9	20. 6	22. 7	24.9	20. 8	18.8	15. 8	14.5	17. 5
($p_s - p_a$) (kPa)	1.8	2.0	2.6	3.9	5.4	5.9	6.1	5.8	5.4	4.2	2.9	2.0	3.7
Evaporation loss (%)	1.0	1.1	1.5	1.9	2.4	2.6	2.6	2.3	2.2	1.7	1.3	1.0	1.7
Water Loss due to evaporation (Thousands liters per month)	1,7 23	1,895	2,585	3,274	4,136	4,4 80	4,4 80	3,963	3,7 91	2,929	2,2 40	1,895	
Costs of Water Loss (\$)	4,5 49	5,004	6,824	8,643	10,91 8	11, 82	11, 82	10,46 3	10, 00	7,733	5,9 14	5,004	
Costs of Water Loss Over Time (\$)	15 1,6 37	166,8 01	227,4 56	288,1 10	363,9 29	39 4,2 56	39 4,2 56	348,7 65	33 3,6 02	257,7 83	7,1 28	166,8 01	
Annual Costs of Water Loss (B)								\$98,716					
Costs of Water Loss Over Time (B/r)								\$3,290,525					
Annual Water Costs (A)								\$5,458,935					
Loss in % (B/A)								1.80					
Minimum temperature mean daily													
Dry Bulb Temp (°C)	12.1	13	15.5	18.4	22.2	25	27. 9	27. 8	24. 6	21	16.9	13.8	19.9
Saturation vapor pressure of air (mbar)	14.1	15.0	17.6	21.2	26.8	31.7	37.6	37.4	30.9	24.9	19.2	15.8	23.2
Actual vapor pressure of air (mbar)	5.9	6.0	6.0	5.7	6.4	8.2	10.1	11.2	8.7	7.7	6.7	6.6	7.5
($p_s - p_a$) (kPa)	0.8	0.9	1.2	1.5	2.0	2.3	2.7	2.6	2.2	1.7	1.3	0.9	1.6
Evaporation loss (%)	0.6	0.6	0.8	1.0	1.2	1.4	1.5	1.3	1.2	0.9	0.7	0.6	0.9
Water Loss due to evaporation (Thousands liters per month)	1,034	1,034	1,379	1,723	2,068	2,412	2,585	2,240	2,068	1,551	1,206	1,034	
Costs of Water Loss (\$)	2,729	2,729	3,639	4,549	5,459	6,369	6,824	5,914	5,459	4,094	3,184	2,729	
Costs of Water Loss Over	90,982	90,982	121,310	151,637	181,965	212,292	227,456	197,128	181,965	136,473	106,146	90,982	

Time (\$)														
Annual Costs of Water Loss (B)		\$53,680												
Costs of Water Loss Over Time (B/r)		\$1,789,318												
Annual Water Costs (A)		\$5,458,935												
Loss in % (B/A)		0.98												

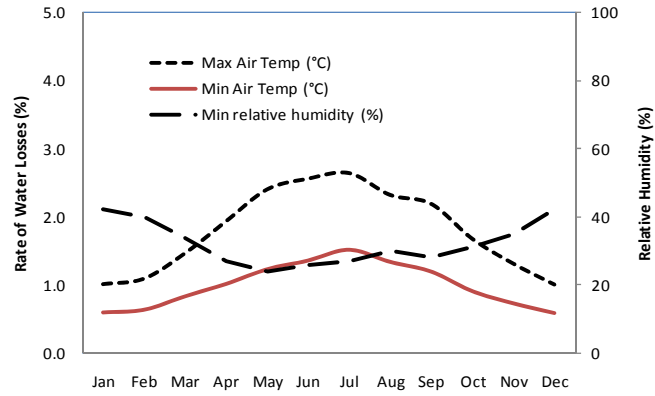


Figure 3: Total percentage of water losses during irrigation due to evaporation and drift at minimum relative humidity and Monthly mean Wind speed in the Emirate of Sharjah, UAE.

Table 6: Total percentage of water losses during irrigation due to evaporation and drift at minimum relative humidity and highest monthly mean Wind speed in the Emirate of Sharjah, UAE.

	Monthly Mean												A v g
	Jan	Feb	Mar	Apr	May	Jun	Jul	Aug	Sep	Oct	Nov	Dec	
Relative Humidity (%)	42	40	34	27	24	26	27	30	28	31	35	42	32.17
Highest monthly mean Wind speed (m/s)	5.7	6.2	6.7	6.7	6.7	6.7	6.7	6.7	6.2	6.2	5.7	5.1	6.2
I. Maximum temperature mean daily													
Dry Bulb Temp (°C)	24.4	25.7	29	34.2	39.1	41.3	42.4	42.2	40.1	36.3	31.1	26.5	34.4
Saturation vapor pressure of air (mbar)	30.6	33.0	40.1	53.9	70.5	79.3	84.0	83.1	74.3	60.5	45.2	34.6	54.5
Actual vapor pressure of air (mbar)	12.8	13.2	13.6	14.5	16.9	20.6	22.7	24.9	20.8	18.8	15.8	14.5	17.5
($p_s - p_a$) (kPa)	1.8	2.0	2.6	3.9	5.4	5.9	6.1	5.8	5.4	4.2	2.9	2.0	3.7
Evaporation loss (%)	1.6	1.9	2.6	3.4	4.2	4.5	4.6	4.4	3.8	3.2	2.3	1.6	2.9
Water Loss due to evaporation (Thousands liters per month)	2,757	3,274	4,480	5,859	7,237	7,754	7,926	7,582	6,548	5,514	3,963	2,757	
Costs of Water Loss (\$)	7,279	8,643	11,828	15,467	19,106	20,471	20,926	20,016	17,287	14,557	10,463	7,279	
Costs of Water Loss Over Time (\$)	242,619	288,110	394,256	515,566	636,876	682,367	697,531	667,203	576,221	485,239	348,765	242,619	
Annual Costs of Water Loss (B)									\$173,321				
Costs of Water Loss Over Time (B/r)									\$5,777,373				
Annual Water Costs (A)									\$5,458,935				
Loss in % (B/A)									3.17				
II. Minimum temperature mean daily													
Dry Bulb Temp (°C)	12.1	13	15.5	18.4	22.2	25	27.9	27.8	24.6	21	16.9	13.8	19.9
Saturation vapor pressure of air (mbar)	14.1	15.0	17.6	21.2	26.8	31.7	37.6	37.4	30.9	24.9	19.2	15.8	23.2
Actual vapor pressure of air (mbar)	5.9	6.0	6.0	5.7	6.4	8.2	10.1	11.2	8.7	7.7	6.7	6.6	7.5
($p_s - p_a$) (kPa)	0.8	0.9	1.2	1.5	2.0	2.3	2.7	2.6	2.2	1.7	1.3	0.9	1.6
Evaporation loss (%)	0.9	1.1	1.4	1.8	2.1	2.4	2.6	2.5	2.1	1.7	1.3	0.9	1.6
Water Loss due to evaporation (Thousands liters per month)	1,551	1,895	2,412	3,102	3,619	4,136	4,480	4,308	3,619	2,929	2,240	1,551	
Costs of Water Loss (\$)	4,094	5,004	6,369	8,188	9,553	10,918	11,828	11,373	9,553	7,733	5,914	4,094	
Costs of Water Loss Over Time (\$)	136,473	166,801	212,292	272,947	318,438	363,929	394,256	379,093	318,438	257,783	197,128	136,473	
Annual Costs of Water Loss (B)									\$94,622				
Costs of Water Loss Over Time (B/r)									\$3,154,051				
Annual Water Costs (A)									\$5,458,935				
Loss in % (B/A)									1.73				

Table 7: Total percentage of water losses during irrigation due to evaporation and drift at maximum relative humidity in Riyadh Saudi Arabia.

	Monthly Mean												A vg
	Jan	Feb	Mar	Apr	Ma y	Jun	Jul	Au g	Sep	Oct	No v	Dec	
Relative Humidity (%)	60	52	47	43	29	19	16	18	21	31	46	60	37
Monthly mean Wind speed (m/s)	3.6	4.0	4.0	4.5	4.5	5.8	4.9	4.9	4.5	3.1	3.1	3.6	4.2
V. Maximum temperature mean daily													
Dry Bulb Temp (°C)	28.0	30.0	35.0	38.0	42.0	44.0	45.0	45.0	43.0	38.0	33.0	28.0	37.4
Saturation vapor pressure of air (mbar)	37.8	42.5	56.3	66.4	82.2	91.3	96.2	96.2	86.7	66.4	50.4	37.8	67.5
Actual vapor pressure of air (mbar)	22.7	22.1	26.5	28.5	23.9	17.4	15.4	17.3	18.2	20.6	23.2	22.7	24.9
($p_s - p_a$) (kPa)	1.5	2.0	3.0	3.8	5.8	7.4	8.1	7.9	6.8	4.6	2.7	1.5	4.6
Evaporation loss (%)	1.0	1.3	1.7	2.2	3.0	4.5	4.1	4.0	3.3	2.0	1.4	1.0	2.5
Water Loss due to evaporation (Thousands liters per month)	167	216	283	366	500	749	683	666	550	333	233	183	
Costs of Water Loss (\$)	266	346	453	586	799	1,199	1,092	1,066	879	533	373	293	
Costs of Water Loss Over Time (\$)	10,658	13,855	18,118	23,447	31,973	47,959	43,696	42,631	35,170	21,315	14,921	11,723	
Annual Costs of Water Loss (B) \$7,887 Costs of Water Loss Over Time (B/r) \$315,467 Annual Water Costs (A) \$319,730 Loss in % (B/A) 2.47													
VI. Minimum temperature mean daily													
Dry Bulb Temp (°C)	3.0	4.0	8.0	12.0	18.0	21.0	23.0	24.0	19.0	14.0	9.0	3.0	13.2
Saturation vapor pressure of air (mbar)	7.6	8.1	10.7	14.0	20.6	24.9	28.1	29.8	22.0	16.0	11.5	7.6	16.7
Actual vapor pressure of air (mbar)	4.5	4.2	5.0	6.0	6.0	4.7	4.5	5.4	4.6	5.0	5.3	4.5	5.0
($p_s - p_a$) (kPa)	0.3	0.4	0.6	0.8	1.5	2.0	2.4	2.4	1.7	1.1	0.6	0.3	1.2
Evaporation loss (%)	0.3	0.4	0.5	0.7	1.1	1.8	1.7	1.8	1.3	0.7	0.5	0.3	0.9
Water Loss due to evaporation (Thousands liters per month)	50	67	83	117	183	300	283	300	216	117	83	50	
Costs of Water Loss (\$)	80	107	133	187	293	480	453	480	346	187	133	80	
Costs of Water Loss Over Time (\$)	3,197	4,263	5,329	7,460	11,723	19,184	18,118	19,184	13,855	7,460	5,329	3,197	
Annual Costs of Water Loss (B) \$2,958 Costs of Water Loss Over Time (B/r) \$118,300 Annual Water Costs (A) \$319,730 Loss in % (B/A) 0.93													

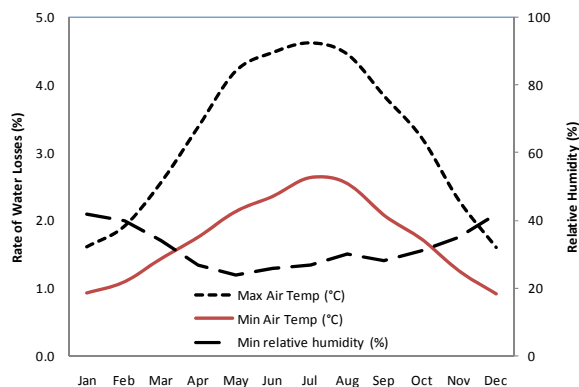


Figure 4: Total percentage of water losses during irrigation due to evaporation and drift at minimum relative humidity and Highest monthly mean Wind speed in the Emirate of Sharjah, UAE.

Table 8. Total percentage of water losses during irrigation due to evaporation and drift at minimum relative humidity in Riyadh Saudi Arabia.

	Monthly Mean												A v g
	Jan	Feb	Mar	Apr	Ma y	Jun	Jul	Au g	Sep	Oct	No v	De c	
Relative Humidity (%)	32	27	24	19	13	8	8	8	9	13	22	33	18
Monthly mean Wind speed (m/s)	3.6	4.0	4.0	4.5	4.5	5.8	4.9	4.9	4.5	3.1	3.1	3.6	4.2
I. Maximum temperature mean daily													
Dry Bulb Temp (°C)	28.0	30.0	35.0	38.0	42.0	44.0	45.0	45.0	43.0	38.0	33.0	28.0	37.4
Saturation vapor pressure of air (mbar)	37.8	42.5	56.3	66.4	82.2	91.3	96.2	96.2	86.7	66.4	50.4	37.8	67.5
Actual vapor pressure of air (mbar)	12.1	11.5	13.5	12.6	10.7	7.3	7.7	7.7	7.8	8.6	11.1	12.5	12.2
$(p_s - p_a)$ (kPa)	2.6	3.1	4.3	5.4	7.2	8.4	8.9	8.9	7.9	5.8	3.9	2.5	5.7
Evaporation loss (%)	1.4	1.8	2.2	2.8	3.4	4.9	4.3	4.3	3.7	2.3	1.8	1.4	2.9
Water Loss due to evaporation (Thousands liters per month)	233	300	366	466	566	816	716	716	616	383	300	233	
Costs of Water Loss (\$)	373	480	586	746	906	1,306	1,146	1,146	986	613	480	373	
Costs of Water Loss Over Time (\$)	14,921	19,184	23,447	29,841	36,236	52,223	45,828	45,828	39,433	24,513	19,184	14,921	
Annual Costs of Water Loss (B)							\$9,139						
Costs of Water Loss Over Time (B/r)							\$365,558						
Annual Water Costs (A)							\$319,730						
Loss in % (B/A)							2.86						
II. Minimum temperature mean daily													
Dry Bulb Temp (°C)	3.0	4.0	8.0	12.0	18.0	21.0	23.0	24.0	19.0	14.0	9.0	3.0	13.2
Saturation vapor pressure of air (mbar)	7.6	8.1	10.7	14.0	20.6	24.9	28.1	29.8	22.0	16.0	11.5	7.6	16.7
Actual vapor pressure of air	2.4	2.2	2.6	2.7	2.7	2.0	2.2	2.4	2.0	2.1	2.5	2.5	2.2

(mbar)													4
($p_s - p_a$) (kPa)	0.5	0.6	0.8	1.1	1.8	2.3	2.6	2.7	2.0	1.4	0.9	0.5	1.4
Evaporation loss (%)	0.5	0.6	0.7	1.0	1.3	2.0	1.8	1.9	1.4	0.9	0.6	0.5	1.1
Water Loss due to evaporation (Thousands liters per month)	83	100	117	167	216	333	300	316	233	150	100	83	
Costs of Water Loss (\$)	133	160	187	266	346	533	480	506	373	240	160	133	
Costs of Water Loss Over Time (\$)	5,3 29	6,3 95	7,4 60	10, 658	13, 855	21, 315	19,1 84	20, 250	14, 921	9,5 92	6,3 95	5,3 29	
Annual Costs of Water Loss (B)							\$3,5 17						
Costs of Water Loss Over Time (B/r)							\$140 ,681						
Annual Water Costs (A)							\$319 ,730						
Loss in % (B/A)							1.1						

Table 9: Cost of Water Loss due to Evaporation in Sharjah

	Cost of Water loss over time in %	Annual costs of Water Loss in value (\$)	Water Loss Costs Over Time in value (\$)
Evaporation and drift at maximum relative humidity and monthly mean wind speed. Maximum temperature mean daily Minimum temperature mean daily	0.59 % <u>0.33 %</u>	32,298 <u>18,196</u>	1,076,623 <u>606,548</u>
Evaporation and drift at maximum relative humidity and highest monthly mean wind speed. Maximum temperature mean daily Minimum temperature mean daily	1.05 % 0.58%	57,773 31,843	1,925,791 1,061,459
Evaporation and drift at minimum relative humidity and monthly mean Wind speed. Maximum temperature mean daily Minimum temperature mean daily	1.80% 0.98 %	98,715 53,679	3,290,524 1,789,317
Evaporation and drift at minimum relative humidity and highest monthly mean Wind speed. Maximum temperature mean daily Minimum temperature mean daily	<u>3.17%</u> 1.73%	<u>173,321</u> 94,621	<u>5,777,373</u> 3,154,051

Table 10: Cost of Water Loss due to Evaporation in Riyadh

	Annual Costs of Water Loss (B)	Annual Costs of Water Consumption	Annual loss in Value (%)	Costs of Water Loss Over Time (B/r)
Maximum relative humidity & maximum temperature daily	\$7,886	\$5,458,935	2.47	\$315,466
Maximum relative humidity & minimum temperature daily	\$2,957	\$5,458,935	0.93	\$118,300
Minimum relative humidity & maximum temperature daily	\$9,138	\$5,458,935	2.86	\$365,557
Minimum relative humidity & minimum temperature daily	\$3,517	\$5,458,935	1.10	\$140,681

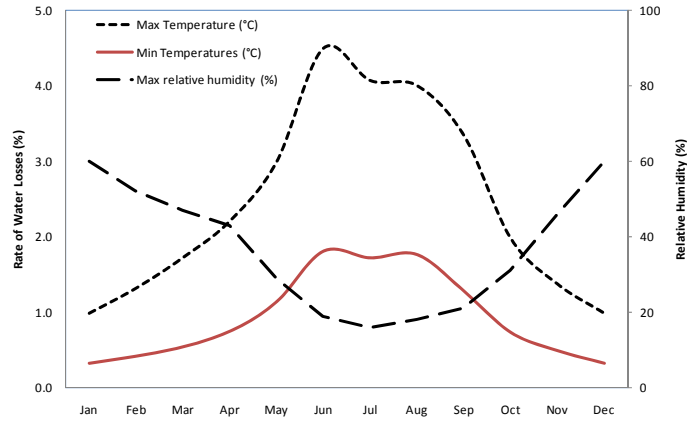


Figure 5: Total percentage of water losses during irrigation due to evaporation and drift at maximum relative humidity in Riyadh Saudi Arabia.

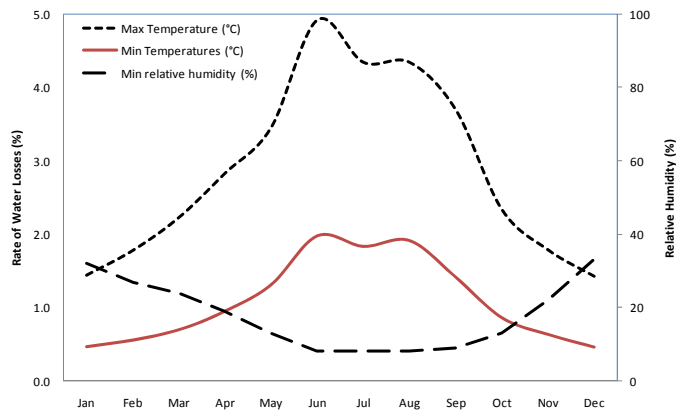


Figure 6: Total percentage of water losses during irrigation due to evaporation and drift at minimum relative humidity in Riyadh Saudi Arabia.

